Proceedings

The 19th IAHR International Symposium on Ice

"USING NEW TECHNOLOGY TO UNDERSTAND WATER-ICE INTERACTION"

July 6 to 11, 2008

VANCOUVER, CANADA

Edited by Martin Jasek
BC Hydro

VOLUME TWO

International Association of Hydraulic Engineering and Research
Ice Research & Engineering

Available from
BC Hydro, 6911 Southpoint Drive (E15)
Burnaby, BC, V3N 4X8, Canada
Attention: Martin Jasek
(martin.jasek@bchydro.com)

ISBN 978-0-9810446-0-6

Printed by St. Joseph Communications, Vancouver, British Columbia

Table of contents

Freeze-up Processes, Rivers and Oceans, River Ice-Structure Interaction

Special Session: Numerical Simulation in Ice Engineering

Ice Measurement

Grasse River Session I: Grasse River Ice Evaluation

Grasse River Session II: Evaluation of Structural Ice Control Alternatives

River Ice Break-up and Ice Jam Formation

Special Session: Remote Sensing

River Ice, Hydropower, and Dam Decommissioning

Mechanical Behaviour of River Ice, Ice Covered Flow, and Thermal Modeling

– Volume 2 –

Ice Friction, Sea Ice Mathematical and Computer Model Formulations

Ice and Navigation, Ice Bergs

Special Session: Ice Crushing Processes

Sea Ice-Shore/Structure Interaction

Ice Properties, Testing, and Physical Modeling

Special Session: Ice Actions on Compliant Structures

Special Session: Oil Spills in Ice

Bohai Sea Papers: Desalination, Ice Thickness, and Climate Change

Sea Ice Ridges

Preface

The International Symposium on Ice is sponsored by the International Association of Hydraulic Engineering and Research (IAHR). It has been a regular biennial forum since 1970 for scientists, engineers and researchers to exchange information on the many cross-disciplinary topics of ice engineering.

This is the 19th IAHR International Symposium on Ice and the general theme this year was "Using New Technology to understand Water-Ice Interaction". The new technology falls into three basic groups, which are: Measurements and Instrumentation, Remote Sensing, and Numerical Simulation. A large portion of the papers used some aspect of these three investigative strategies to solve problems and to give us a better understanding of water-ice interaction.

Special sessions were held on Oil Spills in Ice, Ice on Compliant Structures, Remote Sensing, Numerical Simulation and the Ice Crushing Process. A unique special session of 9 papers on ice process considerations for the remediation options to address PCB contamination in the river bed sediments of the Grasse River was also held. Climate change and environmental considerations were considered in papers throughout the sessions. Other topic areas were Freeze-up Processes in Rivers and Oceans, River Ice break-up and Ice Jam Formation, Ice Measurement Technologies, Ice Effects on Hydropower Generation, the Effect on the Ice Regime due to Dam Decommissioning, Sea Ice Ridging, Ice Properties, Testing and Physical Modelling, Ice – Shore and/or Structure Interaction, Icebergs, Ice and Navigation, and Ice Mechanics.

On behalf of the organizing committee I wish to thank the many people who traveled long distances and at considerable expense to contribute technically, as well as socially, to this event. I know that this event has been an experience that we will all treasure, and that the knowledge exchanged and friendships formed and solidified will help us solve ice problems in the future.

I would like to acknowledge the University of Alberta, the Canadian Hydraulics Centre and Alberta Environment for providing the backbone of support and experience to organize and run the symposium. The sponsors were also of great help to keep registration costs down and we are all indebted to them. Finally I would like to thank BC Hydro for providing staff and resources to organize this event; without this the Symposium would not have been possible.

Best Wishes

Martin Jasek, M.Sc., P.Eng.,
Chair of the Local Organizing Committee
19th IAHR International Symposium on Ice
Senior Engineer, British Columbia Hydro and Power Authority (BC Hydro)

July 2008

Acknowledgements

Principal Sponsor
International Association of Hydraulic Engineering and Research

Sponsors and In-kind Contributors

Alberta Environment
AMEC
ASL Environmental Sciences
BC Hydro
Canadian Society for Civil Engineering
Committee on River Ice Processes and the Environment
Hoskin Scientific
KGS Group
Manitoba Hydro
University of Alberta

Proceedings

Layout Editing
Robyn Andrishak and Asif Siddiqui, University of Alberta

Cover Design
Martin Jasek, BC Hydro

Cover Photos Volume One
Front Cover: Smoky River breaking up into the Peace River, Alberta, April, 2007
Back Cover: Frazil ice pans on the Peace River near Alces River, British Columbia, January 2005
by Martin Jasek, BC Hydro

Cover Photos Volume Two
Front Cover: Edge of the pack ice region in the Beaufort Sea in April, 2007
Back Cover: Ice pile-up in Beaufort Sea
by Garry Timco and used in his keynote lecture entitled "Why Does Ice Fail the Way it Does?" , Canadian Hydraulics Centre

Scientific Committee

- Anne Barker, Canadian Hydraulics Centre (Canada)
- Robert Gagnon, Institute for Ocean Technology, National Research Council of Canada (Canada)
- Faye Hicks, University of Alberta (Canada)
- Koh Izumiyama, National Maritime Research Ins (Japan)
- Martin Jasek, BC Hydro (Canada)
- Tuomo Kärnä, Norwegian University of Science and Technology & Karna Research and Consulting (Finland)
- Michael Lau, Institute for Ocean Technology, National Research Council of Canada (Canada)
- Dan Nixon, BC Hydro (Canada)
- Shigeki Sakai, Iwate University (Japan)
- Garry Timco, Canadian Hydraulics Centre (Canada)
- Andrew Tuthill, Cold Regions Research and Engineering Laboratory (USA)

IAHR Ice Committee

- Karl-Ulrich Evers (Chairman, Germany)
- John Dempsey (Secretary, USA)
- Steve Daly (USA)
- Robert Gagnon (Canada)
- Christian Haas (Germany)
- Faye Hicks (Canada)
- Tuomo Karna (Finland)
- Anund Kvambekk (Norway)
- Victoria Lytle (Australia)
- Igor Stepanov (Russian)
- Takahiro Takeuchi (Japan)
- Galina Tregub (Russian)
- Qianjin Yue (China)
- Hung Tao Shen (USA)
- Pat Langhorne (New Zealand)

Local Organising Committee

- Martin Jasek (BC Hydro, Canada)
- Faye Hicks, (University of Alberta, Canada)
- Garry Timco (Canadian Hydraulics Centre, Canada)
- Robyn Andrishak (University of Alberta, Canada)
- Dan Nixon, (BC Hydro, Canada)
- Julie Elliot (BC Hydro, Canada)
- Katherine Blaney (BC Hydro, Canada)
- Charlie Hare (BC Hydro, Canada)
- Irene Wong (BC Hydro, Canada)
- Cheryl Currie (BC Hydro, Canada)

Previous IAHR Ice Symposia

1970 Reykjavik, Iceland
1972 Leningrad, Russia
1974 Budapest, Hungary
1975 Hanover, USA
1978 Luleå, Sweden
1981 Quebec City, Canada
1984 Hamburg, Germany
1986 Iowa City, USA
1988 Sapporo, Japan
1990 Espoo, Finland
1992 Banff, Canada
1994 Trondheim, Norway
1996 Bejing, China
1998 Potsdam, USA
2000 Gdansk, Poland
2002 Dunedin, New Zealand
2004 St. Petersburg, Russia
2006 Sapporo, Japan

Keynote Papers

19th IAHR International Symposium on Ice
"Using New Technology to Understand Water-Ice Interaction"
Vancouver, British Columbia, Canada, July 6 to 11, 2008

Why Does Ice Fail the Way it Does?

Garry W. Timco
Canadian Hydraulics Centre
National Research Council of Canada
Ottawa, Ont., K1A 0R6 Canada

Abstract
Floating ice has been observed to fail in a variety of ways. Observations of ice show that it can deform in a plastic-like manner, break into small pieces, contain large cracks, and pile-up in large features that can contain a wide range of ice block sizes. In some cases, ice does not fail at all and it exists as large level ice floes. This raises the question: "Why does ice fail the way it does?". This paper explores the various failure modes of ice. The observations are related back to the mechanical properties of the ice and it shows that the unusual mechanical, rheological and fracture properties of ice can explain the observed failure behaviours.

Introduction

When the Organizing Committee invited me to present a keynote lecture at this 19th IAHR Symposium on Ice, I thought about many topics that I could address. However, one particularly leapt to mind. It is something that is important for both sea ice mechanics and river ice behaviour. That is, how and why does ice fail the way it does? This paper will explore this issue. I will do that by taking you on an overview of the ice in the Beaufort Sea. Although I am using this as an illustrative example, many of the aspects are paralleled for river ice. Let's begin our journey.

Nearshore Fast Ice

If you hop into a helicopter and head out over the Beaufort Sea in November, the first thing you see is long stretches of usually wind-swept level ice. Figure 1 is a good example of this. This level ice can extend for several kilometres. It is usually very flat and quite boring. This can be a good thing if you are trying to traverse over ice but not too instructive in terms of ice failure. Or is it? Why is this ice so flat? Let's come back to this question later.

Figure 1. Photograph showing the level wind-swept fast ice close to the shore.

Pockets of Thin Ice

If we fly further offshore, we start to see a lot of features that look like the one in Figure 2. You can see from the colour gradation that something is different here.

Figure 2. Photograph showing an area where there are different ice types with quite different ice thickness.

If you look closely at the bottom part of the photo, you will see a large crack that has separated the ice. The ice at this time of the year is about 0.3 to 0.4 m thick and yet it appears to crack quite easily. Why is this so? The fracture of the ice can be related back to the very low fracture toughness of ice. Several investigators have looked into this, including Urabe et al. (1980), Urabe and Yoshitake (1981a, 1981b), Timco and Frederking (1983), Shen and Lin (1986), Urabe and Inoue (1986), Tuhkuri (1987), DeFranco et al. (1991), DeFranco and Dempsey (1994) and Stehn (1994). The fracture toughness depends on the loading rate and the ice type, with less variation due to temperature and grain size. Typical values of the "opening mode" (i.e. mode-1) fracture toughness (K_{1c}) for small samples were measured in the range of 115 kPa-m$^{0.5}$. Dempsey (1989) has found that a proper experimental arrangement is essential to ensure that the value measured represents the true fracture toughness of ice. Many of these earlier studies did not do this, and so their reported K_{1c} values are not material properties for ice. Kennedy et al. (1994) and Dempsey et al. (1999) report on large-scale field programs to measure the fracture toughness of sea ice.

Dempsey and his colleagues have shown that for thick first-year sea ice, the size independent fracture toughness is on the order of 250 kPa-m$^{0.5}$. But what does this have to do with the large fractures that we see in Figure 2? Well, Dempsey has taken this a step further and has provided estimates for the large-scale tensile strength for sea ice. For the large fracture lengths shown in Figure 2, the tensile strength would have been roughly 0.02 MPa.

Let's look again at Figure 2. In this case, there is a fracture in the ice. The ice at the bottom of the photograph is landfast and typically does not move. What caused the fracture to occur? If there was an offshore wind blowing across the level landfast ice shown in Figure 1, it would induce a stress in the ice cover. We can estimate the shear stress (τ_a) from the wind using $\tau_a = c_d \ \rho_a \ v_a^2$ where c_d is the air drag coefficient, ρ_a is the density of air and v_a is the wind speed. If this wind blows across an ice sheet with a length "L" (i.e., from the shore to the edge of the ice), the tensile stress per unit width in the ice (σ_t) will be $\sigma_t = \tau_a \ L / h$ where h is the ice thickness. This equation shows that the maximum stress in the ice cover will be at the shore line because the wind is "pulling" the whole sheet away from the shore. But the ice doesn't break there – it breaks somewhere further out in the fast ice. Why is this so? I believe that there are several reasons. First, the shore ice is partly anchored by the local coastal topography. Second, there is usually a thickness gradient in the ice, with thicker ice being closer to shore. There are no hard evidence measurements on this for this time of the year but we will make this assumption. It is a reasonable one – the water close to shore is less saline, so it doesn't have the same low freezing point as ice further offshore in more saline water. And third, the currents are relatively slow in this region and ice thickens quickly. With these assumptions, let's look at how things tie together. We can determine the ice thickness that would fracture by re-arranging the above equations as follows:

$$h = c_d \ \rho_a \ v_a^2 \ (L - x) / \sigma_t \qquad [1]$$

where x is the distance offshore of the point where the fracture occurs. Let's assume that the drag coefficient is 0.0028 which is the drag coefficient used by ice-ocean modellers to forecast ice drift along the Canadian east coast (Prinsenberg and Peterson, 2002). If we use ρ_a = 1.3 kg-m^{-3}, a high storm wind speed of 15 m-s^{-1}, and a large-scale tensile strength of 0.02 MPa, and if we assume that the ice sheet extends a distance of 15 km and the fracture distance (x) occurred about 7 km offshore, the estimated ice thickness in this case (using Equation 1) is about 0.3 m! This calculated thickness value is very close to the thickness of the ice at this time of year.

Let's look at Figure 2 once again. We see that there are different colours of ice so we know that there is a wide variation in the ice thickness in this region. This is very important to the ice failure process. If the wind shifts and blows onshore (or in any direction other than the one which caused the ice to open), this region is a potential weak link. A sufficiently large compressive stress will close it and cause the ice there to fail. This failure could take place with a variety of failure modes.

Let's look at how this might happen.

Plate Rafting and Finger Rafting

If we continue our flight further offshore, we get into a completely different type of ice regime. Here, there are large floes moving around and bumping into each other. If the floes are still relatively thin (say, less than 0.5 m) the ice can raft. Typically there are two types of rafting. In one case, which we can call **Plate Rafting**, one ice sheet slides up over another one and as the ice floes converge, the ice sheets continue to slide over or under each other. From the air, and even if you're standing on the ice, this looks like level ice. But this can be very deceiving. Often ice that appears level may actually be rafted and this can significantly increase its thickness. The cold "top" will come in contact with the warmer bottom ice and if there is sufficient thermal reserve (as there is with growing cold ice), it doesn't take long for the ice pieces to freeze together. You can tell if there is rafting by taking a core and doing some thin sections or by estimating the expected ice thickness using an ice-growth equation to see how well they agree. From the air, it's not possible to identity this type of rafting. However we know that it will not occur after the ice is shore fast – it needs movement for this to happen.

The second type of rafting is called **Finger Rafting**. This is an interesting mode of failure. Figure 3 and Figure 4 show two examples. Figure 3 shows a recent finger rafting event since this ice was just outside the edge of the fast ice when the photograph was taken. On the other hand, the finger rafting shown in Figure 4 occurred a considerable time before the photograph was taken so we are seeing a remnant of this process. This rafting feature was well inside the fast ice at the time the photograph was taken so we know it did not occur recently.

Figure 3. Photograph showing recent large-scale finger rafting in the Beaufort Sea in November.

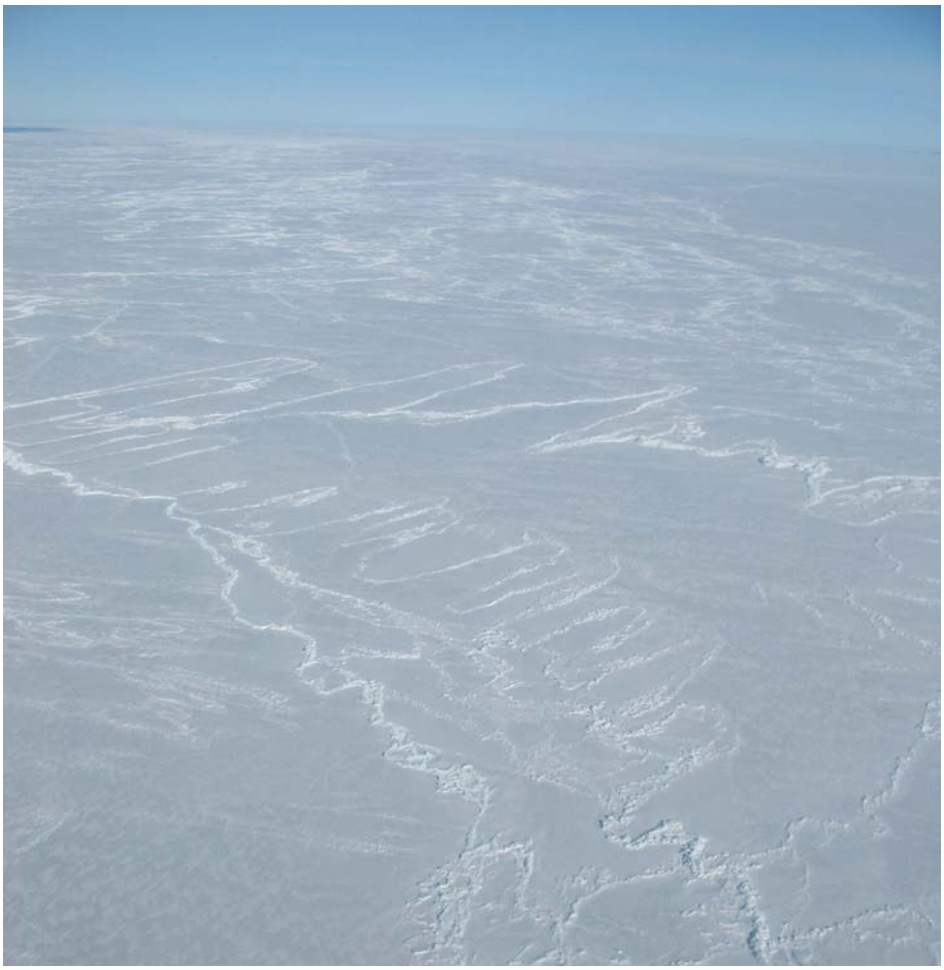

Figure 4. Photograph showing another example of large-scale finger rafting in the Beaufort Sea. This photograph shows the remnants of the rafting process because this ice is well within the shore fast ice region.

During finger rafting, the ice fails by "intertwining" itself with another ice sheet. The reason for the term "finger rafting" is quite obvious because ice appears like interlocked fingers. Once this rafting process starts, the energy in the ice sheets will be dissipated by crushing along the boundaries between the "fingers" and by the friction of one sheet sliding over another. The process can produce large fingers sometimes hundreds of meters long.

Rafting is an interesting phenomena but poorly understood. It is easy to see when it occurs in thin ice (say up to 0.5 m) but it may also occur in thicker ice. There is some anecdotal evidence to this effect but no hard evidence to support this. It can be very important for many situations both for sea ice and also river ice. For the latter, finger rafting generally does not occur because the ice is too brittle and does not "bend" as easily as thin sea ice. Tuhkuri et al. (1999) have done interesting tests to investigate this in the lab and in the field.

Out to the Edge

Let's keep on going and fly to the edge of the competent ice. On our way, we will see many examples of finger rafting and numerous patches of thin ice and very rough ice. But let's go to the ice edge now.

When we get there, we will see some open water and ice that is highly deformed and consists of what appear to be large flat ice floes with very rough edges (see Figure 5). In some cases, there will be a number of large isolated floes just off the edge of the ice boundary (see Figure 6). In some cases, we have to look closely to see if this is the edge of the fast ice, or whether this ice is actually pack ice. You can see the difference if you look closely – pack ice often shows regions of water or thin grey ice between the floes. In any event, this is a place to be very cautious if you plan to land the helicopter. A change in wind direction can send floes moving off to the north.

Figure 5. Photograph showing the edge of the pack ice region in the Beaufort Sea in April. The polar ice was pushed away from this ice edge by an offshore wind.

Figure 6. Photograph showing a large number of individual ice floes at the edge of the landfast ice edge. With a northerly wind, these floes can be pushed together to form a complex ice feature.

Ridging

Figure 5 is a powerful photograph – look at how rough some of the ice is. There are countless regions of rough ice. How did this happen? In this case, if there is an onshore wind, the wind pushes the ice floes together. We can get rafting and finger rafting as we discussed. We can also get ridging as the floes move together. If the floes come together with their broad sides hitting each other, a **Compression Ridge** will often form. These are often snake-like features (see Figure 7) or can be straight (Figure 8 – see also Barker et al, 2008a) that can go on for long distances (often kilometres). They are a more-or-less linear jumbled mess of ice blocks of various sizes. We will discuss the reason for the differences in size in the next section. If the floes slide past each other, a **Shear Ridge** will form. These ridges are also conglomerates of broken ice that are fairly localized in width (as opposed to rafting which can extend for large distances). Shear ridges are usually more linear (i.e., not as snake-like as a compression ridge) and they have very steep walls. We didn't see any during this trip over the ice. Shear ridges are not as common as compression ridges. Timco and Burden (1997) summarized the properties of sea ice ridges. In general, the ridges have a sail height to keel ratio that is just over four (so there is a lot more ice below the ice surface than we see above it). Several investigators have discussed the forces associated with ridge building (e.g., Sayed and Frederking, 1984, 1986; Hopkins, 1998) but we won't go into this here.

Ridges are an important feature in the Arctic. They affect shipping and over-ice transit and they are a factor in the design loads for offshore platforms. The list of references for ridges is far too extensive to treat here. Several years ago, Ken Croasdale, Brian Wright and I wrote a report on ridges and it has a lot of useful information (Timco et al., 2000). It is interesting to note that newly-formed ridges are a loose agglomeration of ice pieces. With time, they begin to freeze together and become more formidable ice objects. Multi-year ridges can occur too (although we didn't see here), that can be extremely thick (up to about 20 m) and very strong.

Figure 7. Photograph showing a compression ridge. Note that the ice is piled up in a quasi-linear fashion and it also meanders in a snake-like fashion. The ice is piled below the ice surface to a depth of over four times the height of the ice above the ice surface.

Figure 8. Photograph showing a section of a compression ridge.

Grounded Ice Features

Let's get closer to the ice surface and look at the types of failure and deformation that there is in the ice. It is striking. There are regions of very large ice features. Figure 9 shows an example. These broken ice piles have grounded on the sea bottom and stabilized there. In many cases in the Beaufort Sea, these **Grounded Ice Features** occur on the relic berm of past drilling sites (see Barker et al. 2008b). Let's take a closer look at them.

Grounded ice features are very distinctive. And they are very rough. They influence much of the failure processes in the Beaufort Sea. For example, Figure 10 shows two radial cracks propagating through an ice sheet that is interacting with a thick grounded ice floe. The cracks are long – they can run for several kilometres. It is interesting to observe these cracks. When I cross the ice, I always try to find the path of least resistance and look for low spots to traverse. Cracks don't seem to care about that. They generally run right through ice ridges and floating rubble fields with no apparent care for the roughness of the ice. Sometimes the ice fracture will bifurcate. There is no obvious reason why they do so. These large scale fractures can be important if they release the confinement of the ice sheet and allow it to move freely. If the ice is under large compression, they do little to relieve the stress.

Figure 9. Photograph showing a grounded rubble field. If you look closely, you will see the author (in red) and colleague Brian Wright traversing this feature.

Figure 10. Photograph showing two large radial fractures in the ice sheet as it pushes against a large grounded ice floe.

Now let's drop down to the ice and see what it looks like. Figure 11 and Figure 12 show some good examples. There are some striking things to note. First, the ice is very rough. You can get an idea of this from Figure 12, which shows a wildlife monitor in the middle of a rubble field. Second, is the haphazard arrangement of the ice blocks. There often does not appear to be any systematic account to explain how the ice blocks got that way. But it is clear that the ice was under considerable compression for the ice blocks to be pushed up this way. Third, the ice blocks have a large variation in sizes. Many of them are relatively small. As we saw in Figure 10, large-scale fracture can occur but in this case there is more to it. There has been a considerable amount of fracturing taking place. Why is this so?

Let's take a look at the process that might occur to make this formation. It is clear that there is considerable out-of-plane movement of the ice during this compression event. The ice blocks in the vicinity of the wildlife monitor in Figure 12 appear to be about 0.8 m or so in thickness. The lengths of the ice blocks are longer than this, about 3 to 4 meters in length and about the same dimensions in width. Why should this be so?

Let's look at an ice sheet that is pushed over top of an existing rubble pile. When that happens, the ice loses its buoyant support because it is no longer in the water (see Figure 13). In that case, we can treat it as if it were a beam that is uniformly loaded (by its own weight). Let's calculate the stress in this beam and compare it to the flexural strength of the ice.

Figure 11. Photograph showing a natural pile-up of ice. Note the wide range of ice block sizes, the general haphazard arrangement and the interesting "balancing" block in the top right section of the photograph.

Figure 12. Photograph showing the roughness of the ice and the wide range of block sizes.

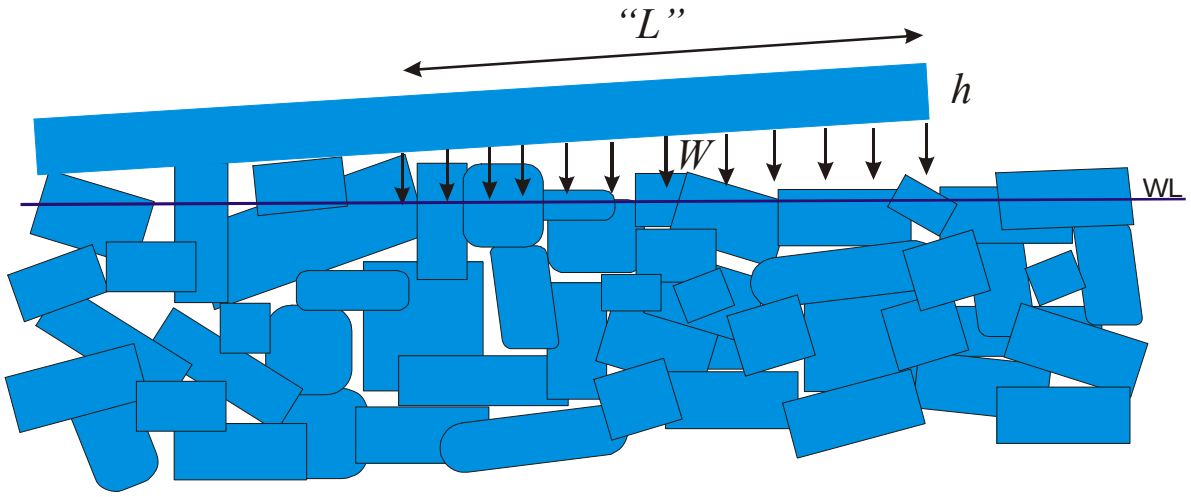

Figure 13. Schematic illustration of an ice sheet being pushed over a rubble field. In this case, the ice loses its buoyant support and it will break at a maximum length "*L*".

For a uniformly loaded beam, the strength is given by $\sigma_f = 6\,W\,L^2 / (b\,h^2)$ where W is the distributive load per unit length, L is the beam length, b is the beam width and h is the ice thickness. In this case, the load per unit length would result from the weight of the ice block so it is $W = \rho_i\ b\ h\ g$ where ρ_i is the density of sea ice (taken as 900 kg-m^{-3} – see Timco and Frederking, 1996), b is the width of the beam, h is the ice thickness, and g = 9.8 m-s^{-2}. We can re-arrange this equation to solve for the maximum length of the ice piece that could exist without the buoyant support of the water. That is given by:

[2] $$L = [\sigma_f\ h / (3\ \rho_i\ g)]^{0.5}$$

Figure 14 shows the calculated length as a function of the ice thickness for various flexural strengths of the ice. Note that it is independent of the width of the ice blocks. Timco and O'Brien (1994) have developed an equation that relates the flexural strength (σ_f) of sea ice to its brine volume (υ_b) as $\sigma_f = 1.76\,e^{-5.88\sqrt{\upsilon_b}}$. We can use this to estimate the flexural strength and using Equation 2, see what this length could be for cold sea ice. Let's assume that the salinity of the ice during the growth phase was about 5 parts per thousand, and that the average ice temperature was -12 °C (this would correspond to an air temperature of about -25°C or so). This would give a flexural strength of about 700 kPa. Let's look again at Figure 12. Here we see a large ice block behind the wildlife monitor which is about 0.8 m thick. So we can estimate that for an ice block of this thickness, the maximum unsupported length before fracture is about 4.5 m. This is not a bad estimate of the block size we actually see. Thus, this simple calculation of the maximum block size in a rubble field appears to provide some explanation for the maximum size of the ice blocks.

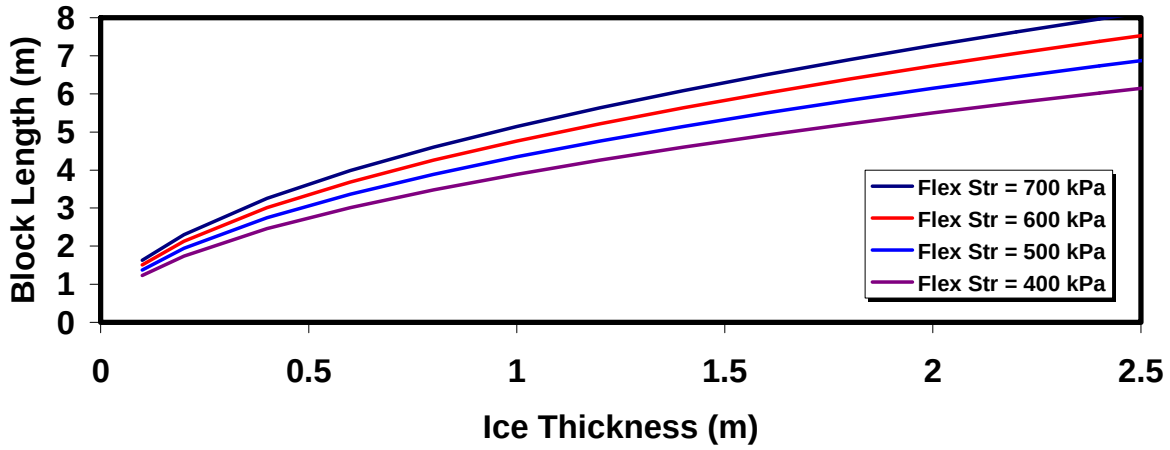

Figure 14. Maximum block length as a function of ice thickness and flexural strength for the simple model developed in Figure 13.

There's more to a rubble field than this. Standing in the middle of a rubble field is quite an awe-inspiring experience. You cannot help but be overwhelmed by the forces required to create it. We discussed the maximum block size above, but in fact you don't see too many large blocks. Many of them have broken into much smaller pieces (see Figure 15). We also see this phenomenon occurring in ridges. This occurs when the ice feature takes shape dynamically. There is always a considerable amount of secondary breakage due to the jumbling of the ice when the ice starts to pile up. You can see this from virtually every photograph of a rubble pile or ridge. You can also see differences in the thickness of the ice blocks in the rubble piles. This is a reflection of the distribution of the ice thickness in the parent ice sheets that formed the rubble pile (Figure 2).

Have a look at Figure 16. It shows a large grounded rubble field with virtually everything we have discussed so far. You can see the large fracture in the ice at the front of the rubble field. Notice also that there are many large blocks, none of which appears to be longer than that proposed in Figure 14. It is easy to imagine that these formed when the ice sheet was pushed over the rubble pile. Also, take a look at the range of sizes of the ice pieces in the rubble field. There is a wide range of block lengths and widths, as well as thickness. Clearly this was a very dynamic pile-up event. There have been some theories on the forces associated with these features (see e.g. Sodhi and Kovacs, 1984). Timco and Barker (2002) have shown that natural pile-up heights can range up 14 m above the waterline. Total pile-up heights from the seabed (i.e. including the ice below the waterline) are then significantly higher than this - up to about 30 m.

Figure 15. Photograph showing a large pile-up of highly broken ice. Note the crack in the ice in foreground. This ice sheet is "bowed" when it rode up over the ice rubble in a Plate Rafting process. This ice block was more than 0.5 m thick suggesting that this type of plate rafting can take place even with thick ice floes.

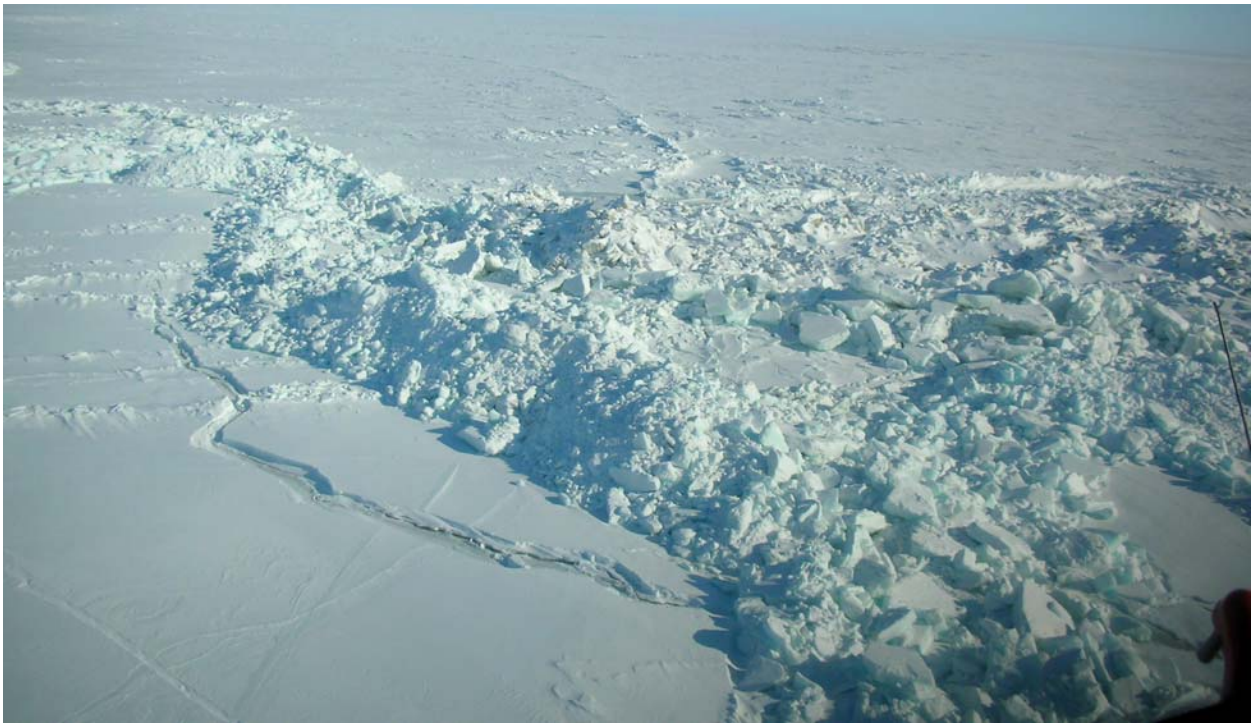

Figure 16. Photograph of a grounded rubble field. Note the large fracture in the foreground, the large blocks in the rubble field, and the wide range of sizes of jumbled ice pieces.

Evidence of remnant forces is everywhere. Figure 17 shows a photograph of Anne Barker standing on top of a large block of ice. But look at the wall behind her. It is about 10 m high above the waterline and well grounded on the seabed. It is a shear vertical cliff. How did this feature form? It appears that the region where Anne is standing was once part of this large grounded rubble pile. However it appeared to be "sheared off" during a storm event. The ice block on which Anne is standing is quite thick and formed late in the winter. This wall was a few hundred meters long. Obviously it took very high forces to create, both in terms of piling the ice to this height and then shearing off the parts that were not well grounded.

Figure 17. Anne Barker standing beside a vertical wall of ice. The total height of the ice feature was more than 10 m above the waterline.

I hope that these few photos and this description give you a sense of these ice features. They dot the landscape in the Beaufort Sea, and although most are formed on relics of previous berms or artificial islands, there are also regions of ice grounded directly on the seabed. They are important. They tend to "anchor" the ice and help establish the boundaries for fast ice. Satellite imagery shows that they often extend the edge of the landfast ice further offshore (Barker et al., 2008b).

Fast Ice Revisited

As you can see from the photographs here, ice fails if floes break apart and ride over one another when they collide. There can be very large forces driving the ice to these failures. But now let's go back and look at the first ice we saw – the level, shore-fast ice. Why is this ice level near the shore? It appears that it is held by the local morphology of the coastline which prevents large movements. But we need these large movements to generate the necessary conditions for the

types of ice failures that we have discussed. Once the fast ice starts to form along the coast, it grows *in situ* and thickens throughout the winter season. After it is firmly anchored, all of the "action" occurs at its edge. We have seen that grounded rubble fields will also help to anchor the fast ice. As the ice edge moves outward, these grounded ice features will help to stabilize the ice sheet. Also, we see from the wind drag on the ice sheet (Equation 1), as ice thickens, more ice fetch is required to create the stress necessary to fracture it. This also contributes to the outward growth of the edges of the land-fast ice.

So far we have looked at a number of ice failure features. These can be explained from the known mechanical and fracture properties of sea ice. But sometimes you see something that is outside the ordinary. Let's look at those now.

Plastic Ice Sculptures

Take a look at Figure 18. This is very different from what we have seen so far. Look closely and you will see that the ice has deformed in a plastic-like manner – see the curvature of the ice blocks. What's going on here?

Figure 18. Plastic-like ice sculptures

This feature was observed at the southern edge of a large grounded rubble field. It was photographed in April when the air (and ice) were starting to warm up after a cold winter. This ice is buckling due to the thermal expansion of the ice cover. This is fast ice that is pushing against the shore and against this feature. I don't know what is happening at the shoreline but it is clear that this ice is failing in a very interesting fashion against the grounded rubble field.

When we were at this site, air bubbles were rising through the water in front of this feature. The water is not snow melt (it was very salty). It resulted from the slow out-of-plane buckling of this thinner ice. Why does this happen? Let's take a quick look at ice rheology to see if we can explain it.

If a load is suddenly placed on ice, the ice immediately deforms elastically. However, depending upon the level of the load and the duration of its application, the behaviour of ice may be influenced by several different strain components. Sinha (1978, 1979, 1989) discussed the rheology of ice and he describes four deformation mechanisms which are important for polycrystalline ice:

1. elastic deformation from the atomic bonds changing length
2. delayed elasticity from sliding at the grain boundaries
3. viscous deformation from the movement of dislocations within grains
4. deformation from the microcracks in the ice.

The total strain in the ice is usually considered as the resultant sum of these separate strain components; i.e.

[3] $$\varepsilon_{ij}^{T} = \varepsilon_{ij}^{e} + \varepsilon_{ij}^{d} + \varepsilon_{ij}^{v} + \varepsilon_{ij}^{c}$$

where the superscripts refer to the total strain (*T*), the elastic strain (*e*), the delayed elastic strain (*d*), the viscous strain (*v*) and the strain due to cracking (*c*). Because ice is an anisotropic material, the strain tensor (*i j*) is used. The first term, which represents the elastic behaviour, and the second term, which represents the delayed elastic response, are of particular importance for situations where relatively small strains are important. The concept of delayed elasticity is interesting since this strain is not permanent. It is fully recoverable after removal of the load. But it is not instantaneous. This delayed elastic creep is sometimes referred to as **primary creep** or recoverable creep. The third term in Equation 3 represents the viscous creep (or **secondary creep**) of the ice. It is permanent, non-recoverable deformation. It becomes apparent when the delayed-elastic strain rate approaches zero. When this occurs, the viscous strain-rate begins to dominate with a rate dependence of the form $\dot{\varepsilon}_v(t) = B\sigma^n$ where *B* is parameter dependent primarily on temperature and ice type. The value of the exponent *n* is normally taken to be 3 (Glen's law). After a long time under compressive loading, the strain rate increases and **tertiary creep** begins. When that happens, microcracks begin to form at grain boundaries. These microcracks, in sufficient numbers, begin to coalesce and cause accelerating deformation rates. This is the fourth term in this equation.

So how does this help explain what we see in Figure 18? Although there have been some studies of the creep of sea ice (Sinha et al. 1992), we still don't know the rheological expression for sea ice so we look again at the one that Sinha (1978, 1979, 1989) developed for freshwater ice. The axial strain (ε_1) for isotropic ice at time *t*, in pure randomly-oriented polycrystalline ice of grain size *d*, subjected to a uni-axial stress σ_1 at a temperature *T* was given by Sinha as:

[4] $$\varepsilon_1 = \left(\frac{\sigma_1}{E}\right) + c_1\left(\frac{d_1}{d}\right)\left(\frac{\sigma_1}{E}\right)^s \left[1 - \exp\text{-}\left(a_T t\right)^b\right] + \dot{\varepsilon}_{vo} t \left(\frac{\sigma_1}{\sigma_o}\right)^n$$

where E is Young's modulus, $\dot{\varepsilon}_{vo}$ is the viscous strain rate for a reference stress σ_o, c_1 is a constant corresponding to the reference grain size d_1, a_T is the inverse relaxation time, and b, s and n are constants. He determined that for ice, $s = 1$ and $b = 1/n$, and $n = 3$ because of intergranular dislocation mechanisms, and provided the following values for pure ice at a temperature of 263 K: $E = 9.5$ GN-m^{-2}; $c_1 = 9 \times 10^{-3}$; $a_T = 2.5 \times 10^{-4}$ s^{-1}; $\dot{\varepsilon}_{vo} = 1.8 \times 10^{-7}$ s^{-1} and $n = 3$. These values represent a system with the grain size d in meters with $d_1 = 1$ m, stress in MPa with $\sigma_o = 1$ MPa, and time t in seconds. The first three terms of this equation correspond to the first three terms in Equation 3 and represent the elastic (term 1), primary creep (term 2), and secondary creep (third term) respectively. The form of the equation for tertiary creep is not well understood although there have been many studies to investigate the role of microcracking in the overall ice behaviour (see e.g. Gold 1960; Sinha 1988, 1989; Jordaan et al. 1992; Schulson 2001).

If we differentiate Equation 4 with respect to time, we see that the delayed elastic strain rate is directly proportional to stress, whereas the viscous creep rate is proportional to the third power of stress (Sinha 1978). This means that the former will decrease more rapidly with time than the later, given increasing stress. In our case, the loading takes place over a long time frame (days) and it occurs at a low rate. When we were looking at the ice feature in Figure 18, we could not observe the ice movement but it was clear that the ice was very slowly deforming and buckling. Thus, the secondary or viscous creep is the important one here. In short, the ice has time to slowly deform and it does this in a plastic-like manner. Sanderson (1984) dealt with this situation in his analysis of the thermal ice forces against an isolated structure. He has shown that the typical strain rates in this case are on the order of 10^{-8} s^{-1}. Very slow indeed!

You don't see many of these types of features because ice loading is usually much more rapid than this and the ice fails in a brittle manner. But there have been recorded observations of these types of failures (creep buckling) at offshore structures (Sudom and Timco, 2008).

Final Comments

I hope that our journey out across the Beaufort Sea has helped reveal the types of ice features encountered there. Our straightforward analysis of these features in terms of the mechanical, fracture, and rheological properties illustrates that they can be reasonably explained. Ice failure is an interesting phenomenon. Ice is a unique material. As we saw, it can readily fracture but it can exhibit plastic–like behaviour as well. This makes every trip onto ice an exciting adventure.

Acknowledgements

All photographs in this paper were taken by the author, Anne Barker or Brian Wright during three field trips to the Canadian Beaufort Sea in November 2005, March 2006, and April 2007. Funding for this research was supplied by the Program of Energy Research and Development (PERD) and the author would like to thank them for their continued support.

References

Barker, A., Timco, G.W. and Wright, B.D. 2008b. Surveying a Four-Week Old First-Year Ridge. Proc 19th IAHR Symposium on Ice, (this volume), Vancouver, B.C., Canada.

Barker, A., De Abreu, R. and Timco, G.W. 2008b. Satellite Detection and Monitoring of Sea Ice Rubble Fields. Proc 19th IAHR Symposium on Ice, (this volume), Vancouver, B.C., Canada.

DeFranco, S.J., Wei, Y. and Dempsey, J.P. 1991. Notch Acuity Effects on Fracture Toughness of Saline Ice. Annals of Glaciology 15, pp 230–235.

DeFranco, S.J. and Dempsey, J.P. 1994. Crack Propagation and Fracture Resistance in Saline Ice. Journal of Glaciology 40, pp 451–462.

Dempsey, J.P. 1989. The Fracture Toughness of Ice. Proc. IUTAM/IAHR Symposium on Ice/Structure Interaction, pp 109-145, St. John's, Nfld., Canada.

Dempsey, J.P., Adamson, R.M. and Mulmule, S.V. 1999. Scale Effects on the *in situ* Tensile Strength and Fracture of Ice. Part II: First-year Sea Ice at Resolute, NWT. Intentional Journal of Fracture 95, pp 347-366.

Gold, L.W. 1960. The Cracking Activity in Ice during Creep. Can. Jour. Physics Vol 38, No. 9, pp 1137-1148.

Hopkins, M.A. 1998. On the Four Stages of Pressure Ridging. Journal Geophysical Research 103, C10, pp 21883-21891.

Jordaan, I.J., Stone, B.M., McKenna, R.F. and Fuglem, M. 1992. Effect of Microcracking on the Deformation of Ice. Can. Geotech. Journ. 29, pp 143-150.

Kennedy, K.P., Mamer, K.J., Dempsey, J.P., Adamson, R.M., Spencer, P.A. and Masterson, D.M. 1994. Large Scale Ice Fracture Experiments: Phase 2. Proc. 12th IAHR Ice Symposium, Vol. 1, pp 315–324, Trondheim, Norway.

Prinsenberg, S. and I.K. Peterson, 2002. Variations in Air-Ice Drag Coefficient due to Ice Surface Roughness. Int. Jour of Offshore and Polar Engineering Vol. 12, No. 2, pp 1- 5.

Sanderson, T.J.O. 1984. Thermal Ice Forces against Isolated Structures. Proc. IAHR Symposium on Ice, Vol. IV, pp 289-299, Hamburg, Germany.

Sayed, M. and Frederking, R.M.W. 1984. Stresses in First-year Ice Pressure Ridges. Proc. 2nd OMAE Symposium, Vol III, pp 173-177, New Orleans, USA.

Sayed, M. and Frederking, R.M.W. 1986. On Modelling of Ice Ridge Formation. Proc IAHR Symp on Ice, Vol 1, pp 603-614, Iowa City, Iowa, USA.

Schulson, E.M. 2001. Brittle Failure of Ice. Eng. Fracture Mechanics 68, pp 1839-1887.

Shen, W. and Lin, S.Z. 1986. Fracture Toughness of Bohai Bay Sea Ice. Proc. 5th OMAE Symposium, Vol. IV, pp 354–357, Tokyo, Japan.

Sinha, N.K. 1978. Rheology of Columnar-Grained Ice. Experimental Mechanics 18, No. 12, pp 464-470.

Sinha, N.K. 1979. Grain-Boundary Sliding in Polycrystalline Materials. Phil. Mag A, 40 (6), pp 825-842.

Sinha, N.K. 1988. Crack-Enhanced Creep in Polycrystalline Material: Strain-Rate Sensitive Strength and Deformation of Ice. Jour. Material Science 23, pp 4415-4428.

Sinha, N.K. 1989. Microcrack-Enhanced Creep in Polycrystalline Material at Elevated Temperatures. Acta Metall. 37, pp 3107-3118.

Sinha, N.K., Zhan, C. and Evgin, E. 1992. Creep of Sea Ice. Proc. 11th OMAE Conference, Vol. 4, pp 261-266, Calgary, AB, Canada.

Sodhi, D.S. and Kovacs, A. 1984. Forces Associated with Ice Pile-up and Ride-up. Proc. IAHR Symposium on Ice, Vol. IV, pp 239-262, Hamburg, Germany.

Stehn, L. 1994. Fracture Toughness and Crack-Growth of Brackish Ice using Chevron-notched Specimens. Journal of Glaciology 40, pp 415–426.

Sudom, D. and Timco, G.W. 2008. Analysis of Loads on the SDC at Paktoa C-60 during an Ice Creep Buckling Event. Proc. 19th IAHR Symposium on Ice, (this volume), Vancouver, B.C., Canada.

Timco, G.W. and Barker, A. 2002. What is the Maximum Pile-Up Height for Ice? Proc. 16th IAHR Symposium on Ice, pp 69-77, Dunedin, New Zealand

Timco, G.W. and Burden, R.P. 1997. An Analysis of the Shapes of Sea Ice Ridges. Cold Regions Science and Technology 25, pp 65-77.

Timco, G.W., Croasdale, K. and Wright B. 2000. An Overview of First-Year Sea Ice Ridges. NRC-CHC Technical Report HYD-TR-047, PERD/CHC Report 5-112, Ottawa, On, Canada.

Timco, G.W. and Frederking, R.M.W. 1983. Flexural Strength and Fracture Toughness of Sea Ice. Cold Regions Science and Technology 8, pp 35–41.

Timco, G.W. and Frederking, R.M.W. 1996. A Review of Sea Ice Density. Cold Regions Science and Technology 24, pp 1-6.

Timco, G.W. and O'Brien, S. 1994. Flexural Strength Equation for Sea Ice. Cold Regions Science and Technology 22, pp 285-298.

Tuhkuri, J. 1987. The Applicability of LEFM and the Fracture Toughness of Sea Ice. Proc. 9th International POAC Conference, Vol. I, pp 21–32. Fairbanks, Alaska, USA.

Tuhkuri, J., Lensu, M and S. Saarinen, 1999. Laboratory and Field Studies on the Mechanics of Ice Ridge Formation. Proc. POAC'99, Vol. 3, pp 1118-1129, Helsinki, Finland.

Urabe, N. and Inoue, M. 1986. Mechanical Properties of Antarctic Sea Ice. Proc. 5th OMAE Symposium Vol. IV, pp 303–309, Tokyo, Japan.

Urabe, N., Iwasaki, T. and Yoshitake, A. 1980. Fracture Toughness of Sea Ice. Cold Regions Science and Technology 3, pp 29–37.

Urabe, N. and Yoshitake, A. 1981a. Strain Rate Dependent Fracture Toughness K_{1C} of Pure Ice and Sea Ice. Proc 6th IAHR Ice Symposium, Vol. II, pp 551–563, Quebec City, PQ, Canada.

Urabe, N. and Yoshitake, A. 1981b. Fracture Toughness of Sea Ice – *in situ* Measurement and its Application. Proc 6th POAC Conference, Vol. I, pp 356–365, Quebec City, PQ, Canada.

19th IAHR International Symposium on Ice
"Using New Technology to Understand Water-Ice Interaction"
Vancouver, British Columbia, Canada, July 6 to 11, 2008

Interactions between ocean, ice shelf, and sea ice

Pat Langhorne[1]
Department of Physics,
University of Otago, Dunedin,
New Zealand
pjl@physics.otago.ac.nz

The presence of ice shelves around 44% of the coastline of Antarctica means that the coastal sea ice in this region is influenced by processes that take place at the base of ice shelves. In particular, theoretical studies estimate that basal meltwater may contribute as much as 0.2 m to the sea ice thickness over significant portions of the sea ice cover. Thus the sea ice in the vicinity of an ice shelf forms due to heat transfer to two heat sinks: the atmosphere and the ocean. The reason the ocean can act as a heat sink is that it, in turn, has interacted with an ice shelf. Over the past decade we have conducted a number of experiments that examine the contribution that platelet ice makes to the landfast sea ice of McMurdo Sound, Antarctica. Our winter measurements have conclusively linked the presence of loose platelet ice in the water column with its incorporation into the sea ice cover. To explain the appearance of ice crystals in the water column we examine the oceanographic changes as autumn progresses into winter. From mid winter a layer develops at the ice-water interface that eventually becomes 10s of meters thick and is 10s of mK below its *in situ* freezing point. We estimate the contribution to the sea ice cover by heat rejection to an oceanic sink and find that it is significant and of the order of magnitude predicted by models. While progress towards understanding and quantifying the contribution of ice shelves to the ocean and sea ice has been made, there are still many mysteries.

[1] The work described in this paper is that of Greg Leonard, Craig Purdie, Inga Smith, and David Dempsey (University of Otago, Dunedin New Zealand) , Mike Williams, Craig Stevens, Natalie Robinson (National Institute of Water and Atmospheric Research, Wellington, New Zealand), and Tim Haskell (Industrial Research Ltd, Lower Hutt, New Zealand), as well as the author.

Sea ice in Antarctica

The extent of the sea ice cover around Antarctica varies annually from 4 to 18 million km^2 (Zwally et al, 2002), with the rapid, spring decrease being a result of ice breakup due to the onslaught of the swell of the Southern Ocean. The percentage of multiyear ice in the Southern Ocean is therefore very small. Sea ice thickness observations, representative of the last 2 decades and corrected by a model estimate of the sampling bias, show that the ice of the marginal ice zone of Antarctica is, on average, 0.5 to 1 m thick (Timmerman et al, 2004). Sea ice near the continent is thicker. If we focus attention on the coast, we immediately note a significant difference between the coastal sea ice of the Antarctic when compared to that of the Arctic.

Figure 1 demonstrates that the sea ice abuts ice shelf along 44% of the coastline of Antarctica (Drewry et al, 1982), with ~30% of this ice shelf having a draft of over 200 m (Weeks and Mellor, 1978). The presence of these deep ice shelf cavities influences the thickness of the sea ice in the vicinity. Modelling studies by Timmermann et al (2002) and Hellmer (2004) have explored the difference in the sea ice thickness distribution between configurations modelled without interaction with ice-shelf cavities in relation to those with ice-shelf cavities. These models predict that over extensive areas of the Southern Ocean sea ice is up to 0.2 m thicker because of the presence of the ice shelf cavity.

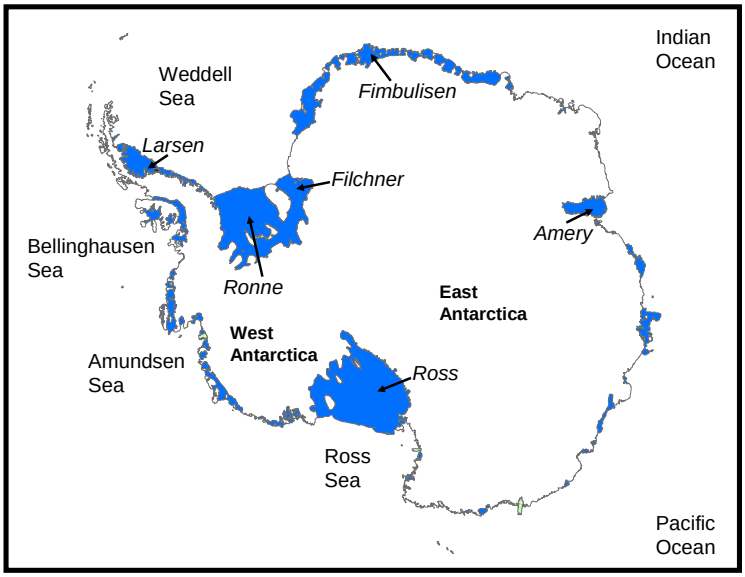

Figure 1: Map of Antarctica with ice shelves highlighted in blue. Only major ice shelves have been labelled.

The ice pump

What is the mechanism that causes the cavity beneath an ice shelf to contribute to sea ice thickness? The contribution arises because melting at the base of the ice shelf produces a flux of relatively fresh, cold water, causing the sea ice cover to be thicker (Hellmer, 2004). Further the freshwater flux stabilizes the water column, reducing deep convection and heat transfer to the surface (Hellmer, 2004). This redistribution of ice mass occurs through a mechanism, sometimes called an ice pump (Lewis and Perkin, 1986). The essential physics lies in the fact that the freezing point of sea water decreases as pressure/depth increases and as salinity increases (Foldvik & Kvinge,1974). The freezing of sea water in the early winter produces saline water that is close to, or at, its surface freezing point. Consider what happens if such a water parcel is moved isothermally downwards through the water column: figure 2 illustrates a hypothetical

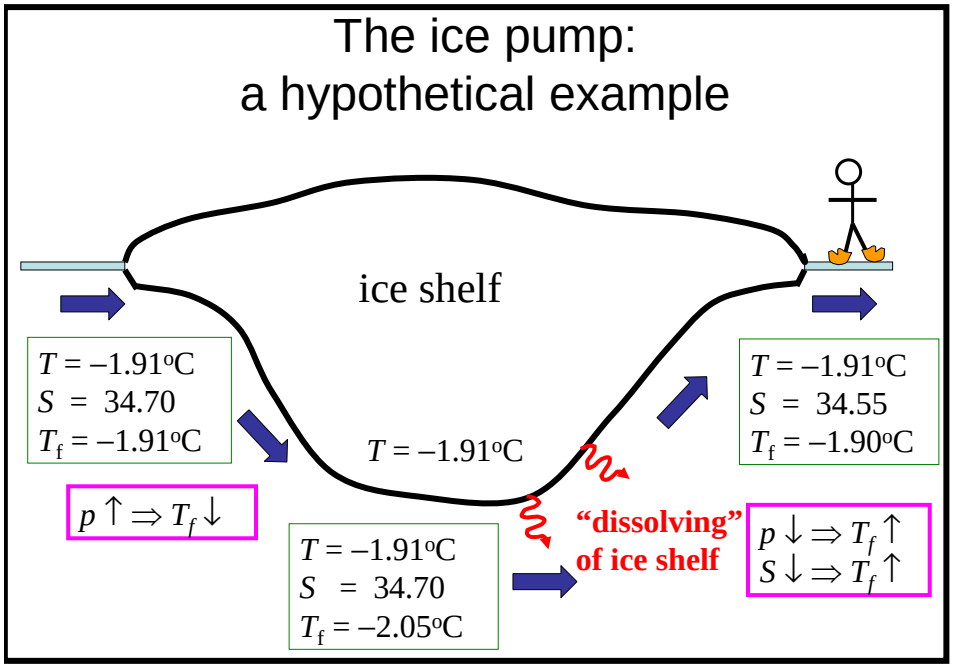

Figure 2: A hypothetical example of the production of supercooled water by interaction with an ice shelf at depth, where T = water temperature, S = salinity, T_f = freezing temperature and p = pressure. Water on the left is at its freezing point: $T = T_f$. It descends isothermally beneath the ice shelf and T_f decreases. Salinity decreases because of dissolving of ice shelf in an attempt to maintain phase equilibrium. As water rises (to right) T_f rises and $T < T_f$.

example. At depth the freezing point is depressed and the water parcel will find itself in an environment where the freezing point is below the actual temperature of the parcel. If it comes into contact with an ice shelf, the fluid of the parcel will therefore be above its freezing point causing the ice of the shelf to dissolve in an attempt to return the fluid to the liquidus. Thus the salinity decreases, raising the freezing point of our parcel. If the water parcel now rises towards the surface, the freezing point rises further because of the release of pressure. Once it reaches the surface the water parcel will be at a temperature below its freezing point: i.e. it is supercooled. These processes are described in detail in Robin (1979) and Jacobs et al (1979; 1992). Crystals of ice may then nucleate in the water to relieve this supercooling.

Models pioneered by Jenkins and colleagues (Jenkins, 1991; Hellmer and Jacobs, 1992; Jenkins and Bombosch, 1995; Bombosch and Jenkins, 1995; Smedsrud and Jenkins, 2004) are more realistic than this simplified picture conveyed in figure 2. These models describe a 2-D, turbulent plume driven by buoyancy to rise up along the upward-sloping base of an ice shelf. The models include the entrainment of warm water from depth, nucleation and precipitation of ice crystals in the plume, secondary nucleation of ice crystals, and freezing and melting at the base of the ice-water interface, with much of the physics informed by advances in the understanding of river ice (for example, Daly, 1984; Hammar and Shen, 1995). Complexities in 3D have been considered, including topography (Williams et al, 1998) and the Earth's rotation (Holland and Feltham, 2006).

Figure 3 (a): Platelet ice attached to a rope from a depth of 10 m in the water column. Photo: Greg Leonard.

Figure 3(b): Platelet ice can be very loosely attached and in large volumes. Photo: Greg Leonard.

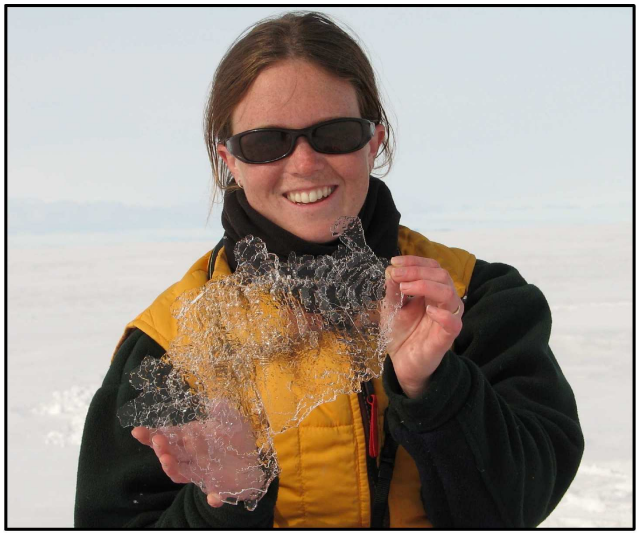

Figure 3(c): Individual platelets, found at the ice-water interface, may be very large. Photo: Brett Grant.

Frazil, marine and platelet ice

At this point we need to introduce some terminology. Ice found as tiny crystals drifting in the oceanic water column at depths from the surface to 250 m (Littlepage, 1965; Dieckmann et al, 1986; Penrose et al, 1994) is usually called *frazil ice*. When these crystals accumulate and consolidate onto the base of an ice shelf (Souchez at al, 1995) it is called *marine ice*. For example, basal melting and freezing rates for the Filchner-Ronne ice shelf have been simulated using a model of the type described above (Holland et al, 2006) and compared to marine ice thicknesses of the region measured by Sandhäger et al (2004). Of course the frazil-laden plume may extend beyond the edge of an ice shelf, depositing its burden beneath the sea ice. This ice is called *platelet ice* (see Figure 3 for examples). Although their origins are believed to be identical, there is a significant difference between marine ice and platelet ice: while marine ice forms in conditions where there is negligible heat flux to the atmosphere, platelet ice forming beneath sea ice does so in an environment where atmospheric heat flux is the dominant term in the heat budget. It is the formation of platelet ice that has been the focus of our attention for the past decade.

Platelet ice in McMurdo Sound, Antarctica

Let us explore the structure of coastal sea ice close to an ice shelf. Platelet ice has been observed at numerous locations around Antarctica, including the Ross Sea (Tison et al, 1998) and the Weddell Sea (Günther and Dieckmann, 1999). However we will focus on McMurdo Sound not only because it is our field site close to the New Zealand and US Bases, but also because the earliest discovery of platelet ice was made there by scientists of the British Antarctic Expedition 1910-1913 (Wright and Priestley, 1922). In the Sound it is common, as illustrated in the example of Figure 4, to find that the predominant ice type of early winter is columnar ice, with platelet ice appearing frozen into the sea ice cover in mid to late winter (Paige, 1966; Jeffries et al, 1993; Gow et al, 1998; Smith et al, 2001; Jones and Hill, 2001; Leonard et al, 2006), Concurrently layers of loose crystals appear at the base of the sea ice cover (Dayton et al, 1969; Crocker and Wadhams, 1989). We will use the term platelet ice to mean both these loose accumulations of ice that are trapped by buoyancy at the ice-water interface, or that attach themselves to mooring lines suspended in the water column (see Figure 3(a) and (b)), as well as crystals that have been frozen into the sea ice cover; so-called *incorporated platelet ice*. Figure 3 (c) shows that individual platelet ice crystals at the ice-water interface can become really very large. A typical ice structure through the late spring sea ice cover of McMurdo Sound in shown in Figure 4.

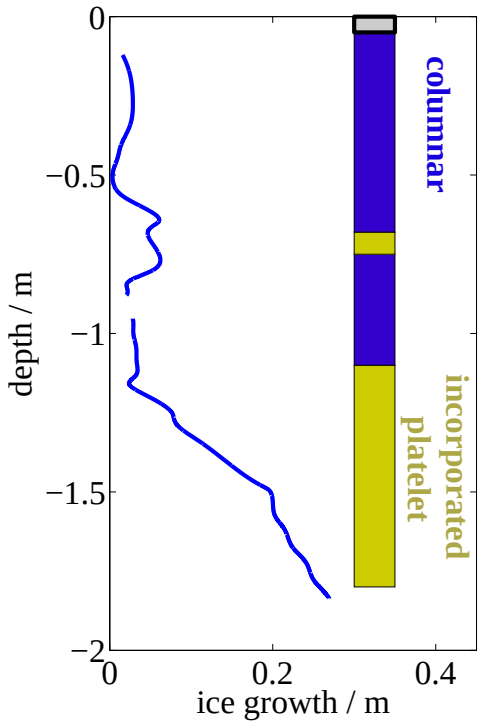

Figure 4: Profile of the cumulative ice thickness due to oceanic heat flux. The ice crystal structure as a function of depth in the sea ice cover is also shown, with layers of frazil ice (grey), columnar ice (blue) and incorporated platelet ice (yellow). [Modified from Purdie et al, 2006]

The most reliable method of identifying incorporated platelet ice is by making thin sections and measuring the orientations of the crystal c-axes. In columnar sea ice (shown in Figure 5), the crystal c-axes lie in the horizontal plane and form a horizontal girdle fabric, represented by points around the perimeter of the Schmidt net. A vertical thin section of columnar sea ice (see Figure 5(a)) graphically illustrates the vertical boundaries of crystals that extend over tens of centimeters, while platelet ice crystals (see Figure 6(a)) have smaller vertical extent and may display fluted edges. The c-axes of platelet ice shown in Figure 6(c) shows the crystals are oriented in a disordered fashion.

Nucleation in the water versus growth at the interface?

In the past few years, there have been three research questions that the New Zealand group has focused upon for the sea ice cover of McMurdo Sound. Work done in McMurdo Sound in the 1980s and 1990s (Jeffries et al, 1993; Gow et al, 1998) identified two possible ways in which

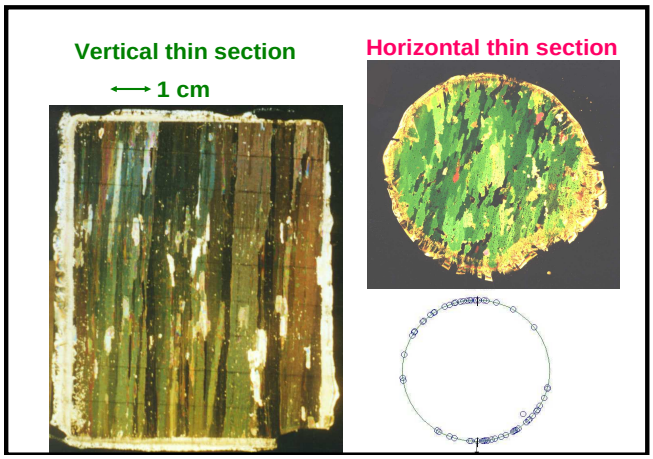

Figure 5: Columnar sea ice, (a) vertical thin section, (b) horizontal thin section and (c) Schmidt net showing distribution of crystal c-axes.

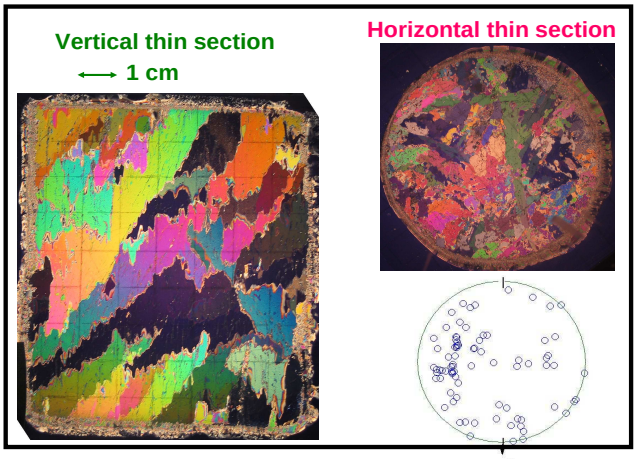

Figure 6: Incorporated platelet ice, (a) vertical thin section, (b) horizontal thin section and (c) Schmidt net showing distribution of crystal c-axes.

platelet ice might find its way into the ice cover: either through unrestrained nucleation of new crystals at the ice-water interface and their subsequent growth there; or by nucleation and growth of crystals in the water column, followed by rise to the underside of the ice cover. Does one process happen to the exclusion of the other? To answer this we conducted an experiment over the winter of 2003, making real-time observations of the freezing of incorporated platelet ice into the sea ice cover.

Figure 7 indicates the relationship between platelet ice amount and the temperature in the water close to the ice-water interface. The top panel shows the temporal evolution through winter of the deviation of the temperature of the water at 10 m (or 20 m) depth from its *in situ* freezing point. Negative values indicate supercooled water. The lower panel shows a rather subjective measure of platelet ice in the water column, derived from the quantity observed on ropes etc. Figure 7 demonstrates that when the temperature of the upper water column was lower, then there were more loose crystals in the water column.

We can also compare the water temperature with the strength of the backscattered signal from an acoustic Doppler current profiler (ADCP). There is now a mounting body of evidence that the acoustic backscatter from such instruments may be used as a proxy for frazil ice in the water column (Dieckmann et

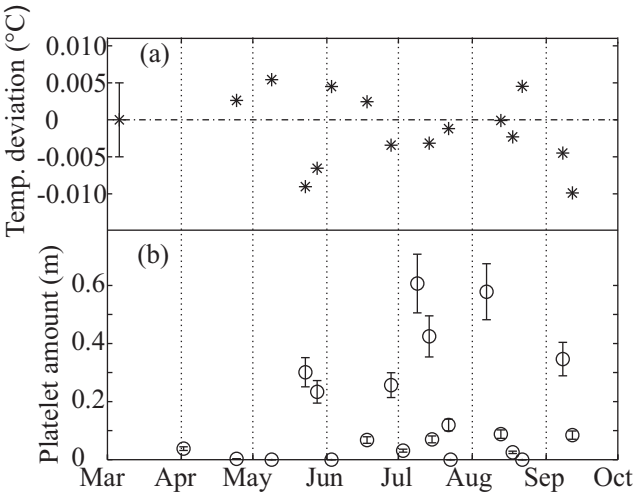

Figure 7: (a) Deviation from in situ freezing temperature at 10/20 m averaged over the previous 48 hours and (b) an estimate of the amount of platelet ice attached to cables. Negative values in 4(a) indicate the presence of supercooling. Error in temperature deviation is shown on left. [From Leonard et al, 2006]

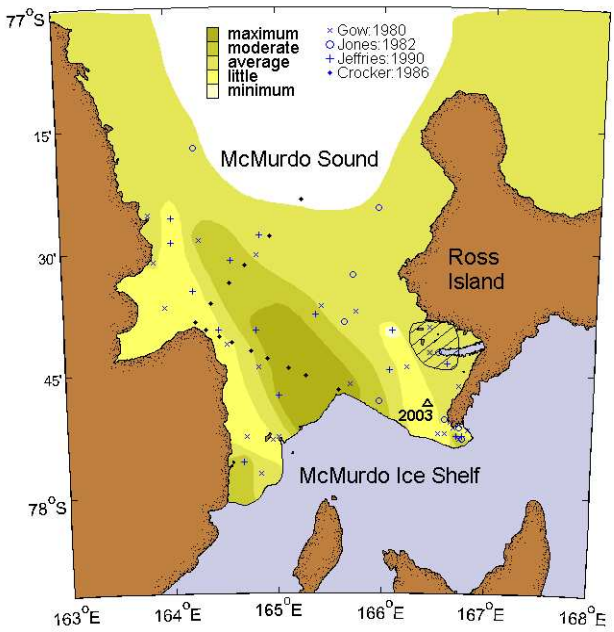

Figure 8: Map of relative abundance of platelet ice over McMurdo Sound, based on measurements of Gow et al, 1998; Jones and Hill, 2001; Jeffries et al, 1993; and Crocker, 1988. Triangle marks the site of the winter 2003 measurements. [From Langhorne et al, 2006]

al, 1986; Penrose et al, 1994; Marko & Jasek, 2008; Jasek and Marko, 2008; Morse and Richard, 2008). Leonard et al (2006) demonstrated that ADCP signal strength in the 2003 experiment correlates with the ocean temperature close to the ice-water interface.

Thus water temperature correlates with platelet "amount" as well as with ADCP signal strength. Finally we compare ADCP signal strength measured close to the interface at the time of freezing with the crystal orientations in the sea ice cover. We find there is excellent correlation between frazil ice in the water column and incorporated platelet ice in the sea ice cover (Leonard et al, 2006), conclusively linking incorporated platelet ice and the time-history of the appearance of ice crystals in the water column. However, once attached, platelet crystals do continue to grow at the interface (Smith, 2001, Smith et al, 2001, Leonard et al, 2006).

Why does platelet growth switch on?

The second research question is concerned with processes in the near surface ocean: what happens in the water column to "switch on" platelet ice growth?

Previous research (Lewis and Perkin, 1985; Barry, 1988; Barry and Dayton, 1988) has shown that in late spring there is a core of relatively warm, saline water near the ocean surface on the eastern side of the Sound, while cold, less saline water occupies the near-surface environment of the western Sound. We compare such observations with a rather subjective map of platelet ice abundance (Barry, 1988; Langhorne et al, 2006), reproduced in Figure 8. Superimposing the best estimate of circulation of the Sound (Robinson, 2004), we may conclude that relatively warm, saline enters on the eastern side of the Sound, while cold, less saline water exits on the west.

However we must remember that this is the situation in late spring and summer when platelet ice is well-established. How do the properties of the water column vary through the winter to bring about the appearance of platelet ice?

Oceanographic measurements in 2003 at the site shown on Figure 8 show the presence of this warm core in late autumn. However by early winter the water column to 250 m has been cooled below its surface freezing point: that is below the freezing point if the water were raised to the surface adiabatically. Lewis and Perkin (1985) have pointed out that the only way in which water may be cooled below its surface freezing point is by having been in contact with an ice shelf. Thus we may conclude that by early winter the water of the upper ocean (to 250 m) close to the 2003 site had interacted in some way with the ice shelf.

There is a second prominent attribute of the near-surface oceanography. Directly beneath the ice-water interface of growing sea ice there is always a layer of water that is well mixed because of the rejection of cold, dense, saline water upon freezing. A particularly striking feature of the McMurdo winter oceanography is the presence of a cold band of water, held by buoyancy at the base of this mixed layer. As winter progresses this mixed layer becomes denser and the cold water of the band is eventually able to gain access to the ice-water interface (Leonard et al, 2006).

What effect does this cold band have on water immediately adjacent to the interface? Leonard et al (2006) have shown that within 0.15 m of the interface the *in situ* supercooling increases from 0.006 ± 0.004^{o}C in mid May (late autumn) to 0.015 ± 0.004^{o}C in September (late winter). Thus as winter progresses, a layer develops immediately below the ice-water interface that eventually becomes 10s of meters thick and is 10s of mK below its *in situ* freezing point. This supercooled layer increases in thickness and in extent of supercooling in an episodic manner through the winter.

What is the contribution of heat flux to the ocean?

Finally we have examined the contribution of heat flux to the ocean to the sea ice thickness in the presence of platelet ice. In other words we ask, what portion of the sea ice thickness has grown as a result of heat flux to the ocean rather than the atmosphere? By equating the oceanic heat flux to the difference between the conductive heat flux through the sea ice and the latent heat released by freezing at the interface (Purdie et al, 2006), we have estimated the contribution to the sea ice cover by heat rejection to an oceanic sink. That is, heat flux to the ocean, F_w, is found from

$$\rho_i L \frac{dH}{dt} = -k \left.\frac{\partial T}{\partial z}\right|_b - F_w \qquad [1]$$

where H is ice thickness, t is time, $\left.\frac{\partial T}{\partial z}\right|_b$ is temperature gradient in the sea ice close to the ice-water interface and ρ_i, L and k are respectively sea ice density, latent heat and thermal conductivity. Figure 4 demonstrates that, at the 2003 winter site, 0.25 m of the total incorporated platelet ice growth of 0.70 m was due to heat flux to the ocean. Thus, approximately 35% of the incorporated platelet ice was due to heat flux to the ocean, the remaining 65% being conducted upwards through the sea ice. This suggests that 10% of the total ice thickness at that site grew as a result of heat flux to the ocean (Langhorne et al, 2006).

Conclusions

Considerable progress has been made over the past two decades in our understanding of the processes that take place at the base of an ice shelf, and how these processes influence the mass balance of the ice shelf, ocean and sea ice. Modelling studies have been particularly successful at providing insights. However there are enormous challenges in making observations to guide and confirm the model predictions. Some of the observational conclusions of the New Zealand group are given below.

- Our experiments conclusively link the presence of platelet ice in the sea ice cover to the time-history of the appearance of ice crystals in the water column.
- Platelet ice forms due to heat flux to the ocean, as well as to the atmosphere. In our experiment 35% of the platelet ice thickness was due to heat flux to the ocean.
- The upper ocean is entirely below its surface freezing point from early winter, implying contact with an ice shelf.
- There is a layer of *in situ* supercooled water adjacent to the ice-water interface that increases in thickness and degree of supercooling as winter progresses.
- There is a band of very cold water held by buoyancy at the base of the mixed layer. As winter progresses and the mixed layer becomes denser due to salt rejection from sea ice formation this cold water gains access to the ice-water interface.

Acknowledgments

This work has been funded by the Marsden Fund, the Foundation for Research, Science and Technology, University of Otago, Industrial Research Ltd and National Institute of Water and Atmospheric Research, New Zealand. We are grateful to Antarctica New Zealand for logistical support. Thanks to J. Leitch, B. Grant, and Drs R. Vennell, C. Petrich, M. McGuinness, and R Frew for their support in collecting and analysing the data presented here.

References

Barry, J. P. (1988), Hydrographic patterns in McMurdo Sound, Antarctica and their relationship to local benthic communities, Polar Biol., 8, 377–391.

Barry, J. P., and P. K. Dayton (1988), Current patterns in McMurdo Sound, Antarctica and their relationship to local biotic communities, Polar Biol., 8, 367–376.

Bombosch, A. and A. Jenkins. 1995. Modelling the formation and deposition of frazil ice beneath Filchner-Ronne Ice Shelf. *J. Geophys. Res.* 100:6983-6992.

Crocker, G.B. (1988) Physical processes in Antarctic landfast sea ice. PhD thesis, University of Cambridge, UK.

Crocker G.B., and P. Wadhams. 1989. Modelling Antarctic fast-ice growth. *J. Glaciol.*, 35:3-8.

Daly, S.F. (1984) Frazil ice dynamics. CRREL Monograph 84-1.

Dayton, P. K., G. A. Robilliard, and A. L. DeVries (1969), Anchor ice formation in McMurdo Sound, Antarctica, and its biological effects, Science, 163, 273– 274.

Dieckmann, G., G. Rohardt, H. Hellmer, and J. Kipfstuhl (1986),The occurrence of ice platelets at 250 m depth near the Filchner Ice Shelf and its significance for sea ice biology, Deep Sea Res., 33, 141–148.

Drewry D., S.R. Jordan, and E. Jankowski (1982) Measured properties of the Antarctic ice sheet: surface configuration, ice thickness, volume and bedrock characteristics. *Annals of Glaciology*, 3, 83-91.

Foldvik, A. and Kvinge, T. (1974) Conditional instability of sea water at the freezing point. Deep Sea Research, 21, p. 169-174.

Gow, A. J., S. F. Ackley, and J. W. Govoni (1998), Physical and structural properties of land-fast sea ice in McMurdo Sound, Antarctica, in *Antarctic Sea Ice: Physical Processes, Interactions and Variability*, Antarctic. Res. Ser., vol. 74, edited by M. O. Jeffries, pp. 355–374, AGU, Washington, D. C.

Günther, S., and G. S. Dieckmann (1999), Seasonal development of algal biomass in snow-covered fast ice and the underlying platelet layer in the Weddell Sea, Antarctica, Antarct. Sci., 11(3), 305– 315.

Hammar, L. and Shen, H.T. (1995) Frazil evolution in channels. J. Hydraulic Res., 33(3), 291-306.

Hellmer, H. H. (2004), Impact of Antarctic ice shelf basal melting on sea ice and deep ocean properties, *Geophys. Res. Lett.*, 31, L10307, doi:10.1029/2004GL019506.

Hellmer, H. H., and S. S. Jacobs (1992), Ocean interactions with the base of the Amery Ice Shelf, Antarctica, J. Geophys. Res., 97, 20,305–20,320.

Holland P. R., D. L. Feltham and A. Jenkins Validity of the Ice Shelf Water plume concept under Filchner-Ronne Ice Shelf, FRISP Report No. 17 (2006), page 48-54

Holland, P. R., and D. L. Feltham, 2006. The effects of rotation and ice shelf topography on frazil-laden ice shelf water plumes. J. Physical Oceanography., 36, 2312-2327.

Jacobs, S.S., A.L. Gordon, and L.D. Ardai. 1979. Circulation and melting beneath the Ross Ice Shelf. *Science*, 203:439-443.

Jacobs, S.S., H.H. Hellmer, C.S.M. Doake, A. Jenkins and R.M. Frolich (1992) Melting of ice shelves and mass balance of Antarctica. *J. Glaciol.* 38(130) 375-387.

Jasek, M and Marko, J.R.. Acoustic detection and study of frazil ice in a freezing river during 2007-2008 winters. In *Proceedings of the 19th IAHR International Symposium on Ice*, 6-11 July, 2008, Vancouver, British Columbia, vol. 1, 395-398.

Jeffries, M. O., W. F. Weeks, R. Shaw, and K. Morris (1993), Structural characteristics of congelation and platelet ice and their role in the development of Antarctic land-fast sea ice, J. Glaciol., 39(132), 223– 238.

Jenkins, A. 1991 A one-dimensional model of ice shelf – ocean interaction. *J. Geophys. Res.* 96: 20,671-20,677.

Jenkins, A. and Bombosch, A. 1995. Modelling the effects of frazil ice crystals on the dynamics and thermodynamics of Ice Shelf Water plumes. *J. Geophys. Res.* 100:6967-6981.

Jones, S. J., and B. Hill (2001), Structure of sea ice in McMurdo Sound, Antarctica, Ann. Glaciol., 33, 5 – 12.

Langhorne, P.J., Purdie, C.R., Smith, I.J., Leonard, G.H., Kempema, E.W., Petrich, C., Gribble, M.A., Bond, P.E. and Haskell, T.G. Antarctic landfast sea ice: the role of platelet ice. In *Proceedings of the 18th IAHR International Symposium on Ice*, 28 Aug-1 Sept 2006, Sapporo, Japan, Vol. 1, 285-292.

Leonard, G. H., C. R. Purdie, P. J. Langhorne, T. G. Haskell, M. J. M. Williams, and R. D. Frew (2006), Observations of platelet ice growth and oceanographic conditions during the winter of 2003 in McMurdo Sound, Antarctica, J. Geophys. Res., 111, C04012, doi:10.1029/2005JC002952.

Lewis, E. L., and R. G. Perkin (1986), Ice pumps and their rates, *J. Geophys. Res.*, 91, 11,756–11,762.

Lewis, E. L., and R. G. Perkin (1985), The winter oceanography of McMurdo Sound, Antarctica, in Oceanology of the Antarctic Continental Shelf, Antarctic Res. Ser., vol. 43, edited by S. Jacobs, pp. 145 – 165, AGU, Washington, D. C.

Littlepage, J.L. 1965. Oceanographic investigations in McMurdo Sound, Antarctica. Antarctic Research Series, Vol. 5 AGU, Publication No. 1297

Marko, J.R. and Jasek, M. Acoustic detection and study of frazil ice in a freezing river during 2004-2005 and 2005-2006 winters. In *Proceedings of the 19th IAHR International Symposium on Ice*, 6-11 July, 2008, Vancouver, British Columbia, vol. 1, 381-394.

Morse, B. and Richard, M. (2008) A field study of suspended frazil particles. Cold Regions Science and Technology, Volume 55, Issue 1, 86-102.

Paige, R.A. (1966) Crystallographic studies of sea ice in McMurdo Sound, Antarctica. *U.S. Naval Civil Engineering Laboratory, Technical Report* R-494.

Penrose, J. D., M. Conde, and T. J. Pauly (1994), Acoustic detection of ice crystals in Antarctic waters, J. Geophys. Res., 99, 12,573– 12,580.

Purdie, C, Langhorne, P., Leonard, G., and Haskell, T. Growth of first year land-fast Antarctic sea ice determined from winter temperature measurements. *Annals of Glaciology*, 44, 170-176 (2006)

Robin, G. de Q. 1979. Formation, flow and disintegration of ice shelves. *J. Glaciol*. 24:259-271

Robinson, N. J. (2004) An oceanographic study of the cavity beneath the McMurdo Ice Shelf, Antarctica. MSc thesis, Victoria University of Wellington, New Zealand, 156 pp.

Sandhäger, H., D.G. Vaughan and A. Lambrecht. Meteoric, marine and total ice thickness maps of Filchner-Ronne-Schelfeis, Antarctica FRISP Report No. 15 (2004)

Smedsrud, L.H. and A. Jenkins. 2004. Frazil ice formation in an ice shelf plume. *J. Geophys. Res.* 109, C03025, doi10.1029/2003JC001851.

Smith, I.J. (2001) Platelet ice in McMurdo Sound, Antarctica. PhD thesis, University of Otago, New Zealand, 224pp.

Smith, I.J., Langhorne, P.J., Haskell, T.G., Trodahl, H.J., Frew, R, and Vennell, R. Platelet ice and the land-fast sea ice of McMurdo Sound, Antarctica. Annals of Glaciology, 33, 21-27 (2001).

Souchez, R., J. L. Tison, R. Lorrain, C. Fl´ehoc, M. Sti´evenard, J. Jouzel, and V. Maggi (1995), Investigating processes of marine ice formation in a floating tongue by a high-resolution isotopic study, *Journal of Geophysical Research, 100*(C4), 7019–7025.

Timmermann, R., A. Beckmann, and H. H. Hellmer, Simulations of ice-ocean dynamics in the Weddell Sea 1. Model configuration and validation, J. Geophys. Res., 107(C3), 3024, doi:10.1029/2000JC000741, 2002.

Timmermann, R., A. Worby, H. Goosse, and T. Fichefet (2004), Utilizing the ASPeCt sea ice thickness data set to evaluate a global coupled sea ice–ocean model, J. Geophys. Res., 109, C07017, doi:10.1029/2003JC002242.

Tison, J. L., R. D. Lorrain, A. Bouzette, M. Dini, A. Bondesan, and M. Stivenard (1998), Linking landfast sea ice variability to marine ice accretion at Hells Gate Ice Shelf, Ross Sea, in Antarctic Sea Ice: Physical Processes, Interactions, and Variability, Antarct. Res. Ser., vol. 74, edited by M. O. Jeffries, pp. 375–407, AGU, Washington, D. C.

Weeks, W. and M. Mellor. 1978. Some elements of iceberg technology. Iceberg Utilization. New York, Pergamon Press, 45-98.

Williams, M. J. M., A. Jenkins, and J. Determann (1998), Physical controls on ocean circulation beneath ice shelves revealed by numerical models, in Ocean, Ice, and Atmosphere: Interactions at the Antarctic Continental Margin, Antarct. Res. Ser., vol. 75, edited by S. S. Jacobs and R. F. Weiss, pp. 285– 299, AGU, Washington, D. C.

Wright, C.S. and R.E. Priestley. 1922. *British (Terra Nova) Antarctic Expedition*, 1910-1913. *Glaciology*, London, Harrison and Sons.

Zwally, H. J., J. C. Comiso, C. L. Parkinson, D. J. Cavalieri, and P. Gloersen, Variability of Antarctic sea ice 1979–1998, J. Geophys. Res., 107(C5), 3041, doi:10.1029/2000JC000733, 2002.

Ice friction, sea ice mathematical and computer model formulations

19th IAHR International Symposium on Ice
"Using New Technology to Understand Water-Ice Interaction"
Vancouver, British Columbia, Canada, July 6 to 11, 2008

The big picture on ice friction

Kietzig, Anne
Hatzikiriakos, Savvas G.
Englezos Peter
Department of Chemical and Biological Engineering
The University of British Columbia
2360 East Mall, Vancouver, BC, V6T 1Z3
akietzig@chml.ubc.ca

Abstract
A review of the many different factors influencing ice friction and their interdependence with respect to different friction regimes clarifies our understanding of the big picture of ice friction and sheds more light on the complexity of ice. Although the study of friction has a long history, ice friction has only been investigated during the last century. Underlying mechanisms of friction on ice are important to our understanding of glacial movements, cargo and ice breaker ship hull design, ice sports, and the grip of shoes and soles on icy roads. The basic physical concepts of boundary, mixed, and hydrodynamic friction apply to ice friction. However, these friction regimes must be described with respect to the thickness of the lubricating liquid-like layer on ice, as well as temperature of the ice, sliding velocity, the contact area between ice and slider, normal load exerted by the sliding object, relative humidity, and also properties of the slider material such as thermal conductivity, hydrophobicity, hardness and surface roughness.

1. Introduction

Reynolds (1901) was the first to scientifically investigate the matter of sliding against ice. He attributed the low friction against ice to pressure melting; this explanation was widely accepted among scientists for almost 40 years. However, Bowden and Tabor (1939) suggested that frictional heating is the main contributor to the low friction coefficient on ice. Heat generated by the first contact between the asperities of the two surfaces melts part of the ice surface. The produced melt water lubricates the succeeding contact between the two surfaces. During motion different friction regimes play an important role depending on several factors, e.g. temperature, velocity, normal load, apparent contact area, roughness, relative humidity, thermal conductivity and hydrophobicity.

2. Friction regimes

Ice friction is generally described with respect to the thickness of the liquid-like layer on ice. Many researchers, such as Bäurle et al. (2006-1), Buhl et al. (2001), Evans et al. (2004), Kozlov and Shugai (1991), Lehtovaara (1987), Makkonen (1994) applied concepts of dry and wet friction to describe friction on ice. The physics of friction clearly show that real dry friction on ice under atmospheric conditions cannot exist, and it is necessary to include the general physical concepts of dry, boundary, mixed, and hydrodynamic friction.

Dry friction is the moving contact between two absolutely clean surfaces, which is characterized by the breakage of adhesive bonds and takes place in total absence of any kind of lubricant or foreign substance (Bowden and Tabor, 1950). The narrow perspective of this definition inhibits any kind of motion, since surfaces without any trace of air or other substances between them will bond together like the bulk of the material. True dry friction thus has only a theoretical importance. A very thin liquid-like film is present on the ice surface under all conditions. Instead of considering dry ice friction, we should actually refer to the physics of boundary friction.

Boundary lubrication on ice is characterized by the temperature (T) in the contact zone being everywhere below the melting temperature (T_m), and the thickness of the lubricating liquid-like layer (h) being far smaller than the surface roughness (R) (Kozlov and Shugai, 1991).

$$\text{everywhere in contact zone: } T < T_m \text{ and } h << R$$

Frictional resistance arises from the shearing of adhesive bonds, which are formed between the mating asperities of the two surfaces in contact. The number of contacting points, which makes up the real area of contact, influences the friction force directly. It depends on the applied load and the hardness of the surfaces but is independent of the sliding speed as long as the film thickness remains constant and no more ice is melted by frictional heating (Bhushan, 2002; Persson, 2000; Bowden and Tabor, 2001). For the width of this regime the thermal conductivities of both surfaces play a fundamental role, since they define where frictional heat acts.

Mixed friction is found when the surface temperature rises above the melting temperature (T_m) of ice at some points within the contact zone, and the thickness of the liquid-like layer (h) is still less than the characteristic roughness of the surfaces (R), the friction regime reaches the so called mixed friction.

$$\text{at some points in contact zone: } T > T_m \text{ and } h < R$$

In this regime, the load of the slider is partly supported by the surface asperities and partly by the lubricating layer. This was just recently confirmed by temperature measurements by Bäurle (2006-1). It is obvious that the increased thickness of the lubricating layer reduces solid-solid adhesion and enhances the lubrication. However, at the same time the lubricating melt water enforces the build-up of capillary water bridges between the asperities, as shown in figure 1.

Figure 1. Capillary bridges between asperities of contacting surfaces during sliding.

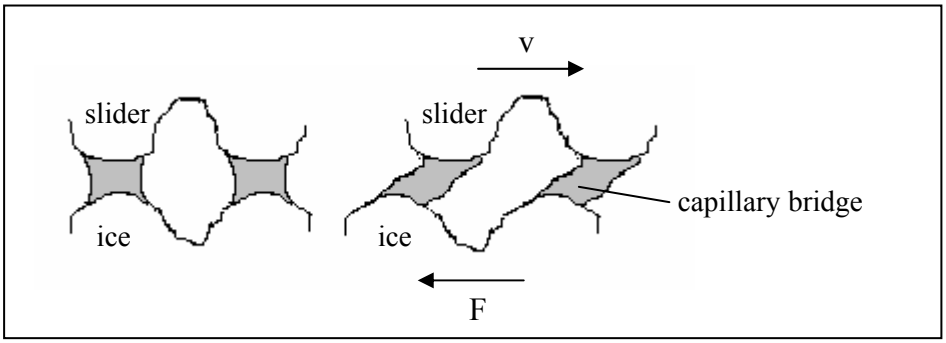

The capillary bridges act as bonds between the surfaces, but do not support the applied load. They exert an additional drag force on the slider, and capillary bridges should be taken into account when discussing friction against ice. The problem herein, however, is that no physical or experimental model was found yet to describe the contribution of capillary bridges to the friction force. Generally, as the name of the friction regimes already tells, thermal conduction, ice melting and capillary drag contribute to the frictional resistance.

Hydrodynamic friction exists if everywhere in the contact zone the temperature is above the melting temperature (T_m), and the thickness of the lubricating layer between the two surfaces is greater than the height of the asperities.

$$\text{everywhere in contact zone: } T > T_m \text{ and } h > R$$

The lubricating layer, not the surface asperities, carries the applied load. If the load is very high, a part of the lubricating layer might be squeezed out between the surfaces. However, for hydrodynamic friction, it is assumed that the thickness of the lubricating layer remains greater than the height of the asperities. The area of real contact is identical to the surface area (A) of the slider (Bhushan, 2002). No solid-solid contact occurs during the sliding movement. Consequently, shearing of the lubricating layer contributes to the friction force. Capillary drag forces must be included in the case of ice friction, since they play a fundamental role in the frictional resistance in the regime of hydrodynamic friction.

The above discussion is summarized in figure 2.

Figure 2. Friction regimes relevant to ice friction in an adaption of the Stribeck curve.

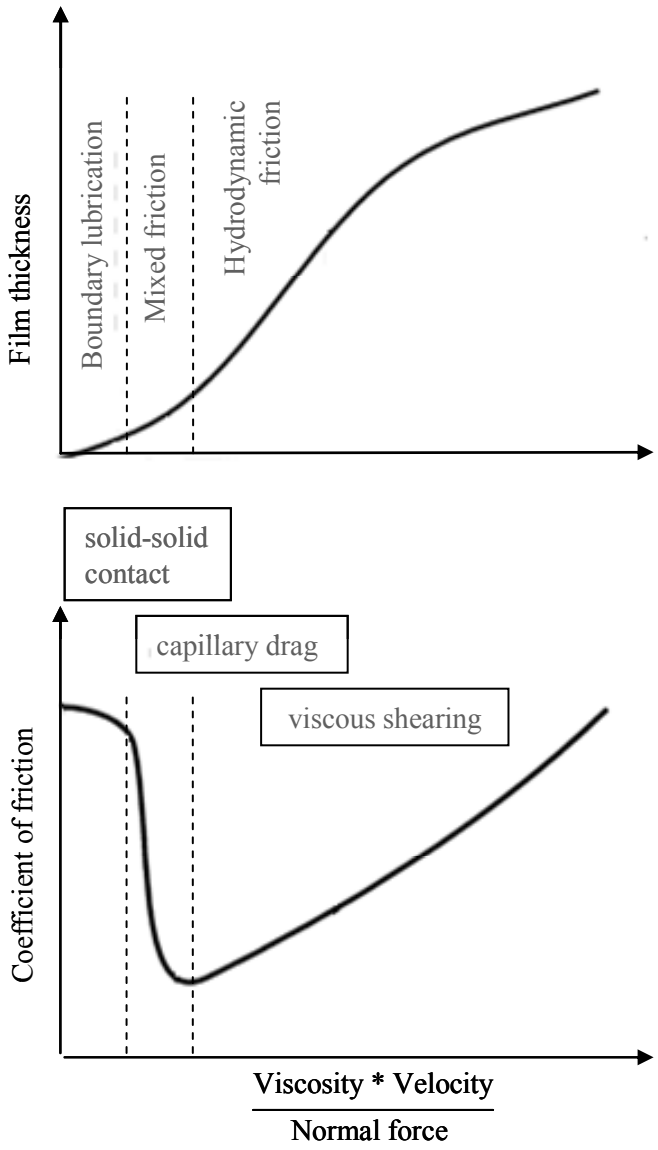

Many researchers (Evans et al., 1976; Oksanen and Keinonen, 1982; Akkok et al., 1987; Stiffler, 1984, 1986) have attempted to model frictional heating theory as it applies in friction against ice. No model so far sufficiently describes the interaction of all physical phenomena contributing to and interacting in ice friction. The biggest problem in modeling is the unknown contribution of drag forces from water bridges.

3. Influence of different parameters on friction coefficient

Many factors influence the thickness of the lubricating liquid-like layer on ice and thus the coefficient of friction, which is widely used to assess the ease of motion on ice and is defined as:

$$F_T = \mu * F_N \quad \textbf{[1]}$$

where F_T is the frictional force, F_N the normal force, and μ the coefficient of friction.

3.1. Temperature

Since the first ice friction studies (Bowden and Hughes, 1939), many researchers have confirmed the dependence of the friction coefficient on temperature (Buhl et al., 2001; Slotfeldt-Ellingsen and Torgersen, 1983; Bowden, 1953; Bowden and Hughes, 1939).

Figure 3. Temperature dependence of ice friction.

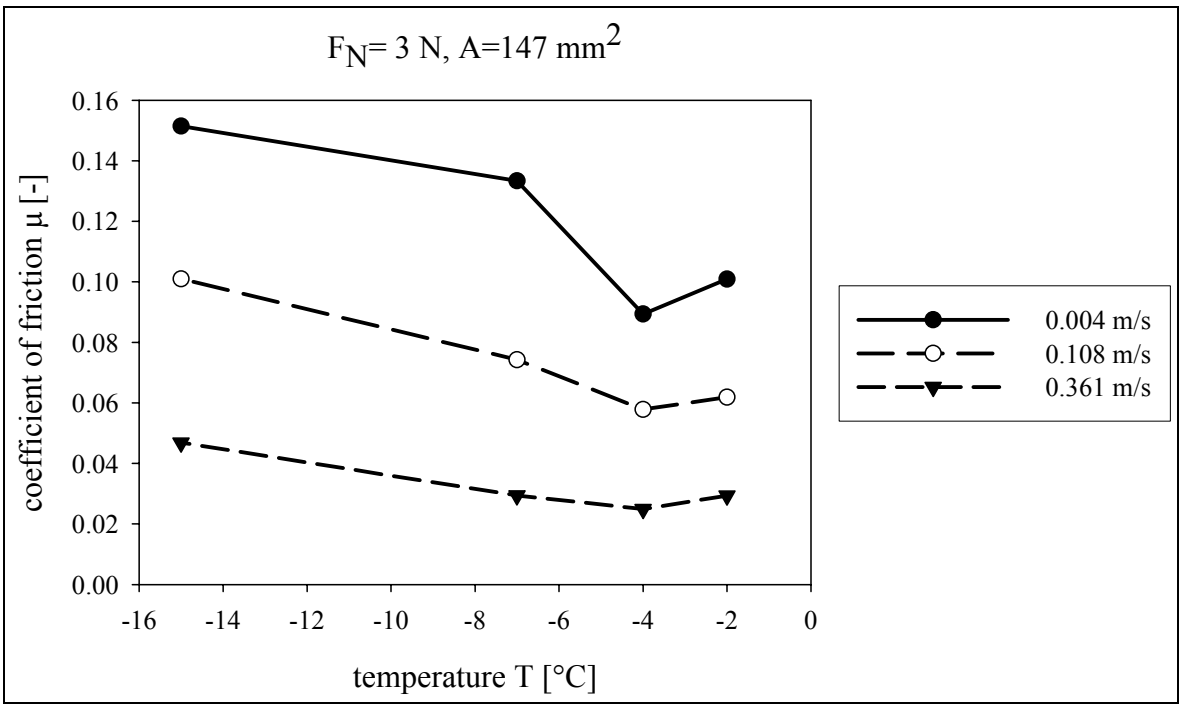

Figure 3 illustrates the temperature dependence of the coefficient of friction for a stainless steel (SS 304L) slider against ice with a normal force of 3 N at 3 different speeds. Overall, the coefficient of friction decreases first with increasing temperature and rises again when the temperature exceeds the optimum temperature for this slider's load and velocity, which is at around 4 °C. At slow speeds this effect is more pronounced. Obviously, at low temperatures and slow speeds the friction is dominated by boundary friction conditions. In the hydrodynamic regime at temperatures close to the melting point the thickness of the lubricating liquid-like layer becomes large enough to not only facilitate the motion but also to add to the resistance through the built-up of capillary bridges. However, the onset of this increase in friction depends largely on the material nature and weight of the slider.

3.2. Velocity

The experimental results regarding the influence of velocity on the friction coefficient are controversial. Bowden and Hughes (1939) and Boden (1953) first observed that friction against ice decreased with increasing velocity, as shown in figure 4.

Figure 4. Velocity dependence of ice friction.

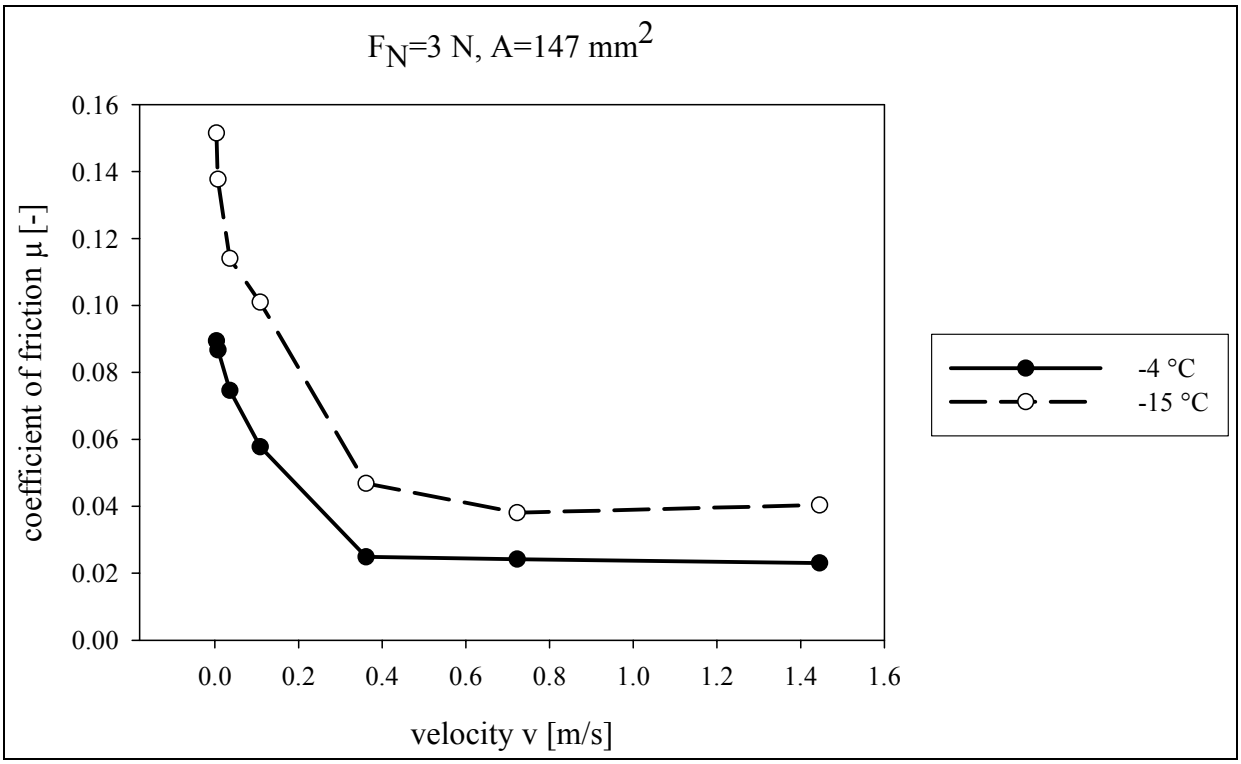

Evans et al. (1976), who were first to model ice friction mathematically, confirmed these findings both experimentally and theoretically. Many other researchers (Kuroiwa, 1977; Calabrese, 1980; Akkok et al., 1986; Montagnat and Schulson, 2003; Marmo et al., 2005) further confirmed the same dependency with different experimental set-ups and materials. Bäurle et al. (2006-1) even extended the study to as high velocities as 10 m/s. These findings showed that at higher velocities more frictional heat is produced than at slower speeds, resulting in a greater melt water production along with more lubricated facilitated motion.

Contradicting results like an increase in the coefficient of friction with velocity were found by Koning et al. (1992), who did friction tests with skaters on ice at -4.6 °C. However, no conclusions about the underlying mechanisms were drawn. Similarly, Jones et al. (1994) found that friction increased with speed during their experiments with a 100 N slider at +1 °C. With ice-against-ice experiments, Oksanen and Keinonen (1982) found the same relationship at temperatures above -5 °C. They extended the mathematical model from Evans et al. (1976) and found that the thickness of the melt water layer and therewith the coefficient of friction is proportional to $v^{1/2}$ for temperatures close to the melting point. Therefore, the increase in friction can be explained through the overproportional increase in drag forces from shearing the lubricating layer. The onset of this increase is obviously largely dependent on the size, weight and material nature of the slider, as was also shown recently by Albracht et al. (2004) and Bäurle et al (2006-1).

3.3. Apparent contact area and load

Generally, research findings agree that the frictional force increases with increasing normal force (Bowden and Hughes, 1939; Bowden, 1953; Lehtovaara, 1987; Bäurle, 2006-2). The impact on the friction coefficient, however, cannot be explained easily.

Bowden and Hughes (1939) first performed experiments on the influence of the geometric area of the slider surface on the friction coefficient. Their experimental results have shown little dependence on the geometric contact area. However, Bäurle (2006-2) studied the influence of the geometric size of the slider under more controlled conditions. Figure 5 illustrates Bäurle's (2006-1, 2006-2) experimental data with exponential curves fitted through the data points.

Figure 5. Area and load dependence of ice friction.

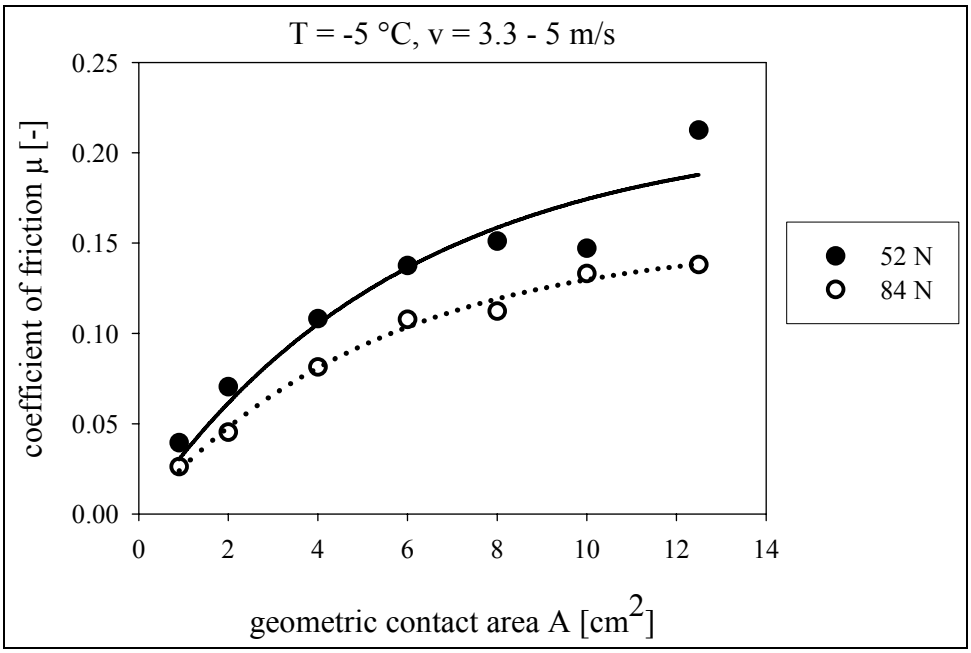

The friction coefficient increases with increasing geometric contact area of the slider. This result contradicts Leaonardo da Vinci's second law of friction, which implies that friction force is independent of the apparent area of contact, and Bowden's discussion on the area of contact (1952). However, the findings can be explained by the nature of the ice and the lubricating liquid-like layer. The larger the geometric area of the slider, the more capillary bridges can be built up between the two surfaces, resulting in the increase of the frictional resistance in the mixed and hydrodynamic friction regimes. Furthermore, the slider with the larger load shows lower friction, due to a greater amount of contacting points, contributing to frictional heating and to a thicker water layer.

3.4. Roughness

In 1699, Amonton attributed friction to roughness (Dawson, 1998). This led to the assumption that smooth surfaces show less friction. Calabrese (1980) measured the friction coefficient as a function of sliding speed for steel with different degrees of roughness and confirmed that roughening increases the friction coefficient. Ducret et al. (2005) came to a similar conclusion after measuring friction of sliders against ice of different roughness. Generally, increasing the roughness of a surface leads to more interlocking asperities during the sliding movement, which increases the wear rate and overall friction in the boundary friction regime. However, few studies exist on the influence of roughness on ice friction. Itagaki et al. (1987) compared different steel types regarding their surface structure and conductivity. Their results imply that smooth surfaces

lead to an increased actual contact area, where adhesive forces between the surfaces result in higher friction compared to rough runners at temperatures around -8 °C. On the other hand, at temperatures closer to the melting point rough sliders show higher friction than smooth ones. This can be explained through the greater surface area that is available for capillary bridges to build up.

3.5. Relative humidity RH

Calabrese (1980) performed friction experiments with steel sliding against ice at different relative humidity conditions. His results are depicted in figure 6.

Figure 6. Relative humidity dependence of ice friction.

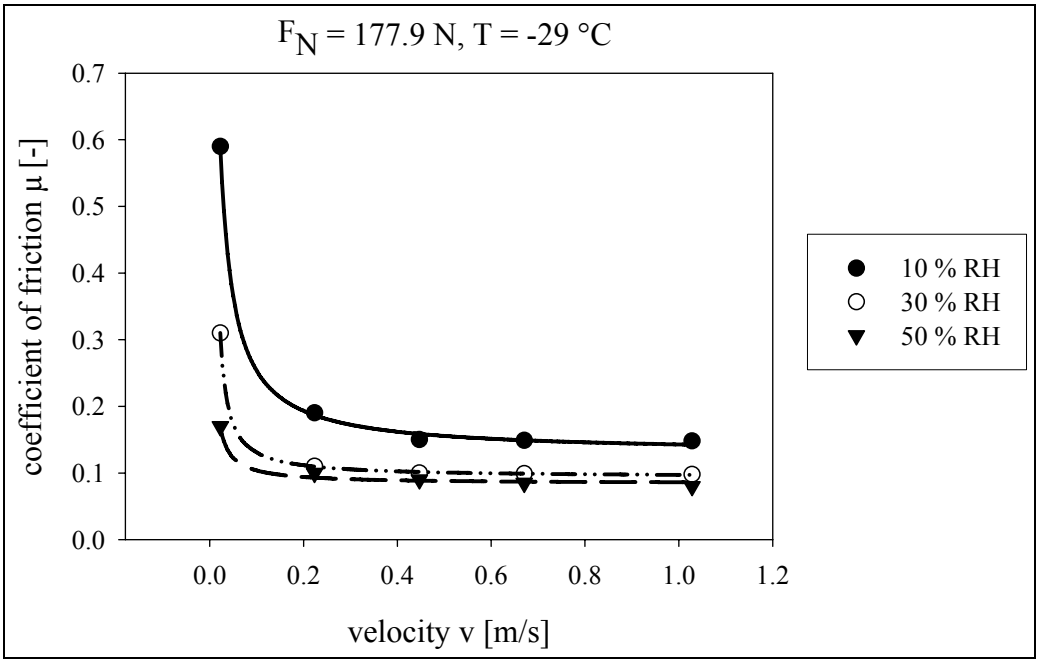

Relative humidity has a strong influence at the onset of the sliding movement. The higher the humidity, the more lubricated is the sliding interface and the lower the frictional resistance. Unfortunately, no further experimental data exist for the influence of humidity at higher temperatures.

3.6. Thermal conductivity k

Applying the frictional heating theory to ice friction, Bowden and Hughes (1939) performed experiments on the influence of the slider's thermal conductivity on the friction coefficient. They compared the friction coefficient of a hollow ski with a copper surface to the one of the same ski construction filled with mercury. Air has a thermal conductivity of about 0.025 W/mK and mercury of 8 W/mK. The friction of the mercury filled ski was higher compared to the hollow air filled ski. Even though no further details are given about the exact experimental conditions, this result implies that the friction of a good thermal conductor is higher because less heat is available at the surface to melt the ice. Further experiments carried out by Itagaki et al. (1987) with steels

of different thermal conductivity have also shown this relationship between thermal conductivity and the friction coefficient. However, Albracht et al. (2004) could not find a significant influence of thermal conductivity on ice friction in their experiments with different materials.

3.7. Hydrophobicity

Bowden (1953) conducted experiments on the wettability of different materials and found that friction was highest for surfaces that wet easily. This can be explained by the enhanced build-up of capillary bridges between the sliding surfaces. However, it should be considered that a change in hydrophobicity was only achieved by using a different material. Therefore, the impact of hydrophobicity cannot be investigated independent of changing thermal conductivity and material hardness. Furthermore, as was pointed out before, roughness and material surface structure also play an important role.

4. Conclusion

It is well understood that friction against ice involves boundary, mixed and hydrodynamic friction. However, it is difficult to predict which regime dominates for a given set of parameters. Different mathematical models were developed to describe friction against ice. The dependence of friction against ice on temperature, velocity and normal load is well understood. However, the influence of material specific parameters such as thermal conductivity, surface roughness, and wettability of the slider are very difficult to isolate. Therefore, their individual impact on ice friction is not easily described. The contribution of capillary drag on ice friction, especially, lacks a profound understanding. Future research is likely to go in these directions.

References

Albracht, F., Reichel, S., Winkler, V., Kern, H, 2004. On the Influences of Friction on Ice, Materialwissenschaft und Werkstofftechnik, 35, 620-625.

Akkok, M., Calabrese, S.J, McC. Ettles, C. M., 1987. Parameters affecting the Kinetic Friction of Ice, Journal of Tribology, 109, 552-561.

Bäurle, L., Szabo, D., Fauve, M., Rhyner, H., Spencer, N.D, 2006-1. Sliding Friction of Polyethylene on Ice: Tribometer Measurements, Tribology Letters, 24, 77-84.

Bäurle, L., Kaempfer, U., Szabo, D., Spencer, N.D, 2006-2. Sliding Friction of Polyethylene on Snow and Ice: Contact area and modeling, Cold Regions Science and Technology, 47, 276-289.

Bhushan, B., 2002. *Introduction to Tribology*, New York, John Wiley & Sons.

Bowden, F.P., Hughes, T. P., 1939. The Mechanism of Sliding on Ice and Snow, Proceedings of the Royal Society of London. Series A, Mathematical and Physical Sciences, 172, 280-298..

Bowden, F.P., 1952. Introduction to the Discussion: The Mechanism of Friction, Proceedings of the Royal Society of London. Series A, Mathematical and Physical Sciences, 212, 440-449.

Bowden, F.P., 1953. Friction on Snow and Ice, Proceedings of the Royal Society of London. Series A, Mathematical and Physical Sciences, 217, 462-478.

Bowden, F.P., Tabor, D., 2001. The Friction and Lubrication of Solids, 3rd ed., New York, Oxford University Press Inc.

Buhl, D., Fauve, M., Rhyner, H., 2001. The Kinetic Friction of Polyethylene on Snow: The Influence of the Snow Temperature and the Load, Cold Regions Science and Technology, 33, 133-140.

Calabrese, S.J., 1980. Frictional Characteristics of Materials Sliding against Ice, Lubrication Engineering, 36, 283-289.

Dowson, D., 1998. History of Tribology, 2nd ed., London, Professional Enginerriner Publishing.

de Koning, J. J., de Groot, G., van Ingen Schenau, G.J., 1992. Ice Friction during Speed Skating, Journal of Biomechanics, 25, 565-571.

Ducret, S., Zahouani, H., Midol, A., Lanteri, P., Mathia, T.G., 2005. Friction and Abrasive Wear of UHWMPE Sliding on Ice, Wear, 258, 26-31.

Evans, D.C.B., Nye, J.F., Cheeseman, K.J., 1976. The Kinetic Friction of Ice, Proceedings of the Royal Society of London. Series A, Mathematical and Physical Sciences 347, 493-512.

Itagaki, K., Lemieux, G.E., Huber, N.P., 1987. Preliminary-Study of Friction between Ice and Sled Runners, Journal De Physique, 48 C-1, 297-301.

Jones, S.J., Kitagawa, H., Izumiyama, K., Shimoda, H., 1994. Friction of Melting ice, Annals of Glaciology 19, 7-12.

Kozlov, I.I., Shugai, A.A., 1991. Experimental Study of High-Speed Friction on Ice, Fluid Dynamics, 26, 145-147.

Kuroiwa, D., 1977. The Kinetic Friction on Snow and Ice, Journal of Glaciology, 19, 141-152.

Lehtovaara, A., 1987. Influence of Vibration on the Kinetic Friction between Plastics and Ice, Wear, 115, 131-138.

Makkonen, L., 1994. Application of a new friction theory to ice and snow, Annals of Glaciology, 19, 155-157.

Marmo, B.A, Blackford, J.R., Jeffree, C.E., 2005. Ice Friction, Wear Features and their Dependence on Sliding Velocity and Temperature, Journal of Glaciology, 51, 391-398.

Montagnat, M., Schulson, E.M., 2003. On friction and Surface Cracking during Sliding of Ice on Ice, Journal of Glaciology, 49 (166), 391-396.

Oksanen, P., Keinonen, J., 1982. The Mechanism of Friction of Ice, Wear, 78, 315-324.

Persson, B.N.J., 2000. Sliding Friction Physical Principles and Applications, 2nd ed., Berlin, Springer-Verlag.

Reynolds, O., 1901. Papers on Mechanical and Physical Subjects, Cambridge, University Press.

Slotfeldt-Ellingsen, D., Torgersen, L., 1983. Water in Ice: Influence on Friction, Journal of Physics D: Applied Physics, 16, 1715-1719.

Stiffler, A.K., 1984. Friction and Wear with a Fully Melting Surface, Journal of Tribology, 106, 416-419.

Stiffler, A.K., 1986. Melt friction and pin-on-disk devices, Journal of Tribology, 108, 105-108.

19th IAHR International Symposium on Ice
"Using New Technology to Understand Water-Ice Interaction"
Vancouver, British Columbia, Canada, July 6 to 11, 2008

On Discontinuities in Anisotropic Plasticity Sea Ice Models

Robert S. Pritchard
IceCasting, Inc.
20 Wilson Ct., San Rafael, CA 94901 USA
pritchardr@asme.org

Mathematical characteristics are derived for quasi-steady, anisotropic plasticity models where ice and mixed layer inertia are neglected. These models are appropriate for resolving daily-averaged ice motions. The focus here is on the mathematical properties of sea ice dynamics models; there are no numerical simulations. Stress characteristics depend on yield surface shape defined by $\phi = 0$. The directions of these characteristics are at angle κ to the *x*-axis

$$\tan\kappa = \frac{-\dfrac{\partial\phi}{\partial\sigma_{xy}} \pm \sqrt{\left(\dfrac{\partial\phi}{\partial\sigma_{xy}}\right)^2 - \dfrac{\partial\phi}{\partial\sigma_{yy}}\dfrac{\partial\phi}{\partial\sigma_{xx}}}}{\dfrac{\partial\phi}{\partial\sigma_{yy}}}.$$

The system of equations is hyperbolic (two real characteristic directions), parabolic (one direction), or elliptic (no directions) depending on whether the discriminant is positive, zero, or negative. The system can behave differently at different locations depending on the stress state σ. Velocity characteristics satisfy a similar equation if ϕ is replaced by the appropriate potential function ψ, and are coincident if a normal flow rule is assumed ($\psi = \phi$). We believe that leads form along characteristic lines. This relationship has been confirmed in a few cases for isotropic models by comparing satellite images with simulated results. It is expected to remain valid for anisotropic model results.

1. Introduction

Large-scale leads are the features that allow pack ice to deform. Lead formation, deformation, and evolution has been modeled most frequently by plasticity constitutive laws that treat the ice cover as a continuum, but admit stress and velocity discontinuities that are interpreted as deforming leads, rafts, and ridges. At smaller scales, fracture mechanics is used to describe the formation and growth of cracks that describe failure of the brittle ice [e.g., *Dempsey*, 2000; *Schulson and Hibler*, 1991; *Schulson, et al.*, 2006] More recently, *Schreyer, et al*. [2006] introduced a decohesion model to describe failure. Our goal here is to derive the mathematical characteristics of a quasi-steady, anisotropic plasticity model and to suggest how leads might form and evolve along them, thus showing that a plasticity model can describe this behavior.

*Shapiro and Burn*s [1975] and *Marko and Thomson* [1977] first described the rectilinear patterns seen in many sea ice images. *Shapiro and Burns* [1975] and several other authors [*Nye*, 1975; *Sodhi*, 1977; *Erlingsson*, 1988; *Pritchard*, 1988] described the mathematical characteristics associated with isotropic plasticity models of sea ice dynamics and argued that the sliplines are aligned with the rectilinear lead patterns. However, since the development of anisotropic plasticity laws within the past decade or so [*Coon, et al.*, 1992, 1998; *Pritchard*, 1998a; *Hibler and Schulson*, 2000; *Taylor, et al.*, 2006], there has been no comparable description of mathematical characteristics associated with the anisotropic plasticity laws. This paper aims to provide that description. Unfortunately, the characteristic analysis has not yet been completed for the fully time-dependent set of equations that describe sea ice dynamics behavior. Thus, the analysis presented here describes only characteristics and their potential discontinuities for the quasi-steady system of equations. These models resolve temporal changes having periods of a day or longer, but not synoptic scale motions that include inertial and tidal oscillations.

For many years, isotropic plasticity laws have been used in numerical models. This approach began with the Aidjex elastic-plastic (EP) model [*Coon, et al*., 1974; *Pritchard*, 1981] then continued with the *Hibler* [1979] viscous-plastic (VP) model and the *Hunke and Dukowicz* [1997] elastic-viscous-plastic (EVP) model. Many studies since that time have used these models. Later, an anisotropic plasticity law (AEP) was introduced to describe lead formation directly [*Coon, et al.*, 1992, 1998; *Pritchard*, 1998a]. The AEP model is quite fundamental and simple; all behavior can be described in terms of the deformation of ice having a single orientation. It can be thought of as an evolving lead that may raft or ridge. The AEP law assembles the oriented behavior by incorporating the amounts of ice in all orientations. Isotropy is a state where each orientation of ice covers the same area fraction [*Pritchard*, 1998a].

2. A Quasi-Steady Anisotropic Sea Ice Dynamics Model

The highest resolution continuum models attempt to describe ice behavior over length scales of order 10 to 20 km and time scales of order 3 hours. These models include tidal and inertial oscillations, and require a fully dynamics formulation. We have not yet studied the mathematical characteristics of these fully dynamic models, but have limited our attention to the more tractable quasi-steady formulations. In the quasi-steady formulations, all time derivatives are neglected. This approximation is appropriate if time is resolved to no shorter than about a day. The essential elements of such quasi-steady ice dynamics models are described next.

3.1. Quasi-steady Momentum Balance

The horizontal momentum equation describes the balance between Coriolis and sea surface tilt accelerations, external forcing by wind and water tractions, and internal stress divergence

$$m\left(f\mathbf{k}\times\mathbf{v}+g\nabla\eta\right)=\boldsymbol{\tau}_a-\boldsymbol{\tau}_w+\nabla\cdot\boldsymbol{\sigma} \qquad [1]$$

where m is areal mass density, $\mathbf{v}$ is ice drift velocity, f is the Coriolis parameter, $\mathbf{k}$ is a unit upward normal, $\times$ is the vector cross product, g is the gravitational constant, η is sea surface elevation, $\boldsymbol{\tau}_a$ is air stress, $\boldsymbol{\tau}_w$ is water stress, and $\nabla\cdot\boldsymbol{\sigma}$ is divergence of the internal stress $\boldsymbol{\sigma}$, a second-order tensor having horizontal Cartesian components

$$\boldsymbol{\sigma}=\begin{bmatrix}\sigma_{xx} & \sigma_{xy}\\ \sigma_{xy} & \sigma_{yy}\end{bmatrix}. \qquad [2]$$

The air and water stress are usually modeled as quadratic functions wind and ice velocity relative to the current beneath the mixed layer [e.g., *McPhee*, 1982]. Only the highest order derivatives affect the characteristic directions so it is not necessary to specify the air or water stress laws in detail. The governing equations in characteristic coordinates do depend on the specific form of the water stress law, but those solutions are beyond the scope of this paper.

3.2. Anisotropic Elastic-Plastic (AEP) Constitutive Law

When a lead is open, a uniaxial stress state exists. Figure 1 (left) shows the yield surface for a new lead with zero strength. It is a line parallel to the $\sigma_{\xi\xi}$-axis, and it is independent of this stress component, although one could allow the tensile strength to decrease with increasing confining pressure [*Schreyer, et al.*, 2006]). The direction of each such feature must be retained as part of the solution. Since behavior can differ in different directions, the constitutive law must be expressed in the three stress components $\left(\sigma_{xx},\sigma_{yy},\sigma_{xy}\right)$, rather than stress invariants as in isotropic laws. As ice grows in the lead, its strength increases. The rectangle shown in Figure 1 (right) is a simple yield surface that can be used for a lead containing ice having nonzero strength [*Coon et al.*, 1992, 1998]. The tensile, shear, and compressive strengths are independently defined. Each may depend on the ice conditions in the lead. This arbitrary shape can be replaced by a more realistic shape when more information is available. A thickness distribution is needed for each lead to define strength parameters in terms of ice conditions. Both thermal growth or melt and mechanical redistribution can affect its evolution.

The yield surface for a lead may be expressed easily in coordinates ξ and η, which are aligned along and across the lead, respectively. The stress components in these directions are $\left(\sigma_{\xi\xi},\sigma_{\eta\eta},\sigma_{\xi\eta}\right)$. Each lead yield surface must be expressed in global coordinates. This is accomplished by using the transformation for the stress tensor $\boldsymbol{\sigma}=\mathbf{Q}^{\mathbf{t}}\cdot\overline{\boldsymbol{\sigma}}\cdot\mathbf{Q}$, where $\boldsymbol{\sigma}$ and $\overline{\boldsymbol{\sigma}}$ are stress components expressed in global and lead coordinates, respectively, and $\mathbf{Q}$ is rotation

$$\mathbf{Q}=\begin{bmatrix}\cos\theta & -\sin\theta\\ \sin\theta & \cos\theta\end{bmatrix}. \qquad [3]$$

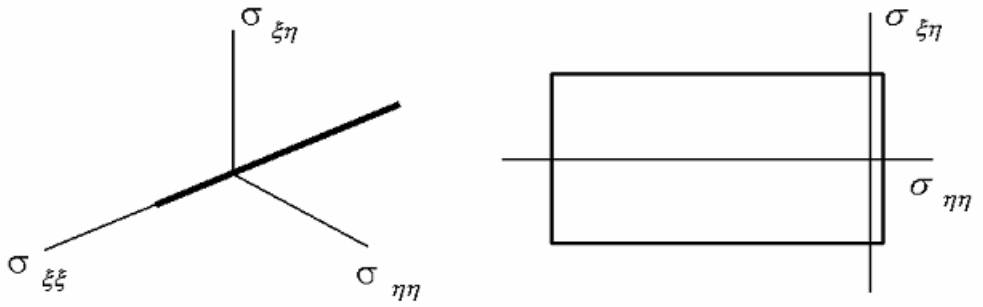

Figure 1. Lead yield surface. Left: A new lead. Right: An evolving lead.

Graphically, the yield surface for a lead in the θ direction is in a plane through the pressure axis σ_I that has angle 2θ from the σ_{xx} -axis. Thus, for an open lead the yield surface line is at this angle on the tensile cut-off cone.

To form the composite yield surface, a yield surface is determined for ice having each orientation. The stress state cannot violate the yield criterion of any of these features

$$\phi_j\left(\boldsymbol{\sigma}, \mathrm{K}_j\right) \le 0 \qquad \textbf{[4]}$$

where K_j represents strength variables that depend on the thickness distribution of the *j*-th feature. Then the composite yield surface is the limiting surface of stress states that are within all of the individual surfaces. This is an advantage of the *Coon et al*. [1992, 1998] constitutive law. It requires only that we determine the yield surface and flow rule for ice having a single orientation and it combines this information into a complete yield surface and flow rule.

Coon, et al. [1998] define isotropic ice as all of the consolidated multiyear and heavy first-year ice surrounding the leads. *Pritchard* [1998a] defined isotropy as a state containing equal fractions of ice having all orientations. These definitions are similar, but the latter requires that the isotropic yield surface have a (belted) diamond shape. It must be composed of the tensile cut-off cone (with generators at a 45 degree angle to the pressure axis), a compressive cone with the same angle to the pressure axis, and a cylinder whose shape depends on the shear strength of the lead yield surface. The isotropic yield surface is shown in Figure 2 for the lead yield surface shown in Figure 1. Here $p*$ and p_o are isotropic compressive and tensile strengths.

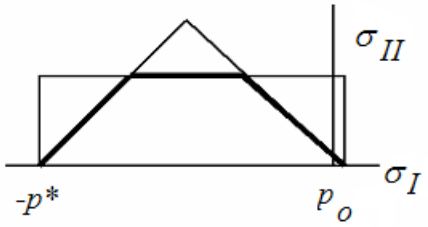

Figure 2. Isotropic belted diamond yield surface.

Plastic stretching is defined to be orthogonal to a potential function ψ. If a normal flow rule is assumed, then the potential function equals the yield surface $\psi = \phi$. If the stress state is at the intersection of more than one of the individual yield criteria (and this will occur frequently), then the plastic stretching is composed of contributions from each of the deforming features

$$\mathbf{D}_p = \sum_{j=1}^{m} \lambda_j \mathbf{N}_j \qquad \textbf{[5]}$$

where $\mathbf{N}_j = \partial \psi_j / \partial \boldsymbol{\sigma}$. If a normal flow rule is assumed, the tensor is orthogonal to the yield surface ϕ_j. Here *m* is the number of branches undergoing plastic deformation. The multipliers λ_j must be nonnegative. Plastic stretching of the *j*-th lead controls its redistribution. The flow rule for each lead may also be expressed in lead coordinates and transformed into global coordinates using $\mathbf{N}_j = \mathbf{Q}_j^t \cdot \overline{\mathbf{N}} \cdot \mathbf{Q}_j$ (there is no sum on j in this equation). A similar relationship exists for stretching, plastic stretching, and stress.

For the EP law, stress satisfies a linear elastic relationship

$$\boldsymbol{\sigma} = \mathbf{M} : \mathbf{e} \qquad [6]$$

where **M** is elastic modulus tensor and **e** is elastic strain. To date, the linear elastic behavior and the kinematic relationship remain identical to the isotropic EP model relationships. It would be more consistent to introduce different elastic moduli for ice having each orientation because the moduli must depend on the thicknesses of ice having that orientation. The elastic strain rate and plastic stretching are related by the kinematic expression [*Pritchard*, 1975]

$$\dot{\mathbf{e}} - \mathbf{W} \cdot \mathbf{e} + \mathbf{e} \cdot \mathbf{W} = \mathbf{D} - \mathbf{D}_p \qquad \textbf{[7]}$$

where **D** is stretching and **W** is spin, which are the symmetric and anti-symmetric parts of the velocity gradient, respectively. If rotation satisfies $d\mathbf{R}/dt = \mathbf{W} \cdot \mathbf{R}$, equation [7] becomes

$$\frac{d}{dt}\left(\mathbf{R}^t \cdot \mathbf{e} \cdot \mathbf{R}\right) = \mathbf{R}^t \cdot \left(\mathbf{D} - \mathbf{D}_p\right) \cdot \mathbf{R}. \qquad \textbf{[8]}$$

Quasi-steady behavior requires that we neglect the material derivative on the left hand side. Thus, in a quasi-steady model plastic stretching equals total stretching

$$\mathbf{D}_p = \mathbf{D}. \qquad [9]$$

This is also the kinematic relationship for the VP constitutive law. Thus, in the case of quasi-steady plastic flow, the EP and VP laws are identical to each other.

3. Mathematical Characteristics

Across a deforming lead, raft, or ridge, the stress tensor and velocity vector can be discontinuous. A continuum model can describe this ice state by including open water in the local thickness distribution and a velocity discontinuity in the velocity field. The stress tensor can be described similarly, but we must consider the traction vector $\mathbf{t} = \boldsymbol{\sigma} \cdot \mathbf{n}$, where **n** is the unit vector orthogonal to the lead. When the lead is closed, the traction must be continuous [e.g.,

Nye, 1975], which does not preclude the normal stress component along the lead from being discontinuous. It is well known that discontinuous behavior can occur only across mathematical characteristics or sliplines of plasticity models [e.g., *Courant and Hilbert*, 1962]. Following *Pritchard* [1988], we derive the mathematical characteristics for the quasi-static model that depends only on the two spatial dimensions, not time.

When stress is on a smooth part of the yield surface, the system of equations has six variables: three stress components $(\sigma_{xx}, \sigma_{yy}, \sigma_{xy})$, two velocity components (u, v), and the scalar multiplier λ. These variables must satisfy two momentum equations, three flow rule equations, and the yield constraint. When stress is at the intersection of two (or more) yield constraints with different slopes, the stress state is constrained by extra equations and plastic flow is composed of contributions from neighboring surfaces. This case is not analyzed here, although it is discussed.

The highest order derivatives of stress appear in the momentum equations [1]. The quasi-steady momentum equations balance of Coriolis and tilt accelerations, loads from wind and current, and stress divergence has components [e.g., *Pritchard*, 1988, 2001]

$$\begin{aligned} \frac{\partial \sigma_{xx}}{\partial x} + \frac{\partial \sigma_{xy}}{\partial y} &= -\tau_{ax} + \tau_{wx} - mf\left(v - v_g\right) \\ \frac{\partial \sigma_{xy}}{\partial x} + \frac{\partial \sigma_{yy}}{\partial x} &= -\tau_{ay} + \tau_{wy} + mf\left(u - u_g\right) \end{aligned} \qquad \textbf{[10]}$$

where (u_g, v_g) is the geostrophic ocean current and water stress (τ_{wx}, τ_{wy}) is a quadratic function of the relative velocity $(u - u_g, v - v_g)$. Details are not needed to determine characteristics because only the highest-order velocity derivatives appear in the flow rule equations. Again, following *Pritchard* [1988], we form the ratios of the shear component to each normal component of the flow rule in equation [5], reducing the flow rule to two equations and eliminating the scalar λ. These two equations involve velocity derivatives and stress-dependent derivatives of the potential surface

$$\begin{aligned} \frac{\partial \psi}{\partial \sigma_{xx}}\left(\frac{\partial u}{\partial y} + \frac{\partial v}{\partial x}\right) - 2\frac{\partial \psi}{\partial \sigma_{xy}}\frac{\partial u}{\partial x} &= 0 \\ \frac{\partial \psi}{\partial \sigma_{yy}}\left(\frac{\partial u}{\partial y} + \frac{\partial v}{\partial x}\right) - 2\frac{\partial \psi}{\partial \sigma_{xy}}\frac{\partial v}{\partial y} &= 0 \end{aligned} \qquad \textbf{[11]}$$

A non-normal flow rule is allowed by using the potential function ψ. The final equation is the yield constraint [4]. It enters the analysis as a differential form, but we await a coordinate transformation to characteristic directions before describing it.

The characteristic analysis is performed most simply if the velocity and stress components are affixed into a five-component solution vector (shown here as the transform)

$$\mathbf{Z}^t = \left\{ u \quad v \quad \sigma_{xx} \quad \sigma_{yy} \quad \sigma_{xy} \right\}. \qquad \textbf{[12]}$$

Two new independent coordinates ξ and η are introduced, with coordinate mappings

$$\begin{aligned} x &= X(\xi,\eta) \\ y &= Y(\xi,\eta) \end{aligned} . \qquad \textbf{[13]}$$

Along each such direction, the governing equations have a derivative only in that coordinate, not the other. If the subscripted coefficients $X_\xi = \partial X / \partial \xi$, etc are partial derivatives, then the derivatives of **Z** along Cartesian coordinates are related to these characteristic directions by

$$\begin{aligned} J\frac{\partial \mathbf{Z}}{\partial x} &= Y_\eta \frac{\partial \mathbf{Z}}{\partial \xi} - Y_\xi \frac{\partial \mathbf{Z}}{\partial \eta} \\ J\frac{\partial \mathbf{Z}}{\partial y} &= -X_\eta \frac{\partial \mathbf{Z}}{\partial \xi} + X_\xi \frac{\partial \mathbf{Z}}{\partial \eta} \end{aligned} \qquad \textbf{[14]}$$

where Jacobian $J = X_\xi Y_\eta - X_\eta Y_\xi$.

The final equations are introduced by differentiating the yield constraint along the characteristic directions. Since there are two such characteristic coordinates, there will actually be two such constraints, $\partial\phi/\partial\xi = 0$ and $\partial\phi/\partial\eta = 0$. If we assume the yield constraint is satisfied along the ξ coordinate direction, its derivative expands to the form

$$\frac{\partial \phi}{\partial \xi} = \frac{\partial \phi}{\partial \sigma_{xx}}\frac{\partial \sigma_{xx}}{\partial \xi} + \frac{\partial \phi}{\partial \sigma_{yy}}\frac{\partial \sigma_{yy}}{\partial \xi} + 2\frac{\partial \phi}{\partial \sigma_{xy}}\frac{\partial \sigma_{xy}}{\partial \xi} + \frac{\partial \sigma}{\partial \mathbf{K}} : \frac{\partial \mathbf{K}}{\partial \xi} \qquad \textbf{[15]}$$

where **:** is the double inner product and the material parameter tensor **K** can have an arbitrary number of components. An analogous equation is satisfied along the η coordinate direction. The factor '2' appears because one must consider all four components of the stress tensor when forming the derivative, even though the off diagonal terms have equal values.

If all transformed equations are affixed into a matrix form, the governing partial differential equation expressed in characteristic coordinates becomes

$$\mathbf{P}\frac{\partial \mathbf{Z}}{\partial \xi} + \mathbf{Q}\frac{\partial \mathbf{Z}}{\partial \eta} + J\mathbf{F} = 0 . \qquad \textbf{[16]}$$

Coefficient matrices **P** and **Q** and the forcing vector **F** are

$$\mathbf{P} = \begin{bmatrix} -X_\eta \frac{\partial \psi}{\partial \sigma_{xx}} - 2Y_\eta \frac{\partial \psi}{\partial \sigma_{xy}} & Y_\eta \frac{\partial \psi}{\partial \sigma_{xx}} & 0 & 0 & 0 \\ -X_\eta \frac{\partial \psi}{\partial \sigma_{yy}} & Y_\eta \frac{\partial \psi}{\partial \sigma_{yy}} + 2X_\eta \frac{\partial \psi}{\partial \sigma_{xy}} & 0 & 0 & 0 \\ 0 & 0 & Y_\eta & 0 & -X_\eta \\ 0 & 0 & 0 & -X_\eta & Y_\eta \\ 0 & 0 & \frac{\partial \phi}{\partial \sigma_{xx}} & \frac{\partial \phi}{\partial \sigma_{yy}} & 2\frac{\partial \phi}{\partial \sigma_{xy}} \end{bmatrix} \qquad \textbf{[17]}$$

$$\mathbf{Q}=\begin{bmatrix} X_\xi\dfrac{\partial\psi}{\partial\sigma_{xx}}+2Y_\xi\dfrac{\partial\psi}{\partial\sigma_{xy}} & -Y_\xi\dfrac{\partial\psi}{\partial\sigma_{xx}} & 0 & 0 & 0 \\ X_\xi\dfrac{\partial\psi}{\partial\sigma_{yy}} & -Y_\xi\dfrac{\partial\psi}{\partial\sigma_{yy}}-2X_\xi\dfrac{\partial\psi}{\partial\sigma_{xy}} & 0 & 0 & 0 \\ 0 & 0 & -Y_\xi & 0 & X_\xi \\ 0 & 0 & 0 & X_\xi & -Y_\xi \\ 0 & 0 & \dfrac{\partial\phi}{\partial\sigma_{xx}} & \dfrac{\partial\phi}{\partial\sigma_{yy}} & 2\dfrac{\partial\phi}{\partial\sigma_{xy}} \end{bmatrix} \quad \textbf{[18]}$$

$$\mathbf{F}=\begin{Bmatrix} 0 \\ 0 \\ -\tau_{ax}+\tau_{wx}-mf\left(v-v_g\right) \\ -\tau_{ay}+\tau_{wy}+mf\left(u-u_g\right) \\ \dfrac{\partial\phi}{\partial\mathrm{K}}:\dfrac{\partial\mathrm{K}}{\partial\xi}+\dfrac{\partial\phi}{\partial\mathrm{K}}:\dfrac{\partial\mathrm{K}}{\partial\eta} \end{Bmatrix}. \quad \textbf{[19]}$$

This set of partial differential equations can be reduced to a set that has a derivative only in the ξ coordinate direction if and only $\mathbf{Q}\partial\mathbf{Z}/\partial\eta=0$. A nontrivial partial derivative solution then exists only if the determinant of the coefficient matrix is zero $|\mathbf{Q}|=0$. Expanding the elements of **Q** gives two separate solutions, one for the momentum and yield constraint equations and the other for the flow rule.

Along the ξ-direction(s), stress characteristics satisfy

$$Y_\xi Y_\xi\frac{\partial\phi}{\partial\sigma_{yy}}+2X_\xi Y_\xi\frac{\partial\phi}{\partial\sigma_{xy}}+X_\xi X_\xi\frac{\partial\phi}{\partial\sigma_{xx}}=0 \quad \textbf{[20]}$$

which is derived by forming the determinant of the last three rows and columns. This is a remarkably simple result for the general anisotropic plasticity law. When written in this form, it correctly treats the special cases when either X_ξ or Y_ξ is zero. It is a bit clearer if direction cosines are introduced to describe the coordinate mappings. To this end let the ξ-axis makes angle κ with the *x*-axis, i.e., $X_\xi=\cos\kappa$ and $Y_\xi=\sin\kappa$. Substituting and simplifying gives

$$\tan\kappa=\frac{-\dfrac{\partial\phi}{\partial\sigma_{xy}}\pm\sqrt{\left(\dfrac{\partial\phi}{\partial\sigma_{xy}}\right)^2-\dfrac{\partial\phi}{\partial\sigma_{yy}}\dfrac{\partial\phi}{\partial\sigma_{xx}}}}{\dfrac{\partial\phi}{\partial\sigma_{yy}}}. \quad \textbf{[21]}$$

Along the ξ-direction(s), the velocity characteristics satisfy

$$\left(X_\xi \frac{\partial \psi}{\partial \sigma_{xx}} + 2Y_\xi \frac{\partial \psi}{\partial \sigma_{xy}} \right)\left(-Y_\xi \frac{\partial \psi}{\partial \sigma_{yy}} - 2X_\xi \frac{\partial \psi}{\partial \sigma_{xy}} \right) - \left(-Y_\xi \frac{\partial \psi}{\partial \sigma_{xx}} \right)\left(X_\xi \frac{\partial \psi}{\partial \sigma_{yy}} \right) = 0 \qquad \textbf{[22]}$$

which simplifies to

$$Y_\xi Y_\xi \frac{\partial \psi}{\partial \sigma_{yy}} + 2X_\xi Y_\xi \frac{\partial \psi}{\partial \sigma_{xy}} + X_\xi X_\xi \frac{\partial \psi}{\partial \sigma_{xx}} = 0 \qquad \textbf{[23]}$$

if $\partial\psi / \partial\sigma_{xy} \neq 0$. This exception is included in equation [23] if x and y are principal coordinates of stretching. For a normal flow rule ($\psi = \phi$), the velocity and stress characteristics are aligned.

Equation [20] has two real solutions if the discriminant in equation [21] is positive (hyperbolic), one if zero (parabolic), and none if negative (elliptic). A similar result follows from equation [23]. The second characteristic coordinate direction η satisfies the same equations as seen when we set $|\mathbf{P}| = 0$. Thus, all roots have been determined from equations [20] and [23]. We next discuss these conditions for several simple examples: failure from an isotropic state, and failure in a specified direction.

3.3. Isotropic Failure

The isotropic yield surface can be described by rewriting equation [4] into the isotropic form

$$\phi = \sigma_{II} - b(\sigma_I, p^*, p_o) \qquad \textbf{[24]}$$

where b defines the yield surface shape, $\sigma_I = \frac{1}{2}\boldsymbol{\sigma} : \mathbf{1}$ is the negative pressure, $\sigma_{II} = \sqrt{\frac{1}{2}\boldsymbol{\sigma}' : \boldsymbol{\sigma}'}$ is the shear stress invariant, and $\boldsymbol{\sigma}' = \boldsymbol{\sigma} - \sigma_I \mathbf{1}$ is the deviatoric stress tensor. The gradient with respect to stress is

$$\frac{\partial \phi}{\partial \boldsymbol{\sigma}} = -b'\mathbf{1} + \frac{\boldsymbol{\sigma}'}{\sigma_{II}} \qquad \textbf{[25]}$$

where $b' = \partial b / \partial \sigma_I$. Substituting these derivatives into equation [20] gives

$$X_\xi X_\xi \left(-b' + \frac{\sigma'_{xx}}{\sigma_{II}} \right) + Y_\xi Y_\xi \left(-b' + \frac{\sigma'_{yy}}{\sigma_{II}} \right) + 2X_\xi Y_\xi \left(\frac{\sigma'_{xy}}{\sigma_{II}} \right) = 0. \qquad \textbf{[26]}$$

Express the stress components in terms of the stress invariants and principal direction γ

$$\boldsymbol{\sigma} = \begin{bmatrix} \sigma_I + \sigma_{II}\cos\gamma & \sigma_{II}\sin\gamma \\ \sigma_{II}\sin\gamma & \sigma_I - \sigma_{II}\cos\gamma \end{bmatrix}. \qquad \textbf{[27]}$$

Finally, substitute these components into equation [26] and simplify to

$$cos2(\kappa - \gamma) = b'. \qquad \textbf{[28]}$$

in agreement with *Pritchard* [1988]. Two real characteristic directions exist when $|b'| < 1$, the hyperbolic case. They are symmetric about the principal stress axis. One real characteristic

direction exists when $|b'| = 1$, the parabolic case. It is aligned with the direction of larger principal stress $\kappa = \gamma$. No real characteristic directions exist when $|b'| > 1$, the elliptic case.

3.4. Failure across Vertical Line

Consider the case when the yield surface ϕ is independent of the normal stress component σ_{yy}. Two solutions to equation [20] exist for the characteristic equation: the first is aligned with the *y*-axis

$$X_\xi = 0 \qquad \textbf{[29]}$$

and the second is aligned at angle

$$\tan\kappa = -\frac{1}{2}\frac{\partial\phi/\partial\sigma_{xx}}{\partial\phi/\partial\sigma_{xy}}. \qquad \textbf{[30]}$$

In this case, a lead can form along the direction of the *y*-axis. Two special cases arise. If the yield surface slope is vertical, the second characteristic satisfies $\kappa = \pi/2$ and it is therefore aligned with the first characteristic direction. This system is parabolic as there is only one real direction. If the slope is less than vertical, the second characteristic direction is at an acute angle to the *x*-axis. Since any coordinate system could be used, this case describes the formation of a lead in any direction (when expressed in lead coordinates).

4. Discussion, Summary, and Conclusions

We have derived the conditions under which real characteristic directions exist at a point. Stress characteristics depend on yield surface shape. The system is hyperbolic (two directions), parabolic (one direction), or elliptic (no directions) depending on whether the discriminant *D*

$$D = \left(\frac{\partial\phi}{\partial\sigma_{xy}}\right)^2 - \frac{\partial\phi}{\partial\sigma_{yy}}\frac{\partial\phi}{\partial\sigma_{xx}} \qquad [\textbf{31}]$$

is positive, zero, or negative. The directions of these characteristics are at angle κ to the *x*-axis

$$\tan\kappa = \frac{-\frac{\partial\phi}{\partial\sigma_{xy}} \pm \sqrt{\left(\frac{\partial\phi}{\partial\sigma_{xy}}\right)^2 - \frac{\partial\phi}{\partial\sigma_{yy}}\frac{\partial\phi}{\partial\sigma_{xx}}}}{\frac{\partial\phi}{\partial\sigma_{yy}}}. \qquad [21bis]$$

The anisotropic elastic-plastic constitutive law has many desirable properties. Lead systems can form and evolve. It is tractable to numerical solution methods [*Pritchard*, 1998b]. The yield surface can be chosen from simple identifiable deformation processes. However, it seemed that the system must be parabolic when stress is on the tensile cutoff cone. Although this property might be desirable, it is also a strong limitation. The AEP law can be extended by allowing a lead yield surface to depend on the confining stress along the lead direction [*Schreyer, et al.,* 2006], which could allow the system to be hyperbolic if desired.

Thus far, we have assumed that the yield surface is smooth. However, in many cases, two different surfaces (perhaps a lead and the isotropic surface) intersect to form a corner. We have introduced the methodology for defining plasticity behavior in this case, but have not presented the characteristic analysis. *Pritchard* [1988] showed that no real characteristic directions could exist when stress is at a corner on an isotropic yield surface. The same might be true for the anisotropic model, but we must study this case in more detail. We now argue as follows. Assume that two surfaces intersect at an angle, but that the intersection is made smooth by a small fillet radius. The previous analysis shows that real characteristics may exist when stress is on the fillet radius and that their orientations vary smoothly between orientations determined from the neighboring surfaces. We ignore pathological cases here. As the fillet radius is shrunk toward zero, the characteristic directions span the same range, but the stress approaches a single state. Thus, at a single stress state, many directions would be characteristic, which is meaningless. We could look at the velocity characteristics expressed in terms of the stretching tensor, but this work has not yet been completed.

We have tacitly assumed that leads form along characteristic lines. *Pritchard* [1981] showed this to be true in a Beaufort Sea simulation and the assumption has been made by others who have studied characteristics [e.g., *Shapiro and Burn*s, 1975; *Nye*, 1975; *Sodhi*, 1977; *Erlingsson*, 1988; *Pritchard*, 1988], but more simulations are needed to confirm this association. The essential point is that leads are important features for offshore operators, whether physical scientists, biologists, navigators, or drillers. Furthermore, they are easily seen in satellite images and are therefore useful for testing model behavior.

This analysis has been limited to quasi-steady plasticity models. While valuable for models resolving daily ice motions, more work is needed to understand fully dynamics systems where time is an independent variable, not simply a parameter.

As we learn more about the existence of discontinuous model behavior, it would be wise to incorporate them into our numerical methods explicitly. Numerical schemes used today do not describe discontinuities explicitly, but instead approximate them as large differences over a few discrete elements or cells. *Schreyer, et al*. [2006] introduced an explicit description for velocity discontinuities in a decohesion law that might also be useful for describing the discontinuities that appear along characteristic sliplines.

5. References

Coon, M. D., G. A. Maykut, R. S. Pritchard, D. A. Rothrock, and A. S. Thorndike (1974). Modeling the pack ice as an elastic-plastic material. *Aidjex Bulletin* No. 24, Seattle, University of Washington, pp.1-105.

Coon, M. D., Echert, D. C., and Knoke, G. S. (1992). Pack Ice Anisotropic Constitutive Law. *IAHR 92, Proceedings of the 11th International Symposium on Ice*. Banff, Alberta.

Coon, M., G. Knoke, D. Echert, and R. Pritchard (1998), The architecture of an anisotropic elastic-plastic sea ice mechanics constitutive law, *J. Geophys. Res.*, *103* (C10), doi:10.1029/98JC01259, pp.21915-21925.

Courant, R., and D. Hilbert (1962), *Methods of Mathematical Physics*, Interscience Publishers, New York.

Dempsey, J. (2000), Research trends in ice mechanics, *Int'l. J. of Solids and Structures*, *37*, pp.131-153.

Erlingsson, B. (1988), Two-dimensional deformation patterns in sea ice, *J. Glaciol.*, *34*, pp.301-308.

Hibler, W. D., III (1979). "A dynamic thermodynamic sea ice model." *J. Phys. Ocean*., 9, pp.817-846.

Hunke, E. C., and Dukowicz, J. K. (1997). "An elastic-viscous-plastic model for sea ice dynamics." *J. Phys. Ocean*. 27, pp.1849-1867.

Marko, J., and R. Thomson (1977), Rectilinear Leads and Internal Motions in the Ice Pack of the Western Arctic Ocean, *J. Geophys. Res.*, *82*(6), pp.979-987.

McPhee, M. G. (1982), Sea ice drag laws and simple boundary layer concepts, including applications to rapid melting, CRREL Rep. No. 82-4, Cold Regions Research and Engr. Lab., Hanover, NH.

Nye, J. F. (1975), Discontinuities in the AIDJEX model, in *AIDJEX Bulletin* No. 28, pp. 119-126, University of Washington, Seattle.

Pritchard, R. S. (1975), An Elastic-Plastic Constitutive Law for Sea Ice, *J. Appl. Mech.*, *42* (E2), pp.379-384.

Pritchard, R. S. (1981), Mechanical behavior of pack ice, in *Mechanics of Structured Media*, edited by A. P. S. Selvadurai, pp. 371-405, Elsevier, Amsterdam.

Pritchard, R. S. (1988). "Mathematical characteristics of sea ice dynamics models." *J. Geophys. Res*. **93**(C12), pp.15,609-15,618.

Pritchard, R. S. (1998a). "Ice Conditions in an Anisotropic Sea Ice Dynamics Model." *Int'l. J. of Offshore and Polar Engineering,* 8(1), pp.9-15.

Pritchard, R. S. (1998b), Integrating an Anisotropic Plasticity Law for Sea Ice, paper presented at Ice in Surface Waters, Proceedings of the 14th Int'l Symposium on Ice, July 27-31, A. Balkema, Clarkson University, Potsdam, NY, pp.821-827.

Pritchard, R. S. (2001). "Long-term sea ice dynamics simulations using an elastic-plastic constitutive law." *J. Geophys. Res*. **106**(C12), pp.31,333-33,343.

Schreyer, H. L., D. L. Sulsky, L. B. Munday, M. D. Coon, and R. Kwok (2006), Elastic-decohesive constitutive model for sea ice, *J. Geophys. Res.*, *111* (C11), C11S26, doi:10.1029/2005JC003334.

Schulson, E. M., A. L. Fortt, D. Iliescu, and C. E. Renshaw (2006), Failure envelope of first-year Arctic sea ice: The role of friction in conpressive fracture, *J. Geophys. Res.*, *111* C11S25, doi:10.1029/2005JC003235.

Schulson, E. M., and W. D. Hibler, III (1991), The fracture of ice on scales large and small: Arctic leads and wing cracks, *J. Glaciol.*, *37*, pp.319-322.

Shapiro, L. H., and H. H. Burns (1975), Satellite Observations of Sea Ice Movement in the Bering Strait Region, in *Climate of the Arctic*, edited by G. Weller and S. A. Bowling, pp.79-386, Geophysical Institute, University of Alaska, Fairbanks, AK.

Sodhi, D. S. (1977), Ice Arching and the Drift of Pack Ice Through restricted channels, CRREL, Hanover, NH.

Taylor, P. D., D. L. Feltham, P. R. Sammonds, and D. Hatton (2006), Continuum sea ice rheology determined from subcontinuum mechanics, *J. Geophys. Res.*, *111* (C11), C11015, doi:10.1029/2005JC002996.

19th IAHR International Symposium on Ice
"Using New Technology to Understand Water-Ice Interaction"
Vancouver, British Columbia, Canada, July 6 to 11, 2008

Sea-Ice Linear Kinematic Features as Mathematical Characteristics of Coulombic Faulting with Dilatation

W. D. Hibler, III[1], E. M. Schulson[2], R. Kwok[3]
[1]*University of Alaska Fairbanks, Fairbanks, AK 99712* billh@iarc.uaf.edu
[2]*Thayer School of Engineering, Dartmouth College, Hanover, NH 03755*
[3]*Jet Propulsion Laboratory, Pasadena California*

Abstract

Numerical simulations with initial random weaknesses have successfully simulated oriented linear kinematic features. With coulombic plastic rheologies such simulations tend to yield more prominent faulting features than those with smoothly varying yield curves with a normal flow rule (Hutchings et. al., 2005). Less well appreciated is the dependence of the simulated intersecting angles of such features on the flow rule and degree of dilatation in fixed flow coulombic failure criteria. To rectify this situation a general derivation of the equations of motion for a system undergoing plastic flow and forming linear kinematic features is presented which demonstrates that optimal intersecting faults coincide with the mathematical characteristics of plastic flow in such faults. These characteristics depend on the flow rule as well as the friction angle of the coulombic failure criterion, a result which is verified numerically using numerical simulations with heterogeneous strengths and fixed wind forcing together with weakening or strengthening. Also presented is a scaling relation for spacing of linear kinematic features depending on wind stress gradient, average ice strength, and the distribution of weaknesses in the ice pack.

1. Introduction

Detailed spatial observations of the Arctic pack ice velocity field from SAR imagery (e.g., Kwok, 2001) show concentrated regions of deformation, especially shear strain. A perspective view of such features, commonly referred to as linear kinematic features (lkf), is shown in Figure 1. Since the Arctic pack ice is most commonly considered (Hibler, 1979;Pritchard, 2001)) to be some type of highly heterogeneous rigid plastic continuum, the similarity of these features to slip lines observed in classical plasticity theory has been noted by a number of authors(Pritchard, 1988; Overland et. al., 1995). While not necessarily inconsistent with plastic deformation features other authors have emphasized the similarity between these features and the brittle fracture of biaxially stressed pack ice in the laboratory (Schulson and Hibler, 2004).

Another seemingly similar, but quantitatively different explanation of these zones is to associate them with coulombic failure zones in two dimensions (Marko and Thompson, 1977, Overland et. al., 1995). In this strictly static force based explanation, sliding friction along any surface (line) in two dimensions is related to the normal force acting normal to the surface via some friction coefficient in an analogous manner to say a particle sliding down an inclined plane. With this idealization for a given stress state with fixed principal axes ratio it is easy to show by rotating the stress tensor to given co-ordinate system, that there are conjugate lines along which failure can occur at a minimum stress level with the intersection of the most likely failure directions dependent on the friction coefficient. This explanation differs subtly from the plastic flow definition (Mendelson, 1968) with the slip line being a particular manifestation of plastic flow, possibly smooth, occurring over a region. In the friction only based argument, for example, there is considered to be a discontinuous slip no matter how small the scale is. In plane strain plastic flow based on von mises plasticity theory, on the other hand, in a region of smooth plastic flow occurring over a finite region (which for plane strain must be pure shear flow with no dilatation) there are still sets of slip lines in existence even though there is no particular discontinuity occurring in say, the middle of the flowing region.

Analogous to two dimensional analyses used in soil mechanics , rheologies of two dimensional pack ice do not always assume normal flow. This is mainly because the system is being described as two dimensional only as opposed to a special case of three dimensional plasticity; plane strain for two dimensional systems from Von Mises theory for example. Two dimensional pack ice rheologies necessarily become more complex because of this.

The extension of slip line/characteristic theory to normal flow rheologies in two dimensions, most notably the elliptical yield curve proposed for sea ice by Hibler(1979), has been carried out by Pritchard (1988). In the case of pure shearing deformation, he recovers the classic Von Mises result yielding slip lines intersecting at 90^{o}, while flow with dilation characteristics occurs with more acute intersection angles. As in classic plastic flow, these characteristics can exist in a region of smooth plastic flow. However, the concept is that these characteristics would be associated with linear kinematic feature directions and character given appropriate boundary conditions and flow field. In some sense this derivation points out some of the limitations of normal flow rule descriptions of two dimensional sea ice failure and flow. For example suppose

we have a coulombic failure criterion, based on the friction coefficient concept, with no dilatation.

In this paper an the slip line/characteristic line theory is extended to more general two dimensional pack ice rheologies largely making use of a more direct physical model of linear kinematic features; namely that they are a zone of plastic failure and flow obeying both the friction and flow characteristics of an assumed rheology, possibly coulombic. This approach reduces to the normal flow results in that limit, but otherwise yields different results. The most notable result is that intersection angles of characteristics, or in our case linear kinematic features, depends not only on the friction coefficient but the assumed flow characteristics of the material, especially the material failing in the failure zone. A true slip line can be recovered in this derivation by assuming no dilatation, and the angles will be less than 90^o for a non zero friction coefficient. However, they will differ (larger) from angles based on simple static friction arguments. The difference can be traced to the essential physical model rather than the mathematics. Here for such a case plastic flow over a finite region must be allowed for, so for example, the failure zone is considered to be an arbitraily narrow region of pure shearing flow. We note that since this is effectively an implict assumption in plastic continuum models of pack ice, it is not surprising that this theory has generally been shown to be consistent (Hutchings et al, 2005; also see examples below) with simulated linear kinematic features using such models.

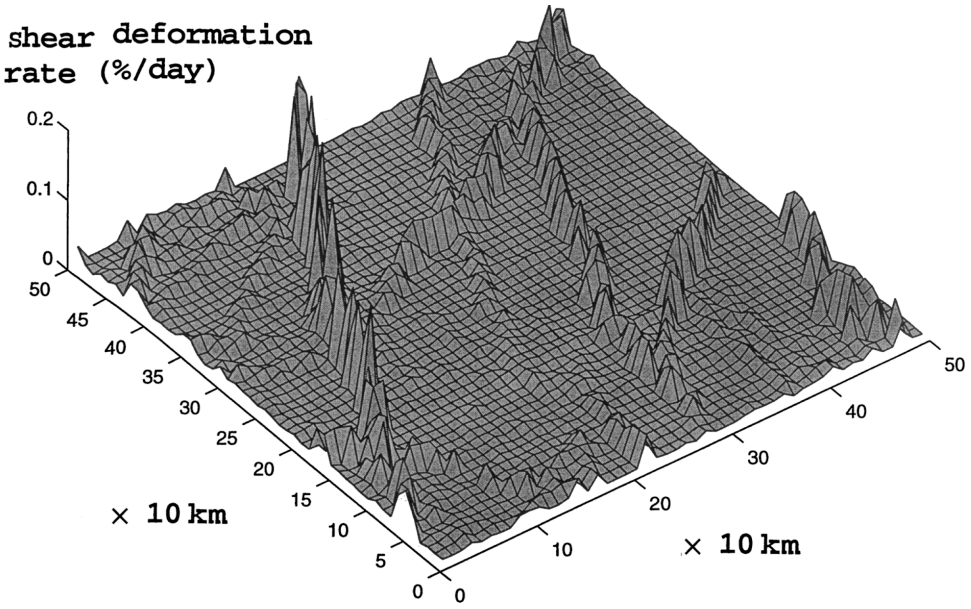

Figure 1. Example of intersecting linear kinematic features obtained from sequential synthetic aperture radar (SAR) images over a three-day period in the central Arctic Basin (see Kwok (2001)).

2. Conceptual framework and scale independent assumptions

To describe the large scale sea ice continuum we consider a rigid 'plastic' rheology with some type of non normal flow rule. The yield curve (Figure 2a) we will use later in the paper with the viscous plastic (Hibler, 1979) numerical approximation of rigid plastic flow is the modified coulombic rheology of Hibler and Schulson (2000). The two dimensional failure stress of this rheology has been taken from biaxial compression brittle failure tests (Schulson and Nickoleyev, 1995) of fresh water Ice. The flow rule for the coulombic failure portion of this yield curve is taken to vary smoothly from pure dilation at the tensile cusp to pure shear at the intersection of the compressive cap and the constant coulombic failure surface. It can be shown to be fully energy dissipative. This overall yield curve reflects the qualitative character of the failure observed in the laboratory inasmuch as under compressional failure of uniform ice an failure zone with initial divergence forms. The initial opening is due largely to a series of oriented wing cracks forming and then deforming in the failure zone. More details on the rheology and its non normal flow rule are given in Hibler and Schulson(2000). The main point here is that it has a non normal flow rule. An additional implicit assumption is that this yield curve applies to all scales from the laboratory to the geophysical scale, albeit with different strengths (Schulson and Hibler, 2004).

The basic idea of linear kinematic features as a plastic failure zone may be gotten from Figure 2b which shows numerical simulation results of deformation under a constant stress ratio forcing at the boundaries of a rectangular grid. (See Hibler and Schulson (2000) for grid and numerical details.) Basically in this numerical simulation a center grid cell has been taken weaker than all the other cells so as to initiate or nucleate symmetric damage (actually deformation) strikes.

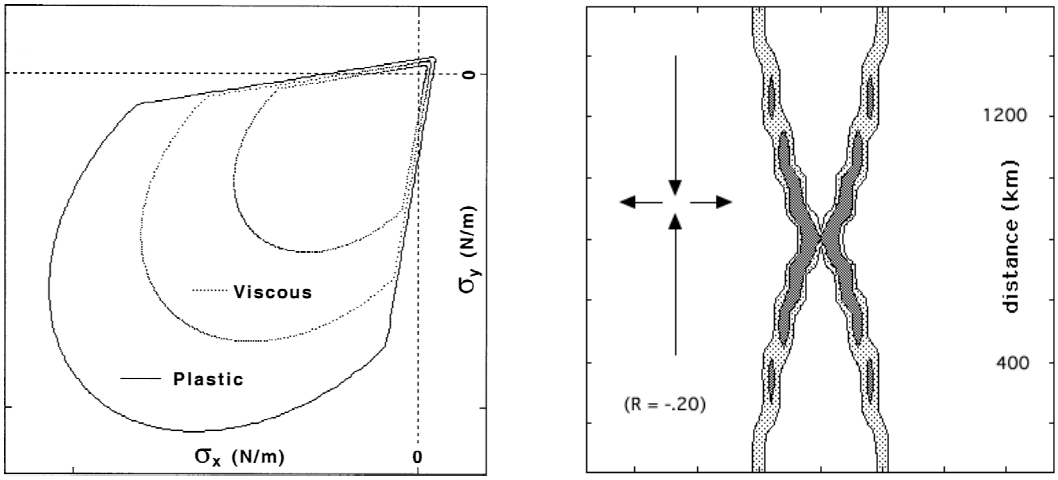

Figure 2. a(left hand panel):A coulombic yield curve with non normal flow rule based on laboratory observations of the brittle failure of ice. The dotted lines are stress states for very small strain rates. 2b(right hand panel): intersecting deformation failure zones obtained by using this yield curve in a numerical bi-axial stress experiment with a single weakness at the center of the grid. See Hibler and Schulson (2000), for more details and scale of deformation in 2b. Darker shades indicate higher strain rate invariants.

Although the forcing is much simpler than that applying on the geophysical scale, these deformation zones bear a pronounced similarity to the linear kinematic features shown in Figure 1 above. What we wish to do here is to show that these oriented deformation zones are effectively mathematical characteristics of the equations of motion of a plastic system obeying a yield curve, say, similar to Figure 2a. The fact that they have qualitative similarities to the oriented deformation features in Figure 1 is already clear. To carry out an analysis demonstrating this we will further idealize these failure zones as shown in Figure 3a to be an arbitrarily thin deformation zone with the ice on either side moving rigidly. In this deformation zone and the adjacent rigid ice normal continuity of stresses applies so that referring to the figure σ_{11} and σ_{12} are both continuous, while σ_{22} may be different in the thin ice and the thick ice as the two stresses do not share a common face.

While there are substantial similarities between these oriented failure zones and the slip lines that occur when classical volume conserving 3-D plasticity theory (say Von Mises) is applied to a two dimensional plate, there are important differences. Some of these differences may be deduced from the two dimensional yield curve and pure shear flow (rule) (Figure 3b) that applies from Von Mises Theory applied to a two dimensional plate undergoing plane strain (Mendelson, 1968). The main point is that the Von Mises yield curve, being a very special case of the full three dimensional cylinder yield surface, for plane strain has very restrictive deformation allowable (only pure shear) with a particular type of failure along (dictated by the tangent to yield curve) such that the friction characteristics are independent of confining stress. In this case the idealization of Figure 3a still applies, with the caveat that pure slip along the deformation zone is now occurring and hence pure shear in the zone.

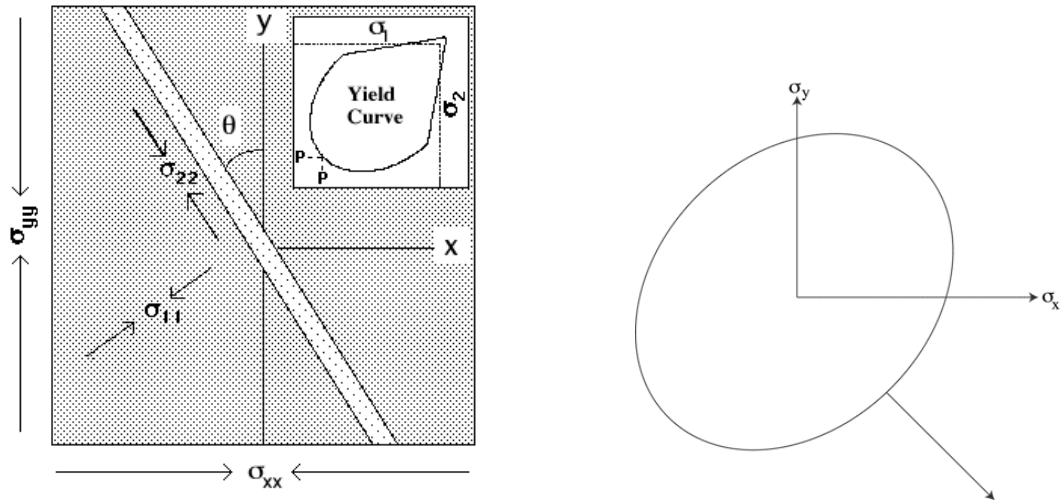

Figure 3. a(left hand panel): Schematic of narrow idealized deformation zone occurring thru relatively 'rigid' sea ice. 3b (right hand panel): Schematic of particular allowable flow and stress for von-mises plain strain occurring in a thin two dimensional plate.

3. Equations of motion of Plastic Flow in Oriented Failure Zones

To obtain the equations of motion in the region of the failure zone consider two intersection failure zones as shown in Fig 4a with a close up view of the strain along one of the failure zones shown in Fig 4b. Two intersecting failure zones are not essential to the argument; rather the important point is that the principal stresses in the rigid ice are taken to be aligned as shown by the boundary arrows in Fig 4a. Since wind and water drag body forces apply to this system the stresses in the rigid ice are not constant. However, by considering the failure zone sufficiently small the stress and strain state there (and the boundary stresses along the sides) may be considered constant.

Considering this region to be in steady state motion (accelerations may also be considered as d'alembert forces) under fixed wind and water drag forces, we may derive the equations of motion in the normal engineering fashion (Fung, 1977) by considering the region of 4a (or 4b) to be arbitrarily small with the stresses on opposing faces to differ by differential amounts $d\sigma$. Note that with the failure zones present, we are essentially carrying out a double limiting process here whereby the failure zones are arbitrarily small compared to the scale of the differential element used to obtain the stress derivative. Summing up the stresses on the face and going to the limit of $d\sigma \sim 0$ we obtain the normal equation of motion for the differential element

$$\frac{\partial \sigma_{ij}}{\partial x_j} = F_i^{\mathbf{a}} + F_i^{\mathbf{w}} + F_i^{\mathbf{d}} \qquad (1)$$

where we have used tensor notation with repeated subscripts summed over i,j =1 to 2 for the two dimensional system. Here $F_i^{\mathbf{a}}$, $F_i^{\mathbf{w}}$, and $F_i^{\mathbf{d}}$ are the i'th cartesian components of the wind drag and water drag forces and acceleration expressed as a d'alembert force.

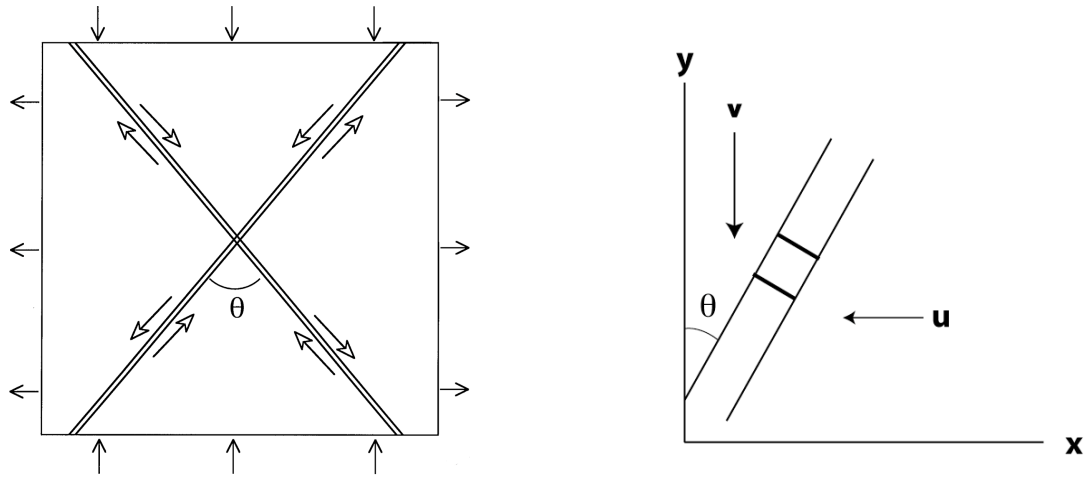

Figure 4. a(left hand panel) Schematic of strain and stress in the region of two intersecting narrow failure zones. 4b(right hand panel): amplified view of one of the idealized narrow failure zones together with rigid motion vectors on either side of the zone.

3.1 Relation of stress and strain rate to failure zone orientation

To proceed further we need to relate the stresses at the faces of the failure zone to the failure zone orientation. For this purpose we consider a coulombic failure curve with fixed dilatation and friction shown in principal axis space in Figure 5a. More general cases may be considered by linearizing the stress strain relations in the stress region of interest. Figure 5b shows the various stresses and principal axes in the failure zone with the boundary stresses represented in terms of ratios. In the case of Fig 5a, the principal axis yield curve may be related to shear and compressive stresses along any given face at failure in a well known manner by $\sigma_s = \mu\sigma_n + b$ where σ_s is the shear stress along the line, σ_n is the normal stress, μ is the coefficient of friction and b is some constant related to cohesive strength (see for example Hibler and Schulson, 2000). In the case of plane strain with von mises plastic flow $\mu = 0$.

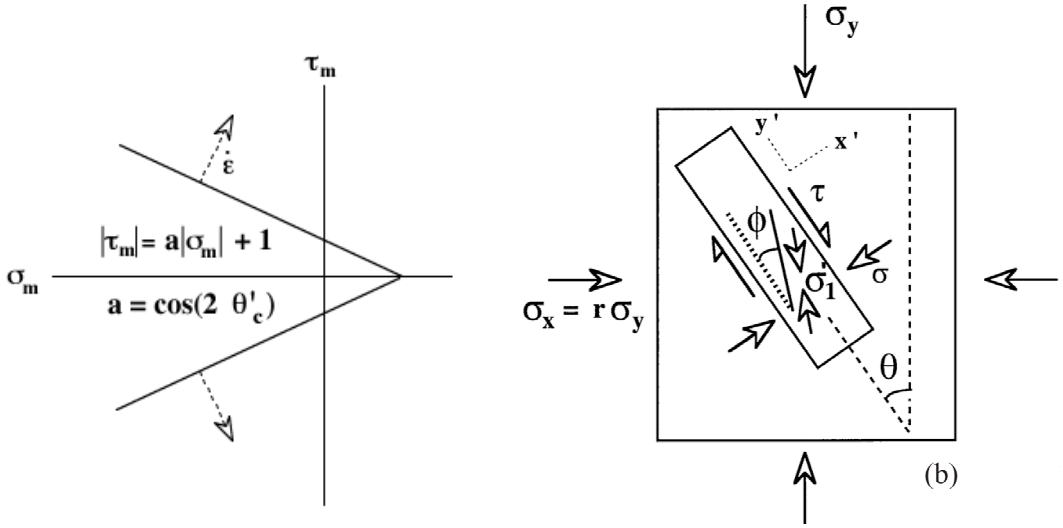

Figure 5. a(left hand panel): Coulombic yield curve and flow rule for fixed dilatation in principal axes space. 5b (right hand panel): Stress states in rigid ice and in a narrow deformation zone.

To derive the orientation dependence for a the fixed dilatation fixed friction failure criterion (Fig. 5a) we take the failure in the deformation zone to be given by $\sigma_s' = \sigma_c' + 1$ where without loss of generality for this argument we have taken a particular cohesive stress so that $\sigma_s' = 1$ at $\sigma_c' = 0$. Referring to Figure 5b, the appropriate mohrs circle construction for the stress state in the deformation zone is given in Figure 6a. From these figures the shear and compressive stresses across the deformation zone are given by

$$\tau = (a\sigma_c' + 1)\sin(2\phi) = \sigma_y \frac{(1-r)}{2}\sin(2\theta) \qquad (2)$$

$$\sigma = \sigma_c^{'} - (a\sigma_c^{'} + 1)\cos(2\phi) = \frac{(1+r)}{2}\sigma_y - \sigma_y \frac{(1-r)}{2}\cos(2\theta) \qquad (3)$$

where the first term on the right-hand sides of (2) and (3) comes from the deformation zone ice stresses and the second term comes from the 'rigid ice' ice stresses. Note that ϕ is the orientation of the principal axes of the stress state inside the failure zone and may be determined (see below) from the flow rule and the isotropy of the material inside the zone. Eliminating σ_c' from equations (1) and (2) we obtain an equation relating the stresses in the rigid ice next to the failure zone to the orientation of the failure zone and principal directions inside the failure zone

$$\frac{(1+r)}{2}\sigma_y - \sigma_y \frac{(1-r)}{2}\cos(2\theta) = \sigma_y \frac{(1-r)}{2}\sin(2\theta)\left[\frac{1-a\cos(2\phi)}{a\sin(2\phi)}\right] - \frac{1}{a} \; . \qquad (4)$$

To find the orientation of the failure zone and hence effectively the equations of motion we minimize σ_y with respect to θ by differentiating (4) with respect to θ and then setting $d\sigma_y/d\theta$ equal to zero. In the special case that the dilatation angle in Fig. 5a is constant then ϕ is also fixed as it is dictated by the strain rate during plastic failure at the interface and since the failure zone is arbitrarily thin there is no strain rate on a face perpendicular to the failure zone. Under these conditions (see also the strain mohrs circle construction in Fig. 6b) this procedure yields a preferred lead orientation angle θ_c satisfying

$$\tan(2\theta_c) = \pm\frac{1-a\cos(2\phi)}{a\sin(2\phi)} = \frac{1}{\mu_e} \qquad (5)$$

where we may think of μ_e as the effective internal angle of friction coefficient for normal and shear stresses along a face (line) parallel to the failure zone. Hence knowing the stress state in a region we may determine the orientation of an expected failure zone by rotating the stress tensor to a given face until the normal and shear stresses on that face agree with a relationship $\tau' = \mu_e \sigma_n' + b$ where b is some cohesive stress not critical to the direction argument.

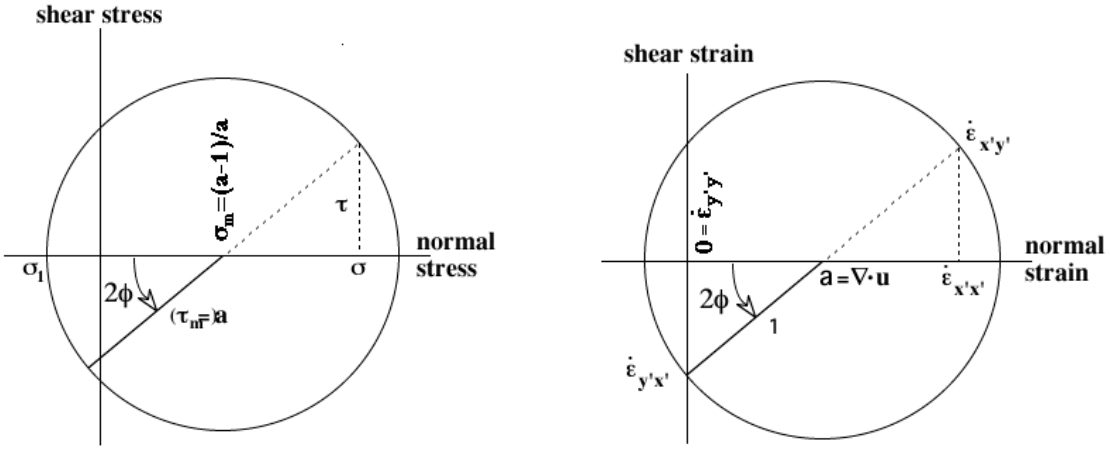

Figure 6. a(left hand panel): mohrs circle construction for the stress state inside the deformation zone of Figure 5b. 6b (right hand panel): mohrs circle construction for the strain rate state inside the deformation zone of Figure 5b.

Clearly the important point here is that the flow rule enters this process by dictating the angle ϕ inside the deformation zone. In the special case of a normal flow rule the failure angle θ is the same as would be deduced by the friction across an arbitrary face related to the compression across that face by a friction coefficient which is directly related to the principal axis slope of the yield curve in Figure 5a. This algebra is shown more completely by Hibler and Schulson (2000), but briefly that from figure 5a and the mohrs circle constructions in Figure (10) and assuming isotropy it is easy to show that $\cos(2\phi) = a$. Substituting this result into Equation (5) yields $\tan(2\theta) = +- \tan(2\phi)$ so that $\theta_c = \phi$. Relating the slope of the failure surface in Fig. 5a to the internal angle of friction across a face μ (see Hibler and Schulson, 2000), one then obtains $\tan(2\theta_c) = +-1/\mu$ which is the classic result for orientation of failure, based only on stresses and friction.

An important part of the result here is that the deformation angle will be equal to the internal angle of friction result only for a normal flow rule. Analysis of the above equations shows that 'fixed dilatation' flow rules always yield larger intersection angles than a normal flow rule. For example, for a coulombic model as in Figure 9a, but with a pure shear flow rule as proposed for example by Flato and Hibler (1992) and with small dilatation by Tremblay and Mysak (1997), internal angles of friction (β) of 90^o, 55^o,44^o and 30^o yield intersecting deformation angles of 45^o. 51^o, 55^o and 63^o. These can be compared to the predicted intersection angles for a normal flow rule of 0^o, 37^o, 46^o and 60^o. For the von mises case at the allowable failure stress the tangent stress line corresponds to a zero internal angle of friction and hence intersection angles of 90^o occur for the normal flow rule which applies.

3.2 Characteristics of velocity equations of motion

At this point we turn to obtaining the velocity equations of motion in the deformation zone or alternatively the velocity gradients between the 'rigid motions' on the zone boundaries. While the algebra above is somewhat extensive, it ultimately reduces to an effective friction coefficient μ_e (Equation 5), dependent on the flow and friction characteristics of the assumed yield surface of material failing in the deformation zone. In particular the effective stress equations of motion for the plastic failure occurring in the coulombic failure zone are simply that the compressional stress σ on the face is given by some value

$$\sigma = E1 \qquad (6)$$

where E1 is given more specifically by Eq. 3; and within some cohesive constants the shear stress τ across this face is given by

$$\tau = \mu_e \sigma \qquad (7)$$

where μ_e is the effective friction coefficient in Eq. 5. It is important to note here that all the information on the flow rule enters in this analysis via ϕ, the principal angle of the strain rate in the failure zone, which in turn depends on the fact that there is no stretching or compressing strain along the lead together with the dilatational flow rule.

To determine the equations of motion in terms of velocity derivatives and hence determine the mathematical characteristics, we write the stress conditions (6) and (7) on the faces of the failure zone in strain rates in the zone. To do that in a form complete enough to determine the characteristics we utilize the general framework developed by Hibler (1977;1979) for expressing plastic stress in terms of strain rate via a generalized Reiner-Rivlin fluid. In particular, referring to Figure 5b for the configuration and orientation of the x and y cartesian axes, within constant pressure terms not relevant to the characteristics argument, the three stress components in the lead are given by

$$\sigma_{xx} = (\eta + \zeta)\frac{\partial u}{\partial x} + \zeta \frac{\partial v}{\partial y} \tag{8}$$

$$\sigma_{yy} = (\eta + \zeta)\frac{\partial v}{\partial y} + \zeta \frac{\partial u}{\partial x} \tag{9}$$

$$\sigma_{xy} = \eta\left[\frac{\partial u}{\partial y} + \frac{\partial v}{\partial x}\right] \tag{10}$$

where η and ζ are in general functions of the invariants of the strain rates so that these equations may be effectively viewed as linearized equations in the region of interest in the deformation zone.

At this point we need to determine the strain rate in the lead . A rather tedious approach would be to determine the strain rate in the lead co-ordinate system and the principal axes of the strain rate. One could then rotate the strain rate to the x, y co-ordinate system. However a much more direct approach is to use a generalized tensor Gauss theorem and integrate around the square box in the failure zone noted in Figure 5b. In this figure we have assumed the relative symmetry of the 'rigid motion' of the ice surrounding the failure zone.

Carrying out these integrations and utilizing the stress strain rate equations 8-10 rotated to yield stresses on the face parallel to the lead, it is easy to show that the resulting stress equations 6,7 are given in terms of velocity gradients across the failure zone by

$$\frac{\partial u}{\partial x} + \gamma \frac{\partial v}{\partial y} = A \tag{11}$$

$$\frac{\partial u}{\partial y} + \gamma' \frac{\partial v}{\partial x} = B \tag{12}$$

where $\gamma\gamma' = \tan^2\theta$ and θ is now defined as in Figure 5b and is the appropriate angle for the failure zone for this particular effective friction. Moreover A and B are functions of other constants and angles defined above. However, it is well know that this system of two first order equations represents a hyperbolic second order partial differential equation with a characteristic equation (Mendelson,1968)

$$\left(\frac{dy}{dx}\right)^2 - \tan^2\theta = 0. \tag{13}$$

Solution of this simple characteristic equation yields two real characteristics with slopes

$$\frac{dy}{dx} = \pm\tan\theta \tag{14}$$

which since the θ in Fig. 5b is chosen to be the angle of the stress zone with the specified stress conditions, clearly coincide with directions of the two possible deformation zones locally. As a very easy special case, consider pure shear across the failure zone. In this case it is very easy to derive equations (11) and (12) with $\gamma=\gamma'=1$. Hence characteristics are slip lines with intersections at 90^o for this special shear case corresponding to von mises plane strain (Figure 3b).

Briefly summarizing the above derivation: by writing down the equations of motion using a double limiting procedure the problem of orientation of deformation zones is reduced to either an energy minimization or confined stress minimization problem locally. Solving this minimization problem yields orientation of the deformation zones and information on the stresses at the faces of the deformation zones. Expressing the two stresses on the face in the case that the intersection angle is properly solved for yields effectively two equations of motion for the velocity gradients in the deformation zone. These two partial differential equations trivially have characteristics aligned with failure zone. As the stress state smoothly curves (as long as plastic flow is occurring) in an actual boundary value solution of sea ice drift using some approximation of rigid plastic flow, the characteristics smoothly curve in space and could be traced out over any plastic flow region in a numerical simulation.

Finally, we note that while the von mises plain strain problem is very restrictive, the normal flow rule two dimensional elliptical yield curve proposed by Hibler(1979) whereby the other stress states in say, Figure 3b, are available, has been widely applied to the modeling of sea ice dynamics. Pritchard (1988) has analyzed this case with more traditional energy methods and finds sets of characteristics that are consistent with our deformation zone analysis here for the case of normal flow. Insight into this special case of normal flow and differences with the non normal flow case may be gotten from numerical results in Hibler and Schulson (2000) showing that stresses in the deformation zone and the 'rigid ice' region are identical on all faces at the optimum orientation angle for a normal flow rule, but not for a non normal flow rule. Hence strictly speaking the theory here really only applies when weaknesses, cracks, etc cause zones of failure to develop, whereas normal flow rule theory can apply to uniform strength plastic flow everywhere with mathematical slip lines everywhere although not necessarily observable as a relatively discontinuous slip line.

4. A simple spatial scaling argument for linear kinematic features

As opposed to von mises plain strain, linear kinematic features, which we argue develop in a similar manner to brittle coulomb failure in the laboratory, almost certainly largely arise from the presence of imperfections, cracks and generally heterogeneity in strengths and orientation of weaknesses in the sea ice pack. In addition to the heterogeneous character of pack ice, however, irregular boundary conditions arising from complex shore lines can result in particular failure zones as demonstrated by Pritchard et. al. (1977) in the Beaufort sea. This concept of random weaknesses can also be used to develop a general scaling theory for the spacing between linear kinematic features, a procedure which yields insight into the general character of sea ice flow yielding collections of deformation zones as opposed to regions of smooth plastic flow.

Considering sea ice to be a one dimensional plastic system with zero stress under opening and fixed stress under closing, the one dimensional flow for a constant strength system under a ramped wind field can be analytically obtained (see e.g., Hibler1984) yielding a result shown schematically in Figure 7a. This result is consistent with two dimensional viscous-plastic simulations with fixed strength and uni-directional wind forcing (Hibler,1984). This result is counter intuitive at first glance because except for an initial region of rigid flow the system is uniformly converging (or diverging depending on the wind direction. Moreover in this uniform converging region the ice is undergoing free drift because the plastic stresses are constant spatially with zero gradient.

In practice, however, the basic paradigm for the formation of oriented flaws under wind fields with uniform stress gradient, is the presence of weaknesses, possibly oriented, within the ice field which can nucleate failure zones. These failure zones divide the ice into relatively rigid plates separated by faults. In principle a scaling derivation for spacing may be carried out by considering two-dimensional plates, but the mathematics is somewhat involved. The basic concept can be understood more simply by considering a one-dimensional ice pack with equally spaced random strength weaknesses.

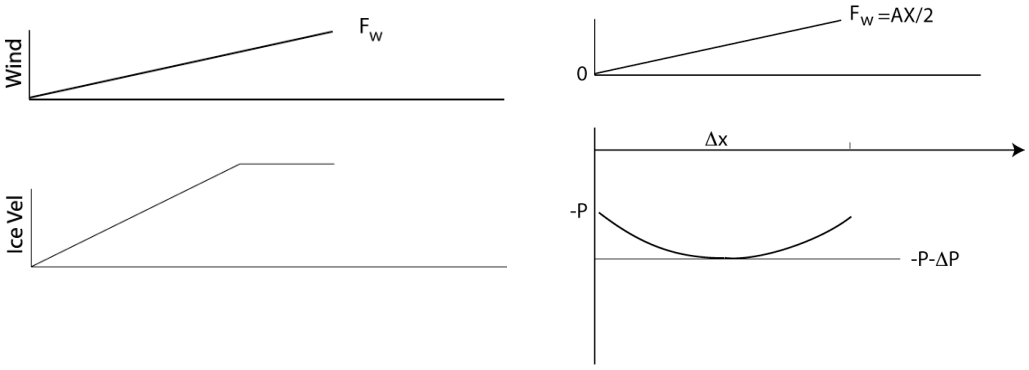

Figure 7. a(left hand panel): Schematic of wind speed and ice velocity for constant ice strength boundary value solutioin. This general behavior applies whether the wind direction is to the right or left, with the ice velocity being negative when the wind direction is to the left. 7b (right hand panel): Schematic of stress variation and wind variation over a rigid region in the one dimensional spacing analysis.

For such a one dimensional system assume that the ice is confined by a wall on one side, and a free stress boundary condition on the other side (Figure 7b). The ice is forced along x toward the wall by a wind stress with constant gradient $F_a = (Ax/2)$, and by a linear water drag F_w. The velocity profile of the failing area will be stepwise, with regions between weak flaws moving rigidly. On a single rigid region between, say, two equal strength flaws of equal compressive failure strength -P, there is a balance between the water drag and the average air drag

$$F_w = \overline{\frac{Ax_o}{2}}, \tag{15}$$

where x_o is the length of the rigid region. Locally within the rigid region there is an imbalance between air and water body forces, that is balanced by the stress gradient according to

$$\frac{\partial \sigma}{\partial x} = F_a - F_w. \tag{16}$$

Integrating the stress over the rigid region, and applying boundary conditions we find that the ice stress in the rigid region (see Figure 11b) is

$$\sigma = \frac{Ax^2}{2} - \frac{Ax_o x}{2} - P. \tag{17}$$

Let us imagine now that there are other stronger flaws within the rigid piece, with say the weakest 'stronger' flaw having a strength –P - ΔP. If this flaw occurs in the middle, it is clear that there will be a maximum allowable value of of x_o beyond which the rigid 'floe' breaks in the middle. This argument leads to a scaling for the spacing Δx between failure zones of

$$\Delta x \approx \sqrt{\frac{\Delta P}{\frac{\partial F_a}{\partial x}}} \tag{18}$$

Since in this simple one dimensional case each weakness can be considered a 'floe' boundary, it is clear that depending on the gradient of the wind field collections of floes will clump together to form a relatively rigid region.

Hutchings et. al. (2005) have tested this scaling argument with the viscous plastic rheology (Hibler, 1979) via a series of one-dimensional numerical experiments with random weaknesses. A typical one d simulation (not shown) easily demonstrates the formation of initial failure points with stepwise motion as assumed in the theoretical example above. The scaling was verified by carrying out a variety of simulations with different wind gradients providing excellent agreement with this simple one dimensional theory. This simulation also demonstrates the ability of the highly nonlinear viscous plastic rheology, whereby rigid flow is modeled by a state of very slow and very viscous flow, to simulate rigid motion and effective discontinuities in velocity.

An important aspect of this scaling argument is that it is not necessary to have a discrete length scale that is dictated by say, ice floe size. Indeed, depending on the boundary conditions and body force gradient discrete floes may 'stick' together, a concept which brings rheologies based on a uniform kinematics of collections of different floe shapes (Bratchie, 1984; Wilchinsky and Feltham, 2006) into question. Instead we imagine that random weaknesses at all scales in the pack ice provide the basis for spacing between linear kinematic features together with gradients in the body forcing fields. One likely source of weaknesses, could be randomly oriented cracks of different lengths with the length serving effectively as an anisotropic strength of varying magnitude. In general this overall view is consistent with a scale-invariant view of pack ice rheology, proposed by Schulson and Hibler (2003), whereby the same 'plastic' rheology is assumed to apply at all scales.

5. Simulation of oriented features for a particular non normal coulombic failure criterion.

For a two dimensional system with random weaknesses, the formation of oriented failure lines requires weakening to occur. This is because localized weaknesses will typically be surrounded by stronger ice that prevents oriented failure strikes from propagating, especially in the presence of water drag (not present in Figure 4a) Plastic failure points when a random distribution of strengths is utilized can however serve as nucleation sites for initiating failure leading to oriented concentrated failure zones. In practice if the wind and water drag are chosen properly as well as weakening rates this general procedure can be very effective in simulating linear kinematic features (Hibler,2001; Hutchings et. al. 2005).

Since the rheology (Hibler and Schulson,2000) shown in Fig. 2a has a variable flow rule with a fixed friction angle over the non convergent region of the yield curve the theoretical intersection angle between linear kinematic features depends on the overall strain state induced in the pack ice. Moreover, because of the varying flow rule the theoretical expected angle for characteristics is difficult to determine analytically and is most easily done by numerically minimizing the dissipation energy in an ideal weak deformation zone as shown in Fig 3b. Numerically determining the expected intersection angle for given strain rates yields Fig. 8a which shows the angles for the modified Coulombic rheology of Figure 2a. Also shown are the expected angles for a normal flow rule elliptical yield curve, also determined numerically. However these elliptical results apply to any normal flow rule rheology by the above analysis.

Because of the dependence of characteristics on strain, a particularly effective procedure to simulate intersecting linear kinematic features is to construct a wind field forcing so that the expected ice drift state would be expected to have a uniform strain everywhere. In addition, since steady solutions without, say, inertial oscillations typically display pure shearing due to coriolis forcing (true also observationally when inertial periods are averaged over) to get a variety of strain rates for comparison to theory it helps greatly to consider water drag with no turning angle. This overall procedure can effectively be used to compare theoretical and expected 'characteristics' or angles of intersecting deformation zones (Hutchings et. al.,2005)

How effective this procedure can be is demonstrated in Figure 8b and Figure 9 where a wind field guaranteeing free drift with principal axes ratio of one to 4 (with no water drag turning angle) is used together with free drift boundary dirchelet conditions. To obviate advection

effects, the simulation is carried out in a virtual mode where by the ice is not advected but is weakened gradually in time as divergence occurs locally. Hence there is really no true time scale for weakening as the ice does not advect. As can be seen from Figure 9b, the initial deformation field is rather chaotic without any clear oriented structure. However as weakening is allowed to occur lineated fields in the strain rate begin to form with approximately 60^o intersection angles, and after sufficient weakening as shown in Figure 12b become very pronounced. Similar results for this idealized forcing can be obtained for the elliptical yield curve with normal flow. There is some dependence on the wind gradient in the simulations with stronger wind gradient inducing more oriented features with somewhat smaller intersection angles.

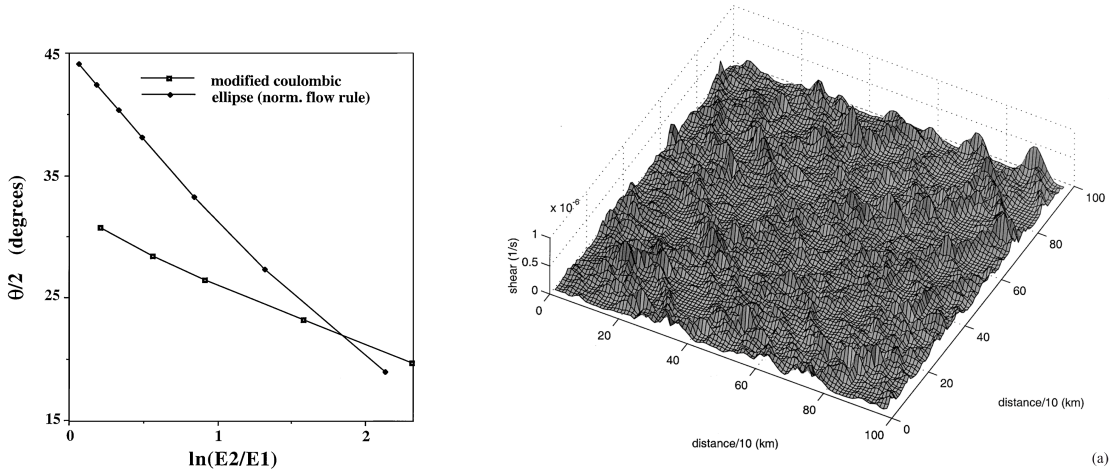

Figure 8. a(right hand panel):Numerically determined half intersection angles versus ratio of absolute strain rates for dilatory strain rates up to pure shear for the modified coulombic yield curve of Figure 2a and for a elliptical yield curve with normal flow rule. 8b (right hand panel): Shear strain field simulated by utilizing a wind field such that uniform dilatory strain is expected over a region of pack ice, together with spatially random strengths. This panel shows the simulated shear without weakening or strengthening.

The multi-scale character of deformation (Fig. 8b) and linear kinematic features (Fig. 9) demonstrated by these viscous-plastic (vp) simulations also refute the assertion by Weiss et. al. (2007) that a vp rheology cannot be used to effectively simulate essential features of fracture. The difficulty of course, is that in Weiss et al.'s comparison of strain to stress, a non-stiff viscous closure was assumed to apply to the vp conceptual model. To properly simulate features as in Fig. 8b and 9 a very stiff closure must be used (strain<.001/day for creep) so that 'rigid' motion is effectively modeled and to insure that 'rigid' deformation energy losses are negligible. These limits are off the scale in the so called 'viscous' comparison of Weiss et. al (2007) ; instead their comparison applies to plastic failure. Moreover with random weaknesses, as used here, there will be a nested set of yield surfaces similar to what Weiss et. al. (2007) claim can only be achieved by non vp models with different yield surface shapes.

Although not shown complications arise when a turning angle in the wind is utilized (see Hutchings et. al.,2005). Beyond the pure strain problem, here the two dimensional wind stress field is not alligned with the resulting ice strain field in contrast to the no turning angle drag case. As a consequence orientated deformation zones in only one direction are preferentially obtained

with this direction depending on whether a 'high' or 'low' pressure forcing is used. Since most sea ice models used in climate models make use of the ellptical yield curve, or if not than a normal flow rule, the pure shear case yields a much more pronounced 90 degree intersection angle not in agreement with observations. Inspection of very high resolution simulations by Mazlowski et. al, (2000) for example, is an example of this. The modified coulombic failure does better although the angle is still a bit large. In general much of the issue here may be due the simple boundary layer drag being used here which also damps out inertial variability (Heil and Hibler, 2002) In reality, and resulting from embedded simulations, where no boundary layer drag is used, the ice undergoes substantial inertial variability with attendant wide swings in the deformation rate rate ratios. Indeed, Hutchings et al (2005) showed that including an imbedded model in basin wide simulations resulted in enchanced linear kinematic features. A major point here is that the embedded model has no artificial energy loss to water drag, so considerably more energy is available for forming complex deformation features.

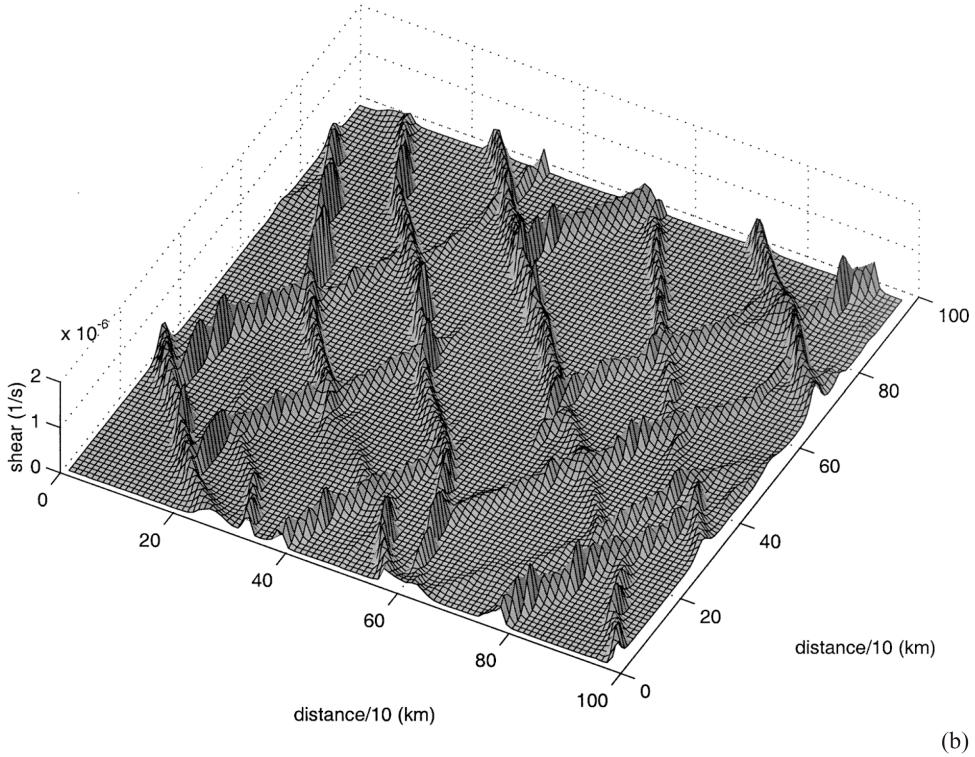

Figure 9. Simulated linear kinematic features obtained by utilizing a wind field such that uniform dilatory strain is expected over a region of pack ice. Random strengths are allowed initially and weakening without advection is allowed to occur. Linear kinematic features develop naturally in the simulation as weakening progresses and serve to divide the pack into regions of relatively rigid motion.

6. Concluding Remarks

The basic theme of this paper has been to introduce a general theory for failure zones in the Arctic pack ice which are construed to be narrow zones where plastic failure, in general obeying a non normal flow rule, is occurring. The main results of this theory are that not only the friction

characteristics but the assumed flow characteristics affect the expected intersection angles of expected linear kinematic features. Numerical simulations of a heterogeneous ice pack clearly demonstrate the capability of existing nonlinear viscous plastic rheologies to simulate such features, provided damage, in terms of weakening pack ice in the zone, is allowed to occur. Moreover the intersection angles simulated agree generally with the theory, and in the limit of largely pure shear deformation are significantly more acute than normal flow rule rheologies. The angles are less acute than what may be obtained from simple sliding friction arguments. However such arguments must necessarily assume a clean sliding friction across a given line over very long distances. Because of the complex failure processes occurring on both the geophysical scale (irregular flows, jagged leads, cracks and ridges) as well as on the lab scale (complex wing crack formation) it seems that in practice a finite failure zone is indeed a very physical assumption.

We also note that the overall conceptual framework used here differs considerably from the kinematics of floes approach used to develop ice rheology utilized by a number authors. Here a complex mix of heterogeneous and possibly oriented weaknesses with the application of dynamics leads to the formation of typical 'ice floe' scales, or at least the scale for separation of major linear kinematic features. The essential concept here is that the kinematic approach (specifying a given plane strain field on a system of idealized floes) is almost impossible to justify as arising from an actual solution of body forces applied to the pack ice, inasmuch as depending on the boundary conditions and external forces, various flows end up either sticking together or possibly fracturing. Otherwise a true momentum balance is not achieved.

References

Bratchie, I., 1984. Rheology of an ice-floe field, *Annals of Glaciology,*5, 23-8.

Fung, Y. C. 1977. *A first course in continuum Mechanics,*2nd Ed. Englewood Cliffs, NJ, Prentice Hall.

Flato, G. M. and Hibler, W. D. III, 1992. On modeling pack ice as a cavitating fluid, *J. Phys. Oceanogr.,*22, 626-51.

Heil, P. and Hibler, W. D. III, 2002. Modeling the high-frequency component of Arctic sea-ice drift and deformation, *J. Phys. Oceanogr.,* **32**(11), 3039-57.

Hibler, W. D. III, 1979. A dynamic thermodynamic sea ice model, *J. Phys. Oceanography,***9**, 815-46.

Hibler, W. D. III and E. M. Schulson, 2000. On modeling the anisotropic failure and flow of flawed sea ice. *J. Geophys. Res.* **105**(C7), 17105-19.

Hibler, W. D. III, 2001. Modeling the formation and evolution of oriented fractures in sea ice, *Annals of Glaciol.,***33**, 157-164.

Hibler, W. D. III, 1977. A viscous sea ice law as a stochastic average of plasticity, *J. Geophys. Res.,* 82, 3932-8.

Hutchings, J. K., P. Heil, and W. D. Hibler III, 2005: Modeling Linear Kinematic features in sea ice, *Monthly Weather Rev.,* 133, 3481-97.

Kwok, R. 2001. Deformation of the Arctic Ocean sea ice cover between November 1996 and April 1997: a qualitative survey. In Dempsey, J. P. and Shen, H. H., eds, *Proceedings of IUTAM Conference*, University of Alaska Fairbanks, June 2000. Dordrecht, Kluwer Academic Publishers, pp. 315-22.

Maslowski, W., Newton, B., Schlosser, P. Semtner, A. and Martinson, D. 2000. Modeling recent climate variability in the Arctic Ocean,Geophys. Res. Lett. 27, 3743-6.

Marko, J. R. and Thompson, R. E., 1977. Rectilinear leads and internal motions in the pack ice of the western Arctic Ocean, *J. Geophys. Res.*, 82, 7787-802.

Mendelson, Alexander, 1968. Plasticity: Theory and Application, Krieger Publishing Company, Florida, 353pp.

Overland, J. E., Walter, B. A., Curtin, T. B. and Turet, P. 1995. Hierarchy and sea ice mechanics: a case study from the Beaufort Sea. *J. Geophys. Res.,* **100**, 4559-71.

Pritchard, R. S., 2001. Sea ice dynamics models. In Dempsey, J. P. and Shen, H. H., eds., *Scaling Laws in Ice Mechanics and Ice Dynamics, Proceedings of IUTAM Conference,* University of Alaska Fairbanks, June 2000. Dordrecht, Kluwer Academic Publishers, pp. 265-88.

Pritchard, R. S., 1988. Mathematical characteristics of sea ice dynamics models, *J. Geophys. Res.,* **93**, 15609-18.

Pritchard, R., Coon, M. D. and McPhee, M. G. 1977. Simulation of sea ice dynamics during AIDJEX, *J. Pressure Vessel Technol.* 99j, 491-7.

Schulson, E. M. and Nickolayev, O. Y. 1995. Failure of columnar saline ice under biaxial compression: failure envelopes and the brittle-to-ductile transition, *J. Geophys. Res.* **100**, 22383-400.

Schulson, E. M. and W. D. Hibler, III, 2004: Fracture of the winter sea ice cover on the Arctic Ocean, *Comptes Rendus Physique* 5, 753-767.-

Tremblay, L. B. and Mysak, L. A. 1997. Modeling sea ice as a granular material, including the dilatancy effect. *J. Phys. Oceanogr.* 27, 2342-60.

Weiss, J., E. M. Schulson, H. L. Stern, 2007. Sea ice rheology from in-situ, satellite and laaboratory observations :Fracture and friction, *Earth and Planetary Science Letter,* 255, 1-8.

Wilchinsky, A. V. and D. L. Feltham, 2006. Modelling the rheology of sea ice as a collection of diamond-shaped floes, J. Non-Newtonian Fluid Mech. 138, 22-32.

19th IAHR International Symposium on Ice
"Using New Technology to Understand Water-Ice Interaction"
Vancouver, British Columbia, Canada, July 6 to 11, 2008

Numerical Simulation of Development of Sea Ice Microstructure Under Temperature Gradient

Yoshiki Kawano*[1] Tetsuya Ohashi*[2]
**1 Graduate Student of Kitami Institute of Technology Dept. of Mechanical Engineering*
**2 Kitami Institute of Technology Dept. of Mechanical Engineering*
Koencho 165, Kitami-shi, Hokkaido, 090-8507 Japan

kawa@newton.mech.kitami-it.ac.jp

Developments of sea ice polycrystals from the sea surface are simulated under two-dimensional approximation by combining numerical models for crystal growth, salinity diffusion and flux of heat. Anisotropic growth of ice crystals from a number of nuclei and their mutual impingements are numerically reproduced by a simple and novel technique, named Voronoi dynamics. In an extreme case where the growth rate is isotropic and the initial salinity is zero, resultant microstructure consists of Voronoi polyhedron. Discharge of salt from solidified region and salinity condensation at the solid-liquid interface are also taken into the simulation. Diffusion process of salinity and heat flux are evaluated by solving equations for diffusion and heat conduction, and growth of ice crystals is affected by these two factors. Results show that layer of granular grains are formed near the sea surface and columnar shaped grains develop below it. Brine regions are mainly formed along grain boundaries in the layer of granular grains, while in the region of columnar shaped grains, brine regions exist both along grain boundaries and inside grains. Columnar shaped crystal grains consist of ice platelets growing in the vertical direction and brine layers are sandwiched between them. Mechanism for the formation of this substructure, ice platelets and brine layers is discussed in terms of Mullins-Sekerka type instability of solid-liquid interface and temperature gradient due to cooling from sea surface. These microstructural features are in accordance with experimental observations.

1. Introduction

Sea ice covers a vast area of oceans near the north and south poles and has many impacts on the environment of the earth (e.g. Weeks and Ackley (1982), , Wakatsuchi (2002), Eicken (2003)). An important effect among those is that the sea ice reflects sunlight and obstructs thermal energy to be absorbed in sea water. Therefore, the process of growth and decay of sea ice is a matter of interest.

When the sea water starts to freeze, most of salt content is discharged from ice crystals into liquid area because the solubility limit of salt in the crystal lattice of ice is very small. However, a number of small volumes of saline water, called brine regions, and air pores remain in crystal grains of ice or at grain boundaries. That is, sea ice is a porous material which is composed of pure ice crystals, brines and air inclusions. Microstructures of such ice crystals with many brine regions play a major role in the macroscopic mechanical response of ice sheet. For example, strength of sea ice is affected by brine content and its distribution in the sea ice, as well as its grain size and temperature. Assure (1958) developed pore microstructural model of sea ice and analyzed the relationship between the brine volume and macroscopic strength of sea ice. By using a Monte Carlo percolation model, Golden *et al*. (1998) showed that sea ice has a fluid permeability when volume fraction of brine regions is higher than 5 %. As stated above, physical behaviors of sea ice are closely linked to its microstructures and studies on the microstructure are very important.

Shape of ice crystals is determined by the environmental conditions under which the ice has formed (Weeks and Ackley (1982)), and its behaviors also changes with the shape. So far, the growth process of ice crystals at molecular scale were studied by using molecular dynamics simulations (Noda *et al*. (2004)), and pattern formation of ice crystals were analyzed by using a discotic ice crystal model (Yokoyama *et al*. (2000)). Experimental observations of pattern formation of ice crystals in supercooled water (Shimada *et al*. (1997)) were also made. However, behaviors of sea ice are also largely influenced by their mesoscopic structure where a lot of crystal grains and brine regions contribute. In this paper, we focus our attention at the growth process and interaction of many ice crystals and formation mechanism of brine regions at mesoscopic level.

In the previous studies, we developed a simple and numerically efficient simulation technique named Voronoi dynamics for the anisotropic growth of ice crystals and their impingements (Ohashi *et. al*. (2004), Kawano and Ohashi (2006), Ohashi and Kawano (2007)). Diffusion and condensation process of salinity in the seawater was also taken into account recently (Ohashi and Kawano (2007)), and it was found that Mullins-Sekerka type instability was formed at liquid-solid interface when the diffusion process governed the growth. This effect induced branching of individual crystals and resulted in a formation of lamellar shaped structure of ice platelets and brine layers. However, the effect of temperature gradient was not considered in the simulation. In this paper, heat transfer by conduction is incorporated into the model and we simulate cooling process of seawater from the sea surface.

2. Numerical procedure

2.1 Crystal growth model and solidification condition

Let us imagine the process where crystal grains grow from nuclei of crystals and impinge each other. During this process, crystal grains which have faster growth rate and earlier nucleation time occupy larger areas than others. In order to reproduce such process numerically, we use following technique, named Voronoi dynamics (Fig. 1).

(1) We assume a simulation space which is divided into small cells, and nuclei are put in the space. Each nucleus has a certain growth rate $\boldsymbol{g}$, character number $\boldsymbol{k}$ and nucleation time. All the cells are initially given character number "-1", which means the cells are liquid (Fig.1 (a)).
(2) A time increment $\boldsymbol{\Delta t}$ is set so as that $\boldsymbol{\Delta t} \times$ (the maximum growth rate) is less than the minimum size of the cell.
(3) Then, we advance the time from $\boldsymbol{t}$ to $\boldsymbol{t}+\boldsymbol{\Delta t}$, and check if growths from nuclei reach to each cell. If growth of a nucleus with the character number $\boldsymbol{k}$ reaches to a cell, and if the cell is touching to a cell that was already solidified and had character number $\boldsymbol{k}$, the character number of the cell is changed from -1 to $\boldsymbol{k}$, which means the cell is solidified (Fig.1 (b)).
(4) The procedure (3) is repeated with a time interval $\boldsymbol{\Delta t}$ and solidification of cells progresses. After a certain time increments, aggregates of solidified cells with the same character number are formed and each of them are individual crystal grains (Fig.1 (c)).

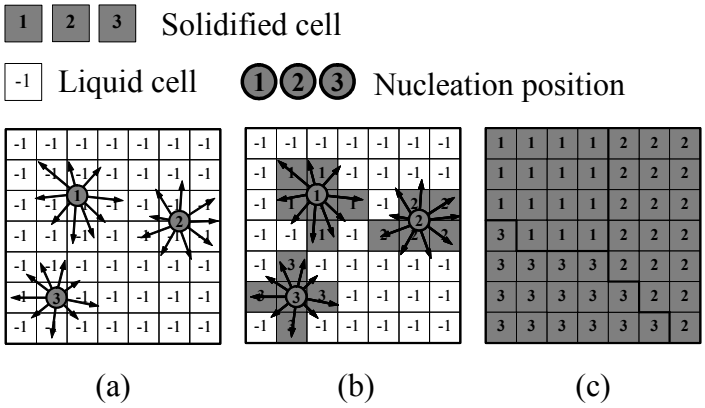

Figure 1. Schematic illustration of Voronoi dynamics technique.

In the above procedure, crystal structures are built up as a result of scrambles for the area (cells) by the nuclei, and only the geometrical effect by the mutual impingement of growth of the crystallites is considered. However, when ice crystals grow in sea water, salt content in sea water is discharged from ice crystals into solid-liquid interface during crystal growth, and the salinity is condensed at the interface and such high salinity impedes the growth of crystals. To reproduce this effect, we incorporate the following model into the Voronoi dynamics scheme.

When a liquid cell solidifies, salt content in the cell is discharged to its neighboring cells. Fig.3 schematically illustrates the movement of salt content from a newly solidified cell. We assume that the salt is equally distributed from the newly solidified cell to its neighboring non-solidified cell(s).

Relationship between salinity $\boldsymbol{S_b}$ and solidification temperature $\boldsymbol{T_s}$ of sea water is approximately given by a monotonically decreasing function of $\boldsymbol{S_b}$ [2]:

$$T_s = \frac{54.11 S_b}{S_b - 1000} + 273.15 \quad \left(250.15 \le T_s \le 273.15\right). \qquad [1]$$

Liquid cells can solidify when the temperature is lower than the solidification point, and this condition is added to the solidification condition of Voronoi dynamics.

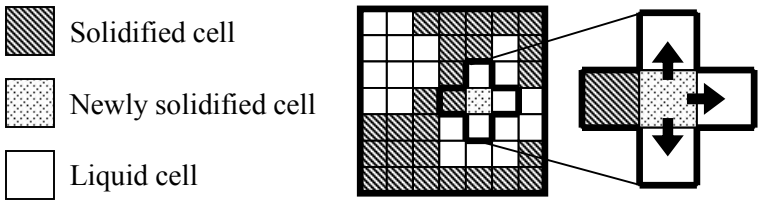

Figure 2. Discharge of salinity from newly solidified cell. All the discharged salinity is distributed equally to neighboring liquid cells.

2.2 Salinity diffusion and conduction of heat

Diffusion of salinity is expressed by Fick's second low:

$$\frac{\partial \boldsymbol{C}_{salt}}{\partial \boldsymbol{t}} = \boldsymbol{D}\left(\frac{\partial^2 \boldsymbol{C}_{salt}}{\partial \boldsymbol{x}^2} + \frac{\partial^2 \boldsymbol{C}_{salt}}{\partial \boldsymbol{y}^2} \right), \qquad [2]$$

where $\boldsymbol{C}_{salt}$ and $\boldsymbol{D}$ denote density and diffusion coefficient of salt, respectively. Salinity diffusion process occurs only between liquid cells. Temperature $\boldsymbol{T}$ changes by conduction of heat and the temperature distribution is governed by the following equation:

$$\frac{\partial \boldsymbol{T}}{\partial \boldsymbol{t}} = \boldsymbol{a}\left(\frac{\partial^2 \boldsymbol{T}}{\partial \boldsymbol{x}^2} + \frac{\partial^2 \boldsymbol{T}}{\partial \boldsymbol{y}^2} \right), \qquad [3]$$

where $\boldsymbol{a}$ is the thermal diffusivity. Physical constants for seawater or pure ice are used in each of the cells in accordance with their liquid or solid state. Eqs. [2] and [3] are discretized by using the same space grid as the one used for the Voronoi dynamics and solved by finite difference method with forward Euler's time integration scheme.

2.3 Growth rate model of nuclei

Generally, ice crystals have a six-fold symmetricity in the basal plane and growth rate is not isotropic. For the expression of such anisotropic growth characteristics, we assume that c-axis of nuclei is normal to the simulation space and the growth rate $\boldsymbol{g}$ in the basal plane is expressed by a simple equation given by:

$$\boldsymbol{g}^{(k)}(\theta) = \boldsymbol{g}_0 + \boldsymbol{g}_{ax} \times \cos\left(\boldsymbol{n}_s \theta + \alpha^{(k)} \right), \qquad [4]$$

where, g_0 denotes the average growth rate, g_{ax} gives the magnitude of deviation from the average, and integer number n_s(=6) defines the number of symmetricity, and θ is the direction of growth. α, which is given by a random number between 0 and 2π, defines the orientation of crystallites (Fig. 3).

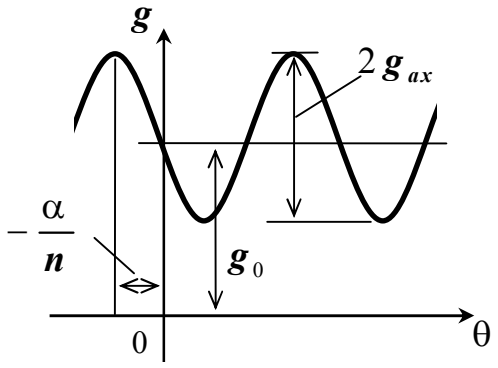

Figure 3. Anisotropic growth rate given by eq. [4].

3. Results and discussion

Let us assume a homogeneous sea water area for the simulation space. Dimension of the space is $50\times150mm^2$ and the space stands vertically. The upper edge of the space coincides to the sea surface and the space is filled with sea water with salinity 35 ‰. 30 points are randomly chosen near the upper edge of the simulation space as the candidate position for nucleation of crystallites. The nucleation is supposed to takes place when the temperature at the candidate position becomes lower than the solidification temperature T_s. Physical constants of ice and seawater used in the both simulations are shown in Table.1. Two simulations are performed with different conditions for temperature and growth rate of crystals.

Table 1. Physical constants used in the present simulations.

	Ice	Seawater
Diffusion coefficient of salt D [m^2/s]		6.8×10^{-10}
Specific heat c[J/kgK]	2040	4217
Diffusivity of heat a[m^2/s]	1.17×10^{-6}	0.139×10^{-6}
Density ρ[kg/m^3]	916.8	1000

In the first simulation, we assume that g_0=0.00106mm/s, $R_{anisotropy}$=0.3 and n_s=6. The whole simulation space is kept at -4°C during crystal growth. Obtained results are shown in Fig. 4.

In the second simulation, g_0=0.1 mm/s and initial temperature in the whole simulation space is -1°C. Then, the sea surface is cooled and kept at -5°C, while the bottom of the space is kept at -1°C. In this condition, temperature gradient is developed in the specimen with progress of time. Obtained results are shown in Fig. 5.

Figs.4 (a)-(e) and Fig.5 (l) show salinity distributions and Figs.5 (a)-(e) depict distributions of degree of supercooling σ[%] which is defined by:

$$\sigma = \frac{T_s - T}{T_s} \times 100 \,. \qquad [8]$$

In these figures, white regions show crystals. Fig.4 (f) and Fig.5 (f) show crystal structure at t=5000s, where individual grains are identified by different gray colors. Figs.5 (g)-(k) show change of temperature distribution with time. Fig. 5 (l) is the salinity distribution at t=5000s.

Fig. 4 shows the results of the first simulation where temperature is maintained uniform and constant throughout the simulation schedule. In the initial stage of crystal growth (Fig.4(a), (b)), the crystallites grow mostly independently in stellar shape. Salt is discharged from solidified area to their environments and high salinity layers build up around them. Degree of supercooling near the ice-seawater interface is small due to the high salinity layers and crystal growth becomes to be governed by salinity diffusion process. Once this condition is formed, solidification progresses more at protrudent place where diffusion of salinity is quicker. The protrusion is amplified with time and the growth is unstable. As a result, the solid-liquid interfaces which are initially smooth become to be rough and areas of condensed seawater are formed at small concave regions between protruded solid regions.

In the concave region, space for diffusion is limited and its salinity is not easily lowered. Thus, the condensed sea water in the concave regions becomes to be difficult to solidify, and the regions turn out to be non-solidified regions within the grains. This phenomenon is observed not only in the early stages of crystal growth where granular shaped grains are formed near the surface but also in the stages where columnar shaped grains are formed at lower part of the sea ice (Fig.4 (c)-(e)).

Next, we observe the result of the simulation with considering the effect of temperature gradient (Fig. 5). In the early stages of the crystal growth (Fig.5(a)), where ice crystals has not completely covered the sea surface, a layer of high degrees of supercooling build up near the sea surface. Thus, growth rates of the crystals become faster in horizontal direction than in downward direction, and the growth mainly develops near the surface (Fig.5 (b)). Since the diffusivity of heat is higher in the ice crystal than that in the seawater, then the temperature in and around the crystal becomes lower (Fig.5 (g), (h)). Once the surface is covered by the sea ice

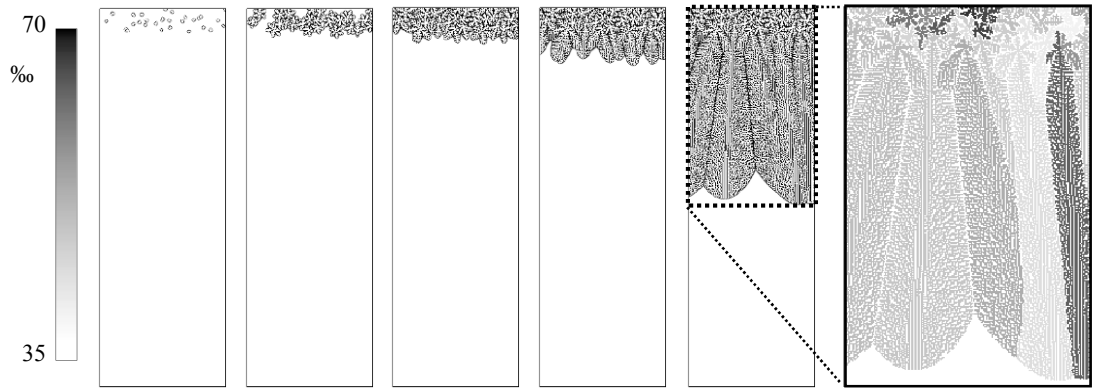

Figure 4. Obtained results when temperature gradient does not exist. (a)-(e) are salinity distributions and (f) shows crystal structure.

and the thickness of the sea ice increases (Figs. 5 (i), (j)), temperature distribution in the horizontal direction becomes more uniform. After that, fluctuation of temperature in the horizontal direction is kept very small and temperature at deeper level decreases with time (Fig.5 (k)).

Growth of ice crystals at solid-liquid interface becomes unstable by the effect of high salinity layers, which is similar to the case shown in Fig.4, and condensed seawater is trapped within the ice crystals in the granular zone. However, in the zone of columnar crystals, formation process of brine regions differs from that obtained in the first simulation. In the zone of columnar shaped grains of Fig. 5, growth rate of most grains in the downward direction becomes almost the same due to the effect of uniform temperature in the horizontal direction. Then, growth rates of thin ice arms protruded from irregularities at interface

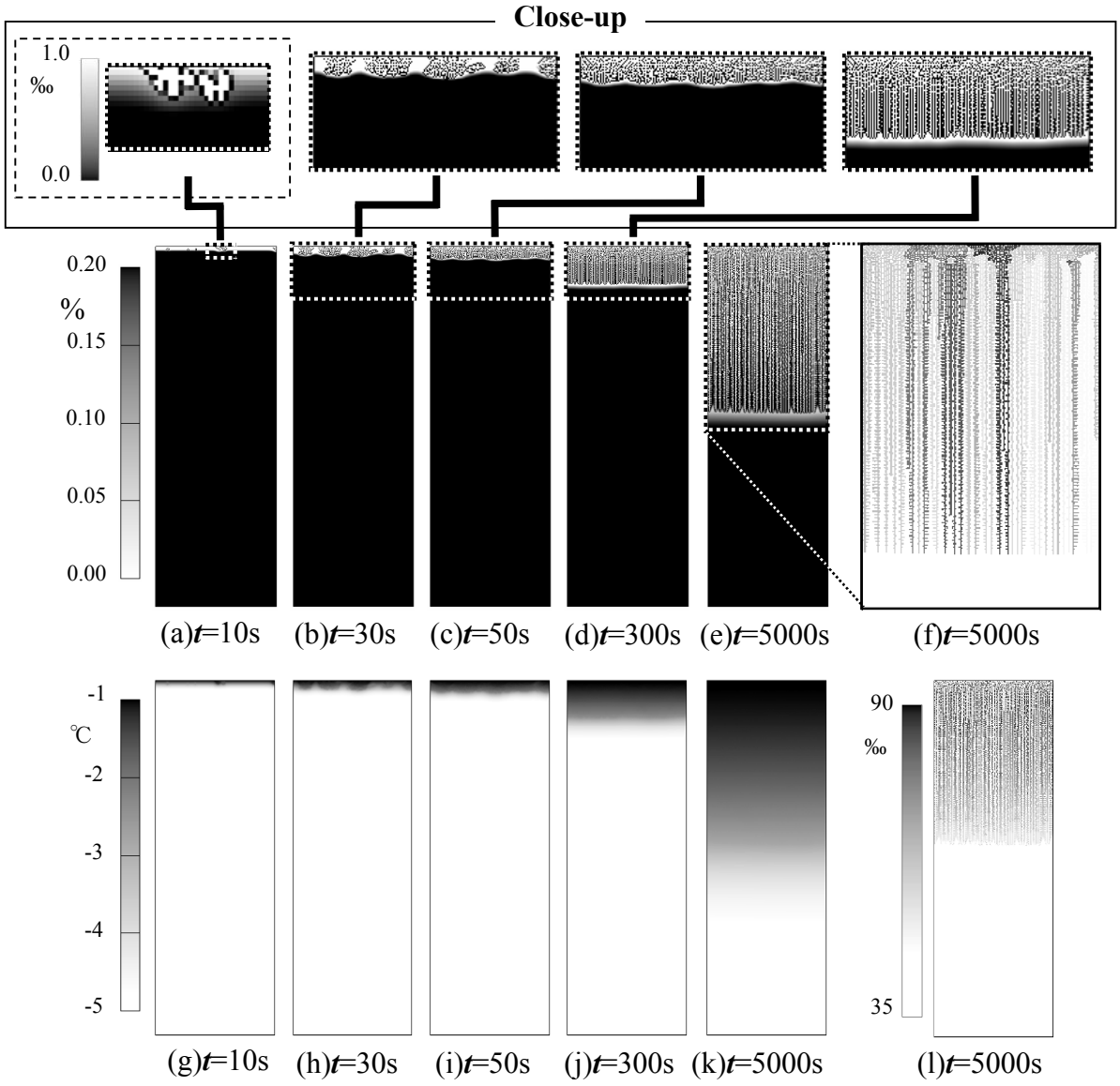

Figure 5. Obtained results when temperature gradient exists in the specimen. (a)-(e) are distributions of degrees of supercooling of seawater, (f) is crystal structure, (g)-(k) are temperature distributions and (l) shows salinity distribution.

also become almost the same and growth directions also align. Areas of condensed sea water are left behind between the protrusions, and the tips of the protrusions keep advancing in the downward direction without connecting each other due to the condensed seawater between them and high temperature around the tips (Fig.5 (d)). As a result, in the columnar zone ice, lamellar-like structure which consists of brine layers and thin ice plates are formed in the vertical direction (Fig. 5 (e), (f)).

Fig.5 (l) shows the distribution of salinity at t=5000 s. We find that salinity near the sea surface is higher. This is because the temperature is lower near the sea surface (Fig.5 (k)) and solidification is easier. As a result, areas of brine regions near the sea surface become smaller than those in the lower part of the sea ice.

4. Conclusion

In this paper, we numerically simulated the growth process of sea ice polycrystals by using models for crystal growth, salinity diffusion and heat conduction. The results can be summarized as follows.

1. By the effect of temperature gradient, fine branching arms of growing crystals aligned in vertical direction, and they formed lamellar like structure.
2. By the effect of temperature gradient, sizes of brine regions became smaller near sea surface than those at deep place of the sea ice.
3. By the effect of temperature gradient, salinity in the brines at shallower place in the sea ice crystal was higher than those at deeper place.

References

Assur, A,. 1958, Composition of sea ice and its tensile strength, Proceedings of the Arctic Sea Ice Conference, Easton, 106-138.

Eicken, H., 2003, Growth, Microstructure and Properties of Sea Ice, In: Thomas, D.N., Dieckmann, G.S. (Eds.), Sea Ice: An Introduction to its Physics, Chemistry, Biology and Geology. Blackwell, Oxford, 22-81.

Golden, K.M. Ackley, S.F., Lytle, V.I., 1998, The Percolation Phase Transition in Sea Ice, SIENCE, Vol. 282, pp. 2238-2241.

Kawano, Y., Ohashi, T., 2006, Numerical simulation for development of polycrystal microstructure of sea ice and brine formation by salinity concentration, Proc 21th int. symp. on Okhotsk sea & sea ice, 95-.98.

Kawano, Y., Ohashi, T., 2006, Numerical simulation of development of sea ice microstructure by Voronoi dynamics technique, Proc. 18th IAHR Int. Symp. on Ice, Vol. 2, 97-103

Noda, H., Von der Eerden, J. P., Furukawa, Y., 2004, A clear observation of crystal growth of ice from water in a molecular dynamics simulation with a six-site potential model of H_2O, Journal of Crystal Growth, Vol. 266, 297-302.

Okagaki, O., 1998, Conduction of heat (Netsu Dendo), In: Nobuhiro S. (Ed.), Engineering of heat transmission (Dennetsu Kogaku), Morikita press, 5 (in Japanese).

Ohashi, T., Sasaki, M., Yoshimura, Y., 2004, Proc. 19th int. symp. on Okhotsk sea & sea ice, 180-185.

Ohashi, T., Kawano, Y., 2007, Numerical simulation of salinity diffusion and growth instability in the microstructure evolution of sea ice, Proc. 22th int. symp. on Okhotsk sea & sea ice, 11-16

Shimada, W., Furukawa, Y., 1997, Pattern formation of ice crystals during free growth in super cooled water, J. Phys. Chem. B, Vol. 101, pp. 6171-6173.

The Japan Society of Mechanical Engineers ed., 2003, Data book of Engineering of Heat Transmission (Dennetsu Kogaku Shiryo), 353 (in Japanese).

Wakatuchi, M., 2002, freezing sea (Koru Umi), In: Hukuda, M., Akira, K., Takahashi, S. (Eds.), Science in polar region (Kyokuti no Kagaku), 15-26 (in Japanese).

Weeks, W.F. and Ackley, S.F.,1982 ,The growth, structure and properties of sea ice, CRREL Monograph.

Yokoyama, E., Sekerka, R.F., 2000, Growth trajectories of disk crystals of ice growing from supercooled water, J. Phys. Chem. B, Vol. 104, 65-67.

Toba, Y., 1970, Kaimen kyokai katei, In: Physical oceanography (Kaiyo butsuri), Tokai univ. press, Tokyo, 145-263 (in Japanese).

Ice and navigation, ice bergs

19th IAHR International Symposium on Ice
"Using New Technology to Understand Water-Ice Interaction"
Vancouver, British Columbia, Canada, July 6 to 11, 2008

First Ice Model testing of the Arctic Tandem Offloading Terminal

Arnor Jensen[1], Basile Bonnemaire[1,2], Sveinung Løset[2], Kåre G. Breivik[4], Karl U. Evers[5], Ola Ravndal[3], Vegard Aksnes[2], Trine Lundamo[1], Christian Lønøy[2]
[1]*Barlindhaug Consult as, Tromsø, Norway*
[2]*The Norwegian University of Science and Technology (NTNU), Trondheim, Norway*
[3]*StatoilHydro, Stavanger, Norway*
[4]*Sevan Marine, Arendal, Norway*
[5]*Hamburg Ship Model Basin (HSVA),Germany*

A new concept for offshore offloading in ice-infested waters is tested in the Large Ice Tank at the Hamburg Ship Model Basin. The test scale was 1:24, and the model was equipped with propulsion and a dry mooring system. The concept, Arctic Tandem Offloading Terminal (ATOT), comprises two units; a moored offloading icebreaker (OIB) and an offloading tanker moored in tandem.

The three basic operational modes of the ATOT are; the OIB moored alone, close loading mode and distant loading mode. These modes are related to the following physical environmental conditions: 1) the OIB moored alone in severe ice conditions, 2) close loading in medium and heavy ice conditions, 3) distant loading mode in light ice conditions and open water. The system is disconnectable making it promising for year-around operation in challenging environments such as the Eastern Barents and Kara Seas.

The OIB is connected to a sub-surface turret mooring and riser system while the tanker is moored on a dry mooring through deck winches on the OIB. The OIB is a purpose designed vessel for operation in ice with azimuth propulsion units fore and aft with an installed power of 20-40 MW depending on the ice conditions to operate in. The sub surface mooring system of the OIB contains a heavy duty spread mooring system with a preliminary horizontal station keeping load capacity up to 40 MN. The mooring system will be connected via a quick disconnectable turret system to the OIB. During the summer of 2007 a series of model testing of the concept was performed showing promising capabilities.

1 Introduction

All-year offshore offloading of hydrocarbons is considered to be a critical factor for safe and sound oil production in ice-infested waters. The present experience with offshore offloading in ice is quite meager. Exceptions are the loading of oil at Varandey in the Pechora Sea and extended-season operations off Sakhalin. Meanwhile substantial efforts are made to identify the technical challenges and to develop robust concepts for all-year offshore offloading in Arctic waters. StatoilHydro has together with industry partners developed a new offshore offloading terminal for oil in ice intended for both shallow and deep waters. This concept, the Arctic Tandem Offloading Terminal (ATOT), is in an early development stage and the concept features and preliminary design are presented herein. The concept is designed for conditions occurring in the Barents Sea, Kara Sea and off Sakhalin and is tested in extreme first year sea ice conditions met in those areas.

The model tests were performed at the Large Ice Model Basin at Hamburg Ship Model Basin (HSVA). The ice tank is 78 m long, 10 m wide and 2.5 m deep. The model test was performed in a model scale, λ=24 which fulfils the Froude and Cauchy similarities (Aston, 1986). Level ice and first year sea ice ridges were produced according to HSVA in-house developed ice production method and to ITTC-Recommended practice (1999a,b,c). Details of ridge production are found in Jensen et al. (2002) and Høyland et al. (2002).

2 Potential concepts for arctic waters

An overview of some concepts for offloading in ice is presented in Bonnemaire et al. (2007). The concepts are grouped into: 1) A variety of fixed terminal designs, 2) Loading behind a GBS structure 3) Tandem loading from a fixed tower or moored vessel, 4) Single anchored vessels and 5) Sub surface moored vessels. There are various obstacles connected to all these concepts such as ice drift and drift changes. The present work aims at presenting possible solutions to key challenges and also use of attractive elements of the offloading concepts outlined in Figure 1.

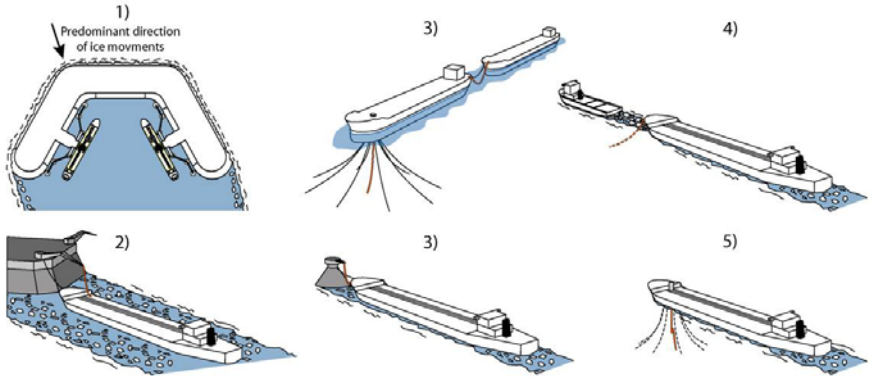

Figure 1. Offloading concepts for operations in the Arctic. 1) Terminal with pronounced ice drift direction, 2) Loading from a Gravity Base Structure, 3) Tandem loading from a production vessel and a loading tower, respectively 4) Single anchored vessel with ice management and a sub surface solution.

3 Some major challenges in ice related to mooring

In cold waters the presence of ice creates a number of additional challenges compared to open water operations. The major factors are:

- Ice features: type of ice, dimensions and velocities.
- Physical ice properties: strengths, temperature and porosity.

First-year sea ice ridges may exert severe loadings on a moored structure and the keel imposes a risk for the sub surface system.

Important operational enhancement of a moored vessel in ice is done by introduction of propulsion appendices. These are important to reduce risk for overloading due to lack of control of ice accumulation and pile up. Examples are found in Bonnemaire et al. (2007).

Drift and dynamic motions of the ice will govern the challenges related to the operability of a moored vessel in ice, and such motions may also cause the main ice load events. On the other hand, land-fast ice may create other challenges related to operations. Drift of sea ice, with land as an escalation parameter, is also a source for tight ice conditions and pressure in the ice cover, which in some cases will make operations and management very challenging and probably impossible to perform. The variability of the ice drift is high and changes in drift directions, zero drift periods and drift speeds of 1 m/s may be expected dependent on the location.

Figure 1 shows the different concepts that were evaluated and Figure 2 displays results in terms of downtime corresponding to the needed loading window, presented by Bonnemaire (2005). From Figure 2 it is seen that the significant change in downtime occurs when the loading window exceeds 5-6 hours, which is linked to tidal oscillations in the ice cover.

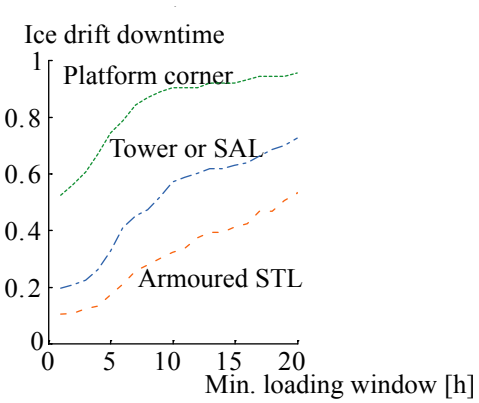

Figure 2 Operability in drifting ice; Downtime due to ice drift events for different loading concepts with full ice management (Bonnemaire, 2005).

Severe ridges may have keels with drafts exceeding the draft of a moored vessel. Icebreaking bows operate in downwards bending and ice is pushed down as shown in Figure 3. This poses risk for the sub surface systems such as mooring and risers which have to be considered in the design. Impact can be reduced by hull design, clearing of appendices from the hull and installation of propulsion units.

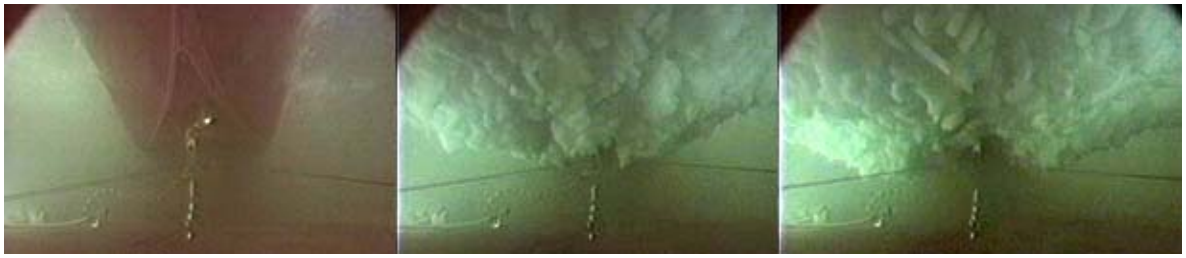

Figure 3 Under-water pictures taken during testing of tanker concept in severe ice ridge conditions. Constant ice impact, but no accumulation of ice was experienced during the tests (Bonnemaire et al., 2007).

4 Features of the ATOT concept in ice conditions and the modeling technique

The Arctic Tandem Offloading Terminal (ATOT) concept comprises two units; a moored offloading icebreaker (OIB) and an offloading tanker in tandem. The three basic operational modes of the ATOT are: the OIB moored alone, close loading mode and distant loading mode. These modes are related to the physical environmental conditions: 1) the OIB moored alone in very severe ice conditions, 2) close loading in medium and heavy ice conditions, 3) distant loading mode in light ice conditions and open water. The latter is primarily affected by waves, and was not a part of the test program. The station-keeping is built around a heavy sub surface turret mooring on the OIB and a limited force controlled mooring system based on wire winches between the tanker and OIB in close loading and a flexible hawser system in distant loading mode. Loading is performed via a double riser system.

Figure 4 The tested Arctic Tandem Offloading Terminal (ATOT) in close loading mode in ice.

4.1 Mooring and riser systems

The basic mooring system of the tanker is in tandem at the OIB stern. The distant mooring system has a preliminary design of two hawser winches with 150 kN pull in capacity and 2 MN maximum load capacity. In far mode the tanker is moored 60 m behind the OIB. The tested configuration for ice operations is the mooring system for close loading comprising two wire winches on the OIB aft deck, with a preliminary design of 2 MN pull power and 3 MN brake power, with a payout rate of 1 m/s. The system is able to disconnect within seconds. The load capacity is based on an operating philosophy that the tanker should have a rapid loading cycle, i.e. stay in the wake as short as possible and avoid any load scenarios that involve changing drift

directions of the ice. Figure 5b) gives an overview of the tanker mooring system, and details of the model set-up is found in Aksnes et al., (2008).

The loading has a preliminary design consisting of two 20 inch risers, flexible hoses between the OIB and the tanker via an A-frame at the aft of the OIB, and bow loading at the tanker. Double risers enhance the loading capacity, and make a loading window of 6 hours possible. Also the flow insurance will be enhanced by several bypass systems that enable circulation in the system. Figure 5a shows a principle sketch of a flow diagram for the ATOT.

Connection of the tanker will be done by pilot lines from the OIB. This system has to be developed in more details, but the standard pneumatic line thrower (shooting lines) is a well-proven solution. Also use of a service vessel is a possible solution, as a standard or a backup solution.

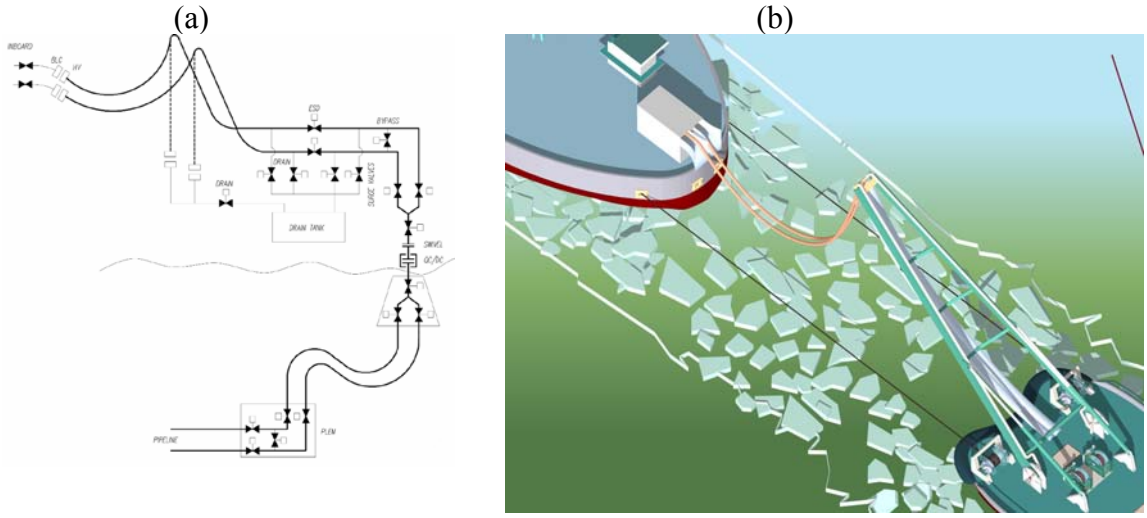

Figure 5. a) Flow diagram for the ATOT showing the turret and flexible hose system, b) the tanker mooring arrangement and tanker hose system in distant loading mode.

The sub surface mooring system of the OIB contains a heavy duty spread mooring system with a preliminary horizontal station keeping load capacity up to 40 MN. The mooring system will be connected via a quick disconnectable turret system to the OIB. The double 20 inch riser system needs a special protection towards ice impact. The present design contains an armored riser system, designed for ice impact of blocks that could be up to 100 to 200 tons. Figure 6 gives an overview of the sub surface turret and riser design. Model testing was performed with a dry mooring system, reported in Bonnemaire et al. (2008b). A dry system gives some important additional features in ice model testing, as the system can move in both X-Y directions, and drift curvatures are possible to model.

Connection of a turret system in ice is pointed out as a challenging operation. This is not tested so far. One of the concept features is that the number of connections of the sub surface system should be limited.

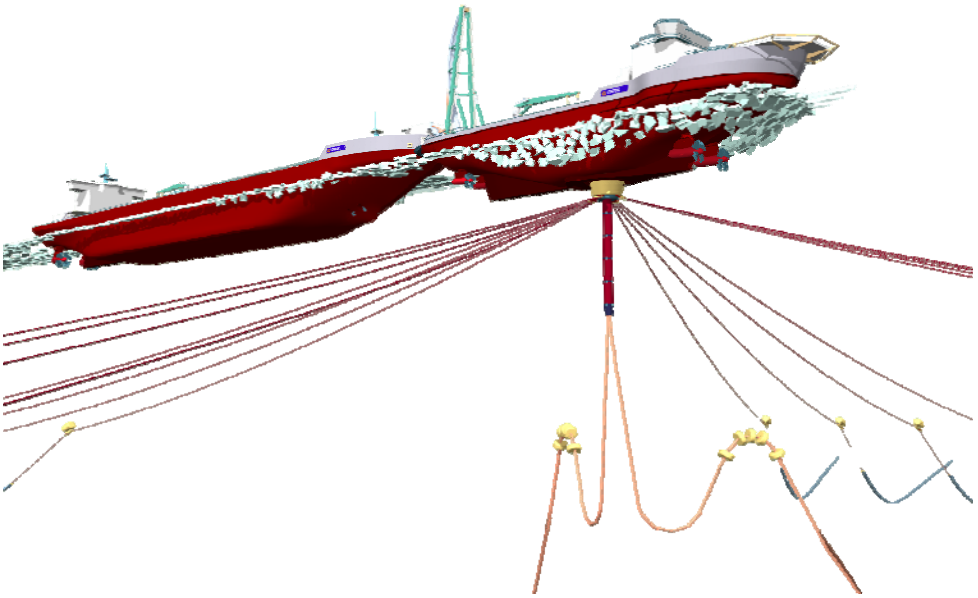

Figure 6 The ATOT in close loading mode in ice with the sub surface mooring and riser system displayed.

4.2 Vessel design

The most basic principle in ice breaking processes is the difference between crushing and bending failure of ice. Transport and escape of ice are critical for maintaining a safe station-keeping in ice. These are important aspects in design of a vessel operating in ice. Typically the icebreaking vessels have a high capacity breaking feature in front and aft while the sides have very limited capabilities in breaking. Figure 7 gives an overview of the icebreaking tanker. The characteristic features, without large modifications of a traditional tanker, will be a long parallel mid-body vessel with flat hull sides. The tanker will also have a variable draft in ballast and loaded conditions. These limitations restrict the capability of the tanker for ice breaking operations even though the tanker has good ice breaking capability both ahead and astern.

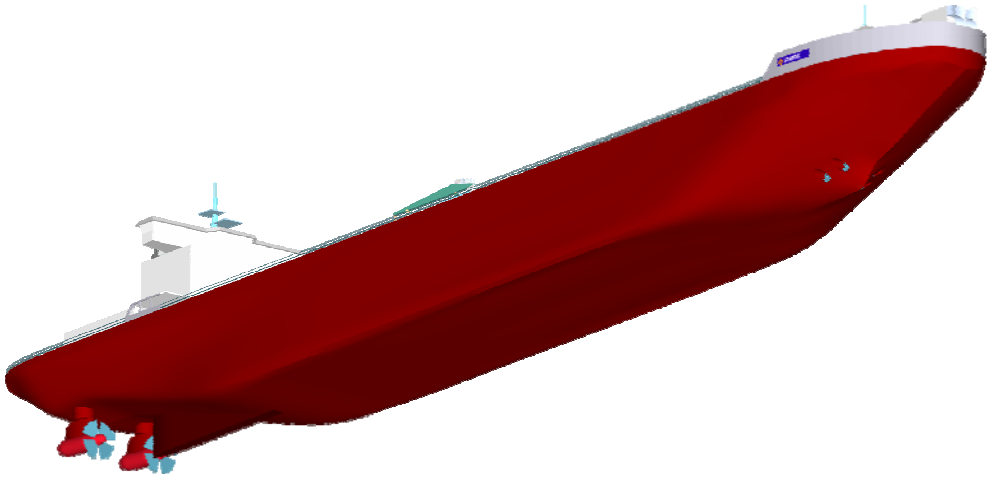

Figure 7 Tanker design, 265 m L_{pp}, 80 000 DWT, for both ahead and astern ice breaking.

Table 1 Dimensions of the tanker model and corresponding values in full scale

TANKER	Full scale	model scale
LOA, m	287.6	11.98
Lpp m	264.2	11.00
B midship, m	35.5	1.48
T, m	15	0.63
Displacement (appr.), t	108 000	7.81
Dead weight, t	80 000	5.78

The OIB is a highly specialized vessel designed with an optimized hull design as an icebreaker with a reamer solution, but at the time same presenting proper open water performances. This is obtained by allowing trimming of the vessel in ice to a draft of 14 m and thereby making use of the reamers while in light ice conditions and open water the draft is only 12 m (see Figure 8). The vessel is further equipped with azimuth propulsion units both fore and aft. The azimuth propulsion enhances the maneuverability of the vessel in ice. When the OIB operates in single mode on its turret, the propulsion will operate in a semi-DP mode to maintain stability and heading of the OIB in severe ice conditions. The installed power will be dependent on ice conditions and type of propulsion, and is foreseen to be in the range of 20 MW to 30 MW. The corresponding bollard pull is 2.5 MN to 4.5 MN dependent of power and propulsion design (i.e. nozzles). This bollard pull will enable the vessel to operate in severe heavy ice and straight drift without mooring assistance.

Figure 8 Preliminary OIB hull and propulsion design, 109 m L_{pp}, 21 000 tons displacement.

Table 2 Dimensions of the OIB model and corresponding values in full scale

OIB	Full scale	model scale
LOA, m	133	5.54
Lpp m	108.8	4.53
B midship, m	26-30	1.08 – 1.25
T, m	13.5 - 14.0	0.58
Displacement (appr.), t	20 800	1.50
Stem angle, °	20	20
Flare angle , °	25	25
Buttock angle , °	18	18

4.3 Ice operations

The basic mode of loading in ice is close loading. This mode eases the operations in ice by reducing the impact from ice on the tanker due to the wake made by the OIB. Further this mode limits the freedom between the tanker and the OIB. The latter has an aft propulsion system that is designed to minimize ice impact and do ice clearing and avoid possible accumulation of ice. The forward propulsion units of the OIB will also be used for reducing the ice transport along the hull and thus minimize the impact from ice on the sub surface systems. A second and important effect will be the channel widening and thereby increased maneuverability of the OIB. Details of the operation and model setup are found in Bonnemaire et al. (2008a).

The ATOT quick disconnection system is designed to release the tanker within a short time window (seconds). Further the OIB has a quick disconnection system via a sub surface turret system. Prepared for disconnection the turret can be released within a minute. The disconnection ability together with a risk management system secures a safe operation of the system, and the design loads and performance of the ATOT in the three modes define the operation envelope:

- The possibility of disconnection associates a high reliability level required for safe operation and the regularity level needed for cost-effective development and operation.
- The operational envelope and design philosophy can be defined, i.e. shut down procedures as a part of the overall safety, and rare events such as multi-year ice, icebergs could be disregarded in design as a shut down condition.
- The collision risk is higher when operating in ice, but the likelihood for a collision is reduced with the disconnectable system of the OIB compared to a scenario with a fixed structure. The mooring also makes a softer system that enables energy accumulation without structural damage.
- Sub surface connection in ice is considered as a much more extensive operation in ice than open water. The sub surface mooring has a strong design, further the OIB is a high capacity ice breaking vessel. Together this enables the OIB to stay on in severe ice conditions, and reduce the number of connections/disconnections to a minimum.
- The concept also operates with a standby/escort icebreaker vessel, included in the risk management system as an observation and ice watch/management vessel.
- The variability in ice drift and sudden drift changes represent a challenge. Thus the best approach to maintain a high uptime in such ice conditions is to restrict the loading window. Loading windows in the range of six hours is believed to have a downtime less than 40 %, and possibly in the range of 20-30 % in actual drift conditions as measured in the Eastern Barents Sea.

5 Model test program and measurements

An extensive measurement program was introduced for the testing. The test set-up included a number of sensors that gave various measurements. The following measurements were performed:

- Carriage speed and position,
- OIB response: surge, sway and heave positions and acceleration, pitch and roll angles and yaw angle rate,
- Tanker response: relative surge, sway, yaw between the vessels, relative elevation between the OIB stern and the tanker bow.
- OIB azimuth propellers: rotation speed, angular position, torque, thrust (only starbord bow), horizontal forces on the pods,
- OIB mooring forces: tri-axial forces between the vessel and the mooring column, and the tension in each mooring cable
- Tanker mooring forces: linear forces in the mooring lines
- Dummy mooring buoy: tri-axial forces between the bucket and the OIB hull.

In addition, underwater and above water video records and pictures documented the tests.

The model testing include all together a program of four ice sheets, two with the OIB operation alone in single mode, and two with the ATOT in close loading mode. Tables 3 to 6 give an overview of the performed tests.

Table 3. Model test #1000 series, OIB alone

#1000 series – OIB alone – Stiff mooring – Level ice, ridges and rubble field		
	Model scale	***Full scale***
Ice drift speed:	0.102 m/s	0.5 m/s
Level ice thickness:	44 mm	1.05 m
Average ice strength:	24 kPa	575 kPa
Max ridge keel depth + sail height:	650 + 90 mm	15.6 + 2.16 m
Ridge consolidation:	Severe (~ 3 level ice thickness)	
Rubble field thickness:	180 mm	4.3 m
Mooring stiffness:	7.7 kN/m	4.4 MN/m
Propulsion power:	4 x 105 W	4 x 7.1 MW

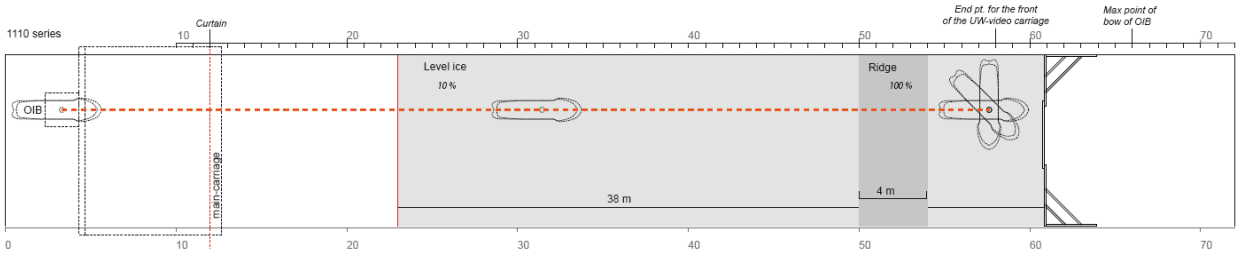

Figure 9 Example of testing trace; overview of model test #1110, OIB in straight mode in level ice and ridges, spot turning in level ice.

Table 4. Model test #2000 series, OIB alone

#2000 series – OIB alone – Soft mooring – Level ice, ridges and broken ice		
	Model scale	*Full scale*
Ice drift speed:	0.102 m/s (#2120: 0.306 m/s)	0.5 m/s (#2120: 1.5 m/s)
Level ice thickness:	39 mm	0.94 m
Average ice strength:	15 kPa	360 kPa
Max ridge keel depth + sail height:	370 + 140 mm	8.9 + 3.4 m
Ridge consolidation:	Light (~ 1 level ice thickness)	
Mooring stiffness:	3.9 kN/m	2.2 MN/m
Propulsion power:	4 x 60 W	4 x 4 MW

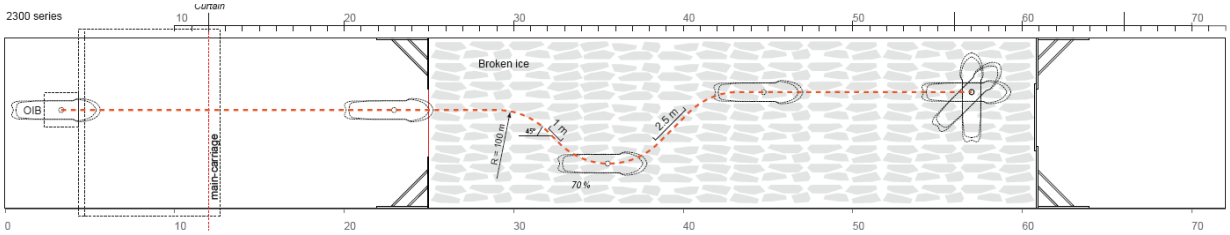

Figure 10 Example of testing trace; overview of model test #2300, OIB in variable ice drift, broken ice.

Table 5. Model test #3000 series, OIB and tanker in close tow

#3000 series – OIB + tanker in close tow – Soft mooring – Level ice, ridges and broken ice		
	Model scale	*Full scale*
Ice drift speed:	0.102 m/s	0.5 m/s
Level ice thickness:	43 mm	1.02 m
Average ice strength:	30 kPa	720
Max ridge keel depth + sail height:	540 + 90 mm	13.0 + 2.2 m
Ridge consolidation:	Medium (~ 2 level ice thicknesses)	
Mooring stiffness:	3.9 kN/m	2.2 MN/m
Propulsion power:	4 x 105 W	4 x 7.1 MW

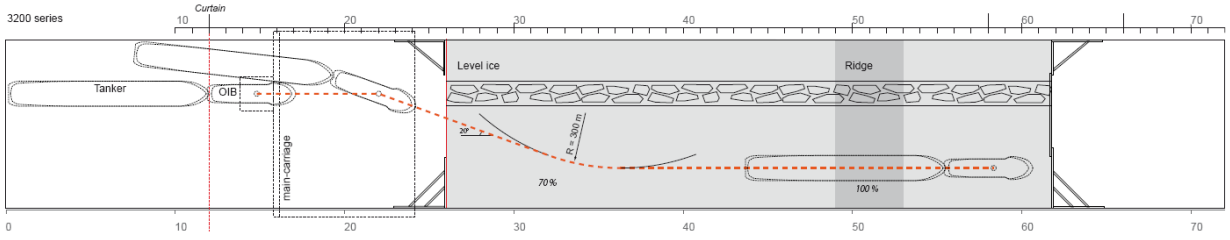

Figure 11 Example of testing trace; overview of model test #3200, OIB and tanker in close tow in variable level ice drift and strait ice ridge drift, partially managed ice on the side.

Table 6. Model test #4000 series, OIB alone

#4000 series – OIB + tanker in close tow – Stiff mooring – Level ice, ridges and broken ice		
	Model scale	*Full scale*
Ice drift speed:	0.102 m/s	0.5 m/s
Level ice thickness:	48 mm	1.16 m
Average ice strength:	20 kPa	480 kPa
Max ridge keel depth + sail height:	620 + 80 mm	14.9 + 1.9 m
Ridge consolidation:	Medium (~ 2 level ice thicknesses)	
Mooring stiffness:	7.7 kN/m	4.4 MN/m
Propulsion power:	4 x 105 W	4 x 7.1 MW

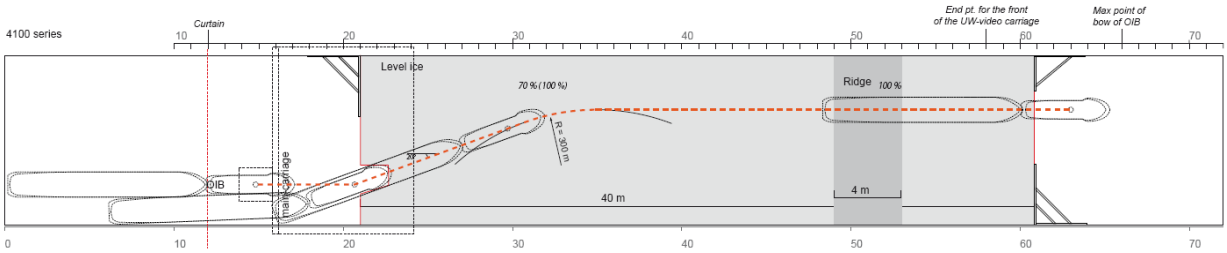

Figure 12 Example of testing trace; overview of model test #4100, OIB and tanker in close towin variable level ice drift and strait ice ridge drift, intact ice sheet.

6 Some test results and model performance

6.1 Maneuverability, yaw stability and hull design of the moored concept

The maneuverability and yaw stability of the moored OIB are two linked effects for which a compromise may have to be found. It was seen for the OIB moored alone:

- The helmsman could steer the vessel in level and broken ice without using 100 % of the installed propeller power.
- The turn on the spot trials of the OIB in level ice were quite satisfactory. By oscillating in yaw, the vessel is breaking the ice with the inclined sides of the bow reamers and stern. The limited vertical sides of the vessel are then not impeding much the vessel motions.
- The OIB is designed with very little stability in yaw in drifting level and broken ice as the mooring centre is close to the vessel centre point. The hull design is not optimized for increased stability in yaw and needs to be taken further. In slow ice drift changes, the OIB is not designed to yaw on its own to follow the ice drift direction changes, active propulsion is needed. In sideway drift, the OIB is neither forced to yaw, inducing risk of large mooring forces in both cases. These mooring load increases can be avoided by turning on the spot with the propellers during sudden changes of drift direction. During slow changes of drift direction, the helmsman needs to be well informed on the actual and upcoming ice drift direction to steer the OIB heading.

- In unmanaged ice ridges, if the ice ridge drift presents an angle with the OIB heading, it can be difficult for the helmsman to steer the OIB during the ridge action, causing large sideway mooring load increase. However, the OIB has to be prepared and be positioned well ahead of these events if possible.

(a) (b)

Figure 13 Model testing of the OIB in single mode operation, a) in severe First Year Sea Ice Ridge, b) manoeuvring in ice.

The effects were different for the OIB when the shuttle tanker was moored in close tow:

- The OIB – shuttle train is very stable in yaw as the mooring centre is in the fore part of the train. In slow drift changes in broken ice, the train follows the ice drift.
- In level ice, the helmsman has little control over the OIB steering as the tanker with its long parallel vertical sides is embedded in the level ice. In case of ice drift changes, the OIB can be pushed to "over-steer" and will drift sideways causing increased mooring forces (see Aksnes et al., 2008).

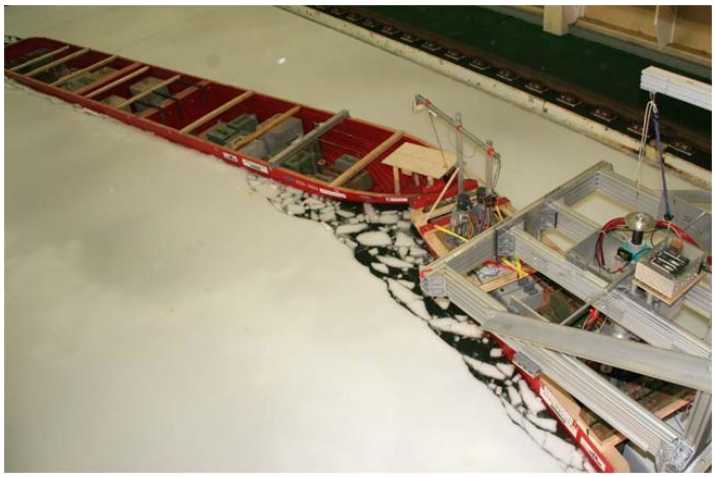

Figure 14 OIB and tanker in close loading mode in changing drift conditions, intact level ice.

The OIB is equipped with reamers on the bow sides. The reamers are inclined and making an angle of 45° with the waterline in a vertical plane transverse to the vessel. In level ice, the reamers are breaking the ice downwards and the broken pieces are tilted. During severe loading the Pitching of the vessel will influence the effect of the reamers.

Figure 15 Breaking of level ice by the reamers in level ice

6.2 Comparison of the measured mooring loads with some expected mooring loads

Results on measured loads and observed sub surface ice interactions are presented by Bonnemaire (2008a,b) and Aksnes (2008).

Table 7 Comparison of maximum measured longitudinal mooring loads ($F_{x,corr}$ measured loads corrected for the propeller forces) with mooring load estimates ($F_{x,est}$)

	run #	$F_{x,est}$ / $F_{x,cor}$		
Ice ridges – straight drift				
OIB	1 110	0.83	1st run	h_k = 15.5 m
	2 200	0.79	2nd run	h_k = 8.9 m
OIB + tanker	3 100	1.28	1st run	h_k = 13 m
	3 200	1.25	2nd run	h_k = 13 m
	4 120	0.91	1st run	h_k = 14.9 m
	4 210	0.91	2nd run	h_k = 14.9 m
Average:		0.99		
Straight ice drift – level ice				
OIB	1110	0.56	1st run	
	2110	0.79	1st run	
	2200	0.74	2nd run	
OIB + tanker	3100	0.87	1st run	
	4120	0.74	1st run	
Average:		0.74		

Prior to the testing campaign a feasibility study of the ATOT was performed. It is possible to estimate the maximum mooring loads that may apply on the moored vessels under certain ice interaction scenarios. These loads estimations are based on extrapolation of measured mooring loads on full scale moored vessels in ice or during model testing of vessels in ice. The extrapolation consists on a scaling and correction of the loads to account for the change in ice

properties and ship geometry. It is thus interesting to compare the measured loads with the expected ones.

Table 7 compares some measured maximum mooring loads with mooring loads estimates. The ability of the mooring load estimates to predict the measured loads vary from test to test, but it is seen that:

- In ridges, the load estimates fit very well with the measured longitudinal mooring load corrected for the thrusters forces (99 % fitting on average, See Bonnemaire et al., 2008 for further details).
- In level ice, the mooring load estimates are under predicting the measured loads (corrected for the thrusters forces), giving only 75 % of the measured load.

7 Conclusions and further work

The ATOT concept is in an early stage of development. The system is designed to operate in challenging first-year ice conditions. There are several challenges that will be addressed based on the model testing.

- The present work shows very promising performance of the ATOT concept.
- Ice loads and impacts on the OIB mooring and tanker mooring is found to be within reasonable design limits.
- The effect of an efficient propulsion system is mainly found to enhance the maneuvering and ice clearing performance, mooring load reduction (see Bonnemaire 2008) is not apparent.
- The performance, including dynamic stability of the ATOT in close loading, performance and limitations regarding variability of ice drift is investigated, and showed promising results
- The performance including dynamic stability of the single OIB in changing ice conditions and severe first-year ice are being studied, and heading stability is a challenge that has to be further investigated.
- Subsurface loading system will have challenges related to transport of ice and ice impact.

Acknowledgements

The work described in this publication was supported by the European Community's Sixth Framework Program through the grant to the budget of the Integrated Infrastructure Initiative HYDRALAB III, Contract no. 022441(RII3). The authors would like to thank the Hamburg Ship Model Basin (HSVA), especially the ice tank crew, for the hospitality, technical and scientific support and the professional execution of the test program in the Research Infrastructure ARCTECLAB. The authors would also like to thank StatoilHydro for funding of the project, fabrication of the physical models, Aker Pusnes in Arendal for their professional work on concept development, ILS in Helsinki for their work on the OIB hulls design and use of tanker lines. Truls Liset's talent for 3D illustrations is also acknowledged.

References

Aksnes, V., B.Bonnemaire, S. Løset and C. Lønøy, 2008. Model testing of the Arctic Tandem Offloading Terminal – Tandem Mooring forces and Relative Motions Between Vessels. Proceedings of the 19th International Symposium on Ice. Vancouver, British Columbia, Canada.

Aston G., D., 1986, River and Lake Ice Engineering. Water Resources Publications, Book Crafters Inc., Chelsea, Michigan.

Bonnemaire, B., A. Jensen, O.T. Gudmestad, T. Lundamo, and S. Løset (2007): Challenges Related to Station-keeping in Ice. Technology as a differentiator in Arctic conditions, 9th annual INTSOK Conference, Houston, Texas, March 2007, 23 p.

Bonnemaire B. (2005): Arctic Offshore Loading Downtime due to Variability in Ice Drift Direction. Journal of Navigation.

Bonnemaire, B., S. Løset and O.T. Gudmestad (2003): Riser Armours for Subsea Offshore Loading of Hydrocarbons in Ice-Infested Waters. Proceedings of the Russian Arctic Offshore Conference, RAO, St Petersburg, Russia, pp. 220-223.

Bonnemaire, B., T. Lundamo, K.U. Evers, S. Løset and Arnor Jensen, 2008a. Model testing of the Arctic Offloading Terminal – Mooring Ice Ridge Loads. Proceedings of the 19th International Symposium on Ice. Vancouver, British Columbia, Canada.

Bonnemaire, B., T. Lundamo, A. Jensen and K.H. Rupp, 2008b. Subsurface Ice Interaction under a Moored Offloading Icebreaker. Proceedings of the 19th International Symposium on Ice. Vancouver, British Columbia, Canada.

Høyland, K.V., A. Jensen, P. Liferov, J. Heinonen, K.U. Evers, S. Løset and M. Maattanen (2001): Physical modelling of first-year sea ice ridges – Part I: Production, consolidation and physical properties. The 16th Int. Conference on Port and Ocean Engineering under Arctic Conditions (POAC), Ottawa, Canada 12th –17th August 2001, Vol. 3, pp. 1483-1492.

Høyland, K.V. (2005): Ridges in the Barents Sea. Proceedings of the 18h Int. Conference on Port and Ocean Engineering under Arctic Conditions (POAC), Potsdam, USA, June 27-30, 2005, Vol. 2, pp. 949-959.

ITTC-Recommended practice (1999a), Testing and Extrapolation Methods Ice testing, General Guidelines. International Towing Tank Conference, Report 7.5-02-04-01, 5 pages.

ITTC-Recommended practice (1999b), Testing and Extrapolation Methods, Ice testing, Test Methods for Model Ice Properties. International Towing Tank Conference, Report 7.5-02-04-02, 4 pages.

ITTC-Recommended practice (1999b), Testing and Extrapolation Methods, Ice testing, Tests in Deformed ice. International Towing Tank Conference, Report 7.5-02-04-02.4, 4 pages.

Jensen, A., S. Løset, K.V. Høyland, P. Liferov, J. Heinonen, K.U. Evers, and M. Maattanen (2001): Physical modelling of first-year sea ice ridges – Part II: Mechanical properties. The 16th Int. Conference on Port and Ocean Engineering under Arctic Conditions (POAC), Ottawa, Canada 12th –17th August 2001, Vol. 3, pp. 1493-1502.

Løset, S., K.N. Shkhinek, O.T. Gudmestad and K.V. Høyland (2006): Actions from Ice on Arctic Offshore and Costal Structures. Krasnodar, St Petersburg, Russia, 2006, 271 p.

19th IAHR International Symposium on Ice
"Using New Technology to Understand Water-Ice Interaction"
Vancouver, British Columbia, Canada, July 6 to 11, 2008

Model Testing of the Arctic Tandem Offloading Terminal Mooring Ice Ridge Loads

Basile Bonnemaire[1,2], Trine Lundamo[1], Karl-U. Evers[3], Sveinung Løset[2], Arnor Jensen[1]
[1]*Barlindhaug Consult AS, Tromsø, Norway*
[2]*The Norwegian University of Science and Technology (NTNU), Trondheim, Norway*
[3]*Hamburgische Schiffbau-Versuchsanstalt GmbH (HSVA), Hamburg, Germany*
basile.bonnemaire@barlindhaug.no, trine.lundamo@barlindhaug.no, evers@hsva.de, sveinung.loset@ntnu.no, arnor.jensen@barlindhaug.no

A new concept for offshore offloading in ice-infested waters is proposed. The concept, Arctic Tandem Offloading Terminal (ATOT), comprises two units; a turret moored offloading icebreaker (OIB) and an offloading tanker in tandem. The concept was tested at scale 1:24 at the HSVA ice tank in Hamburg, Germany.

The model tests included the simulation of ridge penetration of deep ice ridges. Four ice ridges up to 15.5 m deep were built and the offloading concept was towed several times through these ridges. It was observed that the side mooring loads which are highly dependent on the boundary conditions contributed significantly (30 % on average) to the maximum mooring loads.

The OIB was equipped with 4 powerful azimuth propellers, 2 at the bow and 2 at the stern. During ridge interactions those were used for ice milling and for mooring load reduction. It was seen that their thrust effect was limited due to heavy ice interaction.

The measured mooring loads are compared with mooring load estimates based on former measurements (model and full scale). The correlation between estimates and measurements is rather good.

1 Introduction

The Arctic Tandem Offloading Terminal (ATOT) is a new concept for offshore offloading in ice-infested waters. The concept comprises two units (see Figure 1): a turret moored offloading icebreaker (OIB) and an shuttle tanker moored in tandem at the OIB aft. The OIB is interacting with the incoming ice which may be intact or managed. The loading tanker is moored at the aft of the OIB in tandem, at a distance of 60 m in open water (distant tow) or inside a notch at the OIB stern in ice conditions (close tow as shown in Figure 1). See Jensen et al. (2008) for more details on the concept.

To ensure a proper operability rate for the concept, the downtime due to severe ice conditions or ice events should be limited. The OIB design basis is that it should be able to withstand the interaction from severe ice conditions, such as unmanaged deep ice ridges in straight drift. The operational strategy is that the tanker may disconnect and reconnect to the OIB if required by the ice conditions, but that the OIB should be able to remain moored as long as possible.

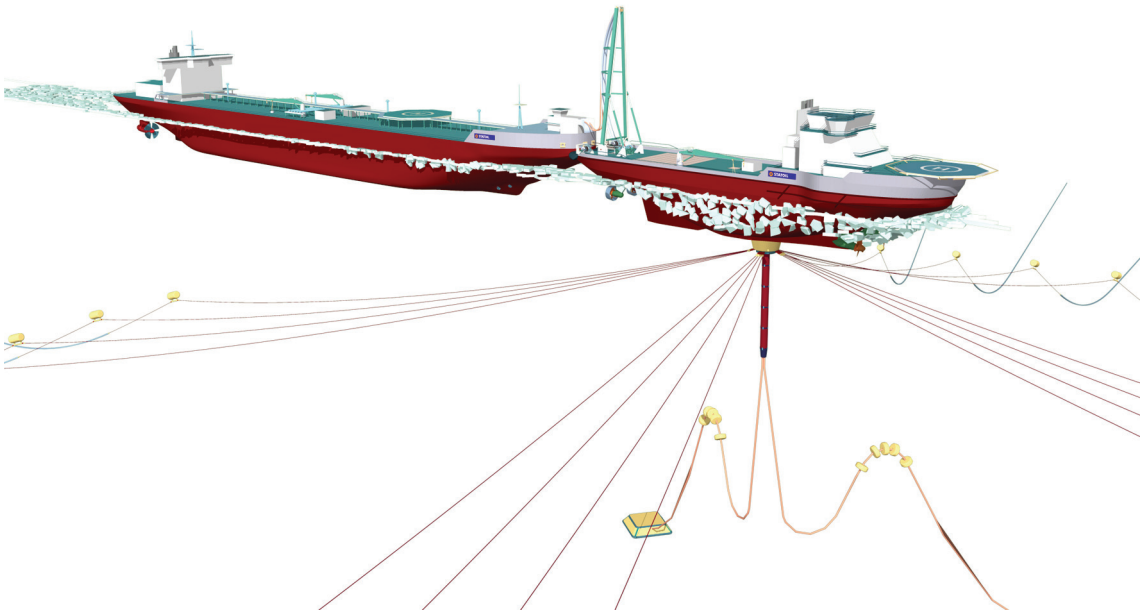

Figure 1 Sketch of the ATOT concept with the turret moored OIB and the tanker moored in close tow

The OIB is thus moored on a strong mooring via a sub-surface loading buoy connected inside a turret. The OIB is optimized for icebreaking with in particular a spoon icebreaking bow. Reamers on the side of the OIB increase its maneuverability in ice and break a wider channel to reduce the ice forces on the tanker. The OIB is equipped with 4 strong azimuth thrusters, 2 at the bow and 2 at the aft.

The ATOT concept was tested at the HSVA ice tank (Hamburg, Germany) during summer 2007 (see companion papers Jensen et al., 2008, Aksnes et al., 2008 and Bonnemaire et al., 2008). The concept was subjected to heavy ice interactions and the vessels responses were monitored.

This paper presents the analysis of the mooring loads during the ice ridge interactions with straight ice drift. The effect of the thrusters milling the incoming ice is discussed. The measured mooring loads are compared to load estimates based on former measurements.

2 Model Setup

The testing program included testing of the two vessels, the OIB and the shuttle tanker moored in close tow. The OIB was moored on the main carriage of the ice tank and pulled through the testing area to simulate different ice drift scenarios.

The chosen model scale was 1:24, and Froude scaling was chosen to respect inertia and gravity forces which are dominant in the present problem. The flexural strength of the ice sheet was also scaled accordingly. The model ice is prepared following a special technique developed in house (see Evers and Jochmann, 1993).

Four ice sheets were produced in a similar manner, all included a long part of level ice (around 30 m) followed by an embedded ridge and some more level ice (about 7 m). The physical properties of the ice sheets are summarized in Table 1.

Table 1 Physical properties of the produced ice sheets, level ice and ridged ice (h_i: level ice thickness, σ_f bending strength of the level ice, h_k, h_s and w_k, keel depth, sail height and keel width of the ridges).

	Model scale			*Full scale*		
Ice sheet	h_i [m]	σ_f [kPa]	(h_k + h_s) x w_k [m]	h_i [m]	σ_f [kPa]	(h_k + h_s) x w_k [m]
2000	0.039	15	(0.37 + 0.14) x 4.5	0.94	360	(8.9 + 3.4) x 108
3000	0.043	30	(0.54 + 0.09) x 4	1.03	720	(13.0 + 2.2) x 96
4000	0.048	20	(0.62 + 0.08) x 4	1.15	480	(14.9 + 1.9) x 96
1000	0.044	24	(0.65 + 0.10) x 4	1.06	580	(15.5 + 2.3) x 96

2.1 Model of the vessels

Models of the two vessels were built at a scale 1:24 and equipped for the testing. Table 2 gives the main dimensions of these vessels in model and full scales (see also Figure 2 and Figure 3).

Table 2 Dimensions of the OIB and the tanker models and corresponding values in full scale

	OIB		Tanker	
	Full scale	model scale	Full scale	model scale
LOA, m	133	5.54	287.6	11.98
Lpp, m	108.8	4.53	264.2	11.00
Breadth, m	26-30	1.08 – 1.25	35.5	1.48
Draught, m	13.5 - 14.0	0.58	15	0.63
Displacement (appr.), t	20 800	1.50	108 000	7.81

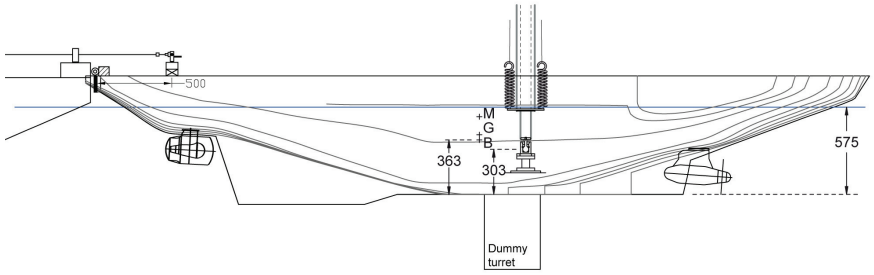

Figure 2 Side drawing of the OIB model with the mooring column and the tanker at the stern (mm, model scale)

Figure 3 The OIB penetrating a ridge, with the tanker moored in close tow in the background

2.2 Thrusters design

The OIB model was equipped with models of azimuth propellers both at the bow and at the stern of the vessel. The latter were equipped with nozzles. All propellers were fully controllable in real time by the captain on the bridge. The available power from the propellers is given in Table 3. It was increased between test series 2000 and 3000. The power increase aims at giving the propellers a power reserve so that they will not stop when interacting with ice. More details on the thrusters use and operational strategy is found in Bonnemaire et al. (2008).

Table 3 Installed propeller power on the OIB model (full-scale value in parenthesis)

		Installed power	Thrust
Tests 2000 and open water tests	Bow:	2 x 60 W (2 x 4 MW)	2 x 45 N (2 x 620 kN)
	Stern:	2 x 60 W (2 x 4 MW)	2 x 48 N (2 x 660 kN)
Tests 3000, 4000 and 1000	Bow:	2 x 105 W (2 x 7.1 MW)	2 x 66 N (2 x 910 kN)
	Stern:	2 x 105 W (2 x 7.1 MW)	2 x 72 N (2 x 995 kN)

2.3 Anchoring of the OIB

For practical reasons, a dry mooring mounted over the vessel is easier to handle. A new system giving mooring characteristics independent of the vessel excursion was developed for the test series.

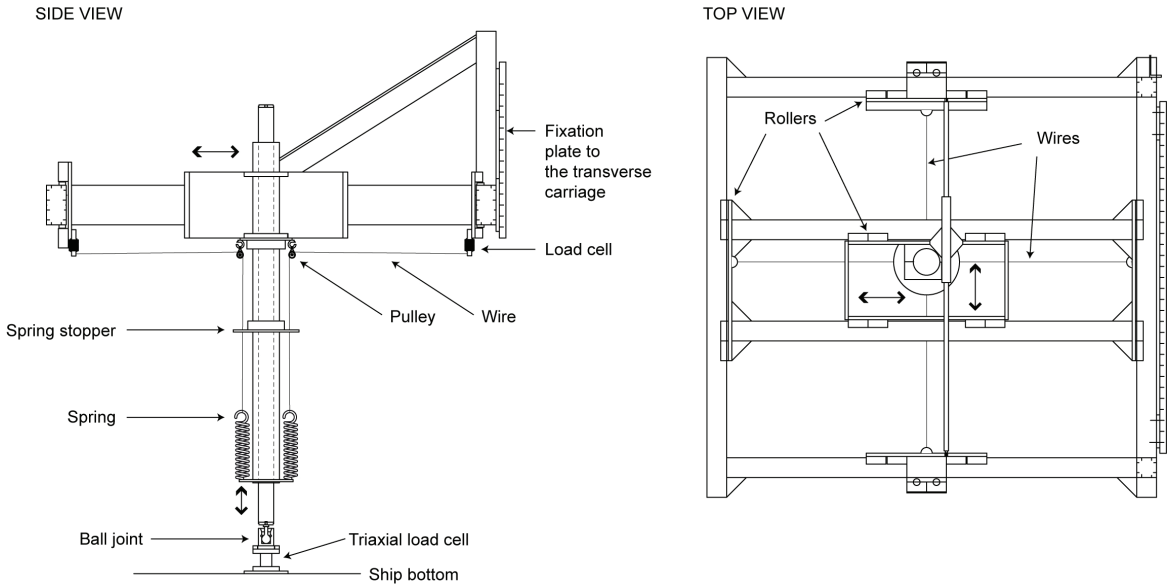

Figure 4 Dry mooring elevation and side view, at rest and under tension

Figure 4 present sketches of the dry mooring principles. A vertical column is fixed to the bottom of the boat via a universal joint and a 3D load cell. The column is thus fixed in surge, sway and heave to the vessel. However the column is free to heave in the mooring frame. The column is mounted on a crossed beam carriage that can move in x and y directions. On each beam is mounted a cable – spring and load cell mooring line system that control the force in surge and sway between the vessel and the towing carriage.

Some advantages of this system are:

- The pulling direction of each mooring line is independent of the vessel offset, as it is practically with a full scale mooring system.
- Large offsets can be achieved (± 0.3 m with the present springs)
- By choosing the springs stiffness one can obtain a perfectly elliptical or circular mooring characteristic (in the horizontal plane).

However the mooring vertical force is not modeled, though it might not be a problem. The application point for the mooring force is also vertically elevated (see Figure 2), as the force is applied some distance over the hull bottom. In full scale, this force will be applied on the bottom part of the mooring buoy. This will somewhat influence the heave and pitch response of the vessel, and more important increase artificially the roll stability under side drift.

a) b)

Figure 5 a) View of the mooring frame, b) The dry mooring mounted on the transverse carriage and connected to the OIB

One interesting concern is the influence of the vessel mooring characteristic (in particular the eigen-periods of the moored vessel) on the ice load on the vessel. The vessel response will be dependant on the mooring stiffness. 2 set of springs were used to achieve to different mooring stiffness's. A soft mooring was used for the open water tests, 2000 and 3000 series, and a stiff mooring was installed during series 4000 and 1000. The mooring stiffness's are presented in Table 4.

Table 4 Mooring stiffness and extensibility together with resonance periods of the moored vessel

	Model scale				*Full scale*			
Mooring config.	Mooring stiffness	Mooring extensibility	Approx surge resonance period		Mooring stiffness	Mooring extensibility	Approx surge resonance period	
			OIB	OIB + tanker			OIB	OIB + tanker
1. Soft	3.9 kN/m	± 0.3 m	3.6 s	9.5 s	2.2 MN/m	± 7.2 m	17.5 s	47 s
2. Stiff	7.7 kN/m	± 0.3 m	2.8 s	7 s	4.4 MN/m	± 7.2 m	13.7 s	34.3 s

2.4 Mooring of the tanker in close tow

In two test series (3000 and 4000 series), a tanker model is moored in close tow at the stern of the OIB. The tanker is then connected to the OIB via two lines and a weight system limiting the tension in the lines to simulate the towing winches at the OIB stern, Reference is made to Aksnes et al. (2008) for more details on the mooring of the tanker.

3 Ice ridge mooring loads

Each of the four ice sheets included an ice ridge (see Table 1). The recorded mooring loads during ice ridge penetration events at 0.5 m/s ice drift speed (full scale) are analyzed in the following. In each ice sheet, the ridges were penetrated several times at different positions. The boundary conditions give higher confinement during the first penetration.

Table 5 Comparison of maximum measured mooring loads during ice ridge events in straight drift (measured loads and measured loads corrected to account for the propeller forces) with mooring load estimates [subscripts definitions: *x*: longitudinal force, *tot*: total horizontal mooring force, *cor*: corrected measurements, *est*: mooring load estimates]

	run #	$F_{x,cor}$ / F_x	$F_{tot,cor}$ / F_{tot}	$F_{x,est}$ / F_x	$F_{x,est}$ / $F_{x,cor}$		
OIB	1 110	1.08	1.15	0.89	0.83	1st run	h_k = 15.5 m
	2 200	1.47	1.16	1.15	0.79	2nd run	h_k = 8.9 m
OIB + tanker	3 100	1.25	1.21	1.60	1.28	1st run	h_k = 13 m
	4 120	1.04	1.05	0.95	0.91	1st run	h_k = 14.9 m
	3 200	1.17	1.21	1.45	1.25	2nd run	h_k = 13 m
	4 210	1.09	1.10	1.00	0.91	2nd run	h_k = 14.9 m
			Average :	1.17	0.99		

In all tests, a difference was observed between the maximum longitudinal force and the total horizontal mooring load (see Figure 6). This difference is due to the non negligible contribution of the transverse mooring forces in sway.

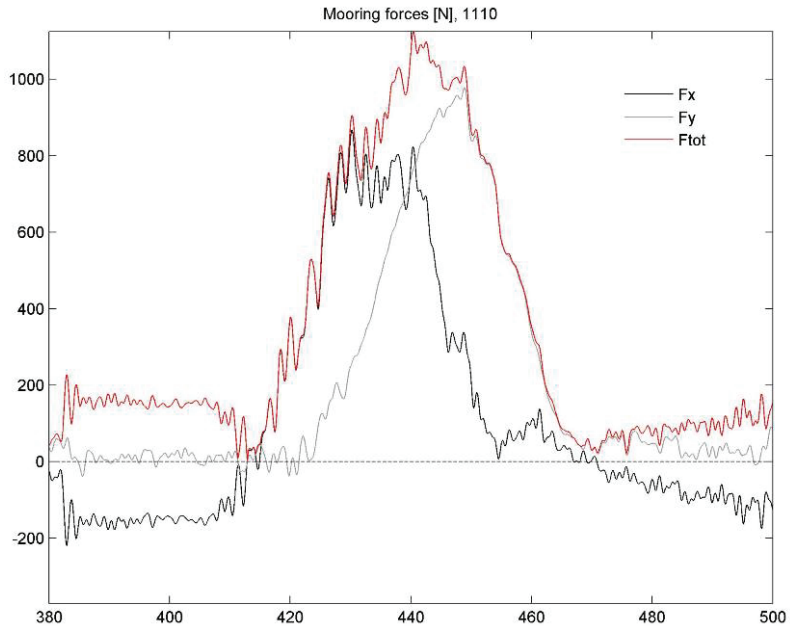

Figure 6 Recorded turret mooring forces in time during a ridge interaction (run 1110) (model scale, Fx, longitudinal mooring load, Fy, transverse mooring load, Ftot, total horizontal mooring load)

As seen in the example in Figure 6, during the ice ridge interaction, the mooring load in surge is first increasing. The vessel penetrates the ridge and the failure starts. Depending on the failure main direction, side loads are then building up. The two load components (in surge and sway) are not simultaneous. The max total mooring load was on average 30 % higher than the max longitudinal mooring load. The difference was often larger during the second penetration of an ice ridge, as the boundary conditions were not identical on each side of the vessel.

It seems that the level of the transverse mooring loads depends little on the longitudinal loads and more on:

- The angle of penetration of the vessel in the ridge compared to the ice drift direction,
- The direction of failure propagation in the ridge. If the ridge is split, the vessel bow will try to follow the split.
- The degree of embedment of the ridge.

It is thus important to consider these two load components (longitudinal and transverse) separated when performing load estimations. This also underlines that ice management on the sides of the moored vessel is also of high importance.

4 Effect of the moored tanker in tandem on the OIB mooring loads

The OIB breaks the ice in front of the tanker. But the OIB is narrower and the effect of the reamers is limited during the ridge interactions due to pronounced pitch motion of the OIB in severe load events. The tanker moored in tandem at the stern of the OIB is then subjected to an ice load increase when entering the ridge.

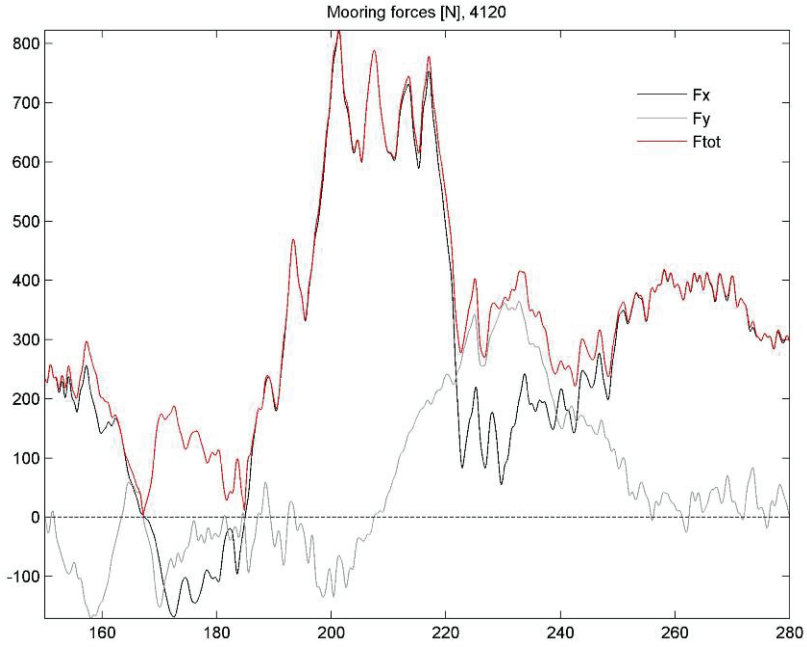

Figure 7 Recorded mooring forces in time during a ridge interaction in run 4120. The tanker is moored in close tow behind the OIB (model scale values, Fx, longitudinal mooring load, Fy, transverse mooring load, Ftot, total horizontal mooring load)

An example of the measured turret mooring loads is given in Figure 7. The tanker interacts with the ice ridge when the OIB is drifting out of the ice ridge. The load peaks due to these effects are not simultaneous (see time series in Figure 7, the OIB penetrates the ridge at 200 – 220 s and the tanker at 250 – 270 s). The tanker moored in tandem has little consequences on the ridge mooring design ice loads (as also reflected in Table 1).

5 Effect of the propeller use on the mooring loads levels

The OIB is equipped with 4 powerful azimuth propellers and their use is important in the operational strategy of the concept. The absolute effect of their use is difficult to quantify from the model test results, as all tests were run with the propellers installed on the vessel. The following part discusses the mooring loads and the measured forces on the propeller drives (which are the sum of the thrust forces and the ice forces on the propeller drive).

During the ice ridge interactions the propellers were running backwards at nearly full power with an outward angle of 20 – 30°. The aim is to combine efficient ice milling and subsurface ice management together with some possible mooring load reduction due to the rubble disturbance and the propeller thrust. The measured mooring forces are thus corrected by subtracting the forces on the propeller drives, such as:

$$F_{x,cor} = F_x - F_{x,prop} \quad \textbf{[1]}$$

The ratios between the maximum corrected mooring loads and the maximum measured loads are reported in Table 5. The comparison of the measured mooring forces and their correction shows that the mooring forces are reduced by 14% due to the propeller action during a ridge interaction. An important condition for this mooring load decrease is that the propellers do not stop rotating under during the interaction with the ice ridge.

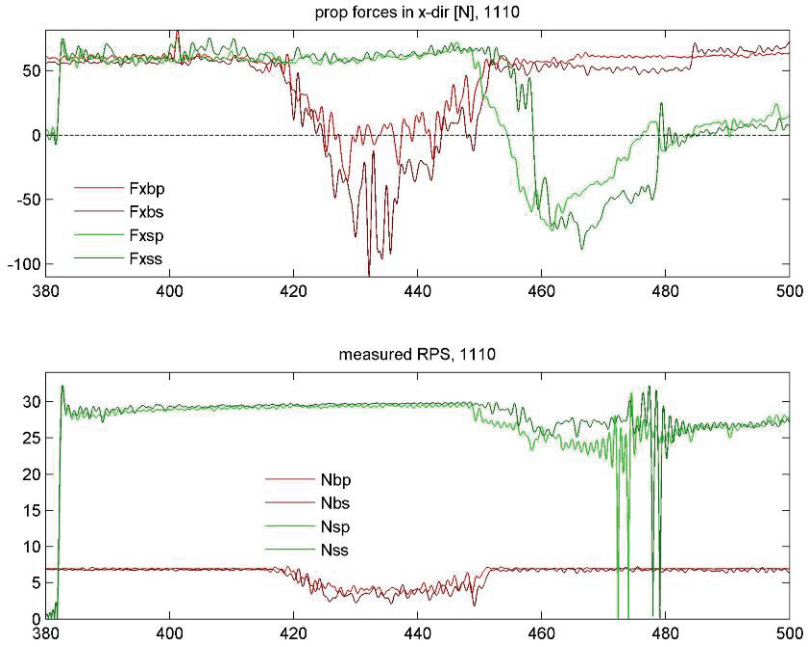

Figure 8 Measured longitudinal loads on the azimuth propeller drives and rotation speed during an ice ridge interaction. At 4230 s the bow of the OIB is in the ridge, at 470 s, the stern of the OIB is in the ridge (model scale values, b: bow, s: tern, p: port: s: starboard)

The loads from the propeller drives on the vessel were always reduced during the ice ridge interaction (see Figure 8). Their maximum effect was on average only 38 % of the measured thrust before entering the ridge. This is probably due to:

- Increased ice forces on the drives,
- Required power to break the ice,
- Disturbed flow upstream the propellers.

This effect was seen on both bow and stern propellers. In some cases (such as seen in Figure 8) the total load was opposite to the thrust. However the perturbation on the bow and stern propellers was delayed in time, such as full efficiency was always available on one set of propellers. Figure 8 shows also that the ice interaction is non negligible with the stern propellers with events of coughing on the stern propellers (see also Bonnemaire et al., 2008). The same type of thrust reduction is seen in during the tests in the rubble field (1320).

6 Comparison of the measured mooring loads with estimates of expected mooring loads

In order to get an estimate of the expected mooring loads on a moored vessel in certain conditions, it is possible to scale and correct exiting measurements. This will give an estimation of the load level. The procedure includes:

- Froude scaling of the problem (forces, geometry…) to account for the size difference between the structures
- Correction of the load to account for differences in aspect ratio or hull form (such as buttock and flare angles) using empirical formulas
- Correction of the load to account for differences between the target ice properties and the original ice properties (thickness and flexural strength corrections)

Such correction laws are reported by Wright (1999, based on work by Keinonen et al., 1989, 1991) and by Elvebakk and Lindberg (1998).

Mooring load estimates were calculated for the moored OIB in the tested ice conditions by scaling results from:

- Two model test series of turret moored tankers in ice (see Løset et al., 1998 and Jensen, 2002)
- Full scale measurements of mooring loads of the Kulluk conical drilling vessel (see Wright, 1999).

Table 5 compares the measured maximum mooring loads during interactions with ridges in straight drift with mooring loads estimates (estimates for the same ice conditions, reported as $F_{x,est}$ in Table 5). The ability of the mooring load estimates to predict the measured loads vary from test to test, but it is seen that:

- The load estimates fit well with the measured longitudinal mooring load corrected for the thrusters forces (99 % fitting on average, with an error of about 20 % for each estimate).
- The load estimate are on average 17 % over the measured longitudinal mooring loads, this is in agreement with what was found on the effect of propellers during ridge interactions.

- The mooring load estimates are under the total measured mooring load. But the total mooring load includes side mooring loads which are not taken into account in the estimates.

7 Conclusions

The present paper discusses the mooring loads measured on the OIB mooring during interactions with ice ridges in straight drift. Some main observations are:

- The level of the mooring loads during the ice ridge interactions was often set by the transverse loads. In reality, those will depend on the embedment of the ridge. The max total mooring load was on average 30 % higher than the max longitudinal mooring load.
- The OIB mooring load increase due to the interaction between the ice ridge and the tanker moored in close tow is delayed in time and do not cumulate with the OIB turret mooring peak loads.
- The effect of the propellers milling the incoming ice and having a thrust directed backwards reduced slightly the mooring loads during the ridge interactions (14 % on average), but the thrusters efficiency was largely reduced due to the ice interactions on the propellers.
- The comparison of the measured mooring loads with mooring load estimates based on other mooring load measurements showed a good fit for the longitudinal mooring loads in ice ridges. However, the estimations do not account for the side mooring loads that are highly dependent on the boundary conditions

The present analysis of the mooring loads needs to be refined further. A particular aspect of relevance is the back-calculation of the ice force applying on the vessel and analysis of the effect of the use of different mooring stiffness's on the ice load.

Acknowledgements

The work described in this publication was supported by the European Community's Sixth Framework Program through the grant to the budget of the Integrated Infrastructure Initiative HYDRALAB III, Contract no. 022441(RII3). The authors would like to thank the Hamburg Ship Model Basin (HSVA), especially the ice tank crew, for the hospitality, technical and scientific support and the professional execution of the test program in the Research Infrastructure ARCTECLAB. The authors would also like to thank StatoilHydro for funding of the fabrication of the physical models, as well as NTNU students Vegard Aksnes and Christian Lønøy for the courageous and valuable help they provided during those long weeks in Hamburg. Truls Liset's talent for 3D illustrations is also acknowledged.

References

Aksnes V., Bonnemaire B., Løset S. and Lønøy C. (2008): Model Testing of the Arctic Tandem Offloading Terminal – Tandem Mooring Forces and Relative Motions between Vessels. *Proceedings of the 19th International Symposium on Ice. Vancouver*, British Columbia, Canada.

Bonnemaire, B., Lundamo, T., Jensen, A. and Rupp KH, 2008. Subsurface Ice Interactions under a Moored Offloading Icebreaker. Proceedings of the 19th International Symposium on Ice. Vancouver, British Columbia, Canada.

Elvebakk, T. and E. Lindberg (1998): Ice model testing of coast guard patrol vessel KBV201. M.Sc. Thesis Chalmers University of Technology Report no: X-98/96, 68 p.

Evers, K. U. and Jochmann, P., 1993. An Advanced Technique to Improve the Mechanical Properties of Model Ice Developed at the HSVA Ice Tank. *Proceedings of the 12th International Conference on Port and Ocean Engineering under Arctic Conditions*. Hamburg, Germany, pp. 877-888.

Jensen, A., Bonnemaire, B., Rupp, K. H., Løset, S., Breivik, K. G., Evers, K. U., Ravndal, O., Aksnes, V., Lundamo, T. and Lønøy, C., 2008. First Ice Tank Model Testing of the Arctic Tandem Offloading Terminal. *Proceedings of the 19th International Symposium on Ice*. Vancouver, British Columbia, Canada.

Jensen, A. (2002): Evaluation of Concepts for Loading of Hydrocarbons in Ice-infested Waters. Doctoral Thesis, NTNU, Norwegian University of Science and Technology, Trondheim.

Keinonen, A. J., R. P. Browne and C. Revill, 1989. "Icebreaker Design Synthesis – Analysis of Contemporary Icebreaker Performance". Report for Transportation Development Centre, Transport Canada. TP 9992E, September 1989.

Keinonen, A. J., R. P. Browne and C. Revill, 1991. "Icebreaker Design Synthesis – Phase 2 - Analysis of Contemporary Icebreaker Performance." Report for Transportation Development Centre, Transport Canada. TP 10923E, September 1991.

Løset, S., Ø. Kanestrøm and T. Pytte (1998): Model Tests of a Submerged Turret Loading Concept in Level Ice, Broken Ice and Pressure Ridges. Cold Regions Science and Technology, Vol. 27, pp. 57-73.

Wright, B. and Associates (1999): Evaluation of Full Scale Data for Moored Vessel Stationkeeping in Pack Ice (With Reference to Grand Banks Development). Report submitted to the National Research Council of Canada, PERD/CHC Report 26-200, 103 p.

19th IAHR International Symposium on Ice
"Using New Technology to Understand Water-Ice Interaction"
Vancouver, British Columbia, Canada, July 6 to 11, 2008

Back-calculation of the Ice Load Applying on a Moored Vessel

Trine Lundamo[1], Basile Bonnemaire[1,2], Arnor Jensen[1], Ove T. Gudmestad[3,2]
[1]Barlindhaug Consult as, Tromsø, Norway
[2]The Norwegian University of Science and Technology (NTNU), Trondheim, Norway
[3]StatoilHydro, Stavanger, Norway
Trine.Lundamo@barlindhaug.no, basile.bonnemaire@barlindhaug.no,
Arnor.Jensen@barlindhaug.no, otg@statoilhydro.com

Studies on moored vessels in ice usually report on the mooring loads which reflect the structural response of the vessel and rarely on the actual ice load. In the present study, results from model tests of an Arctic Shuttle barge at the HSVA ice tank in 1999 are reanalyzed.

A numerical model of the moored vessel is established to back-calculate the ice load applying on the vessel in both heave and surge. As the heave of the vessel was not measured, it was back-calculated using a numerical model of the mooring.

The implementation of the dynamic model seems to give realistic time series for the ice load applying on the vessel. The surge components of the mooring and the ice loads present similar trends, but the vertical loads differ a lot in magnitude. The statistical properties of the signals differ as well. The longitudinal ice load presents a larger standard deviation, which is increasing during ice ridge interactions. The distribution of the measured and the calculated loads are also compared.

1 Introduction

Though activities have been on-going in ice covered seas for decades, the experience with the operation of moored structures is limited. There exist, however, some full scale experiences with moored vessels in ice, in particular in the Beaufort Sea, with the operation of moored drilling vessels. With the growing interest for field developments in the Arctic in areas with mid to deep waters, there is an increasing need to solve the challenges associated with the operations of a moored long-body vessel in ice. One particular challenge is the required high operability, even in harsh ice conditions.

Many studies on moored structures in ice report the horizontal mooring loads (see e.g. Løset et al., 1998, Wright, 1999, Jensen, 2002). However, the mooring loads reflect the structural response of the moored vessel and will differ from the ice loads applied on the vessel. The ice load is challenging to measure in both model and full scale as this load applies over a large area of the hull.

The present common practice for the designer is to use measured mooring loads and to scale them using scaling and empirical laws to a particular design. Then the structure's response is scaled rather than the ice action.

The present paper describes an attempt to back-calculate the horizontal and vertical ice loads applying on a vessel from measured mooring loads during ice tank testing. A numerical model is presented, and some properties of the calculated ice loads are discussed.

2 Test setup from HSVA

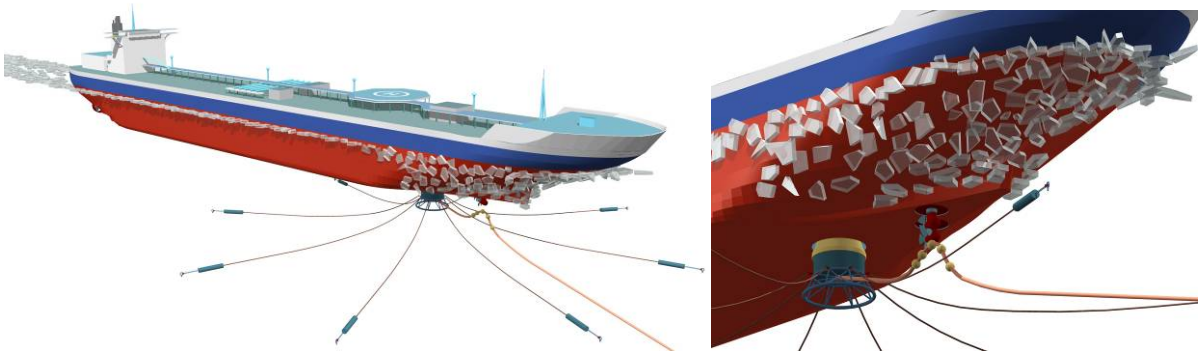

Figure 1. Sketch of the model tanker in loading position, connected to the mooring system, and close up view of the turret area with the loading buoy, the model riser, the bow retrievable propellers and the mooring lines (with their springs).

The model test of the Arctic Shuttle Barge concept for loading oil took place in the HSVA ice tank in Hamburg (Germany) in the autumn of 1999, and was performed at a model scale 1:25. Froude scaling was chosen to respect inertia and gravity loads, which are dominant in the present problem. The flexural strength of the ice sheet was also scaled accordingly.

The concept is based on a turret moored barge and a pusher that works as the main propulsion and connects/disconnects to a notch in the aft of the barge (see Jensen et al., 2000b). The barge is moored on a spread mooring fixed to the loading buoy of the offloading terminal (see Figure 1).

The barge has a bow with high icebreaking capability. The bow form is important for the concept and can be characterized as a spoon bow with 22º stem angle and highly flared frames in the icebreaking zone. Table 1 shows other geometrical features for the barge. A wedge-shaped plough at the bow of the barge serves as an ice clearing system of the turret/moon pool area (see Jensen, 2002, for more details on the test setup).

Table 1. Main geometrical features of the Arctic Shuttle Barge, full scale (Jensen et al., 2000a).

Parameters	Ballast	Loaded
Water line length, L_{pp} [m]	255	255
Vessel beam (width), B_w [m]	38	38
Vessel draft, D [m]	11.5	16
Mass [t]	80 000	120 000

3 Test matrix and testing procedures

The test matrix for the barge in moored condition is shown in Table 2. All tests were run at the same ice drift speed of 0.5 m/s (full scale), and with the barge bow retrievable propellers (see Figure 1) washing backwards and 45° outwards. The analyzed tests were performed in 2 ice sheets, each including an embedded ice ridge.

Table 2. Test matrix (full scale) for the moored Arctic Shuttle Barge. Model scale data is given in brackets (from Jensen et al., 2000b). The ice drift speed is v = 0.5 m/s (0.1 m/s).

Test number	Test setup
3000	Level ice (Ballast condition) h = 1.2m (48 mm); σ_f = 750 kPa (30 kPa)
3100	Ridge (Ballast condition) h_k = 14.5 m (580 mm)
4000	Level ice (Loaded condition) h = 1.2 m (48 mm); σ_f = 750 kPa (30 kPa)
4100	Ridge (Loaded condition) h_k = 11.3 m (450 mm)

The tests were performed with the barge being towed by a mooring system that was placed on a false bottom, see Figure 2. The system was towed through level ice and pressure ridges. During the tests, loads in each mooring line and the total loads in a triaxial load cell in the loading buoy

were recorded. The surge motion of the barge was also measured. Figure 2 show sketches of the setup of the mooring system (Jensen et al., 2000b).

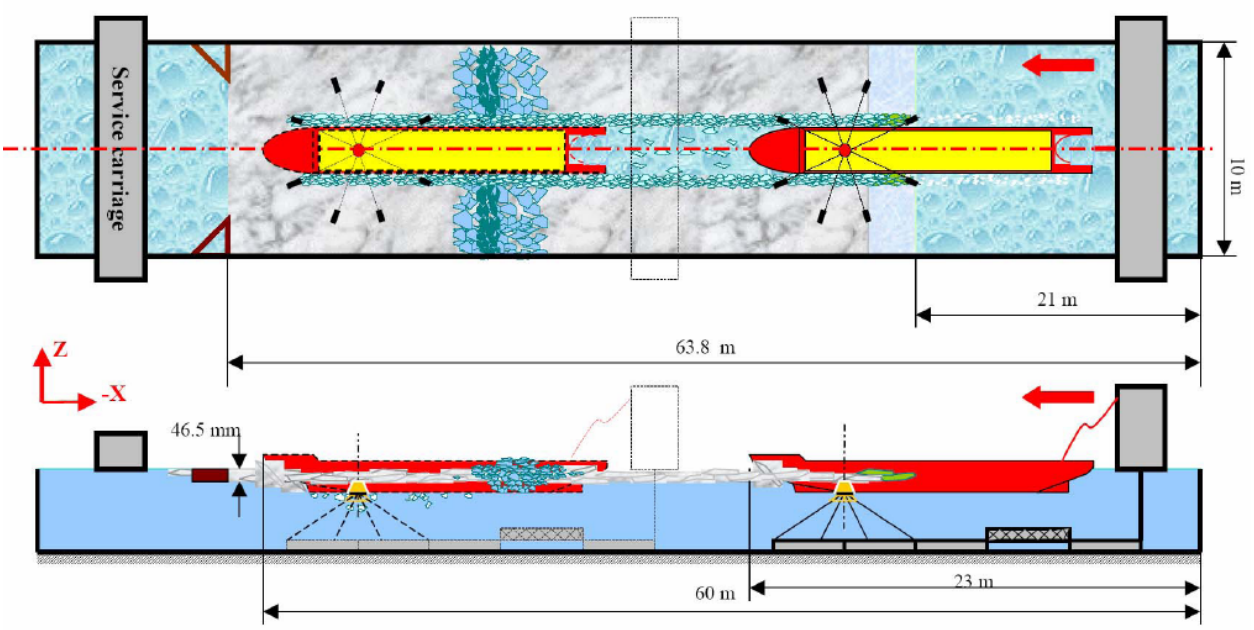

Figure 2. Tank setup during the Arctic Shuttle Barge tests (Jensen et al., 2000b).

4 Data pre-analysis

4.1 Determination of the low-pass cut-off frequency F_{cut}

The measured signals need to be filtered for the high frequency noise. This is all the more important when one studies the derivative of the signals with respect to time (e.g. when determining the acceleration from the measured variation of the position). For each derivation, the signals are thus amplified in the frequency domain proportionally to the frequency. The high frequency noise is thus amplified at each derivation.

A cut-off frequency for the filtering is required; its choice should ensure that all processes that will be further analyzed remain in the filtered signal. It appears that all processes (except propeller actions) have natural frequencies below 0.5 Hz. However, some uncertainty lies in the frequency spreading of the ice processes. The bending failure of the ice is thought to have a frequency range of 0.1-0.5 Hz (applying linear bending theory), but ice will present other failure modes as well and will interact in diverse manners along the hull.

The energy recorded in the frequency domain over 0.6 Hz was compared during measurements when the system is at rest and when the system is interacting with ice. The similarity in the amount of energy suggests that the frequency domain of interest is below 0.6 Hz, and the frequencies that correspond to the ice action seem to be no higher than 0.6 Hz. From these considerations 0.6 Hz was chosen as a cut off frequency.

4.2 Windowing function

The signals are thus filtered by a low-pass filter with a cut-off frequency F_{cut} (0.6 Hz here). The frequencies above this limit are removed by using a square window function. This window zeroes out the responses at higher frequencies that are thought of as noise and not a part of the signal. Equation 1 shows the principle behind the windowing function.

$$Y(f > F_{cut}) = 0 \quad \textbf{[1]}$$

Here Y is the Fourier transform of the signal, and f is the frequency vector. By performing an inverse Fourier transformation, the cleaned signal is found in the time domain. Figure 3 shows a typical signal before and after the filtering process.

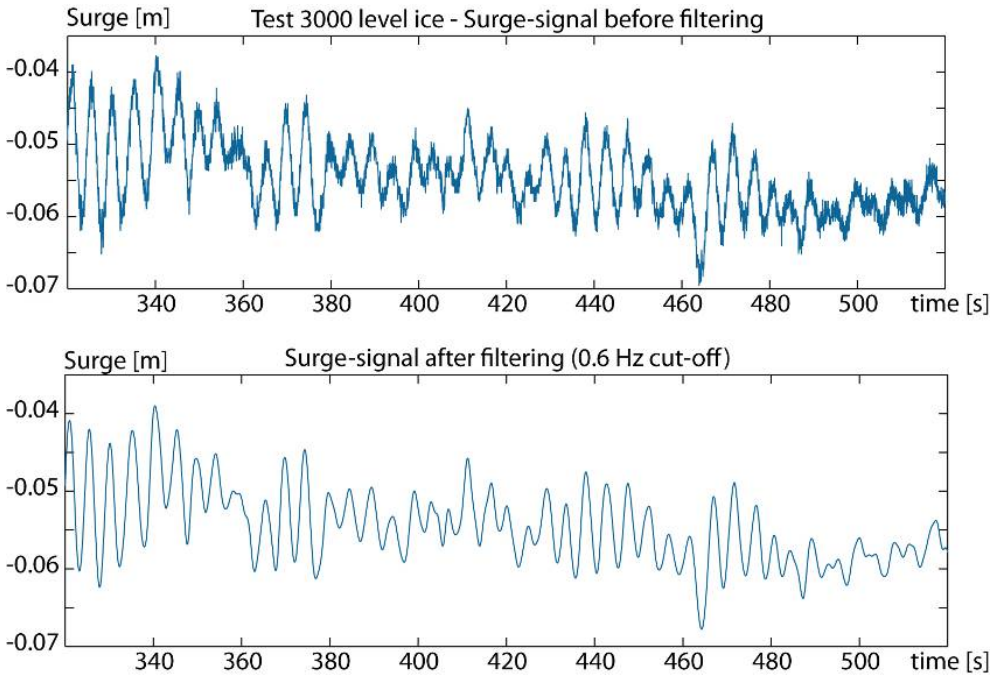

Figure 3. Example of surge measurements (run 3000), with the signal before and after filtering (0.6 Hz cut-off frequency).

5 Dynamic ice loads on a moored vessel

Many studies on moored structures in ice report the horizontal mooring loads. However, the mooring loads reflect the structural response of the moored vessel and will differ from the ice loads applied on the vessel. Figure 4 shows a two-dimensional model of a turret moored tanker where the ice loads in the x- and z-directions are marked.

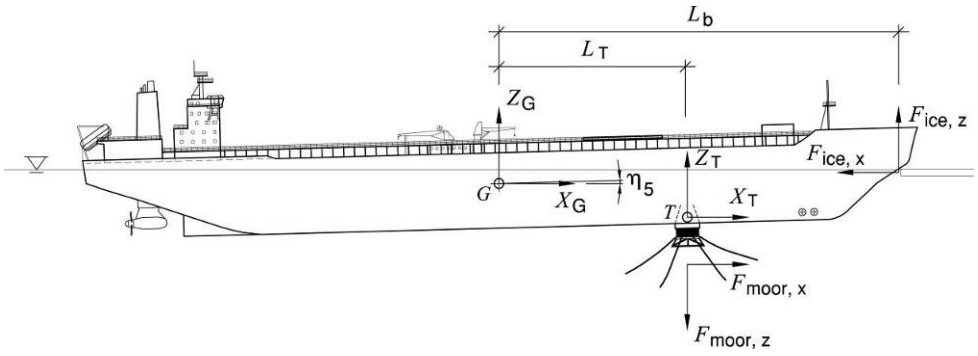

Figure 4. 2D modelling of a turret moored tanker responding to the interaction with ice.

These ice loads applying on the vessel can be back-calculated from the measured mooring loads and motions of the vessel by considering the system dynamic equilibrium:

$$\mathbf{M}\ddot{\boldsymbol{\eta}} = \mathbf{F}_{ice}(t) + \mathbf{F}_{moor}(t) - \mathbf{A}\ddot{\boldsymbol{\eta}} - 2\mathbf{B}(\mathbf{M}+\mathbf{A})\dot{\boldsymbol{\eta}} - \mathbf{C}\boldsymbol{\eta} \quad [2]$$

where $\mathbf{M}$ is the tanker mass matrix, $\boldsymbol{\eta}$ the vessel displacement matrix, $\mathbf{F}_{ice}$ the ice loads, $\mathbf{F}_{moor}$ the mooring loads, $\mathbf{A}$ the added mass, $\mathbf{B}$ the damping matrix and $\mathbf{C}$ the restoring matrix. The system is solved in the *X*-*Z* vertical plane with the vessel centre of gravity as reference point (origin):

$$\mathbf{F}_{ice}(t) = (\mathbf{M}+\mathbf{A}) \circ \ddot{\boldsymbol{\eta}} + 2\mathbf{B} \circ (\mathbf{M}+\mathbf{A}) \circ \dot{\boldsymbol{\eta}} + \mathbf{C}\boldsymbol{\eta} - \mathbf{F}_{moor}(t), \quad [3]$$

where the circle, $\circ$, denotes element-wise multiplication, and:

$$\boldsymbol{\eta} = \begin{bmatrix} \eta_1(t) \\ \eta_3(t) \\ \eta_5(t) \end{bmatrix}, \quad [4]$$

$$\mathbf{M}+\mathbf{A} = \begin{bmatrix} M + A_{11} \\ M + A_{33} \\ I_{yy} + A_{55} \end{bmatrix}, \quad [5]$$

$$\mathbf{B} = \begin{bmatrix} \zeta_1 \\ \zeta_3 \\ \zeta_5 \end{bmatrix}, \quad \zeta_j = \alpha_j \sqrt{\frac{C_{jj}}{M + A_{jj}}}, \quad [6]$$

$$\mathbf{C} = \begin{bmatrix} 0 & 0 & 0 \\ 0 & C_{33} & C_{35} \\ 0 & C_{35} & C_{55} \end{bmatrix}, \quad [7]$$

$$\mathbf{F}_{moor}(t) = \begin{bmatrix} F_{moor,x}(t) \\ F_{moor,z}(t) \\ F_{moor,z}(t) L_T + F_{moor,x}(t) Z_T \end{bmatrix}, \quad [8]$$

$$\mathbf{F}_{ice}(t)=\begin{bmatrix} F_{ice,x}(t) \\ F_{ice,z}(t) \\ F_{ice,z}(t)L_B+F_{ice,x}(t)Z_{ice} \end{bmatrix}. \quad \textbf{[9]}$$

And where η_1, η_3 and η_5 are the surge, heave and pitch motions of the barge, Z_T and Z_{ice} the vertical distance between the centre of gravity and the point of applications of the mooring and ice loads.

The vertical motions of the barge were not measured. A 3D numerical model of the mooring used in the model tests was elaborated to calculate the 3D characteristic of the mooring ($f_{characteristic}$). By knowing the surge and sway of the turret and the vertical mooring load (measured), it is possible to back-calculate the vessel turret heave z_t as shown in Equation 10 (see also the graphical representation of the vertical mooring characteristic in Figure 5):

$$z_t=\eta_3+\eta_5 L_T=f^{-1}_{characteristic}\left(\eta_1,\eta_2,F_{moor,z}\right) \quad \textbf{[10]}$$

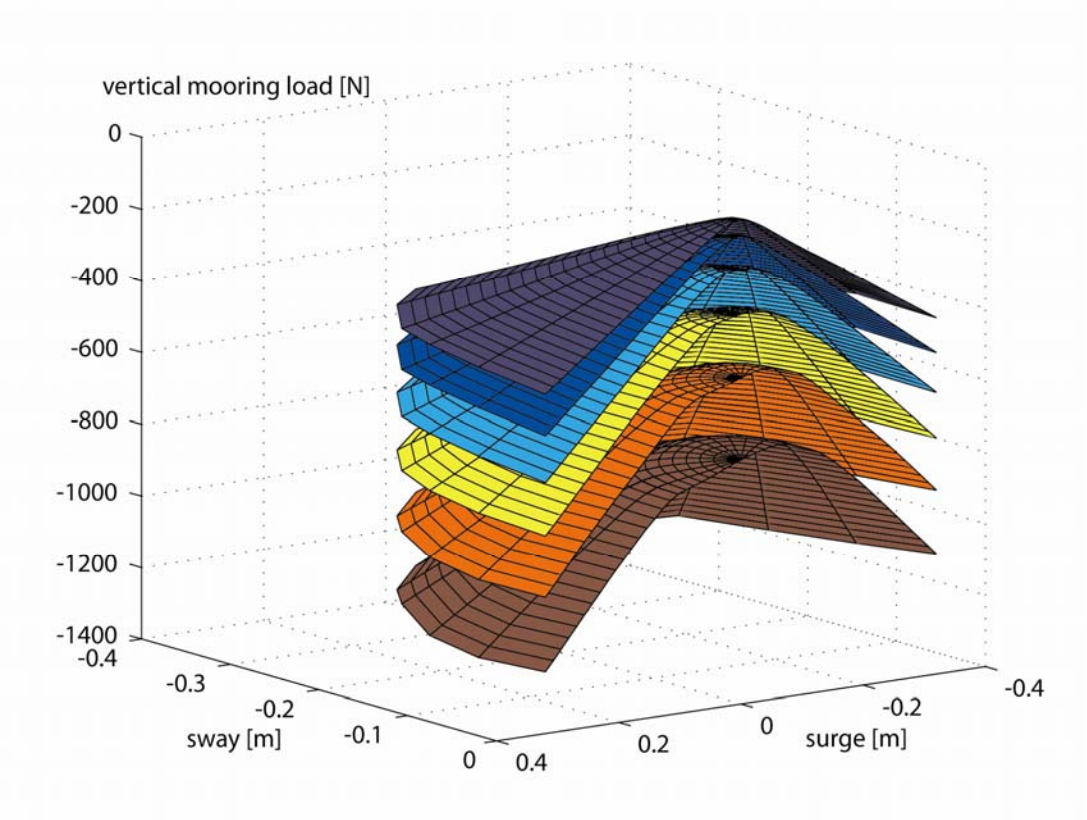

Figure 5. Vertical mooring load characteristics for test 3000 for various surge and sway values. Each surface corresponds to different turret heave values (model scale values).

The model presented in Equations 3 to 9 is a simple model with 3 degrees of freedom (surge heave and pitch). The following assumptions are done:

- The model accounts for the pitch-heave coupling in the restoring loads,
- The calculated ice loads are for one chosen point of applications. The ice load level (in particular the vertical ice load) depends on the choice of the point of application,
- A constant damping coefficient was used for each event. Damping was measured from the recorded time series.

6 Comparison of the mooring loads and the ice loads time series

Figure 6 and Figure 7 give examples of time series of the mooring (F_x and F_z) and ice loads ($F_{ice,x}$ and $F_{ice,z}$) in the horizontal and vertical directions, during level ice interaction (Figure 6) and ice ridge interaction (Figure 7) with the moored vessel.
It is seen that:

- As expected, the horizontal mooring and ice loads have the same slowly varying tendency.
- The vertical ice load is much larger than the measured vertical mooring load. Most of the vertical resistance of the vessel is given by the vessel's response (heave and pitch) and little by the mooring.
- The level of the vertical load is higher than the horizontal load. This is determined partially by the vessel's flare. The chosen horizontal arm of the vertical ice load is also important (and may vary during ice ridge interactions)
- The signals show different properties in the frequency plan, the mooring being a more narrow banded type of signal.

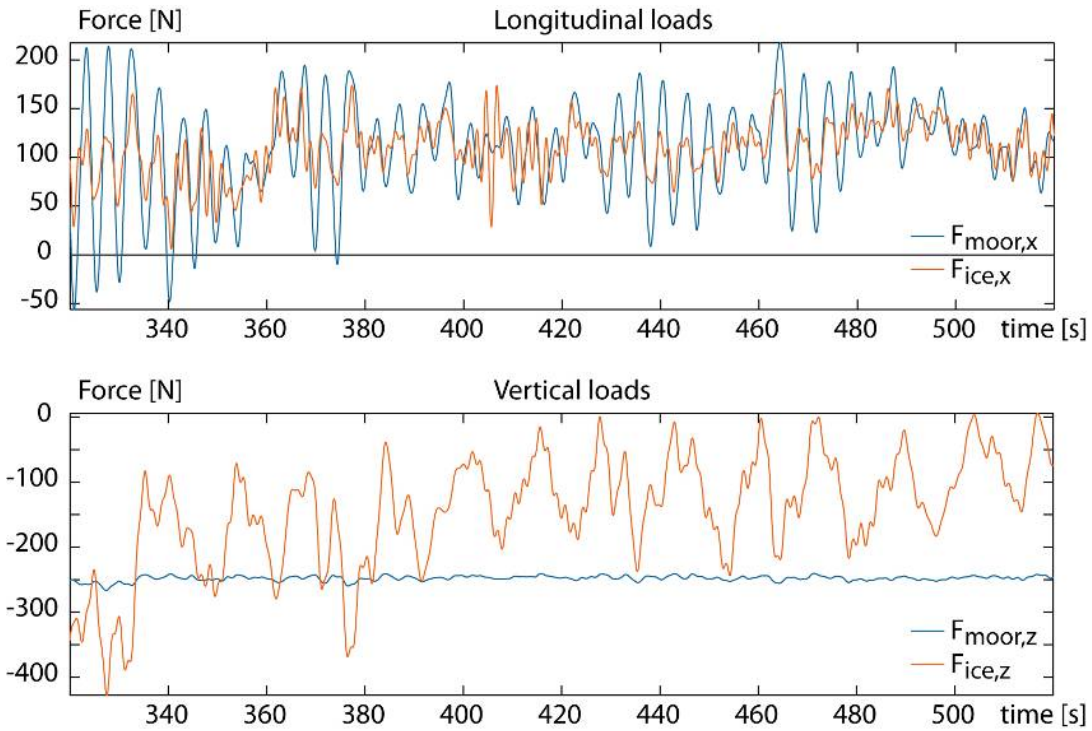

Figure 6. Measured and calculated time series for F_x, $F_{ice,x}$, F_z and $F_{ice,z}$ for the 3000 test series (level ice, model scale values).

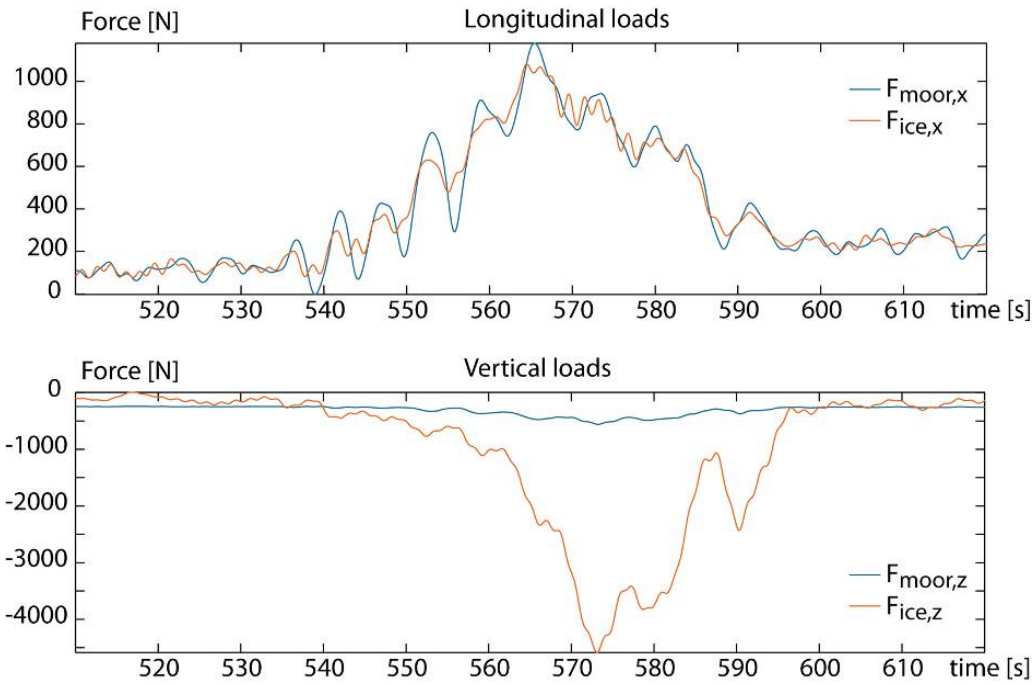

Figure 7. Measured and calculated time series for F_x, $F_{ice,x}$, F_z and $F_{ice,z}$ for the 3100 test series (Ridged ice, model scale values).

7 Statistical analysis of the mooring and ice loads

The statistical properties of the ice load applying on the vessel are of high relevance for the designer. Since usually the mooring loads are reported and not the ice load applying on the vessel, it is of interest to compare the mooring load and ice load statistical values.

Table 3 presents the analysis of some statistical properties of the measured mooring loads and the back-calculated ice load. The statistical properties are computed on the high frequency part of the signal (The signals are filtered by a high-pass filter with a cut-off frequency of 0.05). The quantities analyzed in Table 3 are:

- σ: Standard deviation of the high frequency part of the load (see an example of the high frequency component of the loads in Figure 8),
- A: Maximum amplitude of the high frequency part of the load.

Table 3. Analysis of some statistical properties of the longitudinal mooring and ice load applying on the moored vessel (model scale values). Note: the standard deviation and maximum amplitude values are measured at the high frequency part of the signal.

		Standard deviation σ [N]		Max amplitude A / std. dev. σ		std. dev. ratio	Max amp. ratio
		Mooring F_x	Ice load $F_{ice,x}$	Mooring F_x	Ice load $F_{ice,x}$	$\sigma_{Fx}/\sigma_{Fice,x}$	$A_{Fx}/A_{Fice,x}$
Level ice	3000	38	20	3.1	4.0	1.9	1.5
Level ice	4000	76	41	2.9	4.1	1.9	1.3
Ridges	3100	92	51	3.7	2.7	1.8	2.5
Ridges	4100	113	64	3.0	3.3	1.8	1.6

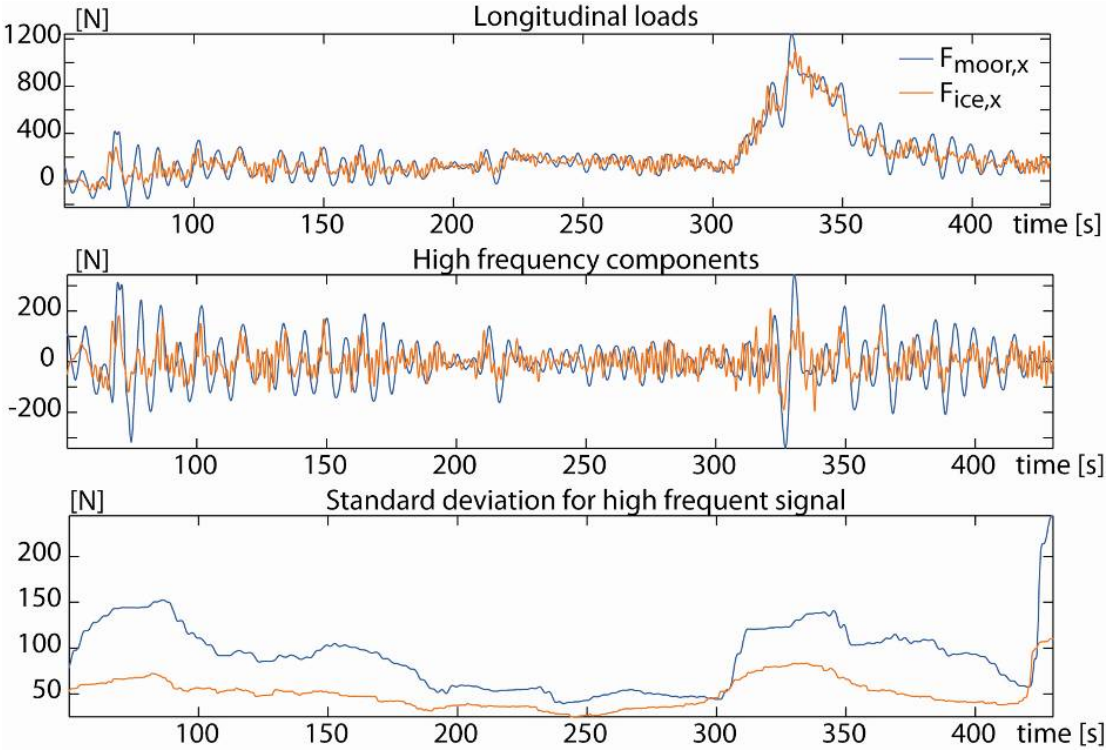

Figure 8. F_x and $F_{ice,x}$ for the 3000 test series (model scale value). Total signal, high frequency component and standard deviation variation are plotted.

From the results presented in Table 3, it is observed that:

- The standard deviation of the longitudinal ice load is approximately 2 times less than the standard deviation of the longitudinal mooring load.
- Comparatively, in level ice, the difference between the max amplitude of the longitudinal ice and mooring load is reduced.
- This effect is illustrated (Table 3) by looking at the ratio A / σ, which is close to 3 for the longitudinal mooring and ice loads, except for the ice load in level ice.
- The standard deviation of the signals increase from level ice interaction to ice ridge interaction. Proportionally this increase is greater for the longitudinal ice load. This increase is illustrated in Figure 8.

Figure 9 shows the normalized distribution of the measured and calculated loads. A clear difference in shape is seen between level ice events (3000 and 4000) and ice ridge events (3100 and 4100). The calculated ice load seems to have a narrower distribution also. However, analysis of more realizations is necessary to draw conclusions on the fitting of the distributions.

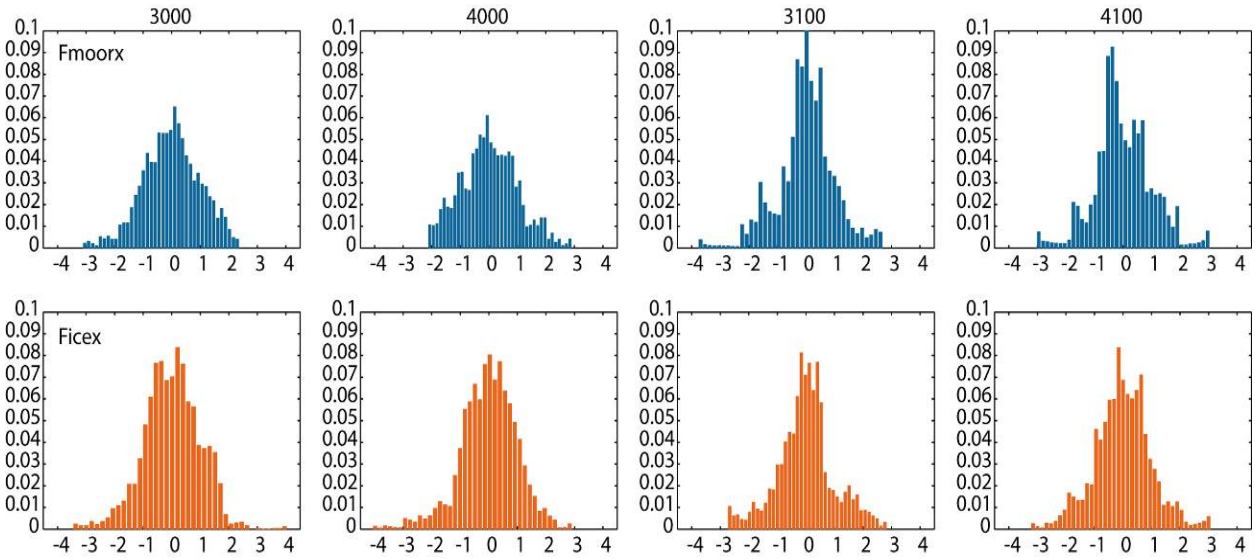

Figure 9. Distributions of the measured mooring load and back-calculated ice load in the longitudinal direction (normalized distributions) for ice level events 3000 and 4000 and for ridged events 3100 and 4100.

8 Conclusions

Data measurements from the ice tank testing of the moored Arctic Shuttle Barge test at HSVA in 1999 have been studied and reanalyzed. The conclusions are the following:

- The implementation of a simple dynamic model seems to give realistic time series for the ice load applying on the longitudinal and vertical directions on the vessel,
- Though the surge components of the mooring and ice loads present similar trends, the vertical loads differ a lot in magnitude,
- The standard deviation of the mooring load in the longitudinal direction is approximately 2 times the standard deviation of the ice load,
- The ratio of the max amplitude to the standard deviation is close to 3 for both the mooring load and ice load in ridges. However, in level ice, it is 4 for the ice load and 3 for the mooring load.

This underlines that it is important to avoid transferring the measured mooring loads to the ice loads applying on the vessel. Further analysis of the back-calculated ice load is of interest, such as a spectral analysis (see e.g. Bonnemaire et al., 2007).

Acknowledgements

The authors would like to thank HSVA (in particular Karl-U. Evers) for the cooperation during the presented R&D project. The financial support of StatoilHydro for the re-analysis of the data is acknowledged.

References

Bonnemaire, B., A. Jensen, O. T. Gudmestad, T. Lundamo and S. Løset (2007): Challenges related to station-keeping in ice. INTSOK Conference, Houston 2007.

Jensen, A., S. Løset, J. Hellmann, O.T. Gudmestad and O. Ravndal. (2000a): Model tests of an arctic tanker concept for loading oil Part I: Maneuvering into loading position. Proceedings of the 15th International Symposium on Ice (IAHR), Gdansk, Poland, 28. August 1 2000, Vol. 1, pp. 341351.

Jensen, A., S. Løset, K.V. Høyland, J. Hellmann and B.P. Vodahl. (2000b): Model tests of an arctic tanker concept for loading oil. Part II: Barge in moored position. Proceedings of the 15th International Symposium on Ice (IAHR), Gdansk, Poland, 28 August 1 September 2000, Vol.1, pp.353370.

Jensen, A. (2002): Evaluation of Concepts for Loading of Hydrocarbons in Ice-infested Waters. Doctoral Thesis, NTNU, The Norwegian University of Science and Technology, Trondheim.

Løset, S., Ø. Kanestrøm and T. Pytte (1998): Model Tests of a Submerged Turret Loading Concept in Level Ice, Broken Ice and Pressure Ridges. Cold Regions Science and Technology, Vol. 27, pp. 57-73.

Wright, B. and Associates (1999): Evaluation of Full Scale Data for Moored Vessel Station keeping in Pack Ice (With Reference to Grand Banks Development). Report submitted to the National Research Council of Canada, PERD/CHC Report 26-200, 103 pp.

19th IAHR International Symposium on Ice
"Using New Technology to Understand Water-Ice Interaction"
Vancouver, British Columbia, Canada, July 6 to 11, 2008

Subsurface Ice Interactions under a Moored Offloading Icebreaker

Basile Bonnemaire[1,2], Trine Lundamo[1], Arnor Jensen[1], Karl-H. Rupp[3]
[1]Barlindhaug Consult AS, Tromsø, Norway
[2]The Norwegian University of Science and Technology (NTNU), Trondheim, Norway
[3]Hamburgische Schiffbau-Versuchsanstalt GmbH (HSVA), Hamburg, Germany
basile.bonnemaire@barlindhaug.no, trine.lundamo@barlindhaug.no,
arnor.jensen@barlindhaug.no, rupp@hsva.de

The Arctic Tandem Offloading Terminal (ATOT) is a new concept for offshore offloading in ice-infested waters. The concept comprises two units; a turret moored offloading icebreaker (OIB) and an offloading tanker in tandem. The concept was tested at scale 1:24 at the HSVA ice tank in Hamburg, Germany.

Subsurface ice transport is critical for the concept as risks of damage of the loading hoses by drifting ice should be avoided. The OIB design included a passive barrier, a wedge under the bow to deviate the drifting ice. It worked fine in level ice, but the wedge was not fully efficient during the interaction with deeper ice formations. The bow propellers were also used to wash away the incoming ice, however, ice interaction with the sub-surface loading and the stern propellers could not be avoided.

The horizontal loads from ice hitting the subsurface loading buoy were measured. These reached 460 kN during interaction with the deepest ridge, the load level was seen to be correlated with the ice ridge keel depth. The measured loads are in the same range as load estimates from either ice block impacts simulations or rubble load solutions found in the literature.

1 Introduction

The Arctic Tandem Offloading Terminal (ATOT) is a new concept for offshore offloading in ice-infested waters. The concept comprises two units; a turret moored offloading icebreaker (OIB) and an offloading tanker moored in tandem at the OIB aft. The operational strategy for the OIB sets that it should be able to stay moored in severe ice conditions, though it can be in a "ready to disconnect" mode and the tanker is disconnected in these conditions.

The moored OIB should be designed to interact with deep ice formations such as ice ridges or rubble fields. Interaction with these types of features will generate a certain amount of rubble that will have to pass by the OIB. This will generate a sub-surface ice transport around the OIB hull. The OIB is moored on a loading buoy fixed in an internal turret. Mooring lines and flow lines are connected to the loading buoy and vulnerable to ice interactions (see Figure 1):

- The design criterion of the upper part of the mooring lines is set mainly by the global mooring load on the vessel. The mooring lines will normally be strong enough to withstand the interaction from ice rubble. However, fatigue effects from the interaction with the ice rubble could be relevant design concerns.
- The flow lines are more vulnerable to ice actions and interaction should be avoided.

Figure 1 Subsurface view of the Offloading Icebreaker (OIB) moored on its loading buoy. The buoy is connected to a mooring made of 4 clusters and to a protected riser

Subsurface ice transport includes an associated risk (e.g. of damage of flow lines) that needs to be reduced (either reducing the probability or the consequence of interaction). Several means are considered for the OIB design:

- Passive deviation. A wedge under the spoon like shaped buoy is present ahead of the turret area. It aims at deviating the ice pieces that may drift towards the loading buoy.

- Active sub-surface ice management. The azimuth bow thrusters are used actively to mill and blow the incoming ice away from the turret area.
- Passive protection. The flow lines can be protected to resist some interaction with the incoming rubble (see Bonnemaire, 2003, Bonnemaire, 2005 or Tikhonov et al., 2004 for examples of riser protections)

The ATOT concept was tested at the HSVA ice tank (Hamburg, Germany) during summer 2007 (see companion papers Jensen et al., 2008, Aksnes et al., 2008 and Bonnemaire et al., 2008). The present paper discusses observations on the subsurface ice transport and the measured ice impact forces on the loading turret.

2 Ice tank modeling setup

The OIB is a highly specialized vessel designed with an optimized hull design as an icebreaker with a reamer solution. The vessel is further equipped with azimuth propulsion units both fore and aft. The installed power will be dependent of ice conditions and type of propulsion, and is foreseen to be in the range of 20 MW to 30 MW. A more detailed description of the ATOT concept and the OIB in particular is found in Jensen et al. (2008).

The ATOT concept was tested at the HSVA ice tank at a scale 1:24. Froude scaling was respected. Various ice conditions were tested, including severe ice ridges, level ice, broken ice fields, rubble fields and different types of ice drift changes. 4 ice sheets were produced numbered from 1000 to 4000.

2.1 Model of the vessel

Table 1 gives the main dimensions of the OIB in model and full scales. Figure 2 shows the lines of the OIB model. The model was moored on a dry mooring. A mooring column was fixed to the bottom of the hull via a ball joint and a load cell (further details can be found in Bonnemaire et al., 2008)

Table 1 Dimensions of the OIB model and corresponding values in full scale

OIB	Full scale	model scale
LOA, m	133	5.54
Lpp m	108.8	4.53
Breadth, m	26-30	1.08 – 1.25
Ice draught, m	13.5 - 14.0	0.58
Displacement (appr.), t	20 800	1.50
Stem angle, °	20	20
Flare angle , °	25	25
Buttock angle , °	18	18

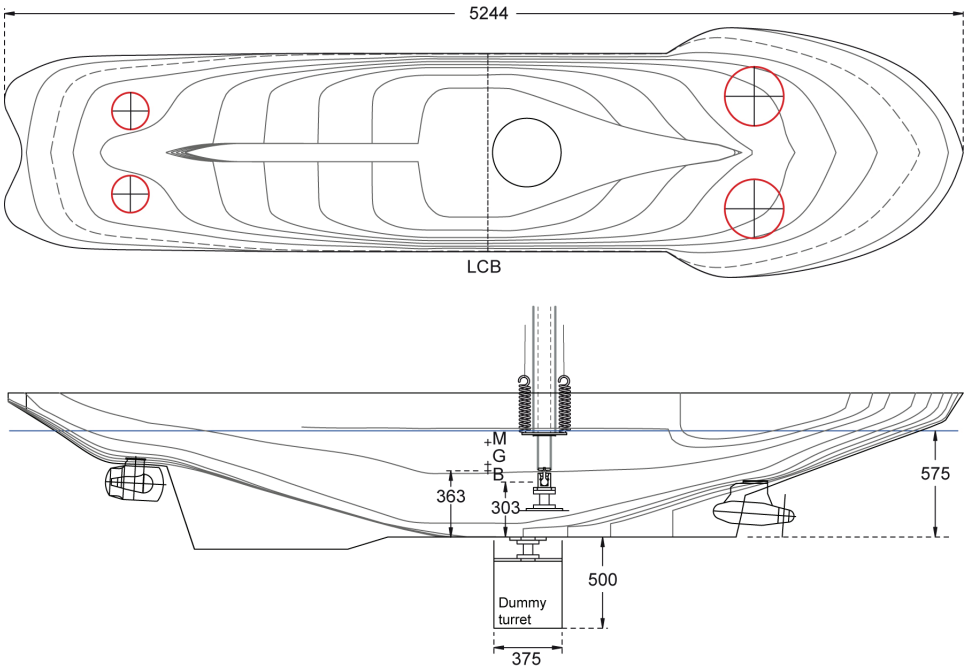

Figure 2 Drawings of the OIB model with its mooring column and the dummy turret (mm, model scale).

2.2 Thrusters design and operation strategy

The OIB model was equipped with models of azimuth propellers both at the bow and at the stern of the vessel (see Figure 3). The latter were equipped with nozzles. The available power from the propellers is given in Table 2. It was increased between test series 2000 and 3000. The power increase aims at giving the propellers a power reserve so that they will not stop when interacting with ice.

Figure 3 a) View of the bow azimuth propellers, b) View of the stern nozzle azimuth propellers

The working range of the azimuth propellers was also limited in heading (see example in Figure 4). The main focus was then:

- One propeller should not blow ice towards a neighboring propeller

- The propeller jet should not be directed towards the turret and riser area
- When the tanker is connected, the stern propellers should not act directly on the tanker.

Table 2 Installed propeller power on the OIB model (full-scale value in parenthesis)

		Installed power	Thrust
Tests 2000 and open water tests	Bow:	2 x 60 W (2 x 4 MW)	2 x 45 N (2 x 620 kN)
	Stern:	2 x 60 W (2 x 4 MW)	2 x 48 N (2 x 660 kN)
Tests 3000, 4000 and 1000	Bow:	2 x 105 W (2 x 7.1 MW)	2 x 66 N (2 x 910 kN)
	Stern:	2 x 105 W (2 x 7.1 MW)	2 x 72 N (2 x 995 kN)

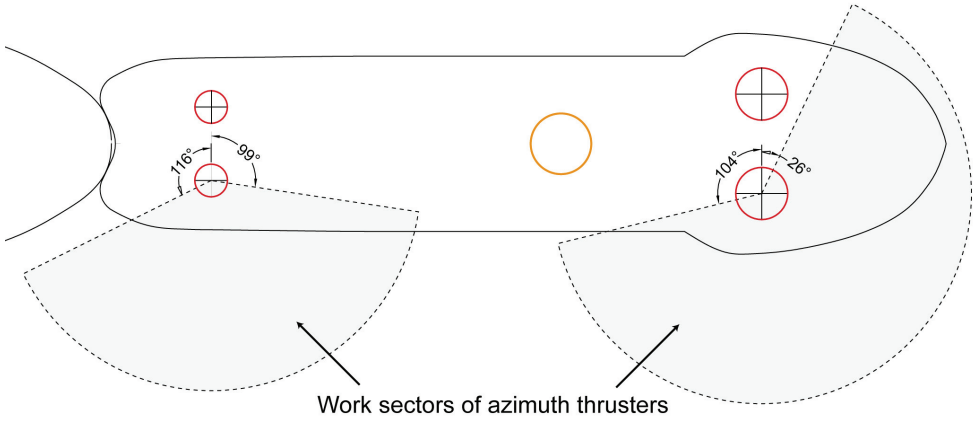

Figure 4 Example of the allowable working area for the azimuth propellers for the OIB when a tanker is moored in close tow

Table 3 Operation strategy for the azimuth propellers in different ice conditions (as defined prior to testing. The numbering indicates the priority level)

	Level ice conditions- Straight or turning mode	Fist year sea ice Ridges with the tanker moored	Severe ice condition, OIB in single mode
Bow Propellers: Two open azimuth propellers	1. Maintain stability (heading) of the OIB (and the tanker) 2. Reduce mooring loads on the vessels by ice clearing 3. Load reduction by bollard pull	1. Clear away ice from the sub surface turret area 2. Maintain stability (heading) of the OIB (and the tanker) 3. Load reduction, by ice clearing 4. Load reduction by bollard pull	1. Clear away ice from the sub surface turret area 2. Maintain stability (heading) of the OIB
Stern propellers: Two nozzle azimuth propellers	1. Widening of the wake and sideways ice breaking (if possible) 2. Maintain stability of the vessels (heading) 3. Load reduction on the moorings	1. Widening of the wake and sideways ice breaking (if possible) 2. Clear away ice from the tanker and OIB 3. Load reduction on the moorings	1. Maintain stability of the vessels (heading) 2. Clear away ice from the OIB 3. Load reduction by bollard pull

A preliminary operation strategy was developed prior to testing to define the helmsman priorities for the use of the bow and stern propellers. This strategy (presented in Table 3) set a priority list for the following operations:

- Maintain stability,
- Reduce mooring loads by ice clearing,
- Reduce mooring load by bollard pull,
- Clear the turret area from ice interactions.

2.3 Dummy turret model

A cylinder was placed under the OIB hull to represent the mooring buoy and its extension sticking out of the hull. The cylinder (see sketch in Figure 2 and pictures in Figure 5) is connected to the OIB hull via a load cell, and the ice impact forces on the cylinder can be recorded.

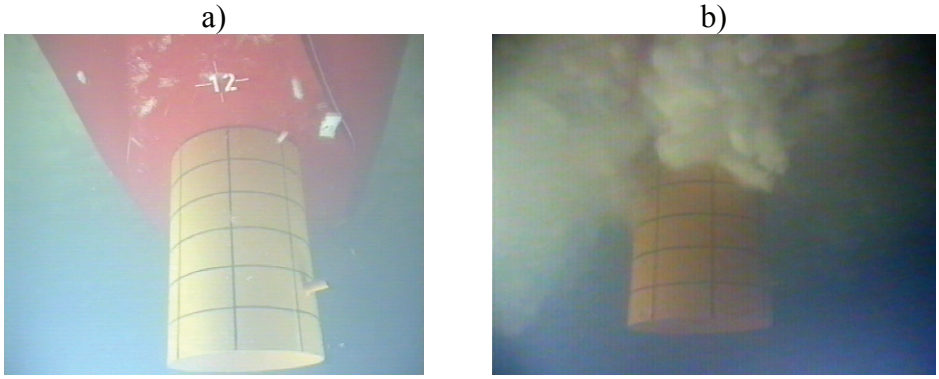

Figure 5 Underwater views of the dummy turret, a) in open water, b) during a ridge interaction (test 4120). The horizontal lines on the bucket are 2 m distant (full scale)

2.4 Ice conditions

The model ice is prepared following a special technique developed in house (see Evers and Jochmann, 1993). Four ice sheets were produced in a similar manner, all included a long part of level ice (around 30 m) followed by an embedded ridge and some more level ice (about 7 m). The physical properties of the ice sheets are summarized in Table 4.

Table 4 Physical properties of the produced ice sheets, level ice and ridged ice (h_i: level ice thickness, σ_f bending strength of the level ice, h_k, h_s and w_k, keel depth, sail height and keel width of the ridges).

	Model scale			*Full scale*		
Ice sheet	h_i [m]	σ_f [kPa]	(h_k + h_s) x w_k [m]	h_i [m]	σ_f [kPa]	(h_k + h_s) x w_k [m]
2000	0.039	15	(0.37 + 0.14) x 4.5	0.94	360	(8.9 + 3.4) x 108
3000	0.043	30	(0.54 + 0.09) x 4	1.03	720	(13.0 + 2.2) x 96
4000	0.048	20	(0.62 + 0.08) x 4	1.15	480	(14.9 + 1.9) x 96
1000	0.044	24	(0.65 + 0.10) x 4	1.06	580	(15.5 + 2.3) x 96

2.5 Monitoring setup

It is challenging to monitor the sub-surface ice transport. In the present tests, qualitative observations with underwater videos gave an impression on the extent of the subsurface ice transport. In addition, some quantitative measurements gave some indications on the ice actions on the sub-surface appendices:

- Horizontal forces acting between the bow propellers and the OIB hull,
- Torque, rotation speed and thrust measurements of the thrusters
- Tri-axial forces between the dummy turret and the OIB hull

3 Ice clearing by the bow thrusters

From the under water video visualizations, it is seen that:

- In level ice, the bow propellers are efficient to clear the ice. The propellers break the already broken incoming ice into smaller pieces and blow it away. The sub-bow wedge deviates the rest of the incoming ice (see Figure 6).
- During interaction with ice ridges, the propellers are submerged in the rubble ice. The ice seems to come out of the thrusters at least partially crushed into thin particles. The propellers do not manage to clear the turret area from ice, but the incoming ice is at least partially milled, probably reducing the ice forces.

Ice clearing using bow propellers is challenging as the helmsman has no control or feedback from the efficiency of the operation.

Figure 6 Underwater view of the bow propellers clearing ice drifting under the vessel hull (run 3100)

4 Ice accumulation on the stern propellers

From underwater videos, it was possible to see that sometime a rubble ice accumulation was formed ahead of the stern propellers (see Figure 7). These accumulations formed essentially after an interaction with a ridge. The ice rubble traveled around the mooting buoy and further aft along the hull. The accumulation is lying on each side of the stern keel and against the azimuth propellers. The propeller nozzle and the keel act as walls preventing the ice from drifting by.

It is also possible to detect these events on the time series plot of the forces applying on the stern propeller drives. When the accumulation forms, two effects are combined: the thrust of the propeller is reduced, and the accumulation is applying a force on the propellers.

Such obstruction of the stern propeller should be avoided. Several aspects have to be reviewed further to minimize this effect:

- Propeller design: The propellers included a nozzle for propulsion efficiency. The nozzle may favor the accumulations.
- Hull design: The underside of the hull is transversally horizontal between the turret and the back propellers. The ice is thus not pushed sideways by its own buoyancy.
- Thrusters operation: The stern propellers could blow partially frontward. In this case the thrusters operational strategy should be revised.

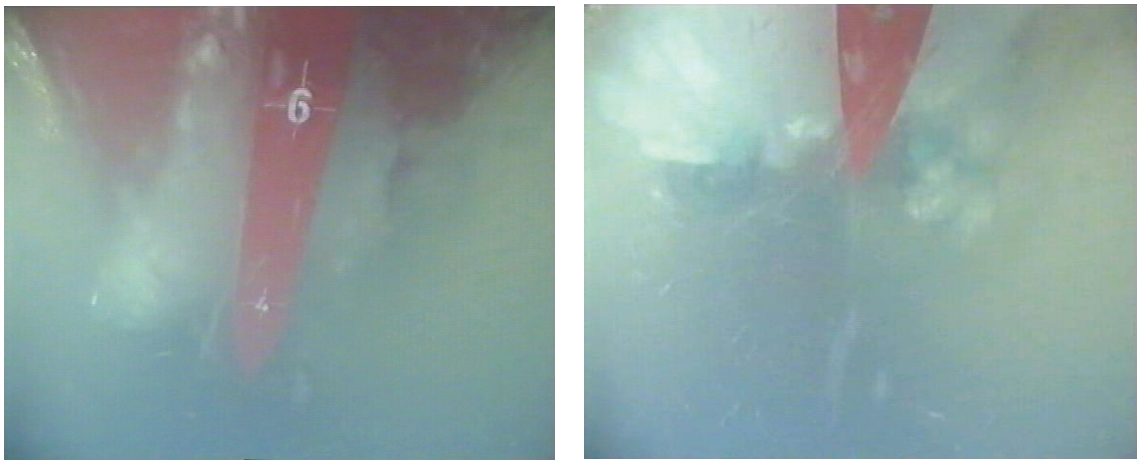

Figure 7 Underwater view of a rubble accumulation in front of the stern propellers after a ridge interaction (run 3100, the stern keel is visible in the foreground)

5 External forces on the loading buoy

5.1 Measurements corrections

The dummy turret simulating the presence of the loading buoy was connected via a tri-axial load cell to the ship hull. The forces measured by the load cell include external actions on the turret, effect of the vessel tilt and inertia effects. The measured forces have to be corrected as described in Equation 1 for forces in longitudinal direction to detect any substantial interaction on the turret. ($F_{1,buoy,ext}$: external forces on the buoy in longitudinal direction, $F_{1,buoy,ext}$: measured force

in longitudinal direction, M_{buoy}, mass of the dummy turret including added mass, η_5, OIB pitch, $\eta_{1,buoy}$, surge of the dummy turret):

$$F_{1,buoy,ext} = F_{1,buoy,meas} - M_{buoy} g \sin(\eta_5) - M_{buoy} \ddot{\eta}_{1,buoy} \quad \textbf{[1]}$$

Load increases were recorded during the ice ridge interactions (see examples in Figure 8). Table 5 gives the maximum recorded horizontal longitudinal forces measured on the loading buoy during the ice ridge events (up to 460 kN in run 1110). The ice ridges were penetrated several times at different positions. The boundary conditions give higher confinement during the first penetration.

Underwater videos of all ridge interactions are not available. It is thus difficult to estimate the amount of ice interacting with the turret. For runs 3100 and 4120 (see Figure 5b and Figure 9), it is seen that the ice interacts on an area that is around 4 m thick in full scale.

Table 5 Maximum longitudinal forces on the loading buoy during ice ridge events. All tests are performed at 0.5 m/s ice drift speed, except 2120 (1.5 m/s). Values in grey indicate no major interaction

run #	$F_{1,buoy,ext}$ [N] model scale	$F_{1,buoy,ext}$ [kN] full scale	Setup	Ridge penetration	Keel depth
1110	33	456	OIB	1st	hk = 15.5 m
4120	13	180	OIB + tanker	1st	hk = 14.9 m
4210	*4.5*	*62*	OIB + tanker	2nd	
3100	*5*	*69*	OIB + tanker	1st	hk = 13 m
3200	12.5	174	OIB + tanker	2nd	
2120	11	152	OIB, fast drift	1st	hk = 8.9 m
2200	*5*	*69*	OIB	2nd	

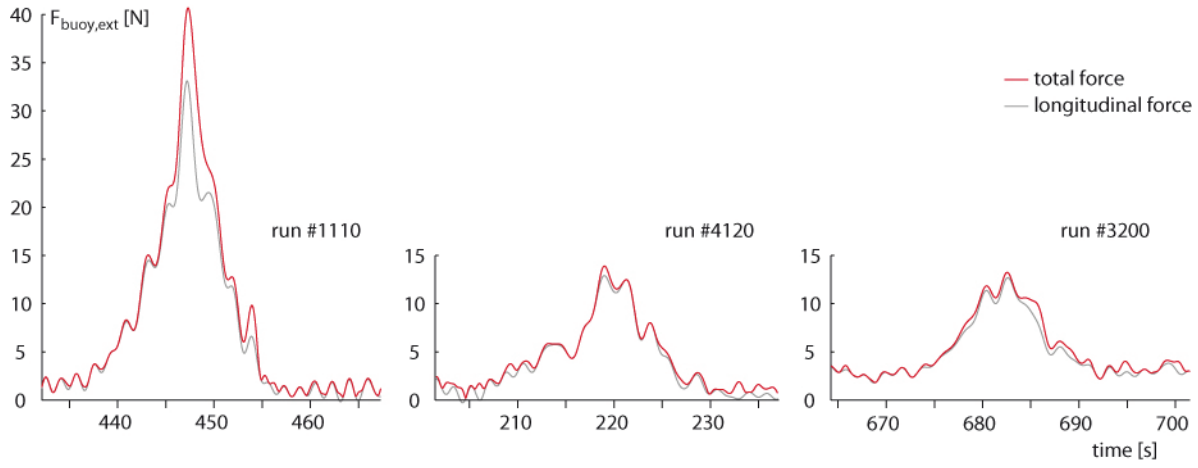

Figure 8 Time series of the longitudinal and total external forces applying on the dummy turret during 3 ridge interactions (runs 1110, 4120, 3200; model scale values)

Figure 9 Underwater view of the loading buoy during interaction with a ridge (run 3100) (each horizontal line is distant of 2 m in full scale)

5.2 Discussion on the measured forces

The external actions on the turret can result from interaction with ice rubble, but also from the propeller wash from the bow propellers. Calibration tests were run with the OIB moored in open water and bow propellers at full power. A load level of 10 N, 3.5 N and 1.5 N was measured on the dummy turret with the bow thrusters with respectively 0° (full ahead), 20° and 30° outward heading. During the ice ridge interactions, the bow propellers always had at least 20° heading, the load contribution from the propeller wash in Table 5 is thus small.

As seen in Table 5, there is a correlation of the external forces with the ice ridge depth. However, there is a substantial variation. Relatively high loads were also measured with the shallowest ridge (2000 series); but the first penetration was performed at high drift speed (1.5 m/s full scale).

5.3 Comparison to force estimates

Mellor (1980) developed a solution to estimate the quasi-static action from rubble of an ice ridge keel on a narrow vertical structure (see Equation 2). Using this solution (with average values), one gets that the action of 4 m rubble on the dummy turret gives an horizontal load of:

$$F = 0.5D\eta^2(1-\nu)(\rho_w - \rho_i)gh^2 = 200 \text{ kN} \quad \textbf{[2]}$$

where D is effective structure width (9 m), η the passive pressure coefficient ($\approx \tan(45° + \varphi/2)$, φ the rubble internal friction (30°), ν is the rubble porosity (0.3), ρ_w the water density (1025 kg/m^3), ρ_i the ice density (890 kg/m^3), g the gravitational constant and h the ice rubble thickness (4 m).

This load is of the same order as measured during run 4120 where an accumulation 4 m thick of rubble was observed (see Figure 5). In 3100, 4 m of the buoy are hidden also, but the load is

lower. However it is unsure how much of the cloud is ice rubble or slush from the milled ice by the propellers.

Simulations of impacts of single ice blocks are also found in the literature:

- Bonnemaire (2003) reports on model tests of simulations of ice impact on a protected riser. The ice block was 160 t (8 m diameter, 4 m thick, based on observations from previous ice tank model tests) and the impact speed 1.2 m/s. The maximum horizontal load was around 330 kN.
- Bonnemaire (2005) reports on numerical simulations from ice impacts on an other type of riser with higher tension. The ice block is similar and the maximum horizontal load 470 kN (0.5 m/s impact speed).
- Tikhonov et al. (2004) reports on numerical simulations of the impact of ice blocks on a stiff cylindrical protection for a drill-string. The maximum load under the impact of a 6.3 t ice block (3 m diameter, 1 m thick) at 0.95 m/s is then estimated to be 480 kN.

The two first investigations concern the interaction between ice and a flexible riser. The maximum loads were observed for impacts close to the riser top, where it is stiffer laterally. These impact loads are very short and may not be captured by the measuring system in the case of the ATOT model tests. However the reported load levels are of the same order as the highest measured ice loads.

6 Conclusions

Special focus was given on sub-surface ice transport during the ice tank testing of the Arctic Tandem Offloading Terminal (ATOT). The concept itself was designed to limit this effect to reduce the risks of ice interaction in the turret area. The main observations are:

- The wedge under the vessel bow was efficient in level ice but its capacity was exceeded in ice ridges
- The bow propellers were efficient in milling and clearing the ice, reducing probably the ice interactions on the turret. However, it is difficult to have control on the bridge of the efficiency of the ice management by propeller wash
- The dummy turret representing the offloading buoy was instrumented with a load cell. Ice loads up to 460 kN were measured due to interaction with ice rubble on the loading buoy. The extent in depths of the interaction was not observed in all tests.
- The measured loads are in the same range as estimations using a solution given by Mellor (1980) and as load estimations from ice impact simulations found in the literature.

The reported load levels (less than 500 kN) may not be a high design concern for the loading buoy in comparison with the expected mooring loads that will apply on this buoy. however, this might be a threat to the flow lines if they are subjected to this kind of transverse load level.

Acknowledgements

The work described in this publication was supported by the European Community's Sixth Framework Program through the grant to the budget of the Integrated Infrastructure Initiative HYDRALAB III, Contract no. 022441(RII3). The authors would like to thank the Hamburg Ship

Model Basin (HSVA), especially the ice tank crew, for the hospitality, technical and scientific support and the professional execution of the test program in the Research Infrastructure ARCTECLAB. The authors would also like to thank StatoilHydro for funding of the fabrication of the physical models, as well as NTNU students Vegard Aksnes and Christian Lønøy for the courageous and valuable help they provided during those long weeks in Hamburg. Truls Liset's talent for 3D illustrations is also acknowledged.

References

Aksnes V., Bonnemaire B., Løset S. and Lønøy C. (2008): Model Testing of the Arctic Tandem Offloading Terminal – Tandem Mooring Forces and Relative Motions between Vessels. *Proceedings of the 19th International Symposium on Ice. Vancouver*, British Columbia, Canada.

Bonnemaire, B., 2003: Model Tests of a Riser Armour for Subsea Offshore Loading of Hydrocarbons in Shallow Ice-Infested Waters. *Proceedings of the Russian Arctic Offshore Conference*, RAO, St Petersburg, Russia, pp. 426 – 430.

Bonnemaire, B., 2005: Response of an Armoured Riser to Wave and Ice Actions, and Impacts from Ice Blocks, IJOPE, *International Journal of Offshore and Polar Engineering*, vol. 15, no. 4.

Bonnemaire, B., Lundamo, T., Evers, K. U., Løset, S. and Jensen, A., 2008. Model Testing of the Arctic Tandem Offloading Terminal – Mooring Ice Ridge Loads. Proceedings of the 19th International Symposium on Ice. Vancouver, British Columbia, Canada.

Evers, K. U. and Jochmann, P., 1993. An Advanced Technique to Improve the Mechanical Properties of Model Ice Developed at the HSVA Ice Tank. *Proceedings of the 12th International Conference on Port and Ocean Engineering under Arctic Conditions*. Hamburg, Germany, pp. 877-888.

Jensen, A., Bonnemaire, B., Rupp, K. H., Løset, S., Breivik, K. G., Evers, K. U., Ravndal, O., Aksnes, V., Lundamo, T. and Lønøy, C., 2008. First Ice Tank Model Testing of the Arctic Tandem Offloading Terminal. *Proceedings of the 19th International Symposium on Ice*. Vancouver, British Columbia, Canada.

Mellor, M., 1980. Ship resistance in thick brash ice. *Cold Regions Science and Technology,* Vol. 3 No. 4: 305-321.

Tikhonov, V.S., A.I. Safronov and M.Ya. Gelfat, 2004: Dynamic analysis of the drillstring protection sys from ice floe. *Proceedings of the 14th International Offshore and Polar Engineering Conference*

19th IAHR International Symposium on Ice
"Using New Technology to Understand Water-Ice Interaction"
Vancouver, British Columbia, Canada, July 6 to 11, 2008

The CCTII Arctic Transportation Project

G.W. Timco[1], I. Kubat[1], M.E. Johnston[1], B. O'Connell[2], and T. Carrieres[3]
[1]*National Research Council - Canadian Hydraulics Centre, Ottawa, Ont., Canada*
[2]*Canadian Coast Guard, Ottawa, Ont., Canada*
[3]*Canadian Ice Service, Ottawa, Ont., Canada*
garry.timco@nrc.gc.ca
ivana.kubat@nrc.gc.ca
michelle.johnston@nrc.gc.ca
barb.oconnell@dfo-mpo.gc.ca
Tom.Carrieres@ec.gc.ca

Abstract

This paper presents an overview of the Canadian Climate Change Technology and Innovation Initiative (CCTII) Arctic Transportation Project. This project investigated the ability to navigate the waters of the Canadian Arctic on a year-round basis. Four tasks were performed to provide improvements in navigation. The first task reviewed historical ice conditions in the Arctic and addressed the issue of shipping regulations for vessels in Canada's Arctic. The second task addressed the issue of visually identifying multi-year ice from the bridge of the vessel, helicopters and satellite photographs. The third task investigated two different approaches for improved ice information onboard a vessel. These included a bow-mounted video camera and a high speed radar system with advanced signal processing. These systems were evaluated in two years of dedicated trials on board the icebreaker CCGS Henry Larsen. The fourth task developed technology for improved predictions of ice movement between the Arctic islands.

Introduction

An extensive drilling program in the Canadian High Arctic between 1969 and 1987 identified sixteen Tcf of discovered gas reserves with estimates of undiscovered potential up to sixty Tcf. Recently, the Canadian Energy Research Institute (CERI, 2004) evaluated the economics for development and concluded that development is viable. One of the main difficulties is to ensure that a reliable transportation system exists for bringing the gas to southern markets. Large tankers are one of the proposed methods for transit. Timco et al. (2005) conducted a scoping study to identify the key research areas that would improve year-round transportation in the Arctic. Fifteen Captains who operate vessels in the Arctic were interviewed in the study. Unanimously, they picked the detection of multi-year (MY) ice as the key research area. This identification of MY ice must be possible on both a regional scale and local scale (i.e. in the immediate vicinity of the vessel). The second priority related to improved knowledge of ice drift, leads and pressure. Based on these results, a four year comprehensive research program was performed to improve ice information in these areas (Timco and Gorman, 2007). There were four main Tasks in this research program:

1. Determine the year-round ice conditions that a tanker would encounter and determine the Polar Class of the necessary vessel based on Transport Canada regulations. This will have a pronounced influence on the cost of ship construction.
2. Collect detailed ground-truthed information on the presence and properties of multi-year ice and compare this information to predictions of ice conditions from satellite imagery. Data would be collected for two years, by the CIS Ice Service Specialists (ISS) on six CCG icebreakers. This information would be a unique collection showing the many facets of multi-year ice as observed from the Bridge of the vessel, helicopters and satellites.
3. Develop two types of sensors for the detection of multi-year ice. One sensor would be based on the high speed radar that has been developed for the detection of small icebergs. The second system would consist of a video system mounted at the bow of the vessel to give better visibility in fog conditions.
4. The fourth task was the collection of ice drift patterns in the High Arctic and the application of ice modeling to these specific regions.

This paper presents an overview and the results of these four tasks.

Task 1: Ice Conditions and Vessel Class

The objective of this Task was to provide detailed information on the ice conditions that would be encountered by a tanker operating year-round in the High Arctic and to determine the class of a vessel necessary to meet Transport Canada Regulations.

Transport Canada has the responsibility for regulating shipping in Canadian Arctic as part of the Arctic Shipping Pollution Prevention Regulations (ASPPR, 1989). There are two systems regulating shipping north of the 60°N in Canada, the Zone/Date System (ZDS) and the Arctic Ice Regime Shipping System (AIRSS, 1996). In both systems, vessels are assigned vessel classes: "Type" vessels and Arctic Classes in the ZDS, and "Type" vessels and CAC vessels in AIRSS. Type vessels are designed to operate in moderate first-year (FY) ice conditions, while the higher class Arctic Class and CAC vessels are designed to operate in severe multi-year (MY) ice

conditions. Vessel classes/categories Type B to CAC 3 were evaluated for year-round shipping in the Canadian Arctic during this task of the project.

Two routes were defined for transportation of gas to the southern markets (Figure 1): the "Western" route for shipping the gas to a terminal in the Beaufort Sea and then by a pipeline to Southern Canada, and the "Eastern" route for delivering the gas to a terminal on the East Coast of Canada. Both the Western and Eastern routes have two segments with one common to both, the Bridport route. The Bridport route leads from Bridport Inlet through Viscount Melville Sound to Barrow Strait with two options of going around Lowther Island. Information on ice conditions was obtained from the Canadian Ice Service (CIS) from historical digital ice charts. The analysis to evaluate ice conditions and the operability of different vessel classes throughout the year in the selected shipping routes is based on a methodology described in detail in Kubat *et al* (2005). The analysis was done for every second year between 1985 and 2005. The results showed that there is a high inter-annual variability in ice conditions encountered in the shipping lanes. It was interesting to note that during some warmer years, the ice conditions were more severe than during some colder years. It is due to ice conditions of the previous year – if the year was cold with severe ice, then the ice doesn't melt completely during summer. It becomes more severe during winter, and a longer time is then needed for ice to melt in the following year, even if the year is relatively warm. Also, in a warm year the first-year ice melts faster and the old ice floes are allowed to drift into shipping lanes. As a result, the ice conditions during the shipping season might be worse than those in the previous colder year.

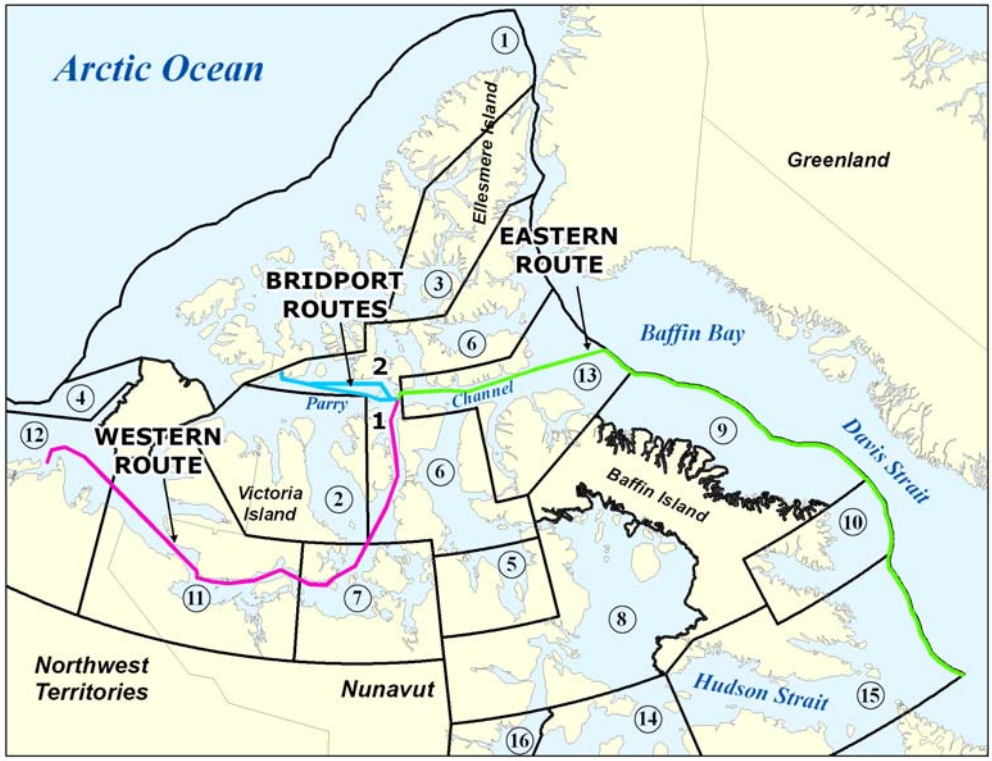

Figure 1. Shipping routes for transporting gas from Melville Island

In addition to this analysis, the occurrence of MY and FY ice in the shipping lanes was examined. This was done by normalizing the percentage of MY and FY ice coverage in each ice regime to the whole length of the shipping route. Results showed that there is not unity in severity of ice conditions for all the routes. For example in 2005 the ice conditions in the Bridport routes are quite light (i.e. much less MY ice is present in the shipping lanes) compared to other years, while in the Western and Eastern routes the conditions are more severe than in previous years. Mostly the ice conditions in the Western route are more severe than in the Eastern route; however during 1995 and 2001, more MY ice was present in the Eastern shipping lane than in the Western route. In general, the high presence of MY ice in all shipping lanes indicates potential danger to vessels, mainly to Type class vessels, and consequently increases requirements for a vessel class. Kubat *et al* (2007a) provides a detailed description of the analysis carried out during Task 1.

The results of this study showed that in order to operate safely in the Canadian Arctic on a year-round basis and in accordance to the existing Transport Canada Regulations, a vessel would have to be built to CAC2 or higher class specifications.

Task 2: Identification of Regional Multi-Year Ice

The objective of Task 2 of the project was to develop a guide to help identify old ice from the ship's bridge, an offshore structure and during an aerial reconnaissance. Old ice is a term that is used to describe sea ice that has survived one or more summers' melt. It includes both multi-year ice and second-year ice. Multi-year ice has been identified as one of the most important hazards facing shipping in the north, in winter and summer. Old ice is associated with the greatest number of ship damage events that occur in ice covered waters (Kubat and Timco, 2003), and it causes the highest loads on offshore structures (Timco and Johnston, 2004).

Despite the hazard that old ice poses for shipping, the mariner currently has very little information at his disposal to help decide when the ice is multi-year or when it is second-year. Differentiating multi-year ice from second-year ice, and even first-year ice at times, is not always straightforward – even for the seasoned mariner or the highly trained Ice Service Specialists (ISS). In fact, the term "old ice" is often used when second-year ice cannot be distinguished from multi-year ice. That sometimes less-than-clear distinction underscores how difficult it can be to differentiate the two ice types.

The NRC Canadian Hydraulics Centre published a guide called *Understanding and Identifying Old Ice in Summer* (Johnston and Timco, 2008; see Figure 2). It was a culmination of three years of work that presents old ice from four different perspectives: on-ice observations, ship-based observations, aerial observations, and satellite observations. The following sections describe the different components of the Guide.

On-ice Observations: *Understanding and Identifying Old Ice in Summer* begins with a primer on old ice. Much of our understanding of old ice comes from the on-ice observations that have been made over the years. The primer uses on-ice measurements such as the thickness, temperature, salinity and strength to show some of the fundamental differences between multi-year and second-year ice. It also discusses how old ice moves (and decays) through the Arctic. As such,

the primer provides context for understanding the ship-based, aerial and satellite observations of old ice that are included in the Guide.

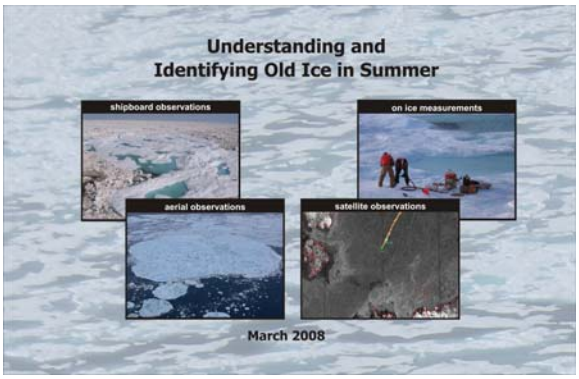

Figure 2. Cover page of guide called *Understanding and Identifying Old Ice in Summer*

Ship-based Observations: A large part of the Guide is devoted to the ship-based observations of multi-year and second-year ice that were collected over a period of three years. More than 200 ship-based observations of old ice were made from early July to October. The observations were made from ten different vessels in all regions of the Canadian Arctic. The information was generously provided by experienced personnel such as the Ice Service Specialists (ISS) from the Canadian Ice Service (CIS), two Commanding Officers acting in the capacity of ice observers on foreign ships, and a keen post-graduate student from the University of Manitoba. The ships that participated in the program were icebreakers, except for the M.V. *Bremen*, which navigated the Northwest Passage while Captain N. Thomas of the Canadian Coast Guard acted in the capacity of an ice observer.

The observations are categorized by the region in which they were collected: western Arctic, central Arctic, eastern Arctic or sub-Arctic (Figure 3). The number of observations that were collected by each ship depended upon how much old ice was encountered during the voyage, but it also depended upon the amount of time that was available for making observations. The amount of ice that was encountered, and the characteristics of that old ice, depended upon the area in which the ship operated, and the time of year.

The Guide includes large format photographs of the old ice features, along with supplementary information about what factors were taken into account in deciding whether the ice was multi-year or second-year – parameters that included the estimated ice thickness, color of the ice, melt pond extent and shape, pond drainage features, surface roughness and degree of weathering. The Guide also provides information about the ship response after impacting the floe, if applicable.

Figure 4 includes some examples of the old ice that was encountered along the shipping routes during summer. Clearly, "old ice" is a general term that covers a broad spectrum of ice. The photographs show that the differences between multi-year and second-year ice range from highly evident, to extremely subtle. The photographs underscore the importance of having a Guide to assist with identifying the varied forms of old ice, and the key parameters should be used to classify old ice.

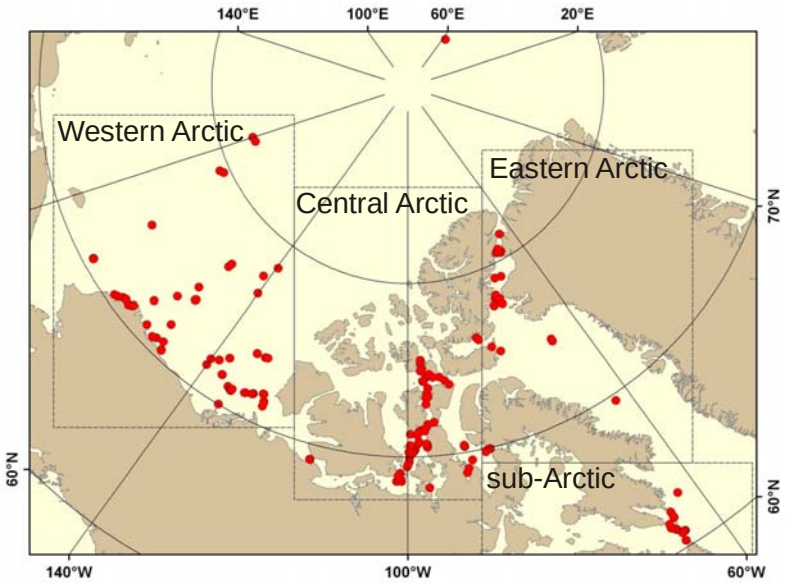

Figure 3. Map showing where old ice observations were made in 2005, 2006 and 2007

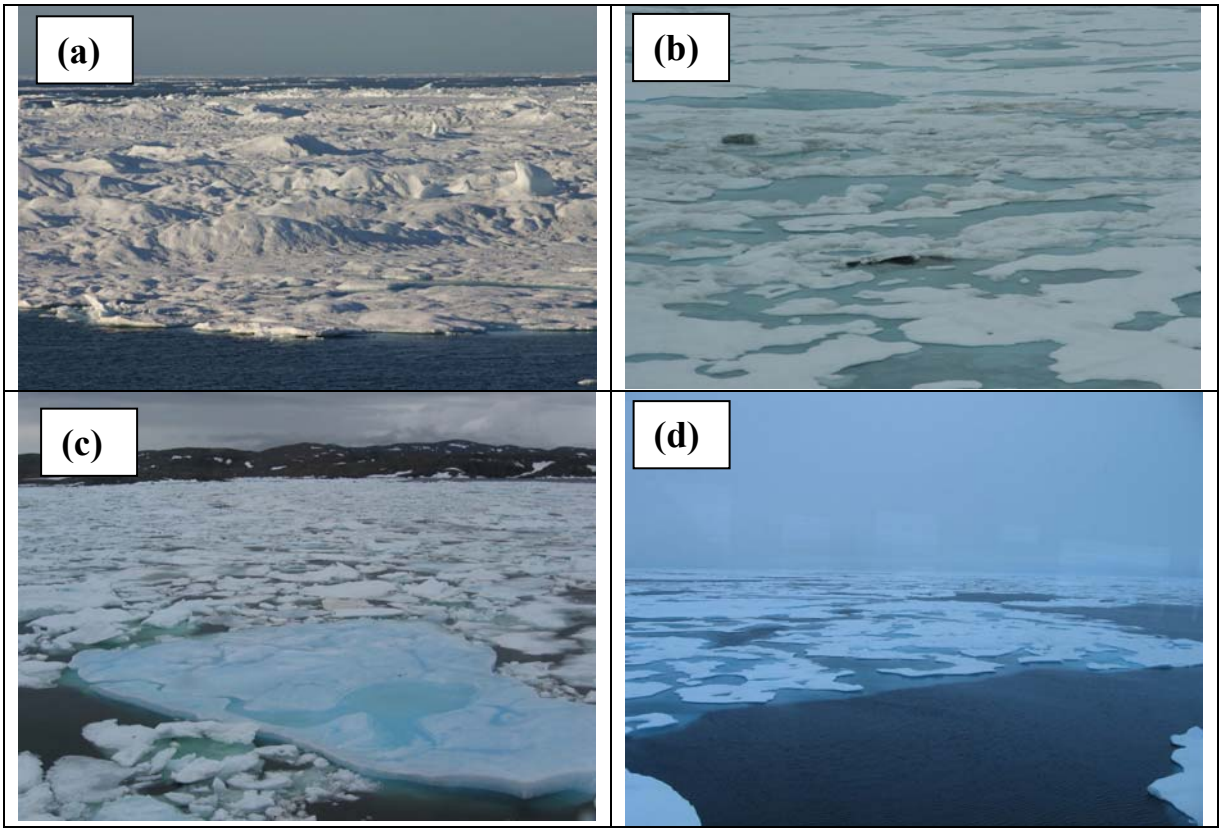

Figure 4. Observations of old ice included in the Guide (a) multi-year ice in the Western Arctic, (b) multi-year ice in the Central Arctic, (c) multi-year ice in sub-Arctic and (d) second-year ice in the Western Arctic.

Aerial Observations: The aerial observations were made while conducting reconnaissance flights with a helicopter. The aerial reconnaissance is one of the Commanding Officer's key lines of defence for navigating safely and efficiently through severe ice. The bird's eye view provides an important perspective of old ice because often it provides the only source of information about the path of least resistance through the ice field. The aerial observations in the Guide provide several examples about how old ice appears from the air.

Satellite Observations: The last section of the Guide includes some satellite images that have been "validated" with complimentary information from the on-ice, ship-based or aerial observations. This is an important section of the Guide because most ships transiting ice covered waters now use some form of satellite imagery, as a navigation aid (short term) and/or for planning purposes (longer term). The satellite images that were included in the Guide were selected from the images that were sent to the bridges of the Canadian Coast Guard (CCG) icebreakers in support of ice operations, courtesy of the Canadian Ice Service (CIS).

Task 3: Local Detection of Multi-Year Ice

Task 3 of the CCTII Initiative investigated two different approaches (video camera and ice hazard radar) for the improved detection of dangerous ice in poor visibility (snowfall, darkness, fog) and in heavy sea conditions. These were tested during trials onboard the CCG icebreaker *CCGS Henry Larsen* in 2006 and 2007.

Bow Mounted Video Camera

Ship captains have observed that objects can occasionally be detected earlier in fog by video cameras than with the naked eye. To quantify this, a video camera with a weatherproof housing was mounted on the bow of the icebreaker *CCGS Henry Larsen* in May 2006. After several months in its exposed location, water was able to penetrate the camera causing irreparable damage so it was replaced with a more rugged camera. The stainless steel Moondance® ruggedized pan-tilt-zoom camera, which is designed to work under extreme weather environments and corrosive conditions was mounted on the bow of the vessel (Figure 5). The display monitor was installed on a console table with other navigation systems close to the bridge windows for convenience. The camera has the ability to use ambient light to enhance the video image at night. During the trial in July 2007, the bridge team assessed the ability of the video system to improve visibility from the bridge, especially in low light, snow and fog conditions. The camera proved itself as a valuable tool to be used in conjunction with the bridge lookouts and radars.

Marine Radar for Improved Ice Detection

Standard marine radars have been developed as target detectors (for other ships, coastlines and hazards) and are not designed to provide a high definition image. They may not detect small floes of multi-year ice or dangerous glacial ice such as bergy bits or growlers early enough to avoid a collision. Transport Canada's Transportation Development Centre (TDC) has conducted significant research projects for the detection of small objects such as swimmers and glacial ice in various sea conditions. As part of this project, the Canadian Coast Guard collaborated with TDC to develop an "Ice Hazard Radar System" for improved recognition of dangerous ice features.

Figure 5. Video camera mounted on the bow of the CCGS Henry Larsen and the video display on the bridge of the vessel.

Rutter Technologies, St. John's, developed the computer display system which was installed on the bridge of the *CCGS Henry Larsen* in June 2006. The system was connected to the vessel's standard x-band marine radar in slave-mode. The radar signal is converted to 256 grey scale and digitized into a high-resolution image similar to a satellite image, which allows the user to identify complex ice patterns. A trial was conducted on board the icebreaker in August 2006 in Nares Strait during a scientific program. Figure 6 shows an example of the improvement with this ice radar.

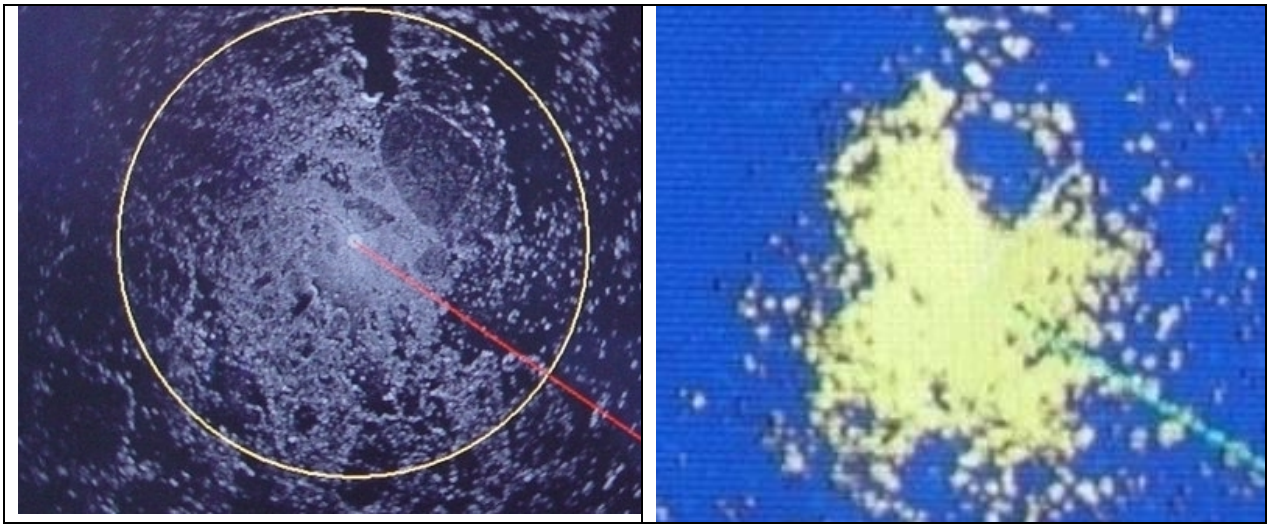

Figure 6. The ice radar (left) provides more clarity of ice features, such as the shape of multi-year floes, than the standard radar (right). August 2006

The Captain, Ship Officers and team evaluated the capability of the radar processing system for displaying ice imagery. Captain Vanthiel stated "The radar is proving to be a very useful tool for tactical ice information. It allows the bridge watchkeeper to differentiate the different ice features and easily discern the water leads."

During the winter of 2007, Innovation Maritime, Rimouski (Quebec), modified a Sperry Bridgemaster E radar so that the scanner could rotate at high speeds up to 120 rpm. Typical marine radar scanners rotate at 25 to 30 rpm. When combined with Rutter Technologies' *Sigma S6*® advanced digital radar processing that uses scan-to-scan averaging techniques, the radar produces high resolution images which allow the user to detect small icebergs which are nearly impossible to see with conventional radar.

In June 2007, the high-speed scanner was installed on the *CCGS Henry Larsen* and connected to the ice radar display system on the bridge. The icebreaker departed St. John's on July 4th and a trial was conducted in Hudson Strait and Frobisher Bay, ending July 12, 2007. The radar was able to detect bergy bits and growlers from decaying icebergs at more than three nautical miles. The ice was not detected on the standard radar until about a half mile from the vessel. Figures 7 and 8 show images that were taken during the Arctic 2007 trial on the *CCGS Henry Larsen*.

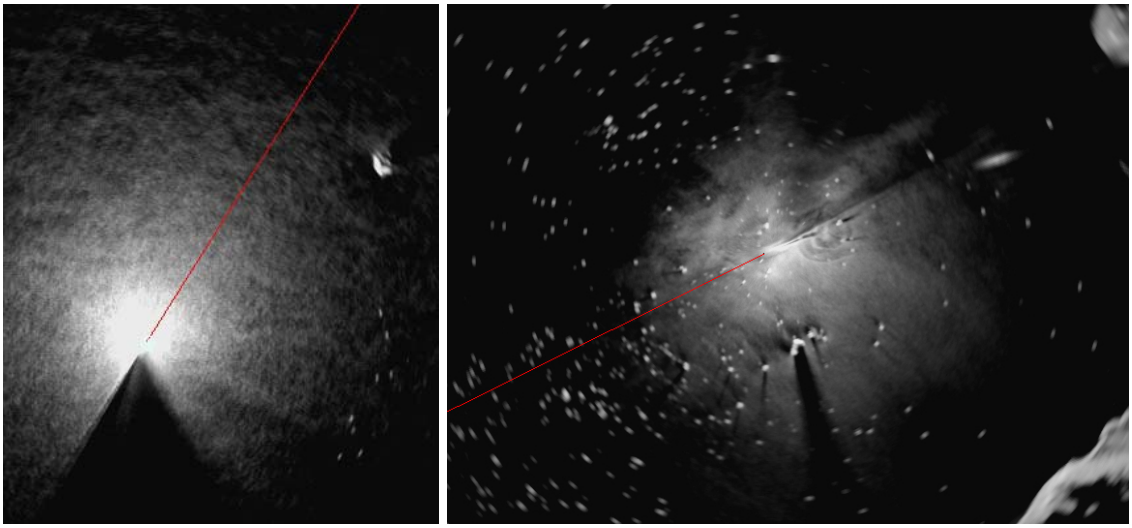

Figure 7. Left: Bergy bits and growlers drifting away from an iceberg. Right: Icebergs, growlers and bergy bits. July 2007

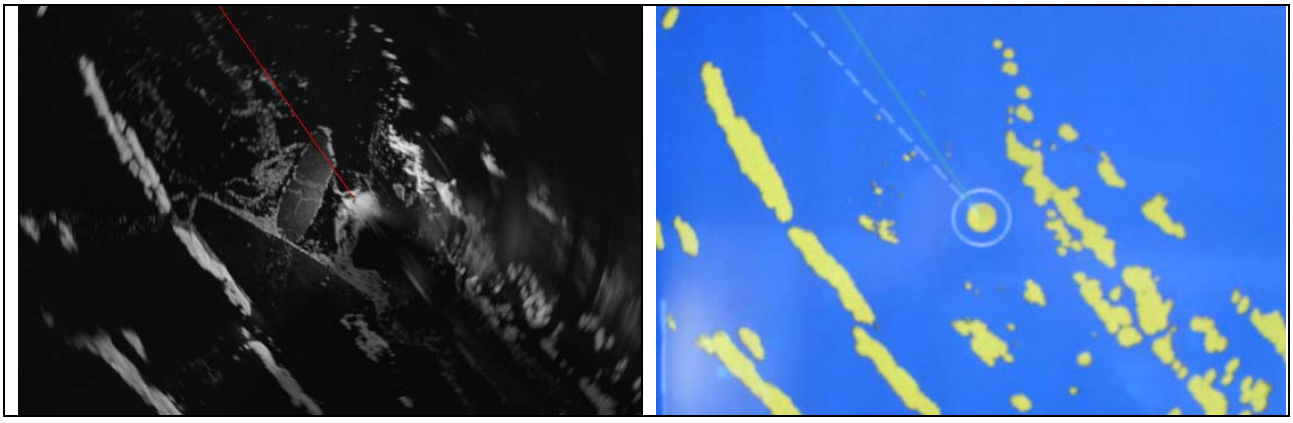

Figure 8. Left: Ice Hazard Radar image Right: Conventional radar image. July 2007

The Captain reported "The imagery provides a real-time picture of the vessel's surroundings. Within a 2 nautical mile radius of the vessel, this imagery presented has a distinctive 3D appearance, tantamount to embossed, indicating ridges, floe edges providing a much clearer image than the 2D blips available on the standard radar. A clear high-definition radar image portraying the mariner's immediate surroundings provided by Sigma S6 technology is a godsend."

The Canadian Coast Guard, Transport Canada, TDC, and Rutter Technologies will continue to develop the ice radar processing capability and assess the system on the *CCGS Henry Larsen* during the ice seasons off the north-east coast of Newfoundland and Labrador and in the Arctic. This technology has proven itself to be a significant improvement over conventional marine radar.

Task 4: Improved Modelling of Ice Drift in the High Arctic

The objective of this task was to investigate ice drift patterns in the High Arctic and develop a framework for the prediction of ice drift, the presence of leads, and internal pressure in the ice.

The Canadian Arctic Archipelago (CAA) presents significant challenges to numerical ice modelling and accurate ice forecasts. The CAA has many narrow straits and bays that are often of similar width to the ice floes that traverse them. This and other factors lead to large areas of consolidated and landfast ice. Multiyear and deformed ice is prevalent and shear zones form along main channels. Winds play a dominant role in ice drift and the steep topography results in significant wind steering. Ocean currents in this area are not well modelled or understood either mainly due to relatively low traffic volumes and the difficulty and cost of conducting research in this remote area.

As a start towards tackling some of these problems, a number of studies have been conducted to better understand the ice behaviour in the CAA. Alt (2005) and Alt *et al.* (2005) identified many of the unique ice features of the CAA including locations of their occurrence and frequency. An atlas of ice drift patterns was prepared using ice drift data derived from sequential RADARSAT imagery for 2003 (Papineau, 2005).

Collaboration between the Canadian Ice Service, NRC-CHC and McGill University led to the development of a model (described in Sayed *et al* 1999, 2002) that deals with small scales and ice conditions typical of the CAA. Model improvements addressed the advection scheme, the ridging formulation, and the numerical solution approach. The main innovation of the model is a Particle-In-Cell (PIC) approach to model ice advection, whereby the ice cover is represented by discrete particles. Each particle carries attributes that describe ice conditions (thickness and concentration of level and deformed (ridged) ice), and variables associated with the ice (velocity, position, etc). In the present PIC implementation, the momentum and continuity equations are solved over an Eulerian grid. This approach allows a history of each particle to be maintained. Another important innovation is a new thickness redistribution model (Savage, 2008) that accounts for continuous evolution of the ice thickness and ice concentration without resorting ice to discrete categories.

Figure 9 shows the results of an idealized test case of a long channel with parallel boundaries used to examine the pressure distributions that may be encountered in long channels with converging ends. The figure shows profiles of the pressure along the centerline of the channels for a case with tidal current applied from the beginning of a run. The profiles show the changes in pressure during a 12-hour cycle for cases with and without tidal currents. One result is that tides reduce ice pressure.

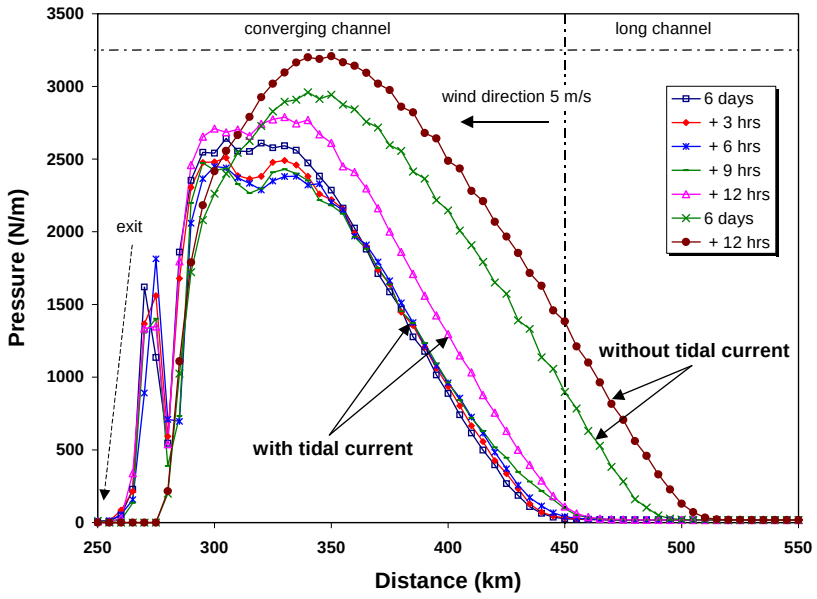

Figure 9. Profiles of the pressure along the centre of the channel at different phases of the tidal cycle after 6 days. Profiles for the same case without tidal current are shown after 6 days and 12 hours later (from Kubat *et al* 2007b).

Conclusions

Overall this project was very successful on all counts. A number of researchers in different organizations worked together to advance the knowledge of multi-year ice detection, and ice movement in the Canadian Arctic. All four tasks will continue to develop. The detection and identification of multi-year ice will be an increasing priority in the Arctic. Continued research by the NRC-CHC and Coast Guard personnel will continue onboard Coast Guard icebreakers. The Canadian Ice Service will begin to use RADARSAT2 to better identify multi-year ice. Finally, the NRC-CHC is developing a system for predicting the real-time locations of pressured ice in the High Arctic.

Acknowledgements

The authors would like to acknowledge with thanks the financial support of the Canadian government through the Climate Change Technology and Innovation Initiative program, Transport Canada, the Canadian Coast Guard, and the Program of Energy Research and Development. The authors would like to acknowledge the input of Anne Collins, Bob Gorman, Charles Gautier, Francois Choquette, John Falkingham, Capt. J. Broderick and Capt. J. Vanthiel. The data collection provided by the Ice Service Specialists of the Canadian Ice Service was superb and their contribution is gratefully acknowledged. The support and assistance of the

Captain and crew of the CCGS Henry Larsen during the trials are greatly appreciated. The Canadian Coast Guard Technical Services in St. John's have also helped to make this project a success.

References

AIRSS, 1996. Arctic ice regime shipping system (AIRSS) standards. Transport Canada Report TP 12259E, Ottawa, Ont., Canada.

Alt, B., 2005. Presence and climatology of old ice and consolidated ice in the Lancaster Sound area of the Canadian Arctic Archipelago. Contract Report to Canadian Ice Service, 31 pages, Ottawa, ON, Canada.

Alt, B. and Lindsay D.G., 2005. Preliminary investigations of unique features of the Canadian Arctic Archipelago sea ice conditions as they relate to short range forecast modelling with emphasis on differences from East Coast. Contract Report to Canadian Ice Service, Report be05-05, 68 pages, Ottawa, ON, Canada.

ASPPR, 1989, Proposals for the revision of the Arctic shipping pollution prevention regulations. Transport Canada Report TP 9981, Ottawa. Ont., Canada.

CERI, 2004. Economics of High Arctic gas development. Canadian Energy Research Institute Report, Calgary, AB, Canada.

Johnston, M.E. and Timco, G.W., 2008. Understanding and identifying old ice in summer. NRC Canadian Hydraulics Centre Report, Ottawa, ON, Canada.

Kubat, I., Collins, A., Gorman, B., and Timco, G.W., 2005. A methodology to evaluate Canada's Arctic shipping regulation. Proceedings POAC'05, pp 693-703, Potsdam, NY, USA.

Kubat, I., Collins, A. and Timco, G.W., 2007a. Year-round shipping in the Canadian Arctic: ice conditions and regulatory requirements. Proceedings POAC'07, Vol. 1, pp 446-456, Dalian, China.

Kubat, I., Sayed, M., Savage, S. and Carrieres, T., 2007b. Flow of ice through long converging channels. Proceedings POAC'07, Vol. 2, pp 673-684, Dalian, China.

Kubat, I. and Timco, G.W., 2003. Vessel damage in the Canadian Arctic. Proceedings POAC'03, Vol. 1, pp 203-212, Trondheim, Norway.

Papineau, M.A., 2005. Understanding the ice motion in the Canadian Arctic summer 2003 using Radarsat-1 data. Canadian Ice Service Internal Report, 94 pages, Ottawa, ON, Canada.

Savage, S.B., 2008. Two-component sea ice thickness redistribution model. Cold Regions Science and Technology, Vol. 51, No. 1, pp 20-37.

Sayed, M, and Carrieres, T. 1999. Overview of a new operational ice forecasting model. Proceedings ISOPE99, Vol. II, pp 622-627, Brest, France.

Sayed, M., Carrieres, T., Tran, H. and Savage, S.B., 2002. Development of an operational ice dynamics model for the Canadian Ice Service. Proceedings ISOPE02, pp 841-848, Kitakyushu, Japan.

Timco, G.W. and Gorman, R., 2007. Survey of Canadian Arctic Captains: current status and research needs. Proceedings POAC'07, Vol. 2, pp 695-704, Dalian, China.

Timco, G.W., Gorman, B., Falkingham, J. and O'Connell, B. 2005. Scoping study: ice information requirements for marine transportation of natural gas from the High Arctic. NRC Report CHC-TR-029, Ottawa, Ont., Canada.

Timco, G.W. and Johnston, M., 2004. Ice loads on the caisson structures in the Canadian Beaufort Sea. Cold Regions Science and Technology, Vol. 38, pp 185-209.

19th IAHR International Symposium on Ice
"Using New Technology to Understand Water-Ice Interaction"
Vancouver, British Columbia, Canada, July 6 to 11, 2008

Model Testing of the Arctic Tandem Offloading Terminal – Tandem Mooring Forces and Relative Motions between Vessels

Vegard Aksnes[1], Basile Bonnemaire[2,1], Sveinung Løset[1] and Christian Lønøy[1]
[1]*Norwegian University of Science and Technology (NTNU), Trondheim, Norway.*
[2]*Barlindhaug Consult AS, Tromsø, Norway.*
vegard.aksnes@ntnu.no, basile.bonnemaire@barlindhaug.no, sveinung.loset@ntnu.no and lonoy@stud.ntnu.no

The Arctic Tandem Offloading Terminal (ATOT) is an innovative concept for offloading of hydrocarbons in ice-infested waters. The concept includes an offloading icebreaker (OIB) with a submerged turret loading system and a shuttle tanker. The OIB is moored to a turret buoy, and shuttle tankers moor at the stern of the OIB for offloading. The ATOT concept has been tested in model scale in the Large Ice Model Basin at HSVA in Hamburg, Germany. This paper discusses results from two tests in level ice and ridges; that is, the measured forces in the tandem mooring system between the vessels as well as the relative motions between the tanker and the OIB. The interaction between the ATOT and ridges is studied and it is seen that the largest tandem mooring forces are occurring during ridge penetration. The qualitative behaviour of the ATOT during slow changes of ice drift direction is analysed.

1. Introduction

The Arctic Tandem Offloading Terminal (ATOT) is a concept for offloading of hydrocarbons in ice-infested waters. The concept includes an offloading icebreaker (OIB) which is moored to a submerged turret and a shuttle tanker which is moored at the stern of the OIB, see Figure 1. The ATOT concept was tested in June 2007 in the Large Ice Model Basin at HSVA in Hamburg, Germany and the general results from these tests are described by Jensen et al. (2008). The tests were performed in level ice, ice ridges and broken ice. Two other companion papers describe different aspects of the model tests of ATOT; the turret mooring forces caused by ridges are discussed in Bonnemaire et al. (2008a) and the subsurface ice interaction under the OIB is analysed in Bonnemaire et al. (2008b). This paper focuses on the measured forces in the tandem mooring system between the vessels and the relative motions between the OIB and the tanker in level ice and ridges.

The tandem mooring system is explained in full scale and in model scale. Further, the ice conditions and the test runs are described. Instrumentation and processing procedures are then followed by results and a discussion about the forces in the tandem mooring system and their connections to ice conditions and relative vessel motions.

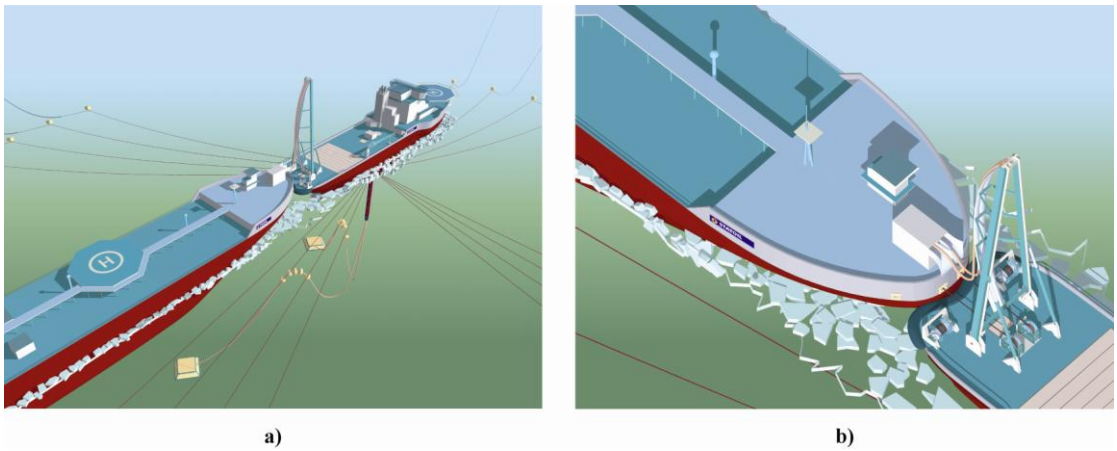

Figure 1. a) The ATOT concept in full scale. **b)** Close-up view of the tandem mooring system in full scale.

2. Model setup

The Large Ice Model Basin at HSVA is 78 m long, 10 m wide and 2.5 m deep. Froude scaling was used because of the importance of gravitational and inertial forces, see Ashton (1986), and the scaling ratio was $\lambda = 24$. In this text, all presented values are scaled to represent full scale data. The length between perpendiculars of the OIB was 109 m, there were two different draughts, 12 and 14 m, for open water and ice respectively and thus the beam varied between 26 and 30 m. It had a displacement of 21000 t and was equipped with reamers to increase manoeuvrability and to reduce the ice forces on the tanker. The length of the tanker was 288 m, the beam and draught was 35.5 and 15 m respectively, and it had a displacement of 108000 t. The OIB was equipped with four azimuth propellers with a power of 7.1 MW each, two at the bow and two at the stern, while the tanker was passive, with no propulsion. Further details regarding the vessels can be found in Jensen et al. (2008).

For practical reasons, the turret mooring system of the OIB was modelled with a dry mooring system. The stiffness of the mooring system was different in the two test runs. In test run 3100 it was 2.2 MN/m and in test run 4100 it was 4.4 MN/m, adapted to 150 m and 40 m water depth respectively. In the model tests the ice sheet was frozen to the tank walls and the OIB was pulled by the mooring system through the ice to simulate ice drift. More details about the dry mooring system and the related mooring forces can be found in Bonnemaire et al. (2008a).

The tandem mooring system has two basic operational modes, distant loading and close loading. Distant loading is intended for loading in open water and light ice conditions, that is, ice coverage of less than 20 %, while close loading is the preferred operational mode in medium and severe ice conditions.

The tandem mooring system consists in full scale of two mooring lines which are fixed to the bow of the tanker and are reeled on to two hawser winches located at the stern of the OIB as shown in Figure 1. The preliminary design of each of the winches is a pull in capacity of 2 MN, a braking capacity of 3 MN and a payout rate of 1 m/s. It is possible to disconnect the mooring lines and the risers within seconds. The loading system consists of two 20 inch risers with a transfer rate of 9000 m^3/h, which makes a loading time of 6 hours achievable for the present tanker. The ice drift is often tidal driven and changes of ice drift direction are believed to cause the highest mooring forces, as reported by Danielewicz et al. (1995) and Comfort et al. (1999). By loading within half a tidal cycle it is therefore assumed that the worst scenarios are avoided. The influence of changes of ice drift direction on different loading concepts is discussed in Bonnemaire (2006). During changes of ice drift direction, the tandem mooring system will be active and provide a constant pretension in the mooring lines as long as there is no opening between the vessels.

In the model tests, the tanker was moored in close tow at the notch of the OIB. The notch was equipped with a fender system which consisted of a row of thick cylindrical fenders and a row of thinner block fenders as shown in Figure 2. The stiffness of the fender system in surge was tested in cold conditions and estimated to be 16.1 MN/m at 0 - 0.4 m penetration and 164 MN/m at 0.4 - 0.5 m penetration. The model scale mooring system consisted of two steel wires which were connected to load cells mounted on hinges at the stern of the OIB. The wires ran through steel guiders at the tanker bow and to a weight system in the tanker, as shown in Figure 3. One meter of each of the wires was replaced with synthetic rope to model the elasticity of the mooring lines.

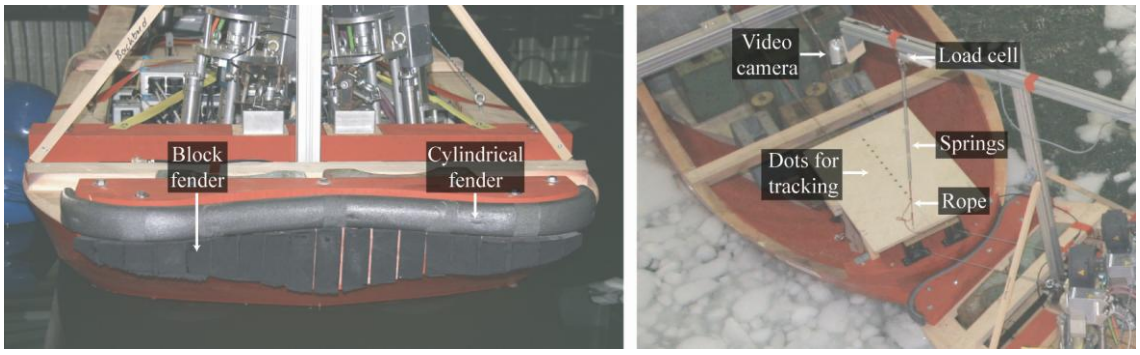

Figure 2. The fender system and the setup for measuring the relative motions.

The model of the tandem mooring system worked as follows:

- The weight system consisted of two times two weights. The upper weights were 2 x 1.2 MN and modelled the pretension in the lines, while the lower weights were 2 x 1.8 MN, so that the total weight represented the breaking capacity of the winches.
- When there was a distance between the tanker bow and the fender system both weights were lifted with a distance between them. The mooring line forces were then constant and did not depend on the distance from the tanker bow to the fender, as long as there was no contact. This simulated the payout of the winches at constant breaking force.
- At the moment when there was contact between the tanker bow and the fender, there was also contact between the lower weight and the floor of the tanker.
- As the tanker bow compressed the fender, the distance between the weights decreased and finally the upper weight was in contact with the lower one. At this point, the mooring lines would be slack, the mooring forces would be zero and the tanker bow would have penetrated into the stiffer part of the fender.
- The weight system did not model the pretension correctly during changes of drift direction. When the vessels were in contact with each other and there was a large yaw angle, one mooring line became slack, while the other was subjected to higher tension than the pretension.

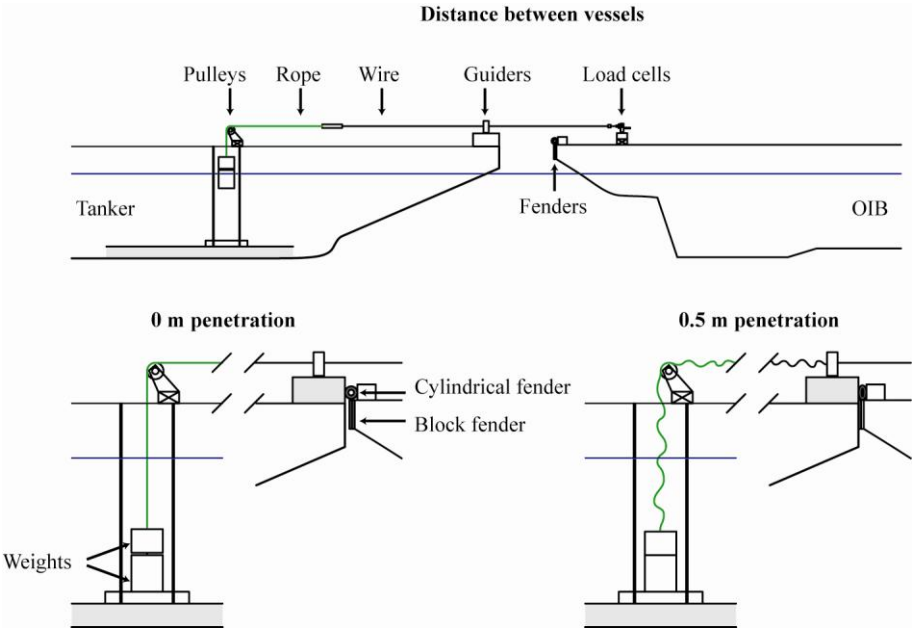

Figure 3. The tandem mooring system as modelled in the ice tank.

3. Test runs

The ATOT concept was tested in unbroken level ice and ridges, in level ice and ridges with a broken channel nearby and in broken ice with a drift speed of 0.5 m/s. The ice drift was straight or slowly varying in level ice and broken ice, but always straight in ridges. In this text, only intact level ice and ridges are considered. Figure 4 shows sketches of the vessel traces in each of the test runs.

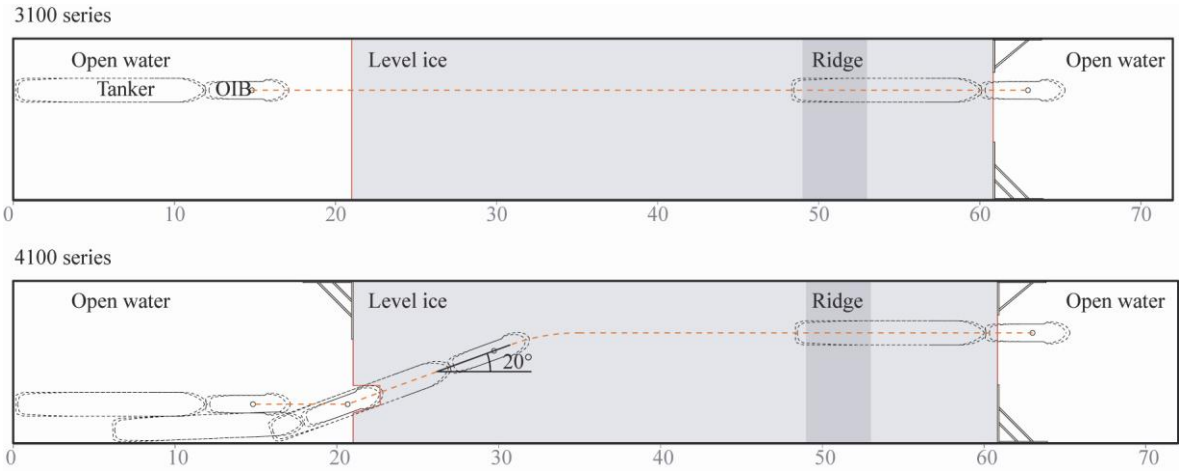

Figure 4. The figure shows the traces of the vessels from the test runs.

The model ice was prepared as described by Evers and Jochmann (1993) and the ice ridges by pushing level ice against a beam as outlined by Høyland et al. (2001). The main characteristics of the level ice and the ridges are summarized in Table 1. Both ridges had a consolidated layer of approximately two level ice thicknesses, in order to model first-year ridges.

Table 1. The main characteristics of the level ice and the ridges are listed in the table below. The notation is as follows: h_i is level ice thickness, σ_f is flexural strength, h_k is ridge keel depth, h_s is ridge sail height and w_k is ridge width.

Test run	h_i [m]	σ_f [kPa]	h_k [m]	h_s [m]	w_k [m]
3100	1.03	720	13.0	2.2	96
4100	1.15	480	14.9	1.9	96

4. Measurements

More than 60 different channels were recorded during each test run. The most relevant measurements regarding the tandem mooring system will be described here, meaning the measurements of the relative horizontal and vertical motion of the vessels as well as the forces in the tandem mooring system.

- The forces in each of the mooring lines in the tandem system were measured with uniaxial load cells of type HBM U9B and sampled at a frequency of 100 Hz. In the time series plots later in the text, “port” and “starboard” will refer to the mooring lines on port and starboard side, respectively.
- The motion of the OIB was measured in all 6 degrees of freedom, see Figure 5 for definition of the modes of rigid body motion, but the absolute tanker motions were not measured directly. However, the relative horizontal and vertical motions between the vessels were measured as described below:
- The relative horizontal motions between the vessels were recorded with a video camera fixed at the stern of the OIB and looking downwards on a dotted plate fixed in the bow of the tanker, see Figure 2. The motion of the dots was then tracked with the free software

Video Spot Tracker developed by the Department of Computer Science, University of North Carolina at Chapel Hill. By fitting a straight line to the dots, the relative surge, sway and yaw motions of the tanker relative to the OIB were found. The motions were found in a coordinate system fixed to the uncompressed fender, as shown in Figure 5. It can be seen that relative surge is negative when there is space between the tanker bow and the midpoint of the fender system, while relative surge is positive when the fender system is compressed.

- The relative vertical motion was measured with a mechanical spring system. Three springs were connected in series, with one end fixed to a load cell which was mounted on a beam, fixed to the OIB. The vessels were aligned and the other end of the system of springs was connected to a point in the bow of the tanker directly under the load cell. The stiffness of the springs was estimated and by recording the force in the springs, we found the relative vertical motion between the vessels by applying Hooke's law. From this, the pitch and heave motion of the tanker could be found. In our coordinate system, the pitch angle is increasing when the bow is moving downwards.

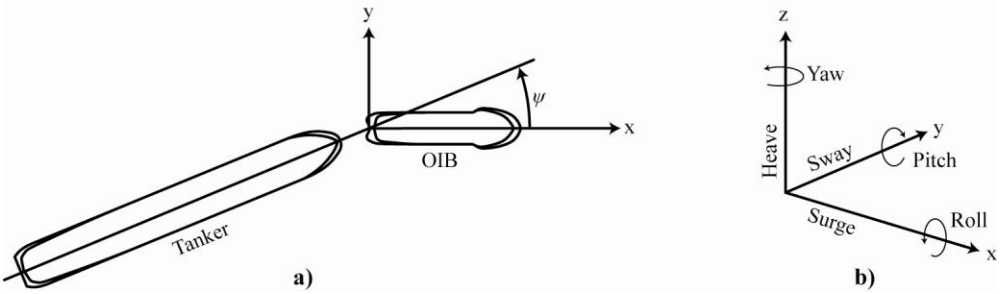

Figure 5. The sketches show **a)** the coordinate system fixed to the centre of the uncompressed fender at the stern of the OIB, which the tanker bow moves relative to and **b)** the six modes of rigid body motion.

5. Results

This section contains plotted time series of the total tandem mooring forces as well as the mooring forces in each individual mooring line. In Figures 6 and 7, the number ❶ indicates when the bow of the tanker entered level ice and the moment when the bow of the tanker started to penetrate the ridge is marked with the number ❷. Note that both vessels are embedded in ice at the end of the time series. In addition to mooring forces, the relative yaw angle and the relative surge between the OIB and the tanker in test run 4100 are plotted. The pitch motion of the tanker and the OIB is given for test run 3100. Key numbers from each of the test runs are highlighted in the text, and the maximal tandem mooring forces are summarized in Table 2.

Table 2. Maximal tandem mooring forces in individual mooring lines and in total from both test runs.

Test run	Max mooring forces in level/broken ice			Max mooring forces in ridges		
	Port [MN]	Starboard [MN]	Total [MN]	Port [MN]	Starboard [MN]	Total [MN]
3100	2.4	2.0	3.7	2.6	3.3	5.9
4100	3.9	3.9	7.8	3.2	3.0	6.2

Test run 3100

The tandem mooring forces from test run 3100 are shown in Figure 6. The maximal total mooring force was 3.7 MN and 5.9 MN in level ice and the ridge, respectively. The mean total mooring force was calculated from $t = 800$ s to $t = 1800$ s, that is, the time period when the tanker was totally embedded in level ice, giving a mean of 3.0 MN with standard deviation 0.4 MN. The relative yaw angle is not plotted since the ice drift was straight throughout the entire test run. The lower plot of Figure 6 shows the pitch motion of both vessels.

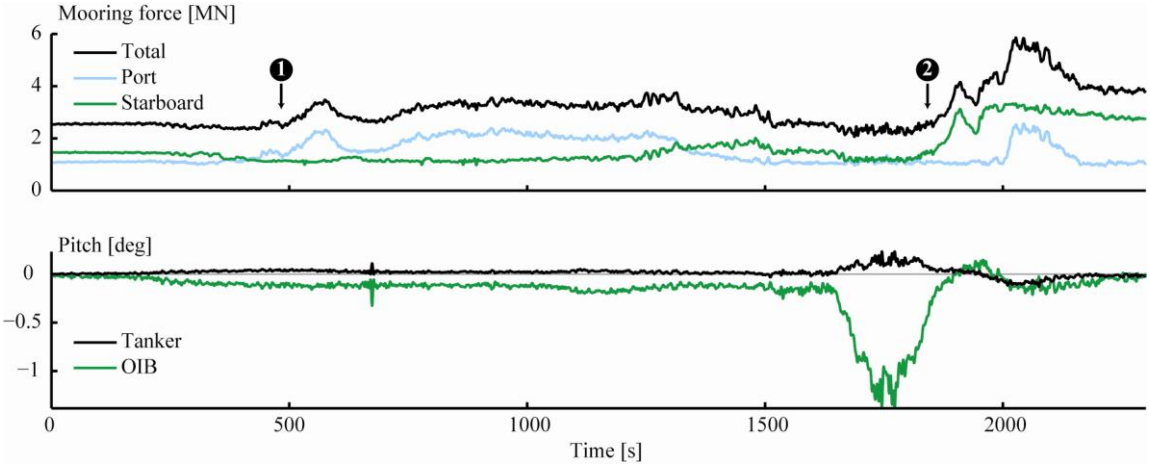

Figure 6. Tandem mooring forces between the vessels and pitch angle of both vessels during test run 3100.

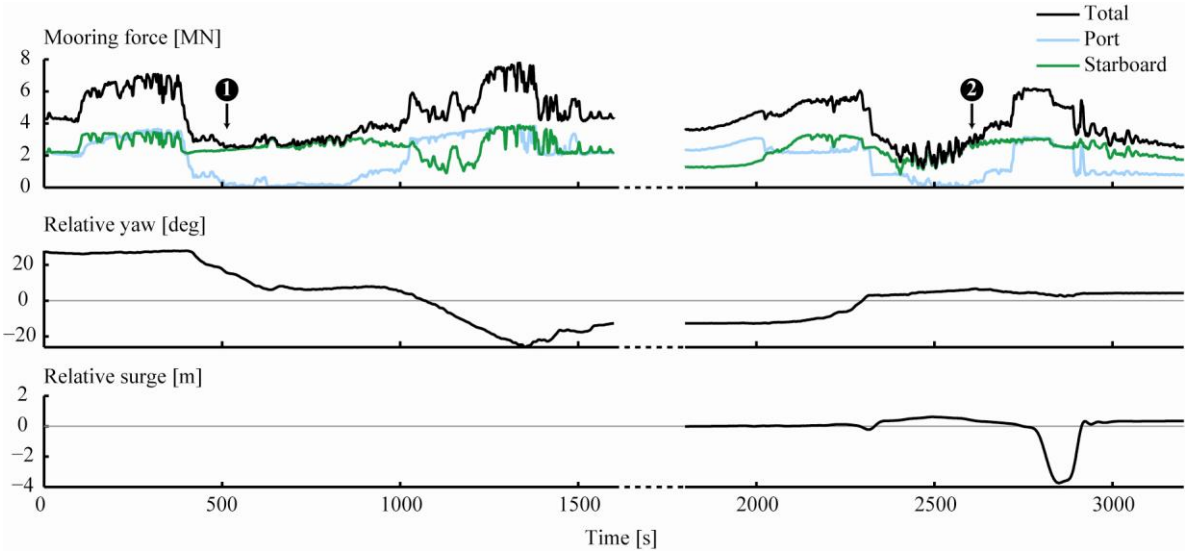

Figure 7. Tandem mooring forces, relative yaw and relative surge between the vessels during test run 4100.

Test run 4100

In Figure 7, the recorded time series of the tandem mooring forces and the video tracked relative yaw angle from test run 4100 are plotted. The test run was temporarily stopped before the OIB

entered the ridge, thus there is a gap in the time series indicated by a dashed interval on the time axis. The maximal total mooring force was 7.9 MN in level ice and 6.2 MN in the ridge. The extreme relative yaw angles were 28º and -26º. The figure also shows the relative surge between the tanker and the OIB during the last part of test run 4100. The largest displacement was 3.7 m. Figure 8 shows a drawing sequence of how the heading of the vessels changed during a change of ice drift direction of 20º.

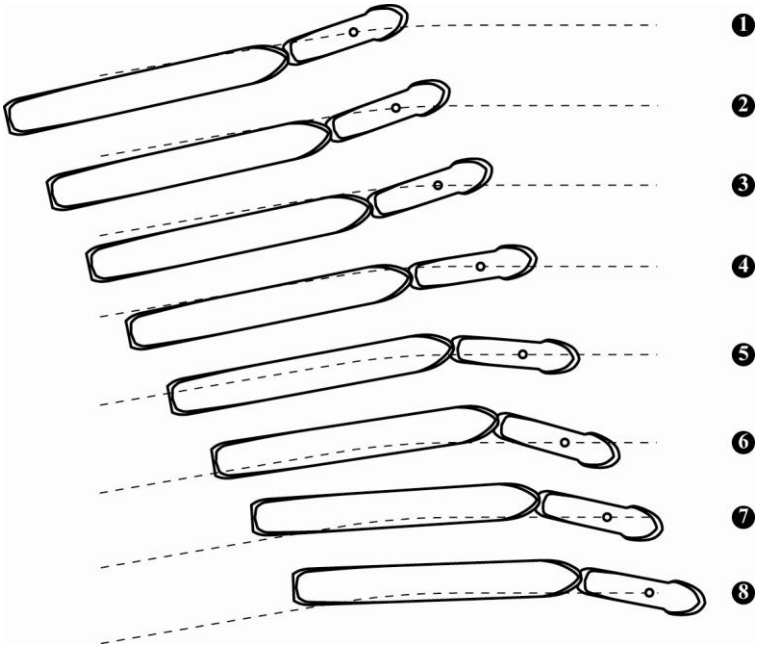

Figure 8. Drawing sequence of the vessel heading and alignment during a change of ice drift direction. The ice drift direction is indicated by a dotted line and the time step between each drawing is 122 seconds.

6. Discussion

The discussion will be divided into three parts; ridge interaction in test runs 3100 and 4100, large yaw motions during test run 4100 and mean tandem mooring forces in the part of test run 3100 where both vessels were embedded in level ice.

Interaction with ridges

During both test runs, the total tandem mooring force increased significantly when the tanker started to penetrate the ridge. In test run 3100, the largest total tandem mooring force was 5.9 MN, which is just below the total capacity of the hawser winches. Consequently, there was no significant relative surge motion between the tanker and the OIB.

The situation was different in test run 4100. The maximal total tandem mooring force was then 6.5 MN and this is above the capacity of 6 MN. At this event, both weights were lifted off the tanker floor and the distance between the vessels increased, as can be seen in Figure 7. In full scale, the winches would have started to pay out. The largest relative distance between the vessels was 3.7 m. However, the tanker came back to the OIB before the OIB stopped at the end

of the basin. This means that in this case it would not have been necessary to start the disconnection procedure in a corresponding full scale situation.

The large tandem mooring forces were induced by large ridge forces on the tanker. They were larger in test run 4100 than in 3100 and this indicates that the forces exerted by the ridge were more severe in the former. When the OIB penetrated the ridges, it was exposed to large vertical ice forces because larger vertical forces are needed to fail the consolidated layer of a ridge in bending than to fail level ice. This resulted in pitch motions of the vessel. In test runs 3100 and 4100 the maximal pitch angle of the OIB was -1.4º and -1.9º, respectively. The volume of the ridge keel in test run 4100 was larger than it was in 3100, which may have caused larger vertical ice forces and hence larger pitch motions. The tanker pitched considerably less than the OIB and this was mainly because the ridge already had failed, but also because it has a larger restoring capacity due to larger water plane area.

The pitch motion of the OIB in ridges reduced the effect of the reamers. In fact, the effective beam of the OIB was estimated to be 28.5 and 28 m in the ridges in test runs 3100 and 4100, respectively, compared to 30 m in level ice. This caused a smaller channel for the tanker. The contact area between intact ice and the tanker hull increased and thus larger forces were induced in the tandem mooring system.

Spencer et al. (1997) studied model tests of a tanker moored behind a terminal and the effect of the terminal size on the mooring forces. They presented a relationship between peak mooring force reduction and the ratio between terminal diameter and the beam of the tanker. However, it is difficult to use the results by Spencer et al. (1997) to compare the difference in mooring forces between 3100 and 4100, since the difference in effective beam of the OIB is less than 2 %. The difference in the tandem mooring forces could be caused by the fact the ridge in 4100 was bigger and by inhomogeneities in the ridge, in addition to the difference in width of the wake after the OIB.

Slow change of ice drift direction

During the first part of test run 4100 there was a slow change of ice drift direction of 20º. A drawing sequence of the heading of both the OIB and the tanker during this drift change is shown in Figure 8. A qualitative description of this event follows:

- The OIB met the new drift direction first. It experienced local ice forces caused by bending failure in the bow area and by crushing failure further aft. Crushing forces are in general larger than forces caused by bending failure and in combination with use of azimuth propellers, this made it possible for the OIB to turn, see steps 3 to 5 in Figure 8.
- The yaw motion of the OIB pulled the tanker by the tandem mooring system and the tanker slowly started to change heading. However, the inertia of the tanker and the fact that the tanker had a long vertical sided parallel body, forced the tanker to continue in its old path and thus pushed the stern of the OIB as can be seen in step 6 in Figure 8.
- At this time the tanker bow reached the port side of the wake after the OIB. In the starboard bow area of the tanker, the ice was mainly broken by the OIB, giving a low lateral pressure. In front of amidships on the starboard side of the tanker, intact ice was met and combined crushing and buckling failure against the tanker hull resulted in large ice forces, see Figure 9. On the port side of the tanker, the ice was partly broken. The

milder ice conditions in the bow area and on the port side in combination with crushing on the starboard side of the hull, made the tanker vane efficiently, see steps 6 to 8 in Figure 8. At step 8, the tanker was almost aligned with the new drift direction.

- It should be noted that there was no propulsion on the tanker, and with for instance azimuth propellers, it might have turned more efficiently.

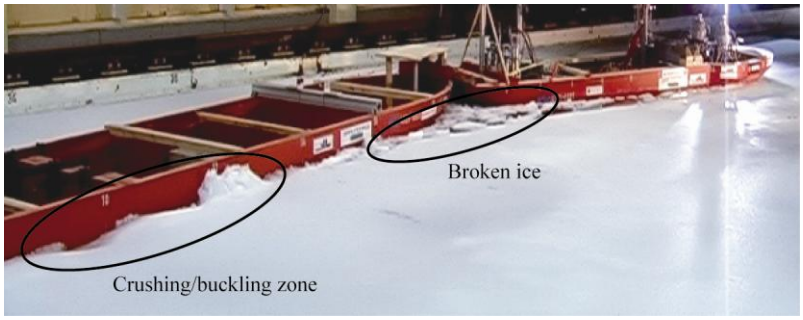

Figure 9. The picture shows the crushing/buckling zone on the hull of the tanker during the slow change of ice drift direction during test run 4100. An area with broken ice is indicated to illustrate the milder ice conditions in the bow of the tanker.

The plot in Figure 7 shows large mooring forces. However, the model of the tandem mooring system did not represent the full scale system well with respect to mooring forces when there was significant yaw between the vessels. It can be seen that during moderate yaw motions, one line was slack, while the other line was exposed to high tension. In full scale, the hawser winches would have been active and provided constant tension, evenly distributed in the mooring lines. At about 1300 s, there was a large relative yaw (up to 26º) between the vessels and the distribution of mooring forces between the mooring lines was even. Both weights were lifted off the tanker floor because of the large yaw angle, but the vessels stayed close to each other and the disconnection procedure would not have been initiated in full scale.

The mooring forces at this incident were larger than what one would expect from the weight system. This can be explained by the friction between the mooring lines and the guiders, both made of steel. Using the standard formula for the friction force between a rope and a cylindrical pole, see for instance Irgens (2005), the friction force F_{fric} between one mooring line and a guider can be expressed as

$$F_{fric} = F_{lc}(1 - e^{-\mu\psi}) \qquad \textbf{[1]}$$

In Equation [1], F_{lc} is the force measured in the load cell. A typical static friction coefficient between steel and steel is μ = 0.6. The measured force in the load cell was 3.9 MN and the relative yaw angle was approximately ψ = 25º (0.44 rad). An approximate value for the friction force is then F_{fric} = 0.9 MN. This example illustrates why the measured forces were higher than what they should be according to the weight system. The friction between the mooring lines and the guiders could have been reduced in model scale by using pulleys.

Mean tandem mooring forces

The mean total mooring force and standard deviation was estimated for the part of test run 3100 where the whole tanker is embedded in level ice and the drift direction was straight. This gave a mean total mooring force of 3.0 MN, which is half of the capacity. The standard deviation was 0.4 MN. The period over which the mean and standard deviation was estimated corresponds to approximately two times the length of the tanker.

7. Conclusions

Results from model tests of a tandem mooring system in level ice and ridges have been reported. The main findings were the following:

- The tandem mooring loads were higher in ridges than in level ice when the ice drift was straight.
- The capacity of the winches was overloaded once, due to large tandem mooring forces induced by interaction between the tanker and a ridge.
- The maximal relative distance between the vessels during this incident was 3.7 m. The tanker bow came back to the stern of the OIB while the tanker still was in the ridge, i.e. the disconnection procedure would not have been initiated in full scale.
- The OIB pitched significantly in the ridges and the effects of the reamers were reduced. This caused high tandem mooring forces during ridge interaction.
- The model of the full scale tandem mooring system did not work well with respect to mooring loads when there was relative yaw between the vessels.
- The tanker vaned efficiently when there was a slow change of ice drift direction, but over steered the OIB before they aligned.

Acknowledgements

The work described in this publication was supported by the European Community's Sixth Framework Program through the grant to the budget of the Integrated Infrastructure Initiative HYDRALAB III, Contract no. 022441(RII3). The authors would like to thank the Hamburg Ship Model Basin (HSVA), especially the ice tank crew, for the hospitality, technical and scientific support and the professional execution of the test program in the Research Infrastructure ARCTECLAB. We would also like to thank StatoilHydro for funding of the physical models. The video tracking was done with *Video Spot Tracker*, developed by the University of North Carolina at Chapel Hill and is available at URL: http://www.cs.unc.edu/Research/nano/cismm /download/spottracker/video_spot_tracker.html. The opportunity to use this software is highly appreciated.

References

Ashton, G. D., ed., 1986. *River and Lake Ice Engineering*. Water Resources Publications, Book Crafters Inc., Chelsea, Michigan.

Bonnemaire, B., 2006. Arctic Offshore Loading Downtime Due to Variability in Ice Drift Direction. *The Journal of Navigation*, vol. 59, pp. 9-26.

Bonnemaire, B., Lundamo, T., Evers, K. U., Løset, S. and Jensen, A., 2008a. Model Testing of the Arctic Tandem Offloading Terminal – Mooring Ice Ridge Loads. *Proceedings of the 19th International Symposium on Ice*. Vancouver, British Columbia, Canada.

Bonnemaire, B., Lundamo, T., Jensen, A. and Rupp, K. H., 2008b. Subsurface Ice Interactions under a Moored Offloading Icebreaker. *Proceedings of the 19th International Symposium on Ice.* Vancouver, British Columbia, Canada.

Comfort, G., Singh, S. and Spencer, D., 1999. *Evaluation of Ice Model Test Data for Moored Structures*. Report submitted to the National Research Council of Canada, PERD/CHC Report 26–195, 77 p.

Danielewicz, B. W., Jolles, W. H., Dunderdale, P., Keinonen, A., Browne, R. P., Spencer, D. and Jones, S. J, 1995. *Loading of Tankers from Arctic Platforms.* Prepared for Transport Development Centre, Policy and Coordination, Transport Canada, Report no. TP 12531E, Montreal Canada.

Evers, K. U. and Jochmann, P., 1993. An Advanced Technique to Improve the Mechanical Properties of Model Ice Developed at the HSVA Ice Tank. *Proceedings of the 12th International Conference on Port and Ocean Engineering under Arctic Conditions.* Hamburg, Germany, pp. 877-888.

Høyland, K. V., Jensen, A., Liferov, P., Heinonen, J., Evers, K. U., Løset, S. and Määttänen, M., 2001. Physical Modelling of First-Year Ridges – Part I: Production, Consolidation and Physical Properties. *Proceedings of the 16th International Conference on Port and Ocean Engineering under Arctic Conditions, Vol. 3*. Ottawa, Canada, pp. 1483-1492.

Irgens, F., 2005. *Statikk*. Tapir akademiske forlag, Trondheim, Norway.

Jensen, A., Bonnemaire, B., Rupp, K. H., Løset, S., Breivik, K. G., Evers, K. U., Ravndal, O., Aksnes, V., Lundamo, T. and Lønøy, C., 2008. First Ice Tank Model Testing of the Arctic Tandem Offloading Terminal. *Proceedings of the 19th International Symposium on Ice*. Vancouver, British Columbia, Canada.

Spencer, D., Jones, S. J. and Jolles, W., 1997. Effect of ice drift angle on a mooring hawser. *Proceedings of the International Conference on Offshore Mechanics and Arctic Engineering (OMAE)*, Yokohama, Japan, pp. 127–133.

19th IAHR International Symposium on Ice
"Using New Technology to Understand Water-Ice Interaction"
Vancouver, British Columbia, Canada, July 6 to 11, 2008

Iceberg towing: analysis of field experiments and numerical simulations

Aleksey Marchenko[1,2] and Christian Ulrich[3]
[1)] *The University Centre in Svalbard (UNIS), Spitsbergen, Norway*
[2)] *Norwegian University of Science and Technology (NTNU), Trondheim, Norway*
[3)]*Hamburg University of Technology, Germany*

aleksey.marchenko@unis.no
christian.ulrich@tu-harburg.de

Abstract
Experiments on icebergs towing in the Barents Sea in 2004 and 2005 are analyzed. Mathematical model of iceberg towing is developed to simulate the tension in the towing rope by the towing with one branch and two branches rope. Numerical simulations demonstrate that monotonic increasing of ship propulsion causes numerous hitches of rope tension following with few minutes interval between successive hitches. Peak tensions of the rope created by the hitches can exceed rope strength. Rotational mode of iceberg motion is constructed and investigated. It is shown that iceberg rotation during the towing increases rope tension significantly in comparison with the towing without iceberg rotation.

1. Introduction

The towing of icebergs by ships is used to prevent iceberg impacts on offshore structures and communication lines. The experience of icebergs towing was accumulated during several tens of years in Canada shelf, where numerous icebergs produced by Greenland glaciers drift to the South by East Greenland current. Glaciers of Svalbard, Franz Josef Land and Novaya Zemlya are the sources of icebergs in the Barents Sea. Barents Sea icebergs are much smaller than Greenland icebergs. Nevertheless the mass of Barents Sea icebergs can be sufficiently big (up to several millions of tons) to create damage of ships and offshore platforms (Loset and Carsten, 1996). In 2003 more than hundred icebergs were observed around Stockman Gas Deposit area. Horizontal sizes of icebergs from Novaya Zemlya and Franz Josef Land are varied from several tens to several hundreds meters (Zubakin et a., 2006).

The experimental towings of the iceberg were carried out in the Barents Sea near the northern Novaya Zemlya in the April of 2004 and 2005 in research cruises of RV ”Mikhail Somov”. In both experiments the towing was occurred by poly-steel rope composed from seven patterns of 110 m length. The rope was outlined around the iceberg and then fastened by the double-bit bollard on the ship stern.

Mean diameter of the iceberg in 2004 was estimated as 32 m, and its mean draft was about 11 m (Fig. 1a). The iceberg mass estimated as 8000 tons. The iceberg was drifting on the open water partially covered by very thin ice - nilas. The towing rope was outlined around the iceberg by small boat. The towing was occurred during 40 minutes with mean speed 0.8 m/s (Marchenko and Gudoshnikov, 2005). The photograph of the towing is shown in Figure 1a. During the towing parts of the rope connected to the ship with length about 200 m hanged in the air, while the other parts were floating on sea or ice surface. Iceberg towing was occurred in calm conditions without surface waves and strong wind.

Mean diameter of the iceberg in 2005 was about 80 m, and its draft exceeded 40 m (Fig. 1b). The iceberg mass was estimated as 200000 tons. The iceberg was partially frozen in the edge of an ice floe, which thickness was about 40 cm near the iceberg. Other floes were floating around the iceberg. Ice free water from one side of the iceberg gave possibility to moor the ship to the iceberg for one day period to study its properties. On the second day the rope was removed from the ship on the iceberg surface and then outlined around the iceberg manually.

The towing was occurred on the second day in conditions of sufficiently strong wind up to 20 m/s without surface waves. During the towing almost all rope between the ship and the iceberg hanged in the air, and only its small parts were floating on water surface near the iceberg. The rope length between the ship stern and the iceberg is estimated as 450 m. After approximately 30 minutes of the towing the ship was decelerated due to the approach to a floe in front of the ship. In this time iceberg rotation was observed visually from the ship due to the depression of the tension in one branch of the towing rope (Fig. 2a). Another branch of the rope had sufficiently strong tension keeping significant part of the rope above water surface. After 10-15 minutes the ship accelerated and the rope was broken (Fig. 2b). The situation of the rope break up is explained in Fig. 3.

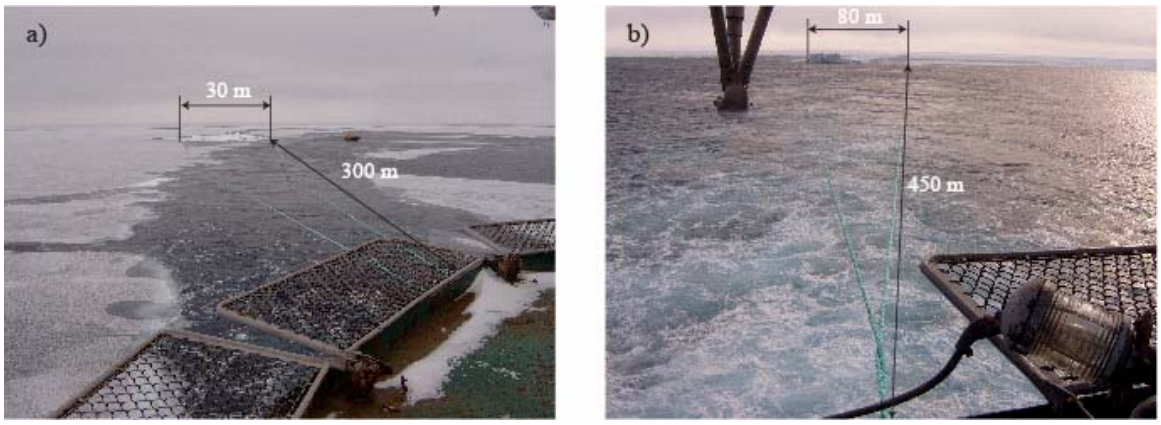

Figure 1. Iceberg towing in 2004 (a) and 2005 (b).

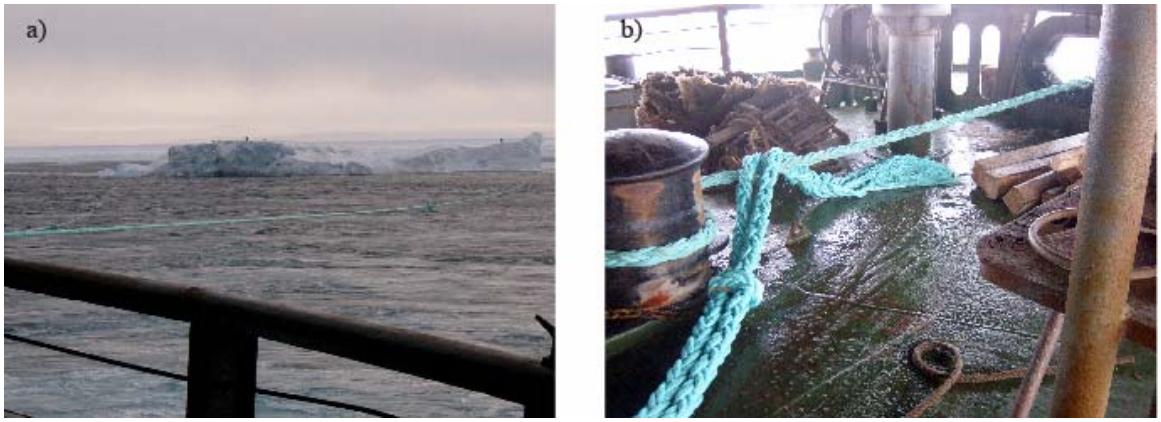

Figure 2. The depression of the tension in left branch of the rope created by ship deceleration and iceberg rotation (a). Broken towing rope (b).

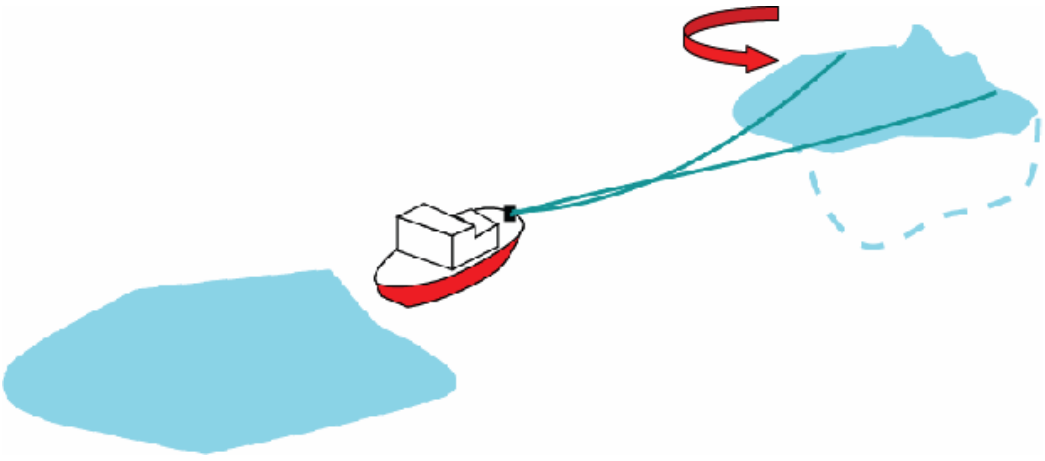

Figure 3. Iceberg rotation caused by ship deceleration.

2. Formulas for the calculation of rope tension

It is assumed that gravity, tension and inertial forces determine the motion of the rope. The force balance at the rope is expressed as follows

$$\frac{W}{g}\mathbf{a} = \frac{d}{ds}\boldsymbol{\sigma} + \mathbf{W} \qquad [1]$$

where $\mathbf{W} = (0,-W)$ is the weight of the rope of unit length, $\boldsymbol{\sigma}$ is the rope tension, $\mathbf{a}$ is the rope acceleration, and ds is infinitesimal length of the rope (Fig. 4). The rope tension is written as $\boldsymbol{\sigma} = \sigma\boldsymbol{\tau}$, where $\boldsymbol{\tau}$ is unit tangential vector to the rope. Using Frenet formulas equation (1) is written as follows

$$\frac{W}{g}\mathbf{a} = \frac{d\sigma}{ds}\boldsymbol{\tau} - \sigma k\mathbf{n} + \mathbf{W}, \qquad [2]$$

where $\mathbf{n}$ is unit tangential vector to the rope and $k = \eta_{xx}\left(1+\eta_x^2\right)^{-3/2}$ is the rope curvature. It is assumed that the rope shape is described by equation $z = \eta(x,t)$.

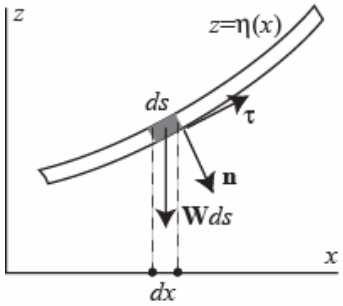

Figure 4. Scheme of forces applied to extended rope.

In steady case the integration of the projection of equation (2) on $\boldsymbol{\tau}$-direction leads to the formula $\sigma = \sigma_0 + W\eta$. The projection of (2) on $\mathbf{n}$-direction is reduced to the equation

$$\sigma\frac{d^2\eta}{dx^2} = W\sqrt{1+\left(\frac{d\eta}{dx}\right)^2} \qquad [3]$$

Let us perform the solution of equation (3) as $\eta = \eta_0 + \delta\eta$, where η_0 is the solution of equation

$$\sigma_0\frac{d^2\eta}{dx^2} = W \qquad [4]$$

Assuming that the rope is fixed at $z = H_s$ by $x = 0$ and at $z = 0$ by $x = A$ we find

$$\eta_0 = \frac{W}{\sigma_0}\left(\frac{x^2}{2} - Ax\right) + H_s \qquad [5]$$

If the rope is floating by $x > A$, then the tension σ_0 is found from the condition $d\eta / dx = 0$ by $x = A$ as (Marchenko and Gudoshnikov, 2005)

$$\sigma_0 = \frac{WA^2}{2H_s} \qquad [6]$$

From (6) follows that $WH_s << \sigma_0$ and consequently $W\eta << \sigma_0$, when $A >> \sqrt{2}H_s$. This inequality is typically occurred for the towing of icebergs, when the distance A is about the distance between the ship and the body (200-500 m) and H_s is free board of the ship (5-10 m). It means also that $\eta_x << 1$. Therefore further $\eta = \eta_0$ is assumed.

The length of the rope above the water surface is calculated with formula when

$$l_{0A} = \int_0^A \sqrt{1 + \eta_x^2}\, dx \qquad [7]$$

Substituting the expression from formula (6) into (7) we find

$$l_{0A} = \frac{\sigma_0}{2W}\left(\frac{WA}{\sigma_0}\sqrt{1 + \left(\frac{WA}{\sigma_0}\right)^2} + \operatorname{arcsinh}\left(\frac{WA}{\sigma_0}\right)\right) \qquad [8]$$

With using Taylor series this expression is simplified with accuracy to high order terms as follows

$$l_{0A} = A\left(1 + \frac{2}{3}\frac{H_s^2}{A^2}\right) \qquad [9]$$

Expressing the rope length as $l_r = l_{0A} + X - A$, where X is the coordinate of rope fastening at the iceberg (Fig. 5), we find

$$A = \frac{2}{3}\frac{H_s^2}{l_r - X} \qquad [10]$$

After substitution of formula (10) into formula (6) the rope tensions is expressed as

$$\sigma_0(l_r, X) = \frac{2}{9}\frac{WH_s^3}{(l_r - X)^2} \qquad [11]$$

In steady solution the rope tension is in a balance to the rope weight. The influence of rope inertia becomes important when $W\partial^2\eta/\partial t^2 \approx g\sigma_0\partial^2\eta/\partial x^2$. Using formula (6) one finds the ratio between representative time (T) and length scale (L) of nonstationary perturbations as $T = LA^{-1}\sqrt{2H_s/g}$. Assuming $L = A$ and $H_s = 7$ m we estimate $T = 1.2$ s.

3. The estimation of rope tension

Visual analysis of the photographs of the rope during the towing in 2005 has shown that both branches of the towing rope with length about 450 m hanged in the air. Substituting in formula (6) numerical values

$$W = 25\ \mathrm{Nm}^{-1},\ A = 450\ \mathrm{m},\ H_s \approx 7\ \mathrm{m}. \qquad [12]$$

we estimate the tension in each branch of the rope as $\sigma \approx 36.9$ T. Therefore total force applied to the iceberg by the ship was about $2\sigma \approx 73.8$ T. This load is closed to critical tension of the rope $\sigma_{cr} \approx 80$ T. Thus the rope would be broken if this load would be applied to one branch of the rope.

Iceberg rotation due to ship acceleration created the depression of the left branch of the rope (Fig. 2a). When ship was accelerated most of the load became applied to the right branch of the rope. It can be the reason for the break up of towing rope in 2005.

4. Equations of iceberg motion under the towing

Let us consider model iceberg with the shape of vertical cylinder with radius R and draft H (Fig. 5). The equation of momentum balance describing iceberg motion under the towing is written as follows

$$M_i\frac{d\mathbf{v}_i}{dt} = \mathbf{F}_{wi} + \mathbf{T},\ \ \frac{d\mathbf{x}_i}{dt} = \mathbf{v}_i \qquad [13]$$

where M_i is iceberg mass, $\mathbf{v}_i = (v_{i,x}, v_{i,y})$ is the vector of iceberg velocity in the horizontal plane (x, y), $\mathbf{F}_{wi}$ is the force applied to the iceberg by the water, $\mathbf{T}$ is the force applied to the iceberg by the rope, and vector $\mathbf{x}_i = (x_i, y_i)$ shows the location of iceberg centre mass at the plane (x, y).

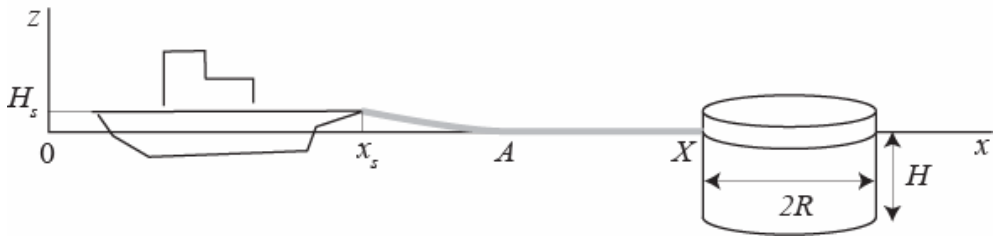

Figure 5. The scheme of cylindrical iceberg towing.

The force $\mathbf{F}_{wi}$ is equal to a sum of the force due to added mass effect and form drag

$$\mathbf{F}_{wi} = M_{ad}\frac{d(\mathbf{v}_w - \mathbf{v}_i)}{dt} + \rho_w C_d S_i |\mathbf{v}_w - \mathbf{v}_i|(\mathbf{v}_w - \mathbf{v}_i) \qquad [14]$$

where $M_{ad} = \pi\rho_w R^2 H$ is added mass of the iceberg, $\mathbf{v}_w$ is mean horizontal water velocity in the vicinity of the iceberg, ρ_w is water density, C_d is form drag coefficient, $S_i = 2RH$ is the effective area of vertical cross-section of submerged part of the iceberg.

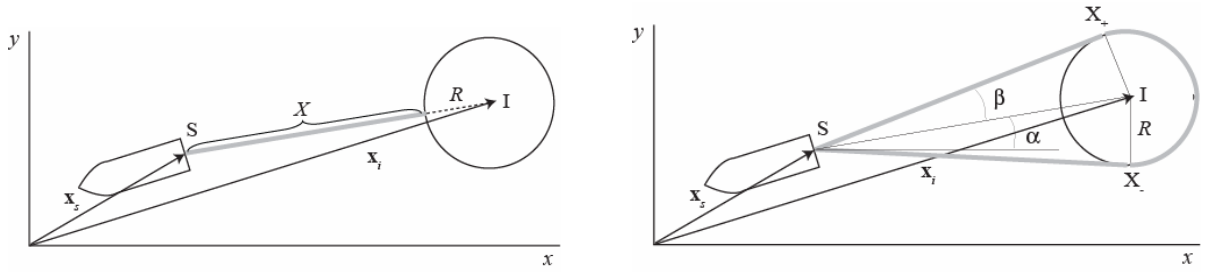

a) b)

Figure 6. Iceberg towing with one rope branch (a) and with two branch rope (b).

The vector of rope tension by iceberg towing with one rope branch (Fig. 6a) is calculated by formulas

$$\mathbf{T} = \mathbf{e}_{IS}\sigma_0(l_r, X), \quad \mathbf{e}_{IS} = \frac{\mathbf{x}_s - \mathbf{x}_i}{X_{IS}}, \quad X_{IS} = |\mathbf{x}_s - \mathbf{x}_i| \qquad [15]$$

The value of σ_0 is calculated with formula (11), where $X = X_{IS} - R$. Vector $\mathbf{x}_s = (x_s, y_s)$ is associated with the coordinates of fastening point of the rope at ship stern.

The vector of rope tension by iceberg towing with two branches of the rope (Fig. 5b) is calculated by formulas

$$\mathbf{T} = \mathbf{T}_+ + \mathbf{T}_- \qquad [16]$$

$$\mathbf{T}_\pm = T_\pm(\cos\alpha_\pm, \sin\alpha_\pm),\ T_\pm = \sigma_0(l_\pm, X),\ X = \sqrt{X_{IS}^2 - R^2},\ X_{IS} = |\mathbf{x}_s - \mathbf{x}_i|$$

$$\alpha_\pm = \alpha \pm \beta,\ \alpha = \arcsin\frac{y_s - y_i}{X_{IS}},\ \beta = \arcsin\frac{R}{X_{IS}}$$

Rope length l_+ between points S and X_+ and rope length l_- between points S and X_- can be different.

The conservation of angular momentum of the iceberg is written as follows

$$I_i \frac{d^2\varphi}{dt^2} = R(T_- - T_+) \qquad [17]$$

where I_i represents the iceberg's inertia and φ is the angle of iceberg rotation around its vertical axes.

Five equations (13) and (17) together with formulas (14), (15) and (16) form closed system of ordinary differential equations for the finding of unknown functions $x_i(t)$, $y_i(t)$, $v_{i,x}(t)$, $v_{i,y}(t)$ and $\varphi(t)$, when functions $x_s(t)$ and $y_s(t)$ are given. In the other case equations (12) and (16) have to be completed by equations describing the ship motion.

4. Simulations of iceberg towing with one branch rope

Let us consider iceberg towing in calm water ($\mathbf{v}_w = 0$) in the direction of x-axis with one branch rope when the ship motion is described by equations

$$M_s \frac{dv_s}{dt} = F_{ws} - T + P,\ \frac{dx_s}{dt} = v_s \qquad [18]$$

where $M_s = 15000\,\mathrm{t}$ is the ship mass, v_s and x_s are the velocity and the location of the ship, P is the power of ship propulsion and T is rope tension calculated with formula (15). The force applied to the ship by the water is defined as follows

$$F_{ws} = -\rho_w C_s S_s |v_s| v_s \qquad [19]$$

where drag coefficient $C_s = 0.003$ and the area of wetted surface of the ship hull is $S_s = 1000\,\mathrm{m}^3$. The ship propulsion is defined by formula

$$P = -\rho_w C_s V_s^2 \tanh^2(5t/t_s) \qquad [20]$$

where t_s is the time of ship acceleration to the speed V_s in the case when rope tension is absent ($T = 0$).

Results of numerical simulations computed with $M_i = 200000\,\text{t}$, $M_{ad} = M_i/2$, $H_s = 7\,\text{m}$, $W = 45\,\text{N/m}$, $l_r = 450\,\text{m}$, $S_i = 3200\,\text{m}^2$ and $C_i = 0.6$ are shown in Fig. 7.

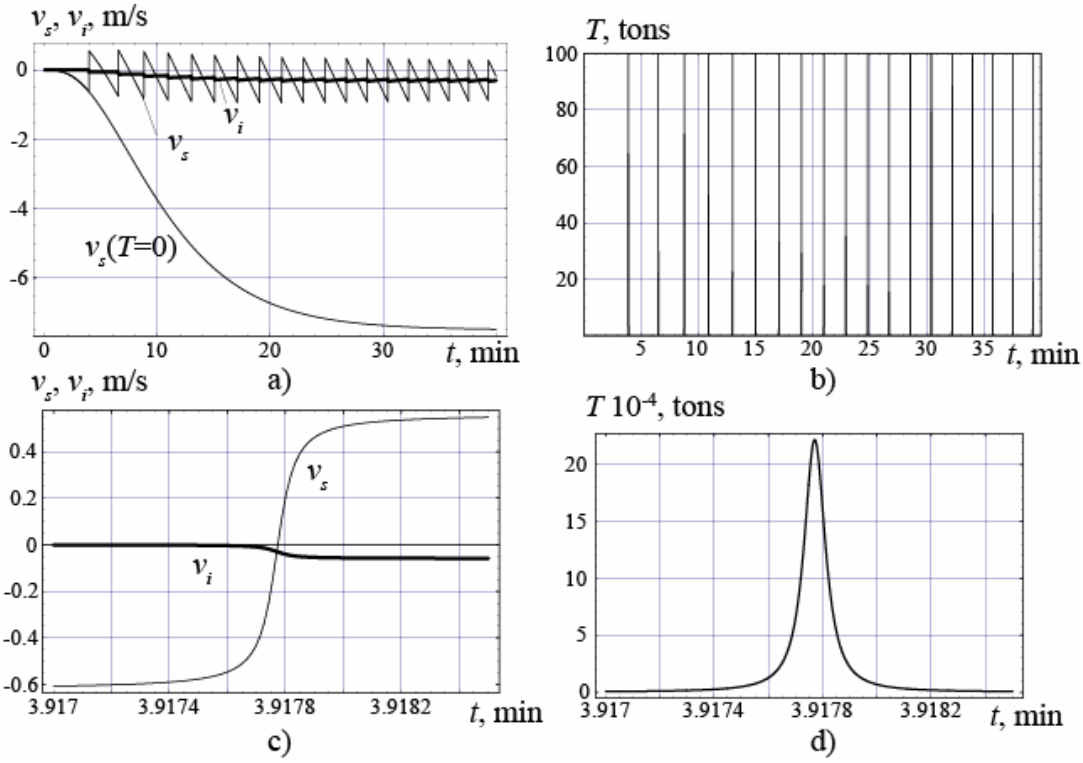

Figure 7. Velocities of ship and iceberg (a,c). Vertical lines show the times of peak tension of the rope (b). Rope tension in the vicinity of local maxima (d).

The line marked by $v_s(T=0)$ in Fig. 7a shows ship velocity versus the time if the ship would be accelerated by the propulsion (20) with $T = 0$. Ship velocity increases to 7.5 m/s during 30 min. Lines v_s and v_i show the speeds of the ship and the iceberg during the towing. Since the iceberg mass is much bigger than the ship mass the iceberg motion looks more monotonic in comparison with ship motion. The ship speed is changed from negative to positive values due to the influence of the rope tension. Each change of the sign of the ship velocity is created by the hitch of the rope. Vertical lines in Fig. 7b show the times of rope hitches. The time interval between two successive hitches is about few minutes. Peak tensions of the rope decrease with the time.

Ship speed and iceberg speed in the vicinity of the first hitch of the rope is shown in Fig. 7c versus the time. In the moment of peak tension the iceberg and the ship move in opposite directions. Fig. 7d shows rope tension versus the time in the vicinity of the first hitch of the rope. One can see that peak value of the tension is very high and it is realized in very short time about 0.001 s, when the rope inertia can be of importance.

5. Rotational mode of iceberg motion

Rotational mode of iceberg motion is described by equations (17) and (16). Equations (13) are satisfied with assumptions $d\mathbf{x}_s / dt = 0$ and $d\mathbf{x}_i / dt = 0$. In this case the points X_+ and X_- are fixed in the space and the sum of rope length $l_{r,-}$ between points S and X_- and rope length $l_{r,+}$ between points S and X_+ is a constant

$$l_{r,+} + l_{r,-} = 2L \qquad [21]$$

Temporal variations of $l_{r,-}$ and $l_{r,+}$ are related to angular velocity of the iceberg as follows

$$\frac{dl_{r,+}}{dt} = -R\frac{d\varphi}{dt}, \quad \frac{dl_{r,-}}{dt} = R\frac{d\varphi}{dt} \qquad [22]$$

Absolute values of the rope tensions T_+ and T_- determined by formulas (11) and (16) are expressed as follows

$$T_+ = \frac{C}{(l_{r,+} - c)^2}, \quad T_- = \frac{C}{(l_{r,-} - c)^2} \qquad [23]$$

where $C = 2WH_s^3 / 9$ and $c = |SX_-| = |SX_+|$.

Substituting formulas (21)-(23) in equation (17) we find

$$I_i \frac{d^2 l}{dt^2} = -R^2 C\left(\frac{1}{(2L - l - c)^2} - \frac{1}{(l - c)^2}\right), \; l = l_{r,+} \qquad [24]$$

Equations (24) is integrated once by time after its multiplication on dl / dt. Let us introduce new dimensionless variables $n \in (-1,1)$ and t' by formulas

$$n = \frac{l - L}{l_0 - L}, \; t' = t2R\sqrt{\frac{C\beta}{I_i(1-\alpha^2)}}, \quad \beta = \frac{L - c}{(L - l_0)^4}, \quad \alpha^2 = \left(\frac{L - c}{L - l_0}\right)^2 \qquad [25]$$

where $l = l_0$ when $dl / dt = 0$. Since $l_0 > c$, constant $\alpha > 1$. The value of constant α is increased with the increasing of the initial length of the rope l_0 when the distance c is fixed. Integrating equation (24) by the time and substituting dimensionless variables we find

$$\frac{dn}{dt'} = \sqrt{\frac{1 - n^2}{\alpha^2 - n^2}}, \qquad T = 4\int_{-1}^{0}\sqrt{\frac{\alpha^2 - n^2}{1 - n^2}}dn \qquad [26]$$

where T is dimensionless period of the solution. When $\alpha >> 1$ the solution of (26) has period $2\pi\alpha$ and it is approximated by the formula $n = \sin(t/\alpha)$. Therefore the period of angular oscillations is increased with the increasing of constant α or the initial rope length l_0. Phase diagram of the solution and period T versus constant α are shown in Fig. 8. One can see that maximal angular velocity of iceberg rotation (it is proportional to dn/dt') is increased with the decreasing of constant α or the initial rope length l_0.

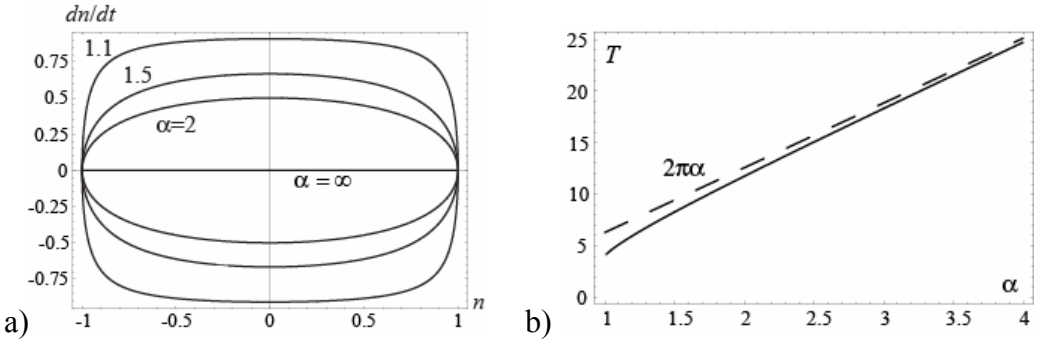

Figure 8. Phase diagram of periodical solutions of equation (26) constructed with different values of α (a) and dimensionless period T versus constant α (b).

6. The influence of iceberg rotation on rope tension

In this simulation the ship motion is given as fixed input value. A towing in calm water ($\mathbf{v}_w = 0$) with two branch rope is considered. The calculations have been carried out with $M_i = 200000\,\text{t}$, $M_{ad} = M_i/2$ (no added mass for the rotation), $H_s = 7\,\text{m}$, $W = 45\,\text{N/m}$, $S_i = 3200\,\text{m}^2$ and $C_i = 0.6$.

The initial conditions for the simulations were related to the equilibrium towing in the direction of x-axis with the velocities $v_i = v_s = 0.1\,\text{m/s}$. For these velocities the rope tension was calculated as 10 000 N for each branch. When the ship accelerates from the initial 0.1 m/s up to 0.2 m/s in 320 s, we can observe four hitches in the rope with the peak tension of $3.5 \cdot 10^5 N$ (Fig. 9a). To simulate the influence of iceberg rotation to the peak tensions, we induce a tension of $1.26 \cdot 10^5 N$ to one rope branch right at the beginning of the ship's acceleration. This scenario represents a rotated iceberg which experiences an increasing of tensions in both rope branches due to ship's acceleration. The maximum peak tension is $9.6 \cdot 10^5 N$ is shown in Fig. 9b. This maximum value occurs at the branch of the rope with the lower initial tension. Comparing Fig. 9a and Fig. 9b we conclude that iceberg rotation increases peak tension of the rope approximately in two times.

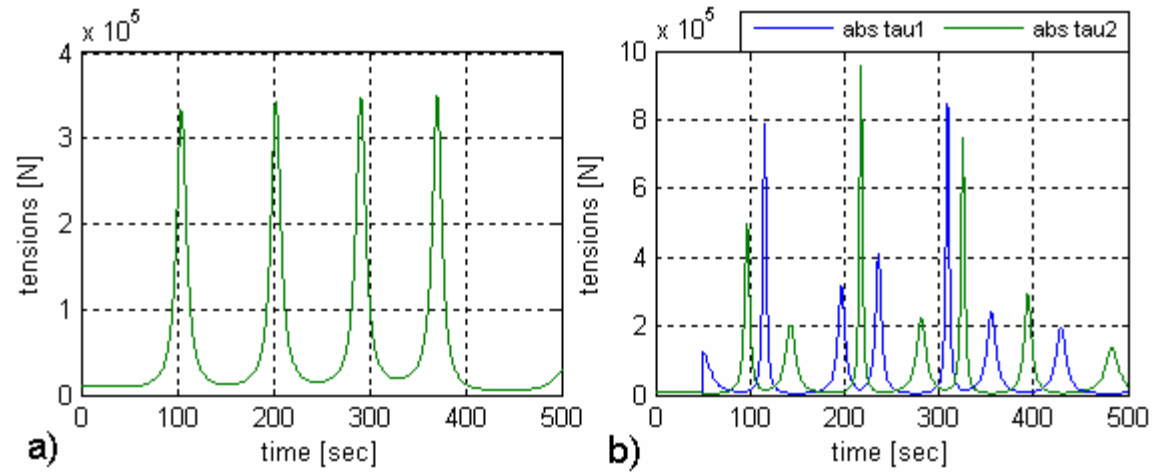

Figure 9. Peak tensions of both rope branches; a) shows the tension due to ship's acceleration without iceberg rotation; b) displays the scenario of ship's acceleration when the iceberg has some initial rotation.

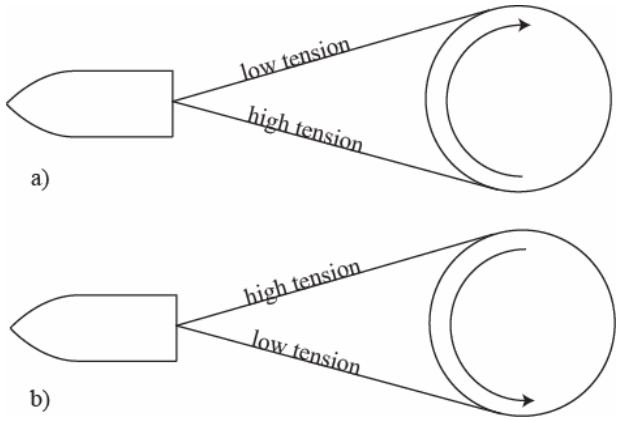

Figure 10. Scheme of iceberg rotation in initial time of the towing (a) and after the peak tension in the branch with low initial tension (b).

The scheme of iceberg rotation during the towing is shown in Fig. 10. In initial time the tension in one rope branch is higher the in other rope branch (a). It creates clockwise iceberg rotation until the tension in the second rope branch reaches its peak value. After that the iceberg starts to rotate in counter clockwise direction (b).

6. Conclusions

Iceberg towing by a ship and towing rope is accompanied by the hitches of the rope tension following successively with few minutes interval. These hitches can lead to the break up of the towing rope. Small acceleration in initial period of the towing will reduce peak tensions of the rope. Peak values of rope tension computed for the case of iceberg towing with two branches rope are smaller those values computed for the towing with one branch rope.

There is rotational mode of iceberg motion under the towing with two branches rope. This mode can be excited due to the change of towing direction or due to unequal tension in rope branches in initial time. Iceberg rotation can increase peak values of rope tensions significantly. This effect created the break up of the rope in iceberg towing experiment in the Barents Sea in 2005.

References

Loset, S, and T. Carstens (1996): Sea ice and icebergs in the Western Barents sea in 1987. Cold Reg. Sci. Techn., Vol. 24, N4, pp. 323-340.

Marchenko, A. and Yu.. Gudoshnikov (2005): The influence of surface waves on iceberg towing. Proc. of 18th Int. Conference on Port and Ocean Engineering under Arctic Conditions (POAC'05), Vol. 2, Clarkson University, Potsdam, NY, pp.543-553.

Zubakin, G.K., Shelomentsev, A.G., Onshuus, D.K., Eide, L.I. and I.V.Buzin (2005): Distribution of icebergs in the Barents Sea based on archived data and observations of 2003. of 18th Int. Conference on Port and Ocean Engineering under Arctic Conditions (POAC'05), Vol. 2, Clarkson University, Potsdam, NY, pp.575-583.

19th IAHR International Symposium on Ice
"Using New Technology to Understand Water-Ice Interaction"
Vancouver, British Columbia, Canada, July 6 to 11, 2008

A Review of Recent Iceberg Scour Survey Data from the Labrador Shelf

Tony King
C-CORE
Morrissey Road, St. John's, NL, Canada, A1B 3X5
tony.king@c-core.ca

Gary Sonnichsen
Geological Survey of Canada (Atlantic)
Bedford Institute of Oceanography, Dartmouth, NS, Canada, B2Y 4A2
gsonic@nrcan.gc.ca

Offshore Labrador holds considerable promise for natural gas development, with discovered reserves of 4.2 TCF natural gas and 123 million barrels natural gas liquids established during the drilling of 28 wells (with 5 significant discoveries) during the late 1970s and early 1980s. Increasing demand for natural gas has renewed interest in exploration and development on the Labrador Shelf and Slope. Iceberg scour is a significant consideration for pipelines and subsea structures in this region. Recently, a number of multibeam seabed surveys have been conducted to establish baseline surveys for future repetitive mapping and to determine scour geometric parameters (i.e. length, width, depth, orientation) for engineering design. In this paper, multibeam surveys conducted in 2003 and 2006, covering almost 1000 km^2 of seabed, are examined and distributions of key geometric parameters of scour features are presented according to location and water depth. Issues related to the discrimination of relict and recent iceberg scour features are discussed, as well as a comparison with scour parameters established during previous (pre-1990) surveys and how the perception of iceberg scour risk has changed with the availability of more recent data.

1. Introduction

Offshore Labrador holds considerable promise for natural gas development, with total discovered reserves of 4.2 TCF of natural gas and 123 million barrels of natural gas liquids established during the drilling of 28 wells (with 5 significant discoveries) during the late 1970s and early 1980s. Iceberg scours, formed when iceberg keels contact and deform seabed sediments, are a significant design consideration for subsea facilities on the Labrador Shelf. An early assessment of iceberg risk on the Labrador Shelf (Petro-Canada, 1983) determined that a pipeline with a cover depth of 2.5 m, running from central Makkovik Bank to a landfall at Cape Harrison, would be directly impacted by a scouring iceberg keel approximately 4 times a year. Later work (King, 2002) identified conservative elements in the earlier analysis and determined the contact rate would be on the order of one every 25 years, with the potential for substantial reductions in risk with additional data collection and analysis to define scour geometry and rates. Since then the Geological Survey of Canada (Atlantic) (GSCA) and C-CORE, separately and in collaboration, have performed a number of investigations to define iceberg scour risk, as well as other environmental considerations relevant to the development of Labrador gas. Increasing demand for natural gas has renewed interest in Labrador Shelf and Slope exploration, and on May 17th, 2007, the Canada-Newfoundland and Labrador Offshore Petroleum Board offered four parcels on, or near, the Makkovik Bank with a deadline of August 1, 2008 to submit bids.

Figure 1 shows multibeam surveys conducted on Makkovik Bank in 2003 and 2006 for the analysis of iceberg scour parameters. The 2003 surveys were conducted using a Reson 8101 multibeam transducer and supporting equipment mounted on the MV Marine Eagle (Fugro-Jacques Geosurveys Inc., 2005). The surveys covered significant gas discoveries (Bjarni and North Bjarni) and sidescan sonar mosaics produced during the Environmental Studies Research Funds (ESRF) Dynamics of Iceberg Grounding and Scouring (DIGS) program (Hodgson et al., 1988). The sites were selected to provide a baseline dataset for future repetitive mapping exercises, to aid in the interpretation of the seafloor topography and composition, and to assess the severity, distribution and frequency of seabed iceberg scours. The 2006 survey was conducted as part of GSC Expedition 2006038. CCGS Matthew deployed a launch during daylight hours to collect multibeam bathymetric data in depths less than approximately 100 m using its Simrad EM3000 system. Concurrently, the Matthew worked further offshore and collected EM710 multibeam data and Knudsen 3.5 kHz sub-bottom data on a 24 hour basis, as weather allowed. Data were cleaned and processed onboard and provided to the GSC for geological analysis and interpretation. Other multibeam surveys in the area, such as those performed in deeper water to examine slope stability issues, are not included.

Additional funds were raised from public and industry sources after the 2003 survey program to perform a detailed analysis of the scour features. This included the development of a suite of software tools by FJG to map scour features, automatically extract data and perform quality control on the resulting dataset (Davis et al., 2005). The software and analysis techniques developed represent a significant advancement in the analysis of iceberg scour and resulted in the production of a large high-quality ice scour dataset for the Makkovik Bank region.

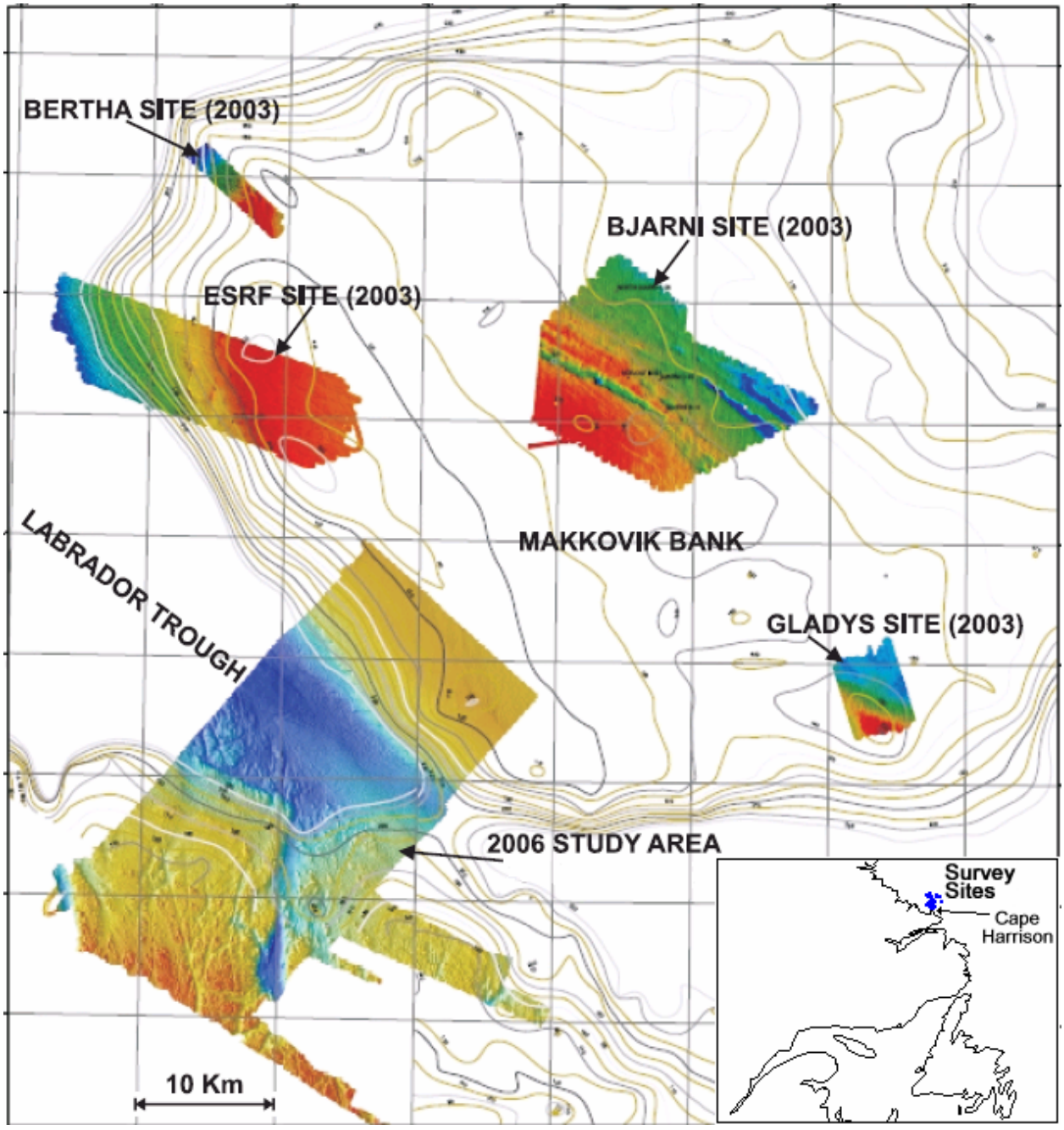

Figure 1. Multibeam survey sites (from Fugro Jacques GeoSurveys, 2007 with modifications).

2. Data Summary

Table 1 summarizes the scour features mapped from the 2003 and 2006 survey sites. Each scour feature was characterized as a scour (linear furrows), pit (circular or oval features), or a scour with an associated pit (typically a terminal pit). The proportion of scours and pits in the overall population is of interest for use in risk analyses, since the difference in formation rates, plan dimensions and depth distributions for the two types of features influences the probability of interaction with subsea structures. Over 11,000 iceberg scour features have been mapped, resulting in over 150,000 measurements of parameters such as width, depth, orientation and sidewall slopes at profiles located at regular intervals along each scour feature, as well as

parameters such as length and rise-up for each scour feature. The distance between successive profiles used for the analysis of 2003 data was 10 m, whereas the profile interval used for the 2006 data was 50 m. Within each survey site, variations in scour parameters were noted according to water depth, seabed slope and sediment type, but significant variations in scour parameters were noted between the Makkovik Bank and inner shelf in the 2006 Study Area (see Figure 2), with the inner shelf scour regime notably more severe. Thus, in any further presentation of parameters on a site-by-site basis, a distinction will be made between the inner shelf and Makkovik Bank portions of the 2006 Study Area.

Table 1. Data summary for survey areas.

Site	Scours	Pits	Scours with Pits	Total Profiles
Bertha	255	131	36	11,236
Gladys	825	269	214	31,018
Bjarni	1,181	943	285	42,375
ESRF	1,925	233	259	37,081
2006 Study Area	3,089	1,574	262	28,339

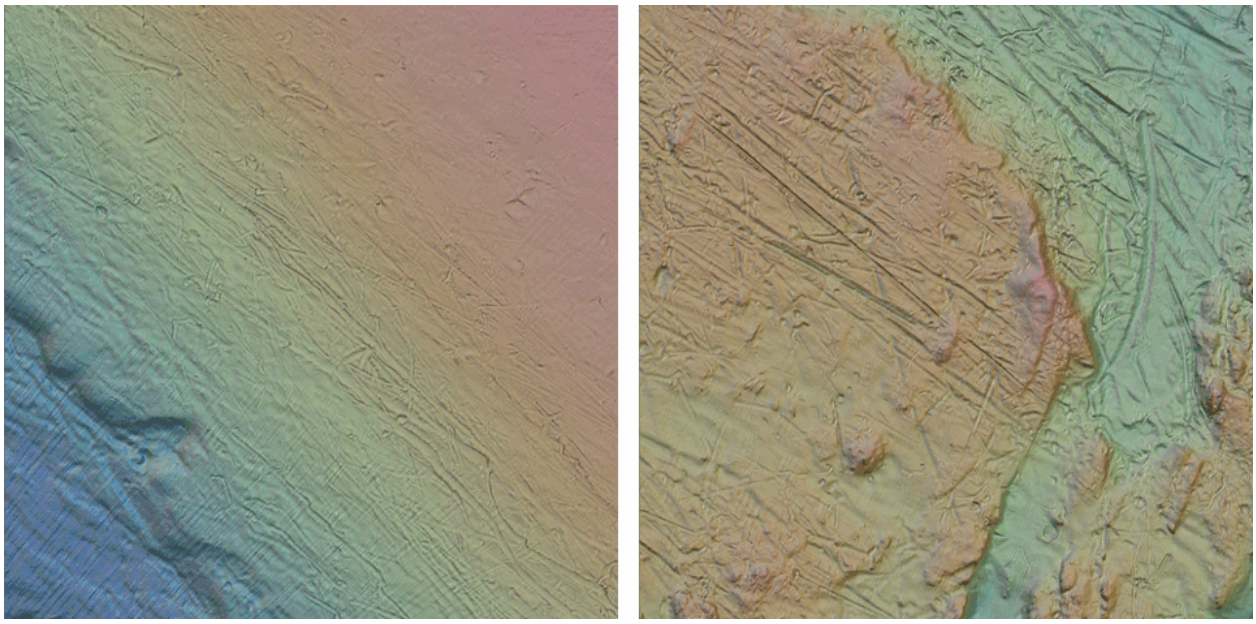

Figure 2. Comparison of scour severity on southwestern flank of Makkovik Bank (left) and inner shelf (right) in 2006 Study Area (samples shown 5 km × 5 km).

3. Scour Parameters

Other than scour rate, the primary parameters of interest for assessing risk to pipelines and subsea structures are scour depth, width, length, orientation and rise-up. It should be noted that parameters presented here do not account for infill effects or the presence of relict scours (see Section 6).

The scour depth distribution is the parameter that most significantly influences pipeline burial requirements. Table 2 gives a breakdown of scour depth distributions according to survey site and soil type. It should be noted that scour data from the 2006 survey have not been classified according to sediment type and thus are not reflected in the sediment type statistics. A

comparison of scour depths based on sediment type is complicated by the fact that different sediment types are more common at different water depths, and water depth in itself has a significant effect on scour depth. Figure 3 shows mean scour depth as a function of water depth for the various survey sites. In the 80 – 220 m water depth range all sites except the 2006 Survey Inner Shelf follow the same positive correlation between water depth and mean scour depth. The contrast between the 2006 Survey Inner Shelf and the other sites is remarkable, with some of the deepest scours occurring in the sediment between bedrock outcroppings, but the reason for the discrepancy has yet to be established. The decrease of mean scour depths in water depths in excess of 220 m may be due to infill of relict scours.

Distributions of scour incision width, length and rise-up are given in Table 3. While the mean widths do not exhibit the same variability as mean depth, widest scours do occur in the 2006 Survey Inner Shelf, as with scour depth. Mean scour lengths for most sites are relatively short compared with the observed mean scour length on the northeast Grand Banks, which is on the order of 588 m, or 650 m corrected for truncation of scours at the edges of survey areas (C-CORE, 2001). However, mosaic size on the Makkovik Bank is larger than on the northeast Grand Banks so the influence of scour truncation would be less. Scour rise-up is of interest since it can be used to estimate the tendency of an iceberg keel to penetrate into an open excavation such as a glory hole. Mean rise-up values are all greater than those observed on the northeast Grand Banks, where mean rise-up is on the order of 1 m. Rise-up values from the 2006 Survey exceed all other sites, with an extreme of almost 90 m on the inner shelf.

The Regional Ice Scour Database (Geonautics, 1989) gives a mean scour depth of 1.35 m for the Labrador Shelf. The Bjarni wellsite survey (Geomarine, 1976) gives a mean scour depth of 1.45 m, and the mean scour depth at the ESRF site (Hodgson et al., 1988) was 0.94 m. Mean scour width from the ESRF site was 21 m (lower) and mean rise-up was 1.8 m (comparable). Mean scour length determined from the previous surveys were comparable with values presented here.

Table 2. Scour depths based on site and sediment type.

		Water Depth (m)	Mean Depth (m)	Standard Deviation (m)	Maximum Depth (m)
Site	Bertha	103 – 145	0.50	0.58	4.95
	Gladys	121 – 146	0.38	0.41	6.01
	Bjarni	127 – 166	0.40	0.43	5.63
	ESRF	88 – 220	0.42	0.60	5.70
	2006 Study Area (Makkovik Bank)	95 – 361	0.70	0.73	6.23
	2006 Study Area (Inner Shelf)	41 – 334	1.81	1.27	10.38
Sediment	Till	88 – 138	0.37	0.44	3.56
	Till with Discontinuous Sand Veneer	93 – 161	0.36	0.41	6.01
	Sand Veneer	113 – 170	0.42	0.46	5.24
	Sand	96 – 128	0.22	0.26	3.28
	Silt	120 – 220	0.81	0.86	5.70

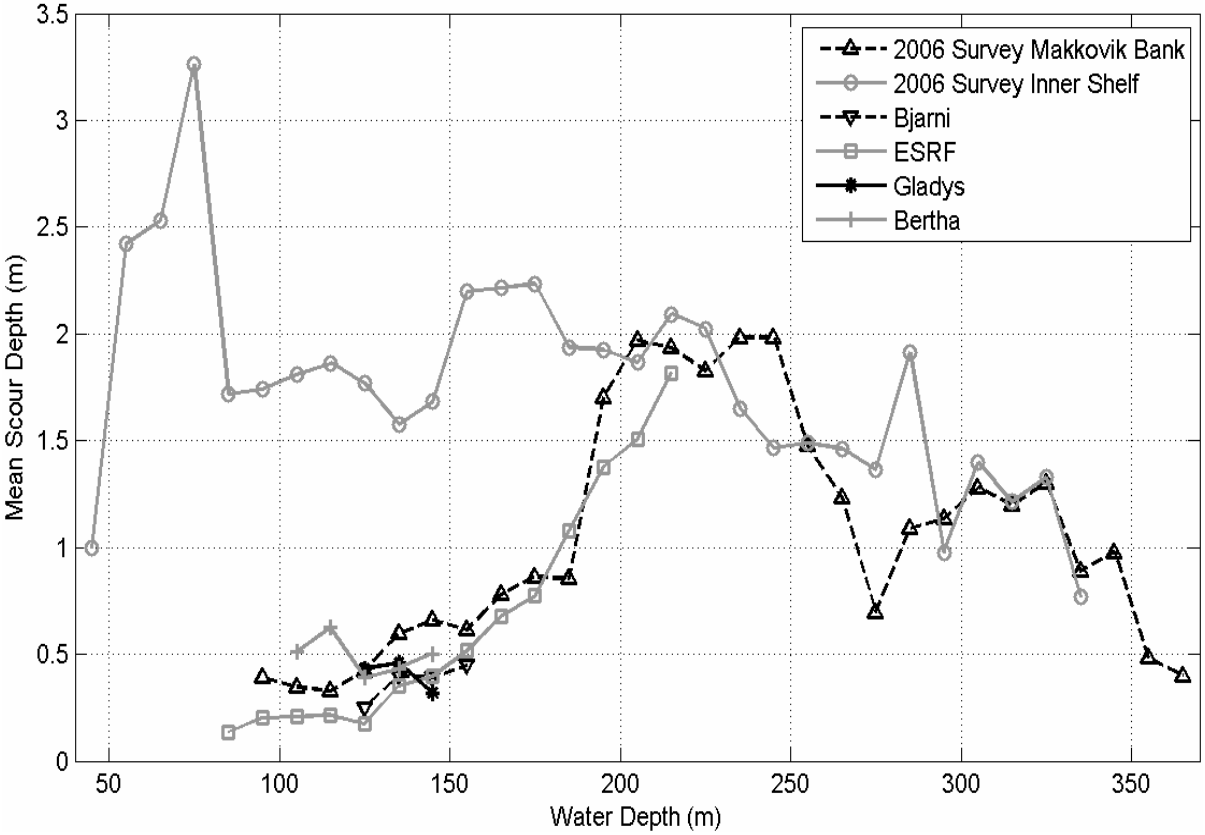

Figure 3. Variation of mean scour depth with water depth.

Table 3. Scour width, length and rise-up distributions.

Site		Width (m)			Length (m)			Rise-up (m)		
		Mean	S.D.	Max.	Mean	S.D.	Max.	Mean	S.D.	Max.
Site	Bertha	37.3	24.3	194	241	248	1825	1.7	1.4	9.9
	Gladys	35.7	21.7	204	282	364	4167	1.3	1.2	11.9
	Bjarni	42.3	25.2	213	360	422	3832	1.5	1.4	17.0
	ESRF	32.0	17.8	190	288	411	5455	1.5	2.3	32.1
	2006 Study Area (Makkovik Bank)	45.6	23.5	264	575	707	7375	3.2	4.6	36.8
	2006 Study Area (Inner Shelf)	54.6	25.3	219	457	551	7410	4.0	5.2	86.6
Sediment	Till	36.1	23.4	204.0	223	203	2039	1.3	1.4	16.5
	Till with Discontinuous Sand Veneer	37.3	22.4	213.4	321	402	4167	1.3	1.2	13.3
	Sand Veneer	32.7	20.1	190.0	307	392	4430	1.9	2.6	27.9
	Sand	29.1	14.3	169.1	218	242	2058	1.5	2.2	14.2
	Silt	40.2	23.8	188.0	417	654	5455	2.6	3.4	32.1

Scour orientation for each site is shown in Figure 4. Distributions of scour orientation at the 2003 sites are similar to those previously observed during the DIGS study (Hodgson et al., 1988).

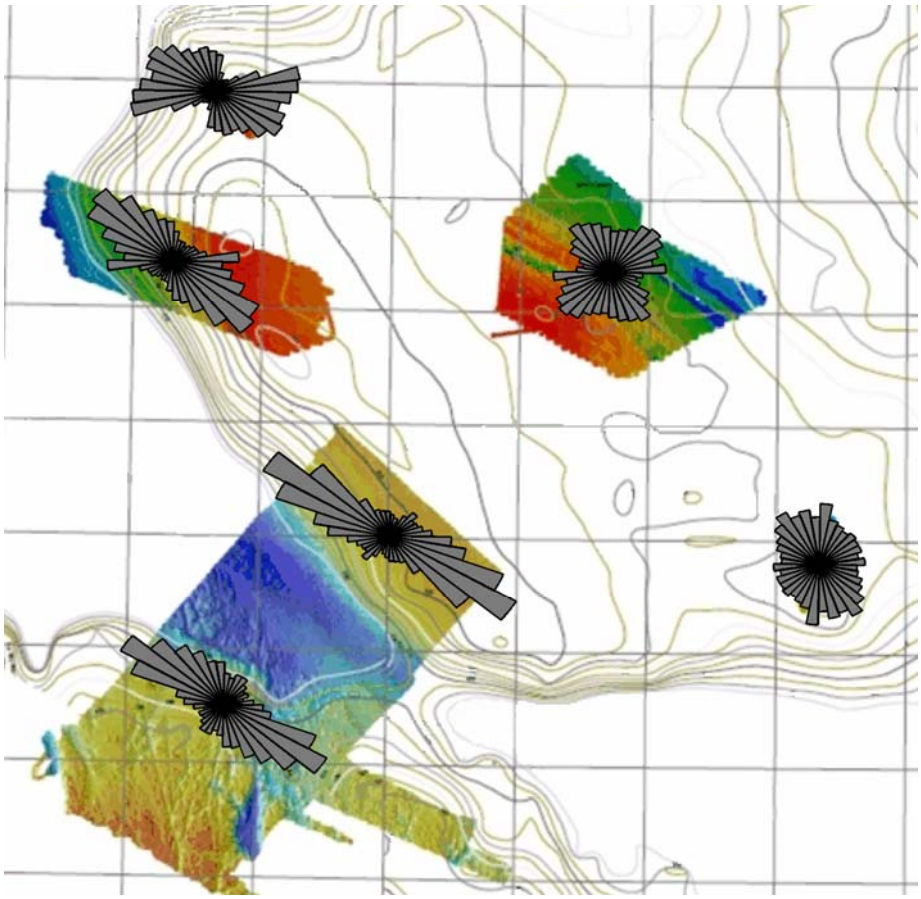

Figure 4. Scour orientation for the various survey sites.

4. Pit Dimensions

Unlike scours, which are linear features, pits are round or oval in plan dimensions. Their reduced dimensions, compared with scours, indicates that a pitting iceberg is less likely to interact with a subsea structure than a scouring iceberg. Coupled with the fact that pits form less frequently than scours, pits pose less of a hazard to subsea facilities. This is offset somewhat by the deeper depths associated with pits. Pits may occur as isolated features or may be associated with a scour, typically, but not necessarily, in the form of a terminal pit. Pits form when environmental driving forces are insufficient to initiate, or continue, the scouring process.

Table 4 gives pit depths and diameters for each site and sediment type. As noted with scours, sediment types were not assigned to the 2006 scour data and thus the 2006 features are not represented in the sediment type breakdown. Little variation in mean pit depth is apparent in the 2003 sites, but they are noticeably deeper in the 2006 data, particularly in the inner shelf. A maximum pit depth of 16.51 m was measured in 200 m water depth in the 2006 data (inner shelf). Mean pit depth variations with soil type do not seem to follow any discernable pattern. The mean pit diameter was calculated as the mean of the pit length and maximum width. The pit diameters in the 2006 data are not notably different from the 2003 data (and lowest of all for the 2006 Makkovik bank data subset). There appears to be no relationship between soil type and pit diameter.

Figure 5 shows variations in mean pit depth as a function of water depth for each site. In general, the same trends in mean pit depth are noted as for scour depth. The ratio of pits to scours is relatively consistent for the various water depth ranges.

Table 4. Pit dimensions based on site and sediment type.

		Pit Depth (m)			Pit Diameter (m)		
		Mean	S.D.	Max.	Mean	S.D.	Max.
Site	Bertha	0.99	0.70	3.77	60.8	30.2	191.0
	Gladys	1.01	0.83	6.89	56.6	28.6	243.6
	Bjarni	0.99	0.93	7.87	63.8	36.4	270.2
	ESRF	0.92	1.07	10.17	55.2	28.1	182.9
	2006 Study Area (Makkovik Bank)	1.12	1.08	11.06	42.1	25.2	200.9
	2006 Study Area (Inner Shelf)	2.44	1.60	16.51	58.4	33.9	276.1
Sediment	Till	0.97	0.79	5.93	59.8	29.5	191.0
	Till with Discontinuous Sand Veneer	0.94	0.87	7.87	60.6	34.8	270.2
	Sand Veneer	1.26	1.14	7.09	64.5	31.7	182.9
	Sand	0.56	0.55	3.85	59.9	26.0	109.9
	Silt	1.22	1.10	10.17	60.5	29.2	156.9

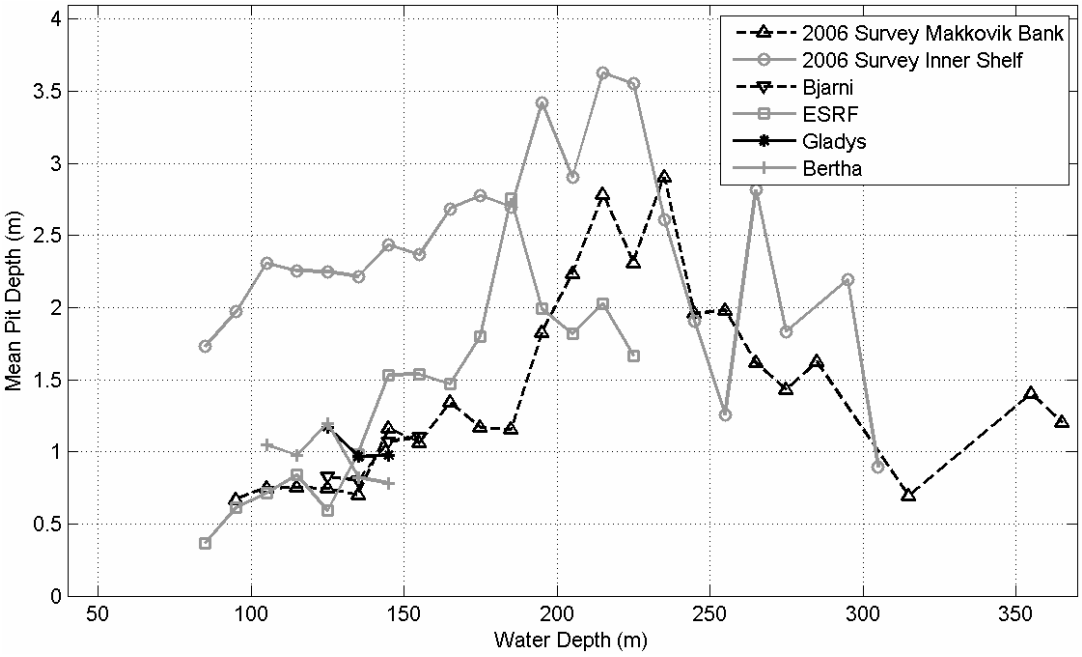

Figure 5. Variation of mean pit depth with water depth.

5. Scour Rate

The 2003 multibeam data were collected over the sites of earlier sidescan sonar surveys in order to establish iceberg scouring rates based on the number of new scours created over the time interval between surveys. Fugro Jacques GeoSurveys (FJG, 2005) compared the 2003 multibeam data with Bjarni and North Bjarni wellsite surveys (Geomarine Associates, 1976, 1980) and with surveys conducted as part of the DIGS (Dynamics of Iceberg Grounding and Scouring) program (Hodgson et al., 1988). Quality issues with earlier surveys were encountered, for example the

line-drawn scour interpretations produced by the Bjarni wellsite survey investigations could not be correlated with the 2003 data with confidence. Therefore, effort focused on the 37 km^2 ESRF sidescan mosaic on the western flank of the Makkovik Bank, which represents the best of the available baseline data. Surficial sand and bedform distributions were noted to be very similar between the 1985 and 2003 surveys (18 year duration), with no measurable indication of net bedform migration (within system resolution). As shown in Figure 6, only one new scour event was identified with confidence. Most scours mapped from the 2003 data (59%) existed in the 1985 survey. Some scours (25%) were outside of the 1985 survey. The rest were classified as "undetermined" due to their subtlety and lack of textural contrast and continuity, as well as positional uncertainties with the 1985 data. Most of the undetermined scours were on the western face of the shallow-most till ridge, in an area of exposed coarse-grained substrate with limited contrast. Similar contrast issues were noted at the edge of the sidescan mosaic. In order to estimate scour rate, two sub-sample areas (totaling 20.5 km^2) were defined that avoided the shallow ridge till and the edges of the sidescan mosaic. Inside these sub-sample areas were 32 undetermined features and 1 new scour. Using the assumption that 50 to 100% of undetermined features were new (likely conservative), the mean scour rate at that location is estimated to be between 0.04 to 0.08 $km^{-2}yr^{-1}$ (C-CORE, 2007).

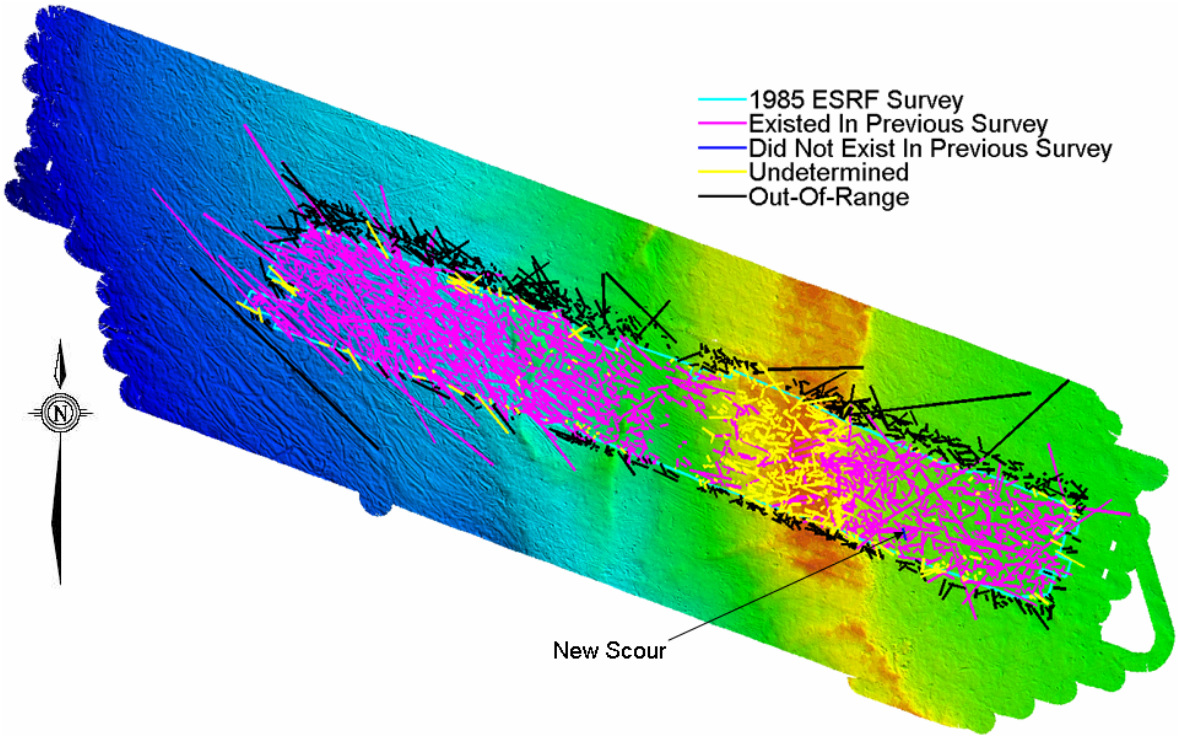

Figure 6. Repetitive mapping analysis of ESRF site (C-CORE, 2007).

6. Relict Scour

One of the factors that complicate the interpretation of scour parameters from seabed records is the presence of preserved relict scours. A relict scour is a very old scour that may not be representative of the modern scouring regime caused by icebergs calved from western Greenland and northern Canada tidewater glaciers. Relict ice scours have been excavated on the prairies (Woodworth-Lynas, 1992) and observed preserved in "fossil" form in rock. Relict scours have also been documented in the Laurentian Channel and on the St. Pierre Bank (King, 1976). An

analysis of pollen in a sediment core from an iceberg pit off Notre Dame Bay at 260 m water depth indicated an age of 9,500 years, while the analysis of a core from a scour in Conception Bay at a water depth of 183 m indicated an age of 6,500 years (Mudie, 1986). Fillon and Harmes (1982) stated that the deglaciation of the Saglek Bank, on the northern Labrador Shelf, occurred between 6000 to 8400 years ago. This is within the age range noted for relict scours on the Grand Banks and suggests that relict scours should also be common in the vicinity of the Makkovik Bank. Relict scour marks have also been observed in water depths greater than is generally considered to be possible for modern scouring. Lewis and Blasco (1990) report scours at water depths of 750 m, well beyond the maximum observed iceberg draft of approximately 220 m (Petra, 2007). A mixture of relict and modern scours has been noted in water depths around 180 m (Barrie, 1980).

The presence of relict scours interferes with the derivation of scour parameters. Relict scours, which tend to be both wider and deeper than modern scours, influence the evaluation of geometric parameters for modern scours. Seabed scour rate estimates based on seabed scour density (i.e. Lewis and Parrott, 1987) are influenced by the presence of relict scours. It also makes it difficult to define the lower water depth limit of modern scouring. To date, no reliable technique has been developed for distinguishing modern and relict scour based solely on multibeam seabed records.

7. Implications for Risk

The Bjarni Development Study (Petro-Canada, 1983) assessed iceberg scour risk to a network of three pipelines (2 redundant production pipelines and a pigging pipeline) running from Bjarni/North Bjarni on the Makkovik Bank to a landfall at Cape Harrison on the Labrador coast. The scour rate was estimated using iceberg flux, an iceberg draft distribution based on measured drafts, and the assumption that icebergs that could scour in a particular water depth was the proportion of the iceberg population with drafts ≥ water depth and ≤ water depth plus 10 m (based on the observation that iceberg scour rise-up could be on the order of 10 m). An exponential scour depth distribution with a mean value of 1.45 m was used, based on scour data collected at the Bjarni wellsite (Geomarine, 1976). It was determined that a pipeline trenched to a cover depth of 2.5 m would be directly impacted 4 times annually by scouring icebergs.

King (2002) used a geometric iceberg grounding model calibrated using scour rate estimates from the northeast Grand Banks (C-CORE, 2001) and revised scour depth parameters to evaluate scour risk for the pipelines on the Labrador Shelf. A review of the Geomarine (1976) scour data showed that almost no depths were recorded that were less than 1 m, indicating issues related to instrument resolution. Scour data from the DIGS program (Hodgson et al., 1988) were analyzed to account for the effect of sub-resolution scours and a mean scour depth of 0.75 m was selected. The revised iceberg contact rate for the pipeline discussed above was reduced from 4 times per year to approximately 1 contact in 25 years.

Incorporation of the latest scour rate and depth data into the risk analysis have resulted in further reductions in risk levels. The scour rate inferred from the repetitive mapping of the ESRF site was used to calibrate scour rates estimated using the geometric iceberg grounding model, and scour geometry obtained from the 2003 survey was used to develop water depth/scour length and depth relationships. As with previous risk analyses, pipeline landfall via the inner shelf was

assumed to pass through a sheltered channel, thus near-shore scour parameters would not dominate. A recent (2007) industry-sponsored multibeam survey (not discussed here) has addressed this issue. Based on these revised parameters, the return period for pipeline contact was revised from 25 years to over 300 years. It should be noted that additional burial would be required to account for the effect of sub-scour soil displacements (Woodworth-Lynas et al., 1996; Nobahar et al., 2007).

8. Conclusions and Future Work

Recent survey programs on the Labrador Shelf have significantly increased the understanding of iceberg scour parameters and risk in the region. Repetitive mapping of the ESRF site has provided a basis for estimating scour rates, although there is uncertainty due to limitations in the quality of the baseline sidescan survey. While the scour rate estimated from the repetitive mapping agrees well with grounding rates estimated using a geometric grounding model (King et al., 2003), this comparison was based on an exposed site and using these data to estimate iceberg scour rates in sheltered areas (i.e. the central or southern Makkovik Bank which is sheltered by the shallow ridge on the western flank) is not appropriate and would be expected to overestimate iceberg scour risk in those areas.

A seabed mapping program has been scheduled for the summer of 2008. This program will resurvey the 2003 survey areas, as well as establish new baseline surveys for future repetitive mapping efforts. The repetitive mapping of the 2003 survey will allow a multibeam-to-multibeam comparison for the identification of new scour and pit features, which will reduce the level of uncertainty associated with the current scour rate estimate, as well as provide some insight to scour rates in the central and southern Makkovik Bank. The new baseline surveys will also be processed to give additional site-specific scour parameters. Of particular interest is the southern flank of the Makkovik Bank (along a potential pipeline route from Bjarni/North Bjarni to Cape Harrison) where it is expected that scour conditions (depths) are more benign than those currently inferred from the analysis of the ESRF data.

9. References

Barrie, J.V. (1980). Iceberg-seabed interaction (northern Labrador Sea). Annals of Glaciology. (1), pp 71-76.

C-CORE (2001). Iceberg Scour Characteristics at White Rose. Contract Report Prepared for Husky Oil Operations Ltd., C-CORE Report Number 00-C44, May, 2001.

C-CORE (2007). Location, Environmental and Other Factors Influencing Exploration and Development of Labrador Gas. C-CORE Report R-06-088-525 V2, May.

Davis, L., Ralph, T., Cumming, E., Sonnichsen, G., and King, T. (2005). Morphometric Analysis of Iceberg Scours using Multibeam Sonar Bathymetry Data, Eastern Canadian Continental Shelf. POAC ’05 Conference Proceedings, Potsdam, NY, June.

Fillon, H.F. and Harmes, R.A. (1982). Northern Labrador Shelf Glacial Chronology and Depositional Environments. Can. Journal of Earth Sciences, Vol. 19, No. 1, pp. 162-192.

Fugro Jacques GeoSurveys Inc. (2005). Analysis and Interpretation of Iceberg Scour Survey Data, Makkovik Bank, Labrador Shelf. FJG Project No. 4020SG. Contract Report submitted to C-CORE. July.

Fugro Jacques GeoSurveys Inc. (2007). Labrador Trough Ice Scour Analysis Eastern Canadian Continental Shelf. Report No. 7017SG-001-RPT Rev 0 (Draft B). Prepared for Geological Survey of Canada (Atlantic), September.

Geomarine Associates Ltd. (1976). Bjarni Wellsite Bathymetry and Iceberg Scours. Contract Report Prepared for the Labrador Group.

Geomarine Associates Ltd. (1980). Wellsite Survey Report, North Bjarni F-06, Makkovik Bank, Labrador, August 20 - August 25, 1980. Report Prepared for the Labrador Group.

Geonautics Ltd. (1989). Regional Ice Scour Data Base Studies. Environmental Studies Research Funds, Report No. 105, 168 pp.

Hodgson, G.J., Lever, J.H., Woodworth-Lynas, C.M.T. and Lewis, C.F.M. (eds.), (1988). The Dynamics of Iceberg Grounding and Scouring (DIGS) Experiment and Repetitive Mapping of the Eastern Canadian Continental Shelf. Environmental Studies Research Funds Report No. 094. Two vols. Ottawa. 315p.

King, L.H. (1976). Relict Iceberg Furrows on the Laurentian Channel and Western Grand Banks. Can. J. Earth Sci., 13, pp. 1082-1092.

King, A.D. (2002). Iceberg Scour Risk Analysis for Pipelines on the Labrador Shelf. M.Eng. Thesis, Memorial University of Newfoundland, St. John's, Canada, 212 p.

King, A.D., McKenna, R.F., Jordaan, I.J., and Sonnichsen, G.V. (2003). A Model for Predicting Iceberg Grounding Rates on the Seabed. POAC '03, Trondheim, Norway.

Lewis, C.F.M. and Parrott, D.R. (1987). Iceberg Scour Rate Studies, Grand Banks of Newfoundland. *In* Current Research, Part A. Geological Survey of Canada, Paper 87-1A, pp. 825-833.

Lewis, C.F.M. and Blasco, S.M. (1990). Character and Distribution of Sea-ice and Iceberg Scours, *in* Proceedings of the Workshop on Ice Scouring and Design of Offshore Pipelines, Calgary, Alberta. Pp. 56-101.

Mudie P.J. (1986). Palynology as a Method for Dating Iceberg Scours. *In* Ice Scour and Seabed Engineering. Lewis, C.F.M., Parrott, D.R., Simpkin, P.G., and Buckley, J.T. (eds). Environmental Studies Revolving Funds Report No. 049. Ottawa, pp. 233-239.

Nobahar, A., Kenny, S., King, A., Mckenna, R., and Phillips. R. (2007). "Analysis and Design of Buried Pipelines for Ice Gouging Hazard: a Probabilistic Approach". Journal of Offshore Mechanics and Arctic Engineering, August, Vol. 129, pp 219-228.

PETRA International Ltd. (2007). Bathymetric Range of Modern Iceberg Scouring, Central Labrador Sea. Final Report No. 07-03: Prepared for Geological Survey of Canada (Atlantic). 54 pages including appendices.

Petro-Canada (1983). Bjarni/North Bjarni Production Perspectives Study. Prepared by Petro-Canada Resources – Frontier Development Group for The Labrador Group of Companies. 10 volumes.

Woodworth-Lynas, C.M.T. (1992). The Geology of Ice Scour. PhD. Thesis, University of Wales, 269p.

Woodworth-Lynas, C.M.T., Nixon, J.F., Phillips, R. and Palmer, A. (1996). Subgouge Deformations and the Security of Arctic Marine Pipelines. Proceedings of Offshore Technology Conference, Houston, May 1996, Vol. 4, pp 657-664.

19th IAHR International Symposium on Ice
"Using New Technology to Understand Water-Ice Interaction"
Vancouver, British Columbia, Canada, July 6 to 11, 2008

Iceberg Calving Frequency from Field Observations

Stephen Bruneau[1], Eugene Manning[2], Kris Rogers[3]
[1] *Assistant Professor Engineering, Memorial University of Newfoundland*
[2] *M.Eng Candidate, Memorial University of Newfoundland*
[3] *Engineering Student, Memorial University of Newfoundland*

One of the primary mechanisms of iceberg deterioration is calving. Calving in this context is an event in which a piece or pieces of ice abruptly break free of a parent iceberg. These events occur regularly though the interval and quantities calved are observed to vary considerably depending upon ambient environmental conditions. Scarcity of field data supporting analytical modeling of this phenomenon has led to an ongoing program of iceberg observation. This paper describes the program methodology and the results of the most recent dataset collected from St. John's Newfoundland in June 2007.

1. Introduction

Understanding the nature and rate of various iceberg mass-reducing mechanisms is important for accurate forecasting of iceberg position and size. Forecasts which are based on drift and deterioration models are required because it is not presently feasible to continuously monitor all bergs entering waters where they may be a risk to commercial activities (Kubat et al, 2007).

It is observed that icebergs loose mass through the action of melting and calving and that these mechanisms are highly correlated. Owing to the discrete and visible nature of calving events specifically, it has been determined that relatively low cost field work provides indicative data of this phenomenon. Experiments by the author in 1998 and later analyzed by Crocker (Ballicater, 2005) demonstrated the viability of using shore-based time lapse recordings for obtaining this data. Icebergs trapped on the coast of Newfoundland, and in particular in an exposed location near Signal Hill, St. John's, could be observed for extended periods of time and provide near-ideal circumstances for recording calving rates and quantities under conditions approximating open sea.

In the 1998 test program a time lapse VHS machine was used in conjunction with a personal Hi8 video camera. In subsequent years various other camera and recorder arrangements were used. In 2004 a similar video camera and web-cameras were used with a laptop providing image capture and storage functions. Specialized software for gathering and post-processing high numbers of still frames was employed in that work. As an experiment that year, a digital still camera with time lapse capabilities was packaged with auxiliary batteries and memory to provide an alternate means of data acquisition at remote sites. This work met with mixed success as conditions were less than ideal for iceberg work in 2004. In 2005 the Canadian Ice Services provided funding for some new equipment – two laptop/video camera packages. These were to be deployed with the older gear in an attempt to substantially increase data collection. The year proved to be a rare near-zero iceberg season around Newfoundland and so a one-week excursion to Greenland was alternately planned and executed. That program proved to be most interesting and useful information resulted though the applicability of results to lower latitudes remains questionable. In 2006 another very low iceberg season did not permit convenient field research and no data was obtained. Icebergs arrived around St. John's in June of 2007 and equipment was again deployed on Signal Hill. This paper describes that fieldwork and includes a discussion of observed deterioration mechanisms in general.

2. Field Observations of Iceberg Deterioration

Melting can be observed by inference only as it must be interpreted from the transition and evolution of iceberg shape, size and texture over time. From numerous hours of first hand observation it has been inferred that melting results primarily from multi-directional complex fluid flows over the submerged ice surface. The rate is accelerated at the waterline as a result of wave action and higher surface water temperatures. Swell and wind-waves increase fluid flow/replacement rates and thus available heat from the surrounding ocean is more readily available. Wave run-up, diffraction, reflection, refraction and interference are observed to contribute overall to an impossibly chaotic fluid flow regime around the waterline of icebergs under most conditions. Below the wave zone it is postulated that a continuum of current speeds

and directions result from berg translation, wind shear, prevailing oceanic and tidal actions and vortex shedding as they interact with berg shape. These combine with near-berg convective actions driven by buoyant melt-water, heavy chilled seawater, and ascending bubble flows to create a flow regime best described as complex.

At times, surface melting above water is visible through the presence of running and dripping water and a glistening appearance – though the latter is not always the case when rapid evaporation "dries" the surface. The melting above water accelerates in warm temperatures, high winds and direct sunlight, but occurs over a much smaller surface and does not appear to match the surface retreat rate observed for the below water portion when revealed, and is thus, likely to be a relatively small component of iceberg deterioration overall.

The melting surface of the submerged portion of an iceberg is characterized globally by long (10s of meters) sweeping curved surfaces devoid of the flat multifaceted and angular fracture surfaces often seen above water after calving events. It is not uncommon to see crevasses and sometimes narrowly supported globular and wing-like appendages below water or revealed above after berg repositioning. On a medium and small scale the surface is dominated by two distinct shapes: *furrows* and *cusps*. Parallel furrows are carved by ascending bubble flows which scour the ice with accelerated heat transfer on vertical and downward facing surfaces. These may be small (approx 1 meter length) if the surface is small and the berg has not been in a stable equilibrium for long; or quite pronounced (many meters long, 10's cm deep and wide) where melting is fast, the berg is stable, water is relatively calm and the berg is large enough to have expansive surfaces below its (vertically tangential) waistline. Most remarkable is the formation of a complete cuspate surface of striking uniformity, akin to the surface of a golf ball. The individual cusp-like depressions are of the scale of 1-50cm and are of smooth parabolic or spherical dimple shape. It appears that this complexion describes the entire wetted surface of an iceberg though this is only surmised from observing bergs after rollover and from various subsurface photos.

It is believed that this cuspate surface is an artifact of fluid flow structures which may be initiated by some surface irregularity and then evolve due to characteristic vortex sizes depending upon fluid flow rates. Indications of this type of phenomenon occur elsewhere in nature as described by Leighly (1948) and Villien et al (2001). In this case, the gouge-like action results from accelerated melting in regions of heightened flow rates and on incoming/convergent zones within each cusp. The spatial distribution of these cusps appears independent of berg orientation and are approximately uniform in size over any one observed surface – though they are not necessarily of the same size over the entire berg. It is also noteworthy that the cusp size appears to vary between icebergs or bobbing ice fragment observed in different locations and under different sea state conditions. It is surmised that the cusp size is controlled by sea state (relative surface flow rate) and duration of action and that water temperature controls the rate at which the "scalloped" surface evolves and develops to maturity. The presence of bubbles in the ice which create a tiny surface void when overtaken by the melting surface may be the catalyst for cusp formation in the first instance. But it is not necessary for bubbles to be present for cusps to exist as is the case where the scalloped appearance is uninterrupted over bubble-free re-frozen crevasse features (clear blue streaks) in icebergs. Whether salinity, density, core ice temperature, crystal shape and size, or some other material or fluid parameter plays a role in the development

of these surface structures is not known. But understanding and describing this phenomenon may be important for analytical modeling as it may indicate true convective action and significantly (20% estimated) increase iceberg surface area.

Mass loss due to **calving** is observed to occur over a wide range of scales. Melting furrows and wave wash continuously cut channels which eventually cause the isolation and parting of small fragments above and below water. This is common and regularly observed at close range under warm water conditions – but may not be significant due to the relative quantities involved (under 100 Kg each typically). Spalling of vertical surfaces and overhanging slabs occurs presumably as a result of reduced support conditions due to wave-induced notching or undercutting at the waterline. Weakening of ice near the surface due to warming and thermal stress cracks likely precipitates calving of vulnerable sections. The quantity of ice calved varies widely in these events.

Major calving events usually occur as a result of a shift in the equilibrium position of an actively melting berg. The shift usually creates overhanging conditions on one side where once only steep or vertical surfaces prevailed. Avalanches of ice are observed to take place in these cases and this is then followed by a reversal of orientation to compensate for the new loss – often resulting in a similar large-scale calving event on the opposite side. This breakup is common and is observed locally as the death nell – because the remaining pieces often depart in various directions and appear to melt away rapidly. Grounded bergs sometimes undergo global failure presumably due to tide-induced buoyant flexural stresses in which the berg parts into two smaller bergs, the smaller of which may be considered the calved portion. The nature of underwater calving events is not known and has not been observed directly by this author, however, instances of ice chipping and erosion due to seabed grinding and bumping is common in rough seas as observed when viewing at close range is possible.

3. Field Program, Signal Hill, St. John's, June 2007

On the morning of June 3rd 2007 an iceberg was observed in the distance from Signal Hill St. John's as it drifted a general course to the South West. There were approximately two other bergs within sight at that time. Fortuitously, the author photographed this distant iceberg and returned the next day to find that it had drifted in to shore and apparently grounded in the general vicinity referred to as Quidi Vidi. The berg was again photographed in the same area the following few days confirming it had grounded and that it may be a suitable candidate for extended study. It may be useful to note that it was assumed it would remain somewhat stationary because it had drifted into place in a tabular form. These, is has been observed in the past will remain in place through a considerable period of deterioration owing to the fact that the flat-top and bottom geometry results in a minimum draught and thus subsequent melting or calving events which may cause imbalances serve to increase the downward reach of one side or another of the ice mass – further anchoring the berg in place.

Figure 1. provides the reader with an impression of the changing shape of the iceberg over time. Note that the images are not scaled equally and so size is not to be gleaned from these.

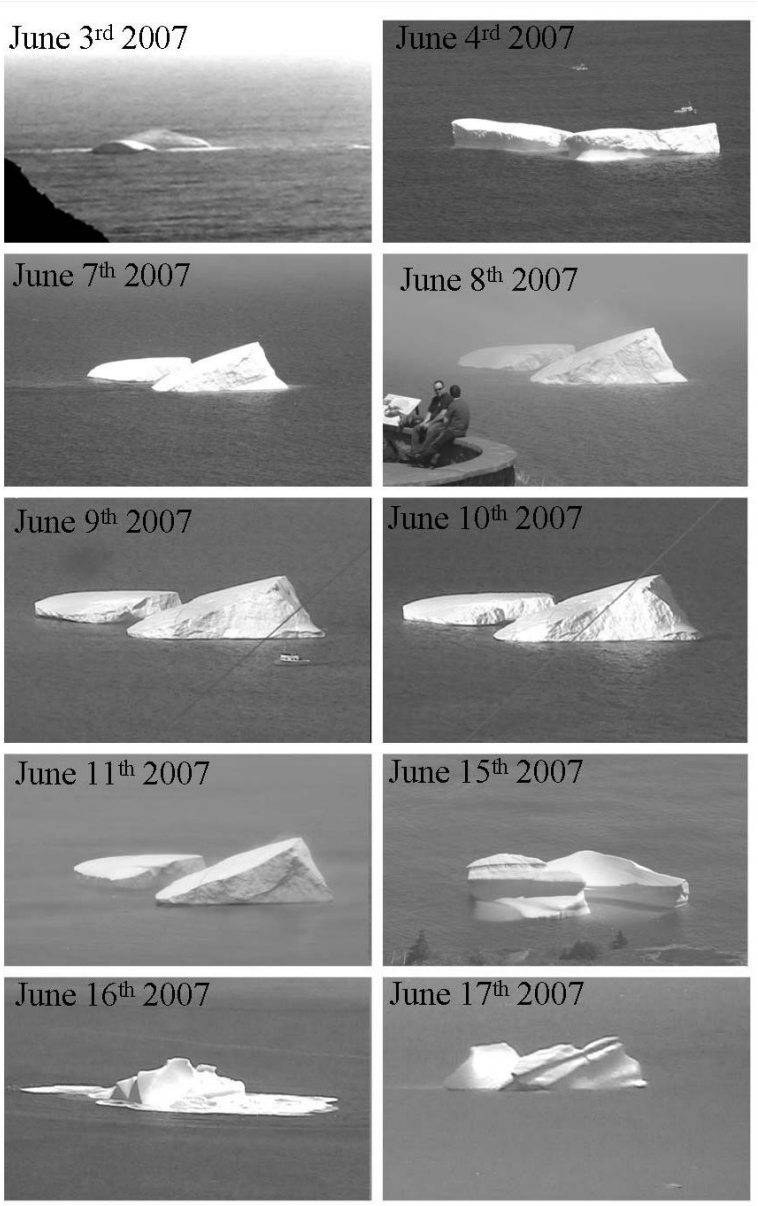

Figure 1. Images of the iceberg subject throughout the observation period – not to scale.

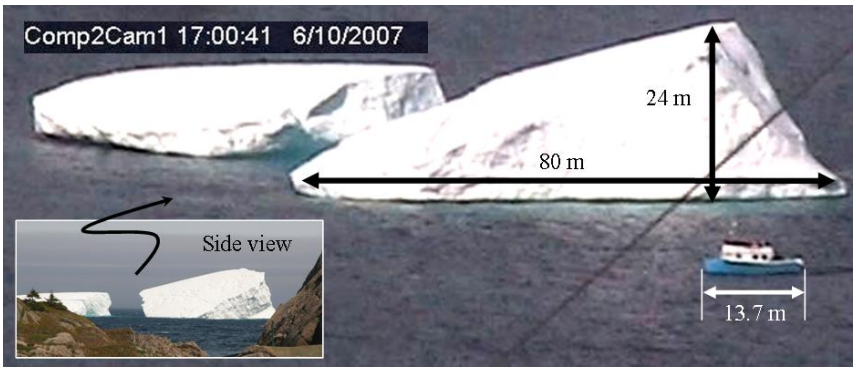

Figure 2. Approximate size of iceberg subject scaled from a known tour boat.

The berg mass likely exceeded one million tones when it was first sighted. Figure 2. illustrates the manner in which approximate scaling was determined throughout the field program. A vessel of known size in close proximity is photographed near the berg allowing direct scaling to take place. Viewing the berg from various approach angles facilitates the volumetric calculation. In the figure, the near portion of the berg is a wedge shape for which a triangle of base 80m and height 25m is an approximation. The side view indicates a wedge width of approximately twice the height, or 50m. The volume above waterline is thus approximately 0.5x80x25x50 or 50,000 m^3. If the glacial ice density is 900 kg/m^3 and the seawater is 1029kg/m^3 then the total ice volume would be 8 times the above water portion, or, 400,000 m^3 equal to 360,000 tones.

On June 9th, through a prior agreement with Parks Canada, Historic sites, two independent recording stations (laptop, tripod, video camera . . .) were configured and triggered from within the Marconi room in Cabot Tower on Signal Hill. Approximately Parallel camera records for 9 days were managed through twice-daily visits to the Tower. As is often the case, fog, darkness and iceberg repositioning out sight meant that a cumulative total of only 72.25 hours of unambiguous eligible records were obtained. In all instances the better of the two views from the camera setups was selected for any particular recording interval. (The strategy with two cameras being a near field view with good resolution and high risk of iceberg departure from the viewfinder, and, a wide angle with poorer resolution but a fighting chance of keeping the berg within sight during unmanned periods.)

In a manner similar to that described in some detail in previous work (Ballicater 2005) the time lapse data were reduced and scrutinized for calving events. The observed events are listed in Table 1. according to the following size classifications: Small: Single growler, few bits of brash. Medium: A few large pieces, several smaller and a noticeable halo of brash in the surrounding water. Large: noticeable change in berg shape and orientation, large quantities of floating ice rubble of all sizes, some sintered piles of brash noticeable.

Table 1. Summary of Calving Events at Signal Hill June 2007

Date/Time	Calving event size
6/09/10:04	Small
6/09/13:55	Small
6/09/15:22	Small
6/09/16:23	Medium
6/09/17:01	Small
6/09/21:28	Small
6/10/10:21	Small
6/10/11:06	Medium
6/10/17:11	Large
6/10/18:13	Small
6/11/4:41	Small
6/11/7:45	Small
6/11/14:36	Small
6/11/16:31	Large
6/11/17:07	Small
6/12/9:01	Medium
6/12/10:38	Small
6/12/11:31	Medium
6/12/12:58	Small
6/15/9:34	Small
6/15/11:42	Large
6/16/8:00	Medium
6/16/11:30	Large

These results have been graphically represented below (Figure 3.) on a timeline whereby periods of valid data are differentiated from lost time.

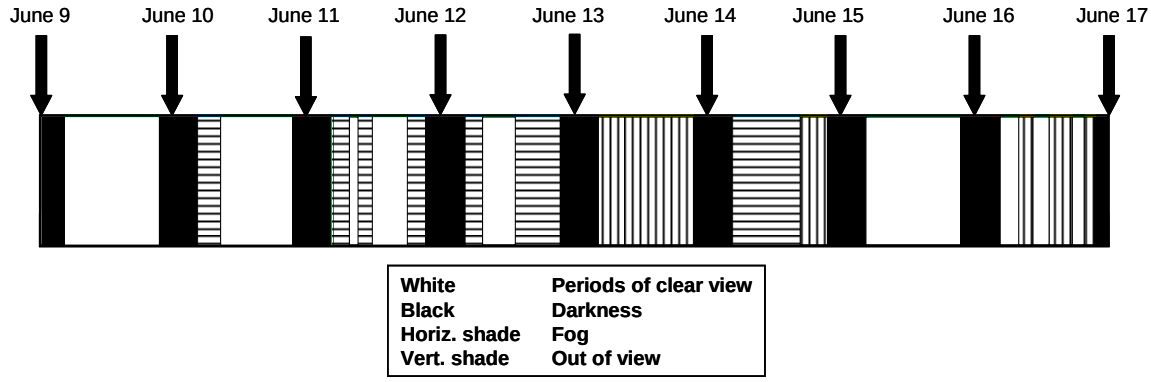

Figure 3. Field program timeline including lost time and clear viewing.

Underscoring the challenging nature of this work is the fact that this iceberg broke into two pieces of roughly equivalent size, and both pieces remained in very close proximity for some time. It was judged that the calving events coming from the two adjacent pieces would continue to be recognized as coming from a single berg until one or the other of the halves moved off by a distance at least equal to one berg length. This judgment became moot as under the cover of fog both pieces drifted off site and only the larger of the two was seen again.

Fisheries and Oceans Canada catalog sea surface temperatures in the oceans surrounding the country. The temperatures are recorded by satellite and weekly and monthly composite means are produced for various regions. Though resolution at the precise location of observation is somewhat vague, the composite for June 3 – 9th indicates a temperature in the range of 6 - 8^{o}C, as did the composite for the period of June 10 – 16th (Figure 4.).

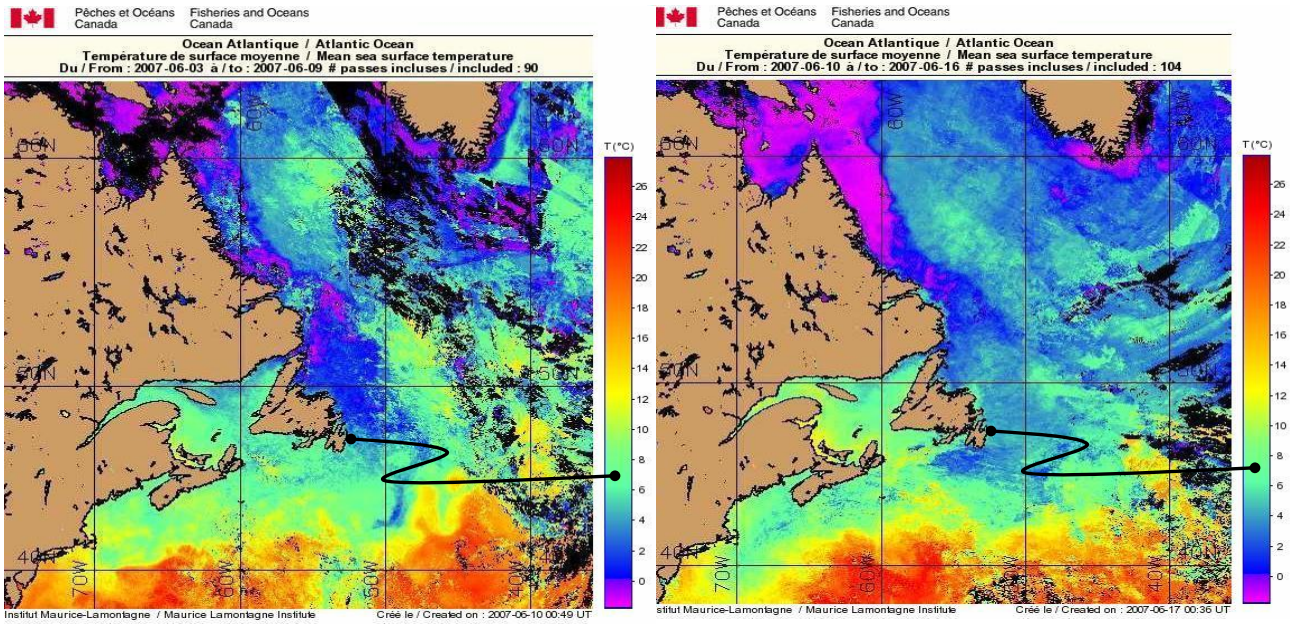

Figure 4. Weekly Mean Surface Temperatures June 3-9 & June 10-16 from DFO, 2007

The Marine Environmental Data Service of DFO also provides hydrographic information for many specific sites, and significantly this includes data from a station not four kilometers from

the berg grounding site. On June 15th, 2007 at 47.55°N and 52.59°W a STD profile was obtained as shown in Figure 5. for the vicinity indicated.

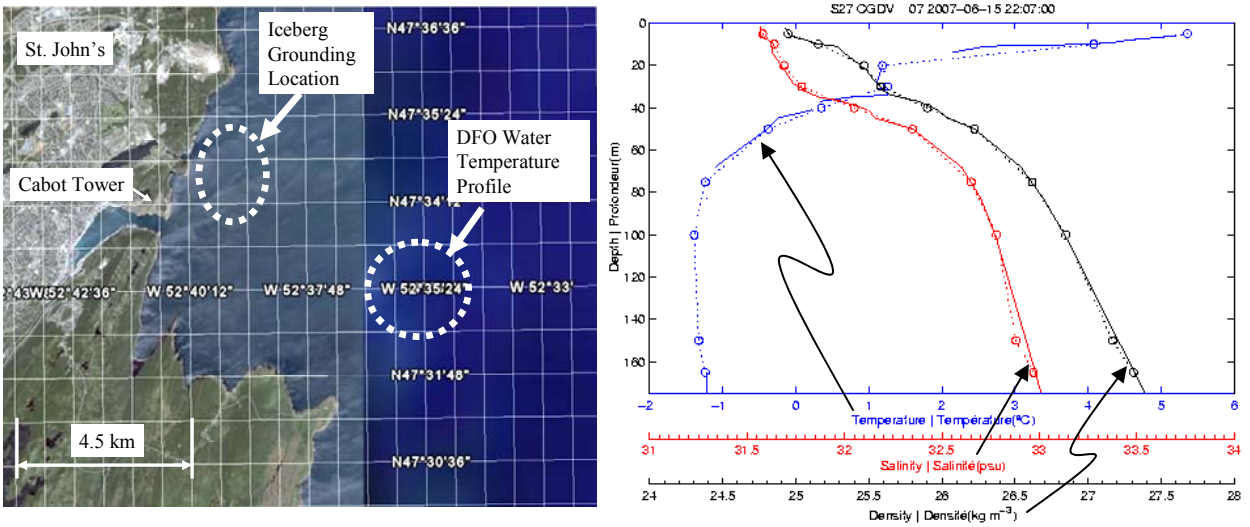

Figure 5. Relative location of iceberg subject and DFO-MEDS station and STD measurements.

The STD profile plotted below indicates a near surface (10 m or less) temperature between 5 and 6 degrees C though the resolution at this depth is vague, and it appears readings above 5 meters are non-existent. Extrapolation suggests the surface temperature tending towards 6 or 8 C which fits well with the remote sensing data. Based on this information the sea surface temperature at the location of the berg closer to land than the DFO station was assumed to be 8 C for the period of investigation. Future work on iceberg melting may be carried out to better account for the distribution of temperature with depth on the bases of the available data.

4. Analysis and Discussion

During the 72.25 hours of observation time 14 small, 5 medium and 4 large events were recorded. The average calving interval during this time period for both medium and large events combined was 8.0 hours. The plot below indicates the relative goodness-of-fit of the present data with past work. Previous investigations resulting in calving interval data have been undertaken from both air and on land. The calving intervals from 2000 to 2003 were obtained from CFR flights and the data in 1998 and 2004 were obtained from video observations much like the present 2007 data (Ballicater 2005). The round markers on the graph represent the calving intervals for medium and large events. Only the medium and large events were used because it is unlikely that the smaller events were able to be seen during the observations from the air. Upper and lower limits have been added to the 2007 data to represent the range of the actual calving interval. The upper limit is developed by recording the large calving events. During the 2007 observations there were 4 large events leading to a calving interval of 18.1 hours. The lower limit is developed by recording all (small, medium and large) calving events, this leads to a calving interval of 3.1 hours. The upper and lower limits have been displayed on Figure 6 for the 1998, 2000 and 2004 data points as well.

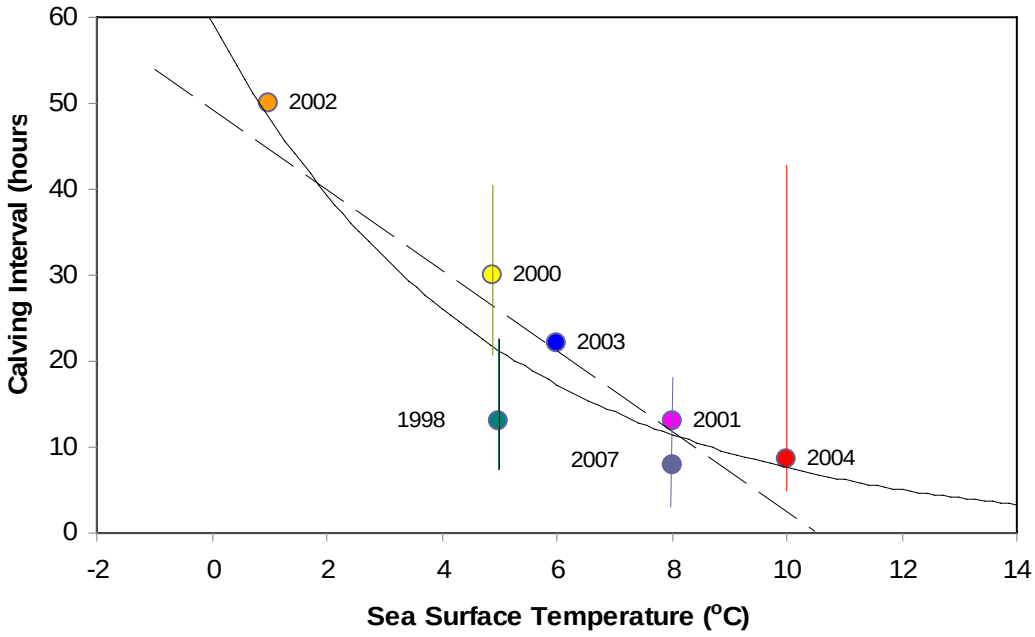

Figure 6. Iceberg calving interval from present (2007), and prior work (from Ballicater, 2005).

The straight dashed line on the graph represents the best linear fit through all data points. The equation of the line is given by:

$t_c = 49.2 - 4.66T_w$

Where t_c is the calving interval in hours and T_w is the surface water temperature.

Reasonable agreement results from the linear model ($R^2 = 0.8084$) but it poses problems reconciling with natural tendencies towards the extremes. To avoid a calving interval tending towards zero as temperatures rise past 10°C, and, appreciable calving rates in waters well below zero, a declining exponential best fit was applied with the resulting curve formulation:

$t_c = 59.4 * e^{(-0.205T_w)}$

Whether this fit is better or not within the context of CIS iceberg modeling is unknown. By comparison, in Ballicater (2005) similarly derived empirical formulas from the 4 CFR data points were expressed as:

$t_c = 55.3 - 5.3T_w$ $\quad$ $t_c = 62 * e^{(-0.20T_w)}$

Note that subtle changes in coefficients and exponents have resulted from the addition of new data to the analysis.

Conclusions and Recommendations

Observations of iceberg deterioration have been made and a range of complex mechanisms have been described. Calving events are one of the least difficult mechanisms to quantify owing to the discrete and visible nature of them. Calving frequency is also proportional to melt rate and so modeling of the calving phenomenon presents an opportunity to capture overall iceberg ablation rates. This work analyzed time lapse recording of an iceberg grounded near St. John's in 2007. Calving intervals were determined for periods of uninterrupted viewing and the results were plotted against previous work. The calving frequency appears to agree generally with the body of data presented, however, a trend towards higher frequencies (lower intervals) from this and other shore-based monitoring programs is noted. This discrepancy may be a result of observer differences in the cataloging of event significance, the difficulty with capturing all events with repeat flight data, or perhaps the actual tendency towards higher calving rates for bergs in grounded situations near the coast – perhaps through higher sea states, higher temperatures of greater stresses and impact accelerations.

It is proposed to carry out further investigations of this nature with better equipment and to begin to correlate overall ablation rates to calving frequencies. Considerable data have been collected in this year (2008) to date and more is likely as this iceberg season appears higher than average and somewhat early.

Acknowledgments

The author would like to thank the Canadian Ice Services, Tom Carriers scientific authority, for financially supporting this work. Support in-kind from Parks Canada Historic Sites, Scott Andrews was greatly appreciated, and the support of Dr Greg Crocker, Ballicater consulting is also recognized.

References

Ballicater Consulting Ltd (2005) Iceberg Observations Ilulissat Greenland. Contract Report Prepared for Canadian Ice Service, Environment Canada and Canadian Hydraulics Centre, National Research Council of Canada, Ballicater Report 05-02, August 2005.

Kubat, I., Sayad, M., Savage, S., Carriers, T, and Crocker, G. (2007). An operational Iceberg Deterioration Model. Proc. 17th ISOPE Conference, Lisbon, Portugal, July 1-6, 2007 pp 652 – 657.

Leighly, J. (1948) Cuspate Surfaces of Melting Ice and Firn. Geograph. Rev. 38:300-306.

Villien, B., Zheng, Y. Lister, D. (2001) The Scalloping Phenomenon and its Significance in Flow-Assisted Corrosion. Twenty Sixth Annual CNS-CAN Student Conference, Toronto, Ontario, Canada, June 10-13, 2001

Special Session: Ice crushing processes

19th IAHR International Symposium on Ice
"Using New Technology to Understand Water-Ice Interaction"
Vancouver, British Columbia, Canada, July 6 to 11, 2008

Ice Pressure Distribution during Ice-Structure Interaction: Measurements of Ice Force Panels on Confederation Bridge Pier

Dhruba Tripathi, Thomas G. Brown, Derek C. Mayne
Department of Civil Engineering, University of Calgary
Calgary Canada
ice@ucalgary.ca

Abstract

Full scale data obtained from the ice force panels (IFP) installed on the conical surface of a Confederation Bridge pier is analyzed to determine the pressure pattern and its distribution. The IFPs provided pressure measurements over 40 m^2 of the conical portion of the bridge pier with a resolution of 0.25 m^2. Details of the IFPs, data screening and preparation, methodology used in the analysis of the data, and results obtained from the analysis are discussed. Raw data from the bridge, in the form of electrical signals, is converted into pressure and then is normalized to perform three different analyses: 1) Panel activation analysis 2) Detailed pressure distribution analysis and 3) Correlation matrix analysis. These analyses are helpful in determining the relative distribution of pressure in the contact area, the relationship between pressure on one panel sector with the pressures on adjacent panels, and the extent to which ice pressures are present over the area of the instrumented cone.

1 Introduction

One of the most frequent hazards faced by offshore structures in Arctic regions is interaction with ice features. Understanding ice-structure interaction behavior can be helpful in achieving structural safety and economy on offshore structures by providing better design and construction guidance.

Ice-structure interaction, however, is a complex process. When ice interacts with a structure, the ice in the interaction area is highly damaged and the crushed ice is subjected to a complex system of loads and deformations. Researchers have observed, in experiments, that the load from ice is transmitted through small discrete areas of intense pressure (Jordaan 2001). It is also been argued that the array of high pressure spots can form a high pressure line, the pattern of which depends on the geometry of the contact area (Daley et al. 1998; Riska et al. 2002). These patterns are generally observed when ice interacts with vertical or nearly vertical structural faces, where ice fails in crushing. When ice interacts with inclined or conical structures the ice force distribution pattern can be different from that of the vertical structures. This paper attempts to analyze data collected from ice force panels (IFPs) installed on the Confederation Bridge, under the assumption that this data can provide valuable insight into trends and patterns of ice force distribution on conical structures.

IFPs installed on the Confederation Bridge were unique in how they measure local ice pressure during ice-structure interaction. The IFPs were installed in 1996 and the data loggers started collecting data in 1998 (Brown et al. 1997, 1998) until the IFPs were damaged during an ice event in 2003 and were removed from the bridge pier.

This paper deals with process and methodology of data screening, data analysis, and presentation of preliminary results of the analysis. Introduction to Confederation Bridge ice force monitoring and details on IFPs are covered in Sections 2 and 3. Section 4 covers the details on data preparation process for analysis. Section 5 deals with panel activation analysis, detailed pressure distribution analysis and correlation analysis. The conclusion and future works are provided at the end of the paper.

2 Confederation Bridge and Ice Force Monitoring

The data source for the current research, the Confederation Bridge, is a 12.9 km bridge connecting two provinces, Prince Edward Island and New Brunswick, over Northumberland Strait in Atlantic Canada. The bridge is constructed in a sequence of two pier portal frame systems connected by a drop-in span. The Confederation Bridge piers are cylindrical in shape with conical ice-shields at the waterline. The conical surface of the ice-shield causes flexural failure of ice, which is less severe than crushing failure generally seen in vertical face interaction. Apart from causing less severe ice failure, conical shape also reduces the probability of cyclic ice loading at a frequency equal to the natural frequency of the structure (Brown 2006).

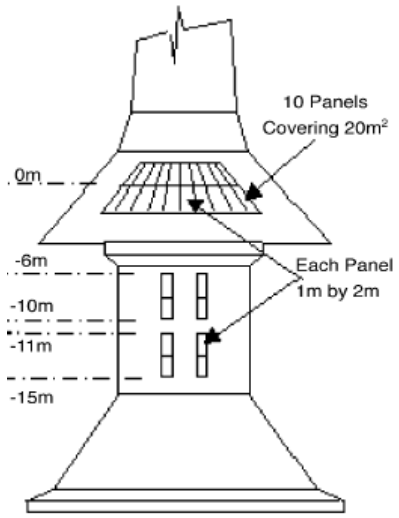

Figure 1. Layout of Ice Force Panels on the Confederation Bridge pier P31 (Lemée and Brown 2005)

Confederation Bridge is monitored by a comprehensive ice force monitoring system. Global load is measured by tiltmeters located in two of the bridge pier shafts (pier P31 and P32). Local ice load is measured by IFPs installed on the conical and cylindrical portion of pier P31. To measure other parameters necessary for understanding ice characteristics and ice kinematics, various other monitoring sensors are installed in different parts of the bridge (Tiwari 2005; Cheung et al. 1997). These monitoring sensors measure parameters like ice thickness, ice velocity, wind velocity, air temperature, and ridge keel profile.

Tiltmeters and IFPs operate in two different modes; slow-speed mode and high-speed mode. They operate in slow-speed mode throughout the monitoring period. When the ice force measured by the tiltmeter exceeds a certain predefined threshold, the tiltmeters and IFP sensors start collecting data in high speed mode. The high speed data is termed "triggered data" and is used in the analysis of the IFP data.

3 Ice Force Panels (IFPs)

Custom made Integrated Deformation Elastic Alloy Laminate (IDEAL) ice force panels supplied by Weir-Jones Engineering Consultants Ltd, Vancouver were installed on the NW face of pier P31 of the bridge (Figures 1 and 2). The panels measure local ice pressure on the lower conical portion of the pier and vertical pier shaft below the conical section. These large flat panels had a rated capacity of 12 MPa. Calibration and operation details of ice force panels are given in Frederking (1996).

The ice force panels on the conical portion were trapezoidal in shape to accommodate the conical shape. Ten pairs of 2000 mm long panels, totaling 20 panels, were installed, one panel above the water line and another below the waterline. The upper panels were 827 mm wide at the top and 1000 mm at the bottom. The lower panels were 1000mm wide at the top and 1173 mm at the bottom. A total of 40m^2 of the conical surface was covered by IFPs.

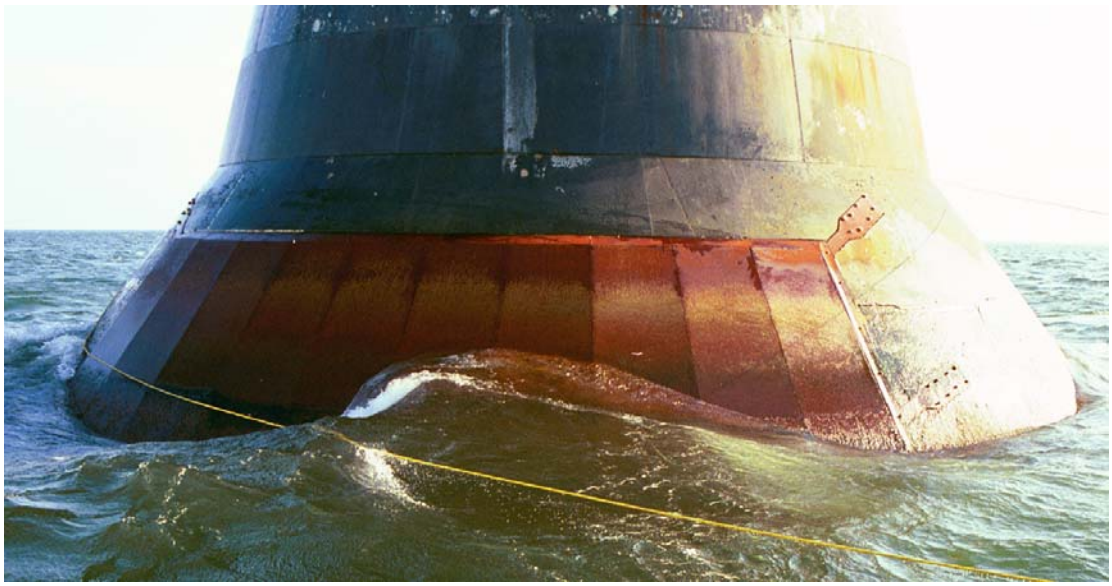

Figure 2. Photograph of ice force panels on pier P31 (Photo by D.C. Mayne).

In addition to the panels on the conical portion, eight 1m by 2 m rectangular ice force panels were installed on the pier shaft with a total area of 16m^2.

The front and back face of each panel was made of 6.35 mm and 3.15 mm thick mild steel plates respectively. Between the front and back faces of the panels an array of tabular rings were installed in equilateral triangular pattern (82.55 mm at centers) as shown in Figure 3. The tabular rings were 19 mm high, 25.4 mm in diameter, and made of 1.65 mm thick plates. Each panel was further divided into 8 sectors of nominal area 500 mm by 500 mm. Out of a typical 30 rings in each sector, 2 were instrumented with strain gauges to measure response of load. Hence ice panel data can only be considered as a representation of actual absolute load and needs to be treated accordingly.

Data collected by IFPs are large text files. When IFPs collect data in trigger mode, during an ice event, 120 IFP sectors in the conical portion of the pier record data every 34 milliseconds. The remaining 40 sectors in the conical portion and 64 sectors in the cylindrical portion of the pier record data every 68 milliseconds. These data are saved in two different text files with extension T2 and T3 respectively (Figure 4) with sizes exceeding one or more gigabytes in some cases. Analyzing all the data at once is impractical, thus data from the sectors most vulnerable to ice action (the shaded portion in Figure 4) are analyzed, and, for clarity, data from eight sectors are shown in the charts in this paper. Data preparation and filtering processes are covered in the next section.

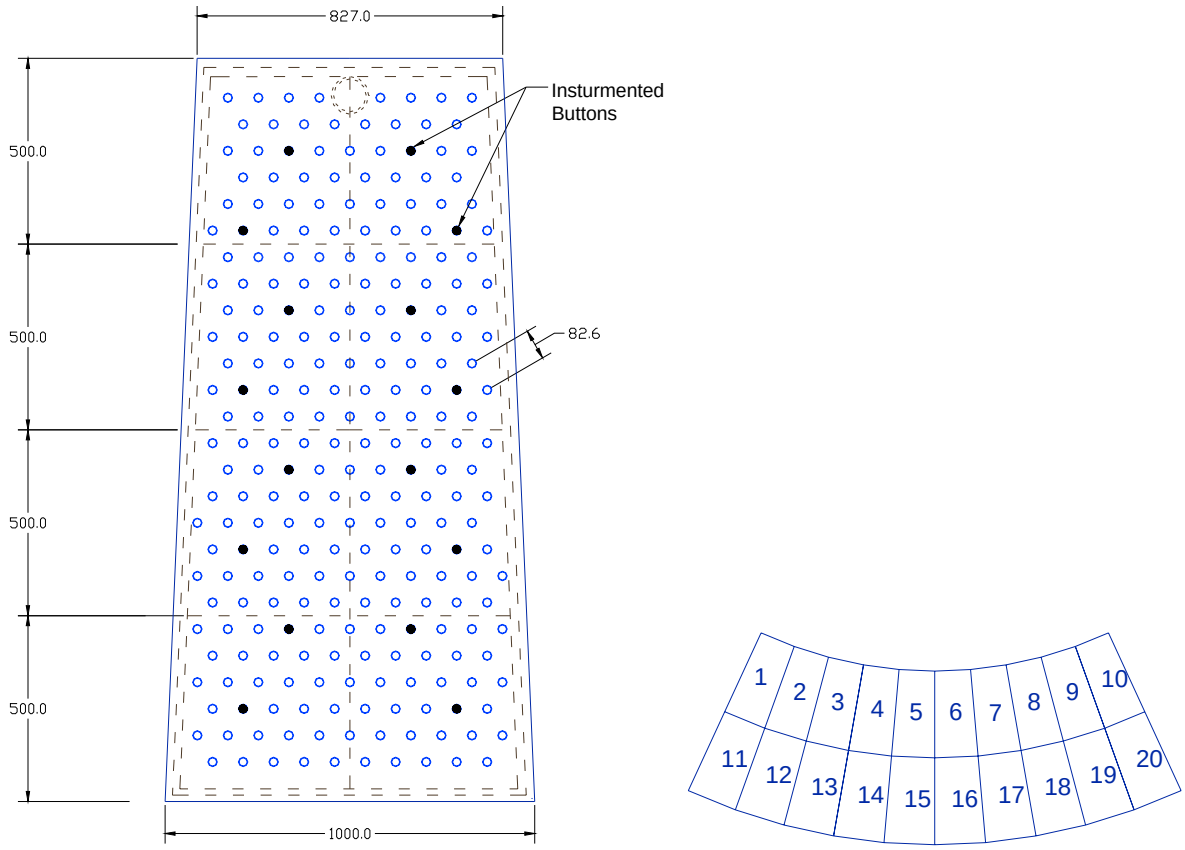

Figure 3. Instrumentation details of a typical IFP (left). Layout and numbering of panels on the conical portion of Confederation Bridge pier P31 (right)

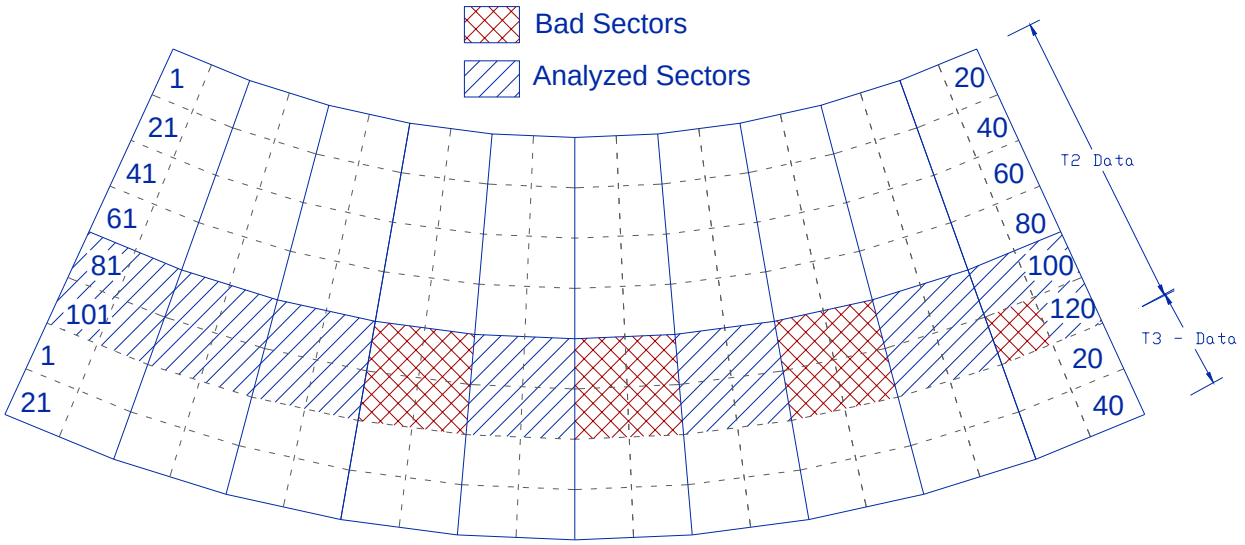

Figure 4. Division and numbering of individual sectors on the conical portion of the pier P31 and sectors analyzed in the paper

4 Data Preparation

Raw tiltmeter data is collected in the form of electrical signals based on the structural response of the bridge during an ice event. When a significant load is measured by tiltmeters installed in the pier shaft of the bridge, the IFP sensors are triggered to collect data. Triggering usually is caused by an incoming ice feature, but sometimes environmental parameters can also cause false triggering and such data are filtered before analysis. Wind is one of the major environmental factors that cause high loads and hence triggering of IFPs. To remove the loads caused by wind, empirical wind correction factors (Bruce and Croasdale 2001) are used in the analysis of tiltmeter data. The IFP data corresponding to the events identified from tiltmeter data is used for further modification and analysis.

Some sectors in various panels had wiring problems, so recorded data were deemed unreliable. Such sectors are named BAD and the data recorded by them was dropped during analysis. Remaining data are converted to ice pressure by using conversion factors (Bruce et al. 1999) of individual pressure panel sectors. The pressure in an individual panel sector, y_{ip}, in MPa is obtained by equation [1].

$$y_{ip} = \frac{(x_i - A_i)}{B_i C_i} \qquad \textbf{[1]}$$

where, x_i is the IFP reading in milliVolts, and i corresponds to the IFP sector number. A_i a baseline correction factor, and B_i, and C_i are constants obtained from the calibration of pressure panels.

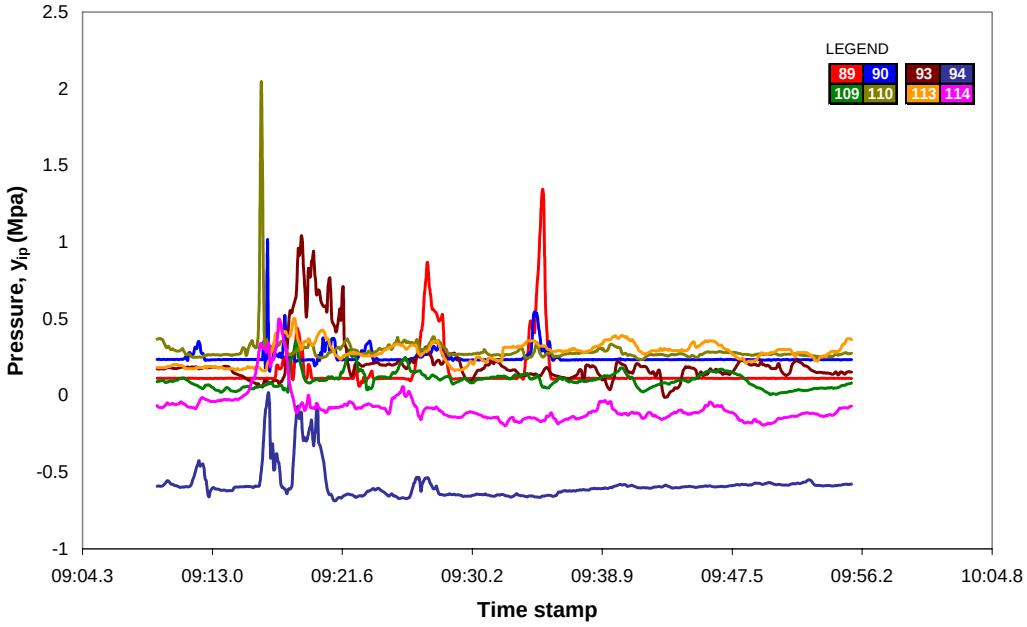

Figure 5. A raw panel pressure plot (Individual line represents response of one particular sector in the pressure panel).

The baselines of individual panels have shifted away from the ideal zero level, as shown in Figure 5, an example of panel pressures obtained from a 1998 event. As the pressure panels are attached to the face of the conical portion of the bridge pier, it can be safely assumed that ice cannot cause negative pressures on the panels. The negative values and high values of pressures in Figure 5 can be attributed to errors in baselines. They are corrected by normalizing against the minimum (y_{min}) of all the readings for a particular event by Eq. [2].

$$y_{iMIN} = y_{ip} - y_{\min} \quad \textbf{[2]}$$

where y_{iMIN} is the normalized pressure and is plotted against time-stamp in Figure 6. The plot in Figure 6 shows positive values for all the sectors, but still the baselines vary for different sectors. To rectify errors in baseline the value y_{iMIN} is averaged and subtracted from y_{iMIN} to obtain $y_{iMINAvg}$:

$$y_{iMINAvg} = y_{iMIN} - \bar{y}_{iMIN} \quad \textbf{[3]}$$

A plot of $y_{iMINAvg}$, Figure 7, still indicates some negative peaks. It is assumed that the negative peaks are caused by interference with electric signals in the logging system. To reduce the effects of negative peaks, average of only the negative values of data $\bar{y}_{iMINAvgNeg}$ is further subtracted from $y_{iMINAvg}$ to obtain the normalized pressure value, y_i, to be used in analysis:

$$y_i = y_{iMINAvg} - \bar{y}_{iMINAvgNeg} \quad \textbf{[4]}$$

The plot of y_i in Figure 8 gives a much better distribution of pressure in panel sectors. This data is used for detailed pressure distribution analysis.

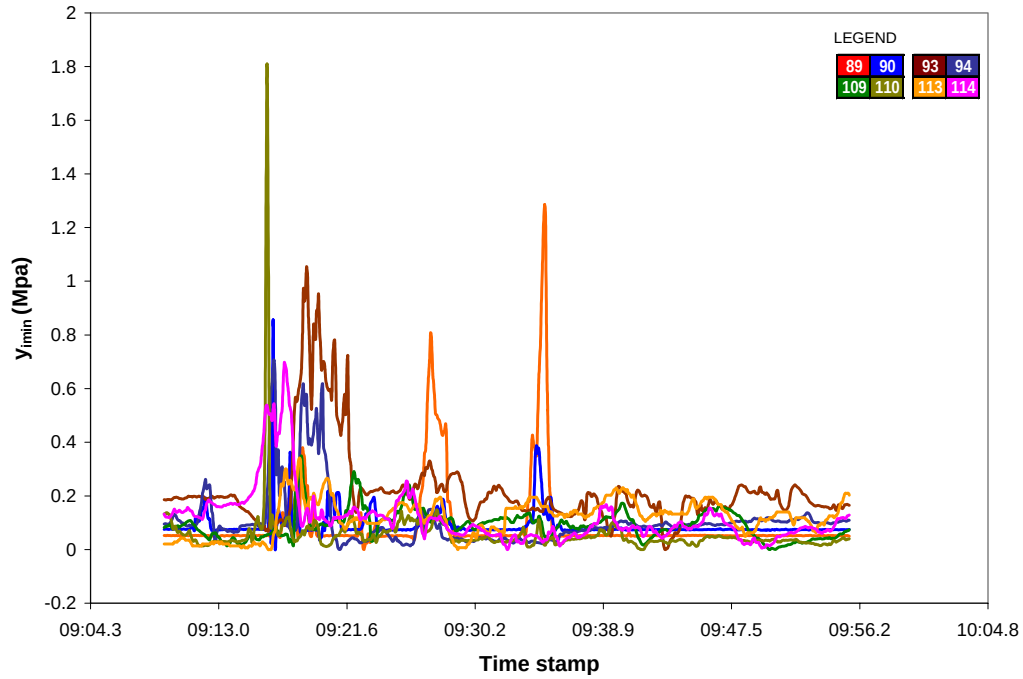

Figure 6. Plot of y_{iMIN} against time stamp

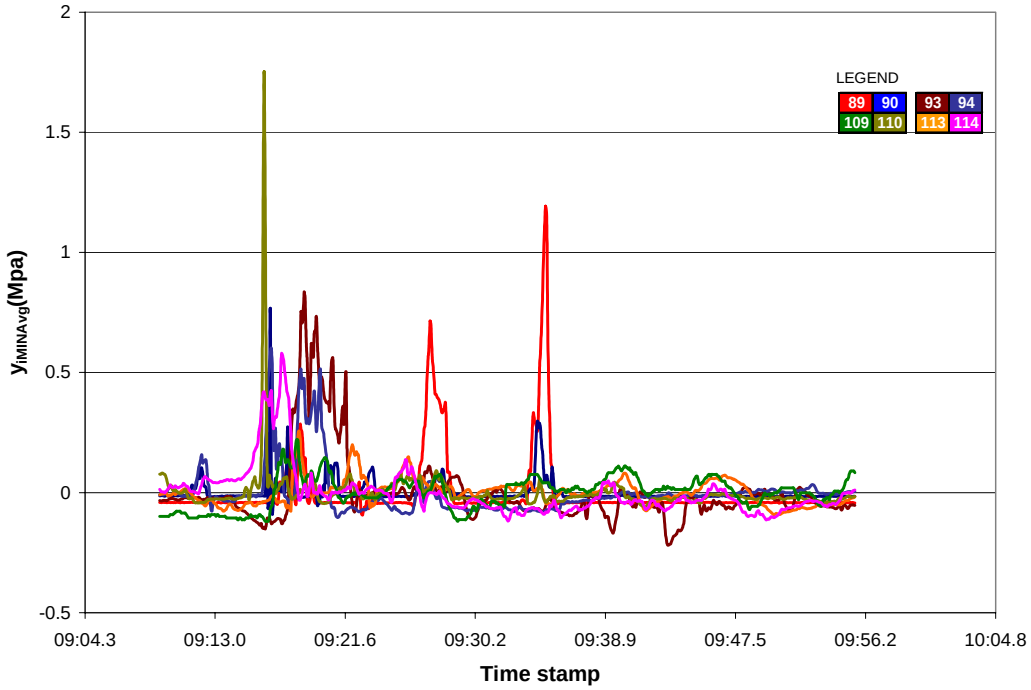

Figure 7. Plot of $y_{iMINAvg}$ against time stamp

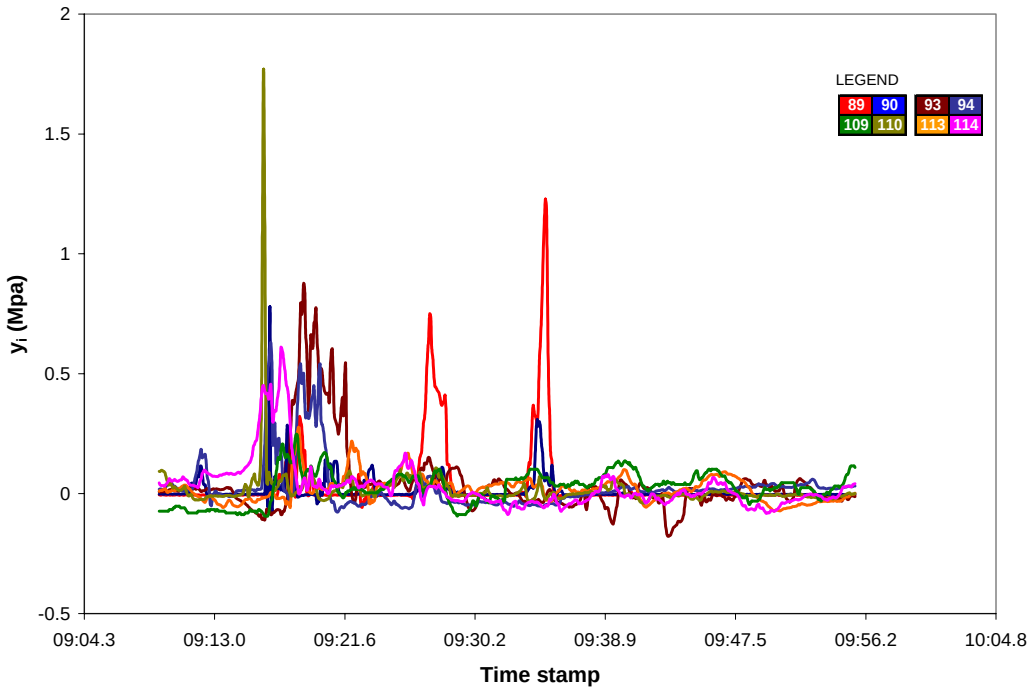

Figure 8. Plot of final pressure data used in detailed pressure distribution analysis

5 Data Analysis

Three main parametric analyses performed in this study are:

- Panel activation analysis
- Detailed pressure distribution analysis
- Correlation analysis

To determine panel activation, ice loads on each panel for an event are calculated and compared with a predefined pressure threshold. From this we can determine the number of panels being acted upon by ice. For this purpose the normalized pressure, y_i, is checked against 0.3 MPa pressure thresholds to find the number of pressure panel sectors active during the selected event. Panel activation is then compared with integrated ice loads on the pressure panel sectors (Mayne 2007). The integrated load is calculated by adding all the normalized positive pressure multiplied by effective area of panel sectors.

$$Integrated\ load = \sum[\, y_i\, a_i\, cos(\alpha_i)] \qquad \textbf{[5]}$$

where, y_i is the normalized pressure, a_i is the nominal area of individual sector, and α_i is the angle of sector i with respect to the line of action of ice force.

Panel activation analysis gives relative distribution of peaks in different panel sectors. In a panel activation plot, the number of activated sectors at a certain instant is plotted as a bar. In a typical panel activation plot, Figure 9, three sectors out of eight were activated at 12:09:16 PM, 12:09:17 PM, and 12:09:19 PM; and one or two sectors were active at other times. It can be seen in Figure 9 that the intensity of integrated load follows the pattern of active panels.

A general picture of ice force distribution on different sectors of pressure panels was obtained from the panel activation analysis. However, during calibration of the panels it was found that highly localized ice loads (less than 78 to 150 mm in diameter) were either missed by the panels or loads were over-predicted depending on the location of application. The panels could only provide reliable results when ice exerts uniform pressure to the 500 mm x 500 mm sector (Frederking 1996). This implies that panels interacting with ice edges might give misleading loads and some panels might not be active even though they seem to be active. Hence, a more detailed analysis for pressure distribution is conducted to obtain actual peaks due to ice loads.

In detailed pressure distribution analysis, peaks higher than a predefined threshold are identified only when the peak is supported by at least five more adjacent peaks on the both sides. In other words, the peaks are identified only if the ice load is caused for a minimum of 0.34 seconds. To obtain the peaks of pressure on the panel a computer program was prepared based on a similar program (Tiwari 2005), used to identify events in tiltmeter data. The computer program gives pressure peaks registered by each sectors over time duration as shown in Figure 10. The pressure peaks are comparable with the panel activation plot of Figure 9.

Pressure peaks obtained from pressure distribution analysis are collected for all the selected events in 1998 to prepare a histogram, Figure 11, that gives the relative distribution of pressure peaks over the year. It can be seen that the magnitude of peaks decrease as the intensity of peak pressure increase.

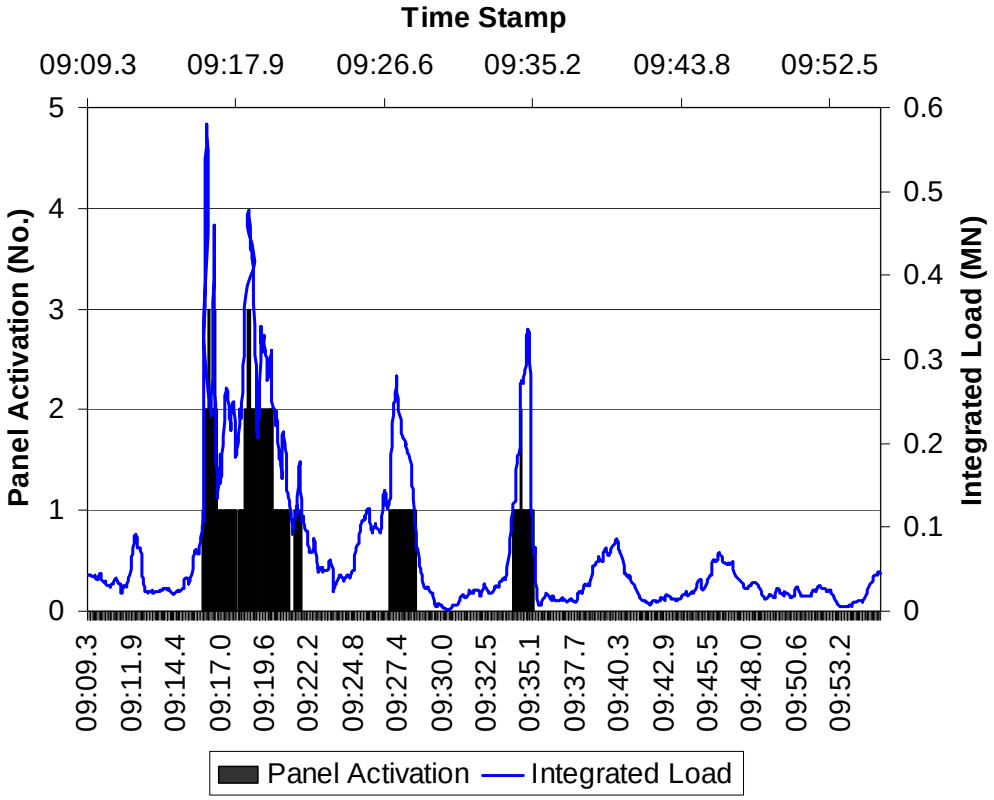

Figure 9. A panel activation plot showing number of active sectors out of eight different analyzed sectors. Integrated load plot is overlaid for comparison.

To obtain the spatial distribution of ice force on panels, correlation matrices are prepared. The correlation matrices give correlation coefficients that indicate the strength and direction of a linear relationship of pressure between the sectors of pressure panel. A sample correlation matrix for an event is shown in Table 1. As expected, the matrix shows positive correlation with adjacent panels although the strength of correlation is not so strong.

Table 1. Sample correlation matrix showing correlation coefficients (IFP sectors 81-86)

Variables	IFP11Z5c81	IFP11Z1c82	IFP12Z5c83	IFP12Z1c84	IFP13Z5c85	IFP13Z1c86
IFP11Z5c81	**1**	**0.056**	0.010	**-0.225**	0.003	**-0.145**
IFP11Z1c82	**0.056**	**1**	**0.161**	**0.177**	**0.055**	0.017
IFP12Z5c83	0.010	**0.161**	**1**	**0.082**	0.033	0.015
IFP12Z1c84	**-0.225**	**0.177**	**0.082**	**1**	**0.234**	**0.279**
IFP13Z5c85	0.003	**0.055**	0.033	**0.234**	**1**	**0.190**
IFP13Z1c86	**-0.145**	0.017	0.015	**0.279**	**0.190**	**1**

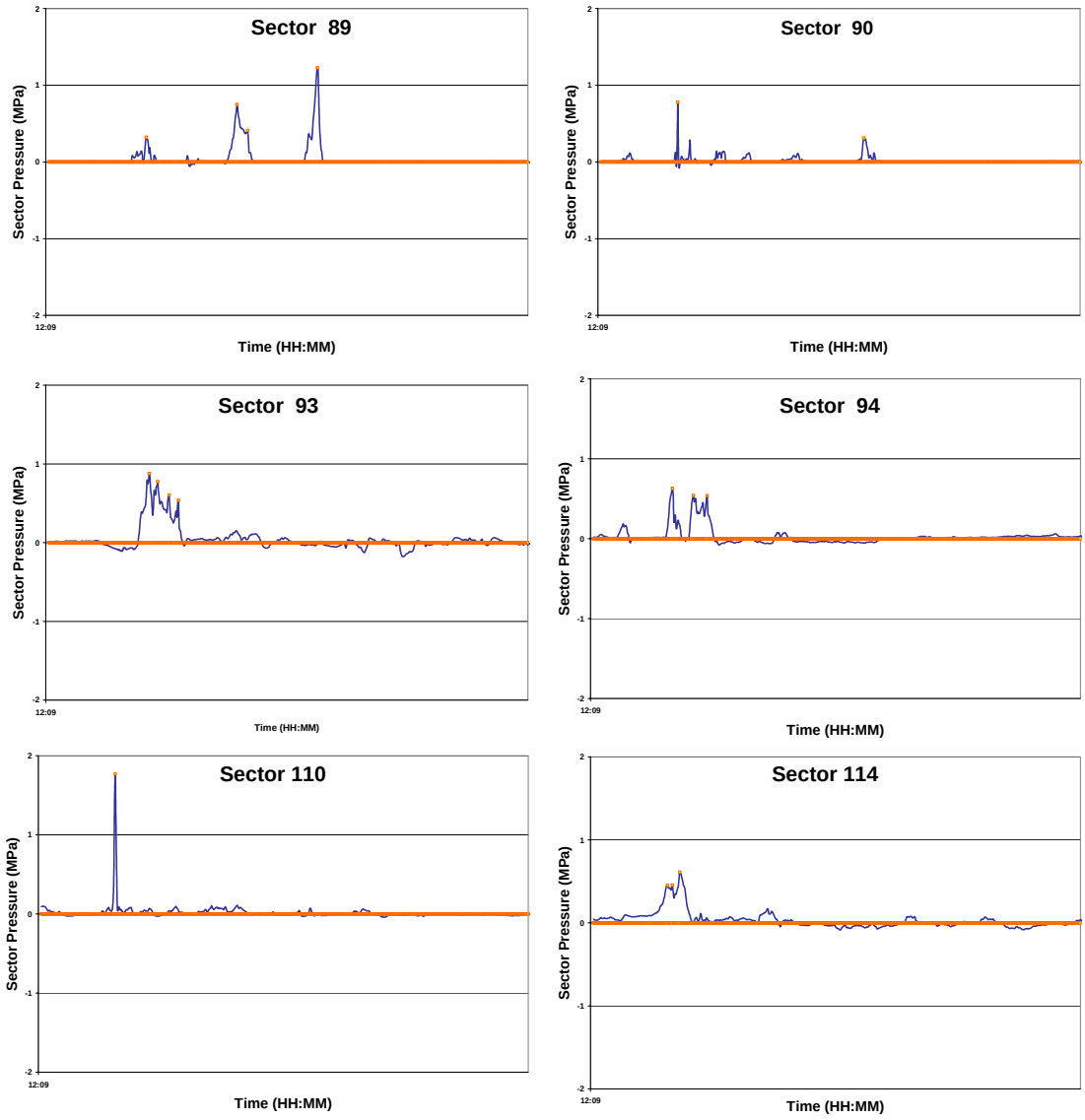

Figure 10. Sample charts showing peaks on sectors 89, 90, 93, 94, 110 and 114 respectively for an event

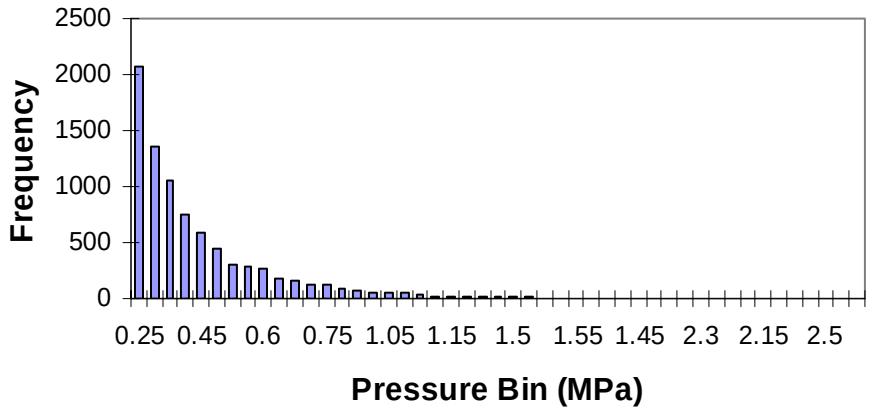

Figure 11. Ice pressure distribution on selected events of 1998

6 Conclusion and Further Works

The analysis of pressure panel data is in its initial stages and hence this paper focuses on procedures of analysis rather than results and final conclusions. Much of the IFP data is still unexplored, however these preliminary analyses have reinforced the initial belief that something new in the field of ice force distribution and ice-structure interaction mechanism can be deduced from the IFP data of the Confederation Bridge.

The analyses discussed were done on one year data and for a limited number of panel sectors. The panel sectors used for the analysis were located near the mean sea level hence covering most of the level ice loads. The analysis can be extended to cover ice loads caused by ride-up and pile-up by analyzing data from panel sectors located in upper portion of the cone (Sectors 1-80, Figure 4). Data from sectors located at the bottom portion of IFP assembly give ice force distribution due to thicker ice and keels of ice ridges. Future IFP data analysis will be extended to include the entire panel so a better ice-load scenario can be obtained. Pressure distribution analysis will be further extended to include spatial and temporal distribution of peaks to compare with panel activation analysis and correlation matrices.

Acknowledgements

The authors would like to acknowledge the support of Strait Crossing Bridge Ltd., Public Works and Government Services Canada, the National Science and Engineering Research Council (NSERC) and Canadian Hydraulics Centre.

Reference

Brown, J. R., Croasdale, K.R. (1997). Confederation Bridge Ice Force Monitoring Joint Industry Project Annual Report - 1997, IFN Engineering Ltd.

Brown, T. G. (2006). Confederation Bridge – An innovative approach to ice forces. The 2006 Annual Conference of the Transportation Association of Canada, Charlottetown, Canada.

Brown, T. G., Bruce, J. R., Croasdale, K.R. (1998). Confederation Bridge Ice Force Monitoring Joint Industry Project Annual Report - 1998, IFN Engineering Ltd.

Bruce, J. R., Croasdale, K.R. (2001). Confederation Bridge Ice Force Monitoring Joint Industry Project Annual Report – 2001, IFN Engineering Ltd. **2001**.

Cheung, M. S., Tardos, G.S, Brown, T., Dilger, T.W., Ghali, A., and Lau, D.T. (1997). "Field monitoring and research on performance of the Confideration Bridge." Canadian Journal of Civil Engineering **24**(6): 75-84.

Daley, C., Tuhkuri, J., Riska, K. (1998). "The role of discrete failures in local ice loads." Cold Regions Science and Technology **27**: 197-211.

Frederking, R. (1996). IFP Calibration Report, National Research Council of Canada.

Jordaan, I. J. (2001). "Mechanics of Ice-Structure Interaction." Engineering Fracture Mechanics **68**: 1923-1960.

Lemée, E., Brown, T. (2005). "Review of ridge failure against the confederation bridge." Cold Regions Science and Technology **42**: 1-15.

Mayne, D. (2007). Level Ice and Rubble Actions on Offshore Conical and Sloping Structures. Department of Civil Engineering. Calgary, University of Calgary. **PhD**.

Riska, K., Uto, S., Tuhkuri, J. (2002). "Pressure distribution and response of multiplate panels under ice loading." Cold Regions Science and Technology **34**: 209-225.

Tiwari, D. (2005). Information Management in Monitoring of the Confederation Bridge for Ice Force Issues. Department of Civil Engineering. Calgary, University of Calgary. **MSc**.

19th IAHR International Symposium on Ice
"Using New Technology to Understand Water-Ice Interaction"
Vancouver, British Columbia, Canada, July 6 to 11, 2008

Experimental studies on anisotropy and strength properties of model ice

Nina Krupina, Alexey Chernov, Vladimir Likhomanov, Pavel Nickolayev, and Evgeny Shakhov

Arctic and Antarctic Research Institute, Saint-Petersburg, Russia
olks@aari.nw.ru; dspi@aari.nw.ru

Abstract

In 2006–2007 AARI performed works according to grant RFFI № 06-08-01288 "Research on failure criteria and fracture resistance of ice at complex laboratory loading". The experiments took place in a big ice tank of AARI capable for obtaining ice of the given properties. Tank water salinity was about 15‰. Air temperature above the ice tank was maintained at the level of –15°C. As a result, lab ice of natural freezing with thickness of 45 cm analogous to the in-situ ice was made. If accounting that temperature regime in the laboratory is rather stable and it completely lacks solar radiation and snow effect the tank-frozen ice becomes more homogenous than the in-situ ice, i.e. the ideal (pattern) conditions for experiments are created. Uniaxial compression tests were conducted on cylindrical samples of 250 mm height and 142 mm diameter taken both perpendicular and parallel to the ice surface. Transverse sizes of samples were at least one order larger than the sizes of ice crystals. The load was applied along the samples' axis. The total amount of test samples comprised 398. During each experiment time-sample force and time-sample strain dependencies were fixed. Primary processing of the test data included plotting of strain-stress diagrams for each specimen which were normalized by maximum values for each sample. The high degree of non-linearity of obtained diagrams was identified. Statistic processing showed that strain-stress diagrams for sea ice can be approximated with high accuracy by an exponential function, whereas distribution of values of power parameters follows the log-normal law.

For more detailed analysis a finite element model of sample loading with account of physical and mechanical ice properties was developed. The obtained results of numerical modeling were used for comparison of the calculated model of strain-stress state and the real failure. Based on comparison an attempt to work out ice failure criteria depending on the sample loading rate and ice temperature was made.

1. Purpose of experiments

The research on ice behaviour at failure is a very difficult task. Since ice represents anisotropic substance which in natural conditions exists at temperatures close to melting temperature its failure is considerably influenced by a number of factors such as temperature, salinity, crystal structure, direction of load application etc. The main purpose of this paper is to identify dependency of failure parameters on loading rate regarding relative stability of values of other external factors.

In spite of the fact that cylindrical and prismatic sample tests present one of the most wide-spread method for definition of compressive strength of ice and many Russian and foreign scientist perform these tests as a rule they are aimed at definition of ice strength in a specific geographical area in given conditions and include testing of several samples. Methodological tests designed for testing several dozens of samples of homogeneous structure in the same conditions have not been conducted before.

The authors of this paper have big experience in performing both laboratory and in-situ experiments targeted at definition of ice strength properties. However, financial support for all field tests was provided by large oil and gas companies and, consequently, all the data are unavailable during 5 years after test performance. That's why this paper contains description and results of tests on research of ice failure characteristics at complex loading of small samples conducted only in the ice tank in Arctic and Antarctic Research Institute (AARI).

2. General description of works

In February 2007 in the framework of grant RFBR[1] № 06-08-01288 "Investigation of crashing parameters and cracking resistance of ice under compound loading in laboratory condition" AARI staff performed a set of experimental works in the large ice tank located in the Institute. Experiments also included:

- ✓ Tests of ice samples at compression parallel and perpendicular to the ice cover surface;
- ✓ Tests of ice strength at large-scale compression;
- ✓ Tests of ice strength at application of cylindrical indenter;
- ✓ Research on characteristics of cracikng resistance;
- ✓ Research on evolution of vertical profiles of temperature, salinity and density of building-up laboratory ice of natural freezing;
- ✓ Modeling of an artificial meltwater pool.

Characteristics of the large ice tank in AARI are given in Table 1. Fig. 1 shows general view of the tank with the ice field prepared for tests.

[1] RFBR – Russian Foundation for Basic Research, www.rffi.ru

Table 1. Characteristics of the large ice tank in AARI

Length	30 m
Width	5 m
Total area of ice field	150 m^2
Depth	1.8 m
Maximum depth	4 m
Minimum air temperature	–20°C
Maximum ice salinity	5 ‰
Maximum ice thickness	55 cm

Figure 1. Large ice tank in AARI

Equipment of the large ice tank in AARI provides laboratory ice of natural freezing similar to sea ice. Water salinity in the tank was 15 ‰. Air temperature in the room with ice tank during ice preparation ranged –14...–17° C. Temperature diagram is presented on Fig. 2. As a result 45 cm thick lab ice of natural freezing similar to sea ice was obtained. Since temperature regime in the laboratory is quite stable and there is no solar radiation and snow influence tank-produced ice was more homogeneous than sea ice because ideal (pattern) conditions for experiments are created.

Even before ice formation a thermistor line was installed which thermistors were placed in such position that each series of measurement includes air temperature above ice surface, ice surface temperature, ice bulk temperature, under ice water layer temperature (for evaluation of warm flow from water). Thermistor line's registration was made once in 3 days. Besides temperature measurements vertical profiles of ice salinity and density were defined, it allowed to fix changes of built-up ice properties.

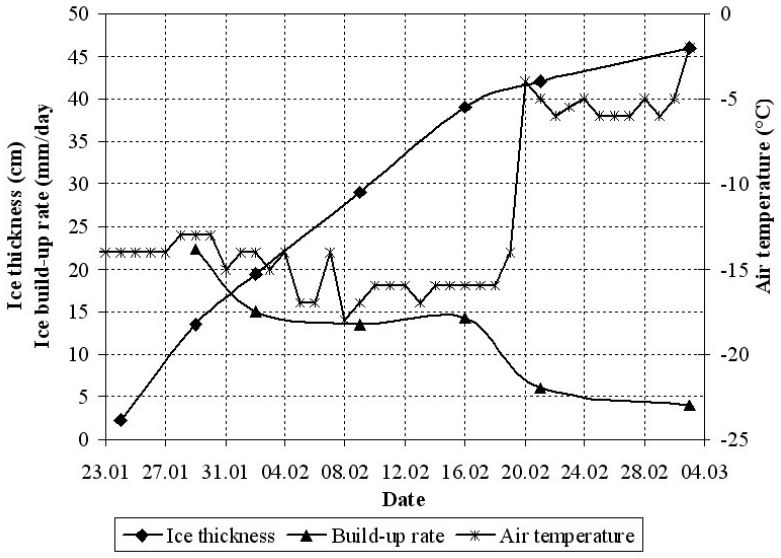

Figure 2. Temperature regime in the large ice tank and ice build-up rate during conduction of experiments

When ice grew up to 40 cm an artificial meltwater pool on its surface was created in order to study behaviour of liquid (frozen artificial meltwater pool) on ice surface.

When ice thickness reached 45 cm experiments for studying ice sample failure mechanisms were performed. Cylindrical specimens of 250 mm height and 100 mm or 142 mm diameter were tested (transversal sample sizes exceeded at least at order the sizes of ice crystals). In order to identify anisotropy of compressive ice properties specimen axis was oriented both parallel and perpendicular to ice cover surface. Samples were loaded along its axis. The specimens perpendicular to direction of growth of the ice cover (i.e. parallel to the ice cover surface) were sampled from several fixed horizons – 10, 22 and 35 cm from the upper ice surface. Unfortunately, crystal structure of ice was not investigated.

This article is devoted only to experiments concerning the mechanism of ice sample failure.

3. Description of equipment

The temperature in ice samples was measured with precision electronic thermometer GTH175/MO manufactured by GREISINGER ELECTRONIC (Germany) (temperature range: from –199.9°C up to +199.9°C, measurement error: not more than 0.1°C). The temperature in sample was determined shortly after its extraction by means of drilling holes in the core and placing the thermometer probe into them. The temperature was measured throughout the entire ice thickness. The temperature was also measured in fragments of ice samples immediately after the test. The salinity was determined by conductivity of melted ice with conductivity meter InoLab Cond 720. The device provides the measurement error not more than 0.1‰. Ice density was evaluated by results of measuring ice sample dimensions and its weighing with electronic

balance TVN-4K manufactured by PetVes Ltd (Russia). The minimal weighing limit of balance TVN-4K was 40 g. The maximal weighing limit equated 4 kg. The measurement error of balance was not more than 2 g. Except a few cases the temperature, density, and salinity of ice were evaluated for all samples, which were tested to determine ice strength.

Figure 3. Equipment for the compression tests: hydraulic press (*1*); pressure gauge (*2*); displacement gauge (*3*); ice specimen (*4*)

Figure 4. Equipment for ice specimen preparation

An upgraded hydraulic press GP-10 manufactured at the Experimental Workshop of the Arctic and Antarctic Research Institute (AARI) was employed for the compression tests. The machine is designed to exert a force up to 98 kN (10 t). The press was provided with a pressure gauge *WIKA ECO-TRONIC* manufactured by *WIKA* (the range of measured pressure 0 to 400 bar, output current 4 to 20 μA, supply voltage 10 to 30 V DC). For measurement of absolute deformations of a sample and, thus, for definition of ice deformation during ice press test the linear displacement gauge DPL-2 produced by *Microsensor technologies*, *Ltd*. (Russia) was installed. This transducer provided recording displacement of the hydraulic cylinder piston. Fig. 3 shows the press prepared for test conduction. Signals from both sensors were applied to the input of multifunctional board *DAQCard-6062E* manufactured by *National Instruments Corporation (USA)* that was installed in a portable computer. The board provided the analog-to-digital transformation of the signal. Principal specification data of the board are as follows: up to 16 input channels, sampling rate up to 500 thousands readings per second, 12 bit resolution. The software of the measuring system, which provided data acquisition and display during the testing, was *VI Logger*, version 1.0.1 package executed in *Measurement & Automation Explorer*, version 2.2.0.3010 (all vended by *National Instruments Corporation, USA)*. The press was calibrated by a certified dynamometer DOSM-3-10. Compression tests were performed at a constant strain rate with recording of loading process by computer.

Since test results considerably depend on accuracy of ice sampling regarding its geometric parameters (sample length and diameter, parallelism of sample ends, squareness of sample ends to its axis) a special stand which allows to prepare samples of the given length and provides squareness of sample ends to its axis was created. The stand was equipped by core latch and

electric chain saw fixed at swinging holder (see Fig. 4). The prepared samples were weighed and measured to define ice density.

3. Temperature, salinity and density of ice samples

Temperature, salinity and density of ice are important factors influencing its strength and deformation properties. These parameters were obtained for the most of tested samples. In Fig. 5 summed up measurement results are given in form of histograms. Despite ideal conditions of ice formation (constant air temperature, constant water salinity, absence of mixing and precipitation etc.) there is a significant scatter of both salinity and ice density values. However, it is mostly connected with variability of ice thickness parameters. To illustrate this fact Fig. 6 shows vertical profiles of ice density and salinity.

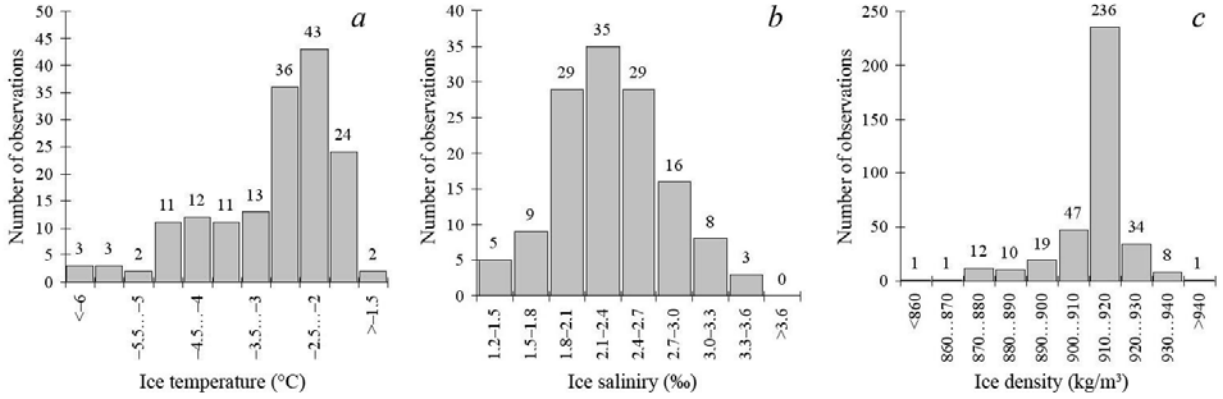

Figure 5. Histograms of ice temperature (*a*), ice salinity (*b*) and ice density (*c*) distribution

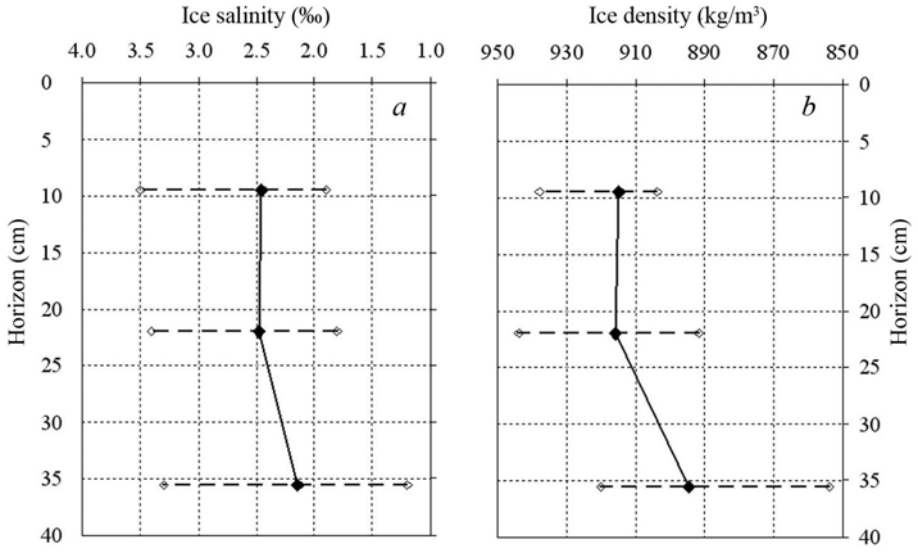

Figure 6. Vertical profiles of ice salinity and density distribution (mean value and variation range within the layer 10 cm)

4. Ice strength measurements results

As it was mentioned above the main purpose of experiment was to study ice failure characteristics in different loading conditions. Therefore, series of tests of small ice samples at compression parallel and perpendicular to the ice cover surface were performed. Summed up results are given in Table 2 and in Fig. 7. Variability of properties along ice thickness is observed: at test parallel to ice cover surface strength limit considerably decreases in direction from the upper to bottom ice surface. One should mention that definition of compressive ice strength was not the main goal of experiments, however, definition of this value showed that despite stable external conditions during ice formation and relatively homogeneous physical ice properties the scatter of values is very big (maximum-minimum values ratio ranges from 3 to 10). It means that in order to evaluate ice failure parameters one cannot use only determined approach but should apply probability methods. In particular distribution of strength limits is well described by Gamma-distribution (Fig. 7). Analogous conformity is usually observed during in-situ data analysis.

Table 2. Generalized data on the strength of ice samples at compression

Parameter	Number of observations	Compressive strength (MPa)			
		Minimum	Maximum	Average	Standard deviation
Compression perpendicular to the ice cover surface	205	0.72	6.97	3.26	1.37
Compression parallel to the ice cover surface	192	0.45	3.01	1.62	0.51
upper layer	64	1.10	3.01	1.90	0.48
middle layer	54	0.60	2.81	1.54	0.42
bottom layer	64	0.45	2.39	1.37	0.45

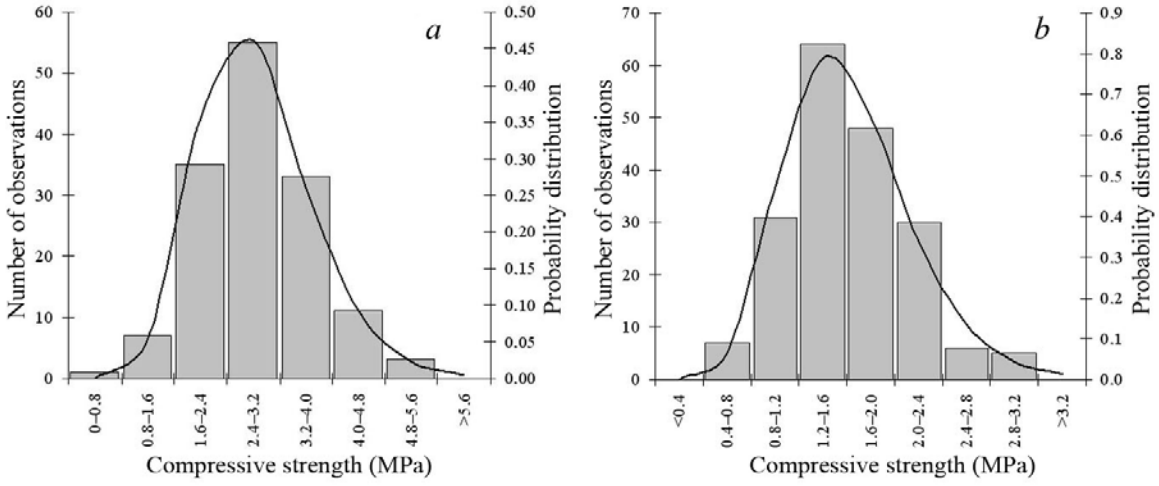

Figure 7. Histograms of distribution of strength limit during ice sample tests at compression parallel (*a*) and perpendicular (*b*) to the ice cover surface and their approximation by Gamma distribution

The main parameter varying during experiments was the loading rate. Fig. 8 shows histograms of relative deformation rates[2] for ice samples compressed perpendicular to the ice cover surface. The majority of tests was carried out at relative deformation rate close to the one required in normative documents for conducting ice research i.e. close to the value 10^{-4} 1/c. However, rate variation ranges from $5 \cdot 10^{-5}$ to $5 \cdot 10^{-3}$.

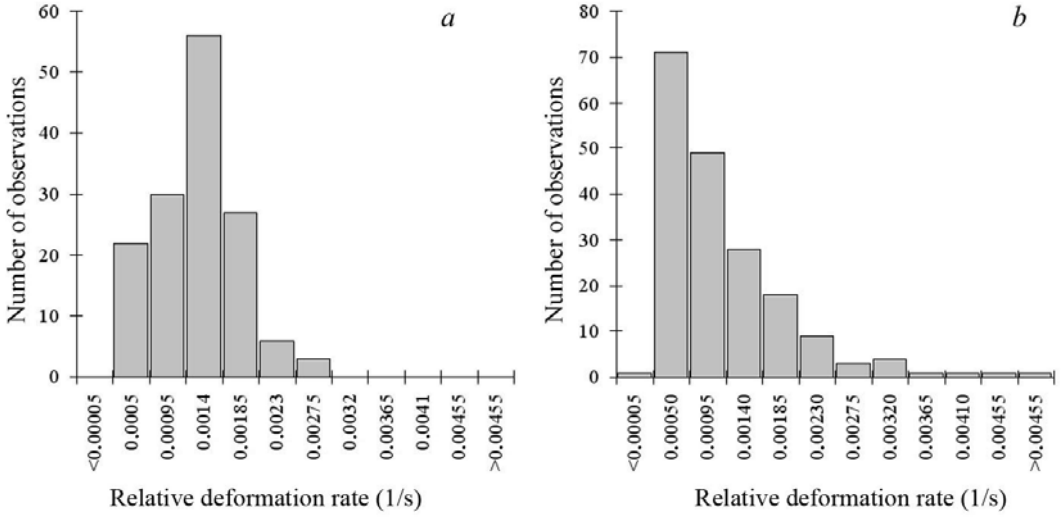

Figure 8. Histograms of distribution of relative deformation rate during ice sample tests at compression parallel (*a*) and perpendicular (*b*) to the ice cover surface

Ice strength is traditionally considered to decrease while loading rate increase. However the conducted tests did not reveal this rule. Fig. 9 presents dependencies of strength limit on deformation rate. It can be observed that there is no correlation between these two values. As a result the following analysis was carried out for the whole selection without division into various ranges of deformation rates.

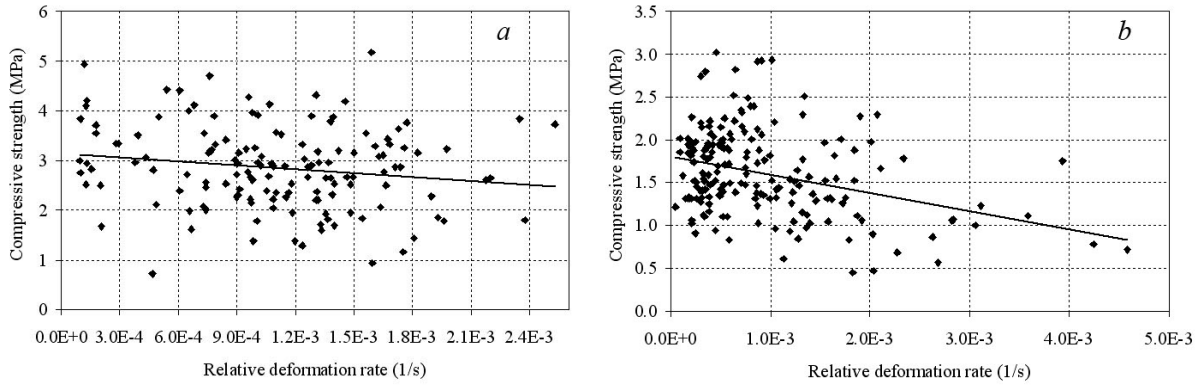

Figure 9. Dependency at compression perpendicular (*a*) and parallel (*b*) to the ice cover surface

[2] In this case moving of press rod corresponds to sample deformation, therefore, relative deformation rate implies moving of press rod-sample length ratio.

5. Working out of failure criterion

To calculate ice impact on engineering objects with the help of finite element modeling one should know in detail material ice properties, in particular, characteristics of ice behaviour during loading. At first sight these characteristics can be obtained by analysis of experimental data acquired during compressive tests of samples.

Using measurement equipment dependencies of the force applied to the sample and moving of press rod on time were obtained for each sample. This article illustrates two examples of sample tests at compression perpendicular to the ice cover surface: № 201 and № 111. Both specimens have diameter of 100 mm and height 250 mm. The temperature of tested samples was –2,8° C, salinity – 2,6 ‰, density – 915 kg/m^3. The relative deformation rate during test formed the main difference between these two samples. For sample № 111 it was $1{,}54 \cdot 10^{-4}$ 1/c, for № 201 – $1{,}33 \cdot 10^{-3}$ 1/s, i.e. there was approximately 10-fold difference. Fig. 10 shows examples of the initial records.

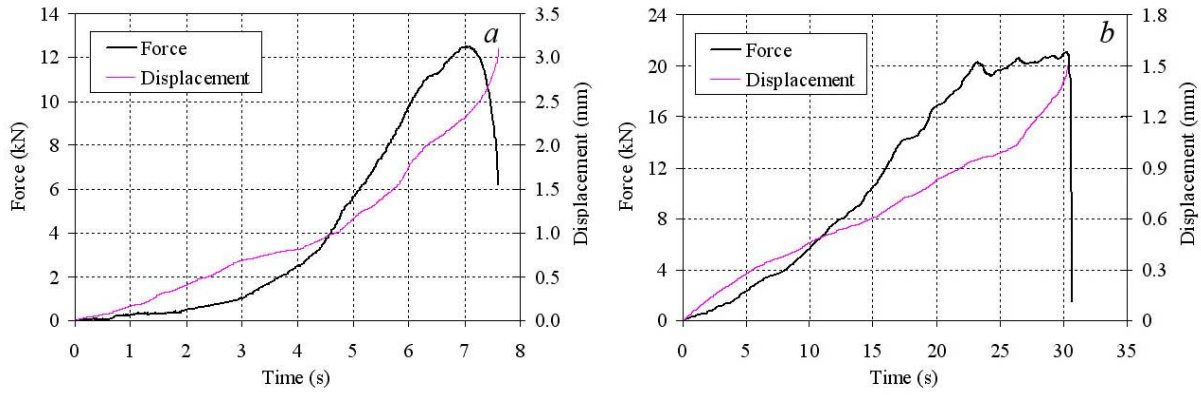

Figure 10. Records of loading process for samples № 201 (*a*) and 111 (*b*)

Since each sample initially has dependencies of the force applied to the sample and moving of press rod on time, rod moving being numerically equal to absolute sample deformation, primary processing of experimental data implied replotting of diagram of dependency of the force applied to the sample and moving of press rod on time in strain-stress diagram. Deformations and stresses were calculated according to the formulae:

$$\sigma(t) = \frac{F(t)}{S};\ \ \varepsilon(t) = \frac{\Delta l(t)}{l}, \tag{1}$$

where $F(t)$ – dependency of the force applied to the ice sample on time; $\sigma(t)$ – dependency of stresses occurred in the sample on time; $\varepsilon(t)$ – dependency of relative sample deformations on time; S – cross section area; l – length of sample.

Due to big variation of values of maximum relative deformations and maximum stresses all strain-stress diagrams were normalized according to maximum values, as a result a set of curves

in dimensionless coordinates was obtained. Fig. 11 presents example of normalized diagrams for samples № 111 and 201.

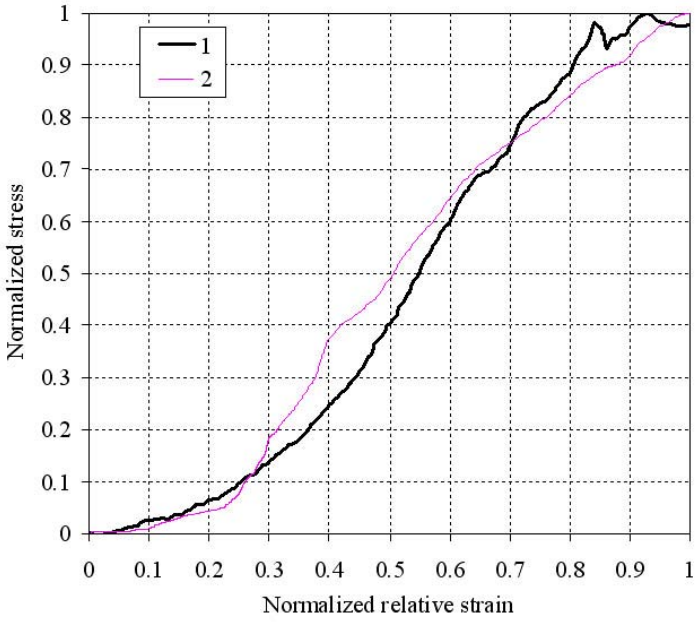

Figure 11. Normalized strain-stress diagrams for samples № 111 (curve *1*) and № 201 (curve *2*)

Even during experimental results primary processing stage high degree of non-linearity of strain-stress diagram was identified and it was defined that the best approximation of dimensionless diagrams is described by the power function $\bar{\sigma} = \bar{\varepsilon}^a$. Using package supplement DataFit the values of coefficient *a* were calculated for each sample (curve). Analysis of the results showed that values of coefficient *a* present random varieties distributed according to the lognormal law. As an average value at compression perpendicular to the ice cover surface dimensionless strain-stress dependency can be described by the quadratic function (average calculated value of coefficient *a* = 2,001). For compression parallel to the ice cover surface average value of power parameter is less than 2 and depends on horizon of ice thickness, namely, upper horizon – 1,586; middle horizon – 1,784; bottom horizon – 1,866.

In conclusion one can say that at first sight of material ice properties description referring to finite element modeling one can recommend to use dependency of stresses $\sigma(\varepsilon)$ on strains in a specimen ε as following:

$$\sigma(\varepsilon) = \sigma_{\max}\left(\frac{\varepsilon}{\varepsilon_{\max}}\right)^a \qquad (2)$$

where $\sigma_{\max}$ – ice strength compressive limit; $\varepsilon_{\max}$ – ultimate sample deformation; *a* – power indicator which value is selected regarding direction of force application to the ice cover surface.

In order to check applicability of the proposed dependency a finite element model was developed which uses experiment-produced non-linear deformation ice characteristics. The model realizes 2D axis symmetrical mode and sample loading in form of upper plane moving.

In many cases characteristic picture of sample failure presents occurrence of vertical cracks (Fig. 12). This type of failure is caused by normal tensile stresses applied perpendicular to vertical plane passing across the sample axis. Numerical modeling reveals the presence of an area of such stresses (Fig. 13), that witnesses quality conformity of strain-stress state of the finite element model and actual nature of sample failure.

Figure 12. Characteristic picture of ice sample failure

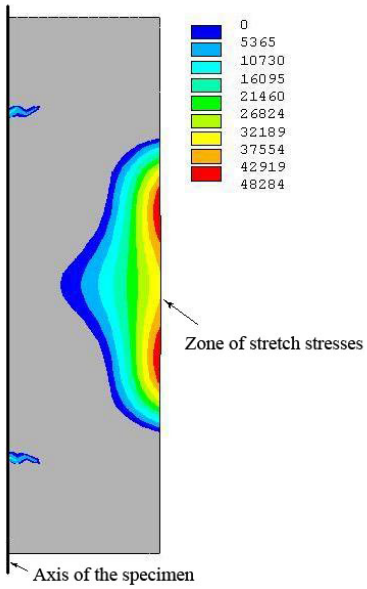

Figure 13. Strain-stress state of the finite element model

6. Results

1. The methodology of conduction of tests on studying of strength ice characteristics in the ice tank in AARI is worked out; the list of external factors (ice temperature, ice build-up rate and, consequently, changing of ice crystal structure, loading rate during ice strength tests etc.) which should be varied during implementation of such woks is defined.

2. It is the first in international practice large-scale experiment on research on ice failure mechanics which was conducted in the laboratory; the unique data allowing to start development of ice failure criteria required for finite element modeling of ice influence on ships and structures were obtained.

3. Mechanic and mathematic mode of ice failure applicable for material ice description at modeling of ice interaction with various objects was worked out, this model can be updated through a series of additional experiments conducted in different conditions.

4. In future joint analysis of lab and in-situ test results is going to be carried out and once should also take into consideration the data obtained in course of large-scale experiments, i.e. experiments for definition of ice strength at compression parallel to the ice cover surface during which not a small sample but a cut ice-cover thickness block of ice is loaded.

19th IAHR International Symposium on Ice
"Using New Technology to Understand Water-Ice Interaction"
Vancouver, British Columbia, Canada, July 6 to 11, 2008

2-Dimensional Edge Crushing Tests on Thick Sections of Ice Confined at the Section Face

R.E. Gagnon and A. Bugden
Institute for Ocean Technology
National Research Council of Canada
St. John's, NL, Canada, A1B 3T5
Robert.Gagnon@NRC.CA
Austin.Bugden@NRC.CA

Abstract

A crushing apparatus incorporating the novel characteristics of the apparatus used by Gagnon and Bugden (2007), and fabricated at 3 times the scale, has been used to conduct crushing experiments on polycrystalline ice, large single crystals of ice and iceberg ice at -10^{o}C. The results confirmed that the behaviours of the different ice types were essentially invariant for the change of scale and that the apparatus functioned as intended at the larger scale, that is, it provided visual data of a 2-D slice of ice during crushing as though it was part of a larger piece of ice. Rectangular thick sections (3 cm thickness) of ice were confined between two thick borosilicate glass plates and crushed from one edge face at a rate in the range 1.5 – 2.5 cm/s using a transparent acrylic platen (3 cm thickness) inserted between the plates. Three identical pressure sensors, of the same type used before, were placed side-by-side to measure pressure across the full breadth of the platen/ice contact area between the glass plates as the samples were being crushed. The pressure data corroborated with the smaller-scale pressure data from the earlier tests and the apparatus served as a test bed to demonstrate that the pressure-sensing technology could function effectively in the side-by-side configuration. This technology will be used to obtain high spatial resolution pressure data during an upcoming full-scale study of ship / bergy bit impacts within the next few years.

Gagnon, R.E. and Bugden, A., 2007. Ice Crushing Tests Using a Modified Novel Apparatus. Proceedings of POAC-07, 235-244.

1. Introduction

Various techniques have been utilized to gain insight into ice crushing processes. Such knowledge is essential for reliable assessment of ice/structure interactions forces and pressures that are needed for design and operational purposes. Following on from the successful tests using the first apparatus incorporating this method (Gagnon and Bugden, 2007) we present results from a larger apparatus (3 times the scale). The purpose was to both demonstrate the effectiveness of the method and to study the behaviour of ice, at the larger scale. The experiments with this larger apparatus also provided the opportunity to test multiple pressure sensors, in a side-by-side configuration, that were successfully used singly in the smaller apparatus. These types of experiments provide rich visual observations of ice crushing processes coupled with in situ pressure measurements.

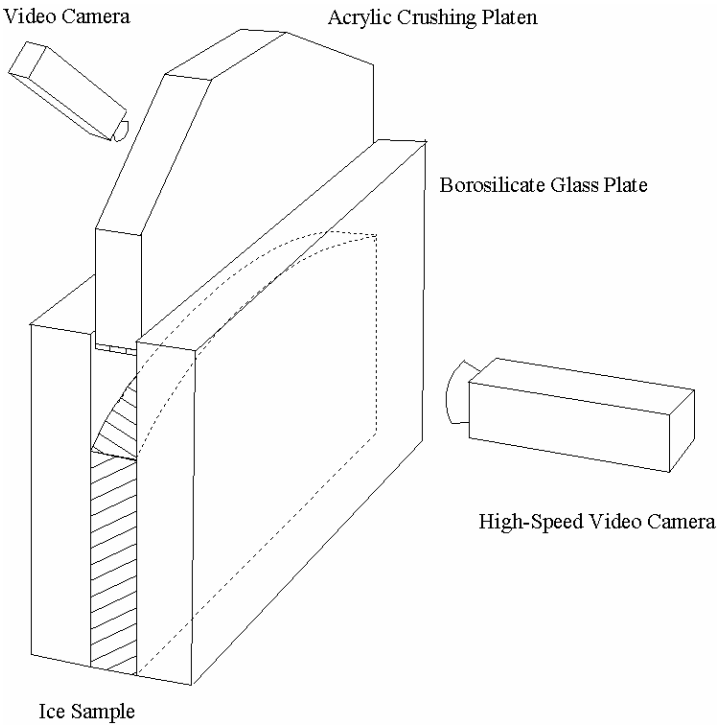

Figure 1. Conceptual schematic of the ice crushing test method and present configuration.

2. Apparatus and Setup

Figure 1 shows the concept for these experiments and has been described in detail for the smaller scale apparatus (Gagnon, 2004; Gagnon and Daley, 2005; Gagnon and Bugden, 2007). The ice is confined between rigid flat transparent plates and crushed at one of its edges by an acrylic platen inserted between the plates. Visual data are acquired by side-viewing using a high-speed video camera (1000 images/s) and from above through the transparent platen itself using a regular video camera and in one instance using a moderately high-speed video camera (240 images/s). Figure 2 shows the present 3 x scale apparatus mounted in the test frame.

Figure 2. Crushing apparatus and sample mounted in the test frame with the high-speed camera in the foreground.

Thick steel plates, with a rectangular port for viewing, hold transparent thick borosilicate glass plates in place that serve to confine the ice laterally during tests. Figure 3 shows the acrylic crushing platen with the three pressure sensing strips attached and how they function. The calibration for the pressure sensing strips has been given in Gagnon and Bugden (2007).

Tests were conducted at -10^{o}C with the crushing platen moving at nominal speeds in the range 15-25 mm/s.

3. Test Using a Single-Crystal Sample

Figure 4 shows an image from one of the crushing experiments using a single-crystal sample of ice, where the c-axis is in the plane of the image and vertically oriented. The crushing rate was nominally 17 mm/s. Various aspects of the test are indicated to assist the reader in following the description below. Figure 5 shows a series of six images from the high-speed video record of the test on the single-crystal sample. Figure 6 shows the corresponding load record where the points at which the images were acquired are indicated.

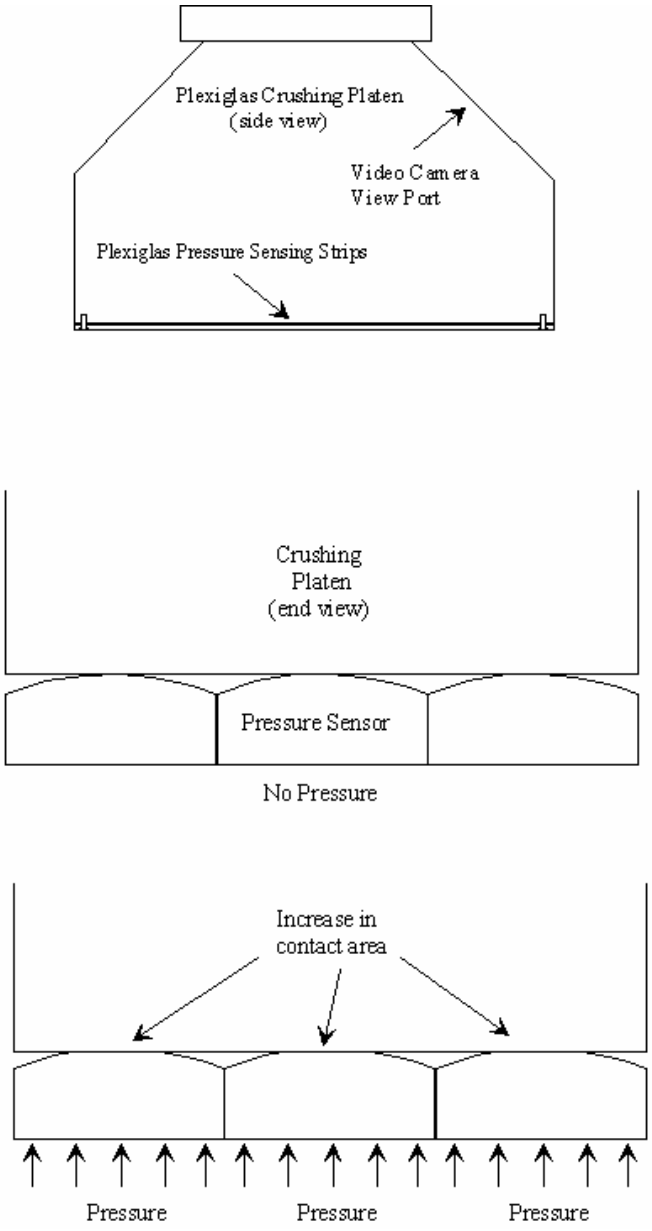

Figure 3. Schematics of the crushing platen (top) and pressure sensor working principle (middle and bottom).

The first image in Figure 5 shows some cracking behavior as load is accumulating, however the cracks have not extended far enough to create spalls that would result in a reduction in contact area and load. High pressure (50-70 MPa) exists throughout the contact zone. The second image was taken after the first spalling event and the spall debris is seen at the left side of the contact zone. The corresponding drop in load is evident in the load record (Figure 6). The third image was taken after the second spall event, to the right of the central contact zone. The ice in the central peak, while somewhat fractured, is still relatively intact and experiences high pressure at the platen interface, while the shattered spall debris on either side of the peak can only support low pressure (< 6 MPa) since it is not confined. The fourth image shows the ice just prior to a very large spalling event that shatters most of the

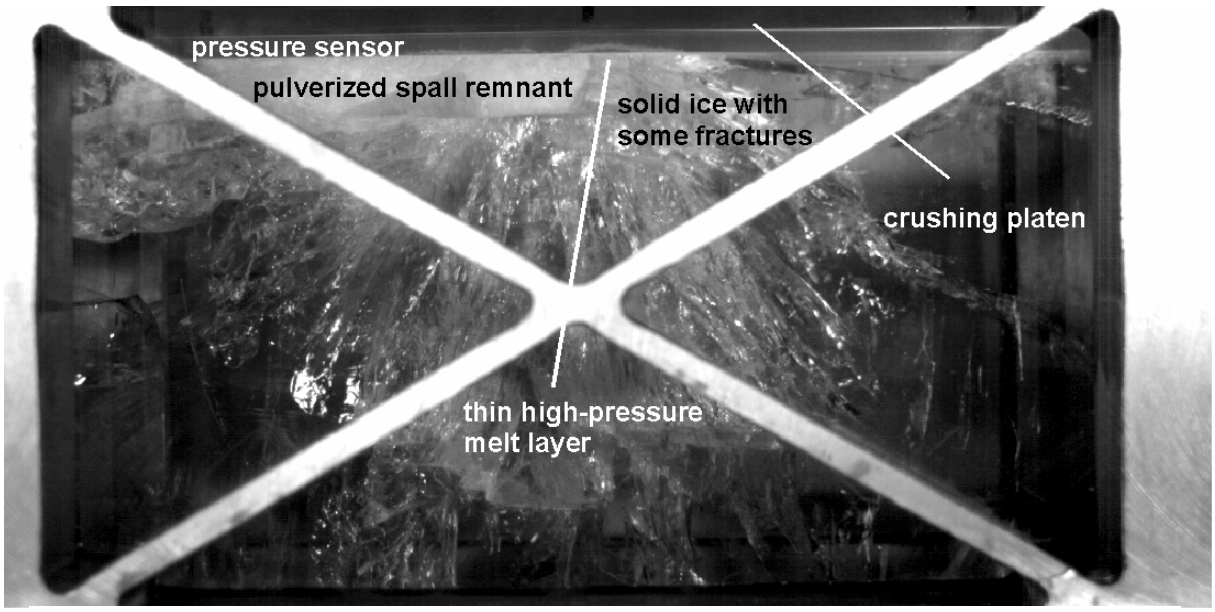

Figure 4. Image from the high-speed video record of a test on a single-crystal ice sample indicating various aspects of the apparatus and ice behavior. The ice slab is in the plane of the image as shown in Figure 1.

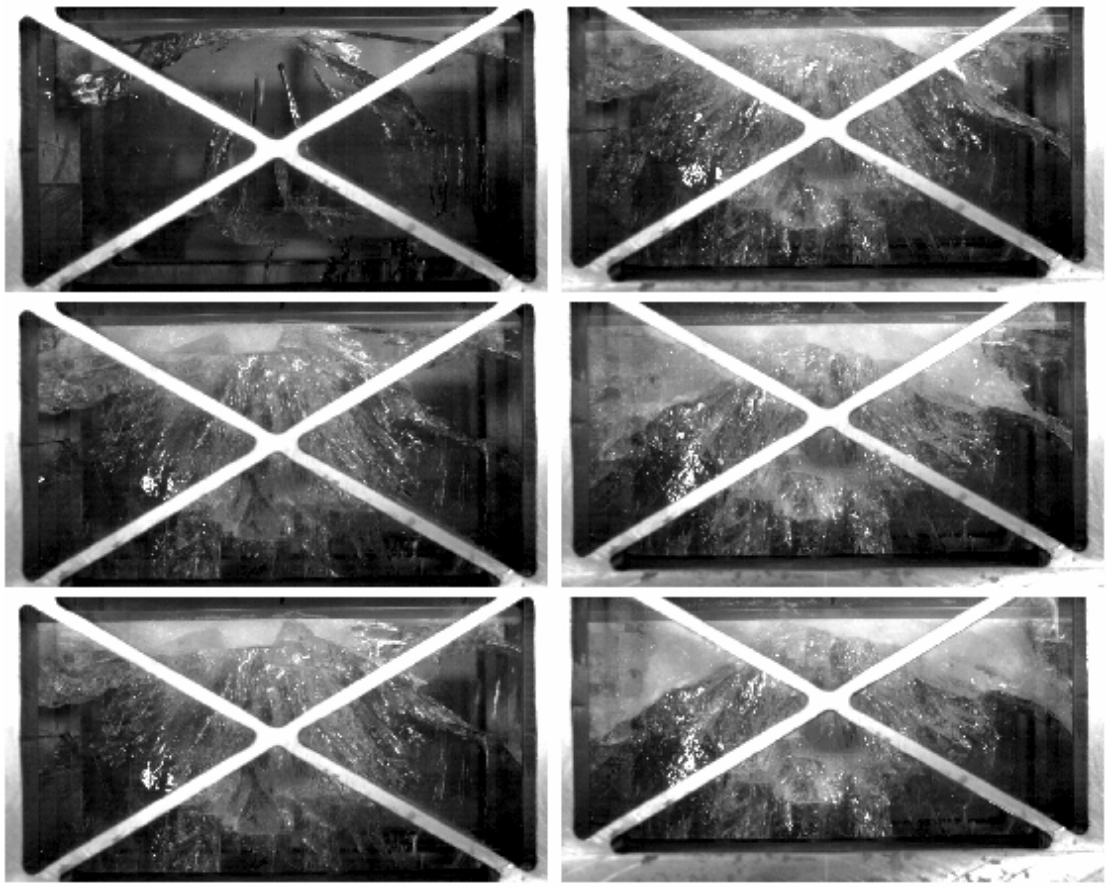

Figure 5. Sequence of high-speed digital images (from top left to bottom right) of a test on a single-crystal ice specimen. Figure 6 shows the corresponding points in time on the load record for the images.

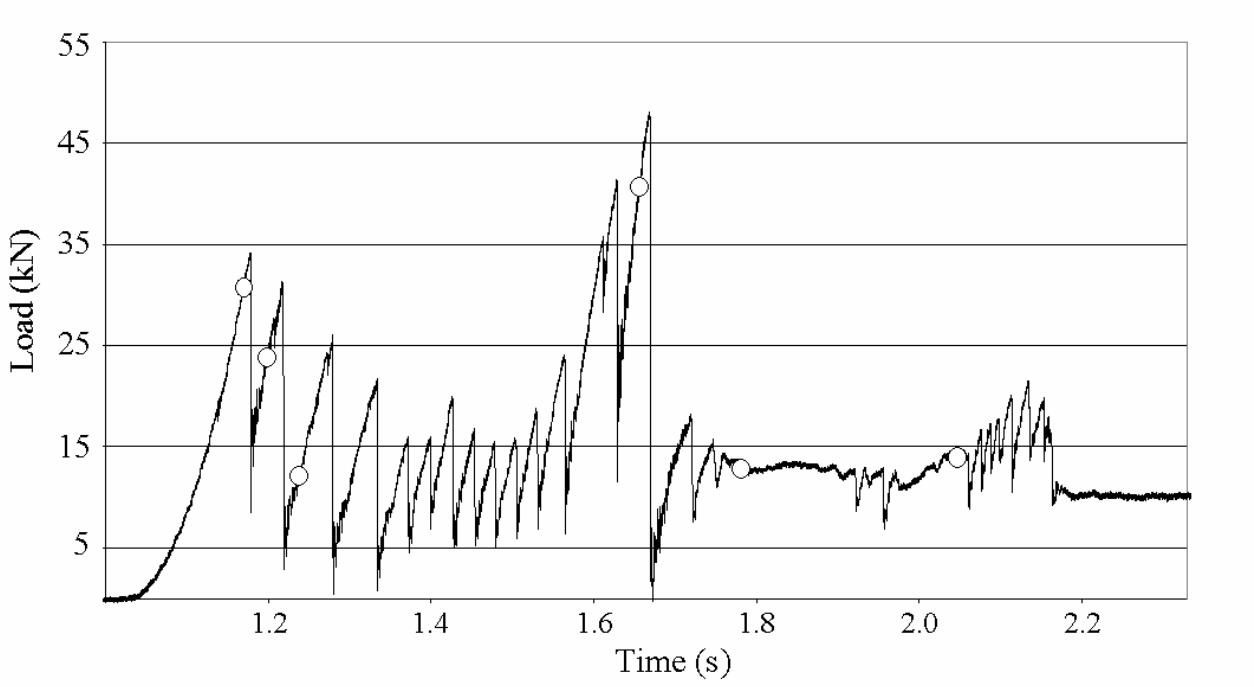

Figure 6. Load record for the test shown in Figure 5 with markers (open circles) corresponding to the six images.

so this mushy contact leads to a period of extrusion where no sawteeth are evident in the load record (i.e. the smooth region just following the time when image 5 was taken (Figure 6)). The final image was taken just prior to the onset of a series of spall induced load drops that start when fresh intact ice pushes up through the mushy material and makes contact with the platen.

Figure 7 shows two images from the downward-looking view through the transparent crushing platen. For most tests a regular video camera was used however for this test a moderately high-speed camera (240 images/s) was used (Sony HDR-FX7). The images show the output from the three pressure sensing strips overlaying the view of the ice behaviour. The two images show the sensor and ice behaviour just prior to (left image) and immediately after (right image) the second spall event in Figure 6 where roughly half of the intact ice spalls away from the upper region of ice/platen contact. The time span between the images is 1/120 s. We note in one region that solid intact ice fully spans the width of the space between the borosilicate plates, as is the intention of the apparatus design. We also note in the left image that the pressure sensors each show near full width contact, indicating pressures in the 50 - 70 MPa range, and that the pressure sharply diminishes to much lower values above and below the intact ice region where ice is pulverized. The widths of the pressure sensor contact indicators in the right image for the intact ice are less than the corresponding widths in the left image only because a spall event and load drop has just occurred. This is due to inertial effects of the ice/apparatus system during the rapid load drop. As load accumulates during the ascending portion of the subsequent load sawtooth (3rd sawtooth, Figure 7) the pressure sensor contact widths eventually increase to similar values as shown in the left image.

Experiments were also performed using lab-grown polycrystalline ice and iceberg ice. Similar behaviours were observed to that of single crystal samples but with generally lower load values and fewer spalling events. These characteristics were also observed in the tests using the smaller scale apparatus and have been discussed before (Gagnon and Bugden, 2007).

Figure 8 shows an image from the high-speed video record of a test using polycrystalline ice. The crushing rate was nominally 25 mm/s. The characteristic shape of the contact zone is evident, that is, a relatively intact central region (in spite of many intergranular cracks), with pulverized ice at the sides. An image from the downward looking regular video camera is inset to the approximate location and scale. It shows high pressure in the central intact ice region and low pressure at the sides as expected. The ability of the polycrystalline ice to maintain its strength and intactness even with many small internal cracks at grain boundaries is remarkable and was previously noted in the experiments with the smaller apparatus (Gagnon and Bugden, 2007).

Figure 9 shows a similar image to that in Figure 8 but in this case iceberg ice was used. The crushing rate was nominally 25 mm/s. The features of the contact zone and pressure distribution are similar to that of Figure 8 and are basically the same as that observed for iceberg ice tested in the smaller apparatus (Gagnon and Bugden, 2007). A noteworthy comparative feature of Figures 8 and 9 is that the pressure sensors indicate that more load is borne by the pulverized ice to the sides of the intact ice in the center of the contact region in Figure 9 than in Figure 8. This is probably associated with the fact that the peaked shape of the intact ice has shallower angles in the case of the iceberg ice, i.e. the pulverized ice is somewhat more confined. The capacity of the pulverized material to support substantial pressure and load, depending on its degree of confinement, was observed and discussed by Gagnon and Bugden (2007).

Figure 7. Images from the downward-viewing camera just before (left) and just after (right) the second spall event in Figure 6. Each image is 3 cm wide.

Another aspect that was characteristic of all experiments was the production and flow of melt from the high-pressure contact zones. The melt could be seen wetting the surrounding pulverized ice and was also evident running up the sides of the crushing platen in the thin space between the platen and the glass plates where it refroze to the glass as a very thin layer of ice (Figure 10). In certain instances, near the end of some tests, liquid could also be seen squeezing up between the

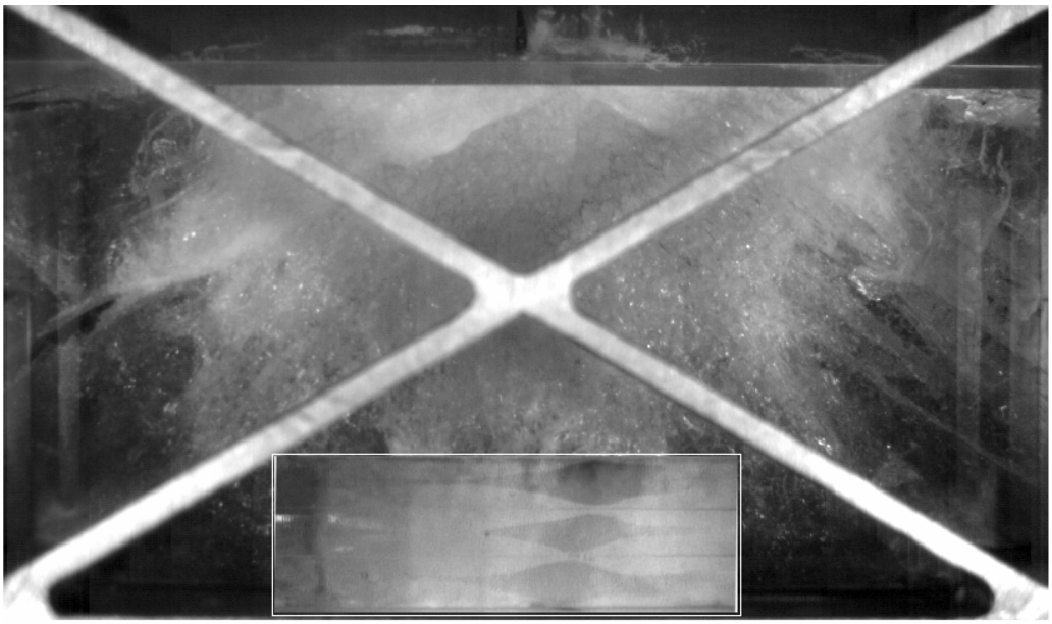

Figure 8. An image from the high-speed video record of a test using lab-grown polycrystalline ice. A corresponding image of the platen/ice contact and pressure sensors from the top-viewing camera is inset to the approximate scale and location.

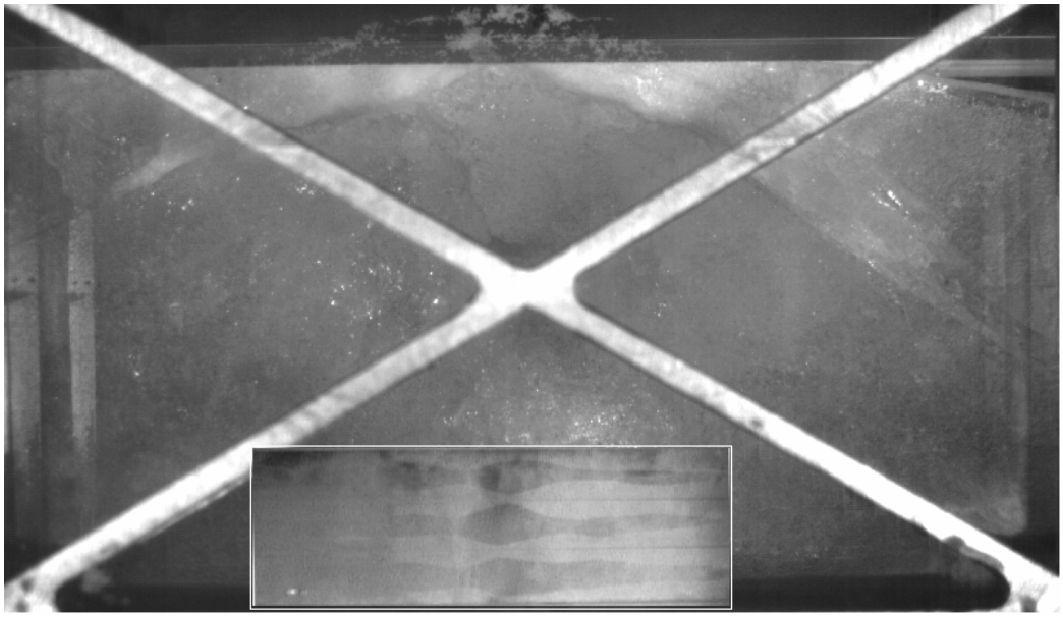

Figure 9. An image from the high-speed video record of a test using iceberg ice. A corresponding image of the platen/ice contact and pressure sensors from the top-viewing camera is inset to the approximate scale and location.

pressure sensor strips and into the thin space between the strip's gently curved surfaces and the flat head of the crushing platen. The production and flow of the melt has been explained and discussed extensively in previous studies (Gagnon, 1994a; Gagnon, 1994b; Gagnon, 1999).

All of the behaviours observed in these tests have been seen and discussed before in the context of the smaller apparatus. If anything was different in the behaviour of ice in the large apparatus it was possibly that there were longer episodes of repetitive spalling events (sawteeth) than with the smaller setup. This was most evident in the tests with single crystals. This implies that for the case of the single crystal samples, at least, that the larger scale somehow reduced the number of times that the whole contact region of intact ice was shattered and pulverized leading to mushy sections in the load records rather than sawteeth.

Not surprisingly, loads using the larger apparatus were roughly 3 to 5 times that for tests using the smaller apparatus.

Figure 10. A thin layer of refrozen melt left on the inside of one of the borosilcate glass plates following a crushing test. The thin ice layer is visible just above the X shape in the photo and extends towards the upper right. The changing horizontal location of the ice layer on the glass from top to bottom is a rough 'strip-chart' record of the horizontal position of the high-pressure intact ice zone at the platen/ice interface as the test progressed.

4. Conclusions

2-D edge crushing experiments using a larger scale apparatus than the original one have shown essentially the same ice behaviours as the former smaller scale apparatus for tests with various types of ice. The pressure sensor technology functioned properly when configured in a side-by side orientation. Consequently the technology will be used on the front surface of a large impact panel intended for head-on ship/bergy bit collisions in a future field study.

5. Acknowledgements

The authors would like to thank the Program of Energy Research and Development (PERD) and IOT for their financial support of this research.

6. References

Gagnon, R.E., 1994a. Generation of Melt During Crushing Experiments on Freshwater Ice. Cold Regions Science and Technology, 1994, Vol. 22, No. 4, 385-398.

Gagnon, R.E., 1994b. Melt Layer Thickness Measurements During Crushing Experiments on Freshwater Ice. Journal of Glaciology, 1994, Vol. 40, No. 134, 119-124.

Gagnon, R., 2004. Side-Viewing High-Speed Video Observations of Ice Crushing. Proceedings of IAHR 2004, St. Petersburg, Russia, Vol. 2, 289-298.

Gagnon, R. E., 1999. Consistent Observations of Ice Crushing in Laboratory Tests and Field Experiments Covering Three Orders of Magnitude in Scale. Proceedings of the 15th International Conference on Port and Ocean Engineering under Arctic Conditions, POAC-99, Helsinki, Finland, Vol. 2, 858-869.

Gagnon, R.E. and Bugden, A., 2007. Ice Crushing Tests Using a Modified Novel Apparatus. Proceedings of POAC-07, 235-244.

Gagnon, R.E. and Daley, C., 2005. Dual-axis video observations of ice crushing utilizing high-speed video for one perspective, Proceedings of POAC 2005, Potsdam, New York, Vol. 1, 271-282.

19th IAHR International Symposium on Ice
"Using New Technology to Understand Water-Ice Interaction"
Vancouver, British Columbia, Canada, July 6 to 11, 2008

High-Speed Imaging of Mechanisms Responsible for Sawtooth Cyclic Loading During Ice Crushing

R.E. Gagnon
Institute for Ocean Technology
National Research Council of Canada
St. John's, NL, Canada, A1B 3T5
Robert.Gagnon@NRC.CA

Abstract

High-speed imaging (30,000 images/s) has been used to observe the behavior of mono-crystalline freshwater ice during crushing at –10°C. The ice contact zone consisted of an intact high-pressure central area surrounded by pulverized spall debris and partially refrozen melt. A sawtooth pattern was evident in the load record, similar to that observed in other ice crushing and indentation studies. The spalling behavior that is responsible for any particular load drop in the load record was found to be caused by the presence of small stable fractures in the high-pressure intact ice zone that were created during the preceding spall event and associated load drop. The small fractures are roughly centered in the intact ice region and this explains why the magnitude of the load drops is typically half the prior load value. The removal of ice from the intact ice zone by the viscous radial flow of a thin layer of melt has been described before (Gagnon, R.E. 1994. Melt Layer Thickness Measurements During Crushing Experiments on Freshwater Ice. Journal of Glaciology, 1994, Vol. 40, No. 134, 119-124). This process explains why the small fractures are roughly centered in the high-pressure contact zone. There the flow is stagnant and less ice has melted, relative to the non-central areas, and this leads to high non-uniform stresses in the ice that cause the fractures.

1. Introduction

Ice crushing and indentation has been studied intensively over the past few decades. Some characteristics of the ice behavior recur during field and lab studies and at various scales (Gagnon, 1999). One intriguing aspect has been the apparent cyclic sawtooth pattern in load that has been described frequently and attributed to spalling behavior. Figures 1 and 2 show examples, from earlier studies, of the sawtooth load behavior, and associated pressure and displacement data, for lab and field experiments respectively. Aspects of the sawtooth patterns, such as their regularity, have not been addressed in any detail so far and no explanations for the size of spalls, and the associated magnitude of the load drops, have been offered. An explanation is provided here based on observations of ice crushing behavior from images acquired at very high speed (30,000 images per second).

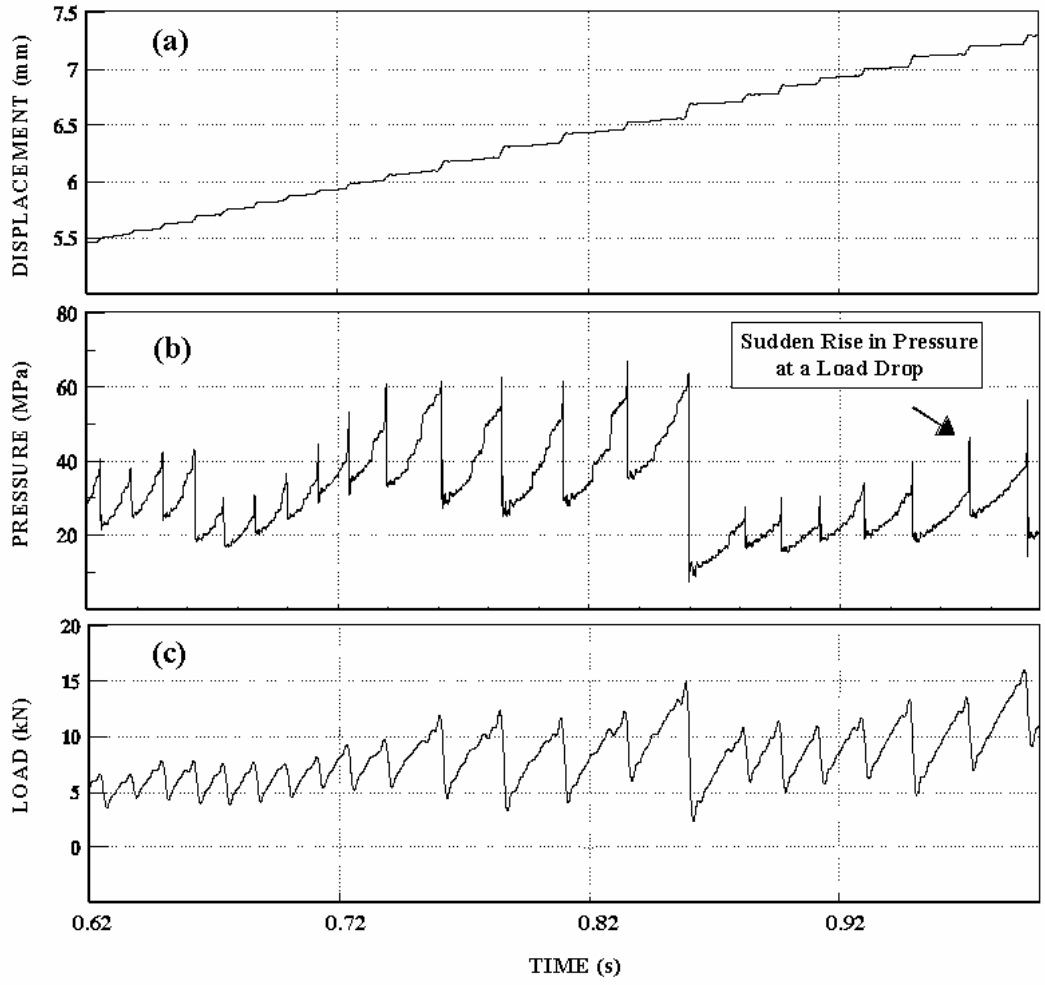

Figure 1. Sections of the displacement (a), pressure (b) and load (c) data from a test using a crushing apparatus similar to the one in this study. The sudden rises in pressure in (b) at the load drops correspond to the spikes in pressure on the remaining ice when a spall breaks away from the contact zone. (From Gagnon, 1994)

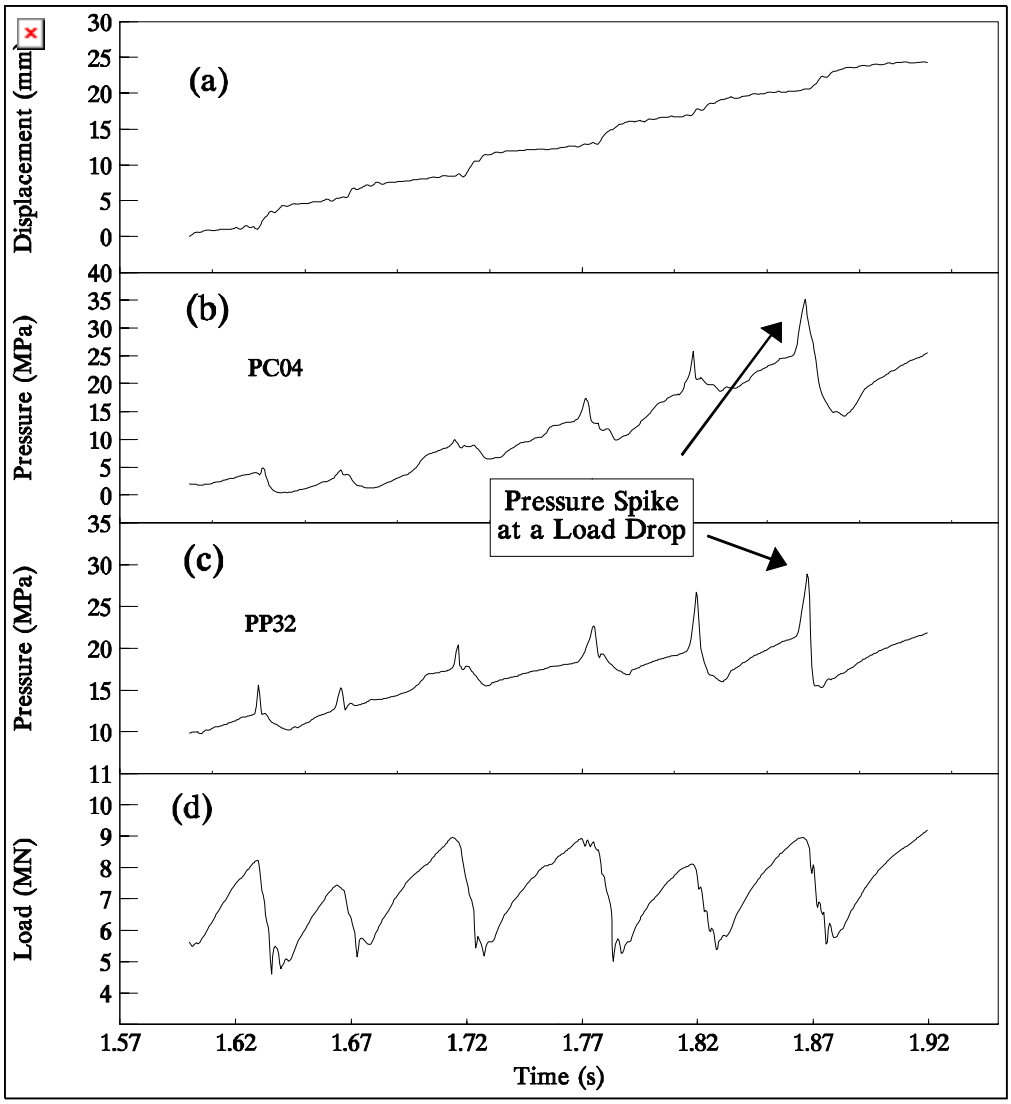

Figure 2. Time series of displacement (a), piston/diaphragm pressure sensor output (b), PVDF pressure sensor output (c) and load (d) for a segment of test Tfr4. The displacement data has not been corrected to account for the ice compliance. The correction would make the gently sloping plateaus almost horizontal. (From Gagnon, 1998)

2. Apparatus and Test Parameters

Figure 3 shows the test setup, where the ice, confined in a rigid holder, is pressed against a transparent Plexiglas™ crushing plate (5 cm thickness) in a testing frame as high-speed images are acquired from the opposite side of the plate. The ice sample was mono-crystalline with the c-axis oriented vertically. The specimen was initially a block 13 cm x 13 cm x 10 cm with the top trimmed to the shape of a truncated pyramid with a slope of about 40°. Details of the procedure for preparing the ice specimen and mounting it in the ice holder are given by Gagnon (1994). A single crystal was used primarily to avoid intergranular cracking that would normally obscure visual observations. The ice holder has been described before and the method of growing large

single crystals (Gagnon, 1994). The test was carried out at -10^{o}C and the actuator was moving at a nominal rate of 32 mm/s. The load data for the test were acquired at 20,000 samples per second.

3. Test Results and Discussion

Figure 4 shows an image acquired during the crushing test. The figure is annotated to illustrate features of the ice behavior to assist the reader in understanding the discussion that follows. The region of the image showing white material surrounding a central dark region corresponds to the area of contact where the top of the pyramid-shaped ice sample is being crushed against the Plexiglas crushing plate.

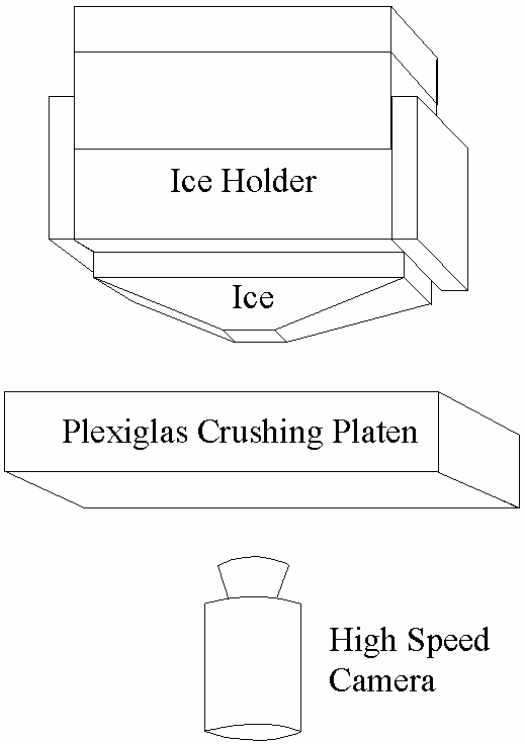

Figure 3. Crushing apparatus with camera for viewing the contact zone during experiments.

Figure 5 shows 6 images from a portion of the high-speed video record of the test. The camera (Fastcam-APX RS) was running at a capture rate of 30,000 images per second and each image was 256 x 256 pixels in size, the maximum allowable resolution for the camera at this image acquisition rate. The images run from the top left to the bottom right of the figure and are not consecutive but rather were chosen to show relevant features of the ice behavior, particularly during load drop events that are caused by spalling. Image 2 in the figure is the same as that shown in Figure 4. The particular locations of the images in the time series of the load record of the test are shown in Figure 6. The oscillating pattern in the load record between the load drops is elastic resonance in the ice/apparatus system, primarily due to flexure of the Plexiglas crushing plate.

The first image shows the ice contact just prior to a spall event, (i.e. designated Spall Event 1). The dark irregular shape somewhat to the left of center shows the region of ice / crushing plate contact where the ice is essentially intact and where the pressure is high (roughly 70 MPa (Gagnon, 1994)). Surrounding this is white material that is a mix of pulverized spall debris and partially refrozen melt from earlier in the test. The melt was created in the high-pressure region by a process that has been described before (Gagnon, 1994). Essentially a thin layer of liquid flows under pressure radially out of the high-pressure zone and this generates heat that causes melting and more liquid flow (Figure 7). The flow rate is much faster during the load drops than on the ascending portions of the sawtooth load pattern. It is noted that while the nominal speed of the crushing plate towards the ice is 32 mm/s, the maximum actual relative speeds of the ice moving towards the plate during periods when load increases and at load drops are around 0.019 m/s and 0.3 m/s respectively, due to the compliance of the ice/apparatus system (1.4×10^{-8} m/N). Images 2 and 3 show the formation of small stable cracks in the dark intact ice zone and

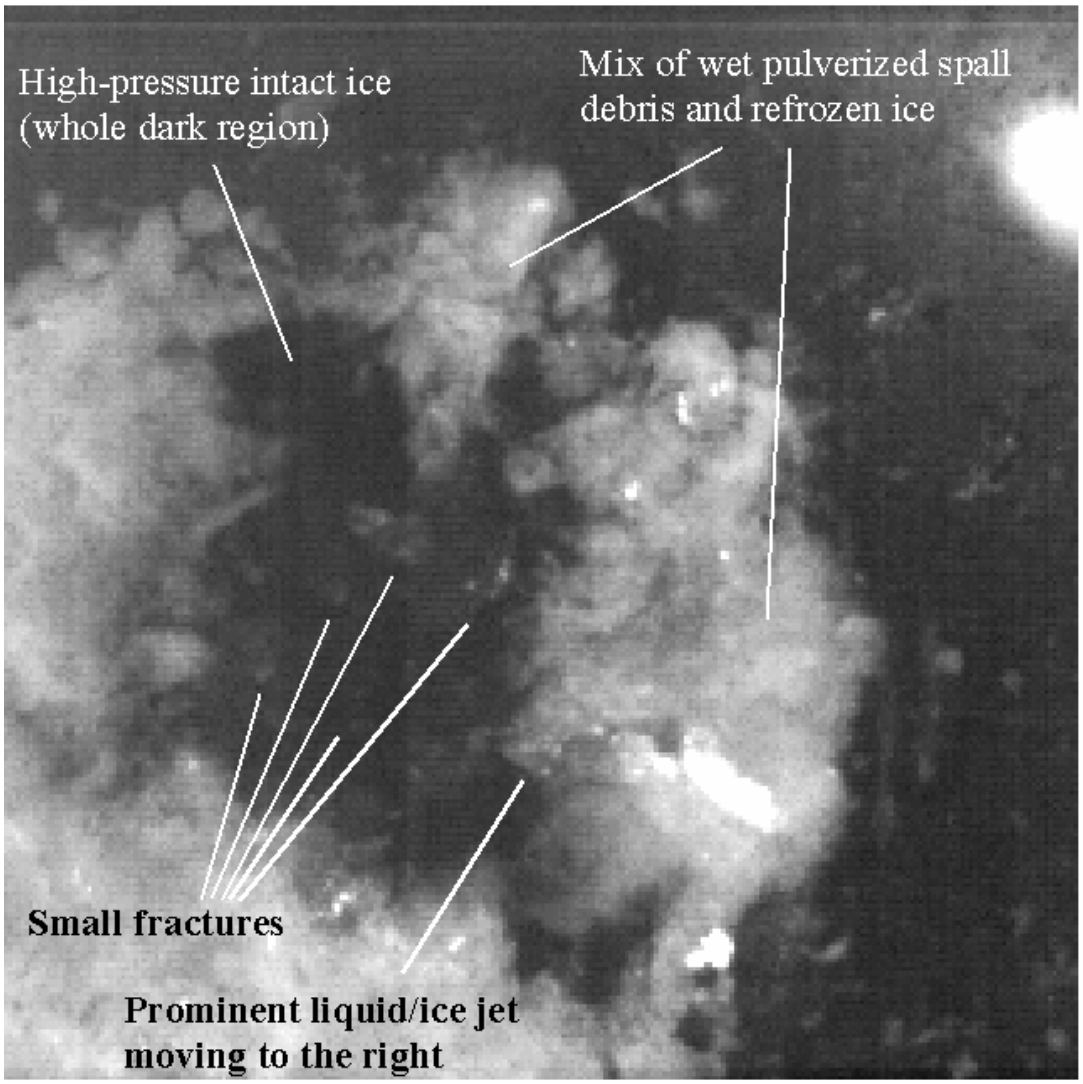

Figure 4. Image from the high-speed video record indicating various aspects of the ice behavior. The image is 43 mm wide.

production of fresh white material around the periphery of the dark zone due to the rapid exit of refreezing liquid and pulverization of the new spalls. This behavior is much easier to see when viewing the actual high-speed video record of the test, such as the movie segments shown at the IAHR 2008 session (contact author for information). Figure 4 serves as an aid to identify these aspects. The rapid exit and refreezing of melt is particularly evident in the form of a liquid/ice jet indicated in the figure. In this case, the velocity of the thin layer of ice produced indicates a lower-limit estimate for the liquid flow rate that produced the ice of about 15 m/s during the load drop. The thin piece of ice moving to the right in Image 3 of Figure 5, that shows as the bright object in the liquid/ice jet region, was used for the velocity estimate. Later in the high-speed image record the flat piece of ice was observed to be extremely thin (on the order of one image pixel, corresponding to 0.17 mm) after it had rotated somewhat to give an edge-on view while moving to the right. At another instance in the high-speed image record an estimate for an even higher lower-limit of fluid flow speed (about 40 m/s) at load drops was made. These high fluid

flow and freezing rates are extraordinary and can only be observed with a camera that has at least the speed and resolution of the one used here. The rapid melt and fluid flow stops at the

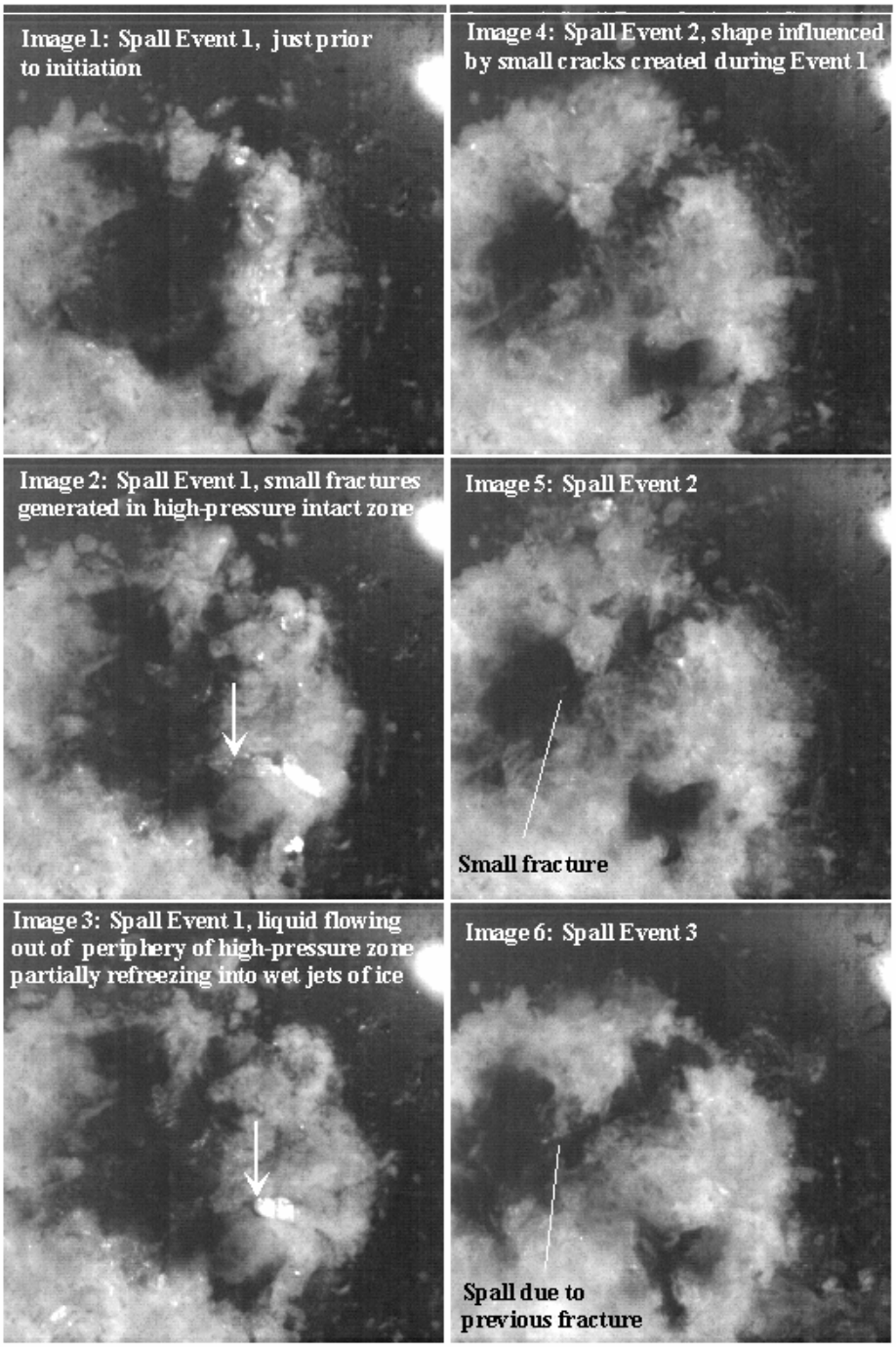

Figure 5. Images from the high-speed video record indicating various aspects of the ice behavior. The arrow in images 2 and 3 is a marker that follows the edge of a freshly frozen thin piece of ice as it moves to the right. Figure 6 shows the corresponding points in time on the load record for the images.

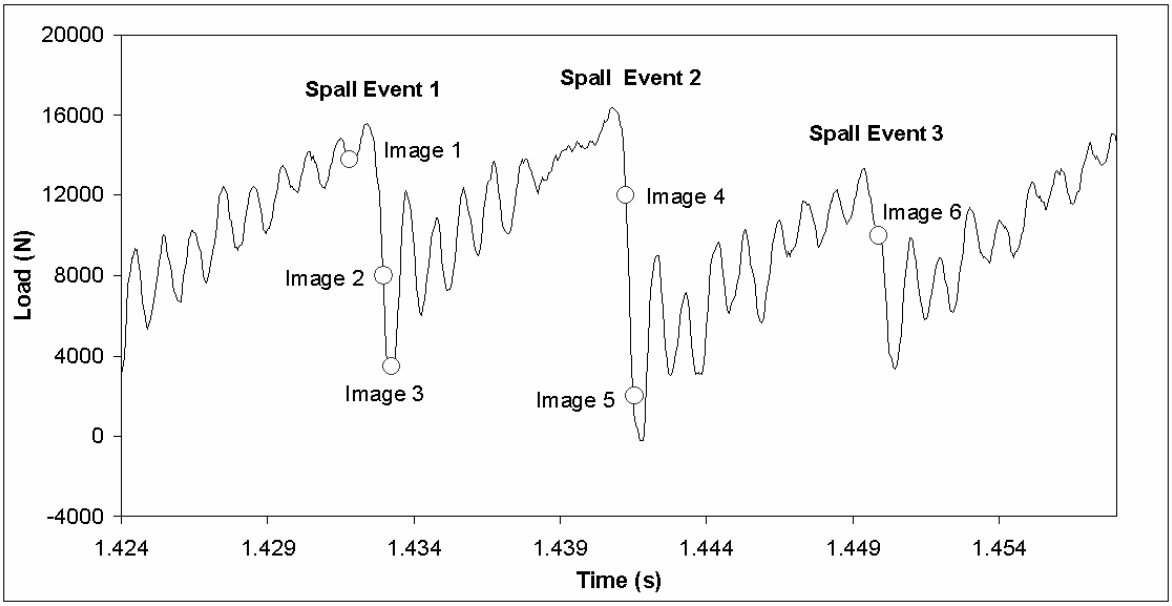

Figure 6. Load record for the test shown in Figure 5 with markers (open circles) corresponding to the six images. The oscillating pattern in the load record between the load drops is elastic resonance in the ice/apparatus system.

end of the spall event and bottom of the load drop. Further relatively slow melting and flow continues to occur during the ascending portion of the following load sawtooth, thereby expanding the intact ice contact area due to the melting, until the next spall event occurs. The next load drop is precipitated by the spall event (Spall Event 2) shown in Image 4. The spalling initiates at the small stable cracks that were created during the previous spall event and the spalling shape is somewhat determined by the distribution of the small cracks. Three regions of remaining intact ice are present after Spall Event 2. From this sequence of events we can surmise that the seeds of a spalling event (i.e. the small cracks) are planted in the previous spalling event. Image 5 was taken a little later during Spall Event 2 and a small fracture has occurred in one portion of the intact ice, similar to the fractures that were evident in Images 2 and 3. Image 6 was acquired during the next spall event (Spall Event 3) and shows spalling that initiated in the vicinity of the small crack shown in Image 5. Hence, to summarize, the small cracks arising in the remaining intact ice during Spall Event 1 lead to Spall Event 2. And in turn the small crack that arose in the remaining intact ice during Spall Event 2 lead to Spall Event 3.

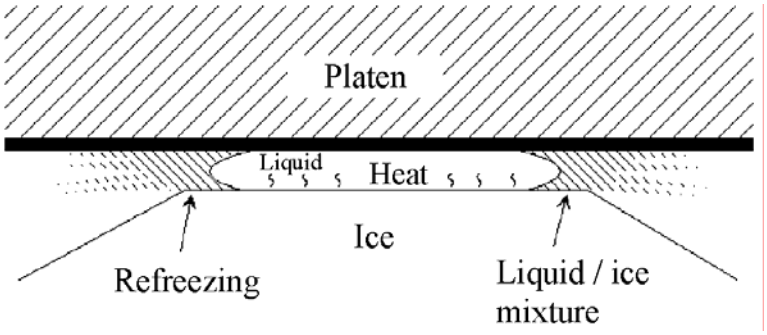

Figure 7. Schematic of the process of high-pressure viscous flow of melt that occurs when the ice moves against the crushing platen. The thickness of the liquid layer is highly exaggerated. (From Gagnon, 1994)

The nature of the small cracks is not entirely clear. They may all be cracks of the ordinary type, that is, where molecular bonds are broken in the ice resulting in a void between the wall faces of the crack. Intriguingly, there may also be instances when 'compression fractures' occur (Knight and Knight, 1972; Baumann et al., 1984; Gagnon et al., 1994). In this case internal melting creates melt figures (liquid-filled fractures) inside the ice when rapid adiabatic pressurization occurs, such as during load drops where the pressure on the remaining intact ice initially increases rapidly (as in Figures 1 and 2). This speculation requires more detailed experiments for verification. In either case the result is the same, the strength of the ice gets compromised due to the presence of the cracks, whatever their nature. The stress required to make these cracks propagate in order to precipitate a spall and a load drop determines the peak load on the load sawtooth.

The regularity of the sawtooth load pattern appears to stem from two effects associated with the small fractures: 1. The fractures are roughly the same size regardless of the size of the load sawtooth or load drop. That is, they seem to be regulated by the stress in the ice during the load drop when the cracks are created rather than by the total load. 2. The cracks occur in the approximate center of the remaining intact ice during a load drop because there is little or no liquid flow and melt there and consequently the ice experiences more compressive stress than in the peripheral regions where ice is removed by melting due to the viscous flow of the liquid layer. The small fractures are stable since they do not propagate very far during the load drop, probably because the stress is highly localized and non-uniform in the stagnant central zone of the intact ice. Hence, when a subsequent spall occurs its nucleation point and ultimate shape are determined from the position and distribution of the cracks created during the previous load drop, and the spalling roughly reduces the initial intact ice contact area by one half. The drop in load due to the spall is consequently half the peak load on the sawtooth just prior to the spall event. The spalling initiates when the stress in the area where the small fractures reside reaches a value to make the fractures propagate. The consequence is that the magnitude of the rise in load on a sawtooth following a spalling and load drop event is not arbitrary but determined by the stress required to start the small fractures propagating.

The observations in this study lead to the interpretation given above. For the present test results, at least, the interpretation is reasonable. In the present case a relatively small ice sample was used and it was mono-crystalline. It is noted, however, that similar crushing behaviors during tests using single crystals and polycrystalline samples have been observed (Gagnon and Bugden, 2007), and therefore the interpretation given here may be applicable to the polycrystalline case. Along the same lines, similar crushing behaviors of ice at different scales have been observed (Gagnon, 1999) and the present interpretation could again be applicable at various scales.

In this study not much attention has been given to the white material surrounding the high-pressure intact ice, consisting of pulverized spall debris and partially refrozen melt, and its role both as a confining and load bearing medium that develops as the crushing progresses further into the ice. This is beyond the scope of the present study, however these issues are discussed to some extent by Gagnon and Bugden (2007).

4. Conclusions

In situ observations of ice crushing processes obtained from a high-speed imaging camera has revealed processes that can explain the sawtooth cyclic load pattern that is often characteristic of ice crushing and indentation experiments. Small stable cracks that occur in the roughly central region of the high-pressure intact ice zone during spalling events serve as nucleation sites for the next spall event and associated load drop. The roughly central location of the small cracks, and their distribution, determines the size and shape of the next spall. While the present test was conducted on a large single crystal of ice at a relatively small scale in the laboratory the results are probably relevant to the case of polycrystalline ice at various scales. This type of study was made possible through the use of a very high speed imaging system with adequate resolution.

5. Acknowledgements

The author would like to thank the Program of Energy Research and Development (PERD) and IOT for their financial support of this research. The author is also grateful to Austin Bugden for technical assistance during the test program.

6. References

Baumann, K., Bilgram, J.H. and Känzig, W. 1984. Superheated ice. Z. Phys. B, 56(4), 315-325.

Gagnon, R.E. 1994. Melt Layer Thickness Measurements During Crushing Experiments on Freshwater Ice. Journal of Glaciology, 1994, Vol. 40, No. 134, 119-124.

Gagnon, R.E. 1998. Analysis of Visual Data from Medium Scale Indentation Experiments at Hobson's Choice Ice Island. Cold Regions Science and Technology, Vol. 28, 45-58.

Gagnon, R. E. 1999. Consistent Observations of Ice Crushing in Laboratory Tests and Field Experiments Covering Three Orders of Magnitude in Scale. Proceedings of the 15th International Conference on Port and Ocean Engineering under Arctic Conditions, POAC-99, Helsinki, Finland, Vol. 2, 858-869.

Gagnon, R. E. and Bugden, A. 2007. Ice Crushing Tests Using a Modified Novel Apparatus. Proceedings of POAC-07, 235-244.

Gagnon, R.E., Tulk, C. and Kiefte, H. 1994. Internal Melt Figures in Ice by Rapid Adiabatic Compression. Journal of Glaciology, 1994, Vol. 40, No. 134, 132-134.

Knight, C.A. and Knight, N.C. 1972. Superheated ice: true compression fractures and fast internal melting. Science, 178(4061), 613-614.

19th IAHR International Symposium on Ice
"Using New Technology to Understand Water-Ice Interaction"
Vancouver, British Columbia, Canada, July 6 to 11, 2008

A New Impact Panel to Study Bergy Bit / Ship Collisions

R.E. Gagnon
Institute for Ocean Technology
National Research Council of Canada
St. John's, NL, Canada, A1B 3T5
Robert.Gagnon@NRC.CA

Abstract

A new design has been generated for an impact panel that is intended for use in a second bergy bit / ship collision field study. The design incorporates new technology to measure impact loads and pressure distribution at fine spatial resolution. The panel consists of 6 large sensing modules. Each module is a solid acrylic block with dimensions 1m x 1m x 0.46 m, giving the impact panel a total sensing area of 6 m^2. Each module sits on four flat-jack type load cells. All 6 modules are housed in a 3m x 2m rigid steel structure that is welded to the hull of the vessel at the bow center. The top surface of each module is covered with a new pressure-sensing mechano-optical technology capable of measuring pressure with an effective unit sensing area of about 1.3 cm x 1.3 cm. Data from the sensing modules are recorded by cameras operating at a capture rate of 250 images/s that are situated at the back end of each sensing module. A secondary means of measuring pressure at an array of locations on each module surface consists of strain gauges imbedded in the acrylic close to the impacting surface. The panel is intended for use within the next few years in a full-scale study of ship / bergy bit collisions with impact loads in the 0 – 20 MN range.

1. Introduction

In June 2001 the first Bergy Bit Impact Field Study was conducted using the CCGS Terry Fox. This successful program demonstrated that a strong vessel could be instrumented to obtain detailed load and pressure distribution data during intentional impact experiments with bergy bits (Gagnon et al., 2008). Bergy bit impacts are a major hazard for tankers and other vessels operating off the East Coast, and similarly in the Arctic regions where resource development, tourism, mineral transport, etc are on the increase. The recent sinking of the Explorer cruise ship in the Antarctic following a collision with what was likely a bergy bit illustrates this point. Large chunks of multiyear sea ice pose similar hazards in the Arctic regions.

While the first Bergy Bit Impact Field Study was a success, the results showed that the maximum obtainable loads were in the 5 MN range due to the shape of the Terry Fox hull and the position of the impact panels. Both panels, an internal strain-gauge panel and an external panel, were located on the port side of the bow, where only glancing impacts could be achieved. Since that time we have verified this result using extensive numerical simulations. The simulations showed that loads that are of the greatest interest (i.e. 10-20 MN) could not be attained with the impact panels in that location, even when unacceptably risky high-speed impact scenarios were simulated.

Fortunately, the solution that would facilitate a safe and effective field study that would achieve impact loads in the desired range is to mount an impact panel with a vertical orientation at the center of the bow of the Terry Fox. Simulations and calculations show that loads of approximately 20 MN can be achieved with impacts on bergy bits in the 2000 tonne range at moderate speeds, where the maximum acceleration would not exceed the safe range for ship and crew operations, that is, around 0.3 g.

A key element that remains to be resolved in relation to ship and structure collisions with sea ice and glacial ice concerns the distribution of pressure within the contact zone. Several studies, including the first Terry Fox field study, showed the existence of high-pressure zones, regions of relatively intact ice surrounded by low pressure pulverized ice. Do these high-pressure zones increase in size as impact load increases, and just as important, does the pressure in the high-pressure zones increase as their size increases? These are critical questions that must be addressed. The data from the external impact panel used in the first bergy bit impact study suggested the affirmative to both questions (Gagnon, 2008), however, the load range was quite limited and it remains to be seen if the trends continue throughout the full range of interest. The new impact panel described below, used on the Terry Fox for head-on bergy bit collisions, has the capability to resolve these issues.

2. Impact Panel Details

2.1. Attachment to the Bow of the Vessel

The impact panel is modular in design and is 3 m wide and 2 m in height at the front impacting surface. Figure 1 shows its location on the Terry Fox bow. The top of the panel is at the waterline. The panel consists of six 1 m x 1 m modular sensor inserts, each with its own

independent array of sensors for measuring load and pressure. The sensor inserts fit into the slots of the box-like structure of the panel, referred to as the backing structure (Figure 2). The backing structure is fabricated using 1" steel plate, welded at all joins. To enable divers to weld the panel to the hull of the Terry Fox it is necessary to do the attachment as a multi-stage process. First a mounting frame must be welded to the hull (Figures 2 and 3). The back end of the frame conforms to the vessel and its shape enables full access for welding all of the conforming metal surfaces to the hull. The front of the mounting frame has several seating pads that mate and bolt to matching seating pads on the back end of the backing structure. Once the backing structure is bolted on then the sensor inserts are individually installed in the six slots. This strategy is similar to that used during the first Terry Fox field study. Removal of the panel from the vessel is accomplished in the reverse order. All electrical cables from the inserts would feed up through a protective conduit welded to the upper hull running from the top of the panel up the side of the ship's bulwarks from where the cables continue on to the data acquisition hut situated on the vessel's fore-deck.

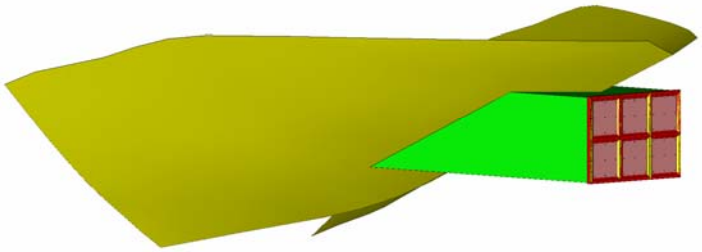

Figure. 1. Impact panel on the CCGS Terry Fox bow.

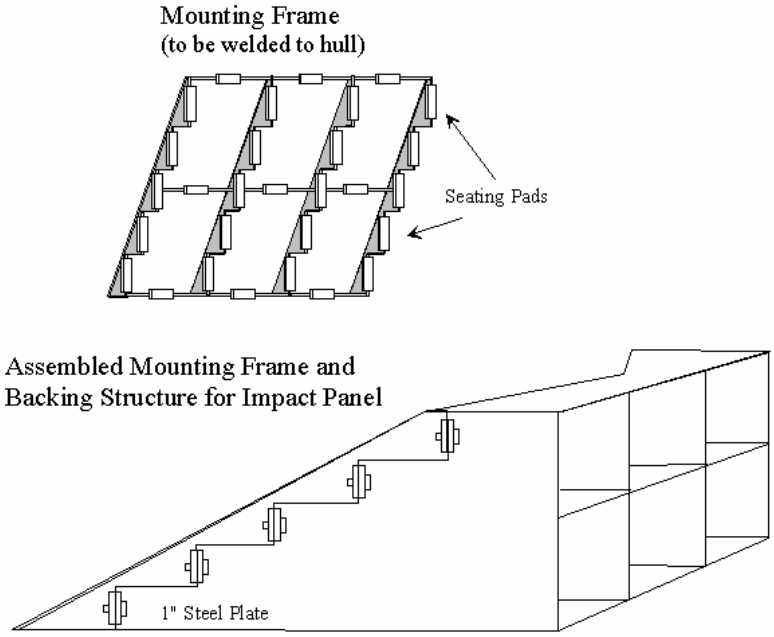

Figure. 2. Mounting frame and backing structure.

2.2. Details of the Impact Panel Sensing Capabilities

A staged strategy will be used for the design and fabrication the impact panel since some of the technology is novel and it is prudent to conduct tests in the lab prior to committing to the final details. A 1/ 6 portion (one sensor insert) of the panel (Figure 4) will be fabricated for extensive testing during the summer of 2008 at IOT and in the Structures Lab of Memorial University. This instrument is referred to as the impact module. Final details of the full impact panel design would be contingent on the results of the lab tests using the impact module. Following the

proofing of the impact panel design, the impact module will be used as a research tool for on-going laboratory studies of ice impacts. The details of the impact module construction and functioning are given below. These are essentially the same details that apply to the full impact panel.

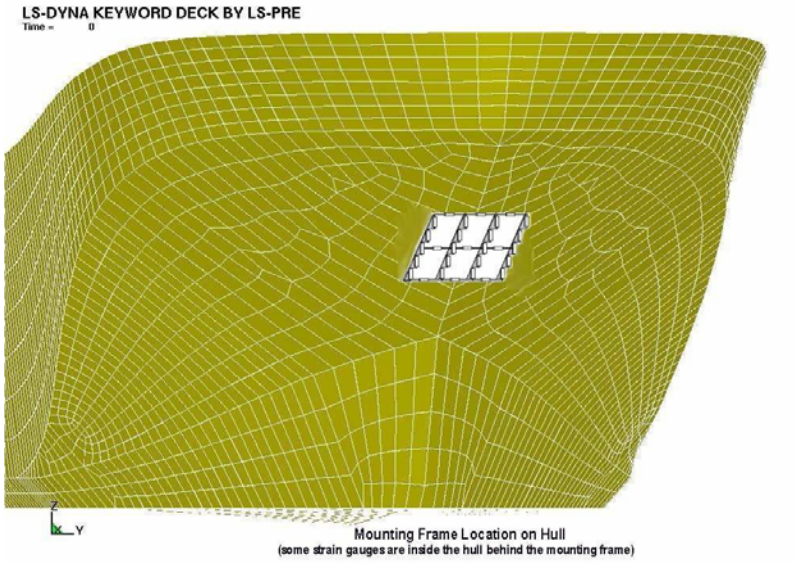

Figure. 3. Mounting frame location on the Terry Fox hull.

The central component of the impact module is a thick transparent block of acrylic measuring 1 m x 1m x 0.46 m (Figure 5). The block rests on four flat-jack type load cells. These cells are metallic envelopes filled with hydraulic fluid. Load applied to the surface of the cell translates into pressure in the fluid, which is monitored by a pressure gauge. The thickness of the acrylic block gives it the flexural strength to withstand high loads while supported at its four corners. The block is held firmly against the load cells by two bolts that pass part-way through opposing corners of the block and that are secured with nuts and thick rubber washers. Also, around the top edge of the block there is a securing plate that bolts to the steel side plating of the impact module with nuts and thick rubber washers (Figure 5). This protects the edges of the block where a thin stainless steel sheet, that covers the

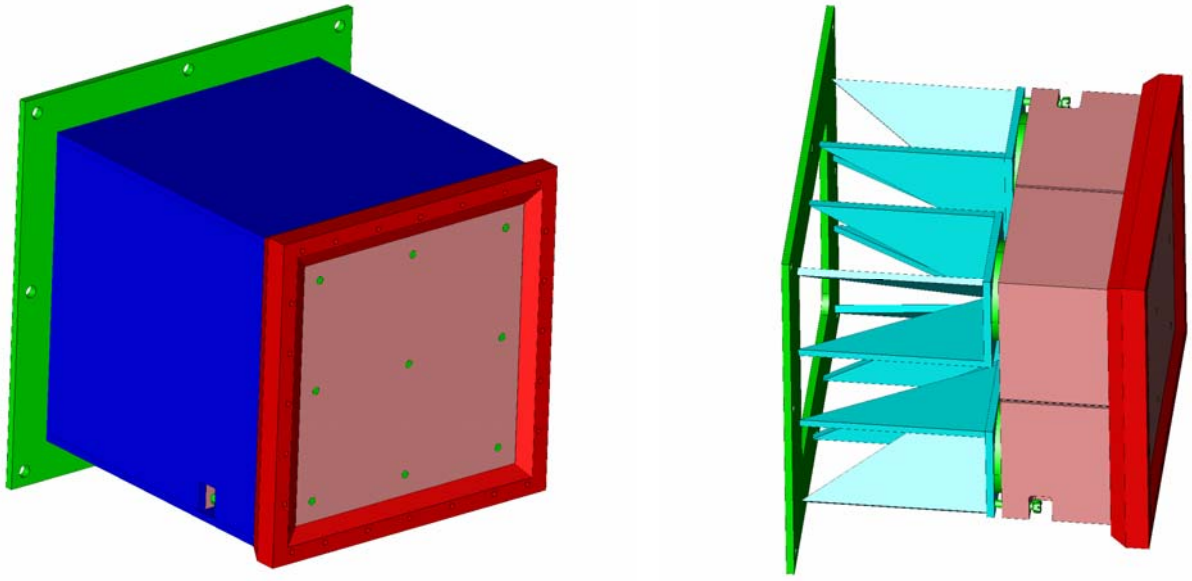

Figure. 4. (Left) Impact module oriented horizontally with the impacting surface in the foreground. (Right) Impact module with side plates removed to show internal structures and components. A protective securing plate is visible around the peripheral edge of the impacting surface.

new pressure sensing technology, is screwed to the block while enabling the load from an ice impact to transfer to the flat load cells.

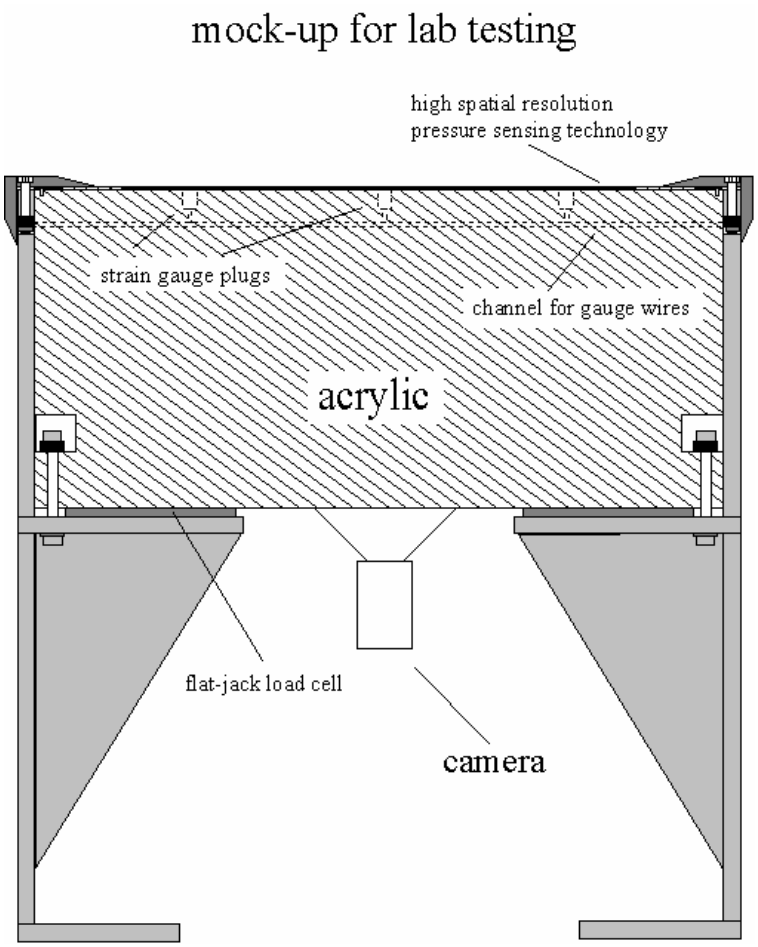

Figure. 5. Sectional view of the impact module.

The top surface of the block is covered by new pressure sensing technology. This new technology consists of many strips of acrylic, 13 mm wide and 4 mm in thickness and ~ 1 m in length, mounted side-by-side on the block's surface. Each strip has a gentle curvature (0.23 m radius) across its width on the face that touches the large acrylic block (Figure 6). Pressure applied to the opposite side of the strips causes them to flatten against the block's surface. The degree of flat contact, i.e. the width of the contact, is a direct measure of the pressure applied and can be calibrated. This type of sensor is very robust and has been used successfully in a number of ice crushing studies (Gagnon and Bugden, 2007; Gagnon and Bugden, 2008; Gagnon and Daley, 2005), in single and multiple strip configurations. Its range of sensitivity is about 0-60 MPa. The pressure sensor strips are covered by a thin sheet of stainless steel that is the contacting surface with the ice during impacts. The unit sensing area for this technology is about 13 mm x 13 mm, hence the top surface of the block is effectively covered by more than 5000 pressure-sensing units. The data acquisition system for the pressure sensing strips is a fast high-resolution video camera (250 images per second) located at the bottom of the block, shown in Figure 5. The acrylic strips are white in color. When not pressed against the acrylic block they make very little contact, and when pressure is applied to them more contact occurs due to elastic flattening of the strips' curved surfaces (Figure 6). The only light source inside the acrylic block is from horizontally oriented LED's around the block perimeter near the top. Light from these LED's normally internally reflects off the top inner block surface. When an acrylic strip is flattened against the block the internal reflection is frustrated, and the light passes through the block's surface to illuminate the white strip where it makes contact. Hence the portion of contact, appearing as white, becomes visible to the camera.

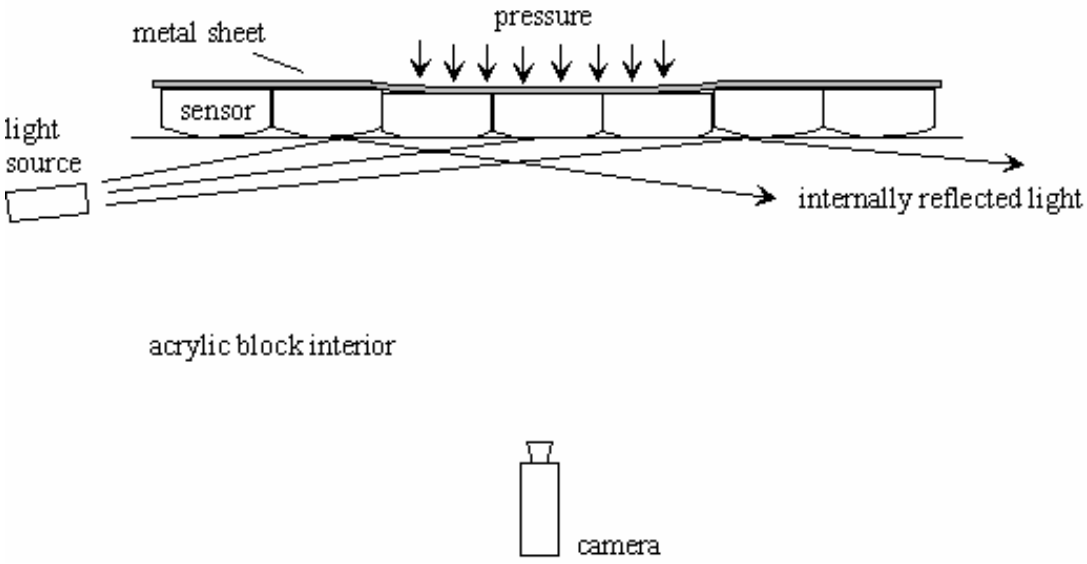

Figure. 6. Schematic showing how the new pressure sensing technology functions. Two of the light rays from the source at the left internally reflect off the block's internal surface where there is no contact with the strips. The center ray illumines the white acrylic strip since the internal reflection is frustrated where the strip is elastically flattened against the block due to the pressure. The curvature of the strips is exaggerated for illustrative purposes.

In addition to the pressure sensing strips the top surface of the block has an array of 9 pressure sensing plugs recessed in it surface. These are small cylinders of acrylic ~ 2 cm diameter that are located and secured in flat-bottomed holes (with slightly larger diameter) machined in the surface to the exact depth corresponding to the height of the plugs. The end of each cylinder is glued to the acrylic at the bottom of the hole with methyl methacrylate glue that has the same properties as the acrylic. Each plug has a strain gauge imbedded in it with sensitivity along the axis of the plug. Load applied to the top of a plug causes it to contract in length and this registers on the strain gauge. The plugs are essentially pressure transducers that have the same mechanical properties as the block itself. The sensors are useful both for corroborating the output from the pressure sensing strips and as backup sensors in the event there is a problem with the strip sensors.

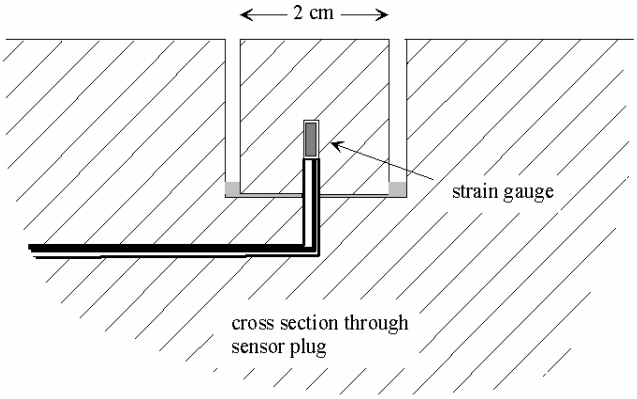

Figure. 7. Sectional view of a strain gauge plug.

In addition to the sensors that are incorporated in the impact panel there will also be a separate device, called MOTAN, installed inside the vessel that determines global loads by measuring the full ship motions that result from impacts. This device was used during the first bergy bit impact field study (Johnston et al., 2008). Furthermore, though not part of the impact panel specifically, there will be an array of strain gauges mounted to the inside of the vessel's hull behind the impact panel. The primary purpose of the gauges would be to monitor any plastic deformation of the hull as a safety precaution. Such deformation is not anticipated, however, since numerical simulations of the impact panel on the hull with various loading scenarios applied did not show any plastic deformation of the impact panel or the hull structure (Figure 8).

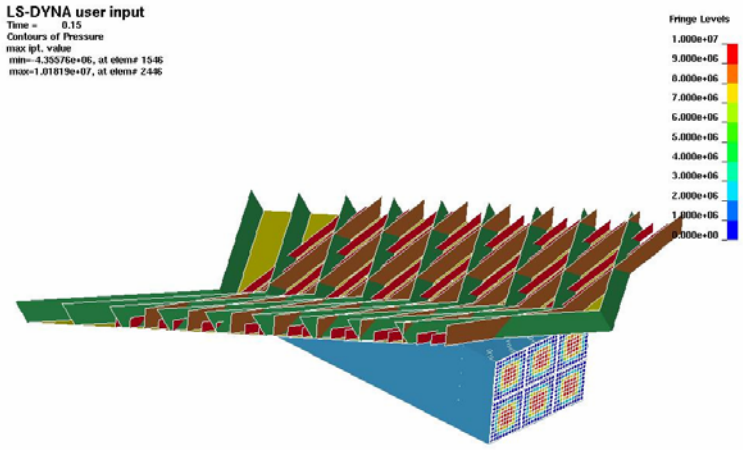

Figure. 8. Finite element stress analysis of the impact panel and Terry Fox hull for a given impact load. The internal structure of the hull, that is, frames and stringers, was included in the simulations.

3. Conclusions

A unique impact panel has been designed for a full-scale ship/bergy bit impact study within the next few years. A device representing a portion of the panel will be fabricated and tested in the lab to proof the technology prior to building the full impact panel. Substantial redundancy is built into the design of the panel to measure loads and pressure distribution. One of the pressure sensing technologies will yield a spatial resolution that effectively amounts to having 30,000 individual pressure sensors on the face of the 3 m x 2 m impact panel.

4. Acknowledgements

The author would like to thank the Program of Energy Research and Development (PERD) and IOT for their financial support of this research. Also, the discussions with Trent Slade regarding the impact panel design details and installation strategies are greatly appreciated.

5. References

Gagnon, R., 2008. Analysis of data from bergy bit impacts using a novel hull-mounted impact panel. Cold Regions Science and Technology, 52, 50–66.

Gagnon, R.E. and Bugden, A., 2007. Ice Crushing Tests Using a Modified Novel Apparatus. Proceedings of POAC-07, 235-244.

Gagnon, R.E. and Bugden, A., 2008. 2-dimensional edge crushing tests on thick sections of ice confined at the section faces. Proceedings of IAHR 2008.

Gagnon, R.E. and Daley, C., 2005. Dual-axis video observations of ice crushing utilizing high-speed video for one perspective. Proceedings of POAC 2005, Potsdam, New York, Vol. 1, 271-282.

Gagnon, R., Cumming, D., Ritch, A., Browne, R., Johnston, M. Frederking, R., McKenna, R. and Ralph, F., 2008. Overview accompaniment for papers on bergy bit impact trials. Cold Regions Science and Technology, 52, 1–6.

Johnston, M., Timco, G.W., Frederking, R. and Miles, M., 2008. Measuring global impact forces on the CCGS Terry Fox with an inertial measurement system called MOTAN. Cold Regions Science and Technology, 52, 67–82.

19th IAHR International Symposium on Ice
"Using New Technology to Understand Water-Ice Interaction"
Vancouver, British Columbia, Canada, July 6 to 11, 2008

The Nature of High Pressure Zones in Compressive Ice Failure

Taylor, R.S.
Memorial University of Newfoundland,
St. John's, NL, A1B 3X5
rtaylor@engr.mun.ca

Frederking, R.M.W.
Canadian Hydraulics Centre, National Research Council Canada,
Ottawa, ON, K1A 0R6,
Robert.Frederking@nrc-cnrc.gc.ca

Jordaan, I.J.
C-CORE,
St. John's, NL, A1B 3X5
ian.jordaan@c-core.ca

In determining design loads for structures in ice, understanding and modeling the nature of high pressure zones (*hpz*s) during compressive failure is key. Medium-scale field indentation tests carried out by the Japan Ocean Industries Association (JOIA) provide pressure data at a resolution previously not available. Measurement data were collected for global and local segmented panel loads using conventional load cells; high resolution interfacial pressures were measured using Tekscan tactile pressure sensors. The aim of this paper is to enhance understanding of the tactile sensor data, how failure processes may be interpreted from these data and guide future efforts to identify and characterize individual *hpz*s. Qualitative and quantitative descriptions of local failure events have been provided. Analysis results, along with a discussion of implications for design load methodology are included.

1. Introduction

In the safe, yet economic design of ships and structures for ice conditions knowledge of local pressure behavior is vital. It is well known that very high local pressures can occur over small areas. Indentation tests on multi-year ice using 10mm diameter sensors (Frederking et al., 1990) indicate local pressures as high as 80 MPa occur. Local pressure measurements reported by Masterson et al. (1993), collected using PVDF sensors during multi-year ice indentation tests, reveal pressures as high as 50 MPa. Ship ram data suggest local pressures may reach as high as 70 MPa (Jordaan, 2001). Small-scale indentation tests on freshwater polycrystalline ice indicate even higher local pressures, with local peak pressures as high as 100 MPa occurring over small areas (Mackey et al., 2007; Jordaan et al., 2008). As a result of the interplay between various failure processes during compressive ice failure, loads are primarily transmitted through localized zones of high pressure (Jordaan, 2001). These *hpz*s often cover only a small portion of the global interaction area and in the case of ice sheets tend to take on "line-like" distributions (Frederking, 2004). Understanding the nature of local failure processes and the links between these processes and the evolution of *hpz*s is of interest in ice mechanics.

The Medium Scale Field Indentation Tests (MSFIT) program, which was sponsored by the Japan Ocean Industries Association (JOIA), included indentation tests on sheets of first-year sea ice. Data from the MSFIT program collected during the winters of 1998, 1999 and 2000 were made available to encourage broader understanding of the results. Data covering a range of ice thicknesses (165mm to 335mm) and speeds (0.03 cm/s to 3.0 cm/s) have been made available; JOIA (2006). Observation of time trace plots for these data suggest brittle-type failure for the medium speed (0.3 cm/s) and high speed (3.0 cm/s) cases, while slow speed (0.03 cm/s) tests produce failure that is more ductile in nature. These observations are consistent with Masterson et al. (1999), who indicate that brittle behavior was observed for rates higher than a few millimeters per second during medium-scale tests. As a starting point, a sample brittle-type event from the 1998 test program has been analyzed to examine the nature of *hpz*s during compressive failure. A general description of the 1998 test program and results are provided in Nakazawa et al. (1999). The present paper is focused on analysis of Tekscan tactile sensor data for the sample event discussed below.

2. Description of Test

Data for the selected event were collected on January 26, 1998. Details of this test are summarized in Table 1 below. The primary reasons for selecting this particular event are that the nominal ice thickness (241 mm) is close to the total height of the tactile film (238 mm) and the time trace suggests that the failure was cyclic and brittle in nature.

Table 1. Characteristics of selected event

Indenter Width	1500 mm	Salinity	6.2 ppt
Indenter Height	400 mm	Ice Strength	1 MPa
Indentation Speed	0.3 cm/s	Ice Density	843 kg/m^3
Ice Thickness	241 mm	Ice Temperature	-2.7 ^{o}C
Ice Temperature	-2.7 ^{o}C	Event Duration	65 seconds

As shown in Figure 1, the indenter apparatus used in these tests was mounted in a testing frame and fitted with several types of load measurement instrumentation. Measurement data were collected for global and local segmented panel loads using conventional load cells; see Figure 1 (a) and (b). Tekscan tactile pressure sensor film was mounted in front of the segmented panels and was used to collect high resolution interfacial pressure measurements; see Figure 1 (c). A detailed description of the instrumentation may be found in Sodhi et al. (1998).

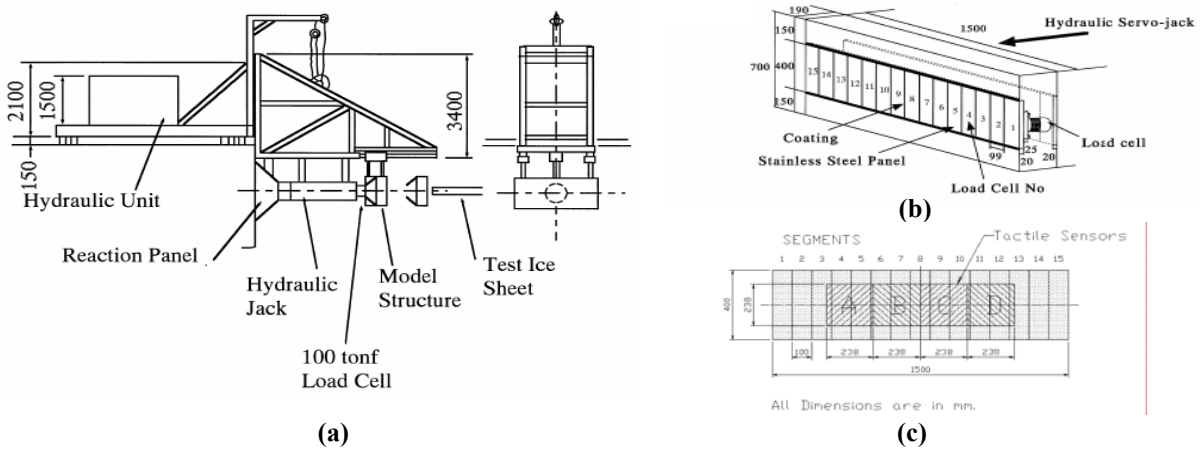

Figure 1. Schematics of: (a) indentation structure and instrumentation; (b) segmented indenter panels; (c) tactile sensors (Sodhi et al., 1998).

As illustrated in Figure 1 (c), the tactile sensor configuration used in the 1998 tests only partially covered the face of the indenter. Four individual tactile sensors, each consisting of a 44 by 44 array of sensor elements, were connected together to form a continuous 44 by 176 sensor array (for a total of 7744 elements). Each sensor element is nominally 5.4 mm by 5.4 mm and the overall dimension of the sensor array is 238 mm high by 952 mm long. For the selected event, sensor data was sampled at a frequency of 12.5 Hz (one 'frame' every 0.08 seconds). Each 'frame' of data consists of a 44 by 176 matrix of values collected for the specified time interval; each element of the data matrix contains a pressure value for the sensor element having the same element indices in the sensor array. Raw data (integer values ranging between 0 and 255 representing pressure intensity) were collected and later calibrated using the procedure described in JOIA (2006). As discussed by Frederking (2004), the manufacturer of the tactile film indicated that error in any reading on the film may be up to +/- 10%. Correspondingly these pressure data are treated as relative.

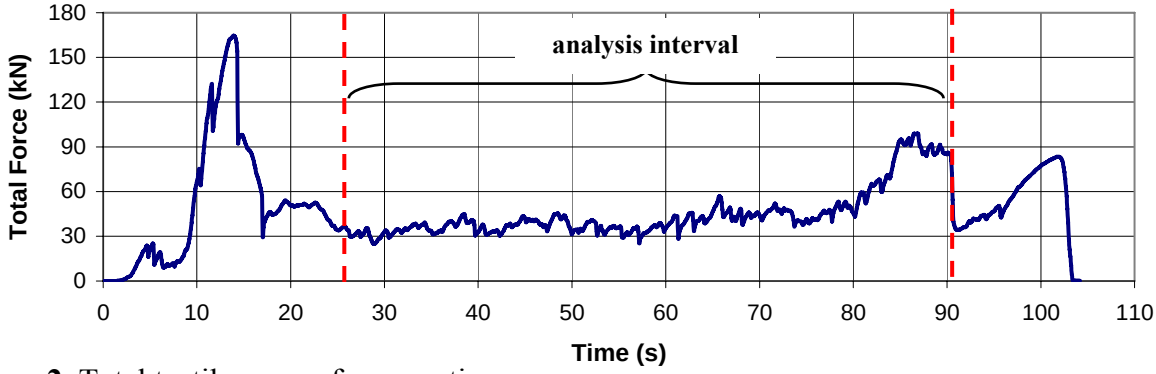

Figure 2. Total tactile sensor force vs. time.

The time trace for the total force measured by the tactile film is shown in Figure 2 above. A large 'break-out' load occurred in the first 25 seconds of the event due to the initial condition resulting from contact of the indenter with the flat sawed edge of the ice. It is interesting to note that, as shown in Figure 3 (a), even during the peak of the 'break-out' phase of the failure process only approximately 27% of the nominal sensor area was actually under load. After this initial 'break-out', the failure process transitioned into a line-type distribution of high pressure zones. During the onset of crushing the total loaded area reduced to approximately 8% of the nominal sensor area; see Figure 3 (b).

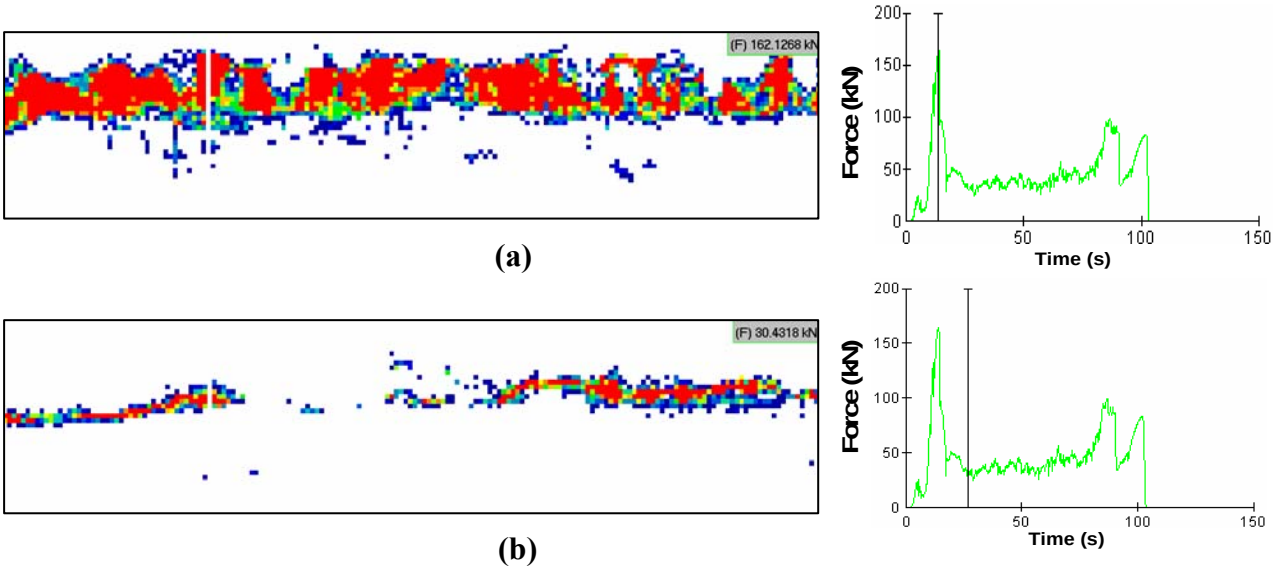

Figure 3. Tactile sensor data for (a) peak of 'break-out' load; (b) onset of crushing.

For the present work only data from the 'analysis interval' between t = 25 seconds and t = 90 seconds have been considered; see Figure 2. Throughout the interaction, *hpz*s were observed to exhibit significant spatial and temporal variation. During the selected interval the average total loaded area was approximately 10% of the nominal sensor area. The average pressure on a loaded sensor element was 2.08 MPa and the average global pressure on the sensor array was 0.208 MPa.

3. Local Failure Processes: Spalling, Crushing and *hpz*s

Localized failure processes serve to limit load build-up within the ice and consequently limit loads applied to the model structure. Examination of the tactile sensor data suggests spalling, pulverization and extrusion processes are in evidence. In the context of this paper, pulverization and extrusion processes are simply referred to as 'crushing'. Both spalling and crushing processes may be associated with various mechanisms within the ice, such as macro fracture, microfracture, recrystallization, and pressure melting. These mechanisms play different roles in the formation and evolution of *hpz*s; the reader is referred to Jordaan et al. (2008) and Jordaan (2001) for further detail.

Both spalling and crushing processes tend to cause decreases in load. It is important to distinguish between consequences of individual spalling and crushing events in terms of their observed effect on tactile sensor data. As shown in Figure 5 (a), crushing is typified by a sudden decrease in *hpz* intensity, without an appreciable shift of the position of the *hpz* (represented below by a centerline). While some variation in area may result from the extrusion of material, significant loss of contact area is generally not expected. Any decrease in total area associated with crushing often occurs near the periphery of the *hpz*. Considering the illustration in Figure 5 (b) it may be seen that spalls, by comparison, typically result in appreciable area losses, which are often asymmetric in nature (i.e. only on one side of the *hpz*). In addition to affecting the intensity, spalls generally have a more significant effect on the size, shape and position of the *hpz*. These observations are consistent with those found in laboratory experiments presented by Jordaan et al. (2008).

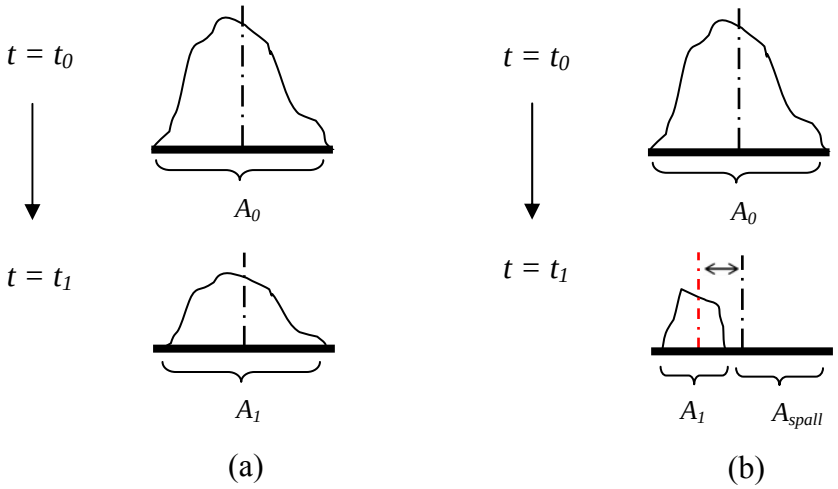

Figure 5. Simplified schematic of *hpz* pressure distribution before ($t = t_0$) and after ($t = t_1$) failure for (a) crushing; (b) spalling.

To investigate the occurrence of spalling and crushing failures, data from the tactile sensor array were first divided into four regions, as shown in Figure 7. Load traces corresponding to the data contained within each region were plotted along with the total sensor data; see Figure 8. Examination of the load traces for each region allowed for assessment of the relative contributions of each region to the drop in total load for each failure event. The objective was to determine if a particular region is associated with the observed load drop, and to study the pressure behavior in the dominant region to identify the type of failure process.

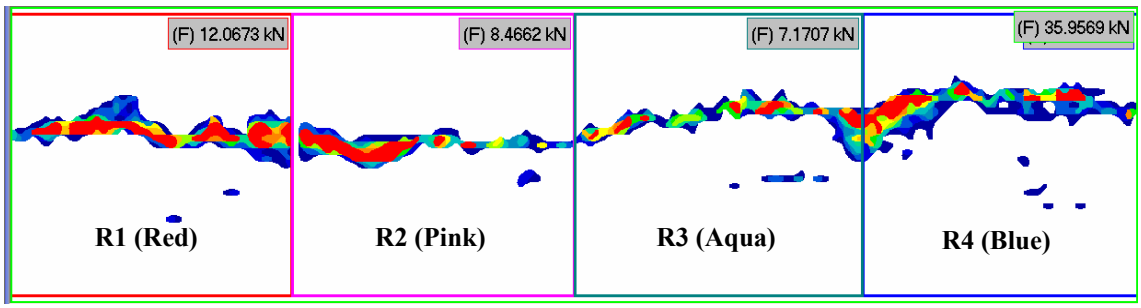

Figure 7. Tactile sensor data regions used in the identification of dominant failure events.

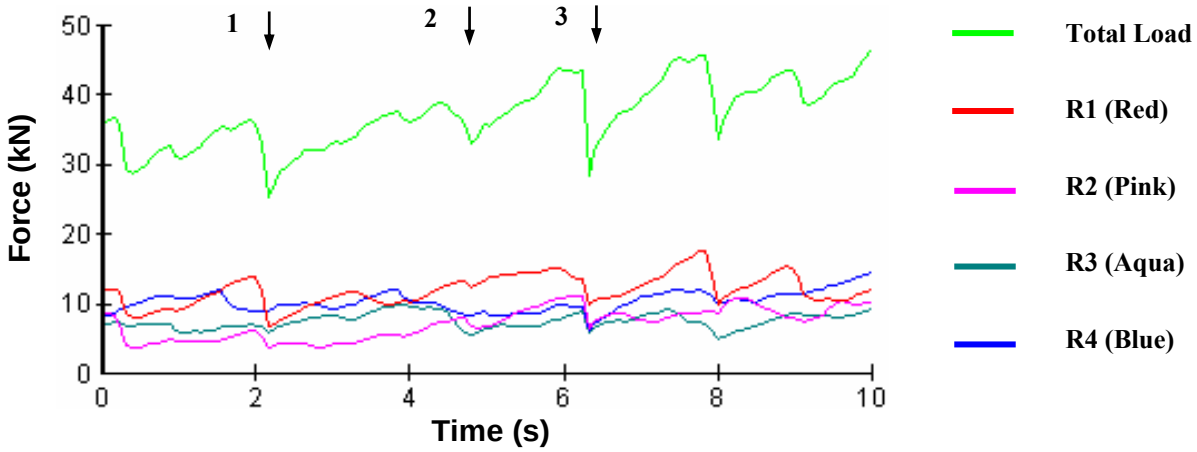

Figure 8. Tactile sensor data for the 10 second interval from 55 to 65 seconds; data correspond to total sensor load, as well as loads for the four regions identified in Figure 7.

In an attempt to enhance the understanding of links between failure processes and pressure distributions, both qualitative and quantitative analysis of tactile sensor data have been undertaken. The qualitative approach has been based primarily on visual interpretation of time traces and spatial pressure maps of tactile data. The quantitative approach aims to link decreases in force, area and pressure with various failure types. In taking such an approach, it is hoped this will aid in the development of criteria for characterizing failure types and their relationship with *hpz* evolution.

Qualitative Interpretation

The degree of influence each region has on the drop in total load for a given failure event has been qualitatively interpreted based on Figure 8, as well as the tactile sensor data. Results are summarized in Table 2 below. The dominant failure types were also identified for each failure event based on examination of the tactile sensor data. For Failure Event 1, the load drop appears to be dominated primarily by activity in region R1, with some influence from the adjacent region, R2. For Failure Event 2, the decrease in load appears to be most heavily influenced by region R3, while activity in regions R1 and R2 appear to have some effect. During Failure Event 3, there appears to be a rapid load drop across all regions, suggesting a simultaneous failure.

Table 2. Classification of the degree of influence of each region on total load drop during identified failure events and assessment of domination failure type using qualitative approach.

Failure Event	Region				Dominant Failure Type
	R1	R2	R3	R4	
1	D	I	I	N	Local Spalling
2	I	I	D	N	Local Crushing
3	D	D	D	D	Simultaneous Crushing
D = Dominant; I = Some Influence; N = Negligible Influence					

Two and three dimensional spatial pressure maps corresponding to the instants before and after the load drop for Failure Events 1, 2 and 3 have been plotted in Figures 9, 10 and 11 respectively.

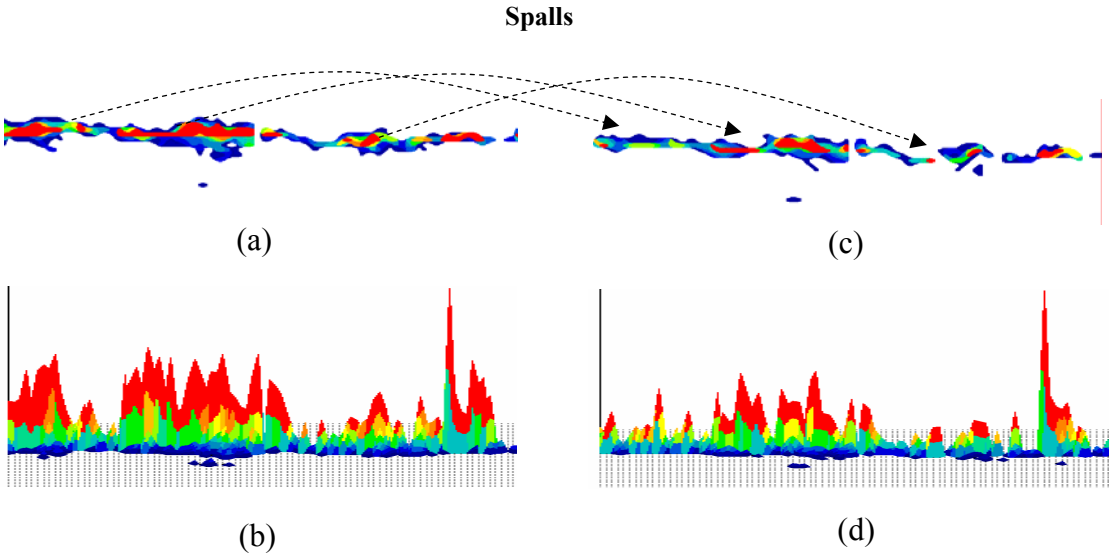

Figure 9. Pressure distributions from selected regions for Failure Event 1 (local spalling): (a) 2-D plan view before failure; (b) 3-D view before failure; (c) 2-D plan view after failure; (d) 3-D view after failure.

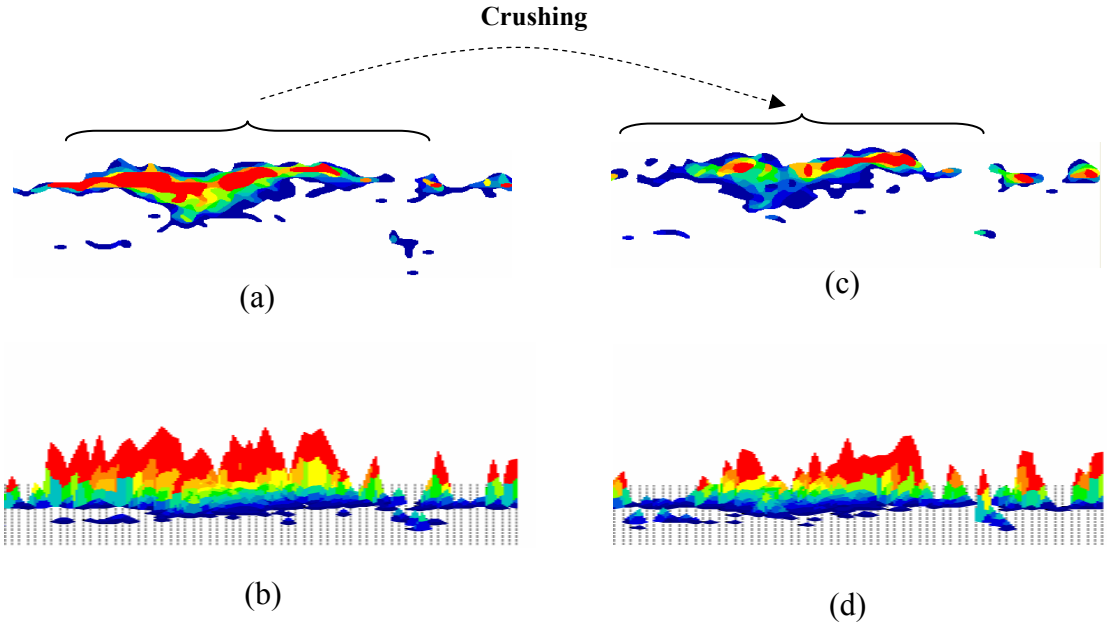

Figure 10. Pressure distributions from selected regions for Failure Event 2 (local crushing): (a) 2-D plan view before failure; (b) 3-D view before failure; (c) 2-D plan view after failure; (d) 3-D view after failure.

Comparison of Figures 9 and 10 illustrates the key differences between spalling failure and crushing failure. Spalling results in appreciable local modification of the shape, intensity and position of *hpz*s and the surrounding area. By comparisons, during crushing the general shape of the contact area does not appreciably change. Rather the extrusion of material along at the face of the indenter results in a decrease in intensity of the *hpz*.

As may be seen from Figure 11, the shape and positions of the *hpz*s do not significantly change during the simultaneous crushing. Rather there is a sudden decrease in intensity due to the extrusion of material. As may be seen, most of the area reduction for this failure occurs near the periphery of the *hpz*s, which is characteristic of a crushing type failure.

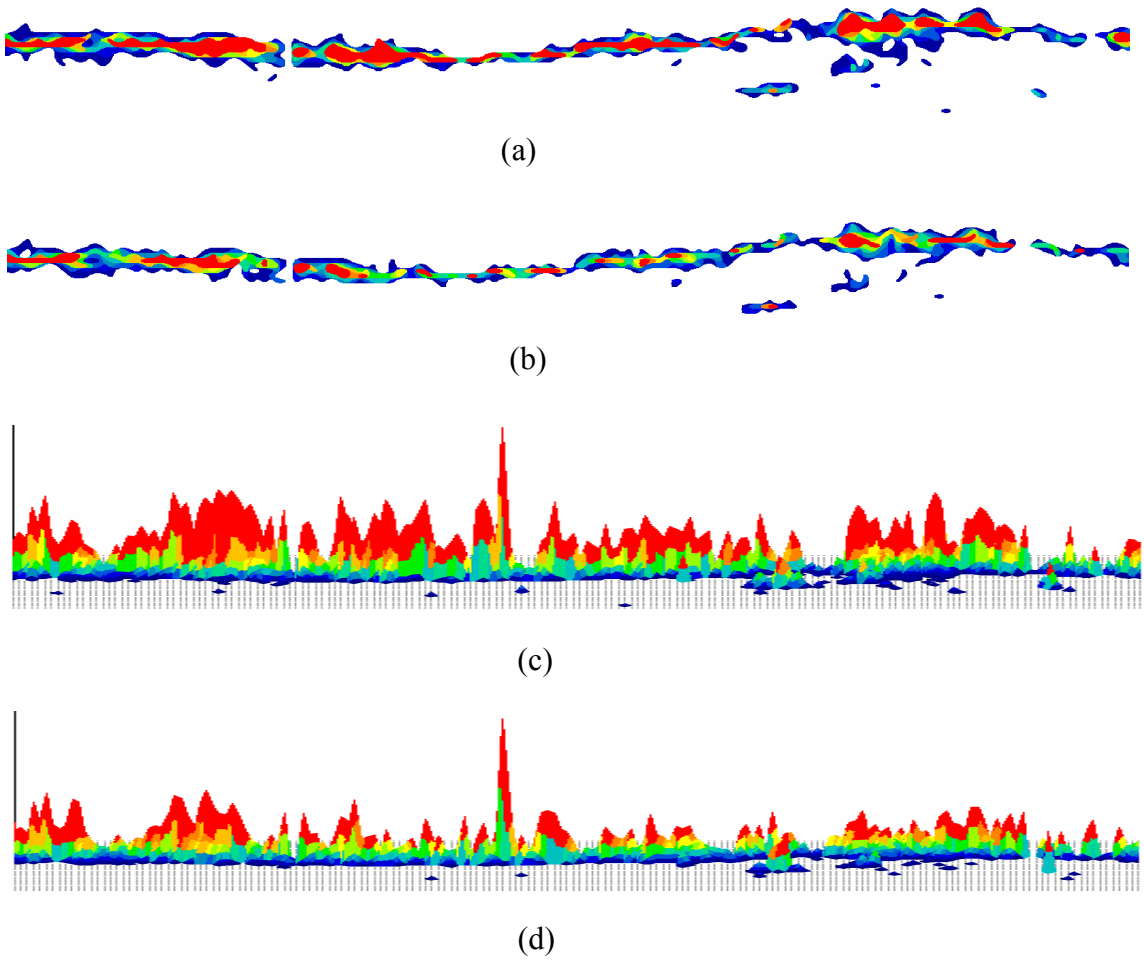

(a)

(b)

(c)

(d)

Figure 11. Pressure distributions from all regions for Failure Event 3 (simultaneous crushing): (a) 2-D plan view before failure; (b) 2-D plan view after failure; (c) 3-D view before failure; (d) 3-D view after failure.

Quantitative Interpretation

Data were extracted for each region and examined in further detail. The percent of total load drop attributed to each region, as well as the percent decrease in area and pressure within each region were determined. These results are summarized in Table 3 below.

Table 3. Percent decrease in force, area and pressure during failure events for each region

Failure Event	Percent Drop in Total Force Attributed to Each Region				Percent Area Reduction in Each Region					Percent Pressure Drop in Each Region				
	R1	R2	R3	R4	R1	R2	R3	R4	Total	R1	R2	R3	R4	Total
1	67	22	9	2	26	-4	-3	12	12	35	40	17	-12	21
2	2	16	60	22	-2	0	2	3	2	4	11	34	9	13
3	25	31	21	22	12	18	10	17	14	19	29	26	21	24

The values from Table 3 well support the qualitative assessment presented in Table 2. For Failure Event 1, activity in region R1 tends to dominate the drop in total force, which is accompanied by both a sizeable reduction in area and a drop in average pressure over the region. As discussed, this type of response is characteristic of a spalling type failure. For Failure Event 1 there appears to be a moderate load drop in region R2, which has a proportionally larger drop in pressure associated with it. From the tactile sensor data it may be interpreted that a smaller spall occurred in region R2, but the ice fragments did not immediately clear. Rather these fragments maintained contact with the sensor, resulting in slight increase in total contact area in region R2, though they contribute little force. The large pressure drop in region R2 then results from the combination of a moderate drop in load accompanied by the slight increase in contact area. Results for Failure Event 2 suggest that the drop in total force is dominated by local crushing in region R3, which has a large load drop, small area reduction and significant decrease in pressure intensity associated with it. For Failure Event 3, the decreases in force, area and pressure are fairly consistent across the width of the indentor suggesting a simultaneous crushing failure. Most of the area reduction for this failure occurs near the periphery of the *hpz*s, which is expected for this type of failure.

4. Discussion and Conclusion

The interplay between fracture and crushing processes is important in the compressive ice failure process. Local spalling, local crushing and simultaneous crushing failures were observed to occur intermittently across the indenter. Further work is needed to determine the frequency of occurrence of each type of failure and explore links between these processes. The mechanics associated with each type of failure are considerably different. As discussed by Jordaan et al. (2008), crushing has been associated primarily with damage processes within *hpz*s, while spalling fracture depends primarily on stress, geometry and flaws.

The high degree of non-simultaneity observed in these data highlights the importance of using design methods that account for probabilistic averaging effects. As discussed by Jordaan et al. (2006), probabilistic averaging results in a standard deviation that is markedly lower for the global load than that of local loads. While the effects of probabilistic averaging are more prominent for wider structures, some effect is still expected on the scale of these tests. Efforts to explore links between correlation structure, *hpz* characteristics, observed failure behavior and the relationship between local and global loads are needed. Statistical aspects of *hpz* characteristics such as size, frequency, persistence and intensity are to be explored in further detail; Taylor et al. (2008). The JOIA dataset is an excellent source of detailed information at a resolution previously not available. These data offer much potential insight into the processes associated with compressive ice failure.

Acknowledgments

The authors would like to acknowledge financial support for this work from the Natural Sciences and Engineering Research Council of Canada (NSERC), and the Japan Ocean Industry Association for making these data available.

References

Frederking, R. M., Jordaan, I. J., McCallum, J. S., 1990. Field tests of ice indentation at medium scale Hobson's Choice Ice Island, 1989. Proc. 10th IAHR Symposium on Ice, v2, Espoo, 931-944.

Frederking, R., 2004. Ice pressure variations during indentation. Proc. 17th IAHR International Symposium on Ice. 2004. v2. p. 307.

Jordaan, I. J., 2001. Mechanics of ice-structure interaction. Engineering Fracture Mechanics. 2001. Vol. 68, 1923-1960.

Jordaan, I., Frederking, R. and Li, C. Mechanics of ice compressive failure, probabilistic averaging and design load estimation. Proc. 18th IAHR International Symposium on Ice, Sapporo, Japan, 2006.

Jordaan, I.J., Wells J., Xiao, J., Derradji-Aouat, A., 2008. Ice crushing and cyclic loading in compression. Proc 19th IAHR Symposium on Ice, Vancouver, British Columbia, Canada.

JOIA, 2006. MSFIT Data CD - 1998, 1999, 2000. Japan Ocean Industries Association.

Mackey, T., Wells, J., Jordaan, I.J., Derradji-Aouat, A., 2007. Experiments on the fracture of polycrystalline ice. Proc. 19th International Conference on Port and Ocean Engineering Under Arctic Conditions (POAC 2007). Dalian, China, vol 1, pp. 339-349.

Masterson, D.M., Frederking, R.M.W., Jordaan, I.J., Spencer, P.A., 1993. Description of Multi-Year Ice Indentation Tests at Hobson's Choice Ice Island – 1990. Proc. 12th International Conference on Offshore Mechanics and Arctic Engineering, vol. IV, pp. 145-155, Glasgow, Scotland.

Masterson, D.M., Spencer, P.A., Nevel, D.E., Nordgren., 1999. Velocity Effects From Multi-Year Ice Tests. Proc. 18th International Conference on Offshore Mechanics and Arctic Engineering, St. John's, NL, Canada.

Nakazawa, N., Akagawa, S., Kawamura, M., Sakai, M., Matsushita, H., Terashima, T., Takeuchi, T., Saeki, H., Hirayama, K., 1999. Medium-scale indentation test (MSFIT): results of winter 1998 tests. Proc. 9th International Offshore and Polar Engineering Conference. 1999. p. 498.

Sodhi, D.S., Takeuchi, T., Nakazawa, N., Akagawa, S., Saeki, H., 1998. Medium-scale indentation tests on sea ice at various speeds. Cold Regions Science and Technology. 1998. 28. pp. 161-182.

Taylor, R.S., Frederking, R.M.W., Jordaan, I.J., 2008. Statistical Characteristics of High Pressure Zones in Compressive Ice Failure. (in preparation).

19th IAHR International Symposium on Ice
"Using New Technology to Understand Water-Ice Interaction"
Vancouver, British Columbia, Canada, July 6 to 11, 2008

Ice Crushing and Cyclic Loading in Compression

Jordaan, I. J.
C-CORE
St. John's, NL, A1B 3X5
Ian.Jordaan@c-core.ca

Wells, J.
Memorial University of Newfoundland
St. John's, NL, A1C 5S7
jenniferw@engr.mun.ca

Xiao, J.
Formally: Memorial University of Newfoundland
St. John's, NL, A1C 5S7
jxiao3@ford.com

Derradji-Aouat, A.
NRC-IOT
St. John's, NL, A1B 3T5
Ahmed.Derradji@nrc-cnrc.gc.ca

Abstract

At very slow loading rates, ice will creep; as the rate is increased, microstructural changes occur and the rate of creep is enhanced as a result. These microstructural changes are referred to as "damage". As the rate of loading is increased further, the damage becomes localized into a layer adjacent to the indentor. This layer is associated with "high-pressure zones" (*hpz*'s). A bulb of pressure develops over these zones with values up to 100 MPa at the centre. Processes within the layer vary with distance from the centre; microfracturing and recrystallization occur near the outside with recrystallization and pressure melting (it is supposed) along grain boundaries in the central part. Cyclic loading can result since the cycle of pressure softening and subsequent hardening upon release of the pressure results in a repetitive cycle. An analysis has been performed using the ABAQUS computer program that encapsulates the principal features of the process. Some results of this analysis are given. It is also shown that the mechanics can be scaled geometrically without any basic change. This explains why the *hpz*'s are found over widely differing scales. Laboratory and field data involving cyclic loading, including Molikpaq and medium scale data, are reviewed and discussed in the context of feedback mechanisms and ice-induced vibration. Finally, data and results from impact tests on other materials, as well as dynamic recrystallization at high speeds are reviewed and discussed in the context of ice compressive failure.

Introduction

The word "crushing" as applied to compressive failure in ice obscures a rather complex process. The failure of ice in compression is a rate dependent process. At very slow loading rates, ice will creep; as the rate is increased, microstructural changes occur and the rate of creep is enhanced as a result. These microstructural changes are referred to as "damage". As the rate of loading is increased further, the damage becomes localized into a layer adjacent to the indentor. This layer is associated with "high-pressure zones" (*hpz*'s). Pressures within the center of these zones can reach values of up to 100 MPa. This means that most of the load transmitted to a structure during an interaction occurs through these areas of localized high pressure. The *hpz's* vary in both intensity and location with time. Their spatial distribution is highly dependent upon the geometry of the contact zone (Figure 3). During an interaction, localized spalls occur close to the edges of the contact zone leaving a fracture plane that is in limited contact with the structure. In the case of a narrow ice sheet, this causes the *hpz*'s to become concentrated in the center of the ice sheet and produces a 'line load'. Across a large interaction area, these zones are distributed throughout the contact zone, which now covers a much larger area. In this case, the distribution of the *hpz*'s can be considered to be random as opposed to the 'line loads' found in ice sheets. The formation and evolution of *hpz's* can be directly linked to crushing failure during an interaction.

Cyclic loading can occur as the result of extended periods of crushing failure. These vibrations are important in design. As an example, ice-induced vibrations were experienced by the Molikpaq during a crushing event on April 12, 1986. In this case, the cyclic loading experienced by the structure was found to have been significant enough to cause partial liquefaction of the core of the structure (Hardy et al., 1998). Load cycling behavior is not limited to full-scale interactions. Vibrations and crushing have been observed both in small-scale laboratory experiments as well as in medium-scale field trials as shown in Figures 2 and 3. Figure 2 shows photographs of crushing events that were observed at three scales of interaction. Figure 3 shows load cycling behavior that was observed at three scales of interaction.

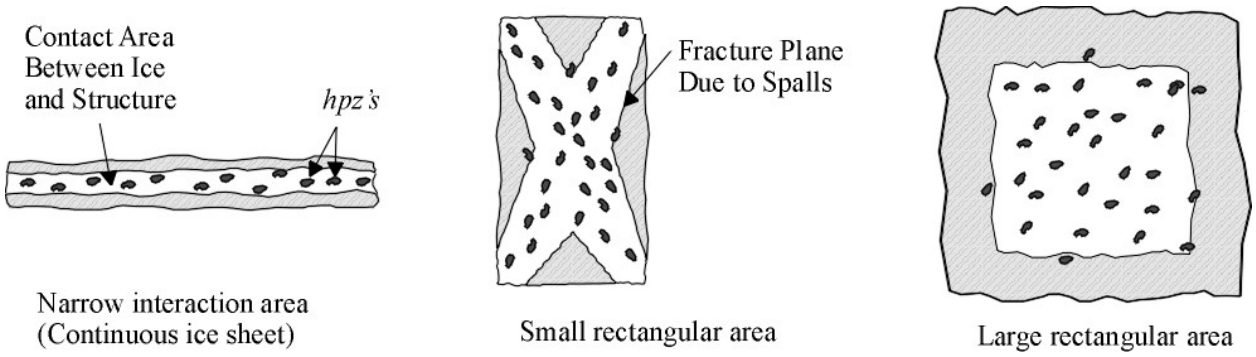

Figure 1. Schematic representation of distributions of *hpz's* for different contact zone geometries.

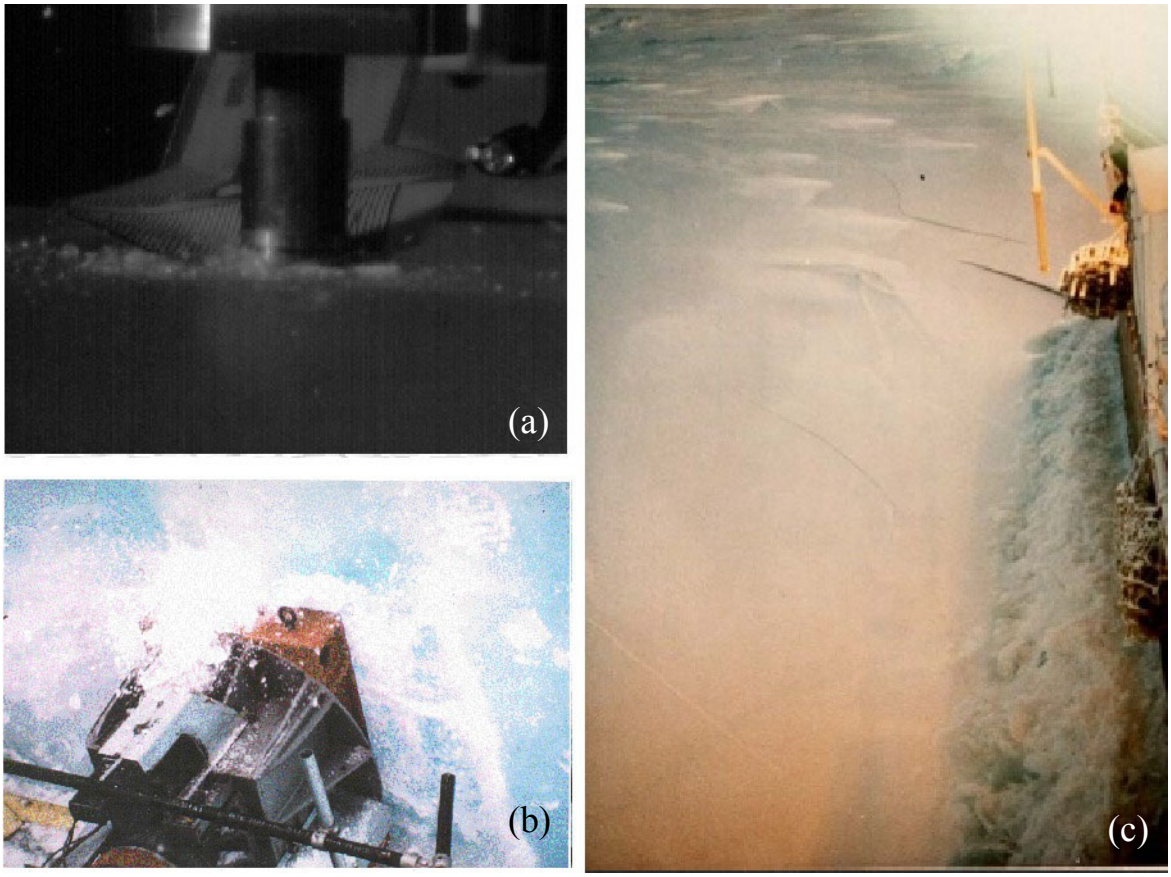

Figure 2. Photographic example of dynamic loading events observed during crushing events at three scales. (a) Small-scale laboratory tests (Embedded crystal paper, in preparation). (b) Extrusion of crushed ice during a medium-scale test at Hobson's Choice (Jordaan, 2001) (c) Mound of crushed ice that developed during the April 12, 1986 event at the Molipaq.

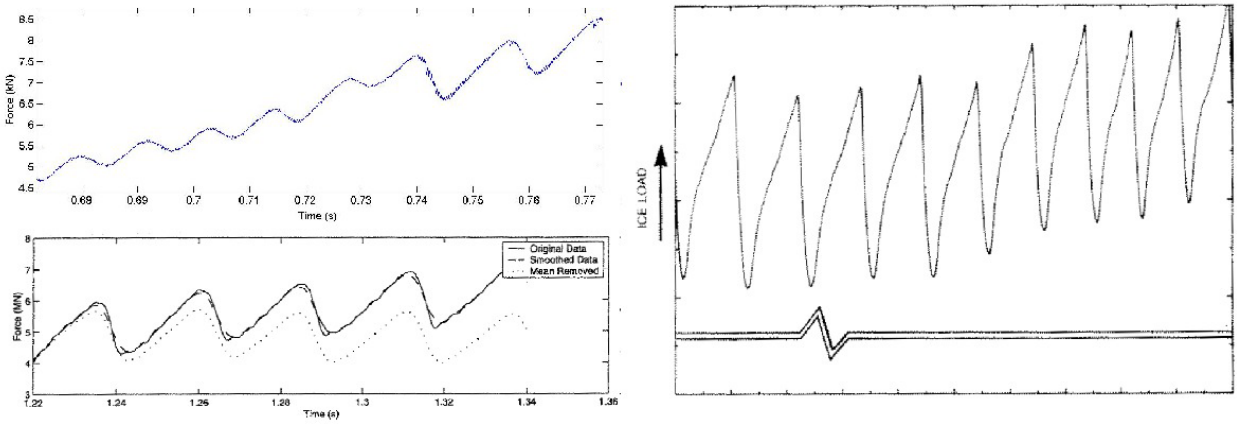

Figure 3. Sample load traces observed during crushing events at three scales. (a) Small-scale laboratory tests (Embedded crystal paper, in preparation), (b) Medium-scale test at Hobson's Choice (Jordaan, 2001), (c) Full-scale crushing event at the Molipaq (Jefferies and Wright, 1988).

High-pressure Zone (*hpz*) Formation and Influence

The formation of high-pressure zones (*hpz*'s) is associated with two processes (Jordaan et al., 1999, Barrette et al. 2002). The first is a concentration of stress in the area of the *hpz*, which results from spalling and fracture processes (Mackey et al., 2007). Since the focus of this paper is on the crushing process, spalling and fracture will not be explored in any detail herein. The second process is the formation of the damaged layer. This layer has been found to exist in both small and medium scale tests and have shown remarkable physical similarity at both scales (Jordaan et al., 2005). The damaged layer that forms under the indenter in tests represents what would be found many times over in a large scale interaction, which would consist of many *hpz's* spread over the entire area of interaction. An initial analysis of the case of more than one hpz interacting with a structure was conducted by Jordaan and Singh (1994). The evolution of a full-scale interaction is strongly dependent on the formation of *hpz's* as they help reduce the total load felt by the structure in a number of ways. The most significant contribution comes through the softening processes that occur within the damaged layer. Within the layer, processes vary with distance from the centre; microfracturing and recrystallization occur near the outside with recrystallization and pressure melting along grain boundaries in the central part (the latter mechanism is hypothesized). The crushing process involves the extrusion of the softened ice from the periphery of the *hpz*, which promotes very regular ice-induced vibrations. Stress concentrations also exist around flaws in the surrounding area. Therefore, during a full-scale interaction, the total load will be significantly reduced by a combination of the localized extrusion of ice from the many *hpz's* and fracture promoted by the presence of flaws. Since the *hpz's* vary in time and space, their presence would promote non-simultaneous failure across a large interaction area. In this paper, we will focus on the contribution of the crushing process to load reduction.

Link Between Ice-Induced Vibrations and *hpz* Formation

Tests have shown that the main mechanism of the ice-induced vibrations can be directly linked to failure processes occurring in the ice. When ice fails by crushing, a repetitive cycle of pressure softening and subsequent hardening upon release of the pressure occurs within the damaged layer as shown in Figure 4. This figure illustrates the behavior of ice in the immediate vicinity of a single *hpz* (Jordaan, 2001). When the ice first encounters the structure, microcracking begins to occur near the outside of the *hpz*, accompanied by extensive recrystallization (A). This leads to a 'white zone' containing cracks and air pockets and eventually causes fragmentation of the ice near the edge of the zone. In the center of the *hpz*, pressure-softening processes occur due to the high confinement and pressure. This causes the formation of a zone of fine-grained, recrystallized ice (B). Extrusion of the crushed and pressure softened ice occurs resulting in a lowering of the pressure in the *hpz* (C). The layer then hardens due to the release of pressure (D). A cycle of pressure softening and hardening develops that produces the load cycling behavior associated with the crushing process. The periods of load cycling are occasional broken up by localized spalls, which reduce the contact area in the vicinity of the *hpz* (E). In the case of a small or medium scale test, these spalls may cause the load cycling to be halted until the pressure builds sufficiently for the cycle of pressure softening and hardening to be renewed. In the case of a full-scale test, these spalls have less significance in the overall crushing process since these interactions involve many *hpz's*.

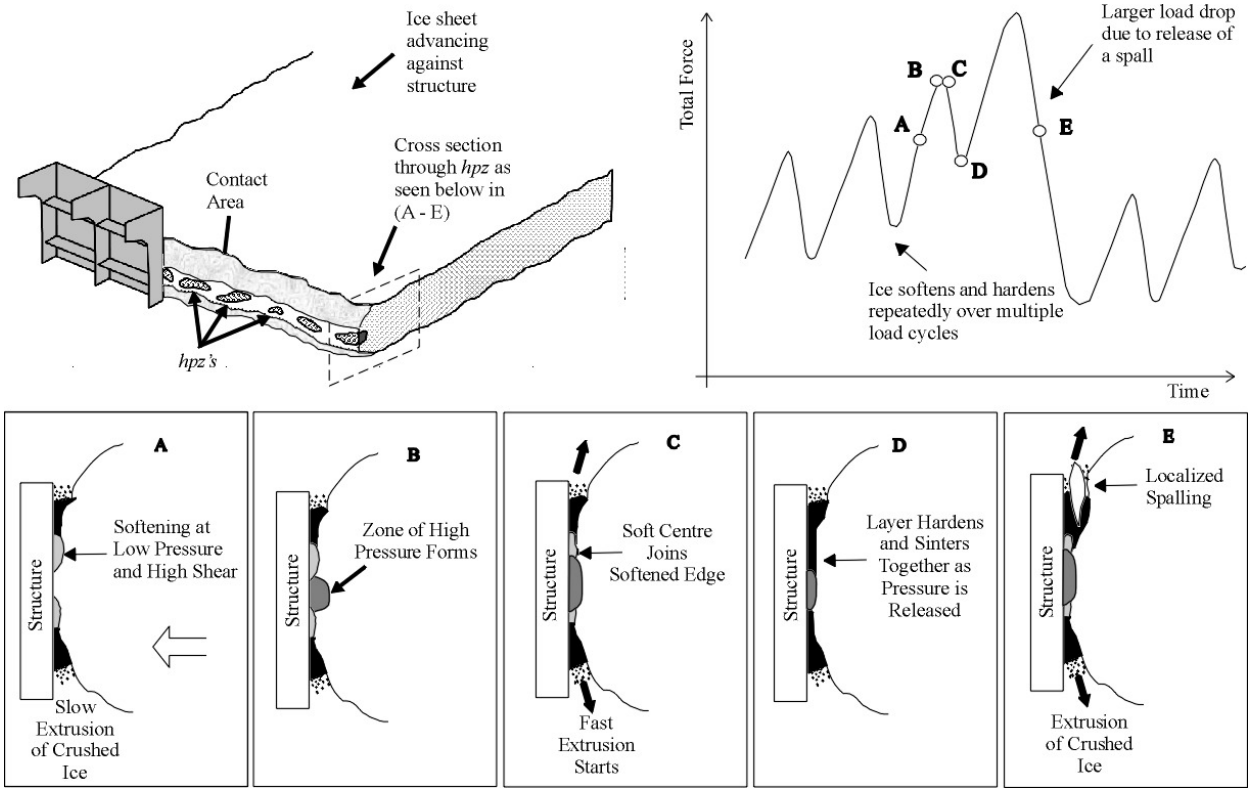

Figure 4. Schematic representation of the link between load cycling and layer dynamics (after Jordaan, 2001).

Laboratory Experiments

A great deal of evidence has been found for the formation of a damaged layer of ice and its relation to the crushing process. In small-scale laboratory tests performed by Barrette et al. (2002) a 2 cm spherical indenter was used to study the failure behavior of the ice in the vicinity of a single, stationary *hpz*. The authors found that the crushing process and load cycling were directly linked and were influenced by both temperature and rate. At relatively warm temperatures, in the range of –2°C, and at a low velocity of 0.2 mm/s, ice fails by a ductile failure mechanism. No extrusion of crushed ice or spalls was seen to occur and a 'smooth' increase in total force was observed. Similar behavior has been modeled previously by Jordaan and Xiao (1992), in which the authors were able to successfully reproduce the smooth increase in total force. In the tests by Barrette et al. (2002), load cycling behavior periodically begins to appear in low temperature tests performed at –10 °C and –20°C with speeds greater than 2 mm/s and continues for speeds increasing to 10 mm/s. This load cycling was accompanied by the extrusion of crushed ice and the formation of damaged layers at the indentation site.

This behavior was studied in greater detail in a recent test series by Wells et al. (2008). In this test series, a 20 mm indenter was again used. The tests were recorded using a high speed video camera with frame rates of 1000 and 1600 fps. A thin, pressure sensitive film (the I-Scan system by Tekscan) dynamically recorded the pressure distribution at the ice-indenter interface. During the tests, crushing events were visually apparent and were classified by the continuous extrusion

of material from under the indenter. The crushing events were accompanied by load cycling, which was apparent on the synchronized load traces. An example of a crushing event is given in the sequence of frames in Figure 5. Each successive drop in load shown in Figure 5 (e) is accompanied by the ejection of material from the indentation area. This extrusion appears on the pressure distribution as regular reductions in contact area from the periphery of the loaded area. The peaks in pressure in this case are mainly concentrated in the central regions of the indenter and remain relatively constant throughout the entire crushing event. This behavior reflects what has been found to occur in the vicinity of *hpz's* during the JOIA program, medium-scale tests. In the case of these tests, when first-year ice sheets were indented with a flat indenter, multiple *hpz's* were distributed across the area of interaction in a 'line-load'. In the vicinity of individual *hpz's* layer dynamics were observed similar to the results shown in Figure 5 (Taylor et al., 2008).

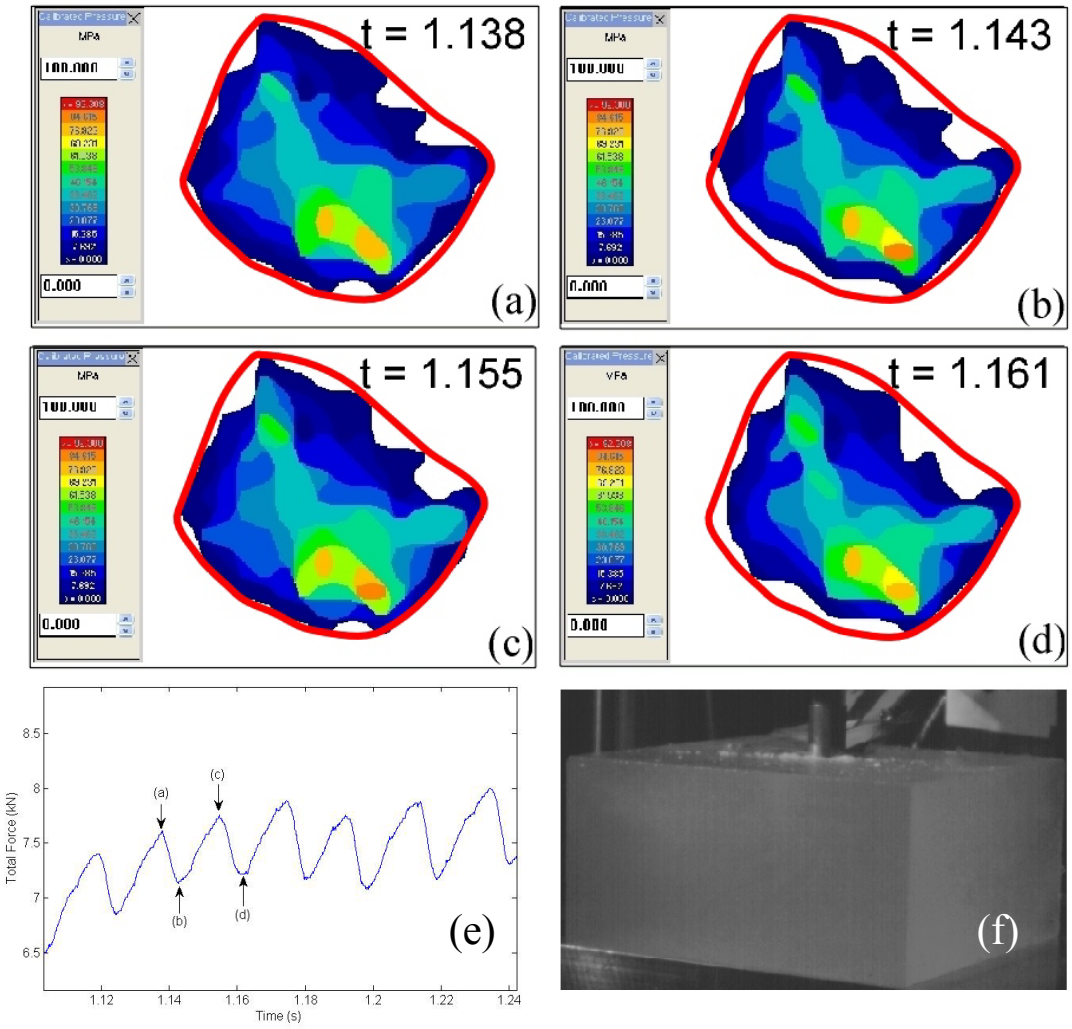

Figure 5. Crushing event during a small-scale laboratory test. (a-d) Pressure distribution recorded during the crushing event. The red circle drawn on the figures represents equal areas. (e) Load cycling observed in the synchronized load trace during the event (f) Frame taken from a high-speed video recording of the event. (Embedded crystal paper, in preparation)

The mechanics involved in this process can be scaled geometrically without any basic change (Jordaan, 2001). This explains why the *hpz*'s are found over widely differing scales. The physical composition of the damaged layer also shows remarkable similarity at both the small and medium scales. It can be assumed that this similarity exists at the full-scale as well. Therefore, it is no surprise that a dependence on loading rate for ice-induced vibrations was observed during the Hobson's choice medium-scale field trials (Jordaan, 2001), similar to what is observed in small-scale tests. Neither extrusion of crushed ice or load cycling behavior was observed in slow rate tests. As the rate is increased, crushing behavior becomes apparent along with damage layer formation. Load cycling begins at rates above 3 mm/s and is accompanied by the production of large quantities of crushed ice (Masterson et al., 1999). The rate dependence of ice-induced vibrations and link to the crushing process has also been observed at the full-scale. In the case of ice-interactions with the Molikpaq, velocities in the range of 2.5 – 10 cm/s promoted high total loads while being accompanied by vibrations in the range of 0.5 – 4 Hz (Sanderson, 1988). Within the range of velocities that cause vibrations, crushing failure was always observed. As an example, in the April 12, 1986 event alluded to earlier, a velocity of approximately 5 cm/s was recorded. While the event was occurring, ice was completely pulverized and extruded upwards, creating piles of crushed ice as high as 8 - 10 m. The crushing was accompanied by ice-induced vibrations with a frequency of 0.8 – 1.4 Hz (Sanderson, 1988).

Dynamic Recrystallization at High Speeds in Compression

A critical feature of the formation of the damaged layer of ice is recrystallization. The high pressures and confinements in the center of hpz's have been found to lead to a zone of recrystallized ice in the center of the damaged layers. There has been ample evidence of grain refinement and recrystallization observed during small and medium scale testing. A few examples will be given herein. Recrystallization has been observed during indentation tests both at the small (Wells et al., 2008; Barrette et al., 2002; Frederking and Gold, 1975; Barnes and Tabor, 1966) and medium (Kennedy, 1990; Jordaan, 2001) scales. For example, Figure 7 shows three examples of damaged layers containing recrystallized zones that were observed during tests by Wells et al. (2008).

Recrystallization in ice has also been observed in other types of testing. Triaxial tests have been used to reproduce the confining pressures felt by ice in the center of *hpz's*. For example, Melanson et al. (1999) found that at low strain rates, very little micro-cracking occurs and the resulting grain size reduction was the result of dynamic recrystallization. Kuon and Jonas (1973) performed a series of tests that were performed by extruding the specimens of ice backwards through a die and hollow ram. It was found that at constant extrusion temperature, the grain size decreased with increasing strain rate. At constant strain rate on the other hand, the grain size increased with temperature. Also, the presence of subgrains was observed within some of the recrystallized grains. The authors speculated that this implies that the subgrains were formed during the deformation and thus, were caused by dynamic recrystallization.

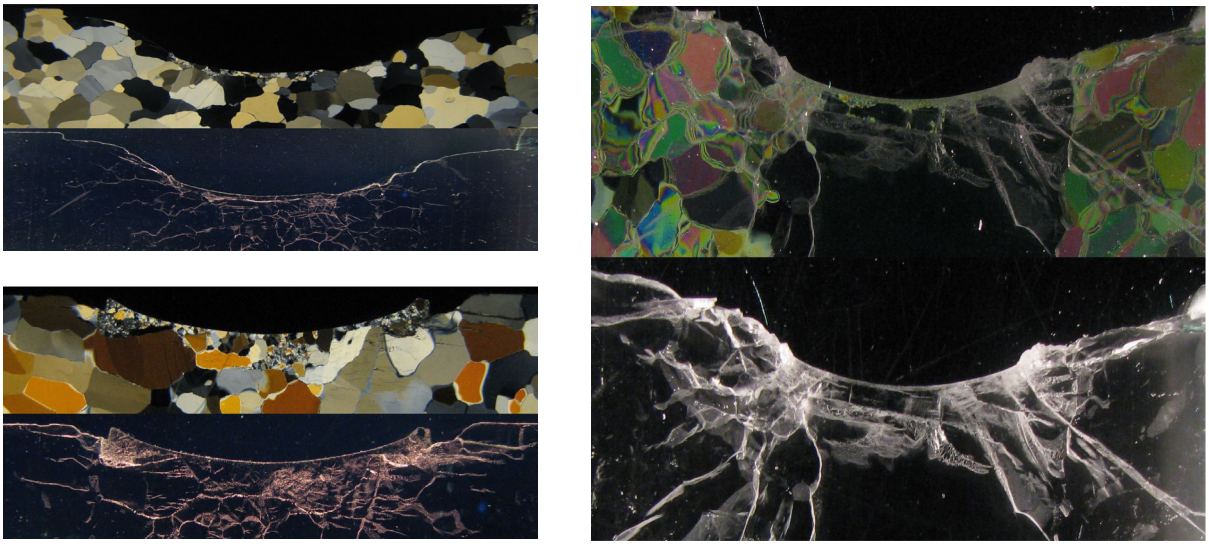

Figure 7. Three examples of thin-sections taken during small-scale tests by Wells et al. (2008). The upper photograph in each picture shows the thin-section viewed using cross-polarized lighting conditions. The lower photograph shows the same thin-section viewed using side-lighting conditions. Each set of photographs show fine-grained recrystallized ice in the damaged layer. The recrystallization is apparent since when viewed under cross-polarized conditions, the grains in these areas are much smaller than the parent grains, yet the side-lighting conditions show that these zones are free from cracks. (Mackey et al., 2007). (a) Indentation speed of v = 3.0 mm/s (b) Indentation speed of v = 10.0 mm/s (c) Indentation speed of v = 5.0 mm/s.

Recrystallization of single-crystals of ice has been studied using thin monocrystalline ice specimens and a transparent glass surface (Offenbacher et al., 1973). The contact zone between the ice and the upper glass plate was observed and it was noted that at loads above ~ 1.5 kg or at lower loads that were held for longer periods of time, cracks were often produced in a direction perpendicular to the c-axis. Recrystallization was found to begin along these cracks and then spread into the ice. The inadvertent presence of a grain boundary caused a similar recrystallization behavior to occur. After a sufficient period of time, the small crystals began to grow at the expense of neighboring crystals. A similar behavior was found to occur during a relatively quick indentation test performed by Wells et al. (2008). Figure 7 (e-f) shows a thin-section taken from an indentation test performed at 10 mm/s. The figure shows the formation of recrystallized grains along cracks that formed within a large single-crystal of ice within the indented sample.

Formation of damaged layers has also been observed to occur during quick impact tests by Kheisin and Cherepanov (1973). During these tests, a cast steel ball was dropped onto fresh water lake ice. After impact, the top 2 cm of ice showed a distinguishable, opaque white layer of total fracturing and compression. The upper portion of the layer (1 – 1.5 cm) was semi-transparent. The authors hypothesized that this was a result of melting and refreezing at the surface. The ice in the layer contained fine-grains which were much smaller than the parent ice and had a random crystal orientation. Additionally, it was observed that after all impacts a layer of finely crushed ice was present. It was hypothesized that particles of submicroscopic size were dispersed throughout the damaged ice. These small particles acted to "lubricate" the system such

that the extruding crushed ice can be considered as a viscous fluid (Kheisin and Cherepanov, 1973).

Finally, there also exists a great deal of precedent for the formation of recrystallized grains in fast impact tests in warm metals (Li et al, 2005; Murr et al., 1998; Duan et al., 2003; and Murr et al, 2002). In all these tests, permanent craters are formed by quickly impacting various warm metals with projectiles. Under certain circumstances, the walls of these impact craters are found to contain recrystallized grains, implying that the process of dynamic recrystallization can occur on a relatively fast time scale as opposed to only occurring during slow creep as had been supposed earlier.

Shear Softening Model as Influenced by Pressure

An analysis has been performed using the ABAQUS computer program that encapsulates the principal features of the process. The analysis was developed based on damage mechanics (Jordaan et al., 1999, 2001). Comprehensive experimental studies (Meglis et al., 1999; Barrette and Jordaan, 2002) of ice under states of stress that are typical of those within *hpz*'s showed that ice softens considerably as a result of previous stress history. The key to the layer development lies in the increase in the softening that occurs at high pressure and shear. Based on previous work Xiao (1997) proposed the model

$$\mathrm{S} = \int_0^t \left\{ f_1(p)\left(\frac{s}{s_0}\right)^{q1} + f_2(p)\exp\left(\frac{s}{s_0}\right) \right\} \mathrm{dt} \qquad \textbf{[1]}$$

where $S = \text{damage}$, $p = \text{pressure}$, $s = \text{von Mises shear stress}$ and $f_1(p)$ and $f_2(p)$ are increasing and decreasing functions of pressure, respectively. From this, the damage rate dS/dt is given by the term in the parenthesis $\{\square\}$ in equation (1). Implementation of particular functions corresponding to this equation are shown in Figure 6. As explained in Barrette and Jordaan (2002), the softening at high pressures and shear is virtually limitless, so that sharp drops in load result, as is observed.

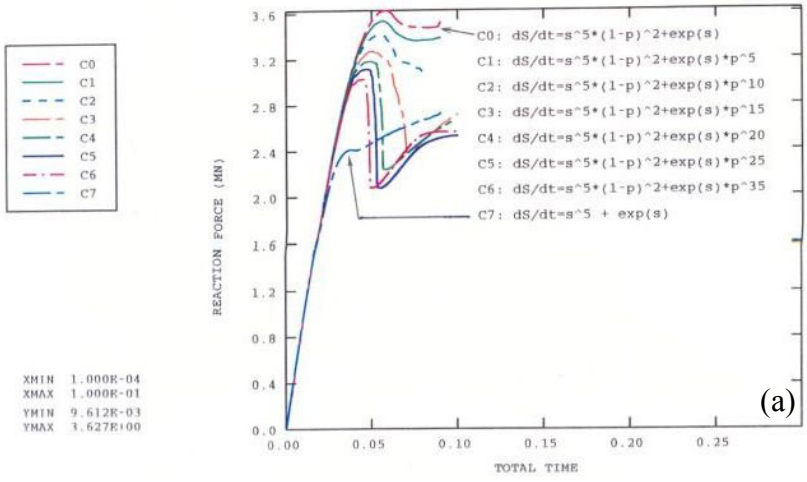

Figure 6. (a) Force-time curves for analysis with the damage model proposed in equation (1)

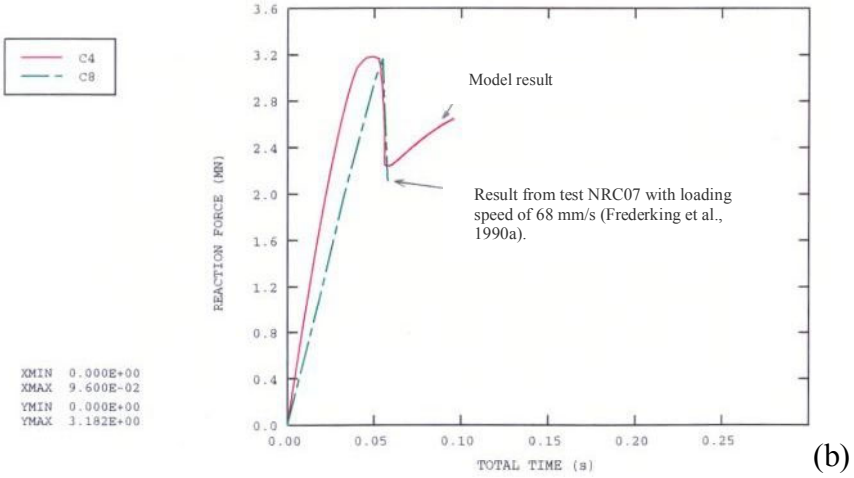

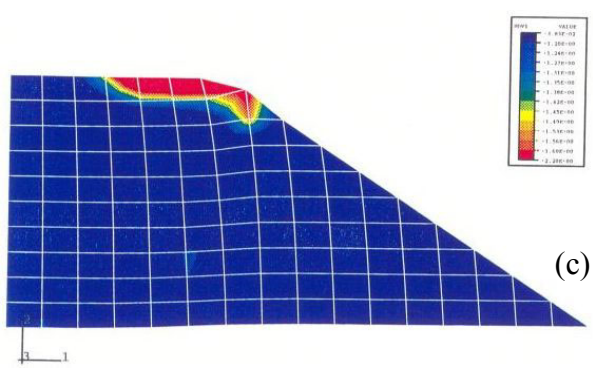

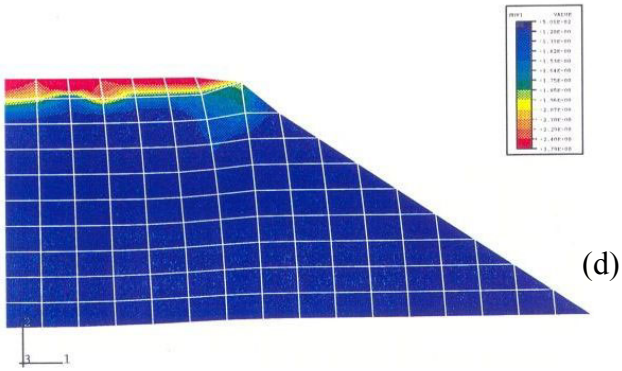

Figure 6 (continued). (b) Force-time curve comparison of model and test results. (c) Damage distribution for $dS/dt = s^5(1-p)^2 + \exp(s)\,p^{10}$; and for (d) $dS/dt = s^5(1-p)^2 + \exp(s)\,p^{15}$. (Xiao, 1997)

Conclusions

The cyclic process of ice failure in compression can lead to dynamic loading. The formation of *hpz's* during an interaction plays a direct role in this process through the creation of a damaged layer of softened ice at the ice-structure interface. Dynamic recrystallization plays an important part in the softening process at high pressures and shear. Vibrations arise from the repetitive cycle of pressure softening and hardening that occurs in the vicinity of the *hpz's* during crushing failure. This behavior is seen at all scales of interaction and has been illustrated by small-scale laboratory tests and modeled by damage mechanics.

Acknowledgements

Financial support for this work has been provided by the Natural Sciences and Engineering Research Council of Canada (NSERC) and by the Program of Energy Research and Development (PERD) of the national research council of Canada.

References

Barnes, P. and Tabor, D., 1966. Plastic flow and pressure melting in the deformation of ice I. Nature, 210: 878-882.

Barrette, P. and Jordaan, I., 2002. Can dynamic recrystallization and bulk pressure melting explain characteristics of ice crushing? Discussion. Ice in the Environment, Proceedings of the 16th international Symposium on Ice, IAHR, Dunedin, New Zealand, 2002, vol. 3:335-354.

Barrette, P. and Jordaan, I., 2002. Compressive Behaviour of Confined Polycrystalline Ice. Final report carried out for the program of energy research and development (PERD) of the national research council of Canada. OERC-2002-02.

Barrette, P., Pond, J. and Jordaan, I. 2002. Ice damage and layer formation in small scale indentation experiments. Ice in the Environment, Proceedings of the 16th international Symposium on Ice, IAHR, Dunedin, New Zealand, 2002, vol. 3:246-253.

Duan, Z. Q., Li, S. X., and Huang, D. W., 2003. Microstructures and adiabatic shear bands formed by ballistic impact in steels and tungsten alloy. Fatigue and Fracture of Engineering Materials and Structures, 26: 1119-1126.

Frederking, R. M. W. et al., 1990. Field tests on ice indentation at medium scale, ice island, april 1989. National Research Council of Canada Report CR 5866.1.

Frederking, R. and Gold, L. W., 1975. Experimental study of edge loading of ice plates. Canadian Geotechnical Jorunal, (12), 4:456-463.

Hardy, M. D., Jefferies, M. G., Rogers, B. T. and Wright, B. D., 1998. DynaMAC: Molikpaq ice loading experience. PERD/CHC Report: 14 – 62 March 1998.

Jefferies, M. G. and Wright, W. H. 1988. Dynamic response of Molikpaq to ice-structure interaction, Proceedings Offshore Mechanics and Arctic Engineering Symposium, OMAE, Houston, Vol. IV, 201-220.

Jordaan, I. J. 2001. Mechanics of ice-structure interaction. Engineering Fracture Mechanics. 68, 1923-1960.

Jordaan, I., Li, C., Barrette, P., Dubal, P. and Meyssonnier, J. 2005. Mechanisms of ice softening under high pressure and shear, Proceedings of the International Conference on Port and Ocean Engineering Under Artic Conditions, 2005.

Jordaan, I. J., Matskevitch, D. G. and Meglis, I. L. 1999. Disintegration of ice under fast compressive loading. International Journal of Fracture. 97, 279 – 300 .

Jordaan, I. J. and Singh, S. K., 1994. Compressive ice failure: critical zones of high pressure. Proceedings 12th International IAHR Ice Symposium, Trondheim, Norway, Vol.1, 505 – 514.

Jordaan, I.J. and Xiao, J. 1999. Compressive ice failure, Proceedings IAHR Symposium on Ice, Potsdam, New York, 1998, Ice in Surface Waters, Ed. H.T. Shen, Balkema, 1999, 2:1025-1031

Jordaan, I. J. and Xiao, J. 1992. Interplay between damage and fracture in ice-structure interaction. Proceedings of the 11th International Symposium on Ice, IAHR, Banff, Alberta, 1992, vol 3: 1448 – 1467.

Kennedy, K., 1990. Dynamic activity and crushed ice behavior in medium-scale ice-structure interactions, Masters Thesis, Memorial University of Newfoundland, Newfoundland, Canada.

Kheisin, D. E. and Cherepanov, N. V., 1973. Change of ice structure in the zone of impact of a solid body against the ice cover surface. Problems of the Arctic and Antarctic, Issues 33–35 (A.F. Treshnikov), Israel Program for Scientific Translations, 239–245.

Kuon, L. G. and Jonas, J. J., 1973. Effect of strain rate and temperature on the microstructure of polycrystalline ice, In Physics and Chemistry of Ice: Proc. from the Symposium on the Physics and Chemistry of Ice, Ottawa, Canada 14-18 August 1972.

Li, G. A., Zhen, L, Lin, C., Gao, R. S., Tan, X., and Xu, C. Y., 2005. Deformation localization and recrystallization in TC4 alloy under impact condition. Materials Science and Engineering A, 395: 98-101

Masterson, D. M., Spencer, P. A., Nevel, D. E. and Nordgren, R. P. 1999. Velocity effects from multiyear ice tests. Proceedings 18th International Conference on Offshore Mechanics and Arctic Engineering (OMAE99). S. John's, Canada, 1999.

Meglis, I., Melanson, P. and Jordaan I.J., 1999. Microstructural change in ice: II. Creep behavior under triaxial stress conditions, Journal of Glaciology, 45(151):438-448 Colour Plates 423-437

Melanson, P.M., Meglis, I. L., Jordaan, I. J., and Stone, B. M., 1999. Microstructural change in ice: I. Constant-deformation-rate tests under triaxial stress conditions, Journal of Glaciology 45 (151), 417-424.

Murr, L. E., Quinones, S. A., Ferreyra T., E., Ayala, A., Valerio, O. L. Horz, F., and Bernhard, R. P., 1998. The low-velocity-to-hypervelocity penetration transition for impact craters in metal targets, Materials Science and Engineering A, 256: 166-182

Murr, L. E., Trillo, E. A., Bujanda, A. A., and Martinez, N. E., 2002. Comparison of residual microstructures associated with impact craters in fcc stainless steel and bcc iron targets: the microtwin versus microband issue. Acta Materialia, 50: 121-131

Offenbacher, I. L., Roselmand, I. C. and Tabor, D., 1973. Friction, deformation, and recrystallization of single crystals of ice Ih under stress, In Physics and Chemistry of Ice: Proc. from the Symposium on the Physics and Chemistry of Ice, Ottawa, Canada 14-18 August 1972.

Sanderson, T. J. O. 1988. Ice mechanics: Risks to offshore structures. Graham & Trotman, London.

Taylor, R.S., Frederking, R, and Jordaan, I. J. 2008. The nature of high pressure zones in compressive ice failure. Proceedings 19th IAHR Symposium on Ice, Vancouver, British Columbia, Canada.

Wells, J., Jordaan, I. and Derradji-Aouat, A. 2008. The influence of embedded flaws on the fracture of polycrystalline ice: laboratory experiments. (In preparation)

Xiao, J. 1997. Damage and fracture of brittle viscoelastic solids with application to ice load models. Phd Thesis, Memorial University of Newfoundland,187 pp.

19th IAHR International Symposium on Ice
"Using New Technology to Understand Water-Ice Interaction"
Vancouver, British Columbia, Canada, July 6 to 11, 2008

Local Ice Pressure Distributions during 1990 Hobson's Choice Ice Island Multi-Year Ice Indentation Tests

R. Frederking and D. Sudom
Canadian Hydraulics Centre
National Research Council of Canada
Ottawa, Ont., K1A 0R6 Canada
robert.frederking@nrc.ca, denise.sudom@nrc.ca

Medium Scale Field Indentation tests on multi-year ice at Hobson's Choice Ice Island in 1990 were examined and local ice pressure distributions determined. Maximum loads of about 10 MN on contact areas of about 1 m^2 were generated in a loading time of 1 to 2 s on multi-year ice. Local pressures of the order of 60 MPa were measured on areas of 0.003 m^2 and less. For areas in the range 0.003 m^2 to 0.1 m^2, the upper bound to local ice pressures is described by the equation

$$P_s = 8\ A^{-0.35}$$

where P_s is local pressure in MPa and A is local area, in m^2, over which the local pressure is averaged. This local pressure-area relation is consistent with pressure-area relations for larger areas. Over the time range of the tests spatial distributions of local pressure were relatively stable, however some high pressure areas were observed to move from one area to another during the test period. The size of these high pressure areas was from 0.01 m^2 to 0.03 m^2.

1. Introduction

The nature of local ice pressure distributions during indentation has been a subject of interest for some time in ice mechanics. It is an important factor in developing an understanding of the ice failure process since it provides a means of scaling-up small-scale laboratory and field measurements to larger scales needed for design of offshore structures and ship hull structures. Obtaining good measurement data on pressure within the contact area was always a problem. If the sensor area was large, the pressure was averaged over too large an area; if the sensor area was small, there were usually insufficient sensors to determine the distribution of pressures. The Medium Scale Field Indentation tests carried out in May 1990 at Hobson's Choice Ice Island north of Ellef Ringnes Island (Masterson et al., 1993) provide a data source where both local ice pressures and global ice loads were measured during crushing failure of ice. The Japan Ocean Industry Association sponsored an extensive series of indentation tests (Nakazawa et al., 1989) in which global loads and local ice pressures were measured in warm sea ice. Some of these data have been made available through the IAHR Ice Crushing Working Group and have been used in a study of High Pressure Zones (Taylor et al., 2008). This paper will examine the Ice Island local ice pressure data to define distributions and how they change with time.

2. Test Set-up

The Ice Island field tests were conducted in a 3 m deep trench cut into a multi-year floe. A hydraulic loading system comprised three hydraulic actuators, each with a capacity of 4 MN, and thus could generate a maximum force of 12 MN. The actuators reacted against one wall of the trench and forced an indenter of specific geometry and characteristics against a specially prepared ice face on the opposite wall. A schematic of the test apparatus in the trench is shown in Figure 1. The actuators were servo controlled to produce a constant velocity of 100 mm/s. The maximum stroke of the actuators was 300 mm, although in most cases the actual stroke was less than 200 mm.

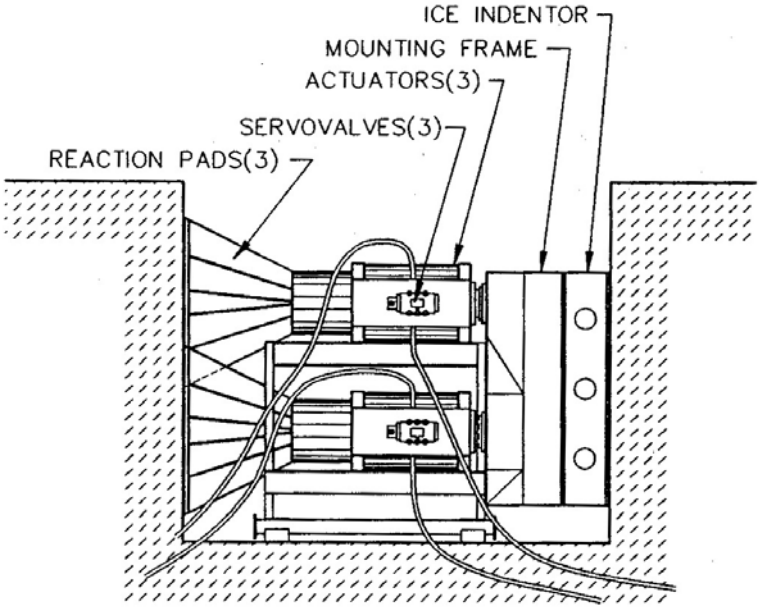

Figure 1. Ice Island test apparatus set-up

A flat rigid indentor, 1.2 m wide and 1.5 m high, was moved by the actuators against a specially shaped ice face, crushing the ice. The indentor, shown in Figure 2, was instrumented with two sets of sensors to measure local ice pressures. The rectangular area near the top of the indentor was a 36 element pressure panel supplied by Helsinki University of Technology (TKK). This type of sensor had been used by TKK in earlier measurements on ships (Joensuu, 1988). The sensor comprised a 9 x 4 rectangular array of piezoelectric film sensors each 36 mm by 36 mm (see Figure 3). A central area 25 mm by 25 mm was actually sensitive to pressure. Because of limitations in the number of channels in the data acquisition system, only 26 channels could be recorded. The overall measurement area was 290 mm wide by 145 mm high, for an area of about 0.04 m^2, and data were recorded for 0.033 m^2 of this area. In the lower part of the indentor there was an array of 12 piston type pressure cells each incorporating a miniature strain gauged load cell. They had a piston diameter of 12.7 mm and a full scale range of 70.2 MPa. The pressure cells were spaced 75 mm on centres and they encompassed an overall measurement area of about 0.09 m^2. The layout of the pressure cells is illustrated in Figure 4.

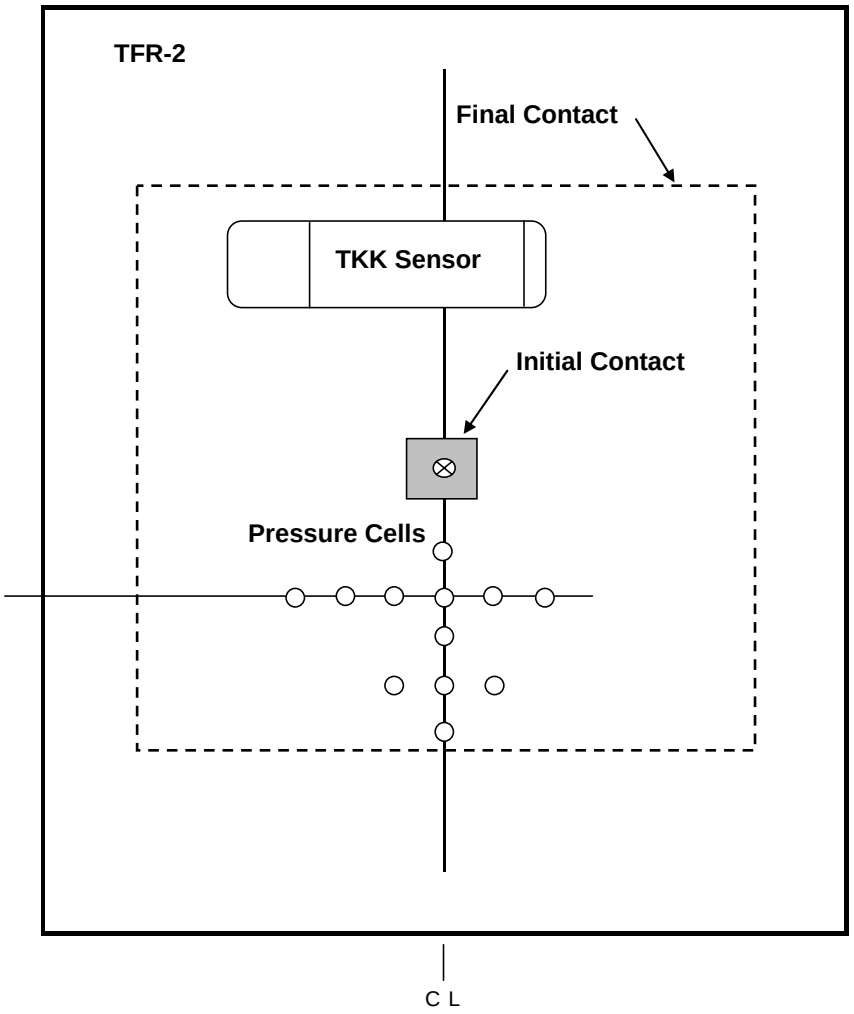

Figure 2. Schematic of the indentor viewed from the ice face

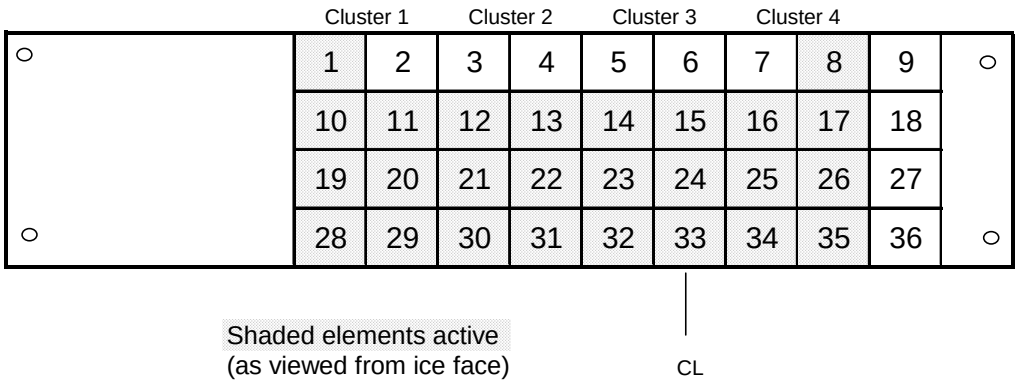

Figure 3. Helsinki University of Technology (TKK) piezoelectric film ice pressure sensor layout, shaded elements recorded

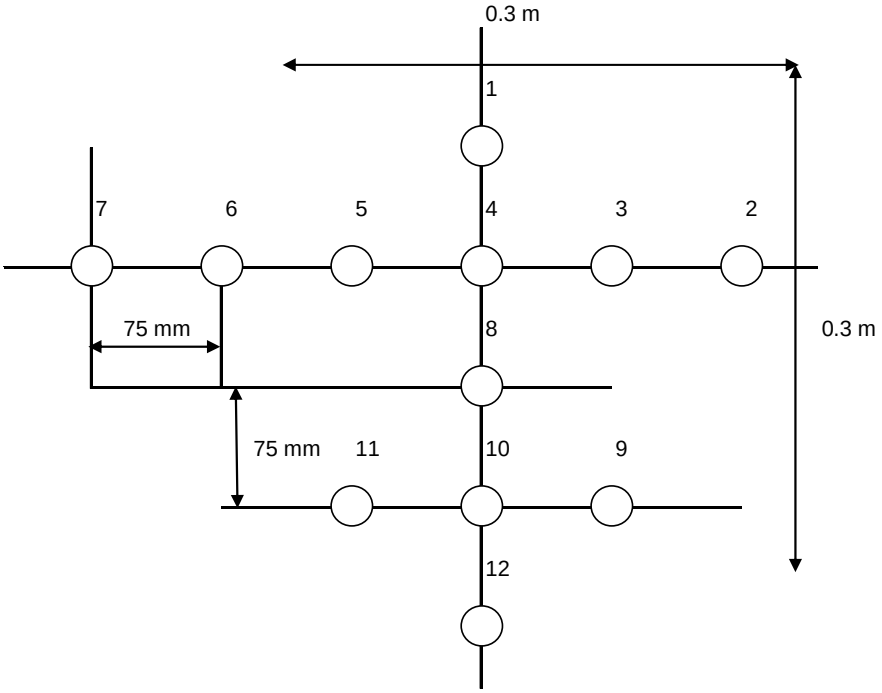

Figure 4. Pressure Cell sensor layout on indentor

In the tests the rigid indentor crushed a pyramidal shaped ice face. This shape was selected to be a simple representation of the edge of an ice feature contacting a ship or structure. The pyramidal shaped protrusion was carved into the face of the trench wall. A cross-section of a typical profile is illustrated in Figure 5. The tip of the pyramid was truncated to present either a 0.1 m square top or a 0.5 m square top with a flat surface. These tests started with an initial contact area of 0.01 m^2 or 0.25 m^2, and nominal contact area increased in a simple geometric relation to the penetration as the indentor advanced into the ice. Ice temperatures for the tests were -10±1° C.

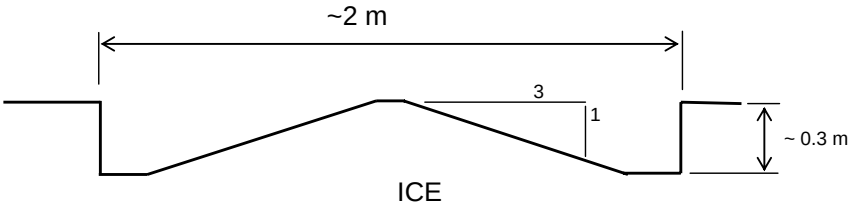

Figure 5. Cross-section of truncated pyramidal face in trench wall at Ice Island

3. Test results

Four tests were carried out with the rigid indentor, all at a constant rate of 100 mm/s. For test TFR-2 the ice edge was a pyramid truncated to a 0.1 m square at the tip. The initial contact of the indentor with the ice was the shaded area in Figure 2, and by the end of the test the nominal contact area was marked by the dashed line. Referring to Figure 2 it can be seen that neither of the areas instrumented for measuring local pressure were in contact with the ice at the start of the test, but were so at the end.

Force and penetration for Test TFR-2 are plotted in Figure 6. The maximum force was almost 12 MN and penetration about 130 mm. The highest force while the ice was actively crushing was about 9.5 MN. Note that as the indentor slowed to a stop a higher load was generated. It can be seen that the servo system generally maintained a constant velocity. The large force drops at about 0.25, 0.6 and 1.25 s occurred when sections of ice spalled away from the face. At the instants when the ice failed (load drops), the indentor surged ahead until the servo system brought it back to follow the programmed rate of 100 mm/s. The smaller fluctuations in the force trace reflect local crushing of the ice at the interface with the indentor. From the force and penetration, nominal area and average pressure can be determined. The nominal area is defined as the area intersected by the face of the indentor and the truncated pyramid. The crushed ice displaced is ignored. Close examination of the start of the test indicated that a force of 0.38 MN was required to initiate crushing on the 0.01 m^2 tip of the pyramid, for a pressure of 38 MPa.

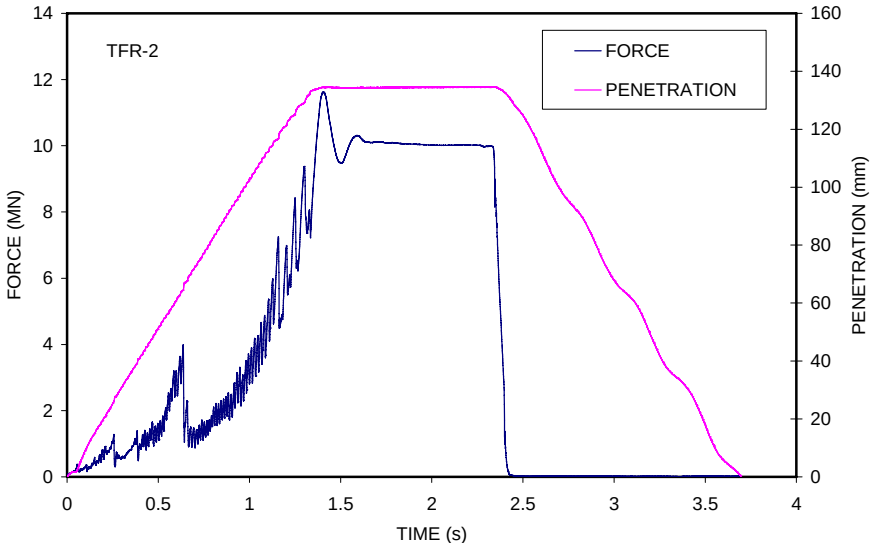

Figure 6. Force and penetration time series for test TFR-2

Average pressure on the indentor (assuming nominal area), together with local pressures from the instrumented sections of the indentor, is plotted in Figure 7. The average pressure at the end of the test assuming nominal area is about 12 MPa on 0.8 m^2, however if it is assumed the crushed ice displaced by the indentor remains at the interface with the indentor, the area in contact is increased by about a factor of 2.5, so the average pressure over 2 m^2 is about 4.8 MPa. The local pressures do not start to respond until about 0.6 s into the test, that is when the indentor has penetrated far enough for the sensors to contact the ice face. The maximum pressure from a single pressure cell (PC) (see PC 6 in Figure 4) reaches a value of almost 60 MPa at the end of the test. The average of the pressure cells (PC), which are assumed to represent an area of 0.09 m^2, reached a value of about 9 MPa at the end of the test. This pressure is always lower than the average pressure over the nominal contact area on the indentor, indicating it was likely in a low pressure area near the edge of the contact area. The maximum pressure from a single element of the piezoelectric film (TKK) sensor was about 10 MPa at the end of the test and the average was about 3.5 MPa. These pressures are surprisingly low. A possible explanation for the low pressures from the TKK sensors is that they were located near the edge of the contact area with the ice where low ice pressures would be expected. Later it will be shown that in this test the TKK sensor gave abnormally low pressures.

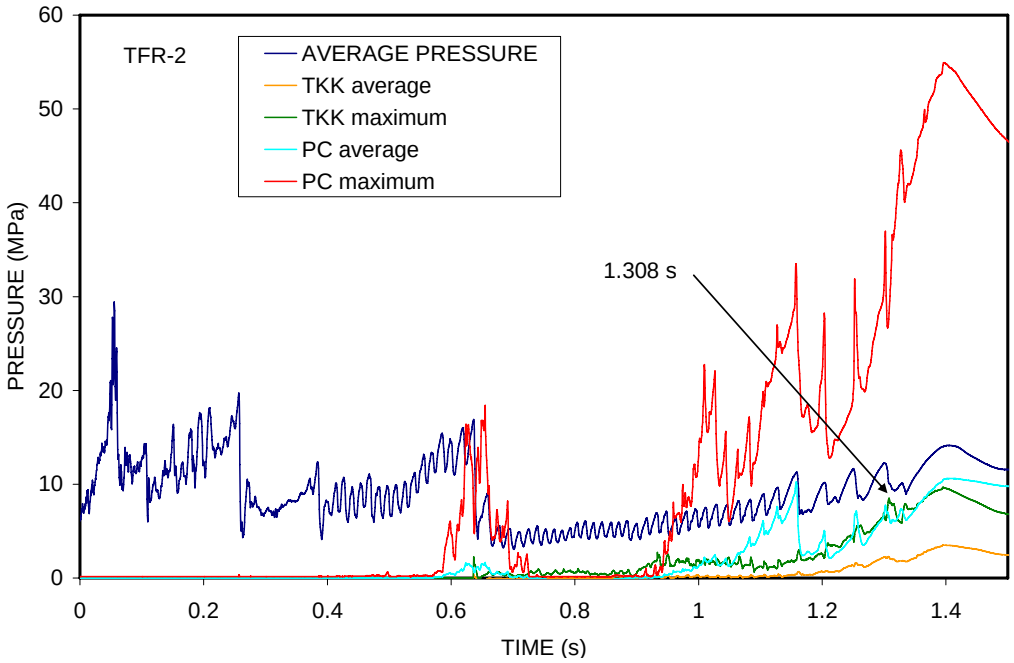

Figure 7. Average and local pressure time series for test TFR-2

A peak in the maximum pressure on the TKK sensor noted at 1.308 s in Figure 7 is used as a point in time for examining the spatial distribution of local pressure on the TKK sensors, see Figure 8. The maximum pressures were in the corner of the sensor (elements 34 and 35 in Figure 3) and generally were higher along the lower edge of the sensor.

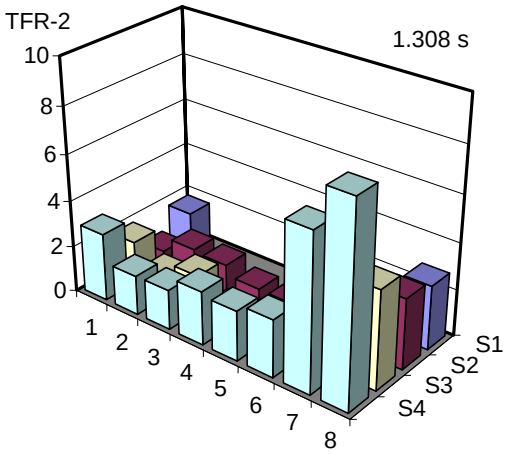

Figure 8. Spatial distribution of local pressure on TKK sensor at time of maximum pressure for test TFR-2

Figure 9 plots the average local pressure on 4 different local areas at the instant of maximum local pressure (1.308 s). The smallest area is one element, 36 mm by 36 mm, (0.0013 m^2) and the local pressure on it is the maximum pressure on the array of elements. The second area is four adjacent elements, 72 mm by 72 mm (0.0052 m^2), the one with the highest pressure and its three neighbours, and the pressure on this area is the average of the pressures on the four elements. The third area is a square of 9 immediately adjacent elements, including the one with the highest pressure, and the local pressure is the average of the pressures on those 9 elements (area = 0.012 m^2). The average on all 26 elements is assumed to apply to an area of 0.033 m^2. The best fit line to the data is a power relation of the form $P = C \cdot A^b$ where C is referred to as the Pressure Coefficient and b is the Exponent.

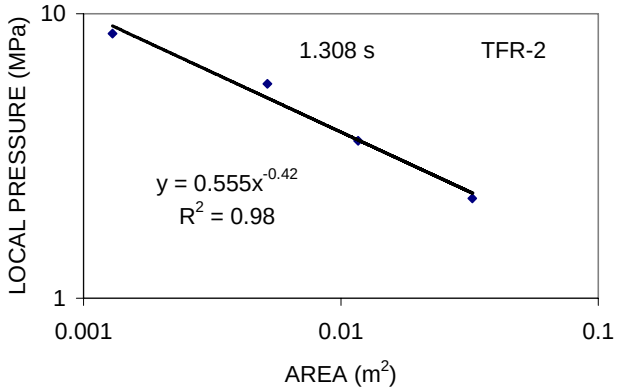

Figure 9. Local pressure versus area on TKK sensor at time of maximum pressure, test TFR-2

As another illustration, for Test TFR-3 the rigid indentor was moved against a pyramid truncated to a 0.5 m square, as shown by the shaded area in Figure 10. The dashed line marks the outline of the nominal contact area at the end of the test. Initially some of the pressure cells (PC) were in the initial contact area but not the piezoelectric film (TKK) sensor. Both sets of local pressure sensors were within the contact area by the end of the test.

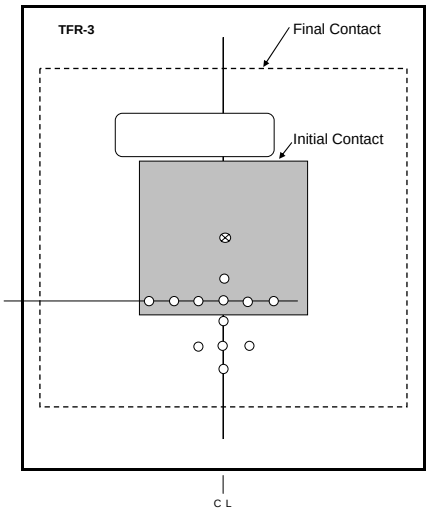

Figure 10. Test TFR-3, truncated pyramid with 0.5 m by 0.5 m square tip

Force and penetration for Test TFR-3 are plotted in Figure 11. The maximum force was almost 12 MN and penetration about 95 mm. The first large force peak and drop, at about 0.1 s, was the break-out of the near perfect contact between the ice face and indentor. Initial failure of the ice on the 0.25 m^2 area required a pressure of 14.7 MPa. In this test the fluctuations in the force were proportionally larger than in test TFR-2. Also it can be noted that while the servo system maintained an average velocity of 100 mm/s, there were steps in the penetration record where slower and faster speeds than the set speed were realized, indicating the servo system was not able to maintain a constant velocity.

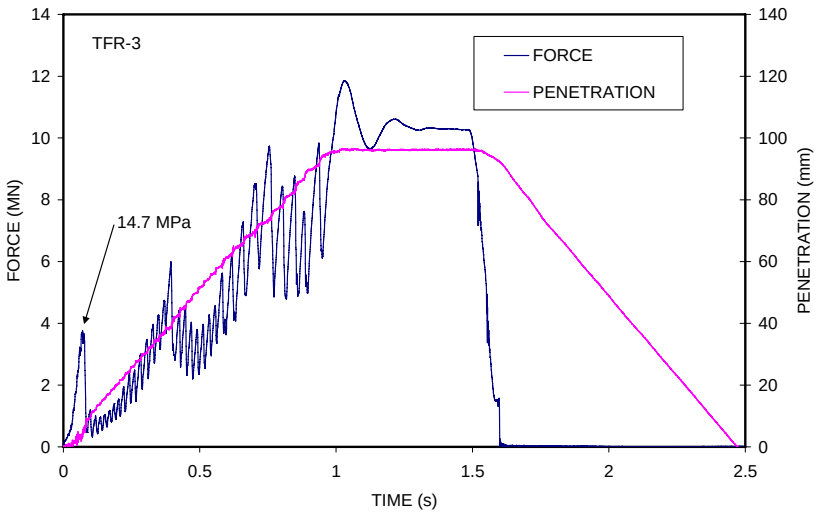

Figure 11. Force and penetration time series for test TFR-3

Average pressure on the indentor, together with local pressures from the instrumented sections of the indentor is plotted in Figure 12. The average pressure at the end of the test was 9.4 MPa on a nominal area of 1.15 m^2. However, taking into account the volume of crushed ice, the final

contact area is increased by a factor of 1.5 so the average pressure at the end of the test was more likely 6.2 MPa on 1.725 m^2. It can be seen that the local pressures from both systems respond immediately and the pressure cell (PC) registers an initial high pressure of about 40 MPa. The initial local ice pressure on the TKK sensor indicated that the indentor was lower with respect to the truncated pyramid than assumed. Later in this test the maximum single pressure cell (PC) reached a value of over 60 MPa and a single TKK element 55 MPa. The average pressure on the whole TKK sensor (with an area of 0.033 m^2) reached a maximum of about 25 MPa at 0.76 s. All the pressures, from the global average pressure determined from the force on the indentor, to the individual and average ice pressures on the two sensing areas are synchronized, rising and falling in unison, only differing in magnitude.

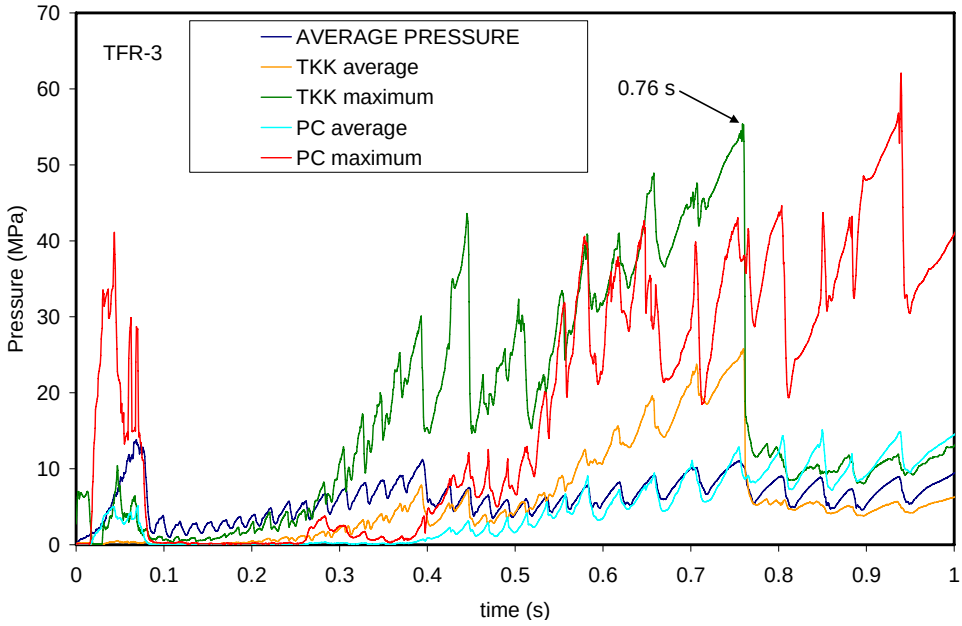

Figure 12. Average and local pressure time series for test TFR-3

The peak in the maximum pressure of TKK sensor was noted at 0.76 s in Figure 12. The spatial distribution of local pressure at this time for the TKK sensors is plotted in Figure 13. The maximum pressures were along the lower edge of the sensor (elements 28 to 35 in Figure 3). The spatial pressure area distribution of pressure at 0.76 s when treated in a similar manner to that in Test TFR-2 had an Exponent of -0.25 and a Pressure Coefficient of 11.4 MPa. The exponent in this case indicates a more uniform pressure distribution than the one in test TFR-2. The Pressure Coefficient for Test TFR-3 is much greater than that for Test TFR-2, indicating higher pressures overall.

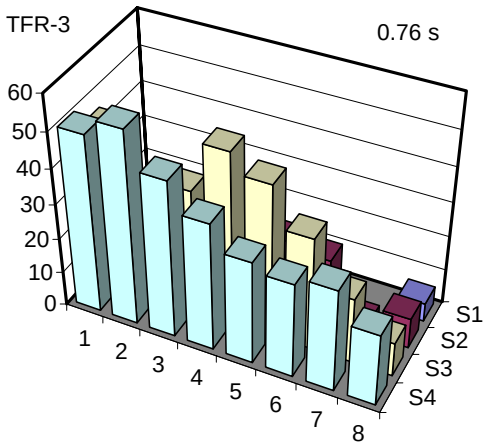

Figure 13. Spatial distribution of local pressure on TKK sensor at time of maximum pressure for test TFR-3

The total measurement width of the TKK sensor was 290 mm, so it offered an opportunity to examine the spatial distribution of local pressure over time. Using a similar approach to Taylor et al. 2008, average local pressures were determined over each of four clusters of elements in Figure 3 (CL1 to CL4). Each cluster comprised six or seven elements (approximately 75 mm by 100 mm). Time series of these pressures are plotted in Figure 14. Over the time interval of the test, less than 1 s, the pressures on the four clusters were generally similar. The only notable relative change with time was the maximum pressure shifted from CL4 at 0.45 s to CL 2 at 0.75 s, indicating that a centre of high pressure had developed and disappeared at CL4, and then another one developed at CL2-CL3-CL1. The TKK sensor data are less complete that those reported by Taylor et al. 2008, however they to indicate mobility of a high pressure zone.

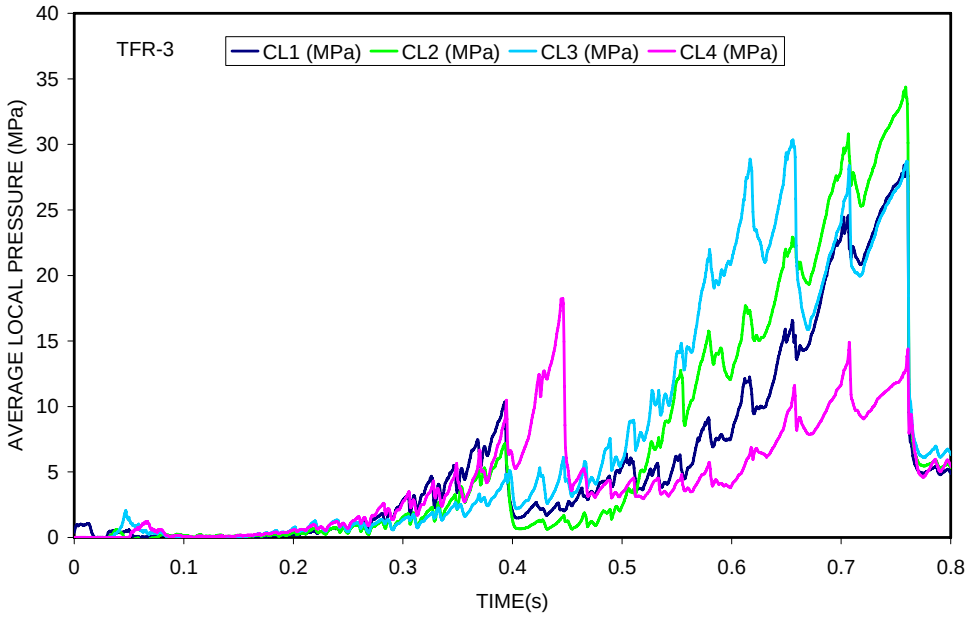

Figure 14. Local cluster pressures on TKK sensor during test TFR-3

Similar exercises can be done for tests TFR-4, which had a similar geometry to test TFR-2 and TFR-5, which had a similar geometry to test TFR-3, however space precludes presenting them.

4. Summary

The local ice pressure results from the TKK sensor and the pressure cells (PC) for all 4 tests are summarized in Table 1. The maximum pressures for both local pressure sensor systems are from a single cell or element. The actual pressure cell area was 0.000125 m^2 and the active area of a single element for the TKK sensor was 0.00625 m^2. What is apparent from these results is that for these very small areas the local pressure is 50 to 60 MPa, independent of area. The average pressure for the pressure cells (PC) is the average of the actual individual cells and the area is taken to be 0.09 m^2, roughly the area encompassed by the cells. There is an implicit assumption in this that the pressure measured on a single cell can be extended to an area 75 mm by 75 mm, or 0.0056 m^2. The area attributed to the TKK sensor average pressure is 0.033 m^2. In this case there is more certainty about the area. For the TKK sensors the local pressure area relation, Pressure Coefficient and Exponent are based on area ranging from 0.013 m^2 to 0.033 m^2.

Table 1. Summary of local pressures and distributions from Ice Island tests

Test No.	Pressure Cells (PC)		TKK Sensors			
	Maximum Pressure 0.00012 m^2	Average Pressure 0.09 m^2	Maximum Pressure 0.00625 m^2	Average Pressure 0.033 m^2	Pressure Coefficient	Exponent
	MPa	MPa	MPa	MPa	MPa	
TFR-2	45.4	10.1	(8.4)*	(2.0)	0.6	-0.42
TFR-3	62.1	15.1	55.3	25.6	11.4	-0.25
TFR-4	52.9	15.7	48.1	23.3	4.5	-0.35
TFR-5	(36.9)	(7.0)	60.7	22.0	3.3	-0.44
average	53	14	55	24	6.5	-0.37

* values in parentheses ignored in averages

The data from Table 1 and the element groups of the TKK sensor are plotted in Figure 15. For areas less than 0.003 m^2 it appears to be a reasonable observation that local ice pressure is independent of area, and is thus an upper bound.

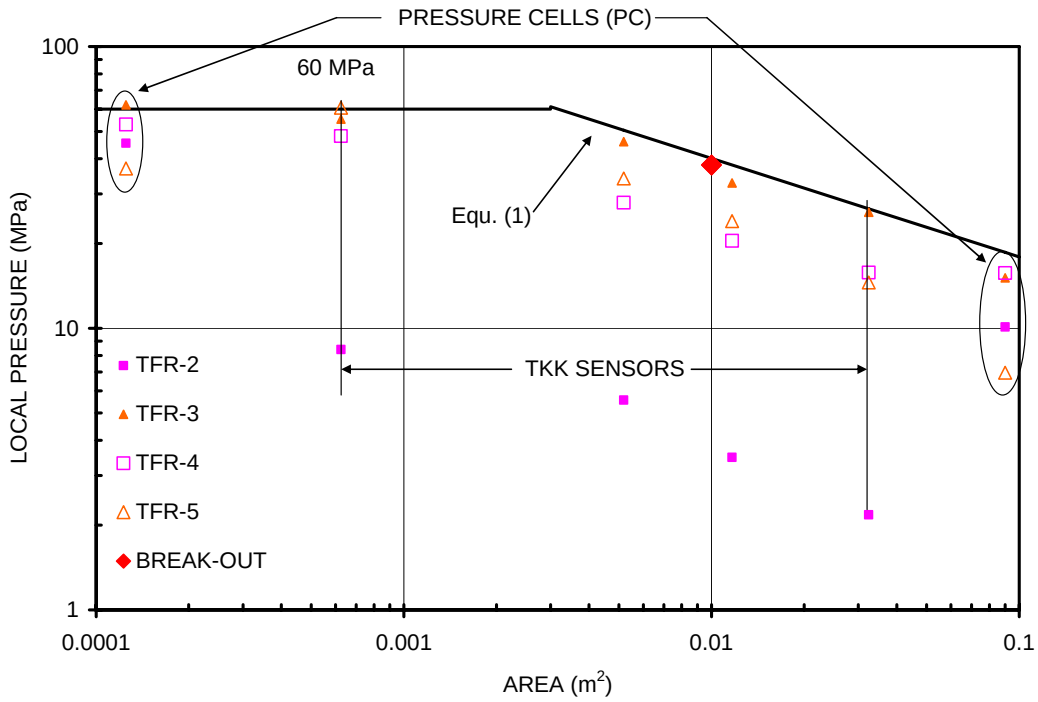

Figure 15. Local pressure versus area on TKK sensor at time of maximum pressure for test

Selecting a value of 8 MPa for an upper envelope value of the Pressure Coefficient and the average value for the Exponent, a power law relation for spatial distribution of local ice pressures can be described by the equation

$$P_s = 8\ A^{-0.35} \qquad \textbf{[1]}$$

where P_s is local pressure in MPa and A is local area, in m^2, over which the local pressure is averaged. This applies for the range 0.003 m^2 to 0.1 m^2. For areas between 0.1 m^2 and 1 m^2, Equation [1] would transition to the pressure-area relation of Masterson et al. (2007),

$$P = 7.4\ A^{-0.7} \qquad \textbf{[2]}$$

which described an upper bound for the area range of 0.1 m^2 to 10 m^2.

Over the time range of the tests, which was about 1 s, spatial distributions of local pressure were relatively stable, however high pressure zones were observed to move from one cluster to another in this time period. Based on the measurements with the TKK sensor, the areas of high pressure appear to be from 0.01 m^2 to 0.03 m^2.

References

Joensuu, A. 1988. Ice Pressure Measurements using PCDF Film. Proceedings, 7th International Conference on Offshore Mechanics and Arctic Engineering (OMAE 1988), Houston, February 7-12, 1988, Vol. IV, p. 153-158.

Masterson, D.M., Frederking, R.M.W., Jordaan, I.J. and Spencer, P.A., 1993. Description of Multi-Year Ice Indentation Tests at Hobson's Choice Ice Island – 1990. Proceedings, 12th International Conference on Offshore Mechanics And Arctic Engineering, OMAE 1993, Glasgow, Scotland, Vol. 4, p.145-155.

Masterson, D.M., Frederking, R.M.W., Wright, B. Karna, T. and Maddock, W.P. 2007. A Revised Pressure-Area Curve. Proceedings, 19th International Conference on Port and Ocean Enginering under Arctic Conditions, Dalian, China, June 27-39, 2007, Vol. 1, pp. 305-314.

Nakazawa, N., Akagawa, S., Kawamura, M., Sakai, M., Matsushita, H., Terashima, T., Takeuchi, T., Saeki, H. and Hirayama, H. 1999. Medium Scale Field Ice Indentation Test (MSFIT) – Results of 1998 Winter Tests. Proceedings, 9th International Offshore and Polar Engineering Conference, Brest, France, May 30 – June 4, 1999, Vol. II, pp 498-504.

Taylor, R.S. Frederking, R.M.W. and Jordaan, I.J. 2008. The Nature of High Pressure Zones in Compressive Ice Failure. Proceedings, 19th IAHR International Symposium on Ice, Vancouver, British Columbia, Canada, July 6-11, 2008 (in press).

Sea ice-shore / structure interaction

19th IAHR International Symposium on Ice
"Using New Technology to Understand Water-Ice Interaction"
Vancouver, British Columbia, Canada, July 6 to 11, 2008

Measurements of stresses in the coastal ice on both sides of a tidal crack

Fabrice Caline and Sébastien Barrault
University Centre in Svalbard, Longyearbyen, Norway
Norwegian University of Science and Technology, Trondheim, Norway
fabrice.caline@unis.no, sebastien.barrault@unis.no

Six stress sensors were frozen-in in two rosettes nearby a breakwater at 15 cm depth on each side of a tidal crack from 6 to 11 May 2007 in Van Mijenfjorden, Svalbard, Norway. An additional rosette was installed some distance from the shore in the level ice. The tidal movement of the ice was recorded with differential GPS equipment a week later. The tide is being recorded continuously in the area. Weekly visual observations of the sea ice were done as well.
This paper gives an order of magnitude of the stresses in the active zone and how they are affected by the tide.
The principal stresses next to the tidal crack during one cycle are presented. They are strongly influenced by the tide and are highest, around 150 kPa, at low tide and in the direction parallel to the crack. It is unknown whether these variations are local to the crack or take place in the whole active zone.

1. Introduction

The main coalmine in Svalbard is situated in Svea, by the inner bay of Van Mijenfjorden called Sveabukta. A coal deposit has been found under Mount Ispallen, on the opposite side of the bay. The mining company SNSG is considering building an access road across the fjord. In this context the University Centre in Svalbard (UNIS) has been looking into methods for protecting this causeway against seawater erosion. The study is relevant for a wide range of coastal structures built in shallow Arctic waters like breakwaters and quays. Due to the presence of seasonal sea ice the main challenge is to build an erosion protection system that sustains ice loads.

Few measurements of sea ice stresses close to the shore have been made. Apart from being the first step for evaluating loads on coastal structures, the study of stresses in the coastal ice is necessary for defining the boundary conditions of thermal and/or mechanical stresses in constrained first-year landfast sea ice. Investigations were done in connection with the construction of a coal loading pier in Svea (Instanes, 1979). Moslet (2001) measured in situ stresses in order to estimate sea-ice loads on this structure. Frederking et al. (1986) and Sayed et al. (1988) measured stresses in the area of Adams Island (Canada). Nikitin et al. (1992) studied the behaviour of the ice in the active zone (see definition in part 2) at a location in the Okhotsk Sea. Stander et al. (1988) also studied the coastal ice while Frederking and Nakawo (1984) studied the sea ice close to the piles of the Nanisivik wharf.

Researchers at UNIS have been investigating level ice stresses in Sveabukta for several years and found thermal expansion to have the most significant effect (Teigen et al., 2005, Barrault and Høyland, 2007). In addition, during the winter of 2007 coastal stresses were measured in one location. During the same period weekly observations of the coastal ice were done and its movement was recorded throughout one tidal cycle with differential GPS equipment. Sea level data were obtained from a tide recorder situated 100 m from land.

2. Proposed terminology

The *ice foot* is determined as the ice frozen to the shore when gradual freezing of sea water from tide and wave spray occurs early in the season. It is in effect a block of ice that is fixed to the ground and does not move with the tide (WMO, 1970). At a certain distance from shore the ice, which is unaffected by the shore, is called *level (floating) ice*. In between is a transition zone which Croasdale (1980) calls *active zone*. The active zone is composed of *coastal ice* which forms simultaneously with the sea ice and is subjected to tidal forces significant enough to create tidal cracks.

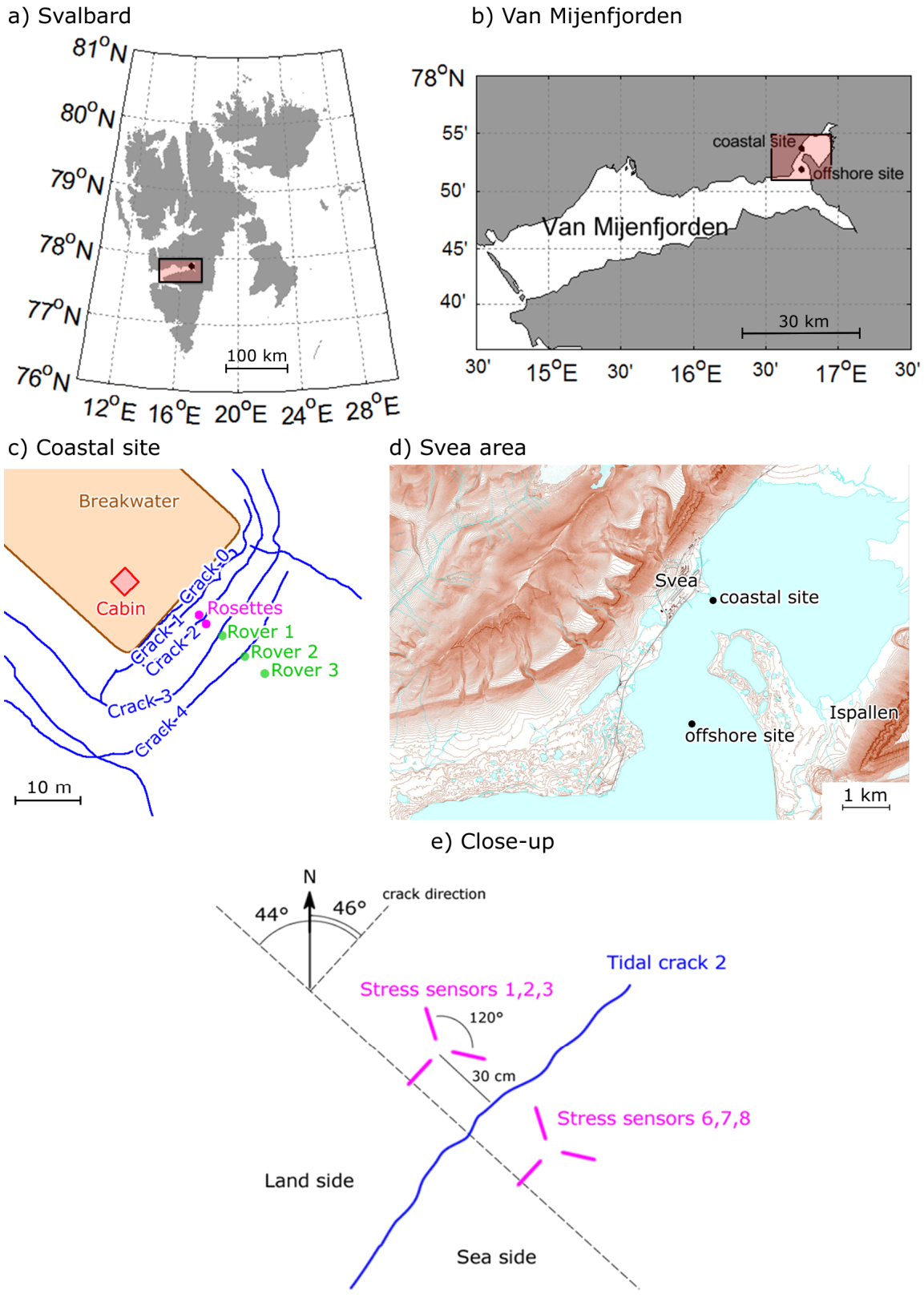

Figure 1. Map of the measurement site and instrument set-up in the innermost basin of Van Mijenfjorden

3. Site and experimental method

A breakwater was built in Sveabukta, the innermost bay of Van Mijenfjorden (Svalbard, Norway) for research purposes. It is 50 m long, 25 m wide and rises 2 m above the mean sea level (MSL), which is taken as the reference level. The depth at the toe is 3.5 m and the slope is 1V:2.5H. During the winter several cracks form in the ice parallel to the breakwater and up to 25 m away. The stress sensors were placed on each side of crack #2 (Figure 1c) which is oriented 46° to the North and runs through the whole 1.6 m thick ice cover.

The instruments are Amplified Solid State Pressure Sensors 242PC100G and they were deployed from 6 to 12 May 2007. These sensors consist of a disc of 10.5 cm in diameter filled with hydraulic oil and a transducer head measuring the voltage difference. Compressive stresses are obtained with ± 0.1 kPa resolution. Tensile stresses are not measured. They were connected to a CR10X Campbell Scientific datalogger. The sensors were deployed as two rosettes on each side of the crack at a depth of 0.18 m. The centre of the rosettes was at 30 cm from the crack. In both rosettes, one sensor measured stresses perpendicular to the crack (Figure 1e) and the angle between each sensor was 120 degrees. Another rosette of three BP stress sensors was frozen-in in the offshore ice 2.6 km away from the breakwater, in the middle of Sveabukta from 16 February to 17 April (Figure 1d). The site, the instrumentation set-up and the logging are described in (Barrault and Høyland 2007).

A Seabird SBE 26Plus tide and wave recorder is permanently placed at 2.5 m depth 100 m from the breakwater. The water level is recorded continuously and averaged every 20 minutes. The ice movement was surveyed with differential GPS equipment on 17 May. A base station was placed on land and three rovers were placed from 8 to 20 m from the shore (Figure 1c). The rover antennas were placed on 1 m-long poles stuck some 20 cm in the snow layer and the position was recorded with 2 cm accuracy every 30 seconds for 20 hours. In additional ice observations and profile measurements were made.

The air temperature of the Svea airport weather station situated at about 1 km west of the site is obtained from the open weather database of the Norwegian Meteorological Institute (http://eklima.met.no).

4. Results

As shown in Figure 2 stresses were identified as periodic events on both sides of the crack with higher pressure on the land side of the crack with a maximal value of 245 kPa compared with 139 kPa on the sea side. The stresses are strongly influenced by the tide and their tidal response is similar during the whole week. There are missing data for the sensor oriented at 46 degrees on the land side. The sensor in fact did not record data when stresses where lower than 24 kPa. During the 6 days of measurements the temperature increased almost linearly from -15 to 0°C. The wind was around 11 $m \cdot s^{-1}$ until 9 May then fell to 5 $m \cdot s^{-1}$. All the time it was blowing from the North-East, i.e. parallel to the tidal crack. The tidal range decreased from 1.26 m on 6 May to 0.56 m on 11 May.

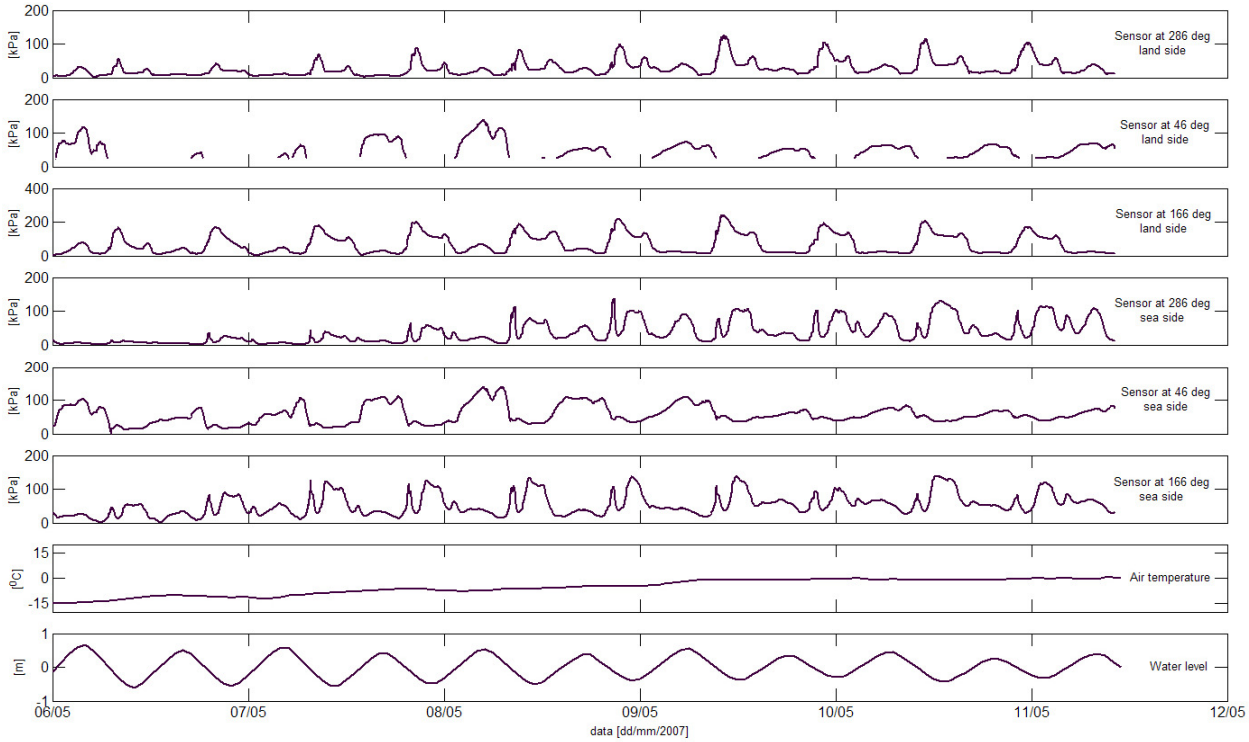

Figure 2. Stresses in the two rosettes on both sides of the crack, air temperature and sea level.

The plot of the calculated principal stresses during one tidal cycle on both sides of the tidal crack (Figure 3) shows they have the same pressure range and their curves have a relatively similar shape. The highest stresses, about 150 kPa, are reached at low tide last for about 3 hours and are oriented parallel with the crack. At high tide the major principal stress is about 70 kPa and oriented perpendicularly to the crack. Finally there is a short 100-150 kPa stress peak oriented parallel the crack when the tide is around mean sea level. This peak is more evident on the sea side.

The results of the DGPS measurements (Figure 4) show that the effect of the tide on the vertical movement of the ice decreases with the proximity to the shore: 20 m from shore, at the location of Rover 3, the ice is completely floating while 8 m from shore, at the location of Rover 1, the ice is moving vertically 60 % less than the sea. The difference in movement is highest at low tide where the sinusoidal curves of the vertical movement of Rover 1 and to a smaller extent Rover 2 are capped. The horizontal movement is perpendicular to the tidal cracks (Figure 4) and is highest at Rover 1 where it attained 22 cm during a tidal cycle.

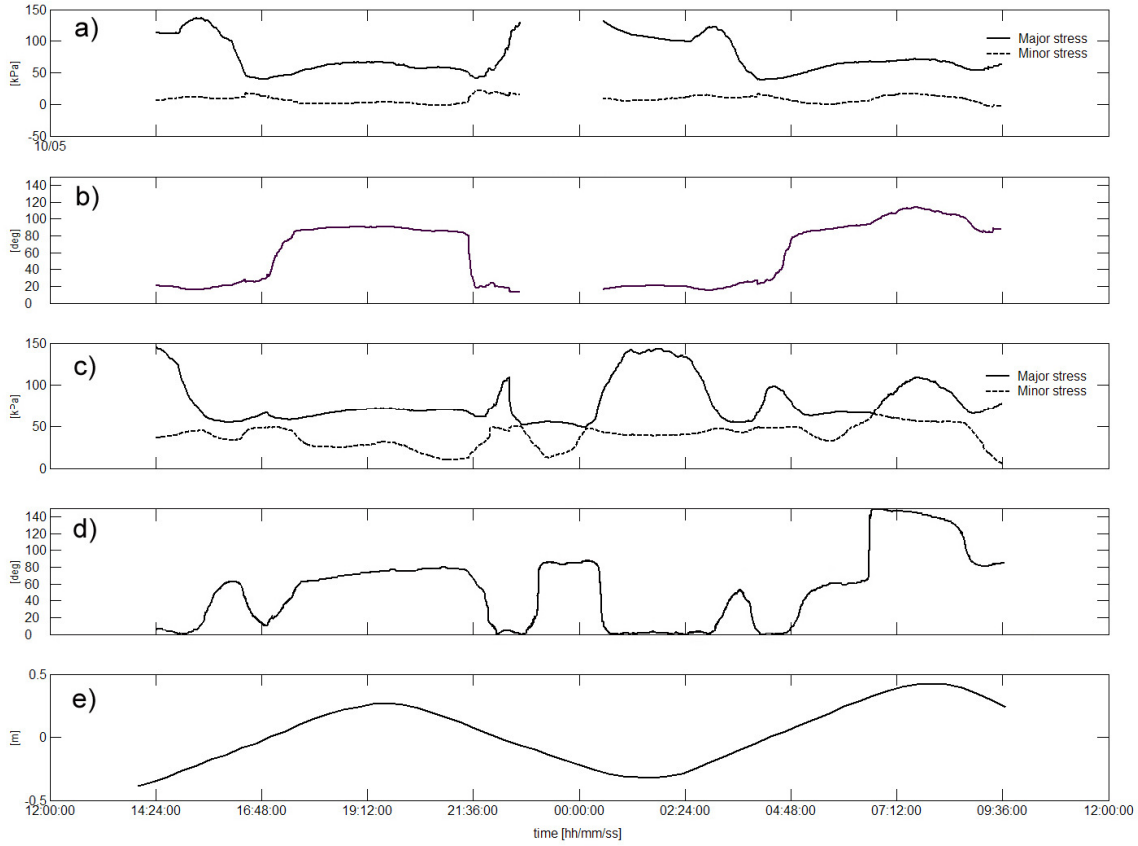

Figure 3. Principal stresses and direction on land side (a and b) and on sea side (c and d) from 10 to 11 May. The sea level is shown on e). The 0 degree reference direction is taken parallel to the tidal crack.

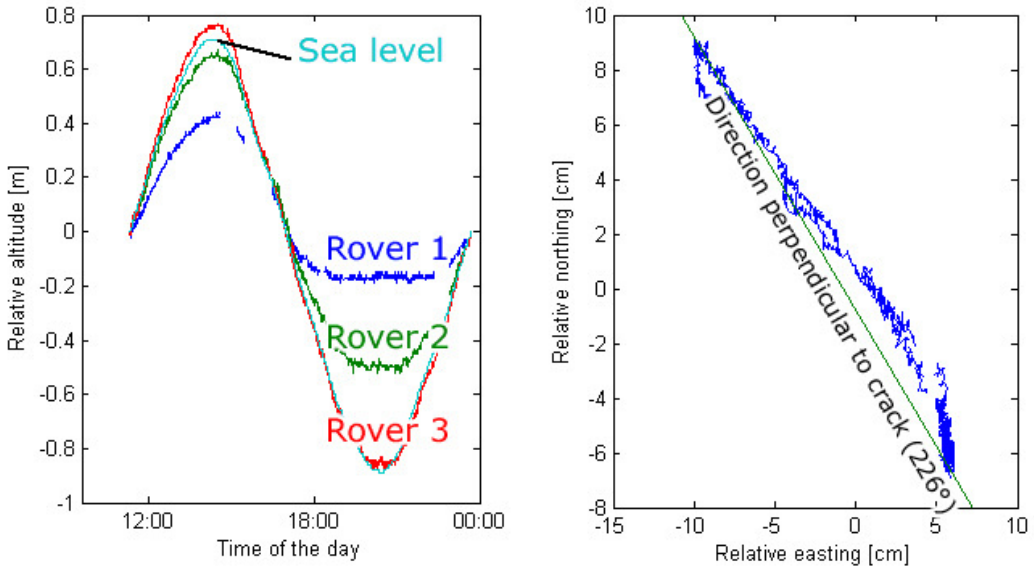

Figure 4. *Left*: DGPS measurement of the vertical movement of the ice top at three locations (Rover 1-3) and sea level during one tidal cycle — *Right*: horizontal movement of Rover 1 during that cycle. Measurements made on 17 May 2007.

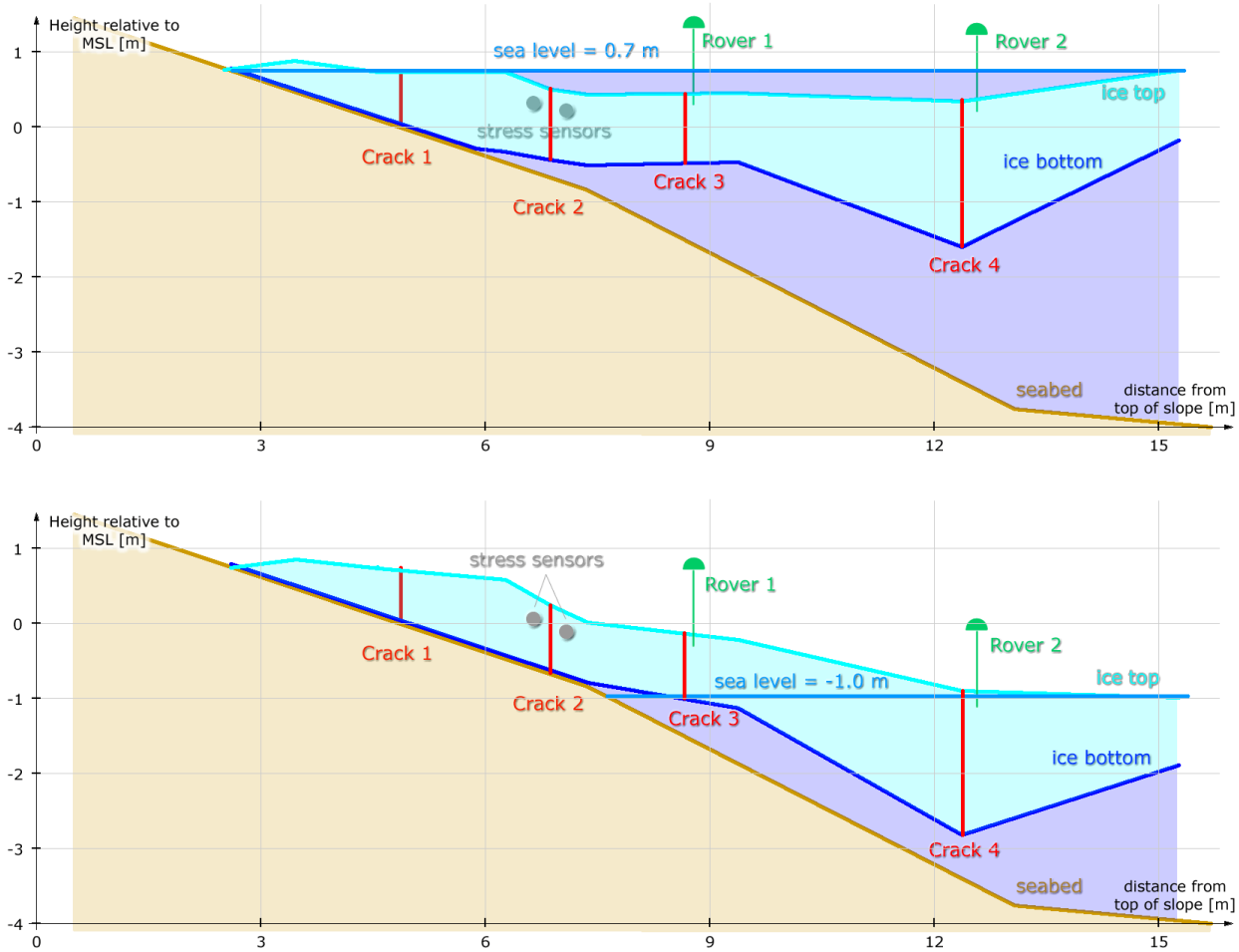

Figure 5. Cross-section of the active zone at high tide (above) and low tide (below)

5. Discussion

Stress data

Stresses in the area close to a coastal crack were measured but it is difficult to say if the stresses in the rest of the active zone vary in the same way. It is possible to give hypotheses of what could have caused the stress variations but testing them would require more measurements. It would be particularly instructive to record stresses at different depths in the 1.6 m-tick ice layer but the current instruments cannot be used because they do not resist to submersion.

Previous studies in Sveabukta (Teigen et al., 2005) showed that the wind does not affect ice stresses below 20 $m \cdot s^{-1}$. Early in the winter 2008, a survey conducted by UNIS researchers measured the tidal current close to the breakwater and found a maximum value of 30 $cm \cdot s^{-1}$. It is unlikely that such a small current would have a major effect on the stresses in the ice cover.

When it comes to thermal effects, the 40 cm-thick snow cover isolated the level ice and no thermal stresses were recorded during the first part of the season. On the coastal ice however the ice was in direct contact with the air through the crack openings. Figure 5 shows that the sea water filled the cracks at every tidal cycle and it is reasonable to suppose that the induced temperature variations would cause thermal stresses. It is expected that the grounding of the ice

(Figure 5) has an effect on the stress distribution in the ice but under a plane strain hypothesis the induced stress variations are expected to be perpendicular rather than parallel to the crack. The plane strain hypothesis might however not be valid since the breakwater is only 25 m wide and there is a rubble accumulation at its western corner which could cause bending in the direction normal to the plane of the cross-section in Figure 5 and hence stress variations in the direction parallel to the crack.

The 20 kPa peak of the stresses perpendicular to the cracks is almost certainly due to the opening and closing of the crack depending on the tide.

The observed stress variations are within the range of values found in the literature. Frederking et al. (1986) measured 70 kPa off the Coast of Adams Island where the tidal range is up to 2 m while Sayed (1988) measured 350 kPa there. Moslet (2001) had 25 kPa in Svea and Nikitin et al. (1992) 500 kPa in the active zone of the Okhotsk Sea with a tidal range of 1.25 m. As in this study they all found that the highest stresses were in antiphase with the tide. However the ice around the breakwater was not translating away from the shore as Frederking and Nakawo (1984) observed around the Nanisivik wharf piles where they measured horizontal displacements of several metres throughout the season. Stander et al. (1988) also recorded horizontal displacements, of several centimetres per day.

DGPS data

The plots of the vertical movement of the ice (Figure 4) show that the coastal ice is not in hydrostatic equilibrium with the sea water. The non-equilibrium is a consequence of friction forces along the cracks. The boundaries are on one side the ice foot which is fixed to the ground and on the other side the level ice which is completely floating. The horizontal movement data are exaggerated because the rover antennas were almost 1 m above the ice top and the vertical movement data reveal that the sections of ice between two cracks has a combined movement of translation and of rotation throughout the tidal cycle. The rotation takes place around a horizontal axis directed like the cracks. A numerical evaluation shows that the correct value of the horizontal movement of the ice at the Rover 1 location is 10 cm rather than 22 cm.

6. Conclusion

Stresses were measured close to a tidal crack in the active zone and showed a strong tidal dependency. The highest stresses were measured in the direction parallel to the tidal crack. The limited amount of stress data makes it difficult to propose more than hypotheses on the mechanical processes taking place in the active zone during a tidal cycle. Close to the tidal cracks the thermal variations caused by the cyclic sea water flooding might create stresses. A simple way to test this hypothesis would be to place a vertical thermistor cable in the ice close to a crack and another one at some distance. The tidal current is expected to have an insignificant effect. In order to measure stresses in more locations and depths in the ices, it is necessary to use a different type of sensors that resist to flooding. A numerical analysis would help optimise the number and location of these sensors.

Acknowledgements
The authors are grateful to Mauri Määttänen from Helsinki Technical University in Finland for the use of his sensors. This survey was supported by the mining company in Svalbard, SNSG and by TOTAL E&P NORGE AS.

References

Barrault, S., Høyland, K.V., 2007. Mechanisms and measurements of generation of stresses in first-year landfast sea ice. 19th International Conference on Port and Ocean Engineering under Arctic Condition (POAC), Dalian, China, 27-30 June, pp 685-694

Croasdale, K.R., 1980. Ice Forces on Fixed, Rigid Structures. Working Group on Ice Forces on Structures, Carstens, T., pp. 34-106.

Frederking, R.M.W., Nakawo, M., 1984. Ice action on Nanisivik wharf, winter 1979-1980. Canadian Journal of Civil Engineering, Vol. 11, No. 4, pp. 996-1003

Frederking, R.M.W., Wessels, E., Maxwell, J.B., Prinsenberg, S., Sayed, M., 1986. Ice pressures and behaviour at Adams Island, winter 1983/1984. Canadian Journal of Civil Engineering, Vol. 13, pp 140-149

Instanes, B., 1979. Coal loading pier in Svea, Svalbard. Proceedings, 5th International Conference on Port and Ocean Engineering under Arctic Conditions (POAC), Trondheim, Norway, Vol. 3, pp. 217-227

Moslet, P.O., 2001. Estimation of loads exerted by sea ice on the quay at Kapp Amsterdam, the Van Mijen fjord. Master thesis, Department of Structural Engineering, NTNU, 93 p.

Nikitin, V.A., Shushlebin, A.I., Sheikin, I.B., 1992. In-Situ Stress Measurements in Fast Ice and Possible Tidal Loads on Structures. Proceedings of the Second International Offshore and Polar Engineering Conference, San Francisco, USA, 14-19 June, Vol. 2, pp. 696-702

Sayed, M., Frederking, R.M.W., Wessels, E., 1988. Field measurements of stresses and deformations in a first-year ice cover adjacent to a wide structure. Canadian Journal of Geotechnics, Vol. 25, No. 4, pp. 726-734

Stander, E., Frederking, R.M.W., Nadreau, J.-P., 1988. The Effects of Tidal Jacking on Ice Displacement and Strain in the Nearshore Environment. Proceedings of the 9th International Symposium on Ice (IAHR), Sapporo, Japan, 23-27 August, Vol. 1, pp. 526-536

Teigen S. H, Høyland K. V., Moslet, P. O, 2005. Thermal stresses in first-year sea ice. Proc. Of Port and Ocean Engineering under Arctic conditions (POAC), Potsdam, USA, pp. 893-906.

WMO, 1970. WMO sea ice nomenclature, (suplement No. 5, 1989). Technical Report MO No. 259.TP.145, World Meteorological Organizartion, Geneva, Switzerland.

19th IAHR International Symposium on Ice
"Using New Technology to Understand Water-Ice Interaction"
Vancouver, British Columbia, Canada, July 6 to 11, 2008

Estimation of Ice Impacts on Armor Stone Revetments at Barrow, Alaska

Steven F. Daly, Jon Zufelt, Leonard Zabilansky, Devinder Sodhi, Kevin Bjella
ERDC Cold Regions Research and Engineering Laboratory
72 Lyme Road, Hanover, NH 03755
steven.f.daly@usace.army.mil

Deirdre Ginter, Kenneth Eisses, John Oliver
US Army Corps of Engineers, Alaska District
Anchorage, AK

A series of four model tests were conducted in the ERDC/CRREL Ice Engineering Environmental Test Basin to simulate the impact of ice shoves from the Arctic Ocean on proposed coastal protection structures to be installed at Barrow, Alaska by the Alaska District of the Corps of Engineers. The structures, designed to protect the shoreline from open-water wave action, are to be constructed by the placement of quarried stones. Ice shoves originating from the Arctic Ocean have long been observed to occur along the shoreline at Barrow, Alaska. The objective of the model tests was to assess the integrity of the proposed structures under the impact of the ice shoves by determining the stability of the stones. A review of available data on ice conditions in the Arctic Ocean off of Barrow, Alaska indicated that representative ice covers are on the order of 1.5-m thick and have a flexural strength of 600 kPa. A 1:20 undistorted model of the proposed armor stone revetment and the immediate shoreline was constructed. The model reproduced approximately 120m of shoreline and covered the distance from the mean water line to the back of the revetment. The model was supported on platform mounted on a rolling gantry with eight wheels that was pushed by the Test Basin carriage into the stationary ice. Each test represented approximately 600 m of prototype ice being driven up the shoreline against the structure. The revetment performance was determined by before and after elevation profiles and visual inspection. The stone placement method, random or selective, and the size of the stones were varied between tests. Selective placement of the stones, that is carefully placing the stones to interlock and support each other, provided a much greater degree of stability during ice shoves than random placement. The size and placement of the stones at the toe of the revetment was also found to be an important factor in the stability of the revetment.

strength, thickness, and temperature of the ice sheet can all play a role. Ice shoves are possible at any location where the shoreline is not protected by barrier islands or shoals

Figure 1. Location of Barrow, Alaska, USA.

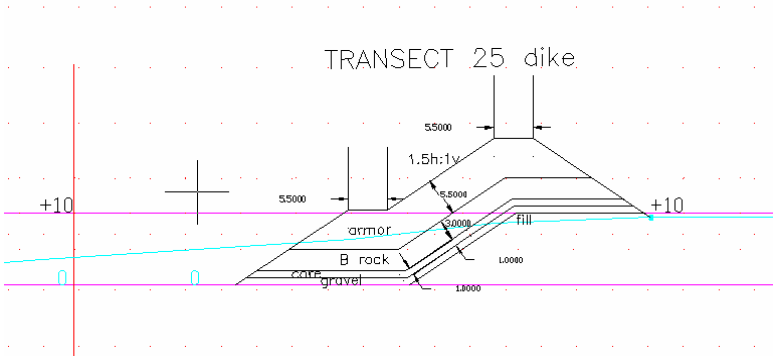

Figure 2. Proposed Coastal Protection Structure.

Ice shoves have occurred at all times of the winter season when ice is present, but seem to be most frequent in spring. Damage can result if the moving ice contacts shore protection, buildings, or other structures. Unless designed correctly, riprap structures are particularly vulnerable. Based on observations made during laboratory tests (Sodhi et al. 1996, Sodhi and Donnelly 1999), damage to riprap appears to take place during pileup events when the incoming ice sheet is forced to go between the riprap and the piled-up ice, bringing with it rocks from the bottom to the surface of an ice pile. To sustain no damage to the riprap protective layer, maximum rock size (D_{100}) should be twice the ice thickness for shallow slopes (1V:3H) and about three times the ice thickness for steeper slopes (1V:1.5H).

4. Ice shoves at Barrow, Alaska.

'Ivu,' as ice shoves are known locally, occur nearly every year at Barrow, Alaska. Usually these ice shoves result only in small piles of sand and gravel left along the beach each spring after the ice melts. Anecdotally, major ice shoves occur about once every five years and can reach inland 100m (328ft) or more. These major ice shoves bulldoze beach material, severely gouge bluffs,

1. Introduction.

The city of Barrow, situated on the coast of the Arctic Ocean, is the northernmost American city (Figure 1). Barrow is susceptible to storms from the north and west that can cause severe coastal erosion. The shoreline is most susceptible to storm activity during the typical open water period from August through October. There is generally enough coastal ice present from November through July to reduce the waves and prevent coastal damage. The Alaska District of the Corps of Engineers is designing an armor stone coastal protection structure to be placed along the shore at Barrow. The structures must not only resist the impacts of waves, they must also resist the impact of sea ice pushed on shore by wind and/or water currents. These ice shoves, or ivus, as they are known locally, occur nearly every year at Barrow, although they are largely undocumented. The forces that ice shoves can generate are potentially quite large, and their impact on this type of coastal structures difficult to estimate. At the present time, there is no guidance for design of armor stone structures to resist ice.

This paper presents the results of a study to determine the likely impact of ice on the stability of the stones that comprise the structure. Four laboratory tests were conducted using a 1:20 scale model of the proposed structure in the ERDC/CRREL Ice Engineering Environmental Test Basin. The model was constructed on a platform supported by a rolling gantry that could be pushed into the ice. The ice grown in the Test Basin was designed to match those expected at Barrow at the model scale. The sea ice properties at Barrow were determined by field measurements. Ice shoves on the model structure were simulated by pushing the rolling gantry and model into the floating ice cover of the basin. The revetment performance was determined by before and after elevation profiles and visual inspection. A variety of armor stone size and toe stone sizes were investigated. Two different types of stone placement were investigated: random placement and selective placement. Selective placement, carefully setting each stone to maximize interlock and support between stones, was found to have a significant impact on the test results.

2. Proposed Coastal Protection Structures.

The proposed coastal protection structures will extend along the coastline at Barrow, Alaska. The structures are to be constructed largely of quarried rock. The structures proposed is a “dike” type structure that will extend along the majority of shoreline (Figure 2). The structure will consist of armor stone, B rock, core rock, gravel, and fill (US Army Corps of Engineers 1995).

3. Ice shoves.

Ice shove is a term to describe the movement of sea or lake ice onto shore by the environmental forces of wind and/or water currents (Kovacs and Sodhi 1988, Gwane 1999). Ice shoves are not predictable and are often associated with storm events. In the Arctic Ocean, ice shoves can be formed of a variety of ice types, but large, intact ice sheets appear to penetrate the furthest and cause the most damages. The shore directed movement causes the ice to ride-up the beach. In most cases as the ice sheet progresses inland, it reaches a point where the ice sheet fails and begins to form a rubble pile of broken pieces. This rubble pile can grow both landward and vertically. While no tested formula has been developed to estimate the size of the ice pile, it is surmised that the magnitude and duration of the environmental forces, the ice type, and the

move across roads and on rare instances severely damage structures and even cause loss of life. The two most recent major ice shoves occurred in January 2006 (Figure 3) and June 2001. There is no program of monitoring and recording ice shoves in Barrow at this time. Descriptions of ice shoves are either anecdotal or are scattered in various scientific reports.

Date	Extent	Date	Extent
July 22 1892	75m inland	Jul-75	15m onto the coast
1913	60 to 90m inland	Jun-76	25m onto the coast
1919	30 to 60m inland	19-Oct-78	10m onto the coast
Jun-43	30m from water edge	Jan. 2 1978	35m from the sea
1953	-	1978	-
1960	-	Jun-01	Up to 5m in ridges
1961	45m onto the beach	Dec-06	60m inland
1968	-	Jan. 26, 2006	30m
1970	-	Dec. 2006	-
1975	-		

Table 1. Recorded ice shoves (ivus) at Barrow, Alaska (various sources).

Figure 3. Ice rubble pile formed in January 2006 at Barrow, AK as the result of an ice shove (www.gi.alaska.edu/snowice/sea-lake-ice/images/ice_events.html)

5. Ice Conditions at Barrow, Alaska.

Four studies (Cole et al 2002, Frankenstein and Abrams 1971, Perovich et al 1998 and UAF Floating Ice Group 2008) provided measurements of sea ice temperature, thickness, and salinity immediately offshore from Barrow (Figure 4). These measurements were used to estimate the flexural strength of the ice based on the equations developed by Timco and O'Brien (1994). These equations require sea ice temperature and brine volume. While brine volume was not

measured in any of these studies, the brine volume was estimated using the equation of Frankenstein and Garner (1967) as suggested by Timco and O'Brien (1994). The data on sea ice temperature, salinity, thickness, and estimated flexural strength are shown in Figure 5. All the measured sea ice parameters varied systematically throughout the winter season: sea ice thickness ranged from 0.2 m (7.87in) in late October to nearly 1.8 m (5.9ft) in early May; depth-averaged salinities ranged from 6-8 ‰ in the fall to 4 ‰ and less in late May; depth-averaged sea ice temperatures declined through autumn to a low of approximately -13°C (9°F) in mid-winter and rose to -2°C (28°F) and warmer in June. The flexural strength measurements averaged around 600kPa throughout most of the winter and dropped off in May and June. This flexural strength compares well to the midwinter peaks of average winters estimated by Timco and O'Brien (1994) for the Canadian Beaufort Sea.

Figure 4. Location of sea ice measurements

6. Overview of the Laboratory Tests

Ice shoves at Barrow are a very real problem as described above. The series of tests described below were developed to allow the structure designers to test their prototype designs and develop new designs based on the laboratory results. It will be seen that the structure design evolved extensively between Test 1 and Test 4.

7. The Ice Engineering Environmental Test Basin.

The Ice Engineering Environmental Test Basin is a refrigerated towing tank for large-scale studies of ice forces on structures such as dams, piers, ships, off-shore platforms and shore protection systems. (http://www.crrel.usace.army.mil/facilitieslabstestsites/ierf_testbasin.html) The Test Basin is a large refrigerated room capable of maintaining a low temperature of -29°C (-20°F). The basin dimensions are 36m long x 9.1m wide by 2.4m deep. (120ft x 30ft x 8ft). Ice sheets are grown with a practical range of ice thickness from 1.9-15.2cm (0.75-6.0in) and ice strength of 20-120kPa (3.0-17.4 psi). The appropriate ice strengths are attained by using urea doped ice and tempering of the ice sheets (Hirayama 1983). There are dedicated instrumentation and data acquisition systems.

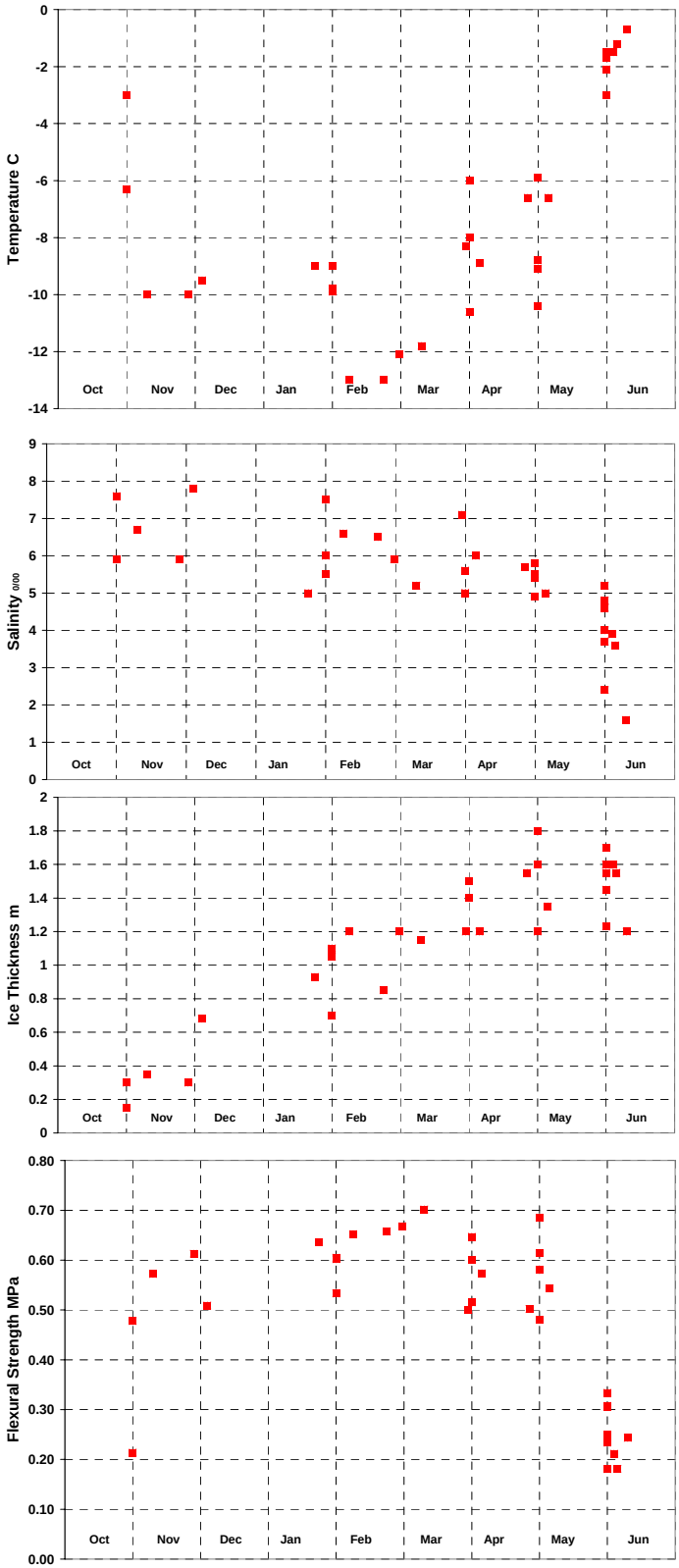

Figure 5. Sea ice properties measured at Barrow, AK and estimated flexural strength

A high force carriage pushes models through an ice sheet at speed up to 200cm s^{-1} (7 ft s^{-1}). A second carriage serves as a movable platform used to measure the engineering properties of the ice and provide access to the test structures.

8. Model Scaling

The weight of the armor stones is the predominant stabilizing force, and is proportional to $\rho_r g D_{50}^3$, where $\rho_r g$ is the specific weight and D_{50} is the median size of the armor stone. The destabilizing force during an interaction between a moving ice sheet and the armor stone revetment is limited by the failure of ice sheet in bending, buckling and crushing. In field observations and previous model tests, ice failure has been observed to take place mainly by bending or buckling of ice sheets. The forces required to fail an ice sheet in bending and buckling are proportional to $\sigma_f h^2$ and $\rho_w g D_{50} L^2$, where σ_f is the flexural strength of ice sheet, h is the ice thickness, and L the characteristic length. An undistorted scale (λ) of 1:20 was selected as an appropriate scale given the capabilities of the Test Basin. All length scales, D_{50}, h, L, and flexural strength, σ_f, scaled with λ. The model densities of water, ice and the granite armor stone were identical to the prototype densities. A review of the ice conditions off of Barrow, Alaska indicated that representative ice covers that are likely to cause the worse damage and occur frequently are on the order of 1.5m (4.9ft) thick with a flexural strength of 600 kPa (90 psi). Conducting a model tests at a scale of 1:20 required a 7.5cm (3in) thick ice sheet having a flexural strength of 30 kPa (4.35 psi). Time for each test included preparation time (operation of bubblers, sensor checking, etc), ice growth, ice tempering (warming the ice to reduce the ice strength), and post test tasks (ice clearing and profiling of the structure). The 1:20 scale allowed a 6 day turnaround time if required. The required flexural strength of 30 kPa (4.35 psi) kept the model ice sheet in a regime to behave in a brittle manner.

9. Test Apparatus and Procedure

A 1:20 undistorted scale model of the coastal protection structure and the immediate shoreline was constructed for each test. The model was approximately 20 by 10 foot (6m x 3m) in overall size and was mounted on a platform supported by a rolling gantry with eight wheels. The gantry was pushed by the Test Basin carriage (Figure 6) into the model ice. The platform on the top of the gantry could be rotated so that the model was completely submerged in the water as described below (Figure 7). The 6m (20 foot) wide model did not experience interference from the test basin walls. At the 1:20 scale, the model reproduced approximately 122m (400 feet) of shoreline and covered the distance from the mean water line to the back of the coastal protection structure (side away from the ocean). A model ice sheet was grown in the 36m long by 9.1m (120 ft x 30 ft) Test Basin with thickness and strength scaled to the values of the prototype ice cover. The scale model was pushed against the stationary ice by the Test Basin carriage. The Test Basin provided approximately 30.5m (100 ft) of usable ice; therefore each test represented approximately 600m (2000 ft) of prototype ice being driven up the shoreline against the structure.

The test procedure was as follows:

1. The model test platform was set in position at the east end of the Test Basin immediately next to the preparation tank. The bubblers located on the bottom of the Test Basin were activated to completely mix the water and maintain a uniform water temperature.

2. The model was hand built to the specifications of the test (See Figure 8 for example). Starting with the second test, the model platform was divided in half and separate models were built on each half. The two models were labeled North (N) and South (S). Typically this required hand selecting rock of the appropriate weight and size. Granite rock was supplied by a local quarry.

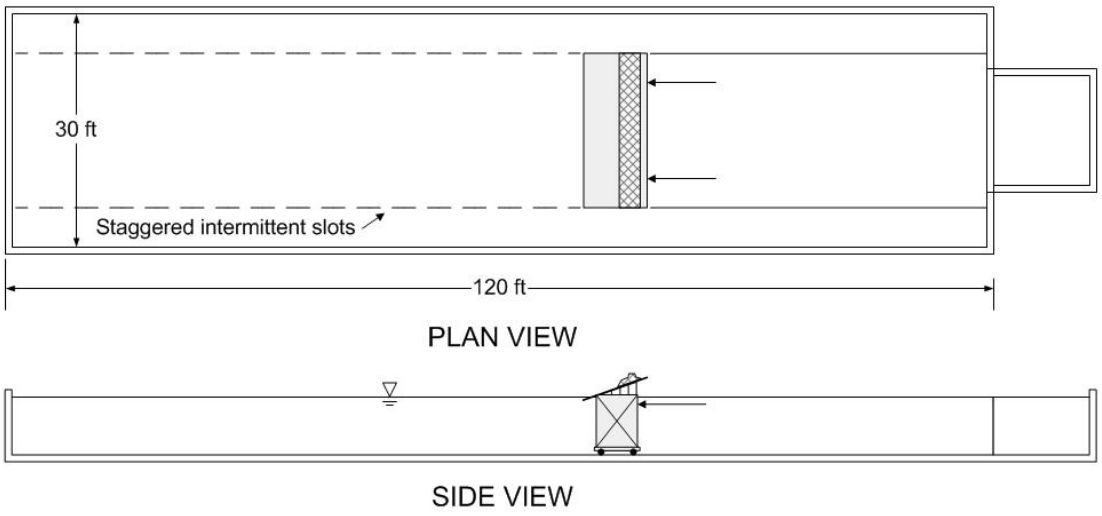

Figure 6. Conceptual views of the coastal protection structure ice model testing apparatus

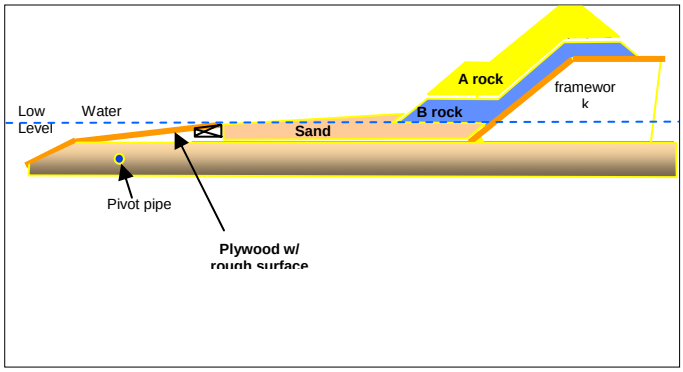

Figure 7. Elevation illustration of the model platform. Note pivot pipe about which the model rotate to submerge the model during ice growth.

3. Elevation profiles of the model were measured using a hand operated laser ranging device from the shoreline to the back of the model. Nine equally spaced profiles were measured on the North and South models. The profile locations were marked to allow profiles to be taken at the same locations following a test.
4. Once the model was constructed, the model and its supporting platform were submerged by rotating the model downward around its front axis. Floating insulation was placed over the submerged model platform to prevent ice from growing in that area.
5. The water temperature was cooled by reducing the Test Basin air temperature until the water became slightly supercooled, with the equilibrium temperature dependant on the concentration of urea in the test basin water. The bubblers were turned off and air of the Test Basin seeded with minute water droplets. The water droplets froze in the air and dropped onto the quiescent water

surface to initiate ice cover formation. The air temperature was maintained at a cold temperature until the required 7.5cm (3in) of ice was grown. The Test Basin air temperature was then allowed to rise and the ice cover "tempered" until the required strength was attained. The ice strength was monitored through periodic cantilever beam tests.

Figure 8. South model of Test 2 prior to test.

6. Once an ice cover of sufficient thickness and strength was prepared, the floating insulation was removed and the model platform rotated above the water surface. The floating ice cover was squared off so that the face of the ice cover and the front of the model were exactly parallel. Two rows of slots were cut in the ice covers at periodic intervals, one row at each edge of the model platform. This prevented interference between the platform and the edge of the tank.
7. The model was slowly pushed until it met the face of the floating ice. At that point, forward motion was halted.
8. The model was pushed through the ice at the set velocity (Figure 9). When the rolling gantry reached the end of the Test Basin and at appropriate intermediate distances, the forward motion of the gantry was halted and the model inspected. At the end of a test, the model was typically covered with ice. The ice was carefully removed to allow the model to be inspected.
9. Elevation profiles were measured again to allow quantitative measurement of the changes that had occurred in the armor stone.

10. Test Series

A series of four tests were performed. An overview of the tests is shown in Table 2. The ice in all the tests was 1.5m (4.9ft) prototype thickness with a prototype flexural strength of 600 kPa (90 psi). Four tests were conducted and are described next. Profiles of the revetments were taken after Test 2 and before and after profiles were measured for Test 3 and 4. The profiles were taken at 30cm (1ft) intervals across the face of each revetment. The profile baseline was roughly at the waterline and each profile extended to the rear of the revetment. The revetment starts at approximately 12.5m (prototype) and the forward slope ends at approximately 27m. For Test 2, each North model profile was subtracted from each South Profile, and then the results were averaged at equal distances from the baseline. For Test 3 and 4, each 'Before' profile was subtracted from each 'After' Profile, and then the results were averaged at equal distances from

the baseline. The total displacement was found by summing the difference between the before and after profiles and then converting to a volume by assuming that each profile represents an equal area.

Figure 9. Test 2.

Test 1. Test one was conducted with 1500kg (1.7 ton) armor stone that was randomly placed. No profiles were measured. This revetment represented the most economic structure required to match the design open water wave climate. This revetment was totally destroyed during the test. A significant portion of the armor stone was removed from the revetment by the ice.

Test 2. Starting with this test, the model platform was divided in half and separate models were built on each half. The stone size was significantly increased from Test 1. The two models, labeled North (N) and South(S), used two different construction techniques: selective placement of stone in the North model, and random placement in the South model. Selective placement required carefully setting each stone to maximize interlock and support between stones (Markle and Davidson 1979). This technique is similar to special placement, except that special placement places a greater emphasis on the stone shape and form. Both selective and special placements are often used in shore protection structures (US Army Corps of Engineers In prep.). They have been found to greatly increase the stability of stones against wave impacts as measured by the stability coefficient in the Hudson equation (US Army Corps of Engineers 1995). It was found that selective placement preformed remarkably better than the random placement, even though the stone size of the North Model 2700-3600 kg (3-4 tons) was slightly larger than the South model, 3600 kg (4 tons). A large portion of the randomly placed armor stone was removed from the model by the ice. The difference between the South model and the North model is displayed in Figure 10, where the material that is removed can be clearly seen.

Test	Date	Model Speed cms^{-1}		Armor Layer $kgx10^3$ (Tons)	Stone Placement	Toe Stone $kgx10^3$ (Tons)	Total Stone Displacement m^3 prototype
1	28-Feb-07	20		1.5 (1.7)	Random	-	Extensive
2	19-Apr-07	10	N	2.7-3.6 (3-4)	Selective	7.2 (8)	Moderate
			S	3.6 (4)	Random	10 (11)	Extensive
3	18-Jul-07	10	N	3.6 (4)	Selective	7.2 (8)	-258.6
			S	3.6 (4)	Selective	11.8 (13)	-104.3
4	29-Aug-07	10	N	3.6 (4)	Selective	11.8 (13)	54.4
						18.1 (20)	25.1
			S	7.2 (8)	Selective	11.8 (13)	132.0
						7.2 (8)	-117.1

Table 2. Test Results

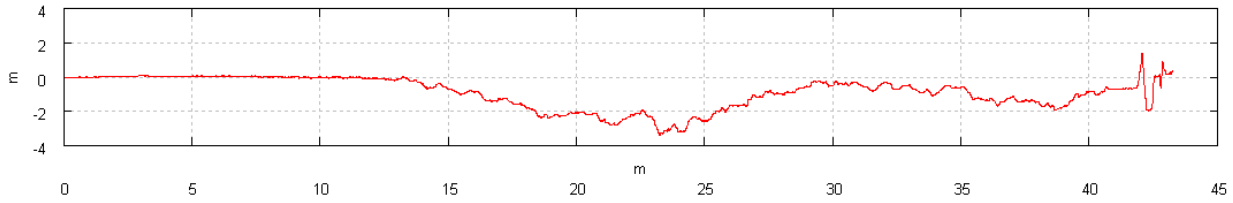

Figure 10. Test 2. Average difference between the North model with selective placement and the South model with random placement after the ice surge (meters prototype).

Test 3. In this test, both the North and South models used selective placement of carefully graded 3600 kg (4 ton) armor stone. The differences were in the type and placement of the toe stone, the stone at the leading edge of the revetment with the North model have smaller toe stones, 7,200 kg (8 ton) than the South, 11,800 kg (13 ton). The results of the test were good, however the before and after profiles revealed that both model had suffered an overall loss of armor stones. The stones were removed from the front face of the revetment for both models and piled further back or removed from the revetment. The South model had fewer stones removed than the North. In fact, the South model results were very good considering that the total displacement listed in Table 2 are for twice the area compared to the results of Test 4. The difference between the before and after profiles for Test 3 is shown in Figure 11.

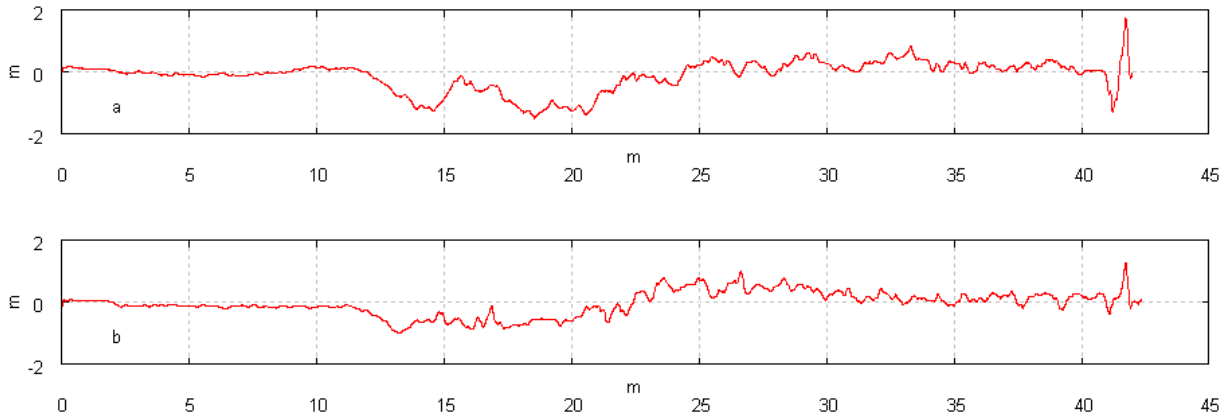

Figure 11. Average difference between the before and after profiles (meters prototype). (a) Test 3 N. (b) Test 3S.

Test 4. In this test, both the North and South models used selective placement of carefully graded armor stone: 3600 kg (4 ton) armor stone in the North model, and 7200 kg (8 ton) armor stone in the South Model In addition, the toe stone was varied for each model, resulting in four separate tests as listed in Table 2. It is interesting that 3600 kg (4 ton) armor stone resulted in less total displacement than the 7200 kg (8 ton) armor stone. Visual inspection of the revetments after the tests suggests that the large majority of 7200 kg (8 ton) were not lost from the revetment but a few were moved around and several of the large 11800 kg (13 ton) toe stones were rolled up the revetment on the south side. The large volume of each individual may have contributed to these results.

11. Discussion

The laboratory tests suggest that for rip-rap shore protection with randomly placed stones (Sodhi et al. 1996, Sodhi and Donnelly 1999) to be stable, the diameter of an average size stone must be 2 to 3 times the ice thickness. If these rip-rap criteria were applied directly to the case of Barrow, where the design ice thickness is 1.5 m, the required diameters would be on the order of 3-4.5m. Stones of this size would be very large, very expensive, and costly to install and transport. The laboratory tests described here suggest that 3600 kg (4 ton) armor stone, which would have a large dimension of roughly 2m, could resist ice shoves very well if selectively placed and due care was taken in the design and placement of the toe stones. Selective placement is a more expensive method of construction than random placement, but the benefits are smaller stone size requirement and greater resistance to ice shoves. Contractors with special placement experience are potentially available in Alaska where other breakwaters have been built using this technique.

12. Acknowledgements

This work was funded by the Alaska District of the Corps of Engineers. Mary Azelton and Merlin Peterson of the Alaska District helped in model assembly. Contributors at CRREL included William Burch and Christopher Donnelly, model design and construction; Jesse Stanley, Rosanne Stoops and Thomas Hall, technical support; and Charles Schelewa, model assembly.

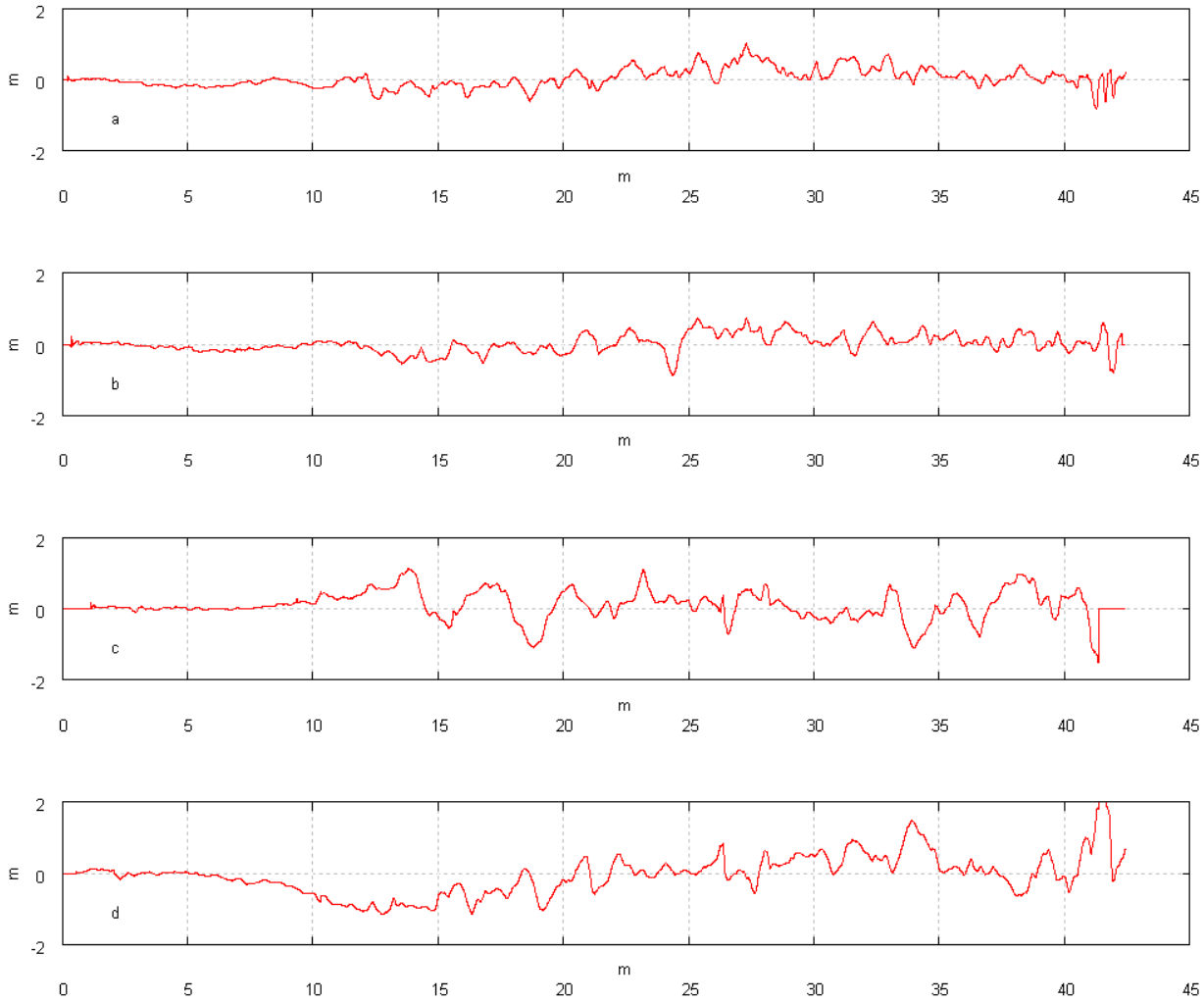

Figure 12. Average difference between the before and after profiles (meters prototype). (a) Test 4N 11,800kg (13 ton) toe stone. (b) Test 4N 18,100kg (20 ton) toe stone. (c) Test 4S 11,800kg (13 ton) toe stone. (d) Test 4S 7,200 (8 ton) toe stone.

13. References

Cole, D.M., H. Eicken, L.H. Shapiro, K. Frey (2002) Some observations of high porosity layers and brine drainage features in first-year sea ice. Proceedings of the International Symposium on Ice, Vol.16(Vol. 2), p.179-186, ; 16th international symposium on Ice, Dunedin, New Zealand, Dec. 2-6, 2002, edited by V.A. Squire and P.J. Langhorne. Publisher: Balkema, Rotterdam, Netherlands.

Frankenstein, G.E. and R. Garner (1967) Equations for determining the brine volume of sea ice from -0.5 to -22.9°C. J. Glaciol., 6(48): 943-944.

Frankenstein, G.E. and W. R. Abrams (1971). Acoustic Reflection Measurements of Sea Ice Thickness, Barrow, Alaska. Canada. Defence Research Board. Defence Research Establishment, Ottawa. Technical note, June 1971; No.71-14, p.29-41. MP-124.

Gawne, K (1999) Assessing the Susceptibility of Shorelines to Inundation by Ice: A Practical Approach. In Proceedings 10th Workshop on River Ice, River ice management with a

changing climate: dealing with extreme events. Edited by J.C. Doering, p. 361-376. Winnipeg, Manitoba, June 8-11, 1999.

Hirayama, K. (1983) Properties of Urea-doped ice in the CRREL Test Basin. CRREL Report 83-8, March 1983.

Kovacs, A. and D.S. Sodhi (1988) Onshore ice pile-up and ride-up: Observations and theoretical assessment. In Arctic Coastal Processes and Slope Protection Design (A.T. Chen and C.B. Leidersdorf, Eds.). New York: American Society of Civil Engineers, p. 108–142.

Markle D. G. and D. D. Davidson (1979) Placed-stone stability tests, Tillamook, Oregon. Technical Report HL-79-16. US Army Waterways Experiment Station, PO Box 631, Vicksburg, MS 39180

Perovich, D.K., D. G. Barber, G. Cota, A.J. Gow, T.C. Grenfell, J. Longacre, R. Maffione, C.D. Mobley, R.G. Onstott, W.S. Pegau, C.S. Roesler (1998) Field observations of the electromagnetic properties of first-year sea ice, IEEE Transactions Geoscience and Remote Sensing 36, 1633-1641, 1998.

Sodhi, D, S.L. Borland; J.M. Stanley (1996) Ice action on riprap: small-scale tests. CRREL Report No: CR 96-12 U.S. Army Cold Regions Research and Engineering Laboratory Report, 64p.

Sodhi, D and C. Donnelly (1999) Ice effects on riprap: model tests. Proceedings 10th International Conference on Cold Regions Engineering, Lincoln, NH, Aug. 16-19, 1999. Putting research into practice. Edited by J.E. Zufelt, p.824-837. Publisher: American Society of Civil Engineers (ASCE). Reston, VA, USA

Timco, G.W. and S. O'Brien (1994) Flexural strength equation for sea ice. Cold Regions Science and Technology, 22 (3), p.285-298, Mar 1994

University of Alaska at Fairbanks Floating Ice Group (2008) Barrow Sea Ice Data. Electronic data at http://www.gi.alaska.edu/snowice/sea-lake-ice/Data/Barrow_data.html#icecores (March 2008)

US Army Corps of Engineers (1995) Engineering and Design - Design of Coastal Revetments, Seawalls, and Bulkheads. Engineering Manual EM 1110-2-1614. http://www.usace.army.mil/publications/eng-manuals/em1110-2-1614/toc.htm (April 2008)

US Army Corps of Engineers (In prep.) Coastal Engineering Manual - Part VI Engineering Manual EM 1110-2-1100

19th IAHR International Symposium on Ice
"Using New Technology to Understand Water-Ice Interaction"
Vancouver, British Columbia, Canada, July 6 to 11, 2008

On the abrasion of coastal structure at estuary zone considering quasi-static pressure of sea ice

Takaharu Kawai[#1] , Shinji Kioka[#2] , Takashi Terashima[#3] , Takahiro Takeuchi[#4]

#1 Cold Region Port and Harbor Engineering Research Center, Sapporo, Japan
#2 Civil Engineering Research Institute of Hokkaido, Sapporo, Japan
#3 Kumashiro System Frontier Co.,LTD, Sapporo, Japan
#4 Hachinohe Institute of Technology, Hachinohe, Japan

#1 Cold Region Port and Harbor Engineering Research Center
Kita bldg. 9F kita 7 nishi 2-8 Kita-ku , Sapporo , Hokkaido , Japan , 060-0807
e-mail:kawai@kanchi.or.jp

Since the movement of sea ice in an open channel of an estuary zone in cold regions is so active due to tidal current, the surface of the structure at the zone is likely to suffer the abrasion due to sea ice movement. Once the type of material of the structure is known, the ice velocity, which is influenced by the nature of sea ice as well as pressure perpendicular to the structure become important factors for the estimation of abrasion depth. In the paper, the method for calculating the abrasive zone and depth at the surface of the structure is shown through sample calculations for the 2nd open channel at Lake Saroma using sinusoidal curve and tide at Mombetsu. It is concluded that the roughness coefficients between sea ice and fluid, which represents the nature of sea ice, play an important part in the estimation.

1. Introduction

In the seaboard area of the east coast of Sakhalin facing to the Sea of Okhotsk, the exploitation of oil and natural gas has started. Since the East Sakhalin Current causes an active sea ice movement in a fixed direction, it is important to evaluate the abrasion amount of the surface in the vicinity of the waterline on the structures built for the resource development. Another similar issue under different conditions is noted in the estuary zones of Lake Saroma and Lake Notori, where lake water is exchanged with seawater of the Sea of Okhotsk through narrow channels. The variation of tidal level alternatively causes both forward and backward active currents accompanying drift ice. This drift ice movement is particularly so active when the lakes are not frozen that the total horizontal movement distance can become more than 1000km a month. There are increasing tendencies to activate the movement particularly in warm winters.

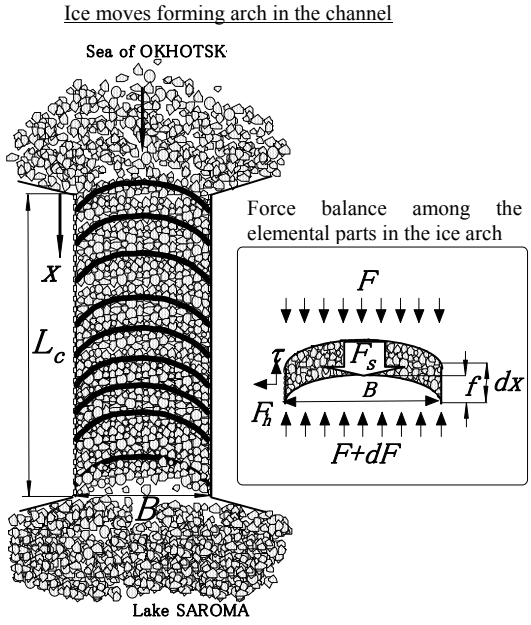

Figure 1. Figure of ice sheet movement at 2nd open channel at Lake Saroma

Thus it is also important to evaluate the abrasion amount for the structural surface of seaside constructions under such conditions, where sea ice movement distance is very long, the movement velocity varies, and the vertical movement due to tidal change is also involved. Terashima et al.(1997) has carried out the measurement of abrasion caused by ice sheets for the steel sheet pile located at the 2nd open channel at Lake Saroma. The present study has reported a theoretical investigation on the method calculating the distribution of abrasion amount, the calculation results for various cases and the effects of ice conditions on abrasion amount.

2. Theory for the calculation of abrasion amount distribution

(1) Parameters affecting abrasion amount

From the past systematic studies concerning the evaluation of abrasion amount due to sea ice movement by Saeki et al.(1985), Asai et al.(1986), Ito et al.(1990,1992) and Hanada et al.(1995), abrasion amount, A [mm], can be evaluated by *Equation* [1].

$$A = m_v \times \sigma_v \times L \qquad [1]$$

where m_v, σ_v and L denote average abrasion rate [mm/(km)/(kgf/cm^2)] depending on the material of construction surface, average contact pressure [kgf/cm^2] and the abrasion distance[km], respectively. Concerning average abrasion rate, m_v, Hanada et al.(1995) has reported practical values for various materials, such as 0.00178 for concrete, 0.00030 for steel and urethane and 0.00078 for Zebron. The present study has been done only for the abrasion of steel by considering the tidal change shown in **Figure 2** and accompanying change in the movement velocity of ice sheets. Thus, for the calculation of abrasion amount distribution, it is necessary to

evaluate contact pressure, σ_v, and abrasion distance, L or the movement velocity of ice sheets, V_i. In reference to the studies by Terashima et al.,[1] it has also been assumed that ice sheets form an arched pattern along the narrow channel. Contact pressure, σ_v , and the movement velocity of ice sheets, V_i, have been evaluated in reference to the studies by Enoki et al.(1992), Ueda et al.(1992), Kawai et al.(1997) and Makita et al.(1998) concerning the fluid resistance of ice sheets under various conditions.

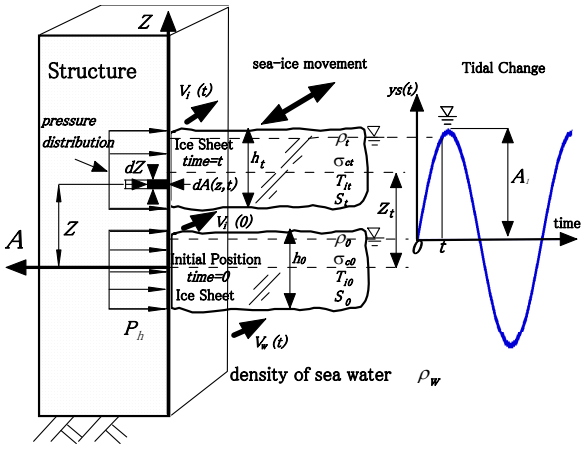

Figure 2. Interaction of structure and ice sheet

(2) Contact pressure acted on the side wall

On the assumption that ice sheets form an arched or parabolic pattern, the contact pressure, F, can be calculated using *Equation* [2]: this is derived from the corresponding application of Jansen's formula and on the basis of the force balance among the elemental parts in the arch shown in **Figure 1**. In this equation, the quasi-static state is assumed and both the inertial force and the pressure resistance among the edges of ice sheets are neglected.

$$F = \frac{F_s l_{ar} B}{2K_0 \tan\phi}\left[1-\exp\left\{-\frac{2K_0 \tan\phi}{B}x\right\}\right] \qquad [2]$$

where F_s denotes the frictional force or the stress per unit area between ice sheets and fluid, expressed by *Equation* [3]; F_s depends on the movement velocity of ice sheets, V_i, and also depends on the fluid velocity under ice sheets, V_w: both the velocities are positive in the x direction. The following equations only concern the flow in the positive x direction as the reversed flow can be calculated by changing the sign.

$$F_s = \frac{1}{2}\rho_w C_f \left(V_w - V_i\right)\left|V_w - V_i\right| \qquad [3]$$

where ρ_w , C_f and V_w denote the density of sea water, the frictional coefficient between ice and fluid and the velocity of tidal current, respectively. Next, the parameter, K_0, in *Equation* [2] can be given by *Equation* [4] on the assumption of the uniform distribution of load to work among the parabolic arch. The parameter l_{ar} is the coefficient of the length of parabolic arch, $l_{ar} \times B$, given by *Equation* [5a].

$$K_0 = \frac{1}{8\left(\frac{f}{B}\right)} \qquad [4]$$

$$l_{ar} = \frac{1}{16\left(\frac{f}{B}\right)}\left\{\frac{1}{2}(r)^2 + 2\ln r - \frac{1}{2}(r)^{-2}\right\} \qquad [5a]$$

where

$$r = 4\left(\frac{f}{B}\right) + \sqrt{\left(\frac{4f}{B}\right)^2 + 1} \qquad [5b]$$

F_h(N/m) and τ(N/m) in **Figure1** are given by *Equations* [6] and [7] using the frictional coefficient between ice sheets and steel sheet pile, μ or $\tan\phi$, where ϕ denotes the internal friction angle of ice sheets.

$$F_h = K_0 F \qquad [6]$$

$$\tau = F_h \tan\phi \qquad [7]$$

Accordingly, the contact pressure, P_h, acted on the side wall, positive in the direction toward the side wall, is expressed as *Equation* [8].

$$P_h = \frac{\rho_w C_f \left(V_w - V_i\right)^2 l_{ar} B}{4h\tan\phi}\left[1 - \exp\left\{-\frac{2K_0 \tan\phi}{B}x\right\}\right] \qquad [8]$$

(3) Flow velocity in the lake estuary zone

Coming and going flows, or forward and backward flows, are caused by tidal change at the 2nd lake estuary zone where there is a narrow channel connecting the Sea of Okhotsk and Lake Saroma. The flow velocity, V_w (t), is given by *Equation* [9], as shown by Kondo(1985), by applying Bernoulli's theorem on the assumption that the water level gradient in the channel is constant as well as that the acceleration term is small enough to neglect because the fluctuation is caused by tidal change.

$$\mathrm{V_w}(t) = \pm\left(f_0 + f_e + \frac{2gn^2}{R^{1/3}}\frac{L_c}{R}\right)^{-0.5}\sqrt{2g\left|y_s(t) - y_b(t)\right|} \qquad [9]$$

where f_0 denotes the loss coefficient at the outlet of the open channel, estimated as 1.0, f_e the loss coefficient at the inlet of the open channel, estimated as 0.5, n Manning's composite roughness coefficient inside the narrow channel, R hydraulic mean depth (m), L the length of the narrow channel (m), $y_s(t)$ the tidal level in the Sea of Okhotsk, and $y_b(t)$ the variation of the water level in Lake Saroma. The variation of water amount of the lake can be calculated by *Equation* [10] based on the equation of continuity.

$$\frac{dy_b(t)}{dt} = \frac{A_s}{S_L} V_w(t) \qquad [10]$$

where A_s denotes the cross section of the narrow channel (m^2) (A_s = B x h where B and h denote the width and water depth of the narrow channel, respectively), and S_L denotes the area of the inner bay or the area contributing to sea water exchange in the 2nd lake estuary zone. The S_L is estimated as 47.7km^2 in reference to Hagino's study.(1985) The Manning's composite roughness coefficient, n, is given by *Equation* [11].

$$n=\left(\frac{s_i n_i^{3/2}+s_b n_b^{3/2}}{s}\right)^{2/3} \qquad [11]$$

where s, s_i and s_b denote the wetted perimeters of the corresponding sections. *Equation* [11] has been deduced for the object where there are ice sheets in the narrow channel, and by considering both of the Manning's roughness coefficients, one between seabed and seawater, n_b, and the other between sea ice and seawater, n_i, and also by assuming the condition that the flow velocity of each section is the same as the average flow velocity. As the data on the tidal level in the Sea of Okhotsk, $y_s(t)$, either the theoretical sine curves or the observed data at Mombetsu City on January 2007 has been used. *Equations* [9] and [10] have been solved using the initial condition of $y_b(0)=0$ to obtain the variation of water level, $y_b(t)$, which is used to deduce the flow velocity at the lake estuary zone, $V_w(t)$, by substitution into *Equation* [9].

Under the assumption that kinetic energy and work are balanced concerning the ice sheets in which an average force is acted along the narrow channel with the length, L_c, *Equation* [12] has been deduced.

$$\begin{aligned}&\int_0^{L_c}\frac{1}{2}\rho_i l_{\mathrm{ar}} BhV_i^2 dx \\ &=\int_0^{L_c}\frac{\rho_w C_f l_{ar} B^2 (V_w-V_i)^2}{4K_0\tan\phi}\left[1-\exp\left\{-\frac{2K_0\tan\phi}{B}x\right\}\right]dx\end{aligned} \qquad [12]$$

It has also been assumed that no acceleration is generated in the narrow channel (width B and length L_c) in the presence of ice, and thus both V_w and V_i do not change with time. Under these conditions, *Equations* [13a] and [13b] are derived.

$$\left(V_w/V_i\right)^2-2\left(V_w/V_i\right)+C=0 \qquad [13a]$$

where

$$C=1-\frac{\frac{1}{2}(\rho_i BhL_c)}{\frac{\rho_w C_f B^2}{4K_0\tan\phi}\left[L_c+\frac{\left(\exp\left\{-\frac{2K_0\tan\phi}{B}L_c\right\}-1\right)}{\frac{2K_0\tan\phi}{B}}\right]} \qquad [13b]$$

Considering that ice does not move faster than seawater, the movement velocity of ice sheets, V_i, can be determined by *Equation* [14] using known values of the flow velocity of sea flow velocity, V_w, obtained from the relation between the tidal level of the open sea and the water level of the lake.

$$m = \left| \frac{V_w}{V_i} \right| = \frac{2 + \sqrt{\left(2^2 - 4 \times C\right)}}{2} > 1 \qquad [14]$$

Accordingly, the contact pressure, $P_h(t,x)$, can be given by *Equation* [15].

$$P_h(t,x) = \frac{\rho_w C_f l_{ar} B V_w{}^2 (1 - \frac{1}{m})^2}{4h \tan\phi} \left[1 - \exp\left\{ - \frac{2K_0 \tan\phi}{B} x \right\} \right] \qquad [15]$$

The overall movement distance of ice sheets, L_t, during time, T, is given by *Equation* [16].

$$L_t = \int_0^T \frac{1}{m} \left| V_w(t) \right| dt \qquad [16]$$

(4) The distribution of abrasion amount

When the thickness center of ice sheets migrating under the influence of tide is located at *z(t)*, the increase of abrasion amount, *dA(z,t)*, of material at the position, *z*, during a time interval, *dt (time=t ～ t+dt)*, can be calculated by *Equations* [17] and [18].

$$dA(z,t) = m_v \times \sigma_v(z,t) \times V_i(t) \times dt \qquad [17]$$

where

$$z(t) = y_S(t) + h_0 \left(\frac{\rho_0}{\rho_w} - 0.5 \right) - h_t \left(\frac{\rho_t}{\rho_w} - 0.5 \right) \qquad [18]$$

The above equations have been deduced under the assumption of $\sigma_v(z,t) = P_h(t,x)$ or the rectangular distribution approximation, as shown in **Figure 2**, in the range of $-h/2 + z(t) \le z \le h/2 + z(t)$. As the initial condition, the location of the ice thickness center is used as the reference, z=0, when the displacement of tide = 0 or $y_s(t)=0$, as shown in **Figure 2**. Although the density of seawater, ρ, the salt concentration, S, the temperature, T, and thickness, h, of ice are actually changing with time, they are assumed to be constant in this work: this assumption results in $\rho_0=\rho_t$ and $h_0=h_t$ in *Equation* [18]. The distribution profile of abrasion amount on the structure surface has been calculated by the time integration of *Equation* [17] at all the locations, z, determined by changing location by a minute amount, dz. Further calculation conditions are shown in **Table 1**.

3. The calculation results of abrasion amount and Consideration

(1) The contact pressure acted on the side wall

Figure 3 shows the calculation results of the contact pressure acted on the side wall, P_h, using *Equation* [15]: it has been deduced under the condition of the quasi-static balance. The calculation has been carried out using $V_i = 1$ *m/s* as the movement velocity of ice sheets and

Table 1. Calculation conditions

Parameter	Numerical value
Ice thickness h [m]	1.0 (on an average)
The density of the sea ice ρ [g/cm^3]	0.9 (on an average)
The density of the sea water ρ [g/cm^3]	1.02
The internal friction angle of the sea ice[degree]	30
The width of sheet pile W [m]	0.3
The shape of 2nd open channel at Saroma Lagoon	Width:50[m] , Length:260[m] ,Depth:5[m]
Tide condition in the calculation Type1(sine tide)	
Tidal level ys [m]	ys=A1sin(2 π t/Tp)
A half amplitude of tidal level A1[m]	0.25 , 0.5 , 0.75
Period of tide Tp[hour]	24
Tide condition in the calculation Type2(actual tidal data at Monbetsu 2007-1)	
Expected tide level at Monbetsu, 30 days , 2007/1/20-2007/2/19, per 0.05[hour]	
The materials of the structure	Steel
Abrasion rate of objective structure mv [mm/km/(kgf/cm2)]	0.00030
A frictional resistance coefficient among the sea ice and sea water	0(no ice) , 0.026(no ice jam) , 0.1 , 0.2 , 0.3 (ice jam fomed)
Parabolic shape of ice arching	hight(f):20[m] , width(B):50[m]
Time interval of the calculation dT [hour]	0.05(=80sec.)
Maninng's roughness coefficient among the sea ice and sea water	0.024
Days of calculation [day]	30

using the conditions shown in **Table 1**. The contact pressure increases with increasing x or with increasing the frictional resistance coefficient between sea ice and seawater, C_f, since the fluid resistance increases. The contact pressure changes depending on the variation of tidal level since it causes the change in flow velocity as well as in flow direction in the narrow channel. Therefore, the calculation of abrasion amount has been carried out using the contact pressure at the center of the channel, $x=L/2$.

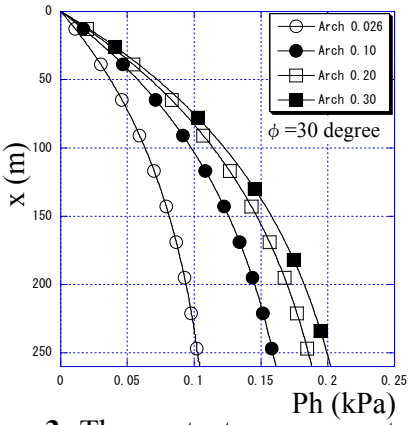

Figure 3. The contact pressure act on side wall

(2) Flow velocity at the lake estuary zone and the movement distance of ice sheets

Figures 4 and 5 show the water level of Lake Saroma, $y_b(t)$, calculated using the theoretical and observed tidal level of the open sea, $y_s(t)$, respectively.

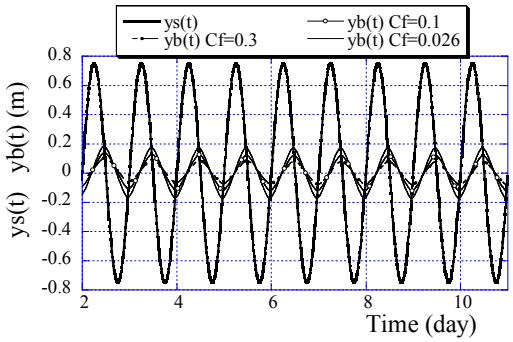

Figure 4. The water level of the lake, calculated using the theoretical tidal level of the open sea

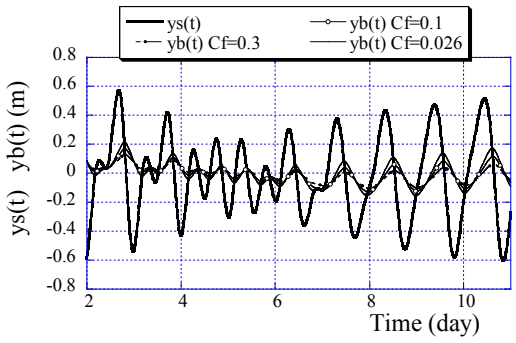

Figure 5. The water level of the lake, calculated using the observed tidal level of the open sea

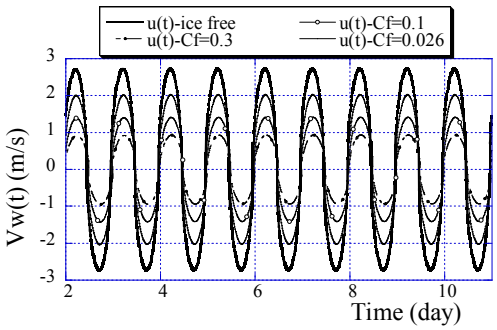

Figure 6. The flow velocity at the lake estuary zone , calculated using the theoretical tidal level

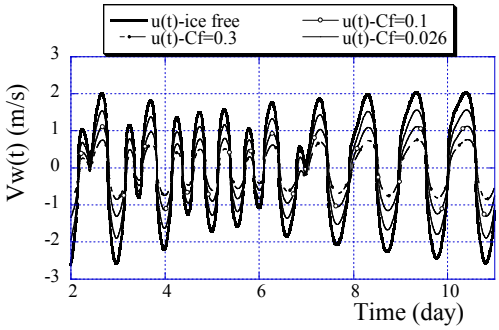

Figure 7. The flow velocity at the lake estuary zone , calculated using the observed tidal level

Figures 6 and 7 show the flow velocity at the open channel, $V_w(t)$, calculated using the theoretical and observed tidal level, respectively. A sine curve with a half-amplitude of 0.75m was used as the theoretical tidal level, while the actual tidal data at Mombetsu City in January 2007 was used as the observed one. For each figure, several calculation results are shown by changing the frictional resistance coefficient, C_f, between ice sheets and seawater. The coefficient is supposed to vary with the conditions of ice sheets: C_f=0 for the ice-free condition, C_f=0.026 for the case showing the ordinary amount of drift ice and C_f=0.10～0.30 for the case showing the formation of ice jam. The above calculation also assumes that the lake is not frozen and then the movement of ice sheets is active. The value of C_f affects the variation of the water level in the lake and also affects the flow velocity at the open channel, $V_w(t)$. With the increase of C_f, the flow velocity, $V_w(t)$, decreases and, on the other hand, the contact pressure acted on the side wall, P_h, increases due to the increase of fluid resistance. The two factors, $V_w(t)$ and P_h, thus are thought to have reverse effects for the evaluation of abrasion amount. Incidentally, the variation of the lake water level shows a delayed phase difference by 2 to 3 hours in comparison with the tidal level of the open sea, as shown in **Figures 4 and 5**. This result as well as the flow velocity under the ice-free condition, as shown in **Figures 6 and 7**, agree well with the studies by Hagino(1985) and Makita(2004). **Figures 8 and 9** show the relations between the overall movement distance L_t and time. They show that ice sheets move more than 1000km during a time as short as 30 days. **Figure 8** shows that L_t decreases with the increase of C_f. This is expected to have significant effect on abrasion amount.

(3) The distribution of abrasion amount

Figures 10 and 11 show the distribution of abrasion amount, A, for C_f = 0.026 and 0.3, respectively, using the theoretical tidal level of the open sea expressed as sine curves with a half-amplitude of 0.25m, 0.50m or 0.75m. The distribution profile of abrasion amount is strongly affected by such parameters as the distribution profile of acted contact pressure, the thickness of ice sheets and the tidal level of concern. For example, Takeuchi et al.(2004) has shown that the Gaussian distribution can approximately be applied when ice sheets are broken mechanically by brittle crushing. But the distribution profile of acted contact pressure is unknown, the uniform or rectangular distribution profile was used in this study. Therefore, field observation will be necessary for the contact pressure and its distribution in order to improve precision.

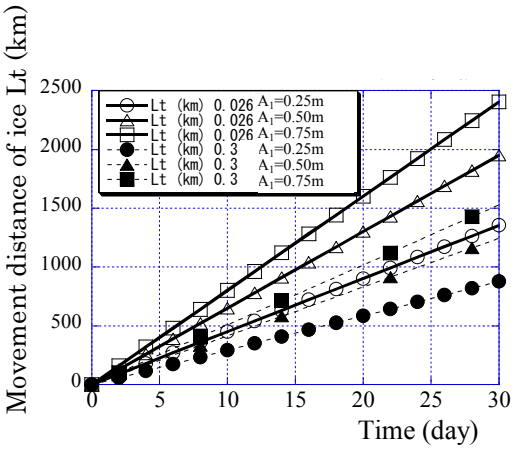

Figure 8. The overall movement distance of ice sheets(theoretical tidal level)

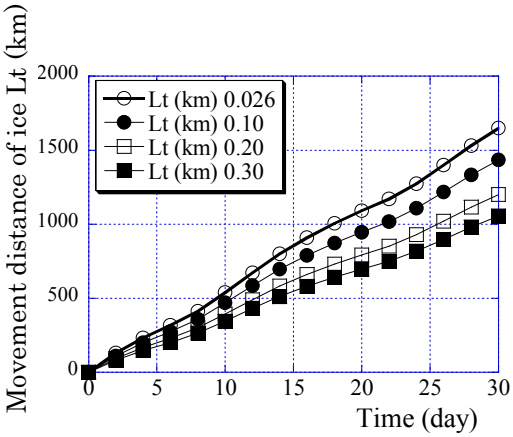

Figure 9. The overall movement distance of ice sheets(observed tidal level)

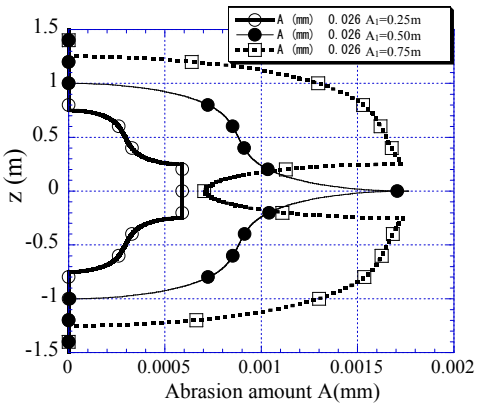

Figure 10. The distribution of abrasion depth using theoretical tidal level (Cf=0.026)

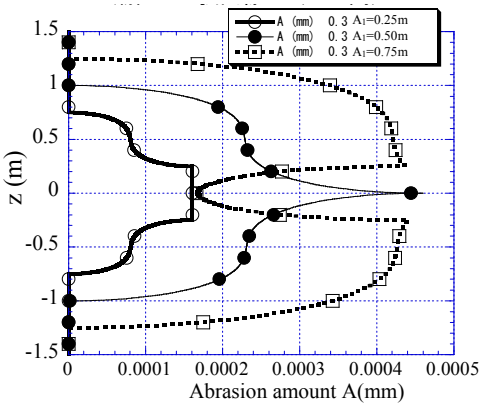

Figure 11. The distribution of abrasion depth using theoretical tidal level (Cf=0.3)

Figure 12 shows the distribution of abrasion amount, A, calculated using various values of frictional resistance coefficient, C_f. The abrasion amount strongly depends on C_f . The distribution profiles reflect the vertical location of ice sheets, determined by tidal level: the profiles are in some agreement with the observed field study results by Terashima et al.(1992) in tendency. **Figure 13** shows the relation between the maximum value of abrasion amount, A_{max}, in ordinate, and frictional resistance coefficient, C_f, in abscissa. The calculation was carried out for the C_f value more than 0.026, the minimum value corresponding to drift ice. No calculation was carried out for smaller C_f values, approximately C_f = 0.007 corresponding to flat ice(Ueda et al.(1992)) for example, because flat ice shows too limited movement to treat practically. Under the calculation conditions, the maximum value of abrasion amount, A_{max}, shows a decrease with increasing frictional resistance coefficient, C_f, either using observed tidal data at Mombetsu City on January 2007 or using the theoretical tidal sine curve. Concerning values of abrasion amount, the present calculation shows a big difference from observed data from the quantitative point of view: the typical value of the maximum abrasion amount, A_{max} = 0.001mm, calculated using C_f = 0.026 and the observed tidal level at Monbetsu City is much smaller than the actual data on corrosion or abrasion rate, 0.2 ~ 0.3mm/year, that Terashima et al.(1997) observed in the splash

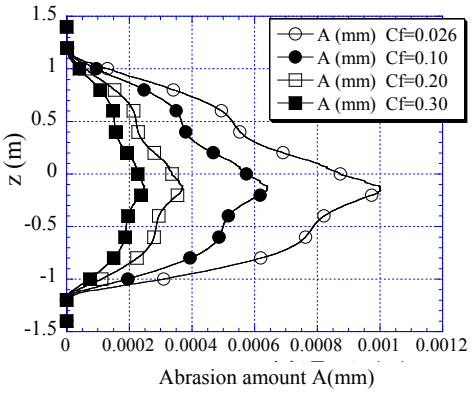

Figure 12. The distribution of abrasion amount using observed tidal level

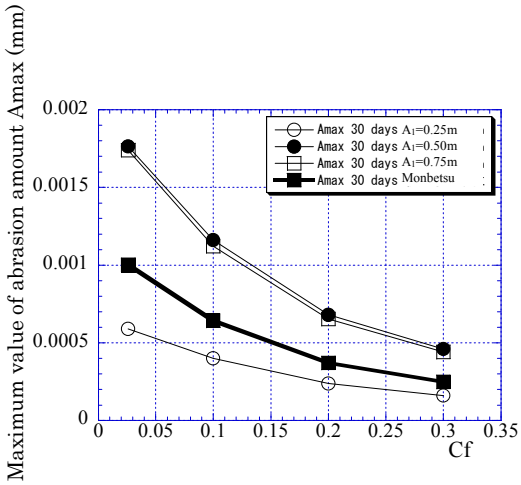

Figure 13. The relation between the maximum value of abrasion amount A_{max} and frictional resistance coefficient C_f

zone susceptible to drift ice. There are many conceivable reasons to explain the difference between the theoretical and observed data. One of the most probable reasons must be about the theoretical contact pressure, P_h, shown in **Figure 3**. It seems too small to contribute to abrasion as it has been deduced from the assumption of the quasi-static balance. The difference seems to suggest that other factors like impact phenomenon should be more effective for abrasion. For future studies of interest, it is significant to carry out calculations on the period of declining drift ice in early spring, using the observed data on tidal level in different years, as well as to perform field observations on the distribution of contact pressure, the thickness and conditions of drift ice and also to investigate the evaluation of C_f values.

4. Conclusions

1) The calculation method is presented on the abrasion amount distribution of construction surface under the conditions that both the movement velocity and the vertical location of ice sheets vary simultaneously.
2) Abrasion amount distribution and its maximum value strongly depend on the frictional resistance coefficient between ice sheets and seawater, C_f, the value indicating the conditions of ice sheets at estuary. The present calculation shows that the maximum value of abrasion amount, A_{max}, decreases with increasing the frictional resistance coefficient, C_f, using C_f = 0.026 as the minimum value: this C_f range corresponds to the conditions of drift ice.
3) Concerning the distribution profile of abrasion amount, the present calculation from the contact pressure, σ_v, under the quasi-static conditions shows some qualitative agreement with observed results reported by Terashima et al.(1997) , but shows a big quantitative difference from the observed data. For future work, it must be necessary to investigate the consideration of other factors such as impact load. Furthermore, it is necessary to make more field investigations on the distribution of the contact pressure and on the thickness and conditions of drift ice as well as to extend the period in calculation.

References

Terashima, T. , Imaizumi, A., Sato K., Nakata, K., Hanada, M., and Saeki H.,1997.Abrasion of steel sheet pile due to a movement of ice floes and its estimation , Proc. of Civil Engineering in the Ocean,Vol.13,pp.813-818 , Japan

Saeki, H., Asai, Y., Izumi, K., and Takeuchi, T., 1985.Study on abrasion of concrete due to sea ice movement, Proc. of Civil Engineering in the Ocean, Vol.1, pp.68-73, Japan

Asai, Y., Konno, K., Kajiya, T., Takeuchi, T., and Hiroshi Saeki,1986.Concrete-sea ice sliding abrasion test , Proc. of Civil Engineering in the Ocean , Vol.2 , pp.85-89,Japan

Itoh, Y. , Asai Y. , Sato, K. , Goto, K., and Saeki, H.,1990. Abrasion test of various construction materials due to movement of sea ice, Proc. of Civil Engineering in the Ocean, Vol.6, pp.167-170, Japan

Ito, Y., Asai, Y., Saeki, H., Oritani, N., and Ishii, C.,1992.Estimation and control method for abrasion of offshore structure due to movement of ice sheet , Proc. of Civil Engineering in the Ocean , Vol.8 , pp.147-151,Japan

Hanada, M. , Hara, F., Itoh, Y., and Saeki, H.,1995.Abrasion of natural stones due to a movement of sea ice sheet , Proc. of Civil Engineering in the Ocean , Vol.11 , pp.229-233 , Japan

Enoki, K., Ishii, C., Kunimatsu, S., and Saeki, H.,1992.Control of the ice floes movement by using Ice Boom, Proc. of Civil Engineering in the Ocean, Vol.8 , pp.153-158 , Japan

Ueda, T., Saeki, H., Yamashita, T., Muraki, Y.,and Enoki, K.,1992. Fluid force acting on floating ice floes and their drifting velocity, Proc. of Civil Engineering in the Ocean, Vol.8 , pp.135-140, Japan

Kawai, T. , Hara, F., Makita, S. , and Saeki, H.,1997.A Study on the fluid resistance of an ice floe and a rubble of ice , Proc. of '97 Cold Region Technology Conference, pp.392-396,Japan

Makita, S., Kawai, T., Saeki, H., and Hara, F.,1998. The experimental study on the fluid resistance of trapped ice floes, Proc. of Civil Engineering in the Ocean, Vol.14, pp.417-422, Japan

Makita, S., Kawai, T., Saeki, H., Enoki, K., and Hara, F.,1998.The Experimental study on the fluid force of rubble field of ice, Proc. of '98 Cold Region Technology Conference, pp.368-375 , Japan

The society of powder technology, 1998, The guide of powder simulation, Japan

Kondo, H., 1985. Effect of freezing of constricted inlets on the tidal current at their entrances, Proc. of '85 Cold Region Technology Conference, pp.103-107, Japan

Hagino, S. , 1985 . Study on sea water exchange characteristics in Lake Saroma, Bulletin of natural research institute of fisheries engineering, No.6, pp.1-15, Japan

Makita, S., Saeki, H.,2004. Influence of aquaculture facility to the water exchange at the semi-closed water area, Proc. of Civil Engineering in the Ocean, Vol.20, pp.395-400, Japan

Takeuchi, T., Akagawa, S., Nakazawa, N., Kioka, S., and Saeki, H.,2004.The distribution of local ice pressure acting on offshore structure ,Proc. of Civil Engineering in the Ocean ,Vol.20 , pp.1235-1240,Japan

19th IAHR International Symposium on Ice
"Using New Technology to Understand Water-Ice Interaction"
Vancouver, British Columbia, Canada, July 6 to 11, 2008

Assessment of "Ice Storm" Possibility in the Bohai Sea

Vadim K. Goncharov
Saint-Petersburg State Marine Technical University
3, Lotsmanskaya str., Saint-Petersburg, 190008, Russia
vkgonch@mail.ru
Natalia Yu. Klementieva, Kirill E. Sazonov
Krylov Shipbuilding Research Institute
44, Moskovskoe sh., Saint-Petersburg, 196158, Russia
nklem@mail.ru, kirsaz@rambler.ru
Zhijun Li, Yongxue Wang, Jing Zhou
Dalian University of Technology
116024 Dalian, China
lizhijun@dlut.edu.cn, wangyx@dlut.edu.cn, zhouj@dlut.edu.cn

"Ice Storm" is one of the most dangerous environmental phenomena that can arise at covered by ice water areas and presents serious hazard for offshore structures because moving with large speed ice floes can damage the structure as result of collision. It the paper the possible mechanism of ice floe capture by wave is stated, and the relationship between the dimensions of ice floe and characteristics of wind induced waves, which are capable to transport ice floes are presented. On the base of created mathematical model and known method of the wind heaving forecast, assessment of possibilities the ice storm occurrence at the Bohai Sea will be carried out and main outcomes will be stated.

1. Introduction

"Ice storm" is a very dangerous natural phenomenon in seas covered with ice. If there is broken ice of low compactness on the water surface (2-3 points), an intensive wind induced heaving can occur. Wind waves with considerable height are capable of involving separate ice floes and transferring them along its slope at a speed of the wave's propagation. These ice floes can hit shelf construction on their way and cause considerable damages. For example, several cases of "ice storms" when berths were damaged are known (Marchenko, 2002). "Ice storm" is extremely dangerous when close to the coastline, where water depth reduces, due to shallow waters effect, the height of waves increase, and wave's profile becomes steeper.

To estimate the possibility of "ice storm" the information on ice cover characteristics in the desired area and on the wind waves parameters, which can be estimated using data of speeds as well as data of directions and periodicity of winds in winter.

2. Weather and Ice Condition at the Bohai Sea

Water area of the Bohai Sea is shown on Figure 1. The average air temperature in winter is about -10°. The ice has sufficient thickness of up to 45 cm (Li et all, 2007; Yakunin et all, 2005) within the period from November till March.

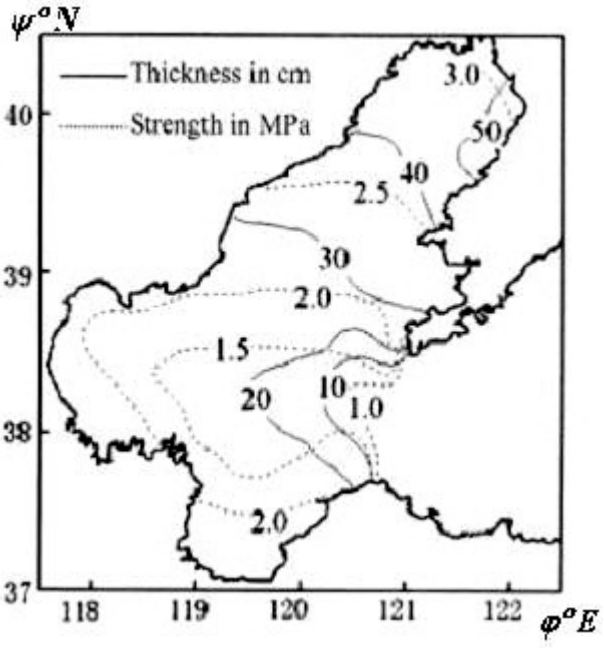

Figure 1. Characteristics of ice cover in the Bohai Sea (Li at all, 2007).

Table No 1 shows the following characteristics of wind for the Bohai Sea for winter season: periodicity of speeds for particular ranges of its value and for the main eight directions according to the data (Davidan et all, 1974). This material was recalculated in the characteristics of periodicity and possibility of winds, the speed of which exceeds the limit of the appropriate value. These results are given in Table No 2.

Table 1. Direction distribution of the wind speed in the Bohai Sea during winter season.

Wind speed, W, m/s	N	NE	E	SE	S	SW	W	NW
0-6	6	12	4	2	2	1	1	1
6-12	12	37	4	1	1	-	-	1
12-16	6	6	1	-	-	-	-	-
>16	1	2	-	-	-	-	-	-
$\sum p$	25	57	9	3	3	1	1	2

As the data of the Tables show, northern and northeastern winds are prevailing as to direction and speed in the Bohai Sea during winter season. The Bohai Sea as well as the entire Yellow Sea is affected by monsoons; winter monsoon features northern winds and it is active within the period from September-October until March-April. Periodicity of northern and northeastern winds reaches 80%. For such winds according to the estimated values of possibility of range limitation exceeding, contained in Table No 2, on Figures 2 and 3 the curves of the winds speed distribution in the logarithmic relative scale for the both axes are shown (for northern and north-eastern winds respectively). The curves of possibility distribution are given approximately using the straight lines and are prolonged into the area of low possibilities that is prolonged beyond the wind speed ranges, stated in initial Table No 2. Using the method it is possible to assess the possibility of wind speed observation, which is not reflected in this Table, as this phenomenon is of low possibility, or because it has not been registered before. As a result of the assessment the following values of the extreme wind speed which could be observed in average once a year were obtained: for the wind of northern direction – 40 m/sec, for the wind of north-eastern direction – 30 m/sec.

Table 2. Repeatability (consequent) and exceedance probability (numerator) of the wind speed gradation for various directions.

Wind speed, W, м/с	N	NE	E	SE	S	SW	W	NW3
0-6	100/24	100/21.1	100/44.4	100/66.7	100/66.7	100/100	100/100	100/50
6-12	76/48	78.9/64.9	55.5/44.4	33.3/33.3	33.3/33.3	-	-	100/50
12-16	28/24	14/10.5	11.1/11.1	-	-	-	-	-
>16	4/4	3.5/3.5	-					

According to the wind speed it is possible, in its turn, to estimate characteristic of the wind induced waves by using empiric formulas and nomograms, obtained as a result of observations of the sea heaving (Davidan et all, 1985; Lappo et all, 1990). As a result of the assessment it was

determined that at extreme speeds of winds of the northern directions the waves of 4.9 m high and 125.8 m long can occur at about 9 sec period. For extreme winds of north-eastern directions the following parameters of waves were obtained: height - 3.7 m, wave length - 122.9 m, and period - 8.9 sec.

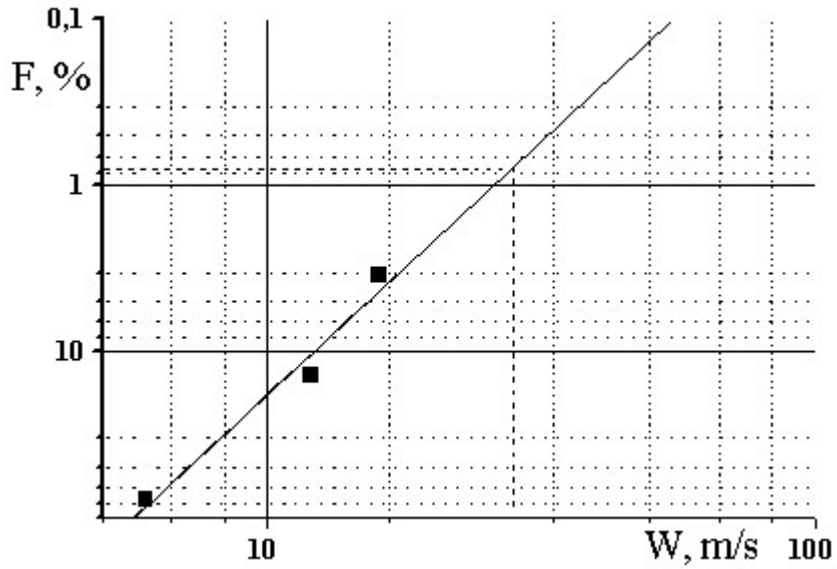

Figure 2. Winds speed distribution in the logarithmic relative scale for the both axes for northern winds during winter season.

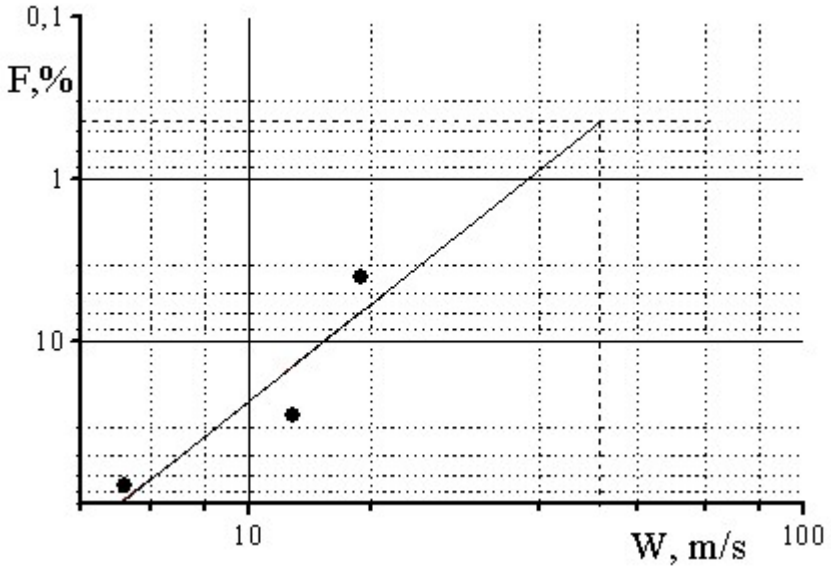

Figure 3. Winds speed distribution in the logarithmic relative scale for the both axes for northern winds during winter season.

3. Model of Ice Floe and Wave Interaction

Separate ice floes floating on the sea surface depending on the correlation of their transverse size and wavelength can be involved into motions of three types. Ice floes of big size will drift under the effect of wind as well as waves (Stocks' wave transfer). Ice floes of small size will combine this drifting with progressive wavering. There is one more possible variant, where an ice floe of intermediate size is in the state of dynamic balance on the wave slope, where its sliding speed under the effect of gravity will happen to be equal to the phase wave speed. It means that in this case the ice floe is involved ("captured") by the wave and moves at a phase wave speed that considerably exceeds speed of the wave drifting. The maximum ice floes size capable of involving into phase wave motion is of great practical interest for assessment of possible damage to shelf or shore constructions crossing the water surface.

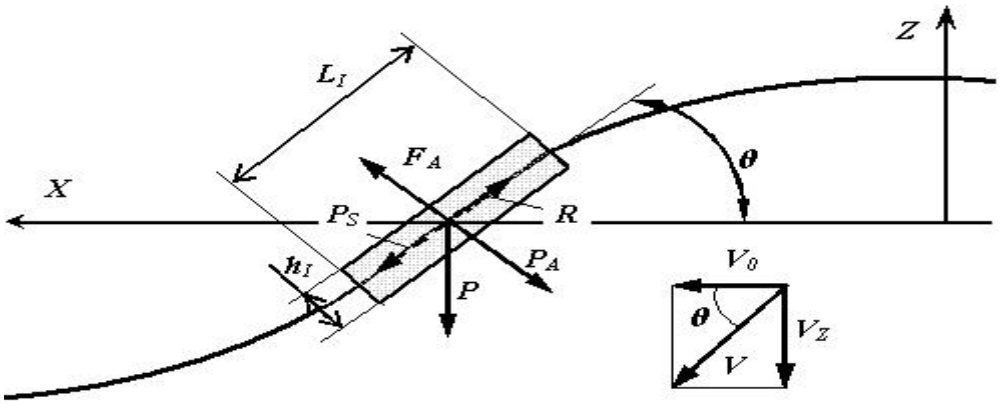

Figure 4. Scheme of the ice floe movement oh the slope of wave.

Figure 4 shows the scheme of allocation of "captured" ice floe on the wave slope and the forces affecting it. Slipping of the ice floe on the wave slope at the average angle θ takes place under the force P_S, representing the vector difference of the floating force F_A and the weight force P, which is equilibrated by the resistance force R. The speed of the slipping is V. If the plane of this speed onto the horizontal axis X happens to be equal to the phase wave speed V_0, the ice floe will be stationary relative to the wave, or will be moving with the wave profile. Such condition can be represented as follows:

$$V \cos\theta = V_0 \qquad \textbf{[1]}$$

Ice floes of smaller size will rise to a crest of wave, slide along back slope and again repeat such cycle with following waves, remaining on the same place after the wave passing. Ice floes of larger size will slide along slope down to the bottom of wave, and ones will be obstacles for breaking of waves. The theoretical analysis of possibility of the occurrence this phenomenon is based on the researches described in (Korotkin, 1973: Marchenko, 2002).

The following forces affect the ice floe "captured" by the wave and moving together with the wave peak: weight force P, floating force F_A and water resistance force R. these forces are determined by the following equations:

$$P = \rho_I \, g \, h_I \, L_I^2 \qquad \textbf{[2]}$$

$$F_A = \rho_W \, g h_{IW} \, L_I^2 \qquad \textbf{[3]}$$

$$R = C_X \frac{\rho_W V^2}{2} S_I \qquad \textbf{[4]}$$

Here ρ_I, ρ_W - ice and water density respectively; g – gravity acceleration, h_I – ice floe thickness; h_{IW} – average draft (immersion) of an ice floe, L_I – feature size of an ice floe; Cx – ice floe resistance coefficient; V – ice floe speed directed along the wave slope; S_I – area of the wetted by water ice floe surface. The average draft of the ice floe can be assessed in case of equation of ice floe buoyancy and projection of its weight onto the normal to the wave slope in given point, that is

$$F_A = P_1 = P \cos\theta \qquad \textbf{[5]}$$

For the real angles oh the wave slope inclination the following form can be accepted

$$h_{IW} = \frac{\rho_I}{\rho_W} h_I \cos\theta \simeq \frac{\rho_I}{\rho_W} h_I \qquad \textbf{[6]}$$

Considering this equation the wetted ice floe surface, determining resistance to the ice floe motion, can be represented as follows

$$S_I \simeq L^2 + 4 \frac{\rho_I}{\rho_W} h_I \, L_I \qquad \textbf{[7]}$$

In order to assess phase wave speed it is reasonable to use the simplest model of progressive waves on the deep water (Eri's model). The disperse correlation for the waves of Eri is as such

$$V_0 = \sqrt{\frac{g \lambda}{2\pi}} \qquad \textbf{[8]}$$

Here λ – is the wavelength. The condition of the ice floe "capture" by the wave can be determined using the equality of projection of the ice floe weight **[2]** onto the tangent to the wave slope and the resistance force **[4]** considering the correlation **[1]**

$$4\pi \frac{\rho_I}{\rho_W} \frac{h_I \, L_I^2}{C_X \, S_I} \sin\theta \cos^2\theta = \lambda \qquad \textbf{[9]}$$

To simplify the following analysis we will use the parameter m – the correlation between the feature size of an ice floe and its thickness

$$L_I = m\,h_I \qquad \textbf{[10]}$$

Substituting **[9]** for the equation **[7]** and considering that $cos^2\theta \approx 1$, the formula **[9]** can be converted in the following way

$$h_I = \frac{1}{4\pi\,\rho_I}\,\frac{C_X\,(m\,\rho_W + 4\,\rho_I)}{m\,\sin\theta_{\max}}\,\lambda \qquad \textbf{[11]}$$

In this formula θ_{max} – is the maximum angle of the wave slope, determined by known formula

$$\theta_{\max} = arctg\,\frac{2\pi\,a}{\lambda} \qquad \textbf{[12]}$$

Here a – is the wave amplitude, which is connected with the waves steepness δ by the correlation

$$\delta = \frac{2\,a}{\lambda} \qquad \textbf{[13]}$$

For the real sea heaving this value is random one that varies from wave to other waves. Therefore, formula **[11]** has to be applied as stochastic equation in relation to the steepness of waves. In the research (Davidan, 1985) it is recommended to use the value δ_a = 0.3 as the average value. In the handbook (Davidan, 1974) for the approximate description of the law of waves steepness values distribution it is recommended to use the following formula based on the experimental data average-out.

$$F(\delta^0) = P\{D \ge \delta^0\} = \exp\left[-0.742\left(\frac{\delta}{\delta_a}\right)^{2.5}\right] \qquad \textbf{[14]}$$

Here δ^0 – standardized value of the heaving steepness according to the average value, that is $\delta^0 = \delta\,/\delta_a$, D – accidental value exceeding δ^0. According to this formula, the assessment of the distribution functions of waves steepness value was accomplished, the results of which are given in Table No 3.

Table 3. Cumulative distribution function of the wind waves steepness.

$F(\delta°)$	0,1	1	2	5	10	20	30	40	50	60	70	80	90	95
$\delta°=\delta/\delta_a$	2,44	2,08	1,94	1,75	1,57	1,36	1,21	1,09	0,97	0,86	0,75	0,62	0,46	0,34

4. Assessment of Conditions for the "Ice Storm" Inception

Inserting values from Table 3 into the formulas **[11]**, **[12]** and **[13]** the calculations of ice thickness of ice floes, which can be involved ("captured") by the waves of different steepness in the Bohai Sea were performed. For the calculations the value C_x = 0.008 was accepted, that corresponds direction of the relatively sharp edge of the ice floe towards the motion direction. Seawater density was accepted as ρ_W = 104.74 kg·sec^2/m^4, that corresponds to the temperature T = 0°C and salinity S = 33 ‰, sea ice density was ρ_I = 94 kg·sec^2/m^4 (T = -2°C and salinity S = 2 ‰ of ice). Figures 5 – 7 show the calculation results for the three values of the parameters m, magnification of which corresponds to the increasing the horizontal size of ice floes. Ice floes thickness and wavelength variation is limited by the values typical for the Bohai Sea and stated in the beginning of given paper. These figures represent the limited curves, corresponding to the equation in the formula **[11]**. The areas of the real ice floes "capture" by waves are located within certain rang near calculated curves for each of the values of the function of wind waves steepness distribution.

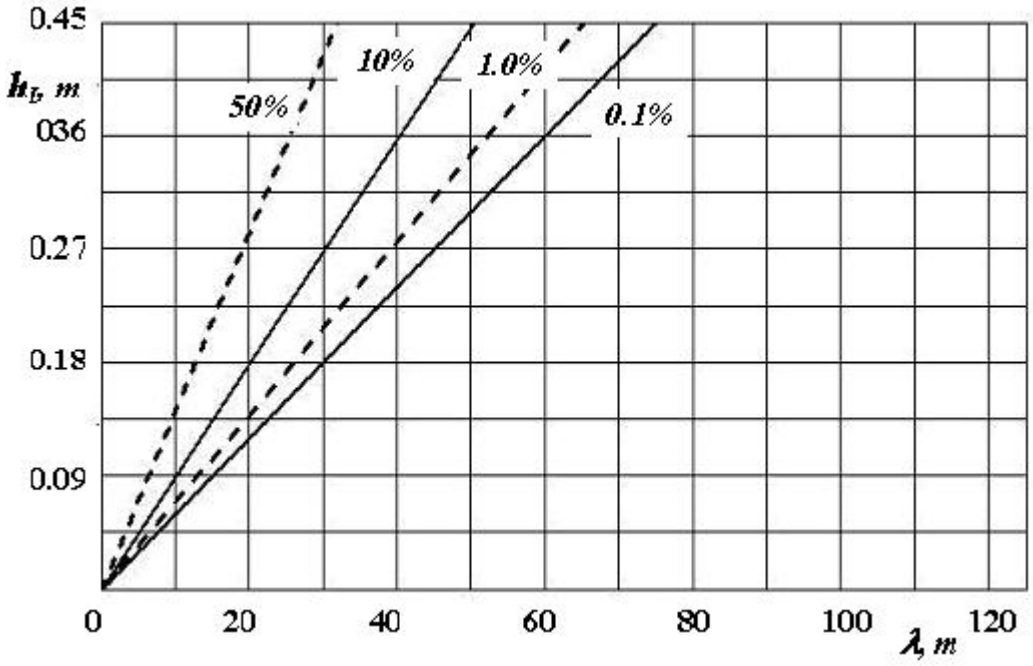

Figure 5. Correlation between the ice floe sizes (m = 5) and characteristics of wind-induced sea heaving when waves are capable to "capture" and transfer ice floes in the Bohai Sea.

Comparison of the calculation results from Figures 5 – 7 shows that at the same ice thickness and wave's steepness with increasing horizontal size of ice floes the waves of greater length are necessary for the ice floes "capture" and future transfer. In other words, with reducing the ice floes size the possibility of "ice storm" increases, but simultaneously due to the ice floes weight reduction the energy of possible stroke against the obstacle is reduced.

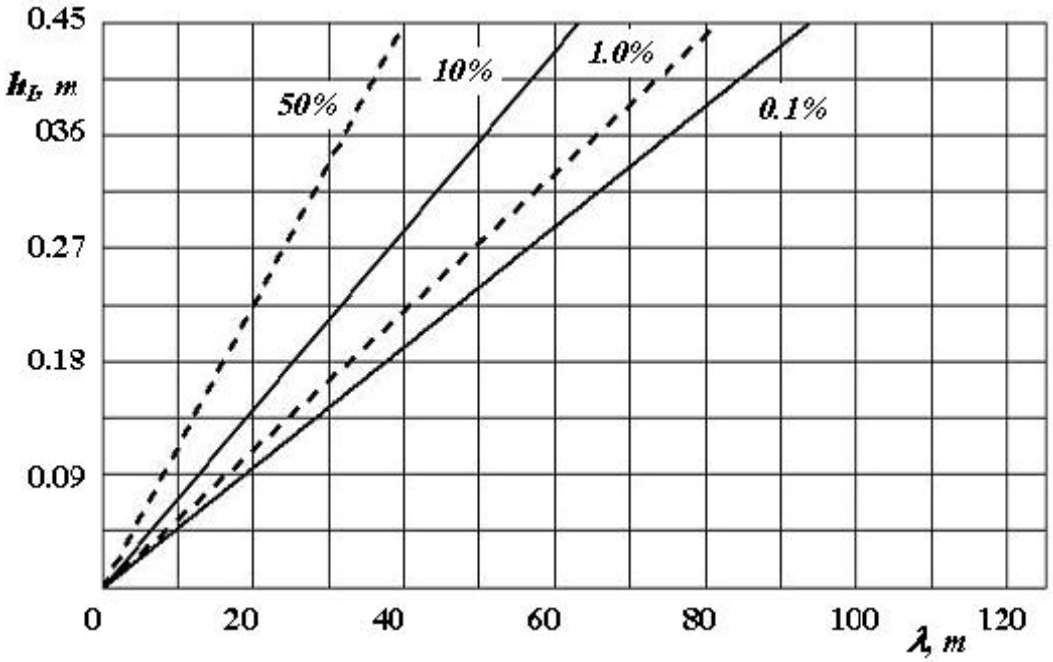

Figure 6. Correlation between the ice floe sizes (m = 10) and characteristics of wind-induced sea heaving when waves are capable to "capture" and transfer ice floes in the Bohai Sea.

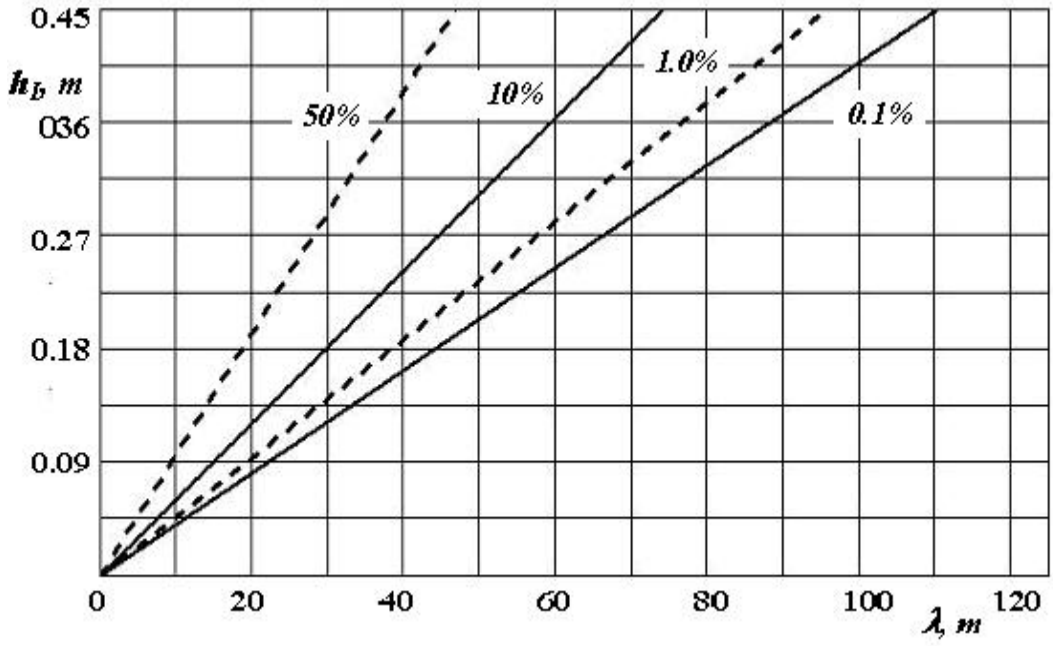

Figure 7. Correlation between the ice floe sizes (m = 25) and characteristics of wind-induced sea heaving when waves are capable to "capture" and transfer ice floes in the Bohai Sea.

5. Conclusion

Carried out studies and assessment show that occurrence of the "ice storm" in the Bohai Sea is real enough natural phenomena. This circumstance should be taken into account at designing the coastal and shelf constructions located in a southern and southwestern parts of the sea on the ways of extreme winds during the winter season. Consequently, for each water area the "dangerous" size of ice floes can be assessed using the described method according to the data of observations for winds and sea heaving in the desired area.

More accurate development of given problem allows to determine more precisely the conditions of "capture" of ice floes by the wind waves. However, taking into account the stochastic character of wind-induced waves, the uncertainty of a result will be kept. Therefore the found solution provides the assessment of conditions of an "ice storm" occurrence and feature sizes of "captured" ice floes with adequate enough for practical tasks.

Acknowledgements

Research was supported by the Russian Foundation for Basic Researches Grant No 06-05-39017 and the National Natural Science Foundation of China Grant No 50439010.

References

Davidan I.N., Lopatukhin L.I., Rozhkov V.A., 1974. Wind and waves in oceans and seas (Handbook). (Давидан И.Н., Лопатухин Л.И., Рожков В.А., Ветер и волны в океанах и морях. Справочник. Л.: Транспорт. 1974. 164 стр.)

Davidan I.N., Lopatukhin L.I., Rozhkov V.A., 1985. Wind induced waves in the world ocean. (Давидан И.Н., Лопатухин Л.И., Рожков В.А., Ветровое волнение в мировом океане. Л.: Гидрометеоиздат. 1985. 256 стр.).

Korotkin A.I., 1973. Mechanism of dolphin moving on the wind and ship waves. (Короткин А.И., О механизме движения дельфинов на корабельных и ветровых волнах. Бионика. No 7. Киев: Наукова Думка». 1973. Стр. 27 – 31).

Lappo D.D., Strekalov C.C., Zavialov V.K., 1990. Loads and effects of wind waves on waterside structures. (Лаппо Д.Д., Стрекалов С.С., Завьялов В.К., Нагрузки и воздействия ветровых волн на гидротехнические сооружения. Л.: ВНИИГ им. Б.Е. Веденеева. 1990. 432 стр.).

Li Z., Zhang L., Li G., 2007. Physical simulation of sea ice effects on coastal and offshore structures. Morskoy Vestnik. No 1(27). 2007. Pp. 81 – 86.

Marchenko A.V., 2002. Ice floes movement under action of gravity waves. Digest: Surface and Inner Waves in Arctic Seas. (Марченко А.В., Движение льдин и ледяных образований под влиянием гравитационных волн. Сборник: Поверхностные и внутренние волны в арктических морях. Ред. Лавренов И.В., Морозова Е.Г. СПб.: Гидрометеоиздат. 2002. 364 стр).

Yakunin L.P., Kardai A.V., Lukjanova N.B., 2005. Distribution of Ice in the Yellow Sea. International Offshore and Polar Engineering Conference, Seoul, Korea.

19th IAHR International Symposium on Ice
"Using New Technology to Understand Water-Ice Interaction"
Vancouver, British Columbia, Canada, July 6 to 11, 2008

The Current State Analysis of the Problem of Probabilistic Ice Interaction with the Seabed and Underwater Pipelines

Alexander T. Bekker, Olga A. Sabodash, Vladimir I. Seliverstov
Far-Eastern National Technical University
10, Pushkinskaya St., Vladivostok, 690950, Russia
abekker@mail.ru, isope@vladivostok.ru, vladsel@mail.ru

Abstract

The analysis of the offshore environment of the freezing seas showed that in these areas the underwater pipelines and the others buried structures could be damaged with high probability by the drifting ice formations of various origins which directly contacted the bottom in the offshore zone.

In this paper the authors analyzed the problems of probabilistic description of ice impacts on the sea bottom and underwater pipelines. The results may be used in order to estimate the normative burial depth of the underwater pipelines in the Arctic seas.

1. General

As known, hazards of the environment have a prime value in designing of underwater pipelines. At designing of the underwater pipeline route in arctic regions the extraordinary combination of natural factors (sea depths up to 60 m; giant ice fields and hummocks; complicated bottom topography; seismic activities, irregular currents and high probability of storm weather) should be considered. At designing and construction of underwater pipelines and other communications in arctic water areas, certainly, the ice cover impact is the main danger natural factor.

Therefore, the basic problem in designing a route of the underwater pipeline under ice conditions is the valid estimate of its burial depth into the soil of the seabed.

Regarding to long-term experience of field surveys of a hydrological mode of freezing water areas it is possible to note that the ice cover of the sea has spatial heterogeneity, permanently moves under influence of currents and wind, and it is also exposed to seasonally-time variability. The bottom relief of the water area also can be reformed at random under influence of currents, heavy sea, inflows, and other factors.

Thus, from the aspect of probability theory the underwater pipeline is assumed to be installed in the environment with stochastic parameters and during operation test loadings and impacts generally in the form of space-time functions. In some cases, as, for example, at the analysis when the pipeline interacts with the sea-bottom, due to poor information about true conditions of operation, loads and soil properties, the information on them will be initially of statistical nature. The specified circumstances cause increase of relative density of probabilistic models at designing of pipelines.

Thus, considering random nature of a process of the ice features penetrate the soil, the problem of designing of the underwater pipeline route has probabilistic aspects. For complex industrial systems it is the most convenient to use the mathematical theory of reliability with application of methods of numerical and statistical simulation to set such problems.

Designing a line of the underwater pipeline in water areas with complex ice conditions it is necessary to distinguish the following problems to be set using the probabilistic approach:

- Determination of optimum value of pipeline installation depth;
- Development of optimum criteria and techniques to determine an optimum variant of the pipeline layout;
- Substantiation of the reliability target level of the pipeline;
- Probabilistic estimations of hummocks parameters and scour parameters;
- Probabilistic simulation of physical process of hummock penetration into the soil;
- Probabilistic models of soil deformation under scours;
- Probabilistic simulation of actual bottom topography of the water area and soils.

Therefore, in this paper the some simulation models of the buried objects behavior under the sea ice impact were analyzed; recommendations on the further application of results in practice of designing of the offshore buried engineering structures in arctic regions were given.

2. Probabilistic models

Owing to lack of the information on the ice conditions of operation, loads and properties of the ground, the information on them will initially be statistical. In the last years the specified circumstances caused increase of specific role of probabilistic models in calculation of the pipelines maintained in ice conditions.

The task of probabilistic simulation modeling of hummocks penetration into the seabed ground was successfully solved by a number of researchers (Beletskiy et al, 1997; Bekker et al, 2005; C-CORE, 2000; Jiao et al, 1991; Kioka et al, 2004; Surkov et al, 1992; Yoon et al, 1997, etc).

The reports (C-CORE, 2000; C-CORE, 2002) recommended to apply probabilistic methods of modeling on the basis of the theory of risk when defining the optimum depth of the pipeline burial. At such approach, the depth of hummock penetration into ground and frequency of the pipeline crossing by gouges along its route should be defined on the comprehensive model of the seabed scouring by hummocks where the following random factors should be taken into account:

(1) Ice conditions, drift speeds and driving forces of the pack-ice;
(2) Geometrical parameters of the hummock keel and strength of the ice features;
(3) Strength of the ground and its physic-mechanical properties;
(4) Bathymetry along the pipeline route.

The general probabilistic approach to estimation of the pipeline burial is shown on Fig. 1. Statistical data on frequency of the pipeline crossing with scours is used to estimate annual excess probability of various scour parameters (such as depth, width, etc.) per unit of the pipeline length. On the basis of these parameters probabilistic models of soil deformation under the scours and models of deflected mode of the pipeline are developed, hence the optimum burial depth of pipeline can be estimated.

Kioka et al (2004) offered probabilistic sceneries for estimation of optimum gouge depth with various input parameters. These authors had been developed a combined method of numerical simulation of penetration depths of drifting hummocks into the soil uniting a Neural-Network model with a mechanical one, considered in earlier works (Kioka et al., 1995). Figure 2 shows the general algorithm of probabilistic simulation of the penetration depths.

The advanced geometrical model of a first-year hummock for the Sea of Okhotsk has been used as a model of a hummock in process (Kioka et al., 2004; Beketsky et al., 1997). Both frequency distributions of scour depths, and dependences between keel depths and scour length left by them at the bottom have been resulted. One hundred thousands of casual variables of hummock keels with a depth range of 15-20 m were simulated during numerical experiments, thus the bottom slope was assumed equal to 1/500. As a result of simulation it has been found that scour depths distribution meets the exponential negative distribution function; and for comparison the authors have been described natural data across the Beaufort Sea (Kioka et al., 2004).

According to (Kioka et al., 2004), the maximal values of scour depth for the given area of the Sea of Okhotsk were 2-2.5 m. The offered model is under further upgrade, especially regarding

development of techniques and various scripts to define optimum parameters of the burial depth of underwater pipeline.

Croasdale et al (2003) has been developed a probabilistic model of ice scours formed at the bottom which was based on a two-dimensional numerical model of hummock-soil interaction, developed by (Been et al., 1990). The purpose of the probabilistic analysis was to research scour depth distribution for designed cases of stopping of a first-year hummocky ridge or local failure of a hummock keel at its penetration into the soil. In model used the statistical analysis data on first-year hummock parameters, resulted from four extensive field programs that had been carried out in Canada and at the Sakhalin offshore in 1997-1998 (Been et al., 1990).

Probabilistic simulation was carried out by methods of Monte-Carlo; thus the distributions used for four random variables (the keel angle, soil friction angle, the cohesion of hummocky ice keel and the dependence between the berm height and scour depth), being normal or close to it. As a result of simulation it was received that the scour depth had been log-normally distributed.

The work showed that the primary factors influencing the final scour depth are keel durability, soil durability, a slope of an angle attack of keel slope (Croasdale et al., 2003). The maximal depths of ice scours at the bottom are equal to 2.04 m (Table 1), and this is perfectly agreed with data of other researchers (Polomoshnov et al., 1999).

Simulation modeling of the process of a hummock penetration into soil, including actual ice/ground conditions, as well as underwater topography of water areas where the deposits were developed offshore Sakhalin, such as Piltun-Astokhskoe, Chaivo, Arkutun-Dagi and Lunskoe, were shown in the studies by (Polomoshnov et al, 1999; Surkov, 2000). Table 1 summary describes the basic characteristics of the recommended the pipeline burial depth on Sakhalin offshore.

Table 1. Recommended values of burial depth of underwater pipelines for Sakhalin at the sea depth H>5 m.

No.	Source	Deposit	Maximal depth, m
1	C-CORE, 2002	Lunsky	2.6-2.8
2	Bekker et al., 2006	Piltun-Astokhskoe	2.37
3	Surkov et al., 2000	Piltun-Astokhskoe	3.78
4	Polomoshnov et al., 1999	Chaivo, Arkutur-Dagi	2.5
5	Croasdale et al, 2003	-	2.04

* without considering litho-dynamic processes.

The analysis of distribution of the hummocks penetration depths into soil (scour depths) showed that they were described by an exponential dependence that was well coordinated to the data on gouges received from the Beaufort Sea. The offered technique has been used in several specific problems to choose an optimum track of the underwater pipeline for Sakhalin offshore.

Bekker et al (Bekker et al, 2005; Bekker et al, 2006) developed a simulation model of interaction between the drifting hummocks and a seabed and determined probabilistic characteristics of the pipeline route parameters. Probabilistic simulation model included the following:

- Statistical simulation of casual parameters of hummocks according to their functions of probability distribution determined by Monte-Carlo method;
- Simulation of a bottom contour of the water area on the basis of GIS technologies.

Initial data for simulation have been accepted by results of natural surveys of hummock parameters in the water areas of the Chaivo, Piltun-Astokhskoe, and Arkutun-Dagi deposits on Sakhalin offshore. Calculation of probabilistic characteristics of hummock penetration depth, using the offered simulation model of interaction (Figure 3), is based on simulation of parameters of five random variables: the height of a hummock sail, the width of the bottom keel, keel depth, angle of slope of keel sides, hummock drift velocity towards penetration. According to calculations, the maximal burial depth of the pipeline is made 2.37 m (Table 1).

Conclusions

Main scientific and practical results of investigations carried out in this study are as follows positions.

1. The research analysis on problem of probabilistic modelling of hummock impact on seabed and underwater pipelines was given that for last ten years the well-defined progressive expertise in this area has accumulated. Usage probabilistic and a simulation methods of modeling processes of interaction in the system “ice-bottom” in most cases allows to receive design parameters of pipeline route, which one can be used for engineering practice.

2. However even the superficial knowledge analysis of studies shows, that now the problem of probabilistic estimation of ice impact on the offshore underwater communications required the further investigations for development of the valid recommendations for engineering practice. Though already now many recommendations are taking account to design and construction of pipelines in Arctic seas, especially, in realization of Sakhalin offshore projects.

3. The analysis of researches is shown, that at present time there is a significant scatter in an estimation of the burial depth of underwater pipelines on different simulation models. The major problem is availability of reliable input statistical data about specific environment conditions, as a rule, of remote water areas.

References

Been, K., Palmer, A., Comfort, G., 1990. Analysis of Subscour Stresses and Probability of Ice Scour-Induced Damage for Buried Submarine Pipelines. Deterministic Models of Ice-Soil-Pipe Interaction, Canada Oil and Gas Lands Administration File 0825-25-6-4, Vol II.

Bekker, A.T., Sabodash, O.A., Truskov, P.A., 2005. Problems of Probabilistic Simulation of an Underwater Pipeline Track under Impact of Drifting Hummocks Offshore Sakhalin Island. Proc. 15th Int. Offshore and Polar Eng. Conf., ISOPE, Seoul, Korea. 62-68.

Bekker, A.T., Sabodash, O.A., 2006. The Probabilistic Approach to Modelling of an Optimal Underwater Pipeline Rout under Impact of Hummocks. Proc 18th IAHR Symposium on Ice, Sapporo, Japan. 325-334.

C-CORE, 2000. An Engineering Assessment of Double Wall versus Single Wall Designs for Offshore Pipelines in an Arctic Environment. Rep 00-C4-Final, Cold Engineering, Tri Ocean Engineering and AGRA Earth& Environmental.

C-CORE, 2002. Ice Hazard&Integrity Analysis for Sakhalin II Project Offshore Pipelines: Probabilistic Assessment&Recommended Burial Depths. 15Jan02 Interim Report, C-CORE Report R-01-19-631-15Jan02.

Croasdale, K.R.&Associates Ltd, BMT Fleet Technology Ltd, 2003. Investigation of the Ice Limits to Gouging. Final Report 4975C.FR / Preliminary phase.

Jiao, G., Bruschi, R., 1991. Methods for Probabilistic Assessment of Environmental Hazards to Submarine Pipelines. Proc. 1st Int. Offshore and Polar Eng. Conf., ISOPE, Edinburgh. Vol. 2. 361-371.

Kioka, S., Saeki, H., 1995. Mechanisms of Ice Gouging. Proc. 5th Int. Offshore and Polar Eng. Conf, ISOPE, Hague, Vol. 2. 398-402.

Kioka, S., Kubouchi, A., Ishikawa, R., Saeki, H., 2004. Application of the Mechanical Model for Ice Scour to a Field Site and Simulation Method of Scour Depths. Proc. 14th Int. Offshore and Polar Eng. Conf., ISOPE, Toulon, France. 891-898.

Polomoshnov, A.M., Astafiev V.N., Surkov G.A., 1999. Method for Selecting Subsea Pipeline Route under Ice Conditions (for Sakhalin Offshore). Proc. 14th Int. Symp. Okhotsk Sea&Sea Ice, Mombetsu, Japan. 130–136.

Surkov, G.A., 2000. Choosing Optimum Underwater Pipeline Burial Profile on Northeast Sakhalin Shelf. Proc. 2nd Ice Scour&Arctic Marine Pipelines Workshop, 15th Int. Symp. on Okhotsk Sea&Sea Ice, Mombetsu, Japan. 207-217.

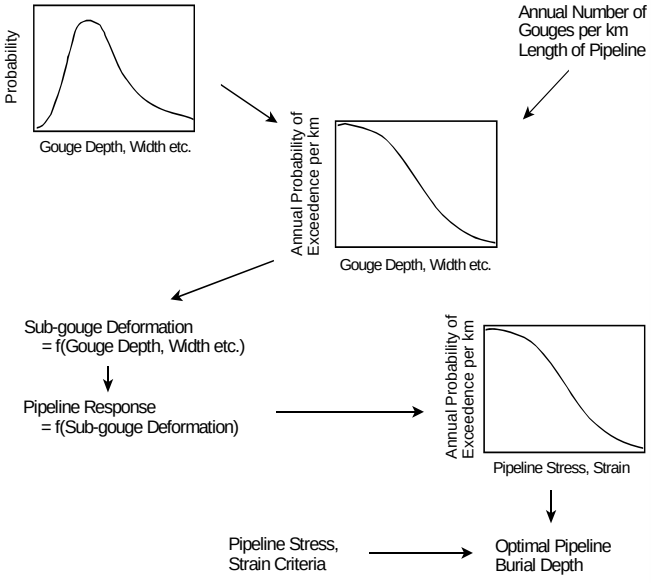

Figure 1. Probabilistic factors affecting estimation of the optimal pipeline burial depth (C-CORE, 2002).

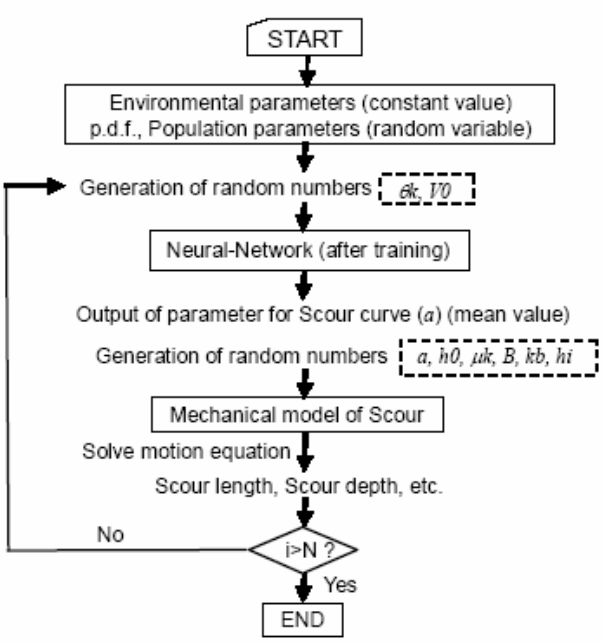

Figure 2. The general block diagram of numerical simulation of scour depth (Kioka et al., 2004).

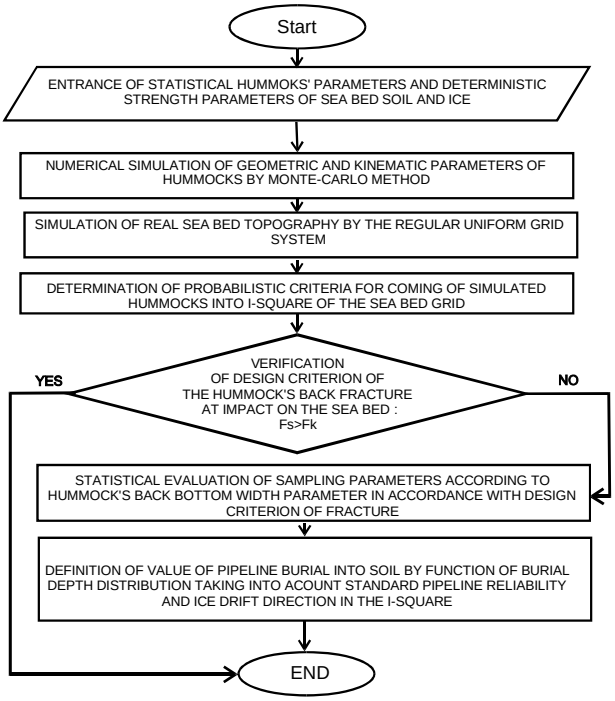

Figure 3. Flow-chart of simulation model of "hummock-sea bed" interaction and the underwater pipeline burial depth calculation (Bekker et al., 2005; Bekker et al., 2006).

19th IAHR International Symposium on Ice
"Using New Technology to Understand Water-Ice Interaction"
Vancouver, British Columbia, Canada, July 6 to 11, 2008

Ice Failure on Conical Structures – Effect of Speed

Thomas G. Brown
University of Calgary
Calgary, Alberta, Canada, T2N 1N4
ice@ucalgary.ca

Abstract:

The effect of speed on the forces resulting from the failure of ice features against conical structures is not well understood, and the information available to facilitate this understanding is both scarce and contradictory. The paper reviews the available information, derived from controlled laboratory experiments, full-scale observations and available theoretical approaches, in an attempt to provide some understanding that addresses the conflicting information. The paper then presents some findings obtained from the Confederation Bridge Ice Monitoring programme in an attempt to provide some full-scale measurements and observations relating measured forces against the interaction speed.

Introduction

Conical structures have proven to be effective in reducing the forces associated with interactions with ice features of all types. The flexural failure of the ice sheet, or the consolidated layer of a first-year ridge, results in significantly less load than the corresponding crushing failure, and the detrimental effects of ride-up or pile-up, which do add to the interaction load, are not sufficient to offset the initial reduction in load. Much has been learnt about the failure of ice against conical structures through full-scale and model-scale research programmes, and observations from permanent structures (Figure 1). These observations (Brown and Maattanen, 2008) have

Figure 1. Typical ice Pile-Up on Confederation Bridge Pier

provided considerable insight into the behaviour of the ride-up or rubble-pile, the failure of the ice sheet, and the loads associated with the interaction. One element that has eluded firm quantification is the effect of the speed of the interacting ice on the resulting load. Mayne and Brown (2000) were able to establish a relation between speed and the height of the associated rubble pile (Figure 2), but a relationship between the interaction force and speed has been more elusive.

First-year ice regimes vary significantly between locations around the northern hemisphere. As a consequence, experience gained in one location may not be applicable in another. As an example of this, flexural-failure induced vibrations, that are damaging, have been experienced in Bohai Bay in China, where the ice is level, uniform, and often snow-free. In Northumberland Strait, first-year ice is seldom level, invariably is snow covered, and frequently consists of ridges and rubble fields. The potential for similar ice-induced vibrations of the Confederation Bridge piers has been investigated, and no such effects have yet been encountered (Azarnejad et al, 1999). In the current analysis, the effect of speed is considered in the context of the total load on the structure, regardless of the nature of the ice feature causing the load.

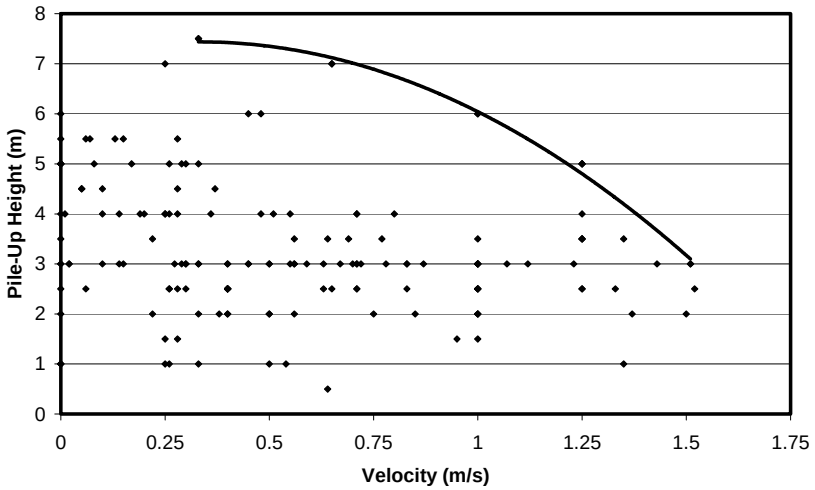

Figure 2. Relationship between height of rubble pile and velocity

Theoretical models have been developed that have included the speed of the interaction in their formulation. Brooks (1981) developed a model, based on the flexural failure of ice in ship interactions, that included the interacting speed as a variable. Lau et al (2000) have reported on observations in ice tank experiments in which they were able to establish an effect of speed, and Lau (1999) incorporated speed as an interaction variable in his model for flexural failure of ice against a fixed conical structure. However, the better-known models for the flexural failure of ice (Croasdale et al, 1994, Nevel, 1992, and Ralston, 1977) do not explicitly include speed of interaction in their formulation. Matskevitch (2002) has analyzed the results of model test data for the effect of speed on loads on conical structures. He concludes that, for a mid-size conical structure, there are no velocity effects for speeds up to 0.5 m/s, and that, for higher speeds, the effect is modeled by the following equation:

$$F / F_{Ralston} = 1 + 0.5(v - 0.5) \qquad \textbf{[1]}$$

The German code (Germanischer Lloyd, 2003), on the basis of JOIA model-scale data (Ishikawa et al. 1999) provides a variation of the Ralston model that explicitly includes the interaction speed. This model includes the effect of speed by adding the term:

$$C_V F_n \sigma_f t^2 \qquad \textbf{[2]}$$

Where C_V is a velocity factor (set at 10.0), and F_n is the Froude number. The code adds other factors to the original Ralston method, but for most conditions, these are equal to unity, except for a reduction factor that is applied to the ride-up term. Figure 3 illustrates the effect of these two approaches for the velocity term on the total load for failure of a typical 0.7 m thick ice sheet against the Confederation Bridge piers. From this, it can be seen that the load almost doubles as the speed increases for zero to 1.5 m/s, suggesting that speed has a significant effect on the resulting force.

During the design process for the piers of Confederation Bridge, ice speed was considered as a design parameter, but only in terms of the inertial effect on the keel of a first-year ridge, as the ridge impacts with the pier. The ice in Northumberland Strait is driven by a combination of tide and wind. Semi-diurnal tides are strong at the bridge site so that they dominate ice movement against the bridge piers. The prevailing winter winds in the southern Gulf of St Lawrence are from the North-West, and therefore tend to drive ice past the bridge axis (which runs South-West/North-East). As a result of the significant ice movements, each pier "sees" several thousands of kilometers of ice every year at speeds to in excess of 1.5 m/s. This speed was a significant factor in the determination of the design ice loads on the piers. Because of the dominance of the tides, ice movements take place in two directions normal to the bridge axis, and thus loads are identified as positive or negative, depending on that direction.

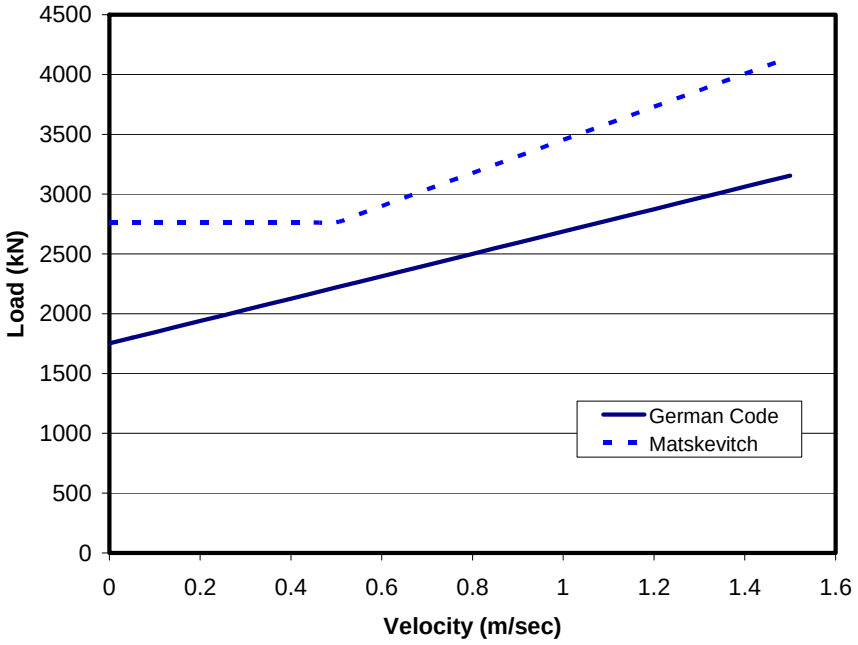

Figure 3. Relation between load and speed

Since opening in 1997, Confederation Bridge has been the subject of a major performance monitoring project that has included the continuous measurement of ice forces on two piers throughout each of the 11 winters (Brown, 1997). The ice monitoring programme has had a number of objectives over the years, including:

- The indirect measurement of ice forces by the measurement of the structural response,
- The measurement of ice pressures on one of the ice breaking cones and the supporting cylindrical pier shaft,
- The observation of ice behaviour with the piers using a CCTV system that is continuously recorded during each winter,
- The measurement of the ice depth by sonar, and, for two winters, measurement of the ice speed by an Acoustic Doppler Current Profiler, and

- The measurement of the atmospheric conditions, including wind speed and direction, atmospheric pressure, and temperature.

This system then provides a great deal of information regarding the interacting ice cover, the prevailing atmospheric conditions, the ice behaviour as it interacts with the piers, and the loads and pressures associated with these interactions. This information can then be used to examine the relationship between aspects of the interacting ice cover and the resulting forces and pressures. Some of these relationships have been investigated in some detail in related work (Lemee, 2003, Mayne, 2007, Tiwari, 2006).

The speed of the interacting ice can be determined in two ways: by direct measurement of the speed using the ADCP data that is available for two winters of the monitoring programme, and by analysis of the CCTV recording of the interacting ice, which is available for all winters, during daylight hours. Analysis of the CCTV data is surprisingly accurate and simple, and has been verified against the ADCP data.

Two sonars, one located on each side of pier P31, were used to measure the depth of the interacting ice. The sonars were located 30 m from the face of the cylindrical pier base, and the signals were transmitted by cable from the sonar to the data acquisition system within the pier. Because of the location of the sonars, the sonar record associated with a particular peak load had to account for the time for the ice to move from the sonar location to the pier face. Sonar data was acquired at a frequency of 2 Hz.

Force is measured indirectly by measuring structure response, in the form of tilts and accelerations. Tilt is measured by very accurate tiltmeters with a resolution of 0.1 μRad, which corresponds to approximately 3 kN of applied force, well below the desired resolution. The relationship between tilt and applied load was established by conducting a full-scale load test on one of the instrumented piers in April, 1997, immediately prior to the bridge opening. The results of this test were subsequently verified using finite element modeling which was also used to determine the corresponding transfer function for the second pier. For the primary instrumented pier, P31, the load test resulted in a relationship between tilt and load of 29 μRad/MN.

Loads are initially identified using data that is averaged over a 17-second interval (Brown, 2007). The tilt data is corrected for the effects of wind and then scanned for peaks that satisfy the criteria to be identified as an “event”. The definition of an event is based on there being a well-defined peak with a minimum load, after correction for wind, of 0.75 MN. Subsequent detailed analysis of an event can then be undertaken using triggered tilt data that is acquired at a rate of 30 Hz. This analysis is considerably more complex, as it requires correction of the tilt data for the attenuation of the tiltmeters, and the removal of the structural frequencies that are present in the measured data (Brown, 2007).

For the purposes of assessing the relationship between load and interaction variables, the average data provides sufficient accuracy and is the basis for the relationships presented in this paper.

Effect of Velocity

Good velocity data was available for three years from 1998 to 2000, inclusive, and data from those years forms the basis for the analysis presented here, Table 1.

Table 1. Data Summary

Year	No. of Events	Maximum Load (MN)	Maximum Ice thick. (m)	Maximum velocity (m/sec)	Maximum Keel Depth (m)
1998	2890	4.25	3.0	1.37	9.5
1999	1635	4.80		1.52	13.8
2000	1261	3.90		1.61	15.0

Although a larger number of events is reported for 1998, the load threshold for an event in 1998 was lower than that used to define an event in the following two years, resulting in more events being identified. Ice thicknesses, as opposed to keel depths, are obtained from image analysis of the video imagery obtained for the particular event. As the video cameras were visible light cameras, this data is only available during daylight hours, and only for a limited number of events, for which image analysis was completed.

Figure 4 summarizes the loads measured for the three years under consideration. This histogram provides not unexpected results, with a significant majority of the measured loads being under 2.0 MN.

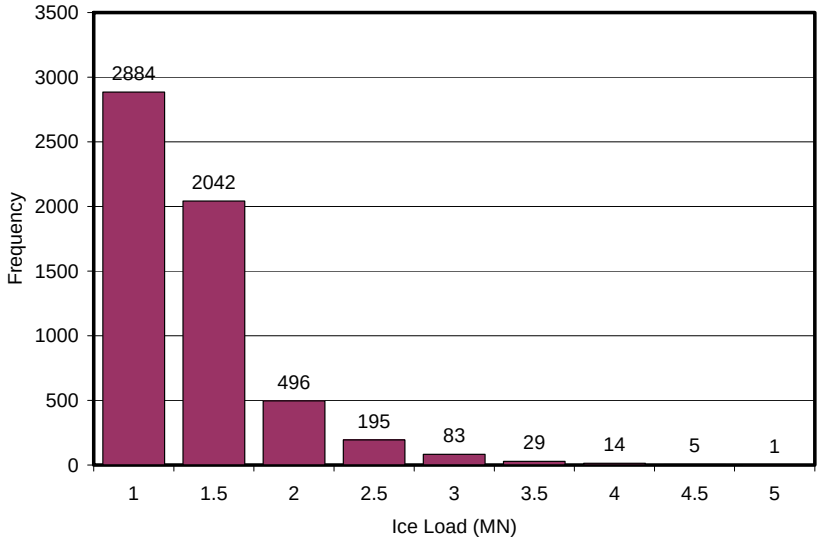

Figure 4. Histogram of all measured loads (1998-2000)

Figure 5 illustrates the relation between the measured load and the speed of the interacting ice for two of the three years, 1999 and 2000. Unfortunately, there is much variability embedded in this plot, as it represents all data for which the speed was measured, encompassing keel depths that

range from zero (level ice) to 15.0 m, and ice thicknesses, including consolidated layer thicknesses, that range from 0.3 m to 3.0 m. This means that the data includes both first-year ridge, and level ice, interactions. Events with zero velocity, representing events limited by limited driving forces have been excluded. The data presented in this figure does not suggest any relationship between the measured load and speed confirmed by any form of regression analysis.

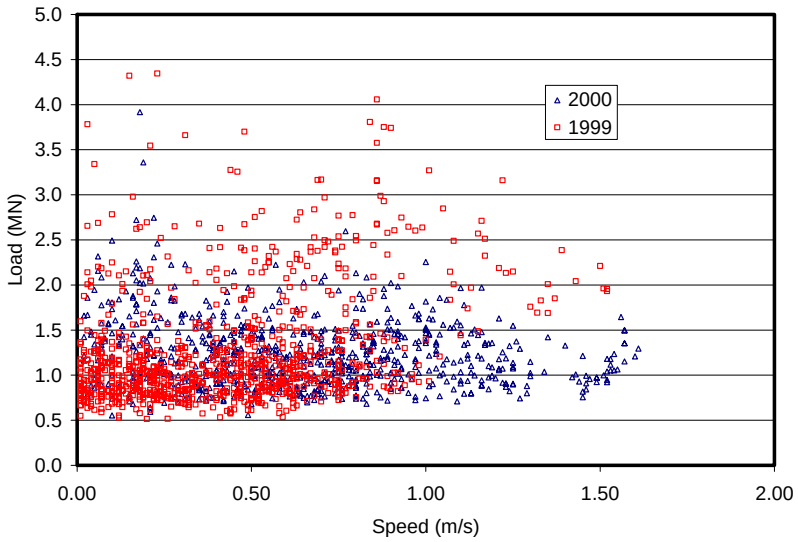

Figure 5. Plot of load against speed for 1999 and 2000

In order to reduce the number of implied variables in Figure 5, Figure 6 presents the corresponding data, limited to those data for which the sonar recording is less than 2 m. There is a weak trend in the data for the 1999 data, but no trend for the 2000 data. The line shown on this figure is a linear fit to the 1999 data for speeds greater than 0.5 m/s. This line shows a weak relation between load and speed. Figure 7 shows the relation between load and speed for all keel depths greater than 6 m., for the 1999 data. Again, there is a weak relationship between load and interacting speed.

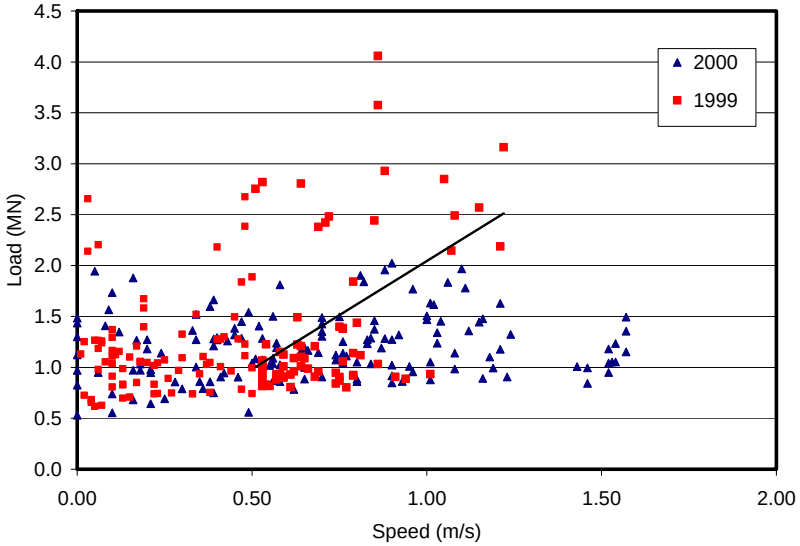

Figure 6. Load against speed for sonar measurements less than 2.0 m

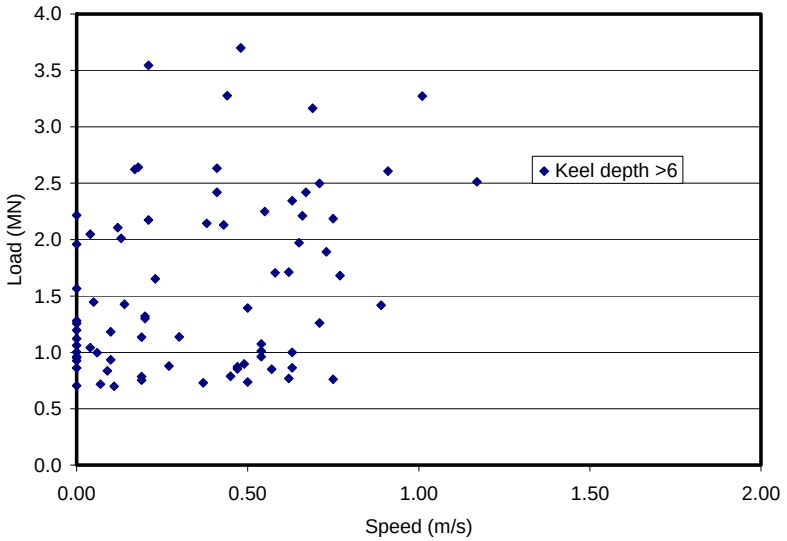

Figure 7. Load against velocity for sonar measurements from 6 to 14m.

Loads resulting from flexural failure of ice depend on the ice thickness in a number of ways (Croasdale et al, 1994, Ralston, 1977). The theoretical flexural failure term depends on the thickness squared, ride up and rubble terms tend to be related to the thickness. This suggests that the thickness effect can be removed by factoring the load by some function of the thickness. Because the rubble piles play such a significant role in the load on the piers of Confederation Bridge, the load has been factored using a linear function of the thickness. The results for the 1998 data, for which the largest number of thickness observations are available, are shown in Figure 8. The corresponding linear regression line is also shown. Again, the correlation is weak, but it is the strongest correlation of any of the relations shown in the figures in this paper.

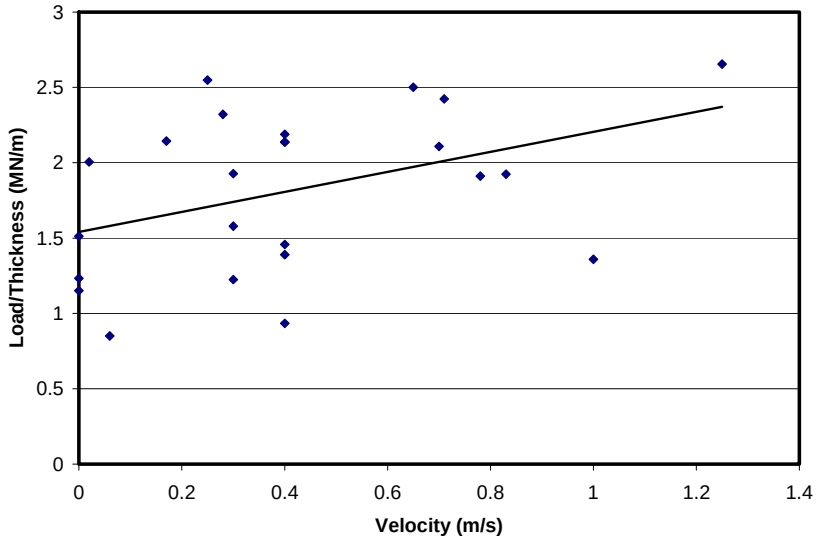

Figure 8. Relation between load/ice thickness and speed

Summary

Most of the most commonly used algorithms for the determination of ice loads on conical structures do not explicitly include the interaction speed as a factor. Nevertheless, speed is recognized as important in the assessment of dynamic effects and the potential for ice-induced vibrations. Accordingly, there is some thought that flexural failure loads should include some factor for ice speed, in addition to the requirement to consider ice-induced vibrations.

Analysis of very large datasets derived from the Confederation Bridge ice monitoring programme suggest that the effect of ice speed on the failure of ice features against a conical structure is very weak, and in many instances, is negligible. Even when much of the variability is removed from the data, the relation between the load and speed is weak.

One may conclude that the effect of speed on the ice load on a conical structure in an ice regime such as experienced in Northumberland Strait, is not significant. Any formal requirement to include speed as a factor in flexural failure of ice must consider the local ice regime, and the nature of the interactions between ice feature and structure.

Previous work has concluded that, as the speed increases, the maximum rubble pile height is reduced as a result of improved clearing of the rubble. As the rubble pile contributes significantly to the load, this reduction may be offsetting any increase in load due to speed. Clearly this is something that needs to be examined in more detail.

Acknowledgement

The author would like to acknowledge the contributions of his students, past and present. He would also like to acknowledge the ongoing support of Strait Crossing Development Inc, Public Works and Government Services Canada, the Program for Energy Research and Development and the Natural Sciences and Engineering Research Council.

References

Azarnejad, A., Mayne, D.C., and Brown, T.G., 1999. Ice dynamics and conical structures. Proceedings of the 18th International conference on Offshore Mechanics and Arctic Engineering, St. Johns, Newfoundland, Paper 1167, 8 pages, CD-Rom.

Brooks, L.D., 1981. Ice resistance equations for fixed conical offshore structures. Proc. POAC 1981, Quebec City, Canada ,Vol I, pp91–99.

Brown, T.G., 1997, "The Confederation Bridge – Early Results from Ice Monitoring Program" *Proceedings*, CSCE Annual Conference, Vol. 1, pp177-186, Sherbrooke, Canada.

Brown, T.G., 2007. Analysis of Ice Event Loads Derived from Structural Response. Journal of Cold Regions Science and Technology, 47, pp224-232.

Brown, T.G. and Maattanen, M., 2008, "Comparison Of Kemi-I And Confederation Bridge Cone Ice Load Measurement Results", Accepted, Journal of Cold Regions Science and Technology, February.

Croasdale, K.R., Cammaert, A.B., and Metge, M., 1994. A Method for the Calculation of Sheet Ice Loads on Sloping Structures. IAHR Ice Symposium, Trondheim, Norway, p874-885.

Germanischer Lloyd, 2003, Guideline for the construction of fixed offshore installations in ice infested waters. GLO-03-319.

Ishikawa, S., Kawasake, T., Yano, S., Kato, K. and Kamesaki, K., 1999. Empirical Formula for Estimation Ice Load on Conical Structures. Proc. International Workshop REIFS '99, February, Mombetsu, Japan, Paper W-18.

Lau, M., 1999. Ice Forces on a Faceted Cone due to the Passage of a Level Ice Field. Thesis submitted in Partial Fulfillment of the Requirements for a PhD Degree, Memorial University of Newfoundland, Canada.

Lau, M., Jones, S.J., Phillips, R., and McKenna, R.F., 2000. Influence of Velocity on Ice-Cone Interaction. Proc. Of the Ice Symposium on Scaling Laws in Ice Mechanics and Ice Dynamics, IUTAM, Fairbanks, Alaska.

Lemee, E., 2003. Ridge Interaction with Bridge Piers, Thesis submitted in Partial Fulfillment of the Requirements for a MSc Degree, University of Calgary, Canada, 165 pages.

Matskevitch, D. G., 2002. Velocity Effects on Conical Structure Ice Loads. Proc. OMAE '02, 21st International Conference on offshore Mechanics and Arctic Engineering, Oslo, Norway, June, pp 635-643.

Mayne, D.C., 2007. Level Ice and Rubble Actions on Offshore Conical and Sloping Structures, Thesis submitted in Partial Fulfillment of the Requirements for a PhD Degree, University of Calgary, Canada, 215 pages.

Mayne, D.C. and Brown, T.G., 2000. Rubble pile observations. Proc. 10th International Offshore and Polar Engineering Conference, Vol. I, Seattle, USA 596–599.

Nevel, D., 1992. Ice forces on cone from floes. Proc. IAHR Symposium on Ice 1992, Vol. 3, Banff, Canada, 1391–1404.

Ralston, T., 1977. Ice force design considerations for conical offshore structures. Proc. POAC 1977, Vol. II, Memorial University of Newfoundland, St. John's, Newfoundland, Canada, 741–752.

Tiwari, D.N. (2005). Information Management in Monitoring of the Confederation Bridge for Ice Force Issues. Thesis submitted in Partial Fulfillment of the Requirements for a MSc Degree, University of Calgary, Calgary, Alberta,

19th IAHR International Symposium on Ice
"Using New Technology to Understand Water-Ice Interaction"
Vancouver, British Columbia, Canada, July 6 to 11, 2008

Analysis of Loads on the SDC at Paktoa C-60 during an Ice Creep Buckling Event

Denise Sudom and Garry Timco
Canadian Hydraulics Centre
National Research Council of Canada
Ottawa, Ont., K1A 0R6 Canada
denise.sudom@nrc.ca, garry.timco@nrc.ca

The Steel Drilling Caisson (SDC) was used by Devon Canada to drill an exploratory well at the Paktoa C-60 site in the Beaufort Sea during the winter of 2005-06. Three major storms were experienced at the site during the deployment; this paper focuses on the final storm event which occurred February 22 to 23, 2006. At that time, the ice surrounding the SDC was landfast and 1 m thick. The ice near the SDC buckled overnight, with total horizontal ice movement of approximately 1 to 1.15 m. In-place inclinometer data showed that late on February 22, a maximum deflection of 35.5 mm occurred in the soil 0.55 m below the foundation skirts of the SDC. This paper examines the available data and uses four different approaches to estimate the ice force on the SDC during this loading event. From this analysis, predicted results from the three most reliable approaches range from approximately 55 to 89 MN. Global pressures are in the range of 0.65 to 1.04 MN/m^2, over an effective structure width of 85 m. The geotechnical sensors provide an interesting approach for inferring the loads on the structure and their response predictions are in general agreement with analytical and empirical-based approaches. Suggestions are made on questions that should be addressed to make this approach more reliable for load predictions.

1. Introduction

During the winter of 2005-06, Devon Canada drilled an exploration well at the Paktoa C-60 site in the Beaufort Sea. The drilling platform consisted of a steel drilling caisson (SDC) mated to a submersible barge (MAT). The SDC is a converted, ice-reinforced supertanker which can be deployed in water depths of 7.6 – 24 m. Resistance to ice forces is provided by the large base area of the MAT combined with a 2-m deep gridded skirt system. The SDC deck is 60 m wide by 218 m long, and the structure is 60 m by 162 m at the waterline. The MAT base is 110 m by 162 m.

The SDC/MAT was ballasted to the seafloor at the Paktoa C-60 site (69° 39.18N, 136° 29.5W) in 13.5 m deep water with the bow oriented towards the northwest. The winter at the drilling site was relatively mild and produced a thinner ice cover than expected. No grounded rubble field formed around this structure at this site (Horizon Systems Group Inc., 2006). This is somewhat surprising since analysis of previous data on caisson structures in the Beaufort Sea indicate that grounded rubble fields often form in this depth of water (Barker and Timco, 2006). Once the ice was landfast, there were three major winter storm events at the Paktoa site. The focus of this paper is the third and final storm event which occurred on February 22 – 23, 2006. During this creep loading event, the 1 m thick ice near the SDC buckled overnight on February 22.

2. Available Data

Devon Canada utilized several types of data measurement programs at the site. Horizon Inc. were contracted to actively monitor the ice and meteorological conditions (including air temperature, and wind speed and direction) at this site during the drilling program. Video was captured by cameras located on the bow and starboard side of the SDC. Klohn-Crippen installed several types of geotechnical sensors (piezometers, manual inclinometers, and in-place inclinometers - IPI) underneath the structure. The Canadian Hydraulics Centre of the National Research Council of Canada approached Devon Canada for access to this data and they agreed to share it with the NRC-CHC.

No piezometer data are available for the February 22 – 23 event. The manual inclinometer readings were taken infrequently, and so are useful only to verify the total deflection of soils between December 10, 2005 and the end of operations on August 17, 2006. Therefore the IPI sensors are the main source of data for soil deflection for the event. The ice was landfast at the time of the event, so the video records are not useful for analysis. The ice conditions were generally recorded twice daily, and detailed descriptions of the February 22 – 23 event are available.

3. February 22-23, 2006 Event

On February 22, 2006, the ice at site was landfast and stable with the landfast ice edge at 15.9 km to the Northwest of Paktoa. The average ice thickness was recorded as 1.0 m.

Temperature dropped from approximately -9C on February 21 0:00 down to -22C by February 22 20:38. The mainly westerly winds reached sustained speeds of over 80 km/h, with much higher gusts. The ice buckled overnight on February 22 along the bow and port bow areas of the SDC, due to the heavy winds and possible ice fracture during the rapid temperature drop. The

total ice movement measured by laser survey was approximately 1 to 1.15 m toward the southeast. Figure 1 shows a sketch of the SDC/MAT with the ice loading direction and approximate location of the ice buckling. The depth of the trough of the buckled ice was measured in one location at 85 cm. (Horizon Systems Group Inc., 2006). On February 23, the trenches were augered and flooded as shown in the photograph in Figure 2.

IPI data are available at 1-minute frequency. The deflection of individual sensors and the total deflection at the location of Sensor 5 are shown in Figure 3. Sensor 5 was located at 0.55 m below the tips of the foundation skirt system. The greatest total vector displacement was 35.5 mm toward the southeast, and occurred on February 22, 2006 21:21. Readings from a calm period (February 14, 2006 00:00) are used to "zero" each of the sensors, and the measurements have been filtered to remove noise.

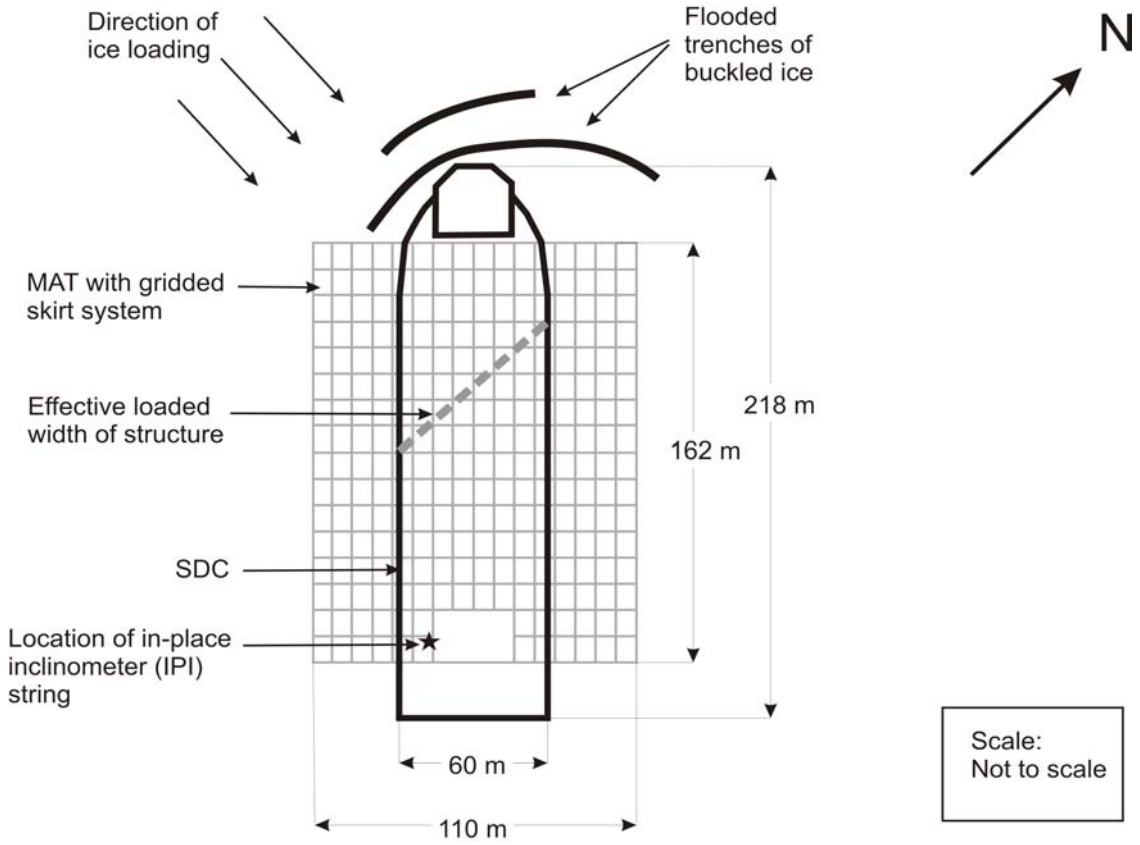

Figure 1. Sketch of ice buckling near the SDC, 23 Feb 2006. The Effective Width of the structure was 85 m, defined perpendicular to the direction of ice movement.

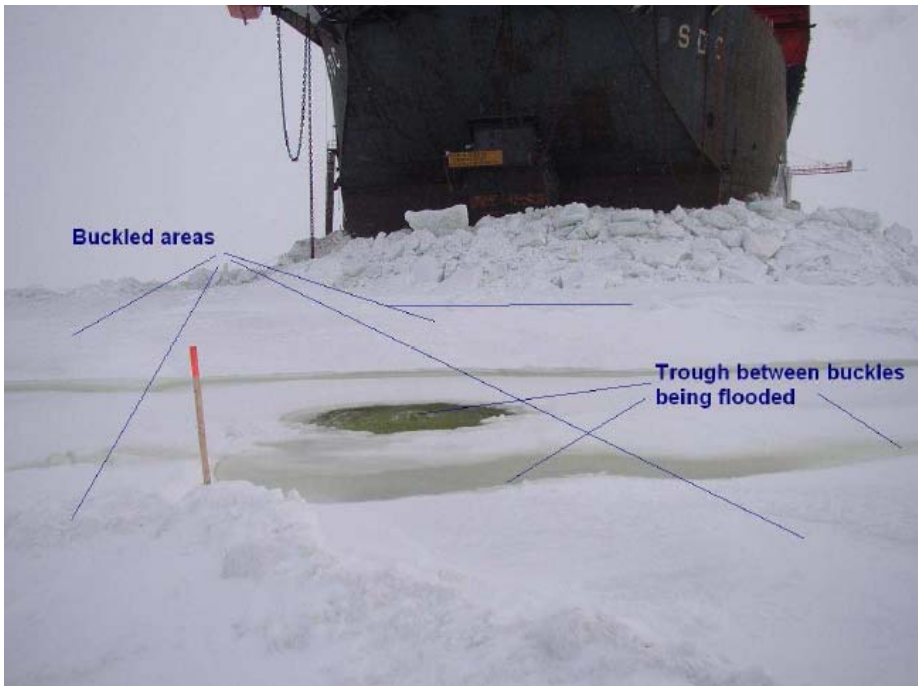

Figure 2. One augered location in buckled ice near the SDC, 23 Feb 2006 (Horizon Systems Group Inc., 2006)

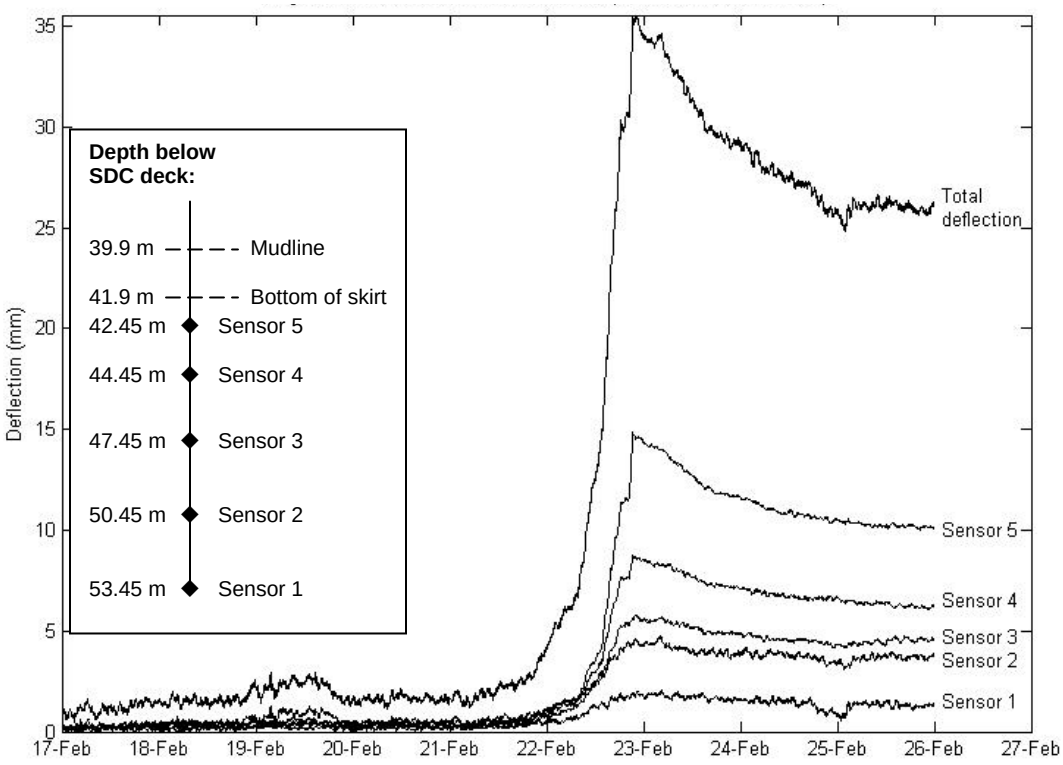

Figure 3. Resultant deflection for individual IPI sensors and total deflection of sensors

4. Load calculations

The information and data on this buckling loading event are quite unique. Although there have been many analyzed ice loading events on caisson structures in the Beaufort Sea (Johnston and Timco, 2003; Timco and Johnston, 2003, 2004; Frederking and Sudom, 2006), the majority of these events did not involve buckling behaviour. The data set for the SDC at Paktoa provides an opportunity to analyze an ice buckling event using several approaches. There were no large load measuring panels used at this site so an absolute reference of ice load is not possible. However it is informative to look at different approaches and see the level of agreement between them. The following section outlines four different approaches for estimating the load on the SDC during the February 22-23, 2006 event.

4.1. Ice Creep Buckling – Buckle Wavelength

Ice creep buckling force was calculated using two methods presented by Sanderson (1988). One approach uses the wavelength of the buckled ice to estimate the force. Sanderson has shown that the buckle wavelength is given by:

$$\lambda_0 = \pi \cdot \sqrt{\frac{\bar{\sigma}\, h}{2\rho_w g}} \qquad \textbf{[1]}$$

where:

λ_0 = half-wavelength of the dominant creep buckle
$\bar{\sigma}$ = average stress (N/m^2)
h = ice thickness (m)
ρ_w = density of seawater (kg/m^3)
g = gravitational acceleration (m/s^2)

For the February 22-23 event, the half-wavelength of the dominant creep buckle is estimated at 20 m, based upon several photographs of the ice surrounding the SDC on February 23. This estimate of wavelength has an accuracy of ± 2m. The average stress calculated using Equation [1] is:

$$\bar{\sigma} = \frac{2\lambda^2 \rho_w g}{\pi^2 h} = [2 * (20\text{ m})^2 * 1020\text{ kg/m}^3 * 9.81\text{ m/s}^2\ ] / (\pi^2 * 1\text{ m}) = 0.81\text{ MPa}.$$

Using the effective loaded structure width of 85 m (perpendicular to the direction of ice movement), the global load is:

$$F = \bar{\sigma} w h = 0.81\text{ MPa} * 85\text{ m} * 1\text{ m} = 69\text{ MN}.$$

Since the buckle half-wavelength may vary by ± 2m, the force is estimated to be in the range of 56 MN to 83 MN.

4.2. Ice Creep Buckling – Time Constant

Sanderson (1988) also showed that the force was related to the time for the ice buckling event. He derived the following equation for the Time Constant of the event:

$$T_0 = \frac{\rho_w g h}{3n\bar{\dot{\varepsilon}}\bar{\sigma}} \qquad \textbf{[2]}$$

where

T_0 = time constant, or length of time over which the dominant creep buckle grows (s)

n = creep index, a constant representing the slope of the line for stress plotted against the log strain-rate; for ice n is generally taken as 3

$\bar{\dot{\varepsilon}}$ = average strain rate (s^{-1})

ρ_w, g, h, and $\bar{\sigma}$ are defined in Section 4.1 of this paper

To calculate the average stress using this approach, the strain rate for the loading event must be estimated. The average strain, $\bar{\varepsilon}$, is the length of deformation divided by the total length over which the stress in the ice was applied. The length of deformation is the lateral distance that the ice moves during the event, which was measured at between 1 m and 1.15 m. However, there is considerable uncertainty regarding the correct value to use for the total length of stressed ice. One approach would be to use the distance from the SDC to the edge of the landfast ice (which was 15.9 km). It is thought that this value is not correct since there was an area of highly ridged ice located 1.85 km west-northwest of the SDC. This ice feature was studied during a reconnaissance flight and appeared almost certainly to be grounded, therefore offering an anchor point to the nearby Paktoa site (John Lindley, Horizon Systems Group, personal communication). Thus, in this calculation, it is assumed that this grounded ice provided an anchor or separation point between the SDC and the edge of the landfast ice. It should be emphasized that this assumption is unsubstantiated, and the use of Equation [2] in this case should not be taken as a reliable estimate of stress.

The peak load on the SDC occurred at 21:21 on February 22, which is 3.5 hours after the end of twilight. The time constant, T_0, is not known since the event occurred during the night and visibility was poor during the storm. Also, creep buckling is a slow process and even if the ice were visible it would be very difficult to establish an exact time when the ice began to buckle. Here a value of 8 hours is used for the calculation. (The actual value of T_0 is not important since it "cancels out" in the calculation of $\bar{\sigma}$.) The average strain rate is:

$$\bar{\dot{\varepsilon}} = \frac{\left(\frac{\Delta l}{l}\right)}{T_0} = (1.075 \text{ m} / 1852 \text{ m}) / 28800 \text{ s} = 2.015\text{E-}08 \text{ s}^{-1}.$$

Using Equation [2], the average stress is calculated as:

$$\bar{\sigma} = \frac{\rho_w g h}{3 n \dot{\bar{\varepsilon}} T_0} = (1020 \text{ kg/m}^3 * 9.81 \text{ m/s}^2 * 1 \text{ m}) / (3 * 3 * 2.015\text{E-}08 \text{ s}^{-1} * 28800 \text{ s})$$

$$\bar{\sigma} = 1.91 \text{ MPa.}$$

The global load is then:

$$F = \bar{\sigma} w h = 1.91 \text{ MPa} * 85 \text{ m} * 1 \text{ m} = 162 \text{ MN.}$$

Due to the accuracy of the measured ice movement (1 m to 1.15 m), the force for this method is best estimated at 152 MN to 175 MN. It should be noted that this range of values is based on the assumption that the total stressed length is 1.85 km, which, as previously discussed, is subject to considerable uncertainty.

4.3. Lateral Force on Shear Skirts

Sladen et al (1992) have presented a method to relate the lateral force on the grid of shear skirts to the deformation. This method is based on a finite element analysis of the load transfer mechanisms between the skirt anchors and the foundation soil. In the following section, the application of this theory is based upon the design of the SDC used at the Paktoa C-60 site.

The shear skirt system was comprised of two series of orthogonal anchors protruding 2 m from the base of the MAT. The grid of anchors is shown in Figure 1. For softer soils such as those present in the uppermost 2 m at the Paktoa C-60 site, the skirts can penetrate almost fully until the base of the MAT contacts the soil. For the lateral force calculations, a penetration depth of 1.8 m is used. In this case, passive resistance is the major component of resistance to lateral forces. Sladen et al (1992) model the soil using the 'Modified Cam Clay' model. The soils at the Paktoa C-60 site are characterized by medium to high plastic, silty clays. The seabed is deformed by ice scour with widths of 1 – 50 m and relief of 0.4 – 1.2 m (Horizon, 2006). The clay at the seabed level is very soft but rapidly increases in strength up to 2 m depth (Klohn Crippen, 2005). The soil is assumed to be consolidated since the event in question occurred several months after setdown of the SDC. The pre-set down seabed undrained shear strength of 30 kPa is used to compute the lateral resistance near the tips of the shear skirts.

When the ice load was first estimated by the authors using this method, the total movement of the SDC was used in the calculation (i.e. the sum of the IPI sensors which gave 35.5 mm). The calculated load value using this approach was much higher than expected. The authors discussed this with one of the authors of the Sladen et al (1992) paper, and it was pointed out that it is only the *local* movement of the soil near the tips of the shear skirts that is required, not the total displacement of 35.5 mm. During the February 22-23 event, the maximum lateral deflection measured by the IPI string is 14.9 mm at the level of the sensor closest to the shear skirts. The ice force acts in a direction 45° from the forward axis of the SDC, so the displacement in each of the x and y directions is similar. In the x or stern direction, the deflection is 10 mm, and in the y or starboard direction the deflection is 11 mm. Using an undrained shear strength of 30 kPa, and assuming the skirts are embedded an average depth of 1.8 m, the lateral resistance was estimated to be 25 kN/m for both the x and y directions. This value is estimated using Figures 19A and 19B in Sladen et al (1992). The number of "rows" of shear skirts in each direction is shown in Figure 1 – there are 17 skirts in each direction, minus the missing pieces around the moonpool of the

SDC. For the stern and starboard directions, the resistance, structure width, and number of shear skirts can be used to calculate the load on the structure:

Force = lateral resistance * width of structure * number of rows of shear skirts

Force in stern direction ≈ 25 MN * 110 m * 16.8 = 46 MN

Force in starboard direction ≈ 25 MN * 162 m * 16.6 = 66 MN

The displacements of 10 and 11 mm in each direction are at the very low end of the scale in the figures used to determine lateral resistance in Sladen et al (1992). Including an estimated error of ±10% in reading these figures, the resultant ice load is estimated as 72 MN to 89 MN.

4.4. Long-Term Creep Load on a Wide Structure

Timco and Johnston (2004) have analyzed ice loading events on wide caisson structures in the Beaufort Sea. They have developed an empirically-based equation that relates the load to the failure mode of the ice. For creep buckling, the global load on a wide structure can be calculated from:

$$L_{gl} = T_{fm} wh \qquad \textbf{[3]}$$

where L_{gl} is the global load on the structure (in MN), w is the width of the structure (in m), and h is the ice thickness (in m). The value of the failure mode parameter, T_{fm}, depends on the type of ice failure for the event being analyzed. For long-term creep, Timco and Johnston (2004) gave a value of T_{fm} = 0.83 MN/m^2. Due to the scatter in the data on which the predictive equations are based, L_{gl} is said to be within ± 15 MN from the calculated value. Using Equation [3] with the effective loaded width of 85 m, the load estimate for the February 22, 2006 event is L_{gl} = 55 to 85 MN.

5. Discussion

Figure 4 compares the results of the four different methods for the calculation of ice loads on the SDC for the February 22, 2006 event. The global pressure (on the right-hand side of the plot) is calculated using an effective loaded area of 85 m^2 for the SDC. This area is the ice thickness (1 m) multiplied by the effective loaded width of the SDC perpendicular to the movement of the ice, as shown in Figure 1.

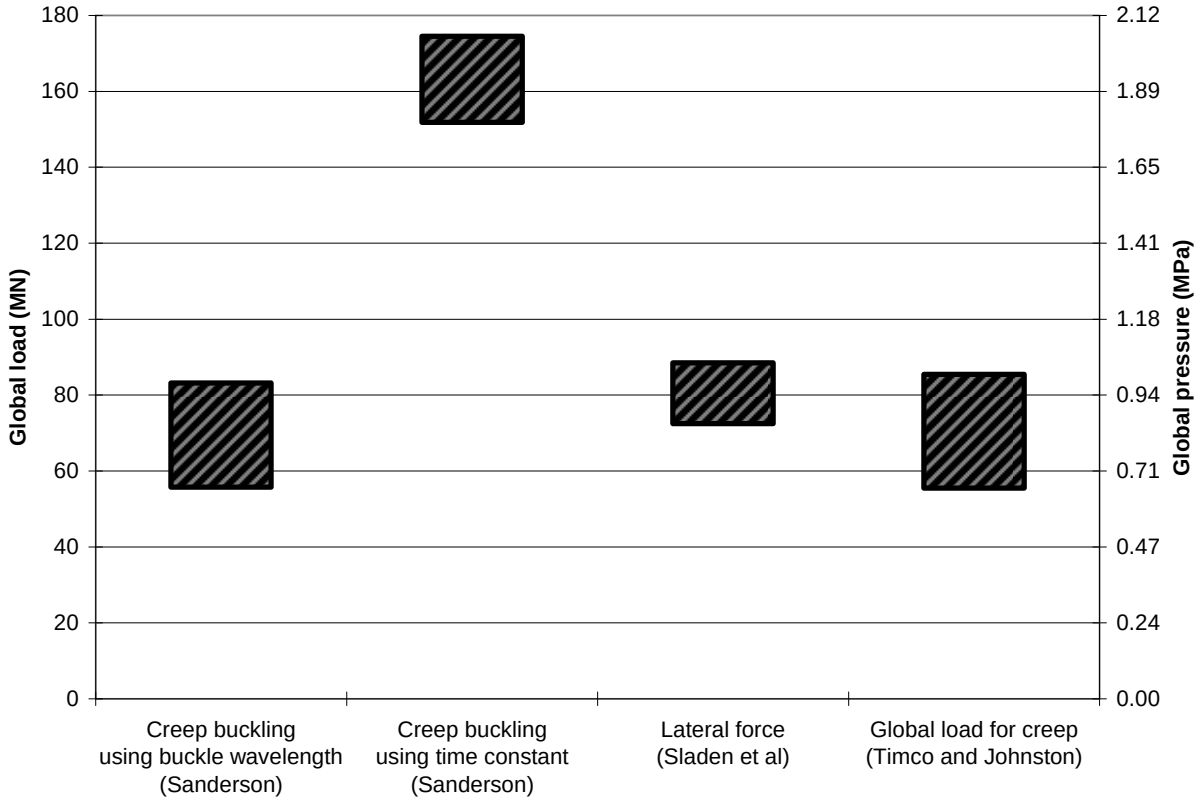

Figure 4. Comparison of estimated ranges for global load on SDC using various methods of ice load calculation

The results in Figure 4 show very reasonable agreement. This is encouraging since the approaches were quite varied. The graph compares predictions based on analytical approaches, geotechnical FE analysis and empirical data of ice loads on wide caisson structures. The use of this large number of approaches could only be done since detailed information on the ice loading event was available for this event. The analysis showed, somewhat surprisingly, relatively good agreement amongst the load prediction methods.

The calculation of global load using the time constant to get ice buckling force (Sanderson, 1988) has the largest uncertainty of any of the methods used. The equation for this method requires the average strain, for which the change in length and the total length over which this deformation occurs must be known. The change is length is the horizontal distance that the ice moves during the event, and was measured at between 1 m and 1.15 m by laser survey. The total length is more difficult to define, and is the main source of error. The total length used for this paper is the distance between the SDC and a rubble field which appeared to be grounded 1.85 km to the west-northwest. This, however, is an unsubstantiated assumption which was made in order to use this approach.

The three other approaches have significantly fewer sources of error. If only these three approaches are used for the load prediction, the estimate of the load ranges from 55 to 89 MN. Using an effective width of 85 m for the structure during the interaction event, the global

pressures range from 0.65 to 1.04 MN/m^2. These values are in good agreement with previous estimates of global loads on wide caisson structures (Timco and Johnston, 2003, 2004).

The Sladen et al (1992) approach, which uses the in-place inclinometers (IPIs) to estimate the load, is especially interesting. In most cases, the detailed information on the ice failure process that is required to use the other three approaches is not known. However, the Sladen et al approach provides a measure of the global load with no required input of the ice failure process. This is very exciting. This approach has the potential to provide estimates of global load using rather simple and inexpensive instrumentation – one of the "Holy Grails" of ice mechanics.

Hewitt et al. (1994) has discussed this approach based on earlier measurements on the SSDC in the Canadian and Alaskan Beaufort Sea. However, before the approach can be used with confidence, several questions must be answered. For example, future research should add the issue of the linearity or non-linearity of response of the soil to the applied load (if the response is non-linear, the analysis would be much more complicated). Second, it would be important to gain an appreciation of the number of IPI strings that would be required for accurate analysis. In the present case, only one string was used. Thus, it was not possible to distinguish between translational and rotational behaviour of the structure, and the assumption of purely translational movement was necessary. Additional strings at different locations in the seabed would be very useful to resolving this issue. With information on the sensitivity of the method to soil type and movement of the structure addressed, it would be necessary to outline a detailed methodology for the accurate use of this approach. Guidance should also be given on the limitations of this approach.

6. Conclusions

This preliminary analysis of the ice creep buckling event near the SDC at the Paktoa C-60 site was quite revealing. Four different approaches were used to estimate the load with quite reasonable agreement. For the three most reliable approaches, estimated global loads due to ice buckling with 1 m thick ice ranged from 55 MN to 89 MN, giving global pressures from 0.65 MN/m^2 to 1.04 MN/m^2. The load prediction using the geotechnical response was especially interesting since it gave reasonable agreement with other predictive approaches. It also pointed to important questions that should be addressed to further develop this approach.

Acknowledgements

The authors would like to thank Bill Livingstone and Peter Millman of Devon Canada for access to the Paktoa data. Thanks are also extended to Sean McDermott of Horizon and Brian Rogers of Klohn-Crippen for the data used in this analysis. Helpful discussions with Kevin Hewitt and Brian Rogers are also acknowledged. Funding for this research was supplied by the Program of Energy Research and Development (PERD) to the ice-structure interaction activity in the Offshore Environmental Factors program.

References

Barker, A. and Timco, G.W., 2006. Rubble Field Quantification in the Beaufort Sea. National Research Council of Canada – Canadian Hydraulics Centre Technical Report CHC-TR-043, Ottawa, Canada.

Frederking, R. and Sudom, D., 2006. Maximum ice force on the Molikpaq during the April 12, 1986 event. Cold Regions Science and Technology, Volume 46, Issue 3, pp. 147-166.

Hewitt, K.J., Kennedy, K.P and Fitzpatrick, P.J. 1994. Global Ice Loads on Arctic Structures interpreted from Foundation Responses. Proceedings 7th Cold Regions Specialty Conference, Edmonton, AB, Canada, pp 223 – 242.

Hewitt, K.J., Sladen, J.A., Williams, D.R., and Brown, J., 1987. Geotechnical Evaluation and Performance of the Canmar SSDC/MAT Mobile Offshore Drilling Unit. Proceedings, 40th Canadian Geotechnical Conference, Regina, Saskatchewan, pp. 364-372.

Horizon Systems Group Inc., 2006. End-of-Well Environmental Monitoring Summary for Paktoa C-60. Horizon Systems Group Report prepared for Devon Canada Corporation, Dartmouth, NS, Canada.

Johnston, M. and Timco, G.W. 2003. Ice Loads on the SSDC during its Beaufort Sea Deployments. Proceedings 17th International Conference on Port and Ocean Engineering under Arctic Conditions, POAC'03, Trondheim, Norway, Vol. 1, pp. 213-222.

Klohn Crippen Consultants Ltd., 2005. SDC at Paktoa C-60 – Geotechnical Evaluation. Klohn Crippen Report prepared for Devon Canada Corporation, Calgary, AB, Canada.

Sanderson, T.J.O., 1988. Ice Mechanics: Risks to Offshore Structures. Graham & Tronman, London, pp. 148-151.

Sladen, J.A., Evison, S.E. and Hewitt, K.J., 1992. Load transfer mechanisms for foundation shear skirts beneath bottom founded arctic offshore exploration structures. Proceedings, 1992 International Conference on Offshore Mechanics and Arctic Engineering (OMAE), Calgary, AB, Canada, Vol. 4, pp. 67-74.

Timco, G. W. and Johnston, M., 2003. Ice loads on the Molikpaq in the Canadian Beaufort Sea. Cold Regions Science and Technology, Volume 37, Issue 1, pp. 51-68.

Timco, G.W. and Johnston, M., 2004. Ice loads on the caisson structures in the Canadian Beaufort Sea. Cold Regions Science and Technology, Vol. 38, Issues 2-3, pp. 185-209.

19th IAHR International Symposium on Ice
"Using New Technology to Understand Water-Ice Interaction"
Vancouver, British Columbia, Canada, July 6 to 11, 2008

Ice Bustles on Quay Piles: Field Studies and Numerical Simulations

Sveinung Løset[1,2] and Aleksey Marchenko[2,1]
[1)]*Norwegian University of Science and Technology (NTNU), Trondheim, Norway*
[2)]*The University Centre in Svalbard (UNIS), Spitsbergen, Norway*
sveinung.loset@ntnu.no
aleksey.marchenko@unis.no

Abstract
In cold climate ice may accrete and form ice bustles on piles exposed to changes in water level. Their formation is related to super-cooling of piles relative to the temperature of surrounding water, when the heat conductivity of the pile material is higher than the heat conductivity of the water. In this case the ice grows laterally from the surface of the pile at larger depths than the thickness of the surrounding level ice. High adhesion between ice and pile keeps the bustles in place during water level changes and allows the bustles to develop over time. The vertical and horizontal size of ice bustles formed on cylindrical quay steel piles (Ø 0.8 m) in the Svea coal harbour, Spitsbergen, was about 1.5 m during the winter and spring of 2007. The ice bustles had cylindrical shapes with slightly downward sloping side walls. Their top surface coincided with water level at maximal tide, and they were almost above the water surface at minimal tide. A mathematical model describing the formation of ice bustle around cylindrical pile was developed with Comsol Multiphysics 3.3a. Ice bustle growth was simulated with constant water level and taking into account tidal variations of the water level. The influence of meteorological conditions, time and tidal amplitude on the sizes of ice bustle is discussed in the paper.

1. Introduction

Low air- and water temperatures combined with waves and water level changes may cause accumulation of ice on coastal structures and piles. These accumulations impose additional gravity actions on the structures and their elements and may be a potential threat for the safety of structure. The situation is not very critical for the strength and stability of heavy gravity structures but may cause problems for mooring and fendering of floating structures and structures of jacket and jack-up types and piers. Sometimes the action linked with the ice accumulation can be comparable with the life action used in the design. Especially critical are these actions in areas with large tide amplitudes (Løset et al., 2006).

The growth of ice on piles (ice bustle) may also increase the water line area and thus cause an increase of the horizontal action from moving ice fields. In this case it is of interest to know the properties of such ice bustles. The paper describes the growth and properties of ice bustles on piles of a quay at Spitsbergen and the numerical modelling of the phenomena.

2. Formation of ice bustles on vertical piles

Fig. 1a shows ice bustles formed on the coal quay piles at Svea in the Van Mijenfjord, Spitsbergen. The tide at the location causes water level variations. Typically the semidiurnal amplitude of the water level is 0.7 m. When the water level is lowering, the water film left on the pile freezes and ice accumulates in cold periods as depicted in Fig. 1b. The piles studied have an utter diameter of 0.80 m. They are made of steel with a wall thickness of 25 mm and filled with concrete. Fig. 1b shows a sketch of the phenomena. The shape of ice bustles can be closed to ring cylinder with inner radius equalling to the pile radius r_p. Utter radius r_b increases with time. The vertical size of the bustles $2A$ is slightly smaller than the maximal variation of water level by the semidiurnal tide. At the low tide phase the significant part of the bustle is lifted out of the water (Fig. 1c). The whole bustle becomes submerged into the water such that the water level is almost coinciding with plane $z = A$ at the high tide phase (Fig. 1d).

The shape of bustles can differ from cylinders significantly. Fig. 2a demonstrates that some of the bustles on the quay piles are not symmetric relatively vertical axis of the pile. Their sizes can be different because of their destruction due to the interaction with surrounding ice. There is frozen slush between bustles below the quay. Fig. 2b shows ice crushing around the bustle when water level decreases. The bustle in this case has almost perfect circular cylindrical shape. Bustles located below the offshore side of the quay in Fig. 2a are smaller than those located more close to the shore, and the shape of their walls is not circular in the horizontal plane. When the water level increases the bustle breaks up surrounding ice by bending deformation (Fig. 2c). It creates water flooding and formation of slush on the surface of surrounding ice. The range of water flooding is bigger than the range of ice crushing around bustles. The slush freezing is probably the main reason for quick extension of bustles in horizontal plane.

Different stages of bustle extension are shown in Fig. 3. Figs. 3a and 3b demonstrate a significant increasing of bustle size $r_b - r_p$ from 0.2-0.3 m to 0.5-0.7 m over 20 days from 15 January to 5 February, 2008. Then their maximal size $r_b - r_p$ was about 0.8 m on 14 February and about 1 m on 4 March, 2008. At this time the bustle was not symmetric relatively to the

vertical axis of the pile. The lateral extension of the bustle according to these observations is shown in Fig. 4a by dots. A linear fit is described as follows

$$r_b - r_p = 0.273 + 0.0162 \cdot t \qquad [1]$$

where the distance $r_b - r_p$ and the time t are measured in metres and days. The line (1) is displayed in Fig. 4a as a solid line. Eq. (1) shows the mean rate of the lateral extension of the bustle $\langle v_r \rangle = 0.0162$ m/day. Fig. 4b shows the air temperature in Svea from 15 January to 8 March, 2008. Mean value of air temperature over this period is equal to $-11.52°C$.

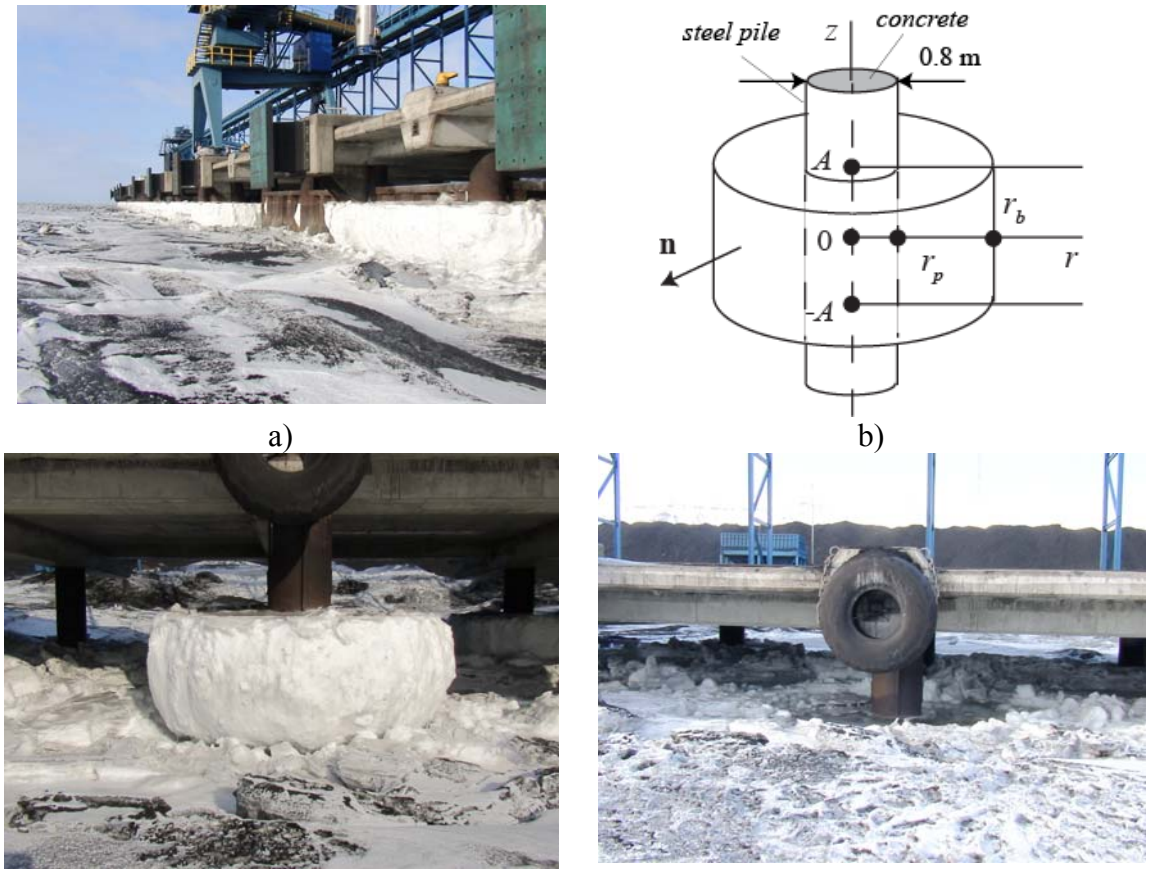

Figure 1. Ice bustles on coal quay piles at low tide (April 2007, Van Mijenfjord, Spitsbergen) (a). Idealized geometrical shape of a bustle in cylindrical coordinates (b). Ice bustle at low tide (c) and high tide (d).

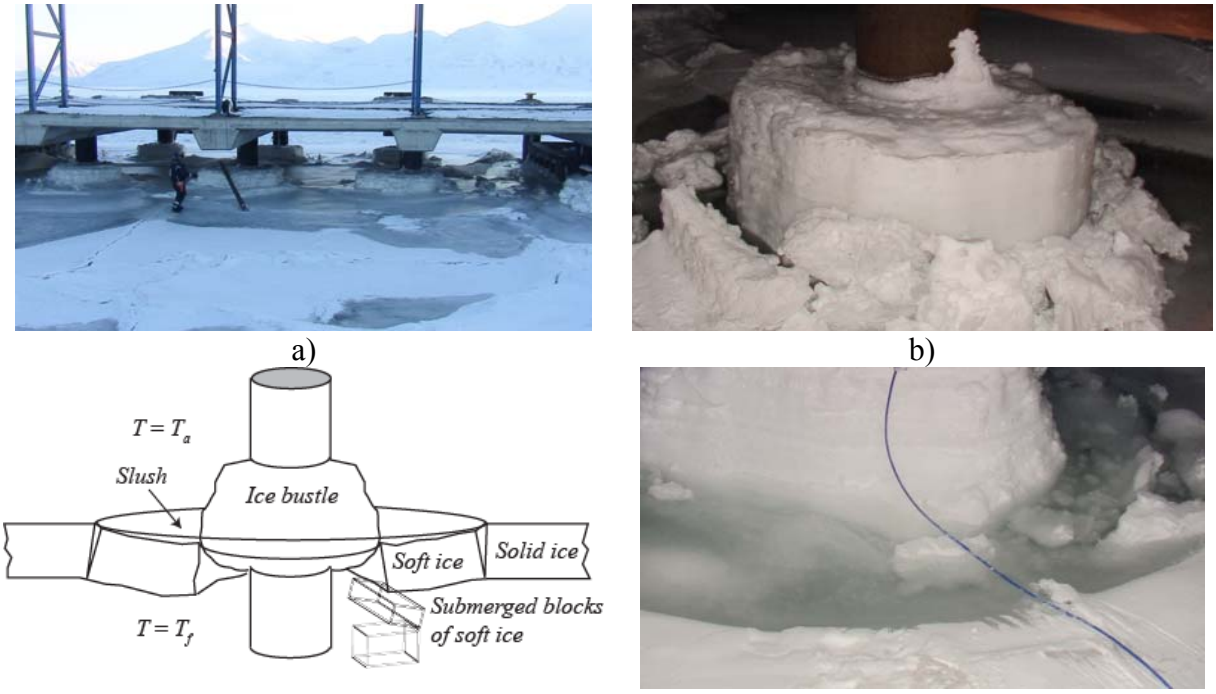

Figure 2. Ice bustles on 4 March 2008 (a), and on 14 February 2008 (b) in the stage of water level decreasing. Ice bustle interaction with surrounding ice in the stage of water level increasing (c, d).

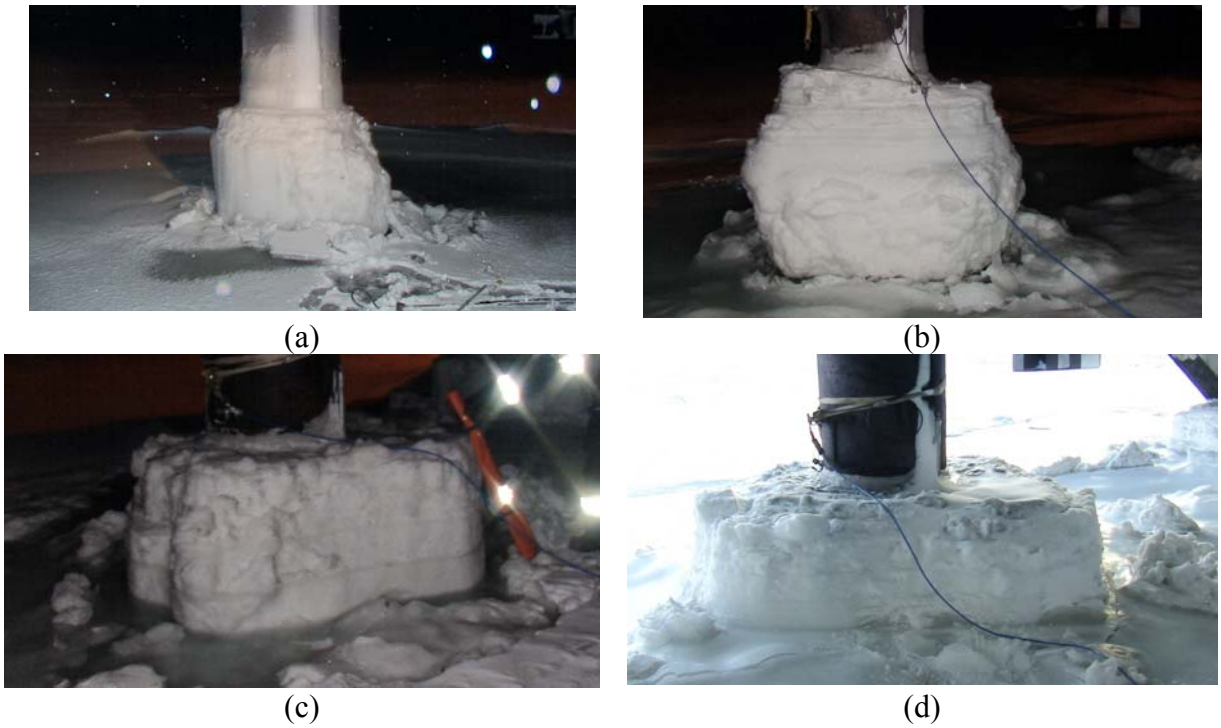

Figure 3. Stages of ice bustle formation: a) 16 January, b) 5 February, c) 14 February and d) 4 March 2008.

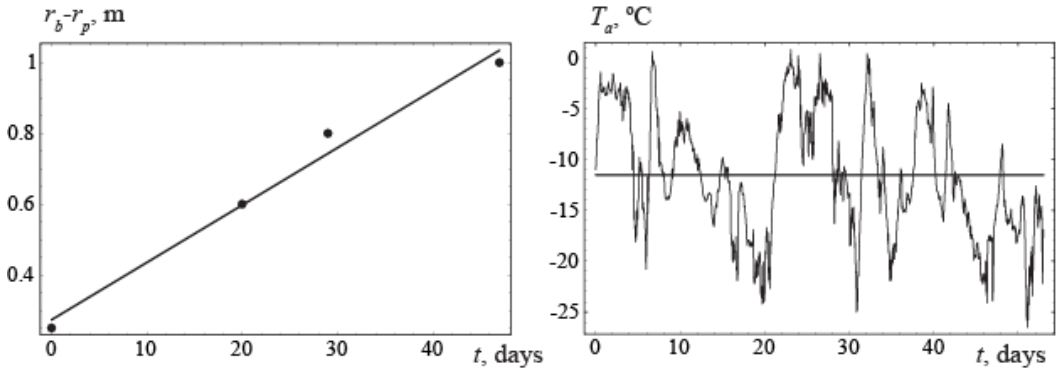

(a) (b)

Figure 4. Lateral extension of the bustle versus time (a), air temperature in Svea from 15 January to 8 March, 2008 (b).

3. Temperature and salinity distribution in the ice bustle

Annually ice bustles have formed on these piles since the quay was built in the 1970ies. The shape and dimensions turn out to be pretty much the same year after year. For the last two years the phenomena has been studied more in detail. Fig. 5a shows the location of vertical and horizontal samples taken in April 2007.

In 2008 one of the bustles was equipped with a vertically deployed thermistor string as shown in Fig. 5b. The resolution along the length of the thermistor string, EBA Engineering (Canada), is 20 cm.

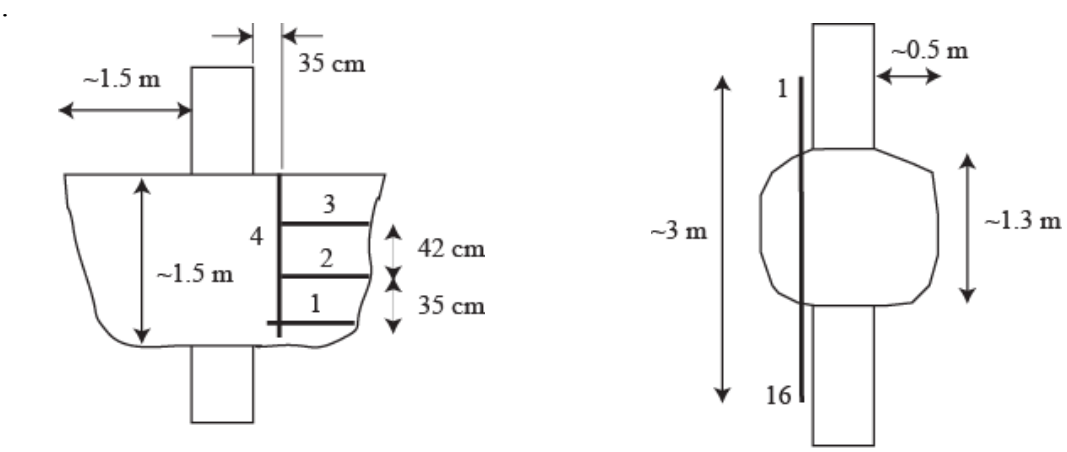

(a) (b)

Figure 5. a) Scheme of horizontal (1,2,3) and vertical (4) ice cores locations on 19 April 2007; b) location of the thermistor string with 16 thermistors related to ice bustle on 5 February 2008.

Fig. 5a shows the shape of the cylindrical bustle as measured 19 April 2007. The rim of the surface is slightly sloping downward with a maximum extent r_b-r_p~1.5 m at the top of the bustle, where r_b and r_p are the radiuses of the cylindrical bustle and the pile.

Three horizontal temperature profiles were taken from cores located at a depth of about 0.53 m, 0.95 m and 1.3 m (Cores #3-1, respectively). The results are shown in Fig. 6a and Table 1. The upper core, Core #3, exhibits an average temperature $\langle T \rangle = -8.3°C$ with a sample standard

deviation $\sigma_T = 0.6°C$. The lowest temperatures are found close to the pile and at the utter surface. The thermal conductivity of steel is about 50 W/mK which is far beyond the corresponding value for ice (~2.2 W/mK). Here the variation is probably caused by fluctuations in the air temperature indicating a relatively low air temperature prior to 19 April 2007. This complies with the observation that the temperature is highest for r_b-r~0.5 m, where r is the polar distance calculated from the axis of the pile, which for all cores is the most thermally sheltered part of the bustle.

Core #2 has a more peculiar profile with the lowest temperature of -10.7°C close to the pile. Then the temperature swings up to a maximum of -7.2°C before it falls down again closer to the rim of the bustle. For Core #2, $\langle T \rangle = -8.7°C$ and $\sigma_T = 1.0°C$. Core #1, the deepest horizontal core, measured the highest average temperature ($\langle T \rangle = -6.9°C$) and $\sigma_T = 0.7°C$. Core #1 is the one that is most influenced by the sea water and it is therefore reasonable that we find the highest temperature here.

The vertical profile exhibits a steady increase of temperature with depth except for a distinct drop in temperature at a depth of 0.75-1.0 m (Fig. 6b). At the same depth we observe a relatively low ice salinity. It is hard to find an explanation for this except that this section contains the oldest part of the bustle which thus has drained for the longest time period.

The salinity was measured with a *Mettler Toledo MX300* salinometer. For the horizontal cores, Core #2 showed the lowest average salinity, $\langle S \rangle = 0.91\,\text{ppt}$ with $\sigma_S = 0.60\,\text{ppt}$ as well as the lowest salinity value of 0.4 ppt at the rim of the bustle. The highest average salinity was measured for Core #1 (bottom), $\langle S \rangle = 1.68\,\text{ppt}$ with $\sigma_S = 0.73\,\text{ppt}$. In average the salinity of all the horizontal cores drops weakly with increasing r_b-r.

Table 1. Temperature and salinity averages ($\langle\rangle$) and sample standard deviations (σ).

Core #	$\langle T \rangle$ (°C)	σ_T (°C)	$\langle S \rangle$ (ppt)	σ_S (ppt)
3	-8.3	0.6	1.03	0.31
2	-8.7	1.0	0.91	0.60
1	-6.9	0.7	1.68	0.73
Vertical	-5.8	2.6	1.78	1.56

In 2008 we were able to monitor a bustle from the first formation and hopefully through the lifetime of the bustle. Fig. 7 displays the first 20 days of records of air temperature (T_a), temperature in upper part of the bustle (T_5) and the temperature below the bustle (T_{13}). The latter temperature, T_{13}, (sea water) shows a constant value of -1.8°C whilst the temperature in the upper part of the bustle is highly correlated with T_a. Fig. 7 shows that T_5 is a smoothening of T_a with a delay of about two days. This delay is due to the relatively low thermal conductivity of ice. Oscillations of the surface temperature (T_5) of the bustle caused by semidiurnal tide are visible during the first 5 days of measurements.

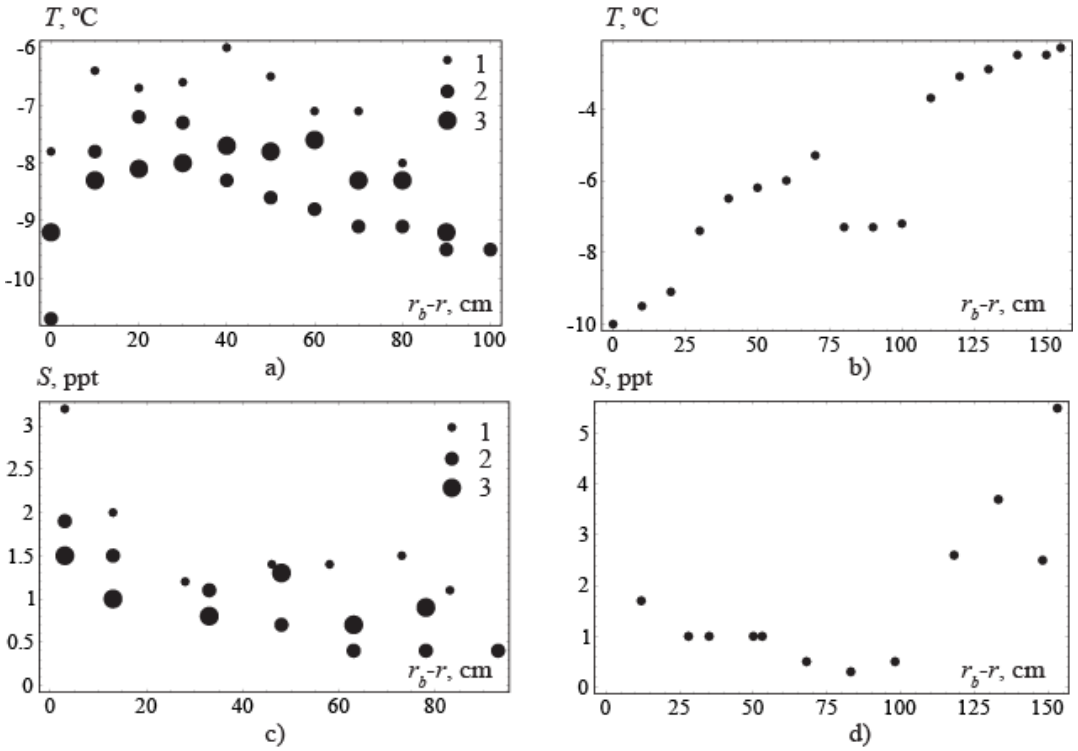

Figure 6. Temperature of horizontal (a) and vertical ice cores (b). Salinity of horizontal (c) and vertical (d) ice cores. The profiles were taken 19 April 2007 and the locations of the horizontal and vertical ice cores are shown in Fig. 5.

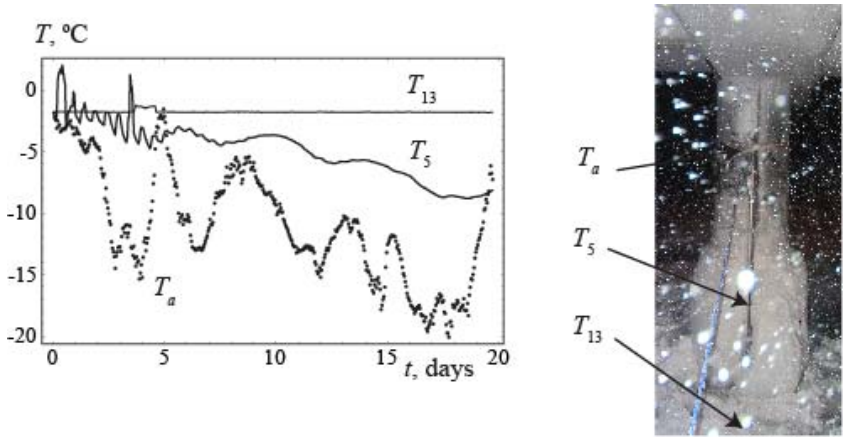

Figure 7. Air temperature (T_a), temperature in upper part of the bustle (T_5) and temperature below the bustle (T_{13}) measured from 16 January to 5 February 2008. The locations of the thermistors are shown in the photographs made on 16 January, 2008.

4. Mathematical modelling of ice bustle growth

The temperature distribution inside the bustle may be described by the equation of heat transfer

$$\rho c_v \frac{\partial T}{\partial t} = k\nabla \cdot (\nabla T), \quad (x, y, z) \in U_b \qquad [2]$$
$$\nabla = \left(\frac{\partial}{\partial x}, \frac{\partial}{\partial y}, \frac{\partial}{\partial z} \right)$$

where ρ, c_v and k are the density, the specific heat capacity and the thermal conductivity of bustle ice, t is the time, x, y and z are horizontal and vertical spatial coordinates, U_b is the bustle volume.

The temperature of the submerged bustle surface is equal to the freezing point $T_f = -1.8^{\circ}\mathrm{C}$, and the temperature above the water bustle surface is equal to air temperature T_a

$$T = T_a, \quad (x, y, z) \in \Sigma_b, \quad z < z_w \qquad [3]$$
$$T = T_f, \quad (x, y, z) \in \Sigma_b, \quad z > z_w$$

where Σ_b is the surface of the bustle, and equation $z = z_w(t)$ describes the elevation of water level by the tide.

The extension of bustle occurred on the submerged surface according to Stefan's law

$$\rho L v_n = k \frac{\partial T}{\partial n}, \quad (x, y, z) \in \Sigma_b, \quad z < z_w \qquad [4]$$

where v_n is the rate of bustle extension in the direction of outward unit normal $\mathbf{n}$ to the bustle surface, and L is latent heat of fusion.

For the simplification of the problem let us assume that the bustle has a cylindrical shape as shown in Fig. 1b. The water level elevation is described as $z_w = a\sin(\omega_t t) + A - a$, where ω_t is the frequency of the semidiurnal tide ($\omega_t = 2\pi / T_t, T_t \approx 12$ hours). From Eq. (4) follows that the mean speed of lateral extension of the bustle $\langle v_r \rangle$ averaged over the time, is calculated with the formula

$$\langle v_r \rangle = -\frac{1}{T_t} \int_{t_0}^{t_0 + T_t} v_r dt, \; v_r = -\frac{\langle F \rangle_h}{\rho L}, \; \langle F \rangle_h = -\frac{k}{2A} \int_{-A}^{A} \left. \frac{\partial T}{\partial r} \right|_{r = r_b} \theta(z_w - z) dz \qquad [5]$$

where $\langle F \rangle_h$ is mean heat flux from the submerged vertical surface of the bustle, v_r is the rate of lateral extension of the bustle averaged over its vertical size, t_0 is initial time, and $\theta(z_w - z) = 1$

when $z < z_w$ and $\theta(z_w - z) = 0$ when $z > z_w$. Mean speed of downward extension of the bustle $\langle v_z \rangle$ averaged over the time is calculated with the formula

$$\langle v_z \rangle = \frac{1}{T_t} \int_{t_0}^{t_0+T_t} v_z dt\,, \quad v_z = \frac{\langle F \rangle_v}{\rho L}\,, \quad \langle F \rangle_v = \frac{k}{r_b - r_p} \int_{r_p}^{r_b} \left. \frac{\partial T}{\partial z} \right|_{z=-A} dr \qquad [6]$$

where $\langle F \rangle_v$ is mean heat flux from ice bustle bottom and v_z is the rate of downward extension of the bustle averaged over its horizontal size.

For the estimate of $\langle v_r \rangle$ and $\langle v_z \rangle$ depending on the horizontal size of the bustle $r_b - r_p$ and air temperature T_a, we consider the heat transfer Eq. (2) with boundary conditions (3) in the case of fixed size of ice bustle, i.e. it is assumed that $\langle F \rangle_h$ and $\langle F \rangle_v$ in Eqs. (5) and (6) can be estimated from the solution of the problem with fixed boundaries of the ice bustle. The problem with fixed boundaries is considered with initial condition $T = T_f$ inside the bustle. Since boundary conditions (3) include periodical function $z_w(t)$, the solution tends asymptotically to the periodical mode. The value of t_0 is determined from the condition that the solution is close to the periodical mode. Numerical estimates show that it happens when $t_0 > t_*$, where $t_* = \rho c_v l^2 / k$ and l is representative length scale. Assuming $\rho = 910\,\text{kg/m}^3$, $c_v = 2.09\,\text{kJ/(kg°C)}$, $k = 2.24\,\text{W/(m°C)}$ and $l = 1\,\text{m}$ we find $t_* = 9.8\,\text{days}$. Fig. 8a shows the rates v_r and v_z versus dimensionless time t_0 / t_* calculated for the bustle with $r_b = 1.8\,\text{m}$, $r_p = 0.4\,\text{m}$ and $A = a = 0.7\,\text{m}$ when $T_a = -10^\circ\text{C}$. Fig. 8b shows the shape of functions $v_r(t)$ and $v_z(t)$ over 7 periods when the solution becomes periodic. One can see that the maximal values of $v_z(t)$ are larger than the maximal values of $v_r(t)$, but the mean value $\langle v_z \rangle = 0.055\,\text{m/day}$ is smaller than the mean value $\langle v_r \rangle = 0.12\,\text{m/day}$.

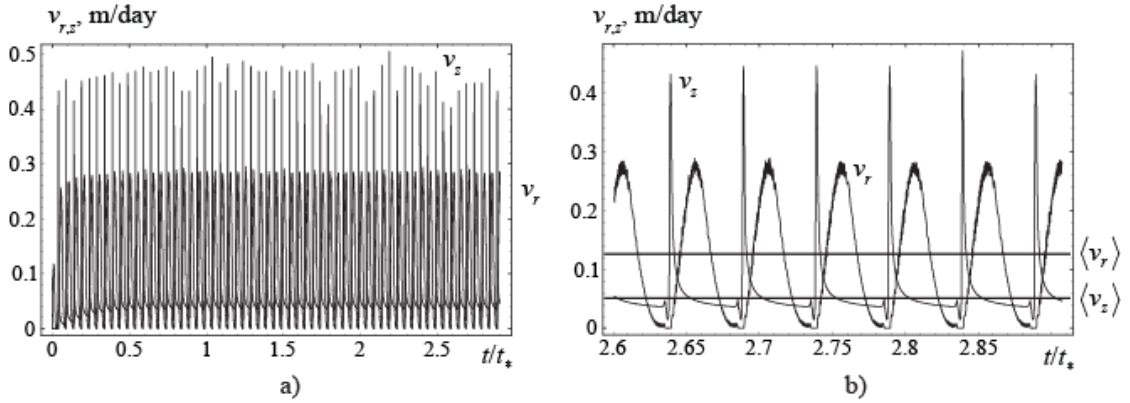

Figure 8. Rates of lateral (v_r) and vertical (v_z) extension of ice bustle calculated with $r_b = 1.8\,\text{m}$, $r_p = 0.4\,\text{m}$, $A = a = 0.7\,\text{m}$ when $T_a = -10^\circ\text{C}$.

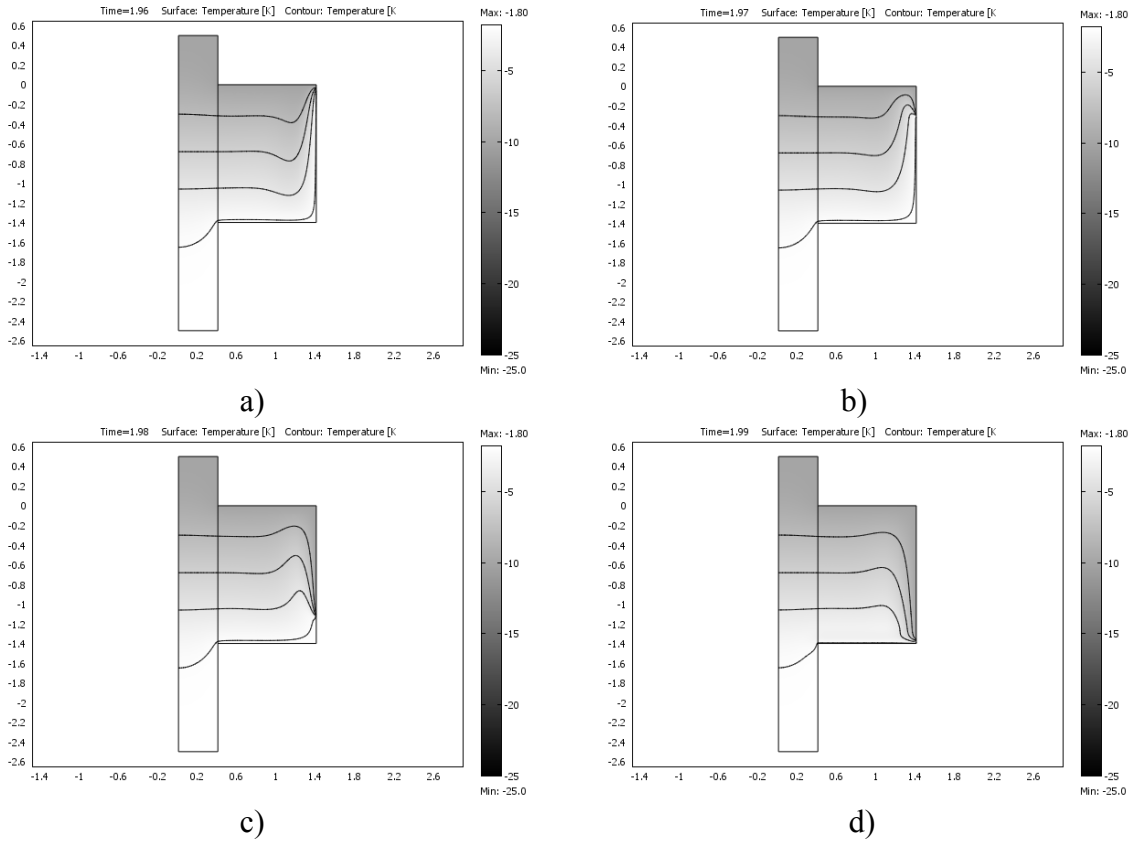

Figure 9. Variation of temperature distribution inside the bustle over one tidal cycle calculated with $T_a = -10^\circ\mathrm{C}$ and $A = a = 0.7$ m. Solid lines show isotherms $-2, -4, -6$ and $-8°\mathrm{C}$.

Temperature distribution inside the ice bustle over one tidal cycle is shown in Fig. 9. The example was calculated with $T_a = -10^\circ\mathrm{C}$ and $A = a = 0.7$ m. Isotherms $-2, -4, -6$ and $-8°\mathrm{C}$ are shown by solid lines beginning from the vicinity of water level, over which the temperature is changed from the freezing point $T_f = -1.8^\circ\mathrm{C}$ to air temperature $T_a = -10^\circ\mathrm{C}$. One can see that the temperature distribution at low tide shown in Fig. 9d is similar to those shown in Fig. 6a. The temperature of the pile above and below the bustle is not affected by the tide.

Results of the processing of numerical simulations data are shown in Fig. 10. The amplitude of the water level oscillations was $a = 0.7$ m in all computed examples. The rates of ice bustle extension, in lateral directions $\langle v_r \rangle$ computed with $2A = 1.4$ m and different values of air temperature T_a and $r_b - r_p$ varied from 0.2 m to 1.4 m, are shown in Fig. 10a. We see that the dependence of $\langle v_r \rangle$ on $r_b - r_p$ is very weak. The dependence on air temperature is approximated by the formula

$$\langle v_r \rangle = -0.031 - 0.015 T_a \qquad [5]$$

where $\langle v_r \rangle$ is measured in m per 10 days, and the air temperature T_a is measured in °C. Assuming $T_a = -11.52^{\circ}\mathrm{C}$ we find $\langle v_r \rangle = 0.013$ m/day. This value is closed to the rate $\langle v_r \rangle = 0.0162$ m/day estimated for lateral extension of bustles in Svea from 15 January to 8 March, 2008 (Section 2).

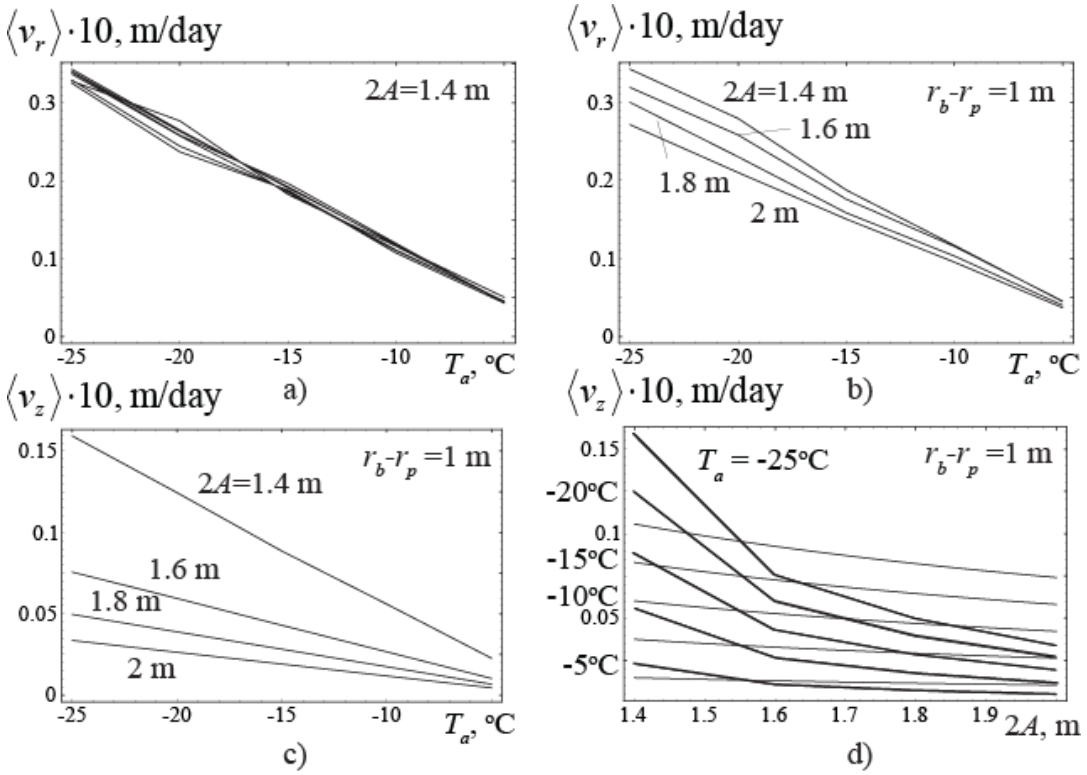

Figure 10. The lateral rate of ice bustle extension $\langle v_r \rangle$ computed with different values of air temperature T_a and different values of $r_b - r_p$ varied from 0.2 m to 1.4 m (a). The lateral rate of ice bustle extension $\langle v_r \rangle$ computed with different values of air temperature T_a and different bustle heights $2A$ (b). Rates of downward bustle extension $\langle v_z \rangle$ computed with different values of air temperature T_a and different bustle heights (c). Rates of downward bustle extension $\langle v_z \rangle$ (thick lines) and rates of level ice thickness growth (thin lines) from ice thickness $2A$ computed with different values of air temperature T_a and $2A$ (d).

Fig. 10b shows strong dependence of the rate of lateral bustle extension on air temperature and weak dependence on bustle height $2A$, which is explained mainly by the averaging over the bustle height $2A$. Fig. 10c shows strong dependence of the rate of downward bustle extension on the bustle height $2A$ and air temperature. Fig. 10d shows the dependence of the rate of downward bustle extension on the bustle height $2A$ (thick lines) in comparison with the dependence of the rate of level ice thickness growth on ice thickness $2A$ (thin lines) computed with different values of air temperature T_a with the formula of degree days of frost

$$\langle v_z \rangle = \frac{k(T_f - T_a)}{2\rho LA} \qquad [6]$$

using $\rho = 910\ \mathrm{kg/m^3}$, $L = 333.4\ \mathrm{kJ/kg}$, $k = 2.24\ \mathrm{W/(m^\circ C)}$ and $T_f = -1.8^\circ\mathrm{C}$. From Fig. 10d follows that the influence of tidal oscillations of water level causes higher rate of downward bustle extension in comparison with the rate of level ice growth when $2A < 1.55\ \mathrm{m}$. The rate of level ice growth is higher than the rate of downward bustle extension when $2A < 1.6\ \mathrm{m}$.

5. Conclusions

In cold climate ice may accrete and form ice bustles on piles exposed to changes in water level. Field studies and numerical simulations have been performed of such a phenomena on a quay in the Van Mijenfjord, Spitsbergen.

The major findings of the study are:

- The tide at the location causes water level variations. When the water level is lowering, the water film left on the pile freezes and ice accumulates in cold periods.
- The vertical extension of the ice bustle was close to twice the amplitude of the semidiurnal tide at the site, 1.4-1.5 m.
- The extension of the ice bustle could be modelled well using Stefan's law.
- The rate of lateral extension of ice bustles increases with decreasing air temperature and is almost independent on bustle height.
- The lateral dimension of the ice bustle was at most 1.5 m measured from the pile surface.

References

Løset, S., K. Shkhinek, O. T. Gudmestad and K. Høyland (2006): Actions from Ice on Arctic Offshore and Coastal Structures. Trondheim, St. Petersburg, Moscow, Krasnodar, Publisher "LAN", ISBN 5-8114-0703-3, 271 p.

19th IAHR International Symposium on Ice
"Using New Technology to Understand Water-Ice Interaction"
Vancouver, British Columbia, Canada, July 6 to 11, 2008

Experimental study on friction between saline ice and steel

Marco Nanetti, Aleksey Marchenko and Knut V. Høyland

The University Centre in Svalbard, Norway (UNIS)
Marco Nanetti: seloselo@virgilio.it - Via Mazzini 112, 40100 Bologna, Italy
Aleksey Marchenko: aleksey.marchenko@unis.no -
the University Centre in Svalbard, P.O 156, 9171 Longyearbyen, Norway
Knut V. Høyland: knut.hoyland@ntnu.no -
the University Centre in Svalbard, P.O 156, 9171 Longyearbyen, Norway

Abstract

A device was developed and designed and small scale laboratory experiments were carried out to study sea ice frictional interaction with steel material by means of a uniaxial compression rig. Sea-ice was artificially grown between a stainless steel piston (of circular cross section) and a hollow cylinder of the same material, coaxial to the former and of the same surface roughness. Three different values for the roughness were tested: 1.2, 10 and 30 μm R_y (maximum asperities height), chosen as representative values for typical surface conditions, from smooth to normally corroded steel. Creep tests (0.2, 0.3, 0.4 and 0.6 kN) were conducted at T = -10 ºC. By pushing the piston head towards the cylinder base, two different types of relative movement were observed: 1) the piston only slid through the ice, 2) the piston slid through the ice and the ice slid on the surface of the outer cylinder. A cyclic stick-slip motion of the piston was detected with a representative frequency of 0.1 Hz. The ratio of the mean rate of axial displacement to the frequency of the stick-slip oscillations was comparable to the nominal roughness length (S_m). The roughness is the most influential parameter affecting the amplitude of the oscillations, while the load has a relevant influence on their frequency. Guidelines for further investigations were recommended.

Key words: Sea ice, friction, roughness, creep, steel, adhesion, uniaxial compression.

1 Introduction

Understanding the interaction of sea ice with offshore structures is of primary importance for the development of technology in cold climate regions. The rheological properties of sea ice (strength, creep, viscosity) as well as the roughness of the contact surface are the main factors influencing the type of interaction with a structure. Ice friction is especially important when considering ice loads on structures. Ice forces act on structures through pressure, adhesion and friction. Friction and adhesion are to a great degree responsible for vertical loads on piles and similar structures, but friction also has influence on horizontal loads especially in the case of drifting ice (Oksanen, 1980). Therefore information on both static and kinetic friction between sea ice in various conditions and construction materials is needed (Nakazawa et al., 1993). Friction also comes into play when considering ice-induced vibrations on structures: vibrations may create serious operational problems and also lead to fatigue failure of structural elements (Løset et al., 2006). The target of this project was to develop a small scale laboratory experiment to study how parameters such as surface roughness, load, relative velocity and temperature, influence the friction between saline ice and steel. For this purpose, the equipment at the UNIS laboratory, a uniaxial compression rig and its load gauges, two cold laboratories, and a tank to grow ice, were used. In addition, the design of a new device was developed for this specific purpose.

Sea ice, as well as freshwater ice, exists mostly at high homological temperatures, and in the case of floating ice, the grains are relatively large. As a crystalline material, sea ice has elastic, visco-elastic, visco-plastic and brittle properties, its actual behavior depending on the type and the state of the sample taken into consideration. The main parameters that influence the ice mechanical behavior are: temperature T, porosity η (brine volume and air volume), grain size d and loading rate. When considering friction between ice and other materials, especially at low speed, the creep properties of ice come into play. See e.g. Barnes et al. (1971) for a treatment of creep.

Surface roughness has an effect on friction and, as summarized by Nakazawa at al. (1993), a number of studies show that the kinetic μ_k and the static μ_s coefficients of friction for ice can be affected by various factors such as normal stress, relative velocity, temperature, and surface roughness itself of the test material. We may add that the other factors affecting the mechanical behavior of ice, such as porosity and grain size, are also likely to be important. Tabata and Tusima (1981) discovered a direct proportionality between the roughness of mean square (RMS) and the friction coefficient between sea ice and stainless steel, underlining the importance of a ploughing effect on the kinetic friction of a rough surface. Nakazawa et al. (1994) showed that the coefficient of friction and the adfreeze bond strength increase with increasing wave height of the irregularities and steepness. Tatinclaux at al. (1986) suggested that the relative size of the crystals with respect to the roughness elements of the surface as well as the morphological characteristics of the roughness other than the simple average, e.g. peak angle and peak radius of curvature of the asperities, must be taken into account.

The existence of the stick-slip motion and the vibrations of structures interacting with ice is well known, but not well explained. Assuming a block which slides on a flat substrate, while pulled via a spring with stiffness k_s at constant speed v_s, the friction force between the two surfaces may either be of a steady type or a stick-slip motion case in which the block alternates between stick and slip. In the steady type of motion, the kinetic friction force is constant after the force has overcome the static friction force. During stick-slip motion the oscillations in the spring force are not always periodic but may behave chaotically (Figure 1.). Experiments do show that stick-slip disappears either if the spring k_s or the sliding speed are high enough (Persson, 2000).

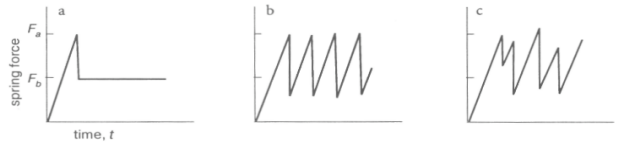

Figure 1. Sliding dynamics a) steady sliding, b) periodic stick-slip motion, c) chaotic motion (Persson, 2000).

For the ice/structure interaction, the stick-slip phenomenon was investigated by Shkhinek et al. (1999) and Kärna et al. (2000). It can be observed when a thin layer of pulverized ice (ongoing crushing) is located between a structure wall and an ice sheet moving against it. The stick-slip occurs due to the uneven distribution of the out of plane (vertical) velocity of ice particles over the contact area and the rate dependence of the friction coefficient. It is typical for very slow ice motion where a gradient of the friction coefficient is maximal. This process results in a saw-tooth form of the pressure signals, where energy accumulations, accompanied by the formation of a stagnation zone and an increase in local and global pressure, alternate to energy discharges, followed by a sudden great increase in the vertical velocity of the ice particles located near the contact surface and a decrease in action. Experiments also show that structures often vibrate even when the ice velocity is low, although one would not expect large variations in action during slow and thus ductile deformation: a resonance effect between the oscillation period during stick-slip motion and one of the structural periods could give a reasonable explanation to the phenomenon (Løset, 2006).

2 Experimental setup and design

Knekkis, a 10 ton uniaxial compression rig with a step engine, was used in the UNIS laboratory. The samples were loaded from below, yet the applied load was measured indirectly by a strain gauge (HBM - load cell U2A) situated above the upper plate. The load cell had an accuracy of 0.01 kN, and the displacement was calculated from the engine rotation. No correction for the upper plate displacement was done. Knekkis could be used for constant velocity tests, creep (constant load) tests or relaxation (constant displacement) tests.

Frysis, a 1.2 m deep metal tank with a surface area of 0.5m x 1m, was used to grow ice in the UNIS cold laboratory. In order to produce ice with a structure resembling that forming in calm sea waters, the walls and the bottom were heated up, to keep a constant temperature above the freezing point. Real seawater from the Adventfjord, outside Longyearbyen, was used to carry out the experiments.

A device (Figure 2.) was specially designed in order to test dynamic friction between saline ice and steel. The main components consisted of an inner cylindrical piston and an outer hollow cylinder, both made out of the same steel material (AISI303). The piston shaft and the inner surface of the cylinder were worked by lathe and both obtained with the same roughness. The piston and the cylinder were kept coaxial by a steel frame (Figure 4.) which was used, in addition, to hang the device over the tank during the ice formation process by means of three metal rings screwed onto the outside. Due to the difference in diameter between the piston shaft and the hollow cylinder, a designed room was left to grow an annulus of ice by freezing sea water. The lower parts of both piston shaft and cylinder ended at the same level (Figure 6.): this structural characteristic allowed the ice grown in addition to be cut off by band saw, before testing; furthermore, during testing, it prevented the ice from being crushed by the piston bottom end. In order to give the device a base in contact with Knekkis' lower plate and to create room for the sliding of the piston, the bottom of the cylinder body had to be connected to an additional hollow steel element (Figure 7.), just before testing. To protect this connection from the formation of ice during the ice growth, a hard plastic ring was designed (Figure 6.). All in all, three devices were produced, equal in dimension, but with three different types of surface roughness: *smooth (sr)*, *middle (mr)* and *high (hr)* (nominal values for the representative lengths are given in Table 1.). Figure 3. shows a sketch of the lathe indenter and the representative dimensions of the asperities.

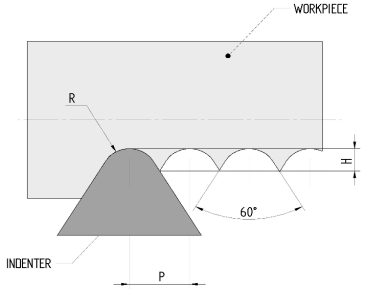

Figure 3. Lathe indenter and representative roughness dimensions.

Table 1. Nominal values for the representative roughness lengths.
Ry [μm] is the maximum height of the asperities → H
Sm [mm] is the mean profile pitch → P

	smooth roughness (sr)	middle roughness (mr)	high roughness (hr)
R_y [μm]	1.2	10	30
S_m [mm]	0.05	0.25	0.4

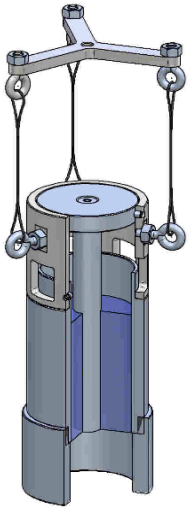

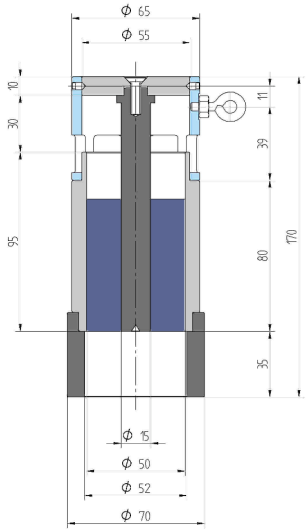

Figure 2.
Ice friction testing device: assemblage.

3 Experimental procedure

The first step of the experimental procedure consisted in the assembly of the device. Once the piston was inserted into the cylinder, the specially designed frame had to be connected (by means of screws) to both elements, in order to keep them coaxial at all times during the ice formation. Growing ice was a crucial phase of the entire experimental procedure since it greatly influenced the whole duration of the process (it required a much longer time (~2.5 days) compared to the other phases) and the testing material was, in fact, the ice which was grown, its quality being therefore an issue. The plastic ring was assembled onto each cylinder to protect the lower part from the formation of ice. Then the part of each cylinder below the metal frame had to be wrapped in a layer of Elastolen (cut from an ordinary sleeping pad) and inserted into a piece of ordinary plastic plumbing (dia.80 mm) (Figure 4.). Each of the three devices could be installed into Frysis, hanging from its own separate wooden beam striding the tank. Ordinary fishing line, resistant and flexible, was used for this purpose. The tank was then filled with sea water up to a couple of mm below the lowest plastic pipe. Then, each device was set plumb, by means of the three lateral screws. The air temperature in the lab was then cooled down to -30 ºC and the appropriate amount of Freezing Degree Hours provided in order to grow ice to the desired thickness. To extract the device from the tank, the harness had to be removed first, by just unscrewing the three lateral rings on the outside of the metal frame. This was possible because the three lines suspending the assemblage loosened since the device had risen a few mm due to ice expansion. Then, by gripping the frame by hand, just a slight force was enough to pull the device out of the plastic pipe. The success of the operation was due to the reduced friction between the wrapping and the plastic because of the formation of small ice crystals and the thermal contraction of the pad (Figure 5.).

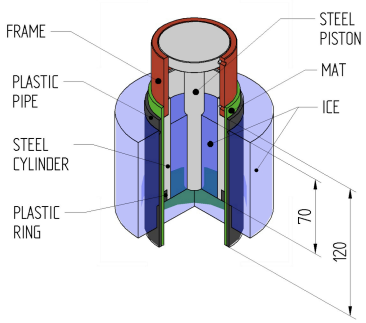

Figure 4. (left) Assemblage during ice formation: sketch.

Figure 5. (right) Device extracted from the tank: the wrapping is easily removable and the ice is ready to be cut off.

The samples were left half a day in the testing cold lab to adapt to the change of temperature. Then the ice that had formed beyond the device bottom had to be evenly cut off. The wrapping mat being removed, a band saw was used to cut the additional ice cylinder. A precision of half a millimeter could be reached by the operator. Subsequently, by means of a metal tool, the cylinder and the piston shaft ends had to be cleared in order to allow only a relative displacement between lateral surfaces (no penetration of the piston into ice was supposed to take place) (Figure 6.). The plastic ring was removed and the bottom steel base assembled (Figure 7.). The upper frame could then be unscrewed and removed. The sample was put in between Knekkis plates and the test

could be started. The tests were interrupted before the piston head touched the cylinder. The duration of constant load tests was therefore variable.

Figure 6. After the ice was cut, the cylinder's and the piston's bottom ends were cleared of ice. Notice the hard plastic ring to protect the connection from the ice formation.

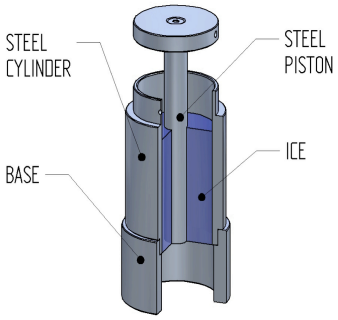

Figure 7. Device ready for testing (sketch).
The addition steel base is assembled at the bottom.

4 Results

During the months of June, July and October 2007, for this project, a total of 14 creep tests[1] were carried out, whose relative data are presented herein and summed up in Table 2..

Table 2. Summary of the performed tests.

test set	date	test code	roughness	test number	constant load	T_{air} [°C]	σ_w [ppt]	σ_{sample} [ppt]	$\delta_{p/i}$ [mm]	$\delta_{i/c}$ [mm]
1	21.06.2007	mr_2_0,3kN	mr	2	0.3 kN	-10	18.4			/
1	22.06.2007	mr_3_0,3kN	mr	3	0.3 kN	-10	18.4	3.2		/
2	26.06.2007	mr_4_0,2kN	mr	4	0.2 kN	-10	18.5	5.8		/
2	27.06.2007	hr_1_0,2KN	hr	1	0.2 kN	-10	18.5	6.3		/
3	04.07.2007	hr_2_0,4KN	hr	2	0.4 kN	-10	18.7	3.2		/
3	04.07.2007	sr_1_0,4kN	sr	1	0.4 kN	-10	18.7	3.0	3.0	17.6
3	04.07.2007	mr_5_0,4kN	mr	5	0.4 kN	-10	18.7	3.0		/
4	09.07.2007	sr_2_0,6kN	sr	2	0.6 kN	-10	19.2		3.7	16.1
4	09.07.2007	hr_3_0,6kN	hr	3	0.6 kN	-10	19.2			/
4	09.07.2007	mr_6_0,6kN	mr	6	0.6 kN	-10	19.2	8.0		/
5	14.07.2007	hr_4_0,2kN	hr	4	0.2 kN	-10		8.1		/
5	14.07.2007	mr_7_0,2kN	mr	7	0.2 kN	-10		7.6		/
5	14.07.2007	sr_3_0,2kN	sr	3	0.2 kN	-10		7.5	7.0	12.6
6	14.10.2007	mp+mc_1_0,3kN	mr	1	0.3 kN	-10				/

T_{air} [°C] = average testing air temperature

σ_w [ppt] = water salinity measured before the freezing process

σ_{sample} [ppt] = sample salinity after testing

$\delta_{p/i}$ [mm] = displacement of the piston relative to the ice

$\delta_{i/c}$ [mm] = displacement of the ice relative to the outer cylinder

[1] The tests were identified with a three-field name:
- indication of the piston and the cylinder's roughness (since the pistons were always assembled with the correspondent cylinders of the same roughness, only one value is indicated, with the exception of test mp+mc_1_0,3kN)
- test number (referred to the number of tests carried out with that specific combination of roughness for piston and cylinder)
- applied constant load.

All the tests were taken at an average air temperature of -10 °C. For every sample, water salinity before freezing (σ_w [ppt]) was measured as well as the salinity of the ice annulus after testing (σ_{sample} [ppt]). The total displacement between Knekkis' punches was automatically registered by the computer, but, in case both a relative displacement ice-piston ($\delta_{p/i}$ [mm]) and a relative displacement ice-cylinder ($\delta_{i/c}$ [mm]) took place during the same test, the entities of the movements were measured manually by calipers. All data were elaborated through Excel and Matlab 7.5.0 (R2007b).

Figure 8. Three samples with three different roughness values are shown after testing. Notice that for sr (left) the ice/cylinder displacement occurred.

To study the effect of axial load on the experiment, different constant loads were used: 0.2, 0.3, 0.4 and 0.6 kN respectively. For each testing load, the relative displacement ice-cylinder was observed exclusively every time the smoothest cylinder was used (Figure 8.). With middle and high roughness surfaces, however, only the piston slid through the ice while no appreciable movement occurred at the interface with the cylinder. Three graphs, one for each value of roughness, are shown below in Figure 9., displaying axial load (ordinate axis on the left, black color) and displacement (ordinate axis on the right, red color) over time for the whole test duration. The three samples are tested with the same load (0.4kN), and they are taken as an example to point out the general trends which were observed. From the curves, two distinct phases can be clearly defined:

- a *first phase* during which the adhesion strength resists the load, the displacement is nearly nil (in the order of tenths of μm) and the load oscillates around the set value.
- a *second phase* begins when the relative motion is set off. The ice yields under the load. The load oscillation features (frequency and amplitude) visibly change. An appreciable displacement takes place with a characteristic stick-slip behavior. There is a clear damping effect of the oscillations with time.

While for middle and high roughness the two phases are clear and distinct, for the smoothest surface the first phase is negligible and the motion starts as soon as the load is applied.

Figure 10a. and Figure 10b. display the axial load and the axial displacement over time for test hr_2_0,4kN as in Figure 9c., but zooming in on the first 100 sec from the beginning of the second phase and on the last 100 sec before the end of the test, respectively. There seems to be a clear connection between the load oscillations and the displacement steps. There are stationary phases during which the ice offers resistance to the load and the displacement is in the order of hundredths of mm alternated to sudden drops in load and quick displacements (in the order of tenths of mm). As can clearly be noticed by comparison, the period of oscillations decreases in time. Hr_2_0,4kN is taken as an example to suggest trends that can be observed in all the other samples with high and middle roughness.

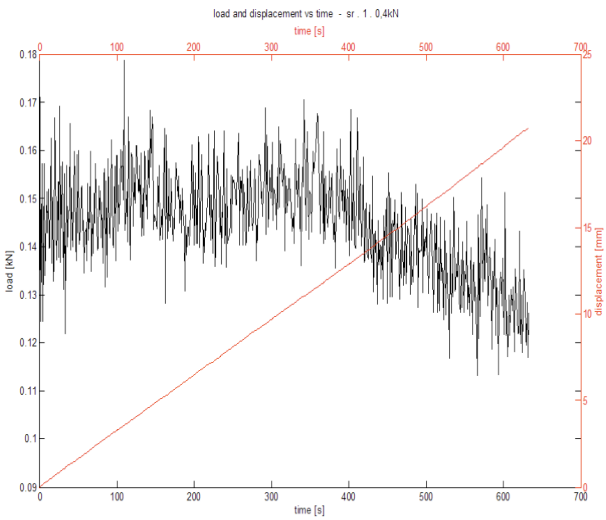

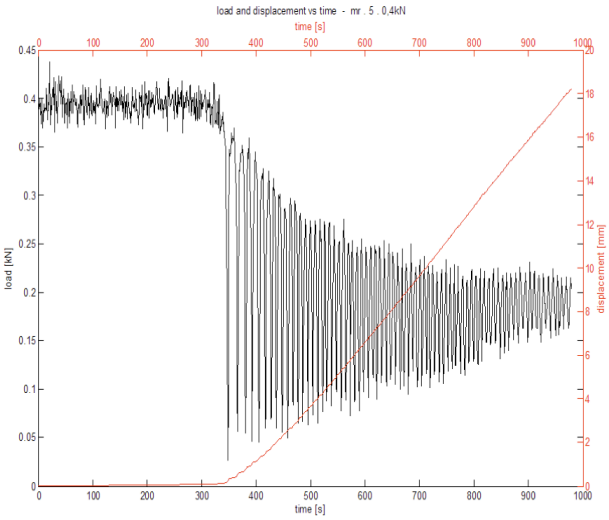

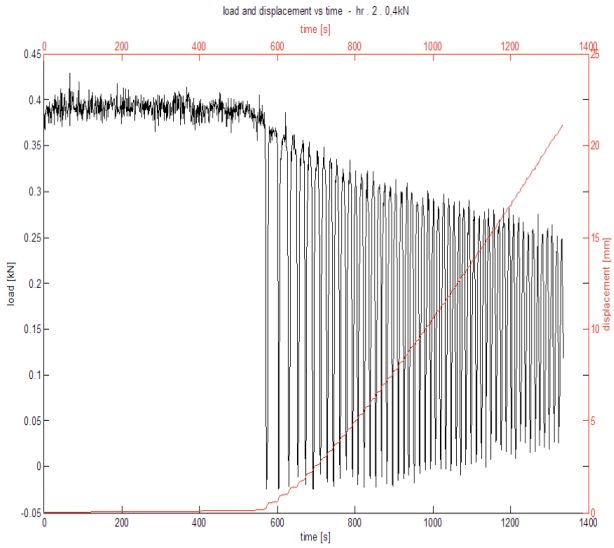

Figure 9a. (above left)
Axial load and axial displacement over time.
Constant load = 0.4 kN. Smooth roughness.

Figure 9b. (above right)
Axial load and axial displacement over time.
Constant load = 0.4 kN. Middle roughness.

Figure 9c. (left)
Axial load and axial displacement over time.
Constant load = 0.4 kN. High roughness.

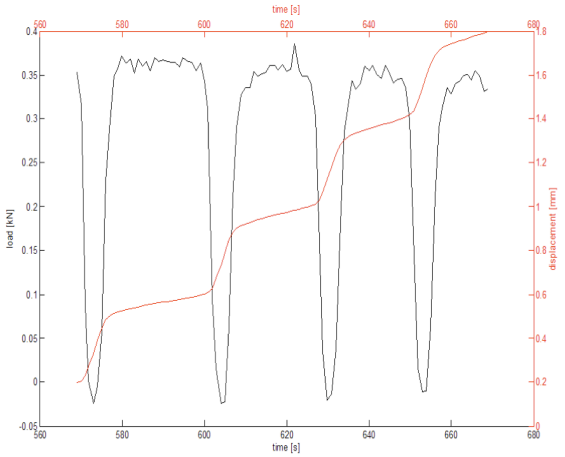

Figure 10a. Axial load and axial displacement over time (from 570 sec to 670 sec). Constant load = 0.4 kN. High roughness. 100 sec lag (beginning of the second phase).

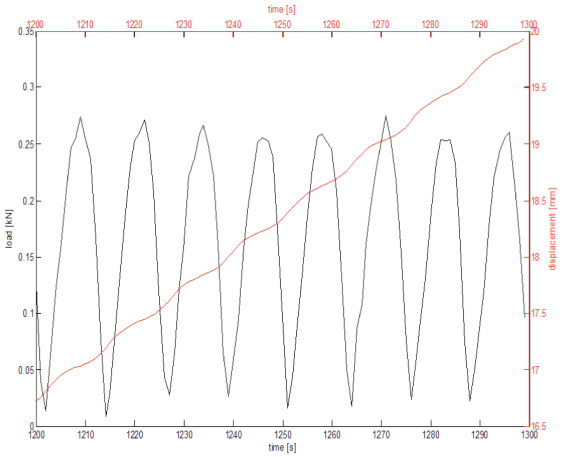

Figure 10b. Axial load and axial displacement over time (from 1200 sec to 1300 sec). Constant load = 0.4 kN. High roughness. 100 sec lag (end of test).

Figures 11a. and 11b. show the variation of the period of load oscillations in time for samples with high and middle roughness, respectively. The higher the load, the smaller the period and the quicker the damping effect over time: with high testing loads, the curves tend to become sub-horizontal after a certain time lag, and therefore the period stabilizes and becomes independent from time. For high loads, the period is clearly longer for samples tested with high roughness than for those tested with middle roughness. For tests hr_1_0,2kN and hr_4_0,2kN the period differs for about a 10 sec offset that seems to be constant during the whole test duration. Sample mr_3_0,3kN has a starting period in the order of the period at which mr_2_0,3kN was interrupted; it is interesting to point this out, since the two tests were performed on the same sample but half a day apart.

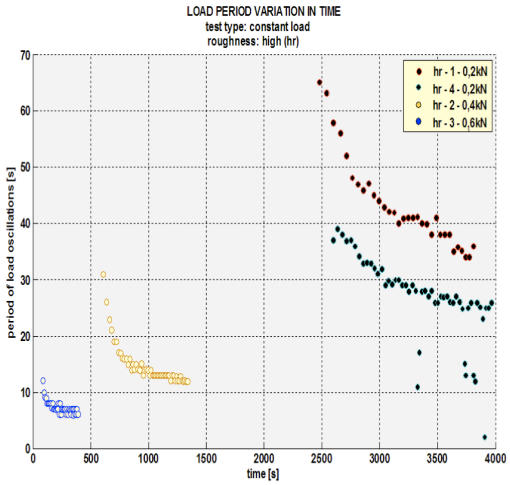

Figure 11a. Variation in time of the load period during the second phase for different constant loads. High surface roughness.

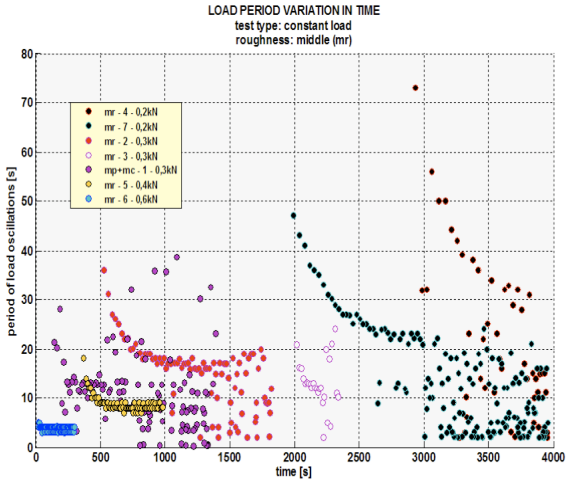

Figure 11b. Variation in time of the load period during the second phase for different constant loads. Middle surface roughness.

Figures 12a. and 12b. show the variation in time of the load amplitude for tests with high and middle roughness, respectively. All the times are initialized at zero, which means time refers to the beginning of the second stage. The load amplitude decreases with time. The higher the load, the quicker the damping effect. In Figure 11a., tests hr_2_0,4kN and hr_3_0,6kN have the same amplitude at the beginning of the second phase (clearly higher than the starting amplitudes of the samples tested with 0.2kN), then the two curves visibly diverge. Hr_1_0,2kN and hr_4_0,2kN have a rather constant difference (about 0.04 kN) throughout the test duration. For the latter pair the amplitude seems to get rather constant as the test approaches the end. In Figure 12b., some curves approach very small values in load amplitude (in the order of a few hundredths of kN). Sample mr_3_0,3kN starts with a considerably high load amplitude compared to the end values of test mr_2_0,3kN, yet the curve is much steeper and it dampens more quickly. It cannot be clearly said that the higher the load the higher the starting values of amplitudes, since there are some inconsistencies: mr_4_0,2kN, mr_7_0,2kN, mp+mc_1_0,3 and mr_6_0,6kN have almost the same starting value of amplitude, then the curves diverge. Values for mr_4_0,2kN are rather scattered.

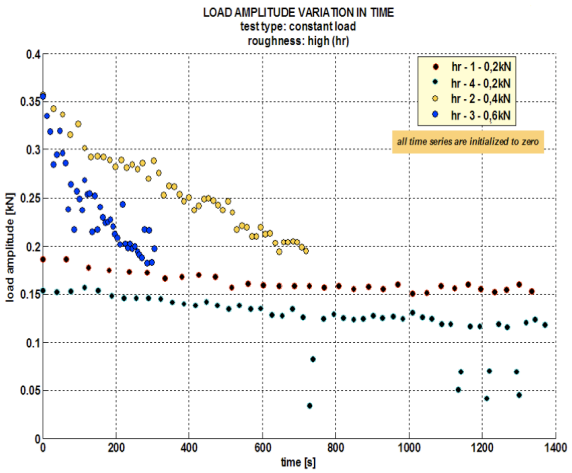

Figure 12a. Variation in time of the load amplitude during the second phase for different constant loads. High surface roughness.

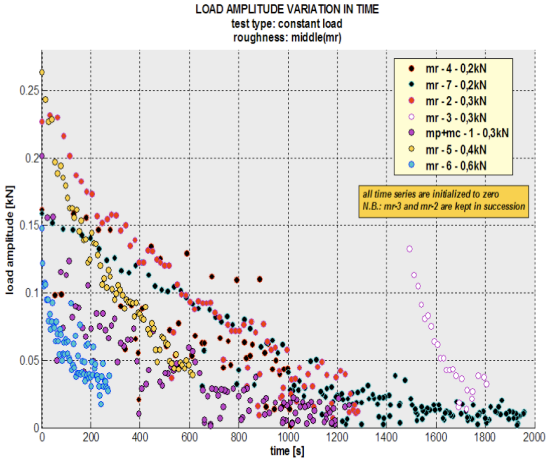

Figure 12b. Variation in time of the load amplitude during the second phase for different constant loads. Middle surface roughness.

Figure 13. shows the variation of the displacement step in time; values for middle and high roughness samples are compared. For every period, the change in displacement (step) was computed and the correspondent period time associated to it. As can be clearly noticed, there are two main values around which the values are plotted: 0.4 mm and 0.25 mm. This means that the displacement step tends to be quite constant with time, especially for samples with high roughness, and it seems independent of the load. Values for middle roughness have a wider range of dispersion (~0.05 mm) than values for high roughness (~0.02 mm). For middle roughness, the scattering greatly increases with time.

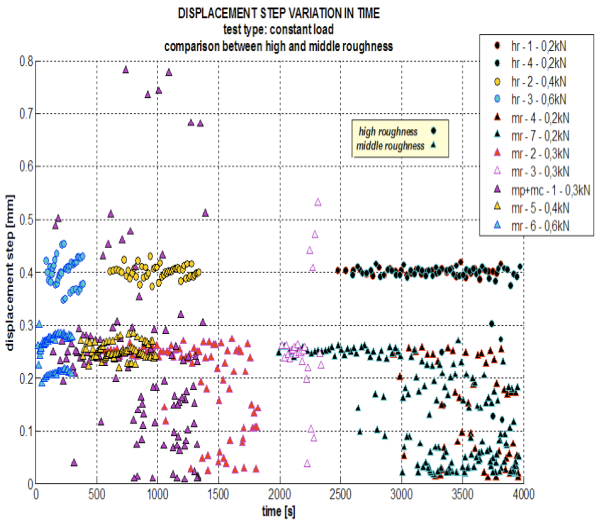

Figure 13. Displacement step variation in time. Values obtained for different roughness (high – middle) are compared taking the effect of load into account.

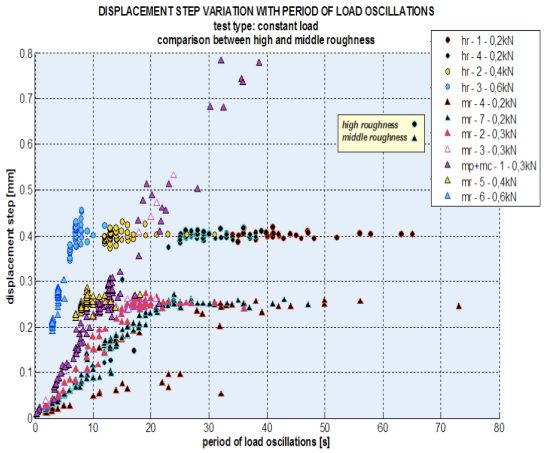

Figure 14. Displacement step variation with period of load oscillations: comparison between high and middle roughness.

Figure 14. displays how the displacement step varies over the period and compares the results for the different values of surface roughness and load. The two distinct values of 0.4 mm and 0.25 mm for high and middle roughness, respectively, can be identified again. The step seems to be constant with decreasing period until a certain threshold value, after which it drops linearly with the period itself. The critical period seems to get shorter, the higher the load. The rate of decreasing step is higher, the higher the load. Furthermore, the higher the load, the shorter the stable phase seems to be. For samples mr_3_0,3kN and mp+mc_1_0,3kN, the threshold cannot be seen at all and the values are aligned even above the 0.25 mm line. It can be noticed, in addition, that the rate of the decreasing displacement step depends on the load but it is independent of the roughness: samples hr_4_0,2kN and mr_7_0,2kN constitute a quite clear example, as do hr_3_0,6kN and mr_6_0,6kN.

In Figure 15. the amplitude variation over the period is compared between high and middle roughness for loads equal to 0.4 kN and 0.6 kN (semi-logarithmic scale). The higher the roughness, the higher the amplitude. More than one main frequency can be identified. The yellow and the blue curves look like the same curve translated of a couple of seconds: the load seems responsible for this. The higher the load, the higher the frequency. In Figure 16. the amplitude variation over period is compared between high and middle roughness for 0.2 kN of load. Test mr_7_0,2kN displays a clear s-shaped curve. The upper part of the curve seems rather continuos while as the amplitude decreases, at the bottom of the curve, many discrete frequencies can be clearly identified within the same amplitude range. The other samples seem to fit the higher part of the same curve. Mr_4_0,2kN gives more scattered results. The data for middle roughness tests dampen down to smaller amplitudes values. For comparison with Figure 15., it can be noticed that the higher the load, the higher the initial level of amplitude but, on the other hand, the narrower the range of measured frequencies; it was confirmed that smaller loads produce low frequency oscillations in the initial stages of sliding.

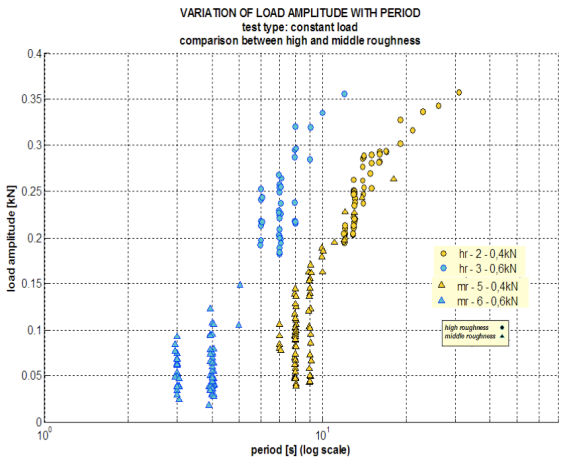

Figure 15. Variation of load amplitude with period (log scale). Comparison between high and middle roughness for 0.4 kN and 0.6 kN.

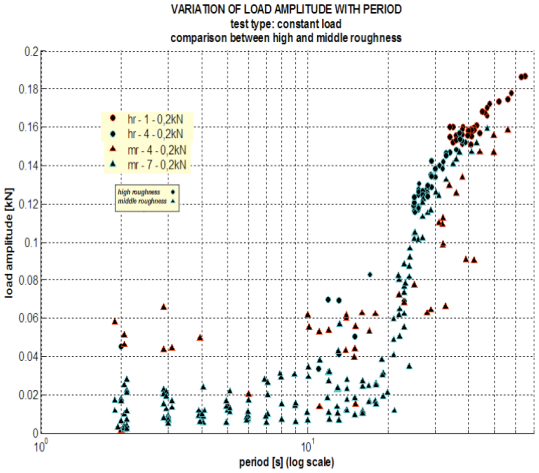

Figure 16. Variation of load amplitude with period (log scale). Comparison between high and middle roughness for 0.2 kN.

5 Discussion

By looking at the graphs displaying axial load and displacement over time (Figure 17.), two distinct phases can be clearly distinguished for samples with high and middle roughness: a first phase during which the displacement is nearly nil and the load oscillates around the set value, followed by a second phase during which sliding occurs in a stick-slip fashion and the load oscillations change in amplitude and period. The period decreases with time and tends to become constant (the higher the load, the more evident this trend). The amplitude is dampened with time: the higher the load, the quicker the effect. For lower loads, the amplitude variation is much shorter and the curves tend to flatten out. The higher the roughness, the higher the load amplitude. As can be observed from Figure 17., the displacement rate seems similar for samples tested with the same load, independently of roughness. The higher the load, the higher the velocity. The duration of the first stage depends on both the load and the roughness: it shortens as the load increases and as the surface asperities flatten out. Mr_4_0,2kN is the only exception. Figure 17a. gives an idea of the repeatability of the experiments. There can be many differences between one sample and another, the test parameters being the same. Therefore, the reason might be sought in the ice´s physical properties such as porosity, structure, etc., which can vary from sample to sample. For instance, mr_4_0,2kN has a lower salinity content than mr_7_0,2kN (-1.8 ppt), hr_1_0,2kN (-0.5 ppt) and hr_4_0,2kN (-2.3 ppt). For smooth roughness, the starting time can be considerate immediate, in the range of the tested loads. Relative sliding between ice and the cylinder occurred only for these samples. This effect could not be explained. When the device was designed, an ice/piston relative sliding was expected: if the system is considered to be in equilibrium during the first stage, the same load is transmitted from the cylinder to the ice annulus, and from this to the piston; on the other hand, the tangential stress on the inner surface of the annulus is 3.3 times higher than the tangential stress on its outer surface, since the ratio of the contact areas is 1 to 3.3. Therefore the visco-plastic deformation of the ice asperities is supposed to be higher at the piston shaft and an ice/piston relative sliding would be expected. The truth is that, while the first phase can be observed for high and middle roughness samples, it is negligible for smooth samples, and therefore, for the last ones, the system can never be in static equilibrium.

Figure 14. gives interesting results. The displacement step seems to have two reference values: ~0.4 mm and ~0.25 mm for high and middle roughness respectively. It is immediately noticeable that these values are comparable with the nominal representative values for the roughness asperities (0.4 mm and 0.25 mm). When the load is applied to the system, the ice absorbs energy to deform elastically at first (immediate deformation) and then visco-elastically-plastically with time. As the asperities deform (some ice might even melt at the interface), the adhesion with steel decreases until the load exceeds the friction force and the slip takes place. It seems that in the slip phase the ice slides for a distance leg equal to the distance between two consecutive asperities. When the ice asperities have overridden the steel asperities of one step, part of the energy is released and the friction force contrasts the load again, some adhesion is regained, and the system needs time to move the following step. Yet, as time passes, the plastic deformation increases, and the time required for the frictional force to be overcome decreases. This is in accordance with what is observed from the graphs. After a certain critical period (function of

load and roughness), the deformation is such that the step decreases in time linearly with the period itself, and at a rate which depends on the load only. From pictures taken with the stereoscope (Figure 18. shows an example), it can be observed that, in reality, the steel surface is composed of many intermediate crests within a representative length. These smaller asperities might have an influence on the load oscillations and give a reasonable explanation to the presence of higher frequencies. Furthermore, the influence of the grain boundaries, in the order of tenths of a mm, as observed from thin sections of the specimens, might be a reason for lower frequencies. Anyway, 0.1 Hz seems a reasonable representative average value for the registered frequencies. For the smoothest roughness the behavior is much more complicated to analyze. The oscillations were more random and no clear correspondence between the displacement step and the representative roughness length could be found. A deeper analysis of random vibrations phenomena is advised.

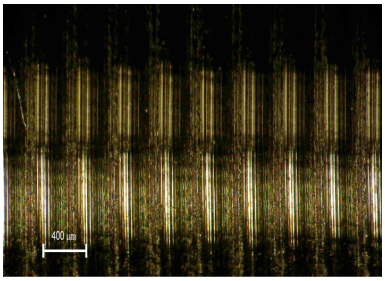

Figure 18. Piston surface roughness magnified 32.5 times (high roughness). Main pitch between asperities: 0.4 mm. Smaller asperities are visible.

5.1 Development of the experiment: guidelines for future studies

The experiment performed has shown interesting results and trends which deserve a deeper analysis. The importance of understanding the stick-slip motion phenomenon can be mostly related to ice-induced vibration on structures. According to present knowledge, the destruction of ice grains at the structure interface during crushing is thought to be responsible for the induced vibrations. This study, on the other hand, reveals that roughness itself might induce vibrations, even in the case of a smooth steel surface. For instance, vibrations could also occur when ice slides on an ice-breaking cone. Furthermore, pure thermal expansion of ice could cause vibrations on structures even if crushing does not take place. If further experiments are carried out, more attention should be paid to the sensitivity of the uniaxial compression rig. A strain gauge whose working range better fits the applied loads is advised. Also considering that Knekkis is a step machine, some of the observed load oscillations (above all in the high frequency range) might be due to a systematic behavior of the machine itself and not to the physics of ice/steel interaction. To understand to what extent this influences the results, a deeper analysis of correlation between data is suggested.

These experiments are quite powerful, above all because they allow researchers to vary many parameters and study their reciprocal influence on friction. Temperature, relative velocity, load, surface roughness (different roughness of cylinder and piston can be combined), and water salinity, are all parameters whose influence can be easily taken into account. Furthermore, a different shape of the indenter, that is the piston cross-section, can be tested: for example a triangular shape (with sharp edges) could be chosen. Some coatings could be applied or even some geo-textile materials interposed. Constant velocity tests are explicitly advised.

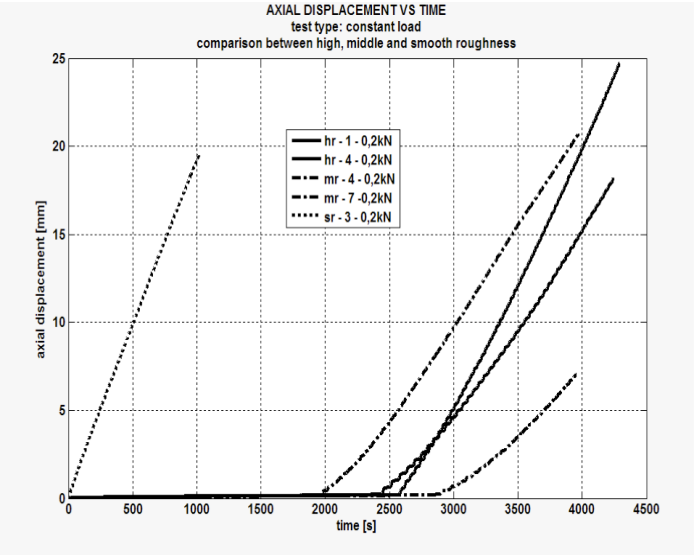

Figure 17a. Axial displacement over time for 0.2 kN of constant load: comparison between samples with high, middle and smooth roughness.

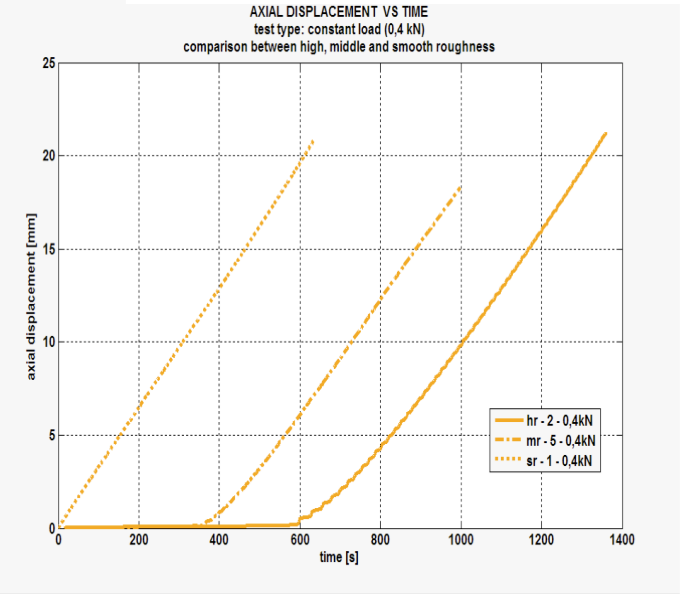

Figure 17b. Axial displacement over time for 0.4 kN of constant load: comparison between samples with high, middle and smooth roughness.

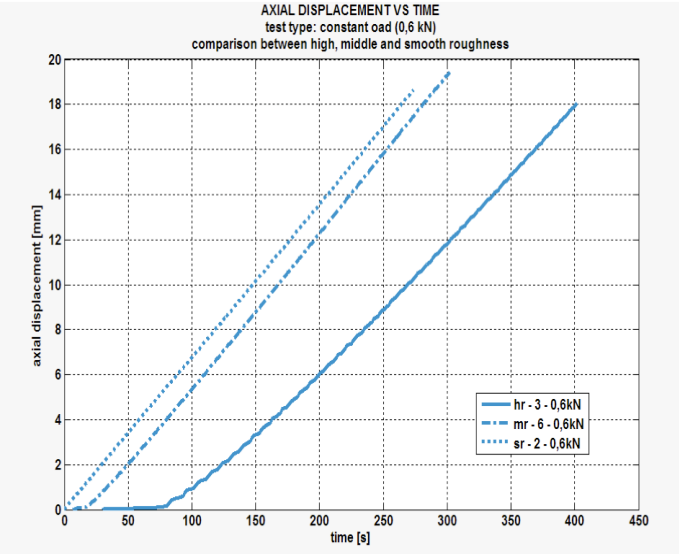

Figure 17c. Axial displacement over time for 0.6 kN of constant load: comparison between samples with high, middle and smooth roughness.

What´s more, an indirect measure of the coefficient of friction could also be attempted. For instance, by applying force sensors onto the cylinder inner surface, the normal force exerted at the contact ice/cylinder could be measured and, subsequently, related to the tangential force (measured by the rig gauges) through the friction coefficient. The above mentioned load sensors should satisfy specific working conditions and dimensional constraints. The Multi-Handle Economical Load & Force Measurement system, comprised of the FlexiForce sensors A201 (flexible printed circuits which use a piezoresistive technology by Tekscan), is suggested as an option for further developments in this direction.

6 Conclusions

The design of a device to test friction between saline ice and steel was presented. The aim of the experimental study was to understand to what extent load and roughness influence friction and how their action is related. All in all, 14 constant load tests were carried out within the cold laboratory at UNIS on samples of laboratory produced saline ice at the temperature of -10 ºC. Three different values of roughness were tested: smooth (R_y = 1.2 μm), middle (R_y = 10 μm) and high (R_y = 30 μm). The tested loads were 0.2, 0.3, 0.4 and 0.6 kN. Particular attention was paid to grow ice from sea water in the laboratory. A numerical value for the coefficient of dynamic friction could not be estimated, but the main conclusions are:

1. A stick-slip motion with a characteristic frequency of 0.1 Hz was observed.
2. For high and middle roughness, the displacement during the slip phase was comparable to the mean nominal pitch of the profile (S_m).
3. The amplitude of the oscillations dampened, most probably due to creep.
4. The higher the load, the earlier the onset of the stick-slip motion and the quicker the damping of both amplitude and period.
5. The smooth-roughness samples failed to show the same characteristics, and their behavior is more difficult to explain.
6. The displacement rate seemed to be independent on the roughness.
7. The higher the roughness, the later the onset of the stick-slip motion, and the higher the amplitude of the oscillations.

The roughness seems to be fundamental in determining the oscillations pattern for the stick-slip motion. This effect can be important in offshore structures design. Ice-induced vibrations can occur not only from crushing ice but also from simple sliding. Guidelines for a future development of the experiment were suggested.

Acknowledgments

Special thanks are due to:

- The Arctic Technology Department within UNIS for financing the whole project.
- Lorenzo Ruggeri from LGT, Rioveggio - Italy, for taking active part in the design and building the experimental device.
- Scott Gregory Gaines for his advice regarding English usage.

References

Barnes, P., Tabor, D., Walker, J.C.F., 1971. The friction and creep of polycrystalline ice. Proc. the Royal Society of London. Great Britain, A324, pp. 127-155.

Kärnä, T., Shkhinek, K.N., Kapustiansky, S.M., Jilenkov, A.G., 2000. Numerical simulation of dynamic ice-structure interaction. VVT Research Notes. Technical Research Centre of Finland, ESPOO.

Løset, S., Shkhinek, K. N., Gudmestad, O. T., and Høyland, K. V. (2006). Actions from Ice on Arctic Offshore and Coastal Structures. LAN St. Petersburg, ISBN S-8114-0703-3. 266 p.

Nakazawa, N., Terashima, T., Saeki, H., Ono, T., 1993. Factors influencing the coefficient of friction between sea ice and various materials. Proc. 12th International Conference on Port and Ocean Engineering under Arctic Conditions, 17-20 August 1993. Hamburg, Vol. 1, pp. 97-105.

Nakazawa, N., Terashima, T., Saeki, H., 1994. Ice-material surface interaction in ice friction and ice adfreeze bonding. Proc. Fourth (1994) International Offshore and Polar Engineering Conference, April 10-15, 1994. Osaka, Japan, Vol. 2.

Oksanen, P., 1980. Coefficient of friction between ice and some construction materials, plastic and coatings. Espoo 1980. Technical Research Centre of Finland, Laboratory of Structural Engineering, Report 7, 73 p.

Persson, B.N.J., 2000. Sliding friction. Physical principals and applications. 2nd edition. Springer, 515 p.

Shkhinek, K.N., Kärnä, T., Kapustiansky, S.M., Jilenkov, A.G., 1999. Numerical simulation of the ice failure process. Proc. POAC Conference, ESPOO. Vol. 2, pp. 877-887.

Tabata, T., Tusima, K., 1981. Friction measurements of sea ice on some plastics and coatings. Proc. of 6th International Conference on Port and Ocean Engineering under Arctic Conditions, July 1981. Quebec, Canada, Vol.1.

Tatinclaux, J.C., Forland, K.A., Murdey, D., 1986. Laboratory and field studies of ice friction coefficient. Proc. IAHR Ice Symposium 1986. Iowa City, Iowa.

19th IAHR International Symposium on Ice
"Using New Technology to Understand Water-Ice Interaction"
Vancouver, British Columbia, Canada, July 6 to 11, 2008

Evaluation of area extent of structure body of marine engineering constructions suffering ice abrasion

Alexander T. Bekker, Tatiyana E. Uvarova, Maria A. Slautenko
Far Eastern State Technical University
Vladivostok, Russia
bekker@mail.primorye.ru

The paper considers an issue of extent of abrasive impact of ice cover on structure body. Complexity and insufficient exploration level of physical process of ice destruction during interaction with sea constructions, structures specificity, comparatively inconsiderable volume of experiments (especially natural) on ice pressure measurement cause urgency of this problem.

The authors have worked out the algorithm and computer program of ice impact calculation defining abrasion extent of structure body with drifting ice fields subject to following factors: ice strength properties, bearing form in the draft, speed and moving direction (drift) of ice fields and compacting of ice cover.

However, it should be noted that structure body abrasion is highly affected with sea level fluctuations. This paper specifies estimation algorithm subject to sea level fluctuations which define area extent of structure body of marine engineering constructions and abrasion degree of its surface.

Introduction

The authors suggest the design procedure of abrasion extent subject to probabilistic characteristics of entry parameters in order to calculate and forecast ice abrasion of construction material. Principal concern is given to the interaction area of ice plate with construction. The program under development on dusting with ice cover subject to level fluctuation will be able to reveal the most unfavourable level of ice loading and as a result to optimize ice belt structure or develop local strengthening of concrete bottom using high-strength concrete.

Problem statement

Construction of marine engineering constructions in the areas of water of freezing seas makes it necessary to thoroughly consider ice impact. Marine constructions are influenced with abrasive impact of ice cover in the zone of variable sea level.

When define construction area suffering abrasive impact of ice formations in present water area, it's necessary to take into account following factors of great importance:

a) sea level fluctuations;

b) thickness variation of drifting ice formations;

c) failure mechanism of ice formation while contacting with marine engineering constructions.

It's common knowledge that abrasive impact depends on ice cover's length (path) that has an abrasive impact on the construction (l) and contact pressure during sliding of ice formation in the contact area (σ) (Yoshishige Itoh, Yoshihiro Tanaka et al, 1995). These characteristics are calculated on the base of program developed by Bekker A.T., Uvarova T.E., Kim S.D. (Bekker AT, Uvarova TE, Kim S. D.,2004).

Material abrasion mechanism as a result of sea ice-floe movement and abrasion intensity subject to level fluctuation was studied by the group of scientists Saeki, H. and Takahiro Takeuchi (Takahiro Takeuchi et al, 2006). They managed to receive dependence of abrasion extent of construction material on sea level fluctuation $dA_z(t)$ in the point of "z" during time period dt, where tidal change is accepted as sinusoid curve W(t) (Fig.1).

$$W(t) = A_1 \sin(\frac{2\pi}{T} t) \qquad \textbf{[1]}$$

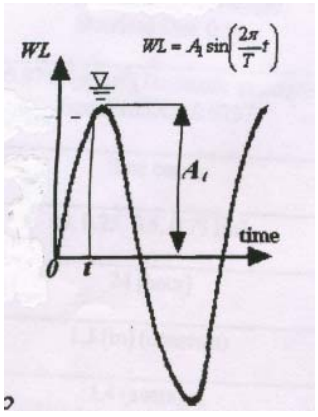

Figure 1. Tidal Change

In addition, even though a tidal change is assumed to follow a sine curve here, active area and total amount of abrasion are strongly influenced by tidal change, especially (A_1). Therefore, it is better to use precise data of tidal change in the considered sea area for the estimation.

However, it should be noted that A_1 value – height of sea level surface above predicted level in the paper (Yoshishige Itoh, Yoshihiro Tanaka et al, 1995) is accepted as constant. In many cases amplitude of level fluctuation can change and we believe that it would be appropriate to accept factual observed data of level fluctuations as a distribution curve for specified area of water.

To account for tidal impacts, amplitude of level fluctuations is set as a distribution curve (Fig. 2), received on the basis of frequency curve of hourly heights of sea level above 0 post that can make it possible to evaluate abrasion of construction material for whole ice period on height.

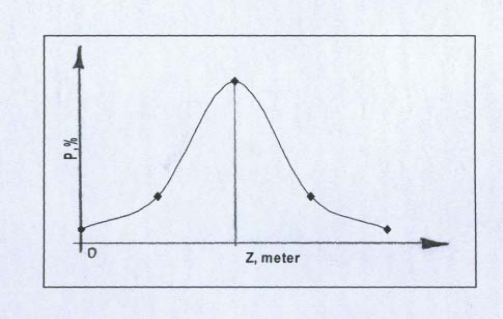

Figure 2. Distribution curve of tidal change

Estimation algorithm of probabilistic characteristics of ice load includes distribution of level fluctuation among other data influencing abrasion extent of the construction. You can see the flow block of the program in the Fig. 3

Order of probabilistic *factors calculation effecting abrasion, and abrasion values of construction material.*

Basic data for calculation are: construction characteristics (diameter of construction **d**, form of bearing **m**), ice cover characteristics (speed of ice drifting **V**, ice field thickness **h**, compacting of ice **N**, ice strength **R**, ice-floe diameter **D)** and value of sea level fluctuation **Z**. Ice cover characteristics, defining ice regime of the area of water, are accepted as chance variables and presented as per decade distributions built on the base of long-term observations in the exact area of sea areas of water.

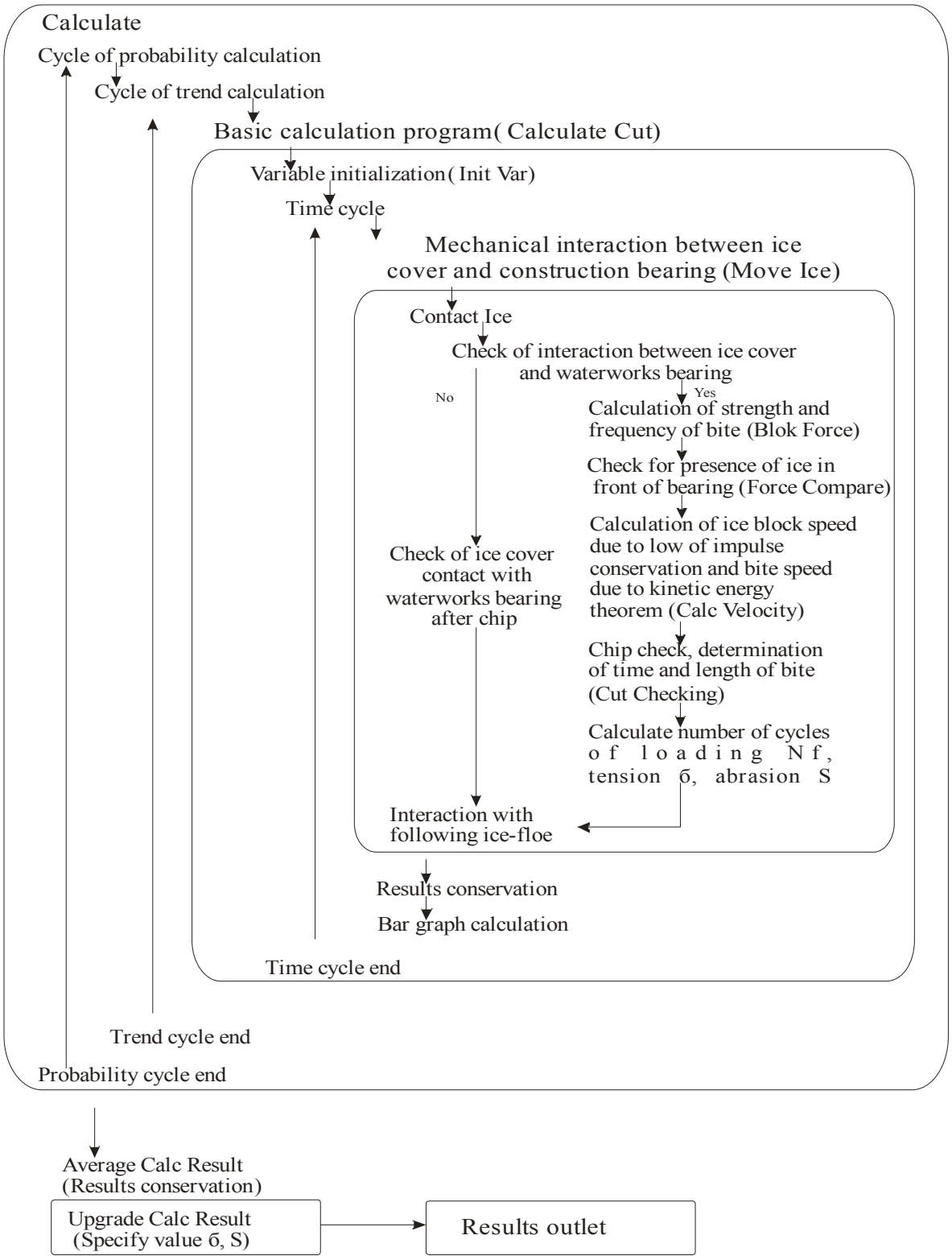

Figure 3. Block diagram of calculation of abrasion impact on construction bearings with drifting ice cover

1. There carried out modeling of ice regime with searching of entry parameters: **h**, **D**, **N**, **R**, **V, Z** so that hug all estimated situations that is all possible parameter combinations.

As a result of **k**-th stage on time (**k**-th decade) and **i**-th parameter combination we imitate (model) specific situation of ice regime with following parameters: $\mathbf{h_{ki}}$, $\mathbf{D_{ki}}$, $\mathbf{N_{ki}}$, $\mathbf{R_{ki}}$, $\mathbf{V_{ki}}$, , $\mathbf{Z_{ki}}$. Besides, there determined probabilities of their appearance $\mathbf{p^h_{ki}}$, $\mathbf{p^D_{ki}}$, $\mathbf{p^N_{ki}}$, $\mathbf{p^R_{ki}}$, $\mathbf{p^V_{ki}}$, $\mathbf{p^Z_{ki}}$

2. There defined time of existence of i-th combination of characteristics of ice regime t_k subject to probabilistic combination of characteristics.

3. On every **i**-th stage of imitation calculation there modeled a process of mechanical interaction between ice fields with MSP bearing of thickness $\mathbf{h_{ki}}$, ice field dimensions $\mathbf{D_{ki}}$, concentration $\mathbf{N_{ki}}$, strength $\mathbf{R_{ki}}$ and speed $\mathbf{V_{ki}}$, also subject to water level fluctuation $\mathbf{Z_{ki}}$ The process under discussion has a length $\mathbf{t_{ki}}$.

Modeling process is accompanied by evaluation of interaction character (stop, bite, bulk) as well as ice plate failure character subject to interference between dimensions and concentration of ice.

As a result of this process's modeling there received ice loading value $\mathbf{F_{ki}}$, time of bite $\boldsymbol{\tau}_{\mathbf{ki}}$, period $\mathbf{T_{ki}}$ and number of cycles $\mathbf{n_{ki}}$ of loading.

4. On the base of findings there modeled an abrasion process of construction material. As a result there received abrasion depth of construction material S subject to sea level fluctuation.

5. The process will be repeated to full search of all possible combinations of ice regime parameters (situations) **NumK** and as a result there defined following characteristics of the process for whole ice period:

- total abrasion depth

$$S = \sum S_i \qquad \textbf{[2]}$$

- spread of abrasion depth subject to level fluctuation

$$S = \mathrm{f}(z) \qquad \textbf{[3]}$$

Average depth of construction's abrasion $\overline{S}$ is accepted as out parameter of the presented model.

Conclusion

Some zones of ice seas' areas of water have ice cover of high dynamics that effect abrasion extent of marine engineering constructions. This paper specifies estimation algorithm of abrasion extent subject to sea level fluctuations. So, considering ice impact on construction from every quarter, one can imagine whole picture of abrasion extent of construction's material with ice cover throughout the surface in the draft in the contact area. It's very important while designing of protective ice belt and detection of the most unfavorable direction of ice impact.

References

Yoshishige Itoh, Yoshihiro Tanaka, Alberto Delgado, Hiroshi Saeki (1995)."Abrasion Mode of a Circular Cylindrical Concrete Structure Due to Sea Ice Movement," *Proc. of 5th Int Offshore and Polar Eng Conf, Netherlands, Vol 2*, pp. 381-388

Bekker AT, Uvarova TE, Kim S. D. (2004). "Numerical Simulation of the Process of Interaction between Drifting Ice Fields and Structure Support". *Proceedings ISOPE Conf.*,v.2,

Vladivostok, p.365-378.

Takahiro Takeuchi, Shinji Kioka, Hiroshi Saeki (2006). “Significance of Tidal Change on Abrasion Area of Structures Due to Sea Ice Movement,” Proc. of 18th IAHR International Symposium on Ice, pp. 129-136

Kim S.D. High-cycle and abrasion influence of drifting ice cover on sea waterworks. Thesis.- Vladivostok City, 2005.

19th IAHR International Symposium on Ice
"Using New Technology to Understand Water-Ice Interaction"
Vancouver, British Columbia, Canada, July 6 to 11, 2008

Ice Rubble Build-Up on a Shoulder Ice Barrier in Shallow Water

Arne Gürtner[1], Karl-Ulrich Evers[2] and Ada Repetto[1]
[1] *Norwegian University of Science and Technology (NTNU), Department of Civil and Transport Engineering, Høgskoleringen 7a, 7491-Trondheim, Norway*
[2] *Hamburg Ship Model Basin (HSVA), Bramfelder Str. 164, D-22305 Hamburg, Germany*
arne.gurtner@ntnu.no, evers@hsva.de, ada.repetto@ntnu.no

ABSTRACT
Ice model tests have been performed on a newly designed ice protection structure, termed the Shoulder Ice Barrier (SIB), in the large ice tank of the Hamburg Ship Model Basin (HSVA). The model tests in ice were part of the SIB concept verification study. This paper analysis the rubble build-up on the SIB under the influence of various observed ice failure modes. Special attention is attributed towards investigating distinct phases of rubble build-up and their accompanying ice forces to the SIB. In the mode where the ice sheet fails on mobile rubble situated upstream, the observed ice forces are typically high of short duration. An attempt of relating ice breaking frequency to the periodical ice failure is herein presented.

1. Introduction

Ice protection structures have been employed in shallow waters to protect offshore exploration and production facilities from impacts of drifting ice (e.g. Potter et al., 1984; Evers et al., 2001; Jochmann et al., 2003). Different ice protection structures have been discussed in the literature to obtain the desired protection. Barker and Timco (2005) presented a summery of the current practice. Yet another design, the Shoulder Ice Barrier (SIB), was presented by Gürtner et al. (2006) and further analysed in Gürtner et al. (2008). The design builds upon stabilizing fragmented ice on the characteristic shoulder section of the SIB, such as to increase the resistance against sliding along the sea bottom. In case of a wide structure, ice fragmentation at the SIB is constrained from bypassing and contributes towards forming grounded ice rubble upstream. The load reducing effect of grounded rubble has, amongst others, been recognized by Potter et al. (1984) and Marshall et al. (1989).

Ice model tests on the SIB were performed in the large ice tank of the Hamburg Ship Model Basin (HSVA) to investigate the general performance under ice loading. Particular emphasis was on the study of the rubble build-up process at the structure. This paper investigates the distinct phases of rubble build-up based on model scale observations. Special emphasis is attributed to the ice failure mode and the accompanying ice force. The ice breaking length is seen to be a vital parameter of the ice accumulation. In this regard, the ice breaking frequency is analysed for the purpose of estimating ice breaking lengths based on the force trace. The method for estimating ice breaking length is verified by visual observations. Finally, the estimates for the breaking length are compared to observations referred in the literature. Throughout this paper full scale magnitudes are presented, unless otherwise mentioned.

2. SIB Model Tests

The SIB model tests commenced in simulated shallow water conditions typically encountered in the Northern Caspian Sea (NCS). For a review of the environmental conditions in the NCS see Gürtner et al. (2006) and the references therein. According to an assumed deployment in the NCS the water depth was, hence, set to 6 m and the simulated ice drift velocity was set to 0.5 m/s. All model tests were conducted in natural grown, columnar grained level ice following the descriptions for preparation of Evers and Jochmann (1993). The ice thickness was 0.64 m and the flexural strength was 760 kPa. The model was scaled according to Froude's law, with a scaling factor of $\lambda = 20$. For details on general model scaling in ice the reader is referred to Schwarz (1977).

The experimental tank at HSVA is 78 m long, 10 m wide and 2.5 m deep. A shallow water bottom was installed to get the anticipated model scale water depth of 30 cm upstream the SIB. The seafloor was simulated by a wooden floor which extended 1.5 m upstream. Hence, seafloor topography was not taken into account. Fig. 1 shows the SIB model in the HSVA test tank. The base model was 1.5 m wide and at each of its sides dummy panels of 1.5 m width were attached to prevent submerged ice from bypassing. Thus, the whole arrangement had a width of 4.5 m, corresponding to 90 m in full scale. The dummy panels were not physically connected to the SIB model. The characteristic shoulder inclination was 10°. The set-up of the model SIB allowed for measurements of vertical forces on the shoulder section. Global ice forces were directly measured by three tri-axial load cells, situated at the interface between the bottom of the SIB and the shallow water bottom.

3. General Results

During the ice model tests, the SIB was pushed into a stationary ice sheet with a constant velocity of 0.5 m/s. Ice forces were sampled with a frequency of 100 Hz.

Fig. 2 depicts the global ice forces on the SIB per structure width as a function of time. Subplot a), b) and c) refer to the horizontal force in direction of rig movement F_x, the in-plane force F_y and the global downward acting vertical force F_z together with the shoulder force $F_{shoulder}$, respectively.

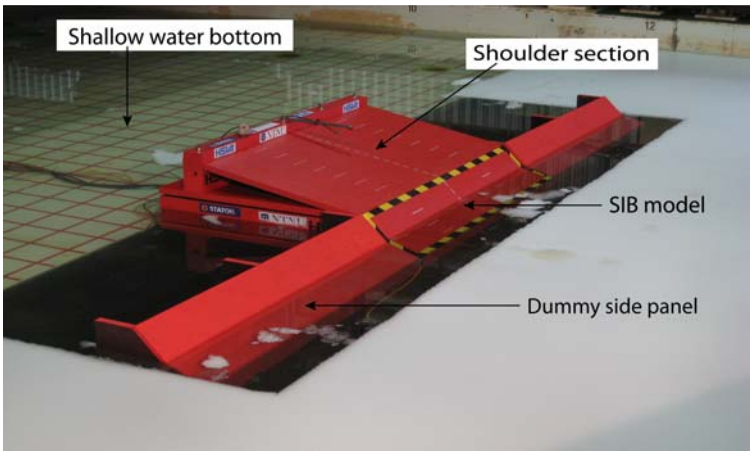

Figure 1. SIB model in the HSVA ice model basin.

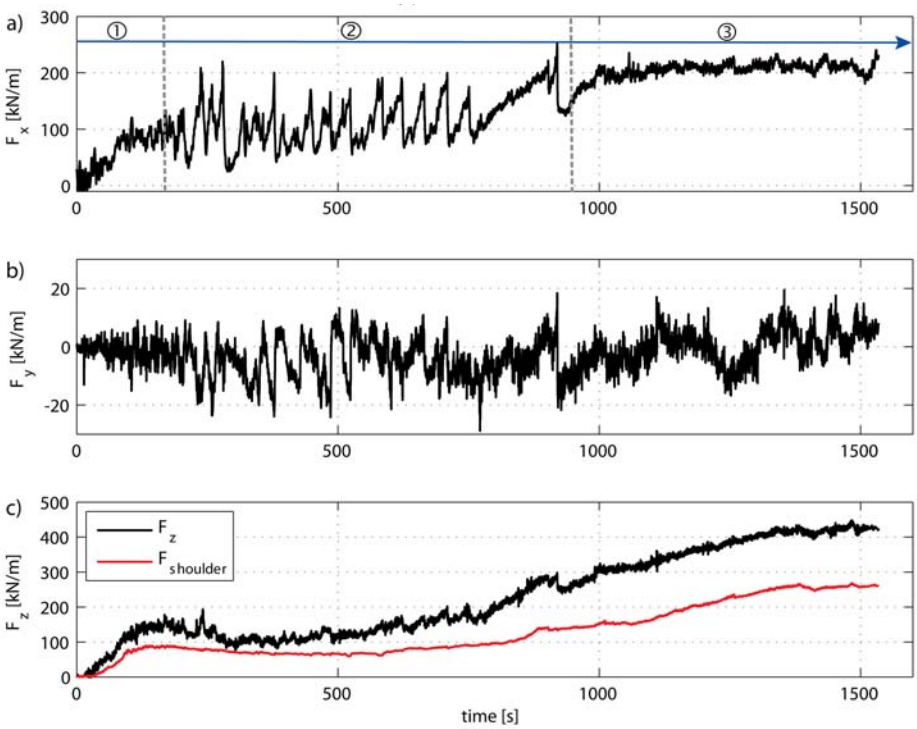

Figure 2. Force summary plot of one particular test run with set-up according to Fig. 1. a) horizontal force subdivided into three phases, b) in-plane ice force and c) global vertical force together with the shoulder force.

From Fig. 2 one may retrieve the fluctuating horizontal force signal during the rubble build-up phase. For convenience, the horizontal force history is subdivided into three main phases ①, ② and ③. Fig. 3 depicts snap-shots referring to these phases. Phase ① comprises steady build-up of horizontal force due to direct ice breaking onto the SIB surface. In this situation the so-called plate failure mode, which initiates planar bending crack zones in the ice with a regular failure pattern, dominates. In phase ② the force signal shifts character into a highly fluctuating force signal with significant peaks of short duration. This phase coincides with the rubble build-up phase, whereupon significant amounts of fragmented ice accumulate upstream. In phase ③ the horizontal force becomes steady. In this paper, special attention will be attributed to phase ②. The fluctuating in-plane forces are a result of asymmetric failure processes observed along the structure width. The influence of asymmetric ice failure is, however, not further analysed. The vertical forces are gradually increasing towards the end of the test run where ice becomes grounded. Shoulder forces are correlated to the global vertical forces. A rapid establishment of the vertical force can be observed. The ratio of the global vertical to the horizontal forces are above 1.5 for phase ③. The shoulder force raises to about 250 kN/m in this phase.

Figure 3. Overview of different phases in relation to Fig. 2,
a) phase ①, b) phase ② and c) phase ③.

For the purpose of investigating the horizontal force signal presented in Fig. 2 a), the original force signal has been converted to a frequency domain representation (Fig. 4 d and e) by applying the Fourier transform. Only the fluctuating force in phase ② is considered, as indicated in Fig. 4 a and the considered time interval is $200 \leq t \leq 800$ [s], as presented in Fig. 4 b). In order to achieve a stationary representation of the process the original force signal is de-trended and filtered (Fig. 4 c). Two different representations of the one-sided auto-spectral density are presented in Fig. 4 d) and e).

Fig. 4 reveals the nature of the frequencies involved during rubble build-up. The averaged spectral density functions have the highest values in the range of low frequencies with dominant frequencies below 0.4 Hz. This behaviour of the force time series has recently been identified as a peculiarity in dynamic ice-structure interactions on slender structures by Kärnä et al. (2007) for local ice crushing on a vertical lighthouse and Gravesen et al. (2005) for ice failure on vertical cylinders and cones.

The Fourier spectrum decreases with increasing frequencies. Subplot e) is plotted on semi-logarithmic scale for the purpose of revealing frequencies which might be in the range of natural frequencies. The otherwise smooth appearance of the curve in subplot e) shows a peak at the natural frequency of the model SIB of about 1.2 Hz. However, for the forces of significance the dependence of the structural response on the force signal can be disregarded.

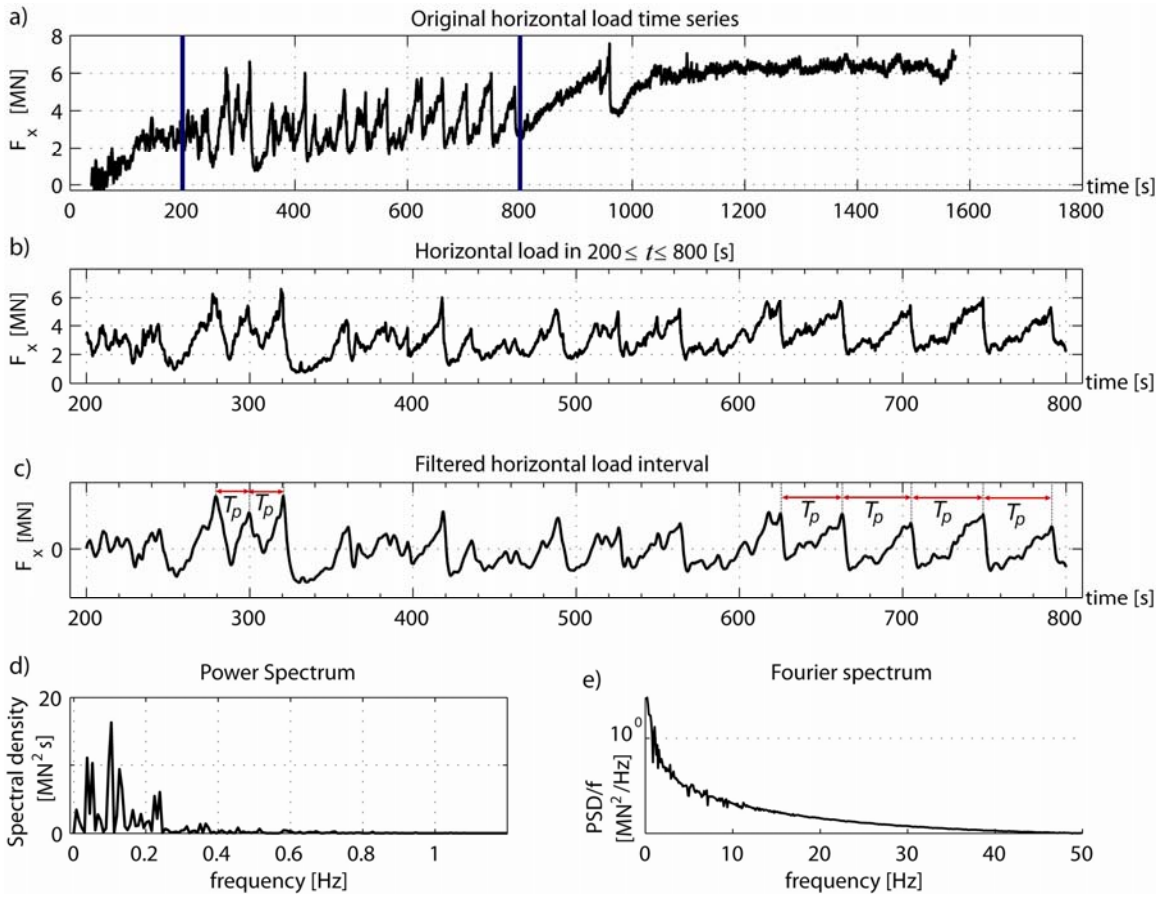

Figure 4. Spectral analysis of horizontal force signal. a) original horizontal force time series, b) extracted interval $200 \le t \le 800$ [s] of fluctuating, c) filtered force signal forces with several indicated peak periods, d) Power spectrum on linear scale and e) Fourier spectrum on semi-logarithmic scale.

4. Estimation of Ice Breaking Length and Rubble Build-Up

In Fig. 4 d) a frequency representation of the horizontal force history was established. The power spectrum showed dominating frequencies below 0.4 Hz. The spectrum will herein be utilized for the purpose of estimating breaking lengths of ice slabs which then govern the rubble build-up. The breaking length is here defined as the physical dimension resulting from flexural failure. The main assumption for employing this estimation method is that the force record incorporates the entire information about flexural failure. This assumption may be justified for phase ② as a result of the fluctuating force.

The power spectrum (Fig. 4 d) shows dominant frequencies in the interval $0.04 \le f \le 0.25$ [Hz]. If we assume that the force spectrum has a peak at the bending failure frequency due to a periodic force, then Eq. 1 may be employed to estimate the breaking length.

$$L_b = \frac{v}{f} \qquad [1]$$

where L_b is the breaking length and v the ice drift velocity. Insertion of the above frequency interval results in breaking lengths of $2\ \text{m} \leq L_b \leq 12.5\ \text{m}$. From the original force history (Fig. 4 c) a change of peak period T_p with time can be observed. Therefore, the power spectrum for phase ② was divided into three successive time intervals of equal length. The detailed power spectrum for the three respective time intervals is shown in Fig. 5.

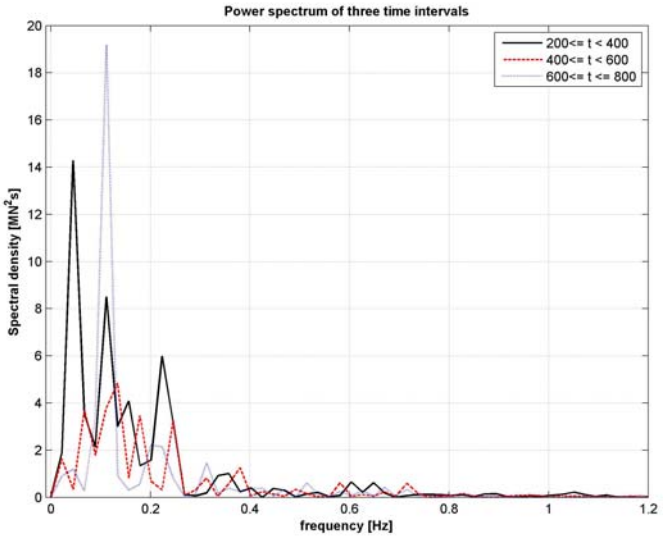

Figure 5. Power spectrum represented for three time intervals (i) $200 \leq t < 400$, (ii) $400 \leq t < 600$, (iii) $600 \leq t \leq 800$, each of 200 seconds length.

In the first interval investigated, the force spectrum centres its energy around three frequencies. That is, the breaking length may, in relation to Eq. 1, be considered to be spread. No dominating frequencies are found in the second interval due to a broad spectrum. The spectral density is considerably lower compared to the other two intervals investigated. A prevalent crushing component is most likely to be the reason for that. This is also in conformance with the force trace, where, in this particular interval, there are less significant force peaks, but a greater amount of local maxima. After 600 seconds the ice force had one dominant frequency of 0.11 Hz. This indicates that ice breaking is rather homogenous.

Due to the peculiarity of model ice, inspection of the rubble pile up did not reveal the original ice blocks involved during build-up. The ice rubble pile showed to be densely packed with vanishing porosity. Fig. 6 depicts the physical inspection. Fig. 7 illustrates the overall extensions of the ice rubble pile at the end of the test run. Note particularly the wedge formation of the rubble pile shown in Fig. 7 b) and c). The maximum ice rubble pile height was measure to be 8.3 m and the upstream extension of grounded ice even exceeded the shallow water bottom of 30 m length.

Figure 6. Physical inspection of the ice rubble pile in the centre.

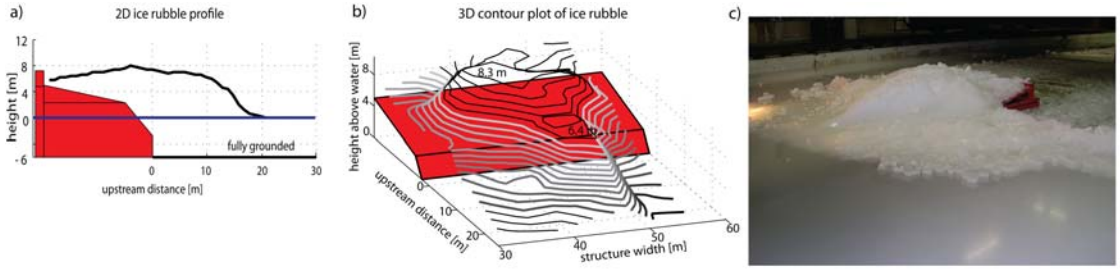

Figure 7. a) Side view of rubble accumulation on the SIB, b) three-dimensional contour plot of the rubble accumulation at the SIB, c) picture showing the model test rubble pile

5. Discussion and Conclusions

In contrast to ice breaking on cones (see review by Li and Yue, 2002), the breaking length of ice impacting a planar sloping structure and particularly the change of ice breaking length with increasing rubble dimensions has, to the authors' knowledge, not been analysed in full scale conditions. Lau et al. (1999), however, analysed the breaking length of ice on sloping structures based on model scale observations for ice thicknesses up to 0.25 m. They found a conversion limit for the non-dimensional ratio of breaking length L_b to characteristic length L_c of $l = L_b / L_c = 0.1$. The equation for the characteristic length based on a plate on elastic foundation is given below (Eq. 2).

$$L_c = \left[\frac{E \cdot h_i^3}{12 \cdot \rho_w \cdot g \cdot (1-\upsilon^2)} \right]^{1/4} \qquad [2]$$

where E is the elastic modulus, h_i the ice thickness, ρ_w is the density of the water, g the gravitational constant and υ the Poissons ratio. Extrapolation of the results to the present ice thickness of 0.64 m is questionable. If however, due to the brittle nature of flexural failure, the breaking is assumed to be purely elastic, then simple elastic theory predicts l = 0.78 (Hetenyi, 1946). Inserting test parameters $E = 5$ GPa (assumed); $h_i = 0.64$ m ; $\rho_w = 1020$; $g = 9.81$ m/s^2 ; $\upsilon = 0.3$ and applying the ratio predicted by elastic theory, the breaking length becomes $L_b \approx 8.1$ m . This length is on the high side of the estimated breaking lengths investigated above. Abdelnour and Sayed (1982), on the other hand, obtained for a model tests of a man made island

in shallow water a ratio of l = 0.5. Applying this ratio would lead to a breaking length of $L_b \approx 5.2$ m, which may be considered to lie in the middle of the estimated breaking length interval.

Visual observation by means of image analysis of the breaking length was only possible for phase ①, since in phase ② rubble accumulations restricted clear sight. As already mentioned, the plate bending mode prevails in phase ①. Fig. 8 shows a plot of the visual observations of the breaking length taken at distinct instances of time. It can be seen that for phase ① the breaking length interval is approximately $1.7\ \text{m} \le L_b \le 5.2\ \text{m}$, which is slightly less compared to observations of Abdelnour and Sayed (1982). For phase ②, only very few observations were possible. The breaking length was here observed to be approximately 8 m.

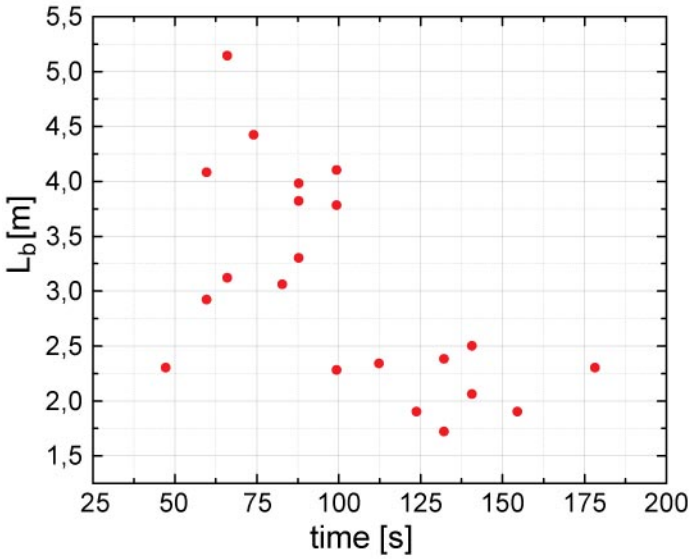

Figure 8. Breaking lengths at distinct time instances measured from image analysis during phase①

From what was presented in this paper it may generally be postulated that ice rubble build-up on offshore structures in shallow waters commences in different phases. In the experiment investigated, three distinct phases have been defined. Each phase is associated with a characteristic horizontal force level. The ice breaking length affects the rubble pile build-up. Global rubble pile build-up is, besides bending failure, governed by various other processes such as shearing and crushing. This alters the observed breaking length which showed to range between $2\ \text{m} \le L_b \le 12.5\ \text{m}$. Visual observations of plate bending failure in phase ① revealed a prevailing breaking length of $2\ \text{m} \le L_b \le 5\ \text{m}$. It has been shown that model scale investigations are able to reproduce observed full scale magnitudes of the breaking length. Due to disintegration of the columnar model ice when applying outer pressure, the ice pile up densities showed to diverge from what can be considered to be observed in nature. Opposed to slender structures, where the ice is able to clear around, the rubble build-up is seen to affect the breaking length. Thus, a constant breaking length cannot be assumed.

Acknowledgments
The work described in this paper was supported by the European Community's Sixth Framework Programme through the grant to the budget of the Integrated Infrastructure Initiative HYDRALAB III, Contract no. 022441(RII3). The authors would like to thank the Hamburg Ship Model Basin (HSVA), especially the ice tank crew, for the hospitality, technical and scientific support and the professional execution of the test programme in the Research Infrastructure ARCTECLAB.

The author furthermore gratefully acknowledges Statoil for funding the SIB model, the PETROMAKS programme, the Research Council of Norway, PetroArctic and StatoilHydro for funding this study.

References

Abdelnour A, Sayed W, (1982): Ice Ride Up on a Man-Made Island. Proceedings of the Offshore Technology Conference. Vol. 3, pp. 141-152, OTC-4313.

Barker, A. and Timco, G. (2005): Ice Rubble Generation for Offshore Production Structures: Current Practices Overview. Canadian Hydraulics Centre Technical Report CHC-TR-030. February 2005. 38p.

Evers, K. U. and P. Jochmann (1993): An Advanced Technique to Improve the Mechanical Properties of Model Ice Developed at the HSVA Ice Tank. Proceedings of the 12th International Conference on Port and Ocean Engineering under Arctic Conditions (POAC), Hamburg, Germany, pp. 877- 888.

Evers, K.-U., Spring, W., Foulkes, J., Kühnlein, W. and Jochmann, P. (2001): Ice Model Testing of an Exploration Platform for Shallow Waters in the North Caspian Sea. Proceedings of the 16th International Conference on Port and Ocean Engineering under Arctic Conditions, Ottawa, Canada, Vol. 1, pp. 254-264.

Gürtner, A., Gudmestad, O.T., Tørum, A. and Løset, S. (2006): Innovative Ice Protection for Shallow Water Drilling – Part I: Presentation of the Concept. 25th International Conference on Offshore Mechanics and Arctic Engineering, Hamburg, Germany. OMAE2006-92181.

Gürtner, A. and Gudmestad, O.T. (2008): Innovative Ice Protection for Shallow Water Drilling – Part II: SIB Model Testing in Ice. 27th International Conference on Offshore Mechanics and Arctic Engineering, Estoril, Portugal. OMAE2006-57015. (*to be published*)

Gravesen, H., Sørensen, S.L., Vølund, P., Barker, A. and Timco, G. (2005): Ice Loading on Danish Wind Turbines: Part 2. Analyses of Dynamic Model Test Results. Journal of Cold Regions Science and Technology, Vol. 41, No. 1, pp. 25-47.

Hetenyi, M. (1946): Beam on Elastic Foundation. University of Michigan Studies, Scientific Series, Vol. XVI, The university of Michigan.

Jochmann, P., Evers, K.-U. and Kühnlein, W.L. (2003): Model Testing of Ice Barriers Used for Reduction of Design Ice Loads. Proceedings of the 22nd International Conference on Offshore Mechanics and Arctic Engineering, Cancun, Mexico. OMAE2003-37385.

Kärnä, T., Qu, Y., Bi, X., Yue, Q. and Kuehnlein, W. (2007): A Spectral Model for Forces Due to Ice Crushing. Journal of Offshore Mechanics and Arctic Engineering, Vol. 129, No. 2, pp. 138-145.

Lau, M., Malgaard, J., Williams, F.M. and Swamidas, A.S.J. (1999): An analysis of Ice Breaking Pattern and Ice Piece Size around Sloping Structures. Proceedings of the 18th International Conference on Offshore Mechanics and Arctic Engineering, St. John's, Newfoundland, Canada. OMAE1999-1151.

Li, F. and Yue, Q. (2002): An Analysis of Amplitude and Period of Alternating Ice Loads on Conical Structures. Proceedings of the 16th IAHR Symposium on Ice, Dunedin, New Zeeland, Vol. 3, pp. 87-93.

Marshall A.R., Frederking R.M., Sayed M., Nadreau J.P., Croasdale K.R. and Jordaan I.J. (1989): Measurements of Load Transmission through Grounded Ice Rubble. Proceedings of the 10th International Conference on Port and Ocean Engineering under Arctic Conditions (POAC), Luleå, Sweden, Vol. 1, pp. 575-584.

Potter, R.E., Bruce, J.C. and Allyn, N.F.B. (1984): Rubble Protection – An Alternative for Arctic Exploration. Proceedings of the 5th International IAHR Symposium on Ice, Hamburg, Germany, Vol. 1, pp. 221-236.

Schwarz, J. (1977): New Developments in Modelling Ice Problems. Proceedings of the 4th International Conference on Port and Ocean Engineering under Artic Conditions (POAC), ST. Johns, Canada, pp. 46-61.

Ice properties, testing, and physical modeling

19th IAHR International Symposium on Ice
"Using New Technology to Understand Water-Ice Interaction"
Vancouver, British Columbia, Canada, July 6 to 11, 2008

Fracture toughness of atmospheric ice

Majid Kermani and Masoud Farzaneh

NSERC/Hydro-Québec/UQAC Industrial Chair on Atmospheric Icing of Power Network Equipment (CIGELE), and Canada Research Chair on Atmospheric Icing Engineering of Power Networks (INGIVRE)
Université du Québec à Chicoutimi, Chicoutimi, Canada G7H 2B1 (www.cigele.ca)
Mkermani@uqac.ca
Mfarzaneh@uqac.ca

Abstract

Fracture toughness of atmospheric ice accumulated in a closed loop wind tunnel at -6 , -10 and -20 ^{o}C with a liquid water content of 2.5 g/m^3 was examined at different strain rates. Ice samples accumulated at each temperature level were tested at the accumulation temperature, but the ice accumulated at -10 ^{o}C was also tested at -3 and -20 ^{o}C. The results of these tests show that fracture toughness of atmospheric ice decreases with decreasing accumulation temperature. This value for the ice accumulated at -10 ^{o}C and tested at the same temperature is 111.17 $KPa\sqrt{m}$, which is in good agreement with the values reported by other researchers. The fracture toughness of atmospheric ice accumulated at -10 ^{o}C and tested at -20 ^{o}C increases, owing to higher strength at very cold temperatures. The fracture toughness of atmospheric ice accumulated at -20 ^{o}C and tested at its accumulation temperature is less than other types because the cavities and possible cracks in this ice decrease its crack propagation resistance.

1. Introduction

Accretion of atmospheric ice on power transmission lines may cause considerable damage to power networks in cold climate regions. Removing the atmospheric ice from network equipment, particularly cables and conductors, has drawn much attention lately and, consequently, many studies on ice adhesion on substrates, ice shedding and its effects on power network elements have been carried out. Studies on atmospheric icing require knowledge of the mechanical properties of the ice under various temperatures and loading conditions.

The present investigation is part of a larger study on the measurement of the mechanical properties of atmospheric ice, such as compressive strength (Kermani et al., 2007a), flexural strength (Kermani et al., 2007b), tensile strength, etc., yet to be published.

The presence of cracks in the ice can weaken it against the loads. This may occur at stresses below its yield strength, where failure would not normally be expected. To study the ice behavior in the presence of cracks, a branch of continuum mechanics called Linear Elastic Fracture Mechanics (LEFM) is used. Most of the studies on the behavior of ice by LEFM concentrate on measuring the fracture toughness of the ice. In fracture mechanics, the determination of fracture toughness is a stress analysis problem which involves the applied stress, loading geometry, sample dimensions and length of the crack which is cut in the ice and sharpened. As noted by Dempsey et al. (1989), some investigations of ice fracture toughness were hindered by experimental difficulties, resulting in unreliable data. Laboratory measurements of the fracture toughness of ice made prior to 1989 are often characterized by a wide variation in results (e.g. Liu and Miller, 1979; Goodman and Tabor, 1978). This scatter is thought to reflect the influence of various testing parameters on experimentally determined values of fracture toughness. However, standardization of testing techniques and characterization of experimental variables by Dempsey et al. (1989) has resulted in more consistent data.

To the best knowledge of authors, no investigation about fracture toughness of atmospheric ice has been published yet. In contrast to atmospheric ice, the fracture toughness of other types of ice has been studied by many investigators (e.g. Dempsey et al., 1989; Liu and Miller, 1979, Goodman and Tabor, 1978; Urabe et al.,1980, Timco and Frederking,1986). In this paper, the fracture toughness of various types of atmospheric ice at various test temperature is investigated.

2. Test conditions

Atmospheric ice and its structure can be influenced by the meteorological conditions prevalent during its formation, such as wind velocity, liquid water content of air, mean volume droplet diameter and temperature. Furthermore, the mechanical properties of atmospheric ice are dependent on temperature, load rate, type and structure. Therefore, the most important aspect in this investigation is selecting the experimental conditions for the ice accumulation and ice tests, which is discussed in the following paragraphs.

2.1 Temperature

Normally atmospheric icing occurs at temperatures ranging between -6 and -20^{o}C, as was acknowledged by other investigators (e.g. Eskandarian, 2005; Mousavi, 2003). Since a typical wintertime temperature in Quebec is -10 ^{o}C, most of the tests in this study were carried out at this temperature. However, to study the temperature dependence of the mechanical behavior of

atmospheric ice, some experiments were done at -3 and -20 ^{o}C, which fall within the typical range of temperatures for Quebec winters.

2.2. Ice accumulation conditions

The ice accumulation conditions for this study were created in the CIGELE atmospheric icing research wind tunnel, which is a closed-loop (air-recirculated) low-speed icing wind tunnel. Icing conditions similar to those encountered during various icing processes in nature can be simulated in this tunnel. The readers are referred to Kermani (2007) for more information about the characteristics of this equipment.

Atmospheric ice was accumulated on an aluminum cylinder (diameter 78 mm and length 590 mm) placed in the middle of the test section of the wind tunnel and rotated at a constant speed of 2 rev/min. Before ice accumulation, the cylinder was cleaned with alcohol and set in place for two hours while the system was cooling down. Once the accumulation was complete, the cylinder was removed from the test section and the accumulated ice was cut with a warm aluminum blade to avoid any mechanical stress that might cause cracks. The resulting ice slices were then carefully prepared using a microtome. The average time interval between ice accumulation and fracture toughness tests was 5 hours. Figure 1 shows the position of the specimens extracted from the accumulated ice on the cylinder, and the load direction in the mechanical tests.

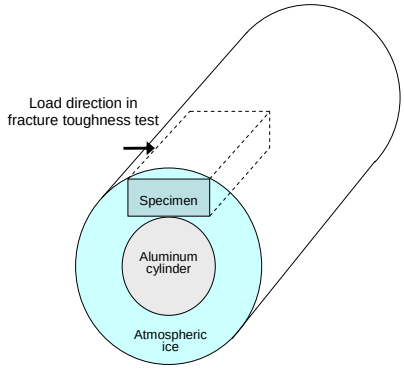

Figure 1. Schematic illustrating specimen position in accumulated atmospheric ice and load direction during test.

Specimen dimensions, as mentioned in ASTM, were determined by averaging three measurements of the three axes of the samples. In preparing the specimens, the guidelines recommended by the IAHR working group on test methods (Schwarz et al., 1981) were used.

Air speeds that typically leads to natural glaze ice formation range from ultra low to medium. In order to make the experimental work more manageable and to obtain a more uniform ice layer, the air velocity value of 10 ms^{-1} was chosen.

The three ambient temperature values, -6, -10 and -20 ^{o}C, were selected for the accumulation of atmospheric ice as representative of warm, medium and cold icing conditions. It was assumed that air pressure was equal to 1 NACA standard atmosphere at sea level (P_{st} =101325 Pa) and that relative humidity ranged from 0.81 to 0.92 %.

The LWC for the CIGELE wind tunnel, as a function of the difference between the air and water line pressures, air speed and the flow rate of water in the supply line, was calibrated by Karev et al.(in press). The LWC for icing conditions in nature varies between 0.5 g/m^3 to 10 g/m^3, which is within the range of the wind tunnel. During calibration, the LWC at the test section of the wind tunnel was measured using the accepted standard technique known as the rotating icing cylinder method (Stallabrass, 1978). The LWC was set at 2.5 g/m^3 in order to obtain solid and uniform atmospheric ice.

The specimens were accumulated at different temperatures and tested at their accumulation temperatures. However, atmospheric ice accumulated at the typical wintertime temperature (-10 ^{o}C) was tested at three temperatures -3, -10 and -20 ^{o}C. The specimens were kept at the test temperature for two hours before each test.

To avoid the effect of grain size, specimen dimensions were chosen according to the guidelines in the ASTM E399-72 and also the recommendations made by Dempsey et al. (1989). The notch root was formed by the saw cut and reshaped by razor blades with a curvature radius of 0.1 mm, in order to increase the notch acuity. Figure 2 shows the experimental setup for measuring the fracture toughness of atmospheric ice. The critical stress intensity factor (K_{IC}) for three-point loading is given by (Dempsey et al., 1989):

$$K_{IC} = 3Ff(a/h)/(4w\sqrt{h}) \quad \textbf{[1]}$$

where F is the load at fracture, a is the notch length, h is the specimen height, w is its width, and the function $f(a/h)$ is:

$$f(a/h) = -1.186(1-\frac{a}{h})^2 + 2.474(1-\frac{a}{h}) - 6.858 + 8.124(1-\frac{a}{h})^{-1} + 0.045(1-\frac{a}{h})^{-2} \quad \textbf{[2]}$$

The loading rate was such that the rate of increase of the fracture toughness was within the range of 70 and 130 $KPa\sqrt{m}/s$ (as mentioned by Dempsey et al., 1989).

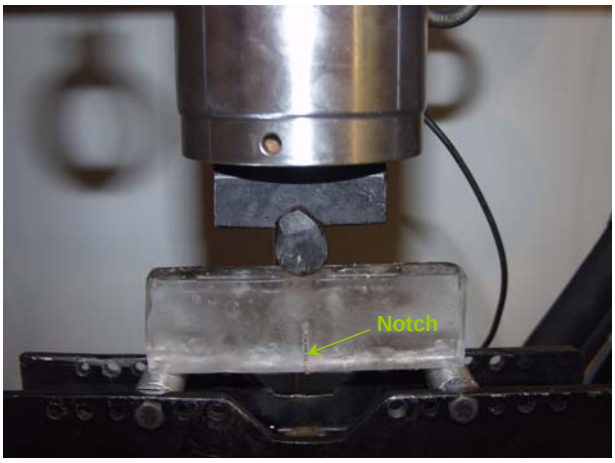

Figure 2. Fracture toughness test of atmospheric ice.

According to ASTM E399, the following conditions should be respected for a valid fracture toughness test:

$$a = h\text{-}a = w \geq 2.5(K_{IC}/\sigma_y) \quad \textbf{[3]}$$

where K_{IC} is the plain strain fracture toughness and σ_y is the yield stress of the material.

Figure 3 shows the specimen dimensions in which a is 20 mm, h is 40 mm, w is 20 mm, and the specimen length is 128 mm. The distance between two roller supports is 120 mm and the force F is applied at the middle of the specimen.

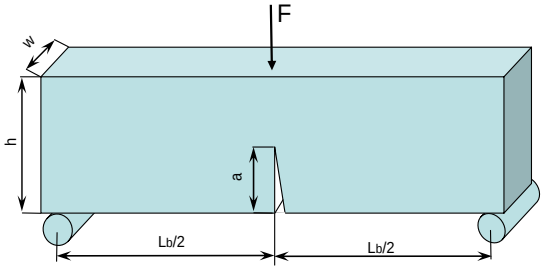

Figure 3. The specimen dimensions in the fracture toughness tests.

In order to verify the application of Linear Elastic Fracture Mechanics (LEFM), an extensometer was installed under the beam to measure the notch mouth opening displacement. Figure 4 shows a typical force–displacement record. The linear fit to data is good ($r^2 = 0.993$) and implies that linear elastic fracture mechanics is applicable.

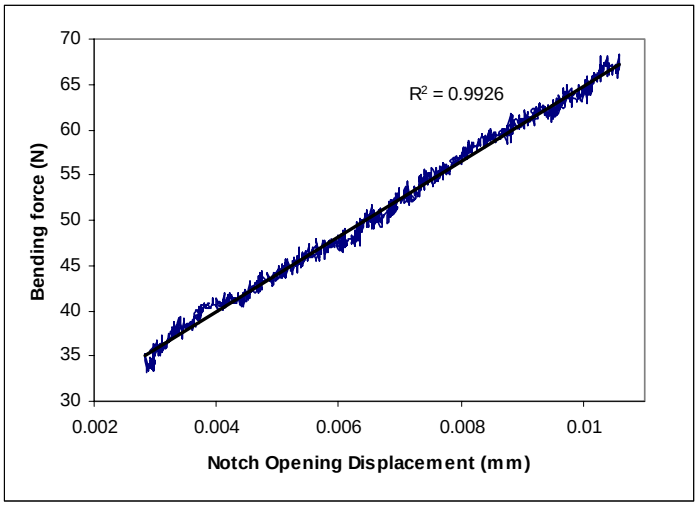

Figure 4. Force versus notch opening displacement in the fracture toughness tests.

3. Test results and discussion

Table 1 shows the results of fracture toughness of atmospheric ice accumulated at -6, -10 and -20 ^{o}C. Again the ice accumulated at -10 ^{o}C was tested at three different temperatures, -3, -10 and -20 ^{o}C.

Figure 5 shows the results of fracture toughness tests for various types of atmospheric ice. The results of these tests show the fracture toughness of atmospheric ice accumulated at -10 ^{o}C decreases and then increases with decreasing test temperature.

Row	T_a (^{o} C)	T_t (^{o}C)	Fracture Toughness (KPa.m^0.5)	Average (KPa.m^0.5)	ST. Dev. (KPa.m^0.5)
1	-6	-6	110.68	137.75	24.86
2	-6	-6	175.45		
3	-6	-6	123.60		
4	-6	-6	146.96		
5	-6	-6	132.08		
6	-10	-3	162.52	128.60	21.65
7	-10	-3	136.74		
8	-10	-3	108.70		
9	-10	-3	120.32		
10	-10	-3	114.71		
11	-10	-10	114.63	111.17	7.93
12	-10	-10	105.04		
13	-10	-10	121.09		
14	-10	-10	101.33		
15	-10	-10	113.77		
16	-10	-20	117.64	143.28	29.13
17	-10	-20	140.95		
18	-10	-20	114.02		
19	-10	-20	160.94		
20	-10	-20	182.83		
21	-20	-20	84.67	108.04	34.44
22	-20	-20	89.80		
23	-20	-20	148.22		
24	-20	-20	142.29		
25	-20	-20	75.22		

Table 1. Results of fracture toughness tests of atmospheric ice.
T_a= Accumulation temperature, T_t= Test temperature.

The average value of fracture toughness at -3 ^{o}C is 128.6 $KPa\sqrt{m}$. Liu and Miller (1979) obtained the average value of 110.5 $KPa\sqrt{m}$ at -4 ^{o}C for fracture toughness of fresh water ice. However, the value of fracture toughness of sea ice reported by Urabe et al. (1980) is about 80 ± 20 $KPa\sqrt{m}$, and they attributed the difference of their results with those of other investigations for fresh water ice to the differences in ice structure.

At -10 ^{o}C, the results of our tests show the average value of 111.17 $KPa\sqrt{m}$. This value agrees well with one reported by Timco and Frederking (1986) for fresh water ice at -10 ^{o}C. They found that $K_{IC} = 188\dot{K}_I^{-0.13}$ for horizontal crack propagation, which is similar to the crack propagation direction in this study. This equation predicts that for loading rates $70 < \dot{K}_I < 130$ $KPa\sqrt{m}/s$, the K_{IC} would range between 99.8 $KPa\sqrt{m}$ and 108.2 $KPa\sqrt{m}$. Dempsey et al. (1989) obtained a

value of fresh water ice fracture toughness in the range of 50 to130 $KPa\sqrt{m}$ for various grain sizes. Smith et al. (1990), in their tests with granular fresh water ice at -10 ^{o}C (porosity < 4%), found the fracture toughness to be between 83 $KPa\sqrt{m}$ and 112 $KPa\sqrt{m}$, within the same load rate of current study. Liu and Loop (1972) reported this value in the range of 96 $KPa\sqrt{m}$ and 116 $KPa\sqrt{m}$ for fresh water ice at -9 ^{o}C. Liu and Miller (1979) reported the average value of 116.3 $KPa\sqrt{m}$ at -9^{o}C for fresh water ice.

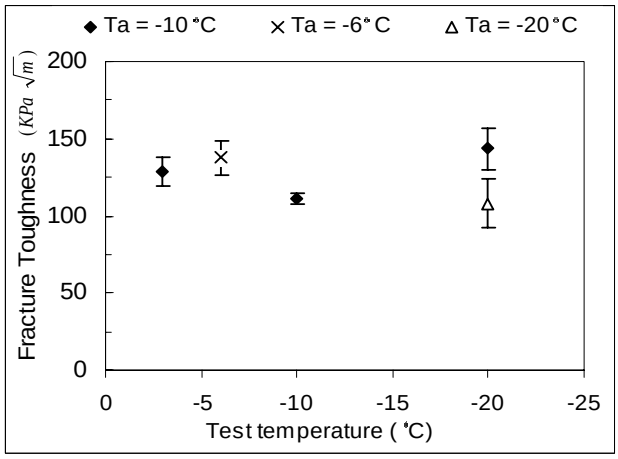

Figure 5. Fracture toughness of various types of atmospheric ice. The error bars in this figure correspond to the standard error in the results for the tests conducted at each set of parameters.

Fischer and Alley (1995) used a modified ring (MR) test to determine the fracture toughness of granular fresh water ice at -15 ^{o}C and obtained results of $145 \pm 35\ KPa\sqrt{m}$. Liu and Miller (1979) obtained the average value of 139 $KPa\sqrt{m}$ for fresh water ice at -18 ^{o}C. Goodman and Tabor (1978) obtained the value of $116 \pm 13\ KPa\sqrt{m}$ for fresh water ice at -13 ^{o}C. Figure 6 compares the fracture toughness values of atmospheric ice found in this study with those of other investigators for fresh water ice.

In Figure 5 (and Table 1), it is observed that the average value of fracture toughness of ice accumulated at -10 ^{o}C and tested at -20 ^{o}C is 143.28 $KPa\sqrt{m}$, while the corresponding value of the ice accumulated at -20 ^{o}C and tested at the same temperature is 108.04 $KPa\sqrt{m}$. Comparing the average value of fracture toughness of the ice accumulated at -10 ^{o}C and tested at -3^{o} C (128.60 $KPa\sqrt{m}$) with the corresponding value of the ice accumulated at -6 ^{o}C and tested at -6 ^{o}C (137.75 $KPa\sqrt{m}$), ignoring the small difference in test temperatures and regardless of overlapping error bars, it seems that the fracture toughness of atmospheric ice decreases with decreasing accumulation temperature. It is obvious that at test temperatures close to the melting point, the ice shows ductile behavior and it is expected that its resistance against crack propagation increases when the temperature approaches the melting point. The fracture toughness of atmospheric ice accumulated at -20 ^{o}C and tested at its accumulation temperature is less than other types because the cavities and possibly pre-existing cracks in this ice lower its

crack propagation resistance (readers are referred to Kermani et al. (2007a) for more information about the structure of these three types of atmospheric ice). The same factor observed in the compression tests and the bending tests led to the weakness of this ice (Kermani et al. 2007a; Kermani et al. 2007b).

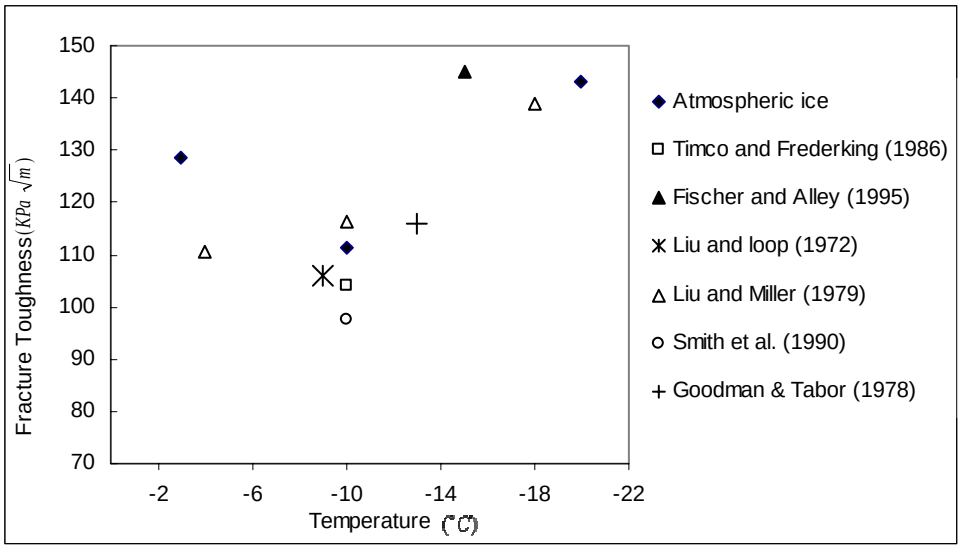

Figure 6. Comparison of fracture toughness of ice with the results of other investigators for fresh water ice.

The dissimilarity between atmospheric and freshwater ice is at the source of some differences between the results of the study herein and those of other investigators for the fracture toughness of freshwater ice. Differences in grain size, void ratio, shape and size of bubbles, and grain growth direction are some examples of this dissimilarity.

As mentioned earlier, the average grain size for atmospheric ice accumulated at -10 and -6 ^{o}C is 0.5 and 1.5 mm, respectively. In the tests of Fischer and Alley (1995) and those of Timco and Frederking (1982), however, the average grain size was found to be between 0.5 and 15 mm, and 1 and 6 mm, respectively.

Another important issue that can cause some differences between the results of our tests and those of other researchers is the test sample size, which is known to affect mechanical properties (Dempsey et al., 1989). The specimen dimensions in our study were 40 mm wide, 20 mm thick and 128 mm long. Timco and Frederking (1982) used sample sizes of 100 x 60 x 450 mm in their study. The height and width of the samples used by Dempsey et al., (1989) were 102 x 25 mm, and the beam length was 314 mm. The large difference in sample size between this study and the previous ones is likely responsible for some of the differences in the results. The difference between test methods is also another important factor. As mentioned earlier, three-point beams were used in this study to measure the fracture toughness of atmospheric ice. The fracture toughness can also be measured using four-point beam (Goodman and Tabor, 1978), modified ring (Fischer and Alley, 1995), circumferentially notched right cylinder (Smith et al., 1990), etc. The inherent scatter of the test results may also have contributed to the discrepancies.

4. Conclusions

The fracture toughness of different types of atmospheric ice was measured using the three-point loading of beam approach. The ice was accumulated on a rotating cylinder in the CIGELE atmospheric icing wind tunnel at LWC of 2.5 g/m^3, wind speed of 10 m/s and various accumulation temperatures. The ice accumulated at -10 ^{o}C was tested at -3, -10 and -20 ^{o}C. The accumulated ice at -6 and -20 ^{o}C was tested at the same temperature as accumulated. The results show that fracture toughness of atmospheric ice decreases with decreasing accumulation temperature. At very cold temperatures (around -20 ^{o}C), the fracture toughness of atmospheric ice increases owing to higher strength. However, the fracture toughness of atmospheric ice accumulated at -20 ^{o}C and tested at its accumulation temperature is less than other types because the cavities and possible cracks in this ice lower its resistance against crack propagation.

The differences between the structure of atmospheric ice and freshwater ice, the specimen dimensions, as well as those between test methods in the current study and those of previous studies, may lead to some discrepancies between our results and those of other investigations on freshwater ice.

5. Acknowledgements

This work was carried out within the framework of the NSERC/Hydro-Quebec/UQAC Industrial Chair on Atmospheric Icing of Power Network Equipment (CIGELE) and the Canada Research Chair on Engineering of Power Network Atmospheric Icing (INGIVRE) at Université du Québec à Chicoutimi. The authors would like to thank the CIGELE partners (Hydro-Québec, Hydro One, Réseau Transport d'Électricité (RTE) and Électricité de France (EDF), Alcan Cable, K-Line Insulators, Tyco Electronics, CQRDA and FUQAC) whose financial support made this research possible.

6. References

Dempsey, J. P., Wei, Y., DeFranco, S., Ruben, R., Frachetti, R.,1989, Fracture toughness of S2 columnar freshwater ice: Crack length and specimen size effects- Part1, The Eighth International Conference on Offshore Mechanics and Arctic Engineering ,PP 83-89.

Druez, J., Nguyeh, D. D. and Lavoie Y., 1986, Mechanical properties of atmospheric ice, Cold Regions Science and Technology, Vol. 13, PP 67-74.

Eskandarian, M., 2005, Ice shedding from overhead electrical lines by mechanical breaking, Ph.D. thesis, University of Quebec at Chicoutimi.

Fischer, M.P. and Alley, R.B., 1995. Fracture toughness of ice and firm determined from the modified ring test, Journal of Glaciology, Vol. 41 , No 138, PP 383- 393.

Goodman D.J. and Tabor D., 1978. Fracture toughness of ice: a Preliminary account of some new experiments, Journal of Glaciology, 21 (85), PP 651-660.

Karev, A. R., Farzaneh, M., Kollar, L. E., 2007, An Icing Wind Tunnel Study on Characteristics of an Artificial Aerosol Cloud, Part II: Liquid Water Content as a Function of Air Speed, submitted to J. of Atmospheric and Oceanic Technology.

Kermani, M. , 2007, Ice shedding from cables and conductors - a model of cracking activity of atmospheric ice in brittle regime, Ph.D. thesis, University of Quebec at Chicoutimi, QC, Canada.

Kermani, M., Farzaneh, M., Gagnon, R. E., 2007a, Compressive strength of atmospheric ice, Cold Regions science and technology, Vol. 49, PP 195–205.
Kermani, M., Farzaneh, M., Gagnon, R. E., 2007b, Bending Strength and Effective Modulus of Atmospheric Ice, Cold Regions Science and Technology, (accepted for publication).
Lavrov, V.V., 1971. Deformation and strength of ice. Transl. from Russian, Natl. Sci. Found., Israel Program for Scientific Translation, Jerusalem, 1-164.
Liu H.W and Miller K.J, 1979, fracture toughness of fresh water ice, Journal of glaciology, Vol. 22, PP 135-143.
Mousavi, M. , 2003, Experimental and theoretical verification of two icing codes, Thesis, University of Quebec at Chicoutimi.
Schwarz, J., Frederking, Gavrillov, R., Petrov, I., Hirayama, K., Mellor M., Tryde P. and Vaudrey K.,1981, Standardized testing methods for measuring mechanical properties of ice, Cold Regions Science and Technology, Vol. 4, 245-253.
Stallabrass, J. R., 1978. An appraisal of the single rotating cylinder method of liquid water content measurement. National Research Council of Canada, Division of Mechanical Engineering, Rep. LTR-LT-92.
Timco, G. W. and Frederking, R. M. W ,1986, The effects of anisotropy and microcracks on the fracture toughness K_{IC} of freshwater ice, Proceedings of the 5th International OMAE Symposium, Tokyo , Japan, Vol. IV ,PP 341-348.
Urabe, N., Iwasaki,T. and Yoshitake, A., 1980, Fracture toughness of sea ice, Cold Regions Science and Technology, 3, 29-37.

19th IAHR International Symposium on Ice
"Using New Technology to Understand Water-Ice Interaction"
Vancouver, British Columbia, Canada, July 6 to 11, 2008

Comparison of physical and mechanical properties of coastal ice and level ice

Magnus Gabrielsen[1,2,3], Sébastien Barrault[1,2], Fabrice Caline[1,2], Knut V. Høyland[2,1]
[1]University Centre in Svalbard, Longyearbyen, Norway
[2]Norwegian University of Science and Technology, Trondheim, Norway
[3]now working at Dr.techn.Olav Olsen AS, Lysaker, Norway
mga@olavolsen.no, sebastien.barrault@unis.no, fabrice.caline@unis.no, knut.hoyland@ntnu.no

Physical and mechanical properties of coastal and level ice were compared. The study is based on the results from horizontal samples taken in March 2007 in Van Mijenfjorden, Svalbard, Norway. The samples were tested in compression and relaxation in a cold laboratory at the University Centre in Svalbard and thin sections were prepared. The results show that the physical properties of the ice are essentially monotone functions of the distance from the shore and that the differences between the ice closest to land and the level ice are important. The porosity varies with a factor 6 while the brine fraction varies with a factor 17. The Young modulus is correlated with the porosity while the residual stress is correlated with the brine content although both correlations are weak. The microscopic analysis shows that the coastal ice is granular while level ice is S2 in the surface and S3 lower down. The size of the grains in the level ice is comparable with the size of the samples, therefore it is important to check their direction when sampling.

1. Introduction

There is a growing interest for constructing coastal structures in ice-infested Arctic waters. Several oil and gas projects are under planning. They will require infrastructure on land. At the same time the reduction of the Arctic ice cover prolongs the shipping season and puts harbour investments on the agenda. Arctic structures must resist ice loads from thermal expansion and tide (Smirnov and Sukhorov, 1994; Nikitin et al., 1992). When the sea ice cover is continuous, the time scale of ice movements is such that the viscosity has an important influence on the maximum loads.

The coastal ice forms in a different way than the level ice and is in addition subjected to important tidal stress variations (Caline and Barrault, 2008). We may therefore expect the physical and mechanical properties of the ice at both locations to differ.

Ice samples were taken at several locations and depths in order to measure physical properties and perform mechanical tests. The main interest was to perform relaxation tests in order to compare the viscous properties of the ice. It was the first time a study based on relaxation tests was made at UNIS, the University Centre in Svalbard.

2. Proposed terminology

The *ice foot* is determined as the ice frozen to the shore when gradual freezing of sea water from tide and wave spray occurs early in the season. It is in effect a block of ice that is fixed to the ground and does not move with the tide (WMO, 1970). At a certain distance from shore the ice, which is unaffected by the shore, is called *level (floating) ice*. In between is a transition zone which Croasdale (1980) calls *active zone*. The active zone is composed of *coastal ice* which forms simultaneously with the sea ice and is subjected to tidal forces significant enough to create tidal cracks (Caline and Barrault, 2008).

3. Site and measurement

The coastal ice and the level ice were surveyed during the winter 2006-07 in the innermost bay of Van Mijenfjorden, Svalbard, Norway (Figure 1). On 14 and 21 March 2007, 6 horizontal ice cores were sampled in level ice at three different depths (H1=10 cm from the ice surface, H2=30 cm, H3=50 cm). On 19 April, 23 horizontal ice cores were sampled in four locations in the coastal ice nearby a breakwater along a profile aligned normal to the shore at 316° from North (Figure 1 c) and e)). All samples had a diameter of 70 mm. They were put in sealed plastic bags and transported to a -20°C storage room at UNIS. The time from sampling to storing was about 3-5 hours and the temperature was kept below the freezing point all the time during transport. The samples were stored from up to three weeks before testing. All samples were tested at -10°C.

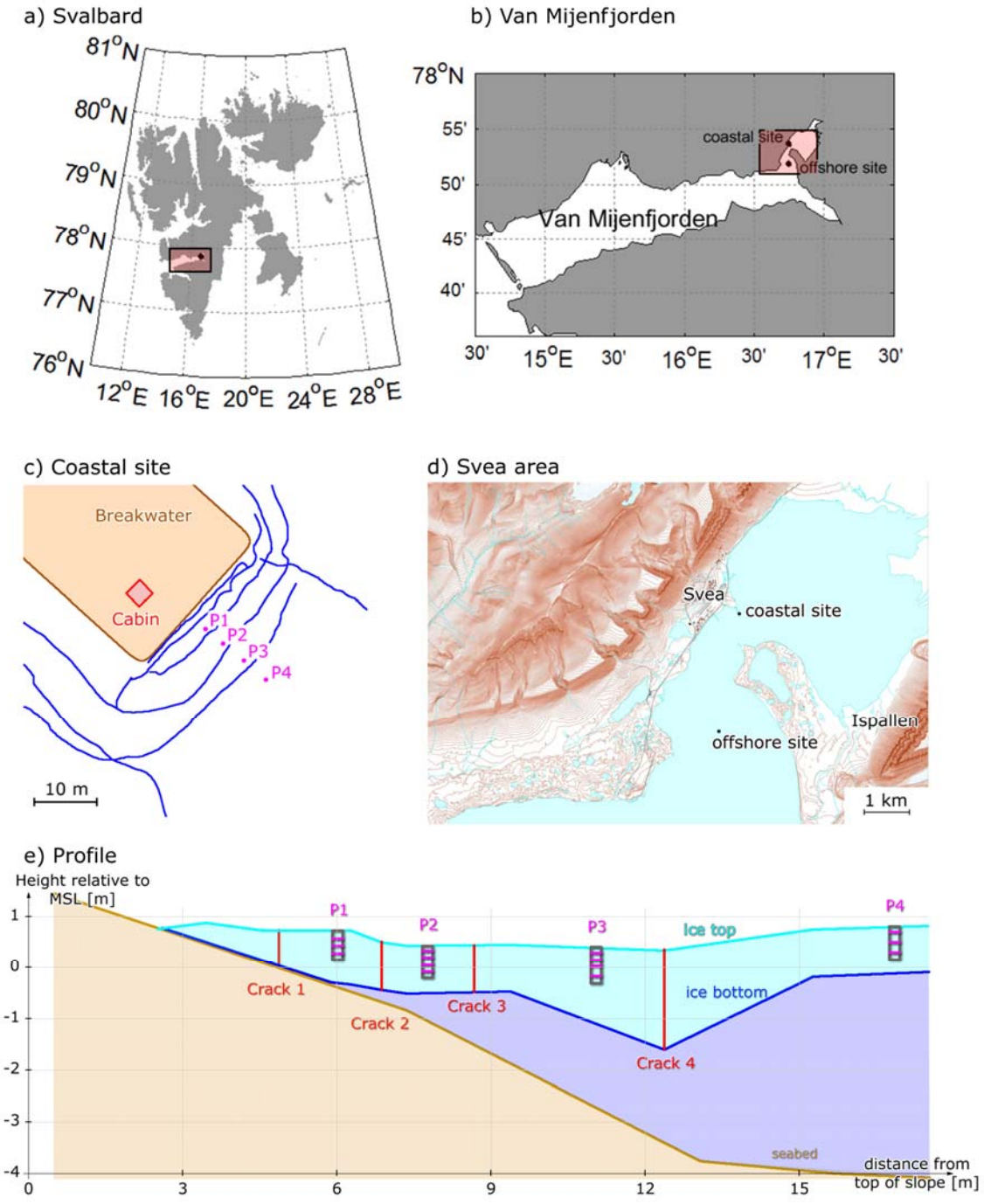

Figure 1. Map of the measurement site and profile in the innermost basin of Van Mijenfjorden

NTNU developed in 1996 a stationary uniaxial compression device, named Knekkis and installed at UNIS. The device can perform maximal strength, creep and relaxation tests. A piston moves upwards and a load cell placed in the upper part of the device records pressure. Data are recorded at a frequency of 0.5 Hz. The relaxation tests were performed by applying a start stress of 500 kPa and keeping the piston immobile for one hour. The compression tests were performed at a constant strain rate of 10^{-3} s^{-1}. For the level ice they were performed on the samples that had

undergone relaxation tests. It was checked that the relaxation tests do not seem to affect the strength or the Young modulus of the samples. For the level ice the data is the average of two samples while for the coastal ice only one test was performed. Young's modulus was taken as the steepest slope of the stress-strain plot. After the tests the samples were melted to measure salinity. Porosity as a function of salinity, density and temperature were calculated from equations developed by Cox and Weeks (1982). Horizontal and vertical thin sections of all level ice samples and four coastal ice samples were made to analyze the ice texture.

4. Results

Formation of the coastal ice

From October to mid-December pancake ice accumulated onshore and consolidated into the ice foot. Below mean sea level the ground remained free of ice. In the end of December the sea was covered with ice which was connected to the shore. In the shore area the ice first moved up and down with the tide but by January it had grown thick enough that it stuck to the ice foot and to the sea bottom so much that it did not move with the same amplitude as the tide. On high tide it resulted in the flooding of the near-shore area and hence the formation of superimposed ice (Figure 2). The structure of the superimposed ice is different from that of the level ice as seen when comparing thin sections in Figures 3-6. The superimposed ice contains much smaller crystals and its porosity is one order of magnitude bigger. It is described as granular and contains more air bubbles. The ice with the lowest density looked more like a mixture of snow and ice. The ice grows faster the closer to the shore. The reasons are a greater heat transfer and the formation of superimposed ice. In the end of January, the ice thickness was 0.80 m at P1 and 0.50 m at P4. In the end of February it was 1.60 m and 0.60 m respectively. In the end of April it was 0.80 m at P4 and it reached 0.95 m in the middle of May.

Figure 2. Pond of surface water close to shore that refreezes on top the coastal ice

Formation of the level ice

Sea ice extended to the offshore site in early January. During a first visit on 14 February the ice was 0.52 m thick. 14 March it reached 0.66 m and a month later ice was 0.58 m thick. The thin sections from level ice H2 and H3 indicate a predominant alignment of the c-axis at an approximate angle of 45° (Figure 6). For the H1 cores the orientation of the c-axis is more random. The vertical thin sections from all three levels clearly show an elongation in the vertical

direction. According to these observations the ice from level H1 is characterised as S2-ice, while ice from level H2 and H3 is characterised as S3-ice.

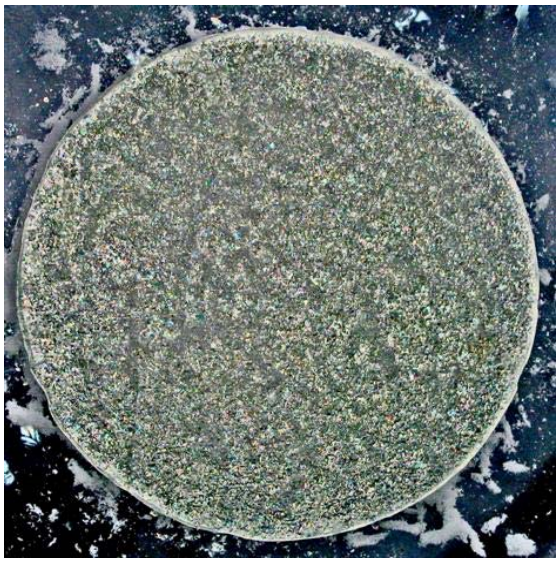

Figure 3. Vertical thin section of P1-H1

Figure 4. Horizontal thin section of P4-H3

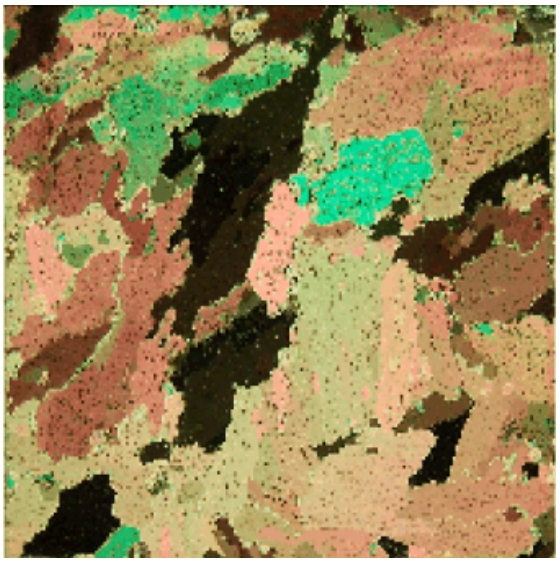

Figure 5. Horizontal thin section of P5-H1

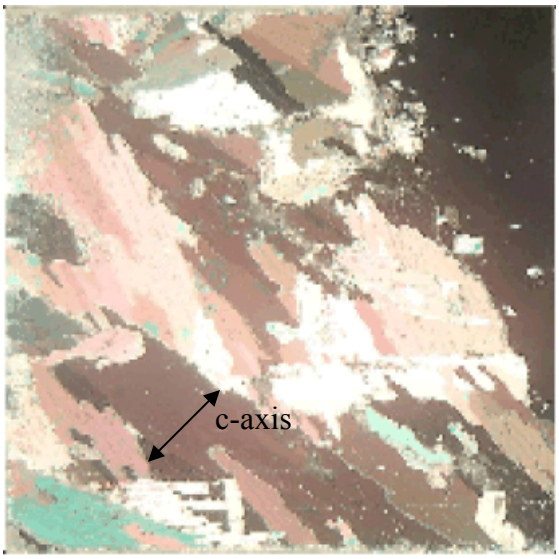

Figure 6. Horizontal thin section of P5-H3

N.B: The diameter of the circular sections and the width of the square sections is 70 mm (Figures 3-6).

Physical and mechanical properties

Table 1 summarises physical and mechanical results obtained in level and coastal ice. All data vary monotonously with the distance from shore. The porosity of coastal ice is decreasing from P1 to P4 and level ice (P5) is 6 times less porous than P1. Air fraction is decreasing as well. In P1 the air fraction is maximal with 99.4 % of the total porosity whereas it is 37 % in the level ice. The brine fraction is highest in the level ice. Ice has the lowest density in P1.

The Young modulus is somewhat higher in the level ice (up to 50% difference) while the residual stress is up to three times higher in the coastal ice than in the level ice.

The residual stress is the only analysed result kept from the relaxation tests. It was chosen not to study the relaxation function partly because it seems that it takes up to 30 minutes for its slope to stabilise after the initial loading and partly because ice is a non-linear visco-elasto-plastic material so no unique relaxation function exists.

Table 1. Comparison of physical and mechanical properties of the floating ice and the coastal ice

		Coastal ice				Level ice
Tested at -10 °C	**Depth**	**P1**	**P2**	**P3**	**P4**	**P5**
Residual stress [kPa]	H1 (10 cm)	170	162	156	156	103
(after one hour relaxation,	H2 (30 cm)	128	150	149	127	76
initial stress 500 kPa)	H3 (50 cm)	132	151	-	104	57
Strength [MPa]	H1	2.7	3.7	2.6	5.1	4.3
(strain rate = 10^{-3} s^{-1})	H2	3.2	3.0	4.2	4.3	4.1
	H3	3.0	4.3	5.2	6.0	3.3
Young's modulus [GPa].	H1	1.1	1.2	1.1	1.2	1.5
	H2	1.1	1.0	1.2	1.2	1.5
	H3	1.0	1.3	1.4	1.6	1.5
Salinity [psu]	H1	0.3	1.0	0.9	2.5	4.6
	H2	0.4	0.9	2.6	6.1	4.6
	H3	0.3	0.7	3.3	4.4	3.7
Density [kg/m^3]	H1	724	789	806	842	916
	H2	720	731	818	861	915
	H3	703	777	-	894	900
Brine fraction [%]	H1	0.13	0.47	0.44	1.26	2.53
	H2	0.17	0.40	1.28	3.15	2.53
	H3	0.13	0.33	-	2.36	2.00
Air fraction [%]	H1	21.2	14.2	12.3	8.6	0.8
	H2	21.6	20.5	11.2	7.0	0.9
	H3	23.5	15.5	-	3.2	2.5
Porosity [%]	H1	21.3	14.7	12.8	9.9	3.4
	H2	21.8	20.9	12.5	10.1	3.5
	H3	23.6	15.8	-	5.5	4.5

As shown in Table 2 ductile failures were observed in all samples except P3-H1 and P5-H3.

Table 2. Failure type of the different samples

	P1	**P2**	**P3**	**P4**	**P5 (level ice)**
H1	Ductile	Ductile	Brittle	Ductile	Ductile
H2	Ductile	Ductile	Ductile	Ductile	Ductile
H3	Ductile	Ductile	Ductile	Ductile	Brittle

5. Discussion

Ice texture analysis

The size and orientation of the crystals have an influence on the results from the mechanical tests. For samples P5-H2 and P5-H3, the crystal size is comparable with the sample size, and the inclination of 45° between loading direction and basal plane direction causes the maximum shear stresses to act along one single basal plane. When the strength of the basal plane is reached through a stress build up, the sample fails in a brittle way.

For samples where crystals have a predominant direction, Peyton (1966) showed that the strength will be lowest when this direction is 45° to the direction of compression while it reaches local maxima at 0° or 90°. It can be seen in Lainey and Tinawi (1984) (after Peyton, 1966 and Wang, 1979) that ice loaded in compression perpendicular or parallel to the c-axis is 2 to 3 times stronger than ice loaded at 45° to it. Since the direction is 45° in the samples analysed in this paper, higher strengths would have been obtained if the samples had been taken in any other directions.

In the coastal ice the size of the crystals compared to the diameter of the samples varies from very small (factor 100) to small (factor 10) as seen in Figures 3 and 4. The unequal grain size originates from the ice formation. Core P1-H1 represents ice formed by snow that gets soaked in sea water at high tide. At low tide the brine is drained, and this causes the ice to be low-saline and very porous. Core P4-H3 represents ice formed directly from sea water.

Residual stresses

In Figure 7 the residual stresses are plotted against the brine content. The two lowest residual stresses (stars) correspond to P5-H2 and P5-H3. As discussed above with strength, the residual stress values would have been expected higher if the samples had been taken with the predominant crystal orientation at 0° or 90° to the direction of compression. It was observed that the residual stress tends to decrease with the brine content, especially when P5-H2 and P5-H3 are not considered. This trend is in accordance with Cole (1997).

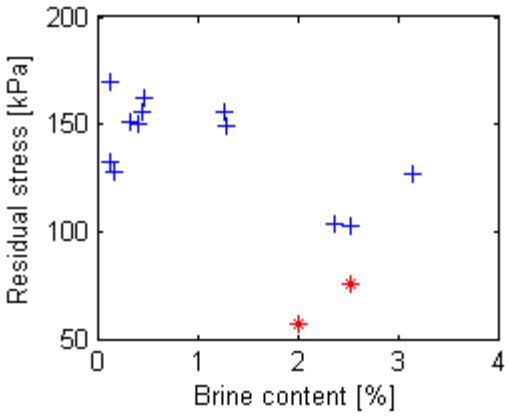

Figure 7. Residual stress vs. brine content

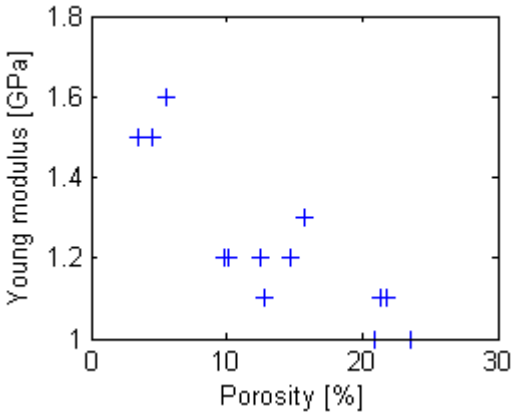

Figure 8. Young modulus vs. porosity

Young modulus

As seen in Figure 8, Young's modulus is decreasing with porosity in accordance with Moslet (2007) and Timco and Frederking (1990). The physical mechanism for elastic deformation is in fact strain of the atomic structure, which is denser the smaller the porosity.

Strength

In Figure 9 the data is split in 3 groups: level ice (star), P3-H1 (circle) and the rest of the coastal ice (cross). The reason why P3-H1 was plotted differently is that it is the only coastal ice sample which failed in a brittle way. It was taken as an indication that its structure is different from that of the other coastal ice samples where, based on the four thin sections, the crystal orientation is random. One good reason why the structure of the ice in P3-H1 would be different is that P3 is located in a place that remained flooded for a couple of weeks in the middle of March and the water froze completely undisturbed. The strengths of the level ice samples are a bit lower than the porosity alone would indicate but the large grains in the level ice reduce its strength (Lee and Schulson, 1986).

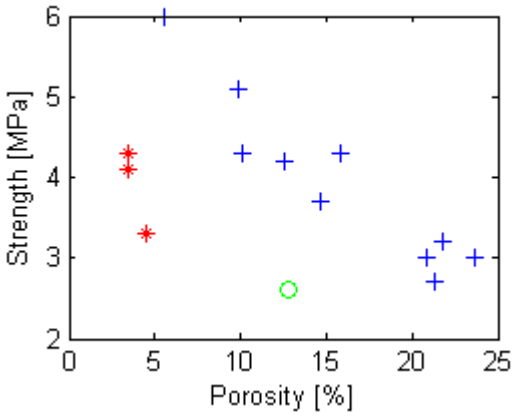

Figure 9. Strength vs. porosity

Mechanical response

Tidal fluctuations have a time constant of 6 hours therefore the ice behaves viscously and the maximum stresses are lower than for a pure elastic material.

Data quality
The margin of error is unknown because of the small number of samples (one per location in the coastal ice). However the strong geographical data dependence is coherent with on-site observations of ice formation and structure. In addition other samples were taken to perform creep and then strength tests and the results show a satisfactory consistency. The storage conditions varied to some extent and the effect of storage time is not well known. Finally note that the coastal ice cores were taken in the top 50 cm while the coastal ice is up to 1.6 m thick (P1). Therefore the results are not fully representative of the coastal ice.

6. Conclusion

Ice was sampled from the level ice and the coastal ice in Van Mijenfjorden on the West Coast of Svalbard, Norway and tests were done to investigate its physical and mechanical properties. The strength, the elastic and the viscous properties were examined by uniaxial compression tests. The strength tests were performed with a nominal strain rate of 10^{-3} s^{-1}. The relaxation tests were done by quickly applying a load of 500 kPa and then allowing the samples to relax. The elastic modulus was taken as the steepest slope of the stress-strain plot.

The level ice has higher density, salinity and brine fraction but lower air fraction and total porosity. It is also stiffer, but significantly more viscous than the coastal ice. The main results are as follows:

- Young's modulus is decreasing with the total porosity as one could expect from the well-known physical mechanism behind elastic deformation
- the strength is also decreasing with porosity but is in addition a function of grain size. The level ice is weaker than the coastal ice even though it is less porous because its grains are up to 100 times bigger.
- the residual stress depended on the brine volume however the orientation of the crystals in the level ice samples may exaggerate this trend in the presented data.

This means that the coastal ice is stronger than level ice when loaded slowly, as with tidal fluctuations, but weaker when loaded faster, as when the wind or a ship pushes the level ice towards the shore.

References

Caline, F. and Barrault, S., 2008. Transmission of level ice stresses to ice foot through a tidal crack. Proceedings of the 19th International Symposium on Ice (IAHR), Vancouver, Canada, 6-11 July.

Cole, D.M., 1997. Modeling the cyclic loading response of sea ice. Int. J. Solids Structures, vol. 35, Nos 31-32, pp. 4067-4075.

Cox, G.F.N. and Weeks, W.F., 1982. Equations for determining the gas and brine volumes in sea ice samples. CRREL Report 82-30.

Croasdale, K.R., 1980. Ice Forces on Fixed, Rigid Structures. Working Group on Ice Forces on Structures, Carstens, T., pp. 34-106.

Lainey, L. and Tinawi, R., 1984. The Mechanical Properties of Sea Ice – a Compilation of Available Data. Canadian Journal of Civil Engineering, 11, pp. 119-127.

Lee, R.W. and Shulson, E.M., 1986. The strength of ductile ice under tension. Journal of Offshore Mechanics and Arctic Engineering, May 1988 vol. 110, pp. 187-191.

Moslet, P.O., 2007. Field Testing of Uniaxial Compression Strength of Columnar Sea Ice. Cold Regions Science and Technology, vol. 48, pp. 1-14.

Nikitin, V.A., Shushlebin, A.I., Sheikin, I.B., 1992. In-Situ Stress Measurements in Fast Ice and Possible Tidal Loads on Structures. Proceedings of the Second International Offshore and Polar Engineering Conference, San Francisco, USA, 14-19 June, vol. 2, pp. 696-702.

Peyton, H.R., 1966. Sea Ice Strength. Technical Report Final Report of Naval Research Arctic Project, 1958-1965, UAG R-182102, University of Alaska, Fairbanks, 285p.

Smirnov, V.N. and Sukhorov, K.K., 1994. Quasi-static thermal stresses in the sea ice. IAHR Ice Symposium, Trondheim, Norway.

Timco, G.W. and Frederking, R.M.W., 1990. Compressive Strength of Sea Ice Sheets. Cold Regions Science and Technology, vol. 17, pp. 227-240.

Wang, Y., 1979. Crystallographic studies and strength tests of field ice in the Alaskan Beaufort Sea. Technical Report, Vol. 1 Exxon, Technical Seminar on Alaskan Beaufort Sea Gravel Island Design.

WMO, 1970. WMO sea ice nomenclature, (suplement No. 5, 1989). Technical Report MO No. 259.TP.145, World Meteorological Organizartion, Geneva, Switzerland.

19th IAHR International Symposium on Ice
"Using New Technology to Understand Water-Ice Interaction"
Vancouver, British Columbia, Canada, July 6 to 11, 2008

Randomness on Strength of Natural Sea Ice

Takahiro Takeuchi[#1], Satoshi Akagawa[#2], Shinji Kioka[#3], Takashi Terashima[#4], Takaharu Kawai[#5]

#1 Hachinohe Institute of Technology, Hachinohe, Japan
#2 Hokkaido University, Sapporo, Japan
#3 Civil Engineering Research Institute of Hokkaido, Sapporo, Japan
#4 Kumashiro System Frontier Co., LTD, Japan
#5 Cold Region Port and Harbor Engineering Research Center, Japan

#1 Hachinohe Institute of Technology, No.88-1, Obiraki, Myo, Hachinohe, Aomori, JAPAN 031-8501
Email : take@hi-tech.ac.jp

The strength of natural sea ice has a lot of scatter due to variations in its growing process. For engineering purposes, it is necessary to understand this strength randomness. The uniaxial compressive strength of natural sea ice at Lake Saroma was analyzed statistically to find an appropriate probability density function that would fit the strength data. Furthermore, peaks occurring in subsequent ice load data obtained in medium scale field indentation tests carried out by the JOIA project were analyzed statistically, since it had been found that each peak load was due to flaking failure of ice in an independent ice failure zone. From a Chi square test for goodness of fit, it was found that both uniaxial compressive strength and peak load fit a log-normal density function with 3 parameters. From this, a method for generating strength and peaks of ice load based on ice failure in the brittle condition can be developed.

Introduction

The physical and mechanical properties of natural sea ice sheet has a lot of scatter. The thickness and strength of natural sea ice are especially important for ice engineering problems such as construction of coastal structures in ice-infested sea areas. In terms of ice thickness, Kioka et al. (2004a,b,2006) proposed a method for generating synthetic data through sea ice surveys along the Okhotsk Sea of Hokkaido, Japan using a bottom-mounted IPS (Ice Profiling Sonar) and ADCP (Acoustic Doppler Current Profiler). A lot of studies (e.g. Michel, 1979; Saeki, 1978; Weeks and Cox, 1984; Lainey, L. and Tinawi, R., 1984; Masaki et al., 1996) have been conducted on the strength of sea ice, and it is well-known that density, temperature, and salinity are the main factors influencing its strength. The uni-axial compressive strength of sea ice is a fundamental value for design of structures, and is strongly related to ice load on vertical structures. If we could determine the distribution of uni-axial compressive strength of natural sea ice, it would be available for generating the data. In this study, first uniaxial compressive strength of natural sea ice at Lake Saroma under brittle condition was analyzed statistically to find an appropriate probability density function that fits strength data. Second, the peaks of subsequent ice load data obtained in medium scale field indentation tests of the JOIA project were analyzed statistically, since it was already found that these peaks were due to flaking failure of ice in an independent ice failure zone (Akagawa et al., 2000). Chi square tests for goodness of fit in terms of probability density functions were conducted based on both uniaxial compressive strength and the peaks of subsequent ice load data.

Uniaxial Compressive Strength

Takeuchi et al. (1994, 1995) conducted uni-axial compressive strength tests using land-fast sea ice in Lake Saroma. Test specimens of natural sea ice were sampled horizontally "in a line" at 15 cm spacings (**Fig.1**) and the strain rate was in the order of 10^{-2} (1/sec), which corresponds to the brittle condition. The specimens were of columnar structure and cylindrical shape, 20cm high and 10cm in diameter. The failure types were shear and longitudinal splitting. **Table 1** summarizes the conditions. **Fig.2 (a) (b)** show the variation in uni-axial compressive strength σ_c over the distance that ice specimen was sampled "in a line". For comparison of data, the ice temperature was kept constant by keeping the specimen immersed in sea water with a constant temperature of around -1.7 to -1.8 degree Celsius. The coefficient of variation in March 1994

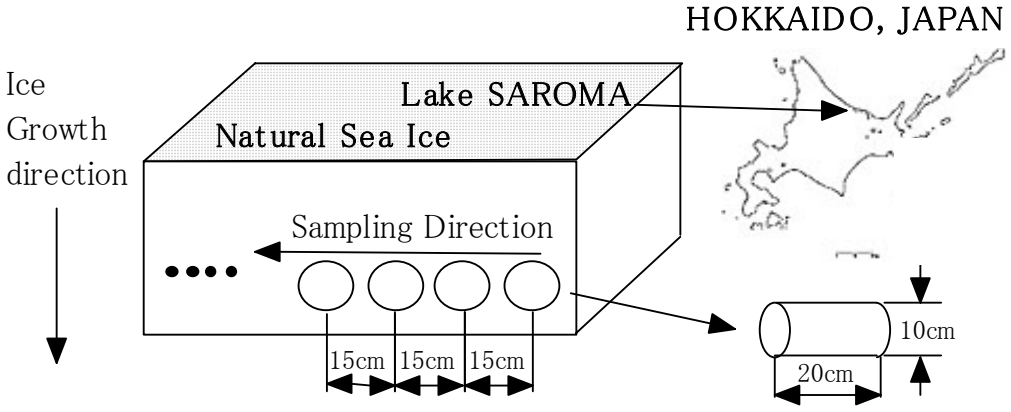

Fig.1 Location of ice specimen, Lake SAROMA, JAPAN.

Table 1. Conditions of uni-axial compressive strength tests

Year/Mon.	Distance in a line (m)	Mean (MPa)	Coefficient of Variation	Total Number of ice sample (N)	Ice temperature (degrees Celsius)
1994/3	19	1.52	0.29	133	-1.8
1995/2	38	1.23	0.26	256	-1.7

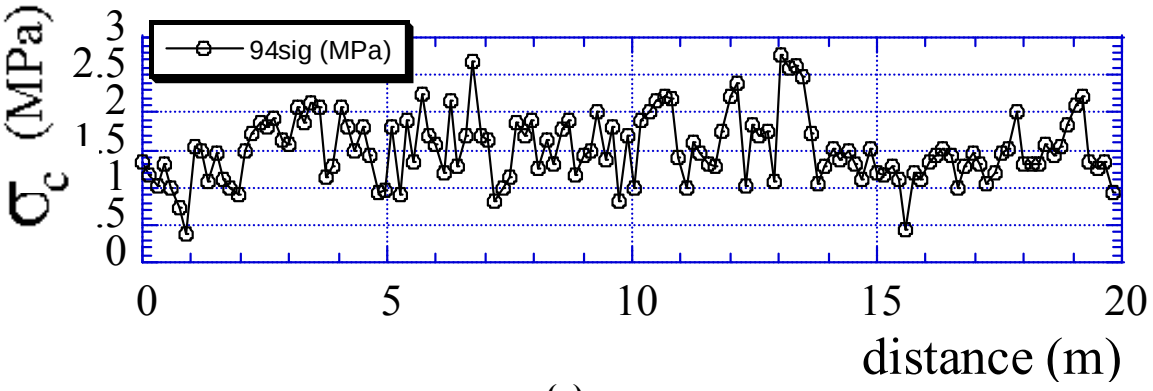

(a)

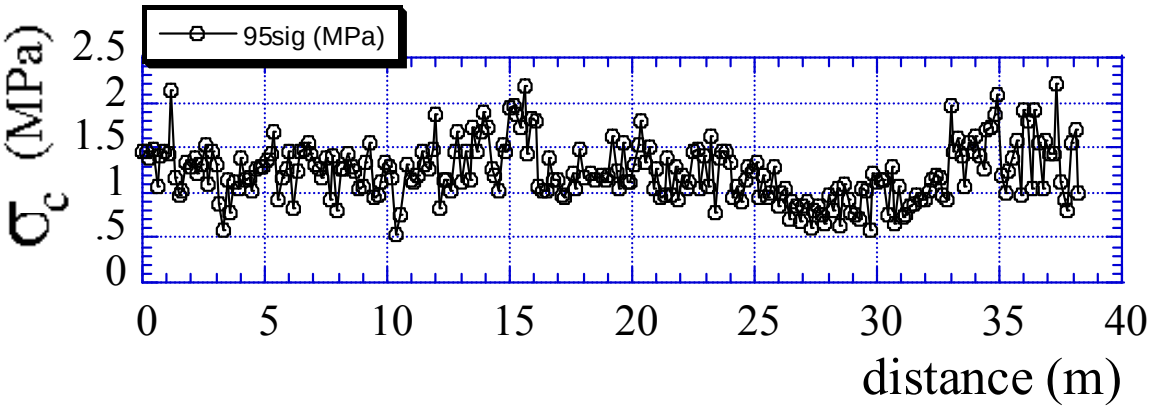

(b)

Fig.2 Uni-axial compressive strength vs. distance in a line.

was slightly larger than that in February 1995, since the structural variation of the ice specimen in March 1994 was more than that in February 1995 due to an increase in porosity caused by factors such as brine drainage channels.

Fig.3&4 show the relation between uni-axial compressive strength and density and salinity. Uni-axial compressive strength appears to be influenced more by density than by salinity, although both data show a lot of scatter. This corresponds to the fact that uni-axial compressive strength depends on ice temperature and density, as reported by Saeki et al. (1978).

To find an appropriate probability density function for fitting strength data, the five functions shown in **Table 2** were used in the analyses.

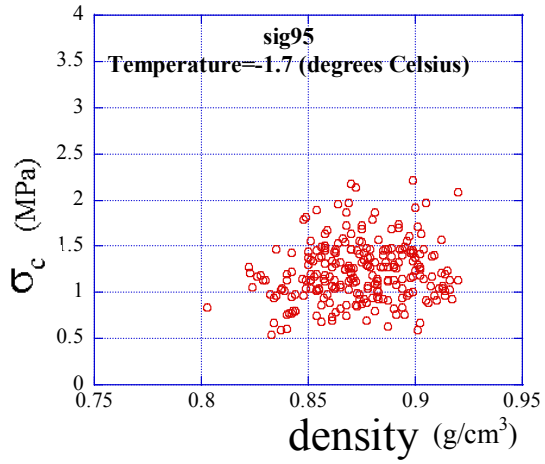

Fig.3 Uni-axial compressive strength vs. density.

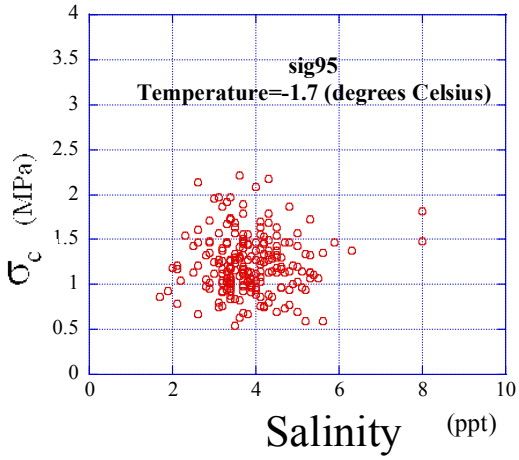

Fig.4 Uni-axial compressive strength vs. Salinity.

Table 2. Probability Distribution Functions

Probability Density Function p.d.f.	Parameters
Normal distribution	
$f_x(x)=\frac{1}{\sqrt{2\pi\sigma_x}}\exp\left\{-\frac{1}{2}\left(\frac{x-\mu_x}{\sigma_x}\right)^2\right\}$	μ_x,σ_x
Log-Normal distribution(2)	
$f_{l2}(x)=\frac{1}{\sqrt{2\pi\sigma_y}}\frac{1}{x}\exp\left\{-\frac{1}{2}\left(\frac{y-\mu_y}{\sigma_y}\right)^2\right\}$ $y=\ln x$	μ_y,σ_y
Log-Normal distribution(3)	
$f_{l3}(x)=\frac{1}{\sqrt{2\pi\sigma_y}}\frac{1}{(x-a)}\exp\left\{-\frac{1}{2}\left(\frac{y-\mu_y}{\sigma_y}\right)^2\right\}$ $y=\ln(x-a)$	μ_y,σ_y ,a
Weibull distribution(2)	
$f_{w2}(x)=\frac{a}{b^a}x^{a-1}\exp\left\{-\left(\frac{x}{b}\right)^a\right\}$ $(0\le x<\infty;a>0,b>0)$	a,b,c
Weibull distribution(3)	
$f_{w3}(x)=\frac{a}{b-c}\left(\frac{x-c}{b-c}\right)^{a-1}\exp\left\{-\left(\frac{x-c}{b-c}\right)^a\right\}$ $(c\le x<\infty;a>0,b>c\ge 0)$	a,b,c

Note: Mean μ_x, Standard Deviation σ_x, a,b,c,

Fig.5(a)&(b) show histograms of uni-axial compressive strength σ_c with theoretical curves of probability density functions. The relation between total number of data (N) and number of histogram (n) can be determined by Sturges' formula [1].

$$n = 1 + \log_2 N \qquad [1]$$

After calculating χ_0^2 from equation [2], χ_0^2 is compared to $\chi^2(\phi,0.05)$ with the degree of freedom ϕ calculated by equation [3] and a one sided test with 5% significant level.

$$\chi_0^2 = \sum_{x=1}^{n}(n_i - m_i)^2 / m_i \qquad [2]$$

n_i is frequency based on test data, and m_i is frequency calculated using the probability density function.

$$\phi = (n-1) - (\textit{parameters}) \qquad [3]$$

The results of Chi square tests for

goodness of fit are listed in **Table 3.** Satisfying $\chi_0^2 < \chi^2(\phi, 0.05)$, log-normal (3-parameters) is the most appropriate probability density function for uni-axial compressive strength. Log-normal (2-parameters) can generate data but with reduced accuracy.

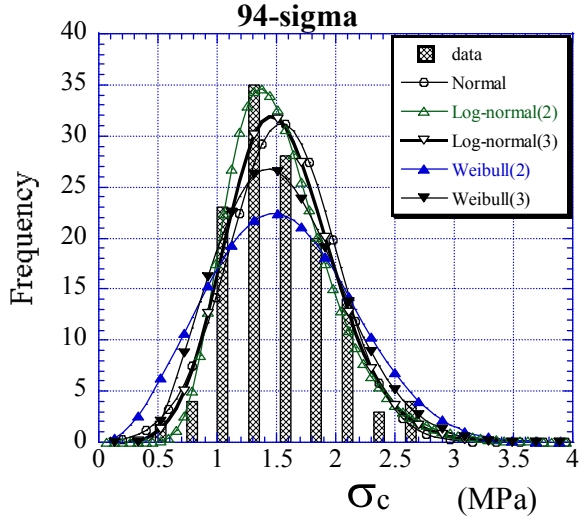

Fig.5(a) Histogram and probability density functions of uni-axial compressive strength (1994)

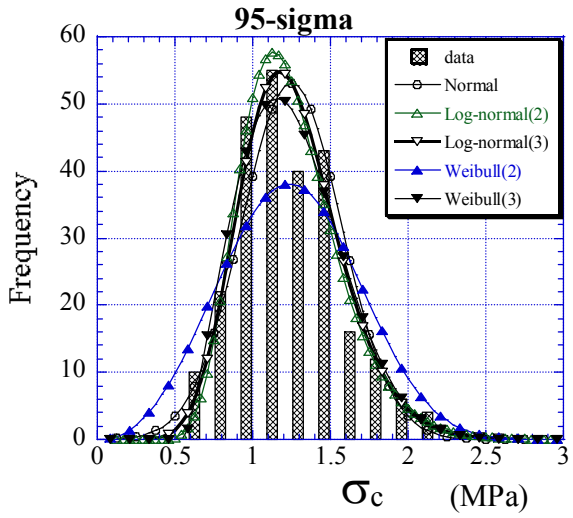

Fig.5(b) Histogram and probability density functions of uni-axial compressive strength (1995)

Table 3. Chi square test for goodness of fit (uni-axial compressive strength)

Year/Mon.	n	N	Probability Distribution Function p.d.f.	χ_0^2	$\chi^2(\phi, 0.05)$
1994/3	9	133	Normal(2)	12.1	12.59
			Log-normal(2)	12.0	12.59
			Log-normal(3)	6.8	11.07
			Weibull(2)	26.4	12.59
			Weibull(3)	11.9	11.07
1995/2	10	256	Normal(2)	18.5	14.07
			Log-normal(2)	10.2	14.07
			Log-normal(3)	7.4	12.59
			Weibull(2)	39.7	14.07
			Weibull(3)	8.3	12.59

Ice Load Data

In medium scale indentation tests on JOIA projects, a lot of indentation test data using natural sea ice were obtained and reported by Takeuchi et al. (2002). Akagawa et al. (2000) investigated the relation between each peak under subsequent load and failure pattern through a plane pressure panel sensor, and found that all peak loads were due to flaking failure of ice in an independent ice failure zone. The top figure in **Fig.6** shows the occurrence of a peak under

subsequent ice load in the independent ice failure zone, and the bottom figures in **Fig.6** are images obtained by pressure panel sensors at four frames. The occurrence of a peak corresponds to flaking failure. These data were obtained at an ice thickness h of 21cm, an indentation velocity V of 30mm/s, a uni-axial compressive strength σ_c of 1 MPa, and a structure width W of 1.5m. V/h is around $1.4*10^{-1}$ (1/s) which is in the brittle range.

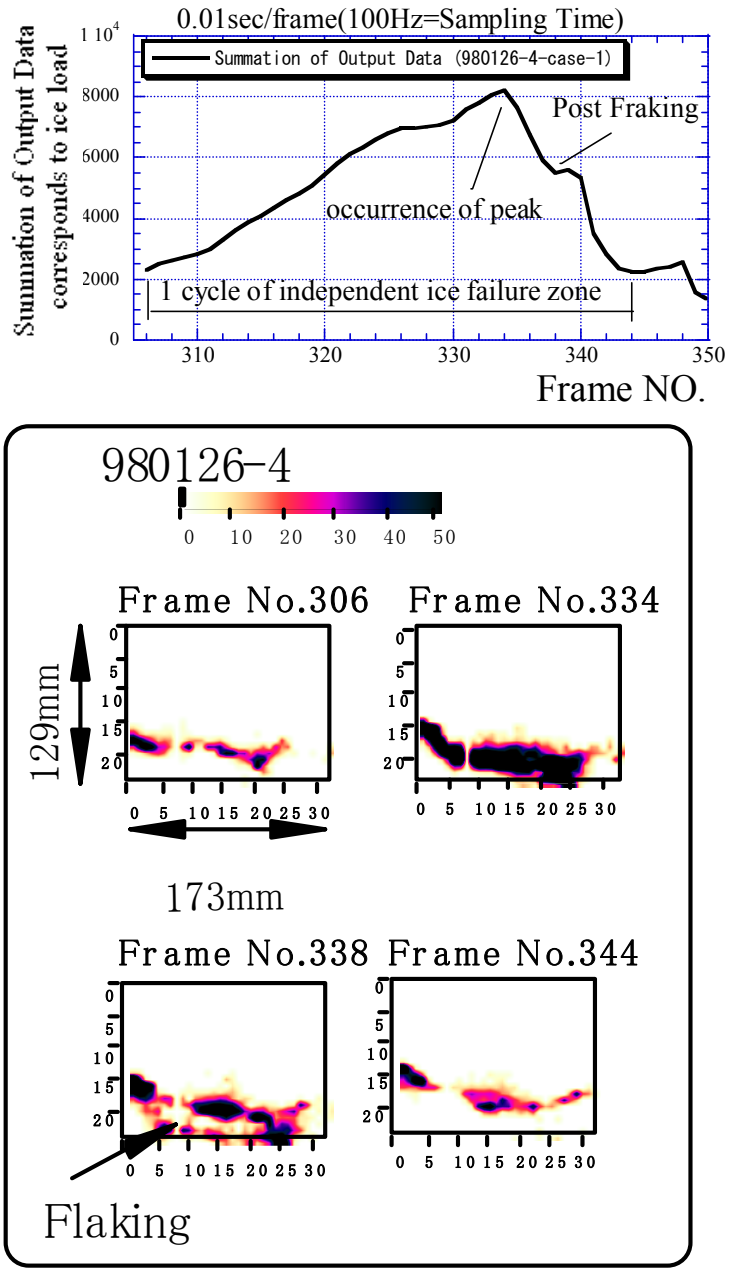

Fig.6 Relationship between flaking failure and occurrence of peak under subsequent load (Akagawa et al., 2000).

In medium scale indentation tests of the JOIA projects, the size of an independent ice failure zone is approximately the same as ice thickness (h), even though it shows scatter. Furthermore, the segmented panels of width 10cm are mounted at the surface of the model structure to measure ice load. Thus, the medium scale indentation test data listed in **Table 4**, which satisfy the brittle condition of V/h> 10^{-3} (1/s), and ice thickness of around a multiple of segmented panels of width 10cm, were used for statistical analysis. Ice load data at both ends of the model structure were not used in the analysis for constraint effect. 27 time series of ice load data for 1996/2/26 test and 12 time series of ice load data for 1996/2/28 test were prepared, and a lot of peak data were taken out for the analysis. **Fig.7 & 8** show examples of ice load data that could be considered to be in an independent ice failure zone. **Fig.9(a)&(b)** show histograms on peaks under subsequent ice load in an independent ice failure zone with the theoretical curves of probability density functions. From **Fig.9(a)&(b)**, log-normal (3-parameters) appear to give a good fit to the data. After calculating χ_0^2 using equation [2], χ_0^2 is compared to $\chi^2(\phi,0.05)$ with the degree of freedom ϕ using equation [3] and a one sided test with 5% significant level similarly.

Table 4. Conditions of peaks under subsequent load used in statistical analysis

	W (m)	h (cm)	σc (MPa)	V (mm/s)	V/h (1/s)	No. of time series in an independent ice failure zone
1996/2/26	3	11.5	1.26	30	$2.6*10^{-1}$	27
1996/2/28	3	20	2.76	6	$3*10^{-2}$	12

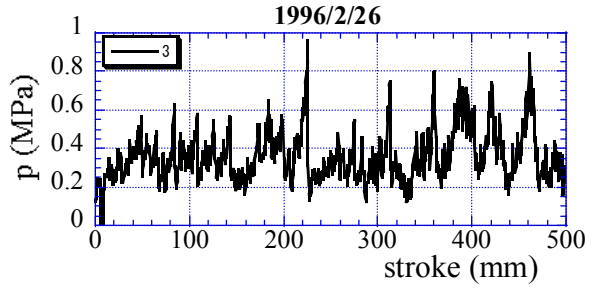

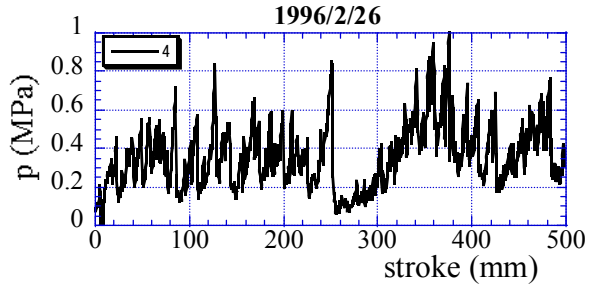

o
o
o

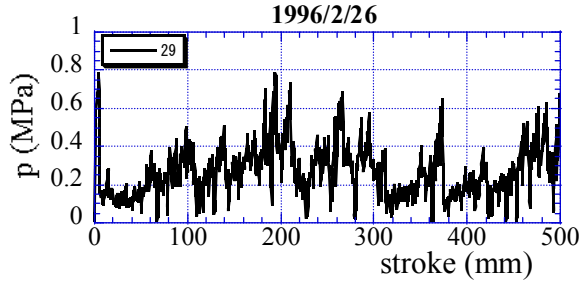

Fig.7 Ice load time series (converted to stroke) for 1996/2/26

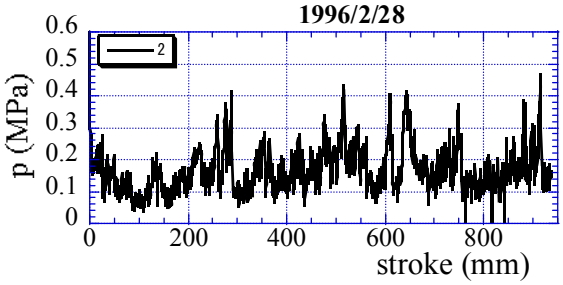

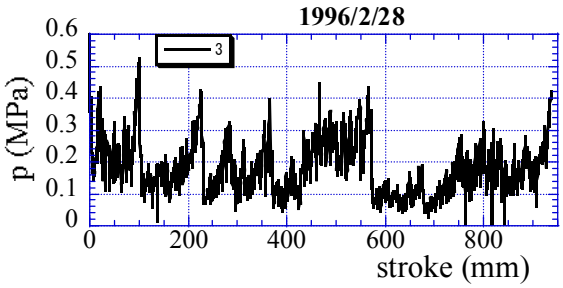

o
o
o

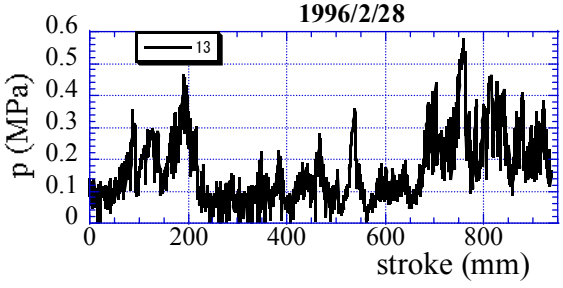

Fig.8 Ice load time series (converted to stroke) for 1996/2/26

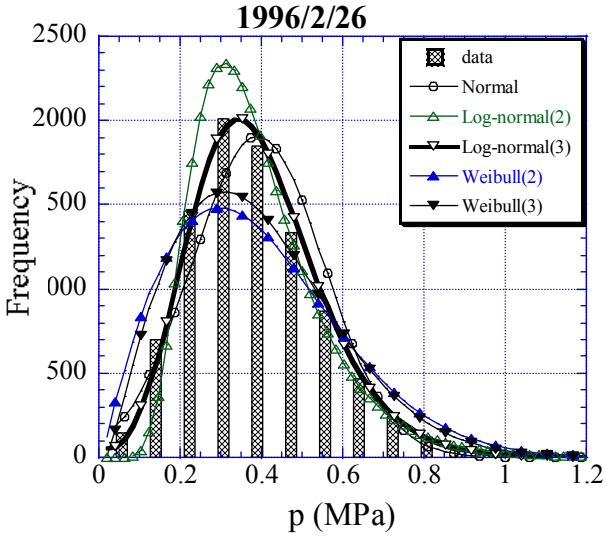

Fig.9(a) Histogram and probability density functions on peaks under subsequent load in an independent ice failure zone.

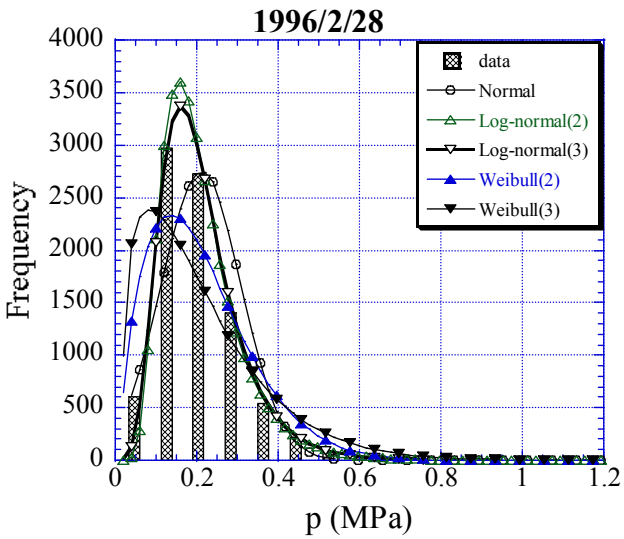

Fig.9(b) Histogram and probability density functions on peaks under subsequent load in an independent ice failure zone.

The results of Chi square tests for goodness of fit are listed in **Table 5.** Satisfying $\chi_0^2 < \chi^2(\phi,0.05)$, log-normal (3-parameters) is the most appropriate probability density function for peak loads. This result is the same as that for uni-axial compressive strength. It is shown that load, based on ice failure, follows a log-normal (3-parameters) distribution.

Table 5. Chi square test for goodness of fit (peaks under subsequent load)

Year/Mon/Day	n	N	Probability Distribution Function p.d.f.	χ_0^2	$\chi^2(\phi,0.05)$
1996/2/26	15	9271	Normal(2)	1927.6	21.0
			Log-normal(2)	2288.8	21.0
			Log-normal(3)	11.3	19.7
			Weibull(2)	1159.9	21.0
			Weibull(3)	699.4	19.7
1996/2/28	15	8603	Normal(2)	33817910.8	21.0
			Log-normal(2)	70.8	21.0
			Log-normal(3)	18.1	19.7
			Weibull(2)	1438.8	21.0
			Weibull(3)	2536.3	19.7

Conclusions

Uni-axial compressive strengths of natural sea ice at Lake Saroma as well as peaks during subsequent ice load obtained in medium scale field indentation tests of the JOIA project were analyzed statistically to find an appropriate probability density function to fit the data. From Chi square test for goodness of fit, it is found that both uniaxial compressive strength and peaks

under subsequent loads in an independent ice failure zone distributed in log-normal density function with 3 parameters.

Acknowledgments
The paper includes data from part of the JOIA Project.

References

Kioka, S., Yamamoto, Y., Honma, D. and Sakikawa, M., 2004a, Analysis and Simulation of Sea Ice Draft Profile on Okhotsk Sea Coast of Hokkaido, Proc 17th International Symposium on Ice, Vol.1, pp191-198.

Kioka, S., Yamamoto, Y., Honma, D. and Sakikawa, M. and Nishita,M.(2004b), "Simulation Method of Ice Bottom Topography," Proc 6th ISOPE PACOMS-2004, pp96-102.

Kioka, S., Yamamoto, Y., Sakai, S., Takeuchi, T (2006), "ANALYSISI OF ICE BOTTOM TOPOGRAPHY ON OKHOTSK SEA COAST OF HOKKAIDO -OBSERVATION RESULTS IN 2004-," Proc 18th IAHR International Symposium on Ice, Vol.1, pp309-316.

Michel,B.:Ice Mechanics, Quebec:Les presses de l'Universite, Laval. 1979

Saeki,H., Nomura,T., and Ozaki,A.: Experimental study on the testing methods of strength and mechanical properties for sea ice, Proc5th IAHR International Symposium on Ice, Part 1,pp.135-150.,1978.

Weeks,W.F. and G.F.N. Cox: The mechanical properties of sea ice: A status report, OCEAN SCIENCE and ENGINEERING, 9(2), pp.135-198. , 1984.

Lainey, L. and Tinawi,R., 1984., The mechanical properties of sea ice – A compilation of available data, Canadian Journal of Civil Engineering, Vol.11, pp.884-923.

Masaki,T., Takeuchi, T., Matsushita, H., Sakai, M. and Saeki, H., 1996. Study on Unconfined compressive strength on sea ice. Cold Region Technology Conference Vol.12, pp.516-521.

Takeuchi, T., Akagawa,S., Iwai, T., Nishio,S. and Katsura, Y., 1994., Characteristics on strength of natural sea ice, Cold Region Technology Conference Vol.10, pp.403-406. 11

Takeuchi, T., Akagawa,S., and Iwai, T.,1995., On the distribution of strength of ion-situ sea ice sheet, Annual Journal of Civil Engineering in the Ocean, VOL.11, pp.241-245, 1995. 6

Takeuchi T., Sakai M., Akagawa S., Nakazawa N. and Saeki H.,2002, ON THE FACTORS INFLUENCING THE SCALING OF ICE FORCES, *Scaling Laws in Ice Mechanics and Ice Dynamics* by J.P.DEMPSEY and H.H.SHEN, KLUWER ACADEMIC PUBLISHERS SOLID MECHANICS AND ITS APPLICATIONS VOLUME94 (ISBN 1-4020-0171-1) pp. 149-160.

Akagawa,S., Nakazawa,N., Sakai,M., Terashima, T., Takeuchi,T. and Saeki, H., 2000, Predominat Ice Failure Mode Producing Peak-Ice-Load Observed in Continuous Ice load Records, Cold Region Technology Conference Vol.16, pp.175-182.

19th IAHR International Symposium on Ice
"Using New Technology to Understand Water-Ice Interaction"
Vancouver, British Columbia, Canada, July 6 to 11, 2008

An Experiment for the Mechanical Properties of Model Ice Grown in a Cold Room

Kyungsik Choi, Jung-Hyun Kim and Young-Kyo Seo
Korea Maritime University, Busan, Korea
kchoi@hhu.ac.kr

ABSTRACT

The ice model basin is an essential part of the facilities for design of icebreaking vessels and Arctic offshore structures. One of the important issues while performing model tests in the ice model basin is to select a realistic model ice material which shows a correct similitude with natural sea ice. Usually in the refrigerated tank, model ice is grown from fresh water with appropriate chemical additives such as brine, urea or EG/AD/S.

The first Korean ice model basin is now under construction at the Maritime Ocean Engineering Research Institute (MOERI) and is scheduled to open in 2009. This study focuses on reviewing material properties of model ice for possible use in the future MOERI ice model basin. The purpose is to correctly reproduce and to check the properties of model ice prior to the completion of MOERI ice model basin facilities. The elastic modulus and the flexural strength of EG/AD/S model ice originally developed by Timco(1986) were evaluated through a series of beam bending test. A cold room facility at the Korea Maritime University (KMU) was used for making model ice specimen. Since the cold room adopts a different freezing procedure in making model ice, the material properties of model ice grown and measured in a cold room slightly differ from published test results grown in the ice model basin. The reason for this difference is discussed in this study and future refinement techniques in making and testing of model ice specimen in a cold room are recommended.

KEY WORDS: EG/AD/S Model ice; Cold room; Flexural strength; Elastic modulus

INTRODUCTION

Full-scale field measurement is of importance in the construction of ships and offshore structures, however, the full-scale tests in ice-covered sea are usually very expensive and difficult. Model tests in a refrigerated ice model basin may substitute this difficulty of full-scale field tests. One of the main issues while performing model tests in the ice model basin is to select a model ice material which follows the appropriate similitude law between the prototype and model scales. Among various material properties of model ice, the most important one is the ratio of elastic modulus to flexural strength (E/σ_f) of model ice. Usually E/σ_f ratio falls in the range of 2,000 ~ 5,000 according to the variation of natural sea ice properties.

Currently there are a number of ice model basins in the world and they are using various types of model ice materials. The model ice is usually grown from fresh water with certain chemical additives such as brine, urea or EG/AD/S. The material properties of those model ice were thoroughly investigated in may references (for example, see Schwarz et al., 1981; Timco, 1984).

The first Korean ice model basin is now under construction at the Maritime Ocean Engineering Research Institute (MOERI) and is scheduled to open in 2009. MOERI ice tank comprises of a square-type main test section (32m×32m), a preparation tank (10m×32m) and a melting pit. MOERI is planning to use EG/AD/S-CD model ice as a primary model ice material in their ice model basin. This study focuses on reviewing material properties of model ice for possible use in the future MOERI ice model basin. The purpose of the study is to correctly reproduce and to check the properties of model ice prior to the completion of MOERI ice model basin facilities.

In this study, the elastic modulus and the flexural strength of EG/AD/S model ice originally developed by Timco(1986), were evaluated and the test results were compared with those of the published reference. A cold room facility at the Korea Maritime University (KMU) was used for making model ice specimen. Since the cold room adopts a different freezing procedure in making model ice, the material properties of model ice grown and measured in a cold room slightly differ from published test results grown in an ice model basin. The reason for this difference is discussed in this study and future refinement techniques in making and testing of model ice specimen in a cold room are recommended.

TESTS IN A COLD ROOM

The ice tank was not available at time of the test hence a cold room facility was substituted for the model ice tests. The KMU cold room designed for ice mechanics research was used to measure the elastic modulus and the flexural strength of EG/AD/S model ice. Details of the cold room facility were described by Kim and Choi (2006). A digitally controlled UTM (universal testing machine) and portable push-pull spring gauges were used to carry out beam bending tests inside the cold room (4m×6m×2.6m).

Procedures in Making Model Ice Specimen

As described by Timco(1986), the EG/AD/S model ice is made of a solution of ethylene glycol(0.46%), aliphatic detergent(0.032%) and sucrose(0.039%) added to fresh water. The specific gravity of EG/AD/S solution is very close to that of fresh water and assumed to change,

as fresh water does, with increasing temperature. The viscosity of the solution is the same as fresh water. The ice formed when the EG/AD/S solution in the ice tank freezes is a crystalline structure that closely models the flexural, shear, and crushing strength of sea ice found in Polar Regions.

In this study, two important material properties of EG/AD/S model ice, i.e., elastic modulus and flexural strength are tested for determination of applicability in an ice model basin. The purpose of the test is to check and also to reproduce correct material properties of model ice prior to the completion of MOERI ice model basin facilities. Another goal in the test is to achieve target strengths of the model ice systematically through a so-called 'warm-up' process. By warming up air temperature right after the desired thickness of model ice sheet was achieved, it is possible to control the strength of model ice according to various test environments.

As mentioned above, a cold room facility was used in making model ice specimen instead of an ice model basin that was not available at the time of test. Freezing procedures used in a cold room are different from those in an ice model basin in many respects. To reduce the gap in test results from different freezing procedures, a series of test procedure in making model ice specimen is adopted as in Table 1.

Table 1. Procedures in making model ice specimen

<table>
<tr><td>Test 1</td><td rowspan="3">Entire solution frozen in plastic containers (Photo. 1)</td><td>Original EG/AD/S</td><td rowspan="2">No seeding</td><td rowspan="3">No warm-up</td></tr>
<tr><td>Test 2</td><td>Higher concentration</td></tr>
<tr><td>Test 3</td><td>Original EG/AD/S</td><td rowspan="2">Seeding</td></tr>
<tr><td>Test 4</td><td>Ice sheet frozen on surface of solution in an ice tank (Photo. 2)</td><td>Original EG/AD/S</td><td>Warm-up process applied</td></tr>
</table>

Original EG/AD/S mixture of the model ice solution was used in all tests except Test 2 where about 10 times higher concentrated solution of three chemical additives is used. Test 2 was intended to see the effect of chemical additives in the freezing process of model ice solution. Seeding of fine powder from solid model ice enhances the freezing process and this technique is applied in Test 3 and 4.

Each chemical ingredient is added to the fresh water in a small container and the solution is blended well at room temperature. The containers holding EG/AD/S mixture are put in the cold room at -18 for 36 hours. Once the entire solution is frozen, the model ice specimens are cut and trimmed by a band saw (Photo. 1). Because no warm-up process was adopted for Test 1, 2 and 3, the flexural strength of model ice specimen turned out to be much stronger than it was assumed. It will be discussed thereafter.

Photo 1. Containers of AG/AD/S mixture solution and the ice specimens cut from frozen model ice solution (Test 1, 2 and 3)

Photo 2. Model ice sheet grown in a small ice tank (Test 4)

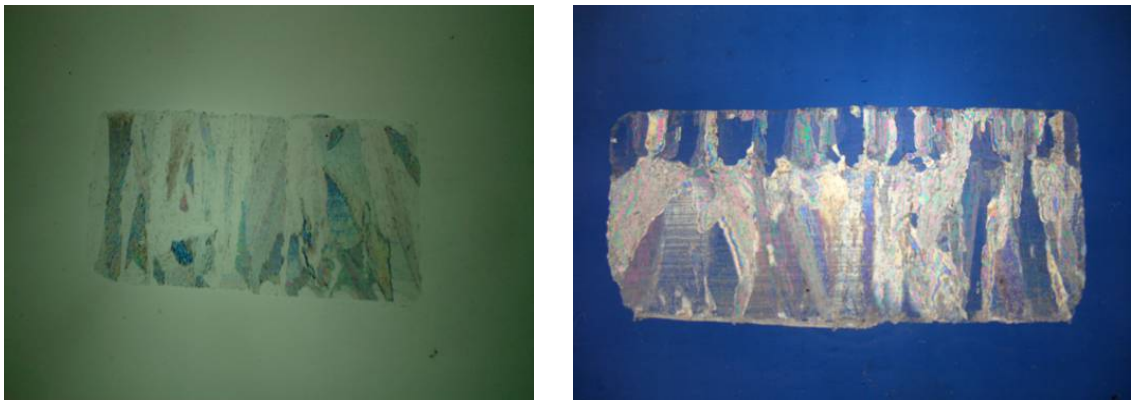

(a) (b)

Photo 3. Thin section photographs of model ice grown in Test 1 (a) and in Test 4 (b)

To apply a wet-seeding technique and warm-up process for Test 4, a miniature ice tank (120×50×50cm) was fabricated to simulate the environment of an actual ice model basin. In the ice tank, the model ice sheet grows up to 30mm at -18 for 6 hours (Photo. 2). After a desired thickness is achieved, the air temperature in the cold room is set to 0 and the warm-up process is allowed for about 6 hours. This tempering process reduces the strength of model ice. Photo. 3 shows thin section photographs of model ice specimen in Test 1 and in Test 4 respectively.

Three-Point Beam Bending Tests

The flexural strength and elastic modulus of ice can be measured by a cantilever beam test or beam bending test. In the actual ice model basin, the cantilever beam tests are performed easily using portable spring gauges and a LVDT system. In the cold room situation, however the cantilever beam tests are very difficult or impossible even in a small ice tank because a relatively large ice sheet is required to carry out cantilever tests. In this study only 3-point beam bending tests are performed in the cold room. Inside the KMU cold room a 20 ton capacity UTM is located for compression and flexural beam tests. For Test 1, 2 and 3 the UTM is used for measuring flexural strength and deflection of model ice specimen. For Test 4 the model ice is too weak to use the UTM, hence a portable push-pull spring gauge is used for measuring flexural strength of model ice specimen.

The model ice specimen prepared for 3-point bending tests has a standardized dimension according to laboratory manuals (Jones, 1993; ITTC, 2002). The length (L) is five to six times the specimen thickness (h) and the width (B) is twice the thickness (Timco, 1981). Since the model ice thickness grown in an actual ice model basin is about 2.5~5 cm, dimension of model ice specimen used in all tests is selected as $h:B:L$ = 25mm:50mm:125mm.

In the 3-point bending tests the flexural strength (σ_f) is determined from the linear elastic beam theory by $\sigma_f = \frac{3PL}{2Bh^2}$ and the elastic modulus (E) by $E = \frac{1}{4B}\frac{P}{\delta}(\frac{L}{h})^3$.

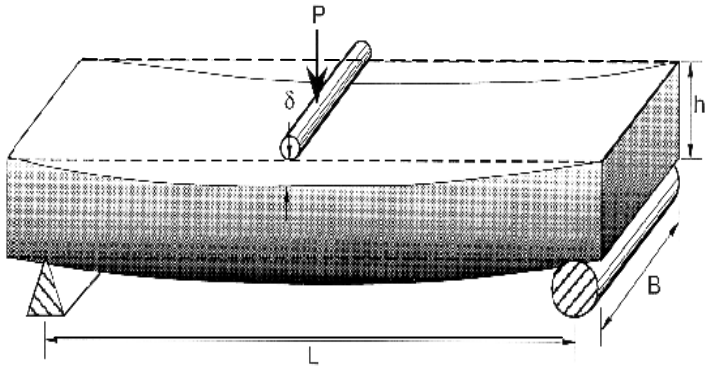

Figure 1. Parameters in the 3-point beam bending test

TEST RESULTS

Figure 2 and Table 2 summarize the results from model ice beam bending tests. In Figure 2 the measured values of flexural strength are plotted against elastic modulus for four different tests. Flexural strength data for Test 1, 2 and 3 (i.e., the cases when no warm-up process was applied) fall in the range greater than 500kPa, which seems to be much stronger than it is expected. Depending on freezing procedures, the model ice specimens show differences in their values of elastic modulus. The elastic modulus of model ice frozen from higher concentration of EG/AD/S solution (Test 2) is smaller than those of Test 1. It seems that the amount of chemical additives diminishes the stiffness of model ice structures.

Data from Test 3 where a seeding technique is applied shows the E/σ_f ratio about 2,000 which is close enough to the published results (Timco, 1986). It seems to be desirable for the model ice material, however, the flexural strength and elastic modulus of model ice are still too high and the similitude law between the actual sea ice and model ice does not satisfied at all.

In order to obtain low strength and also low stiffness for model ice it is necessary to use the warm-up process during model ice preparation. In Figure 2 and Table 2, the data from Test 4 show that the flexural strength of original EG/AD/S model ice falls in the range less than 100kPa with an average of 65kPa. For Test 4, LVDT type devices measuring deflections of model ice sheet can not be used in a cold room condition and therefore it was not possible to obtain the elastic modulus of model ice specimen. However it is believed that the elastic modulus of model ice after a sufficient warm-up time decreases to near 100MPa.

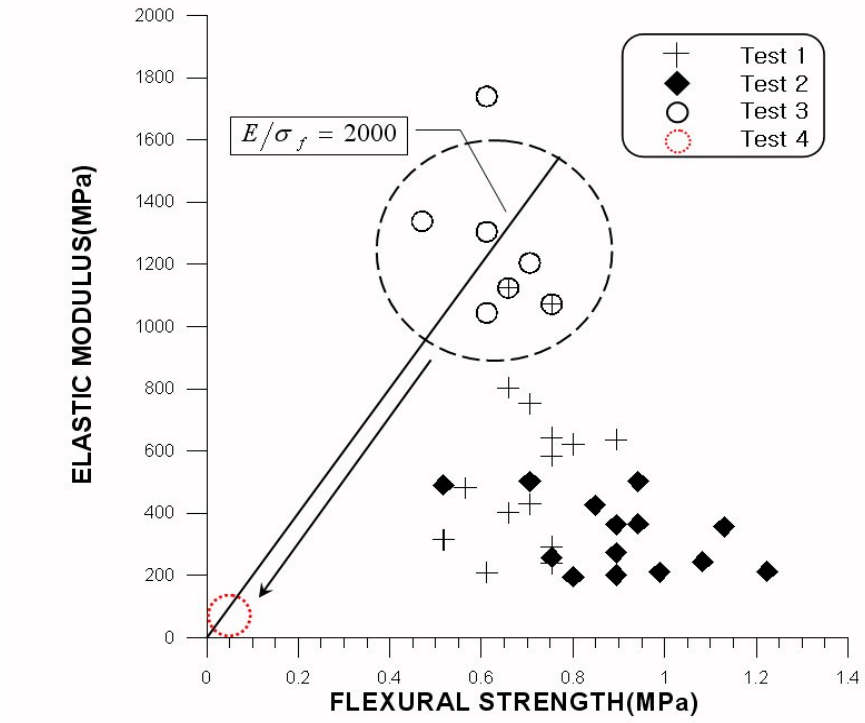

Figure 2. Elastic modulus and flexural strength of model ice measured from beam bending tests

Table 2. Average values in elastic modulus and flexural strength measured from model ice

	Test Procedures	σ_f (kPa)	E (MPa)	E/σ_f	Comment
Test 1	Plastic container	710	578	822	Original EG/AD/S solution
Test 2	No warm-up UTM for bending test	910	328	395	High concentration (EG 0.46%, AD 0.32%, S 0.49%)
Test 3		620	1270	2109	Original EG/AD/S solution
Test 4	Small ice tank Warm-up process Push-pull gauges	65	N/A	N/A	Original EG/AD/S solution

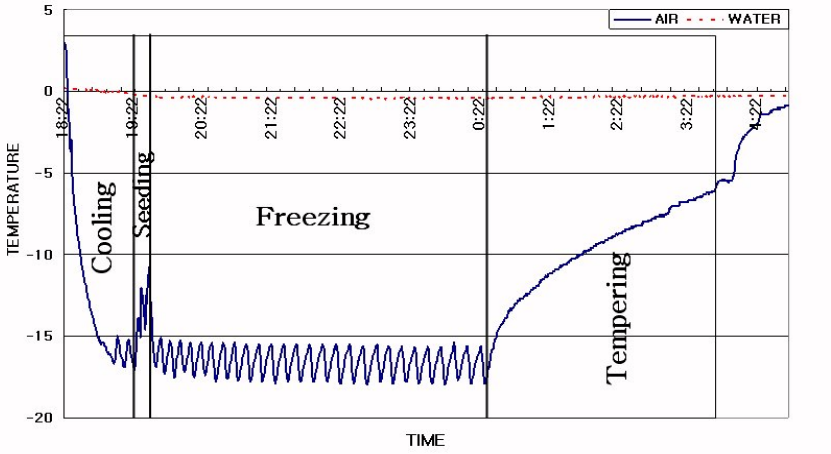

Figure 3. Air and water temperature variation with time in the cold room (Test 4)

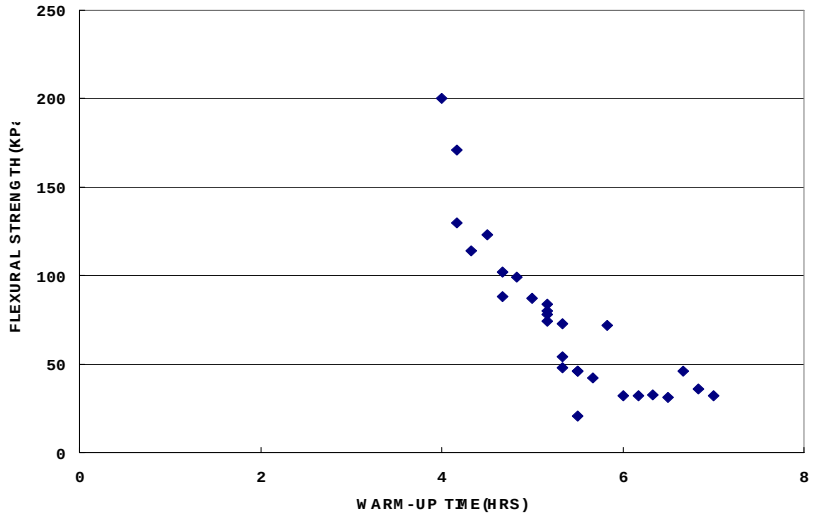

Figure 4. Measured flexural strength of model ice specimen vs. warm-up time (Test 4)

The EG/AD/S model ice has a columnar structure (anisotropic) grown from the top to bottom of ice sheet in the ice tank. During the warm-up period which produces glycol pockets entrapped between ice crystals, ice structures weaken gradually and the strength and stiffness of model ice depend on the length of warm-up time. Figure 3 shows a typical air and water temperature variation with time in the cold room. We can see that the measured strength of model ice specimen decreases with warm-up time as shown in Figure 4.

CONCLUSION

The purpose of the paper is to determine the applicability of EG/AD/S model ice originally developed by Timco(1986) to the MOERI ice model basin facilities. The elastic modulus and the flexural strength of EG/AD/S model ice were evaluated and the test results were compared with those of the published reference. A cold room facility was used for making model ice specimen. It is difficult to make model ice using a cold room because it adopts different freezing procedures from that of an ice model basin.

It was found that the warm-up time is the most important factor in preparation of a good model ice that is correct in similitude law. In order to get a desired strength and stiffness for a model ice it is necessary to control the warm-up time. The relationship between the warm-up/cool-down time and the strength/stiffness will be studied in the future.

ACKNOWLEDGMENT

Research supports provided by the Korea Science and Engineering Foundation through the Advanced Ship Engineering Center (Grant No. ASERC R11-2002-008-01002-0) and Maritime Ocean Engineering Research Institute are greatly acknowledged.

REFERENCES

ITTC, 2002. Testing and Extrapolation Methods - Ice Testing General Guidelines, ITTC Recommended Procedures, Ice Specialist Committee of 23rd ITTC.

Jones, S.J., 1993. Ice Tank Test Procedures at the Institute for Marine Dynamics, NRC Report LM-AVR-20.

Kim, S.Y. and Choi, K. 2006. Standardization of Laboratory Experimental Techniques with a Cold Room in Korea, Proc. of IAHR Symposium on Ice, Sapporo, Japan, pp.113-120.

Schwarz, J. et al., 1981. Standardized Testing Methods for Measuring Mechanical Properties of Ice, Cold Regions Science and Technology, Vol.4, pp.245-253.

Timco, G.W., 1981. On the Test Methods for Model Ice, Cold Regions Science and Technology, Vol.4, pp.81-92.

Timco, G.W., 1984. Ice Forces on Structures: Physical Modeling Techniques, Proc. of IAHR Symposium on Ice, Hamburg, Germany, Vol.4, pp.117-150.

Timco, G.W., 1986. ED/AD/S: A New Type of Model Ice for Refrigerated Towing Tanks, Cold Regions Science and Technology, Vol.12, pp.175-195.

19th IAHR International Symposium on Ice
"Using New Technology to Understand Water-Ice Interaction"
Vancouver, British Columbia, Canada, July 6 to 11, 2008

Latest development in ice model testing

Göran Wilkman, Ann-Cristin Forsén, Tom Mattsson
Aker Arctic Technology Inc.
Merenkulkijankatu 6, 00980 Helsinki Finland
goran.wilkman@akerarctic.fi, ann-cristin.forsen@akerarctic.fi, tom.mattsson@akerarctic.fi

Abstract

The next generation ice model testing facility of Aker Arctic Inc. (AARC) was inaugurated in March 2006. The new facility is located in Helsinki at the Vuosaari Marine Business Park, next to the new Helsinki harbour. This facility is the third in the history of Aker Arctic starting in 1969 with Wärtsilä Ice Model Basin (WIMB).

Today the new facility has been in operation for two a half years. During this period quite a lot of learning and developing has taken place still even the transfer of the ice making happened quite well.

The new facility has also opened new possibilities.

The paper describes the new facilities and highlights the work done so far. Also among other things the further development possibilities of the AARC FGX model ice is discussed.

Making of thick weak ice in the model basin has always been quite a problem. In this respect the enhanced use of AARC FGX ice has given new possibilities in testing. Firstly ice sheets with thickness close to 100 mm were prepared for the new Russian multipurpose icebreaker project to simulate full-scale level ice thickness of 2.85m. Recently model ice with thickness close to 240 mm with flexural strength of 10-20 kPa was manufactured.

The paper will discuss also the processes of making these thick/week ice sheets.

1. History

The first ice model testing facility in Finland was established in 1969. That time Esso (Humble Oil) was looking for the possibilities to transport oil from north slope of Alaska to the market through Canadian Arctic Islands, Manhattan project. Esso initiated the building of the Wärtsilä Icebreaking Model Basin, WIMB; test facility in an underground tunnel (bomb shelter) in conjunction with the Manhattan project where Wärtsilä Ice breaking knowledge had a leading role. The experts of Wärtsilä were in charge both the model testing of the vessel and planning its modifications.

This first facility was intended to be a temporary one , but was successfully operated for 13 years till February 1983. In 1980 it was decided to design and build a new testing facility, Wärtsilä Arctic Research Centre, WARC. WARC was inaugurated on February 17, 1983. Simultaneously with the building process, also a project to make a new model ice (FGX), which would have better physical properties than the traditional saline ice, was started. In November 1989 the parent company changed to Masa-Yards and the name of the arctic centre was changed to MARC, Masa-Yards Arctic Research Centre. The property lease under MARC facility expired in 2005 and the construction of the new facility has started in January 2005. In January 2006 the calibration of the new facility started and commercial work started in March 2007.

2. New facility

The new facility is located in eastern Helsinki, in Vuosaari. Helsinki City is building a new harbour to the area (to be operational in 2008), where the Valmet Shipyard was operating in the seventies and eighties. The new AARC facility is located next to the new harbour at Vuosaari Marine Business Park. Figure 1 shows the location of the facility.

Figure 1. Location of the new testing facility

The area is quite ideal for such purpose. As the new harbour is ready, there will be excellent connections to the centre of city of Helsinki and Helsinki-Vantaa Airport. The old graving dock alongside to the new facility can still be utilized for docking of ships and research installations like strain gauges etc. can be handled at the facility, if needed.

The building of the new facility will follow the similar layout principle as the previous facility. The main principle views are in Figures 2. The main parameters of the test basin are in Table 1.

Table 1. Main parameters of the laboratory basin

	AARC
Length (m)	75
Width (m)	8
Water depth (m)	2,1-2,2
Water volume (m3)	1300

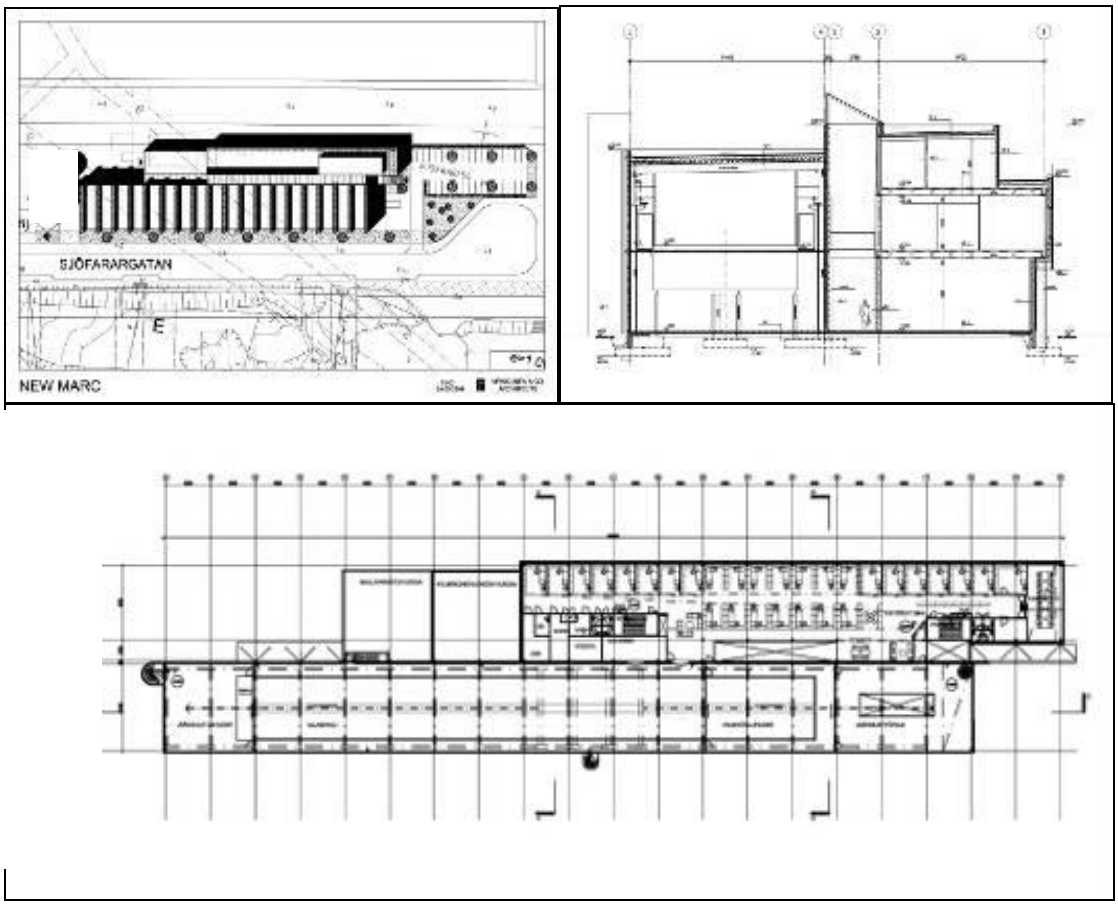

Figure 2. Layout of the new testing facility

Basin

The new basin is 8 meters wide throughout the whole length of the basin. The beam has been increased from the previous facility by 1.5 m to better enable maneuvering tests with ships and larger scales with structure tests. The material of the basin is steel.

One of the most important features in an ice model basin is the underwater visibility. In the new basin the side windows (8pcs.) will be wider and in the bottom of the basin there is a continuous window throughout the whole length of the basin. These improvements enable better visualization of the tests.

The basin area is separated from the preparation/ice melt space and with vertically opened/shut curtain. A view to the basin is shown in Figure 3.

Figure 3. View to basin

Refrigeration system

The new refrigeration system is based on completely new technique. Instead of cooling large amounts of coolant liquid, only 80 kg of freon is cooled and through a heat exchanger liquid CO_2 is cooled and circulated in the refrigeration elements. In total four (4) cooling compressors with a total cooling power of 600 kW is installed. In the former facility there was only one compressor, which made it very difficult and uneconomic to at higher basin hall temperatures, say -6 ºC. Also the new system will be automatic/remote controlled. Machinery arrangement is shown in figures 4.

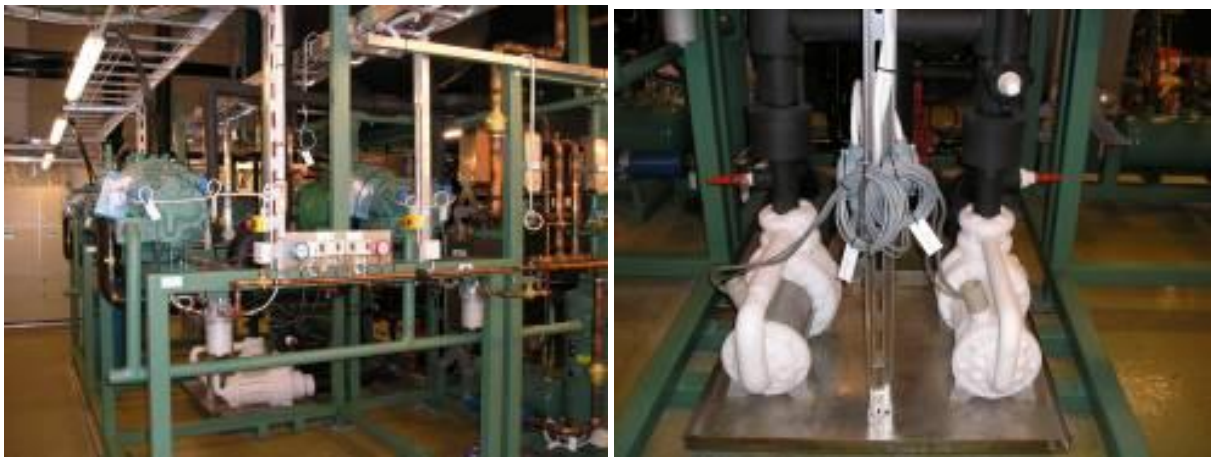

Figure 4. Machinery room views

Carriages
In the new facility there are two carriages:

- measurement/test carriage
- ice treatment/ice making carriage

The carriages are on rails up near the ceiling and the carriages are hanging like any gantry crane. This improved solution also enables better observations from the ice level from the sides of the basin. The features of the carriages are the following:

Both carriages are planned be moved in synchronous mode, one follows the other. Also both the carriages can be taken to the model outfitting area (warm space out from the cold) for installation of models and initial calibration. The measurement carriage is shown in Figures 5.

Figure 5. Measurement carriage

Visual observations
It was already mentioned about the windows around the basin. In addition there is a plan to adopt an online video link to the conference rooms from the cameras recording the tests. Views to the basin through windows are in Figures 6.

Figure 6. View through bottom and side windows

3. Calibration of the new basin

Testing and calibration of the basin and equipment took place in early March 2006.

The first part was to get all the equipment related to ice making process to function according to defined specification; water treatment, refrigeration system and carriages.

The ice making process was in fact adopted directly from the previous laboratory and thus when the conditions are similar, the ice produced follows quite well similar pattern. One of the key parameters is the smoothness of the ice sheet produced. In Figure 7 there are the thickness distribution examples of three different ice sheets of which the target thickness values were 19, 35 and 55 mm. The variation of thickness along the length of the basin is 1- 3mm. The lower value is for the thinner ice. This variation is due to several items like: functioning of the cooling elements in the ceiling, measuring method (manual) and distance from the over water gates. However, the results are very good and the ice sheet exceed the thickness evenness of the previous laboratory. Of course to keep it good, it needs to be tendered continuously.

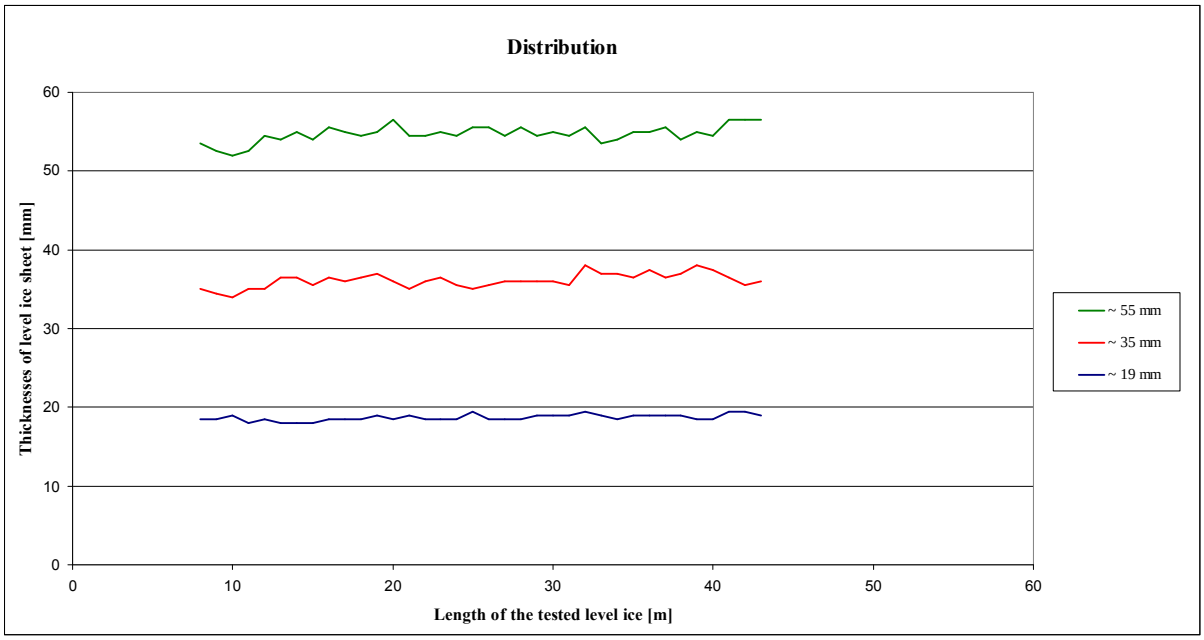

Figure 7. Thickness variation of model ice during calibration

The other interesting parameter is the transversal thickness distribution. This is affected by the same parameters as the longitudinal one added by the evenness of the spraying of the water into the air to form the fine grains which laminate the final thickness. The transversal evenness is due to the angles of the spray nozzles. The transversal profiles are in Figure 8. The example shows that there was some discrepancy in the thickness distribution when moving towards the sides of the basin, but very small with no significant effect.

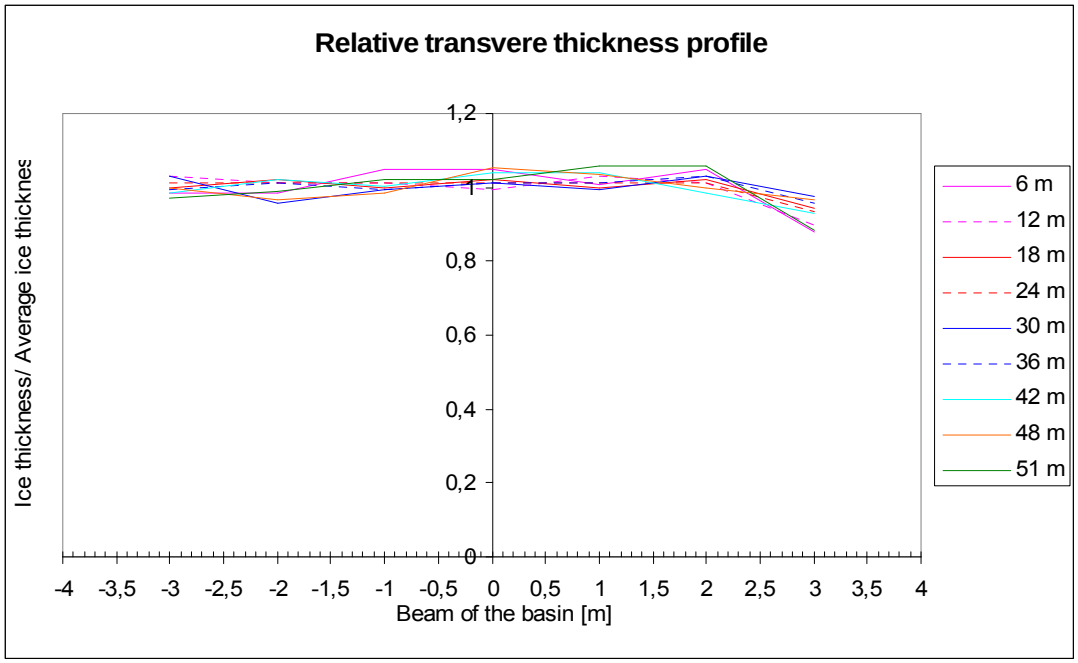

Figure 8. Variation of transversal ice thickness profile

The first model tested was AARC's standard model of icebreaker Otso. IB Otso is the first new generation Baltic Icebreaker built in the middle of eighties. She has a twin propeller (open, fixed pitch) and rudder aft ship and in the waterline there is a stainless steel belt to keep the friction against ice small. IB Otso in action is in Figure 9.

Figure 9. Icebreaker Otso in the Baltic Sea

The test results in the new basin coincide with the results gained in the full-scale ice trials. IB Otso is one of the mostly tested icebreakers both in full- and model scale. The calibration test results are shown in Figure 10.

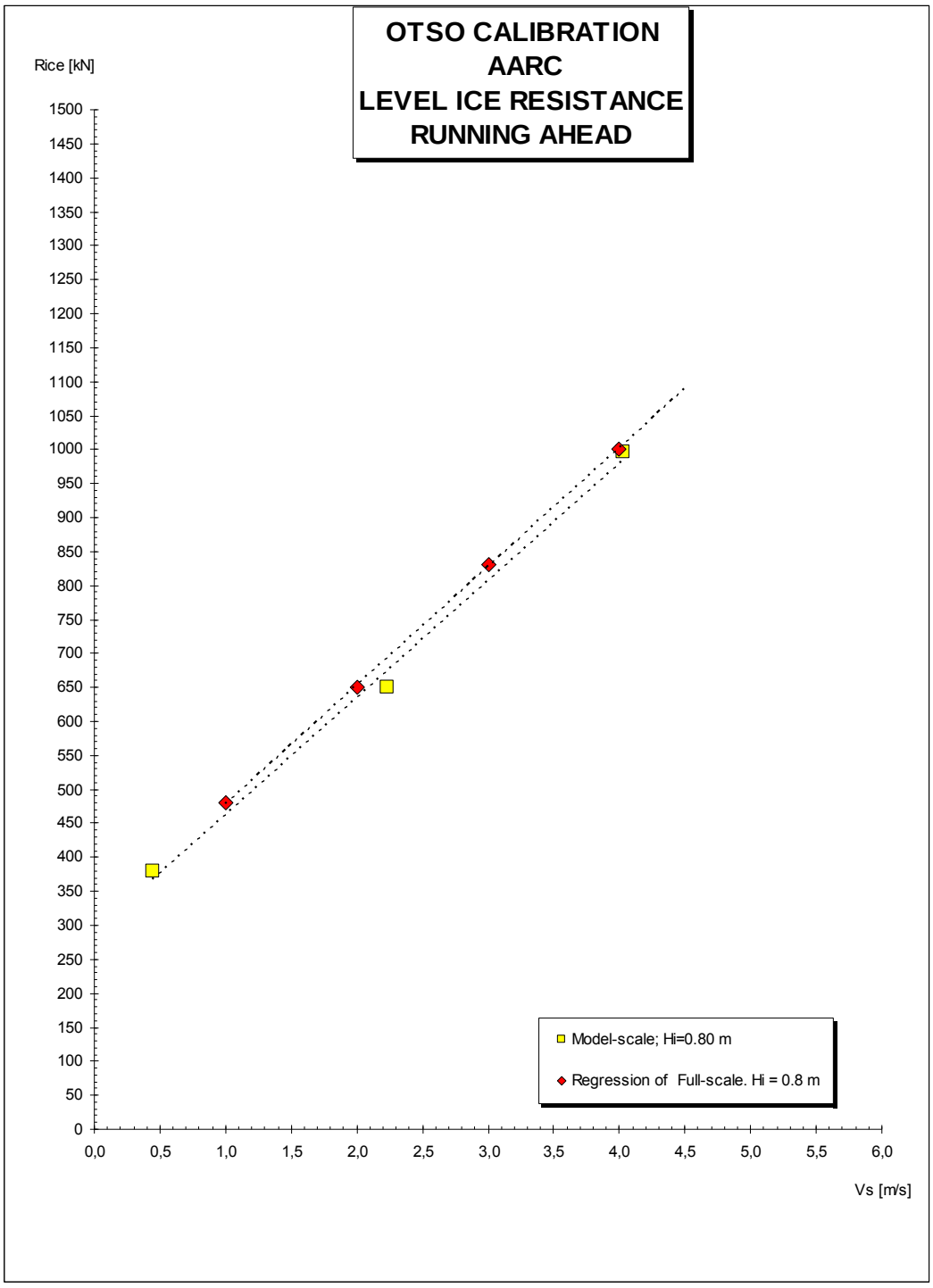

Figure 10. Calibration test results of IB Otso.

In early April after all the calibration, the basin was ready to start tests for projects.

4. Experience during the first two years

During the first year, altogether 80 ice test days was carried out (2005: 61 ice test days). The year started with oil spill tests in the old facility. During the first year 10% of the ice sheets done were consumed for calibration and ice development. During the second year the basin was primaly used for project testing. The selection of the tests (ice sheets produces) by type is in Table 2.

Table 2. Test types by test days at AARC in 2006 and 2007

	2006	*2007*
Ice class Tankers	38	21
Icebreaking LNG carriers	20	9
Icebreakers		5
Offshore structures	6	20
Oil spill (old basin)	4	
Cargo vessels	1	13
Calibration/ice development	8	
Offshore service vessels	3	9
Total	**80**	**77**

In Figures 11 there are some views of the tests during first operational year.

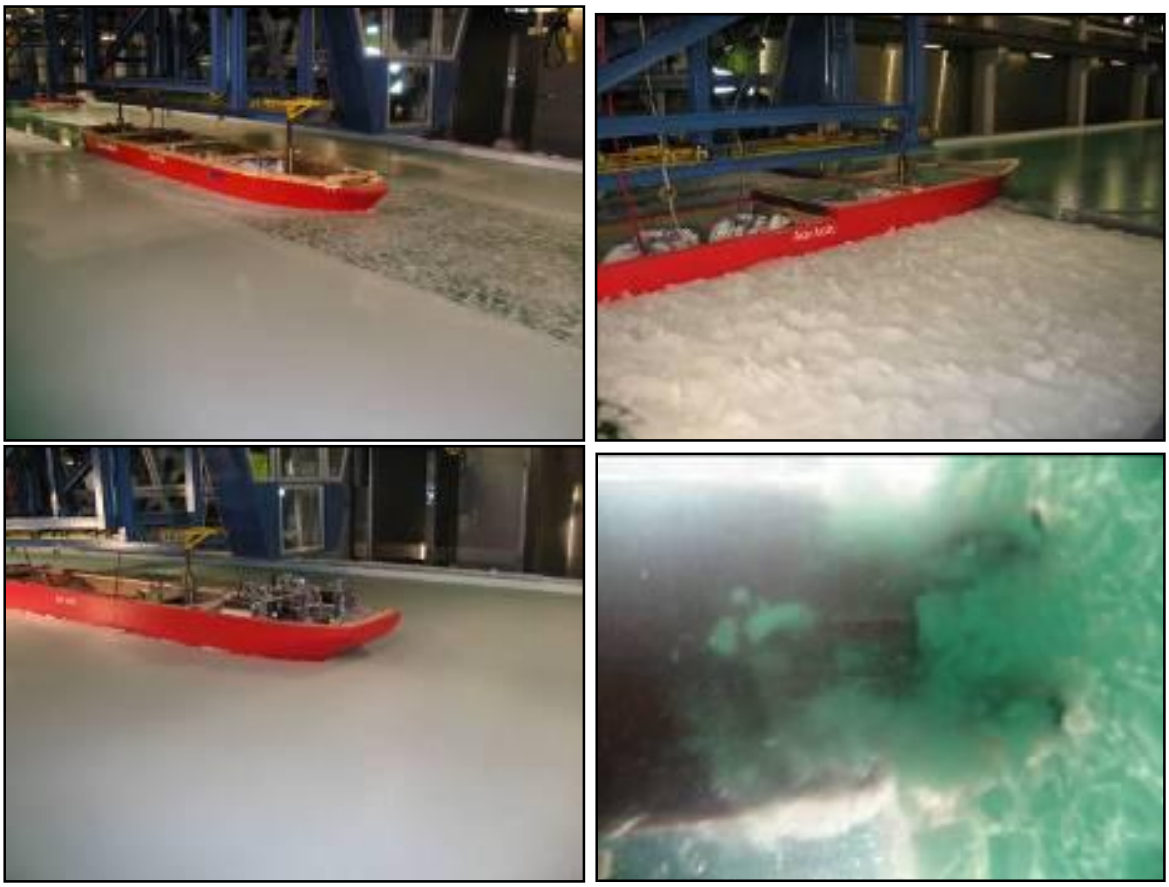

Figure 11. Test views

Also during the first year preliminary testing took place to further develop the AARC FGX-model ice. This work continued in 2007.
Traditionally the limits of the FG and FGX model ice are shown in figure 12 (Nortala-Hoikkanen 1990), where the practical upper limit for ice thickness is 90mm.

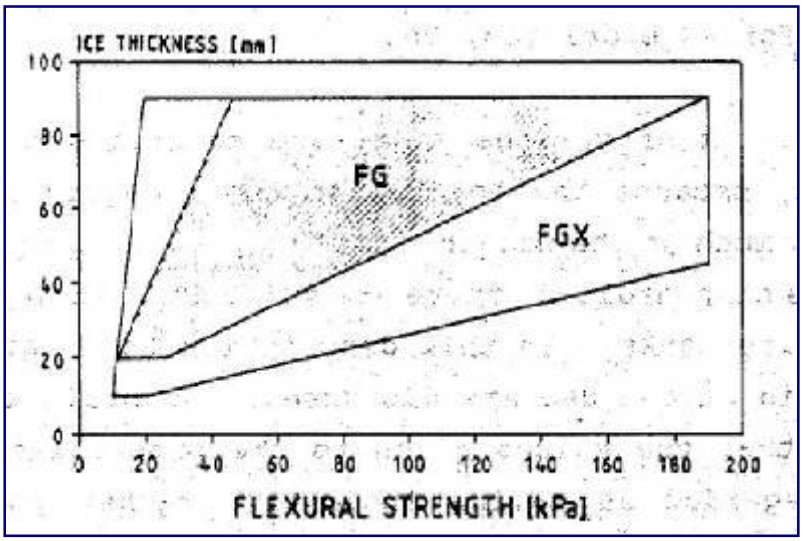

Figure 12. Traditional limits of FG and FGX model ice manufacturing

In spring 2007 there was a request to simulate 2.85 m thick level ice for the new multipurpose nuclear icebreaker project for JSC AISBERG, St. Petersburg, Russia. Due to the scale factor of the model it resulted to be 90mm in model scale. In these tests it was the first time as the former limit in thickness was approached in the new facility.

The ice manufacturing was a success, without any problems, resulting in thickness 90 mm with flexural strength of 18 kPa, which is really weak but brittle. Views of the tests are in Figure 13.

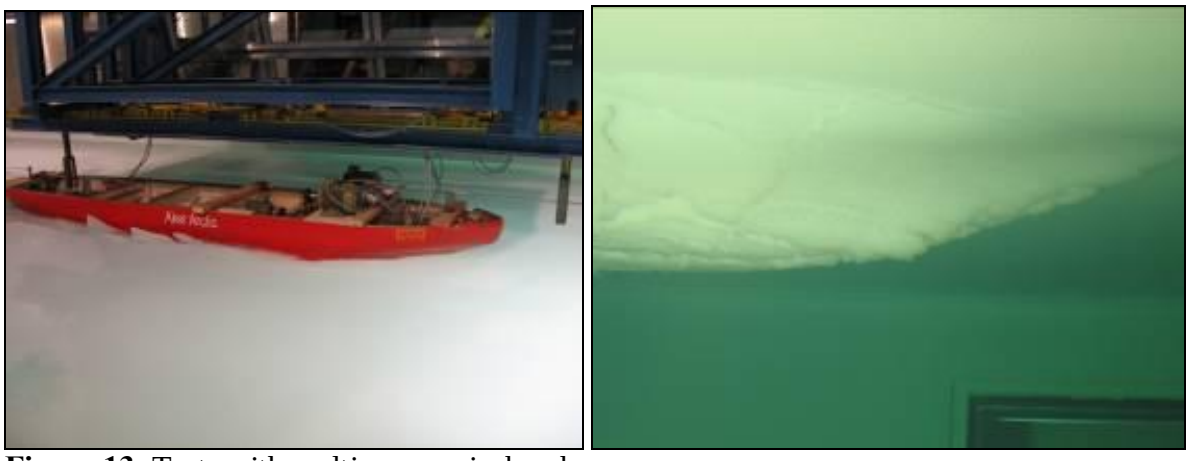
Figure 13. Tests with multipurpose icebreaker

Encouraged by this success it was decided to try to extend the limits of the FGX ice and ice thicknesses around 150, 200 and 230 mm were produced with flexural strength under 20kPa. The extended graph of flexural strength and ice thickness is in Figure 14.

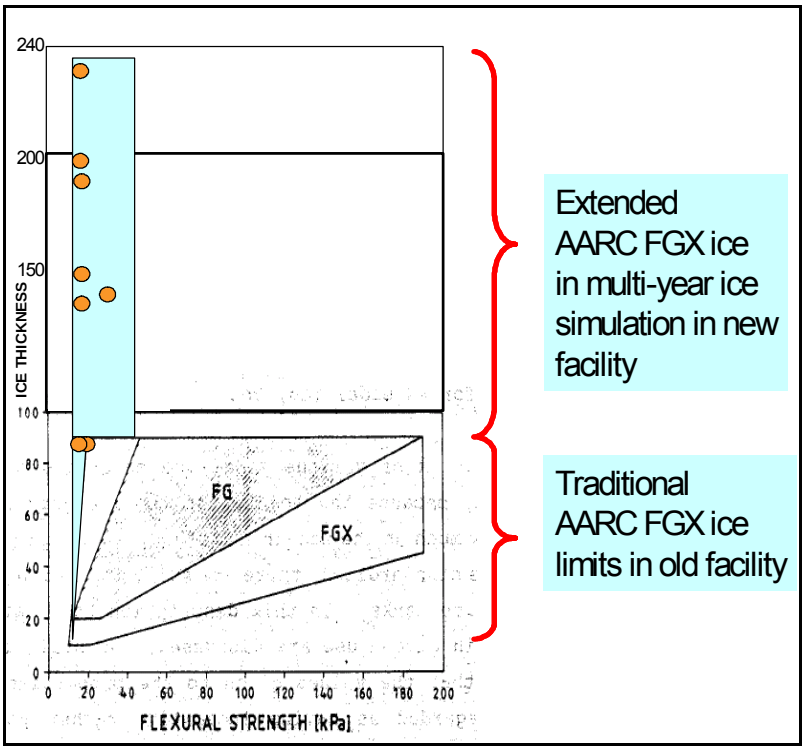

Figure 14. Extended limits of FGX model ice manufacturing

The manufacturing time of thick ice will be of course longer. In table 3 there are the rough times for making different thicknesses.

Table 3. Ice preparation time vs. thickness

Ice thickness mm	*Preparation time prior testing (hours)*	*Number of Ice sheets/week*
15 - 60	5 - 16	4
60 - 90	14 - 24	2-3
90 - 120	24 - 50	2
120 - 200	50 - 70	1-2

5. Conclusion

The new facility is working extremely well and all the results so far on the capability in making thicker ice with scaled ice properties are very promising.

This new development has of course just started and there are still a number of issues to be solved. The number of thick sheets done so far is quite limited and more data is needed on the different phases of the process to properly be able to make thick weak ice.

References

Nortala-Hoikkanen, Anita, 1990. FGX model ice at the Masa-Yards Arctic Research Centre, IAHR Ice Symposium, Espoo, Finland

19th IAHR International Symposium on Ice
"Using New Technology to Understand Water-Ice Interaction"
Vancouver, British Columbia, Canada, July 6 to 11, 2008

Wintertime heat budget of Lake Pääjärvi, Finland

Juho Jakkila[1], Matti Leppäranta[1], Toshiyuki Kawamura[2] and Kunio Shirasawa[2]
[1]*Department of Physics, P.O.Box 64, FIN-00014 University of Helsinki, Finland*
[2]*Institute of Low Temperature Science, Hokkaido University, Sapporo, Hokkaido 060-0819 Japan*

The heat budget of Lake Pääjärvi, located in Southern Finland, was studied basing on field experiment in winter 2003-2004. The data includes meteorological observations, under-ice temperature and current measurements and ice and snow thickness observations. Additional field measurements were done in April 2006 for examining radiative transfer through the ice cover. The obtained data was used for studying the heat exchange at the ice-water interface. Turbulent heat flux from the water was calculated using under-ice water current and temperature measurements. Penetration of shortwave radiation through the ice cover was examined by diffuse attenuation coefficients determined for snow and different ice layers. Heat fluxes at the ice bottom were compared to the heat budget terms at the surface of the ice cover. The main term of the surface heat budget during winter months was longwave radiation loss, which was balanced by heat release from the ice growth and heat flux from the water. In April shortwave radiation became the dominant term of the surface heat budget and penetrated radiation heated the under ice water causing convective currents. Warming of under ice water and convective currents increased the average heat flux from the water from 12 to 20 W/m^2. The increasing amount of penetrated radiation during the melting season heated up the water temperature of the whole lake evenly to 3 ºC already before ice break-up. The penetrated radiation has thus important impact on springtime overturn and the water quality of the lake during the melting season.

1. Introduction

The heat fluxes from the bottom sediments and at the ice-water interface are the driving factors of wintertime circulation of lakes. In winter months the lake gains heat from the sediments and releases it through the ice cover by heat flux from the water (Welch and Bergmann, 1985). During the melting season penetration of shortwave radiation through the ice cover exceeds other fluxes and causes convective currents. The temperature increase due to sediment heat flux and penetrated radiation is highest in the shallow areas, which causes bottom lined advection from the littoral zone to the centre of the lake (Bengtsson, 1996 and Kenney, 1996). The oxygen consumption is as highest in the bottom sediments (Golosov *et al*., 2007), which together with advection may result to the development of oxygen depletion to the deepest part of the lake. Convective currents may also help non-motile algae to suspend near the ice-water boundary during wintertime (Matthews and Heaney, 1987 and Kelley, 1997), which can be beneficial to enhance their growth during the springtime melting period.

The evolution of the ice cover depends on the heat exchange in atmosphere-ice and ice-water interfaces. The traditional approach in the studies of ice evolution has been in the atmosphere-ice interactions. However the heat flux from the water has also significant effect to the ice growth (Shirasawa *et al.*, 2004). Different methods have been used for estimating the heat flux from the water. Turbulent heat fluxes in Arctic oceans have been estimated as a residual from the ice temperature profile and ice thickness measurements (Perovich and Elder, 2002), from the under-ice conductivity-temperature-depth profiles together with turbulent friction velocities estimated from local ice motion (Maykut and McPhee, 1995) and from straight measurements of turbulent eddy fluxes of sensible heat (McPhee, 1992). These experiments indicate large seasonal variability in mean heat flux from the water (1-30 W/m^2) due to penetrated radiation through the ice cover during the melting season. In shallow lakes in Sweden and Karelia the heat flux from the water has been studied from temperature profiles in the viscous sublayer close to the ice bottom (Bengtsson and Svensson, 1996, Bengtsson et al., 1996). The results from stably stratified lakes with low current velocities (1 mm/s) give small heat fluxes in winter ~1 W/m^2 increasing to 2-10 W/m^2 in springtime melting period.

The present study of wintertime heat budget experiment was done in Lake Pääjärvi (Fig 1.) located in southern Finland (61º04'N, 25º08'E). The mean and the maximum depths of the lake are 14.8 m and 87 m, respectively. The area of the lake is 13.4 km^2 with maximum dimensions of 10 km long and 4 km wide. The summer thermocline is typically at 6-8 m depth lowering to 10 m depth until autumn overturn. As a typical humic lake it has a brown colour with light attenuation coefficient ~1.5 m^{-1}.

The objective of the study was to examine the heat exchange at the water-ice interface. The heat flux from the water is calculated using under-ice current and temperature measurements and also as a residual from the heat fluxes in the atmosphere-ice-water system. The penetrated radiation through the ice was calculated by simple radiation transfer model. The water temperature measurements were used for calculating changes in water temperature storage and the results were used for estimation of sediment heat fluxes.

2. Materials and methods

The ice station observations – The ice station data obtained from Lake Pääjärvi in winter 2003-2004 included incoming and reflected shortwave radiation, air and surface radiative temperature, relative humidity, wind speed and direction and under-ice water current and temperature measurements. The meteorological data was compared and replenished with the observations from the nearest weather stations produced by Finnish Meteorological Institute (Lammi biological station and Jokioinen observatory). The ice thickness and snow depth were measured once a week close to the ice station. In addition daily snow thickness and precipitation observations were made in Lammi biological station located on the shore of the lake. These observations were used for data elaboration.

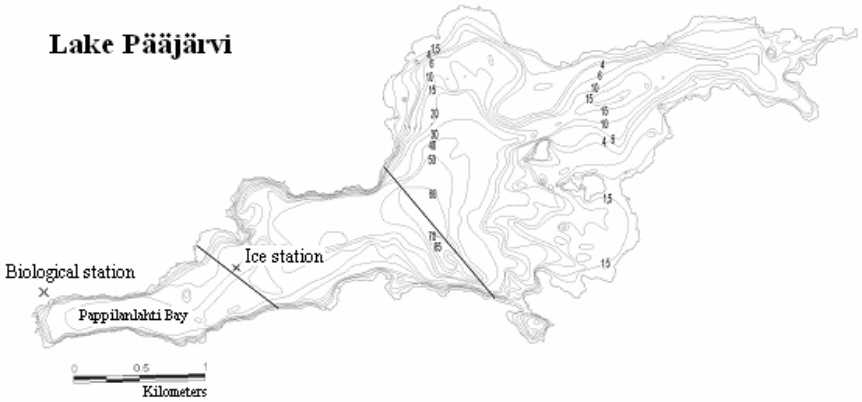

Figure 1. Bathymetry of Lake Pääjärvi. The locations of ice station and Lammi Biological station are shown. The CTD-sections made in Pappilanlahti Bay and in the deepest part of the lake are drawn as straight lines.

Transmission and attenuation of shortwave radiation – The light penetration through the ice cover was studied in spring 2006. The vertical attenuation of irradiance was examined by four scalar PAR-sensors (MDS-MkV/L) deployed on top and bottom of the snow cover, at the granular-congelation ice interface and within the congelation ice layer from 11th to 20th of April. In addition the incoming, reflected and penetrated spectral irradiances were measured by hyperspectral radiometer (Ramses ACC) on 20th, 26th and 28th of April.

Temperature profile measurements – The influence of heat fluxes at the ice bottom on the lake temperature structure was studied by measurements of water temperature profiles. The temperature logger chains were situated in the depths of 1 m, 5 m, 10 m, 20 m, 40 m and 80 m. The loggers were distributed in 5 m depth interval in all logger chains. The water column profiles of conductivity and temperature were measured by Falmouth Scientific micro CTD in two transects shown in figure 1. The data loggers were deployed on 13th of February to measure temperatures in 1 hour intervals whereas CTD-profiles were measured on 12th of February, 4th and 5th of March and 23rd and 25th of March. The both logger chain data and CTD-measurements were used for estimating the changes in heat storage of the lake.

3. Light penetration through the ice cover

The light attenuation measurements in different ice layers were obtained by scalar PAR-sensors deployed on 11th of April 2006. In the beginning of the measurement period congelation ice thickness was 46 cm, while snow-ice layer above was 8 cm and the thickness of snow cover on the ice was 9 cm. Due to fast melting the average attenuation coefficients for snow and snow-ice layers were determined only from two and four days data set seen in figure 2.

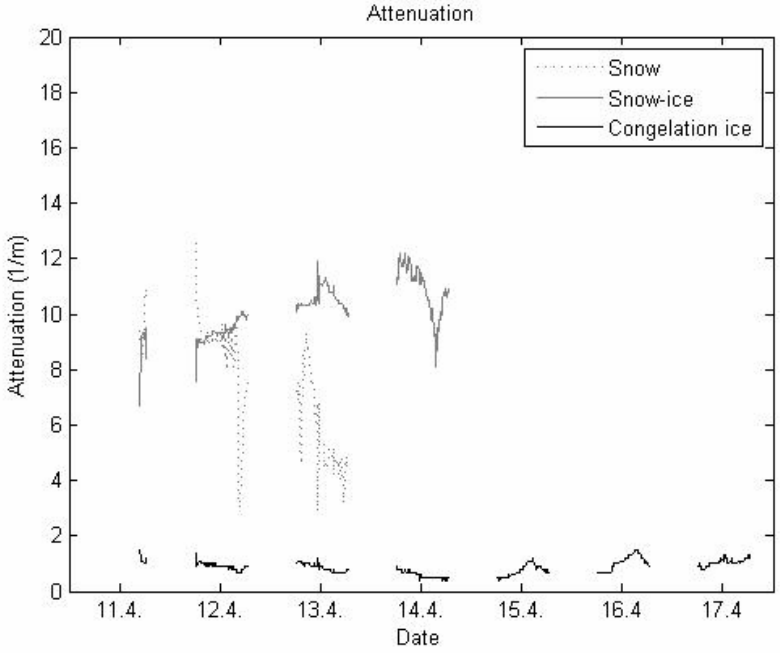

Figure 2. Photosynthetically active radiation (PAR) diffuse attenuation coefficients of snow, snow-ice and congelation ice calculated from scalar irradiance measurements in April 2006.

The diffuse attenuation coefficients for different ice layers are determined using exponential decay law:

$$\kappa_o(\lambda, z) = \ln\left[\frac{E_o(\lambda, z_1)}{E_o(\lambda, z_2)}\right]/(z_2 - z_1), \qquad \textbf{[1]}$$

where κ describes diffuse attenuation coefficient of the layer between measurement depths z_1 and z_2 and E_o is the scalar irradiance at the measurement depth. The scalar attenuation coefficients were calculated from spectrally integrated irradiance profiles over PAR-range (Photosynthetically active radiation, 400-700 nm). The average values for congelation ice was 1.1 m^{-1} and for both snow and snow-ice 10 m^{-1}. Wang *et al.* (2005) achieved similar results from the measurements made on Lake Pääjärvi in March 2003 (9 m^{-1} for snow-ice and only 0.5-0.8 m^{-1} for congelation ice). In winter 2002-2003 the ice cover was thickest ever measured, 80 cm, and the congelation ice layer was exceptionally clear, which is the reason for lower values than obtained in 2006. Wang *et al.* (2005) determined the attenuation coefficients from planar PAR-sensor setup. The difference in planar and scalar measurements depends on angular structure of incoming irradiance and the fraction of up- and downwelling irradiances. The irradiance below the snow surface is highly diffuse and the angular structure of downwelling irradiance can be

assumed to be invariable with depth. The fraction of upwelling irradiance depends on the scattering properties of studied medium. The light scatters effectively in snow and snow-ice layers, while blue ice is more transparent in PAR-range. Compared to planar irradiance measurements the results obtained by the scalar sensors can be assumed to give higher attenuation coefficient for snow-ice layer.

The attenuation coefficients were used for calculating the penetrated radiation Q_{Sp} using the simple exponential decay law modified by Maykut and Untersteiner (1971):

$$E_d(z,\lambda) = (1-\alpha) i_o E_d(0,\lambda) e^{-\kappa_t z_t}, \quad \textbf{[2]}$$

where α is albedo, i_o is the fraction of incident irradiance transmitted through the top 10 cm and z_t is the thickness of ice cover. κ_t describes the average attenuation coefficient of whole ice cover, which can be divided to optically homogenous layers, e.g.:

$$\kappa_t z_t = \kappa_s z_s + \kappa_{gi} z_{gi} + \kappa_{ci} z_{ci}, \quad \textbf{[3]}$$

where subindices *s, gi*, and *ci* represent snow, snow-ice and congelation ice layers. The value of i_o depends on cloudiness and properties of topmost ice layer. Different values for congelation and snow-ice depending on cloud conditions are used according to field observations made by Grenfell and Maykut (1977). The values for κ_x are determined from the field measurements obtained from the PAR-sensor setup.

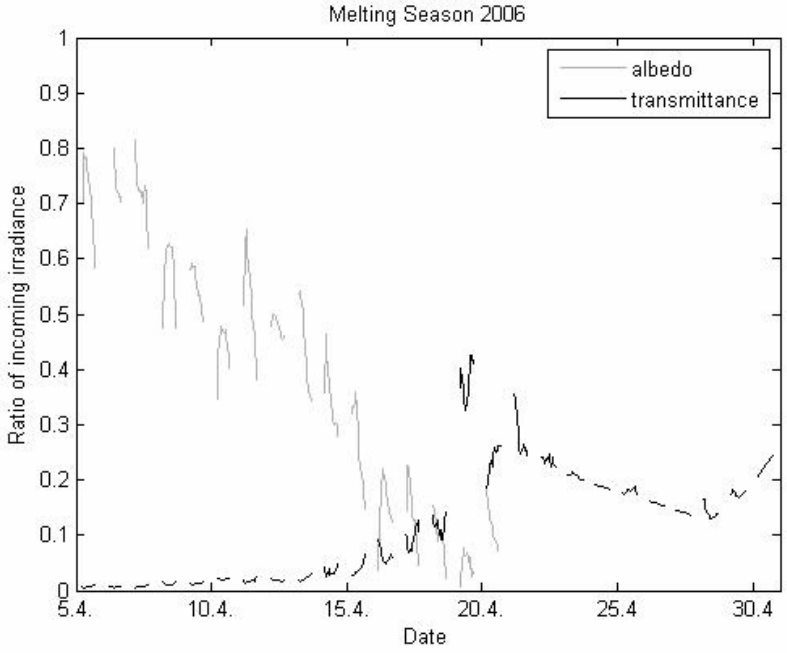

Figure 3. Evolution of albedo and transmittance through the ice cover during the melting season in April 2006.

During the melting season the optical properties of the ice cover experience rapid changes. In April 2006 albedo decreased from 0.8 to 0.1 in two weeks (figure 2) during the snow and snow-

ice melting. Due to decline of albedo and the remarkably smaller light attenuation in congelation ice layer, the transmittance increased from 1 to 40 % of the incoming irradiance (Fig. 3). The increased penetration of shortwave radiation caused internal melting in congelation ice layer. The melting began from the bottom of the ice cover at the edges of ice crystals forming a candled shape. Increased scattering in candled ice layer caused the decline of light transmittance during the ice melting.

4. Heat budget of the ice cover in winter 2003-2004

In winter 2003-2004 Lake Pääjärvi froze up on 17th of December and ice cover broke up on 28th of April. The maximum ice and snow-ice thicknesses were measured on 15th of March, which were 41 cm and 13 cm, respectively. The maximum values for ice thickness and length of the ice season were close to 25 years mean values (Kärkäs, 2002) and the ice season can be considered to be typical in Lake Pääjärvi.

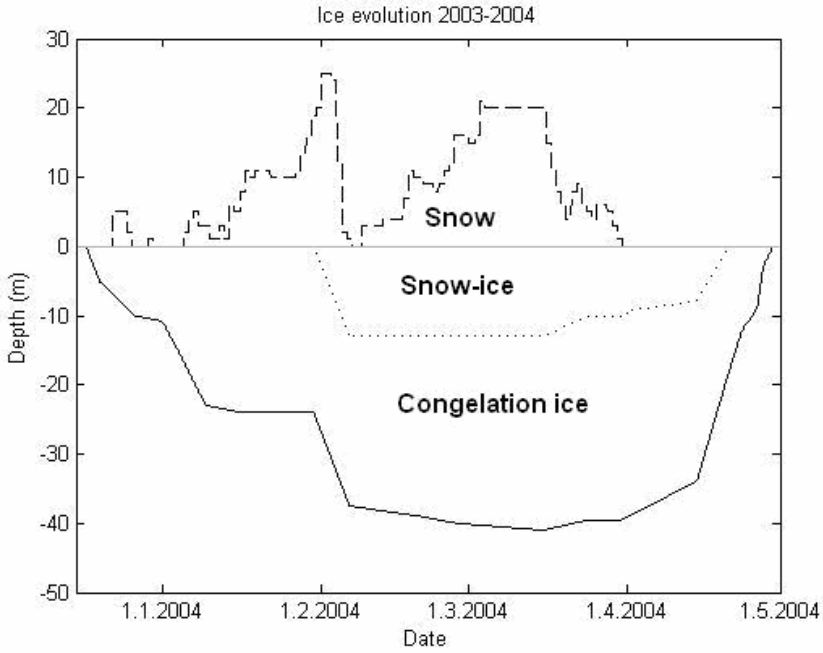

Figure 4. Ice evolution in winter 2003-2004.

During winter months (February-March) vertically averaged water temperature in the deepest part of the lake increased 0.05 K/month (figure 5). The under-ice current and temperature measurements at 5 m depth close to the ice station showed that temperature increasing and water currents retarded slightly between January and March, from 0.10 to 0.05 K/month and from 1.0 to 0.7 cm/s, respectively. The increase in the heat storage of the lake indicates that heat flux from bottom sediments exceeds the heat flux from the water. The sediment heat flux seems to maintain the wintertime circulation during the whole winter, but it weakens towards spring. During the melting season penetration of shortwave radiation through the ice cover heats the under-ice water inducing convective currents. Due to convection penetrated radiation mixed the whole water column increasing water temperatures of the lake uniformly to 3 ^{o}C already before ice break-up on 28th of April as seen in figure 5.

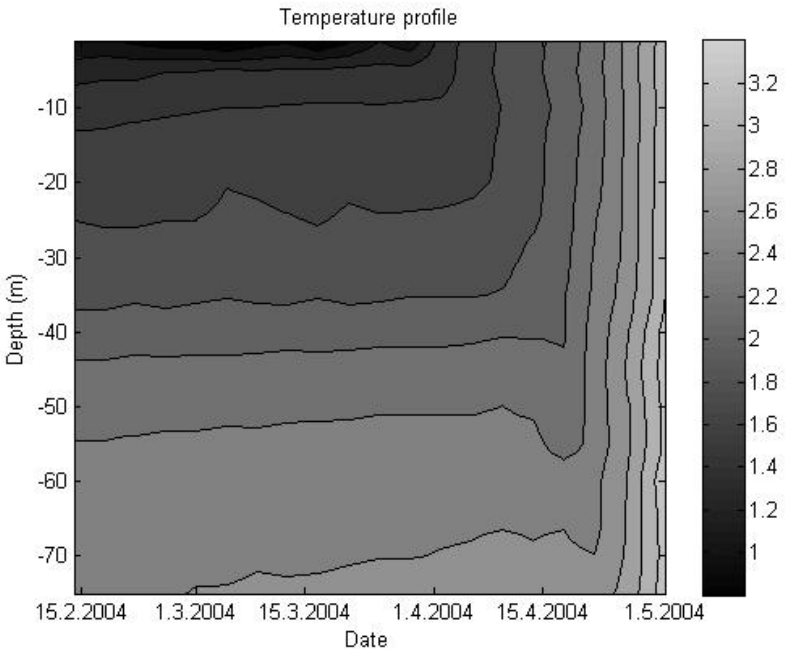

Figure 5. Temperature profile in the deepest part of Lake Pääjärvi in winter 2003-2004. Snow cover had melted on 30th of March and ice cover broke up on 28th of April.

The heat flux from the water was examined from the ice station data using two different methods: The turbulent heat flux was calculated from under-ice temperature and current measurements according to parametrization determined by McPhee (1992):

$$Q_w = \rho_w c_w c_h u_* (T_w - T_o) \quad \textbf{[4]}$$

Here ρ_w is water density, c_w is specific heat capacity of water, c_h is Stanton number, T_w and T_o are water and ice bottom temperatures and u_* is friction velocity near the ice bottom, which was calculated from mean current velocity measurements assuming neutral conditions under ice.

The under-ice currents and high temperature difference near the ice bottom kept the heat fluxes from the water relatively high (~12 W/m^2) during winter months (table 1). The heat flux declined slightly towards spring due to decreasing current velocities. In April the penetrated radiation increased the mean horizontal current speed from 0.7 to 0.9 cm/s, whereas the hourly averaged maximum value increased to 2.7 cm/s. The increase in under-ice currents and temperature profile during the melting period raised the average heat flux from the water from 10 to 20 W/m^2.

Another estimate for the heat flux from the water was provided as a residual of ice surface and ice bottom heat fluxes. Since the changes in ice temperature heat content in long term means are relatively small and can be ignored, the relationship between ice surface and bottom heat exchange can be written as follows:

$$Q_w = \rho_i L_m \frac{dh_i}{dt} - Q_o \,, \quad \textbf{[5]}$$

where ρ_i is ice density, L_m is latent heat of freezing, h_i is ice thickness, t is time and the last term Q_o describes the heat exchange at the ice surface. The surface heat budget consists of radiation and turbulent heat fluxes:

$$Q_o = Q_{Si} - Q_{So} - Q_{Sp} + Q_{Li} - Q_{Lo} + Q_h + Q_e. \quad \textbf{[6]}$$

The incoming (Q_{Si}) and reflected (Q_{So}) shortwave radiation were measured directly in the ice station as well as upwelling longwave radiation Q_{Lo}, which was obtained from surface radiative temperature measurements. The penetrated radiation Q_{Sp} was calculated using the ice attenuation coefficients as illustrated before. The downwelling longwave radiation Q_{Li} was estimated using the parametrization presented by Crawford and Duchon (1998). This combines Brutsaert's (1975) parametrization for clear sky atmospheric emissivity and Deardorff's (1978) cloudiness correction using cloud fraction computed from the incoming shortwave radiation measurements. Nighttime values for cloudiness were taken from the nearest weather station observations (Jokioinen observatory). The turbulent heat fluxes were calculated using the bulk aerodynamic formulae for sensible Q_h and latent heat Q_e. The aerodynamic transfer coefficients for temperature C_h and humidity C_e were calculated using Louis's (1979) parametrization for near surface stability.

Table 1. Heat fluxes (W/m^2) in winter 2003-2004 at the ice surface and at the ice-water interface. The heat released form the ice growth or required for the melting is included to the ice bottom heat fluxes. Positive signs indicate downward and negative upward heat fluxes.

Winter 2003–2004	December (ice season)	January	February	March	April
At the ice surface					
Shortwave radiation	1	1	6	22	117
Longwave radiation	-19	-21	-25	-35	-47
Sensitive heat flux	-10	-4	-4	-1	2
Latent heat flux	-8	-3	-4	-3	-2
At the ice bottom					
Penetrated radiation	1	0	0	1	40
Heat flux from the water	-11	-13	-12	-10	-20
Freezing/melting	-25	-18	-15	6	46
Residuals	**-1**	**4**	**0**	**-14**	**4**

The heat fluxes at the surface and at the bottom of the ice cover are compiled in table 1. The heat release from the ice growth or required for melting is calculated from the ice and snow thickness measurements and included to the ice bottom heat fluxes. The negative sign in the table indicates ice growth or upward heat flux, whereas positive sign ice/snow melting or downward heat flux. The residuals express the difference between heat fluxes at the ice surface and at the ice bottom.

In winter months the heat exchange at the surface of the ice cover was prevailed by longwave radiation, which gives ~20-35 W/m^2 negative flux at the surface of the ice cover. The heat loss

from the surface was balanced by heat release from the ice growth and heat flux from the water. Shortwave radiation and turbulent heat fluxes can be considered as minor terms of the heat budget during winter months. In springtime shortwave radiation takes the dominant role in the surface heat budget. The longwave radiation is still important, but the shortwave radiation changes the sign of net radiation flux to be positive. In April the net radiation flux at the ice surface was 70 W/m^2, from which 40 W/m^2 penetrated through the ice cover and the rest went for ice melting, which was supported by increased heat flux from the water.

The most significant errors in this analysis are related to incoming longwave radiation and heat flux from the water. The cloud fractions calculated from shortwave radiation measurements were used for estimation of incoming longwave radiation. Nighttimes cloud fraction was taken from the observations made in Jokioinen observatory (~100 km west from Lake Pääjärvi). The mean bias error (mbe) for longwave radiation calculated from shortwave radiation measurements in different sites (Lake Pääjärvi and Jokioinen) was -2.4 W/m^2. The mbe between calculated and observed values in Jokioinen was as high as 13 W/m^2. These results indicate that the observation method used for estimating cloud fraction makes even more crucial error to calculation of longwave radiation than cloud conditions in different sites. The turbulent heat flux calculated from under ice temperature and current measurements includes also some errors. The parametrization in equation 4 has been made in Arctic oceans and should be adjusted for boreal lakes in future experiments. For instance the stratification under ice has been assumed to be in neutral conditions. This assumption may overestimate the heat flux from the water, because lakes experiencing relatively small currents in winter conditions are usually stably stratified under ice.

5. Conclusions

The results obtained from the ice station experiment were used for estimating the heat exchange at the ice-water interface. The measured attenuation coefficients for different ice layers using the scalar PAR-sensors gave similar results as observed before in Lake Pääjärvi (Wang *et al.* 2005). The importance of penetrated radiation came up in spring when snow had melted. The ratio between penetrated and incoming irradiance increased gradually to 40 % during snow and snow-ice melting. The transmittance declined to 20 % during congelation ice melting due to increased scattering by candled ice layer. The results for light transmittance through the ice cover are in good accordance with earlier observations in Finnish and Estonian lakes (Leppäranta *et al.*, 2003 and Arst *et al.*, 2006). Warming of under-ice water and convective currents induced by penetrated radiation increased the heat flux from the water to 20 W/m^2 and mixed the whole lake to the uniform temperature already before ice break-up.

Two methods were used for estimating the heat flux from the water. Both methods have some sources of errors, but overall the results are encouraging because the residuals calculated for monthly mean values are relatively low exceeding ±5 W/m^2 only in March. The high error in March was reached due to different cloud conditions in Jokioinen observatory as found out when comparing the shortwave radiation observations from different sites. The achieved results for the heat flux from the water and increasing values in lake heat storage indicate relatively high sediment heat flux (~10 W/m^2) during winter months. In earlier studies made in shallow Swedish and Karelian lakes (Bengtsson and Svensson, 1996 and Bengtsson et al., 1996) the average heat fluxes from bottom sediments have been reported to be ~1 W/m^2. The under-ice current

velocities observed in Lake Pääjärvi (0.7-1.0 cm/s) are much higher than in shallow lakes (~0.1 cm/s), which may result to higher heat fluxes in ice-water and water-sediment boundary layers.

Instead of encouraging results the used methods in this study need still to be developed. The estimated error for incoming longwave radiation brings uncertainties to the accuracy of heat fluxes at the surface of the ice cover. In future experiments net radiation measurements should be included to achieve more accurate results. Also the method for estimating the turbulent heat flux from the water could be improved. The equation used for calculating the turbulent heat flux is parametrized for neutral conditions under ice in Arctic oceans. Additional experiments for measuring the under ice turbulent heat fluxes in stably stratified lakes would be beneficial for future studies.

Acknowledgements

This research has been funded by Academy of Finland and Lammi Biological Station. The work is part of the project 'Hydrodynamic focusing on sediment oxygen consumption to the deepest part of large lakes – a multidisciplinary approach', which has been led by Kalevi Salonen from University of Jyväskylä.

References

Arst, H., Erm, A., Leppäranta, M. and Reinart, A., 2006. Radiative characteristics of ice-covered fresh- and brackish-water bodies. *Proc. Estonian Acad. Sci. Geol.,* 55, 1, pp. 3-23.

Bengtsson, L., 1996. Mixing in ice-covered lakes. *Hydrobiologia,* 322, 1-3, pp. 91-97.

Bengtsson, L. and Svensson, T., 1996. Thermal regime of ice covered Swedish lakes. *Nordic Hydrol.,* 7, pp. 39-56.

Bengtsson L., Malm J., Terzhevik A., Petrov M., Boyarinov P., Glinsky A., Palshin N., 1996. Field investigations of winter thermo- and hydrodynamics in a small Karelian lake. *Limnol. Oceanogr*., 41, pp. 1502-1513.

Brutsaert, W., 1975. On a derivable formula for long-wave radiation from clear skies. *Water Resour. Res*., 11, pp. 742–744.

Crawford, T. M. and Duchon, C. E., 1998. An Improved parameterization for estimating effective atmospheric emissivity for use in calculating daytime downwelling longwave radiation. *Journal of Applied Meteorology*, 38, 4, pp. 474–480.

Deardorff, J. W., 1978. Efficient prediction of ground surface temperature and moisture, with an inclusion of a layer of vegetation. *J. Geophys. Res.,* 83, pp. 1889–1903.

Golosov, S., Maher, O. A., Schipunova, E., Terzhevik A., Zdorovennova, G. and Kirillin, G., 2007. Physical background of the development of oxygen depletion in ice-covered lakes. *Oecologia,* 151, 2, 331-340.

Grenfell, T. C. and Maykut, G. A., 1977. The optical properties of ice and snow in the Arctic Basin. *Journal of Glaciology*, 18, 80, pp. 445-463.

Kärkäs, E., 2000. The ice season of Lake Pääjärvi, southern Finland. - *Geophysica*, 36 pp. 85-94.

Kelley, D.E., 1997. Convection in ice-covered lakes: effects on algal suspension. *J. Plankton Res.*, 19, pp. 1859-1880.

Kenney, B. C., 1996. Physical limnological processes under ice. *Hydrobiologia* 322, 1-3, pp. 85-90.

Leppäranta, M. A., Reinart, A., Erm, A., Arst, H., Hussainov, H., and Sipelgas, L., 2003. Investigations of ice and water properties and under-ice light fields in fresh and brackish water bodies, *Nord. Hydrol*., 34(3), pp. 245–266.

Louis, J-F., 1979. A parametric model of vertical eddy fluxes in the atmosphere. *Boundary Layer Meteorol*., **17**, pp. 187-202.

Matthews, P.C. and Heaney, S.I., 1987. Solar heating and its influence on mixing in ice-covered lakes. *Freshwater biol.* 18, pp. 135-149.

Maykut, G. A. and McPhee, M. G., 1995. Solar heating of the Arctic mixed layer, *J. Geophys. Res.* 100, C12, 24691-24703.

Maykut, G. A. and Untersteiner, N., 1971. Some results from a time dependent thermodynamic model of sea ice. *J. Geophys. Res.*, 76, 1550-1575.

McPhee, M. G., 1992. Turbulent heat flux in the upper ocean under sea ice. *J. Geophys. Res.* 97, C4, pp. 5365-5379.

Perovich D. K. and Elder B., 2002. Estimates of ocean heat flux at SHEBA. *Geophys. Res. Lett.*, 29, 9, 1344.

Shirasawa, K., Leppäranta, M., Saloranta, T., Kawamura, T., Polomoshnov, A. and Surkov, G., 2004. The thickness of coastal fast ice in the sea of Okhotsk. *Cold reg. sci. technol.* vol. 42, 1, 25-40.

Wang, C., Shirasawa, K., Leppäranta, M., Ishikawa, M., Huttunen, O. and Takatsuka, T., 2005. Solar radiation and ice heat budget during winter 2002-2003 in Lake Pääjärvi, Finland. *Internationale Vereinigung Für Theoretiche Und Angewandte Limnologie* 29 (1), 414-417.

19th IAHR International Symposium on Ice
"Using New Technology to Understand Water-Ice Interaction"
Vancouver, British Columbia, Canada, July 6 to 11, 2008

Optical and colored dissolved organic matter properties of landfast ice in the Baltic Sea

Uusikivi Jari
Department of Physics, University of Helsinki, Finland
P.O.Box 64
FI-00014 University of Helsinki, Finland
jari.uusikivi@helsinki.fi
Vähätalo Anssi V
Department of Biological and Environmental Sciences, University of Helsinki, Finland
Granskog Mats A
Artic Centre, University of Lapland, Rovaniemi, Finland
Galí Tàpias Marti
Department of Biological and Environmental Sciences, University of Helsinki, Finland

In March 2007, spectral irradiance measurements were conducted above and beneath the landfast sea ice in Santala Bay near the entrance to the Gulf of Finland, Baltic Sea. The measurements included the spectral albedo, extinction coefficient of the sea ice, and also extinction coefficients separately to granular and columnar ice layers. Ice included particle matter (PM) and colored dissolved organic matter (CDOM) absorption coefficients were measured from melted ice samples to quantify their contribution to light attenuation in ice. PM and CDOM absorption dominate absorption spectrum in the shorter wavelengths (320- 550nm), and are most important reason for high extinction coefficients at ultraviolet in the Baltic Sea ice. CDOM was found to be most significant absorber in the UVR (<380nm) with the exception of the surface ice layer for which the CDOM absorption spectrum was clearly different from the ice layers below. Photochemical reactions induced by high ultraviolet radiation could have altered the composition of CDOM at the ice surface layer. We found that CDOM absorption in the ice cover contributed 42 %, 37%, 33% and 20 % of light attenuation at 305 nm, 322 nm, 360 nm and 550 nm, respectively.

1. Introduction

On the Finnish coast of the Baltic Sea landfast sea ice is generally formed every winter. Although Baltic Sea surface water salinity along the Finnish coast is normally between 2 and 6 practical salinity units the ice cover typically shows sea ice like features, such as brine pockets and irregular crystal boundaries (Kawamura et al. 2001). At parent water salinities higher than about 0.6, the ice formed has these sea ice characteristics, and therefore it is only in proximity of river estuaries that Baltic Sea ice is directly comparable to freshwater ice (Palosuo 1961). Granular surface ice layers, composed of snow-ice and superimposed ice, usually contribute a significant part of landfast ice thickness in the Baltic Sea area, and can contribute up to half of total ice thickness (Kawamura et al. 2001, Granskog et al. 2004), these highly scattering surface layers affect significantly the overall optical properties of the relatively thin Baltic Sea ice cover (Ehn et al. 2004).

Solar radiation and variation in transmitted radiation are normally the most important factors affecting biological activity in and under sea ice (Perovich 2003, Perovich et al. 1993, Perovich 1993). Although Baltic Sea landfast ice harbors an active ecosystem, despite its relatively low salinity (Granskog et al. 2005), very little is known about the bio-optical properties of the Baltic sea ice cover, as very few studies have been conducted to date (Ehn et al. 2004 and references there in). To properly characterize light transmission in the sea ice system the transmission spectra must be divided to individual constituents of light attenuation (Perovich et al. 1993). Most important constituents to light attenuation in sea ice are pure ice, liquid brine, solid salts, the relative fractions of the former are dependent on temperature, further particulate matter (PM) and colored (also called chromophoric) dissolved organic matter (CDOM) incorporated into the ice cover affect the transmission of light through an sea ice cover (Perovich, Roesler & Pegau 1998, Belzile et al. 2000). In situ production of both PM (algae) and CDOM can occur with biological activity in the ice thereby contributing with optically active substances.

It is important to study the whole spectrum of incident and transmitted irradiance through sea ice and into the water column below. Photosynthetically active radiation (PAR), from 400 to 700 nm, is important for biological activity, but it is also equally important to understand the penetration of ultraviolet radiation (UVR), from 280 to 400 nm, through the ice (Perovich 1993). Earlier studies indicate that ice algae are adapted to low light conditions that prevail under snow and ice covers and that such conditions makes algae potentially sensitive to photoinhibition by UVR (Cota et al. 1991, Prezelin, Moline & Matlick 1998). Belzile et al. (2000) found strong absorption in UVR by CDOM and suggested that significant photochemical reactions could occur in and right under sea ice, the result being that CDOM could be photodegraded to components more suitable for the microbial food web (Moran, Zepp 1997, Reche, Pace & Cole 1998). However CDOM photochemistry in sea ice has not been studied and therefore the significance of CDOM to transmitted light spectrum in sea ice and its effects to ice communities is not well known. As CDOM can both shield from harmful UVR radiation and be a precursor for biologically labile compounds that could enhance biological growth, the integrated effect of these opposing processes is yet to be quantified.

Especially interesting is that in the Baltic Sea dissolved organic carbon (DOC) concentrations are 3–4 times higher than in the oceans (Hagstrom et al. 2001) which is also reflected in relatively

high CDOM concentrations, both in water and ice (Ehn et al. 2004), thereby making the potential for photochemical processes in Baltic Sea ice high (Granskog et al. 2006). Baltic Sea ice CDOM has been found to be a mixture of humic materials, incorporated from the underlying water during ice formation, and autochthonous material produced by organisms within the ice (Stedmon et al. 2007). Based on the observations by Kaartokallio et al. (2007), it seems that Baltic Sea ice bacteria are dependent on autochthonous DOM produced in the ice, despite the high background levels of humic materials which appear largely to be refractory. Generally it can be concluded that the relative contribution of CDOM and PM to optical properties in Baltic Sea ice (Ehn et al. 2004) can differ significantly from that in Arctic sea ice (Perovich, Roesler & Pegau 1998).

2. Materials and methods

2.1 Study site

The study site was located at the entrance of the Gulf of Finland, Baltic Sea, near the Finnish coast. Fieldwork was conducted from 13th to 15th March 2007 on landfast sea ice at Santala Bay (59° 55' N, 23° 05' E). Santala Bay is semi enclosed bay sheltered from open sea by islands thereby allowing fast ice to form even in mild winters (see e.g. Granskog et al. 2004). Winter 2007 was mild and at time of measurements the ice cover was about 2 months old. The study period occurred during the onset of ice melt, when the snow had already melted away few days prior to our measurements. Water in the study area had a salinity of 5.3 (practical salinity units) at 2 meters depth. Since surface melting had already started there was a layer of lower salinity right under the ice bottom, with a salinity of 3.3 (Ehn et al. 2004).

2.2 Field sampling

Ice samples were collected using a 9 cm diameter ice core drill on 14 March. The ice core was divided to three parts, surface granular ice layer, middle and bottom, and analyzed for ice structure by thin sections, spectral absorption of colored dissolved organic matter ($a_{CDOM,\lambda}$) and particulate matter ($a_{PM,\lambda}$). Based on structural analyses the ice cover consisted of 31 cm columnar ice and a 6 cm granular ice layer at the surface totalling 37 cm in thickness.

2.3 Laboratory measurements

$a_{CDOM,\lambda}$ and $a_{PM,\lambda}$ were measured from melted ice cores that were filtered through glass fibre filters (Whatman GFF 25-mm, nominal pore size of 0.7-µm) in all glass filtration device (19-mm dimeter of filtering area) with mild vacuum. The filtrate was collected for $a_{CDOM\ ,\lambda}$ measurements. The filters were placed into small dishes, kept in darkness, and $a_{PM,\lambda}$ was measured within few hours or from frozen (-18°C) filters on the next day. The CDOM-spectra were measured against MQ-blanks from 200 nm to 800 nm with 2-nm slits and at 1-nm intervals using a Shimadzu UV-2501 PC spectrophotometer. The absorbance measured with a 10-cm cuvette ($A_{CDOM,\lambda}$) was converted to an absorption coefficient ($a_{CDOM,\lambda} = 2.303\ A_{CDOM}\ 0.1^{-1}$). $a_{PM,\lambda}$ was measured with an ISR-240A integrating sphere by the "transmittance-reflectance"-method (Tassan, Ferrari 2002). The optical density of particles on filter is converted to that in water

suspension. Finally, the absorption coefficient of particles accounts for the ratio of filtered volume to the filter area.

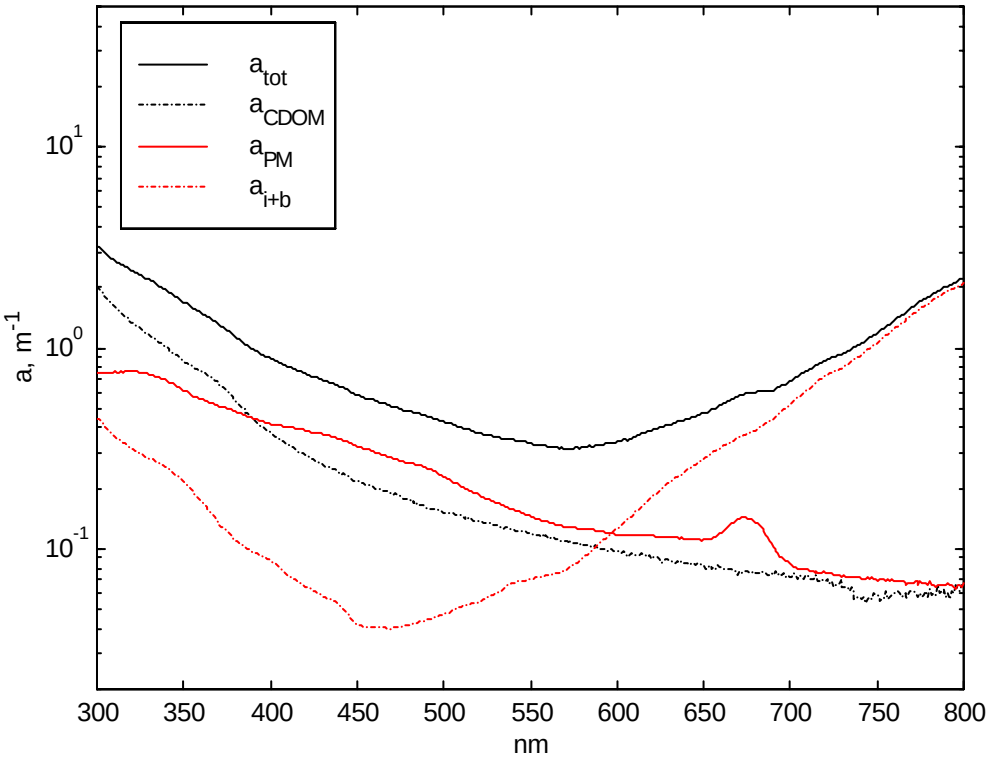

Figure 1. Mean absorption coefficients of all three ice layers in the sea ice cover for particle matter (a_{PM}), colored dissolved organic matter (a_{CDOM}), ice and brine (a_{i+b}) (Grenfell and Perovich 1981, Perovich and Govoni 1991, Smith and Baker 1981) and combined for all of them (a_{tot}) on 14th March 2007 .

2.4 Optical measurements

Incident, reflected and transmitted spectral irradiances were measured simultaneously with three Ramses-ACC VIS hyperspectral radiometers (TriOS Optical Sensors, Germany). These sensors have wavelength range from 320 to 950 nm and sampling band width 3.3 nm. Measurements from two of the sensors were normalized to fit measurements from the third sensor with calibration measurements. To measure transmitted irradiances a metallic arm with floats was used to position the sensors under ice. The arm was installed through a 30 cm x 30 cm hole in the ice and sensors positioned 3 cm below the ice bottom 1 m south of the hole. We also used a Macam SR991 spectroradiometer (Macam Photometrics Ltd., Scotland) equipped with a cosine collector attached to a 4.2 m long optical fibre was used to measure irradiances between 290 nm and 800 nm at 2 nm band width with 5 nm intervals. In this case one single instrument was used to make successive measurements of incident, reflected and transmitted irradiances. This method was observed to produce approximately ±8 % error in transmitted irradiances compared to measurements made simultaneously with the Ramses instruments. Irradiance measurements are represented as an average of at least 3 scans, Macam measurements at least 5 scans. Also upwelling and downwelling irradiances measurements in water column were conducted with

Ramses radiometers. Irradiances in the water column were measured at 50 cm intervals to a depth of 5 m and only in the 370- 750 nm range.

Irradiance attenuation in the interior of the ice was measured with an inverted Ramses radiometer following Grenfell and others (2006). In this set up the sensor was mounted to metal casing pointing downwards to a diffuse reflector surface and then inserted into 5 cm diameter hole which was drilled through the ice and set to different depths at 5 cm intervals. The sensor head was also shaded so that only radiation from reflector surface entered the sensor.

2.5 Attenuation coefficients

Ice was assumed to be thick enough so that light attenuation in ice is asymptotic and could be calculated using exponential decay law ($E_z = E_0\ e^{-Kd,\lambda\ z}$) (Maffione, Voss & Mobley 1998, Maffione 1998). Spectral diffuse attenuation coefficient for downwelling irradiance ($K_{d,\lambda}$) for the whole ice cover was calculated from measured downwelling incident radiation at the surface (E_0) and downwelling radiance (E_z) below the ice cover.

To relate inherent optical properties *a* (absorption coefficient) and *b* (scattering coefficient) to apparent optical property $K_{d,\lambda}$ a simple relation by Kirk 1991 (Kirk 1991) was used

$$K_{d,\lambda} = \sqrt{a^2 + Gab} \qquad \textbf{[1]}$$

where coefficient *G* is dependent on the shape of the scattering phase function and varies between 0.233 and 0.264 (Kirk 1994). Maffione (1998) also found *G* to be weak function of single-scattering albedo $\omega_0 = b/a+b$ and following this in our study *G* was set to 0.233 for granular ice and 0.245 for columnar ice layers in the visible wavelengths. Coefficient *G* in UVR was acquired through iteration to fit measured $K_{d,\lambda}$ with modelled $K_{d,\lambda}$ and assuming that *b* is wavelength independent from 300 to 700 nm (Perovich 1993).

Total spectral absorption coefficient a_{tot} is a sum of all absorbing components in the ice and consists of measured a_{CDOM} and a_{PM} and absorption by ice and brine (a_{i+b}) (Grenfell, Perovich 1981, Perovich, Govoni 1991, Smith, Baker 1981). We estimated brine volume to be 5% throughout the entire ice cover and as the ice was relatively warm no solids salts are expected to be present.

Ice interior $K_{d,\lambda}$ was determined at each wavelength using finite difference equation

$$K_{d,\lambda}(z) = \frac{1}{\langle F(z) \rangle} \frac{\Delta F}{\Delta z} \qquad \textbf{[2]}$$

where z is the depth from the ice surface, *F* is irradiance at given depth measured with diffuse reflector and Δ represents central difference in both numerator ($\Delta F = F(z+dz) - F(z-dz)$, where dz is small increment in depth) and denominator ($\Delta z = (z+dz) - (z-dz)$). Grenfell and others (2006) showed that the depth gradients of vertical irradiance profiles acquired in this manner

were indistinguishable from those measured from undisturbed ice when the measured irradiance field was diffuse.

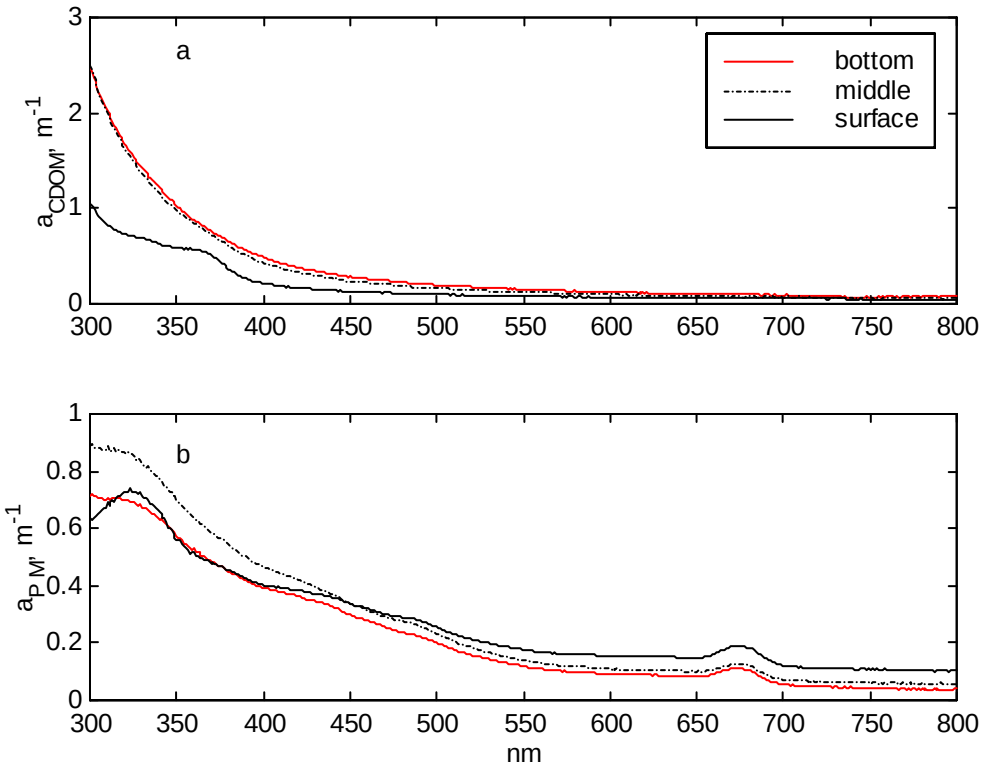

Figure 2. (a) CDOM and (b) PM absorption coefficients for each of the three ice layers.

3. Results and discussion

3.1 Absorption

The ice itself, brine, PM and CDOM contribute to light absorption in sea ice and PM and CDOM were found to be most important absorbing components in the ice cover in UVR and PAR (Figure 1). Absorption by ice and brine was significant only in the longer wavelengths and became larger than the combined $a_{CDOM,\lambda}$ and $a_{PM,\lambda}$ beyond 625. CDOM was found to be most significant absorber in the UVR (<380nm) with the exception of the surface ice layer for which the CDOM absorption spectrum was clearly different from the ice layers below (Figure 2a). In columnar ice layers $a_{CDOM,\lambda}$ exhibited the usual exponential decay with increasing wavelength. Surface layer $a_{CDOM,\lambda}$ deviated clearly from exponential decay. This could be a result of intense UVR conditions at the ice surface layer resulting in high cumulative doses if UVR for CDOM trapped in the ice. That could induce photochemical reactions that have altered the composition of CDOM at the ice surface layer, i.e. CDOM has been photobleached.

$a_{PM,\lambda}$ show characteristic chlorophyll-a absorption peaks at 670 nm and 440 nm. In all ice layers $a_{PM,\lambda}$ had distinct peak between 320 and 340 nm and its magnitude increased towards surface

(Figure 2b). $a_{PM,\lambda}$,320 -340 nm, corresponds to the absorption by mycosporine-like amino acids, UV- protecting pigments(Prezelin, Moline & Matlick 1998, Belzile et al. 2000).

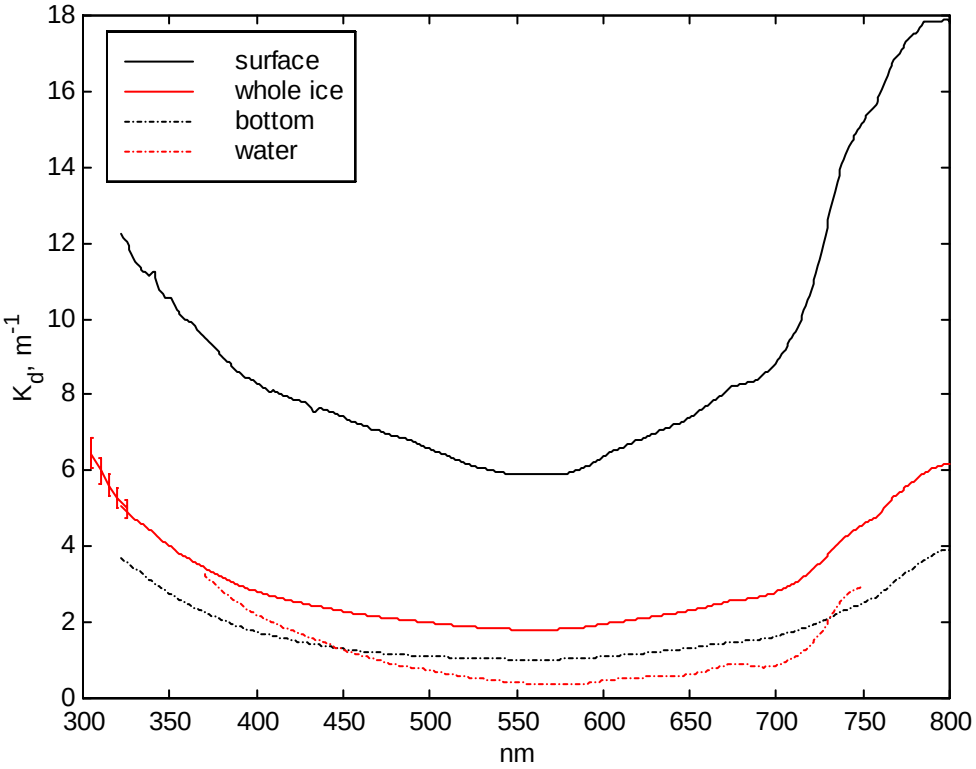

Figure 3. Measured (whole ice cover, bottom and water 20 -70 cm below ice bottom) and modeled (surface) K_d. The error bars between 305 and 325 nm show standard deviation of Macam specroradiometer measurements.

3.2 Light attenuation in ice.

Spectral diffuse attenuation coefficient for downwelling irradiance $K_{d,\lambda}$ was measured for entire ice cover and for columnar ice between 25 and 35 cm from ice surface using Equation 2. Ice cover was assumed to be composed of two optically homogenous layers, surface granular layer and a columnar ice layer below (6 and 31 cm thick, respectively), as was seen in the crystal structure. The $K_{d,\lambda}$ for granular layer was obtained by fitting appropriate attenuation to match with the measured total ice $K_{d,\lambda}$ using the measured columnar ice $K_{d,\lambda}$. Figure 3 shows spectral $K_{d,\lambda}$ in each of the ice layers and whole ice cover, also $K_{d,\lambda}$ for under laying water column is shown. Minimum light attenuation was at around 560 nm in all ice layers and increased towards longer and shorter wavelengths. In visible wavelengths attenuation increased almost linearly with decreasing wavelength until in UVR attenuation increased exponentially.

To examine the role of CDOM in UVR attenuation in ice, scattering coefficients *b* for each layer was calculated with Equation 1, as absorption coefficients and $K_{d,\lambda}$ are known and CDOM does not significantly affect scattering. In columnar ice scattering coefficient was 13 m^{-1} and 430 – 800 m^{-1} in granular ice. Granular ice *b* changed along with surface conditions and albedo (Figure 4), and was lower when ice surface was wet and the freeboard was 0 cm and increased after

surface become dry and freeboard increased to +2cm, resulting in a highly scattering surface layer.

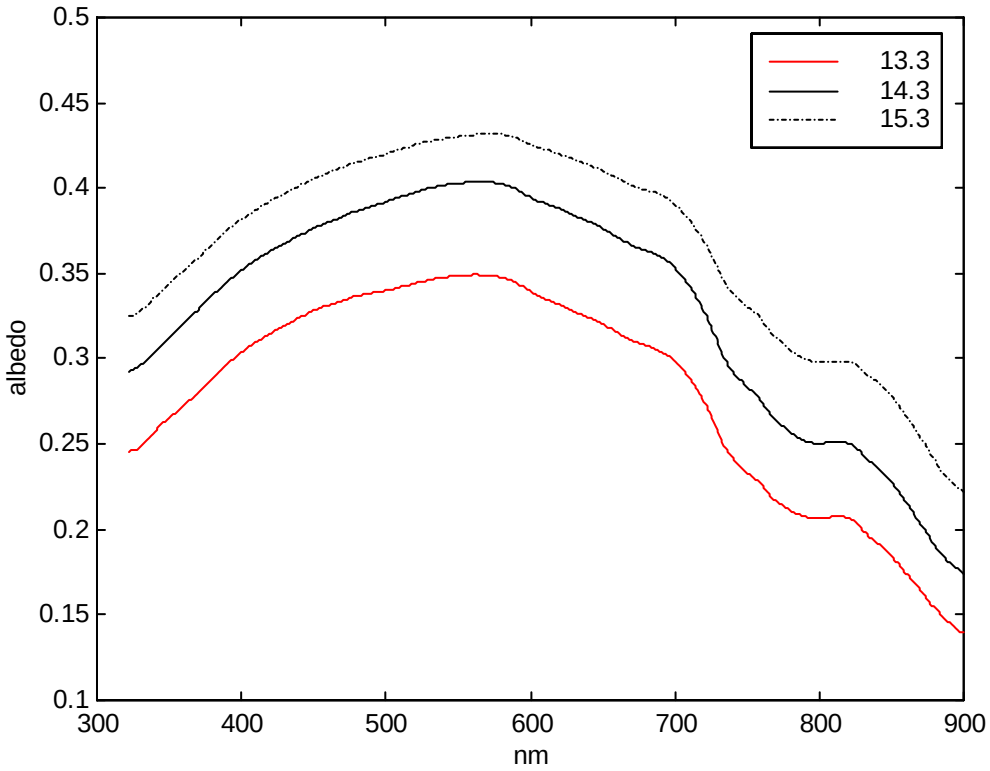

Figure 4. Spectral albedo at three consecutive days March 2007. Surface was wet and freeboard 0 cm on the 13th and then surface dried out and freeboard increased to + 2 cm on the 15th.

Maffione (1998) noted that Equation 1 is valid only when medium is highly scattering and single scattering albedo ω_0 >= 0.95. These measurements had ω_0 = 0.989 in PAR range for entire ice cover. In UVR ω_0 decreased with decreasing wavelength and approached lower limit of diffusion approximation as a result of increased absorption at shorter wavelengths. At 305 nm ω_0 = 0.947, so Equation 1 was still valid in the UVR. Belzile and others (2000) demonstrated that high organic matter content at the bottom of ice could result that the diffusion approximation breaks down at visible wavelengths (i.e. ω_0 < 0.95). This could be a more common case for CDOM rich ice in UVR, as absorption is then very strong in shorter wavelengths. In our study bottom of columnar ice had very strong absorption in UVR by CDOM and PM, at 322 a_{tot} = 2.7 m^{-1}, and relatively low scattering, b = 13 m^{-1}, and this caused ω_0 to drop far below diffusion approximation limit for bottom ice layer. This result demonstrates that despite high scattering nature of sea ice organic matter absorption has a major role in sea ice optical properties, especially so in UVR.

Light attenuation by CDOM played a major role in UVR, but not so much in PAR. Modelled $K_{d,\lambda}$ without CDOM showed that CDOM absorption in ice contributed 42 %, 37%, 33% and 20 % of light attenuation at 305 nm, 322 nm, 360 nm and 550 nm, respectively. CDOM played larger role in light attenuation deeper down in the ice cover, as photochemical reactions appeared to have affected CDOM absorption in the surface layer, especially in the UVR (Figure 2a). In the surface

layer PM appeared to contribute significantly to light attenuation also in the UVR. At 322 nm absorption by CDOM contributed only 23 % of light attenuation in the surface layer compared to 46 % in the columnar ice layer.

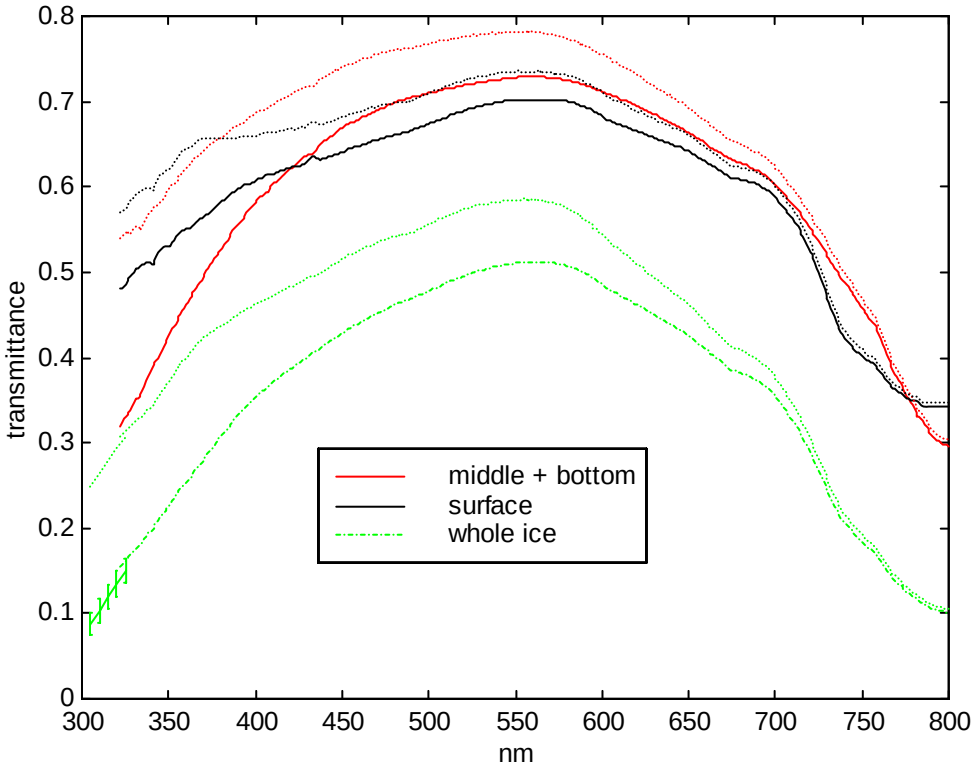

Figure 5. Measured and modeled (as in Fig. 3) transmittance for each ice layer and whole ice and modeled no-CDOM transmittance (dot lines). Also shown error bars as in Fig. 3.

3.3 Transmittance

Transmitted irradiance through each ice layer and whole ice cover with and without CDOM are shown in Figure 5. CDOM has notable effect on transmitted irradiances on all wavelengths shorter than 560 nm. Influence to transmittance is relatively largest in UVR and especially in the shortest wavelengths and for the columnar ice layer. Available UVR in and under ice cover is important to biological activity and DNA damage (Prezelin, Moline & Matlick 1998). CDOM absorption in ice has biggest effect on transmitted irradiances on wavelengths that are the most damaging to biology.

It has been found that UVR damage is not only a function of UVR intensity but that amount of damage depends also on the UVR to PAR ratio, which implies the balance between UVR damage and repair (Neale, Fritz & Davis 2001, Prezelin, Moline & Matlick 1998, Perovich 1993). Transmittance ratio implies how ice cover is modifying incoming irradiance and a large ratio means relatively more UVR and less PAR. Transmittance at 305 nm was 0.09 and PAR transmittance was 0.45 for the whole ice cover, then 305:PAR ratio was 0.20 and 322 nm transmittance was 0.15 and ratio 322:PAR 0.34. Transmittance ratio 322:PAR for columnar and granular ice layers were 0.47 and 0.73, respectively. When compared to simulated no-CDOM

transmittances these were considerably smaller, especially the 305:PAR ratio (2.3 times larger in no-CDOM case) (Figure 5.). Perovich (1993) found with theoretical model work that an approximately 15 cm layer of snow cover on ice would cause similar changes in UVR:PAR ratios than CDOM absorption in this study.

4 Conclusions

Ultraviolet light levels in the water layer are significantly reduced when sea ice cover is present, and even more reduced if ice is snow-covered (Perovich 1993). The results presented in this paper indicate that organic matter within the Baltic Sea ice cover can modify ultraviolet light levels in and below the ice cover significantly, especially when no snow cover is present. Organic matter and especially colored dissolved organic matter not only reduce the absolute ultraviolet light available, but also alter the relative amount of UVR to PAR and thus also modify the biological impact of radiation in ice.

The radiation environment in the surface ice layer was quite extreme from the organic matter point of view, no snow and high spring time incident radiation in addition to a highly scattering layer at the surface. Lack of brine channels in the granular ice layer also restricts migration and so makes dissolved and particulate constituents trapped in the ice more exposed to UVR, resulting in high cumulative doses of UVR. Under these conditions CDOM absorption spectrum is altered significantly by assumed photochemical reactions and biology in surface layer is apparently more exposed to UVR than initially before CDOM photobleaching has occurred. This and the larger UVR:PAR transmittance ratios makes biology in the surface layer much more vulnerable to UVR damage than in the columnar ice layers below with lower UVR:PAR ratios due to absorption by CDOM.

In the columnar ice layers and at the bottom of ice cover UVR intensities were lower and photochemical reactions had not apparently modified the CDOM absorption spectra to any significant degree. Here transmittance ratios were smaller and UVR damage less expected. Modeling transmittance with and without CDOM absorption showed that CDOM was very important in absorbing UVR in the lower ice layers and so modifying the transmittance ratios. Transmitted UVR:PAR ratios at the ice bottom would have been over two times larger were there had not been CDOM absorption in the ice cover.

These results show the pronounce importance of the granular surface layer in light attenuation when compared to thicker arctic ice covers and are therefore directly applicable at least to Baltic Sea ice conditions. Results presented here can also have more widespread importance when this type of ice conditions, young relatively thin first-year sea ice without a snow-cover, are expected to be more common in the arctic and sub-arctic areas because of warmer climate, less snow and thinner sea ice cover.

References

Belzile, C., Johannessen, S.C., Gosselin, M., Demers, S. & Miller, W.L. 2000, "Ultraviolet attenuation by dissolved and particulate constituents of first-year ice during late spring in an Arctic polynya", *Limnology and Oceanography,* vol. 45, no. 6, pp. 1265-1273.

Cota, G.F., Legendre, L., Gosselin, M. & Ingram, R.G. 1991, "Ecology of bottom ice algae: I. Environmental controls and variability", *Journal of Marine Systems,* vol. 2, no. 3-4, pp. 257-277.

Ehn, J., Granskog, M.A., Reinart, A. & Erm, A. 2004, "Optical properties of melting landfast sea ice and underlying seawater in Santala Bay, Gulf of Finland", *Journal of Geophysical Research-Oceans,* vol. 109, no. C9, pp. C09003.

Granskog, M., Kaartokallio, H., Kuosa, H., Thomas, D.N. & Vainio, J. 2006, "Sea ice in the Baltic Sea - A review", *Estuarine Coastal and Shelf Science,* vol. 70, no. 1-2, pp. 145-150.

Granskog, M.A., Kaartokallio, H., Thomas, D.N. & Kuosa, H. 2005, "Influence of freshwater inflow on the inorganic nutrient and dissolved organic matter within coastal sea ice and underlying waters in the Gulf of Finland (Baltic Sea)", *Estuarine Coastal and Shelf Science,* vol. 65, no. 1-2, pp. 109-122.

Granskog, M.A., Lepparanta, M., Kawamura, T., Ehn, J. & Shirasawa, K. 2004, "Seasonal development of the properties and composition of landfast sea ice in the Gulf of Finland, the Baltic Sea", *Journal of Geophysical Research-Oceans,* vol. 109, no. C2, pp. C02020.

Grenfell, T.C., Light, B. & Perovich, D.K. 2006, "Spectral transmission and implications for the partitioning of shortwave radiation in arctic sea ice", *Annals of Glaciology,* vol. 44, pp. 1-6.

Grenfell, T.C. & Perovich, D.K. 1981, "Radiation Absorption-Coefficients of Polycrystalline Ice from 400-1400 Nm", *Journal of Geophysical Research-Oceans and Atmospheres,* vol. 86, no. NC8, pp. 7447-7450.

Hagstrom, A., Azam, F., Kuparinen, J. & Zweifel, U.L. 2001, "Pelagic plankton growth and resource limitations in the Baltic Sea", *Systems Analysis of the Baltic Sea,* vol. 148, pp. 177-210.

Kaartokallio, H., Kuosa, H., Thomas, D.N., Granskog, M.A. & Kivi, K. 2007, "Biomass, composition and activity of organism assemblages along a salinity gradient in sea ice subjected to river discharge in the Baltic Sea", *Polar Biology,* vol. 30, no. 2, pp. 183-197.

Kawamura, T., Shirasawa, K., Ishikawa, N., Lindfors, A., Rasmus, K., Granskog, M.A., Ehn, J., Leppäranta, M., Martma, T. & Vaikmae, R. 2001, "Time-series observations of the structure and properties of brackish ice in the Gulf of Finland", *Annals of Glaciology,* vol. 33, pp. 1-4.

Kirk, J.T.O. 1994, "Characteristics of the Light-Field in Highly Turbid Waters - a Monte-Carlo Study", *Limnology and Oceanography,* vol. 39, no. 3, pp. 702-706.

Kirk, J.T.O. 1991, "Volume Scattering Function, Average Cosines, and the Underwater Light-Field", *Limnology and Oceanography,* vol. 36, no. 3, pp. 455-467.

Maffione, R.A. 1998, "Theoretical developments on the optical properties of highly turbid waters and sea ice", *Limnology and Oceanography,* vol. 43, no. 1, pp. 29-33.

Maffione, R.A., Voss, J.M. & Mobley, C.D. 1998, "Theory and measurements of the complete beam spread function of sea ice", *Limnology and Oceanography,* vol. 43, no. 1, pp. 34-43.

Moran, M.A. & Zepp, R.G. 1997, "Role of photoreactions in the formation of biologically labile compounds from dissolved organic matter", *Limnology and Oceanography,* vol. 42, no. 6, pp. 1307-1316.

Neale, P.J., Fritz, J.J. & Davis, R.F. 2001, "Effects of UV on photosynthesis of Antarctic phytoplankton: models and their application to coastal and pelagic assemblages", *Revista Chilena De Historia Natural,* vol. 74, no. 2, pp. 283-292.

Palosuo, E. 1961, "Crystal structure of brackish and fresh-water ice", *I.A.S.H., Snow and ice comission,* vol. 54, pp. 9-14.

Perovich, D.K. 2003, "Complex yet translucent: The optical properties of sea ice", *Physica B-Condensed Matter,* vol. 338, no. 1-4, pp. 107-114.

Perovich, D.K. 1993, "A Theoretical-Model of Ultraviolet-Light Transmission through Antarctic Sea-Ice", *Journal of Geophysical Research-Oceans,* vol. 98, no. C12, pp. 22579-22587.

Perovich, D.K., Cota, G.F., Maykut, G.A. & Grenfell, T.C. 1993, "Biooptical Observations of First-Year Arctic Sea-Ice", *Geophysical Research Letters,* vol. 20, no. 11, pp. 1059-1062.

Perovich, D.K. & Govoni, J.W. 1991, "Absorption-Coefficients of Ice from 250 to 400 Nm", *Geophysical Research Letters,* vol. 18, no. 7, pp. 1233-1235.

Perovich, D.K., Roesler, C.S. & Pegau, W.S. 1998, "Variability in Arctic sea ice optical properties", *Journal of Geophysical Research-Oceans,* vol. 103, no. C1, pp. 1193-1208.

Prezelin, B.B., Moline, M.A. & Matlick, H.A. 1998, "Icecolors '93: Spectral UV radiation effects on Antarctic frazil ice algae", *Antarctic Sea Ice: Biological Process, Interactions, and Variability,* vol. 73, pp. 45-83.

Reche, I., Pace, M.L. & Cole, J.J. 1998, "Interactions of photobleaching and inorganic nutrients in determining bacterial growth on colored dissolved organic carbon", *Microbial ecology,* vol. 36, no. 3, pp. 270-280.

Smith, R.C. & Baker, K.S. 1981, "Optical-Properties of the Clearest Natural-Waters (200-800 Nm)", *Applied Optics,* vol. 20, no. 2, pp. 177-184.

Stedmon, C.A., Thomas, D.N., Granskog, M., Kaartokallio, H., Papadimitriou, S. & Kuosa, H. 2007, "Characteristics of dissolved organic matter in Baltic coastal sea ice: Allochthonous or autochthonous origins?", *Environmental science & technology,* vol. 41, no. 21, pp. 7273-7279.

Tassan, S. & Ferrari, G.M. 2002, "A sensitivity analysis of the 'Transmittance-Reflectance' method for measuring light absorption by aquatic particles", *Journal of Plankton Research,* vol. 24, no. 8, pp. 757-774.

19th IAHR International Symposium on Ice
"Using New Technology to Understand Water-Ice Interaction"
Vancouver, British Columbia, Canada, July 6 to 11, 2008

Experimental study of phase change in rapidly growing sea ice

Daisuke Yamagishi[1] and Pat J. Langhorne[2]
University of Otago, Dunedin, New Zealand[1,2]
daisuke@physics.otago.ac.nz[1], pjl@physics.otago.ac.nz[2]

Abstract

Sea ice is never completely solid and forms a mushy layer (or skeletal layer) at the temperatures encountered in nature. The amount of liquid in the sea ice determines its physical properties. An effective estimate for the solid volume fraction, Φ_s during sea ice formation which is applicable for in situ measurements was first established by Shirtcliffe et al. (1991). They utilised the measurement of the electrical impedance of the mixture of the solid and the liquid and the conductivity of the liquid in the mushy layer. Improvements were made by Shirtcliffe and Kerr (1992) and Notz (2005); Notz et al. (2005). This research investigated Φ_s of sea ice with an improved device which measured the resistive and capacitative impedance for rapidly growing sea ice with various initial conditions. The results indicate the measurements made from the magnitude of the total impedance were in good agreement with the theoretical values of Φ_s which were obtained from the equations provided from Frankenstein and Garner (1967) and Wettlaufer et al. (2000). Experimentally measured Φ_s was within 0.05 to the theoretically estimated Φ_s. The results conclude that the skeletal layer thickness, and hence Φ_s, are a function of the growth rate of sea ice, and the greater the growth rate, the smaller the mushy layer thickness.

1 Introduction

Sea ice never freezes completely at the temperatures encountered in nature. It forms a mixture of solid and liquid, sometimes called a mushy (or skeletal) layer. This mixture is formed because of cellular growth with entrapped brine in brine channels or pockets between platelets of pure ice. Cellular growth is caused by the constitutional supercooling which arises from the salt rejection during the ice formation (Ackley, 1996). The physical properties of sea ice are determined by the volume fraction of liquid brine in sea ice, Φ_l, and hence the solid volume fraction $\Phi_s\,(= 1 - \Phi_l)$. The effective, in situ measurement of this solid volume fraction, Φ_s, by measuring the electrical impedance of the mushy layer with an applied AC current was first performed by Shirtcliffe et al. (1991) and improved by Shirtcliffe and Kerr (1992) and Notz (2005); Notz et al. (2005). Further improvements by separating resistive and capacitative impedance in the measurement of the solid volume fraction, Φ_s are presented in this report. The relationship between the growth rate of sea ice and thickness of mushy layer is deduced from our measurements.

2 Theory

The first experimental determination of fraction solid was made by Shirtcliffe et al. (1991) who employed a single carbon rod as one electrode, and a number of vertically-separated horizontal platinum wires as the second electrode of the pair. Each pair works as a conductivity probe to measure the AC electrical impedance between a wire and the carbon rod. They considered the ratio of the electrical impedance with respect to a reference state of sea ice, R_0/R, where R is the electrical impedance and subscript 0 denotes the reference state. Since ice is a poor electrical conductor, the measured impedance increases as the ice freezes over the wires. Hence the solid volume fraction is proportional to the increase in impedance. In addition, the electrical conductivity of brine, which is trapped interstitially in sea ice must be taken into account, since the conductivity depends on the temperature and the salinity which does not remain constant during ice formation due to salt rejection. Thus the equation for the solid volume fraction, Φ_s, stated by Shirtcliffe et al. (1991) is

$$\Phi_s = 1 - \frac{\gamma_0 R_0}{\gamma R} \qquad [1]$$

where γ is the conductivity of the liquid region inside the mushy layer, while R is the measured resistance between a carbon electrode and individual wire which changes from the liquid resistance to the combination of liquid and solid resistance as the wire is frozen into the ice. Both R and γ are functions of concentration and temperature, while subscript 0 denotes the values when the ice reaches the wire. The method has since been tested in natural sea ice in Svalbard and showed an increase in solid fraction with the time and ice growth (Notz, 2005; Notz et al., 2005). However, Shirtcliffe and Kerr (1992) and Notz (2005); Notz et al. (2005) have made improvements. In particular, the conductivity probe, Shirtcliffe and Kerr (1992) utilized two closely placed platinum wires at the same level. They measured the electrical impedance between these two wires, allowing a more spatially precise measurement with each pair experiencing the same electrical environment beneath the sea ice cover. Notz (2005); Notz et al. (2005) described the cell made by wires as a simplified equivalent electric circuit between wires. This is a RC circuit in series, where the capacitive

impedance dominates the magnitude of total impedance, $|Z_{tot}|$ measured between two wires (hereafter total impedance denotes magnitude of total impedance unless it is specified)

$$|Z_{total}| = (Z_C^2 + Z_R^2)^{0.5} = \left(\frac{1}{(2\pi f C_d)^2} + R_S \right)^{0.5}. \quad [2]$$

This capacitive impedance arises from a capacitance-like layer, C_d formed by ions around the electrodes. This layer is called an electric double layer and was formulated by Hunter (1987). According to Poisson-Boltzman theory, Notz (2005); Notz et al. (2005) deduced that the capacitance of the electric double layer has a relationship with salinity, S following

$$C_d = AS^{0.5} \quad [3]$$

where A describes the geometrical properties of the conductivity cell and can be treated as constant for a certain solution at constant temperature. Hence in an ideal situation, Notz claimed that if 50 % of the surface of the wires is covered by the ice, then C_d should becomes half of the initial value, causing the capacitive impedance to be doubled. However, the effect of increase in salinity must again be considered and hence equation [1] becomes

$$\Phi_s = 1 - \frac{\gamma_0 Z_0}{\gamma(T, S_{br}) Z} \quad [4]$$

where γ is the conductivity of the brine in the interstices, Z is the measured impedance. Z and γ both depend on the temperature, T and the salinity of the brine, S_{br}. S_{br} in psu is obtained from the liquidus relationship of sea water (Assur, 1958).

3 Equipment and experiments

The perspex freezing cell (figure 1) has dimensions of 48 cm in height, 34.8 cm wide, and 2 cm thick. A pressure relief tube was attached to avoid pressure build up inside the sealed container. The freezing cell is placed inside a box, which was made of polystyrene on five sides and 1.5 cm thick perspex at the front. The cell was then placed in the cold room which operates at a room temperature within 1 ˚C of the freezing point of the salinity of the sea water. For each experiment, sea water was pre-cooled to within 2 ˚C of the freezing point before being cooled from above by circulating cold kerosene at the desired temperature through an aluminium lid. Photographs of growing sea ice were taken at intervals of three to five minutes. The temperature of the sea water and the sea ice were measured by twelve temperature probes located at several positions. An array of nine thermistors were located near the platinum wire conductivity cell and sensors had a vertical displacement of 3, 6, 9, 12, 15, 20, 25, 30, 40 mm from the interface of the lid and sea water. Three thermistors were used as reference probes. One was placed 465 mm directly below the array and two were placed at 5 and 465 mm deep on the other side of the cell. Changes in the impedance of sea water and sea ice were measured by the platinum wire conductivity probe, constructed following the design of Notz (2005); Notz et al. (2005). The probe is made of two platinum wires which have a diameter of 0.25 mm, length of 20 mm and are horizontally separated by 5 mm. This was located at 20 mm below the lid. The main modification from the design of Notz (2005); Notz et al. (2005) was that the signal conditioner in figure 2(a) was designed

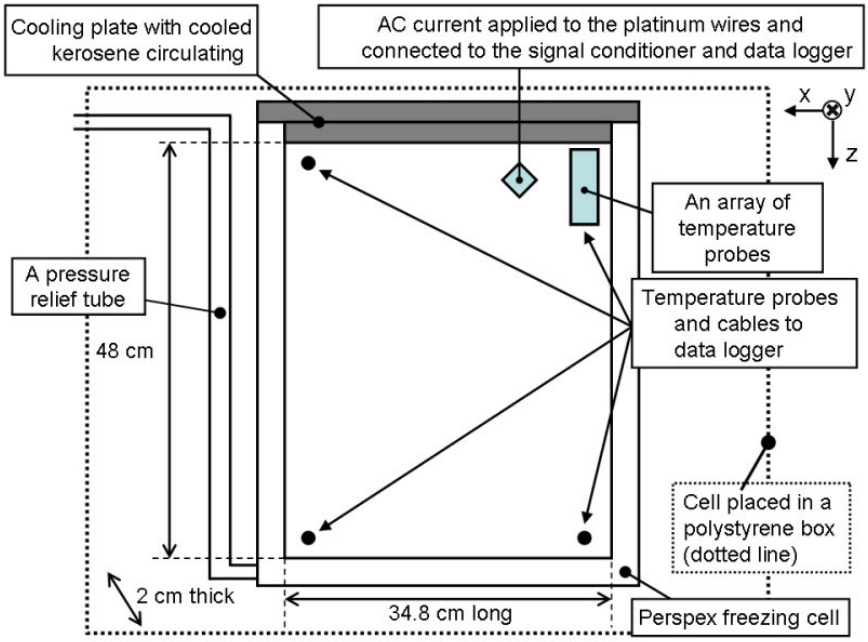

Figure 1: An overview of the freezing cell.

to measure both resistive and capacitive impedance. A 2 kHz AC voltage was applied to the platinum wires (figure 2(a)) and the impedance was deduced from the phasor relationship between the voltage (figure 2(b)) and the current obtained from the reference resistor in figure 2(a). The conductivity probe was calibrated in sea water by changing temperature and salinity. The conductance, G in Ω^{-1}, which is an inverse of the impedance, was derived and empirical equations are obtained

$$\begin{aligned} G^R(S_{br},T) &= (0.0044S_{br}^{0.68}) \\ &\quad + (-1.68\times10^{-3}(T-20)^2 + 0.61(T-20) - 1.39)\times10^{-3} \\ G^C(S_{br},T) &= (0.019S_{br}^{0.17}) \\ &\quad + (-1.42\times10^{-1}(T-20)^2 + 1.88(T-20) + 1.11)\times10^{-4} \\ G^{Z_{tot}}(S_{br},T) &= (0.0065S_{br}^{0.42}) \\ &\quad + (-7.80\times10^{-2}(T-20)^2 + 2.26(T-20) - 6.31)\times10^{-4} \end{aligned} \quad [5]$$

where superscripts R, C and Z_T represent the resistive, capacitative and total impedance respectively. Note that the empirical exponent for salinity is not the same value expected by Notz (2005); Notz et al. (2005) in equation [3]. S_{br} in psu from the liquidus relation (Assur, 1958) and T in ℃. Coefficients and exponents were obtained from a power-law fit. Hence equation [4] becomes

$$\Phi_s = 1 - \frac{G_0^i Z_0^i}{G(S_{br},T)^i Z^i} \quad [6]$$

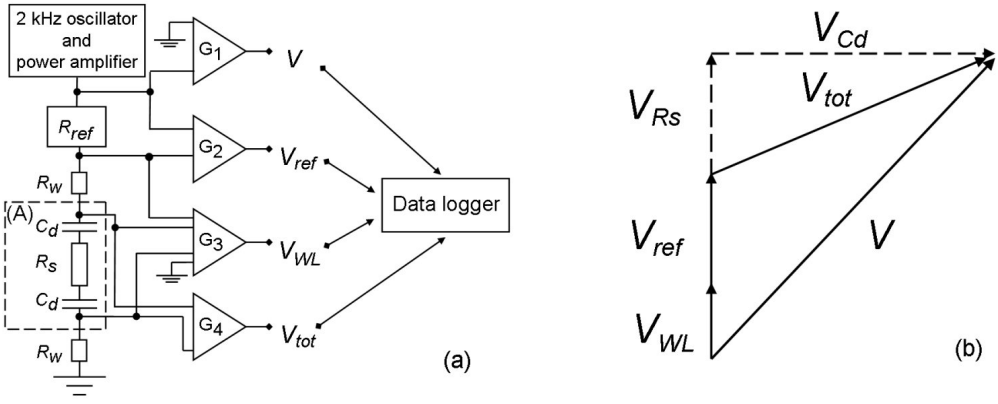

Figure 2: (a) The circuit of the signal conditioner used to measure the impedance between the pair of platinum wires. $G_{1,2,3,4}$ are the filters, rectifiers, and amplifiers. $R_{ref} = 40.2\ \Omega$ is the reference resistance, and (A) is the conductivity cell of two electrodes with the resistance of the solution, R_s and the electric double layer, C_d. R_w is the resistance of the leads which connect the conductivity cell and signal conditioner. The box outputs DC voltages where V is the voltage across the entire circuit, V_{ref} is the voltage across R_{ref} and is a measure of current I, V_{WL} is the voltage loss through the connecting wires, and V_{tot} is the total voltage across the conductivity cell. (b) The phasor diagram of the system. V, V_{ref}, V_{WL}, V_{tot} are same as in figure 2 (a). V_{Cd} and V_{Rs} are the voltages across the resistive and capacitive impedance between the platinum wires. Solid lines represent measured quantities, and dashed lines indicate derived.

where superscript i is the choice of resistive, capacitive, or total impedance. The experimentally obtained solid volume fractions, Φ_s, are compared with theoretically obtained values from the equations of Frankenstein and Garner (1967) and Wettlaufer et al. (2000). In equation [6], subscript 0 denotes the reference state that was chosen at the time when the temperature at the wire depth reached the initial freezing point of the sea water, rather than the time when the ice reached the wire. This time was chosen due to the difficulty of precisely defining the time when ice reached the wire.

4 Results

Five experiments were conducted by freezing sea water with different initial conditions as shown in table 1. Expt 3 was designed to reduce the change in growth rate during the experiment that is observed if the cooling plate temperature is constant. The photographic data allows an estimate of the growth rate of sea ice to be made as shown in figure 3(a). Time evolutions of the temperature gradient and sea ice thickness are shown in figure 4. The growth rates were used to estimate the initial entrapment of the salt (Cox and Weeks, 1988) for each layer of sea ice within a given time interval. An estimate of the time evolution of the salinity of sea ice for each experiment was obtained by following a sequence of several steps. First, the initial entrapment of salt in sea ice was estimated by utilizing the growth rate (figure 3(b)) and the equation from Cox and Weeks (1988). The salinity of sea ice decreases during its growth due to the salt rejection. A main mechanism of desalination in sea ice is gravity drainage. Gravity drainage was estimated next from Cox and Weeks (1988)

Table 1: Initial conditions of each experiment showing the initial salinity of the prepared sea water, S_{br}^{ini}, the temperature of cooling plate, T_{Top}, the mean temperature of upper region of the cell, $\overline{T_{br}^{Up}}$, the mean temperature of the water column, $\overline{T_{br}}$ and the temperature of the cold room, T_{Room}. $*$ indicates T_{Top} was constant throughout the experiment.

	Expt 1	Expt 2	Expt 3				Expt 4	Expt 5
S_{br}^{ini} (psu)	34.0	12.5	34.0				33.6	34.0
Time (mins)	$*$	$*$	0–63	63–141	141–192	192–288	$*$	$*$
T_{Top} (°C)	-10	-20.0	-10.0	-20.0	-25.0	-30.0	-10.0	-15.0
$\overline{T_{br}^{Up}}$ (°C)	-1.41	1.15	-0.69				0.013	0.72
$\overline{T_{br}}$ (°C)	-1.51	1.20	-0.64				0.015	0.35
T_{Room} (°C)	-2.0	-0.5	-2.5				-1.0	-1.0

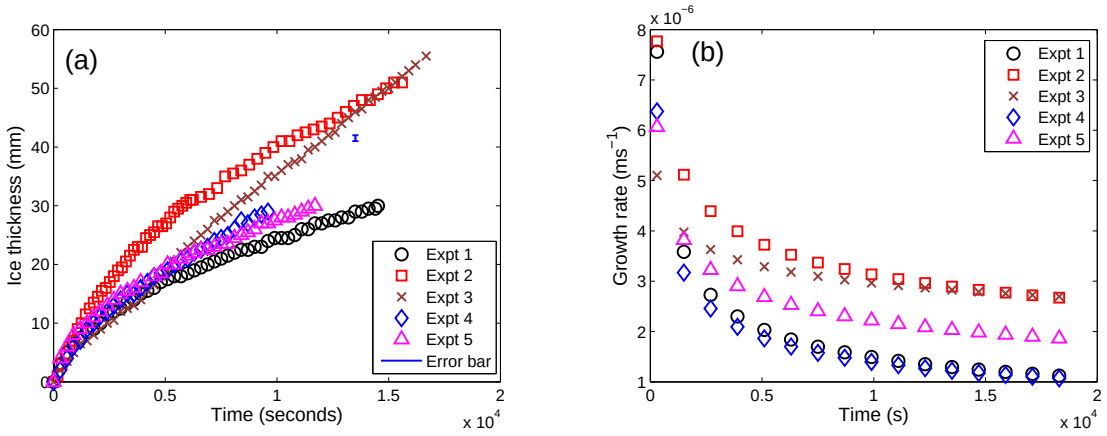

Figure 3: (a) Ice thickness versus time. A representative error in measuring ice thickness, ±0.5 mm, is plotted. (b) Fitted growth rates for experiments.

with the temperature gradient measured from the photographs and temperature data as in figure 4, and an estimated brine volume from Cox and Weeks (1983). The calculated salinity profiles for Expt 1 to 5 are presented in figure 5. This allows us to obtain a better estimate of theoretical solid volume fraction, Φ_s from Frankenstein and Garner (1967). On the other hand, Φ_s from Wettlaufer et al. (2000) requires only temperature data.
The result for Expt 3 presented in figure 6(b) shows the relationship between estimated Φ_s using different impedances, and theoretical Φ_s:

$$\Phi_s^{ZC} < \Phi_s\,(theory) \leqslant \Phi_s^{Ztot} < \Phi_s^{ZR}. \qquad [7]$$

Figure 6(a) shows that although the capacitative impedance is larger than the resistive impedance in the liquid brine (that is at time less than 80 minutes) it is not dominant as expected by Notz (2005); Notz et al. (2005). Figure 6(b) and the relationship in equation [7] show clearly that the total impedance provides the closest estimate of Φ_s to the theoretical value. Thus both the capacitive and the resistive impedance should be taken into account.

In figure 7(a), values of Φ_s are plotted against the ratio of wire depth to ice thickness for all five experiments. This depth ratio, η is given by

$$\eta = \frac{\text{Wire depth}}{h} = \frac{0.020}{h} \qquad [8]$$

where h is ice thickness measured in meter. Figure 7(a) clearly shows for experiments with the similar initial salinities of $S_{br}^{ini} \simeq 34.0$psu that

$$\Phi_s^{Ztot}(\text{Expt 4}) \simeq \Phi_s^{Ztot}(\text{Expt 1}) < \Phi_s^{Ztot}(\text{Expt 5}) < \Phi_s^{Ztot}(\text{Expt 3}), \qquad [9]$$

where their cooling plate temperature, T_{top} ($^\circ$C) are related

$$T_{top}(\text{Expt 4}) = T_{top}(\text{Expt 1}) > T_{top}(\text{Expt 5}) > T_{top}(\text{Expt 3}). \qquad [10]$$

However there are discrepancies in values of Φ_s^{Ztot} at high η between Expt 1 and 4 in spite of the fact that the initial conditions, except the initial brine temperature of the water column, are the same. This may be explained by the variation in growth rate between the experiments. The sea ice grew faster when the initial brine temperature was lower, causing increases in the solid volume fraction. Thus the initial growth rate of Expt 1 is greater than Expt 4. Hence the effect of the growth rate on the thickness of the skeletal layer is investigated.

The skeletal layer (or mushy layer) here is defined as that thickness of sea ice close to the bulk ice-water interface in which the solid volume fraction is less than some arbitrary value. The measurements of the local solid volume fraction, $\Phi_s^{Z_{tot}}$ with respect to η allows an estimate of this skeletal layer thickness to be obtained. From the definition of η, the thickness of the layer between the location of the conductivity probe and the ice-water interface is

$$\text{layer thickness in mm} = h - 20 \text{ mm} = 20 \text{ mm} \left(\frac{1}{\eta} - 1\right). \qquad [11]$$

We may define the skeletal layer of sea ice as that region above the interface in which Φ_s is less than a predetermined value Φ_{sc}. Sea ice is believed to become impermeable at $\Phi_{sc} \sim 0.95$ (Petrich et al., 2006), and this sets an upper bound for the arbitrary choice of Φ_{sc} at the top of the skeletal layer. The arbitrary values of solid volume fraction, Φ_{sc}, on which skeletal layer is defined were chosen as 0.6 and 0.75. The ice thickness ratio was then taken where these values intersect at the interpolated curves of Φ_s for each experiment to obtain the ice thickness. The corresponding growth rate was plotted against the skeletal layer thickness. It is seen in figure 7(b) that the thickness of the skeletal layer is a function of the growth rate.

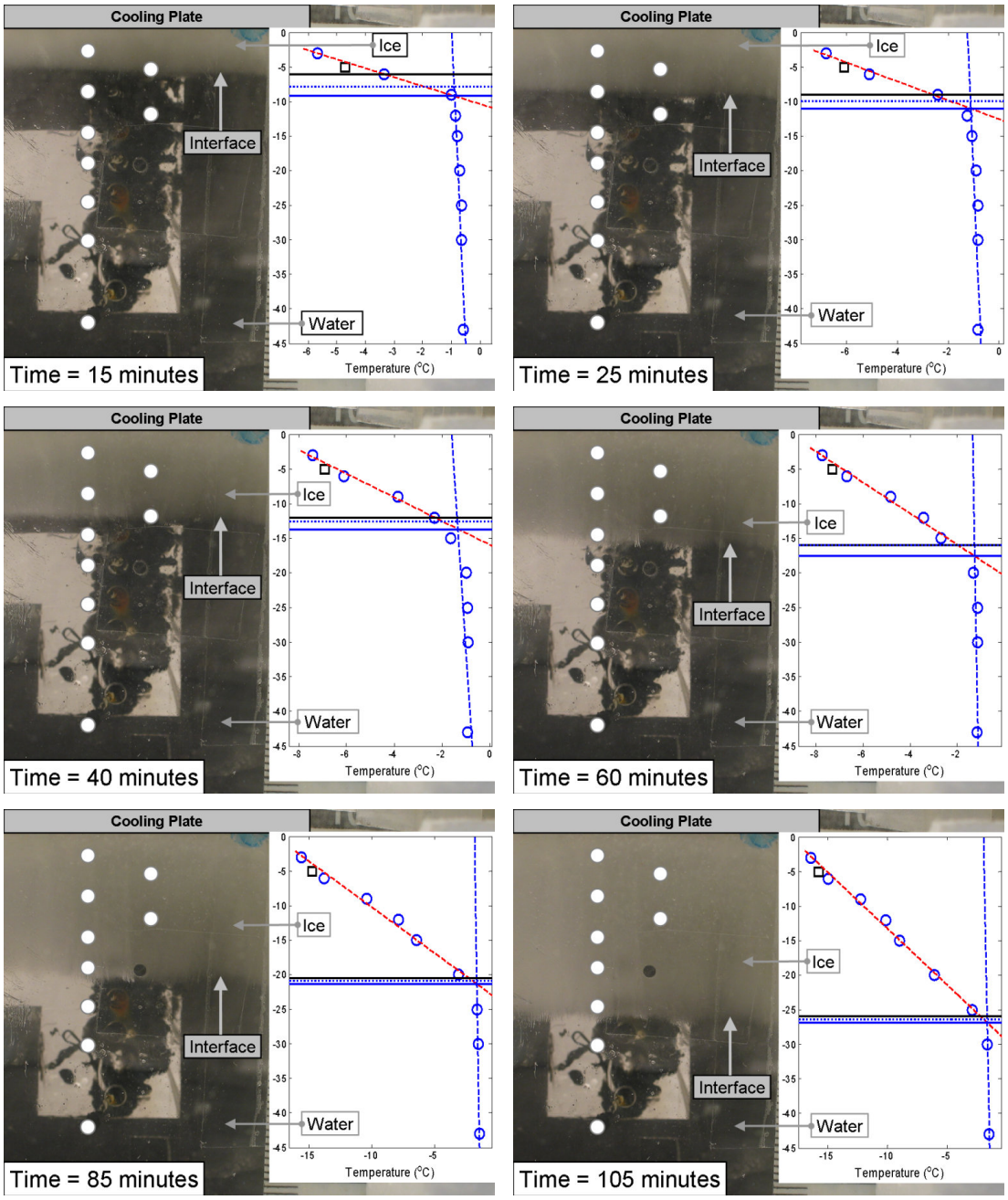

Figure 4: The temperature gradient in the sea ice from the experiment 3. White circles on the photograph represent the position of each temperature probe. The temperature profile on the right of figure has the temperature on the abscissa and depth in mm on the ordinate. Blue circles are the temperature probes, and the black square represents the reference probe at 5 mm deep on the other side of the cell. Dashed red line and dashed blue line are the temperature gradient of sea ice and brine respectively. The horizontal black line is the sea ice-water interface observed from the photograph. The horizontal blue solid line is the sea ice-water interface estimated from the intersection of the temperature gradients of sea ice and brine. The horizontal blue dotted line is the sea ice-water interface estimated from the intersection of the initial freezing point and the temperature gradient of sea ice.

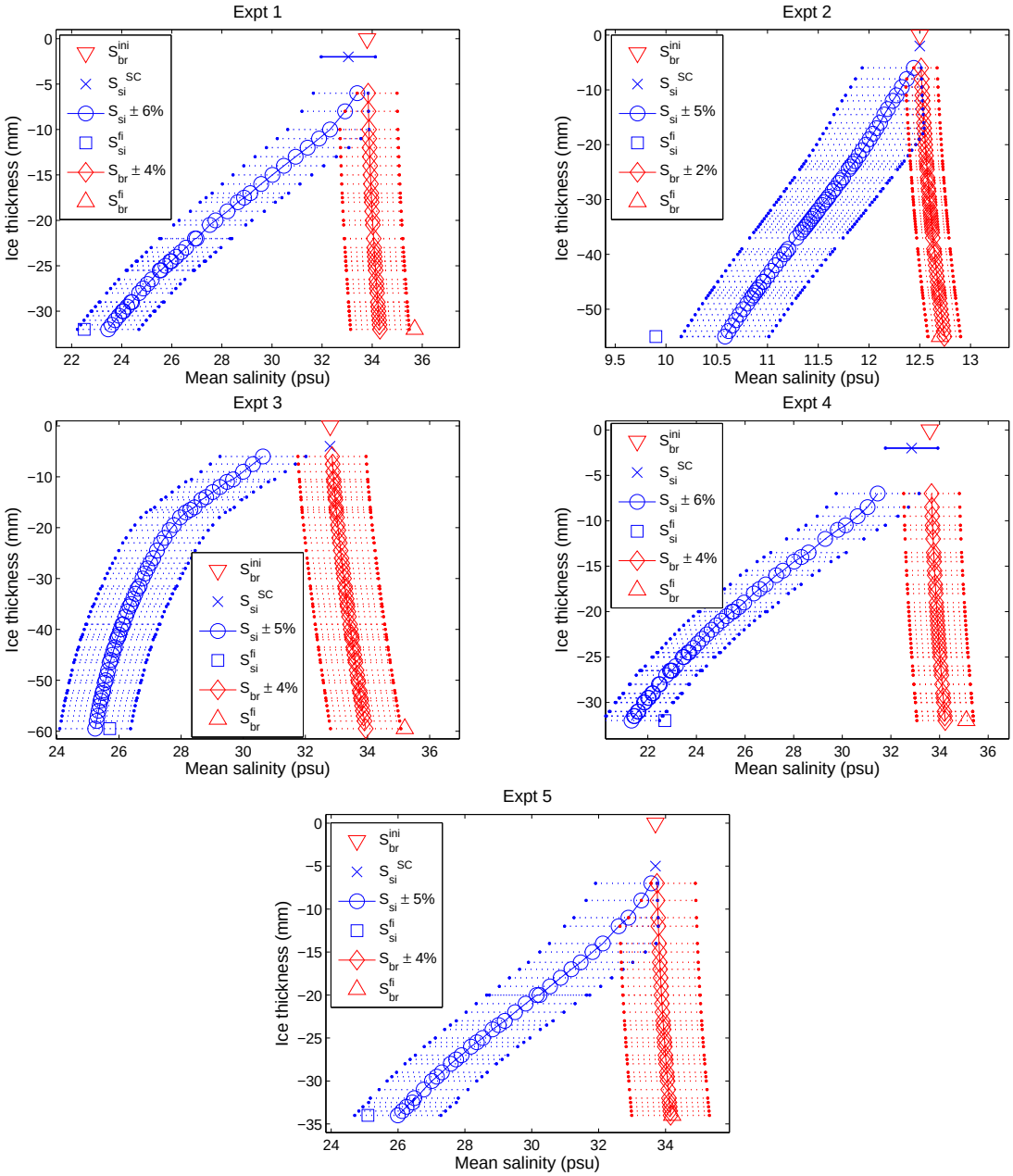

Figure 5: Salinity profile for experiments 1, 2, 3, 4 and 5. S_{br}^{ini} is the initial salinity of the brine , S_{si}^{SC} is the salinity of sea ice estimated from initial ice formation from supercooling. S_{si} and S_{br} are the evolving mean salinity of the sea ice and brine beneath the sea ice respectively with errors. S_{si}^{fi} and S_{br}^{fi} are the measured final salinity of sea ice and brine beneath the sea ice after experiment completion, respectively.

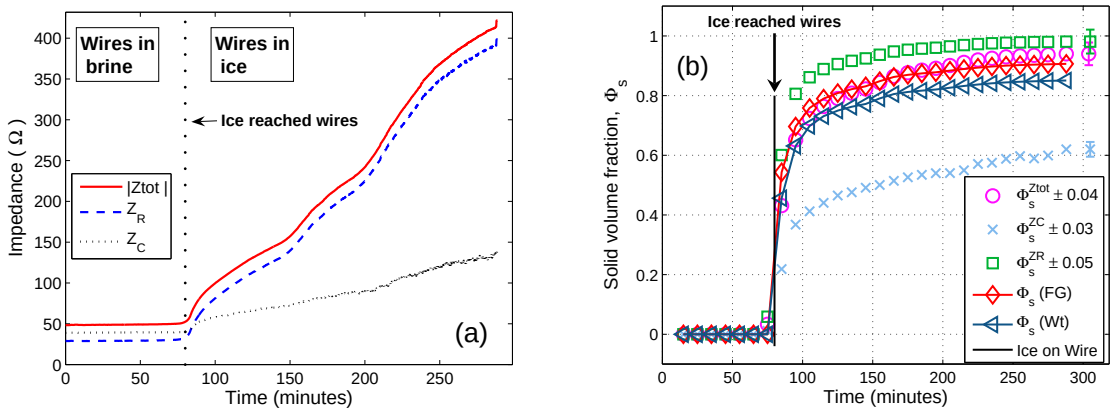

Figure 6: From Experiment 3, (a) Change in impedance with respect to time. $|Ztot|$, Z_R, Z_C are the magnitude of total impedance, the resistive impedance and the capacitive impedance respectively. (b) Experimental and theoretical solid volume fractions. Φ_s^{Ztot}, Φ_s^{ZC}, and Φ_s^{ZR} are the solid volume fraction measured by using corresponding impedance. The measurements were made with the initial freezing point as the reference point. The maximum errors are shown for Φ_s^{Ztot}, Φ_s^{ZC}, and Φ_s^{ZR}. $\Phi_s(FG)$ and $\Phi_s(Wt)$ are theoretical values of solid volume fractions, from Frankenstein and Garner (1967) and Wettlaufer et al. (2000) respectively.

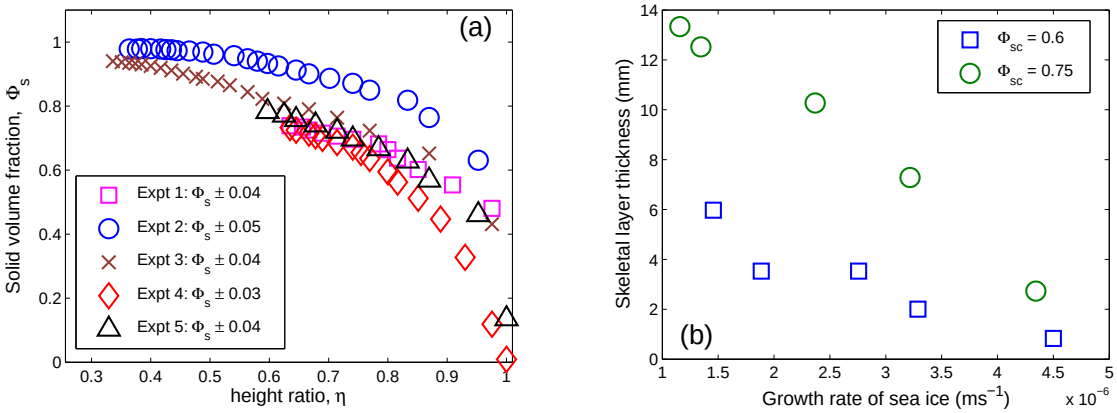

Figure 7: (a) Solid volume fractions, Φ_s vs height ratio, η for Expt 1 to 5. The solid volume fractions were measured by using the total impedance (and the total conductance of brine) with the initial freezing point as the reference point. Initial conditions for each experiment were as shown in table 1. (b) Growth rate vs thickness of skeletal layer for two values of Φ_{sc}.

5 Conclusion

The best in situ measure of solid volume fraction with the two-wire impedance cell is given by taking the magnitude of total (resistive and capacitative) impedance. Values of Φ_s determined in this way are within 0.05 of values determined from the phase diagram for sea ice. It is possible to define a skeletal layer thickness at the ice-water interface region in which the value of solid volume fraction is less than some arbitrary value. By direct measurement it

has been shown in this paper that this skeletal layer thickness is a function of sea ice growth rate.

Acknowledgements
We would like to thank Dr.Dirk Notz for the concept of the conductivity cell used in this research and sharing the information on the signal conditioner. We would also like to thank Dave Hardisty of the electronics workshop in the Physics Department who designed the circuit which measures the resistance and capacitative impedance. Many thanks to Peter Stroud of the mechanical workshop in the Physics Department for building the perspex freezing cell and the aluminium cooling plate with circulation.

References

Ackley, S. F. (1996). Sea ice. *Encyclopedia of Applied Physics*, 17:81–103.

Assur, A. (1958). Composition of the sea ice and its tensile strength. In *In Arctic sea ice*, volume 598, pages 106–138, Easton, Maryland. U.S National Academy of Sciences, Washington, DC, U.S, National Research Council Publication.

Cox, G. F. N. and Weeks, W. F. (1983). Equations for determining the gas and brine volume in sea-ice samples. *Journal of Glaciology*, 29(102).

Cox, G. F. N. and Weeks, W. F. (1988). Profile properties of undeformed first-year sea ice. *CRREL Report*, 88 - 13.

Frankenstein, G. and Garner, R. (1967). Equations for determining the brine volume of sea ice from -0.5 °c to -22.9 °c. *Journal of Glaciology*, 6(48).

Hunter, R. J. (1987). *Foundations of colloid science*. Oxford University Press.

Notz, D. (2005). *Thermodynamic and Fluid-Dynamical Processes in Sea Ice*. PhD thesis, University of Cambridge.

Notz, D., Wettlaufer, J. S., and Worster, M. G. (2005). Instruments and methods. a non-destructive method for measuring the salinity and solid fraction of growing sea ice in situ. *Journal of Glaciology*, 51(172).

Petrich, C., Langhorne, P. J., and Sun, Z. F. (2006). Modelling the interrelationships between permeability, effective porosity and total porosity in sea ice. *Cold Regions Science And Technology*, 44(2):131–144.

Shirtcliffe, T. G. L., Huppert, H. E., and Worster, M. G. (1991). Measurement of the solid fraction in the crystallization of a binary melt. *Jounral of Crystal Growth*, 113:566–574.

Shirtcliffe, T. G. L. and Kerr, R. C. (1992). On the use of electrical resistance and temperature as measures of the solid fraction in a mushy layer. *Jounral of Crystal Growth*, 125:495–501.

Wettlaufer, J. S., Worster, M. G., and Huppert, H. E. (2000). Solidification of leads: Theory, experiment, and field observations. *Journal of Geophyisical Research*, 105:1123–1134.

19th IAHR International Symposium on Ice
"Using New Technology to Understand Water-Ice Interaction"
Vancouver, British Columbia, Canada, July 6 to 11, 2008

Optical Structure and Substances in Ice – Measurements in the Baltic Sea and Some Finnish and Estonian Lakes

Ants Erm[1], Juho Jakkila[2], Jari Uusikivi[2], Antti Kangas[3] and Matti Leppäranta[2]
Marine System Institute at Tallinn University of Technology[1]
Department of Physics,University of Helsinki[2]
Finnish Institute of Marine research[3]
Akadeemia tee 21, 1268 Tallinn, Estonia[1]
Gustaf Hällströmin katu 2a , P.O. Box,Fi-00014 Helsinki, Finland[2]
Erik Palménin aukio 1, P.O. Box 2, FIN-00561 Helsinki, Finland[3]
ants@phys.sea.ee, jjakkila@mappi.helsinki.fi,
uusikivi@cc.helsinki.fi, antti.kangas@fimr.fi, matti.lepparanta@helsinki.fi

Spectral and integral optical properties of ice, ice meltwater and under ice water of some Estonian and Finnish lakes and of the Gulf of Finland were investigated as in the field and in the laboratory. In the field the albedo of ice and snow and irradiation above and under the ice were measured. The main purpose of this study was to answer the question: is it possible to learn about the optical properties of ice by investigating ice meltwater. In the laboratory the beam attenuation spectra of meltwater were measured, and concentrations of optically active substances (OAS) were analyzed. Although there are some irreversible processes going by freezing-melting cycles, especially in hard waters, the inherent optical characteristics of ice cover, including its vertical profile, could be estimated by studying of ice meltwater. The investigations have shown that not only the upper layer of ice (snow-ice) and bottom skeleton layer of sea ice may have an elevated amount of OAS, but there may occur optically denser layers inside the ice-sheet too, where the concentration of OAS could be some tens of g/m^3 while the common level is below 5 g/m^3. Assuming the optical density of distinctive layers is proportional to the amount of OAS, its values can be calculated. Two different approximations for the light field inside of ice were composed and compared: one based on the beam attenuation coefficient of meltwater and an other based on the concentration of the suspended matter. From these approximations more accurate transition coefficients to estimate the optical properties of the ice could be calculated, an specific attenuation coefficient of the suspended matter in ice also.

1. Introduction

The structure and physical properties of ice and snow and concentrations of sediments and other impurities in the ice of the Baltic Sea and some Finnish lakes have been examined since the 1960s (Palosuo 1965, Leppäranta *et al.* 1998, Leppäranta and Kosloff 2000, Leppäranta et al.2001, Erm *et al.* 2003, Leppäranta *et al.* 2003a). In Santala Bay in the Gulf of Finland the ice was investigated very profoundly during four years 1998 - 2002: Kawamura *et al.* 2001, Rasmus *et al.* 2002, Leppäranta *et al.* 2003b, Ehn *et al.* 2004, Granskog *et al.* 2004). The optical studies in the Estonian lakes begin in the frame of Finnish-Estonian co-operation project (Arst *et al.* 2008) in year 2000 at first on the Santala Bay in the Gulf of Finland and in some Estonian lakes (Erm and Reinart 2002, Erm *et al.* 2003, Leppäranta *et al.* 2003b, Arst *et al.* 2006) from 2003 the Finnish lakes in Lammi region were included into the research programme.

Principally the ice sheet formed on the water body would be pure, as by the equilibrium freezing process the pure solid phase must freeze out. In natural conditions there are several types of impurities: suspended particles, some salts, traces of yellow substances and chlorophyll pigments. Sometimes the layers with remarkably higher optical density exist in the ice sheets.

It seems that it is quite simple to study the macrostructural properties of ice sheet – to take the ice samples on the field and analyze the meltwater in the laboratory. We have begun this type of experiments in year 2000 (Erm *et al.* 2003). But there are still problems with interpreting of these data. The optical properties of water are more ore less correlating with the concentration of optically active substances (Arst *et al.* 1999, Erm *et al.* 2002), but the corresponding correlations for the ice samples are very low, especially for the lake samples (Erm and Reinart 2002).

2. Measurements and methods

2.1. Field experiments

The purpose of the current study was to elucidate how the under ice light field is forming, and how the OAS in ice cover influence on it. Many lakes in Estonia and Finland and some bays of the Gulf of Finland were studied in the winters 2004 -2006 (Table 1).

The *in situ* works consisted of measuring the ice thickness (z_{ice}), collecting ice samples and measuring the *albedo*, irradiance $E_d(z,\lambda)$ or $E_d(z)$ (in the PAR region of the spectrum) above and below the ice cover. The optical measurements were made with an experimental equipment for measuring the integral optical parameters (LiCor PAR sensors) or with a Ramses spectral radiometer (Trios Corp.). More detailed the measurement equipment is described in Arst etal, 2006.

The main parameter used to characterize optical properties of water bodies is the diffuse attenuation coefficient $K_d(z,\lambda)$, (Arst 2003):

$$K_d(z,\lambda) = -\frac{1}{E_d(z,\lambda)}\frac{dE_d(z,\lambda)}{dz}, \qquad \textbf{[1]}$$

where $E_d(z,\lambda)$ is the irradiation at the depth z.

For a water layer from z_1 to z_2 $K_d(z)$ could be calculated as

$$K_d(z_2 - z_1) = -\frac{1}{z_2 - z_1} \ln\left(\frac{E_d(z_2)}{E_d(z_1)}\right). \quad \textbf{[2]}$$

In this study the spectral and integral parameters will be discussed, thereby here and after designation without a wavelength index would be read for the integral data. It is quite complicated to measure irradiance profiles inside the ice sheet, but it is possible to apply the Eq. [2] for ice cover. If there is some snow on the ice two series of measurements must be carried out – with and without snow (after the snow will be removed). So, for the ice sheet (without snow) we can consider

$$K_{d,ice} = -\frac{1}{z_{ice}} \ln\left(\frac{E_{d,inc}(1 - A_{ice})}{E_{d,ice}}\right), \quad \textbf{[3]}$$

where $E_{d,inc}$ is the irradiance just above the ice cover, A_{ice} is *albedo* of ice and $E_{d,ice}$ is the irradiance just under the ice, measured directly or calculated from underwater irradiance profile. Knowing now the diffuse attenuation coefficient of the ice $K_{d,ice}$ and the underwater irradiance under the ice cover $E_{d,ice}$ we can calculate the irradiance in the snow-ice boundary

$$E_{d,snow-ice} = E'_{d,ice} \exp(z_{ice} K_{d,ice}), \quad \textbf{[4]}$$

where $E'_{d,ice}$ is the irradiance just under the snow covered ice.

Now we are able to calculate an attenuation coefficient of the snow

$$K_{d,snow} = -\frac{1}{z_{snow}} \ln\left(\frac{E_{d,inc}(1 - A_{snow})}{E_{d,snow-ice}}\right), \quad \textbf{[5]}$$

where z_{snow} is the thickness and A_{snow} the *albedo* of the snow.

2.2. Laboratory measurements

A lot of studies have been carried out to explain the optical properties of natural waters through the amount of OAS (Kutser *et al.* 1998, Arst *et al*. 1999, Herlevi 1999, Erm *et al*. 2002, Paavel *et al.* 2007). These studies have shown that generally there exist a quite good correlation between the diffuse attenuation coefficient and the amount of OAS in the water and different algorithms have been proposed to connect the optical properties with concentrations of OAS. As the concentrations of chlorophyll and yellow substance in ice are commonly negligible, on one hand it seemed to be much easier to find a good algorithm for ice samples. That is why we started laboratory studies of ice meltwater. In reality, the task turned out to be much more complicated than expected.

Commonly two ice samples were taken from the field site. One was melted, and the one was cut to parts by boundaries between the layers with different structure (transparency, bubbles, colour etc.). They were melted separately.

Beam attenuation coefficient spectra ($c^*(\lambda)$) of the meltwater were recorded by spectrometer Hitachi 1000). Spectrometric attenuation coefficients were determined from unfiltered and filtered water samples, respectively, $c^*(\lambda)$ and $c_f^*(\lambda)$.They were obtained as the difference $c(\lambda) - c_d(\lambda)$, where $c(\lambda)$ and $c_d(\lambda)$ are the beam attenuation coefficients for natural and distilled water, respectively (Arst 2003). These measurements were made at a spectral interval of 10 nm in the band 350–700 nm, and to compare the field and laboratory data a mean attenuation coefficient c^*_{PAR} over the band 400-700 nm (PAR) was calculated. The spectra $c^*(\lambda)$ could be compared with $K_d(\lambda)$ from the field data.

The concentration of suspended matter C_s was established by dry weight method using 0.45 μm Millipore membrane filter.

In some cases concentrations of yellow substance, estimated by an optical method (Mäekivi and Arst 1996) using a value of $c_f^*(380)$, and chlorophyll *a* by the spectrophotometric method (Lorenzen 1967) were measured.

3. Results and discussion

The spectral underwater light field was monitored by Ramses radiometer and used to control as the usability of integral PAR sensors and as well the beam attenuation coefficients method in the laboratory. In Fig.1 incident and underwater irradiance spectra taken on the10th of April 2006 in Lake Ormajärvi in Lammi are shown.

Most of the under ice light was apportioned in the range 400-700 nm, that means in the photosynthetically active region (PAR) where our integral sensors were working. A drift of irradiance maximum towards longer wavelengths due to short wave absorbtion by yellow substance is seen also.

In Fig. 2 profiles of underwater irradiance at four wavelengths and integral PAR irradiance are plotted. In the regression formulas, shown near the plots, the first constant is the derived initial irradiance at the zero depth, and the exponents power coefficients correspond to the mean (over the measured depth profile) diffuse attenuation coefficient $K_d(\lambda)$ or K_d. As awaited $K_d(400)$ is much higher as that for longer wavelengths. $K_d(600)$and $K_d(700)$ are comparable with the K_d. The figure also suggests that the euphotic depth is about 5 m, defined as the level where irradiance is 1% of the surface level.

Using underwater spectra together with irradiance and backscattered from the snow and ice (snow removed) $K_d(\lambda)$ of snow and ice could be calculated by Eqs. 5 and 6. The attenuation in snow is increases rapidly in shorter wavelenghts, while $K_d(\lambda)$ of ice is much more uniform (Fig.3). That means we do not loose a very great deal of information using integral data in the analysis.

Before introducing the model a classical example of optical data of ice meltwater must be discussed (Table 2, Fig. 4). Four ice layers of the lake Valkeakotinen (April 2004) were separately investigated in the laboratory .The beam attenuation coefficients $c^*(\lambda)$ and $c_f^*(\lambda)$.were determined and the concentrations of OAS were established.

The water of this lake is very brown (a high concentration of yellow substance) but with a quite low suspended matter amount. Contrary, the ice sheet contained remarkable amount of particles, but practically no yellow substance. The beam attenuation spectra of Lake Valkeakotinen are shown in Fig. 4.

The attenuation spectra of the water beneath the ice are principally different from the meltwater attenuation spectra. The water spectra are mostly influenced by the yellow substance absorbing in the ultra violet and blue light with an exponential increase towards shorter wavelengths, while

the meltwater spectra are linear with only a slight slope and at the red end the spectra are comparable to those in the water. Filtered meltwater is very clear. The values of yellow substance and chlorophyll *a* in table 1, both obtained by optical methods too, reflect traces of some other impurities. So, we can use only two laboratory characteristics in the further discussion – C_S and c^*.

From the field data K_d for the whole ice layer had to be calculated. To fit the model an initial value (the coming into ice) and end value (the level just under the ice) of E_d are needed, but knowing K_d of ice one of these could be fed in and then the other one could be calculated. Assuming K_d to be proportional to c^* as well to C_S at least in one ice sample, the values of K_d for distinctive layers could be calculated:

$$K_{d,c} = k_c c^* \quad \textbf{[7]}$$

for the model 1 (the same for all layers), and

$$K_{d,S} = k_S C_S \quad \textbf{[8]}$$

for the model 2 (the same for all layers also).

Varying values for k_c and k_S, the plots $E_d(z)$ could be fitted so, that the light field inside the ice sheet is consistent and $k_c c^*$ and $k_S C_S$ at the top and bottom of the ice sample equal to the irradiance measured in the field. In such a way two different approximations for the light field in the ice sheet could be composed. Attenuation profiles constructed in this way are shown in the Fig. 5. (Lake Võrtsjärv, 24 March 2005) and Fig. 6 (Lake Valkeakotinen, 15 April 2004).

The ice sample Lake Võrtsjärv (Fig. 5a) consisted from a very dense and opaque layer (5 cm) on the top and more clear lower part (45 cm). Despite the most part of the ice sheet was quite clear, the apparent attenuation coefficient was rather high (1.1 m-1). Using a more realistic approximation, K_d of upper 5 cm layer was 4.4 – 5.8 m^{-1}, and of the lower 35 cm only 0.5-0.8 m^{-1}, see also tables 2 and 3. Explanation for this could be high scattering in snow-ice layer.

The beam attenuation coefficient and concentration of suspended matter in the ice sample of Lake Valkeakotinen are decreasing sheet by sheet from the top of the ice (Tab. 3). Accordingly the irradiance in the ice calculated by models 1 and 2 is changing monotonously (Fig 5 b).

To control the availability of methods, the correlations $K_{d,S}(C_S)$ and $K_{d,c}(c^*)$ were calculated (Fig. 6). The slope factor of $K_{d,S}(C_S)$ corresponds to a specific attenuation constant c'_S of the suspended matter in ice. This models work quite well in most cases, only the very dense layers seem to have some more complicated transformation mechanism. Hereby, four layers (ice 1 of the Lake Võrtsjärv and the both layers of the Lake Äntu-Sinijärv) are excluded from the plots in Fig. 6. A reason that some lakes do not accommodate into the model may be the precipitation of salts from the water by freezing process. These salts probably are the optically inactive components of a solid solution constituted by freezing of water. Similar changes in the water samples during melting–freezing cycles were observed in the previous work by Erm *et al.* (2003). One reason of the quite great distribution of meltwater parameters may be the existence of gas bubbles in the ice. These processes need a further discussion, especially the case of Äntu-Sinijärv, where the precipitation of a very great amount of suspended matter even from filtrated samples was observed.

4. Conclusions

A database from years 2003-2005 of field and laboratory investigations of ice cover, ice samples and ice meltwater samples from years 2003-2005 is analysed and discussed.
Using a method, first proposed in Erm and Reinart (2003), a model to describe the light field inside the ice sheet using the values of suspended matter concentration and beam attenuation coefficients of the ice meltwater samples is developed and discussed.
A model for estimating the diffuse attenuation in an ice sheet based on optical and concentration data of the ice meltwater is discussed.
A mean value of specific attenuation constant of suspended matter in ice (c'_S ~0.7 m^2 g^{-1}) is estimated.

Acknowledgments
Financial support has been provided by the bilateral exchange programme between the Academy of Finland and Estonian Academy of Sciences. The authors are indebted to Mr. Ove Pärn for help in the fieldwork

References

Arst H., Erm A., Hussainov M., Kutser T., Mäekivi S., Reinart A., Herlevi A. (1999). Investigation of Estonian and Finnish lakes by optical measurements in 1992-97. *Proc. Estonian Acad. Sci., Biology, Ecology* 48/1: 5–24.

Arst, H. 2003. Optical Properties and Remote Sensing of Multicomponental Water Bodies. Berlin, Chichester: Springer, Praxis.

Arst, H., Erm, A., Leppäranta, M., Reinart, A. (2006). Radiative characteristics of ice-covered fresh and brackish-water bodies. *Proceedings of the Estonian Academy of Sciences. Geology*, 55, 3 - 23.

Arst, H., Erm, A., Herlevi, A., Kutser, T., Leppäranta, M., Reinart, A., Virta, J. (2008). Optical properties of boreal lake waters in Finland and Estonia. *Boreal Environment Research*, 13, (in press).

Ehn, J., Granskog, M, Reinart, A., Erm, A. (2004). Optical properties of melting landfast sea ice and underlying seawater in Santala Bay, Gulf of Finland. *Journal of Geophysical Research-Ocean*s, 109(C9), 1

Erm, A. and Reinart, A. (2002). Optical properties of the system iyice cover + waterlt in different types of water bodies. In *Proceedings of the Fourth Workshop on Baltic Sea Ice Climate,Norrköping, Sweden (Omstedt, A. & Axell, L., eds), Oceanografi SMH*I, 72, 1Œ10.

Erm, A., Arst, H., Nõges, P., Nõges, T., Reinart, A., Sipelgas, L. (2002). Temporal Variation of the Bio-Optical Properties of Four North Estonian Lakes in 1999-2000. *Geophysica,* 38, 89 - 111.

Erm, A.; Reinart, A.; Arst, H.; Sipelgas, L.; Leppäranta, M. (2003). Optical properties of lake and sea ice. *In: Proceedings of the seminar "Sea ice climate and marine environments in the Okhotsk and Baltic Seas - The present status and prospects": Seminar "Sea ice climate and marine environments in the Okhotsk and Baltic Seas - The present status and prospects"; Finland; 2003. Helsinki: University of Helsinki, 2003, (Report Series in Geophysics*; 46), 93 - 100.

Granskog M., Leppäranta M., Ehn J., Kawamura T., Shirasawa K. (2004). Sea ice structure and properties in Santala Bay, Baltic Sea. *Journal of Geophysical Research* 109, C02020.

Herlevi A., Virta J., Arst H., Erm A. (1999). Results of light absorption measurements in Finnish and Estonian lakes in summer 1997. *Proc. Estonian Acad. Sci., Biology, Ecology* 48/1: 46–62.

Kawamura T., Shirasawa K., Ishikawa N., Lindfors A., Rasmus K., Ehn J., Leppäranta M., Martma T., Vaikmäe R. (2001). A time series of the sea ice structure in the Baltic Sea. *Annals of Glaciology* 33: 1–4.

Kutser, T., Arst, H., Mäekivi, S., Kallaste, K. (1998). Estimation of the water quality of the Baltic Sea and some lakes in Estonia and Finland by passive optical remote sensing measurements on board a vessel. *Lakes and Reservoirs: Research and Management*, 3, 53 - 66.

Leppäranta M., Tikkanen M., Shemeikka P. (1998). Observations of ice and its sediments on the Baltic coast. *Nordic Hydrology* 29: 199–220.

Leppäranta M., Kosloff P. (2000). The thickness and structure of Lake Pääjärvi ice. *Geophysica* 36(1–2): 233–248.

Leppäranta, M., Tikkanen, M., Virkanen J. (2003). Observations of ice impurities in some Finnish lakes. *Proc. Estonian Academy of Science.Chemistry* 52(2): 59–75.

Lepparanta, M., Reinart, A., Erm, A., Arst, H., Hussainov, M., Sipelgas, L. (2003). Investigation of ice and water properties and under-ice light fields in fresh and brackish water bodies. *Nordic Hydrology*, 34(3), 245 - 266.

Lorenzen, C.J. (1967). Determination of chlorophyll and phaeopigments; spectrophotometric equations. *Limnol. Oceanogr.* 12: 343–346.

Mäekivi, S. and Arst, H. (1996). Estimation of the concentration of yellow substance in natural waters by beam attenuation coefficient spectra. *Proc. Estonian Acad. Sci., Ecology* 6(¾): 108–123.

Paavel, B., Arst, H., Herlevi, A. (2007). Dependence of spectral distribution of inherent optical properties of lake waters on the concentrations of different water constituents. *Nordic Hydrology*, 38(3), 265 - 285.

Palosuo E. (1965). Frozen slush on lake ice. *Geophysica* 9(2): 131–147.

Rasmus K., Ehn J., Granskog M., Lindfors A., Pelkonen A., Rasmus S., Leppäranta, M. & Reinart A. 2002. Optical measurements of sea ice in Tvärminne, Gulf of Finland. *Nordic Hydrology* 33(2/3): 207–226.

Table 1. Water bodies discussed in the paper.

Water body	State	Latitude	Longitude	Typical Secchi depth, m	Limnological type
L. Lammi Pääjärvi	Finland	61°03 N	25°07 E	1.5	Mesohumic
L. Valkeakotinen	Finland	61°14 N	25°04 E	0.8	Dystrophic
L. Ormajärvi	Finland	61°06 N	24°57 E	3	Eutrophic
L. Nohipalu Valgjärv	Estonia	58°00 N	27°21 E	3	Oligotrophic/ mesotrophic
L. Äntu Sinijärv	Estonia	59°05 N	26°17 E	15	Alkalitrophic
L. Võrtsjärv	Estonia	58°12 N	26°05 E	0.8	Eutrofic
Gulf of Finland, Toila	Estonia	59°26 N	27°31 E	4	Brakish water

Table 2. The parameters measured in the laboratory from the ice and water of Lake Valkekotinen (15 April 2004).

Sheets from the top	Thickness of the ice layer, cm	$C_{chl}\,a$, mg m^{-3}	C_s, g m^{-3}	$C_{y,e}$, g m^{-3}	c*(PAR), m^{-1}
Ice 1	8.0	0.1	6.3	0.34	3.2
Ice 2	5.5	0.2	4.6	0.29	2.9
Ice 3	6.0	0.7	5.0	0.29	1.7
Ice 4	19.0	0.3	1.8	0.10	0.5
Water		8.8	3.4	33.68	5.3

Table 3. Measured (z_i , A_i, K_d, c^*, C_S) and calculated (k_c, k_S, $K_{d,c}$, $K_{d,S}$) characteristics of investigated lakes.

Lake			z_i	A_i,	K_d	c^*	C_S	$K_{d,c}$	$K_{d,S}$	k_c	k_S
			cm		1/m	1/m	g/m^3	1/m	1/m		m^2/g
L. lami Pääjärvi	**14 Apr. 04**	**total ice**	31.0		2.34	3.14	6.8			**1.35**	**0.70**
		ice 1	8.0	*0.29*		4.15	7.4	**5.60**	**5.18**		
		ice 2	23.0			0.88	2.1	**1.19**	**1.47**		
L. lami Pääjärvi	**18 March 04**	**total ice**	74.0		0.45	1.06	2.4			**0.96**	**0.24**
		ice 1	8.0	*0.29*		0.39	1.5	**0.38**	**0.37**		
		ice 2	38.0			0.49	1.1	**0.47**	**0.27**		
		ice 3	74.0			0.46	1.2	**0.44**	**0.29**		
L. Valkea-kotinen	**19. March 03**	**total ice**	57.0		3.78	2.3	1.2			**1.71**	**0.95**
		ice 1	23.0	*0.43*		7.4	4.6	**7.87**	**7.01**		
		ice 2	34.0			1.7	0.6	**1.03**	**1.61**		
L. Valkea-kotinen	**15Apr. 04**	**total ice**	38.5		2.39	1.62	3.6			**1.475**	**0.66**
		ice 1	8.0	*0.39*		3.18	6.3	**4.69**	**4.15**		
		ice 2	5.5			2.94	4.6	**4.33**	**3.05**		
		ice 3	6.0			1.71	5.0	**2.52**	**3.29**		
		ice 4	19.0			0.55	1.8	**0.81**	**1.18**		
L. Valkea-kotinen	**5 Apr. 05**	**total ice**	74.0		2.06	1.09	2.6			**1.10**	**0.50**
		ice 1	16.0	*0.6*		1.82	3.6	**2.00**	**1.79**		
		ice 2	58.0			1.54	4.0	**1.69**	**2.00**		
L. Ormajärvi	**20 March 03**	**total ice**	31.5	*0.58*	0.86	2.3	0.6			**0.59**	**0.29**
		ice 1	12.0			3.5	1.2	**2.69**	**2.17**		
		ice 2	19.5			1.5	0.5	**0.35**	**0.50**		
L. Ormajärvi	**6 Apr 05**	**total ice**	36.0		1.84	2.28	4.5			**0.80**	**0.50**
		ice 1	15.5	*0.39*		2.17	5.3	***1.78***	**2.56**		
		ice 2	20.5			2.28	2. 7	***1.87***	**1.28**		
L. Nohipalu Valgejärv	**23 March 05**	**total ice**	27.0		1.04	0.61	1.5			**1.30**	**0.40**
		ice 1	7.0	*0.39*		0.92	3.0	**1.20**	**1.20**		
		ice 2	20.0			0.74	2.4	**0.96**	**0.96**		
L. Võrtsjärv	**24 March 05**	**total ice**	41.5		1.07	0.73	3.4			**0.75**	**0.25**
		ice 1	5.5	*0.51*	4.57	6.09	25.2	**4.57**	**6.30**		
		ice 2	36.0			0.77	1.4	**0.58**	**0.35**		
Gulf of Finland (Toila)	**22 March 05**	**total ice**	36.5		1.85	1.27	1.7			**1.10**	**0.60**
		ice 1	6.5	*0.37*		1.54	3.2	**1.69**	**1.95**		
		ice 2	15.0			1.86	3.3	**2.05**	**1.98**		
		ice 3	15.0			1.34	2.6	**1.47**	**1.56**		
L. Äntu-Sinijärv	**2 March 03**	**total ice**	29.0		2.03	5.63	55.1			**0.53**	**0.03**
		ice 1	9.5	*0.61*		5.75	57.6	**3.05**	**1.94**		
		ice 2	19.5			2.45	52.2	**1.30**	**1.76**		

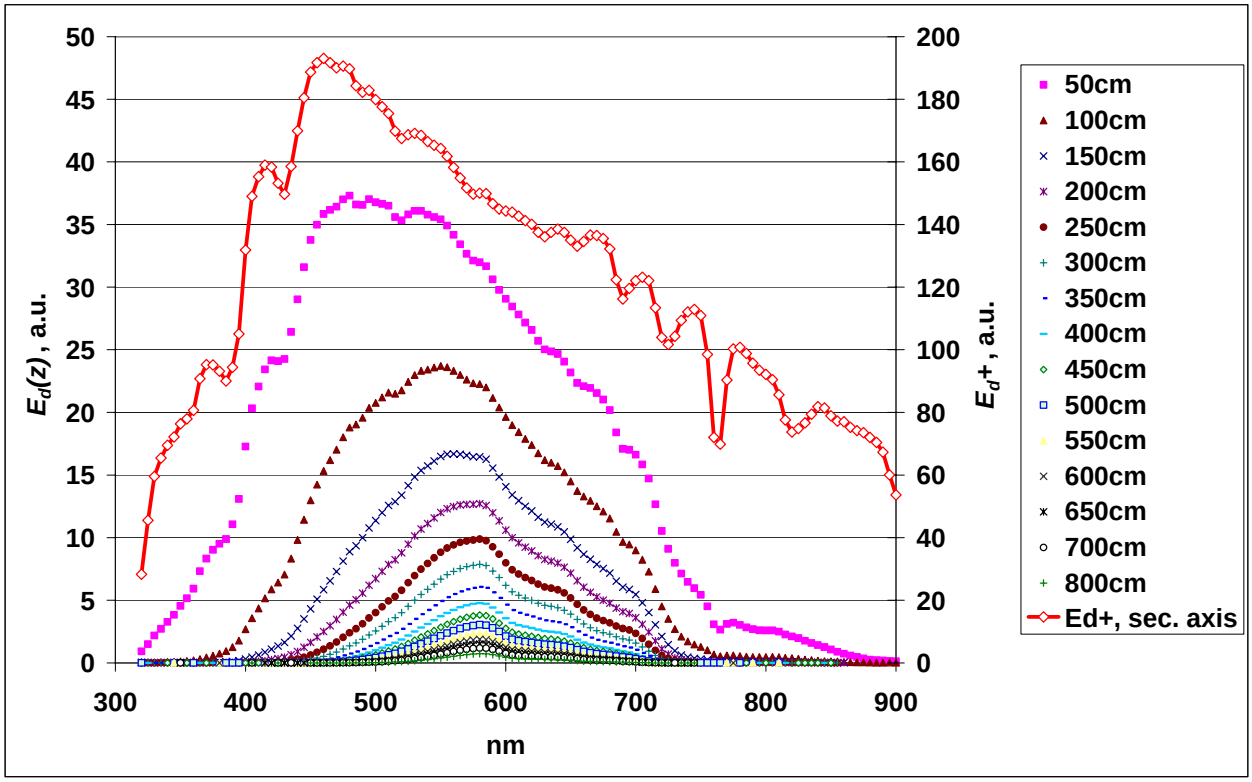

Figure 1. Irradiation spectra of the lake Ormajärvi measured on 10 April 2006. Depth from the top level of ice. Values of the incident irradiation (E_d+) are on se left axis.

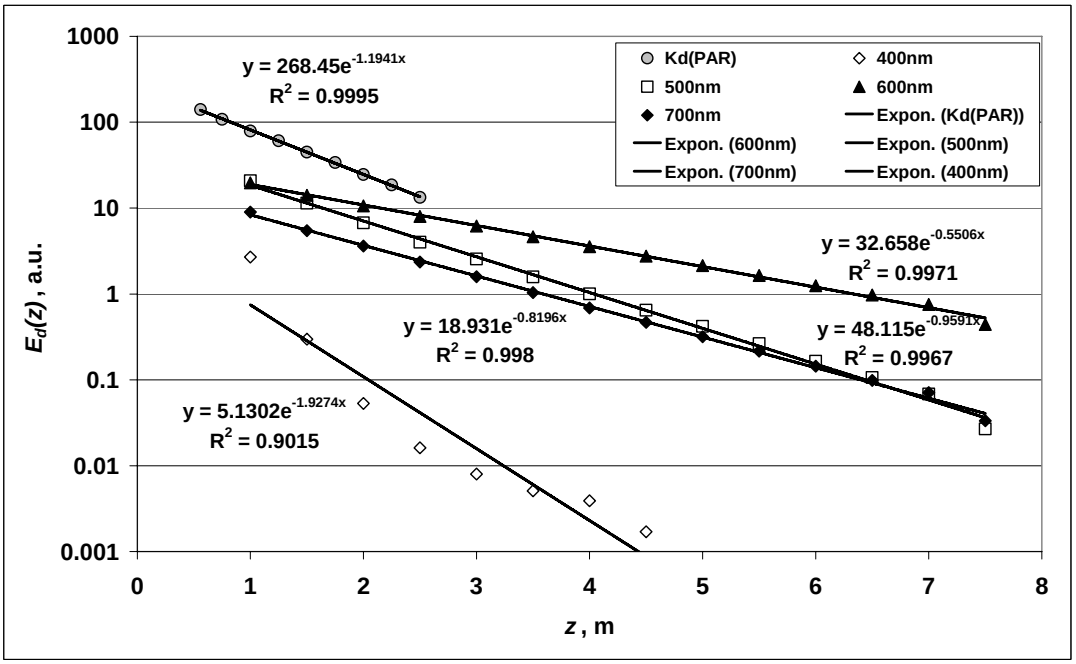

Figure 2. Underwater irradiation profiles of the Lake Ormajärvi (10 Apr. 2006).

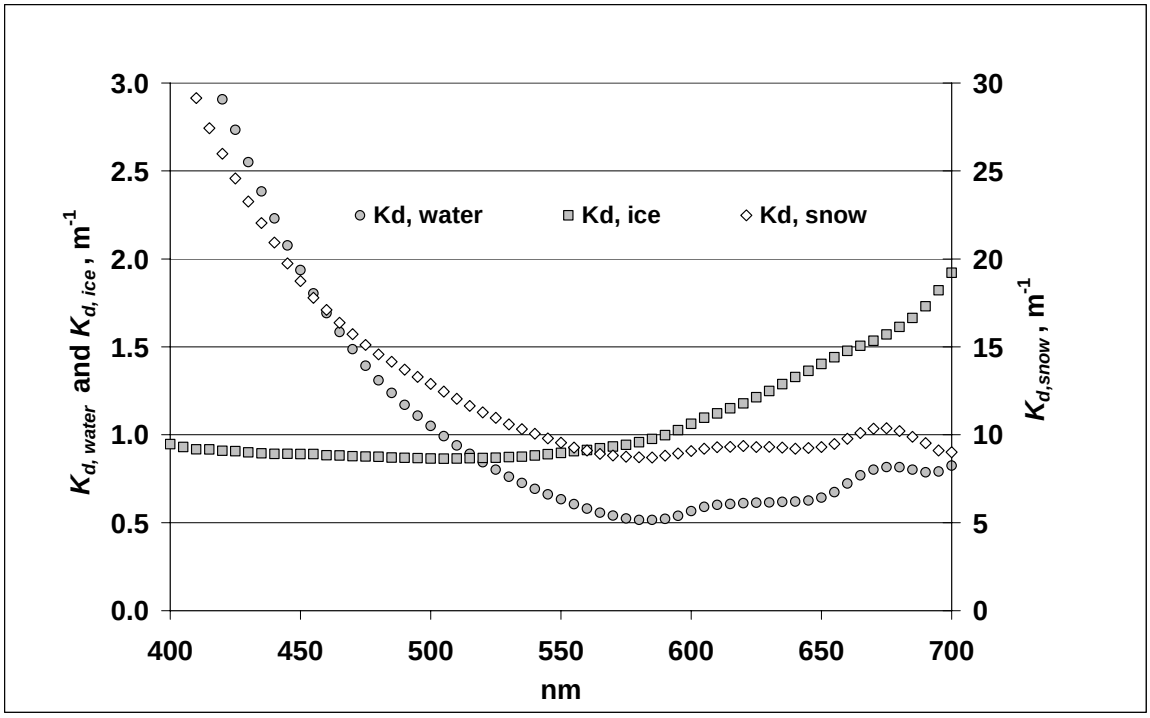

Figure 3. $K_d(\lambda)$ of water, ice and snow of lake Ormajärvi (10 Apr. 2006). The values for snow in the left axis.

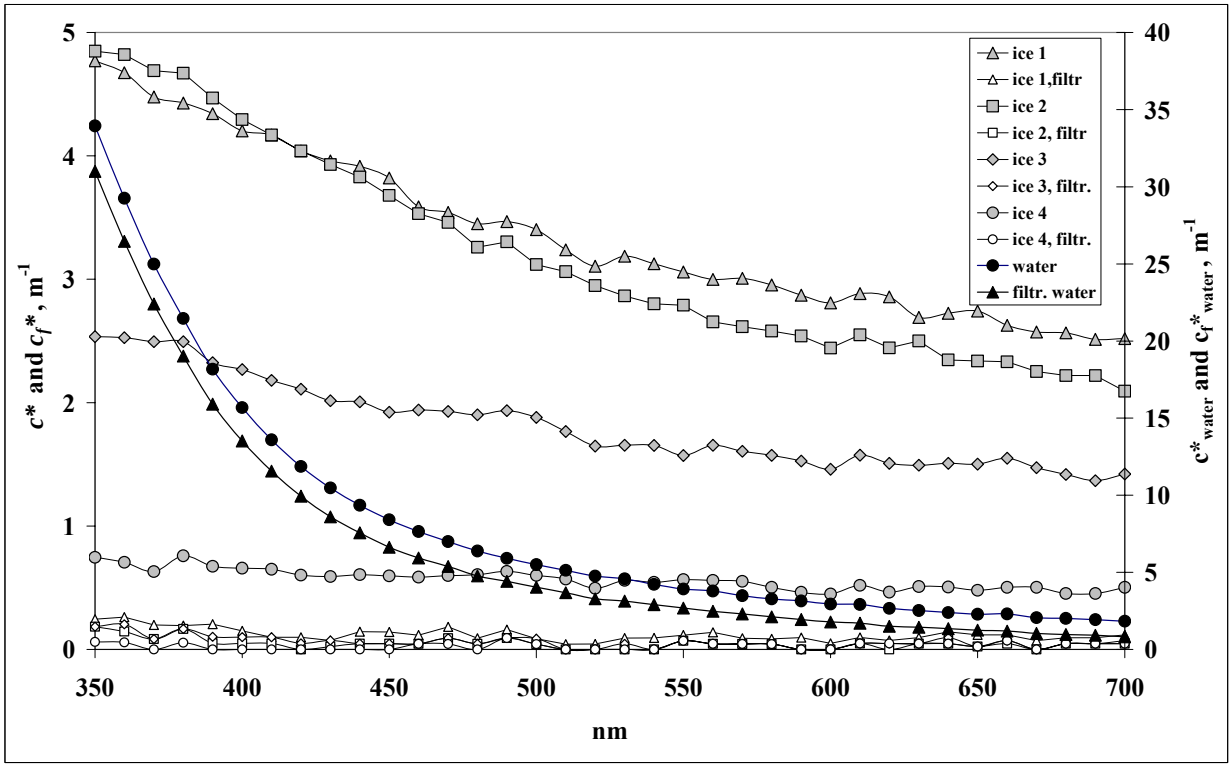

Figure 4. Beam attenuation spectra of the lake Valkeakotinen, 15. Apr. 2004. Ice layers numbered from the top of the ice sheet. Values of the ice meltwater spectra in the right axis and values of the water in the left axis.

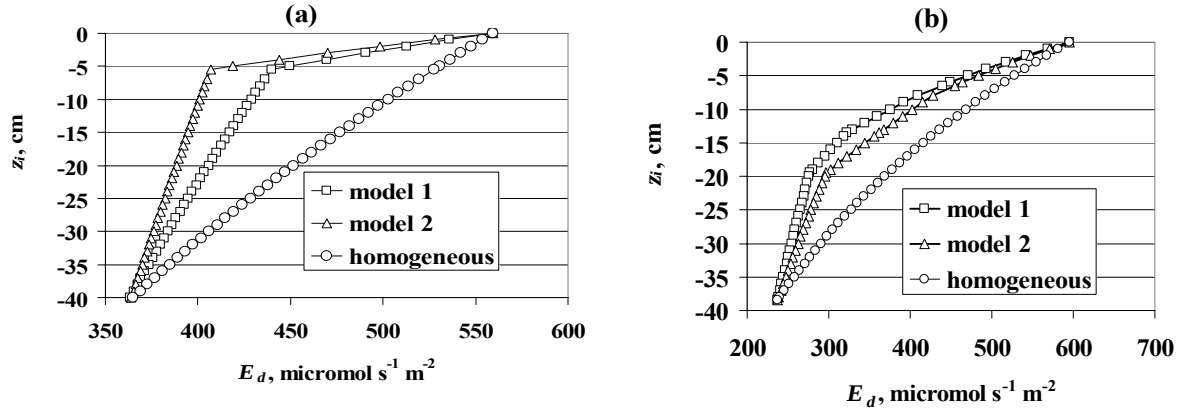

Figure 5. Calculated irradiance profiles in the ice of lake the Lake Võrtsjärv on 24 March 2005 (a) and Lake Valkeakotinen on 15 April 2004 (b).With "homogeneous" profiles constructed by the field irradiance data are designated.

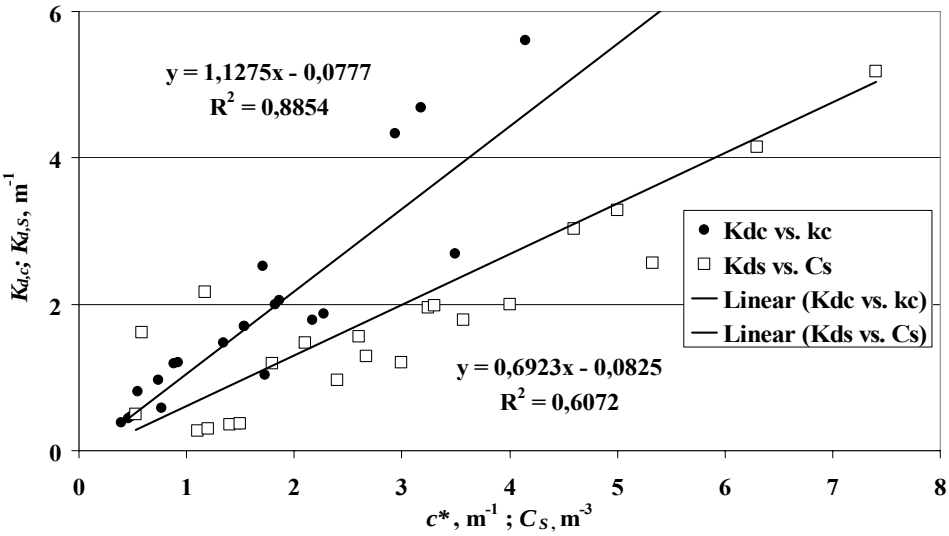

Figure 6. The plots $K_{d,c}$ *(c*)* and $K_{d,s}$ *(C_S)* associating the measured and calculated (by the models) parameters of the ice. Only the values, calculated for the distinctive layers are taken into consideration in the plots. Three layers (ice 1 of the Lake Võrtsjärv and the both layers of the Lake Äntu-Sinijärv) are excluded from the plots.

Special Session: Ice actions on compliant structures

19th IAHR International Symposium on Ice
"Using New Technology to Understand Water-Ice Interaction"
Vancouver, British Columbia, Canada, July 6 to 11, 2008

Ice velocity limit to frequency lock-in vibrations

Mauri Määttänen
Emeritus professor
Helsinki University of Technology
Finland
mauri.maattanen@tkk.fi

Abstract
Scale model tests have proven that at certain ice velocity range the natural mode frequency of the structure can control the ice failure rate while ice is crushing against a vertical structure. Full-scale data indicates the same phenomenon. As this is a resonant type loading the dynamic response of the structure will be severe. In ice load design there is not yet any well established bound for the lock-in vibrations velocity range. The future ISO 19906 Ice load code suggests a conservative upper bound. In this paper data on scale model and full scale measurements, as well as on less accurate in-field observations is assessed. Scale-model data is extrapolated into full-scale by scaling laws. Numerical simulation model results are compared in order to find out the limiting ice velocities. Physical reasoning with parameters that control the possible lock-in vibrations is discussed.

Introduction

Observations and measurements on moving constant thickness ice sheet crushing against the structure have indicated that ice failures often repeat at consistent frequency close to a natural frequency of the structure. This is true both in actual offshore structures and in scale model tests. From the structures point of view this is a resonant type dynamic loading that easily results in severe large amplitude vibrations. The result may be only annoying but can lead to structural fatigue and failure as has been witnessed in first steel lighthouses in the Baltic e.g. Kemi-1 and Kemi-2 in 1974, or in failure of secondary structural components as in Bohai Sea in 2003. In Beaufort Sea the foundation stability of a massive caisson retained structure was threatened, Molikpaq 1986.

Theoretically the response amplitude is limited by the amount of internal damping of the vibration mode in resonance. E.g. if the resonating mode is having 2 % relative damping then the resonant amplitude will be 25 times the amplitude of the same load acting statically. Hence small dynamic loads can cause large vibration amplitudes at resonant frequency.

The structural dynamic response analysis is a straightforward and well defined discipline whenever the load function is known. The Finite Element Method provides good accuracy for the discrete structural model. Also the supporting foundations stiffness and damping properties can be determined with reasonable accuracy. The difficulty in lock-in vibrations is the time dependent ice load function that is not known in advance. Evidently an approach in which the maximum ice crushing load is assumed to be also the dynamic resonant load amplitude will result into over-conservative design.

The nonlinear models of self-excited vibrations can be used in order to find out the ice load and its frequency in crushing. However, the micromechanical models and ice material data that could be used to describe continuous crushing process are far too complicated to be used in numerical integration for self-excited vibration amplitudes. Only greatly simplified models have been realized this far. A robust simplification – ready to be utilized in FE-solution - is to assume a saw tooth like resonant ice force function with amplitude reduced from nominal crushing load. The only remaining difficulty for the user is to judge what is the appropriate reduction factor to the crushing load. This method is adopted also in the forthcoming ISO 19906 Arctic Offshore Structures Ice Load Code.

The measurements have indicated that the amplitude of lock-in vibrations increase together with increasing ice velocity to a certain limit. In this paper we compile the full-scale and model-scale data, and numerical model results in order to bound the limiting velocity. The future ISO 19906 Arctic Offshore Structures ice loads code gives a limit to ice velocity v_t that can cause lock-in vibrations

$$v_t = \gamma_v \, f_n \qquad [1]$$

where $\gamma_v = 0.060$ m and f_n is the natural frequency of the structure. Justification to this equation was presented by Kärnä et. al. (2007) based on an extensive compilation of measurement data. The data suggested a lower value of 0.040 for the coefficient γ_v but a more conservative value was adopted into ISO 19906.

The physical reasoning is that whenever ice velocity is larger than the vibration velocity of the structure at ice action point, the ice failure mode is getting into totally brittle mode and does not allow alternating ductile load build up and brittle ice failure loading cycles. Another limit is the maximum environmentally driven velocity of ice movement at the location of the structure. As the vibration velocity of the structure is directly proportional to the fluctuating ice force, one could expect that also all the parameters that determine the ice force have an influence on the limit velocity. In this paper the applicability of Eq. 1 is assessed with reference to further measurement data and theoretical models.

Full scale data

First reported observations and measurements on frequency lock-in vibrations were from Cook Inlet, Blenkarn, 1970. Ice movement was due to tidal currents up to 2 m/s and ice thickness typically from 10 to 60 cm with a possibility of rafted thicker ice. Ice failures repeated at about 1 Hz that was also the lowest natural frequency of the platform. No specific data was given on the dependence of vibrations in relation to tidal current driven ice velocity. The deck displacements during the vibrations were up to 50 mm. If one assumes 10 mm (20 %) modal amplitude at the ice action point, its vibration velocity would be about 60 mm/s. The ISO 19906 velocity limit at 1 Hz would be 60 mm/s. Hence at the maximum tidal driven ice velocity of 2 m/s no lock-in vibrations should not have been present. Indeed, this was true also during the measurements. From the extensive original data it would be valuable to find out the real limit velocity.

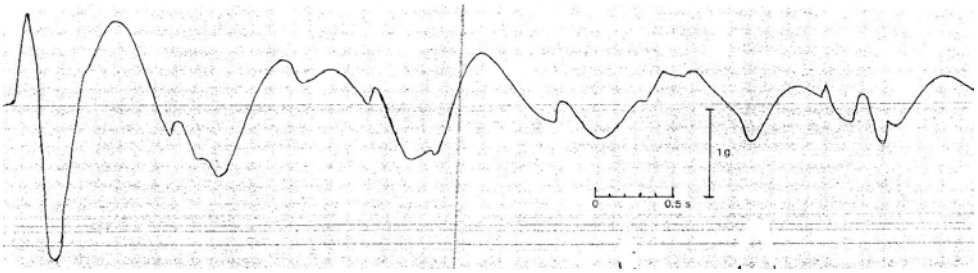

Figure 1. Kemi-1 Steel lighthouse +1 m above MSL acceleration 1973-12-21. Resulting displacement response was in the first mode at 0.85 Hz.

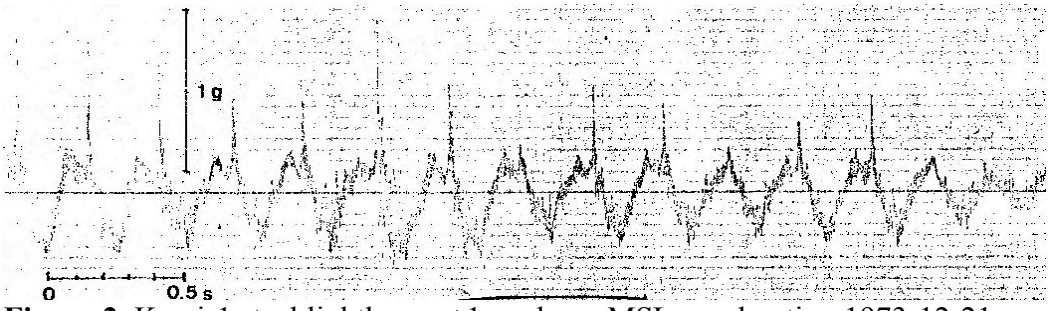

Figure 2. Kemi-1 steel lighthouse +1 m above MSL acceleration 1973-12-21. Resulting displacement response was in the second mode at 3.8 Hz.

The first steel lighthouse Kemi-1 suffered from severe ice-induced vibrations, Määttänen 1974. In December 1973 two different scenarios were measured. With 0.55 m thick ice the first natural

mode was excited at 0.83 - 0.85 Hz, Fig. 1, and with thin 0.10 m thick ice the second mode at 3.8 Hz was prevailing, Fig. 2. In both cases ice velocity was the same, about 55 - 85 mm/s. Later in the winter 1973/74 the superstructure was destroyed due to severe vibrations. Considering the continuous second mode acceleration amplitude 0.3 g at 3.85 Hz results in 125 mm/s velocity amplitude that is almost double to the measured ice velocity. The ISO 19906 velocity limit from Eq. 1 is conservative 230 mm/s.

The concrete caisson lighthouse Kemi-1 – replacing the destroyed steel lighthouse - was massive and stiff with lowest natural frequency at 3.1 Hz, Määttänen 1977. Frequency lock-in vibrations were rare. Only in some instances continuous vibrations were measured by telemetry system while the ice thickness was estimated to be 60 – 70 cm. The only information on ice velocity is the comparison to the ten years later measured typically below 200 mm/s maximum ice velocities in the same location at the same ice thickness range. Due to high stiffness the lock-in vibration velocity amplitude remained small, lower than 100 mm/s. This is well below the ISO 19906 limit velocity 185 mm/s from Eq. 1.

The Swedish lighthouse Norströmsgrund in the Gulf of Bothnia has experienced significant ice-induced vibrations at 2.3 Hz, Engelbrektson 1997. Analysis on lock-in vibrations has shown that during the fully developed steady state vibrations the vibration velocity amplitude has been slightly below the ice moving velocity. However, resonance could occur also at other ice velocities. The ISO 19906 limit velocity for the Norströmsgrund would be 140 mm/s. Even though the dimensions and dynamic properties of the structure, as well as ice conditions, are close to those of Kemi-1 the latter has been less prone to lock-in vibrations. In both locations the thin ice maximum ice drifting speed in up to 0.5 m/s is postulated. Due to missing high velocity data a question remains if the ISO 19906 velocity limit is conservative or not.

In Finland over 100 offshore channel edge markers have been constructed within last 20 years. These structures are slender steel cylinders with underwater diameter from 3 to 4 m, and the above water structure diameter 0.8 m. Water depth varies from 4 to 16 m and superstructure top is typically at 12 m height. The lowest natural frequencies are at the range from 3 to 6 Hz. All these structures are sensitive to ice induced vibrations and exhibit continuous frequency lock-in vibrations. Therefore the lantern and battery pack with solar cells have been isolated from ice induced vibrations, Fig. 1. The temporary data logger with its own batteries for acceleration measurements is isolated in a swing. Telemetry or automatic data logging measurement on superstructure accelerations have been conducted in six different locations, Kärnä et.al 1989, Määttänen 2003 The pitfall in measurements was that true data on ice thickness or velocity was not available. However, ice thickness could be extrapolated roughly based on data from nearby monitoring stations. Due to missing tidal currents the maximum ice velocity is bounded typically to less than 2 % from the prevailing winds.

Figure 3. A modern channel edge marker superstructure.

Fig. 4 gives samples on measured accelerations in Hanko-1 channel

edge marker. Frequency lock-in vibrations persist for long times close to the calculated lowest natural frequency at 4.3 Hz. Ice thickness was from 15 to 40 cm. Maximum winds during the measurement season were below 20 m/s that bounds the maximum ice moving velocity below 400 mm/s. Observing the shape of the first natural mode the amplitude at waterline is 16 % from the top. Hence the maximum measured displacement amplitudes 67 mm corresponds to 290 mm/s structural vibration velocity amplitude at waterline. ISO 19906, Eq. 1, gives the limit ice velocity to 260 mm/s. This is below the measured value. However, most of the vibration measurement displacement amplitude data fell to or below 42 mm corresponding to 182 mm/s vibration velocity amplitude. Similar data as in Hanko-1 has been measured also in other locations along Finnish coast, Kärnä et.al.1989.

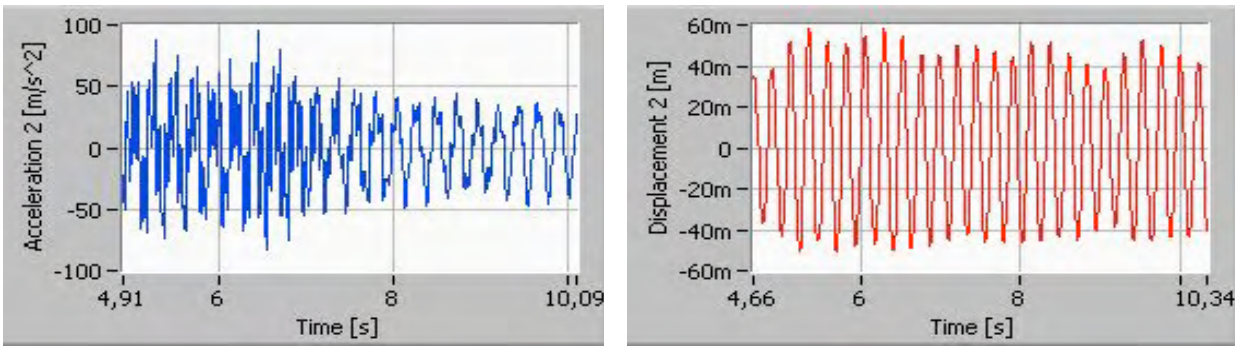

Figure 4. Hanko-1 acceleration and displacement y-component response Feb. 26, 2003. Combined x+y resultants were: max 95 m/s^2 and 67 mm at 4.6 Hz

A vibration isolated lighthouse is an exception in reference to lock-in vibrations. Extensive telemetry measurements in Kemi-2 lighthouse never recorded lock-in vibrations in the dynamically stable superstructure natural modes at 0.32 and 0.93 Hz, Määttänen 1987. Even when ice failures repeated close to the natural frequencies the lock-in state was never established. As expected, the dynamically unstable foundation natural mode at 7.6 Hz experienced lock-in vibrations.

Molikpaq is another exception because generally lock-in vibrations are considered to be a problem for slender and flexible structures, Jeffries et. al. 1988. Molikpaq is a caisson retained island, shallow, 111 - 89 m diameter hexagon, about 30 m tall, stiff and massive structure. However it has experienced severe lock-in vibrations. The mode in question has been the caisson ring ovaling combined with core sand shearing. As the lock-in vibrations are controlled by a natural mode, the mode attracts the otherwise unsynchronized local ice failures to synchronize at the global (modal) deformation rate. Even though ISO 19906 speed limit is not intended for shallow structures, the calculated limit 78 - 90 mm, based on Molikpaq reported frequency of 1.3 – 1.5 Hz, falls close to the range of actual ice movement rate at 60 mm/s. However, if calculated from the measured 0.11 g acceleration the vibration velocity would be over 135 mm/s.

Laboratory tests

Scale-model tests 1979 in CRREL, Määttänen 1983, proved the linear increase of vibration amplitude with ice velocity, resonant peak, and limit velocity when the lock-in vibrations stopped. The model structure had variable stiffness mass and damping, During the tests in Fig. 5 the structural properties were kept unchanged with the lowest natural frequency at 8.5 Hz. Only

pile diameter at waterline, and ice thickness was varied, Table 1. The ice velocity was increased so slowly from 0 to 100 mm/s that vibration amplitudes had time enough to develop into fully developed limit cycles corresponding to each velocity. The resulting vibration amplitude was increasing with velocity. The steady state frequency-lock-in vibrations started at certain velocity after which almost linear dependence on amplitude on velocity prevails, Fig. 5a. The same is true also in other tests Fig. 5b. However, in two tests 49 and 50 the curve peaks and amplitude reduces. Before the maximum velocity of 100 mm/s the lock-in vibration disappears; the limit velocity has been reached. The main difference was ice thickness, cf. tests 37 and 38 to 49 and 50 in Table 1. Evidently the thin ice could not feed enough energy to the structure to overcome the energy dissipation in internal damping with increasing vibration amplitudes. Also the change in diameter manifests the same energy balance: wider structure causes higher loads and more energy input. In other tests 37 – 48 and 51 it would have needed a faster than 100 mm/s ice velocity to reach the "resonance peak" and the disappearance of the lock-in vibrations.

Considering scaling to full-scale the vibration velocity is proportional to ice strength ratio. In CRREL tests the urea ice crushing strength in tests 49 to 51 was 1.4 – 1.5 MPa, e.g. about half of the full-scale ice crushing strength. The velocity limit 90 mm/s in tests would correspond to 180 mm/s full-scale ice velocity. The natural frequency depends inversely to the used scale ratio 1:10 in laboratory tests. Hence the ISO 19906 speed limit in full-scale would be un-conservative, only 50 mm/s.

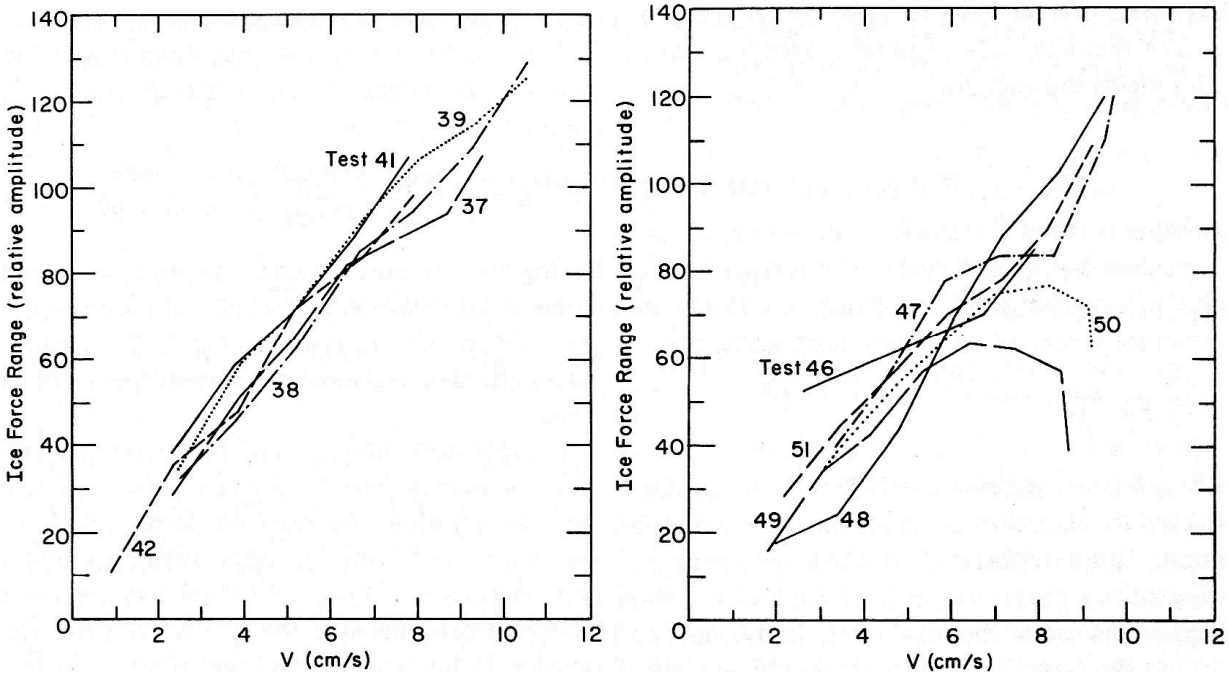

Figure 5. Continuous lock-in vibration amplitude vs. ice velocity
a) Tests 37-42, b) Tests 47 - 51

Table 1. Varied test parameters in Fig. 5 (Ice thickness h and pile diameter D in mm)

Test	37	38	39	41	42	46	47	48	49	50	51
h	50	51	52	53	53	79	79	82	22	21	20
D	64	102	178	178	102	178	178	64	64	102	178

Japanese conducted 1980-82 scale-model tests in Saroma lagoon and observed the linear vibration amplitude vs. ice velocity dependence, Toyama et. al. 1983. In tests the maximum velocity was only 48 mm/s that was too low to reach to the limiting velocity range. However, comparing the test data with a numerical model they concluded that there exists a velocity beyond which the self-excited vibration disappears. Another important finding was that limit velocity is decreasing with increasing structural damping.

A series of ice-induced scale-model tests were conducted in NRC ice tank with PG-model ice, Izumiyama et. al, 1994. The ice velocity was up to 500 mm/s and ice thickness from 20 to 40 mm. The stiffness and the natural frequency of the structure were kept constant. The response data indicates linear dependence between the structures response velocity and ice velocity. A good fit together with data from other sources was presented as

$$U = \beta V \qquad [2]$$

with $\beta = 1.0 \ldots 1.4$. At velocities above 130 … 200 mm/s the response turned into random with much lower velocity amplitudes. They observed that the limiting transition velocity was dependent on crushing load.

Another Japanese test series in ice tank with PG model ice, Izumiyama 1997, indicated the same findings. As the carriage velocity reached up to 500 mm/s, the decay of lock-in vibrations was measured and the data could be divided into steady state vibrations and into more or less random low amplitude response. The change over took place at $S_I = 0.1$ value of the Strouhal number S_I that was defined as

$$S_I = \frac{f_n}{f} = \frac{f_n F_C}{KV} \qquad [3]$$

where f is the frequency of response vibration, f_n the natural frequency and K the stiffness of the structure, F_C is the maximum crushing load, and V the ice velocity. (Normally the Strouhal number is related to von Karman vortex shedding frequency in flow induced structural vibrations and is defined as this frequency times diameter divided by flow velocity). The measurement data was not consistent to all parameters, e.g. with increasing ice thickness the critical velocity should also increase but the thinnest ice gives the smallest $S_I = 0.05$ that corresponds to largest change-over velocity. This was explained to be due to natural variation, or due to difficulties in dealing with thin ice.

Using the limiting measured $S_I = 0.05 \ldots 0.1$ the limit velocity can be solved simply

$$V_c = \frac{f_n \cdot F_C}{S_I \cdot K} = \frac{f_n \cdot \delta_{stat}}{S_I} \qquad [4]$$

The static deflection δ_{stat} takes into account crushing load F_C, ice strength and thickness, pile diameter and aspect ratio effect in relation to structural stiffness. This definition explains the effect of ice thickness and pile diameter in CRELL tests, and natural frequency in Japanese tests.

With a stiffer structure the limit of lock-in vibrations is met at lower ice velocity. This was also verified in scale-model tests by Yan et. al. (2007).

In laboratory tests with fresh water ice it is easy to have continuous ice-induced vibrations to persist at wide velocity range. However, the saline model ice close to the freezing point – as customary during scale model tests – is often so mushy that it is hard or even impossible to excite structure into continuous vibrations. E.g. this author has experienced this in scale model tests in WARC and HSVA basins. Wu et. al. 1976, have also measured the softening ice behaviour in uni-axial ice compressive tests with increasing ice temperature. These observations agree with the theoretical models that are based on decreasing ice strength with increasing loading rate at transition from ductile to brittle ice failure.

Numerical model prediction

The present understanding is that ice-induced lock-in vibrations are a result of a self excited process. The majority of researchers couple the structural response velocity effect on the ice load via ice strength dependence on loading rate, Blenkarn 1970, Määttänen 1977 and 1998, Toyama et. al. 1983, Xu et. al. 1988, Kärnä 1990, Vershinin 1990. With such models it is possible to numerically simulate lock-in vibrations and to predict also the limit velocity. The numerical process cannot produce any more resonant type vibrations if ice velocity results in completely brittle ice failure mode during most of the vibration cycle.

Toyama et. al. 1983 presented a simple one degree of freedom model that defined the ice force during the load build-up phase to be linearly dependent both on indentation distance and on ice velocity. At crushing phase the ice load was kept constant and smaller than maximum elastic ice load. The model predicted the maximum displacement amplitude to be the sum of static maximum ice load displacement and ice velocity divided by natural angular velocity. The linear dependence to velocity was predicted correctly as well as a limit velocity beyond which self-excited vibrations disappeared.

Määttänen 1998 presented a multi-degree of freedom ice-induced vibration model to predict the frequency lock-in and synchronization of ice failures at different locations of the ice action contact zone. This was demonstrated both for a wide – Molikpaq like - structure and a multi-legged jacket platform structure. The model predicts the velocity range where lock-in vibrations persist, starting velocity, the linear increase with ice velocity, and the limit where ice crushing

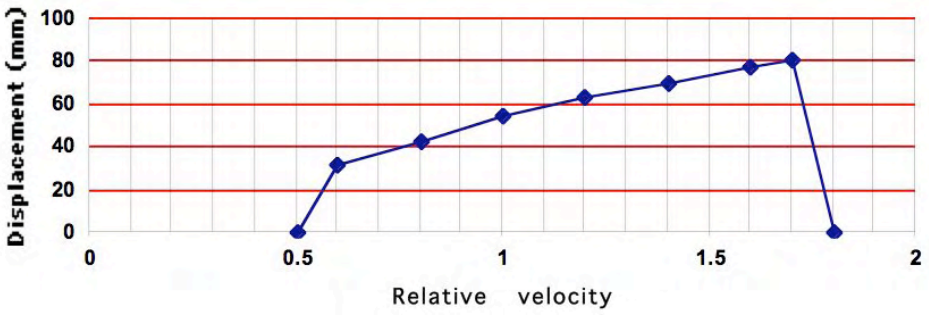

Figure 6. Numerically predicted caisson retained island lock-in vibration displacement amplitude dependence on ice velocity.

failure turns into completely brittle and vibrations disappear (if no randomness in ice properties is observed), Fig. 6. Here relative velocity $v_r = 1$ corresponds to the point that gives the steepest descent rate in the ice crushing strength dependence on stress rate. $v_r = .5$ is at the maximum ice strength, and $v_r = 1.4$ corresponds to velocity where random, in average constant, brittle crushing starts. Hence the lock-in vibrations can persist with nominal ice velocity completely at brittle range if during the vibration cycle the real contact velocity – ice velocity minus vibration velocity – brings ice failure mode to the transition zone from ductile to brittle.

The generic jacket platform was much more sensitive to ice induced vibrations than the caisson retained island. Lock-in was possible with different natural modes, and ice failure synchronization with different legs occurred always. Velocity dependence indicated the same features as in Fig. 6, initiation, linear amplitude increase, and disappearance. This was also similar to results of numerical models on Finnish steel aids-to-navigation structures and their real measurement results.

Yin et. al. (1998) present an analytical lock-in vibration model for a four legged platform. The model predicts lock-in and synchronization to natural frequencies of the structure, as well as jump from one natural mode to another. The results are in agreement with real observations of the North China Sea platform SP62C. The initiation of vibrations started at 100 mm/s ice velocity and had a maximum at 150 mm/s. At 500 mm/s the vibration amplitude dropped significantly. The paper does not give enough data on how the application example scale-ratio in the analytical model corresponds to full scale in order to now compare to ISO 19906 limit velocity prediction.

Physical explanation

Continuous lock-in vibrations during ice crushing include an energy balance process. Moving ice is the source of energy while breaking ice and structural damping are dissipating energy. If energy input and dissipation are equal steady state limit-cycle vibrations prevail.

The details of the energy input and dissipation are not too well understood. While ice edge is pushing the structure, the structure deflects, and energy from ice load is turned into elastic and kinetic energy in the structure. A part of oncoming ice energy is dissipated directly in local plastic deformations at the ice edge contact and in micro-crack formation in ice. After maximum load, as ice starts to crush, a lot of energy is dissipated in the crushing – into ice surface energy and plastic deformation. Most of the stored elastic energy and a part of kinetic energy of the structure are dissipated into ice crushing. Structural damping dissipates a small amount of energy as well. Some energy interchange occurs also in the oncoming ice sheet itself. It stores elastic and kinetic energy and releases them during the crushing phase.

If structure is at rest the initial energy input from ice into the structure will be more than dissipation. If conditions are right a natural mode starts to control structural movements and occurrence of ice crushing. Then vibration amplitudes start to increase which increases the energy losses both to crushing and to damping. However, the energy input does not increase at same rate as dissipation with increasing vibration amplitudes. So after a while a balance is achieved: the energy input is equal to energy dissipation during each crushing cycle. The state of vibrations can be described as a stable limit cycle.

One can easily imagine what happens in the case of slow ice movements. The structure deflects under ice action, ice load increases until ice fails, and the stored elastic energy is dissipated. The structure will again be in rest when a new contact of ice edge occurs and new cycle starts. This is the state of intermittent relaxation oscillations. In other extreme if ice is moving fast, ice loading will be completely brittle that yields into continuous brittle crushing with only random variations in ice loads, random energy interchange, and random dynamic response.

Sodhi 2001, has measured and described alternating ductile load build-up and brittle crushing vibrations. The data clearly shows the effect of the structural vibration velocity that changes the ice failure mode. The decrease of ice load during crushing is due to ice strength dependence on loading rate. The spring-back rate of the structure increases loading rate while crushing occurs. Even though the strength vs. stress rate curve is random at transition from ductile to brittle, the structure feels it as an average. This is because the structural damping is low and it needs tens of cycles to develop into limit cycles. So the random transition zone is averaged in the structural response due to summing. Hence the decreasing part of the ice compressive strength vs. stress or strain rate can also be described as an average negative damping effect.

The phases of ductile load build-up and brittle crushing bring with the ice mechanical properties dependence on grain size, salinity and temperature to the onset and disappearance of lock-in vibrations. Cold fresh water ice is more likely to break in brittle mode than warm saline ice. This has been observed in scale model tests and in full-scale.

Conclusions

Both scale model tests and full-scale measurements on ice crushing have proven the existence of resonant ice-induced lock-in vibrations close to the frequency of a natural mode of the structure. The onset of vibrations occurs after a minimum ice velocity. Above a limit ice velocity the lock-in breaks and only random structural response occurs while ice failure occurs in completely brittle mode. Between minimum and limit velocities vibration amplitude increases proportional to ice velocity.

In scale-model tests the measurement of limit velocity is straightforward provided that the carriage is capable to sufficiently high driving speed. The problem is how to scale-up from the model scale to full-scale. Even though the structural dynamics is well understood, the scaling of ice properties is not. Especially the data on ice strength versus loading rate at different scales is missing.

Full-scale data is scarce and only seldom ice velocity has been high enough to exceed the limit for lock-in vibrations. Many data sets have been measured by a telemetry system. While dynamic structural response can be easily measured and interpreted, there is very little or inaccurate information on ice conditions, thickness and velocity.

Theoretical models simulating lock-in vibrations can predict the onset and limit ice velocity. Most uncertainty is in the ice strength dependence on loading rate that is used to couple together the structural response and ice crushing failure.

The future ISO 19906 ice load code presents a simple equation to the limit velocity for lock-in vibrations. The only parameter is the natural frequency of the structure. Theoretical models and scale model tests indicate that the magnitude of ice force and the stiffness of the structure have also an effect. Measurement data can only be interpreted by observing ice thickness, strength, and the stiffness and the diameter of the structure at waterline.

The findings in this paper suggest that the limit velocity for the ice-induced lock-in vibrations is proportional to the product of natural frequency of the structure and the static deflection due to the excitation ice force. In cases when the natural frequency is high and static deflection large, the ISO limit can be un-conservative. However, comparisons to the simple ISO 19906 velocity limit appear to be conservative in most cases.

References

Blenkarn K. A. (1970): Measurement and analysis of ice forces on Cook Inlet structures. Proc. 2nd Offshore Technology Conference, Houston, TX, OTC 1261, Vol. II, pp. 365-378.

Engelbrektson A.: A refined Ice/structure interaction model based on observations in the Gulf of Bothnia. Proc. ASME OMAE-1997, Vol. IV, pp.373- 376.

Engelbrektson A. (1983): Observations on a Resonance Vibrating Lighthouse Structure in Moving Ice. Proc. POAC 1983, Helsinki, Finland, Vol. II, pp. 855-864.

Huang Y., Shi Q., and Song A. (2007): The interaction between ice and Compliant vertical pile. Proc. POAC-07, Vol. I, pp. 142-152, Dalian, China.

Izumiyama K., Irani M.B., and Timco G. (1994): Influence of compliance of structure on ice load. Proc. IAHR Symposium on Ice 1994, Vol. I, pp. 223-236.

Izumiyama K., and Uto S. (1997): Ice loading on a compliant indentor. Proc. ASME OMAE 1997, Vol.4, pp. 431-436.

Jin D.P., and Hu H.Y. (1998): Ice-induced non-linear vibration of an offshore platform. *Journal of Sound and Vibration*. **214**(3), 431-442.

Jeffries M., and Wright W. (1988): Dynamic response of "Molikpaq" to ice-structure interaction. Proc. ASME OMAE-88, Vol. IV, pp. 201-220. ASME. Houston, USA.

Kärnä,T. and Turunen R. (1989). Dynamic response of narrow structures to ice crushing. *Cold Regions Science and Technology* **17**(1989) pp. 173-187.

Kärnä,T. and Turunen R. (1990). A straightforward technique for analysing structural response to dynamic action. Proc. 9th ASME OMAE 1990, pp. 135- 142.

Kärnä, T., Kamesaki, K. and Tsukuda, H., (1999). A numerical model for dynamic ice-structure interaction. Computers and Structures **72**(1999) 645-658.

Kärnä T., Izumiyama K., Yue Q., Qu Y., Guo F., and Xu N. (2007): An upper bound model for self-excited vibrations. Proc. POAC-07, Vol. I, pp. 177-189.

Määttänen M. (1974): Tutkimus Perämeren teräsrakenteisten majakoiden ja reunamerkkien värähtelyistä, vaurioiden syistä ja rakenteellisesta lujuudesta. (Assesment on the vibrations, damage and structural strength of the Gulf of Bothnia steel aids-to-navigation, in Finnish). University of Oulu/Finnish Board of Navigation, Internal Report, Oulu 1974-01-17.

Määttänen M. (1977): Ice Force Measurements at the Gulf of Bothnia by the Instrumented Kemi-1 Lighthouse. Proc. POAC-1977, Vol. II, pp. 730-740.

Määttänen M. (1983): Dynamic ice structure interaction during continuous crushing. U. S Army Cold Regions Research and Engineering Laboratory, Hanover, NH, USA 03755, CRREL Report 83-5, 53 p.

Määttänen M . (1987): Ten years of ice-induced vibration isolation in lighthouses. Proc. 6th ASME OMAE, Vol. IV, pp. 261-266.

Määttänen M. (1998): Numerical model for ice-induced vibration load lock-in and synchronization. Proc. IAHR Symposium on Ice 1998, Vol. 2, pp. 923-930.

Määttänen M.: Hanko-1 reunamerkin värähtelymittaukset talvella 2003 (Channel edge marker Hanko-1 vibration measurements during winter 2003, in Finnish). Helsinki University of Technology, Laboratory for Mechanics of Materials, Internal Report, Espoo 22.12.2003.

Sodhi D. (2001): Crushing failure during ice-structure interaction. *Engineering Fracture Mechanics*. **68**(2001) 1889-1921

Toyama Y., Sensu T., Minami M. and Yashima N. (1983): Model tests on ice-induced self-excited vibration of cylindrical structures. Proc. 7th POAC 1983, Helsinki, Finland, Vol. II, pp. 834-844.

Vershinin S, and Iliady A. (1990): A new approach to dynamic ice-flexible structure interaction analysis. Proc IAHR Symposium on Ice 1990, Vol. III, pp. 73-80.

Wu. H.C, Chang. K.J, and Schwarz J. (1976): Fracture in the compression of columnar grained ice. *Engineering Fracture Mechanics*, **8**(1976), pp. 365-372.

Xu J. and Wang L. (1988): Ice force oscillator model and its numerical solutions. Proc. ASME OMAE-88, Vol. IV, pp. 171-176.

Yan H., Shi Q., and Song.a (2007): The interaction between ice and a compliant vertical pile. Proc. POAC-07, Vol. 1, pp. 142-153.

Yue, Q. and Bi, X. (2000). Ice-induced jacket structure vibrations in Bohai Sea. *Journal of Cold Regions Science and Engineering*. **14**(2). pp. 81-92.

Yue Q., Bi X., Li F. and Qu Y. (2006): Full-Scale Tests of Dynamic Ice Force in Bohai Bay, Proc. IAHR Symposium on Ice 2006, Vol. 2, pp 139-146.

19th IAHR International Symposium on Ice
"Using New Technology to Understand Water-Ice Interaction"
Vancouver, British Columbia, Canada, July 6 to 11, 2008

Risk analysis of jacket platforms under ice induced vibrations

Dayong Zhang, Qianjin Yue, Baolin Tong

(State Key Laboratory of Structural Analysis of Industrial Equipment,
Dalian University of Technology, Dalian 116023, China)
Dalian University of Technology (DUT)
Linggong Str. 2. Dalian China
zhangdayong_2001@163.com

Abstract: Since the late 1980's, several jacket offshore oil platforms were constructed in the northern part of China's Bohai Sea, where sea water freezes every winter. These platforms were primarily designed to withstand an extreme static ice force. However, the observations on these platforms disclosed that intensive vibrations could be induced by sea ice. Based on monitoring data and structure analysis, the risk and failure modes of ice resist jacket structure are discussed in present paper. The results of the studies lead to the conclusion that jacket structures which only considered the extreme ice force exist potential risks posed by dynamic ice forces.

Key word: ice-resistant structure; ice-induced vibration; failure modes

1. Introduction

It has been known that offshore oil platforms designed in ice infested areas need to withstand not only maximum ice forces, but also dynamic ice forces, which may result in structure vibrations. The phenomenon of ice-induced structure vibrations has been noticed and studied since the early 1960s (Peyton 1968). In the 1970s, lighthouses in the Gulf of Bothnia encountered ice-induced vibrations and one of them collapsed (Engelbrekston, 1977). Further, in the 1980's, the sand base of the caisson structured, named Moligpac and located in the Beaufort Sea, was liquated because

of ice-induced vibrations (Wright and Timco, 1994). Since the late 1980's, ice-induced vibrations was noticed after the first platform was established in Bohai Sea (Yue and Bi, 2001).

Normally, there are two types of steel offshore structures designed to resist ice forces. The first are classed as caisson structures, which are rigid and have a strong ability to withstand extreme ice force and dynamic ice force. The second type is termed as jacket structure, which is more economic advantage as it used less steel in the same depth of water but could be more flexible and easily to be induced vibrations by ice sheet. At present, the design and construction of jacket platforms has been mainly focused in the area of the Cook Inlet and the Bohai Sea and they all met the problems of ice induced vibrations.

The main reason why current design codes for offshore structures deal mainly with enduring an extreme force is that the interactions of ice-structure is very complicated as dynamic ice force is formed during failure process of ice sheet which hardly to simulate this process. The practical dynamic ice force model has not well developed.

The challenging for oil exploitation in Bohai Sea is that it mainly consists of marginal oil field but with relative severe ice condition, so that it has to design economic ice-resist oil platform. The design of oil platform in this area could be divided into three periods. First generation of platform was constructed in early of 1960's, of which did not consider the ice loading. Two of them were pushed over. After that the ice load and ice parameters were overestimated, which caused that some structures were too conservative designed and that influenced the profit of the oil field adversely. Since the middle of the 1980's, large scale ice conditions survey and international cooperation on studies of ice load where carried out. It is now believed that more rational structures were designed based on API RECOMMENDED PRACTICE in the Bohai Sea. But observations on later constructed platforms over the past several winters have shown that strong ice-induced vibrations have evoked some accidents during the drilling operation.

The jacket platforms have been undergoing design improvements since the late 1980s, and further modifications are expected to continue as a greater understanding of the ice-structure interaction is developed. Presently, jacket structures are effectively used in Cook Inlet, where environmental factors such as water depth and ice loads are similar to the conditions in the Bohai Bay. However, unlike Cook Inlet, where large concentrated oil reserves are located, the Bohai Bay is a marginal oil field with jacket structures using 1/5 to 1/3 as much steel. Further, the stiffness of jacket platforms in the Bohai bay results in a frequency of roughly 1Hz, which is only half of that employed for the platforms in the Cook Inlet. The project of full-scale tests in the Bohai Sea concluded that newly designed structures could withstand the static ice force preventing being pushed over, but the structures would be more slender. Thus, they may be too frail to resist the kind of cyclical forces they would encounter during winter periods. Under strong vibrations, some accidents that endanger both structural safety and crew member health would likely be induced. Relatively, jacket structures are so strong that ice-induced vibration in Cook Inlet is not significant.

In the present paper, based on the field monitoring information of oil platforms in the Bohai Gulf, the dynamic behavior of ice resistant jacket structures and potential failure modes provoked by ice induced vibrations are discussed. The results show that ice-induced vibrations not only cause significant cyclical stress of tube nodes, but also a great acceleratory response of the platform deck. This acceleration is sufficiently high to endanger the pipeline systems on the platform, and it is a recurring cause of discomfort to the crew members.

2. Field observations on the platforms

After the drilling platforms at the JZ20-2 and JZ9-3 oil field were put into operation in the beginning of the 1990's, some of the platforms were instrumented for continuous measurements of ice induced-vibrations. It is part of the Sea Ice Management project funded by China National Oil Bohai Company. The objective of the project is to evaluate how the sea ice affects oil platforms. Figure 1 shows the set-up of JZ20-2MUQ and MNW. In the observation, dynamic

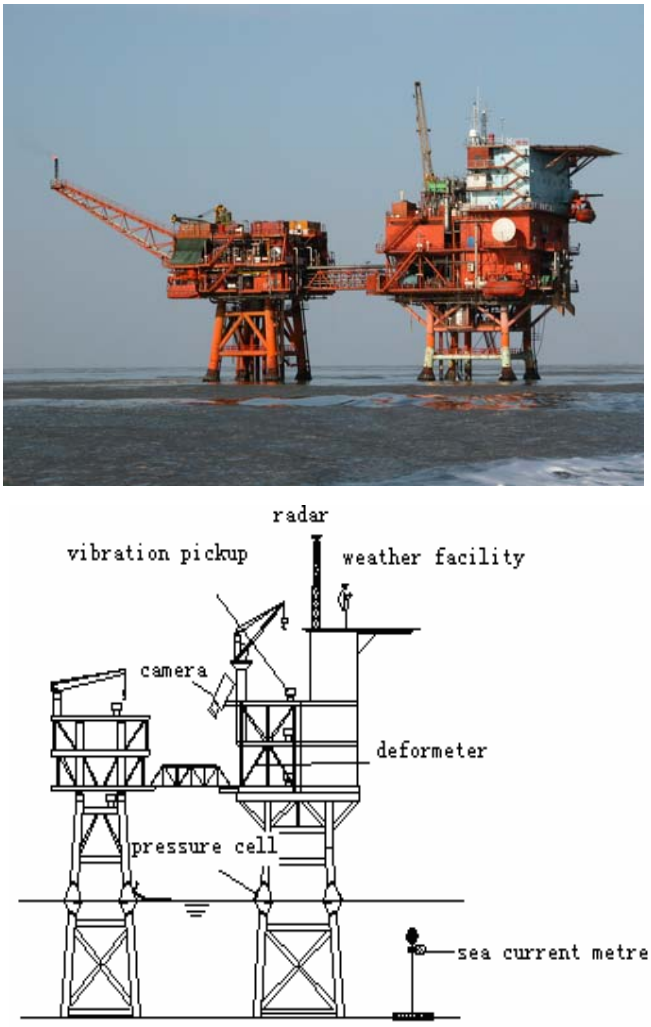

Figure 1. JZ20-2MUQ & MNW platform and sketch of the measurement system on the platforms

response of the platform is measured by several accelerometers placed on decks of different elevations. Ice forces are recorded using ice force panels designed by Dalian University of Technology. The detailed arrangements of the full-scale observation have described by Yue and Bi (1998, 2000). The observation data will not only be useful for dynamic analysis of the Bohai Sea structures but also for those flexible structures in other areas.

The problems of ice-induced vibration of vertical structures are much more complex than those of conical structures, because the crushing process of ice is still not well understood. The maximum vibrations appear in the steady-state vibrations, which have been measured on some vertical platforms in Bohai Bay. The occurrence times are more than twenty in a winter based on response measurement. And the longest time it could last is over 15 minutes. The accelerations of it may reach to 0.6m/s^2 (see Figure 2). The dynamic ice load on the upward facing cone like pulse functions. Yue and Bi (1998), based on full-scale test, developed a load function of ice acting on an upward cone. The period of ice force is relative to the breaking length and ice speed. At high speeds, the significant ice-induced vibration will be evoked (see Figure 3). The maximum acceleration response of deck could be up to 0.8m/s^2.

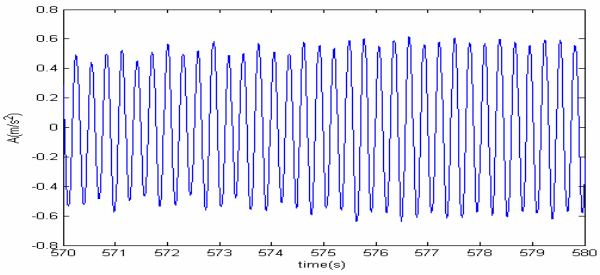

Figure 2. Steady state vibration caused by ice crushing failure

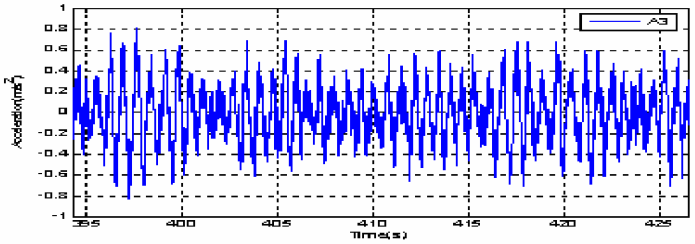

Figure 3. Significant ice-induced vibration of conical structures

3. Cyclical strain analysis of tube nodes under dynamic ice loads

To verify the possibility of structural fatigue failure under ice vibrations, as the difficulty of strain measuring under sea water, one needs to estimate whether the cyclical stress of a hot-spot is greater than the fatigue limit stress. Fatigue damage of the platform is induced by cyclical stress of the tube node. With the typical deck vibration response and finite element model of platform, the writers analyze fatigue stress by ANSYS software, as shown in Fig.4. Here the monitoring data of structural vibrations under typical ice conditions is chosen to validate the significance of the cyclic stress.

According to the type of node and the structural parameters, The SCF (Stress Concentration Factors) of the node is considered consulting the criterion promulgated by DNV (2001). On the other side, according to the *S-N* curve of steel provided by API 2A (1991), shown in Figure 5,

the fatigue limit stress is about 41MPa when limit fatigue life $N = 10^8$. As shown in Figure 4, the cyclical stress amplitudes of the structure induced by typical ice condition are 16 times greater than the fatigue limit stress amplitude in 60 seconds considering the SCF of the node. So the cyclical stress induced by ice forces will cause fatigue damage. Therefore, it is safe to come to the conclusion that the cyclical stress is great enough to evoke fatigue damage and fatigue analysis for the jacket ice-resistant platform in Bohai Bay is necessary.

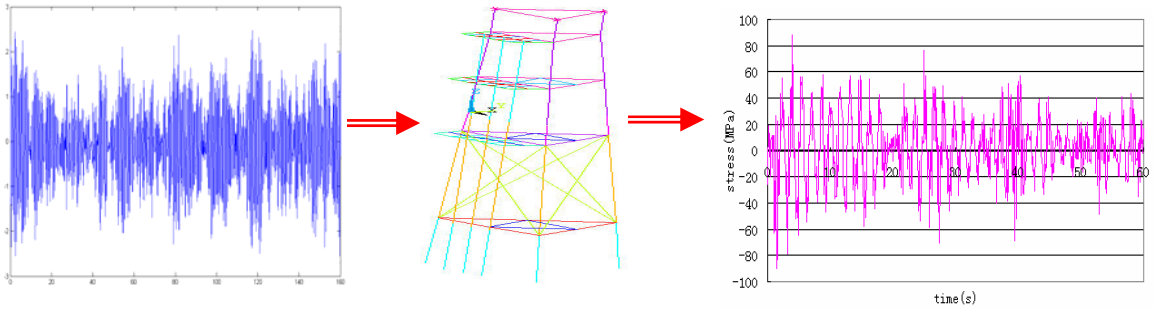

Figure 4. Fatigue stress analysis by ANSYS software based on monitoring data

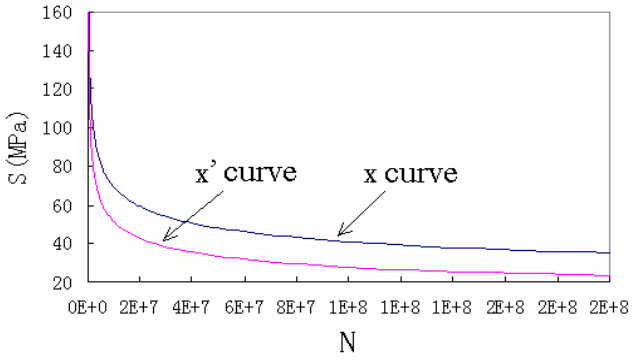

Figure 5. S-N curve of steel provided by API 2A

4. Failure analyses induced by deck accelerations

Based on the data observed on the jacket platforms, sea ice can induce the periodic load and make the offshore jacket structures vibrate with major acceleration. Figure 6 shows the every-day max acceleration of ice-resistant platforms in winter 2006/2007. As production platforms, the vibrations have several times caused accidents. On January 28, 2000 one of the pipelines on the platform suddenly broke during steady-state vibrations as shown in figure 2. This caused high-pressure natural gas to rush out. Figure 7 shows the broken pipeline caused by vibrations. On February 7, 2000 a flange on the pipeline loosened during vibrations and caused leakage. The writers designed all kinds of torque spanners. During the examination and repair of offshore platforms in Spring, we found that connected bolts of 47% the flanges with graphite gaskets are loose and the lowest remnant preload is only 50N.m.

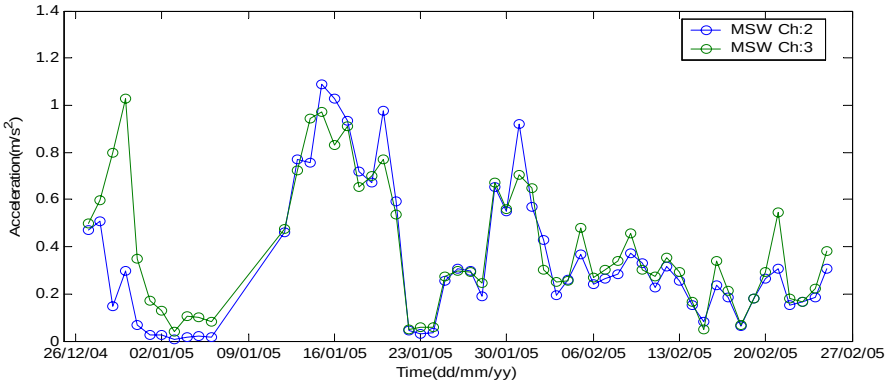

Figure 6. Every-day max acceleration of jacket platform in winter

Figure 7. Broken pipeline caused by vibrations

With number statistics of the data monitored on the platforms of JZ20-2 MUQ and MSW, the mean values of equivalent total exposure time, 4.1 hours and 4.33 hours, respectively. And the mean values of equivalent acceleration are 0.29 m/s^2 and 0.37 m/s^2, respectively. Compared with the ISO standard about human body in vibration environment (GB/T 13442 92), as shown in table 1, it is found that as a living platform, intensive deck vibrations could discomfort the crew members and even affect work efficiency or health.

Table 1. Every stage critical value of human feeling about the relationships between vibration acceleration and duration in level librations

	24h	16h	8h	4h	2.5h	1h	25min	16min	1min
	0.03	0.05	0.07	0.11	0.16	0.27	0.40	0.48	0.63
	0.095	0.158	0.221	0.347	0.504	0.851	1.260	1.512	1.985

	0.19	0.316	0.442	0.694	1.008	1.702	2.52	3.024	3.97

5. Failure causes analysis

The economical ice-resistant jacket platforms are so strong considering only the extreme static ice load, Tab.2 shows the results of maximal deformation and stress of typical ice-resistant structures, such as JZ20-2 MUQ, JZ20-2 NW, JZ20-2MSW, and JZ9-3GCP, under extreme ice loads, here ice thickness is 42cm. The maximal ratios of calculation to the threshold for the deformation and stress are 27.3% and 27.1%, respectively. So the safety reserves of ice-resistant jacket platforms are greater, the structures could stand the push-over ice force.

Table 2. The maximal deformation and stress of ice-resistant platforms under extreme ice forces

platform	Maximal deformation mm		Maximal stress MPa	
	Calculation value	threshold value	Calculation value	threshold value
JZ20-2MUQ	15	168	23	225
JZ20-2MSW	24	130	61	225
JZ20-2NW	12	118	32	225
JZ9-3GCP	24	88	36	225

However, the observations on JZ202 and JZ93 oil field illustrate that both vertical and conical structures are so slender compared with wave-resistant structures in deep sea, which were obtained by their response measurements, as shown in table 3. At a certain ice speed corresponding to a given ice thickness, resonance vibrations, i.e. great dynamic responses, will be induced. Figure 8 shows typical test data. The frequency spectrum of the ice force [Figure 8 (a)] and the acceleration response [Figure 8 (b)] shows that the dominant frequency of the ice force exceeds that of the structure. This means there are many ice conditions which the dominant frequency of the ice force and the structure are nearly equal. So strong ice-induced vibrations took place on jacket platform regardless of whether ice-breaking cones were attached to the legs of structures in Bohai Bay.

Table 3. Structural dominant frequency based on response measurements

Platform	Vertical structures		Conical structures		
	JZ9-3MDP	JZ9-3GCP	JZ20-2MSW	JZ20-2MUQ	JZ20-2NW
Dominant frequency(Hz)	2.37	2.04	1.37	0.87	1.00

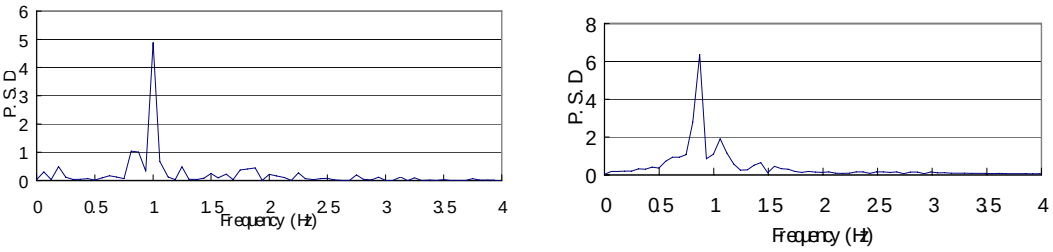

(a) (b)

Figure 8. Power spectrum of ice force (a) and structure response (b)

6. Conclusions

Even though the phenomenon of ice-induced vibration of structure has been observed and investigated about forty years ago, the problem is still not satisfactorily resolved. The main reasons are that no practical dynamical ice force model or design code was given and the failure modes analyses of ice-resistant jacket structure were not definite. The ice conditions and ice-structure interaction play a very important role for oil exploitation and production. Full scale observations made in the Bohai Sea show that ice-resistant jacket platforms in marginal oil fields are quite slender, and their basic frequency is roughly 1-2 Hz. Although under extreme static ice loads the safety reserves of ice-resistant jacket platforms are greater, and the structures could withstand the push-over ice force. Both vertical structures and conical structures encounter significant ice-induced vibrations. The failure modes of ice-resistant platforms in marginal oil fields are quite complicated. It is recommended that the following failure modes should be considered in optimization design and risk assessment:

- Structural safety failure mode, including maximum deformation or strength of structure exceeds accepted value of norm suggested under extreme static ice load; significant cyclical stress of tube node by ice-induced vibrations.
- Human feeling failure mode, involving feeling uncomfortable, degrading work efficiency, and even endangering crew members' health due to significant vibrations of platform deck.
- Facilities on the platforms failure mode, ice-induced vibrations of offshore structure could lead to the associated accidents of facilities on the platform, such as fatigue fracture of pipe and looseness of flanges.

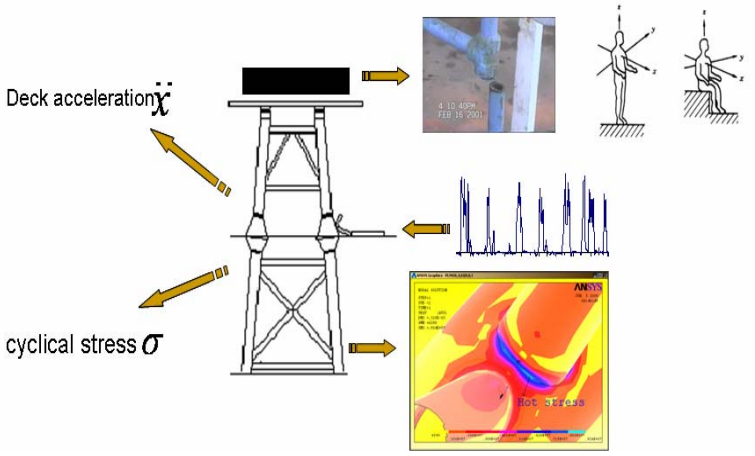

Figure 9. The failure modes of flexibility ice-resistant platform under the ice-induced vibration

The offshore structural vibrations induced by dynamic ice loads may evoke two kinds of risk (see in Figure 9). The intensive shaking of the deck may endanger the facilities on the platform and discomfort the crew members. Additionally, cyclical stress on tubular nodes of the jacket structures may reduce the structural fatigue life. After now, the design of ice-resistant platforms in marginal oil fields should consider ice-induced vibrations and predict the consequences. It will also bring forth studies of relating problems, such as practical dynamic ice force models, fatigue analysis, a complete evaluation of crew member health, dynamic response analysis of pipeline systems exposed to ice-induced vibrations on offshore platforms, vibration mitigation and control. Meanwhile, in order to avoid strong ice-induced vibrations, newly designed ice-resistant structures, such as those more flexible than existing economical jacket structures, should be carried out. These structures should not only resist an extreme static ice force, but also react gently to ice-vibration. More studies should evaluate the usefulness of these new types of ice-resistant structures. In brief, flexible jacket structures are quite suitable in ice marginal oil fields if the dynamic failure modes induced by ice vibration that mentioned in this paper meet their performance requirements.

Acknowledgements

The support of the National Natural Science Foundation of China (No. 10672029) is much appreciated.

Reference

Peyton H R. 1968. Sea ice forces. Ice pressures against structures. National research council of Canada. Canada, Technical Memorandum 92:117-123.

Engelbrekston,A., 1977. Dynamic ice loads on lighthouse structures Proc.4th Int.Conf.on Port and Oc.Engrg.under Arctic Conditions St.John's Canada, 654-864.

Wright B, Timco G., 1994. A review of ice forces and failure modes on the Molikpaq.Proc.12th Int.Symp.On Ice.Trondheim, Norway, 816-824.

Yue, Q.J. Bi, X.J., 2001. Ice-induced jacket structure vibrations in Bohai sea Journal of Cold

Regions Engineering, 14(2):81-92.
Maattanen, M.,et al. 1996. Ice failure and ice loads on a conical structure-Kemi-1 cone full scale ice force measurement data analysis. Proc. of 13th International Symposium on Ice (IAHR). Beijing, China. Vol.1: pp.8-17.
Jochmann, P. and Schwarz, J. 2000. Ice Force Measurements at Lighthouse Norstromsgrund. Winter 1999. LOLEIF Report No 5. EU Contract MAS-CT-97-0098. 48 p + Appendix. Hamburg, Germany, December 2000.
Kärnä, T and Jochmann, P. 2003. Field observations on ice failure modes. Proc. 17th International Conference on Port and Ocean Engineering under Arctic Conditions (POAC'03). Trondheim, Norway, June 16-19, Vol 2, pp. 839 - 848.
Schwarz, J. and Jochmann, P. 2001. Ice force measurement within the LOLEIF-project. Proc. 16th Int. Conf. on Port and Ocean Engineering under Arctic Conditions. Ottawa, Canada, August 12-17, pp. 669 - 680.
Timco, G and Johnston, M. 2003. Ice loads on the Molikpaq in the Canadien Beaufort Sea. Cold Regions Science and Technology 37: 51-68.
Yue, Q., Bi, X., Sun, B., Zhang, T. & Chen, X. 1996. Full scale force measurement on JZ20-2 platform. Proc. IAHR Ice Symp. (IAHR' 96) Beijing. pp. 282-289.
Hirayama, K., Schwarz, J. and Wu H.C. 1973. Model technique for the investigation of tice forces on structures. Proc 2nd Int. Conf. on Port and Ocean Eng. under Arctic Conditions Reikjavik, Iceland, August 27-30, pp. 332 - 344.
Muhonen, A.,Karna, T., Eranti, E., Riska, J. and Järvinen E., 1992. Laboratory indentation test with thick freshwater ice, Volume I. VTT Research Notes 1370. Espoo 1992, 92 p. + App.
Guo, F., Yue, Q., Bi, X., Xu, N. 2007. A medium scale model test system of ice-structure interaction and test results. 19th International Conference on Port and Ocean Engineering under Arctic Conditions (POAC'07). Dalian, China, June 27-30, Vol 1, pp. 216 - 224.
Yue, Q.J. Bi, X.J., 1998. Full-scale tests and analysis of dynamic interaction between ice sheet and conical structures. Proc. of 14th IAHR, Potsdam, Vol.2, 939-945.
DNV, 2001. Recommended practice DNV-RP-C203 fatigue strength analysis of offshore steel structures.
API 2A, 1991. Recommended practice for planning, designing, and constructing fixed offshore structures.
Reduced comfort boundary and evaluation criteria for human exposure to whole-body vibration, exposure to whole-body vibration, GB GB/T 13442-92.

19th IAHR International Symposium on Ice
"Using New Technology to Understand Water-Ice Interaction"
Vancouver, British Columbia, Canada, July 6 to 11, 2008

Theoretical Study on Mechanism of Frequency Lock-in and resonance in Ice-induced Vibration of Compliant Structures

Guojun Huang
Department of Engineering Science, Institute of Mechanics
Chinese Academy of Sciences
15 Bei Si Huan Xi Road, Beijing, 100080, China
Tel: 011-861082544195, Fax: 011-861062561284
E-mail: ghuang@imech.ac.cn

Pengfei Liu
Institute for Ocean Technology, National Research Council Canada
1 Kerwin Place, St. John's, NL, Canada, A1B 3T5
P.O. Box 12093, Postal Station A
Tel: 1-709-772-4575, Fax: 1-709-772-2462
E-mail: Pengfei.Liu@nrc-cnrc.gc.ca

Abstract: This paper presents a theoretical investigation on the mechanism of the frequency lock-in and resonance observed in the ice-induced vibration (IIV) of compliant structures. The study is based on a dynamical model of IIV developed recently by authors (OMAE2006). It is shown that in addition to the conventional resonant frequency lock-in, there exists another type of the frequency lock-in, namely, the separated frequency lock-in, where the predominant frequency of ice force is not locked on the natural structural frequency. Besides, the influence of some important ice and structural properties on the frequency lock-in is studied. From these theoretical studies, it is turned out that the strain rate effect of the ice-crushing strength is responsible for the frequency lock-in and resonance. A self-exciting vibration comes from the strain rate effect through the uneven momentum transfer between ice and structures, dependent on the relative movement directions. The self-exciting vibration is coupled with the forced IIV in a complex nonlinearly dynamical way, leading the system to the stationary vibration with the feature of the frequency lock-in. These theoretical results are instructive to the further systematic experiment study on the frequency loc-in and resonance, and useful for us eventually to devise some effective techniques for the mitigation of intensive IIV.

Key words: ice-induced vibration, compliant structures, frequency lock-in, resonance, ice-crushing strength, strain rate effect

1. Introduction

Resonance in ice-induced vibration (IIV) is an important issue for the structures in ice regions, since it threatens severely the safety of the structures and worsens the working environment for operators. The resonant vibration often companions the frequency lock-in, i.e., both the predominant ice and structural frequency remain to be unchanged and are equal to the natural structural frequency, over an ice velocity span. So a rational understanding of the mechanism underlying the frequency lock-in and resonance is crucial for the controlling and mitigation of IIV.

Some laboratory experiments and field observation have been carried on the lock-in resonant vibration by the previous investigators. For example, Engelbrektson (1983) observed, in the Gulf of Bothnia, that in resonance, the structural acceleration might reach at as high as 0.7g, one order of magnitude more than that of the most of the day, 0.07g. Meanwhile, Määttänen (1983) found, in the laboratory experiment, the resonant frequency lock-in over a wider velocity span. Tsuchiya et al (1985) carried out an IIV experiment in the air to obtain the important data of the resonant frequency lock-in. It is interesting to note, from these experimental results, that the resonant frequency lock-in in IIV is quite similar to that in vortex-induced vibration (VIV), referred to Feng (1968), showing a dynamic analogy between IIV and VIV, although their natures are completely different.

On the other hand, theoretical studies have also been made on the resonant frequency lock-in. Toyama et al (1985), Kärnä & Turune (1990), Shih (1991) and Jin & Hu (1998), among the others, developed their IIV models to determine the critical conditions under which the resonant frequency lock-in arises. Some kinetic or dynamic assumptions, however, were introduced in their models, to capture the features of resonance. In view of the dynamic analogy between IIV and VIV, Xu and Wang (1988) proposed a phenomenological IIV model, named the ice force oscillator model and being alike the wake oscillator model in VIV, to predict the resonant frequency lock-in. Recently, the authors (Huang and Liu, 2006) have developed an IIV model by incorporate the strain rate effect of the ice-crushing strength into the Sodhi's (1994) IIV model. It is capable of capturing the resonant frequency lock-in in a natural way, without the assumptions mentioned above.

The aim of the present work is to study the influence of the ice and structural properties on the frequency lock-in and resonance and to clarify its mechanical and dynamical mechanisms, based on the Huang and Liu's (2006) model. In this paper, we firstly outline the model in Section 2. Then two types of frequency lock-in are presented in Section 3. Next, the influences of the ice and structural properties on the frequency lock-in are studied in Section 4 and its mechanism is discussed in Section 5. Finally, we summarized the work in Section 6.

2. Theoretical model of IIV

For the convenience of the later study and discussion, we summarize briefly the Huang and Liu's (2006) IIV model as follows. The system of a damped single-degree-of-freedom oscillator interacting with a series of moving ice teeth, proposed by Matlock et al (1971) is considered, as an analogue to a cantilevered pier excited by ice floe. The basic interaction process is consisting of three phases, i.e., loading, extrusion and separation phases, as proposed by Sodhi (1994).

The system of the governing equations of motion for the three phases is expressed as

$$M\ddot{x} + C\dot{x} + Kx =$$

$$\begin{cases} k\left[x_0 + vt - x - p(n-1)\right] + F_e & 0 \le \delta < \delta_f \text{ and } \dot{x} \le v \quad \text{(Loading phase)} \\ F_e & \delta_f \le \delta < p \text{ and } \dot{x} \le v \quad \text{(Extrusion phase)} \\ 0 & \dot{x} > v \quad \text{(Separation phase)} \end{cases} \qquad \textbf{[1]}$$

where M , C and K are the structural mass, damping coefficient and elastic stiffness, respectively; x, $\dot{x}$ and $\ddot{x}$ the position, velocity and acceleration of the structure, respectively, with x_0 being the initial value; k the ice stiffness; $\delta = x_0 + vt - x - p(n-1)$ the deflection of the ice tooth, with v, p and n are the velocity of ice floe, the pitch of the ice teeth or the length of the ice-crushing zone and the number of the teeth, respectively; $\delta_f = \dfrac{(F_f - F_e)}{k}$ the failure deflection of ice, with F_e and F_f being the constant extrusion ice force and the ice failure force, respectively.

Following Korzhavin (1962), the ice failure force is given by

$$F_f = Im\kappa hD\sigma_f \qquad \textbf{[2]}$$

in which, I , m and κ are indentation, geometry and contact coefficients, respectively; D is the diameter of the structure and h the thickness of ice floe; σ_f is the ice failure strength, i.e. the ice-crushing strength. In the Sodhi's (1994) model, the ice-crushing strength is set to be constant, while in Huang and Liu's (2006) model, it is dependent on the instantaneous relative velocity between the ice and structure, $v_r = v - v_s$ with $v_s = \dot{x}$. The dependence comes from the well-known strain rate effect of the ice-crushing strength, as illustrated schematically by Figure 1. The figure has also defined some characteristic values. Following Iliescu and Schulson (1999), the relationship of ice-crushing strength versus strain rate may be expressed in a dimensional form and by two separate power laws, as below

$$\bar{\sigma}_f = \begin{cases} (1 - \bar{\sigma}_{fd})(v_r / v_t)^{\alpha} + \bar{\sigma}_{fd} & v_r / v_t \le 1 \\ (1 - \bar{\sigma}_{fb})(v_r / v_t)^{\beta} + \bar{\sigma}_{fb} & v_r / v_t > 1 \end{cases} \qquad \textbf{[3]}$$

where $\bar{\sigma}_f = \dfrac{\sigma_f}{\sigma_{f\max}}$, $\bar{\sigma}_{fd} = \dfrac{\sigma_{fd}}{\sigma_{f\max}}$ and $\bar{\sigma}_{fb} = \dfrac{\sigma_{fb}}{\sigma_{f\max}}$, with $\sigma_{f\max}$ being the maximum ice-crushing strength, corresponding to the transitional ice velocity, v_t , which is defined by $\dot{\varepsilon}_t = v_t / h$; $\alpha > 0$ and $\beta < 0$ are indexes.

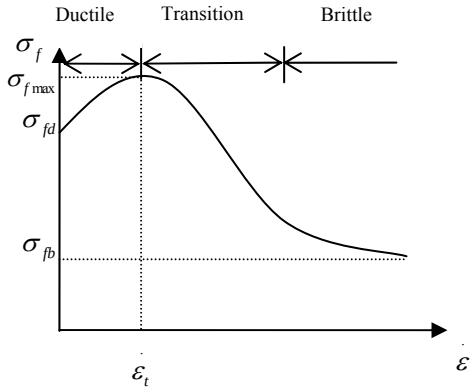

Figure 1. Characteristic plot of ice-crushing strength versus strain rate.

Introducing the following normalized quantities:

$$\begin{cases} \bar{x} = x/\Delta \quad \bar{x}_0 = x_0/\Delta \quad \bar{p} = p/\Delta \quad \bar{\delta} = \delta/\Delta \quad \bar{\delta}_f = \delta_f/\Delta \\ \tau = \omega_n t \quad \bar{k} = k/K \quad \bar{F}_e = F_e/F_{f\max} \quad \bar{v} = v/(\omega_n \Delta) \\ \bar{v}_t = v_t/(\omega_n \Delta) \end{cases} \qquad \textbf{[4]}$$

in which $\Delta = \dfrac{F_{f\max}}{K}$ and $\omega_n = \sqrt{\dfrac{K}{M}}$ are the maximum deflection of the structure corresponding to the static application of the maximum ice failure force, $F_{f\max}$, and the natural angular frequency of the structure, respectively. Then the governing equation [1] can be non-dimensionalised as

$$\ddot{\bar{x}} + 2\xi\dot{\bar{x}} + \bar{x} = \begin{cases} \bar{k}\left[\bar{x}_0 + \bar{v}\tau - \bar{x} - \bar{p}(n-1)\right] + \bar{F}_e & 0 \le \bar{\delta} < \bar{\delta}_f \text{ and } \dot{\bar{x}} \le \bar{v} \\ \bar{F}_e & \bar{\delta}_f \le \bar{\delta} < \bar{p} \text{ and } \dot{\bar{x}} \le \bar{v} \\ 0 & \dot{\bar{x}} > \bar{v} \end{cases} \qquad \textbf{[5]}$$

where $\xi = \dfrac{C}{2M\omega_n}$ is the structural damping ratio, $\ddot{\bar{x}} = \dfrac{d^2\bar{x}}{d\tau^2}$ and $\dot{\bar{x}} = \dfrac{d\bar{x}}{d\tau}$. From the equation [2], we get $\bar{F}_f = \bar{\sigma}_f$ and, then, the instantaneous ice failure condition:

$$\bar{\delta}_f\left(v_r/v_t\right) = \frac{\left[\bar{\sigma}_f(v_r/v_t) - \bar{F}_e\right]}{\bar{k}} \qquad \textbf{[6]}$$

Equation (5) is a highly nonlinear dynamic equation, owing to the discrete ice failure events and its dependence on the instantaneous relative ice velocity. However, since it is piece-wise linear, a closed form solution can be derived for the individual phase. The detailed solutions can be referred to Huang and Liu (2006). The complete solution to Eq. (5) requires numerical computation to obtain the dynamic structural response and the coupled ice force time histories.

3. Frequency lock-in

Now we carry out the numerical simulation on the structural response and the coupled ice force in IIV, applying the IIV model presented in the last section. Special attentions are paid to the frequency lock-in phenomenon. For the purpose of mechanism investigation, the study here is restricted to parametric one. A typical case is chosen in the computation, whose parameters for the properties of the ice and structure are listed in Table 1.

Table 1. Typical parameters of the properties of the ice and structure.

$\overline{k}$	ξ	$\overline{\sigma}_{fd}$	$\overline{\sigma}_{fb}$	α	β	$\overline{v}_t$	$\overline{p}$	$\overline{F}_e$
0.1	0.04	0.7	0.5	0.5	-2	1	10	0.2

Figure 2 shows the dimensionless amplitude of the steady structural deflection, $\overline{x}_{\max} - \overline{x}_{\min}$, as a function of the dimensionless ice velocity, v/v_t. The black solid and red dashed lines correspond to the cases with and without the strain rate effect of the ice-crushing strength involved, respectively. In the latter case, the ice-crushing strength is fixed to be 0.78 $f_{i\max}$ and so the Huang and Liu's (206) model reduces to the Sodhi's model. Comparison between the two results illustrates a remarkable strain rate effect of the ice-crushing strength on the structural response. When the stain rate effect not considered, there exist several narrow response peaks. For the relatively higher ice velocity, v/v_t>2.75, the response remains to be temperate, in accordance with the usual experimental observations. While, with the stain rate effect considered, the response peaks broaden and heighten, indicating that more intensive IIV arises over the ice velocity spans corresponding to the response peaks. Note that, however, the two models give nearly same prediction for the ice velocity outside the velocity spans.

To unveil the cause to the amplifying response after the strain rate effect involved, we have calculated the predominant frequencies of both the structural response and the ice force/ice crushing, f_s and f_i, corresponding to Figure 2. The results with the strain rate effect involved are depicted in Figure 3, which are normalized by the natural frequency of the structure, f_n. The blue solid line presents the predominant frequency of ice force and the red square symbols denote the predominant frequency of response. In the case when the strain rate effect considered, the ice-crushing frequency increases nearly linearly with the increasing ice velocity until v/v_t=2.2. Then it locks on the natural frequency of the structure in the ice velocity span of v/v_t=2.2-2.75. Finally, it jumps into the second blue solid slope line and varies along it, which is nearly the extension line of the first one. Note that, over the ice velocity range of v/v_t=2.6-2.75, the ice-crushing frequency is diplex. That is because there exist two steady vibration states, dependent on the initial conditions of structural movement. Meanwhile, it is interesting to see that there exist two kinds of the frequency lock-in, as the red square symbols shown. In the first two response peaks the predominant structural frequency is separated from the ice-crushing frequency and locked on the natural structural frequency. We term this frequency lock-in the separated frequency lock-in.

While, in the last response peak, the two frequencies are all locked on the natural structural frequency, featuring resonance, and so term it the resonant frequency lock-in. Thus in conjunction to Figure 1, it turns out that the intensifying of vibration results from the frequency lock-in. However, the effect of separated frequency lock-in on the intensifying of IIV is moderate, while the effect of the resonant frequency lock-in mostly remarkable. Hence, avoiding the resonant frequency lock-in is crucial to protect structures from intensive vibrations.

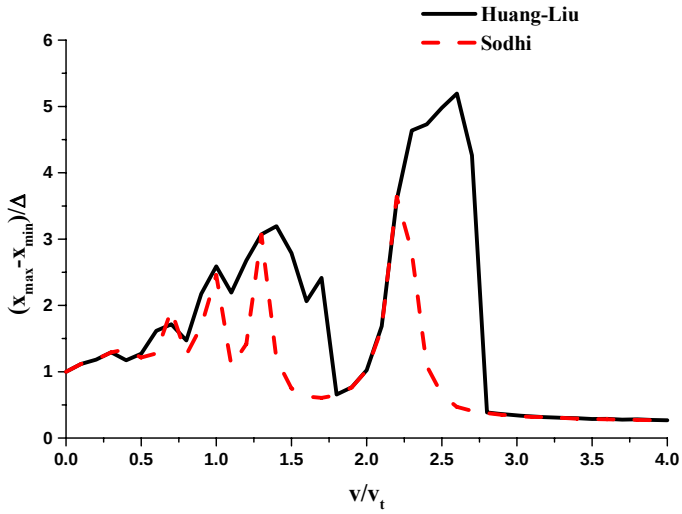

Figure 2. Dependence of the amplitude of structural deflection on the ice velocity predicted from the Sodhi's (1994) and Huang-Liu (2006)'s models, respectively, showing the strain rate effect of th ice-crushing strength on IIV

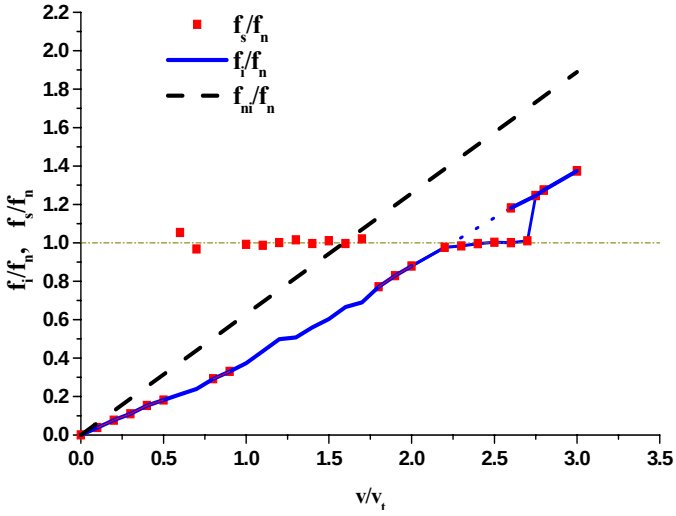

Figure 3. Dependence of the predominant frequencies of the ice force and structural response on the ice velocity, corresponding to Figure 1, with the strain rate effect involved.

In the case without the strain rate effect considered, the ice and structural frequencies are almost equal and vary with the ice velocity along the slope line combined by the blue solid and dashed lines in Figure 3. Neither the separated frequency lock-in nor the resonant frequency lock-in

arises. It demonstrates that both the frequency lock-in come from the strain rate effect. Included in Figure 3 is the natural ice-crushing frequency, $\frac{f_{ni}}{f_n}=\frac{v}{pf_n}=\frac{\pi}{5}\frac{v}{v_t}$, as the black dashed line shown, for comparison. It corresponds to the interaction between ice and rigid structures. It is somewhat different from the actual ice-crushing frequency for compliant structures, because of the movement coupling between the ice and structure.

4. Influencing factors of the frequency lock-in

Since the frequency lock-in is responsible for the intensive IIV, it is worth studying the important influencing factors dominating the frequency lock-in. Seeing the governing equations [5], we make a investigation on the influence of ice and structural properties, including the structural damping ratio, ξ , the structural stiffness, K, the relative ice stiffness, $\bar{k}$, the ice-crushing pitch, $\bar{p}$ and the ductile-brittle transitional velocity, $\bar{v}_t$. Randomness in the ice-crushing strength is also considered.

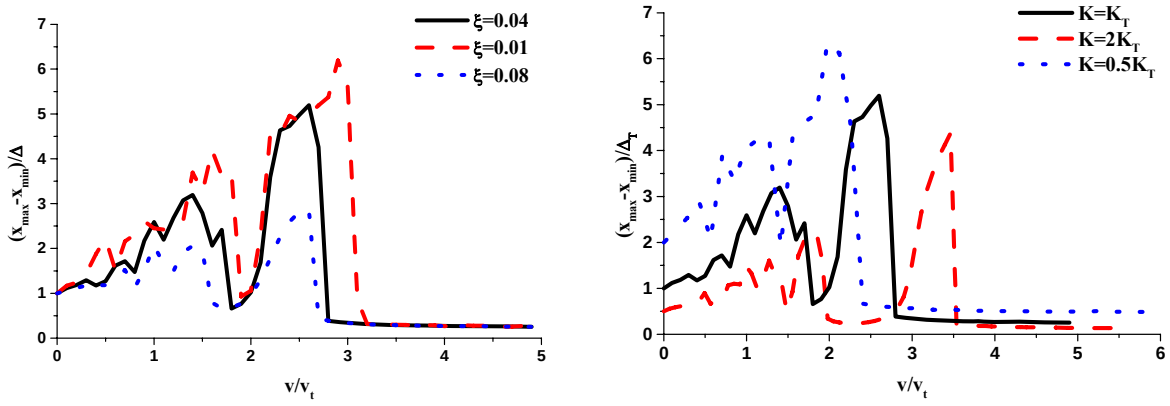

(a) (b)

Figure 4. Influence of the structural properties on the frequency lock-in. (a) damping and (b) stiffness.

Figure 4 presents the effect of the structural damping ratio on the structural response as well as the frequency lock-in. The black solid line corresponds to the typical case, as shown in Figure 2 by the black one. With the structural damping ratio changed from 0.01 to 0.08, while the other parameters are fixed as the same as those listed in Table 1, the structural response varies correspondently, as shown by the blue dotted and red dashed lines, respectively. Note that slight changes in the structural damping ratio lead to appreciable variations both in width and in height of the response peeks. It indicates that the frequency lock-in is sensitive to the structural damping ratio. The more the structural damping ratio, the less the velocity spans of the frequency lock-in and the responses. In view of $\xi=\frac{C}{2M\omega_n}=\frac{C}{2\sqrt{MK}}$, it is demonstrated that increasing the structural damping coefficient, C, is an effective way to protect the light and compliant structures from the intensive vibration. In addition, under certain conditions, the lock-in resonant vibration may arises even in the massive and stiff structure, due to its relatively lower structural damping ratio, as long as the structural damping coefficient is not appreciably large. This result can explain why

the intensive vibration might take place in the large-scale structures, for instance, Molikpaq in Beauforts.

Figure 4 (b) shows the effect of the structural stiffness on the response. The structural deflections for all the cases are scaled uniformly by the maximum structural deflection, Δ_T, for comparison, where and hereafter the subscript T denotes the parameter corresponding to the typical case. When the structural stiffness changes to be, $K = 2K_T$, for example, with the other properties fixed as the same as the typical ones, the corresponding variations in the dimensionless parameters listed in Table 1 are: $\overline{k} = \overline{k}/2$, $\xi = \xi_T / \sqrt{2}$, $\overline{v}_t = \sqrt{2}\overline{v}_{tT}$ and $\overline{p} = 2\overline{p}_T$. Similar variations are also coming from the changing: $K = 0.5K_T$. As the red dashed line and the blue dotted lines shown, it is illustrated that for the relatively stiffer structure, the response peaks are shifted to the higher velocity, while for the relatively compliant structure to the lower velocity, as compared with the typical case. Meanwhile, it is seen that the less the structural stiffness, the broader the ice velocity spans of the frequency lock-in and, correspondently, the more intensive the response, in agreement with the conventional experiences. Nevertheless, it is worthwhile to note that since the ratios among the predominant structural angular frequencies, i.e., ω_n, inside the frequency lock-in spans are 2:1:0.5 for the cases of $K = 2K_T$, K_T and $0.5K_T$, respectively, the ratios among their maximum structural acceleration amplitudes, $a_{A\max} = \varpi_n^2 (x_{\max} - x_{\min})_{\max} / \Delta$ are 8.76:5.20:3.19. That is to say, from this case study, the stiffer structure experiences the resonant vibration with smaller deflection amplitude and larger acceleration amplitude, as compared with the compliant structures.

The influence of the ice properties on the frequency lock-in is presented in Figure 5 (a)-(d), still with the black solid lines corresponding to the typical case. Figure 5 (a) is about the effect of the relative ice stiffness, $\overline{k} = k / K$, for the cases of $k = 2k_T$, k_T and $0.5k_T$ (or $\overline{k} = 2$, 1 and 0.5), with the other parameters being the same as the typical ones listed in Table 1. The corresponding structural responses are depicted by the blue dotted, black solid and red dashed lines, respectively, It is shown that with the ice stiffness increased, the response peaks shift to relatively lower ice velocity with more remarkable separated lock-in response and less intensive resonant lock-in response. The influence of the ice-crushing pitch on the frequency lock-in is graphed in Figure 5 (b) for the different pitches, $\overline{p} = 10,\ 15$ and 20, as shown by the black solid, red dashed and blue dotted lines, respectively. It demonstrates that with increasing ice-crushing pitch, the ice velocity of the frequency lock-in increases and the corresponding vibration intensifies. Figure 5 (c) indicates the results pertaining to the influence of the ductile-brittle transitional ice velocity on the frequency lock-in, for the cases of $\overline{v}_t = 1,\ 2$ and 0.5, as shown by the black solid, red dashed and blue dotted lines respectively. It is seen that the effect is remarkable such that the larger the ductile-brittle transitional ice velocity, the broader the response peak and the more the intensity vibration. In addition, the randomness in the ice-crushing force is considered in the present study. 0% (typical case), 10% and 2 0%, respectively, of the randomness with uniform probabilistic distribution is imposed on $\overline{F}_f$ and $\overline{p}$ and the corresponding results are indicated in Figure 5 (d). It is seen that with the randomness increased, the frequency lock-in tends to be restrained and the probability of resonance is less than that for the deterministic case.

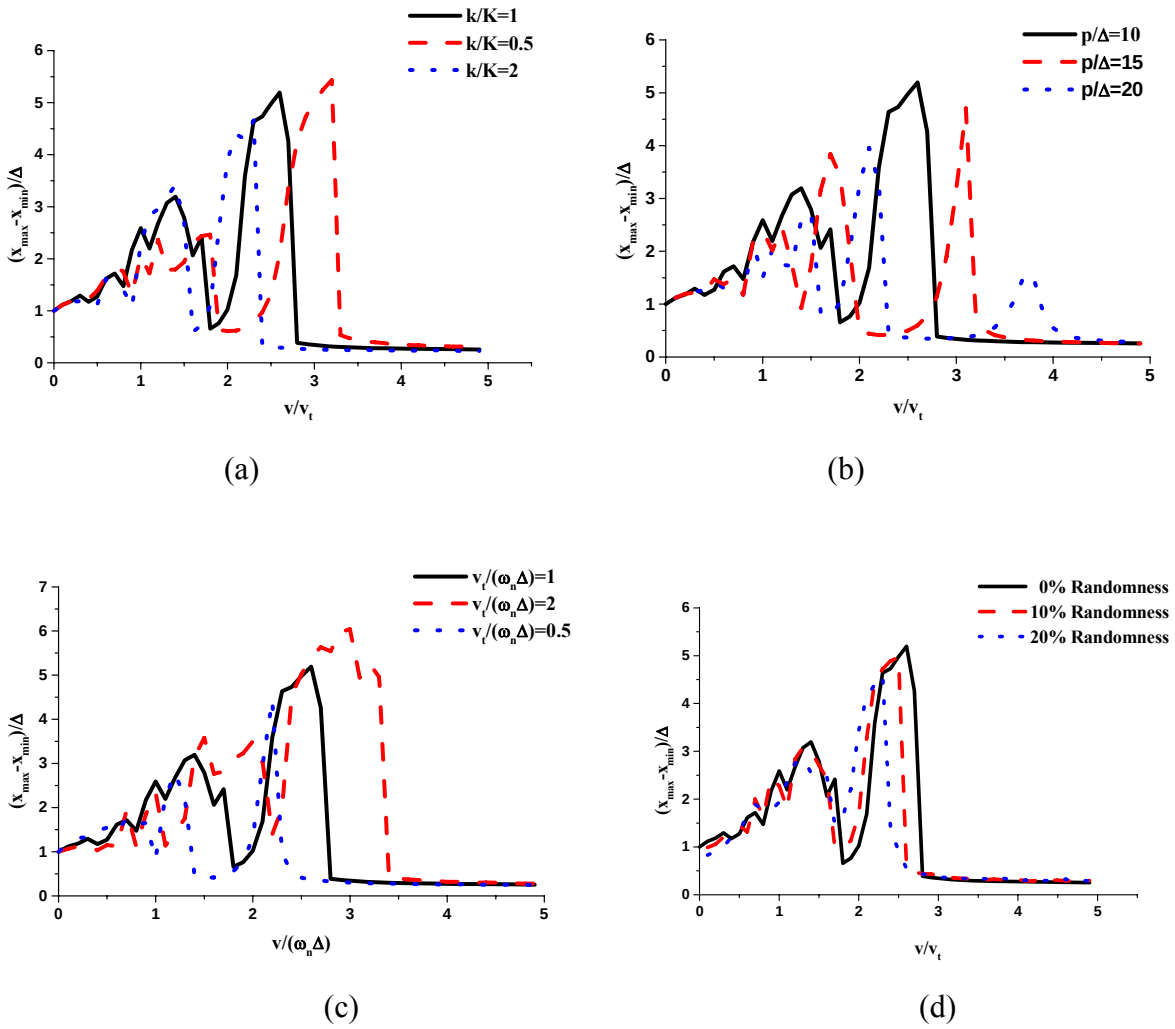

Figure 5. Influence of the ice properties on the frequency lock-in in. (a) ice stiffness, (b) ice-crushing pitch, (c) ductile-brittle transitional ice velocity and (d) randomness in ice-crushing.

5. The mechanism of the frequency lock-in and resonance

So far, it has been clear that the frequency lock-in comes from the strain rate effect of ice-crushing strength. Now we further study the mechanism through which the effect works. To this end, it is helpful to see the time histories of ice force and structural response in the phase of the frequency lock-in. Figure 5 presents the steady profiles of the time history of ice force and structural velocity in the resonant frequency lock-in phase. At v/v_t=2.2, where the ice-crushing frequency begins to reach the natural structural frequency, the resonant vibration behaves in the conventional way, i.e., the ice force and the structural response are in-phase and there exists one deflection cycle along with one ice-crushing event per period, as shown in Figure 5 (a) by the red solid and black dashed lines, respectively. Note that at this velocity, the ice-crushing force is nearly constant, meaning that the strain rate effect is wick. However, the profile of the resonant vibration changes with increasing ice velocity, as indicated in Figure 5 (b) for v/v_t=2.6, which is by the end of the ice velocity span of the resonant frequency lock-in. It is seen that there exist nine deflection cycles along with ten ice-crushing events per period, still nearly one cycle versus

one ice-crushing event. In the period, the phase difference between the ice force and the structural response varies gradually from in-phase ($v_s > 0$) to out-of-phase ($v_s < 0$) so that the response increases gradually until the maximum reached and then decreases gradually to enter the next period. In the spectrum analysis, it has been shown that although there exist multiple response frequencies, both the predominant frequencies of the response and ice force remain to be equal to the natural structural frequency, for all the ice velocity fallen into the resonant lock-in span. That is to say, there exists a self-organization mechanism responsible for the frequency lock-in. This can be understood more clearly by noting, from Figure 5 (b), that when the structure and ice move in the same direction in the loading phase, the structure gains more momentum (the area enclosed by the red ice force curve and the horizontal line of $F = F_e$) from the ice than that when they move in the opposing direction. This is because the relative velocity between the ice and structure in the former case is less than that in the latter case, leading to the higher ice-crushing force and, hence, the longer loading period in the former case, due to the strain rate effect. In the former case, the gaining momentum promotes the vibration, while in the latter case, it restrains the vibration, i.e., the ice-structure interaction plays dual roles in IIV. Intrinsically, the relative domination of the two roles is uneven even when the stain effect not involved, due to the difference in the relative velocity in the two vibration directions, as in the conventional forced vibrations. The strain rate effect makes the unevenness intensify as if it introduces an extra self-exciting. The more the response, the more the unevenness, vice versa. However, this positive feedback of the self-exciting is balanced by the structural damping, leading the system to reach at a stationary state of resonance. Therefore, from the above observation and study, it may be clear that the lock-in resonant vibration is a coupled combination of forced and self-excited ones. The latter is induced by the former due to the strain rate effect and, in turn, affects the former. The resonant frequency lock-in comes from this complex coupling through the dynamical adjustment of the ice-crushing force and the period of the loading phase, being a stationary vibration state.

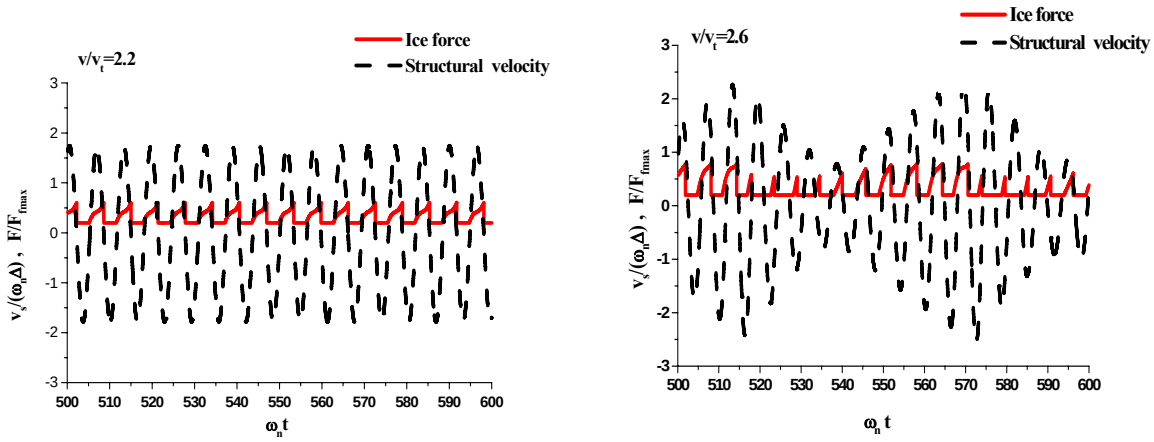

(a) (b)

Figure 6. Time history plots of ice force and structural response in the phase of the resonant frequency lock-in. (a) v/v_t=2.2 and (b) v/v_t=2.6.

Do to the limitation of paper length, we have omitted the result of the time histories of the ice force and response in the first and second separation frequency lock-in spans, It is found that the

two spans correspond to the cases when the ice-crushing frequencies have approached to quart and half the natural structural frequency, respectively, where there exist four and two response cycles per one ice-crushing period, respectively. So that, the frequency adjustment is relative wicker, as compared with that in the resonant span, leading only the predominant response frequency to be locked on natural structural frequency. This is readily understood since the ice–crushing frequency in these spans are far from the natural structural frequency.

In additional to the above mechanical exploration on the mechanism of the frequency lock-in, a survey from the nonlinear dynamics aspect is meaningful. IIV is a complex nonlinear dynamical process, especially when the strain rate effect is incorporated. The steady vibration corresponds to the attractor in the phase plot, i.e., limiting cycles. The frequency lock-in is a bifurcation of the steady solutions. The occurrence of the multiple of the steady response in the resonant frequency lock-in as well as their initial value sensibility is also the typical feature of nonlinear dynamics. When the strain rate effect is not considered, the steady solution is trivial one, without bifurcation, as shown in Figure 3 by the blue slope line. While, when the strain rate effect is considered, bifurcation occurs, coming from the increased non-linearity. In the frequency lock-in spans, the trivial solution loses its stability and the dynamically stationary non-trivial solution, i.e. lock-in ones, become stable. Evidently, the strain rate effect plays a role of the stabilizer in the frequency lock-in.

Finally, we can give a reasonable explanation on the theoretical results about the influence of the ice and structural properties on the frequency lock-in presented in Section 4. The structural damping ratio is an important factor that affects remarkably the width of the lock-in span. The broader the lock-in span, the more the acceleration cycles per period and the more intensity response. The larger ductile-brittle transitional ice velocity, v_t, corresponds to the broader transition zone in the curve of ice-crushing force versus ice velocity and, consequently, to the broader lock-in span. Since the structural stiffness affects the beginning velocity of the lock-in span and its relative velocity to the ice transitional velocity, the role of strain rate effect played in the frequency lock-in varies with them, leading to the shifting and the shape changing of the response peaks. In regard to the ice stiffness, its influence on the frequency lock-in is through affecting the unevenness of the energy transfer between ice and structures. Although the randomness in ice-crushing leads to the stochastic trajectory in the phase plot, the lock-in vibrations may occur, as long as the trajectory falls into inside the attraction basin of the lock-in attractors.

6. Conclusive remarks

In summary, in the present study, the frequency lock-in is analyzed in details based on the IIV model developed previously by the authors. There exist two types of the frequency lock-in, i.e. separated and resonant ones. They all come from the strain rate effect of the ice-crushing strength. The strain rate effect plays a crucial role in inducing the self-exciting vibration through the uneven energy transfer between ice and structures and the corresponding frequency adjustment. These theoretical results are useful for us to plan a systematic experimental study on the frequency lock-in, which is underway by the authors. The comprehensive experimental and

theoretical findings on the frequency lock-in will be instructive for us to devise some techniques for the mitigation of IIV.

Acknowledgments
The authors thank for the financial supports from the National Natural Science Foundation of China (Grant No. 10772184 and No. 10532070). The authors also thank to the National Research Council Canada for its support.

References

Engelbrektson, A., 1983, "Observations of a resonance vibrating lighthouse structure in moving ice," *Proc. 7th POAC Conf.*, Helsinki, Finland, Vol. II, pp. 855-864

Feng, C. C., 1968, "The measurement of vortex-induced effects in flow past stationary and oscillating circulator and D-section cylinder," M. A. Sc. Thesis, University of British Columbia.

Huang Guojun and Liu Pengfei, 2006, " A dynamic model for ice-Induced vibration of structures," Proceedings of 25th International Conference on Offshore Mechanics and Arctic Engineering, June 4-9, Hamburg, Germany,pp:1-7

Iliescu, D., Schulson, E.M., 1999, "Brittle compressive failure of ice: monotonic versus step-loading," *Proc. 18th Int. OMAE Conf.*, CD-ROM: OMAE99-1170, 14pp.

Jin, D. D. and Hu, H. Y., 1998, "Ice-induced non-linear Vibration of Offshore Platform, " J. Sound and Vibration, V214 (3), pp. 431-442.

T. Kärnä and R. Turunen, 1990, A straightforward technique for analyzing structural response to dynamic ice action, Offshore Mechanics and Arctic Engineering, Arctic/polar technology, ASME Vol. 4, pp. 135-142.

Korzhavin, K.N., 1962, "Action of ice on engineering Structures," U.S Army Cold Regions Research and Engineering Laboratory, Hanover, NH, USA, CRREL Draft Translation No. 260.

Määttänen, M., 1983, "Dynamic ice structure interaction during continuous crushing," U.S Army Cold Regions Research and Engineering Laboratory, Hanover, NH, USA 03755, CRREL Report 83-5, 53p.

Matlock, G., Dawkins, W., Panak, J., 1971, "Analytical model for ice-structure interaction," ASCE J. Eng. Mech., EM 4, pp. 1083-1092.

Shih, L. Y., 1991, "Analysis of ice –induced vibration on a flexible structure," Appl. Math. Modeling, Vol. 15, pp632-638

Sodhi, D.S, 1994, "A theoretical model for ice-structure interaction," *Proc. OMAE-94 Conf.*, Vol. IV, ASME, New York. pp. 29-34

Tsuchiya M Kanie S. and Ikejiri K., 1985, ″An experimental study on ice-structure interaction, ″ Proc. Of the 17th Offshore Technology Conference, Astrodomain, Houston, Texas, Vol. 4, pp. 321-327

Toyama, Y., Sensu, T., Minami, M. And Yashima, N., 1983, ″Model tests on ice-induced self-excited vibration of cylindrical structures, ″ Proceedings of the 7th International Conference on Port and Ocean Engineering under Arctic conditions, Helsinki, Finland, Vol. II, pp. 834-844

Xu J. Z. and Wang L. Y., 1988, "Ice force oscillator model and its numerical solution," Proc. 7th Intern. Offshore Mechanics and Arctic Engineering (OMAE) Symposium, Vol. IV, Houston, TX, USA, pp. 171-176

19th IAHR International Symposium on Ice
"Using New Technology to Understand Water-Ice Interaction"
Vancouver, British Columbia, Canada, July 6 to 11, 2008

TMD as an approach to mitigate ice-induced vibrations

L. Zhang Z.L. Fan and Q.J. Yue
(State Key Laboratory of Structural Analysis of Industrial Equipment,
Dalian University of Technology, Dalian 116023, China)
Linggong Str. 2. Dalian. China
jassenzl@gmail.com

Abstract: The problems of ice induced vibrations have been noticed and become a concern since the 1960's, but it has not been well resolved. One reason is that the dynamic interaction between ice and a structure is so complicated that a practical ice force model has not been developed. The recent full scale tests conducted on jacket platforms in the Bohai Sea proved that ice could cause intense vibrations which endanger the facilities on the deck and make discomfort for the crew. In this paper, the strategy of mitigation of ice induced offshore structure vibration is discussed. Based on observation and understanding of the interaction between ice and a structure, the proposed mitigation approach, absorption method for suppressing of ice-induced vibrations is described. The numerical simulations were conducted for a structure attached with a TMD under ice force function and ice force time history to evaluate the performance of the TMD.

Keywords: ice resistant structure, ice-induced vibrations, vibration mitigation, TMD.

1. Introduction

The observations carried out in situ and laboratory have indicated that the cyclical forces can be formed and vibration can be exerted when ice sheet passing through a fixed narrow structure because of failure of ice sheet (Nadreau, 1987; Sodhi, 1987; Montgomery et al., 1980). It seems that the slender or compliant structure such as lighthouse, bridge pier, jacket oil platform and supporting structure of wind turbine will be more easily suffer from ice induced vibrations as their natural frequencies are close to the breaking frequency of ice. Full scale tests conducted on oil platforms in the Bohai Sea demonstrated that jacket structures, which can withstand maximum ice force, may endure intensive ice induced vibrations. The primary analysis disclosed that the vibrations may cause significant cyclical strain and threaten the facilities on the deck (Yue and Bi, 1998, 2000; Yue and Li, 2003). It is urgent to study the ways of suppressing or mitigating the vibrations.

Normally there are two approaches for designing compliant offshore structures to withstand the cyclical environmental force. The conventional way focuses on strength-based design, which enforce the structure, satisfy the requirement of fatigue life, namely, permits the vibration exist on the structure. This requirement can be easily satisfied at the stage of design. However, there have also been other spectacular and different failure modes, such as human comfort, motion-sensitive facilities on the platforms, like pipeline oscillation and flange leakage. For such kinds of requirements, strength-based design is hard to reach. The alternative approach is so-called motion-based design can deal with these issues, which takes its primary objective the satisfaction of motion-related design requirements such as restrictions on acceleration for human comfort or motion-sensitive equipments failure and find optimal mitigation strategies to achieve these design targets as well as satisfy the constraints on strength.

Structural motion control (Yao, 1972; Soong, 1997) is a cost-effective way to reduce vibrations induced by environmental excitations of slender structures, it is enabling technology of motion-based design to implement control device to suppress the structural vibration level to acceptable limits. Due to the structural control methods are more cost-effective, many researcher are attempting to explore its application to offshore structures. Abdel-Rohman (1996) studied the application of certain active and passive control mechanisms to reduce the dynamic response of steel jacket platform under wave-induced loading. Mahadik and Jangid (2003) studied the response of offshore platform with an active tuned mass damper. Due to passive control devices do not require external energy, many researcher conduct the related studies. Määttänen (1987) implemented the isolation device to the water-line structure to mitigate dynamic response of the light-house under ice loading. Kärnä (1994, 2004) discussed the effectiveness of adding TMD to mitigate ice-induced vibration for wind turbines. Patil and Jangid (2005) studied the response of offshore jacket platforms with different kinds of energy dissipation devices under wave loading. Although there had been several studies on mitigating vibrations for offshore structures under environmental loads. However, very few studies are reported on absorption methods to mitigate ice-induced vibrations for offshore platform. Regarding to passive supplementary device, like Tuned Mass Damper (TMD) have been widely and successfully implemented to suppress wind-induced vibrations in tall buildings (Kitamura et al., 1988; Ueda et al., 1992; Kwok et al., 1995), the idea of using TMD to suppress ice-induced vibrations for steel jacket offshore oil platform was presented.

In this study, the authors proposed a passive auxiliary device for mitigating the vibrations of an offshore platform using Tuned Mass Damper. The specific objectives of the study are:

1. Analyzing the characteristic of ice-induced vibrations based on field observation.
2. Comparing the commonly used passive strategies such as isolation, damping dissipation and dynamic vibration absorption, choose the best choice for suppressing ice-induced vibration.
3. Setting up the mathematic model of platform attached with a TMD, and conducting numerical simulations for the platform under simplified ice load function and directly measured ice force to check the performance of TMD system.

2. Ice-induced vibration

Considering the environmental conditions and oil deposit of the Bohai Sea, steel jacket platform is the priority for drilling and exploration of oil and gas. Two kinds of typical jacket platforms, vertical structure and conical structure, are commonly used in the JZ20-2 oil field, China. (Fig. 1).

During the period of platforms on services, intensive ice-induced vibration was found from field observations, and the results were astonishing. Yue and Zhang et al. (2001) studied the problems of ice-induced vibration of vertical structures based on full scale tests. Their results show that the maximum vibrations appear in the steady-state vibrations, as shown in Fig. 2. The occurrence times are more than twenty in a winter based on field measurements. And the longest time could last for over 15 minutes. The maximum amplitude of accelerations may reach to 0.6m/s^2.

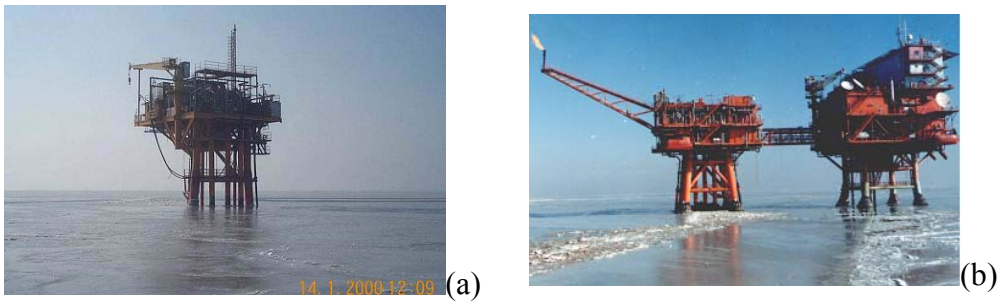

Figure 1. Typical jacket platforms in the Bohai Sea: (a) Vertical Structure-JZ20-2 MSW; (b) Conical Structure-JZ20-2 MNW & MUQ

To reduce ice-induced vibration, ice cones have been installed on several platforms. Investigations made by several researchers demonstrated the effectiveness of adding ice breaking cone in reducing ice force (Frederking and Schwarz, 1982, Shkhinek et al., 1996, Barker et al., 2005, Gravesen et al.,2005). However, Yue and Bi (1998, 2000) found that vibration still existed on platforms after cones had been installed on the legs of structures. They extensively investigated the dynamic response through field observation on MUQ and MNW platforms (see Fig. 1) in the Bohai Sea, their results revealed that ice force on conical structure appears the periodic characteristic and the dominant frequency of ice sheet could be close to the natural frequency of the structure when certain ice thickness occurred, which cause dynamic amplification of platform (see Fig. 3). The maximum acceleration response of deck could be up to 0.8m/s^2.

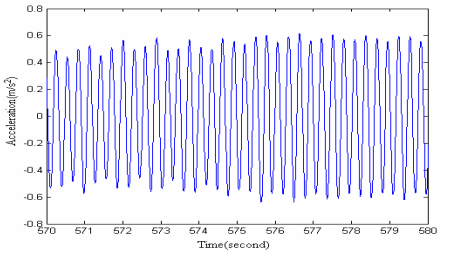

Figure 2. Steady-state vibration of vertical structure

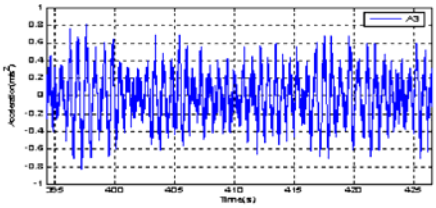

Figure 3.Ice-induced vibration of conical structure

As stated above, we can draw the conclusion that both vertical pile and conical pile of platform can be induced dynamic amplification by ice force. Excessive dynamic vibrations not only affect the working efficiency for personnel on the platform but also create damage to the pipeline and facilities on the platform. Besides these problems, fatigue of the structure is also a concern of the operator of these platforms. Therefore, not only from the view point of ice-resistant structure design but also from the viewpoint of workability and the comfort of personnel, the problem of ice-induced vibrations has become an important issue for discussion, in addition, effective measures have to be taken to lower the level of vibrations to acceptable limits.

3. Strategies of vibration mitigation

The feasible mitigation strategies under consideration for offshore structures are top isolation, damping dissipation and dynamic vibration absorption, respectively. The top isolation is a newly proposed isolation system, in which, the flexible laminated rubber bearings are inserted between the deck and the jacket columns that support it. However, the top isolation method can be only implemented to the newly built offshore structure, in addition, for huge topside of platform, is hard to meet the requirements of high performance of isolator. As for damping dissipation devices, like oil dampers, they need large relative deformation between components of platform when dissipate energy. However, field observation of platforms show that the relative deformation is so small that the purpose of using dampers to reduce vibration is unpractical.

Comparing to these two mitigation method, TMD is an optimal choice. It can be adjusted and implemented for newly built structure as well as existing structure. In general, the work of the tuned mass dampers is adding a secondary vibrating system to a main structure at resonance such that the natural frequency of the secondary system is tuned to the primary system and oscillates to counteract the motion of the primary system. The device is usually located at the top of the building and is connected through a passive spring and damper with the structure.

Considering the use of a TMD to mitigate ice-induced vibration of the platform, the first step is to determine if the undesired vibration response is dominated by a single frequency or whether several other frequencies need to be involved. Field observations (Yue, 2001) demonstrate that response of platform concentrate on its natural frequency. So, it is suitable to use TMD to mitigate ice-induced vibration. Fig. 4 shows the proposed schematic configuration of a TMD attaching to the deck of platform to reduce deck acceleration induced by ice load.

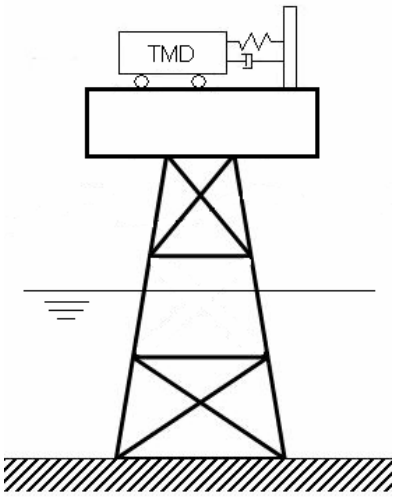

Figure 4. TMD placement scheme

4. Evaluation of vibration reduction

4.1 Description of the offshore platform

The platform studied in this work is a typical offshore platform, JZ20-2MUQ, a well-drilling and gas production platform located in the Bohai Bay. It is a four-leg steel jacket platform, the diameter of pile is 1.6 m and the maximum diameter of breaking cone is 4.3 m. Fig. 5 shows the general arrangements of sensors and instruments on it. It consists of two main components: superstructure and substructure.

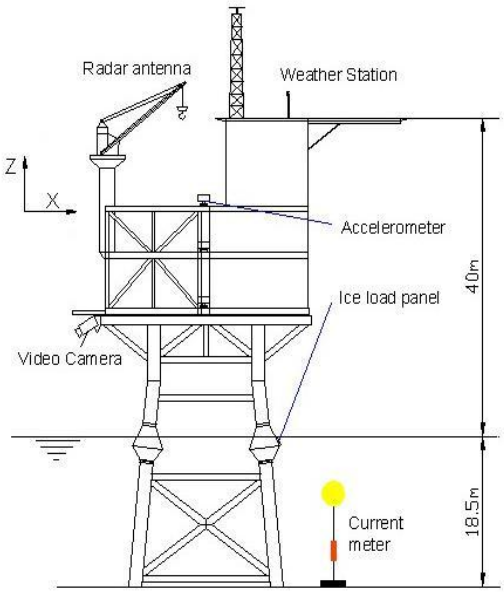

Figure 5. Sketch of JZ20-2 MUQ platform

The in-situ measured natural frequencies and damping ratios of the platform are summarized in Table 1.

Table 1. Main structural parameters for JZ20-2 MUQ platform

Topside mass	2576.8 tons
Jacket structure mass	550 tons
Structural damping ratio	2% of critical in X direction
Natural frequency- field measurement	0.87 Hz in X direction
Water depth	18.5 m

4.2 Mathematical Model of platform attached with a TMD

To simplify analysis, one needs only to consider the dominant modes of structural vibration that will be excited by ice-structure interaction. As stated above, field measurements show that platforms in the Bohai Sea have strong filter ability, they will oscillate at its fundamental frequency even under random ice force action that means the first mode is the most important mode to be concerned. So, it is sufficient to model the structure for its fundamental mode of vibration by single degree of freedom system. Fig. 6 shows the 2-SDOF schematic model of simplified platform attached with a TMD.

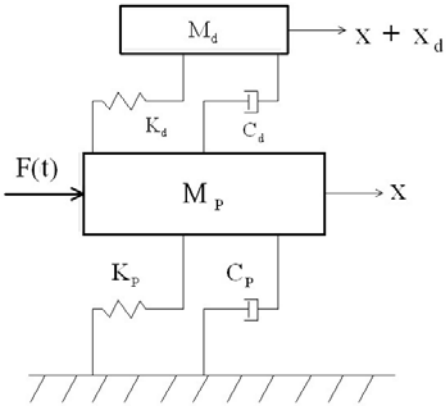

Figure 6. SDOF system coupled with a TMD

The equation of motion of main structure is

$$M_P\ddot{x} + C_P\dot{x} + K_P x = F(t) + F_e(t) \quad [1]$$

$$F_e(t) = C_d\dot{x}_d + K_d x_d \quad [2]$$

The effectiveness of a TMD can be evaluated in terms of equivalent damping force, $F_e(t)$, which is the combination of damping force and elastic force generated by the relative movement between TMD device and structure, as shown in Eq.2. Where x is the displacement of the general model of the platform, x_d is the relative displacement of TMD to the platform and F(t) is the interaction force generated by the ice sheet and the structure.

The effective fundamental mass can be simply obtained by the sum of superstructure mass and substructure mass. So, given the mass M_P, the fundamental natural frequency, and the damping ratio; the system's stiffness K_P, and the damping coefficient C_P can be determined accordingly. The parameters of SDOF system in the X direction are obtained as follows:

$$M_P = 3126.8 \text{ tons}, K_P = 9.3436 \times 10^4 \text{ kN/m and } C_P = 683.5 \text{ kN.s/m}$$

4.3 Parameters selection of TMD

According to Den Hartog's tuning formula (Den Hartog, 1956), the optimum frequency ratio is given by

$$f=\frac{1}{1+\mu},$$

Correspondingly, the damping coefficient

$$C_d=2M_d\omega_d\xi_d,$$

is selected such that the optimum value of the damping ratio, ξ_d, can be obtained by:

$$\xi_d=\sqrt{\frac{3\mu}{8(1+\mu)^3}},$$

Non-dimensional parameters were used to determine the passive TMDs and they are defined as follows:

$\mu=M_d/M_P$: TMD mass to platform mass ratio

$f=\omega_d/\omega_P$: tuning frequency ratio

$\xi_d=\frac{C_d}{2M_d\omega_d}$: TMD damping ratio

In general, the ratio of the mass of TMD to the fundamental generalized mass is set between 0.5% and 2%. A larger mass ratio provides more damping in the structure if the phase lag between the TMD and the structure is kept optimal. The mass ratio was selected to be 0.02 in this study, thus the optimum frequency ratio and TMD damping ratio are f=0.985, and $\varsigma_d=0.065$, respectively.

4.4 Simulation under ice load

Dynamic ice action acting on the structure, i.e. the forces on the structure varies with time, causes a response that varies with time. The time domain simulations are important parts of the design process since ice forces, platform responses, and TMD system movements also vary with

time. The model of 2-DOF was used to conduct these simulations to evaluate the performance of the TMD.

- **Ice load function**

Field observations show that dynamic ice force on an upward cone has a periodic characteristic. Accordingly, Yue and Bi (1998) introduced a model to describe the dynamic ice force, which accurately describes the failure process of ice sheets acting on the cones. The expression for the ice-load function is given in Eq. 3, where F_0 is the amplitude of total horizontal ice force on the cone. This value can be obtained from a static ice force tests or at ice speeds which do not cause dynamic amplification. Time τ represents the period of the breaking process of the ice, period T relates to the breaking length during interaction between ice sheet and cone. Here we assume that τ is about one third of T. Fig. 7 shows an illustration of the described ice load function for a cone.

$$F(t) = \begin{cases} F_0(1-\frac{t}{\tau}) & (0 \le t < \tau) \\ 0 & (\tau \le t < T) \end{cases} \quad [3]$$

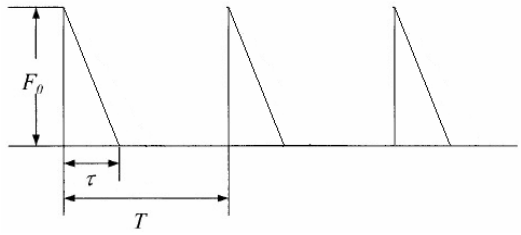

Figure 7. Dynamic ice-load function model

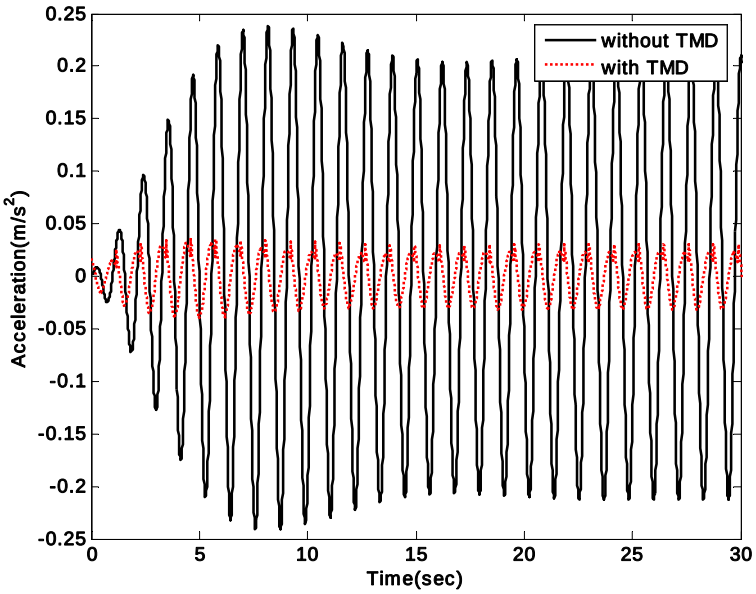

Figure 8. Response of platform model to ice load function

Based on long-term ice force measurements, we set the maximum amplitude of ice force to 55 kN and the frequency at 0.87 Hz. Fig. 8 shows the platform response subjected to the dynamic ice force excitation for the system with and without a TMD. From the simulation results, we can see that for the first couples of cycles, structural response is amplified and after several cycles, it reaches a steady state. The response seems harmonic because the period of ice force function corresponds with the natural oscillation period of the platform. It can also be seen that the TMD is very effective at reducing vibration, the peak value of acceleration decreases from 0.21 m/s^2 to 0.04 m/s^2.

- **Measured ice load**

The typical ice force time history recorded by an ice load panel on the up-ward cone was used to check the reduction effectiveness of TMD. As shown in Fig. 9, it can be found that the ice force has periodic characteristic, each of the peaks represents a breaking event. It should be noted here that the data just recorded from one channel that means it represents the local force. When considering use measured ice force to calculate the ice-induced response, total ice force has to be obtained by transformation. The average of peak ice force in this case is about 55 kN.

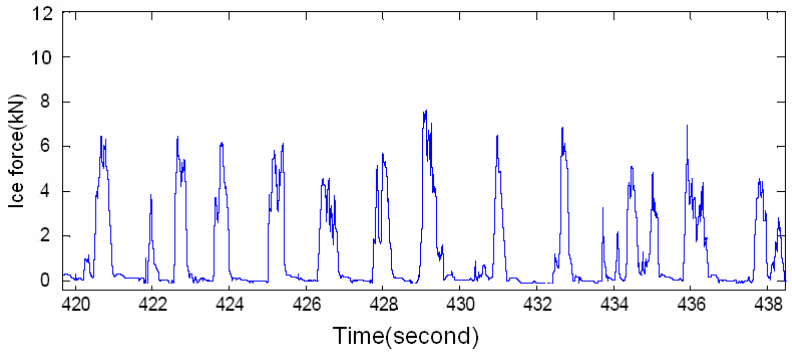

Figure 9. Measured ice force versus time on conical structure Qu, 2003

Fig.10 shows the time history response for two SDOF systems subjected to measured ice force time history. In this case, significant reduction in the acceleration response of the primary system is observed, the average peak of acceleration reduced from 0.107 m/s^2 to 0.04 m/s^2. The good performance is attributed to the effectiveness of tuned mass damper for narrow banded loading as well as its ability to reach a resonant condition and therefore the maximum effective damping force can be obtained.

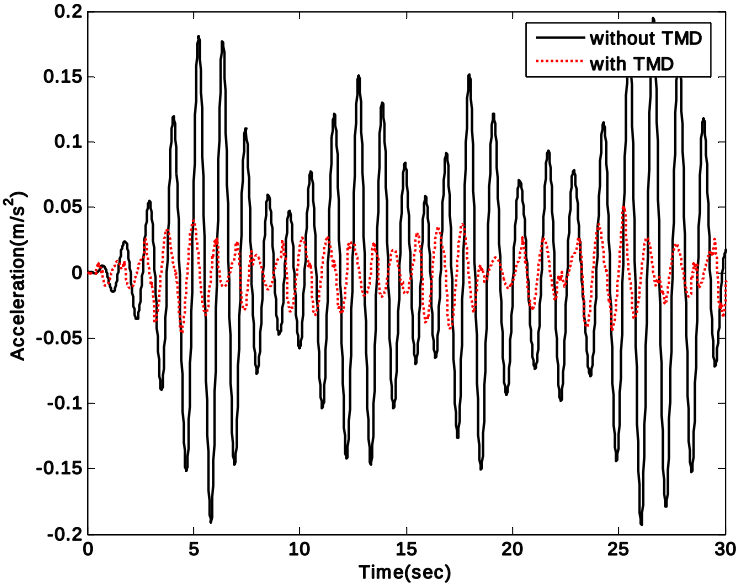

Figure 10. Response of platform model to ice load time history

5. Conclusions

Slender offshore structures, like lighthouse, bridge pier, jacket oil platform and wind turbine supporting structures etc. in ice-infested area are pone to ice-induced vibrations. For such kind of structures, it is hard to eliminated vibration totally, so, motion-based design strategy, which permits vibration exist and seeks optimal vibration mitigation methods to limit the level vibration to acceptable range according certain design objectives. As the enabling technology of motion-based design, structural control strategies are discussed for suppressing ice-induced vibrations for offshore structures. In this study, absorption method, Tuned Mass damper was proposed to be the optimal method comparing other types of methods, like isolation, damping dissipation. Based on full scale measurements for platforms in the Bohai Sea, the conceptual model of TMD device was presented, which is one-directional and sliding type TMD. To check the reduction effectiveness of TMD, numerical simulation was conducted on the JZ20-2 MUQ platform in the Bohai Sea under simplified ice load function and measured ice force time history, respectively. The results show that a TMD can favorably reduce the acceleration of platform, so this absorption mitigation method can be considered to employ to the design stage for the newly built platform as well as improve the performance of existing platforms.

Acknowledgements

The supports of the National High Technology Research and Development Program of China (No. 2001AA602015) and the National Natural Science Foundation of China (No. 10672029) are much appreciated. The authors also would like to thank Dr. Kärnä for kindly reviewing the paper and providing useful suggestions.

References

Abdel-Rohman, M., 1996. Structural control of steel jacket platform, Structural Engineering and Mechanics 4, pp. 25–38.

Barker, A., Timco, G., Gravesen, H. and Volund, P., 2005. Ice loading on a Danish wind turbines: Part 1. Dynamic model tests, Cold Regions Science and Technology. 41, pp. 1–23.

Den Hartog, J.P., 1956. Mechanical Vibrations, 4th ed., McGraw-Hill, New York.

Frederking, R. and Schwarz, J., 1982. Model test of ice forces on fixed and oscillating cones, Cold Regions Science and Technology .6. pp: 61–72.

Gravesen, H., Sorensen, S.L. and Volund, P., Barker, A. and Timco, G., 2005. Ice loading on Danish wind turbines: Part 2. Analyses of dynamic model test results, Cold Regions Science and Technology. 41, pp. 25–47.

Kärnä, T., 1994. Mitigation of steady-state vibrations induced by ice. Proc. 4th International Offshore and Polar Engineering Conference. Osaka, Japan. pp. 534–539.

Kärnä, T., Kolari, Kari . 2004. Mitigation of dynamic ice actions on offshore wind turbines. Proc. Of the third European Conference on Structural Control, 3ECSC. Vienna, Austria, July.

Kitamura, H., Fujita, T., Teramoto, T. and Kihara, H.,1988. Design and Analysis of a Tower Structure with A Tuned Mass Damper, Proc. 9th World Conf. Earthquake Eng., Tokyo, Japan.

Kwok, K.C.S. and Samali, B., 1995. Performance of tuned mass dampers under wind loads, Journal of Engineering Structure. 17. 655-667.

Määttänen, M. (1987). Ten Years of Ice-induced Vibration Isolation in Light-house, Proceedings of Offshore Mechanics and Arctic Engineering, Houston, TX, USA .Vol. 4, pp. 261–266.

Mahadik, A.S. and Jangid, R.S.,2003. Active control of offshore jacket platforms, International Shipbuilding Progress 50, pp. 277–295.

Masashi YAMAMOTO, Yoshiyuki SUZUKI. 2001. Practical applications of structural control systems to buildings in Japan. Journal of Earthquake Engineering and Engineering Vibration. Vol. 21, pp. 32-39.

Montgomery, C. J., Gerad, B., and Lipsett, A. W., 1980. Dynamic response of bridge piers to ice forces. Canadian Journal of Civil Engineering, Ottawa, Canada, 7, 345–356.

Nadreau, J. P., 1987. Ice-induced dynamic behavior of structures. C-CORE, Memorial Univ., St. John's, NF, Canada. pp. 30-34.

Patil, K.C. and Jangid, R.S., 2005. Passive control of offshore jacket platforms. Ocean Engineering, Vol. 32(16), pp. 1933-1949.

Qu,Y. Yue, Q.J. Bi, X.J. and karma, T., 2003. Random ice forces on conical structures, Proceeding of the 17th International Conference on Port and Ocean Engineering Under Arctic Conditions (POAC). Trondheim, Norway, pp. 259–270.

Shkhinek, K., Kapustiansky, S., and Jilenkov, A., 1996. Ice loads onto the sloping structures, International Conference on Development and Commercial Utilization of Technologies in Polar Regions, 24th–26th Sep. 1996, St. Petersburg, Russia), pp. 171–178.

Sodhi, D.S., Morris, C.E. and Cox, G.F.N., 1987. Dynamic analysis of failure modes on ice sheets encountering sloping structures, Proc. 6th Int. Conf. on Offshore Mechanics and Arctic Engineering. Houston. Vol.4, pp. 281-284.

Soong, T.T., Dargush G.F. ,1997. Passive Energy Dissipation Systems in Structural Engineering, Buffalo, USA. John Wiley & Sons.

Takayuki Teramoto, 2000. Japanese Structural Control system for Building, Advanced Technology in Structural Engineering, Structures Congress 2000, Philadelphia, Pennsylvania, USA.

Ueda, T., Nakagak, R. and Koshida, K., 1992. Suppression of wind-induced vibration by dynamic dampers in tower-like structures. Journal of Wind Engineering and Industrial Aerodynamics. 41-44. pp. 1907-1918.

Yao, J.T.P.,1972. Concept of Structural Control. Journal of Structural Division, ASCE. 98 (7), pp. 1567-1574.

Yue, Q.J., Bi X.J., 1998. Full-scale tests and analysis of dynamic interaction between ice sheet and conical structures, Proceeding of 14th International Association for Hydraulic Research (IAHR) Symposium on Ice, Vol. 2, pp. 939–945.

Yue, Q.J. and Bi, X.J., 2000. Ice-Induced Jacket Structure Vibrations in Bohai Sea. Joural of Cold Regions Engineering, Vol.14, No.2, pp. 81–92.

Yue, Q.J., Zhang, X., Bi, X.J. and Shi, Z.M., 2001. Measurement and analysis of ice induced steady state vibration. Proceedings of the 16th International Conference on Port and Ocean Engineering Under Arctic Conditions, vol. 1, pp. 413–420.

Yue, Q.J. and Li, L., 2003. Ice Problems in Bohai Sea Oil Exploitation, Proceeding of the 17th International Conference on Port and Ocean Engineering Under Arctic Conditions (POAC). Trondheim, Norway, June 16-19, pp. 151–163.

19th IAHR International Symposium on Ice
"Using New Technology to Understand Water-Ice Interaction"
Vancouver, British Columbia, Canada, July 6 to 11, 2008

Small-scale data on magnification of ice loads on vertical structures

Tuomo Kärnä[1], Fengwei Guo[1,2], Sveinung Løset[1] and Mauri Määttänen [3]
[1]*Norwegian University of Science and Technology, Norway*
[2]*Dalian University of Technology, China*
[3]*Helsinki University of Technology, Finland (Prof. emeritus)*

Abstract

This paper addresses a condition where a vertical faced structure is subjected to actions posed by sheet ice. Previous laboratory tests as well as full-scale experiments indicate that quasi-static loads can be magnified at a low ice speed if the structure is compliant. Further laboratory tests were carried out to investigate this phenomenon. The test set-up as well as the new results are described.

An extensive database that has been obtained by now shows that the ice load on a vertical structure attains its highest value in conditions where intermittent crushing is the dominating ice failure mode. The new data analyzed in this paper indicates that the waterline displacement of the structure can be used as an explanatory parameter. The new data also indicate that the maximum peak values of the ice load increase with the compliance of the structure, that is, with the waterline displacement.

1. Introduction

Peyton (1966) and Blenkarn (1970) provided field data on ice loads on cylindrical piles. They showed that the global ice load on a narrow and compliant pile may be increased by a factor of two when the ice speed decreased from a value of above 1 m/s to zero. Määttänen (1981) found a similar result while making laboratory indentation tests with a narrow pile. Furthermore, Rogers et al. (1986, Figs. 11 and 12) and Jefferies et al. (1988, Fig. 16) also found a velocity effect in the full-scale data that was obtained while the Molikpaq structure was deployed in 1980's in Tarsuit P-45 and Amauligak I-65.

Later on, Kamesaki et al. (1996) analyzed laboratory data on ice indentation with compliant model structures. Data were available from five test series that had been conducted using compliant vertical indentors. The results had been obtained independently by five different teams in three ice tanks. A reanalysis of the data showed that the global pressure $p_G = p_G(v, u_w, K_w)$ depends on ice velocity v, and the waterline displacement u_w, which is a function of the waterline stiffness K_w of the structure. The data indicated that the global load on a narrow structure may increase by 100% if a stiff model structure is substituted with a compliant structure.

New information on ice loads has recently been complied in the design standard S471-04. This standard does not recognize the earlier experimental findings showing that the external quasi-static global load as well as the local pressures on a compliant structure may be significantly higher than for a stiff structure. Therefore, the objective of this paper is to provide further data on this phenomenon.

2. Test set-up

A special model structure was constructed for laboratory tests. The details of the test set-up are described by Kärnä et al. (2003). Dynamic characteristics of this model structure were adjustable. Two geometrical parameters, H and h depicted in Fig. 1a, were used to vary the waterline stiffness of the structure. In addition, the stiffness of the joints between the model structure and the carriage were adjustable. Figure 1b shows a typical test condition where a cylindrical indenter is penetrating horizontally to the ice sheet.

The model structure was instrumented by using six accelerometers and two displacement transducers. One of the accelerometers was just above the ice level. The two displacement transducers allowed an approximate measurement of the waterline displacement of the indenter. Strain gauges were installed both in the horizontal and vertical beams of the tests structure. The calibration of these instruments was checked several times while building up the test set up and while making tests.

A system-identification approach was adopted to obtain the ice force signals from the measurements. The dynamic characteristics of each test structure were tested by static tests and by using an impact hammer technique (Kärnä et al. 2003). The results of these tests were then used to establish a two-degree of freedom model for the model structure. The ice force acting on the indentor was determined from this model by using two measured accelerations corresponding to this model.

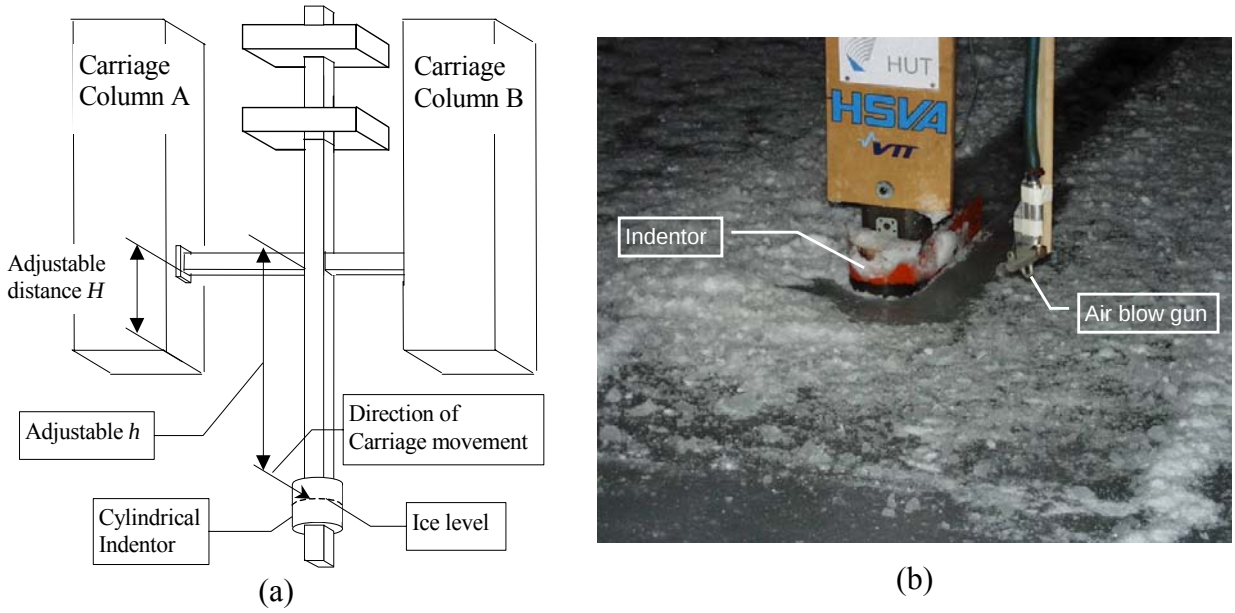

Figure 1. Sketch of the compliant structure (a) and an indentation test with a 114 mm wide cylindrical indentor (b).

The tests were made in the large ice basin of the Hamburg Ship Model Basin (HSVA). This ice basin is 78 m long and 10 m wide. The tests were done using columnar grained model ice. The ice was prepared using a conventional method where pre-cooled water having a salinity of 9 ppt was seeded to initiate the growing process of the ice. The salinity of the ice varied from 2.4 ppt to 4.6 ppt. The ice thickness varied in different ice sheets from 73 mm to 98 mm as shown in Table 1.

Table 1. Variations of the main test parameters. The width of the indentor was w = 114 mm.

Model structure	K (MN/m)	Sheet No	h (mm)	σ_c (MPa)	
				Mean	Stdv
SV5	1.62	1	93	0.486	0.138
SV6	1.29	1	97	0.486	0.265
SV6B	1.47	2	77	0.726	0.108
SV7	0.828	2	98	0.726	0.217
SV8	3.18	3	73	0.486	0.123

Five different variants of the model structure were used. The waterline stiffness was varied as shown in Table 1. The horizontal compressive strength σ_c was measured at different locations of each ice sheet using standard procedures of the test laboratory. The specimen temperature varied from -3°C to -5°C during the compression tests. Most of the actual indentation tests were done at an air temperature of -15°C. Table 1 shows the mean value and the standard deviation of the compressive strength for the three ice sheets that were used for the tests.

3. Data analysis

Categorizing the data

Several series of laboratory tests conducted by Sodhi (1998, 2001) and others with compliant indentors show that the ice crushing process changes its nature when the indentation speed v decreases from a value higher than about 0.1 m/s to a lower value below 0.05 m/s. At high indentation speeds the ice fails in a mode known as continuous brittle crushing. At a lower speed the failure mode is intermittent crushing.

Figure 2 shows typical records of the ice force and the response due to intermittent crushing. A salient feature for this failure mode is that the displacements of the structure play a major role in the ice failure process. Transient vibrations are triggered at each event of a major ice failure. These transients usually decay by the next event of ice failure. Therefore, a quasi-static static balance prevails at the moment of peak loading between the external loading and the internal stresses of the structure.

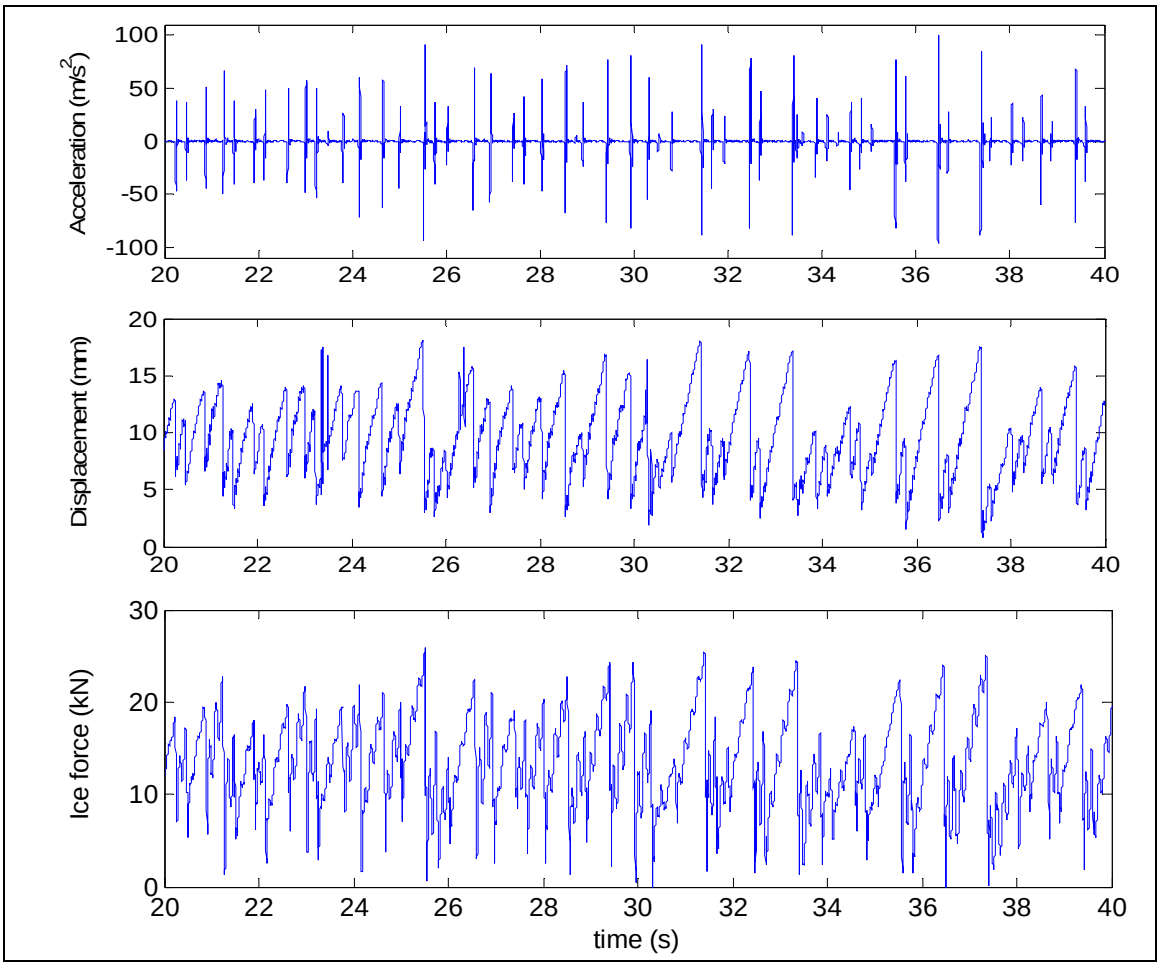

Figure 2. Typical records for the condition of intermittent crushing. Test SC6V-40, v = 40 mm/s.

Figure 3 shows typical records from a test where the ice failed in continuous brittle crushing. In this case the ice force can be characterized as a wide-band random process. A comparison of the

force records of Figures 2 and 3 shows that the peak values of the external load increase when the failure mode changes from continuous crushing into intermittent crushing.

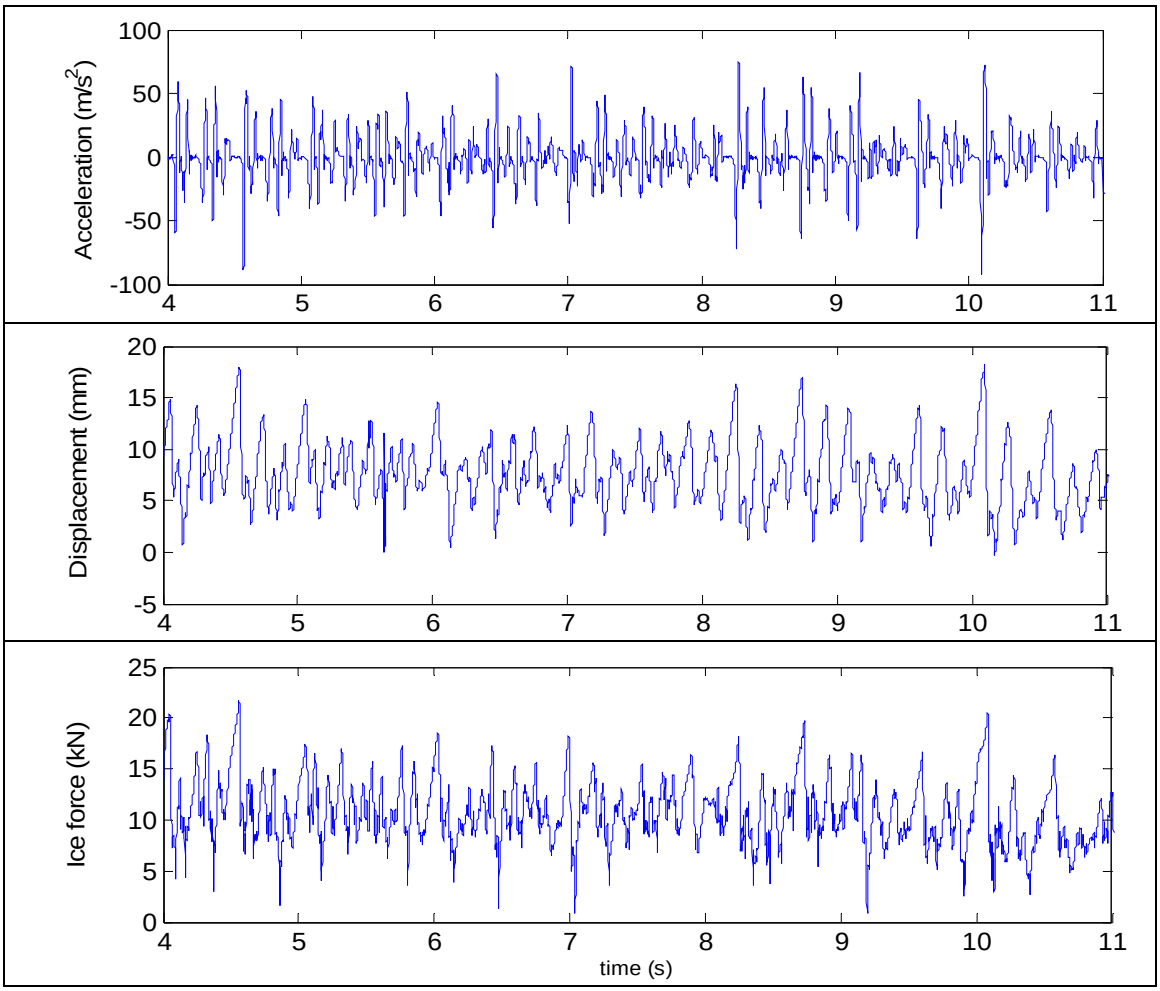

Figure 3. Typical records for the condition of continuous crushing. Test SV6V-200, v = 200 mm/s (Kärnä et al. 2003).

Method of data analysis

It was recognized that the ice strength varied in different areas of the ice sheets. It is deemed , therefore that an isolated maximum value of the ice force record is not the best representative of a test condition and -results. To avoid this problem the ice force was considered as a stochastic process and estimates of the maximum load were determined as follows.

The ice force was first divided to a mean component F^{mean} and a fluctuating component $F_D(t)$ as

$$F(t) = F^{mean} + F_D(t) \quad [1]$$

The maximum peak value of the force record was then estimated as

$$F^{\max} = F^{mean} + k\,\sigma_F \quad [2]$$

where σ_F is the standard deviation of the fluctuating force component. The parameter k was obtained from the expression

$$k = \sqrt{2\ln \nu_0 T} + \frac{0.5772}{\sqrt{2\ln \nu_0 T}} \quad [3]$$

where T is the duration of excitation and ν_0 is the zero-crossing frequency of the fluctuating force component. This expression provides an estimate of the maximum value of a parameter that constitutes a wide-band random process (Davenport, 1964). The zero-crossing frequency is obtained by calculating first spectral moments m_r (r = 0, 2) from the expression

$$m_r = \int_0^\infty f^r G_F(f)\, df \quad [4]$$

where $G_F(f)$ is the one-sided autospectral density function (PSD) of $F_D(t)$. Spectral moments are then used to obtain the zero-crossing frequency as

$$\nu_0 = \sqrt{\frac{m_2}{m_0}}\,. \quad [5]$$

The global pressure p_G was determined for each test as

$$p_G = \frac{F^{\max}}{w \cdot h} \quad [6]$$

where w = 114 mm is the width of the cylindrical indenter.

Normalizing the test results

Figure 4 shows the global pressures obtained in this test series. The results show that the global pressure is for each model structure approximately constant for indentation speeds higher than 100 mm/s or 150 mm/s. A significant magnification of the global pressures can be seen for indentation speeds v < 100 mm/s.

As shown in Table 1, the uniaxial compressive strength varied between the ice sheets and within each ice sheet. Therefore, the data were also investigated in terms of a non dimensional ice load. This was obtained by normalizing the maximum ice load by the expression

$$P_C = \frac{F^{\max}}{\sigma_c \cdot w \cdot h} \quad [7]$$

The results of this transformation are shown in Figure 5a.

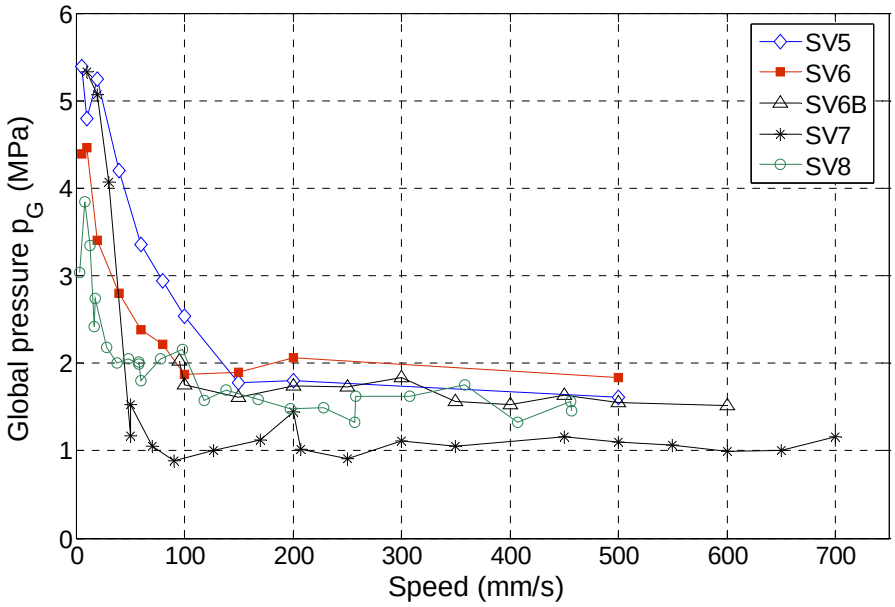

Figure 4. Influence of the indentation speed on the global pressure.

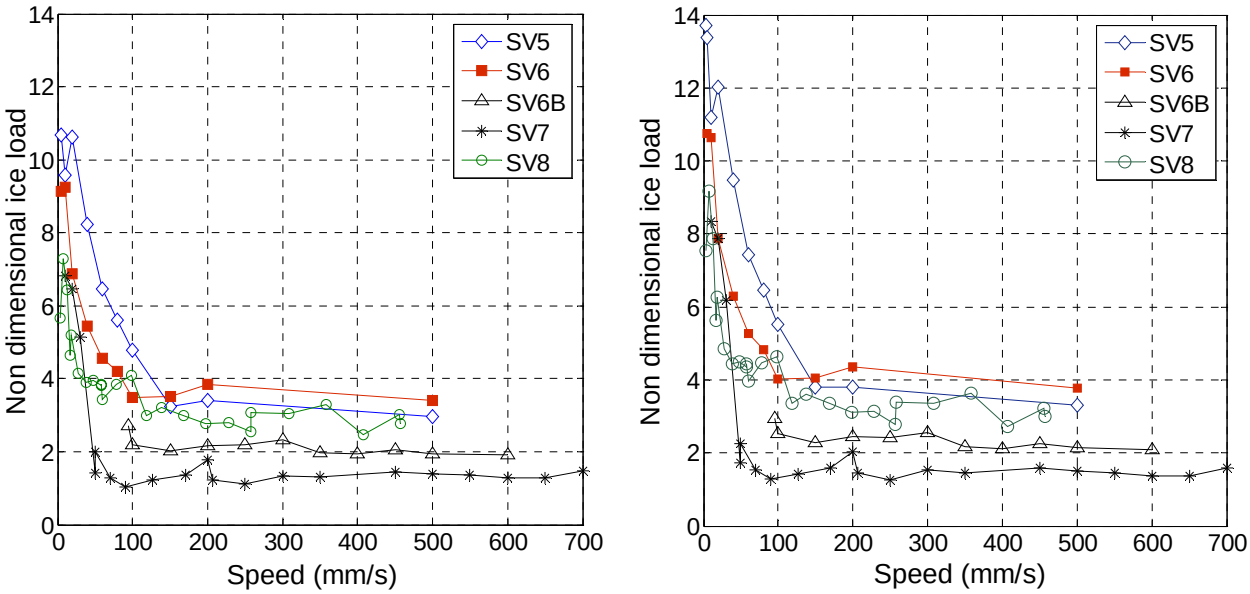

Figure 5. Non-dimensional ice load as a function of indentation speed. (a) Maximum values for each test. (b) Maximum values corresponding to a horizontal penetration distance of L = 50 m.

The duration T of ice action usually has an effect on the maximum value of the ice load. Depending on the indentation speed, the horizontal penetration distance L varied in these tests from 0.2 m to 3.8 m. Therefore, the influence of the test duration was studied in terms of the horizontal penetration distance L. Inserting $T = L/v$ into Eq. (3) yields

$$k(L) = \sqrt{2\ln(\nu_0 L/v)} + \frac{0.5772}{\sqrt{2\ln(\nu_0 L/v)}} \quad [8]$$

This expression can be used to transform the actual test results to correspond a standardized penetration distance L_s. Figure 6 shows how the coefficient k varies with the distance L. This plot is shown by using for the zero up-crossing frequency lower and upper bound values of 2 Hz and 10 Hz, which are relevant for the test data. It can be seen that the coefficient k depends strongly on the distance if $L < 5$ m. On the other hand, the changes in the coefficient k become small for $L > 50$ m.

Due to this parametric study, the test data was standardized to a penetration distance of $L_s = 50$ m. Figure 5b shows the non-dimensional ice load corresponding to this value of indentation distance.

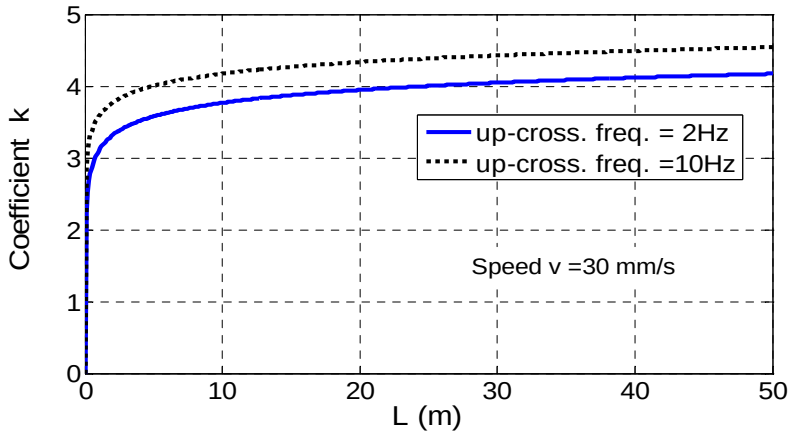

Figure 6. The functional relationship between the coefficient k and the vertical penetration distance.

Load magnification at low ice speeds

The results obtained above confirm that the characteristics of the two failure modes concerned are different. The maximum peak values of the ice load show little variations for indentation speeds from 100 mm/s to 700 mm/s. The ice failure mode is continuous brittle crushing in this speed range. However, the ice load increases with a decrease of the speed if $v < 100$ mm/s. In this range the ice fails in the mode known as intermittent crushing.

The increase of the ice load at low ice speeds is known as a speed effect or also a strain rate effect. On the other hand, recent results show that these higher ice loads are controlled in the conditions discussed here by the displacements of the structure (Sodhi, 1998, 2001; Kärnä and Järvinen, 1999). The higher ice loads can therefore be considered as a result of a magnifying effect, which arises while the ice failure mode changes from continuous into intermittent crushing.

It is proposed herein that the conditions of this transition as well as the amount of load magnification can be described by a compliance parameter. This parameter is defined as the ratio

between the quasi-static waterline displacement and the ice thickness. The waterline displacement is here taken as a value that arises in the conditions of continuous brittle crushing. In the present data this condition occurred when $v > 100$ mm/s or 150 mm/s.

Therefore, the compliance parameter was determined here for conditions of continuous brittle crushing as

$$C_o = \frac{u_{wb}}{h} = \frac{F^{av}_{brittle}}{K \cdot h} \qquad [9]$$

where u_{wb} is the quasi-static waterline displacement and $F^{av}_{brittle}$ is the average of the peak values of the ice load in the velocity range of $v > 150$ mm/s. Based on the measurements, Table 2 shows the compliance parameter C_o for each of the model structures.

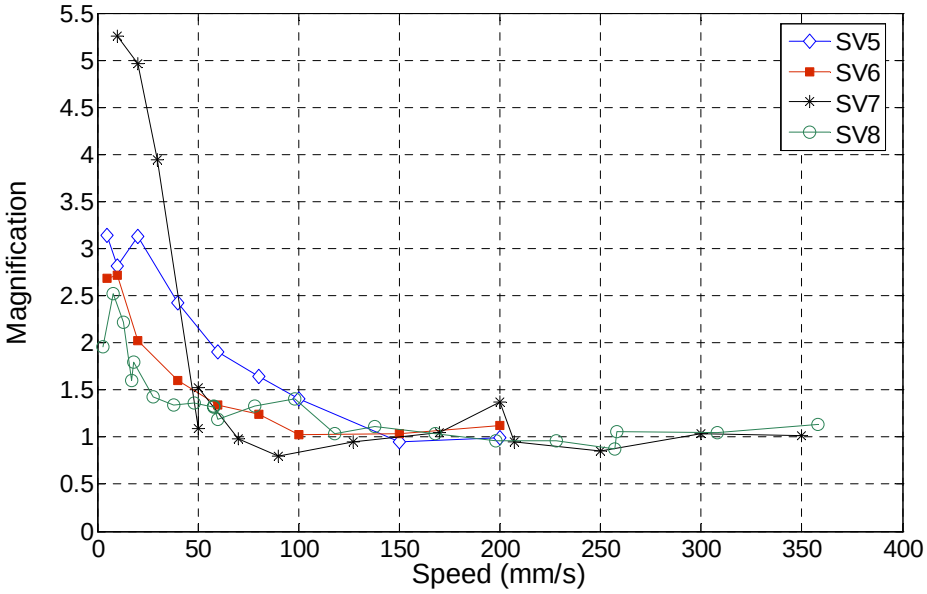

Figure 7. Load magnification at low indentation speeds.

Figures 4 and 5 show that the constant level of the peak loads is different for different test structures. Therefore the data shown in Fig. 5a were normalized further by dividing the non dimensional loads shown in Figure 4a by the average of the non-dimensional load values in the speed range of 150 mm/s to 300 mm/s. The results of this transformation are shown in Figure 7.

This figure shows for each model structure the amount of load magnification occurring at a low indentation speed. The amount of load magnification is also shown in Table 2 for each model structure along with the compliance parameter C_o.

Table 2. Magnification at low indentation speeds.

Model structure	K (MN/m)	$C_o = u_{wb}/h$	Maximum load magnification
SV7	0.83	0.128	5
SV6	1.29	0.127	2.8
SV5	1.62	0.096	3.2
SV8	3.18	0.05	2.5

4. Discussion

Based on several test series of ice actions on vertical structures, Sodhi (2001) has categorized different kinds of modes of ice crushing as shown in Figure 8. This figure suggests that the failure mode known as intermittent crushing will not arise if a structure is very rigid. This experience has been partly confirmed by full-scale tests on a lighthouse where saw-tooth patterned force signals, which are typical of intermittent crushing were met only in conditions of self-induced vibrations (Bjerkås, 2006; Kärnä et al., 2006).

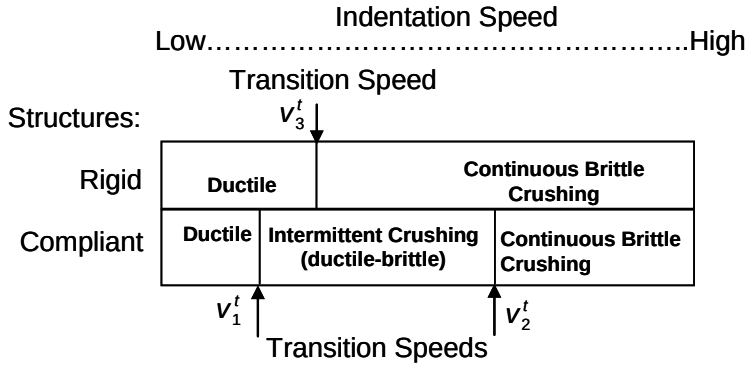

Figure 8. Failure map for ice crushing in terms of indentation speed and the type of structure (Sodhi, 2001). Notice that transition speeds for self-excited vibration are not shown in this figure.

The transition speed between ductile ice failure and intermittent crushing was in the present test series in the range of $v_1^t < 3$ mm/s. The transition speed between intermittent crushing was $v_1^t \approx 100$ mm/s, as shown in Figure 4. It should be appreciated that the results obtained in this paper are relevant for compliant structures. Magnification of the ice load is possible also in conditions where ice acts on a rigid narrow structure or on a local contact area of a rigid structure. The present data do not provide information on this kind of conditions.

Table 2 shows that the compliance parameter $C_o = u_{wb}/h$ varied in the present test series from 0.05 to 0.13. The highest loads were met for model structure at a low indentation speed around 10 mm/s. Table 2 also indicates that the load magnification increases with an increase of the compliance parameter. This tendency can be supported by the data that have been compiled in the lighthouse Norströmsgund in the Baltic Sea. The value of the compliance parameter can be estimated for this structure as 0.005 and the load magnification discussed herein equals to unity.

However, the data obtained in Table 2 are not fully conclusive. More data are needed on structures for which the compliance parameter is in the range from 0.01 to 0.05. It should also be appreciated that these tests were conducted in conditions where the aspect ratio was in the range of 1.2 to 1.6. Other phenomena such as the size effect and flexural failure modes will influence the ice loads of wide structures.

5. Conclusions

Several sets of laboratory tests as well as a few field tests show that ice loads acting on a vertical, compliant offshore structure assume their highest values at a relatively low ice speed. This phenomenon was studied in this paper by analyzing a set of laboratory tests where the stiffness of the model structure was variable. These results show that the maximum ice loads occur at a low ice speed while the ice fails in a mode known as intermittent crushing. This failure mode seems to produce ice loads that are more than two times higher than loads arising at a higher ice speed which promotes ice failure in continuous brittle crushing.

The results also indicate that the load magnification depends on a compliance parameter, which is defined as the ratio between the waterline displacement and the ice thickness. More data are needed to fully clarify how the displacements of the structure influence the maximum ice load.

Acknowledgments

The first and last author would like to thank the Hamburg Ship Model Basin (HSVA, ARCTECLAB), especially the ice tank crew, for the hospitality, technical support and professional execution of the tests that provided data for this paper. The acquisition of the data was financially supported by the Human Potential and Mobility Programme from the European Union through contract HPRI-CT-1999-00035. The authors also express their gratitude to the PETROMAKS program, the Research Council of Norway and to NTNU's PetroArctic project for funding the data analysis.

References

Bjerkås, M. (2006). Ice actions on offshore structures. Norwegian University of Science and Technology. Doctoral thesis, Trondheim, May 2006.

Blenkarn, K. (1970). Measurements and analysis of ice forces on Cook Inlet structures. Offshore Technology Conference. Houston, TX, USA, April 22-24. OTC 1261.

Davenport, A.G. (1964). Note on the distribution of the largest value of a random function with application to gust loading. *The Institution of Civil Engineering Proceedings*. London, Vol 28, pp. 187-196.

Jefferies, M.G. and Wright, W.H. (1988). Dynamic response of Molikpak to ice-structure interaction. Proc. 7th Int. Conf. Offshore Mech. and Arctic Eng., Houston, USA, Vol. 4, pp. 201-220.

Kamesaki, K., Yamauchi, Y and Kärnä, T. (1996) Ice force as a function of structural compliance. Proc. 13th Int. Symp. on Ice. Beijing, 1996. Vol. I, pp. 395 – 402.

Kärnä, T. & Järvinen, E. (1999). Symmetric and asymmetric flaking processes. Proc. 15th Int. Conf. Port Ocean Eng. under Arctic Cond. Helsinki, Finland, August 23-27. Vol 3. pp. 988-1000.

Kärnä, T., Kolari, K., Jochmann, P., Evers, K-U., Bi, X, Määttänen, M and Martonen, P. (2003). Ice action on compliant structures. VTT Research Notes 2223. Espoo 2003, 125 p.

Kärnä, T., Qu, Y. and Yue, Q.J. (2006). Baltic model of global ice forces on vertical structures. Proc. 18th International Symposium on Ice. Int. Ass. Hydr. Eng. Res. Sapporo, Japan, 28-31 Aug. 2006. Vol 1, pp. 253-260.

Määttänen, M. (1981). Laboratory tests for dynamic ice-structure interaction. *Eng. Struct.* 1981, Vo. 3, April, pp. 111-116.

Peyton. H. (1966), Sea Ice Strength. University of Alaska, Geophysical Institute, Report No UAG R-182, December 1966, 285 p.

Rogers, B.T., Hardy, M.D Neth, V.W and Metge, M. (1986). Performance monitoring of the Molikpaq while deployed at Tarsuit P-45. Proc. 3rd Canadian Marine Geotechn. Conf., St.Johns', Newfoundland, 11-13 June 1989.

Sodhi, D. (1998). Nonsimultaneous crushing during edge indentation of freshwater ice sheets. *Cold Regions Science and Technology* 27 (1998) 179-195.

Sodhi, D. (2001). Crushing failure during ice-structure interaction. *Engineering Fracture Mechanics* 68 (2001) 1889-1921.

S471-04. General requirements, design criteria, the environment, and loads. Canadian Standards Association. February 2004. 116 p.

19th IAHR International Symposium on Ice
"Using New Technology to Understand Water-Ice Interaction"
Vancouver, British Columbia, Canada, July 6 to 11, 2008

Field data on the magnification of ice loads on vertical structures

Michael Jefferies[1]
Tuomo Kärnä [2]
Sveinung Løset [2]

[1]Golder Associates, Vancouver, Canada (mjefferies@golder.com)
[2] Norwegian University of Science and Technology

ABSTRACT

This paper addresses interaction of vertical faced structures with moving sheet ice. Data had been obtained from narrow and compliant piles that we exposed to ice actions in Cook Inlet in late 1960's. This data showed that the highest ice loads were obtained at a low ice velocity while ice was failing in a ´ratcheting´ mode. The same phenomenon was termed subsequently as ´phase-locked crushing´ when it was encountered with the much wider Molikpaq structure in the Beaufort Sea in the 1980's. It has also been termed as ´intermittent crushing´ or ´alternating ductile-brittle crushing´ in reports on laboratory tests.

The main features of the Molikpaq data are reviewed and a typical condition of ice-structure interaction studied in detail. The data shows ice load can increase when ice velocity decreases below 0.1 m/s. Under these conditions the data shows a transition from non-simultaneous failure into simultaneous crushing. The overall or 'global' load on the structure increase by about a third because of the synchronized ice crushing.

The data obtained on the Molikpaq structure are compared with data obtained on the lighthouse Norströmsgund in the Baltic Sea. This structure is very stiff at the waterline. Comparisons between the two data sets support the conclusion that the maximum peak values of the ice load increase with the compliance of the structure, that is, with the waterline displacement. Waterline displacement appears to be the feedback mechanism synchronizing the usual non-simultaneous ice failure into a periodic, simultaneous ice crushing across the width of the structure.

1. Introduction

The discovery and exploitation of large oil reserves at Prudhoe Bay raised the possibility of similar resources in the adjacent Canadian Beaufort Shelf, given impetus by the oil price escalation in the early 1970s. Starting in 1972, three companies drilled exploration wells at 33 sites in the Beaufort shelf between the Mackenzie Delta in the west and extending to near the eastern limit of the Tuktoyaktuk Peninsula (see Figure 1). This area is ice covered for about nine months of the year, curtailing operation of drillships. The ice also moves, causing large loads on structures, so exploration adopted artificial islands supporting land-based drilling equipment.

Initially, islands were constructed in the near-shore zone. These islands were relatively inexpensive and easy to develop. As exploration continued, it moved progressively further offshore and into deeper water – eventually as much as 45 m water depth. In the early 1980's, all three companies changed from simple shallow beach islands to caisson type structures to cope with both the exponentially increasing cost and extended construction duration of the earlier simple island forms. This change from shallow beach slopes to near vertical side structures changed the interaction with moving ice. In the shallow beaches of the earlier islands, moving ice sheets could break up and form grounded rubble piles. With the deeper draft and near vertically sided caissons, moving ice could crush directly against the structure and be cleared away by ongoing ice movement – a very different situation from the accumulated experience. The possibility ice interaction with vertical sided structures might have a substantial cyclic aspect was essentially over-looked when all of the caissons were designed.

The uncertainty over ice loads was recognized in the Arctic offshore industry, with all three operators including ice load measurement systems on their structures. Substantial data was accumulated and over many ice loading events. This paper is based on experience with the Gulf Canada Resources platform 'Molikpaq', the structure being shown on Figure 2.

The Molikpaq, was deployed for wells at four sites in the Canadian Beaufort shelf: Tarsiut P-45 during 1984–85; Amauligak I-65 during 1985–86; Amauligak F-24 during 1986–87; and, Isserk I-15 during 1988–89. During 1989-97 the Molikpaq was in cold store at Hershel Island before being towed out of the Canadian Arctic for reconfiguration as an early production platform for the Sakhalin II field in the Sea of Okhotsk. It continues on site there today.

The information presented comes from the 1985-6 Amauligak I-65 deployment, some 75 km offshore and in 32 m depth of water. An ice interaction with the Molikpaq on 12 April 86 caused large loads and concern for platform stability. Unsurprisingly, this event has attracted interest and discussion. However, despite excellent reliability in early ice interaction events, the data acquisition system lost a file during 12 Apr 86, reducingprecision in the ice load measurement (the file contained key data). Subsequently, sensors and data acquisition were upgraded. A second event, on 12 May 86, provides clear ice-structure interaction data and this paper focusses on that event. Subsequently, we report trends from the whole season's experience.

The data presented here was originally documented and reported for a Joint Industry Project (JIP) with an extended confidentiality agreement. That agreement has now expired and the archived data is being transformed into accessible, public domain, files. Scales have been added to previously published figures while others come from the project files.

2. Molikpaq Description

2.1 Overview

In use, the Molikpaq is ballasted down onto a sand berm. The berm is constructed using hydraulically placed sand, with the berm providing the chosen set down depth for the Molikpaq (initially 19 m, subsequently 15 m depth). Figure 3 shows a section of the caisson as deployed on the berm at Amauligak I-65. The sand core provides about 80% of the resistance to ice load (depending on load level) with the caisson acting to reduce the volume of sand and to provide a convenient self-contained unit with all of the drilling and support systems. Information on the way the Molikpaq was deployed can be found in Jefferies et al (1985) – here we concentrate on the interaction of the structure with winter ice.

2.2 Ice Load Measurement

The Molikpaq was equipped with some five hundred transducers and a high speed digital data acquisition system (Jefferies et al, 1989). However, ice loading was by no means the only interest, with foundation behaviour, platform displacement, platform base contact pressures, platform dynamic response also being monitored.

Ice loads were primarily measured by 'Medof' panels deployed in three groups on each of the north and east face of the structure with a further group on the shorter north east face, see Figure 3. The three faces with Medof panels were chosen based on the anticipated direction for the ice movement. Medof panels were the norm for measuring ice load on the offshore platforms constructed in the 1980's. Medof panels only measure ice loads normal to the caisson. Shear forces, from ice sliding along the caisson, were not measured.

An unexpected part of the ice loading experience, apparent from first deployment of the Molikpaq in 1984, was that the ice/structure interaction had a frequency of ice load variation on the structure as high as 4 Hz and inducing extended periods of overall platform vibration with accelerations routinely in excess of 2% g (and in the 12 Apr 86 event exceeding 11% g). The Medof panels were unable to respond to ice load variation at these frequencies, the panels only registering slowly varying average loads.

The Molikpaq was equipped with an extensive set of strain gauges. It quickly became apparent after the first encounters with moving ice that the strain gauges on the upper strut of the bulkheads, essentially immediately behind the Medof panel array (see Figure 4), were highly correlated to loads measured by the adjacent Medof group. These "09" series strain gauges were adopted as the basic transducer for measuring the high frequency component of the ice loading. The 09 series strain gauges were distributed around the caisson matching the distribution of the Medof panels. However, as experienced accumulated and it became apparent that ice loading was from more than the NE sector, further strain gauges (and accelerometers) were installed. After April 1986, three bulkheads on each long side and one bulkhead on each short side, were instrumented with 09 series strain gauges – giving 360 deg coverage for ice load sensing.

Although the 09 strain gauge location was correlated to the ice load from the Medof panels, an ongoing question was the 'gauge factor' relating measured strain to load on the ice face of the bulkhead. Finite element studies, and experience, indicated that the gauge factor depended on the ice thickness. It also varies from bulkhead to bulkhead (presumed caused by local

installation details). A forward modelling approach was adopted to determine the strain gauge factor, implemented for each ice loading event and each group of Medof panels. In the forward modelling approach, the strain gauge factor is determined by computing an equivalent Medof load time series from the strain gauge data, using an assumed gauge factor and the mathematical model of each Medof panel. The estimated load time series from this preocedre is compared with that measured by the Medof panels. The assumed gauge factor is then adjusted, iteratively, to give the best fit. With the gauge factor thus established, the strain gauge can then be used to compute the true load time series. In this way, the integrity of ice load being traceable to the original dead-load calibration of the Medof panels is preserved while overcoming their limited frequency response. The key to forward modelling is an accurate mathematical model of the Medof panels implemented in a data processing algorithm.

The mathematical model of the Medof panels was developed after reviewing their calibration data. The creep and elastic response of the Medof panels was evaluated using data from two sources: (i) the calibration data provided by the manufacturer, Fenco; and, (ii) a series of calibrations by Geotech on two panels removed from the Tarsiut structure. These two panels were the same type as used on the Molikpaq, were fabricated by the same manufacturer, and had very similar calibrations. The purpose of testing the Tarsiut panels was to fully quantify the time dependent aspects of Medof response which were unclear from the original calibration. It was found that the response of each Medof panel to applied load could be represented by a five Kelvin elements in series. The first element comprised the panel stiffness coefficient and a dashpot with a 6 second period representing the compliance in the measuring system. The remaining four Kelvin elements were optimized for the panel creep response.

The reliability of the forward modelling method can be seen from two figures. Figure 5 shows an example of estimated load on the face of the Molikpaq from a group of three 09 strain gauges and the corresponding load-time series that would be observed by the matching group of Medof panels based on the mathematical model of the panels involved. Figure 6 shows the match between the equivalent-Medof response derived from the strain gauges and the actual measured load on the 60 m long north face of the Molikpaq during the ice loading event of 12 May 86. There match would seem impressive to an unbiased observer. Arguably, the strain gauge load factor has been underestimated as the match is very close at peak load but at the expense of average trends – a 5% increase in the strain gauge factor might be a better calibration depending on the preferred weighting between average versus peak load. Overall, forward modelling is more accurate than the correlation approach of Frederking & Sudom (2006).

2.3 Global vs Face Load

The octagonal shape of the Molikpaq has a perhaps poorly appreciated impact on the understanding of ice loading. When ice moves past the Molikpaq, the platform cuts a swathe about 90 m wide in the moving ice (see Figure 2). However, most of the instrumentation is concentrated on the ‘long’ 60 m faces with less instrumentation on the shorter corners. In particular the strain gauges used for measuring the high frequency aspects of ice-structure interaction displayed much greater linearity with load on the long face than the corner face. And, there is no measurement of shear forces on the corners. Finally, the ice itself often showed different failure modes at the short corner faces than on the long face.

Ice loads on the Molikpaq are reported at three levels. First, and most accurate, are the loads per unit length at the instrument locations. These are referred to in the Molikpaq documentation as 'local' loads and are accurate to about ±10% (varying from event to event depending on the uniformity of the ice thickness amongst other things). The next level of integration is the summation of local loads across a 60 m long face. This summation averages the three local loads and multiplies by the length of the face to give the 'face' load. Because of the way it is measured, the 'face' load is actually only the normal component. And, as three is not a good sample of random events, accuracy is degraded as well. Finally, the load exerted on the platform as a whole includes the vector sum of the face loads, the loads on the corner(s), and the unknown shear load. Because of the complexity of the ice failure modes at the corners the total load, referred to as the 'global' load in the Molikpaq documentation, is taken as 90/60 times the vector sum of the face loads – that is taking the average crushing pressure on the face (= 60 m) as applying over the cut swathe in the ice (= 90 m). The global load is the least accurate, about ± 25%. Face load accuracy lies between these limits. We note that Frederking & Sudom (2006) suggest a global load of approximately only 110% of the face load for the 12 Apr 86 event, a proportion that seems too low based on the caisson geometry.

Because of the uncertainties in ice-structure interaction on the corners of the Molikpaq, understanding ice-structure interaction seems easiest if carried out only in terms of the reasonably well measured face loads. We only discuss face loads in this paper.

2.4 Data Acquisition

Two independent data acquisition systems were installed, referred to as 'slow' and a 'burst' in the Molikpaq archive, controlled by a common HP200 series microcomputer. The basis of each system was a HP6944 'multiprogrammer', devices that sequenced through the channels recording voltages and converting them to digital records. The multiprogrammers were controlled by custom software on the HP200, interfacing using the manufacturers HP-IB (instrumentation bus) protocol. In essence, this was high end scientific instrument logging for the era (1984) with the greatest limitation being data storage – the recorded data on each system was limited to 15 MB because of the available hard drive size.

The slow scan unit was used for long term monitoring of all transducers, allowing the recording of extended platform response with all 500 transducers within the storage limit. The slow scanner had two modes of operation, one scanning at 0.3 Hz with mean, minimum and maximum values over a five minute averaging period and the other operating at 1 Hz with all scan data stored to file. Automated triggering, driven by the software on the HP200 computer, was used to change modes. The 1Hz files are referred to as 'fast' files within the Molikpaq archive and the file numbers all start with the letter 'F'. Files are identified by a number indicating the date and start time. There was sufficient data storage for extended monitoring at 1 Hz and it is these files that form much of the overall picture of ice-structure interaction.

The slow scan system could not record the 'dynamic' ice interactions because of the Nyquist limit and the systems maximum 1 Hz scan rate. A second, high-speed data acquisition system sampling at 50 Hz was provided for monitoring cyclic ice action but, because of compromises in the filters, real measurements are in the DC – 10 Hz range. Limited mass storage had two effects on the data acquisition strategy for the high speed (burst) system. First, only a quarter of the

transducers (actually 128) were connected to it. This subset related to the measurement of transient load and response and included ice face bulkhead strain gauges (for load measurement), servo accelerometers (for caisson/core response) and the electric core piezometers (for cyclic excess pore water pressures). Second, the mass storage allowed only three 90 second files of burst data before the hard drive had to be downloaded (manually) to tape back-up. Because of the very limited duration of the burst measurements, which in effect were only a sample within the general picture revealed by the longer term fast files, the burst system was configured with a recursive memory buffer. This buffer allowed continuous high speed scanning but the data was only stored onto a burst file when one of twelve designated trigger channels exceeded a threshold value. Several seconds of data preceding the event trigger were recoverable from the rolling memory buffer. Threshold values were keyboard selectable and automatically increased after each burst file had been triggered, a technique that allowed a series of snapshots to capture the response at the critical moments. Burst files all start with the letter "E" (for event) followed by the date and time at which the burst mode was initiated.

Both burst and fast files were controlled by the same computer with the same clock. There is no difficulty in comparing the two file types as their way they were acquired ensures a common time base. In fact his is an essential aspect as the Medof panels are only recorded as fast files.

2.5 Ice Thickness and Velocity Measurement

The Molikpaq was not equipped with upward looking sonar or any other method for real time measurement of ice thickness. Knowledge of ice thickness was developed from three sources: on-ice surveys; observations of ice fragments; and the Medof panels.

For several loading events the ice was stationary around the Molikpaq for days (or more) ahead of the event. When this allowed, ice observers got onto the ice to drill cored holes and to survey the upstanding pressure ridges. These surveys allow for a good appreciation of the mean and standard deviation of ice thickness, although some holes were fortuitously located so that a thickness-time correlation could be developed for the subsequent ice loading. It was also possible, after some events, to get on ice and survey the ice adjacent to the wake cut by the passage of ice past the structure. The Molikpaq was equipped with video cameras and recorders to document the ice structure interaction, and there was an enthusiastic team of ice observers on the structure documenting the ice failure against the structure. These approaches allowed an assessment of ice thickness, from visual observation looking down at the ice from deck level, when the ice fragmented (as opposed to crushed). Finally, the Medof panels were deployed in a vertical array. If the lowest panel displayed a loading, then the ice was necessarily greater than 2.8 m thick.

Ice velocity was generally well monitored with radar tracking at the larger distances and timing of identified features moving within the calibrated view of the video cameras for close in speeds.

3. The 12 May 86 Ice Loading Event

The process by which phase-locking develops can be understood from the 12 May 86 event as, not only does this event provide a full data set for phase-locked crushing during dynamic loading of the north face in 2 – 3 m thick ice, but it also has extensive documentation of the ice velocity. Most intriguingly, this was an event where the transition from non-simultaneous to phase-locked

crushing was captured on the high speed data record as the ice moved into, and out of, phase-locking several times (in the first two event files) before large amplitude phase locked motion became established later in the event (in the third event file) as the ice slowed down. Arguably, from an ice mechanics view, the 12 May 86 event is by far the most useful of the whole 1986 experience. Some aspects of the 12 May 86 event have been reported by Timco et al (2005). Other aspects of that event were presented in Jefferies & Wright (1988), although without all the details because of the confidentiality agreement then in force.

The 12 May 86 event developed as a 7km by 15 km floe of thick first-year ice with several large multi- year floes embedded within it moved towards the Molikpaq in open water at a constant drift speed of 0.18 m/s. The interaction brought the drift of this flow to a standstill. An aerial reconnaissance photograph after the event, Figure 7, gives an illustration of the situation although this photograph misses the ice loading on the northwest corner as that part of the floe broke away mid-way through the event. Figure 8 shows the ice flow velocity during the interaction based on a detailed evaluation of the video recorded from the fixed camera on the platform (this analysis was carried out by Wes Wright, P.Eng., reproduced here from the files).

The initial impact of the ice with the structure was noted to be at 0301 hrs, but load did not begin to develop until ten minutes later (Figure 6) based on the fast file data. The first burst file was triggered at 03:20:10 when the face load first exceeded 150 MN. A ten-second window of data from this burst file is shown on Figure 9. The first five seconds of this record shows the usual non-simultaneous failure situation with the three loaded zones with statistically similar variation but on different time bases. However, at about 4 seconds, and in no more than 1.5 seconds further, the three loading zones become synchronized in time. This transition is in less than three cycles of the subsequent ice load cycling. The transition from an incoherent oscillation to a coherent one is a known aspect of non-linear dynamic systems in the presence of feedback, the presumed feedback mechanism being the stiffness of the Molikpaq steel caisson which enforces commonality of motion across the entire loaded face. The response was called ‘phase locking’ as that is the general terminology applied to this phenomenon in the study in the dynamics of non-linear systems. An accessible overview of this subject can be found in Glieck (1997).

The very different response of the Molikpaq under phase-locking can be seen from the acceleration record of the mid-side accelerometer mounted near the top of the bulkhead and also plotted on Figure 9. During the non-simultaneous loading, the Molikpaq vibrates but only gently – it is a true randomly excited vibration. However, when the ice crushing synchronized, then the Molikpaq responded with a violent five-fold increase in acceleration.

The nature of the phase-locked loading changed with the ice velocity. During the first burst file, the ice was moving at about 0.09 m/s and the ice-structure interaction was drifting in and out of phase-locking. However, as the ice slowed to about 0.02 m/s, the phase-locked interaction became well established with the characteristic saw-tooth like waveform. Figure 10 presents the data from the third burst file, triggered at 03:25:03 which shows this aspect. Figure 10a is the data as recorded using the unit load calibration procedure described previously. Figure 10b is the same line load data converted to pressure using the ice thickness from the ice observers records (3.5 m in the middle of the face, 2.8m at the east end, 1.8m at the west end).

4. Ice Interaction with Molikpaq 1985-86

The amplified ice loading, when the ice crushing became synchronized across the entire caisson, occupied only a few hours out of the many thousand of hours of structure interaction with moving ice. Most interactions were of the conventionally understood 'non-simultaneous failure' or creep types. For the JIP, the season's data files were examined to identify good records for evaluation of these amplified loading events. The criteria used were: presence of cyclic loading; data available in burst files (i.e. at 50 Hz scanning); field documentation on ice thickness, ice velocity, and other environmental parameters. A total of five events met these criteria and are listed in Table 1 together with some key parameters about them.

Table 1: Amplified cyclic loading events with adequate recorded data for detailed analysis

Date/Time	Synopsis	Ice Thickness & Velocity	Peak Face Load	Crushing Pressure
17 Feb 86 04:01 – 05:30	Common example of moving first year ice. Ice failure was generally crushing with occasional flexural failure when the weight of crushed ice accumulated on top of the ice sheet became too great. Loading was directly on E face with good records. One fast file, three burst files.	0.6 m ±0.1 m 0.03 – 0.06 m/s @ ≈ 90 deg .	60 MN	1.7 MPa
7 Mar 86 15:20 – 17:40	Complex event with two MY floes welded by FY ice. Ice contact was complete on west, northwest and north faces, so the loading only partially captured by the sensors on north face. Cracks in the ice sheet formed early in the event (1545hrs) but did not widen significantly until the end of the event. Two fast files, six burst files.	5m – 6m in MY ice, but < 2.8m for most of the loading ≈ 0.05 m/s @ 145 – 170 deg	300 MN	1.3 MPa
12 April 86 08:28– 08:36	The major load event on the Molikpaq. Crushing of 2 km×1km multi-year floe against the east face. However, the large 9 m multi-year hummock appears to have not crushed, with flexural failure behind it. Three burst files only, hard drive failure leading to loss of fast file data.	3.5 m ± 1 m ≈ 0.06 m/s @ ≈ 90 deg	400 MN	1.5 MPa
12 May 86 03:09–03: 40	Impact of large flow containing thick first year ice with multi-year inclusions. Loading was essentially on the north face, see Figure 7, with excellent records. One fast file, three burst files.	2.7 m ±0.8 m 0.1 m/s decreasing steadily to creep, see Figure 8	250 MN	1.4 MPa
25 June 86 05:01–06:30	Impact of warm first year ice floe (puddles of melt water on ice surface) on west face.	2.1 m ±0.4 m 0.1m/s decelerating to zero	115 MN	0.8 MPa

Data from these five events was systematically evaluated in the JIP. An interesting characteristic of phase-locked loading is the similarity of load-time series shape over a wide range of interactions, allowing data reduction to key parameters: the repeat frequency of the peak loads; the amplitude of the cyclic component (i.e. peak to minimum on a per cycle basis), and the unloading rate. Figure 11 shows the results of interrogating the data to identify conditions associated with occurrence of phase-locked loading, limiting the evaluation to first-year ice only. The data suggests phase-locked loading does not occur in the case of the Molikpaq for velocities greater than about 0.1 m/s but that it can be a common mode with ice velocity of 0.05 m/s.

The normalized amplitude of the phase-locked loading is defined as *(peak – trough)/peak* and this amplitude is plotted against peak load itself on Figure 12. Figure 12 includes all the individual cycles from the event files identified in Table 1. Normalized amplitudes in excess of 0.4 are not uncommon during phase locked loading.

This phase-locked loading can be viewed as an increase in load over the non-simultaneous situation. In non-simultaneous ice crushing, the structure sees an average load across the face. During the transition to phase-locked loading, half the amplitude will appear as a sudden step increase in loading. The Molikpaq data shows that ice loads 25% to 30 % greater than conventionally expected can arise, very quickly, purely as a consequence of phase-locking. This estimate was confirmed in a reanalysis (Fig. 4, Kärnä et al. 2006) of the Molikpaq data provided by Timco and Johnston (2004).

5. Comparisons with other experimental experiences

When the phase locking was first encountered with the Molikpaq, those involved thought it was a new aspect of ice loading. But, on investigating the literature (after the 1986 experience…) it became obvious that the same phenomenon had been encountered much earlier with the Cook Inlet structures. Peyton (1966) and Blenkarn (1970) measured the performance of narrow piles that were exposed to moving ice in Cook Inlet. At velocities of more than about 0.1 m/s, the ice failed by brittle crushing on the vertical pile with a time-varying ice action that had a wide-band random character. When the ice speed decreased below 0.1 m/s, the mode of the time-varying ice-structure interaction changed - the ice force assumed a saw-tooth pattern while the peak values of the ice force increased by a factor of two. A closer study showed that transient vibrations of the structure were triggered at each event of ice failure. Blenkarn (1970) shows this feature in his Fig. 16. In most conditions, these vibrations cease before the next event of ice failure with periods of quasi-static load increase until the next failure event. No dynamic magnification is involved with the structure. The phenomena described by Blenkarn (1970) can be found in the Molikpaq records shown in Fig. 9 and Fig. 12 of Jefferies et al. (1988). Vibrations that are associated with the dynamic ice action have a transient nature, decaying rapidly from the strong inertial response on the unloading occurring at the intermittent ice crushing. This kind of ice-structure interaction is very different from self-excited vibration where the response is in a steady-state mode at a natural frequency of the structure.

Further comparisons can be made with small scale data reported by Kamesaki et al. (1996), and Kärnä et al. (2008). The tests reported in these two papers were made in four different ice tanks using either model ice or freshwater ice. These papers propose that the phase locked (intermittent) crushing is a process that is controlled by the displacements of the structure. The

phenomenon is, therefore, relevant in conditions where the structure can experience significant displacement at the waterline. The data indicates that the global ice load acting on a narrow structure can increase by a factor of two or more if the waterline displacements of the structure are in excess of 1% of the ice thickness. Sodhi and Haehnel (2003) summarize their long-term experiences on small scale tests by saying that *'the effective pressure depends on the relative indentation speed, which in turn depends on the speed of a moving ice floe and the compliance of a structure'*. Analysis of several laboratory tests on compliant, narrow model structures indicate (Kamesaki et al. 1996; Sodhi and Haehnel 2003; Kärnä et al. 2008) that the change from a random ice failure into phased-locked into simultaneous failure occurs when the ice speed decreases to a range below 0.1 m/s. This experience is in a fair agreement with the Molikpaq data shown in Fig. 11.

Recently, field data have been compiled on the lighthouse Norströmsgrund in the Gulf of Bothnia (Schwarz and Jochmann, 2001). Data analysis shows (Kärnä et al. 2006) that local pressures acting on this structure may increase when the ice velocity slows down to the range below 0.01 m/s. Ductile deformations that occur at the ice edge in such ice speeds can significantly modify the contact conditions and enhance local loads. However, global loads acting on this structure did not exhibit any increase at low ice speeds. Phase-locked ice actions have been recorded on this structure, but only in conditions where the structure experiences steady-state vibrations (Bjerkås 2006). Phase-locked (intermittent crushing) that is associated with transient vibrations have not been met in the lighthouse Norströmsgrund.

The static stiffness of the lighthouse Norströmsgrund has been estimated as 1700 MN/m at the waterline. Hence, the waterline displacements are less than 2 mm in operational conditions, where the ice thickness is in the range of $h < 0.6$ m. These displacements are less than 0.3 % of the ice thickness. In the Molikpaq's event of 12 May 1986, the extensometers showed total deformations up to 40 mm (Fig. 7, Timco et al. 2005). Therefore, it is apparent that the ratio between the waterline displacements and the ice thickness was much higher in the May 12 event of Molikpaq than experienced by the Norströmsgrund lighthouse. The difference in the compliances of the Molikpaq and Norströmsgrund structures appears to explain the differences in ice-structure interactions experienced by these two structures. Waterline displacements of a vertical structure appear to provide a feed-back effect that can create an increase in the ice load. This increase can be significant in compliant, narrow structures, but should be considered also in the design of wide structures if the structure is compliant at the waterline.

6. Conclusion

The ice failure mode during crushing of moving ice against a structure is normally one with spatial variability in terms of load at a particular time. However, under certain ice conditions, the structure deflection under load can act to impose a feedback on the ice crushing. Under this feedback, the crushing of ice in the local zones becomes synchronized in time and leads to a characteristic 'saw tooth' like loading with an immediate increase in the peak ice force by as much as 25%. For narrow structures this increase can be up to 100 %. The measured accelerations show that this feedback is not 'resonance' – there are essentially no inertial components to the ice loading. The dynamic aspect arises on synchronized ice crushing at peak load, leading to a flyback of the structure as the load drops to its minimum value. The subsequent structural vibration is very heavily damped, presumably by the crushed ice against the structure.

When first encountered with the Molikpaq, those involved thought that this type of synchronized ice failure was a new phenomenon. It has become clear since that the Cook Inlet structures experienced exactly the same situation 25 years earlier, unfortunately not recognized when the Molikpaq was designed. Laboratory tests that several research teams have conducted on compliant model structures in 1990's and 2000's confirm findings reported in this paper. On the other hand, field data obtained on a lighthouse in the Baltic Sea indicate that an increase in the global quasi-static ice load may not arise if the structure is very stiff at the waterline.

References

Bjerkås, M. , Skiple, A. (2005). Occurrence of intermittent and continuous crushing during ice-structure interaction. Proc. 18th Int. Conf. Port Ocean Eng. under Arctic Cond. Potsdam, NY, USA, Vol. 3, pp. 136-145.

Blenkarn, K. (1970). Measurements and analysis of ice forces on Cook Inlet structures. Offshore Technology Conference. Houston, TX, USA, April 22-24. OTC 1261.

Frederking, R. & Sudom, D. (2006). Maximum ice force on the Molikpaq during the April 12, 1986 even. Cold Regions Science & Technology.

Glieck, J. (1997). Chaos: The making of a new science. Vintage.

Jefferies, M.G., Stewart, H.R., Thomson, R.A.A. and Rogers, B.T. (1985). Molikpaq deployment at Tarsuit P-45. Proc. ASCE Spec. Conf. 'Arctic 85', pp. 1-27.

Jefferies, M.G., Hardy, M.D., and Rogers, B.T. (1989); Instrumentation and monitoring of an offshore arctic platform. In: *Geotech Iinstrumentation in Practice*, 735-748 & 802-803. Thomas Telford, London. ISBN 0 7277 1515 1.

Jefferies, M.G. and Wright, W.H. (1988). Dynamic response of Molikpak to ice-structure interaction. Proc. 7th Int. Conf. Offshore Mech. and Arctic Eng., Houston, USA, Vol. 4, pp. 201-220.

Kamesaki, K., Yamauchi, Y. and Kärnä, T. (1996). Ice force as a function of structural compliance. Proc. IAHR Ice Symposium, Beijing, China, August 27-30, Vol. 1, pp. 396-402.

Kärnä, T., Qu, Y. and Yue, Q. (2006). Extended Baltic model of global ice forces. Proc.18th International Symposium on Ice. Int. Ass. Hydr. Eng. Res. Sapporo, Japan, 28-31 Aug. 2006. Vol. 2, pp. 261-268.

Kärnä, T., Guo, F., Løset, S. and Määttänen, M, (2008). Small-scale data on magnification of ice loads on vertical structures. Proc. 19th IAHR International Symposium on Ice. Vancouver, Canada, July 6-11 (in the same proceedings as this paper).

Peyton. H. (1966), Sea Ice Strength. University of Alaska, Geophysical Institute, Report No UAG R-182, December 1966, 285 p.

Schwarz, J. and Jochmann, P. (2001). Ice force measurements within the LOLIEF project. Proc. 16th INt. Conf. Port Ocean Eng. under Arctic Cond. Ottawa, Canada, August 12-17. Vol. 2, pp. 669-680.

Sodhi, D. and Faehnel, R. (2003). Crushing ice forces on structures. *J. Cold Regions Engineering*. Vol. 17, NO. 4., pp. 153-170.

Timco, G.W. and Johnston, M. (2004). Ice loads on the caisson structures in the Canadian Beaufort Sea. *Cold Regions Science and Technology*, Vol. 38, pp. 185 – 209.

Timco, G.W., Johnston,M.E. and Wright, B.D. (2005). Multi-year ice loads on the Molikpaq_ May 12, 1986 Event. Proc. 18th INt. Conf. Port Ocean Eng. under Arctic Cond., Potsdam, NY, USA, Vol. 1, pp. 453-462,

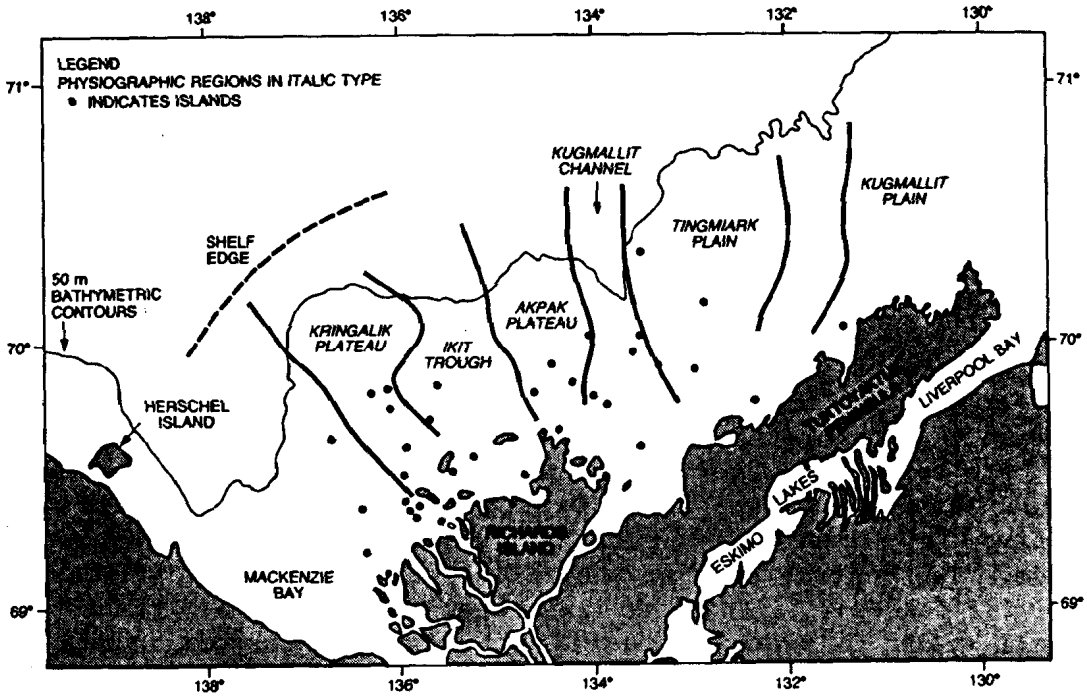

Figure 1. Offshore island locations in Canadian Beaufort Sea

Figure 2. Photograph of Molikpaq in moving first year ice (note arrangement of short and long sides forming the octagonal plan)

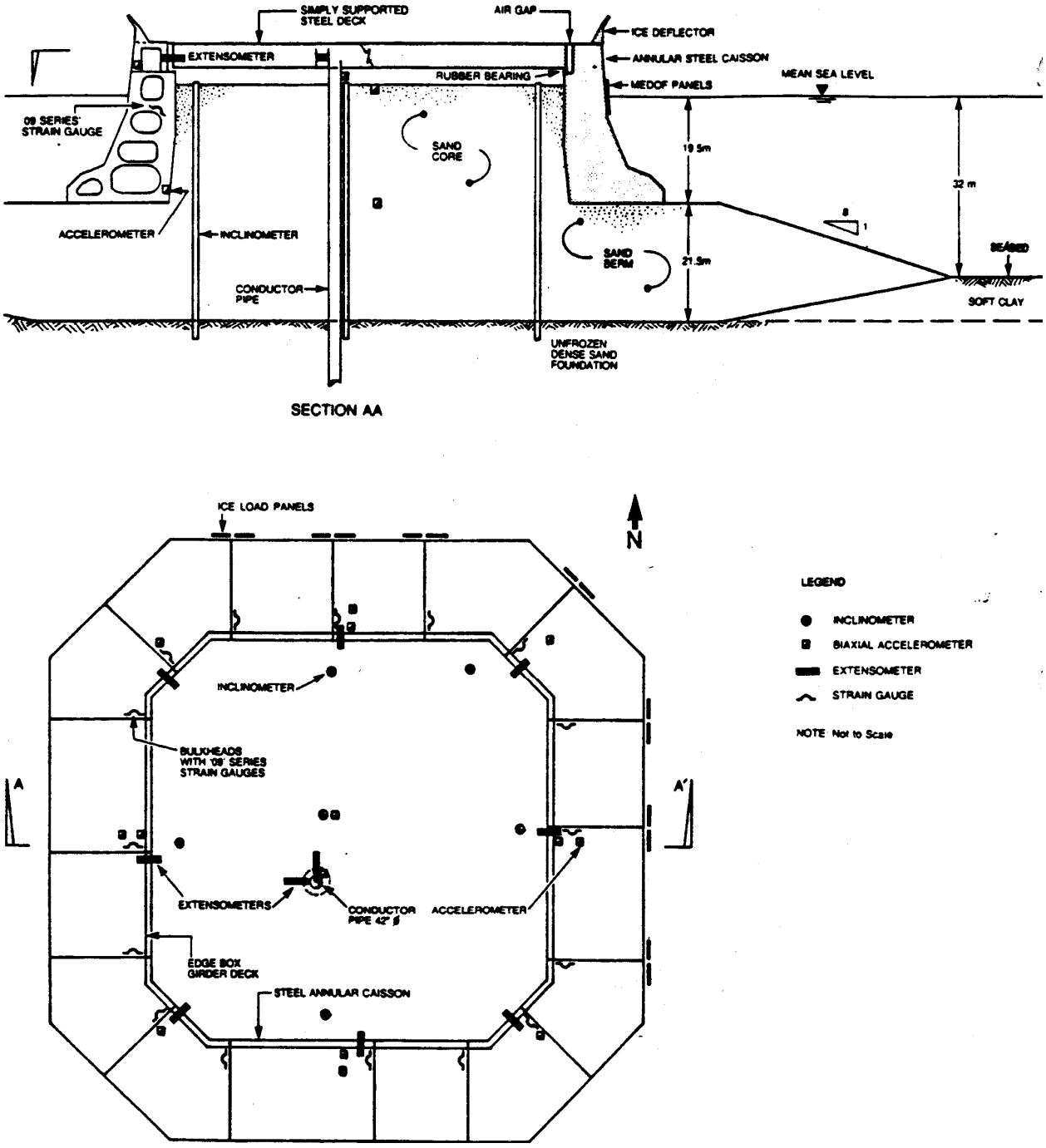

Figure 3. Plan and Section of Molikpaq showing sensor locations

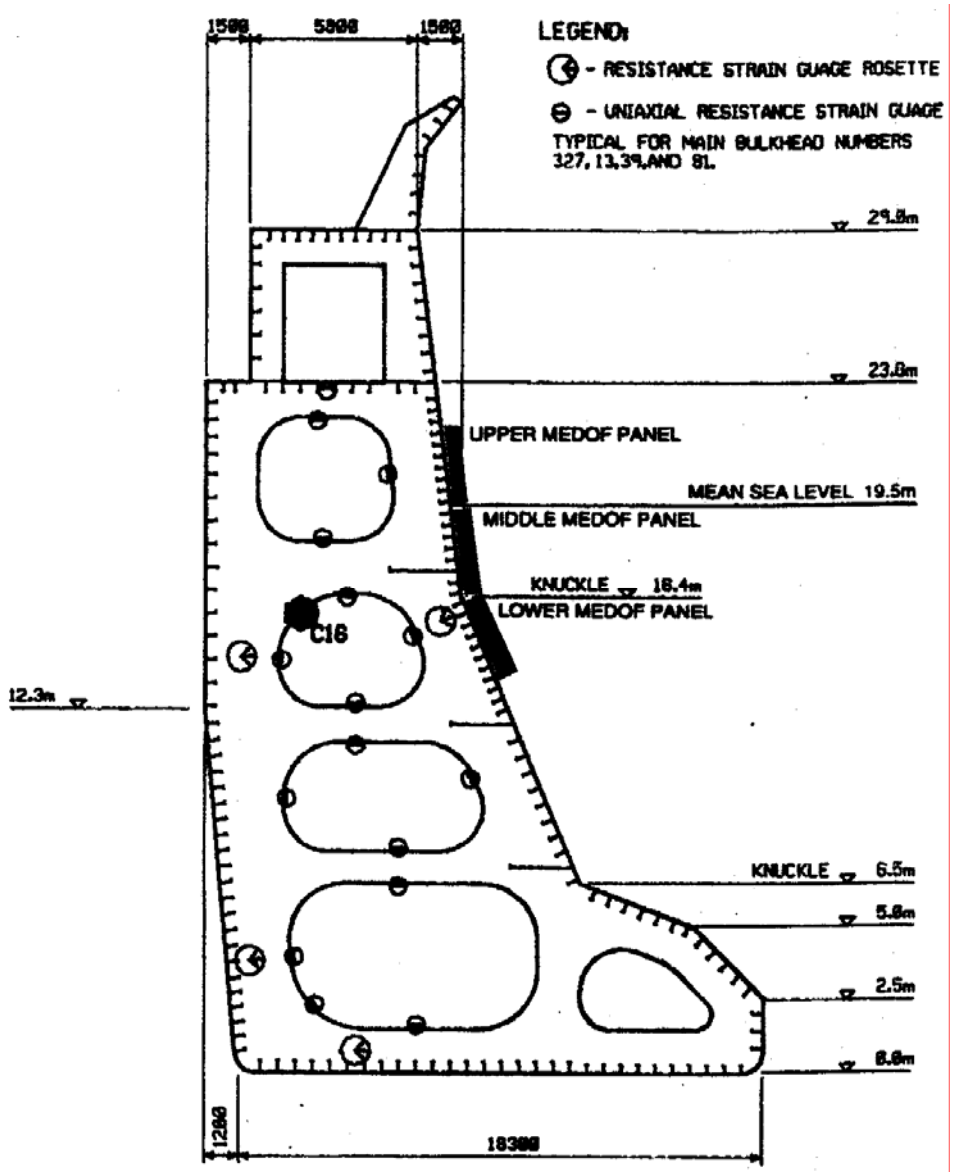

Figure 4. Detail of bulkhead showing location of strain gauges and Medof panel (Location highlighted as 'C16' is that found to have greatest correlation to Medof load)

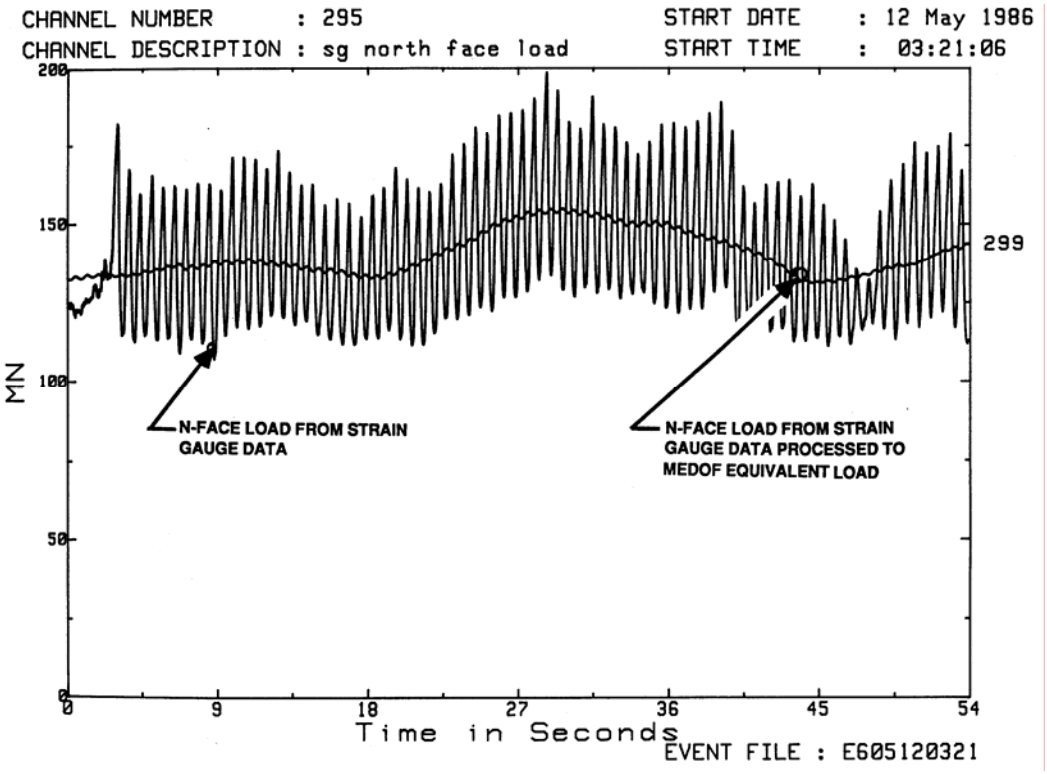

Figure 5. Effect of applying mathematical model of Medof panels to strain gauge load

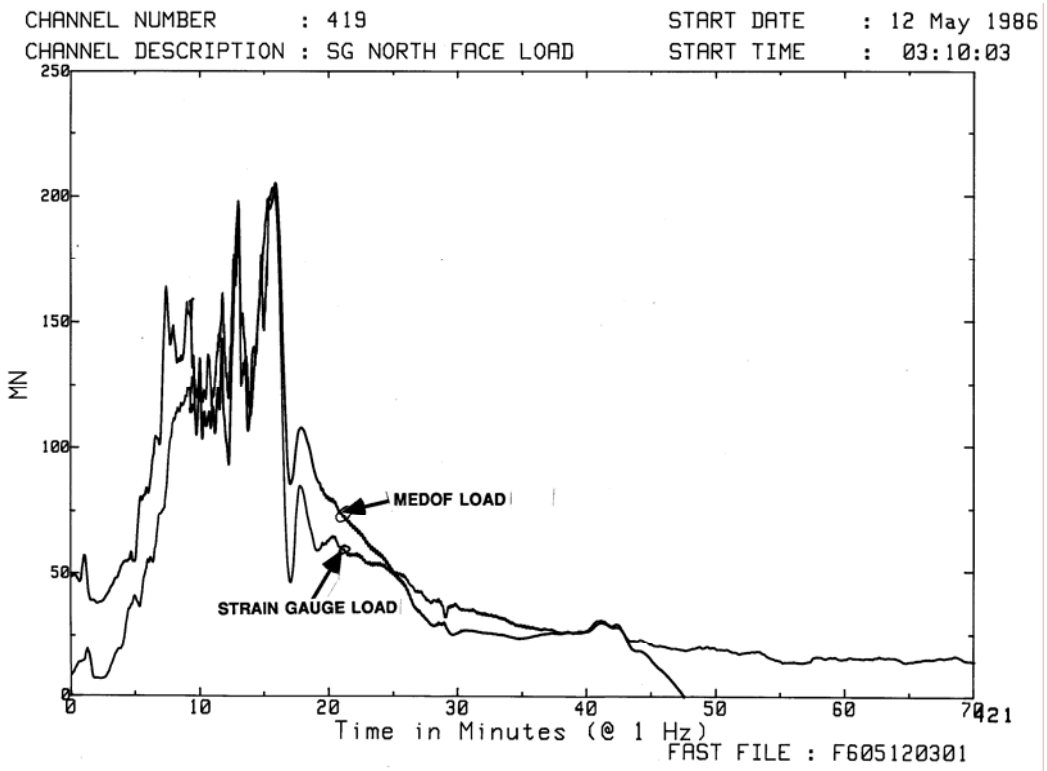

Figure 6. Medof face load from strain gauge algorithm compared to measured Medof face load

Figure 7. Aerial photograph of ice against north and northeast sides of Molikpaq after 12 May 86 event. The photograph was taken during the post-event helicopter ice reconnaissance flight by Volker Neth, P.Eng. (from GCRL project files). The ice had broken away from northwest side during the event and this area was in open water at the end.

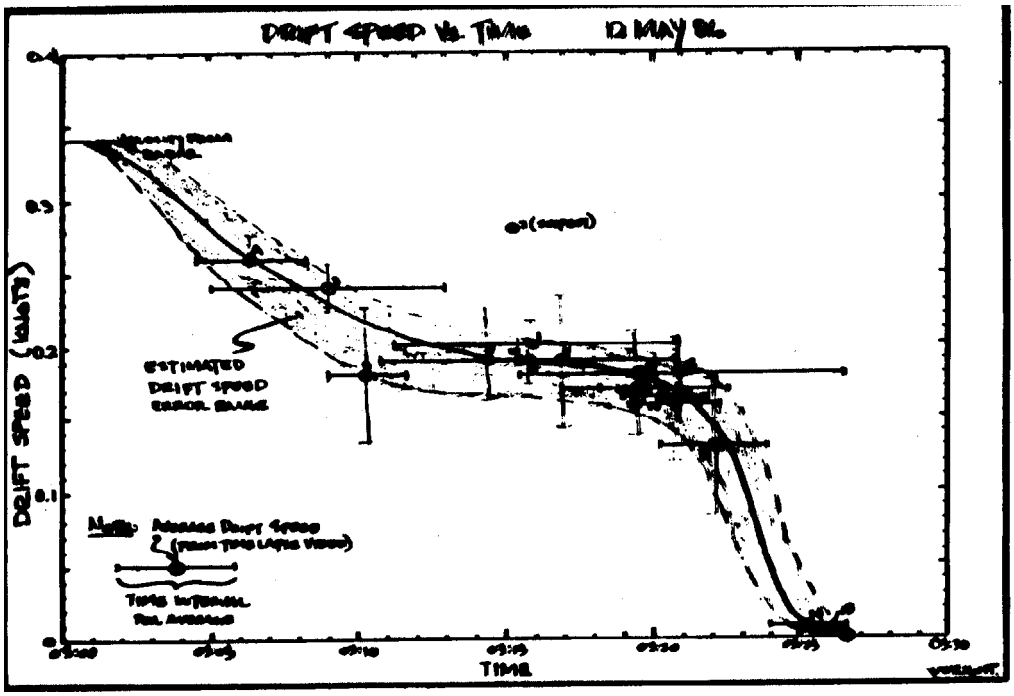

Figure 8. Estimated ice drift speed from timed video observations, 12 May 86 event. Data reduction and evaluation by Wes Wright, P.Eng. Note that the plot starts at 0300hrs and extends to 0330 hrs with ticks at 5 minute intervals.

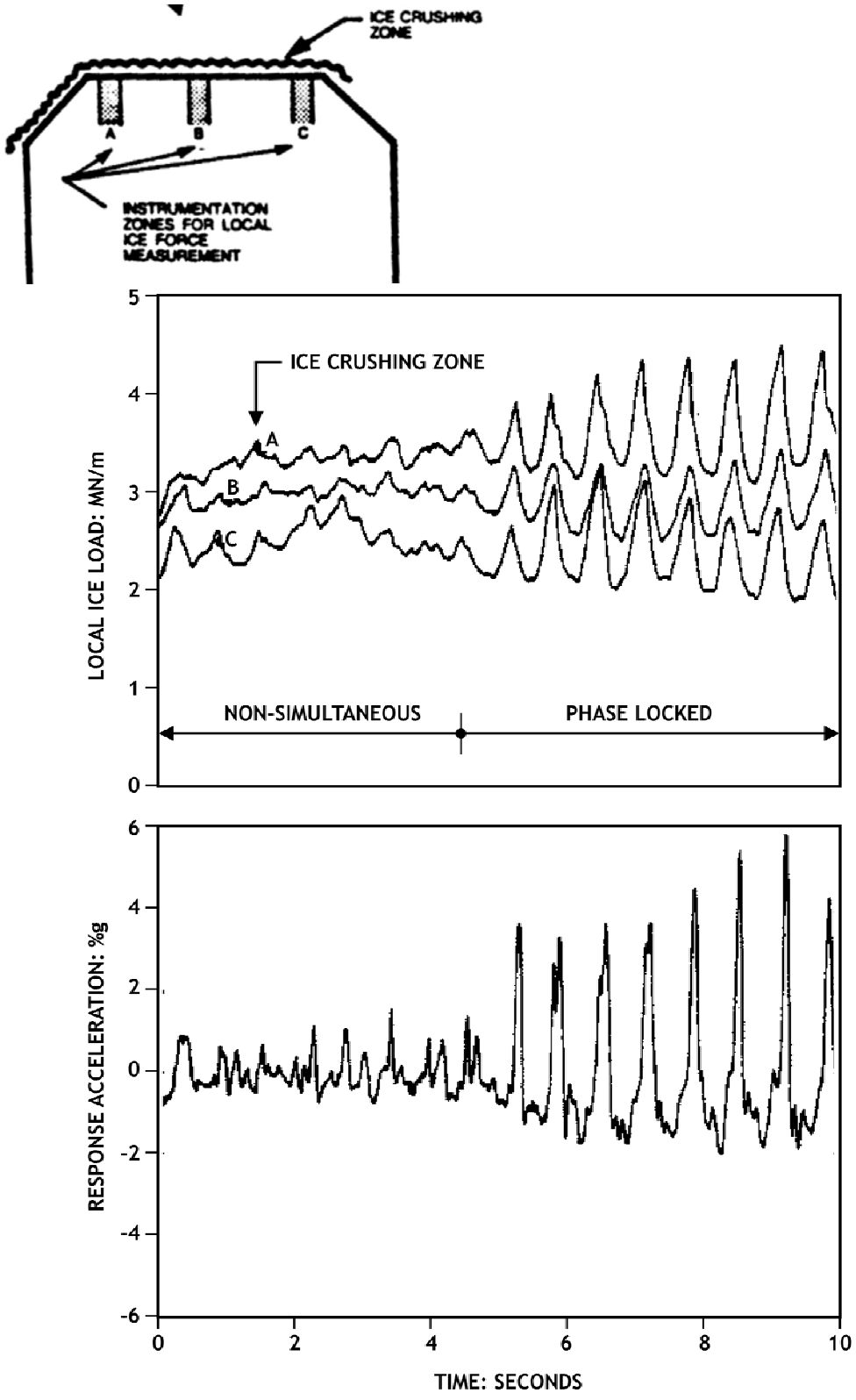

Figure 9. Measured transition from non-simultaneous to phase-locked crushing during 12 May 86 event (after Jefferies & Wright, 1986; scale added by authors)

(a) Unit ice loads as measured time series

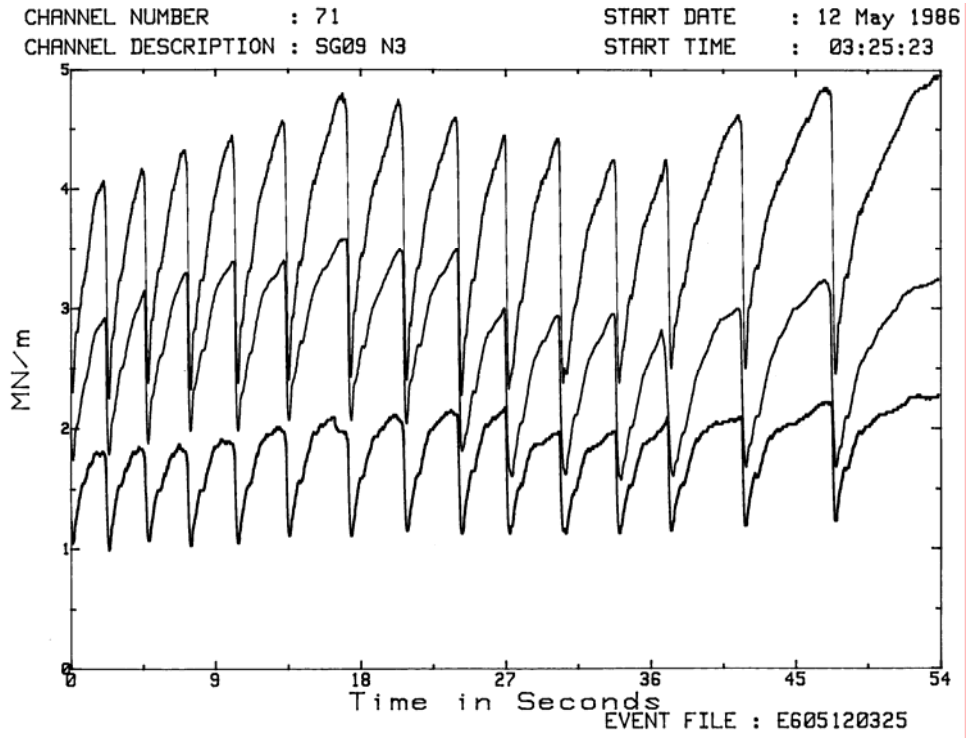

(b) As estimated transient ice pressure

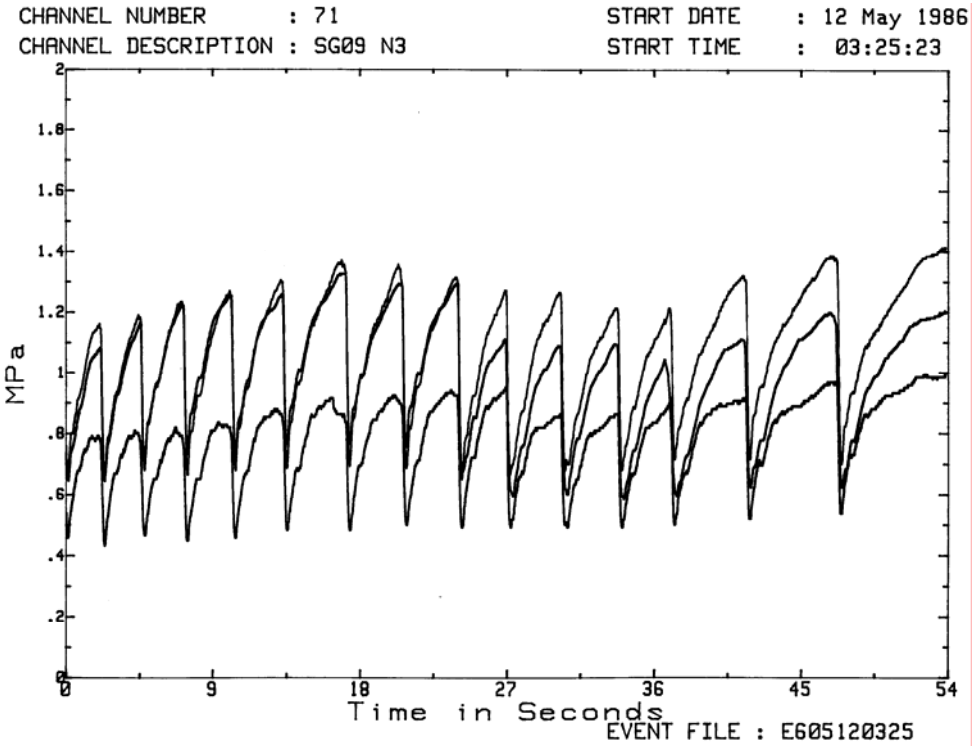

Figure 10. Phase-locked ice failure as time series (locations as per Figure 9)

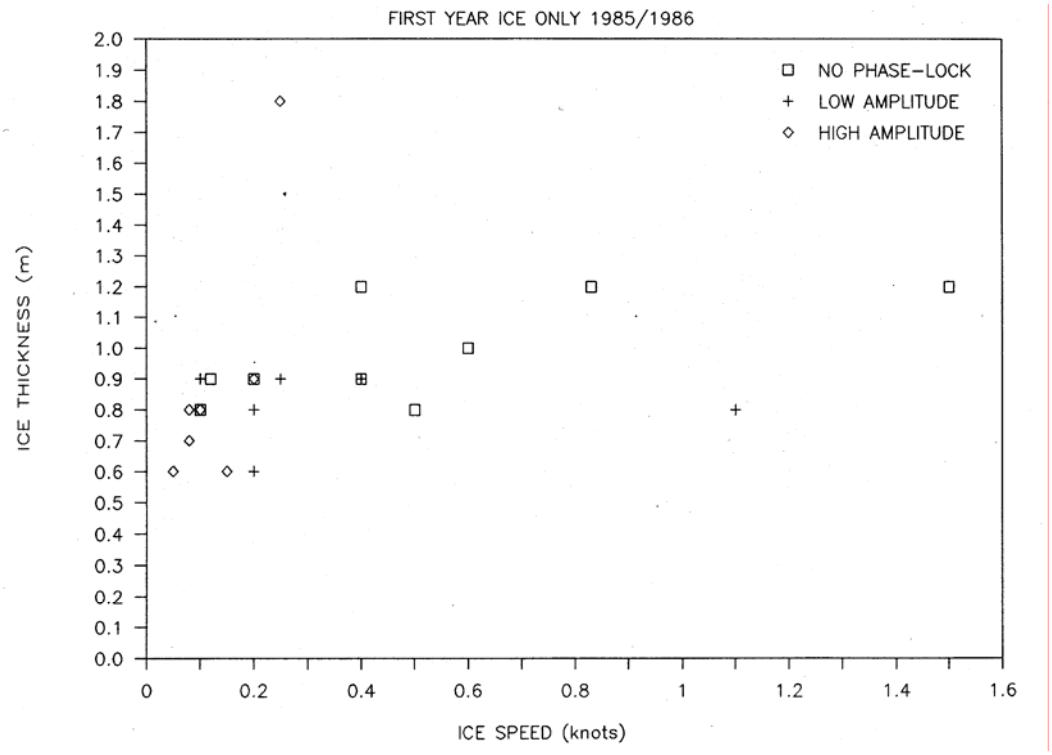

Figure 11. Effect of ice drift speed on occurrence of phase-locked ice crushing in FY ice

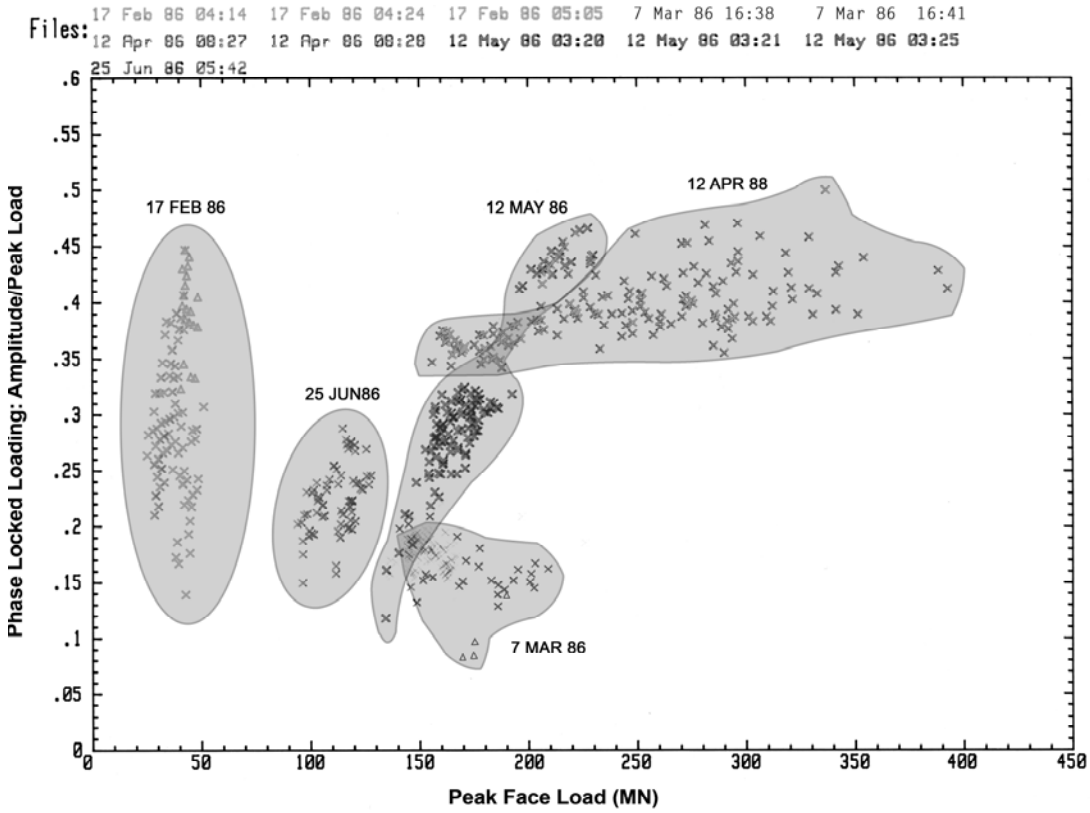

Figure 12: Normalized cyclic amplitude during phase-locked loading 1986 season events

19th IAHR International Symposium on Ice
"Using New Technology to Understand Water-Ice Interaction"
Vancouver, British Columbia, Canada, July 6 to 11, 2008

Time history of dynamic ice force for narrow conical structure

Ning Xu[1], Qianjin Yue[1], Yan Qu[2], Kärnä Tuomo[3,4], Xiangjun Bi[1]
1 Dalian University of Technology, Dalian, China
2 Research center of CNOOC, China
3 Kärnä Research and Consulting, Finland
4 Norwegian University of Science and Technology, Norway

Abstract
This paper presents in detail the dynamic ice force process caused by bending failure of ice sheet acting on narrow cones based on full scale tests conducted on a multi-leg jacket platform which added with ice breaking cones. It is indicated that when ice sheet acting on a narrow cone the broken ice will totally clearing up by side of the cone. That mean the ice force will return to zero before the next action. The direct ice force measurement by ice load panel verified this phenomenon. The narrow cone referring to describe dynamic ice force is defined as broken ice floes could clearing up by side of the cone in the failure period of action.

1 Foreword

Ice action from floating ice sheets is the dominant environmental force for the offshore structures in cold regions. Resistance against the extreme ice force is the fundamental request and traditional design. Wide and rigid structures have always been adopted as the traditional forms to provide the safety.

As the development of ocean exploration, the demand of safety and economics of exploitation structures is enhanced by the different environment and energy distribution. Optimization methods are expected to give better platform designs in order to reduce the ice action as well as the economic payout. Narrow, slender, or flexible structures showed to be a good design for some seas. These structures proved to successfully reduce the ice action by reducing the exposed area, and reduce investment expenses due to short manufacture and construction time and less use of material. However, the remarkable dynamic behavior of such structures gives a series of serious problems and even threatens the exploitation safety. And the mechanics explanation and resolve methods are not well-known. Therefore, these structures are just cautiously used in very few sea areas where the ice condition is mild. Research on the dynamic ice loading is fundamental for conceptual design and the application feasibility of these structures.

The Bohai Bay is a typical sub-arctic area; with around 2 months freeze-up every winter. Considering the shallow water, short and dispersive storage, the choice of proper structures for the exploitation is a key issue. It is possible and necessary to use slender and economical structures. Since the 1960's, extreme force capability deficiency of and remarkable dynamic problems of oil platforms have been resolved successfully.

Jacket platforms with ice-breaking cones are the typical economical ice resistance structures in the Liaodong Bay of Bohai Sea. The main purpose of our work is to solve the existing problems of these structures in ice condition, which is also supported by the Chinese national ocean oil company (CNOOC).

Our work is based on ice mechanics, and focus especially on the loading processes. Research observations and conclusions are founded by theoretic analysis combined with first-hand information from measured full scale data and observations of ice-structure interaction, which are obtained from platforms operating in the Bohai Sea. If the mechanism can be well demonstrated, then the conclusions can be used in the design of structures and widely applied.

This paper presents the significant conclusions of our research on jacket platforms and also the applicability of such structures. Some fundamental definitions and assumption are described. Then the ice-structure interaction process and the time histories of ice force signals are combined to demonstrate the general process.

2 Basic definitions

It is widely accepted that the main failure mode for ice sheet acting on a cone is flexural failure. However, it is still difficult to give the mechanical explanation of the failure process, because of the complicated material composition of natural ice. When acting on a cone, the ice sheet is under a complex three-dimension stress state.

The main discussion on conical structure is the dynamic ice force, which can be explained by the ice-cone interaction process. The most important reasons why general conclusions are not stated are mostly as follows: the general characteristics are not extracted from different results on variant structures; some negligible influence factors are overly considered, especially in some lab study. Clarification and reasonable simplification of the study object is the key issue to application and generalization.

Dynamic force process

The ice force on the structure is induced by the moving ice sheets, driven by environmental forces as wind and currents. When the ice sheets pass through the structures continuously, the alternate ice loads occur. Internal crack starts to form under local pressure in the ice. The pressure will cause further crack growth, and at last the crack will run through because of unbearable large stresses. This process constitutes one period of the alternate ice force, which is mainly composed by a loading and an unloading process.

Loading: A moving ice sheet is continuously acting on the structure with higher and higher pressure; internal cracks of the ice absorb more energy giving a tendency of further crack growth.

Unloading: Near field ice is totally damaged. Unstable internal crack growths and release the energy. Whether the ice force unloading is total is up to whether the fracture ice is separated from the coming formal ice.

Total unloading: If the broken ice is total separated from the intact ice sheet, which will act on the structure during the next force period, it is called total unloading.

If the near field ice is continuously pushed by the later ice sheet to the structure, and there are always certain notable amount of broken ice existing between the structure and the intact ice sheet. Thus the kinetic energy of the coming ice sheet is transferred over to the broken ice. This is not total unloading.

The extreme load takes place at the saturation of the ice crack. For the dynamic ice force, the unloading process is of much more importance.

Clear up process

The clear up process is one behavior of broken ice under gravity, and the friction force (between the slope face and later ice sheet). After the unloading (ice breaking) and before the intact ice sheet make contact with the structure, the broken ice will be cleared away in some way.

There are mainly two kinds of clearing processes. One is total clear up; broken ice has been totally cleared before the next ice period takes place, and there is no influence on the coming ice sheet acting on the structure.

The other kind is when the broken ice can not be totally moved away before the intact ice sheet makes new contact, due to different reasons (steep incline, wide waterline structure, etc.)

Pile up is a typical example. Broken ice could not be moved in time, but instead pile up in front of the structure at the water line, forming a large ice pile up, which supply a gentle slope. The pile up of broken ice will absorb the input energy, reduce the nominal ice pressure, and disturb the ice force period. In these cases, the dynamic effect of structure is weakened significantly, or even disappears.

Wide/narrow structure

The alternating ice force created by the moving ice sheet passing through the structure. If total unloading or total clear up of broken ice takes place during each ice force period, such structures can be regarded as narrow structure. Otherwise it should be categorized as wide structures.

Therefore, it can not just be defined whether the structure is wide or narrow by only the geometrical size. Even the same structure under different ice condition; such like ice thickness, ice velocity and ice strength, will be specified into different classifications. If considered qualitatively, the ratio of conical diameter to ice thickness D/h, can be raise up. As the increases of this ratio, the size of the breaking ice blocks decrease, and the number of broken ice blocks increases. This will weaken the simultaneous of ice force. Then the conical ice force would be disturbed, and the total ice force would be reduced.

For narrow structures, the alternating ice force is obvious. The reason for the alternating force is the quick clearing of broken ice, and dynamic response of the structure will be dominating for the design of the structure. For wide structures, the extreme force is more important.

The cone-diameter at the waterline of the Confederation bridge pier (14m) and Kemi-I lighthouse (10m) is much larger than that of the jacket platforms (4~6m) in the Bohai Bay. When ice acts on these two structures, the pile up always takes place, and this will reduce the periodicity of ice forces acting on the structures.

For multi-leg structures, the pile up problem will be easily induced if the distance between the legs is small (less than 6 times the width of the legs), or there are obstructions between the legs. This condition is similar to wide structures. For example; JZ20-2MSW legs (diameter of 1.2~4m) have a distance of 9.6m, with 3 conductors erected between the legs at the ice-ward side. The pile up is shown in figure 1.

Figure 1. Level ice failure against piled ice in front of JZ20-2 MSW.

Flexible structures

Flexible structures: The structure experiences large deformations under external loading and the dynamic effect is obvious under alternating load. If the frequency of the environmental force is close to the natural frequency of the structures, there will be a large dynamic amplification of the response for the flexible structures.

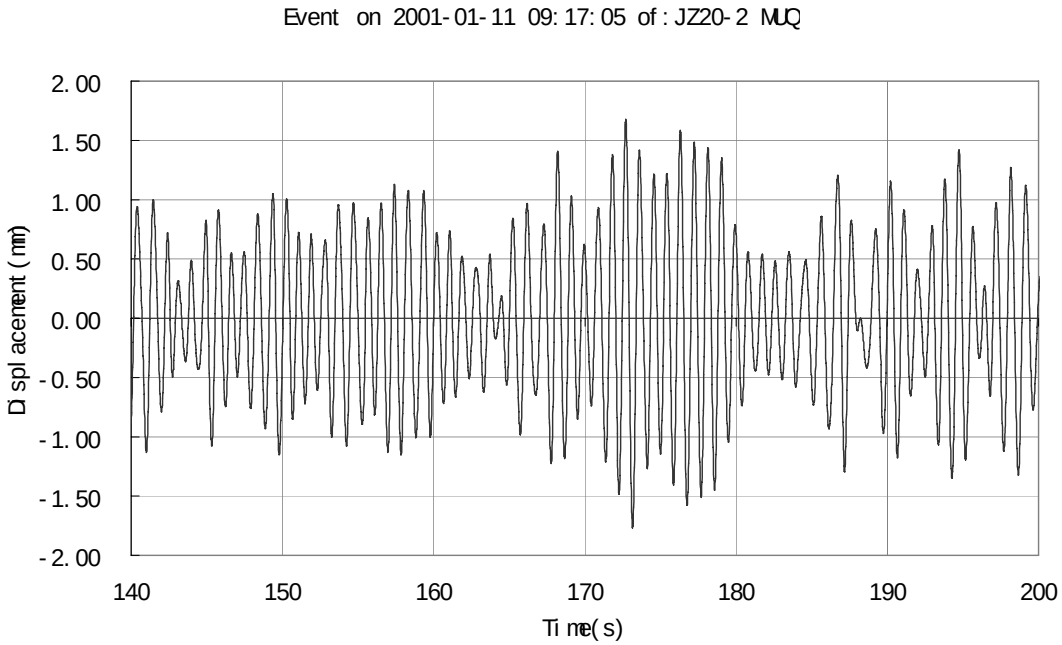

Figure 2. Dynamic response of JZ20-2 MUQ

The jackets in Cook Inlet with large structural stiffness, compared to the Bohai Bay, have not reported occasions of serious vibration. While for the jackets with small structural stiffness in the Bohai bay, where the ice force frequency is close to their natural frequencies, the dynamic amplification of the response is serious. The dynamic character of the response can be seen in fig.2. Based on this, these structures can be considered as flexible structures.

3 Ice-cone interaction process and time history of dynamic ice force analysis

The reasonable assumption and fundamental definitions are the basic of the general conclusion. Herein the real ice force and the ice-structure process are combined.

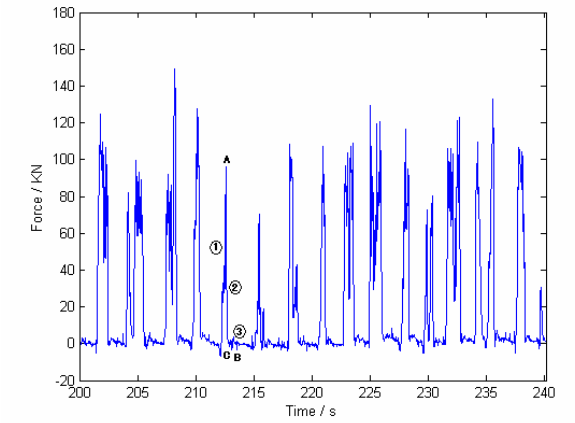

Figure 3. Ice load recorded by the load panels on JZ20-2 MUQ platform at 12:01 of Jan 18, 2001.

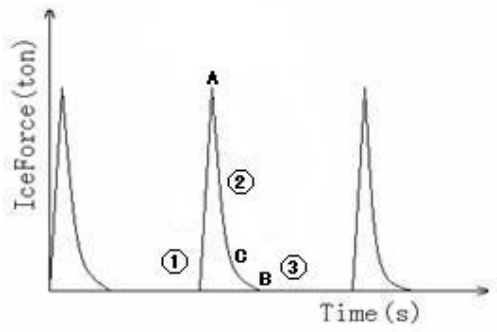

Figure 4. Ice force variation during the interaction between the ice and cone.

The process of ice acting on narrow conical structures is a periodical process, similar to the ice force. This process has been described by Yue (2000 2001). We define the start of each period when a uniform ice sheet starts acting on the cone. The ice-cone interaction process can be described by the following three phases: flexural failure, climbing and clearing up. The corresponding dynamic ice force is loading, unloading and zero force respectively. A typical part of a real ice force history, measured by load panels is show in Fig.3. Figure 4 is the simplified ice force model of the time history. The time history of ice force during ice failure on narrow cone is as follows:

Flexural failure - loading

The moving ice sheet directly crushes onto the cone by certain momentum. The local crushing induces normal pressure on the sloping surface, which can be divided into vertical and horizontal vector components in the center of the destroyed ice interface. The ice sheet is slowly climbing on the cone and gets a small uplift displacement.

The internal stress field in the ice forms and develops quickly by the rapid increasing normal pressure and ice force on the conical surface. When the ice sheet is up to some height, the radial and circumferential cracks begin to occur in the ice sheet from the boundary of the cone. Video measurements from field tests indicate that the radical and circumferential cracks on the cone of JZ20-2 almost appear at the same time. Li Feng (2003, 2005) considers this as a transfer between wedge-plate and board-plate.

When the local stress exceeds the limiting stress, two direction's cracks run through to induce the break of the ice sheet. Thus the flexural failure happens and several uniform ice sheets are produced. Then ice force begins to decrease.

During this period, the ice force will increase almost linear. Corresponding to the real ice force, the ice force in each period is always a triangular pulse; the peak point of the pulse corresponds to the maximum ice force (point A), and also the turning point of the ice force. The typical ice

Figure 5. Ice bending failure against a narrow cone.

sheet flexural failure is shown in Figure 5.

Sea ice climbing-unloading

The breaking broken ice sheet will continue to climb up the slope of the cone, due to the moving ice. The ice force time history is no-linearity, and the ice force decreases slowly because of the friction between the ice and cone. Second breaking (Point C) may happen with steep inclination. After the ice is broken, the ice force fall down to zero (point B) at the end of this phase.

During this phase, broken ice moves in some of the following ways: first, it continues to climb pushed by the intact ice sheet; secondly, it will turn over onto the subsequent ice sheet. Large ice

blocks will probably fall down into the water by the conical inclination due to the long distance between the intact ice sheet and the cone.

Sea ice clearing up-no load

The broken ice sheet will slip down from two sides of the narrow cone, above or below the water lever by the pushing of coming intact ice sheet. There might be so limited amount of broken ice left between the cone and later ice, that this part of ice force can be neglected.

There is no evident ice block/sheet act and no ice force on the conical structure, until the next intact ice sheet's coming.

Then a new period of ice force is coming. These three phases revolve in each narrow conical ice force period.

4 Conclusion

Based on the fundamental definitions and assumptions defined in this paper for conical structure with narrow cones and flexible behavior, we can use the conclusions from jackets in the Bohai Bay. We can then use the research from studies on these structures in design of similar structures in other sea areas. This will make it easier to analyze the applicability for new structures.

5 Acknowledgements

The support of the National Natural Science Foundation of China (No. 10672029) is much appreciated.

Reference

Yue, Q., Bi, X. ,2000. Ice-induced jacket structure vibrations in Bohai Sea. Journal of Cold Regions Engineering. Vol.14, No.2, 81-92.

Yue, Q., Bi, X., Yu, X., Shi, Z., 2001. Ice-induced Vibration and Ice Force Function of Conical Structure. China Civil Engineering Journal.Vol.36, No.2, 16-32

Li F., Yue Q., Shkhinek, K. and Karna, T., 2003. A Qualitative Analysis of Breaking Length of Sheet Ice Against Conical Structure, Proc. 17th International Conference on Port and Ocean Engineering under Arctic Conditions, Trondheim, Norway, 293-304.

LI Feng, YUE Qian-jin., 2005. Qualitative analysis of ice forces on conical structures under different failure modes, Journal of Dalian University of Technology, 06, Vol. 45, No. 6,. 785 - 788.

Qu Yan, Yue Qianjin, Bi Xiangjun and Kärnä Tuomo. 2006. A random ice force model for narrow conical structures. Cold Regions Science and Technology, 45, 148-157.

19th IAHR International Symposium on Ice
"Using New Technology to Understand Water-Ice Interaction"
Vancouver, British Columbia, Canada, July 6 to 11, 2008

Numerical Simulations of Dynamic Response of Narrow Conical Structures due to Ice Actions

Oddgeir Dalane[1], Xu Ning[2], Yue Qianjin[2], Tuomo Kärnä[1,3] and Sveinung Løset[1]
[1]*Norwegian University of Science and Technology (NTNU), Trondheim, Norway.*
[2]*Dalian University of Technology (DUT), Dalian, China.*
[3]*Karna Research and Consulting, Helsinki, Finland.*
oddgeir.dalane@ntnu.no, xuning@student.dlut.edu.cn, yueqj@dlut.edu.cn,
tuomo.karna@gmail.com, sveinung.loset@ntnu.no

Abstract

This paper addresses a condition where a conical structure is exposed to the action of sheet ice. The focus is on narrow cones, for which the rubble build-up does not influence the ice actions. Both field data and recent theoretical studies show that the time-varying ice action and the structural response constitute a narrow-band random process under these conditions.

Experiences from structural dynamics indicate that the time of exposure can be a significant parameter if the response has a narrow-band character. This feature has consequences on the numerical simulation of this kind of ice action. There is a chance that the real response will be underestimated if the time of a numerical simulation is not sufficiently long.

This problem is studied by using a numerical method based on data obtained from full-scale structures deployed in the Bohai Bay. The main idea is to find out how long it can take before the maximum response is obtained while main parameters of the load model vary randomly. The results of this simulation are compared with a similar analysis performed on full-scale data.

1. Introduction

Compliant structures are not only affected by the action from ice, but also the response to the action. Vibration and resonant loading conditions must be considered for such structures. Several observations of severe vibrations have been observed and reported from full-scale and model-scale measurements due to ice-structure interaction (Yue et al., 1998; Yue and Bi, 2000; Kärnä et al., 2003; Bjerkås, 2006; Frederking and Sudom, 2006). Under vibrations, large deformations may damage the structure due to high tensions, and accelerations of the structure might destroy equipment and cause uncomfortable working conditions. The conditions where a very large global pressure acts on the structure might not be the conditions where the vibrations are largest. For instance the Kemi lighthouse in the Gulf of Botnia experienced large vibrations that caused failure of the structure when the ice thickness was registered to be very thin (Løset et al., 2006).

Introduction of breaking cones on cylindrical structures has shown to be efficient in order to reduce the ice action (Ralston, 1977; 1980; Frederking and Schwarz, 1982; Gravesen et al., 2005). Therefore, cones were installed on the platform JZ20-2 MUQ in the Bohai Bay in order to reduce the vibrations that were observed while it had vertical legs. Even after these cones were installed on the structure, vibrations were reported.

From experiences with slender structures in ice conditions, it is obvious that dynamic loading needs to be taken into account in the design process. Qu et al. (2006) derived a random load model for conical structures based on full-scale measurements at the JZ20-2 MUQ platform. This model is very useful in order to calculate the response of a system with dynamic loading. However, for dynamic loading another important question is how the maximum value of the simulation will change as a function of the simulation length. This problem will be investigated in the present paper. First an introduction to dynamic loading and estimation of maximum values will be given. Then a short description of the load model and some preparatory derivations for the analysis on how the time of exposure affects the maximum values are stated. Comparisons between measured and calculated responses from the JZ20-2 MUQ platform, operating in the Bohai Bay, will be given.

2. Theoretic background

Dynamical analysis of structures is concerned with time-varying forces and responses. The load on the structure is varying in time with direction, amplitude or length. Dynamic loading results in structural response, displacements and tensions, which also will be time varying. The dynamic analysis can be carried out in two different ways according to how the load is specified; deterministic or stochastic. If the time varying load is given in a way that we may consider it to be exactly known as a function of time, this will also apply for the response and we call the dynamic analysis deterministic (Naess, 2007). The loading process in stochastic analysis is specified using probabilistic concepts and the corresponding displacements and tensions can only be described in the same way.

Extreme response is important in the design processes of structures. For deterministic processes statistical analysis must be performed over several different realizations of time series, while from stochastic processes the statistical parameters can be extracted from the response spectrum.

For a stochastic process the probable extreme value y_n for n observations can be evaluated as a solution of

$$1 - D(y_n) = 1/n \qquad [1]$$

where $D(y_n)$ is the cumulative distribution function of the amplitudes.

A Gaussian narrow-band process will have a Rayleigh probability distribution of amplitudes in the process, with a parameter equal to twice the variance (Ochi, 1990). The probable extreme amplitude expected for a Rayleigh distribution can be obtained by Eq.[1], and will be given as

$$y_n = \sqrt{2m_0}\sqrt{\ln\ n} \qquad [2]$$

where m_0 is the zeroth moment of the spectrum (equal to variance), given as

$$m_i = \int_0^\infty \omega^i S(\omega)\, d\omega \qquad [3]$$

where ω is frequency, $S(\omega)$ is the spectrum of the process in terms of the frequency ω, and i =0, 1, 2 …k according to the order of the moment.

The number of amplitudes, n, of a random process observed in a specified time period is equal to the number of zero crossings in that period. The number of amplitudes for a period of T seconds can then be expressed based on the average number of zero crossings per unit time and given as

$$n = \frac{T}{2\pi}\sqrt{m_2 / m_0} \qquad [4]$$

where m_2 is the second moment of the spectrum defined by Eq.[3].

For a wide-band process it is difficult to solve Eq. [1] analytically. Ochi (1990) gives an approximate solution for a bandwidth parameter ε (ε = [0,1], small ε is a narrow-banded process) less than 0.9 and the probable largest maximum of n amplitudes is given by

$$y_n = \left\{ 2\ln\left(\frac{2\sqrt{1-\varepsilon^2}}{1+\sqrt{1-\varepsilon^2}} n \right) \right\}^{1/2} \sqrt{m_0} \qquad [5]$$

The expected number of positive maxima for a period T seconds is given by Ochi (1990) as

$$n = \frac{T}{4\pi}\left(\frac{1+\sqrt{1-\varepsilon^2}}{\sqrt{1-\varepsilon^2}} \right)\sqrt{\frac{m_2}{m_0}} \qquad [6]$$

We can now show that we will have the same equation for the probable extreme maximum in a time period T seconds for a narrow-band and wide-band process. By inserting Eq.[4] into Eq.[2] and Eq.[6] into Eq.[5], both yield the result

$$y_n = \left\{ 2\ln\left(\frac{T}{2\pi}\sqrt{m_2 / m_0} \right) \right\}^{1/2} \sqrt{m_0} \qquad [7]$$

As can be seen from Eq.[7], the maximum amplitude is no longer a function of the bandwidth parameter when it is given as a function of time. However, it should be remembered that the number of peaks for a wide-band process is much larger than for a narrow-band process during the same period of time. Figure 1 shows the probable extreme maxima in dimensionless form as a function of bandwidth parameter.

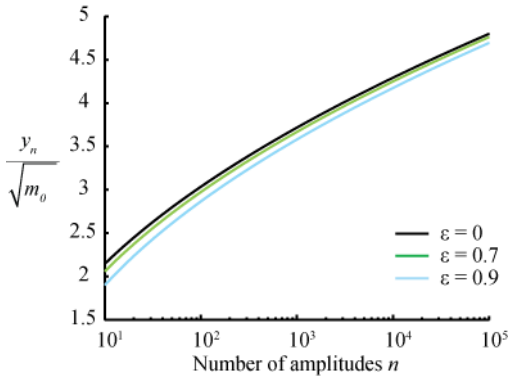

Figure 1. Probable extreme maxima in dimensionless form, as a function of bandwidth parameter ε.

For an engineer it is important to have sufficient length on numerical simulations to catch the maximum events. Numerical simulations are used in order to in best possible way give a presentation of what can be expected in the real world, and it is therefore important to study the similarities between simulations and measured response. For numerical simulations the only consideration with regards to simulation length is time consumption, but the time histories of the measured response are of limited length and comparison studies are therefore limited by the length of these time series. The measured time series might be affected by other loading conditions like wind and current which is not reported in the data. Therefore, it is not possible to directly compare the amplitudes in the numeric simulation with the results form the full time series in the current study, and the results will be presented in a dimensionless form.

3. Load model

The four legged (diameter of 1.7 m) jacket structure JZ20-2 MUQ platform, as shown in Figure 2, is operating in the northern part of the Bohai Bay of China. It has a top mass of 1700 ton and a natural frequency of 0.87 Hz (Yuan, 2007). The platform is equipped with icebreaking cones at the waterline (diameter of 4 m) to reduce the vibrations and loads caused by action from ice during the two months when ice is present each year. The cones were installed after the deployment of the structure due to the vibrations that were observed. The structure is still reported to vibrate and load cells were installed in the winters from 2001 till 2004, which recorded the ice action on the legs. The results from these measurements were analyzed and used

to suggest a time-varying random ice load model for narrow conical structures where the ice fails by bending in a mode where the broken ice pieces are cleared away. This method is described by Qu et al. (2006) and will be used in this paper to generate a time-varying ice load with the general shape illustrated in Figure 3. The method and findings described in Qu et al. (2006) are summarized in this section in order to give a description of the load model used in this paper.

Figure 2: The JZ20-2 MUQ platform (Qu et al., 2006).

Based on statistical analysis of the magnitude and period of the measured ice force, a stochastic function for the ice load time series was developed by Qu et al. (2006). The load function is constructed by a row of load impulses as can be seen in Figure 3. The function of one impulse depends on the random parameters F_{0i} and T_i and is given by

$$f_i(t) = \begin{cases} \dfrac{6F_{0i}}{T_i}t & 0 < t < \dfrac{T_i}{6} \\ 2F_{0i} - \dfrac{6F_{0i}}{T_i}t & \dfrac{T_i}{6} < t < \dfrac{T_i}{3} \\ 0 & \dfrac{T_i}{3} < t < T_i \end{cases} \qquad [8]$$

where i=1 for the first load impulse, which starts at t=0. The load amplitudes F_{0i} are found by selecting random values from a normal distribution $F_{0i} \sim N\left(\overline{F_0}, \sigma_{F_0}^2\right)$ where $\overline{F}_0$ is the mean load and the variance $\sigma_{F_0}^2 = \left(0.4\overline{F}_0\right)^2$. The time period is found by selecting random values from the independent normal distribution $T_i \sim N\left(\overline{T}, \sigma_T^2\right)$, where $\overline{T}$ is the mean period and the variance $\sigma_T^2 = \left(0.5\overline{T}\right)^2$. Methods for defining $\overline{F}_0$ and $\overline{T}$ are suggested in Qu et al. (2006).

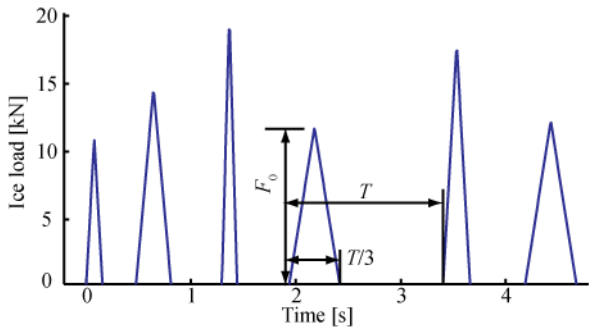

Figure 3. The random ice load function for a narrow conical structure.

The load functions of the individual impulses given by Eq.[8] can be collected to form the full time series by the expression

$$F(t) = \sum_{i=1}^{N} f_i\left(t - t_i^0\right) \qquad [9]$$

where N represents the length of the loading function, $t_1^0 = 0$ and $t_i^0 = \sum_{j=1}^{i-1} T_j$ for $i > 0$. The time series obtained will be used in the analysis of dynamic response of structures in the time domain.

4. Preparatory Derivations

Tuning of the load functions

In the current study the target is to investigate the response from numeric analysis and compare the results with true measured response. In order to apply a load in the numeric analysis that represent the same process as the true measured load history a similarity study was performed in order to tune the numerical load process, meaning to find $\overline{F}_0$ and $\overline{T}$ as required in Eq.[8] to give the same process in the numerical results as the full time results. The similarity study was performed in the frequency and time domain. The time domain was used to study the variance (amplitudes of the ice loading) and for visual study of the periodicity and shape of the loading functions. The frequency domain was more efficient for studies of the frequency composition of the time series. It is important that the energy is concentrated around the same frequencies and that the peak frequencies coincide.

One measured time series can be treated as one realization created by the random time function. Therefore, the frequency domain study was based on a confidence interval study. Three criteria for similarity were stated; equality in load amplitudes, coinciding peak frequencies and that the power density function of the numerical realizations should lie inside a 95% confidence interval of the true time series.

MATLAB was used to create power density spectra of the measured ice force time series, where the trends were removed (Leis, 2002) (no padding or tapering). The density spectra were then smoothed with a Daniell window (Bloomfield, 2000) to obtain a better and less biased realization of the spectra. The modified Daniell window for a span m is given as

$$g_i = \begin{cases} \dfrac{1}{2(m-1)} & \text{for } i = 1 \text{ or } i = m \\ \dfrac{1}{m-1} & i \text{ otherwise} \end{cases} \qquad [10]$$

where g_i is the i weight of the filter and i corresponds to a discrete position in the time series. The Daniell window is shaped as a trapezium as shown by Eq.[10] where the two end points are half as large as the other weights. It can then be shown that the distribution of the estimated spectrum $\hat{S}(f)$ can be shown to be approximately χ^2 with degrees of freedom (Bloomfield, 2000)

$$v = \frac{2}{g^2} \qquad [11]$$

where $g^2 = \sum_i g_i^2$ is the sum of squared Daniell weights. A 95% confidence interval for the estimated spectrum can then be given as

$$\frac{v\hat{S}(f)}{\chi_v^2(0.975)} \le S(f) \le \frac{v\hat{S}(f)}{\chi_v^2(0.025)} \qquad [12]$$

where $\chi_v^2(0.975)$ and $\chi_v^2(0.025)$ are the 97.5% and 2.5% points of the χ^2 distribution with v degrees of freedom.

Numerical model for response calculations

The dynamic response of a multi-degree-of-freedom-system exposed to a time-varying external load *F(t)* can be computed by modal analysis (Chopra, 2007). For the current problem this method is very convenient to use in order to simplify the dynamic loading conditions. Modal analysis is clearly described in textbooks considering dynamic analysis e.g. Chopra (2007) and Clough and Penzien (1975). The method was also thoroughly described in Kärnä et al. (2006) for a vertical structure exposed to ice actions similar to the problem at hand. The structure may then be modeled as several independent single-degree-of-freedom systems representing one mode of vibration which can be summarized to give the total response.

In this study the JZ20-2 MUQ platform have been simplified as a single degree of freedom system (SDOF) according to modal analysis. The structure have been modelled in the finite element program ANSYS and the parameters to define the system for its first mode have been calculated by the program (Yuan, 2007).

From acceleration to displacement of the measured response

The response of the JZ20-2 MUQ platform is measured by accelerometers as described in Qu et al. (2006). The deflections of the structure can be found by numerical integration of the measured accelerations. Due to unknown numerically initial conditions and also different distortions in the measurements called baseline offsets, the numerical integrated results will often

have a drift off (Boore et al., 2002). The distortion problems generally manifest themselves at long periods because small offsets in acceleration can produce large errors during double integration. One simple method to correct for these errors is to apply a high-pass filter to the acceleration records. The disadvantage with this method is that you might ignore the pseudo-static response, and it is therefore only useful for a transient signal, sinusoidal signal or free response that does not have a pseudo-static response (Park et al., 2005). The load process for the response signals used in this study is well known; the loads are measured at the same time with load cells and in addition we know how the response of such loading should look like. Therefore, we can apply a high-pass filter with a cut off frequency based on the frequency representation of the load histories and structural parameters that characterizes the response process. By performing this action on the acceleration signal, then integrate twice and detrend the last result, we will obtain the displacement history for the dynamic process. The last detrend operation is in order to take the initial velocity into account.

5. Results

The results from different simulations will be presented herein. A part of a time series obtained by the numerical program is shown in Figure 4. The randomness in the method for establishing the time series ensured unique results in the time domain for each test run, but as long as the time series got long the spectra was similar for the different analysis with the same conditions.

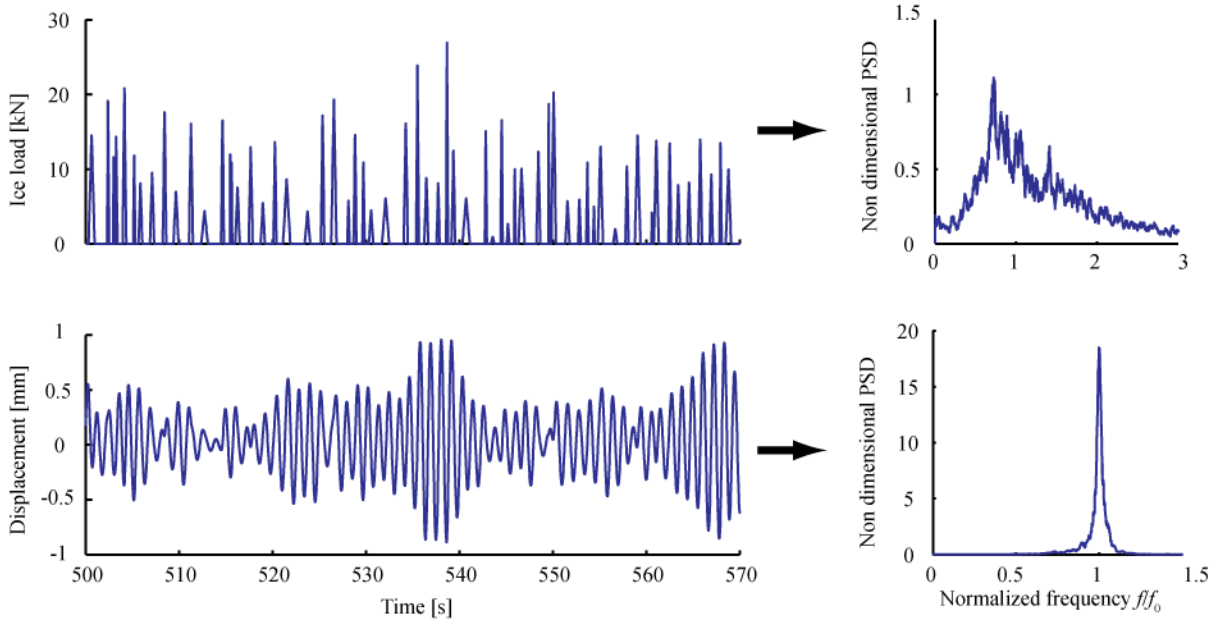

Figure 4. Loading process with accompanying response, given in the time domain and a nondimensional representation in the frequency domain (divided by variance and multiplied with the natural frequency f_0).

The numerical simulations were found to have three different loading periods giving large dynamic amplification for the system. Figure 5 shows the dynamic amplification for a system exerted to several equal loads (period and amplitude) after each other, as a function of loading period T as defined in Figure 3.

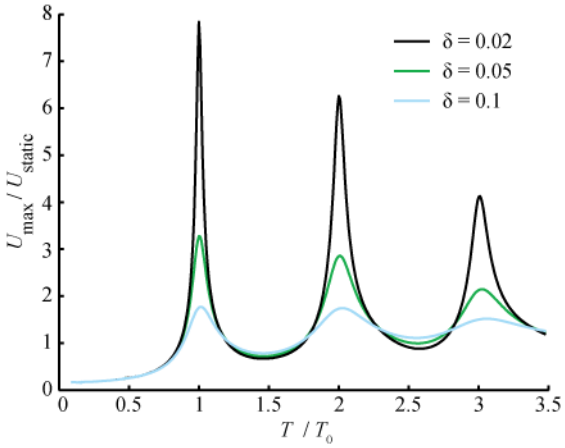

Figure 5. Dynamic amplification as a function of loading period *T*.

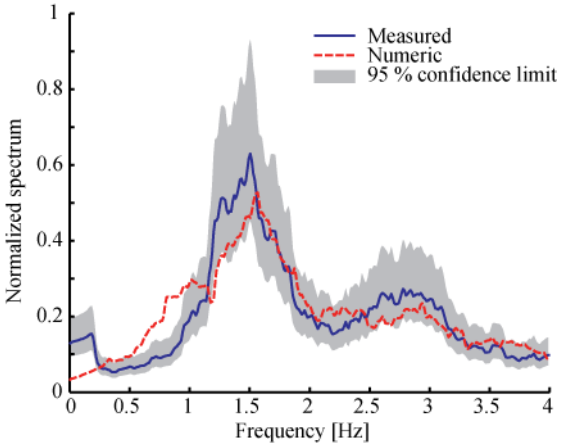

Figure 6. Spectrum of a measured time series with 95% confidence limits together with the spectrum of a numerical time series.

A truncated Fourier series *G*, was created based on a load signal *F*, consisting of several equal load pulses inserted after each other with period equal *T* and amplitude equal F_0. The result is given by Eq.[13] and illustrated in Figure 7.

$$G(t) = \frac{F_0}{2}\left[\frac{1}{3} + \frac{6}{\pi^2}\cos\left(\frac{2\pi t}{T} - \pi/3\right) - \frac{9}{2\pi^2}\cos\left(\frac{4\pi t}{T} + \pi/3\right) - \frac{8}{3\pi^2}\cos\left(\frac{6\pi t}{T}\right)\right] \qquad [13]$$

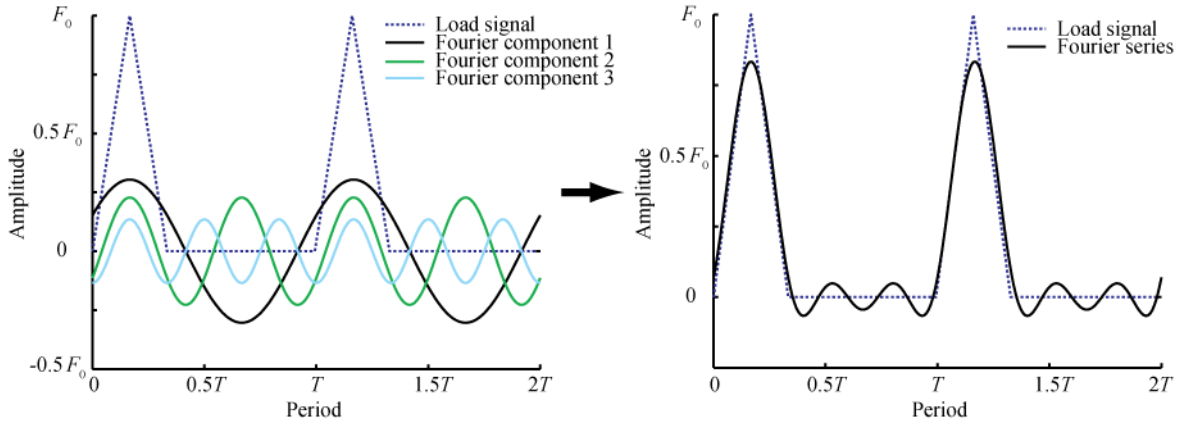

Figure 7. Separate Fourier components and the corresponding truncated Fourier series of a load signal.

The numerical spectra of load histories made by the load function defined by Eq.[9] were compared to the measured load spectra as shown in Figure 6. It was found that the numerical spectra could be tuned by changing $\overline{F}_0$ and $\overline{T}$ of the normal distributions the random variables are picked from, to fit inside the confidence limits for the measured spectrum. It was also found that the biased numerical spectrum made by an average of 100 numerical created time series fitted well to the measured spectrum.

The mean period $\overline{T}$ was found to correspond to the peak frequency of the measured spectrum, and was the average period between load peaks in the measured time series. It was found that the numerical load time series in general had a more wide-band characteristic than the measured time series.

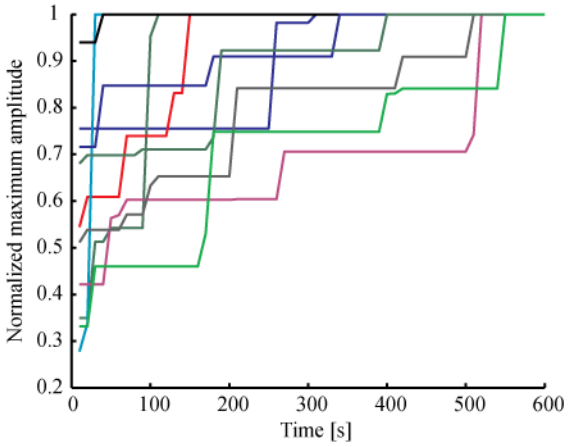

Figure 8. The largest response normalized over the maximum response for increasing intervals of measured time series.

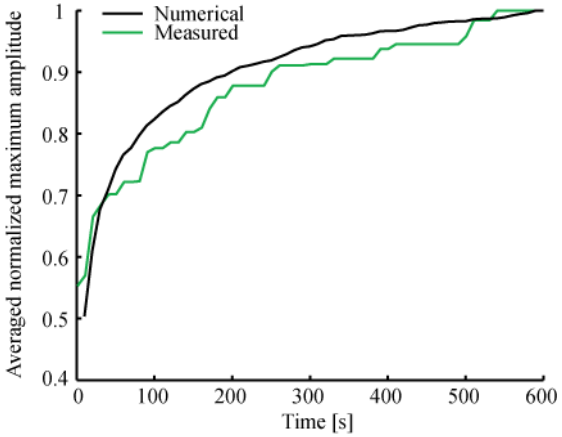

Figure 9. Maximum values as function of time for numeric and measured.

Figure 8 shows the largest values of the response normalized over the maximum response in the particular time series, for increasing time interval lengths. The maximum values were found for intervals increased with 10 seconds for each step. A total of 10 measured time series were studied. The maximum response was found to happen at different times; from very early to very late in the time series. Figure 9 shows how the averaged maximum amplitude of 10 measured and 100 numerical time series varies as a function of time. The amplitudes at the different time intervals have been normalized by the maximum in the particular time series similar to Figure 8, and then averaged. Figure 10 shows the result for several different numerically simulated condition lengths, where 200 numerical time series were averaged for each condition. The figures give an indication of the ability to capture the maximum response for an ensemble of simulations with simulation lengths different from the true length of the simulated condition. It was found that the maximum amplitude increased with the length of the time series.

A linear relation was found between required simulation times and lengths of loading conditions, ranging from 700 s to 10800 s (3 hours), to obtain an averaged normalized maximum amplitude higher than 0.9. The result is shown in Figure 11 and the required simulation time was found to be

$$R = 0.16L + 170 \qquad [14]$$

where R is required simulation time in seconds and L is condition length in seconds.

The time when the maximum amplitude in the numerical simulation occurred, had a uniform distribution as shown in Figure 12.

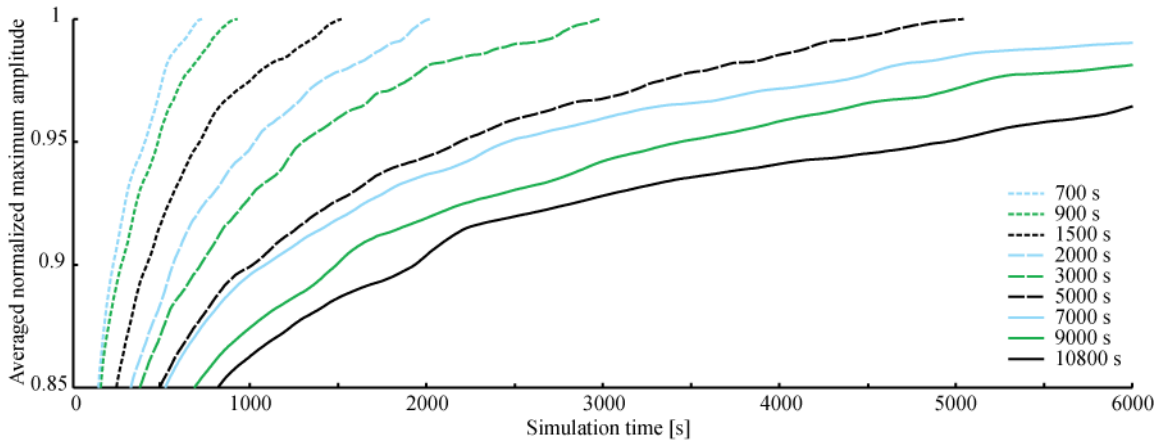

Figure 10. Averaged normalized maximum amplitude as a function of simulation time for different condition lengths.

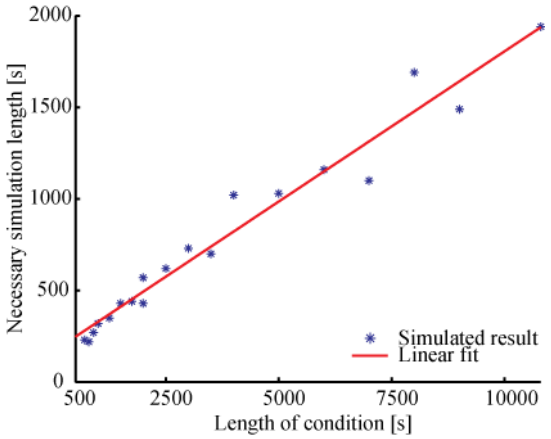

Figure 11. Required simulation time to get an averaged normalized maximum amplitude above 0.9 for different condition lengths.

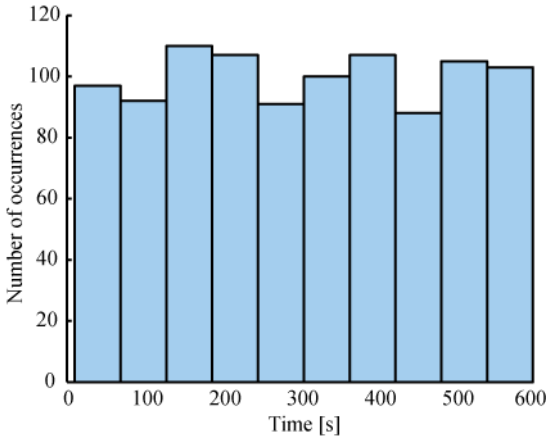

Figure 12. Histogram for the time of occurrence of 1000 numerical maximums.

6. Discussion

The load model by Qu et al. (2006) has three conditions were dynamic amplification of the loading occurs, as shown in Figure 5. The load model is divided into three parts where the triangular impulse lasts for one third of the total period T_i as shown in Eq.[8]. The physical explanation of having three dynamic amplification periods can be described by the help of a Fourier series and thereby expressing the load as a sum of harmonic functions. In order to coincide the peaks of the structures transfer function with the different Fourier components of the load function; the Fourier component of highest amplitude will have a period T_i of Eq.[8] equal to the natural period of the structure T_0, the second highest amplitude will for $2T_0$ and the lowest for $3T_0$. The loading corresponding to $3T_0$ corresponds to a triangular impulse with length equal to the natural period of the structure, and hence gives the largest amplification for one single triangular load.

It was found that the loading process obtained by the model by Qu et al. (2006) could be tuned by certain $\overline{F}_0$ and $\overline{T}$ to fit inside the 95% confidence of the measured time series. However, in general it was found that the load process by Qu et al. (2006) was a more wide-banded process

than the measured ones. This means that the real ice load histories had more of its energy focused around the peak frequency of the process. In the time domain this will give more rapid load impulses. The durations of the triangular loading were similar, but there was less time between each triangular load in the measured time series. For some of the time series an adjustment of the model by Qu et al. (2006) where the loading lasted for half of T_i instead of one third of T_i, gave a more narrow-banded spectrum and better fit to the real spectrum.

The response in the numerical calculations is narrow-banded for loading at frequencies close to or higher than the natural frequency of the structure, as shown in Figure 4. The response is then very similar to free vibration where impulse loads cause the system to oscillate continuously. This response was found to be Gaussian and the relation for simulation length as given in Eq.[7] can be used. In this study we wanted to investigate when these maximal values happened and the result for the numerical simulations are shown in Figure 8 to Figure 12. The same results were found for the numerical simulations and the true measured structural response. The maximal value in a time series could take place in the beginning and in the end of the time series with equal probability. Figure 9 shows how the average amplitude as a fraction of maximal response would look like. From this figure it can be seen that a simulation time of 50 seconds for a loading condition which is stable for 600 seconds, would in average give us a value of 70 % of the real maximum of a 600 seconds response signal. This means that the response most likely would be underestimated for this short simulation time. The graph shown in Figure 9 for the numerical simulation can be divided into three parts based on the slope of the graph; very steep inclination from 0 – 100 seconds, a smaller inclination between 100 – 400 seconds and even smaller inclination from 400 – 600 seconds. The same observation can be done for all of the graphs shown in Figure 10, but at different times. This shows that after a certain simulation length further increase of simulation time does not change the results significantly. It is important to have a simulation length that can be defined in this regime in order to get several simulation results for the same condition that not differ significantly. Figure 10 can be used to find a required simulation length for numerical calculations to obtain a desired level of accuracy for different condition lengths. To obtain simulation results that in average give 0.9 of the maximum response for the actual condition, the simulation length is given by Eq.[14]. With regards to simulation time it must also be remembered that depending on the damping in the system, it takes some time before the steady state condition is obtained.

Conclusions

Measured and numerically obtained response for the platform JZ20-2 MUQ operating in the Bohai Bay, have been compared and studied. The main findings are:

- The load model by Qu et al. (2006) was successfully used to create load data similar to measured full-scale data.
- The load model by Qu et al. (2006) gives dynamic amplified response for three different loading conditions; namely a mean period $\overline{T}$, of one, two and three times the natural period of the structure.
- The response was found to be a narrow-banded random process for loading frequencies on or higher than the natural frequency of the structure.
- The time when the maximum amplitude of the response for a certain time series took place was found to have a uniform distribution over the entire time series length.

- Figure 10 can be used to choose a simulation time based on the condition length and desired accuracy for the result.
- A required simulation time R to obtain an average response higher than 0.9 of the maximum response for a given condition length L, can be given as $R = 0.16L + 170$ where both R and L are in seconds.

Acknowledgments

The authors express their gratitude to the PETROMAKS program, the Research Council of Norway and to NTNU's PetroArctic project for contribution to the study. In addition the support of the National Natural Science Foundation of China (No. 10672029) is much appreciated.

References

Bjerkås, M. (2006). Ice Actions on Offshore Structures. Doctoral Theses 2006:9, Norwegian University of Science and Technology (NTNU), Norway, 173 p.

Bloomfield, P. (2000). Fourier Analysis Of Time Series: An Introduction, Second edition: New York, John Wiley & Sons, Inc., 261 p.

Boore, D. M., Stephens, C. D. and Joyner, W. B. (2002). Comments on Baseline Correction of Digital Strong-Motion Data: Examples from the 1999 Hector Mine, California, Earthquake. Bulletin of the Seismological Society of America, Vol. 92, No. 4 May 2002, pp. 1543-1560

Chopra, A.K. (2007). Dynamics of Structures: Theory and Applications to Earthquake Engineering. Pearson Prentice Hall, New Jersey 2007, 876 p.

Clough, R.W and Penzien, J. (1975). Dynamics of Structures. McGraw-Hill, New York 1975, 634 p.

Frederking, R., Schwarz, J. (1982). Model test of ice forces on fixed and oscillating cones. Journal of Cold Regions Science and Engineering, Volume 6, Issue 1, 61-72.

Frederking, R.and Sudom, D. (2006). Maximum ice force on the Molikpaq during the April 12, 1986 event. Journal of Cold Regions Science and Technology, Volume 46, Issue 3 , December 2006, pp. 147-166.

Gravesen, H., Sorensen, S.L., Volund, P., Barker, A. Timco, G. (2005). Ice loading on Danish wind turbines: Part 2. Analysis of dynamic model test results. Journal of Cold Regions Science and Engineering, Volume 41, Issue 1, 25-47.

Kärnä, T., Kolari, K., Jochmann, P., Evers, K.-U., Xiangjun, B., Määttänen, M., Martonen, P. (2003). Test on dynamic ice-structure interaction. Proceedings of the 22th International Conference on Offshore Mechanics and Arctic Engineering (OMAE2003), Cancun, Mexico, June 8-13 2003.

Kärnä, T., Qu, Y., Yue, Q. (2006). An Equivalent Lateral Force for Continuous Crushing. Proceedings of the 25th International Conference on Offshore Mechanics and Arctic Engineering (OMAE2006), Hamburg, Germany, June 4-9 2006.

Leis, J. (2002). Digital Signal Processing: A MATLAB-Based Tutorial Approach. Baldock, Research Studies Press.

Løset, S., Shkhinek, K., Gudmestad, O.T. and Høyland, K.V. (2006). Actions from ice on Arctic offshore and costal structures. "LAN" design, St. Petersburg, 271 p.

Naess, A. (2007). An Introduction to Random Vibrations. Lecture Notes, Norwegian University of Science and Technology (NTNU).

Ochi, M.K. (1990). Applied Probability and Stochastic Processes: In Engineering and Physical Sciences, John Wiley and Sons Inc., New York, pp. 520.

Park, K.T., Kim, S.H., Park, H.S. and Lee, K.W. (2005). The determination of bridge displacement using measured acceleration. Engineering Structures 27, pp. 371-378.

Qu, Y., Yue, Q., Bi, X. and Kärnä, T. (2006). A random ice force model for narrow conical structures. Journal of Cold Region Science and Technology, Volume 45, Issue 3, pp.148-157.

Ralston, T.D. (1977). Ice Force Design Considerations for Conical Offshore Structures. Proc. POAC 1977, Vol II, p. 741-752. Memorial University of Newfoundland, Newfoundland, Canada.

Ralston, T.D. (1980). Plastic Limit Analysis of Sheet Ice Loads on Conical Structures. International Union of Theoretical and Applied Mechanics symposium on Physics and Mechanics of Ice, Springer-Verlag, New York, p. 289-308.

Yuan, L. (2007). Research on Dynamic Analysis and Structural Lectotype of Ice-resistant Offshore Platforms. PhD Thesis, Dalian University of Technology, China

Yue, Q., Bi, X. and Yu, X. (1998). Full-scale test and analysis of dynamic interaction between ice sheet and conical structures. Proc. of 14th International Association for Hydraulic Research Symposium on Ice (IAHR), Vol II.

Yue, Q. and Bi, X. (2000). Ice Induced Jacket Structure Vibration in Bohai Bay. Journal of Cold Region Science and technology, Volume 14, Issue 2, pp. 81-91.

Special Session: Oil spills in ice

19th IAHR International Symposium on Ice
"Using New Technology to Understand Water-Ice Interaction"
Vancouver, British Columbia, Canada, July 6 to 11, 2008

Numerical Simulation of Interactions of the Oil Slick and Currents Under Ice Cover

Yoshitaka Matsuzaki[1] and Shigeki Sakai[2]

[1]Port and Airport Research Institute
3-1-1 Nagase, Yokosuka, Kanagawa 239-0826 Japan
matsuzaki-y@pari.go.jp
[2]Iwate University
4-3-5 Ueda, Morioka, Iwate 020-0066 JAPAN
sakai@iwate-u.ac.jp

The full operation of crude oil and natural gas offshore the island of Sakhalin has just started. If oil spills, a coastal area along the Sea of Okhotsk in Hokkaido, Japan might suffer serious environmental damage from the spilled oil since there is a strong southward ocean current in the Sea of Okhotsk. The sea surface in this area is covered by ice in winter; therefore it would be impossible to find the spilled oil.
In this study, we propose a numerical model which can treat interactions of oil slick and currents. This numerical model is able to simulate the deformation and movement of the oil slick by current in arbitrary conditions of oil properties and ice bottom configurations.

1. INTRODUCTION

The full operation of crude oil and natural gas offshore the island of Sakhalin has just started. If oil spills, a coastal area along the Sea of Okhotsk in Hokkaido, Japan might suffer serious environmental damage from the spilled oil since there is a strong southward ocean current in the Sea of Okhotsk. The sea surface in this area is covered by ice in winter; therefore it would be impossible to find the spilled oil.

At the last IAHR Symposium on Ice, we proposed a numerical model to simulate the deformation and movement of an oil slick induced by a current under the ice cover. In this numerical model, effects of current on the oil slick are described by an increment of the oil thickness along the edge of the oil slick that the current acts on. While the numerical model accurately simulates our experimental results, properties of oil (the density and viscosity of the oil) and effects of the ice sheet bottom roughness could not be examined since the relations between the increment of the oil slick thickness and the current velocity were obtained by experiments under a level ice with just one kind of oil.

In this study, we propose a numerical model which can treat interactions of oil slick and currents. This numerical model is able to simulate the deformation and movement of the oil slick by current in arbitrary conditions of oil properties and ice bottom configurations.

2. NUMERICAL SIMULATION METHOD

2.1 GOVERNING EQUATIONS

In this study, incompressible Navier-Stokes equation, the continuity equation and color function equation were employed as governing equations.

$$\frac{Du}{Dt} = -\frac{1}{\rho_*}\frac{\partial P}{\partial x} + \frac{1}{\rho_*}\left\{\frac{\partial}{\partial x}\left(\mu_* \frac{\partial u}{\partial x}\right) + \frac{\partial}{\partial y}\left(\mu_* \frac{\partial u}{\partial y}\right)\right\} + \frac{1}{\rho_*}F_{sx} + G_x \quad \textbf{[1]}$$

$$\frac{Dv}{Dt} = -\frac{1}{\rho_*}\frac{\partial P}{\partial y} + \frac{1}{\rho_*}\left\{\frac{\partial}{\partial x}\left(\mu_* \frac{\partial v}{\partial x}\right) + \frac{\partial}{\partial y}\left(\mu_* \frac{\partial v}{\partial y}\right)\right\} + \frac{1}{\rho_*}F_{sy} + G_y \quad \textbf{[2]}$$

$$\frac{\partial u}{\partial x} + \frac{\partial v}{\partial y} = 0 \quad \textbf{[3]}$$

$$\frac{D\phi}{Dt} = 0 \quad \textbf{[4]}$$

Where u, v are velocity in x, y direction respectively, P is pressure, ρ is density, μ is coefficient of viscosity, F_s is interfacial tension, G is external force (gravity force), φ is color function (φ=0~1). In this paper, governing equations were written 2-dimensional space. 2-dimensional space can be written 3-dimensional space to expand the governing equations to z direction. Color function φ was used to decide the position of oil and water. φ=1 means oil, and φ=0 means water. Density ρ and coefficient of viscosity μ were decided at each cell from color function φ.

2.2 NUMERICAL SOLUTION

Figure 1 shows calculation algorism. In this study, we split Navier-Stokes equation between advection term and non-advection term. Advection term of Navier-Stokes equation and color function equation were calculated by CIP (Constrained Interpolated Profile) method. CIP method is one of the calculation approaches to solve advection term. CIP method is calculation method satisfied profile between calculation grids approximately using calculation value (u,v,φ) and its spatial differential value (du/dx, du/dy, dv/dx, dv/dy, dφ/dx, dφ/dy).

Non-advection term was calculated by SMAC method.
In general, difference at calculation of viscous term in single-phase flow is as follows;

$$\nabla^2 u_{i+1/2,j} = \frac{u_{i+3/2,j} - 2u_{i+1/2,j} + u_{i-1/2,j}}{\Delta x^2} + \frac{u_{i+1/2,j+1} - 2u_{i+1/2,j} + u_{i+1/2,j-1}}{\Delta y^2} \quad \textbf{[5]}$$

In calculation of viscous term in multi-phase flow, using velocity next to the cell like equation [5] doesn't seem to describe change of velocity between two flows accurately. Figure 2 shows change of velocity between two fluids. We think change of velocity is like this figure.
In this study, viscous term was transformed into difference equation as follows.
Viscous stress from (i+1/2,j-1) to (i+1/2,j-1/2) is equal to it from (i+1/2,j□1/2) to (i+1/2,j). From balance of stress,

$$\tau_{i+1/2,j-1/2\square j} = \tau_{i+1/2,j-1\square j-1/2} \quad \textbf{[6]}$$

Oil and water are Newtonian fluid,

$$\tau = \mu \frac{\partial u}{\partial y} \quad \textbf{[7]}$$

Therefore,

$$\mu_{i+1/2,j} \frac{u_{i+1/2,j} - u_{i+1/2,j-1/2}}{\frac{\Delta y}{2}} = \mu_{i+1/2,j-1} \frac{u_{i+1/2,j-1/2} - u_{i+1/2,j-1}}{\frac{\Delta y}{2}} \quad \textbf{[8]}$$

$$u_{i+1/2,j-1/2} = \frac{\mu_{i+1/2,j-1} \cdot u_{i+1/2,j-1} + \mu_{i+1/2,j} \cdot u_{i+1/2,j}}{\mu_{i+1/2,j-1} + \mu_{i+1/2,j}} \quad \textbf{[9]}$$

So, difference at calculation of viscous term in multi-phase flow is as follows;

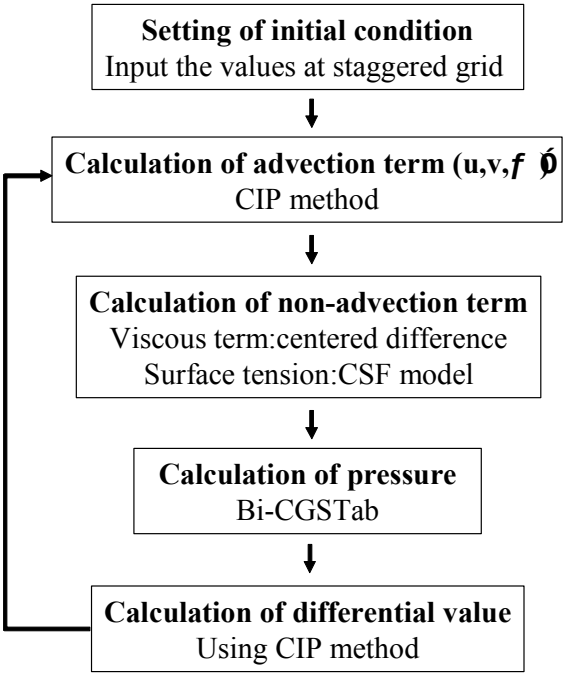

Figure 1. Calculation algorism

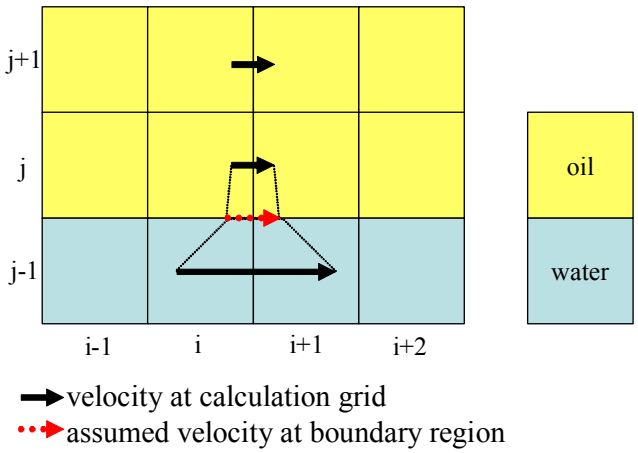

Figure 2. Change of velocity between two fluids

$$\nabla^2 u_{i+1/2,j} = \frac{1}{\rho_{i+1/2,j}} \frac{1}{\Delta x} \left(\mu_{i+1,j} \frac{u_{i+3/2,j} - u_{i+1/2,j}}{\Delta x} - \mu_{i,j} \frac{u_{i+1/2,j} - u_{i-1/2,j}}{\Delta x} \right) + \frac{\mu_{i+1/2,j}}{\rho_{i+1/2,j}} \frac{1}{\left(\frac{\Delta y}{2}\right)^2} \left(u_{i+1/2,j+1/2} - 2u_{i+1/2,j} + u_{i+1/2,j-1/2} \right) \quad [10]$$

Color function has value from 0 to1 and the value was decided at each cell by color function equation. φ=1 means oil, and φ=0 means water, so property values ρ, μ at boundary region were decided as follows;

$$\rho_* = \rho_o\phi + \rho_w(1-\phi) \quad \textbf{[11]}$$

$$\upsilon_* = \upsilon_o\phi + \upsilon_w(1-\phi) \quad \textbf{[12]}$$

Surface tension was given by CSF (the Continuum Surface Tension) model. This model is flowed the concept that replace pressure difference at boundary surface by volume force at tiny boundary region.

If boundary region become complicated, it is difficult to capture boundary region closely. In this study, we caught a boundary region sharply by converting color function φ in a tangent function as follows;

$$H(\phi) = \tan[(0.9\pi(\phi - 0.5))] \quad \textbf{[13]}$$

In order to prevent the tangent function from becoming infinity, 0.9 was given as a coefficient. Tangent function was inverse transformed when the value was necessary.

3. NUMERICAL RESULTS

Calculation in case there was the current under the ice cover was performed. Calculation conditions are Table 1. Figure 3 shows boundary conditions. Current was taken as 0.005× (acceleration of gravity)×(Elapsed time) to 20cm/s. Counter side was free boundary condition. Non-slip condition at the ice bottom was used, and free slip condition at sides were used.

Figure 4 shows comparisons of numerical and experimental results of the deformation and movement of the oil slick. Top are experimental results, bottom are numerical results, and upper is plane view and downside is cross-sectional view. In the plane view of numerical results, a shade in the oil slick shape corresponds to the thickness. Oil thickness increase by current and oil slick move to flow direction. The calculated shapes of the oil slick agree with the experimental results.

Figure 5 shows comparisons of numerical and experimental results of the movement speed which was calculated from the position of the center of oil slick. Two figures in Figure 5 correspond to that in Figure 4, respectively. In general, the present model simulates experimental results of the oil speed.

But rear oil lag compared to the experimental results. In this study, we adopted non-slip condition at the ice bottom, so we might have to use free-slip condition and give any friction to the oil slick from ice bottom roughness.

Table 1. Calculation conditions

Time Step (sec)	1.0×10^{-4}
Acceleration Coefficient of Gravity (m/s^2)	9.8
Temparature (K)	273
Surface Tension Coefficient (N/m)	2.641×10^{-2}
Water Viscosity (Pa.sec)	1.79×10^{-3}
Oil Viscosity (Pa.sec)	2.54×10^{-1}
Water Density (kg/m^3)	1000
Oil Density (kg/m^3)	878

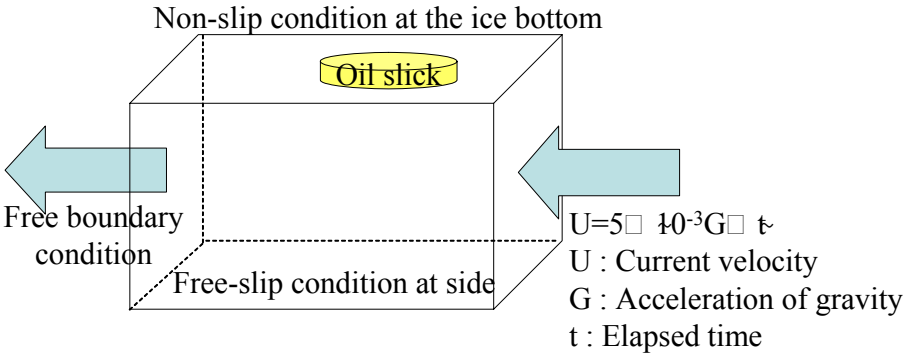

Figure 3. Boundary conditions

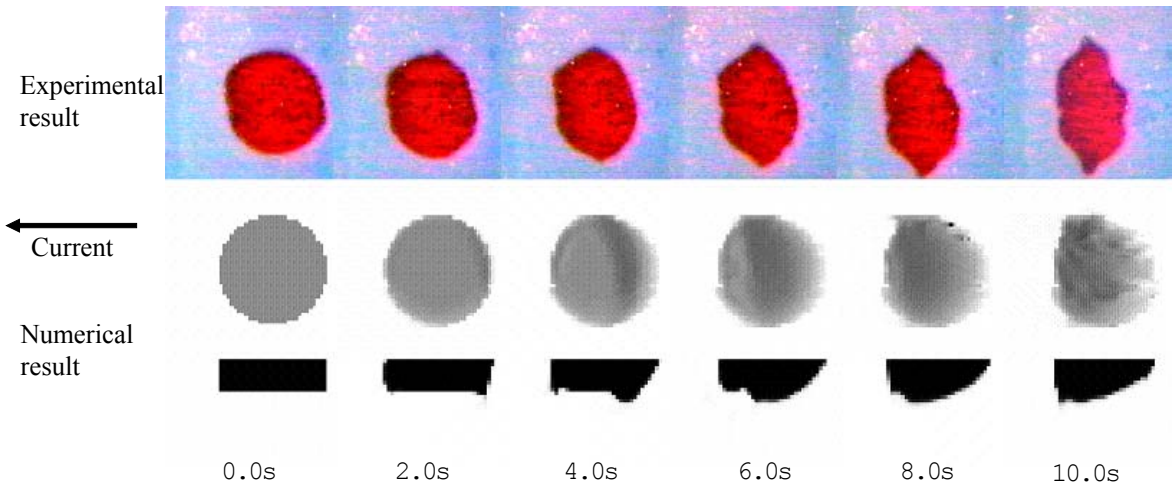

(a) Initial area of the oil slick 1500cm^2
Current velocity 20cm/s

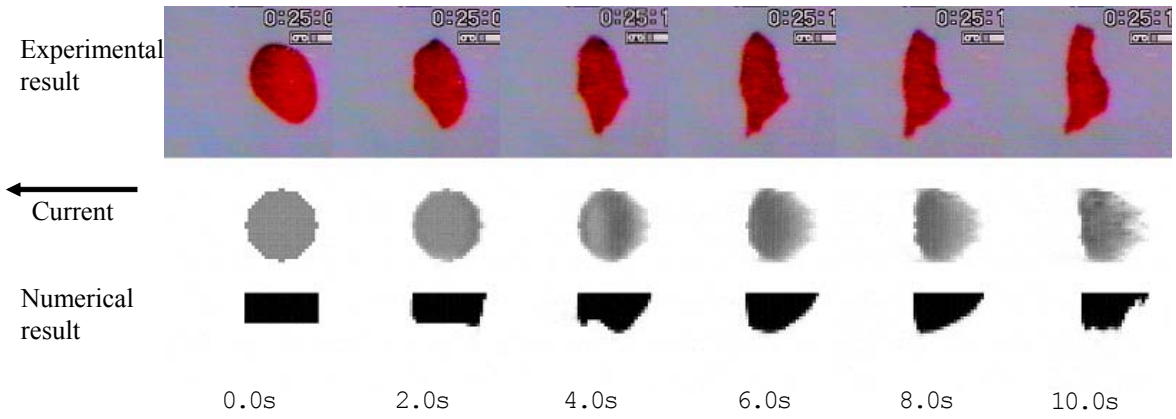

(b) Initial area of the oil slick 800cm^2
Current velocity 20cm/s

Figure 4. Comparisons between numerical and experimental results of oil slick deformation

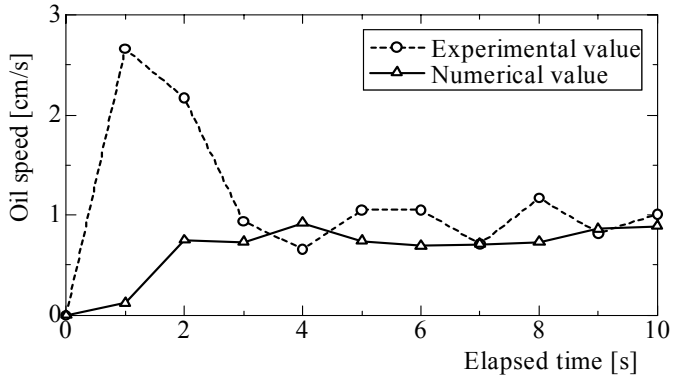

(a) Initial area of the oil slick 1500cm^2
Current velocity 20cm/s

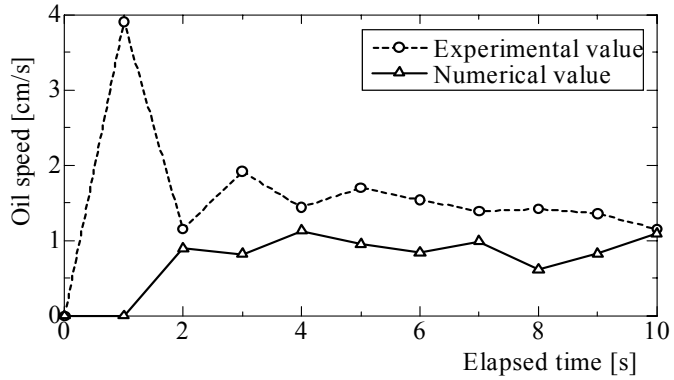

(b) Initial area of the oil slick 800cm^2
Current velocity 20cm/s

Figure 5. Comparisons between numerical and experimental results of oil speed

4. EFFECTS OF OIL PROPERTIES

Characteristics of the deformation and movement of the oil slick by currents under the ice will depend on properties of the oil. In particular, the density of oil, the oil-water interfacial tension, and viscosity of the oil are dominant factors to characterize the deformation and movement. Figure 6 shows the effects of the density of oil, the oil-water interfacial tension, and the viscosity of oil on the deformation of the oil slick. Bench mark is same result of the Figure 4 (b). Difference of calculation conditions are as follows. In case1 and case2, the densities of oil are 800kg/m^3 and 950kg/m^3, respectively. In case3 and case4, the coefficients of interfacial tension are 1.3205×10^{-2}N/m and 5.282×10^{-2}N/m, respectively. In case5 and case6, the coefficients of viscosities are 0.127Pa.sec and 0.508Pa.sec, respectively.

Figure 7, 8, 9 show the effects of the density of oil, the interfacial tension and the viscosity of oil on the relations between the oil speed and the current velocity, respectively. Figure 7 illustrates the influence of the density on the oil speed. When the density is larger, the movement speed is larger. Figure8, 9 show that the oil speed is larger when the interfacial tension is larger and the viscosity is smaller.

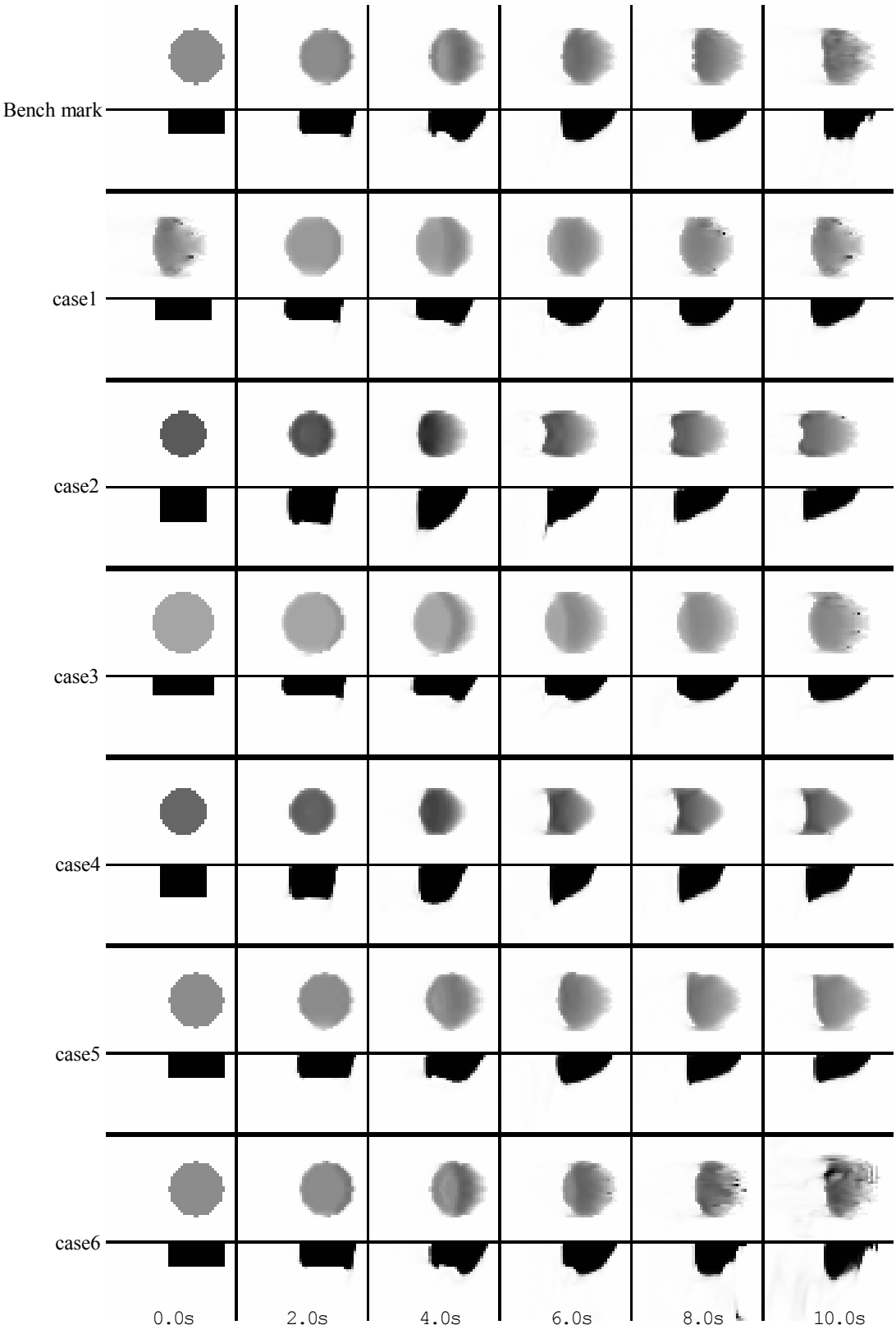

Figure 6. Comparisons between numerical and experimental results of oil slick deformation

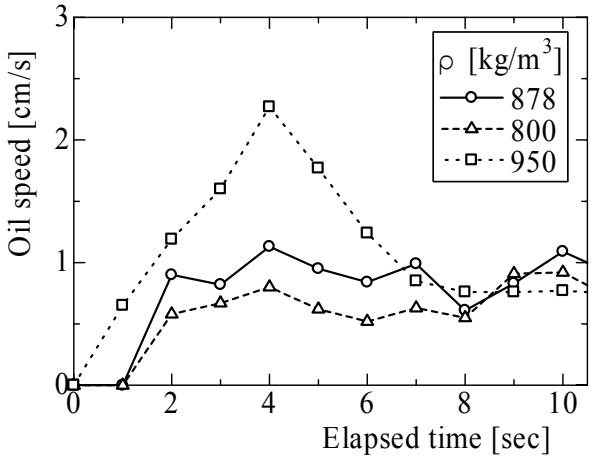

Figure 7. Effects of density of oil on movement speed

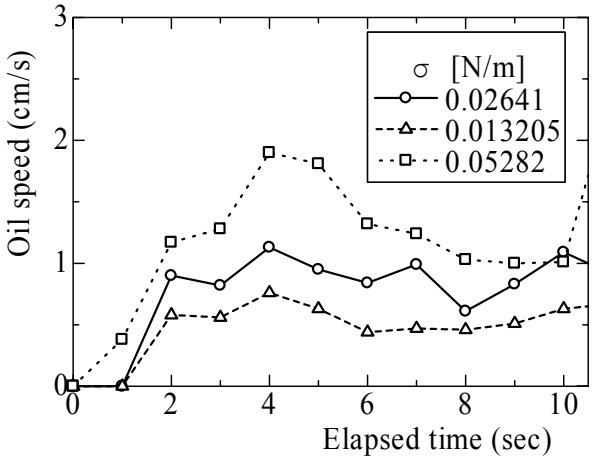

Figure 8. Effects of interfacial tension of oil on movement speed

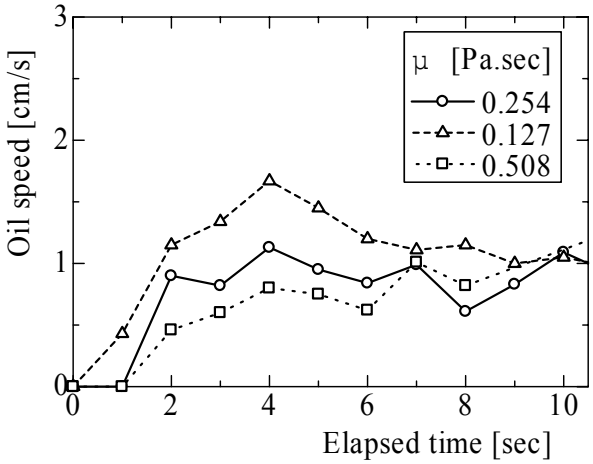

Figure 9. Effects of viscosity of oil on movement speed

5. CONCLUTIONS

Results of this study can be summarized as follows.

1. In this study, we developed the numerical simulation be able to treat interactions of oil slick and currents.
2. The present simulation method simulates experimental results of the deformation and movement of the oil slick under the ice cover.
3. The present model can treat in arbitrary conditions, for example, difference of density of oil, coefficient of interfacial tension and viscosity, value of current velocity and ice bottom configurations.
4. The calculated results show the effects of the oil properties on the oil movement speed.

References

Yoshitaka Matsuzaki, Toshinori Ogasawara, Shigeki sakai, Koh Izumiyama and Shigeo Kanada, 2006. NUMERICAL SIMULATION OF CURRENT-INDUCED DEFORMATION AND MOVEMENT OF THE OIL SLICK UNDER THE ICE COVER. Proc 18th IAHR Symposium on Ice, pp.219-226

Takashi Yabe, Feng Xiao and Takayuki Utsumi, 2001. The Constrained Interpolation Profile Method for Multiphase Analysis. Journal of Computational Physics 169, pp.556-593

J. U. BRACKBILL, D. B. KOTHE, AND C. ZEMACH, 1992. A Continuum Method for Modeling Surface Tension. Journal of Computational Physics 100, pp.335-354

19th IAHR International Symposium on Ice
"Using New Technology to Understand Water-Ice Interaction"
Vancouver, British Columbia, Canada, July 6 to 11, 2008

R & D Study of an Oil Recovery Device for Ice-covered Waters

Koh Izumiyama, Shigeo Kanada, Haruhito Shimoda
Daisuke Wako and Tadanori Takimoto
National Maritime Research Institute
6-38-1, Shinkawa, Mitaka, Tokyo 181-0004 Japan
koh@nmri.go.jp, kanada@nmri.go.jp, shimoda@nmri.go.jp
wako@nmri.go.jp and takimoto@nmri.go.jp

Abstract

Ice-covered waters in the arctic and sub-arctic regions are regaining a growing interest as the fields for the exploitation and transportation of hydrocarbon resources. Ice-covered waters, meanwhile, are sensitive and vulnerable to pollution. Oil spilling at sea from ships or other facilities can cause disastrous damages to the ocean environment. Recognizing the sensitive and vulnerable environment of ice-covered waters, there have been studies done on the fate and behavior of spilled oil in ice and on the response measures to the pollution. However, our understanding of these problems is still significantly limited compared with of those in open water conditions.

This paper presents the results of an R & D study at National Maritime Research Institute (NMRI) of an oil recovery device to be used in ice-covered waters – NMRI-ORDICE. Oil recovery in ice-covered waters has to go through two different processes of oil-ice separation and then oil recovery from water. NMRI-ORDICE uses air-bubbling to separate oil from ice. A new design of NMRI-ORDICE was made in 2006. This paper describes two major elements in the design. Based on the design a model was manufactured. A series of model testing was performed in 2007 in the ice model basin of NMRI. The model was tested in various ice conditions. Two machine oils with different viscosity were used in the test. Data obtained in the test are presented. Test results are discussed in terms of recovery rate, which is the ratio of recovered oil volume to that released, oil fraction, which is the ratio of oil volume to the total liquids volume recovered, the effects of brash and slush ice and oil viscosity.

1. Introduction

Ice-covered waters in the arctic and sub-arctic regions are regaining a growing interest as the fields for the exploitation and transportation of hydrocarbon resources. Commercial production of oil has commenced in 1999 in the continental shelf of Sakhalin Island in the Sea of Okhotsk (Sakhalin Energy). Although the production has been limited in non-ice seasons, it will enter a year-round operation phase in the near future. A giant oil field was discovered in 2000 in North Caspian Sea, where air temperature can be as low as -30 degrees-C in winter, to be one of the recent largest discoveries in the world (Agip KCO). The oil field was declared to be commercial in 2002, and the production is planned to start in 2008. Baltic Sea is seeing a soaring surface traffic to and from the oil terminals located in the coast of the Gulf of Finland (Rytkonen, 2005). Winter shipping is not an exception. Baltic ice-covered waters are sailed by increasing number of ships.

The environment of ice-covered waters, meanwhile, is sensitive and vulnerable to pollution. In waters with temperate conditions, pollutants released in the environment can be disintegrated into harmless substances through biodegradation processes. In ice-covered waters, however, the unique conditions such as low temperatures and insufficient intensities of sunlight retard the biodegradability and pollutants can persist and accumulate in the environment. In addition, human use of ice-covered waters has been minimal due to the harsh conditions. Little is known of the environmental consequences of large scale pollutions in such waters. Developments in ice-covered waters require full considerations and precautionary measures for the environment protection.

Oil spilling from ships or other facilities is one of major, and probably most frequently observed, causes of pollution at sea. A large scale oil spill brings about acute and disastrous damages to the ocean environment. It can also result in serious impacts on industries such as fisheries and tourism of the affected regions. Recognizing the particularly sensitive and vulnerable environment of ice-covered waters, there have been studies done on issues related to oil spilling in ice including the fate and behavior of spilled oil in ice and on the response measures to the pollution (Evers et al, 2004). Our understanding of these problems, however, is still significantly limited compared with of those in open water conditions.

Mechanical recovery of spilled oil is the most desirable response method from the environmental point of view. However, mechanical recovery of oil spilled in ice-covered waters is a complicated problem. It has to go through two different processes – separation of oil from the ice and then recovery of oil from the water. Although some modification may be needed, conventional techniques for open water conditions could be applicable to the latter process. The former process, however, calls for new ideas. There have been various techniques studied of the oil-ice separation mechanisms. MORICE project developed a recovery device that lifts ice from the water by a rotating grated belt (Jensen and Mullin, 2003). Oil left on the water surface is recovered by a brush-drum recovery unit. Lamor Oil Ice Separator (LOIS) also uses a grated belt to separate oil from the ice (Finnish Environment Institute). Contrary to the MOICE concept, the grated belt submerges ice into the water and let oil rise to the surface. The belt also vibrates to promote oil separation from the ice.

National Maritime Research Institute (NMRI) has been carrying out an R & D study of an oil recovery device for ice-covered waters (hereinafter termed NMRI-ORDICE). It is based on a concept to separate oil and ice by way of air-bubbling in the water. The study has undergone two phases. In the first phase, a review was made of the existing techniques and ideas for oil recovery in ice. It was followed by a small scale model test at the ice model basin of NMRI to examine the effectiveness of the oil-ice separation concept using air-bubbling (Narita et al, 2001). In the second phase a lager model, 6 m in length and 5 m in width, was manufactured and tested for various ice conditions (Izumiyama et al, 2005).

The third phase started in 2006 when the study was incorporated in a larger research project at NMRI on the shipping safety and oil pollution prevention in the Sea of Okhotsk. In 2006 results of the previous studies were reviewed and a new design of NMRI-ORDICE was made. A model of NMRI-ORDICE was manufactured for ice model basin test based on the new design. In 2007 two series of model tests were performed. The first series was to study the basic performance of the newly designed NMRI-ORDICE and to find out possible further improvements of the design. Based on the result of the test, some modifications were made of the model. The second series of tests was performed for the modified model to quantitatively assess the oil recovery performance of NMRI-ORDICE. This paper describes the outline of NMRI-ORDICE including the new design, and presents and discusses the result of the second series tests.

2. Oil Recovery Concept

Figure 1 is an aerial photograph taken at an experimental oil spill performed in icy water off Nova Scotia, Canada (S.L. Ross Environmental Research Limited and D.F. Dickins Associates Limited, 1987). The photograph shows the spilled oil spreading over the free surface in broken ice. NMRI-ORDICE has been developed to function in the ice conditions as shown in the photograph.

Figure 2 schematically shows the oil recovery concept by NMRI-ORDICE. NMRI-ORDICE is a self-floating device. It is composed of an oil-ice separation channel, oil recovery ducts and air-bubbling units on the bottom of the channel. The oil-ice separation channel and the oil recovery duct are separated by a grating. To recover oil from the ice, oil and ice are brought in the separation channel. Air bubbles are released from the bubbling units beneath. The rising air bubbles entrain the surrounding water mass to create plume jets in the water. The jets generate horizontal currents at the surface or at the bottom of ice. The currents transport the oil and ice toward the recovery duct. The grating stops the ice but allow the oil to go through it and to enter the recovery duct. Oil is recovered from the duct and cleaned ice is returned to the sea. Oil spilled from underwater sources such as a pipeline may be trapped in depressions and pockets located in the underside of ice. Air-bubbling is effective to separate such oil, because air can displace it from the hollows.

Figure 1. Aerial Photograph at an Experimental Oil Spill

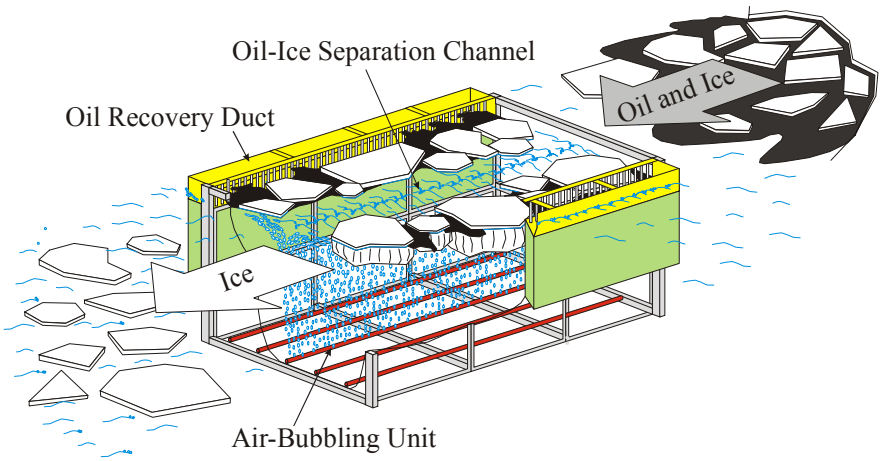

Figure 2. Schematic of Oil Recovery by NMRI-ORDICE

3. New Design incorporated in NMRI-ORDICE

A new design of NMRI-ORDICE was made through brain-storming discussions. There are many points that were incorporated in the new design. Two major elements of the new design are described below.

Air-bubbling System

Model testing in the phase-2 study revealed a problem associated with oil recovery from broken ice (Izumiyama et al, 2005). It was observed, particularly in tests with high ice concentrations, that ice acted as a barrier in front of the grating to hamper oil flow into the recovery duct. This slowed down the recovery operation. To solve the problem a mechanism to shift air-bubbling tubes sideways was introduced. This aimed to "pack off" the oil to the recovery duct by gradually shifting the location of plume jets. The test showed that the mechanism worked well.

The new design adopted an improved air-bubbling system. Figure 3 schematically compares the previous and new systems. In the previous system, air bubbles are released from tubes installed in the bottom of the oil-ice separation channel. The tubes span the whole length of the channel and can be shifted sideways. This system enables to create linearly aligned plume jets at any lateral locations in the channel. In the new system, numbers of short and fixed air-bubbling units, instead of the long movable tubes, are installed on the bottom of the separation channel. Air flow to each unit can be controlled separately. The packing-off effect as in the previous system can also be achieved in this system by releasing air from bubbling units alternatively toward the recovery duct. Furthermore, the new system provides a wide range of options of oil recovery operation. It is possible, for instance, to drive oil to any intended directions by selecting appropriate units. Also, the fixed bubbler design is expected to be mechanically less problematic than the movable tube design.

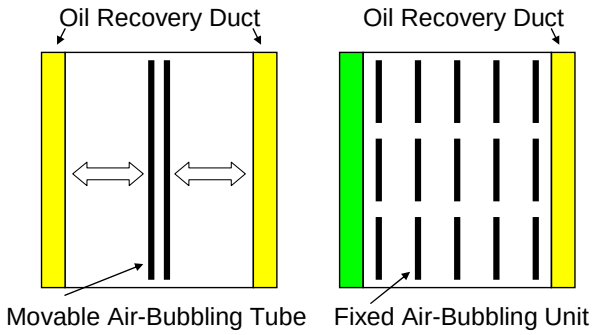

Figure 3. Schematic Comparison of Air-bubbling Systems

Oil Recovery System

The previous studies at NMRI mainly focused on the oil-ice separation process recognizing that this is the crucial point for the development of oil recovery device in ice-covered conditions. In the previous model test, oil was recovered manually from the ducts. In the present study, oil recovery mechanism after the separation from ice is also regarded as an important issue to be worked on for the development of NMRI-ORDICE. Existing oil skimming technologies were reviewed and a system for NMRI-ORDICE was designed.

There have been many types of skimmers developed for oil recovery in open water conditions. They can be categorized into weir skimmers, oleophillic skimmers, bucket skimmers and suction skimmers (DeCola, E. et al, 2006). After reviewing the principles and functions of these skimming systems, particularly in terms of the applicability to low temperature conditions, it was concluded that NMRI-ORDICE is to be outfitted with a weir type oil recovery system. Wire skimmers draw oil from the surface by creating a sump in the water. The captured oil is pumped out of the sump and sent to a storage.

A wire type oil recovery system with a motor-driven gate was designed for NMRI-ORDICE. Figure 4 schematically shows the system. A gate is placed on the front face of the recovery duct. The gate is driven by a motor vertically. To recover oil the gate is lowered so that its top side comes slightly below the surface. Oil, together with water, then overflows the gate and is captured in the duct. The flow rate can be controlled by adjusting the elevation of the gate. The gate is fitted with an inclined plate to direct the liquids. This is to prevent the liquids from flowing over the back of the gate. Oil and water captured in the duct are pumped to a storage tank.

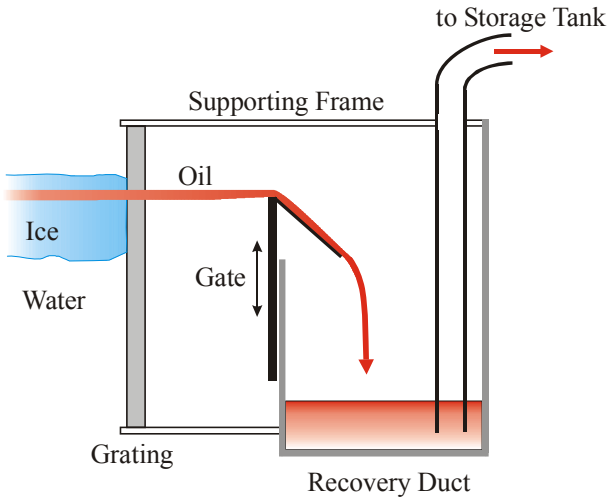

Figure 4. Oil Recovery by NMRI-ORDICE

4. Model Testing

Model Tested

A model of NMRI-ORDICE was designed and manufactured in 2006. The model was tested in 2007 in the ice model basin of NMRI. The basin is 35m in length, 6 m in width and 1.8m in depth. It is housed in a cold chamber and ice is grown at the air temperature of -20 degrees-C. Saline ice was used for the test. The basin is spanned by a main carriage with a towing capacity of 50 kN. There is also a smaller working carriage.

Figure 5 and Figure 6 show the outline and photograph of the model, respectively. The model is 6.6 m in allover length including ice deflectors, 4.8 m in width and 1.6m in depth. It is made of stainless steel and displaces about two tonnes. The oil-ice separation channel is 6.0m in length and 3.5m in width. The channel is supported by two 0.4 m wide floaters on either side. The starboard floater is double-bottomed and functions as the oil recovery duct. The model is equipped with wheels. It stands on them when assembled in the drained basin. In the test the

model floats by itself. The oil-ice separation channel can be closed by fore and aft motor-driven gates of 4 m in width and 0.8 m in height.

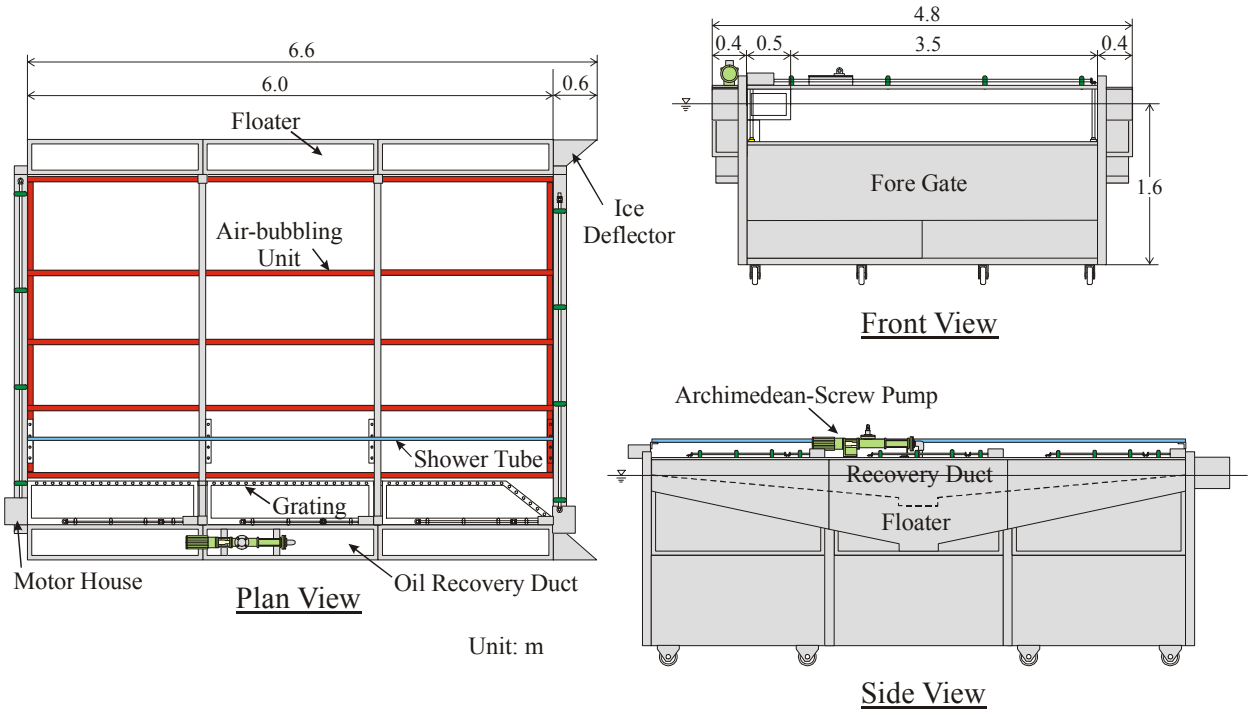

Figure 5. Outline of Model

A grating composed of vertical bars of 20 mm in diameter is located in front of the oil recovery duct. The bars can be set by inserting them into holes located at constant intervals in the upper and lower supporting frames. This design enables to perform tests for different bar spacings. In the present test, the center-to-center spacing of neighboring bars was set to the minimum value of 50 mm. Behind the grating there are three oil recovery gates. The gate is watertight and 1.8 m in width and 0.5 m in height. Three motors drive the gates separately. They can be driven also together. There is a 0.5 m spacing between the grating and the gates.

Figure 6. Photograph of Model assembled in Ice Model Basin

As a supplemental function for oil recovery, the model is outfitted also with a showering system. A 6 m long tube is installed in front of the grating spanning the whole length of the separation channel. The tube is equipped with nozzles at constant intervals. Pressurized water pumped to the tube comes out of the nozzles to generate fan-shaped sprays. The tube can be turned on the axis so that the spray direction is changed. With this system the surface area up to the grating can be swept by a shower from the turning tube.

Air-bubbling units are installed on the bottom of the oil-ice separation channel. In total there are 15 units in the arrangement of 3 lengthwise by 5 widthwise. Each unit is a stainless tube of 2 m in length and with a rectangular cross section of 30 mm by 30 mm. Holes of 1 mm in diameter are drilled in the tube at 100 mm intervals. They are loacated not in the topside but in the underside of the tube. A preliminary test showed that this configuration gave a more simultaneous and uniform bubble generation along the unit. In addition to the units, 4 m long air-bubbling tubes are installed beneath the fore and aft gates. A 3.7 kW air compressor with the maximum pressure of 0.93 MPa provides air to the units and tubes via a regulation tank and a control panel. Figure 7 is a photograph of the panel. Air flow rate to each unit and tube can be controlled separately by valves and flow meters on the panel. Typical flow rate used in the test was 100 *l*/min/unit.

Figure 7. Flow Control Panel

Liquids captured in the recovery duct are transported to a storage tank by an Archimedean-screw pump (Nemo Pump, Heishin Ltd.). An ordinary volute pump was used in the first series of tests in 2007. However, this pump turned out to disperse oil in water. Pumped water had a milky whitish appearance, and it was difficult to determine the oil-water interface in the storage tank even a long time after a test. This pump was then replaced by the Archimedean-screw pump. The new pump disperses little oil in water. The oil-water interface can be clearly seen in the storage tank as shown later in Figure 8. Also, the Archimedean-screw pump is able to transport small ice pieces and slush ice that pass through the grating and are captured in the recovery duct together with oil and water. This is another advantage of this pump as an element of the model.

Test Conditions and Methods

Table 1 summarizes the test conditions. For the test ice sheet was grown in the basin to a thickness of 100 mm. Ice was then cut out in circular floes of different diameters ranging from 0.3 m to 2 m to represent broken ice conditions at sea. In the test ice floes were brought in the oil-ice separation channel of the model and oil was released in it. The test was performed for a wide range of ice concentration in the separation channel. This was done by changing the amount of ice in the channel. The numbers of ice floes with different diameters were determined so that they keep the same ratio. The ratio was determined based on field observation of ice floe size in the Sea of Okhotsk (Izumiyama et al, 2005). Some tests were performed to study the effects of brash and slush ice presence on the recovery performance. These ice features were created by breaking and pulverizing ice blocks taken from the basin.

Two machine oils of different viscosity were used for the test. Oil properties given in Table 1 are values at 0 degree-C. For comparison, viscosity of Arabian Light and Heavy crude oils is 32 and 130 mPa-s at 0 degree-C, respectively (Environment Canada), and Sakhalin Vityaz oil is reported to be of 4 mPa-s at 15 degrees-C (Petroleum Association of Japan). Most of the test was performed with the lower viscosity oil, while the higher viscosity oil was used in two tests.

Table 1. Test Conditions

Ice	Floe Diameter, m	0.3, 0.67, 1.0, 2.0 m		
	Concentration, %	36 – 89 %		
Oil	Viscosity, mPa-s	57		1450
	Density, kg/m^3	881		890
	Volume, *l*	70	140	40
Air Flow Rate, *l*/min/unit		100		
Recovery Operation Period, min		10		

After each test oil and water volumes recovered in the storage tank were measured. The storage tank is made of transparent acrylic resin. Figure 8 is a photograph of the tank after a test. An oil-water interface is clearly seen in the photograph. Depth of the oil layer and the total depth of liquids were measured to calculate recovered volumes. As shown in Figure 9, oil layer was observed to gradually shrink with time and leveled off about one hour after a test. This can be understood as a process in which water entrained in the oil layer drained out of it because of the higher density. For the sake of test efficiency, a test routine was set so that the oil and water depths in the storage tank were measured 20 minutes after a test, and the net volume of the recovered oil was calculated using the time curves as shown in Figure 9. In some tests, particularly tests with slush ice, also a fair amount of ice was transported to the storage tank together with oil and water. The ice located between the oil and water. Although such ice was mixed with oil and difficult to be distinguished from the oil layer above, careful observation enabled to determine the oil-ice interface.

Figure 8. Oil and Water in the Storage Tank

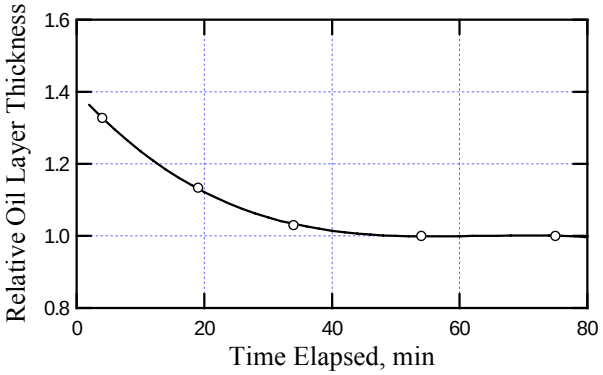

Figure 9. Oil Layer Shrinkage with Time

The model was tested in two modes – a standing mode and a moving mode. In the standing mode, the model was located still in the northern end of the basin with the fore and aft gates closed. Oil and ice were enclosed in the separation channel. Oil recovery test was carried out for a period of 10 minutes. Oil volume recovered in this period was measured in the storage tank after the test. If practically the whole volume of oil was recovered before the appointed time, the test was then finished. Tests were performed for different ice conditions and oil volumes. Oil recovery process

was filmed by VTR cameras on the main carriage located behind the model and on the chamber ceiling above the model.

In the moving mode, oil and ice were located on the surface in front of the model. The model was connected to the main carriage and pushed through the oil and ice at a constant speed with the fore and aft gates open. This test was performed to observe oil and ice behavior flowing into, through and out of the separation channel. However, the test was possible for only a very low range of model speed due to a large squat of the model. The tested speed range was too low to be compared with practical operation speeds in full-scale conditions. It was decided to perform this test with a smaller model in 2008. This paper presents test results in the standing mode.

5. Test Results

Figure 10 shows the oil recovery process observed in test No. 8. The figure shows series of frames taken by the VTR camera located behind the model. Each frame shows the oil and ice conditions in the separation channel at the indicated time during the course of the test. The small drawing in the top right corner of each frame shows the air-bubbling units working at the time of the frame.

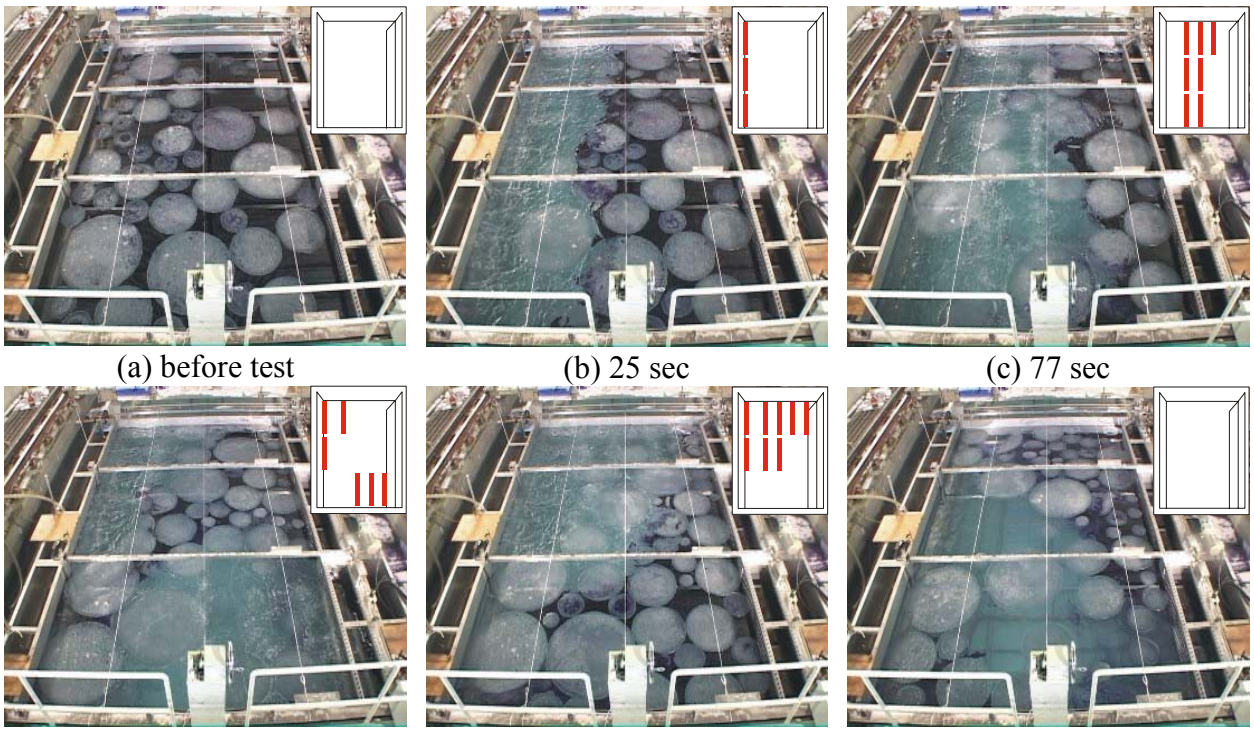

Figure 10. Oil Recovery Process (Test No. 8)

A brief description of oil recovery processes shown in each frame of Figure 10 is given below. Although there were no particular procedures determined for oil recovery operation in the present study, the figure shows a typical air-bubbling unit operation for oil recovery conducted in the present test.

(a) The condition in the oil-ice separation channel before the test is shown. In this test oil volume and ice concentration in the separation channel were 65 *l* and 63.5 %, respectively.
(b) Oil recovery operation started with air-bubbling from the units located beneath the port floater. Oil and ice were sent toward the starboard floater which is the recovery duct.
(c) Air bubbling from the units in the second row started, and the third row followed then. Oil was further sent toward the recovery duct. Oil recovery was performed with these units working. When oil was recovered from a gate, bubbler units also in the forth and fifth rows in front of the gate were used. This operation was repeated for each gate. Note that some ice floes had returned to the port side of the channel beyond the plume jets in the third row.
(d) An amount of oil evaded the above recovery operation and remained unrecovered in the channel. A second-round recovery operation was made for the remaining oil. More complicated bubbler operation is required to efficiently recover the smaller volume of oil than the first-round. This frame shows that the bubbling units were operated so that oil was directed to the fore recovery section.
(e) This frame shows that oil was directed to the aft recovery section.
(f) Test was over. After a ten-minute operation, some volume of oil was left unrecovered in the channel. In this test it was about 10 % of the oil volume released before the test.

Table 2. Summary of Test Results

Test No.	Ice Concentration %	Oil Viscosity	Shower	Oil Volume Released, *l*	Recovery Rate, %	Oil Fraction, %	Remarks
5	38.1	low	OFF	66	85.8	30.3	
6	38.1	low	OFF	66	97.2	36.8	
7	63.5	low	OFF	63	65.5	26.6	
8	63.5	low	OFF	65	90.8	31.5	
9	88.9	low	OFF	65	64.5	21.8	
10	88.9	low	OFF	64	36.9	13.2	
11	63.5	low	OFF	61	80.4	21.8	
12	63.5	low	OFF	141	79.8	45.1	
13	63.5	low	OFF	141	84.3	56.2	
14	38.1	low	OFF	140	87.3	48.6	
15	38.1	low	OFF	140	99.0	57.9	
16	40.4	low	OFF	70	97.0	39.7	test finished in 7 minutes
17	40.4	low	OFF	70	98.0	41.8	
18	80.7	low	OFF	69	74.9	12.3	
19	47.5	low	OFF	70	54.4	23.5	operation not successfully
20	47.5	low	OFF	70	89.2	24.5	
21	47.5	low	OFF	69	90.2	28.0	test finished in 9 minutes
22	71.3	low	OFF	67	77.2	20.1	
23	71.3	low	OFF	67	84.5	22.2	
24	35.6, brash/slush ice	low	OFF	66	43.9	7.8	
25	35.6, brash/slush ice	low	OFF	66	64.2	11.7	test finished before appointed time due to limitation in storage tank
26	brash ice	low	ON	64	59.2	11.4	
27	brash ice	low	OFF	64	64.4	15.5	
28	brash/slush ice	low	OFF	63	28.3	6.4	
29	brash/slush ice	low	ON	63	42.5	9.4	
30	brash/slush ice	low	ON	62	55.1	14.2	
31	35.6	high	OFF	40	94.4	17.3	some oil may be left in hose due to high viscosity
32	35.6	high	OFF	40	95.0	20.1	

Table 2 summarizes the test results. In total 32 tests were performed in the standing mode. Tests No. 1 through 4 are not included in the table, because they were performed for open water (no ice) conditions or as preliminary tests with ice. Two dimensionless parameters of recovery rate and oil fraction were defined to analyze test results. Recovery rate is the ratio of oil volume recovered in a test to that released in the separation channel before the test. Oil fraction is the ratio of the recovered oil volume to the total volume of liquids (and ice) pumped to the storage tank. Table 2 gives these two parameters.

6. Discussion

The present model test provided data that enabled us to quantitatively assess the oil recovery performance of NMRI-ORDICE. Test results are discussed below from viewpoints of recovery rate, oil fraction, the effects of brash and slush ice, and oil viscosity.

Recovery Rate

Model test in the previous study showed that the time required to recover a certain volume oil was a function of ice concentration in the oil-ice separation channel (Izumiyama et al, 2005). The required time decreased with the increase of ice concentration. The present test was performed in a way that the oil recovery operation was made for a period of 10 minutes, and liquids volume recovered in the period was measured. Figure 11 shows the correlation of recovery rate to ice concentration. Although the plot shows some scatter, there is a general trend of recovery rate increasing with the decrease of ice concentration. In the tests with ice concentration of 40%, almost all the oil was recovered within 10 minutes. This trend shows qualitatively the same result as obtained in the previous test. It is interesting to note that the trend is independent of either oil volume or viscosity. On the contrary, the presence of brash and slush ice significantly lowers recovery rate. This will be discussed later.

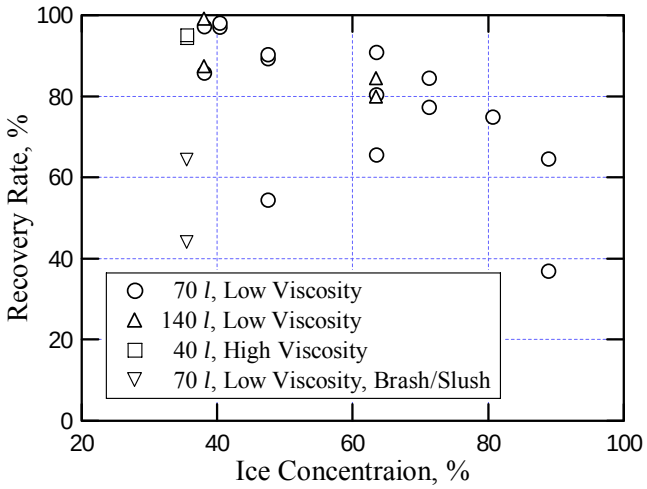

Figure 11. Correlation of Recovery Rate and Ice Concentration

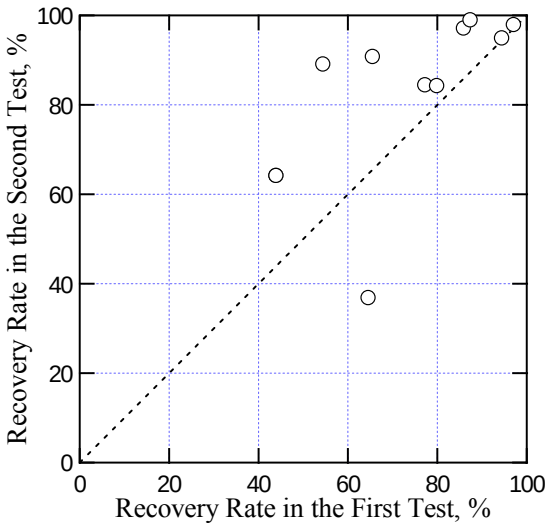

Figure 12. Comparison of Recovery Rate in First and Second Tests

A possible reason for the scattering in data in Figure 11 is the way to operate the air-bubblers and recovery gates. There were no predetermined operation procedures for these systems. A person

operated the air-bubbling units. He observed the oil and ice conditions in the separation channel and selected the bubbling units to be used on a case-by-case basis. Another person operated the recovery gates. He watched oil overflowing the gate and controlled the gate height. As shown in Table 2, two or three consecutive tests were made for the same conditions. Figure 12 compares recovery rate in the first and second tests in such cases. The figure shows that the second test give higher recovery rate than that in the first test, except for one case. It is reasonable to assume that the operators' practice in the first test resulted in the higher recovery rate in the second test. Scatter in recovery rate shown in Figure 11 will therefore have attributed to the different degrees of operators' skill. This suggests also a possibility that recovery rate in the high ice concentration region could be improved by training or by establishing certain routines for efficient recovery.

Oil Fraction

A drawback associated with the wire type skimming principle is that it can capture not only oil but also an amount of water. Too much water inclusion in the recovered liquids can lead problems in the succeeding oil spill response processes such as the storage and the final disposal of recovered oil. In the present test oil fraction in the recovered liquids was measured as a parameter to examine this issue.

An important parameter that affects oil fraction is oil thickness on the surface. Average oil thickness, h_O, in the separation channel is given by

$$h_O = \frac{V_O}{A(1-C)}, \qquad \textbf{[1]}$$

where V_O, A, and C are oil volume, channel area and ice concentration, respectively. Figure 13 shows correlation of oil fraction to average oil thickness. Data from tests with low and relatively high ice concentrations are shown. The figure shows a good linear correlation between oil fraction and average oil thickness, and, as is naturally expected, oil fraction increases with oil thickness.

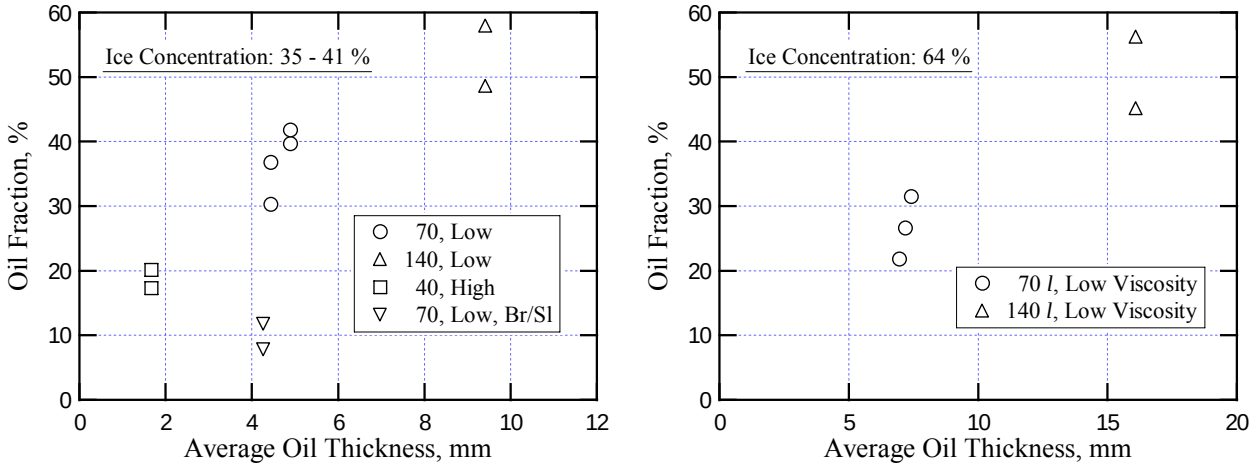

(a) Ice Concentration of 35 – 41 % (b) Ice Concentration of 64 %

Figure 13. Correlation of Oil Fraction and Average Oil Thickness

Figure 13 also shows that oil fraction depends not only on oil thickness but also on ice concentration. As is defined in equation [1], average oil thickness in the separation channel increases with ice concentration. However, oil fraction in the tests with the higher ice concentration is slightly lower than that obtained in tests with lower concentration. Figure 11 shows low recovery rate in high ice concentrations. This will attribute to that high ice concentration hindered and slowed down oil flow through the grating. It is reasonable to assume oil thickness at the recovery gate will therefore be thin and resulted in low oil fraction. Figure 13 indicates that although it is a useful parameter, oil fraction can not be simply explained by the average oil thickness given by equation [1].

Oil fraction will be inversely interrelated with recovery rate. In the present test, recovery gates were operated so that water inclusion in the recovered liquids could be minimized to have high oil fraction. Oil recovery speed in such an operation is low, and not the whole volume of oil may be recovered within a fixed period as shown in Figure 11. On the other hand, the gates can be operated also in such a way to recover oil as quick as possible. If the test had been performed in this way, recovery rate would have been higher even in high ice concentration conditions. However, oil fraction would have naturally been lower. Tactics for oil recovery operation should be selected based on consideration of this trade-off between recovery rate and oil fraction.

Presence of Brash and Slush Ice

Table 2 and Figure 11 show that tests No. 24 and 25 with brash and slush ice gave significantly low recovery rate compared with other tests for the similar ice concentrations. The presence of brash and slush ice lowered also oil fraction as shown in Figure 13. In the present test brash ice was sized to about 60 to 100 mm in diameter so that it was stopped by the grating, while slush ice was about 2 to 30 mm in diameter that was smaller than the opening in the grating. In these tests, a 92 kg brash ice and 81 kg slush ice were put in the separation channel together with circular floes. Brash and slush ice spread over the surfaces among the floes. Tests No. 26 and 27 were performed for a 244 kg brash ice with no ice floes. After these tests an additional 67 kg brash ice and 107 kg slush ice were put in the channel. Tests No. 28 through 30 were performed for this condition.

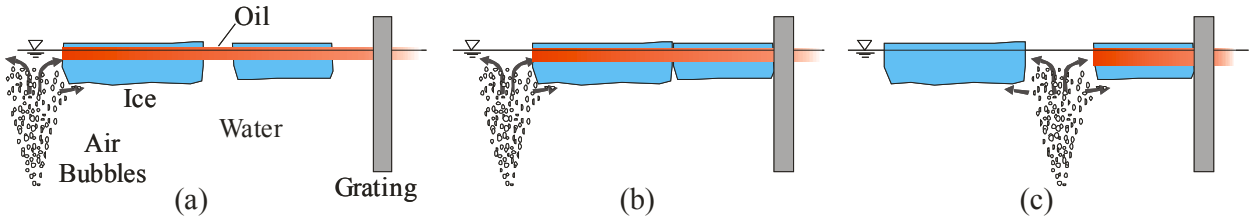

Figure 14. Schematic of Oil-Ice Separation Process

A key mechanism for oil-ice separation by NMRI-ORDICE is seen in Figure 10 (c). The frame shows that some ice floes returned to the port side of the separation channel. Figure 14 schematically explains the process. (a): Horizontal currents induced by plume jets transport oil and ice toward the grating. (b): Ice floes are stopped by the grating while the plume jets shifting toward it. (c): With further shifting of the plume jets, the ice floe located outside is eventually sent back away from the grating. It is important that plume jets generate horizontal currents not

only toward the grating but also to the opposite direction. Ice floes first receive currents toward the grating and then to the opposite direction as the plume jets shifting toward the grating, while oil receives only the grating-directed currents because of its compressibility (oil layer thickening). This is the oil-ice separation mechanism by way of shifting plume jets.

It was observed that the above mechanism didn't work well on brash ice. Because of the small size, brash ice reacted to bubble-induced currents similarly to oil, and was difficult to be separated from oil. As a result, brash ice accumulated at the grating to obstacle oil flow. The blockage by brash ice largely lowered recovery rate as shown in Figure 11.

Slush ice was observed to pass through the grating and to complicate oil recovery at the gate. When the gate was lowered, slush ice was drawn together with oil to the recovery duct. This often resulted in slush ice accumulations at the gate to hamper oil from flowing into the duct. The operator lowered the gate more to enhance oil recovery in such a situation. This led more water intake to the recovery duct and lowered oil fraction as shown in Figure 13.

In tests No. 26, 29 and 30, the shower system was used with an aim to improve oil recovery performance in conditions with brash and slush ice present. However, the system was installed to the model only near the end of the series. It was used only in the above three tests. It is difficult to assess the effectiveness the shower system from the results of the present test. It is planned to perform more tests with the shower system in 2008.

Oil Viscosity

Viscosity of oil is a parameter that is often discussed in association with recovery efficiency of skimmers. One of the concerns related to the effects of oil viscosity on the recovery performance of NMRI-ORDICE is that oil of high viscosity may be caught at the grating and lower the recovery efficiency. To prevent such problem opening in the grating should be wide enough. However, the wider opening in the grating will allow the more ice to pass through it. This will complicate the recovery gate operation as discussed above.

In the present test two machine oils of different viscosity were used as shown in Table 1. As far as the present test conditions concerned, no significant difference is seen between the test results for these oils. However, this issue needs to be studied further. A new series of tests is planned in 2008. A larger model of the grating will be made and tested for a wider range of oil viscosity.

7. Summary

This paper presented the results of a study at National Maritime Research Institute to develop NMRI-ORDICE, an oil recovery device for ice-covered waters. The device uses air-bubbling to separate oil from ice. The study has undergone two phases, and the third phase started in 2006. A new design for NMRI-ORDICE was given through brainstorming discussions. Two major elements of the new design – air-bubbling and oil recovery systems – are described in this paper. Based on the design a model of NMRI-ORDICE was manufactured. The model was tested in 2007. The test was performed for various ice conditions and two machine oils of different viscosity. Test results are discussed in terms of recovery rate, which is the ratio of recovered oil volume to that released, oil fraction, which is the ratio of oil volume to the total liquids volume recovered, the effects of brash and slush ice, and oil viscosity.

Although the present model test provided data that enabled us to quantitatively assess the oil recovery performance of NMRI-ORDICE, there still are issues that require further studies. More model testing is planned in 2008 of these issues. They include behavior of ice flowing into and through NMRI-ORDICE, effectiveness of showing as a supplementary system for oil-ice separation and the effects of oil viscosity on recovery performance.

References

Agip KCO Home Page: http://www.agipkco.com/wps/wcm/connect/AgipKCO+EN/Home.

DeCola, E., Robertson, T., Fletcher, S. and Harvey, S., 2006. Offshore Oil Spill Response in Dynamic Ice Conditions: A Report to WWF on Considerations for Sakhalin II Project, Alaska, Nuka Research, 73 p.

Environment Canada, 1992. A Catalogue of Crude Oil and Oil Product Properties (1992 Edition).

Evers, K-U, Jensen, H. Dieckmann, G. and Gerdes, B., 2004. State of the Art Report on the Oil Weathering and on the Effectiveness of Responses Alternatives. Deliverable D.4.1.1 (a), Arctic Operation Platform (ARCOP).

Finnish Environment Institute (SYKE) Home Page: http://www.ymparisto.fi/default.asp?node=5297&lan=en.

Izumiyama, K. Kanada, S., Uto, S. and Otsuka, N., 2005. Development of a Recovery Unit for Oil in Ice. Proc 18th International Conference on Port and Ocean Engineering under Arctic Conditions (POAC'05), Vol. 2, pp. 863-872.

Jensen, H. and Mullin, J., 2003. MORICE – new technology for mechanical oil recovery in ice infested waters. Marine Pollution Bulletin 47 (2003) 453 469.

Narita, S., Kanada, S. and Shimoda, H, 2001. A New Oil-Recovery Method for Broken Ice Conditions. Proceedings of the 23rd Arctic and Marine Oil Spill Program (AMOP) Technical Seminar, pp. 357 - 372.

Petroleum Association of Japan, 2004. Experimental Study of Vityaz Crude Oil Properties over Time (in Japanese). p. 22.

Rytkonen, J., 2005. On the Marine Oil Transportation and Terminal Development in the Gulf of Finland. Expert Article 13, Baltic Rim Economies, Bimonthly Review 1-2005.

Sakhalin Energy Home Page: http://www.sakhalinenergy.com/en/

S.L. Ross Environmental Research Limited and D.F. Dickins Associates Limited. 1987. Field Research Spills to Investigate the Physical and Chemical Fate of Oil in Pack Ice. Environmental Studies Revolving Funds Report No. 062. Ottawa. 118p.

19th IAHR International Symposium on Ice
"Using New Technology to Understand Water-Ice Interaction"
Vancouver, British Columbia, Canada, July 6 to 11, 2008

Physical Simulation Technique on the Behaviour of Oil Spills in Grease Ice under Wave Actions

Zhijun Li
State Key Laboratory of Coastal and Offshore Engineering, Dalian University of Technology
2#, Linggong Road, Dalian 116024, China
lizhijuun@dlut.edu.cn
Bruce Hollebone, Merv Fingas, Ben Fieldhouse
Emergencies Science and Technology Division, Environment Canada
335 River Road South, Ottawa, Ontario K1A 0H3, Canada,
Bruce.Hollebone@ec.gc.ca, Merv.Fingas@ec.gc.ca,Ben.Fieldhouse@ec.gc.ca

Abstract

For the laboratory studies of wave-grease ice, wave-grease ice-spilled oil interactions, especially the emulsion of oil under waves, a physical simulation technique is built up, and the wave energy at the level as that used in chemical laboratory. The main part of the technique is a mini wave flume. Its wave making power is from an oscillator in chemical laboratory, made of glass with insulation materials around its five sides for using in cold room. The reasons of using glass and plastic materials in the technology are that these materials do not absorb spilled oil and the wave in the flume can be monitored by videos and cameras. The wave parameters are obtained from these photos following image analysis technology. Based on ice growth theory and a series of cold room tests, the cold room temperatures for grease ice making and keeping with and without waves have been determined. Under these temperatures, an invariable amount of grease ice keeps under the wave actions. The relations of wave parameters of wave height, wave length and wave frequency with adjust parameters of the position of oscillator power transfer bar holes, the oscillator frequencies, the flume water depths have been established following a series of wave making capability tests. Based on these relations, the wave parameters can be controlled when testing. Hence, it is possible that the physical simulation technique performs the tests of interactions among wave, grease ice and spilled oil.

Introduction

When spilled oil occurs on the sea surface, it spreads and forms as an oil slick. The movement of oil particles is governed by the advection and turbulent diffusion due to current, wave and wind actions. The slick spreads over the water surface along with compositions of the oil changing due to a balance among gravitational, viscous and surface tension forces. Depending on turbulence, the formation of oil-in-water or water-in-oil emulsion may take place. The transport and fate processes of oil spills are a comparative intractable problem, thereby many investigators have studied in this domain by field tests, laboratory tests, and numerical studies (Kawamura et al., 1986; Chao et al., 2001; Li et al., 2008).

There are two facts that Arctic and Subarctic regions of the world contain significant oil and gas deposits that are expected to account for a considerable portion of the world's future production (IUCN, 1993) and there are sea ice coved areas where the platforms and/or ships operation. Significant researches have been done to through understand the interactions that oil and oil-gas mixtures spilled in ice infested waters (Fingas and Hollebone, 2003; Braddock et al., 2003). Initial ice formation at or near the sea surface occurs in the form of small platelets and needle-like crystals called frazil, with continued freezing a soupy mixture of sea water and unconsolidated frazil called grease ice is created, and then nilas ice and young ice. Until the ice becoming young ice sheet, the interactions between wave and grease ice or nilas are obvious as the wave can make them fluctuation. What will happen while it goes with oil spill? In this condition, the ice can move with wave and a part of wave energy maybe brings on the emulsion of the spilled oil. However, up to now, there is not more reported literatures involved the interactions of grease ice-spilled oil-wave.

Emergencies Science and Technology Division, Environment Canada, studies the physical and chemical processes of oil emulsion under wave actions profoundly and has a lot of achievements (Fingas et al.,1996; Fingas, 2005). These achievements absorbed Chinese scientist attention (Liu, et al., 1995; Yan and Xu, 2002; Wang L., et al., 2004). However all these achievements are adapt for no more than open water conditions. If it is involved ice, these achievements can not be seemly. The authors look for a new system for studying the oil emulsion in grease ice underexperimental conditions. From literature study, a flume of 0.8 m-width, 1 m-depth and 24 m-length has been used to investigate the spilled oil-wave interactions in open water in China (Zhao et al., 2004); a container of 2.2 L - cubage has been used in Canada (Fingas, 2005). All these study methods can not perform the tests with grease ice. Thus we designed a physical simulation technique to perform the tests of wave energy effect on spilled oil emulsion in the condition of grease ice with wave in Emergencies Science and Technology Division, Environment Canada. The developed test system has ability for the simulation tests in wave, wave-ice, wave-oil and wave-ice-oil. Its size is 10 times bigger than Canadian container, but much smaller than that reported by Zhao et al. (2004). This paper gives the concept design of the developed test system, and then introduces the experimental certifications of the system capability, including temperature controlling, wave-making, grease ice making.

Test System

As the energy of regular wave is easy to evaluate, a mini wave making flume, of 130 cm-length, 15 cm-width and 50 cm-depth, with a capacity of creating regular wave, made of glass, has been

build and placed in a higher accurate temperature-controlled cold room. The reasons to use glass are two, one keeps away the stick between oil and container, the other is useful for take wave profile from lateral side by camera. For remove the thermal effect from air temperature, the insulation materials are used to around the glass flume. The front side is moveable for camera photos using. A paddle for wave making is set up in the flume and moves vertically. The surface of the paddle is painted to keep away the oil absorbing. The power for the paddle vertical movement is derived from oscillator. For searching the suitable cold room temperature to make and keep grease ice, and for adjusting the wave length, height and frequency, a series of tests were performed under different temperatures, water depths, frequencies of the oscillator movement and the positions of the connect hole of power transfer bar. The sketch map of the mini making flume is shown in Figure 1.

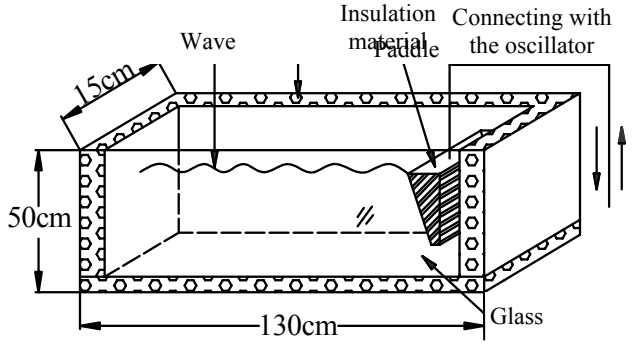

Figure 1. The wave making flume

Key Problems

Because the capability of this new developed system has not been through understood, the key problems are necessary to illuminate by theoretical analysis and experimental studies. For the physical simulation study of ice-wave-oil based on this new system, the key problems can be summarized as following: how evaluate the wave energy; how prepare the grease ice; how keep the amount grease ice invariable under wave actions; how pour the crude oil samples into the grease ice.

1. Wave Energy

The energy of regular wave can be expressed as Equation [1] (Gao et al., 1990). The wave shape often deformed due to the small containers in chemical laboratories, but the wave height almost keeps invariable according to the same energy level as reported by Owens and Belore (2004).

$$D = (1/8)L\rho gH^2 \qquad \textbf{[1]}$$

Where D is the energy in J/m^2; ρ is the density of sea water; g is the acceleration due to gravity; H is wave height; and L is wave length.

Therefore the key parameters to evaluate regular wave energy in the mini wave making flume are wave height and wave length. The water depth of the flume, the movement frequency of oscillator and the movement distance of the paddle shaped like a wedge are the dominant factors controlling wave parameters. Therefore, a series of tests under different water depths, different

oscillator frequencies and different positions of connect hole in the power transfer bar are performed to determine the relations between wave parameters and wave-making system parameters.

2. Grease Ice Making

The method for grease ice making is that put the sea salt into water, and make the artificial sea water with the salinity of 33‰ w/w. The water is poured into the mini flume. The grease ice formed in the cold room under –20 ºC in 14-16 hours.

3. Grease Ice Keeping

While there are waves in the small glass flume, a part of the wave makes grease ice melting in the flume. However, the amount of grease ice must be keep invariable during the tests. Therefore the air temperature in the cold room should be little lower than the water freezing point for counteracting the dissipative energy roused by wave movement. The dissipative energy can be evaluated by Stefan ice thickness evaluate method, in other words, the cold room temperature when testing can be evaluated in advance.

While the grease ice making, the cold room temperature is set up at –1.5 ºC and keeps 24 h for the thermal balance of 40 kg water from normal room temperature to –1.5 ºC. And then the air temperature in the cold room is set up at –3.0 ºC, and the grease ice formed in the flume over 14-16 h. During the processes, the water temperature, air temperature in the cold room, grease ice frozen time and grease ice thickness (h_{grease}) are recorded regularly.

After the test system start to make wave, the grease ice thicknesses are measured at 2h, 3h, 4h, 5h and 6h. Assuming the grease ice density keeps same, the grease ice thickness (h_{grease}) variation at different time can be obtained as following.

$$h_{ilost} = (h_{grease} - h_i) \qquad \textbf{[2]}$$

Where, h_{ilost} is the grease ice thickness wastage, and h_i is the measure grease ice thickness at time i.

Assuming the ice thicknesses before and after wave actions can be calculated according to the Stefan ice thickness calculation formula (Li and Riska, 2002), then there are three steps to get the air temperature in the cold room as an inverse problem.

$$h = \lambda\sqrt{\theta T} \qquad \textbf{[3]}$$

First step is that using the recorded data of grease ice thickness, air temperature, and time to calculated λ. Second step is that the ice thickness wastage at time i is expressed as Equation [4]. The third step is that the air temperature in the cold room (θ_{wave}) while wave making is calculated based on the measured ice thickness, air temperature (θ_{air}) and the measurement time.

$$h_{ilost} = \lambda\sqrt{\theta_{air} T_{total}} - \lambda\sqrt{\theta_{wave} T_{wave}} = h_{grease} - h_i \qquad \textbf{[4]}$$

Let the air temperature in the cold room to be θ_{wave} and start wave making again. The grease ice thickness is measured subsequently. If theses grease ice thicknesses do not keep same value, the slight adjust is needed. The methods also can be used for the assessment of the dissipative energy for crude oil emulsion.

4. Crude Oil Samples

Pouring the crude oil samples from ice surface or ice bottom was governed by the relatively density between crude oil and water in the flume.

Evaluation of the Capability of the Test System

1. Temperature

The temperature probes with the accurate of 0.5 °C, thermocouples of Type K with Teflon skin, have been utilized in the test. As their accurate does not suitable for our testing, it is necessary to calibrated them. This work was performed in the temperature range from –20 to 45 °C by using a device with accurate of 0.1 °C, which made by OMEGA ENGINEERING, INC. Even there is good linear relation between measured temperature and the device temperature, but for the small range, there is still some fluctuation that makes the practical error is 0.2 °C. Figure 2 gives one of these probes calibration curves.

For the tests, the salty water was made by adding salt into fresh water, and the salinity is 33‰ w/w, approaching the salinity of natural sea water. The freezing point of the artificial sea water is the key parameter for calculating the energy to keep the grease ice. Figure 3 gives the process for detecting the freezing point of the artificial sea water under the ambient temperature of –5 °C. From the curve, the supercooling temperature during water cooling and the freezing point in the crystal developing period are –3.36 °C and –1.884 °C, respectively.

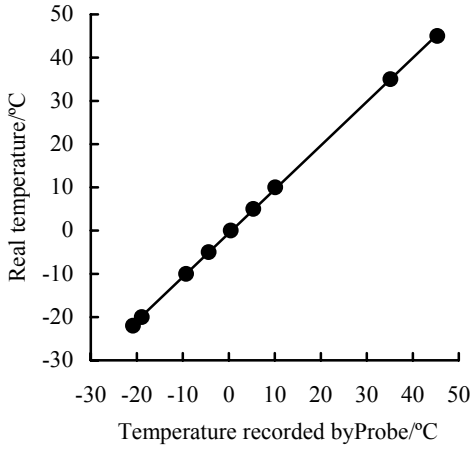

Figure 2. Calibration of a temperature probe

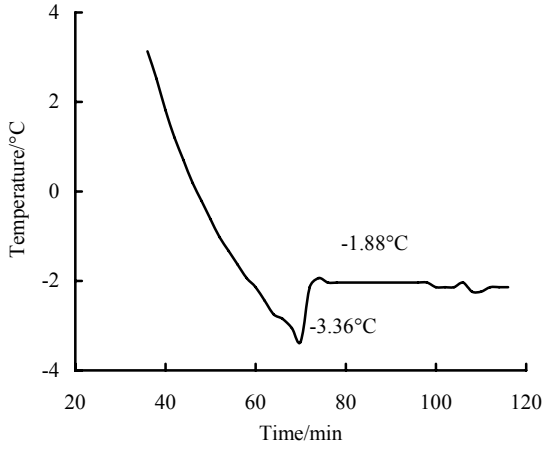

Figure 3. Artificial sea water freezing process under ambient temperature of –5 °C

In addition, the air temperature in the cold room is the crucial parameter for energy evaluation, and we also need the temperature controlling device to set up the air temperature in the cold room. Hence, the air temperature distribution in the cold room and the air temperature in the vicinity of the temperature probe of the temperature controlling are necessary to measure and compare. From measurements, there was no obvious horizontal difference in the cold room, but the temperature probe for cold room temperature controlling is 0.2 °C higher than the real temperature in the cold room.

2. Wave Parameters

The small flume for the test is shown in Figure 4 and Figure 5. For getting different wave conditions, 4 connect holes has been preset in the power transfer bar which connected with oscillator. In addition, the frequency of the oscillator, the water depth can be adjusted expediently. A video camera and a stroboscope are used to detect the wave height, wave length and oscillator frequency. A series of 5-10 min tests were performed to determine how these 3 factors (connect hole position, oscillator frequency and water depth) effect on the wave parameters (wave height and wave length).

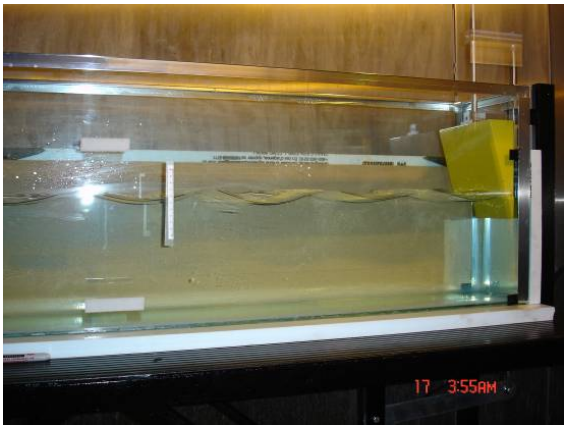

Figure 4. Picture of the flume with wave

Figure 5. Oscillator and power transfer bar

A series of images are extracted from the video record of each test. Using the image analysis technique (Lu, et al., 2004), the shape of wave surface can be obtained (see Figure 6), and then the wave height, wave length and wave frequency can be calculated.

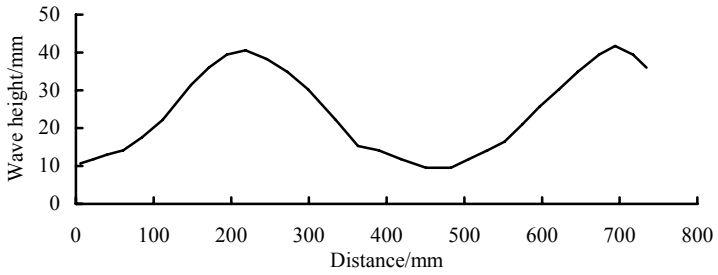

Figure 6. The wave surface from image analysis

The effects of connect hole position in power transfer bar on the wave elements are shown in Figure 7. For ascertaining the relation of wave frequency and oscillator frequency, a series of tests were performed at the water depth of 191 mm. The relation is given in Figure 8. The results of tests under 2 Hz of the oscillator movement show that the wave height and wavelength increase nonlinearly as the water depth increased from 191 mm to 336 mm (see Figure 9).

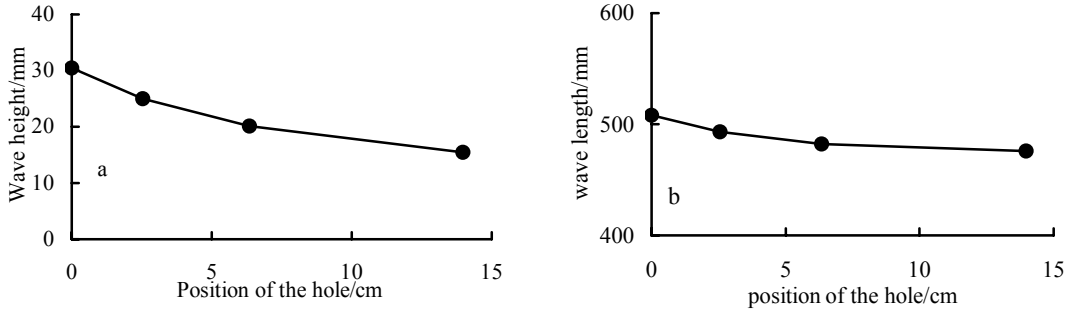

Figure 7. The variations of wave height and length with hole positions

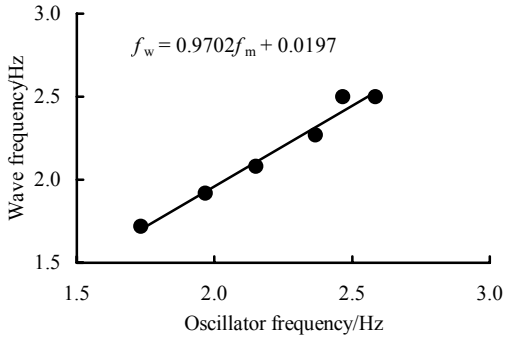

Figure 8. The relation of wave frequency and machine frequency

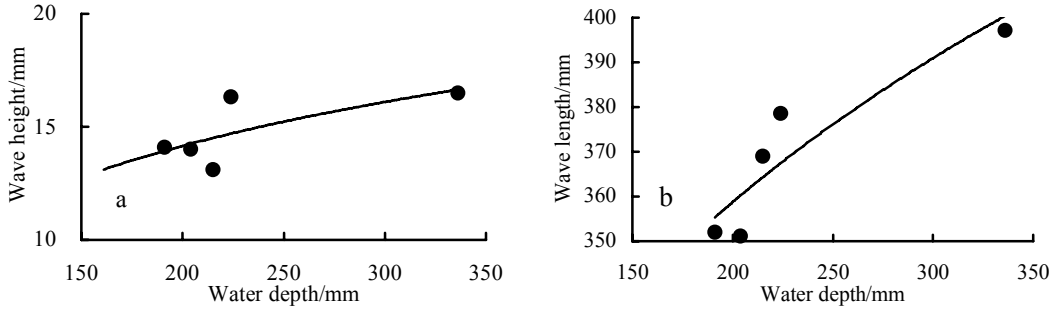

Figure 9. The water depth effect on wave parameters

3. Grease Ice

The grease ice is frozen in the flume in the cold room under –2 °C for 14-16h. The freezing growth ice has similar crystal size as natural ice. If considering the used crude oil properties is natural, and ice crystal keeps natural strictly. Figure 10a and 10b show the grease ice in state

case and in the case with wave movement. If considering the effect of ice crystals and particles movements on the crude oil migrations and movements, the problem is that crystal is large, but wave height is small, so the ice absorbs the energy remarkably. It is necessary to consider the simulation laws in this case, thus maybe using snow particles to simulate grease ice is better.

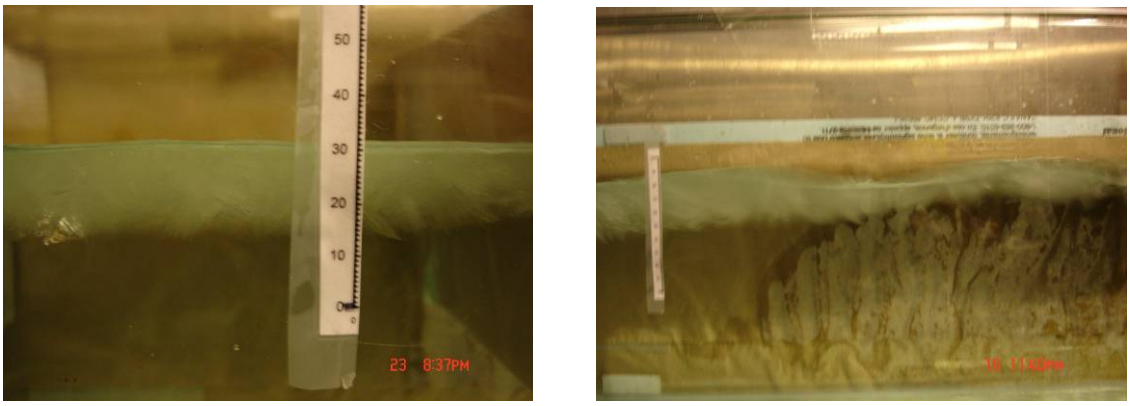

(a) (b)

Figure 10. Picture of grease ice growing in state case (a) and wave action case (b)

Conclusions

On the wave contribution for the oil emulsion in laboratory study, there are two scales of experimental techniques. One is the size of chemical laboratory oscillator, and the other is the hydrodynamic laboratory water flume. Both are not belong to same scale. The new developed mini flume is the same power level as chemical laboratory and 10 times bigger than chemical containers. Therefore the test results can be compared with chemical laboratory test results.

By using the oscillator in chemical laboratory, the power for the mini wave flume is resolved. For keeping away the stick between oil and container, oil and paddle, oil and temperature probes, the mini wave flume is made of glass; the surface of the paddle is painted and the temperature probes coated with Teflon.

The energy for grease ice forming can be evaluated suitably by Stefan ice thickness evaluation method. Using this method, also can determine the cold room air temperature suitably, under the air temperature, the amount of grease ice keeps same during the actions of wave.

The wave height, wave length and wave frequency depend on the connect hole position in the power transfer bar, oscillator frequency and water depth. From the series of tests, the relationships between them are obtained. Therefore, the waves parameters can be controlled by adjust position of the hole in the power transfer bar, oscillator frequency and water depth.

Acknowledgments

This work was finished during performing Canada-China Scholars Exchange Program. We are grateful for the financial support for the work in Canada to Canadian Bureau for International

Education and China Scholarship Council, for the final support for the paper writing to Changjiang River Scholar and Innovative Team Developing Plan (IRT0420).

References

Braddock J. F., Lindstrom J. E., Prince R. C., 2003, Weathering of a subarctic oil spill over 25 years: the Caribou-Poker Creeks Research Watershed experiment. Cold Regions Science and Technology, 36:11-23.

Chao X., Shankar N. J., Cheong, H. F., 2001. Two- and three-dimensional oil spill model for coastal waters. Ocean Engineering, 28:1557-1573.

Fingas M. F., Fieldhous B., Mullin J. V., 1996. Studies of water-in–oil emulsions: Stability studies. Spill Science and Technology Bulletin, 3(4):189-190.

Fingas M. F., Hollebone B., 2003. Review of behaviour of oil in freezing environments. Marine Pollution Bulletin, 47:333-340.

Fingas M. F., 2005. Measurement of energy in laboratory vessels_III. Proceedings of the 28th Arctic and Marine Oilspill Program Technical Seminar, Ottawa, Canada, Environment Canada, 1: 1-16.

Gao M., Zhao Y., Huang G., 1990. An integrated analysis and proposal of practical method of evaluation of berthing energy and motions of mooring ships under waves on deepwater piers. Hydro-Science and Engineering, 1990(4): 367-379(in Chinese).

International Union for the Conservation of Nature (IUCN), 1993. Oil and gas exploration and production in Arctic and Subarctic Onshore Regions. IUCN Gland, Switzerland and Cambridge, UK, 1993 with E&P Forum, London, UK, vol. viii. 56 .

Kawamura P., Mackay D., Goral M., 1986. Spreading of chemicalson ice and snow. Manuscript Report EE79, Environment Canada,Ottawa, 106.

Li Z., Riska K., 2002. Index for estimating physical and mechanical parameters of model ice. Journal of Cold Regions Engineering, 16(2): 72-82.

Li Z., Lee K., King T., et al., 2008. Assessment of chemical dispersant effectiveness in a wave tank under regular non-breaking and breaking wave conditions. Marine Pollution Bulletin, doi:10.1016/j.marpolbul.2008.01.031.

Liu H., Zhang Y., Wang W., et al., 1995. The Interficial property of oil spill dispersant on sea and its diffusion effect. Acta Oceanologica Sinica, 17(6):65-71 (in Chinese).

Lu P., Li Z., Dong X., et al., 2004. Sea ice thickness and concentration in Arctic obtaining from remote sensing images. Chinese Journal of Polar Science, 15(2):91-97.

Owens C. K., Belore R. S., 2004. Dispersant effectiveness testing in cold water and brash ice. Proceedings of the 27th Arctic and Marine Oilspill Program Technical Seminar, Edmonton, Canada, Environment Canada, 2004, 2: 819-842.

Wang L., He Y., Wang Y., et al., 2004. Oil spill identification by near-infrared spectroscopy coupled with clustering analysis based on principle components. Marine Environmental Science, 23(2): 58-60(in Chinese).

Yan Z., Xu H., 2002. Review of the studies on emulsification of spilled oil. Environmental Protection in Transportation, 23(2): 1-6(in Chinese).

Zhao Y., Ma Y., Wu J., et al., 2004. Assessment on the emulsification principle of dispersants with a wave through by simulating the movement of the surf. Marine Environmental Science, 23(4): 67-70(in Chinese).

Bohai Sea Papers: Desalination, ice thickness, and climate change

19th IAHR International Symposium on Ice
"Using New Technology to Understand Water-Ice Interaction"
Vancouver, British Columbia, Canada, July 6 to 11, 2008

Sea ice desalination in solid state by temperature control

Wei GU, Yingjun XU, Weijia CUI, Ning LI, Shuqing HUANG and Peijun. SHI

College of Resources Science & technology and Key Laboratory of Resource Engineering of Beijing Normal University, State Key Laboratory of Earth Surface Processes and Resource Ecology, and Key Laboratory of Environmental Changes and Natural Disaster of Ministry of Education
No.19 Xinjiekouwai Street, Haidian, Beijing, 100875, P. R. China
weigu@bnu.edu.cn , yingjxu@ires.cn

Abstract

In view of severe scarcity of fresh water in the Bohai Rim and the abundance in sea ice in Bohai Sea, a tester to obtain fresh water from sea ice by desalination through controlling temperature was designed in this paper. A field trial of Bohai sea ice desalination and an indoor observation trial of salt movement with a type of blue trailer in the sea ice body were completed. The results showed that the micro-structural characteristics of sea ice as a hybrid of crystal and brine symbiotically formed the technology basis, and the brine in the sea ice body moved down along the micro-pipelines rapidly and drained away through gravitation and washing function of water melted from ice crystals. When the air temperature was controlled within the range of 2□ to 6□ and the sea ice temperature was controlled within the range of -1.5□ to 2□ about from five days to seven days, the salinity of sea ice pieces might descend under 1‰, the product rate of the desalted water would be more than 60% and the output of single device could be up to 381.6 m3 during the ice period in a year. Desalted water quality could reach the irrigation water quality standard completely and could accord with the environmental quality standard of drinking water and surface water in China with the exception of NH3. The trial cost of water produced from sea ice was about 4.47 RBM/m^3.

Keywords: Water resources; Bohai Sea; Sea ice desalination; Greenhouse; Temperature control

1. Introduction

As the only inland sea in China, Bohai Sea located at 37º07'- 41º0'N, 117°35'- 121º10'E. Its area is approximately 9.0×10^4 km^2, and average water depth is 25m. The land region around Bohai Sea is also one of the most important developing areas in China. Fresh water shortage is a key point that badly restricts the integral sustainable development. The point has become the bottle neck of the regional economy and society development in North China, especially in the Bohai Rim. In this area, the total quantity of fresh water is only 2% of that of the entire country, but nurses 18.15% of the total population and provides over 24.91% of the total GNP (Wang et al., 2003) of the country. The average per capita quantity of fresh water in most coastal cities of China is less than 500 m^3, only accounting for roughly 1/5 of the average level in China, among which Tianjin, DaLian, Qingdao and Beijing are even below 180 m^3. So, seeking and enlarging new fresh water resources for these regions in North China is a fundamental approach. Presently, desalination of seawater including very saline water is developing into a type of ripe and reliable industrial technology to expand the fresh water resources. It is also the crucial and useful way, for this area, to take full advantage of access to sea water including brackish water as a source of freshwater by desalination.

Bohai Sea is known as Chinese only "freezing" sea, being the southernmost (37º07'- 41º0'N) on the Northern Hemisphere. It has abundant sea ice in a normal ice year. The potential reserve of sea ice can be up to 1.0×10^{12} m^3 in a heavy ice year. Some tentative plans have been provided for using the sea ice resource during these years, considering that the sea ice salinity is much lower than that of seawater, which could be transformed into fresh water by simpler treatment with small cost (Wang et al., 2003, Gu et al., 2003, Shi et al., 2002). Those attempts may help to find a kind of fresh water resources, and also to break a new path for sea ice study from the point of resources while the traditional research was emphasized mainly on the reduction and prevention of sea ice disaster and on global climate response to ice and snow sphere (Chen et al., 2004, Bai et al.,1999, Liu et al.,1998, Arunachalam et al., 1993). Now, to use sea ice as fresh water in the Bohai Rim (Wang et al., 2003, Shi et al., 2002) even in North China, is a new concept in the field of unconventional water resources exploitation and utilization (Gu et al., 2003). That has drawn great attention and forceful support from the government at all levels and society in China.

Recently, many case studies on the resourcization and utilization of sea ice were conducted in the Bohai sea region and a series of active progresses were made accordingly. Some work has been done in these areas: (1) the process and mechanism of sea ice formation and desalination (2003, Shi et al., 2002); (2) the estimation of sea ice resource gross in Bohai Sea in a normal ice year, a light ice year and a heavy ice year during the period of grand ice by remote sensing (Gu et al., 2002, 2003, Shi et al., 2003,2004, Xie et al., 2003); (3) the engineering exploitation of sea ice; (4) the methods and technologies on sea ice desalination (Chen et al., 2004, Xu et al., 2002, 2003); (5) the comprehensive utilization of melted sea ice in agriculture and fresh water from sea ice by desalination as irrigating water (Xu et al., 2003, Xiao et al., 2003), and so on. So far, the further development and perfection of the sea ice desalting technology has been the key to really using sea ice resources toward the engineering of the seawater desalination application. In this paper, elementary principle of sea ice desalination in solid state is provided based on the analysis of sea ice crystal microstructure, a system of sea ice desalting through temperature control in a

greenhouse is designed, and corresponding trials are conducted to acquire the parameters for the industrialization of this technology in the future.

2. Micro-structural analysis and basic desalting principle for sea ice

Seawater begins to turn into sea ice when its heat lost is under the critical point. Sea ice is the product of seawater freezing. Owning to the drainage of massive salt from sea ice during the natural formation process of seawater-to-sea ice, most of the salt is dissolved in seawater and the remaining is locked in the ice as "brine". Therefore, the salinity of sea ice is much lower than that of seawater. Usually the salinity of seawater is 28‰-32‰ in Bohai Sea while that of sea ice is 4‰-11‰ (Xu et al., 2003). So, about 80% salt may be removed away from seawater during the freezing process.

According to the researches done in the past, sea ice in Bohai Sea is a kind of composite with complex, random constitution, mainly made up of polygonal pure ice crystal, brine, air and solid impurity (Liu et al., 1998, Li et al., 1997), and its component will change with environmental conditions, space-time, etc. The pure ice crystal is freshwater itself while the brine is high saline water by the separation of salt from seawater during the freezing process, which accounts for the main of sea ice salinity. The fundamental characteristics of sea ice microstructure is that polygonal pure ice crystals arrange with each other tightly in crystal frame and configuration, so that brine and air are closed by two or more ice crystal wall like a cell. The cells are so-called saltwater bubbles or brine pockets (Col et al., 1998) (Figure1-a), which are usually in the shape of a micro-ball or a long micro-tube. The micro-structural characteristics of sea ice as a hybrid of crystal and brine symbiotically construct the technology basis for the brine in sea ice to transport. If the brine in sea ice is removed by some means, the aim to get fresh water from sea ice by desalination can be achieved.

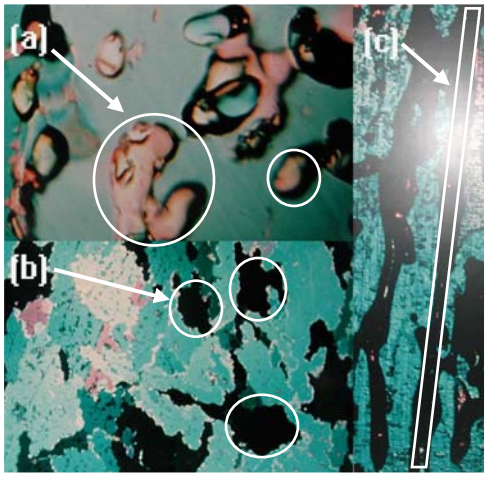

Figure1. Images of sea ice micro-structure by ellipsometer

(The environmental temperature is within the scope of -8□-2□; the thickness of the sea ice sample is 2 cm and that of the treated sample is 2mm, magnification: ×200. (a) brine pockets shaped during the course of sea water freezing, where most salt of sea ice is concentrated, (b) chinks formed during the course of sea water freezing, which always appear among sea ice crystals, (c) brine micro-pipelines shaped during the course of sea ice crystals melting lightly, along which brine in brine pockets is drained from the sea ice body.)

As a rule, the freezing point of freshwater is about 0□ and that of sea ice in Bohai Sea is from -1.51 to -1.76□. Moreover, the brine with high concentration will retain in liquid phase under the conditions of temperature range, -30 -0 . Due to the brine in sea ice unfreezing and its density being larger than that of pure ice crystal, it will have a tendency to move down along the chinks among the ice crystals for its deadweight (Figure1-b). Supposing the chinks between the ice crystals interlink and transfix one another in the direction of gravity, namely many brine pockets break and join to be so-called brine micro-pipelines or micro-tubes (Figure1-c) in this paper, the brine will be discharged outside ice body through gravitation and sea ice will be transformed into freshwater from very saline water.

Therefore, a desalination trial of sea ice through a double-course control of sea ice temperature and air temperature was conducted, according to the micro-structural characteristics of ice crystals and brine pockets arranging in the sea ice body. This double-course temperature control could speed the formation of the micro-pipelines in sea ice body and enlarge the micro-tubes. Then, rapid disposal of salt was realized with very low desalting costs using natural energy.

3. Materials and methods

3.1 Tester and its mechanism

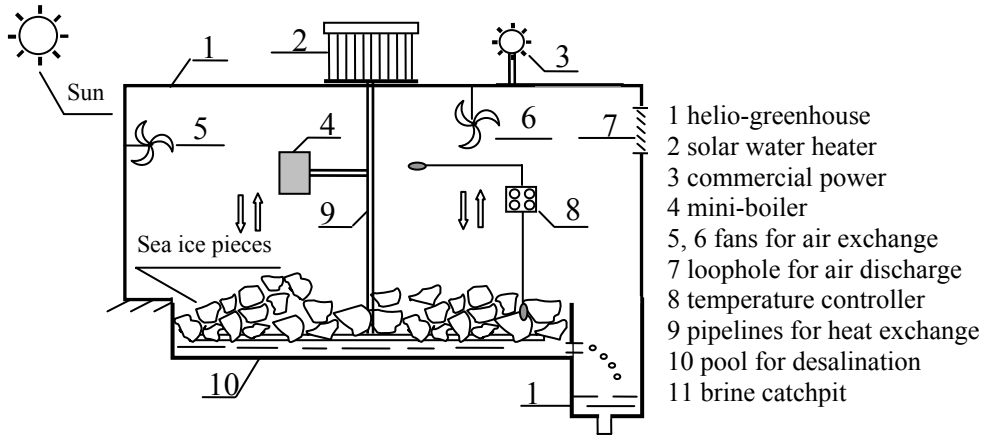

Figure 2. The schematic diagram of the tester configuration

A desalinator as the tester for sea ice desalting by temperature control was designed based on greenhouse principle. Greenhouse principle is a better choice in agrometeorology in that solar energy can be deposited and transformed into heat in a greenhouse. Its structure was shown in Fig.2, with subunits such as heat supply, compulsive ventilation, hot water circulation, pool for desalination, brine catchpit, temperature control, and so on.

The mechanism was illuminated as follows: The sea ice pieces in the pool and indoor air were heated by shortwave radiation of sunlight through the transparent plastic film coping of the greenhouse in daylight, heat exchange happened between them and the sea ice pieces began to melt away. At the same time, data on the room temperature were sent to the temperature controller by temperature sensor and the room temperature was dynamically adjusted to a certain scope by fans. The fans were used for air discharge and exchange. The pieces could be kept

melting lightly, which resulted in the formation and enlargement of the brine micro-pipelines in sea ice body. Subsequently the brine inside the sea ice was discharged continuously along the micro-pipelines by gravitation and was drained into the catchpit as a tiny conflux. The brine salinity in the catchpit was monitored synchronously. When the salinity was under a certain value, the desalting could be controlled to finish. As a result, the sea ice pieces were turned into limnetic ones and they might be removed away and conserved. During night time, the heat for the light melting of sea ice was delivered by the hot water from the mini-boiler or solar water heater. The heat exchange took place between the hot water and the pieces through the circuit of pipelines to keep the pieces melting lightly.

3.2 Operational conditions

The followings were the operational conditions of the desalinator based on the mechanism above. The plane size of the heliogreenhouse was 40m×7m. The two pools in the greenhouse were both designed with the size of 16m×5.5m×0.6m and their cubage was 52 m^3. The gradient of the pools' underside was 1/1000. The lowest point of the pool bottom surface was the catchpit at a corner of the pool. The catchpit opened its mouth to the top of the pools. Its upside height was the same as the pools' while its deepness was lower than that of the pools. Furthermore, its cubage was not smaller than 3 m^3. The air temperature inside the greenhouse was controlled within the scope of 4 -6 , and that of the sea ice pieces was -1.5 -2 at the same time. The standard salinity of the water melted from the sea ice in catchpit was not more than 1‰ for stopping desalting process.

3.3 Field trials of desalination

A field trial of desalination was conducted in Sino-Czechoslovakia Friendship Farm in Hebei Province, which was on the seashore of the Bohai Bay and located at 36° 22' N, 117° 21'E, from January 24th to January 31st in 2005. The salinity of seawater was approximately 32.7‰, that of the sea ice pieces from Bohai Bay was approximately 5.0‰-5.2 ‰, and average ice thickness was approximately 10cm-15cm.

About 48m^3 raw material sea ice pieces were respectively piled up in 1$^{\#}$ and 2$^{\#}$ pools, which could be converted into 30.2m^3 water approximately, supposing the density of sea ice was 0.9×10^3kg/ m^3 and the rate of gap between sea ice pieces 30%. The solar radiation intensity and the air temperature were monitored at the same time, using a WS automatic weather station (Beijing Havesting Science and Technology Co., Ltd., Beijing, China). When the water salinity in the catchpit was less than 1‰, the sea ice pieces in the pools could be collected as freshwater ice. The salinity was quantified using a UC-78 salinometer (Central Kaeaku Co., Ltd., Japan).

3.4 Water quality analysis of the fresh freshwater from the desalted sea ice

When the salinity of the desalted pieces was less than 1‰, the pieces melted away naturally. A water quality analysis was subsequently carried on the water sample from the melted pieces using a Dionex-600 IC (DIONEX, America) and an ULTIMA ICP (JY, France). The methods of water quality analysis and appraisal adopted included three professional standards, which were drinking water quality standard, surface water environment quality standard and agricultural irrigation water quality standard. The specific indexes chosen in the water quality analysis and appraisal, included sulfate ($SO4^{2-}$), Cl^-, fluoride (F^-), As, Se, Hg, Cd, Cr, Pb, ammonia nitrogen

(NH^{4+}), phosphate (PO_4^{3-}), Zn, Cu, Fe, Mn, nitrate (NO_3^-), total dissolved solid (TDS), and total salt content (TS) , etc.

3.5 Observation of salt movement in sea ice

Blue tracer was used to observe the movement of salt during the melting process of sea ice in order to conduct research on the movement of brine in sea ice body at the level of the ice crystal microstructure. Sea ice pieces were placed indoors at normal room temperature (10 -15) as they grew naturally. Then a drop of blue tracer was dripped on the upside of the sea ice pieces and its diffusion process in ice body was observed carefully and kinescoped using a V50 digital camera (Lenovo, China).

4. Results and discussions

4.1 Desalination effects of sea ice

The average solar radiation intensities outdoors and indoors were 119.2w/m^2 and 62.4w/m^2, respectively. Hence, it was deducible that the solar radiation came into the greenhouse at the ratio of 52.35%. The average air temperature indoors was 4.8 - 5.4 .

We could learn from table 1 and table 2 that the salinity of the water melted from the sea ice pieces in the two pools diminished day by day and would drop to under 1‰ through the course of desalination by controlling temperature during from five days to seven days. The water desalted was 53% in proportion to the sea ice pieces as raw materials ($1^{\#}$ product about 11.3m^3 freshwater and the product rate was 62.33% or so, while $2^{\#}$ did about 16.9m^3 and the rate was about 43.66%.), the output of single device was about 31.8m^3 every time and 381.6 m^3 during the ice period in a year supposed total days for desalination were 72d, and the average production was 5.3m^3/d.

Table 1. Salinity and amount of the water melted from seaice in different testers

Date	$1^{\#}$ Salinity ‰	$1^{\#}$ Amount m^3	$2^{\#}$ Salinity ‰	$2^{\#}$ Amount m^3
Jan. 24	6.8	1.2	13.4	2.1
Jan. 25	5.2	1.9	11.9	2.9
Jan. 26	4.1	2.1	7.7	2.5
Jan. 27	2.6	1.4	3.2	1.6
Jan. 28	1.3	2.8	2.4	7.8
Jan. 29	0.3	1.9	1.1	6.4
Jan. 30	0.3	2.5	0.8	9.3
Jan.31	0.2	-	0.2	-

Table 2. Effect of sea ice desalination by controlling temperature in different testers

Pool code	Sea ice (solid)		Product water (liquid)		Product rate %	Daily production m^3/d	Total production m^3/a
	Amount m^3	Salinity ‰	Amount m^3	Salinity ‰			
$1^{\#}$	48	5.1	18.7	0.3	62.33	3.12	224.4
$2^{\#}$	48	5.2	13.1	1.1	43.66	2.18	157.2

The drainage of the salt from sea ice body would be very fast and the sea ice pieces could exist in solid state better under a rational temperature. Such, the amount of the water produced would be on a rise if the temperature indoors was controlled well. In addition, it could also increase more

than 10% of output if the melted water with a salinity of over 1‰ discharged from sea ice frozen again.

4.2 Water quality analysis

The 19 general chemical and toxicity indexes selected, totally accorded with the water quality standard of field irrigation. With the exception of ammonia nitrogen, the indexes else reached the drinking water and surface water quality level. But ammonia nitrogen was unstable and might have transgressed the water body due to dynamical factors. So, as far as the indexes were concerned, the freshwater desalted from sea ice by temperature control, not only could be used as agricultural irrigation water, but also be used as industrial, life and urban ecological water available, etc.

Table 3 Water quality analysis results of desalinized sea ice pieces*

Indexes	Sample1#	Sample2#	I	D	S
SO_4^{2-}	11.3	3.06	-	250	250
Cl^-	70.1	24.4	250	250	250
Fe	0.14	0.16	-	0.3	0.3
Mn	0.0001	0.02	-	0.1	0.1
Cu	0.002	0.006	1	1	0.01
Zn	0.009	0.002	2	1	0.05
NO_3^-	0.36	0.22	-	20	10
NH_4^+	0.22	0.53	-	0.1	0.1
NO_2^-	n.a.	n.a.	-	0.05	0.1
PO_4^{3-}	n.a.	n.a.	-	-	0. 1
F^-	n.a.	n.a.	2	1	1
Se	0.015	0.013	0.02	0.01	0.01
As	0.007	0.007	0.05	0.05	0.05
Hg	0.0006	0.0005	0.001	0.001	0.0005
Cd	0.0002	0.003	0.005	0.01	0.005
Cr	0.002	0.004	0.1	0.05	0.05
Pb	0.007	0.0009	0.1	0.05	0.05
TDS	17.8	12.9	-	450	-
TS	121	41	1000	-	-

*mg/L is the unit for all; I indicates agricultural irrigation water quality standard. D indicates drinking water quality standard. S indicates surface water quality standard of China. n.a. denotes not applicable.

4.3 Microstructure and salt movement

Figure3 shows the detention of the blue tracer in a sea ice sample at different moments. At the beginning, the tracer stayed between the ice crystal chinks in upper strata of the ice body and mainly spreading horizontally before the brine micro-tubes took shape. At this time, the tracer concentration was relatively high and presented in rhizomorphous form (Figure3-a). Some time later, the temperature of sea ice rose and reached unanimity with that of environment, the chinks between the ice crystals were interconnected. Thus, the brine passways were formed progressively and the tracer spreading downwards quickly (Figure3-b and Figure 3-c). At last, the tracer came to the bottom sheet of the ice body, of which some was discharged out of the ice body and some distributed in a cloud bulk in the under part ice sheet with a great-reduced concentration (Figure3-d). Those indirectly proved enough that the movement and transportation of the salt in sea ice body might be related to the microstructure of sea ice crystals and the columnlike microstructure of sea ice crystals would help the salt to move downwards fast. Under most circumstances, the horizontal movement of the salt in the upper strata was greater than that

in the middle ice sheet and that in the under part was also relatively large before the salt was discharged from the ice body.

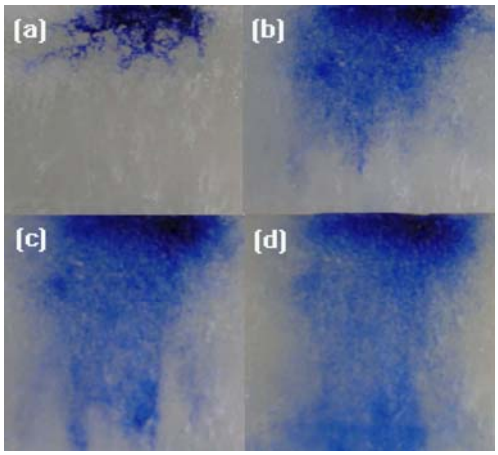

Figure3. Pictures of blue tracer diffusing process in a sea ice cube sample

(The environmental temperature is within the scope of 10 -15 . The thickness of the sea ice sample is 18 cm. (a) 30min, (b) 240min, (c) 480min, (d) 560min)

The diffusing process of the tracer in sea ice body could be interpreted as follows. Initially, the brine and the ice crystals were in the balance of phase state in the ice sheet of middle and upper part of ice body. Then the ice crystals around the brine pockets began to melt a little during the limited heating course. The chinks between the ice crystals became greater and expanded to the upper and lower ends of the ice body. At last, the brine with greater concentration moved downwards by gravitation and a large amount run off quickly when the chinks were interlinked as brine micro-pipelines and the micro-pipelines were connected with large numbers of different dimensional opening micro-holes in the under part ice sheet from head to foot. Of course, the continuous rise in temperature would not only lead to the formation of the micro-passways for the brine to be drained from the ice body, but result in the melting of some ice crystals. The ice crystals were considered as freshwater themselves, whose density was less than the brine. The water melted from the ice crystals floated on the brine in the chinks among the ice crystals and replaced the brine in the original position for its static pressure to push the brine out when the micro-passways were smaller in size. When the micro-passways were larger in size, the water melted from the ice crystals would play a very important role in eluviating, even washing the brine (salt) away from the ice body. It was the two functions that helped the salinity of the ice to drop ultimately.

The purpose of getting freshwater desalted from sea ice was realized ultimately by melting the ice crystals within its limits. The melting was controlled by dynamically adjusting the temperature of the sea ice pieces to wave around the freezing point of the corresponding sea water with a given salinity. That resulted in the brine draining along the micro-passways from the sea ice body for its gravitation and the static pressure of the water melted from the ice crystals.

4.4 Technological craft characteristics and desalination trial cost estimating

The characteristics of the desalination technology to get freshwater ice from sea ice by controlling the temperature of the air and the sea ice pieces were very obvious and striking. Depending on the natural energy (solar radiation) mainly, the system only consumed a very little energy. Because the desalination process was a sheer physics course and involved no chemical reagent, it was friendly towards the environment and the brine discharged might be recycled to obtain salt through evaporation. So, the utilization ratio of the sea ice pieces as raw materials was relatively large. Furthermore, the desalinator was of simple systematic structure and the maintaining of the system cost little. Correspondingly, it was safe to run and easy to popularize.

The experimental cost of the product freshwater desalted from the sea ice pieces was estimated on the basis of the unit cost analysis by dividing the desalination course into different segments according to the energy consumption. In the field trial, the price of the sea ice pieces as raw materials was about 1.29 RMB/m^3. One ton of the product freshwater consumed about 3.1 m^3 raw materials worth 3.99 RMB and the corresponding energy consumption cost 0.48 RMB. The experimental cost of the product freshwater was 4.47 RMB/m^3. It will be reduced by a relatively large margin with the enlargement of the production scale in the future.

5. Conclusions

It was feasible to obtain fresh water desalted from the sea ice pieces by controlling the temperature. When the air temperature was 2□-6□ and the sea ice temperature was -1.5□-2□, the effective desalination would be achieved in a course of from five days to seven days. Generally, the annual product fresh water of the single facility could be up to 381.6 m^3, the output rate of product fresh water could be more than 60%, and the experimental cost of the product freshwater was 4.47 RMB/m^3.The chemical and toxicity indexes of the fresh water product could reach the water quality standard of agricultural irrigation. With the exception of ammonia nitrogen, the indexes could also accord with the drinking and surface water quality standard of China. The microstructure characteristics of the double-phase mixture of the liquid and solid made up the foundation of the desalination technology through temperature control and the column structure of sea ice crystal would help the salt shift down fast. When the sea ice was piled up on the land surface, the brine in sea ice body would overall move downwards along the micro-passways under the gravitation and washing function with the rising of the environment temperature. The desalinator was mostly driven by natural energy including solar radiation and gravitation potential energy. The systematic energy consumption was very low and the desalination process was good for environmental protection. The maintaining of the system cost little for its simple systematic structure. Correspondingly, it was safe to run and easy to popularize. As the extension of seawater desalinization technology, the sea ice desalination technology will be expected as a new one with the developing prospects of solving the problem in short supply of fresh water in the Bohai rim, as through updating and perfecting. With the development of the technology and the promotion of the industrialization demonstration project, it can be well predicted that the sea ice will become a kind of new-type reserve resource of freshwater in North China which is in great short of fresh water.

Acknowledgements

Financial supports from National High Technology Research & Development Program of China ("863" Program, No. 2004AA2Z4020), the Emphasis Project of National Natural Science

Foundation of China (NSFC, No. 40335048), the Major Project of National Scientific & Technical Support Plans of China (No. 2006BAB03A03), and the Emphasis Project of National High Technology Research and Development Program of China ("863" Program, No. 2006AA100206), are highly appreciated. The authors would like to thank Researchers Weibin Chen and Xueren Xu from the National Marine Environmental Monitoring Center of China and Professor Akio Mouri from the Scientific Centre of Floating Ice in Khotsk of Hokkaido in Japan, for their kind help in completing the analysis of sea ice microstructure in this paper and are indebted to anonymous references for their valuable comments for the revision of this paper.

References

Arunachalam, V. M. and Muggerridge, D.B., 1993. Ice pressures on vertical and sloping structures through dimensional analysisi and similarity theory, Cold Regions Science and Technology, 21, 231-245.

Bai, S., Liu, Q.Z and Li, H., 1999. Sea ice in the Baohai Sea of China, Marine Forecasts, 16,1-9.

Chen, W.B., Xu, X.R., and Zhou, C.G., 2004. Testing study on desalination role of the gray-white ice in the Bohai Sea by the centrifugal rotational speed, Acta Oceanologica Sinica, 26, 25-32.

Col, D., and Shapior, L., 1998. Observations of Brine Drainage Networks and Microstructure of First-year Sea Ice, J Geophys Res., 103C10, 21739-21750.

Gu, S.G., and Shi, P.J., 2004. Estimation of seaice resources in Liaodong Bay on decomposing mixed pixels, Journal of Beijing Normal University(Natural Science Edition), 40, 411-416.

Gu, W., Gu, S.G., Shi, P.J., Liu, Y. and Cui, W.J., 2003. The temoral change characteristics of seaoce thickness and regeneration period of seaice in Liao-dong gulf, Resources Sicence, 25, 24-32.

Gu, W., Shi, P.J., Liu,Y., Xie, F. and Cai, X.P., 2002. The characteristics of temporal and spatial distribution of negative accumulated temperature in Bohai Sea and north Yellow Sea Journal of Natural Resources, 17, 168-173.

Gu, W., Zhang, Q.Y., Xie, F., Li, N. and Cui, W.J., 2003. Estimation of the amount of seaice resources in Liaodong Gulf by climate statistics, Resources Sicence, 25, 9-16.

Li, Z.J., Ding, D.W., Yan Qilun, Jin, H.T. and Guo, H., 1997. Preliminary study on the sea crystals and chlorophyll in Liaodong Bay, Marine environmental Sicence, 16, 21-27.

Liu, Q.Z, Bai, S. and Wu, H.D., 1998. Research on sea ice in China, Marine Forecasts, 15, 8-14.

Shi, P.J., Fan,Y.D., Hasi, Yuan, Y. and Xie, F.,2002. Calculation gross seaice resources using AVHER and MODIS data, Journal of Natural Resources, 17, 138-143.

Shi, P.J., Gu, W., Xie, F., Yuan, Y. and Jing, G.F., 2003. Spatial characteristics of seaice resources of Liaodong Gulf in winter, Resources Sicence, 25, 2-9.

Shi, P.J., Hasi, Yuan, Y., Zhou, J.H., and Xie, F., 2002. The desalination of Bohai seaice and its value as fresh water resource, Journal of Natural Resources, 17, 354-359.

Wang, J.A., Su, Y. and Liu M.X., 2003. The exploitation and utilizationof the ice in Bohai Sea used as freshwater resources and region sustainable development, Journal of Beijing Normal University (Social Science Edition), 3, 85-72.

Xiao, J.G., Xie, L.X., Wang, J.Z., Feng, G., Shi, S.F., Hu, Y.L. and Xia, S.Y., 2003. Efeects of the Bohai seaice melt~water on wheat growth and soil salt accumulation, Resources Sicence, 25, 37-43.

Xie, F., Gu, W., Yuan, Y. and Chen, Y.H., 2003. Study on the remote senseing estimation of seaice resources in Liaodong Gulf using remote sensing, Resources Sicence, 25,17-23.

Xu, X.R. Chen, W.B., Liu, X.M., Zhang, G.G., Lin, Z.S. and Guan, D.M., 2003. Quality status of the water melting from seaice in the sea area near the Changxing Island, Marine environmental Sicence, 22, 33-36.

Xu, X.R., Chen, W.B., Liu, X.M. Fu, Y.N., Sun, Y.H. and Guan, D.M., 2003. Method of desalinatimg seaice: soaking to desalt, Resources Sicence, 25, 33-36.

Xu, X.R., Chen, W.B., Liu, X.M., Fu, Y.N., Sun, Y.H., Lin, Z.S. and Guan, D.M., 2003. Study on the method of desalting sea ice: soaking and centrifuging to desalt sea ice, Marine Sicences, 27, 50-53.

19th IAHR International Symposium on Ice
"Using New Technology to Understand Water-Ice Interaction"
Vancouver, British Columbia, Canada, July 6 to 11, 2008

The calculation of Bohai sea ice thickness

Yingjun XU, Wei GU, Shuai YUAN, Ning LI, Weijia CUI and Peijun SHI

College of Resources Science & technology and Key Laboratory of Resource Engineering of Beijing Normal University, State Key Laboratory of Earth Surface Processes and Resource Ecology, and Key Laboratory of Environmental Changes and Natural Disaster of Ministry of Education
No.19 Xinjiekouwai Street, Haidian, Beijing, 100875, P. R. China
yingjxu@ires.cn, weigu@bnu.edu.cn

Abstract

To discover water sources of agriculture irrigation for regions around Bohai Sea in China, sea ice in Bohai Sea is considered as a new kind of fresh water resource due to its lower salinity than seawater, and it is feasible after many experiments. So it is vital to know the quantity of the sea ice in Bohai Sea. Thickness is one of the most important parameters to estimate the quantity of sea ice. There are many methods to calculate the sea ice thickness. Remote sensing is one of the most feasible methods because of the high-temporal and multiple spatial resolutions. Then an appropriate method should be used to calculate the sea ice thickness based on Remote Sensing. This paper comes up with a method to calculate the sea ice thickness based on the solar shortwave radiation theories. Using the methods above, this paper comes up with the time series of sea ice thickness from 1987 to 2007. The thickness time series are important to the sea ice resources calculation. And the thickness time series are also an indication of climate change. It is an evidence of global warming according to the variation of the sea ice thickness or sea ice resources.

Key words: Bohai Sea, Seaice, Thickness, Resources calculation, RS

1. Introduction

The Ring Region of Bohai Sea in China includes Liaoning, Hebei, Shandong Province and Tianjin City. This region occupies only 2% percent of the total water resource in China with an average value of 500m^3/person, which makes it a region with the heaviest water burden and the most severe conflict of water supply and need(Wang et al., 2003). In these years, scientists provided a new way to solve the water shortage problem in this region: Sea Ice Desalination (SID). SID uses sea ice as a kind of fresh water resource to supply the fresh water reservation of north China and solve the fresh water shortage problem (Shi et al., 2002). The assessment of the volume of sea ice resource, including two important indices of sea ice area and thickness, is the primary and basic job for SID. The assessment of sea ice area and the construction of its time series, takes an important part in the assessment of the volume of sea ice resource.There are several main methods for calculating the sea ice thickness by then. Both regular and Remote Sensing data are used in these methods, which include ice thickness calculation from temperature data(Gu et al., 2003), from albedo(Greenfell et al.,1991 □ Allison et al., 1993), from thermodynamics relationship(Untersteiner, 1971) and from numerical mode(Bai et al.,1998).

Whatever researches in China(Yang, 2000) or other counties(Grenfell, 1984), researches for assessing and measuring the thickness of annual sea ice or less than 1m thick sea ice were mainly focused on the exploration of ice's albedo information. There are neither constructed basic physical theories nor effective database for the parameters about ice thickness in the Bohai Sea for correlation model construction and validation, not to say the large region satellite data for real situation observation at the same time. The mentioned ice thickness calculation methods by using albedo actually can not validate the form of the relation between albedo and ice thickness although they have noticed that.

This study selected the Bohai Sea ice (at the lowest latitude in the Northern Hemisphere) as the object for research. On the base of the research on relationship between albedo and sea ice thickness, the remote sensing inversion model was constructed for the thickness of sea ice. A lot of works were done in the calculation of model parameters, a time series of sea ice thickness from 1987 to 2007 were constructed by combining sea ice area distribution. A primary analysis for the thickness error was made.

2. Data and Methods

The Bohai Sea is located off northeast China, from about 37–41°N to 117–123 °E, and is surrounded by land to the west, north, south, and northeast (Figure 1). It opens to the Yellow Sea only in the southeast by way of the Bohai Strait. On average, the water depth is 18 m. In such a half-enclosed and very shallow sea, the local weather plays an essential role in sea ice conditions.

This study has used 1200 images of AVHRR remote sensing data, which can be divided into two parts: one was provided by WebPanda, the other was from National Satellite Meteorological Center of China. Basic calibrations and geometry were made for the data and the data product were the albedo for visible light and the brightness temperature of radiation. According to the relationship between sea ice thickness and albedo (Figure. 2), the remote sensing inversion

model for the thickness of Bohai Sea ice was constructed under the theory of Solar Shortwave Radiation Theory. The calculation formula is:

$$\alpha_{(h)} = \alpha_{(\max)}[1 - k \cdot \exp(-\mu_\alpha h)] \quad \textbf{[1]}$$

Where $\alpha_{(h)}$ is the sea ice albedo of the solar shortwave radiation and it varies from the ice thickness, $\alpha_{(\max)}$ is the albedo of the infinity ice thickness, α_{sea} is the albedo of the sea water, k is related to the $\alpha_{(\max)}$ and α_{sea}, and μ_α could be calculated by the field experiment in the study area.

Based on the field experiment, the μ_α should be 2.6599 and the value is varies when there are sands in the sea water or in the sea ice. So it is hard to use a simple figure to calculate the sea ice thickness. According to the actual situation in Bohai Sea, this paper divides the Bohai Sea into four subareas. In each area, different parameters are used to calculate the sea ice thickness. In order to improve the accuracy, the parameter has to be calculated many times based on the field experiment.

For the obtained Bohai Sea ice thickness, error should be calculated. According to the field observed sea ice thickness with the fixed points and the macro characteristic data for the sea ice, the errors in sea ice thickness calculation and main reasons for them were analyzed. The macro characteristic of sea ice means the sea ice characteristic on a scale and resolution discernable by the satellite remote sensing image(like NOAA's Resolution of 1.1km×1.1km). The target of this is to achieve the satellite remote sensing survey of the macro characteristic of sea ice thickness by using field collected data to correct the inversion mode of satellite remote sensing parameters.

3. Results and discussion

3.1 The distribution of sea ice thickness

The calculated sea ice thickness by regional parameters was shown as Figure 1. It was displayed that the sea ice in the full ice period of Bohai Sea was mainly located in Liaodong Bay. There were little large areas of sea ice in other sea regions except some fixed coastal ice distributions. The distribution of sea ice thickness also showed some pattern: the coastal fixed ice was thicker than float ice. The thickness of the coastal ice was regularly more than 40cm. Some of the ice was thicker than 1m because of the effect of accumulation. However, the thickness of coastal accumulated ice was hard for accurate assessment because that it was the blind zone for the model inversion. So in the inversion of sea ice thickness on February, 4th, 2003, the maximum assessment for the sea ice thickness was only 76cm.

The thickness distribution for the sea ice was not even. Taking Liaodong Bay as an instance, the sea ice in the eastern bay (where sea ice thicker than 20cm was mainly located) was obviously thicker than that in the western bay. It was generally considered that the sea ice movement driven by winter monsoon was the basic reason for this distribution pattern. But for the warmer year, the situation is different. Fig.2 shows that there are no obvious differences between Eastern Bay and Western Bay when Liaodong Bay is the only area covered by sea ice. The thick sea ice(11~20cm) are distributing at the middle part and the Northern part of Liaodong Bay. The thickness of coastwise fast ice is about 30cm and the area is small.

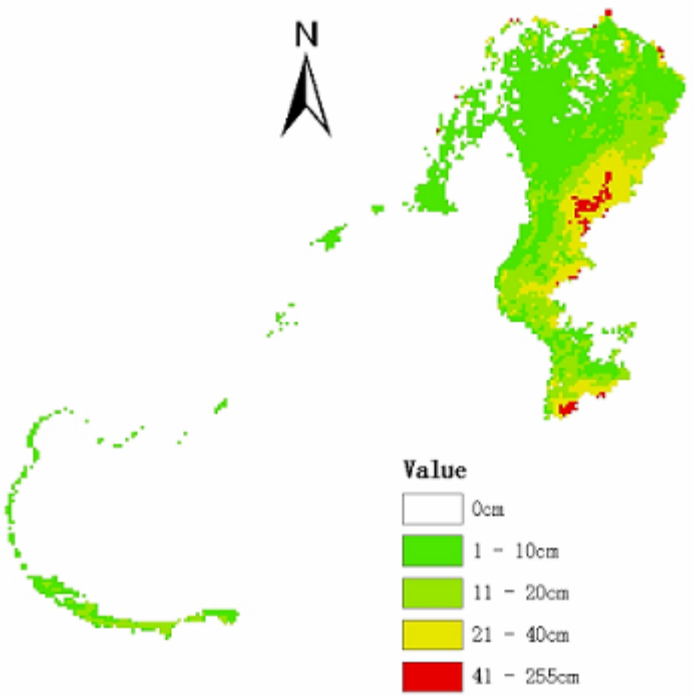

Figure 1. The distribution of sea ice thickness obtained by inversion on February 4, 2003

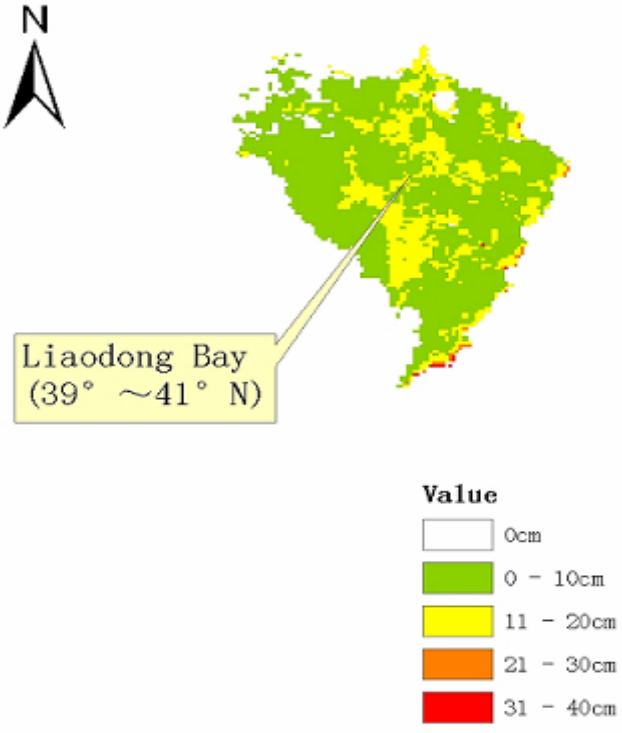

Figure 2. The distribution of sea ice thickness obtained by inversion on January 31, 2007

3.2 The error analysis for sea ice thickness assessment

In the process of calculating Bohai Sea ice thickness by regional parameters, the inversion model for sea ice thickness displayed relatively good stability. However, parameters in different regions had temporal changes, so there would be big or small errors if a same parameter (μ) was used to calculate sea ice images in different regions with a time scale of 20 years. Related researches showed that parameters such as albedo of images in different spot and at different time are different because of the changes in instrument and climate situations. The ideal situation is to firstly calculate the inversion parameter(μ) for every image according to the results obtained by a series of experiments combining real situation of each study region(Latitude, Mud Content in the water, etc), and then calculate the sea ice thickness of every image by the obtained parameters. However, limited by the present condition, we could not reverse to past to do the related experiments. In addition the calculation of different parameter for every image can not show the uniformity of the inversion model. The inversion result of this research showed that the application of single parameter for each region basically met the distribution pattern of Bohai Sea ice thickness. In order to validate the effect of inversion model, field measurement and assessment for sea ice thickness were done in Bohai Sea. The sampling spots were displayed in Figure 3. (Black points are sample positions in actual nautical experiments□.

Figure 3. Actual measured ice type position on Jun. 30, 2005

Table 1. NOAA/AVHRR on January, 30, 2005

Lat.	Long.	Actual thickness	Calculated thickness
40°18′14″N	121°50′38″E	16cm	20 cm
40°18′54″N	121°44′31″E	8cm	6 cm
40°19′04″N	121°34′04″E	16.5cm	19 cm
40°18′50″N	121°29′32″E	7~22cm	12 cm
40°19′12″N	121°21′35″E	5~25cm	17 cm
40°19′21″N	121°12′06″E	12~20cm	14 cm

Table 2. NOAA/AVHRR on March, 2, 2006

Lat.	Long.	Actual thickness	Calculated thickness
40°22′43″N	121°54′55″E	12cm	17 cm
40°25′30″N	121°52′14″E	8~20cm	29 cm
40°32′09″N	121°57′12″E	5~12cm	12 cm
40°38′18″N	121°57′55″E	5~12cm	5 cm

Table.1 and Table.2 showed that the good effect of the inversion model, which has the maximum error of 25% and minimum error of 15% for the sea ice thickness. The other calculated thickness values were all in the ranges of observation for the sea ice thickness. However, this model was mainly for inversion of the ice thickness of the smooth ice, there would be big error if there were concaves, convexes and coverage on the sea ice. In a resolution of 1km, overlapped ice, compiled ice and hummocked ice were not discernable. We could only get an average result for each single pixel, but the complied ice and other smooth ice both determined the remote sensing features of the pixel. So the ice thickness obtained by inversion was only an average sea ice thickness for each pixel, including the average effect of smooth ice and other kinds of compiled ice. In addition, because there were disturbs in non-transparent ice and sea fog, it was hard to determine the inversion parameter of μ. And the thickness inversion effects of NOAA images in old times could not be evaluated because we could not get inversion parameter (μ) from experiments.

4. Conclusion

The extraction method of sea ice thickness from NOAA remote sensing images was provided by combining solar shortwave radiation theory on the basis of the relationship between sea ice thickness and its albedo. By comprehensively analyzing the sea ice and mud in Bohai Sea, it was divided into four regions. The sea ice thickness in different regions was extracted from using the inversion model from 1987-2007. And a time series was constructed for sea ice thickness.

It was shown by the inversion result of sea ice thickness that the Bohai sea ice had uneven distribution in thickness in the full ice period. Usually the sea ice in the eastern Liaodong Bay(where sea ice with more than 20cm thickness were located) was obviously thicker that that in the western bay. It was generally considered that the sea ice movement driven by winter monsoon was the basic reason for this distribution pattern. there are no obvious differences between Eastern Bay and Western Bay when Liaodong Bay is the only area covered by sea ice.

Analysis showed that the maximum error for the sea ice thickness obtained by inversion was 25%, and the minimum error was 15%. However, this model was mainly focused on thickness of smooth ice and had some limitations. It had not considered concaves, convexes, coverage, non-transparent ice and sea fog, which could greatly influence effect of the sea ice thickness inversion because their disturbance in the confirmation of inversion parameter of μ.

Acknowledgements

Financial supports from National High Technology Research & Development Program of China (“863” Program, No. 2004AA2Z4020), the Emphasis Project of National Natural Science

Foundation of China (NSFC, No. 40335048), the Major Project of National Scientific & Technical Support Plans of China (No. 2006BAB03A03), and the Emphasis Project of National High Technology Research and Development Program of China (“863” Program, No. 2006AA100206)□are highly appreciated. The authors would like to thank the project group for their help and are indebted to anonymous references for their valuable comments for the revision of this paper.

References

Allison, I., Brandt, R.E. and Warren, S.G.,1993. East Antarctic sea ice: Albedo, thickness distribution, and snow cover, J. Geophys. Res., 98, 12417-12429.

Bai,S.,Wu,H.D.,1998. Numerical sea ice forecast for the Bohai Sea, Acta meteorologica sinica,2,139-153.

Flato, G. M. and Brown, R. D.,1996. Variability and climate sensitivity of landfast Arctic sea ice, J. Geophys. Res., 101, 25767-25777.

Grenfell, T. C. and Maykut, G.A.,1977. The optical properties of ice and snow in the Arctic Basin, J. Glaciol., 18, 445-463.

Grenfell, T. C.,1979. The effect of ice thickness on the exchange of solar radiation over the polar oceans, J. Glaciol., 22, 305-320.

Grenfell, T. C.,1983. A theoretical model of the optic properties of sea ice in the visible and near infrared, J. Geophys. Res., 88, 9723-9735.

Grenfell, T. C., and Perovich, D. K.,1984. Spectral albedos of sea ice and incident solar irradiance in the southern Beaufort Sea, J. Geophys. Res., 89, 3573-3580.

Grenfell, T. C.,1991. A radiative transfer model for sea ice with vertical structure variations, J. Geophys. Res., 96, 16991-17001.

Gu,W.,Zhang,Q.Y.,and et al., 2003. Estimation of the amount of sea ice resources in Liaodong Gulf by climate statistics, Resources science, 3, 9-16.

Lindasy, R. and Rothrock, D.A.,1993. The calculation of surface temperature and albedo of Arctic sea ice from AVHRR, Ann. Glaciol. ,17, 391-397.

Lindasy, R.and Rothrock, D.A.,1994. Arctic sea ice albedo from AVHRR, J. Climate, 7, 1737-1749.

Wang,J.A., Su.Y.and Liu,M.X., 2003. The Exploitation and Utilization of the Ice in Bohai Sea Used as Freshwater Resources and Region Sustainable Development, Journal of BeiJing Normal University, 3,85-92.

Unterstainer, N.,1964. Calculation of temperature regime and heat budget of sea ice in the central Arctic, J. Geophys. Res., 69,4755-4766.

Shi,P.J.,Ha,S.,and et al., 2002. The desalinization of Bohai sea and its use value as fresh water resource, Journal of natural resources, 3, 353-360.

Yang, G.J.,1999. Features of ice conditions in the Bohai Sea, Marine forecasts, 3,10-20.

19th IAHR International Symposium on Ice
"Using New Technology to Understand Water-Ice Interaction"
Vancouver, British Columbia, Canada, July 6 to 11, 2008

The Response of Bohai Sea Ice Area to the Climate Change

Shuai YUAN, Yingjun. XU, Wei. GU, Ning. LI, Weijia CUI and Peijun. SHI

College of Resources Science & technology and Key Laboratory of Resource Engineering of Beijing Normal University, State Key Laboratory of Earth Surface Processes and Resource Ecology, and Key Laboratory of Environmental Changes and Natural Disaster of Ministry of Education
No.19 Xinjiekouwai Street, Haidian, Beijing, 100875, P. R. China
yingjxu@ires.cn

Abstract

To discover the new water sources for regions around Bohai Sea in China, sea ice in Bohai Sea is considered as a new kind of fresh water resource due to its lower salinity than that of sea water. It is feasible after desalination and other experiments. So it is vital to know the quantity of the sea ice in Bohai Sea, and its response to the climate change which will affect the future use of the sea ice. Sea ice area is one of the most important parameters to estimate the quantity of sea ice. So a time series of sea ice area of Bohai Sea were established after data collecting and data processing. And this paper makes a primary study of the response of sea ice area to the climate change.

Keywords: Bohai Sea; Seaice area; NOAA/AVHRR; Climate change; Response

1. Introduction

The Ring Region of Bohai Sea in China includes Liaoning, Hebei, Shandong Province and Tianjin City. This region occupies only 2% percent of the total water resource in China with an average value of 500m3/person, which makes it a region with the heaviest water burden and the most severe conflict of water supply and need(Wang et al., 2003). In these years, scientists provided a new way to solve the water shortage problem in this region: Sea Ice Desalination (SID). SID uses sea ice as a kind of fresh water resource to supply the fresh water reservation of north China and solve the fresh water shortage problem (Shi et al., 2002). The assessment of the volume of sea ice resource, including two important indices of sea ice area and thickness, is the primary and basic job for SID. The extraction of sea ice area and the construction of its time series, takes an important part in the assessment of the volume of sea ice resource.

In Bohai Sea, there is a close relationship between sea ice and climate change. It is proved by some scientific research that climate change has caused changes in sea ice, especially the sea ice in polar areas Flato et al., 1996 . The cryosphere is of great significance in global change, both for its large response to the changing climate and as an important mechanism of climate forcing through its feedback (Houghton et al., 2001; Polyakov et al., 2002; Serreze and Francis, 2006 Garrison &Ackley 1983). The sea ice in the Northern Hemisphere has experienced an evident decline in its extent and thickness as the climate has warmed over the past few decades (Parkinson et al., 1999; Lindsay and Zhang, 2005; Stroeve, 2005). Therefore, as the sea ice in the lowest latitude in the Northern Hemisphere, the Bohai sea ice is an important indicator for regional climate change because its great sensitivity to intra-annual and inter-annual changes and changes of regional climate. Sea ice severity is a qualitative data applied frequently in researches for the relationship between sea ice and climate. Based on time series of sea ice area, this article made quantitative analysis for the response of Bohai sea ice to climate change from the prospective of the variations of sea ice area.

2. Data and Method

The Bohai Sea is located off northeast China, from about 37–41°N to 117–123 °E, and is surrounded by land to the west, north, south, and northeast (Figure 1). It opens to the Yellow Sea only in the southeast by way of the Bohai Strait. On average, the water depth is 18 m. In such a half-enclosed and very shallow sea, the local weather plays an essential role in sea ice conditions. Observations indicate that, in this particular region, the dynamical factors such as wind stress and surface ocean currents are not so important in the distribution of sea ice (Zhang, 1986). In the present study, thus, we do not address the influence of wind related ice-dynamics. We focus only on the sea ice area due to temperature variability.

The data used in this research can be divided into two parts, one is the daily data from meteorological stations around the Bohai Sea (Dalian, Yingkou and Dagui), the other is NOAA/AVHRR Remote Sensing data from 1987 to 2007(December to March) including 1200 images.There were differences in the data format and time series length among different meteorological stations around Bohai Sea. After data analysis and reorganization with the consideration of these limits in data, a database for those stations was constructed for data usage and analysis.

Based on the characteristics of high reflectance and low brightness temperature, the clouds can be removed by a compositive threshold. But we don't use the image with clouds which covers the sea ice. For it is hard to estimate the sea ice area covered by cloud. As for the land, it can be out with a vector boundary. It is hard to differentiate sea water and sea ice with a simple threshold because of the sands in the sea water. The sea water with sands has a similar reflectance as the sea ice. But the sea ice and the sea water nearby are different in reflectance. According to the actual situation in Bohai Sea, this paper divides the Bohai Sea into four subareas. In each subarea, a threshold is defined to differentiate the sea ice from the sea water. In order to improve the accuracy, the threshold has to be rectified based on the original image and feasible field experiments. A time series of Bohai sea ice from 1987 to 2007 was constructed on the base of those 583 extracted NOAA images for Bohai sea ice area.

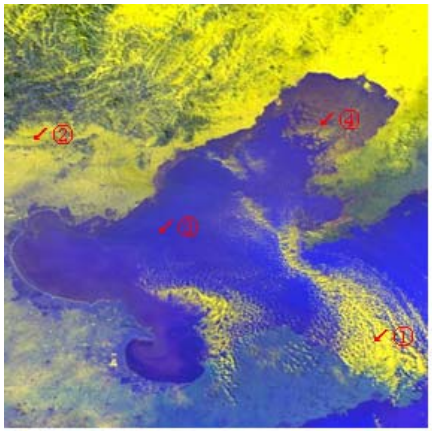

Figure 1. Study area NOAA/AVHRR image
(clouds land sea water sea ice)

3. Results and discussions

3.1 Sea ice area and ice severity

The sea ice can quantitatively represent variation of the Bohai sea ice. And there is good relationship between changes in sea ice area and sea ice severity. In recent 20 years, the maximum sea ice area is below 20,000km^2 in the full ice period of Bohai Sea, which means a less than 3 sea ice severity. This is in accordance with the reduction of global sea ice area caused by global warming. Although the total trend for Bohai sea ice area is decreasing, there is more than 20,000km^2 of sea ice in some years, such as the winter in 2000 with a sea ice severity of 4 and a total sea ice area of 25,000km^2. In this study, the remote sensing data begins later than the sea ice severity (More than 50 years). However, in the future studies, the time series for the sea ice variations can be extended by using good relationship between sea ice severity and sea ice area under the support of related meteorological data. This extended time series can support quantitative researches for sea ice variations in a long time scale.

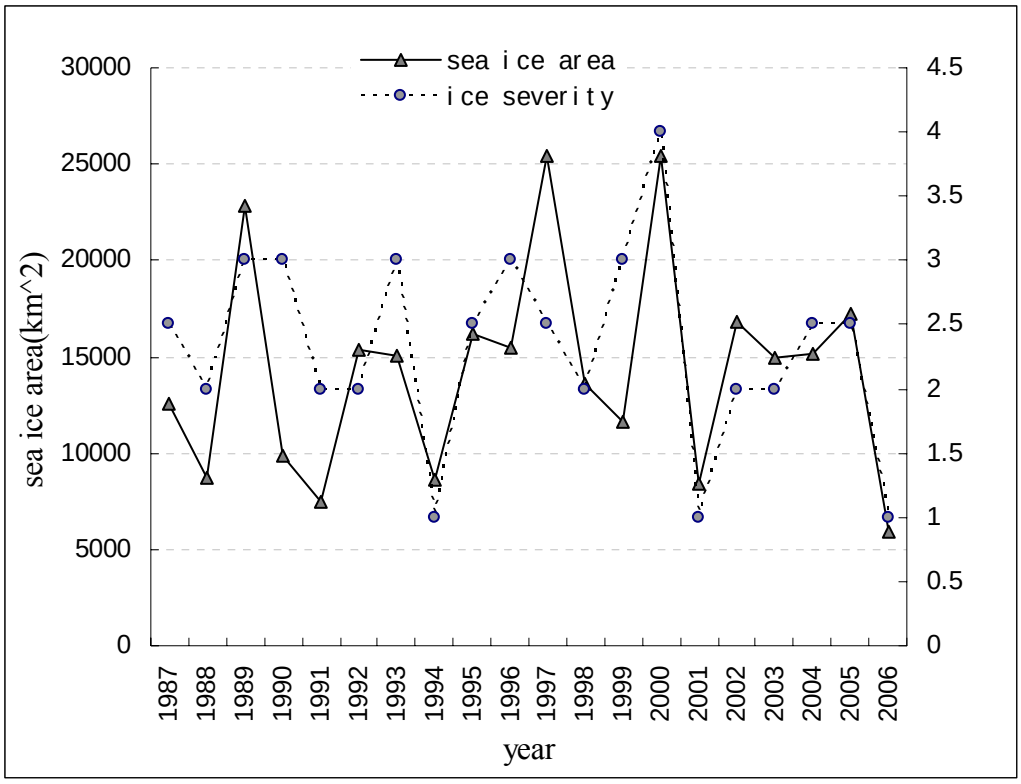

Figure 2. The sea ice area and the ice severity

3.2 Intra-annual variations of sea ice area

Bohai sea ice is 'annual' sea ice, which means the sea ice area experiences the circle of 'zero-generating-maximum-reducing-zero' in one year. So the intra-annual variation for Bohai sea ice is significant with a ratio of 17.2 between the maximum and the minimum sea ice area obtained by remote sensing images. The intra-annual variation mode for Bohai sea ice corresponds to the winter temperature variation model in Bohai sea: 'Temperature decreases that the sea ice freezes-Temperature keeps on dropping-Lowest temperature in winter-Temperature begins to increase-Temperature keeps on increasing that sea ice totally melts'. The Generating-Disappearing course for the 'annual' sea ice should be the response to the regional temperature variation.

Table 1. Sea ice area variation in 2000/2001

date	$12/15^0$	$12/20^0$	$12/25^0$	$01/03^1$	$02/01^1$	$02/09^1$	$02/15^1$	$02/19^1$	$03/07^1$
area km^2	4346	7553	11065	9380	11081	25469	14888	17255	1476

12/15 refers to 15^{th}, Dec. ^{0}refers to 2000. ^{1}refers to 2001

3.3 The response of inter-annual variations of sea ice area to climate change

(1) The response of sea ice area to variation in winter average temperature.

The variation of temperature of Bohai in winter has important influences to the generating of sea ice and the changes of its area. The winter average temperature basically represents the trend of local winter temperature variation, which is one of the main controlling factors for the distribution of Bohai sea ice area. Figure3 shows the response of sea ice to winter average temperature variation around Bohai see. An inverse correlation between sea ice area and winter

average temperature is shown: Sea ice area decreases when winter average temperature and vice versa. In winter, the variation range is 18000km^2 for the sea ice area and 4 for the winter average temperature. If the winter average temperature is considered as the single factor for sea ice area change, the ratio should be 4500 km^2/ , which means the sea ice area decreases 4500 km^2 while winter average temperature increases 1 . However, this relationship was not very strict. For instance, the maximum value for sea ice area appeared in 2000, but the winter mean temperature in that year was not the lowest value, which appeared in 1999. Global Warming's impact to sea ice area was both delicate and profound, which displayed in to prospective, one is that there was not obvious reduction in total sea ice area under the background of global warming, another is that there was actually reducing periods for sea ice area in recent 20 years.

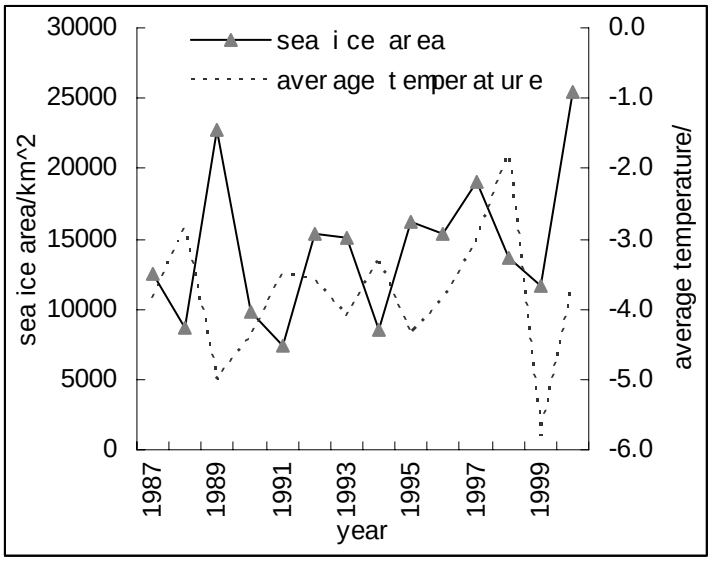

Figure 3. The response of sea ice are to the average temperature in winter

(2) Lowest temperature

The temperature in Dalian Meteorological station represents the sea ice situation in Liaodong Bay pretty well (Bai et al., 2001). The sea ice area in Liaodong Bay takes the main part of that in Bohai Sea (more than 74%), so the variation of winter lowest temperature in Dalian Meteorological Station is an important reference to Bohai sea ice variation. It is shown in Figure 4 that sea ice area becomes bigger when lowest temperature turns lower. Two exceptions were the years of 1987 and 1988, when the lowest temperature(about -8) was obviously higher than other years but the sea ice areas were also very big. Although temperature is a very important index with great influence to sea ice area, the single temperature index (for instance, the winter average temperature and lowest temperature) can not perfectly indicate variation of sea ice area. Therefore, the total tendency for the response of sea ice area to climate change is clear, however, the situation of sea ice area in a specific year needs comprehensive analysis with more factors, for instance, wind, sea current and so on.

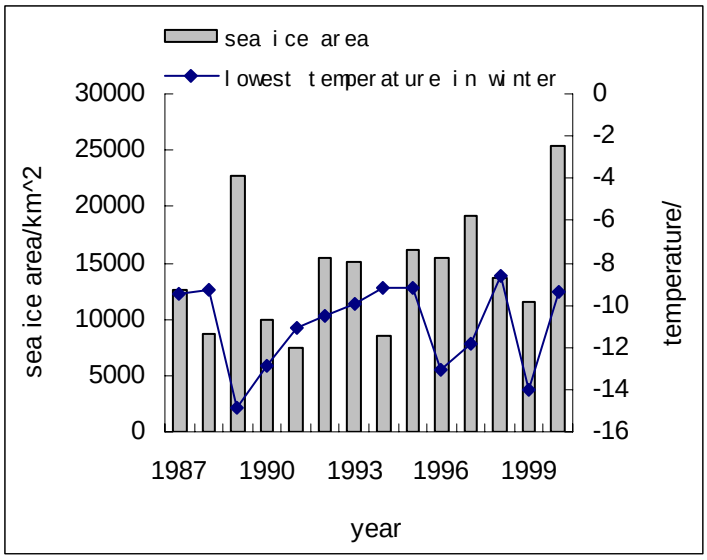

Figure 4. The sea ice area and the lowest temperature in winter

(3) Sea ice area and Cold Waves

When the generating process of sea ice is analyzed, the cold wave is another important climate factor the sea ice forming. By combining temperature condition for sea ice freezing and referencing the national standard for the cold wave, the definition of cold wave is given: When the daily average temperature at one station was below - □ and more than 8□ lower than the day before, a cold wave happened at that station. Figure 5 shows the frequency of cold waves happened in Dalian in recent years, which is calculated by the definition. There is basically no record for more than two cold waves in one year after 1990 with the exception of 1998, when two cold waves happened. In years of 1987 and 1998, when the big sea ice area can not be explained by lowest temperature, the sea ice area is closely related to cold wave, because these two years were high years for cold waves, 3 times and 2 times for each year respectively.

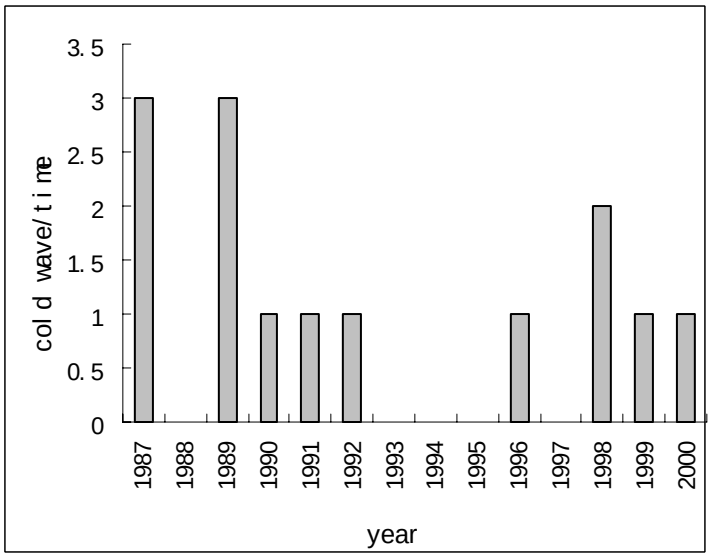

Figure 5. The sea ice area and the cold waves

The response of sea ice area variation to regional climate change is very sensitive, which is result of the comprehensive effect from different kinds of climate factor. Any single factor can hardly explain the whole information included in the variation of sea ice, so it is a very complicated question to understand the response of sea ice area variation to regional climate change.

4. Conclusions

From the time series of Bohai sea ice constructed by using NOAA/AVHRR remote sensing images, it is shown that Bohai sea ice area was commonly less than 20,000km^2 in recent 20 years. Although in some years, the sea ice area could be bigger than 25,000 km^2, it is still in a period of relatively smaller sea ice area. There is good correspondence between sea ice area and the sea ice severity data, which is qualitatively descriptive. By combining related meteorological data, the time series of sea ice area could be extended with the purpose of supporting quantitative index for the future sea ice area research. There is a non-strictly inverse correlation between sea ice area and regional winter average temperature. According to primary assessment, the sea ice area decreases (increases) 4500 km^2 while winter average temperature increases (decreases) 1□. The global warming is an important reason for the recent 20 years' period of relatively smaller Bohai sea ice area, but there was no obvious reduction in the sea ice area for this reason. In most years, the variations of sea ice are closely related to winter's lowest temperature. Although in some years, variations between winter lowest temperature and sea ice area contradict the regular pattern, the cold waves in those years can give good explanations for those contradictions. The variation of sea ice area contains different kinds of climate information, so it has sensitive and complicated responses to regional climate change.

Acknowledgements

Financial supports from National High Technology Research & Development Program of China ("863" Program, No. 2004AA2Z4020), the Emphasis Project of National Natural Science Foundation of China (NSFC, No. 40335048), the Major Project of National Scientific & Technical Support Plans of China (No. 2006BAB03A03), and the Emphasis Project of National High Technology Research and Development Program of China ("863" Program, No. 2006AA100206), are highly appreciated. The authors are indebted to anonymous references for their valuable comments for the revision of this paper.

References

Bai,S.,Liu,Q.Z.,Wu,H.D.and Wang,Y.L.,2001. Relation of ice conditions with climate change in the Bohai Sea and the northern Huanghai Sea, Acta oceanologica sinica, 5,33-41.

Flato, G. M., R. D. Brown. ,1996. Variability and climate sensitivity of landfast Arctic sea ice, J. Geophys. Res., 101, 25767-25777.

Garrison, D. L. Ackley, S. F. Buck, K. R. ,1983.A physical mechanism for establishing algal populations in frazil ice, Nature 306(5941), 363 365

Gong, D.Y.,Kim, S.J., and Ho,C.H. ,2007. Arctic Oscillation and ice severity in the Bohai Sea, East Asia, international journal of climatology, 27,1287-1302.

Houghton, J.T., Ding, Y.H., Griggs, D.J., Noguer, M., vander Linden P.J., Dai X.S., Maskell K, Johnson C.A. ,2001.Climate Change 2001: The Scientific Basis. Contribution of Working

Group I to the Third Assessment Report of the Intergovernmental Panel on Climate Change, Cambridge University Press: Cambridge, 881.
Lindsay, R.W., Zhang, J. (2005). The thinning of Arctic sea ice, 1988-2003: have we passed a tipping point? , Journal of Climate, 15, 4879-4894.
Parkinson, C.L., Cavalieri, D.J., Gloersen, P., Zwally, H.J., Comiso, J.C.(1999).Arctic Sea ice extents, areas, and trends, 1978-1996, Journal of Geophysical Research, 104, 20837-20856.
Polyakov, I., Alekseev, G., Bekryaev, R., Bhatt, U., Colony, R., Johnson, M. Karklin, V., Makshtas, A., Walsh, D., Yulin, A.(2002). Observationally based assessment of polar amplification of global warming, Geophysical Research Letters, 18, 1878-1881.
Serreze M.C., Francis, J.A. (2006). The Arctic amplification debate, Climatic Change, 3,241-264.
Shi,P.J.,Ha,S.,and et al(2002). The desalinization of Bohai sea and its use value as fresh water resource, Journal of natural resources, 3, 353-360.
Stroeve, J.C. (2005). Tracking the Arctic's shrinking ice cover: another extreme September minimum in 2004, Geophysical Research Letters, 32(4), L04501.
Wang,J.A., Su.Y.and Liu,M.X.(2003) The Exploitation and Utilization of the Ice in Bohai Sea Used a s Freshwater Resources and Region Sustainable Development, Journal of BeiJing Normal University, 3,85-92.
Zhang, F.J. (1986). Sea ice in China, China Ocean Press: Beijing.

Sea ice ridges

19th IAHR International Symposium on Ice
"Using New Technology to Understand Water-Ice Interaction"
Vancouver, British Columbia, Canada, July 6 to 11, 2008

The consolidation in second- and multi-year sea ice ridges Part I: Measurements in early winter

Knut V. Høyland[1,2], Sébastien Barrault[1,2], Sebastian Gerland[3], Harvey Goodwin[3], Marcel Nicolaus[3], Ole Morten Olsen[3], Eero Rinne[4]
[1]*The Norwegian University of Science and Technology (NTNU), Trondheim, Norway*
knut.høyland@ntnu.no
[2]*The University Centre in Svalbard (UNIS), Longyearbyen, Norway*
sebastien.barrault@unis.no
[3]*The Norwegian Polar Institute (NPI), Tromsø, Norway*
sebastian.gerland@npolar.no (harvey.goodwin@...,marcel.nicolaus@..., ole.morten.olsen@...)
[4]*The Finnish Institute of Marine Research (FIMR), Helsinki, Finland*
eero.rinne@iki.fi

.

Second-year sea ice in the Fram Strait has been investigated in September 2006 and 2007 with respect to consolidation. This is the first time measurements on these early winter second-year ridges are presented. Their geometry and macro-porosity were examined by drilling 2" holes and showed almost zero macro-porosity (i.e. almost completely consolidated). The ice keels were less than 7.1 m. Ice cores were sampled for the determination of temperature, salinity and density and further for calculation of air and brine porosity. The mean salinity of the keels was about 1.8 ppt, similar to what has been found in old ridges in April in the Beaufort Sea (1.4 and 1.6 ppt), but clearly lower than in blocks from keels of first-year ridges (about 4-6 ppt). The relative air volume was 4.9 (2006) and 2.1 (2007), and no obvious difference from neither first-year ridges nor old is apparent. We suggest that the most important processes that transform first-year to multi-year ridges occur in the summer.

1. Introduction

Sea ice ridges are formed from compression or shear in the ice cover, and are important features in most ice covered seas. They are interesting in both engineering- and climate related studies. For engineers the prime interest is the direct ridge action on ships and offshore - or coastal structures, but also the indirect effect caused by ridging in small-scale ice dynamical models are important. The latter for predicting the internal pressure in drifting ice. In this way sea ice ridges often govern the design for Arctic marine structures/installations when icebergs are not present or when they can be managed.

The World Meteorological Organization (WMO, 1970) defines different floating sea ice features, and categorizes both according to type and age. Let us firstly discuss the types of ice features. We let the icebergs live their non-salty lives undisturbed and concentrate on floating sea ice. It consists of mechanically un-deformed ice, often called level ice, and mechanically deformed ice such as ridged and rafted ice. Level ice has relatively even top and bottom surfaces during the growth season as opposed to ridges that in principle consist of a clearly distinguishable sail above the waterline and a keel below. However, it is often difficult or impossible to distinguish rafted ice from level ice without ice texture or ice physics examination (or both). Further, during the melt season the level ice top and bottom surface become uneven, and when the freezing starts again it may be quite difficult to visually determine if the unevenness is due to thermal or mechanical activity. In this paper which is about ice ridges we have chosen not to try to distinguish between mechanically deformed and non-deformed ice.

The age of ice is categorized as first-year - and old ice (WMO, 1970), the latter is further subdivided into second- and multi-year ice. But the definition of what is first- and second year ice is not clear. Ice that has lived through one winter and one summer is both first- and second-year ice. The definitions of WMO are as follows:

- First-year ice is sea ice of not more than one winter's growth
- Old ice is sea ice which has survived at least one summer's melt, and can be subdivided into:
    1. Second-year ice that is old ice which has survived only one summer's melt
    2. Multi-year ice is old ice up to 3 m or more thick which has survived at least two summers' melt

First-year ridges have different geometrical and mechanical properties than old ridges and give different engineering challenges, in particular the consistency of the keels are different. In first-year ridges the keels consist of a refrozen or consolidated layer and a relatively large part of unconsolidated rubble. The consolidated layer grows through the winter and usually becomes 1.5-2 times the thickness of the surrounding level ice. In old ridges the entire ridge seems to be consolidated, see Part II of this paper for a review on consolidation and properties in old ridges. The ice in the Fram Strait in September 2006 and 2007 was either at the end of the summer or in the beginning of the winter, but as it seems as the most important processes transforming first-year ridges into second-year ridges occur during the summer we call our ridges second-year throughout this paper.

2. Motivation, site and experimental set-up

The Norwegian Polar Institute (NPI) does systematic monitoring and research in the Fram Strait since the early 1990's, mostly with the research vessel R/V Lance. The main point is to examine the transport of ice and water out of the Arctic through the Fram Strait, and the collection of oceanographic data (CTD) along specific transects and extracting data from Upward Looking Sonars (ULS) and current rigs have been the core. In-situ ice investigation became a part of the work in 2003, and in September 2006 and 2007 UNIS was invited to extend the scientific scope to also examining ice ridges. Selected results from earlier NPI Fram Strait work is presented in Vinje et al. (1994), Hansen et al. (1987) and Gerland et al. (2006).

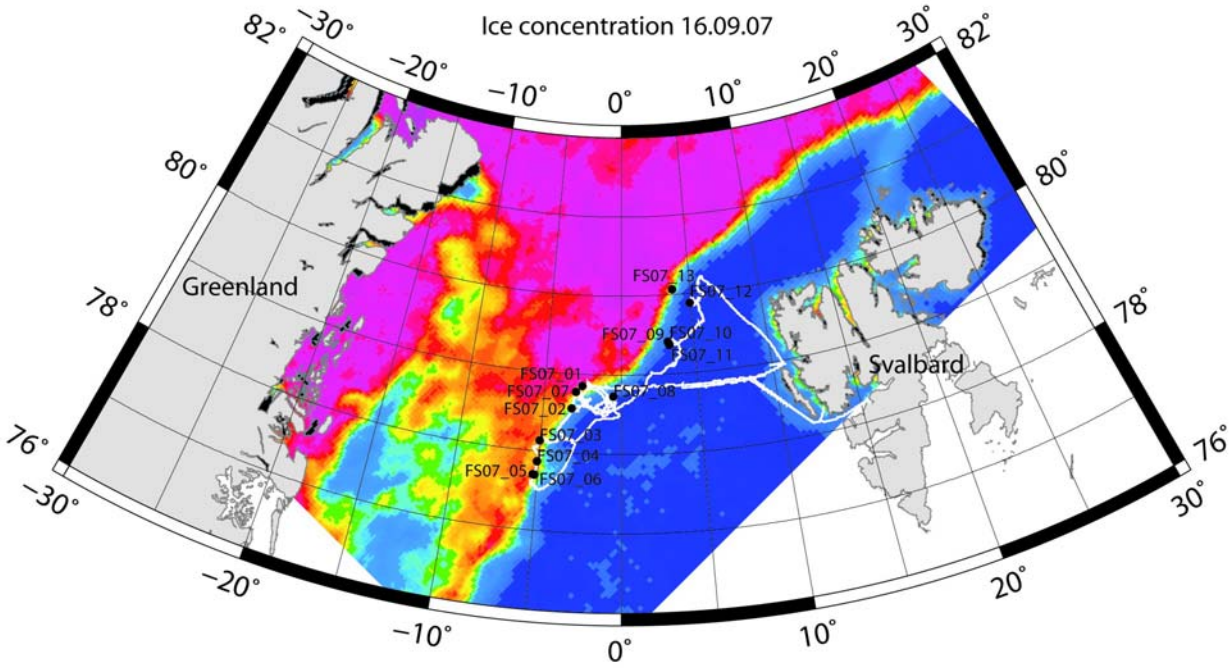

Figure 1. The ice stations and the ice concentration in 2007. Blue is 0% and pink is 100% ice. The ice maps are based on AMSR-E data and the images were downloaded from www.seaice.dk.

Figures 1 and 2 and Table 1 give the locations of the ice stations. The work in 2007 took place further east due to larger ice extent in 2007 compared with 2006. The ship R/V "Lance" is ice enforced, but not an ice breaker so it cannot break very heavy ice.

We had 9 stations in 2006 and 12 stations in 2007 and spent 2-8 hours on each station, measuring ice thickness with an electro-magnetic device (Haas et al., 1997), taking cores for temperature, density, and salinity (T, S and ρ) in ice and snow, drilling geometry profiles over the ridge, measuring surface albedo and how the solar radiation penetrates through the snow, ice and water. In 2007 the temperature, salinity and density profiles were mostly taken in three individual cores next to each others, but in one case (FS09-7#C) we economized and used ice from one core to measure all three properties. In most of the stations in 2006 (except FS06-2 and FS06-4) the temperatures were taken from one individual core whereas salinity and density were measured on the same core, but every alternating 0.1 m throughout the core thickness. We used a 10 cm

core diameter sampler in 2006 and 7 cm in 2007. The air and brine volumes (η_a and η_b) were calculated after Cox and Weeks (1983) and Leppäranta and Manninen (1988). The geometry drilling was done with 2" augers.

In the present paper we concentrate on the T, S and ρ cores, but will also present some thickness profiles from manual drillings.

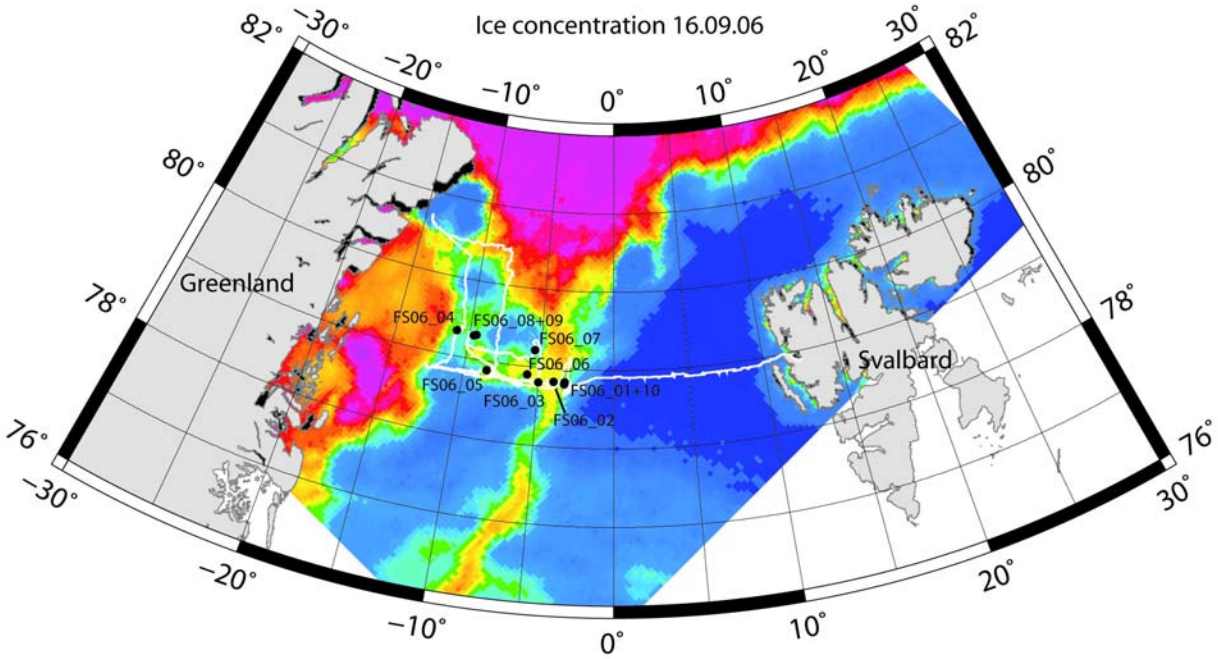

Figure 2. The ice stations and the ice concentration in 2006. Blue is 0% and pink is 100% ice. The ice maps are based on AMSR-E data and the images were downloaded from www.seaice.dk.

3. Results

Geometry and morphology

Table 3 gives the main results and Figures 3 and 4 show two of the seven profiles from 2007. In some of the cross-sections we detected some pores, either in the topmost layer or close to the bottom as given in the two figures. The ice was sometimes porous on top but became gradually more solid with increasing depth; other floes had relatively solid ice throughout the depth. But none of the ridge keel had a consistency typical for first-year ridges with relatively large (decimeters) pores, in other words the macro-porosity in our ridges was close to zero. The bottom surfaces were quite uneven, and at FS07-2 we drilled 3 cores within a 0.3 m radius and the thicknesses were 1.87, 1.93 and 2.51 m. When the floes split and when the ship advanced through the ice and partly breaking it, we could see large ice blocks (1-10 m) floating up from below ridges. The top surface was mostly covered with snow, but when removing the snow the blocks in the sail were little eroded and clearly visible.

Table 1. Stations with ice coring

Name	Date	Position[a]	Cores for T,S and ρ[b]	Geometry drilling # holes
2006				
FS06-1	01.09.06	78°84'N / 3°26'W	S and ρ	1
FS06-2	02.09.06	78°83'N / 3°99'W	T, S and ρ	2
FS06-4	05.09.06	79°32'N / 10°90'W	T, S and ρ	2
FS06-5	08.09.06	78°89'N / 8°46'W	2T, 2S and 2ρ	1
FS06-6	09.09.06	78°90'N / 5°76'W	T, S and ρ	2
FS06-8	11.09.06	79°30'N / 9°52'W	2T, 2S and 2ρ	2
FS06-10	13.09.06	78°80'N / 3°29'W	T, S and ρ	2
2007				
FS07-1	14.09.07	78°50'N / 2°35'W	2T, 2S and ρ	9
FS07-2	15.09.07	78°30'N / 3°20'W	2T, 2S and ρ	4
FS07-3	16.09.07	78°05'N / 5°05'W	T and ρ	9
FS07-4	17.09.07	77°50'N / 5°05'W	T, S and ρ	19
FS07-7	19.09.07	78°40'N / 3°00'W	2T, 2S and ρ	14
FS07-8	23.09.07	79°20'N / 0°40'W	T, S and ρ	6
FS07-9	25.09.07	79°50'N / 3°15'E	3T, 3S and 2ρ	1
FS07-12	26.09.07	78°84'N / 5°00'E	2T, 2S and ρ	10
FS07-13	27.09.07	80°05'N / 5°35'E	T and ρ	3

[a]This gives an approximate average position, the ice was drifting
[b]T – temperature, S – salinity and ρ – density sdf

Physical properties and porosity

Table 3 gives average values of T, S and ρ and the calculated porosities for the different cores. The two most important parameters in relation to the mass transfer and seasonal development are the salinity and the air volume (η_a). The brine volume changes with the temperatures and gives less of an indication of the relative composition of ice, salt and air. The average sail and keel salinities were 0.3 and 2.0 ppt (2006) and 0.5 and 1.7 ppt (2007), and the average relative air volumes for sail and keel were respectively 9 and 5% (2006) and 9 and 2% (2007). Two vertical profiles of temperature and porosities from 2007 are given in Figures 5 and 6. Especially in Figure 6 the effect of the summer heating and the start of the winter are clear. Station FS07-12 was further north than FS07-7 and the air temperature was lower.

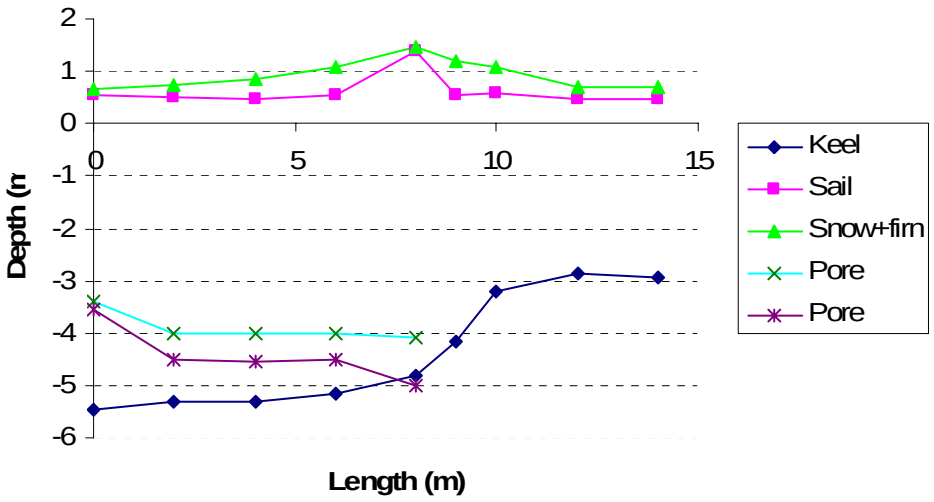

Figure 3. The geometry profile of the ridge at station FS07-3, 16.09.07. There were voids between the two lines marked Pore.

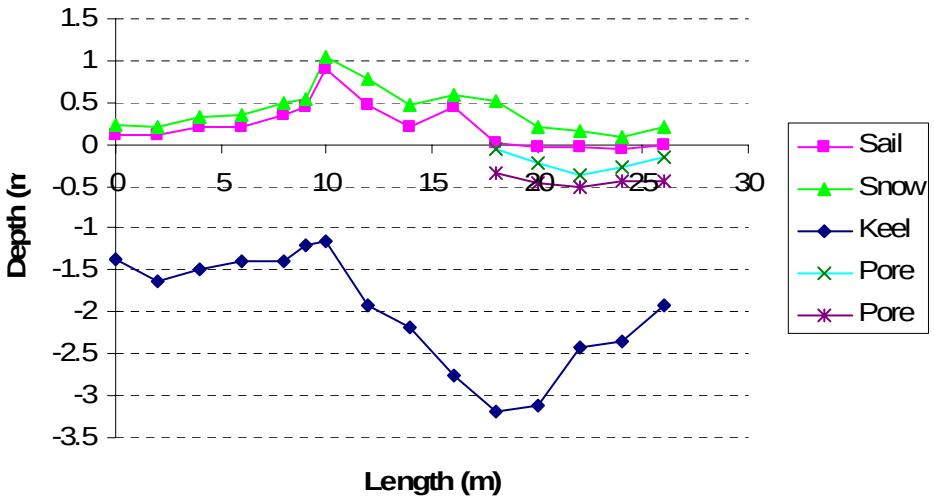

Figure 4. The geometry profile of the ridge at station FS07-7, 19.09.07. There were voids between the two lines marked Pore.

Table 2. Porosity measurements in ridge keel/rubble

Source	η [%]	η_a [%]	η_b [%]	S [ppt]	ρ [kg/l]
First-year – May in the Barents Sea[a]					
2002 (UNIS)	8	3	5	2.1	0.90
2003 (UNIS)				6.8	
2004 (UNIS)	16[b]	4	0.12	3.9	0.89
2005 (UNIS)	23	7	16	5-6	0.87
2006 (UNIS)[c]	19	6	13	5	0.87
2007 (UNIS)	17	6	11	4.5	0.87
First-year – September in the Fram Strait					
2006 (NPI/UNIS)	13	4.9	8.0	2.0	0.88
2007 (NPI/UNIS/NTNU)	10	2.1	6.9	1.8	0.91
Second/multi-year – April in the Beaufort Sea					
Kovacs (1983)	8.47	7.47	0.1	1.37	0.851
Richter-Menge and Cox (1985)	3.2[d] / 3.68[e]	2.7	0.5 / 1.1	1.64	0.90
Cox and Richter-Menge (1985)	0.08				

[a]This is the porosity of the solid pieces of ice that was sampled from the keel, the macroscopic ridge porosity is not included. The salinity and porosity of the entire unconsolidated part is higher

[b]Only 1 m below the consolidated layer

[c] In the Arctic Ocean, off the northern coast of Svalbard

[d]measured at -20°C

[e]measured at -5°C

4. Discussion

Geometry and morphology

The keel depth ranged from about 1.5 m to 7 m so we only examined small to medium ice ridges. The consistency of the ridge keels were clearly different from that of first-year ridges and support earlier observations of old ridges being almost completely consolidated (see Part II for a review). The upper pores were partly refrozen melt ponds with low saline ice/water and the lower ones were remains of ordinary first-year keel porosity. The existence of these indicates that the ridges were less than one year old. In the sail the block structure was often still visible, and the original voids between the blocks were partly refrozen with almost fresh ice, and partly still snow and air filled. These facts also indicate second-year ridges. Finally the fact that the bottom surfaces of the keels were not smooth indicates either ridges less than one year old, or re-ridging under older ridges. In summary we believe the ridges were less than one year old.

Table 3. Main results, the keel depth (h_k), the sail height (h_s), the physical properties (S, T and ρ) and the air and brine

Station Name	Ice thickness[a]		Ice properties									
	h_s [m]	h_k [m]	T [°C]		S [ppt]		ρ [kg/l]		η_a [%]		η [%]	
	Sail	Keel	Sail	Keel	Sail	Keel	Sail	Keel	Sail	Keel	Sail	Keel
2006						**2006**						
FS06-1	0.74 (1.54)	4.33 (5.1)	-1.92	-2.13	0.10	2.35	0.85	0.89	7.36	3.62	0.24	5.19
FS06-4	0.7 (2)	7.15	-1.19	-1.64	0.30	2.34	0.83	0.88	9.63	4.84	1.11	6.69
FS06-5[b]	0.16 (0.76)	1.64	-0.50	-0.82	0.70	1.97	0.80	0.86	13.36	7.37	6.03	11.03
FS06-6	0.45 (1.29)	2.35	-0.40	-0.68	0	1.63	0.84	0.89	8.40	4.11	0	11.43
FS06-8	0.73 (1.16)	2.95	-0.21	-0.84	0.50	1.78	0.88	0.88	5.11	5.08	11.45	9.96
FS06-10	0.8 (1.05)	4.52	-2.34	-2.26	0	1.72	0.83	0.88	9.52	4.51	0	3.53
Average	3.82	0.60	-1.09	-1.40	0.27	1.97	0.84	0.88	8.90	4.92	3.14	7.97
2007						**2007**						
FS07-1#2	0.1	1.4		-1.25	1.27	1.68	0.79	0.87		5.83		6.23
FS07-1#5	0.8	2.1 (2.3)	-1.14	-0.99								
FS07-2	0.3	4.2 (5.5)	-1.10	-1.05	0.43	1.81	0.82	0.90	10.8	2.76	1.71	8.26
FS07-3	0.5 (1.45)	4.6 (5.5)	-1.04	-1.30	0.42	1.94						
FS07-4	0.05 (0.37)	2.1 (2.9)		-0.73		1.02		0.89		3.63		6.65
FS07-7	0.4 (0.9)	3.0 (3.2)	-2.08	-1.90	0.34	2.45	0.79	0.92	13.96	0.47	0.68	6.34
FS07-8	1.1 (1.9)	4.7			0.55	1.88	0.82	0.93				
FS07-9#A	0.15	1.4	-2.00	-0.95	0.05	1.47	0.89	0.93	2.99	0	0.12	7.67
FS07-9#B	0.1	1.5	-2.05	-1.10	0.35	1.28	0.89	0.91	3.07	1.39	0.81	5.64
FS07-9#C	0.05	1.8		-0.70				0.90				
FS07-12	0.35	3.5	-2.94	-1.31	0.77	2.05	0.80	0.93	12.95	0	1.1	7.75
FS07-13	0.1 (0.44)	2.7	-1.75	-1.16			0.71	0.92				
Average	2.92	0.51	-1.64	-1.15	0.52	1.73	0.83	0.91	8.75	2.01	0.88	6.93

[a]The sail and keel thickness in the place where T, S and ρ were measured, the number in parenthesis gives measured peak value in the floe

[b]Density data to be used with caution, brine drained from pockets (r > 1cm) while sampling

Physical properties and porosity

Table 2 compares average values from Table 3 with earlier data from first-year ridges late in the spring (May) in the Barents Sea and with old ridges from the Beaufort Sea in April. Most of the data from the UNIS cruises in May are presented in several publications, but may deviate some from earlier reports (Høyland, 2007). This is because the data below are meant to be the in-situ porosities, whereas most of the earlier published data are measurements done after the mechanical testing, that is some minutes after the samples were collected. In particular the temperature may deviate a bit, but less than 0.3°C.

The two key points are firstly that the keel salinity in the Fram Strait ridges were similar to that of second- or multi-year ridges from the Beaufort in April and clearly less than that of first-year ridges from the Barents Sea in May, and secondly that the relative air volume does not seems to develop in any clear direction. This indicates that the main mass transfer occurs during the summer, and that the drained brine seems to be replaced by newly formed ice.

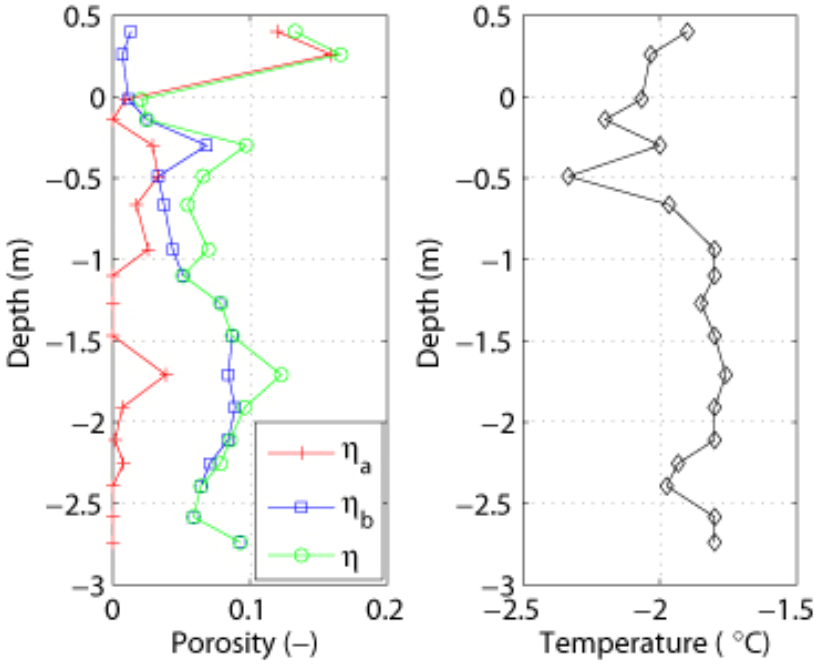

Figure 5. Vertical porosity (air and brine) and temperature profiles from station FS07-7, 19.09.07

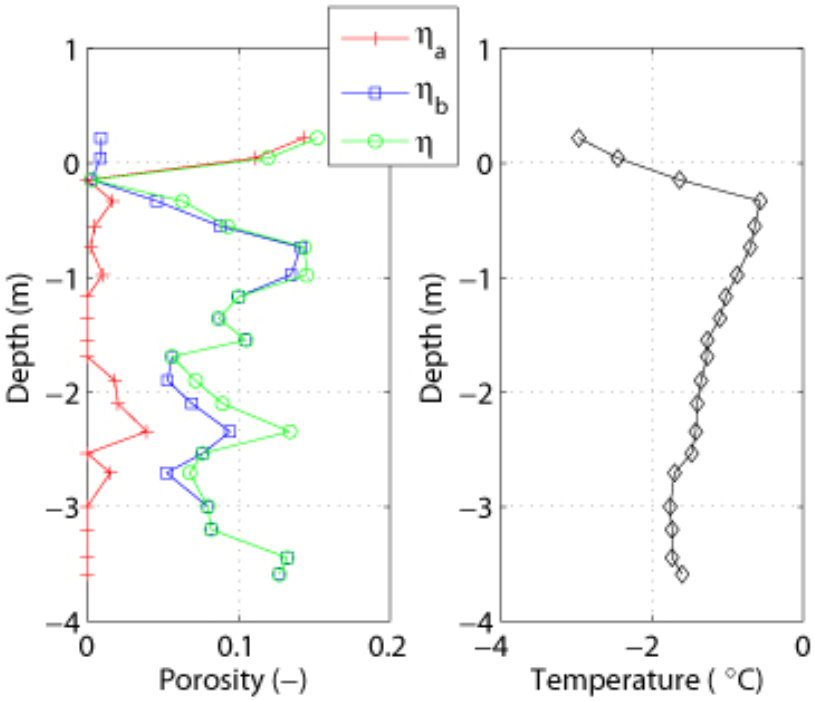

Figure 6. Vertical porosity (air and brine) and temperature profiles from station FS07-12, 26.09.07

5. Conclusion

Second- or multi-year sea ice in the Fram Strait has been investigated in September 2006 and 2007 with respect to consolidation. We drilled geometry/porosity profiles and took cores for determination of temperature, salinity and density. This is the first time measurements on these early winter second-year ridges have been presented and the main conclusions are as follows:

- The maximum keel depth was 7.2 m.
- The keels were almost completely consolidated, clearly different from first-year ridges.
- The salinities of the keels were about 1.8 ppt, similar to what has been found in old ridges in April in the Beaufort (1.4 and 1.6 ppt), but clearly lower than that in blocks from keels of first-year ridges (about 4-6 ppt).
- The relative air volume was 4.9 (2006) and 2.1 (2007), and no obvious difference from neither first-year ridges nor old ridges is apparent.

6. Acknowledgement

We would like to thank the Norwegian Polar Institute (NPI) for funding and operating R/V Lance, further we would like to thank the projects DAMOCLES (EU), iAOOS (Research Council of Norway - IPY), and CryoSat PRODEX (ESA/Norwegian Space Center). Finally we would like to thank the crew on R/V Lance for excellent treatment and help. We always enjoy being on Lance.

References

Cox, G.F. and Richter-Menge, J., 1985. Tensile strength of multi-year pressure ridge sea ice samples. Journal of Energy Resources Technology, (107), pp. 375-380.

Cox, G. F. and Weeks, W.F., 1983. Equations for determining the gas and brine volumes in sea ice samples. Journal of Glaciology, Vol. 29, No. 102, pp. 306-316.

Gerland, S., Haas, C., Hall, R., Holfort, J., Hansen, E., Løyning, T., and Renner, A., 2006. Spring sea ice thickness in the western Fram Strait: Preliminary results. In P. Wadhams and G. Amanatidis (eds.): Arctic Sea Ice Thickness: Past, Present and Future. Climate Change and Natural Hazards Series 10, EUR22416, European Commission, Brussels, 293 pages, pp. 158-164.

Haas, C., Gerland, S., Eicken, H., and Miller, H. (1997). Comparison of sea-ice thickness measurements under summer and winter conditions in the arctic using a small electromagnetic induction device. *Geophysics*, (Vol. 62, No. 3). 749-757.

Hansen, E., Løyning, T., Gerland, S., and Goodwin, H., 1987. Arctic sea ice thickness variability observed over a decade in the Fram Strait. In Extended Abstract. Arctic Climate System Study (ACSYS), 2004. Progress in Understanding the Arctic Climate System: The ACSYS Decade and Beyond. Proceedings of the ACSYS Final Science Conference, St. Petersburg, Russia, 11-14 Nov 2003, volume WCRP-118 (CD); WMO/TD No. 1232. September 2004, 4 pages.

Høyland, K.V., 2007. Morphology and small-scale strength of ridges in the North-western Barents Sea. Cold Regions Science and Technology, (48), pp. 169-187.

Kovacs, A., 1983. Characteristics of multi-year pressure ridges. In Proc. of the 8th Int. Conf. on Port and Ocean Eng. under Arctic Conditions (POAC), Helsinki, Finland, 2: pp. 173-182.

Leppäranta, M. and Manninen, T., 1988. The brine and gas content of sea ice with attention to low salinities and high temperatures. Technical Report 1988(2), Finnish Institute of marine research. 14 p.

Richter-Menge, J. and Cox, G., 1985. Structure, salinity and density of multi-year sea ice pressure ridges. In Proc. of the 4 Int. Conf. on O®shore Mechanics and Arctic Engineering (OMAE), Texas, USA, pp. 194-198.

Vinje, T., Nordlund, N., and Ånund Kvambekk, 1994. Monitoring ice thickness in Fram Strait. J. Geophys research- Oceans, 103(C5).

WMO,1970. WMO sea ice nomenclature, (suplement No. 5, 1989). Technical Report MO No. 259.TP.145, World Meteorological Organizartion, Geneva, Switzerland.

19th IAHR International Symposium on Ice
"Using New Technology to Understand Water-Ice Interaction"
Vancouver, British Columbia, Canada, July 6 to 11, 2008

The consolidation in second- and multi-year sea ice ridges, Part II: Review and speculations

Knut V. Høyland
The Norwegian University of science and Technology (NTNU)
Høyskoleringen 7a, 7491 NTNU, Norway
knut.hoyland@ntnu.no

A review of consolidation in old ridges is done, ridge keels down to 37 m have been reported in the literature and they are reported to be completely consolidated. But information about physical properties only exists down to a depth dept of 10 m. The models for consolidations in first-year ridges cannot explain a consolidation depth of 37 m. During the summer the ridge keels collapse so that the macro-porosity disappears, meltwater drizzles down from the surface and refreezes, and finally brine is drained from the ridge. These are the most important processes that transform first-year ridges to second-year ridges.

1. Introduction

Sea ice ridges are formed from compression or shear in the ice cover, they often govern the design for coastal and offshore structures when icebergs aren't present or when they can be managed. As with sea ice in general one distinguishes between first-year ridges and old ridges. First-year ridges have different geometrical and mechanical properties than old ridges and give different engineering challenges. The main difference seems to be that old ridges are consolidated all the way through the keel. But no physical explanation of this phenomenon has been presented. It is of course interesting to understand why and how this happens. Part I one of this paper (Høyland et al, 2008) presents some measurements on ice ridges done in late summer and early winter and in this paper (Part II) I present a little review and discuss some mechanisms for consolidation in old ridges.

2. Review of work on consolidation of old ridges

Below follows present a small review of the key papers that present information relevant for the consolidation of old (= second- and multi-year) ridges. It is not a complete review of all work performed on second- and multi-year ridges, but I believe it contains the up-to-date published knowledge relevant for consolidation. Timco and Burden (1997) give a more complete overview of the literature on old ridges, but don't discuss consolidation in detail. Table 1 gives an overview of field campaigns, the topic of investigation and the relevant papers. As can be seen all the field studies were done in the first half of the 70's and early in the 80's. The work in the 70's concentrated on geometry and morphology of the ridges and found keels depths up to 40 m. In the 80's the researchers also sampled and measured physico-mechanical properties.

Table 1: The main sources on old ridges

Field campaign/year	Literature
The 70's – Geometry and Morphology	
APOA 1971	Wright et al (1978)
APOA 1975	Wright et al (1981)
APOA-102 1976	Dickins and Wetzel (1981)
1982	Kovacs (1983)
The 80's – Physico-mechanical properties and ice texture	
1981 & 1982	Richter and Cox (1985)
	Cox et al. (1985)
	Cox and Richter-Menge (1985)
	Cox and Richter-Menge (1988)
	Hausler et al. (1987)
1982	Kovacs (1983)
Specific information on vertical profiles of T, S and ρ	
1981 & 1982	Richter-Menge and Cox (1985)
1982	Kovacs (1983)

The main results from these papers are:

- Ridge keels of 31 m (Wright et al., 1978) and 37 m (Dickins and Wetzel, 1981) have been measured. The latter also found a ridge keel deeper than 40 m, but could not measure it due to limitations in their equipment
- Ridges are reported to be consolidated all the way through, though some measurements (Kovacs, 1983) have shown soft ice at the bottom of second- year ridges.
- Vertical profiles and ice samples were only taken down to 10 m
- Mechanical properties are more or less correlated to velocity (strain-rate), temperature, crystal size and structure, air and brine volume as for other types of ice (freshwater- and sea ice).

Of special importance for us is the available information on consolidation, in particular measurements of macro-porosity, ice texture, temperature, salinity and density in the ridge keels. Richter-Menge and Cox (1985) sampled one core throughout the keels in two different ridges (April 1981 and April 1982) with keel depths of 9.5 m and 5 m. They present vertical profiles of salinity and ice texture classification as well as average values for salinity and density. The cores consisted of a mixture of granular, mixed (granular and columnar) and columnar ice, quite similar to what Kankaanpää (1998) and Høyland (2007) found in first-year ridges. Kovacs (1983) also sampled in April 1982 and presents vertical profiles of temperature, salinity and density through a ridge with keel depth of about 5.5 m. Both papers gives sail salinities of 0.6-0.7 ppt and keel salinities of 1.4-1.6 ppt. Their density values vary a bit, but the density is a difficult parameter to measure, and it is not clear to me if the values reflect real differences, or the technics of measurements. The temperature profile of Kovacs (1983) shows increasing temperatures from the waterline and down, and clearly shows that the winter cold has penetrated throughout the ridge keel so that additional first-year ice could form at the bottom.

They both report no, or almost no voids (i.e macro-porosity approximate zero), but Kovacs (1983) found moist areas in the lower keel and 0.15 m of first- year ice on the bottom of the sampled core. Richter-Menge and Cox (1985) also suggest that the lowermost columnar ice in the cores was first-year ice. Kovacs (1983) suggests that the ridges consolidate during the summer as meltwater drizzles down and freeze up.

3. Consolidation

3.1 Model for consolidation in first-year ridges

The consolidation in first-year ice ridges can basically be described by one-dimensional ice growth in a porous medium. The effect of the initial- and oceanic conditions are not clarified (Høyland and Liferov, 2005), but the existing numerical and analytical models based on the assumptions above explain field measurements well (see e.g. Croasdale et al., 1990; Leppäranta et al., 1995; Høyland, 2002b). The simplest model can be derived from Stefan's law and relates the thickness of the consolidated layer to the thickness of the surrounding level ice in the following manner:

$$h_c^2(t) = h_{c,0}^2 + \frac{h_i^2(t) - h_{i,0}^2}{\eta^M} \qquad [1]$$

where h_c, h_i are the thicknesses of respectively the consolidated layer and the level ice, the subindex *0* refers to the initial thickness, and η^M is the macro-porosity. If the same physical processes govern the consolidation of old ridges, the thickness of the consolidated layer can be calculated. I assume the following:

- No melting of h_c during the summer (q_{ocean}=0)
- Level ice melts during summer ($h_{i,0}$=0)
- Annual peak level ice thickness, 3 m
- Initial thickness of the consolidated layer ($h_{c,0}$), 1 m
- Macro-porosity (η^M), 0.35/0.05

and find that the model predict respectively 55 years (η^M=0.35) and 9 years (η^M=0.05) of consolidation before h_c equals 37 m (see Fig 1).

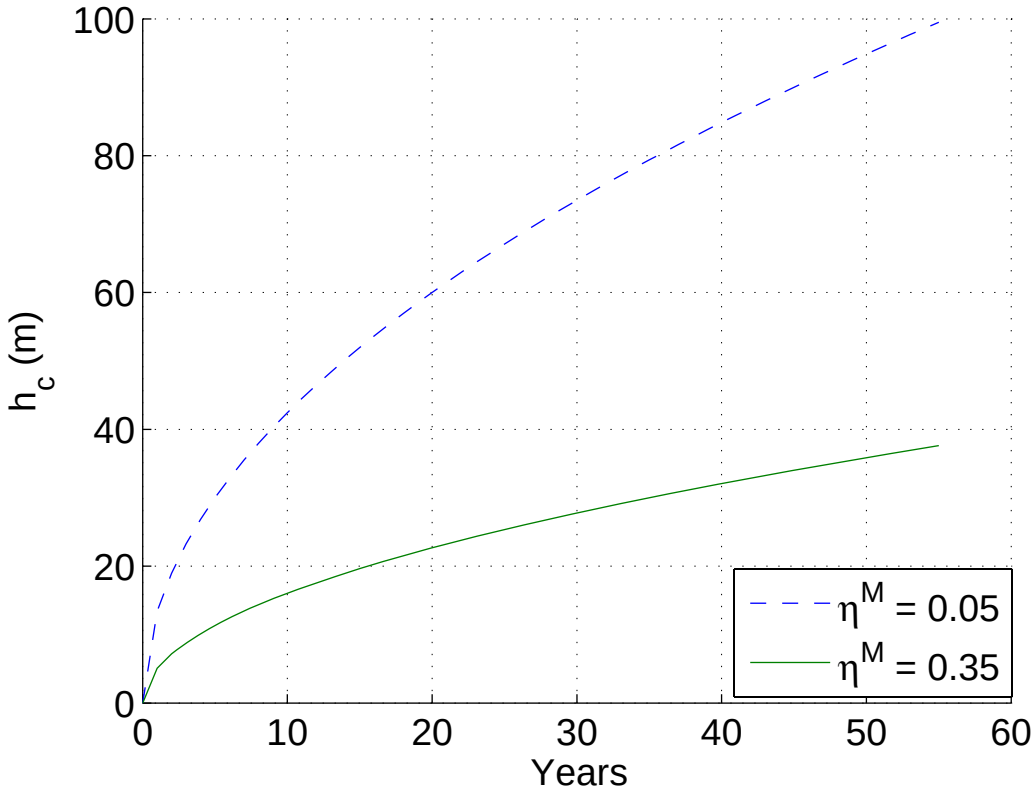

Figure 1: The thickness of the consolidate layer simulated by Stefan's law

The assumptions about no summer melting of h_c is realistic only as long as there is a buffer of unconsolidated layer in the bottom of the keel, in other words basically the first season. But even with this unrealistic assumption the results are not realistic. The thickest ridge reported by Wright et al. (1981) had recognizable blocks in the sail and appeared to be a young multi-year (perhaps second-year) ridge. In other words, *the physical processes governing the consolidation in first-year ridges cannot lead to a consolidation down to 37 m!*.

3.2 Summer consolidation

As indicated in Part I the most important processes that transform first-year ridges into second-year ridges occur during the summer. The oceanic heat melts/erodes ice from below and the solar radiation/above-zero air temperatures melt ice from above. This leads to ridge keel collapse, brine drainage, and refreezing of meltwater. The oceanic flux will melt/erode first-year ridges most of its lifetime (Høyland and Liferov, 2005), but in the case of warmer water during summer this process accelerates. As demonstrated by Marchenko and Høyland (2008) the permeability of ridge keels may give turbulent fluxes inside the unconsolidated rubble, which would lead to effective rubble erosion. Considerable differences in the consistency of the rubble can be felt when drilling and this is related the oceanic conditions the ridge keel live in (Høyland, 2002a). I believe that this thermo-mechanical erosion will lead to a keel collapse during the summer so that the macro-porosity almost disappears. The measurements presented in Part I of this paper support this statement.

The surface melting also has important consequences for the development of the consolidated layer. The surface snow and ice will partly sublimate and partly melt and drizzle down. The meltwater drizzles towards colder temperatures and freezes when meeting the freezing-point of the solution. The freezing releases energy so that some ice has to melt to keep the brine in thermal equilibrium. The measurements presented in Part I indicate that the relative air volume is more or less constant for ridges of different ages. This means that the meltwater that drizzles down and freezes replaces brine. In summary the surface melting produces new ice and drains the ice of salt. It continues as long as there is available meltwater and as long as the ridge keel has enough cold to freeze the ice. When the surface conditions (air temperature and solar radiation) no longer supplies meltwater this process stops and ridge starts consolidating in an *ordinary* way with vertical heat transfer upwards, and the brine drainage slow down. Kovacs (1983} suggests this process as the major contributor to the consolidation in old ridges. At the end of the summer the ridge is very warm (about -1.2ºC) and substantial amounts of surface cooling is needed to consolidate a ridge down to 37 m. The simulations presented in Fig. 1 indicate that this takes many years and cannot explain the relatively young ridge (probably second-year) described by Wright et al. (1981}. In other words re-ridging is a possible explanation for consolidated ridges of 30 m or more.

4. Conclusions

This paper presents a review of work on consolidation of old ridges, and discusses and suggests some mechanisms for consolidation in old ridges. The main conclusions are:

- Ridge keels up to 37 m have been measured (Dickins and Wetzel, 1981).
- They are reported to be consolidated all the way through the keel, but sampling down to only 10 m is reported in the literature.
- The models for consolidation in first-year ridges cannot explain the measured degree of consolidation in old ridges
- The ridge keels collapse during the summer and the macro-porosity becomes close to zero.
- The surface melting produces fresh water that drizzles down in the ridge and freezes.
- Most of the brine is drained during the summer and replaced by new ice.
- Re-ridging may still be necessary to consolidate a keel of 37 m.

Acknowledgments
I would like to thank Aleksey Marchenko and Matti Leppäranta for discussions at 'Pubben' at Svalbard last year.

References

Cox, G. F., Richter, J., Weeks, W. F., and Mellor, M. (1985). A summary of the strength and modulus of ice samples from multi-year pressure ridges. *Journal of Energy Resources Technology*, 107. 93-98.

Cox, G. F. and Richter-Menge, J. (1985). Tensile strength of multi-year pressure ridge sea ice samples. *Journal of Energy Resources Technology*, 107. 375-380.

Cox, G. F. and Richter-Menge, J. (1988). Confined compressive strength of multi-year pressure ridge sea ice sample. *Journal of Offshore Mechanics and Arctic Engineering*, 110. 295-301.

Croasdale, K. R., Allen, N. F. B., and Marcellus, R. W. (1990). Thermal response of ice rubble: predictions and observations. In *Proc. of the 10th Int. Symp. on Ice (IAHR), Espoo, Finland, 20-24 August 1990*, 1: pp. 153-167.

Dickins, D. and Wetzel, V. (1981). Multi-year pressure ridge study, Queen Elizabeth islands. In *Proc. of the 6th Int. Conf. on Port and Ocean Eng. under Arctic Conditions (POAC), Quebec, Canada*, 2: pp. 765-775.

Hausler, F. U., Earle, E. N., and Gerchow, P. (1987). Uniaxial and biaxial compressive strength of ice sampled form multi-year pressure ridges. In *Proc. of the 9th Int. Conf. on Port and Ocean Eng. under Arctic Conditions (POAC), Alaska, USA*, 1: pp. 1:11.

Høyland, K. V. (2002a). Consolidation of first-year sea ice ridges. *Journal of Geophysical research*, 107(C6, 10.1029/2000JC000526). 15,1-15,15.

Høyland, K. V. (2002b). Simulations of the consolidation process in first-year sea ice ridges. *Cold Regions Science and Technology*, (34). 143-158.

Høyland, K. V. (2007). Morphology and small-scale strength of ridges in the North-western Barents Sea. *Cold Regions Science and Technology*, (48). 169-187.

Høyland, K. V., Barrault, S., Goodwin, H., Gerland, S., Nicolaus, M., Olsen, O. M., and Rinne, E. (2008). The consolidation in second- and multi-year ridges, Part I: Measurements in early winter. In *Proc. of the 19th Int. Symp. on Ice (IAHR), Vancouver, Canada*, submitted.

Høyland, K. V. and Liferov, P. (2005). On the initial phase of consolidation. *Cold Regions Science and Technology*, (41, 1). 49-59.

Kankaanpää, P. (1998). *Distribution, morphology and structure of sea ice pressure ridges in*

the Baltic. PhD thesis, Helsinki University. 100 p.

Kovacs, A. (1983). Characteristics of multi-year pressure ridges. In *Proc. of the 8th Int. Conf. on Port and Ocean Eng. under Arctic Conditions (POAC), Helsinki, Finland*, 2: pp. 173-182.

Leppäranta, M., Lensu, M., Koslof, P., and Veitch, B. (1995). The life story of a first-year sea ice ridge. *Cold Regions Science and Technology*, (23). 279-290.

Marchenko, A. and Høyland, K. V. (2008). Properties of sea currents around ridged ice in the Barents Sea. In *Proc. of the 19th Int. Symp. on Ice (IAHR), Vancouver, Canada*, submitted.

Richter, J. and Cox, G. (1985). A preliminary examination of the effect of structure on the compressive strength of ice samples from multi-year pressure ridges. *Journal of Energy Resources Technology*, 107. 99-102.

Richter-Menge, J. and Cox, G. (1985). Structure, salinity and density of multi-year sea ice pressure ridges. In *Proc. of the 4 Int. Conf. on Offshore Mechanics and Arctic Engineering (OMAE), Texas, USA*, :194-198.

Timco, G. W. and Burden, R. (1997). An analysis of the shapes of sea ice ridges. *Cold Regions Science and Technology*, (25). 65-77.

Wright, B. D., Hnatiuk, J., and Kovacs, A. (1978). Sea ice pressure ridges in the Beaufort Sea. In *Proc. of the 5th Int. Symp. on Ice (IAHR),*, pp. 249-271.

Wright, B. D., Hnatiuk, J., and Kovacs, A. (1981). Multi-year pressure ridges in the Canadian Beaufort Sea. *Coastal Engineering*, (5). 125-145.

19th IAHR International Symposium on Ice
"Using New Technology to Understand Water-Ice Interaction"
Vancouver, British Columbia, Canada, July 6 to 11, 2008

Properties of Sea Currents around Ridged Ice in the Barents Sea

Aleksey Marchenko[1,2] and Knut Hoyland[2,1]
[1)] *The University Centre in Svalbard (UNIS), Spitsbergen, Norway*
[2)] *Norwegian University of Science and Technology (NTNU), Trondheim, Norway*
aleksey.marchenko@unis.no
knut.hoyland@ntnu.no

Abstract
During the annual UNIS cruise in the Barents Sea in May 2007 the sea current in the vicinity of a first-year ice ridge was investigated in relation to both the drift of the ice floe and the ridge keel properties. The current and the turbulent heat fluxes inside the ridge keel, as well as the turbulent heat fluxes to the surrounding ice floe are calculated and analyzed depending on local shape of the trajectory of Lance drift.

1. Introduction

Natural drift of an ice floe is determined by wind and water drag forces accumulated over the floe surfaces and by floe interaction with surrounding ice. Offshore platform can be considered as an obstacle reducing natural drift velocity of several floes in the boundary zone near the platform. Floes drift is closed to natural sea ice drift outside the boundary zone. Trails after grounded icebergs have loop shape and show that ice drift velocity changes the direction significantly during the interaction with the iceberg (Vinje and Kvambekk, 1990).

The loop shape of floes drift trajectories in the North-West Barents Sea is explained by coupled influence of wind drag force and water drag forces related to the action of permanent current and tides (Dmitriev et al., 1991). Tidally induced ice drift trajectories are located within region with diameter about several kilometers. The influence of wind and permanent currents extent ice drift trajectories to curves with numerous loops and corner points. Numerical estimates have shown maximal velocities of water current in semidiurnal tide M2 near East Svalbard up to 30 cm/s and major principal axis of the tidal ellipse directed to South-West.

Prevailing winds directed to South-West and permanent sea current of the same direction explain general direction of ice drift to South-West in West Barents Sea in winter and spring time (Mironov, 2004). Ice drift speed is in the range from 0 to 10 cm/s with 80% probability.

Comparative influence of air and water drag forces on ice drift is characterized by the wind coefficient of ice drift k equaling to the ratio of absolute values of ice drift velocity (v) to wind velocity (V_a). The increasing of k is related to the increasing of air drag influence on ice drift in comparison with water drag. According to (Zubov, 1944) representative value of k for the Central Arctic is about 0.02. Using square laws for air-ice and water-ice drag forces ($F_{wi} = \rho_w C_w v^2$ and $F_{ai} = \rho_a C_a V_a^2$) and assuming $F_{ai} \approx F_{wi}$ we find $C_w / C_a \approx \rho_a / (\rho_w k^2) \approx 3$, where C_w and C_a are water-ice and air-ice drag coefficients, ρ_w and ρ_a are water and air densities. Estimates of the ratio C_w / C_a carried out by the analysis of momentum balance equation written for the drifting floe and data on wind and sea currents velocities measured from the floe show the values from 0.16 to 1.65 for the North-East Barents Sea (Marchenko and Gorbatsky, 2005).

Small values of C_w / C_a in the conditions of the Barents Sea were explained by smooth surface of ice bottom due to intensive melting of ice ridge keels in the Barents Sea. At the same time it was shown that surface roughness of Barents Sea ice can be sufficiently high because of the formation of ridge sails by ice rafting (Marchenko and Makshtas, 2005). Gorbatsky and Marchenko (2007) estimated heat fluxes to ice bottom and inside ice ridge keels using the data of ADV (Acoustic Doppler Velocimeter, SonTek 5MHz) and SBE-39 (temperature and pressure recorder) measurements. Representative value of vertical heat fluxes was about several W/m^2, while their maximal values reached 30 W/m^2. They also found mean velocity of sea currents inside ice ridge keels up to 10 cm/s showing high permeability of the keels by sea water.

In the present paper we will discuss the measurements of turbulence and velocities in the water in relation to the navigational data and the temperature profiles in the ice. Main results of the paper are based on the analysis of field data collected on the drifting ice in the North-West

Barents Sea. The expedition was organized in the May of 2007 by RV "Lance". During this time we collected the data on the structure of the ice ridge located near the ship and the data of ADV and SBE-39 measurements below the level ice and around the ridge. The ship has a weather station and also records navigational data.

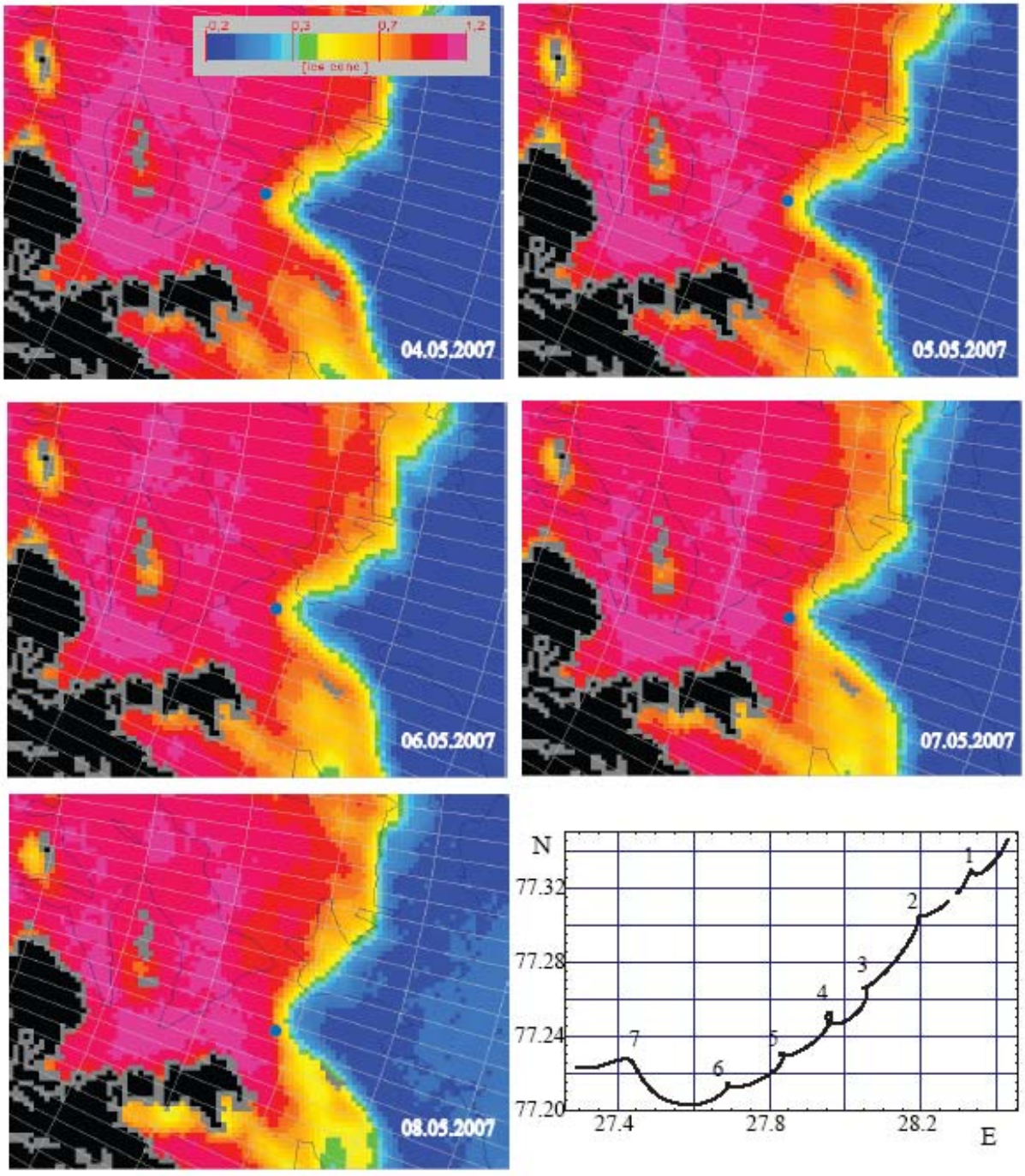

Figure 1. ENVISAT ice maps and trajectory of RV "Lance" drifting with Barents Sea ice from 04 to 08 of May 2007. The ship location is shown by blue dots on ice maps.

2. Site and experimental set-up

The annual field work in the UNIS cruise to the Barents Sea in 2007 took place north-east of Hopen, see Figure 1. We moored to a large ice floe and drifted with it from 4 to 8 May, from 77 35N/28 43E to 77 23N/26 20E. The position of the floe and the ice concentration is given in Figure 1 together with a plot of the drift. The floe was several kilometres in diameter, but we did not attempt to measure its size.

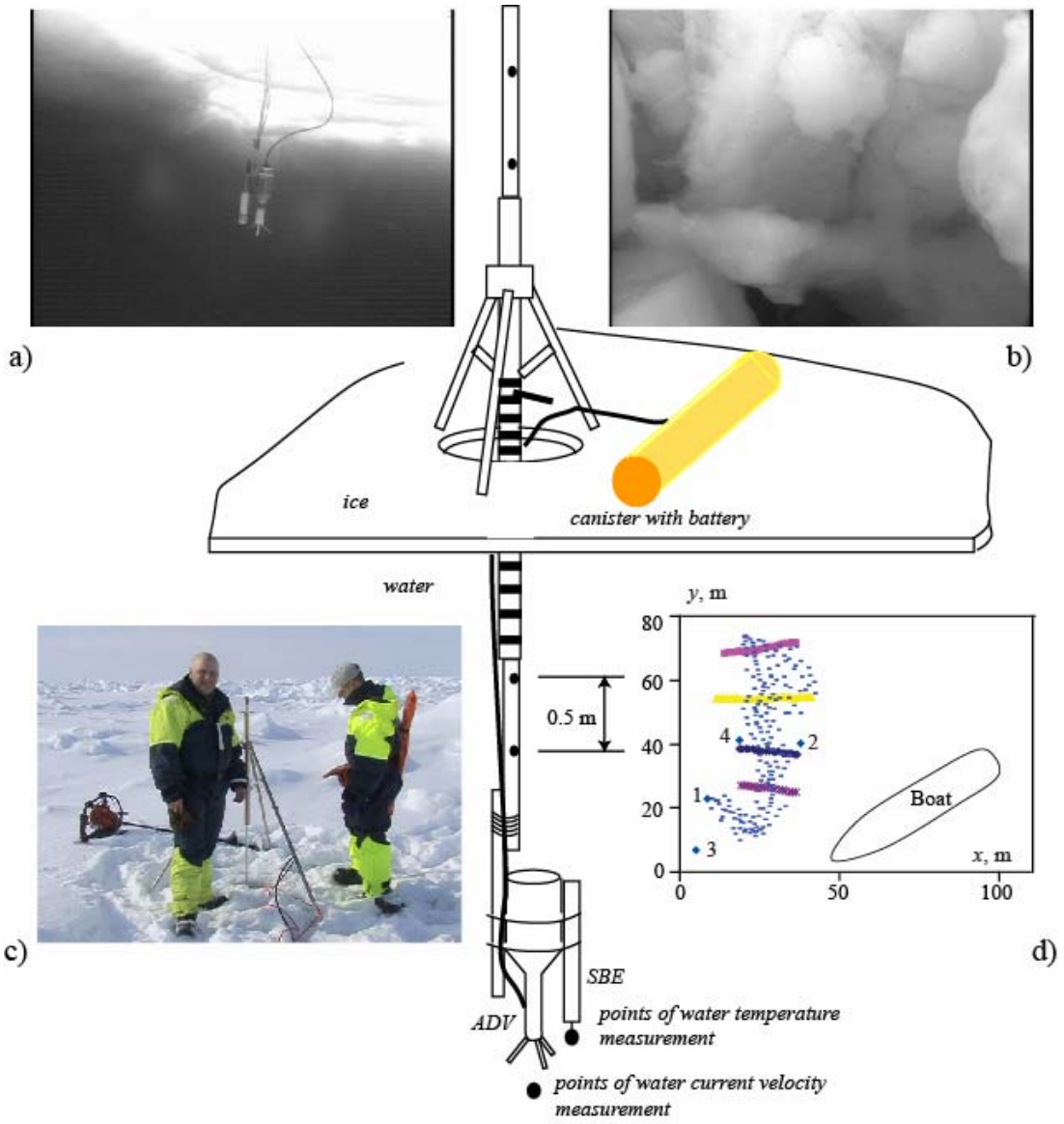

Figure 2. Scheme of the measurement of water velocity and temperature with ADV, and SBE-39 sensors; down looking ADV and SBE-39 below the level ice (a); caves between ice blocks inside ridge keel (b); tripod with ADV and SBE-39 on the ice (c); locations of measurements relatively the ship and the ridge shown by dots (d).

3D vector of sea current velocity relatively the ice ($\mathbf{v}_{wi}$) was measured by down looking 5-MHz ADVOcean Probe SonTek (Acoustic Doppler Velocimeter) fastened on sea ice with the tripod as it is shown in Fig. 2. The fastening gave possibility to lift up and down the ADV on distance divisible to 50 cm within 3 m below the ice for the measurements of the velocity of water sample (~2cm^3) located on 18 cm from the acoustic transmitter. The measurements were carried out below the level ice (location 2 and 3 in Fig. 2d) and inside ice ridge keel (locations 1 and 4 in Fig. 2d). Sampling rate was chosen as 10 Hz at locations 1,2 and 3, and 0.5 Hz at location 4. Measurements of the temperature (T) were carried out with 1 Hz frequency with temperature recorder SBE-39 mounted on the same beam with the ADV (Fig. 2). The time of ADV measurements was 20 min from 10.22 at location 1, 20 min from 11.30 and 20 min from 12.30 at location 2, 5 min by each 15 min from 22.00 on 05.05.2007 to 09.30 on 06.05.2007 at location 3, and 10 hours from 17.42 on 07.05.2007 to 03.30 on 08.05.2007.

The scheme of the works around the ridge is shown in Fig. 3. The works included drilling of four ridge cross-sections (A-D) with 2 inch augers for the calculation of the porosity and measurements of keel geometry. The cross-sections A-D are shown in Fig. 8. Ice cores were sampled from the ridge for the measurement of temperature and salinity profiles. We also measured block sizes in the sail and reproduced the topography of ridge sail with theodolite.

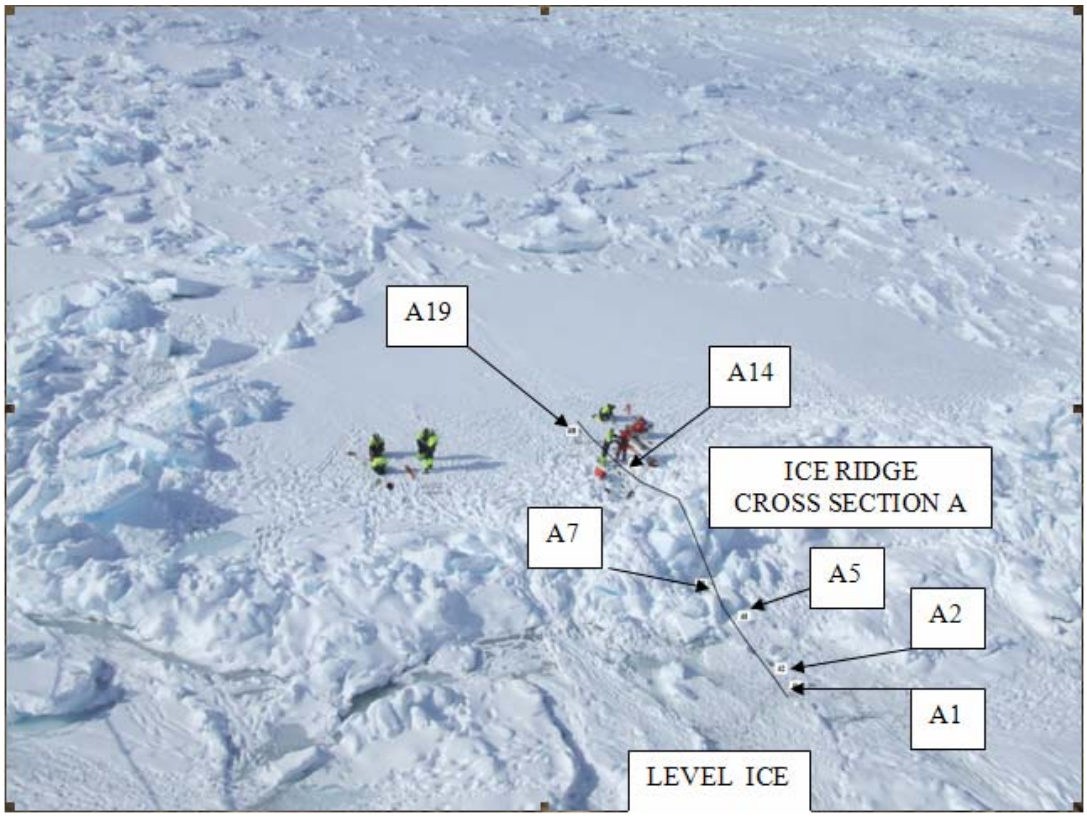

Figure 3. The surface of the ice ridge including the holes for temperature and salinity profiles.

3. Results

3.1. Analysis of navigational data

Trajectories of floe drift and vectors of wind velocity are shown in Fig. 4. The first three days the floe drifted South-West under the influence of North-Eastern wind with a velocity that varied within few meters per second. The floe trajectory is inclined to the west from the wind direction due to the influence of the Coriolis force. The wind direction is changed to South-East on May 7, and floe drift became directed to the West-North. Displacements of the floe to the North were bounded by the resistance of drifting sea ice (Fig. 1).

The floe trajectory included two loops and/or corner points each day due to the influence of semidiurnal tide. Diameters of the loops varied within few hundreds meters. The absolute value of the floe velocity is shown versus the time in Fig. 5. Gray columns show the times when the floe passes loops and corner points. One can see that local the velocity has local minima inside gray regions. Maximal velocity was estimated about 25 cm/s.

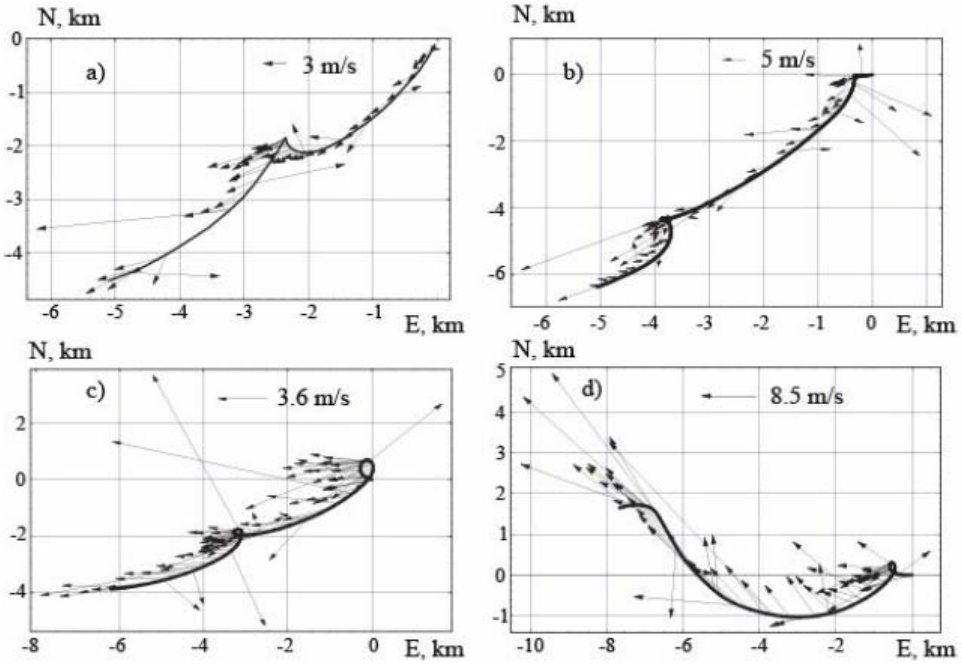

Figure 4. Trajectories of "Lance" drift and vectors of wind velocity a) 4 May, b) 5 May, c) 6 May, d) 7 May.

Figure 6 shows temporal variations of the heading angle of the ship during the drift. The variations were very small in first two days of the drift. On May 6 the heading angle changed on 8^o during 5 hours, and it was changed on 20^o during 18 hours on May 7. The changing of the direction of floe rotation is occurred in gray regions in Fig. 7 in times when the floe passed loops and corner points.

Figure 7 shows the values of wind coefficient of ice drift (k). The coefficient can exceed 0.05 when the floe moves between the loops or corner points. The high values of k demonstrate

prevailing influence of wind drag force on floe drift. When the floe drifted inside a loop the values of k are closed to those estimated for Central Arctic (Zubov, 1944).

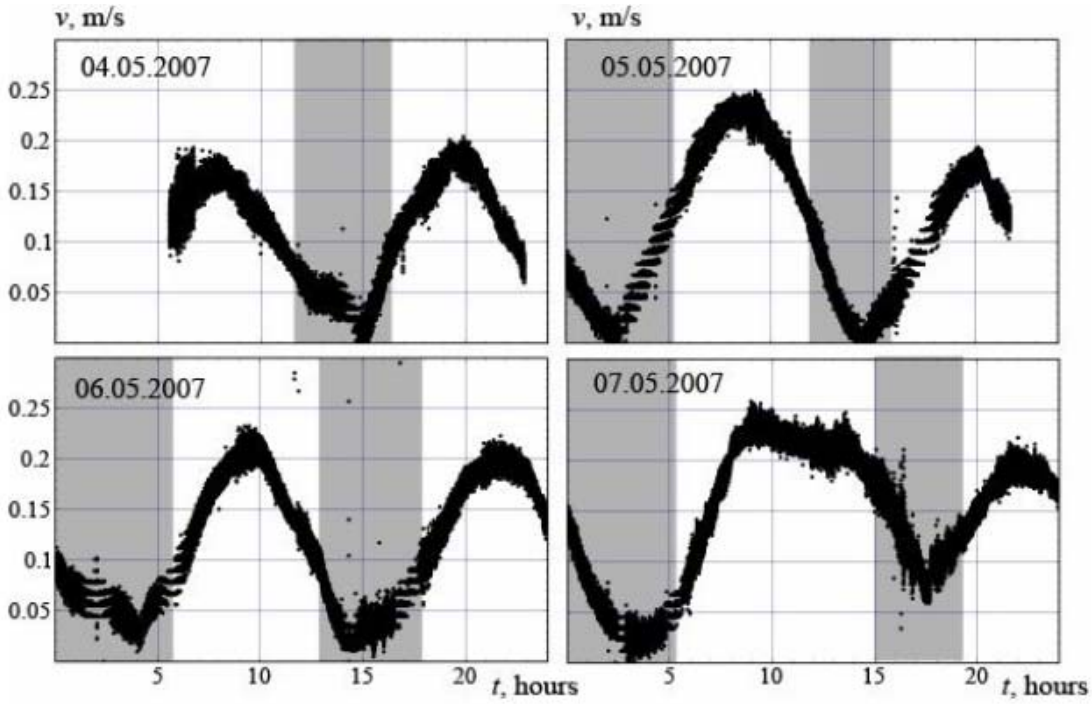

Figure 5. Temporal evolution of absolute drift velocity of RV "Lance" during the drift.

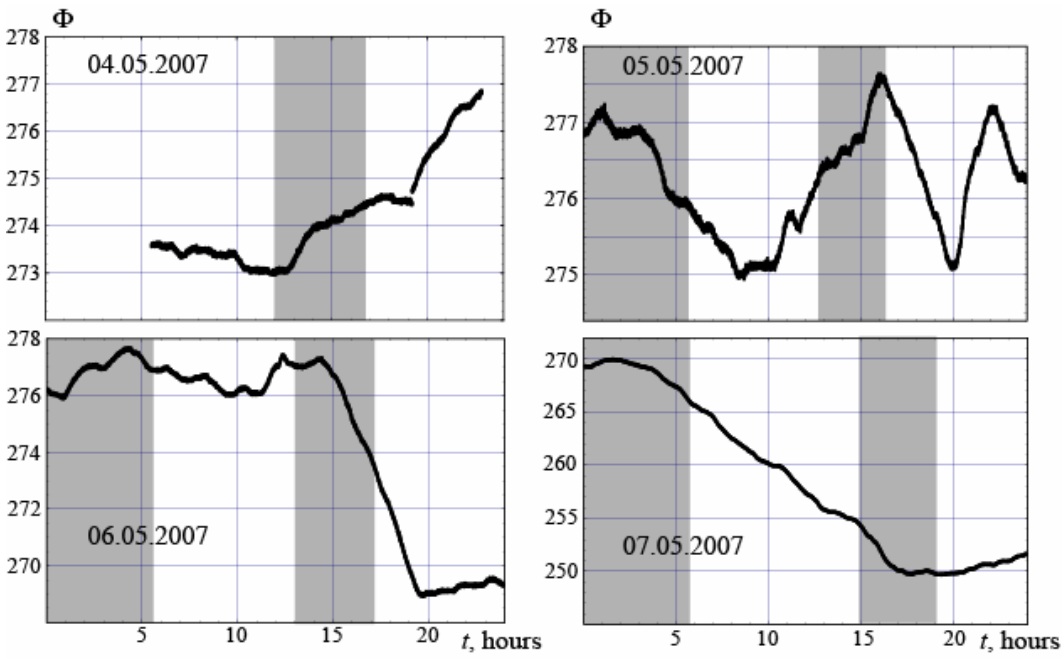

Figure 6. Heading angle Φ of RV "Lance" versus the time during the drift.

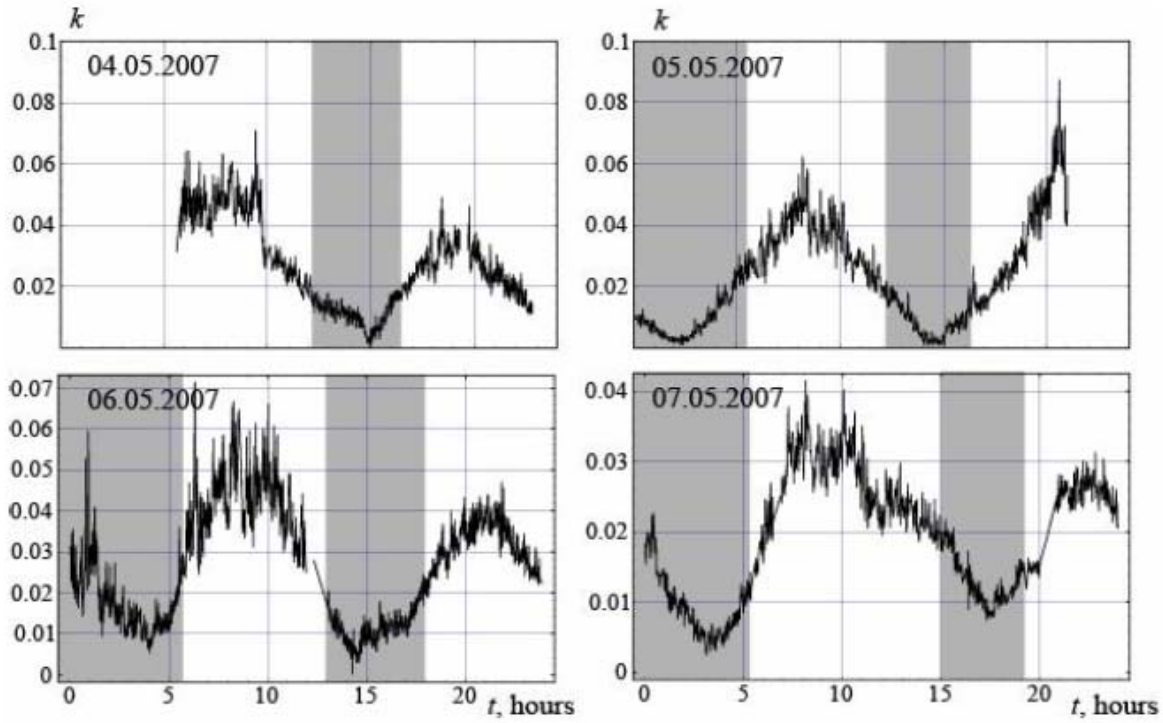

Figure 7. Wind coefficient of ice drift k versus the time.

3.2. Ice ridge structure and topography

Figures 3 and 8 show an overview of the ridge surface. The peak keel depth in the four cross-sections spanned from 5.8 to 7.7 m, and the peak sail height from 1.2 to 2.3 m.

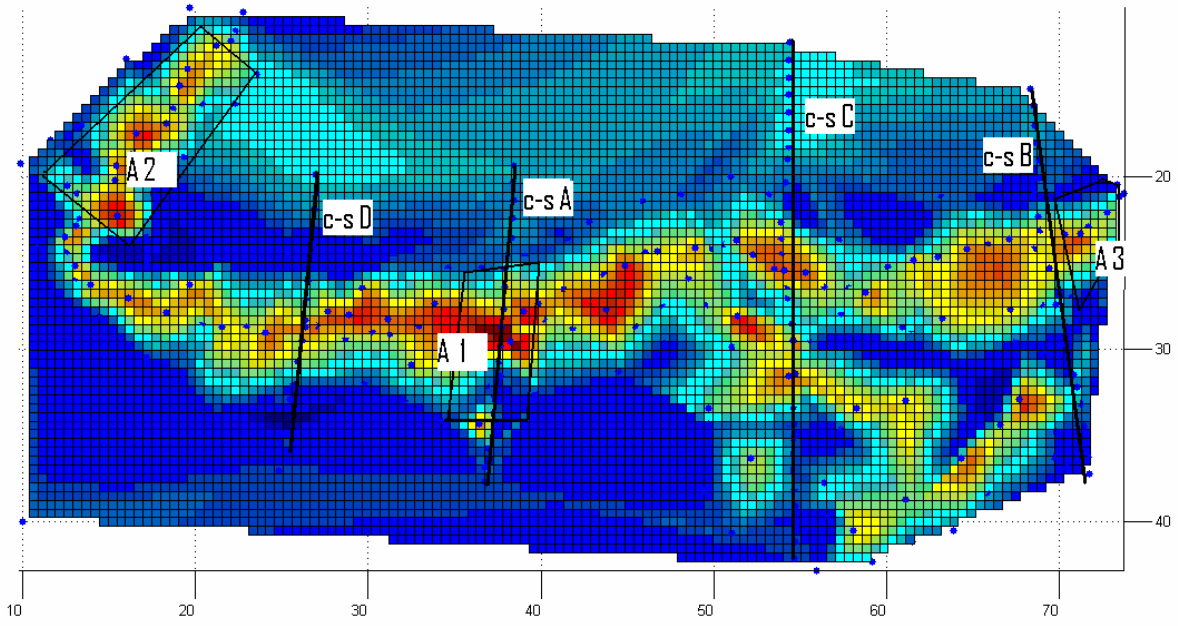

Figure 8. The surface topography of the ridge, including the four cross-sections (c-s A to c-s D) that were drilled and the three areas in which block sizes et c were measured (A1-A3).

3.3 Currents and heat fluxes

ADV measured 3D vector of water velocity relatively the ice ($\mathbf{v}_{wi}$), and SBE-39 measured water temperature (T) in discrete times. Since these times were different for the ADV and SBE we interpolated the data to the same times $t = t_j$ within each burst of ADV measurements ($t_j \in (t_1, t_2)$). These data were used to calculate turbulent heat fluxes in the water below the ice by the formula

$$\mathbf{F} = \rho_w c_{v,w} \langle \mathbf{v}'_{wi} T' \rangle \qquad [1]$$

where ρ_w and $c_{v,w}$ are the density and the specific heat capacity of the water. Velocity and temperature fluctuations ($\mathbf{v}'$ and T') were calculated as follows

$$\mathbf{v}_{wi,j} = \langle \mathbf{v}_{wi} \rangle + \mathbf{v}'_{wi,j}, \ \langle \mathbf{v}_{wi} \rangle = \sum_{j=1}^{N} \mathbf{v}_{wi,j} [\omega (t_2 - t_1)]^{-1} \qquad [2]$$

$$T = \langle T \rangle + T', \ \langle T \rangle = \sum_{j=1}^{N} T_j [\omega (t_2 - t_1)]^{-1}$$

where $\mathbf{v}_{wi,j}$ and T_j are the values measured in the time $t = t_j$, N is the number of samples per burst, and ω is the sampling rate.

The results of measurements at locations 1 and 2 are shown in Table 1. Highest horizontal velocity of sea current 10 cm/s was measured inside ice ridge at location 1. Highest vertical velocity also was measured inside ridge keel. Highest vertical heat flux 24.3 W/m^2 was measured below the level ice. Heat flux measured inside ridge keel at location 1 is smallest.

Table 1. Mean values of eastern ($\langle v_E \rangle$), northern ($\langle v_N \rangle$) and vertical ($\langle v_z \rangle$) components of water velocities, temperature ($\langle T \rangle$) measured in location 1 and 2. F_z is vertical turbulent heat flux calculated with ADV and SBE data.

	1	2_1	2_2
$\langle v_E \rangle$, cm/s	4	-1	-0.7
$\langle v_N \rangle$, cm/s	10	3	2
$\langle v_z \rangle$, cm/s	1	0	0
$\langle T \rangle$, $^\circ$C	-1.84	-1.81	-1.81
F_z, W/m^2	7.2	24.3	18

The results of measurements at locations 3 and 4 are shown in Fig. 9 and Fig. 10. Vectors **H** in Fig. 9d show the ship orientation calculated with the heading angle. Comparing Fig. 9a and Fig. 9b we find that highest mean velocities up to 12 cm/s and vertical velocities of sea currents were measured inside the ridge keel. Figure 9d shows that the angle between vectors **H** and vectors of mean horizontal velocities of sea current inside the ridge keel $\langle \mathbf{v}_w \rangle = (\langle \mathbf{v}_E \rangle, \langle \mathbf{v}_N \rangle)$ are the same

during the measurements period. It is probably because of the current is directed along some channel inside the ridge keel which orientation is fixed in the time. Figure 9c shows water velocities that we measured from the ice take maximal values when the floe passed the loop. It agrees with Fig 7 showing the decreasing of the influence of wind drag force on the ice drift when the floe passed the loops.

Figure 10a shows mean temperature inside ridge keel at location 4 versus the time. High values of the temperature in initial time can explain high value of vertical heat flux 60 W/m^2 calculated at the same time. Later heat fluxes where much smaller. In the initial time the floe passed point with high curvature which is almost corner point (Fig 9d), when the water current relatively the ice takes local maximum.

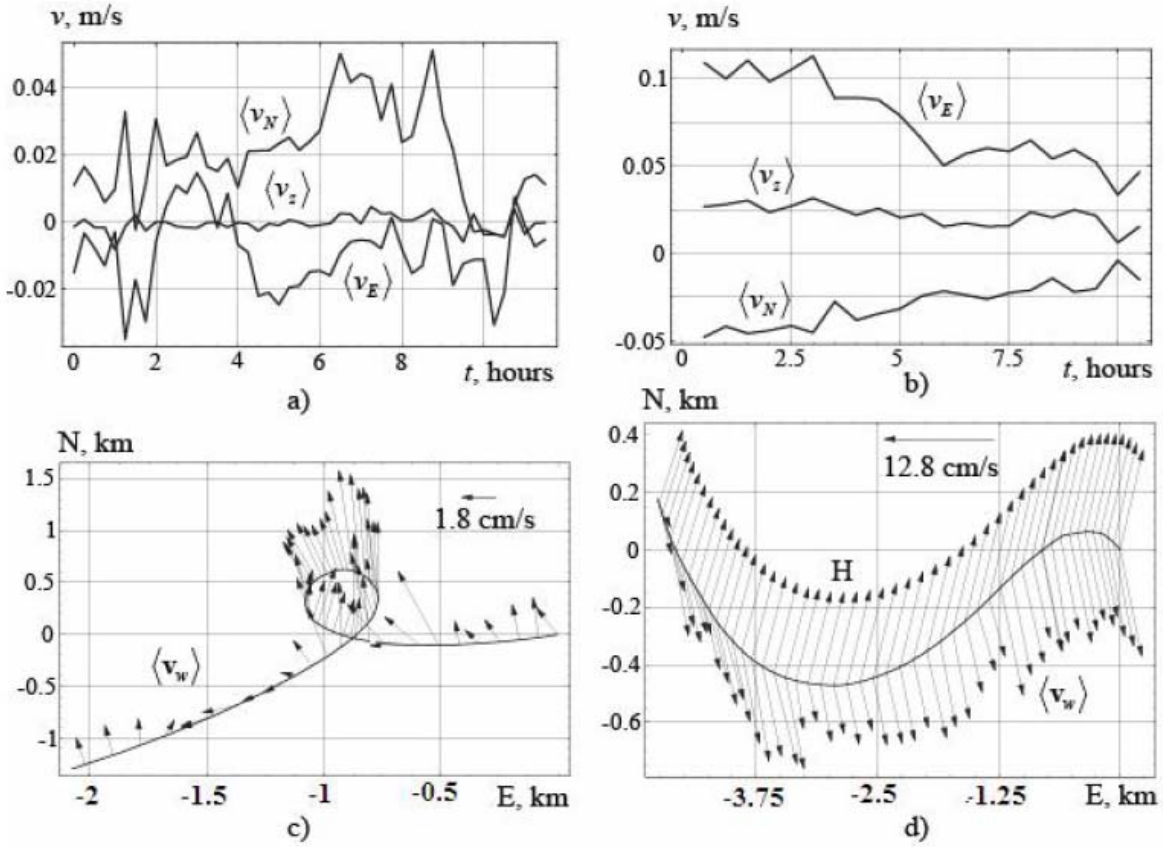

Figure 9. Mean values of eastern ($\langle v_E \rangle$), northern ($\langle v_N \rangle$) and vertical ($\langle v_z \rangle$) components of water velocities (a) measured at locations 3 (a) and 4 (b).Vectors of mean horizontal water velocities $\langle \mathbf{v}_w \rangle$ constructed at different points of floe trajectory at location 3 (a) and 4 (b).

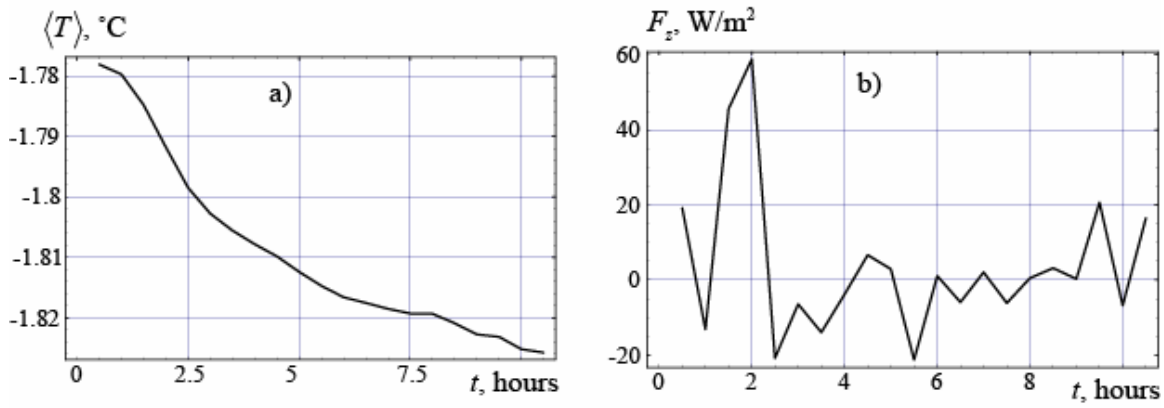

Figure 10. Mean values of water temperature ($\langle T \rangle$) (a) and vertical turbulent heat flux (F_z) (b) calculated using ADV and SBE data from location 4.

3.4 Heat fluxes and turbulent measurements

Figure 11 shows the temperature profile in hole A16. Temperature gradient is negative inside the ridge keel and the heat flux is directed upward from 0.2 m to 1.3 m depth. Temperature gradient becomes positive below 1.3 m, and the heat flux is downward directed in that region. It can happen because of different temperatures of solid ice and slush between ice blocks at 1.3 m depth. By using the vertical temperature gradient the heat flux can be calculated to about 4-5 W/m^2 in three holes A14, A16 and A19. In holes A1, A3, A5 and A7 the ice was warmer, almost isotherm throughout most of the thickness, and this corresponds with the relatively high fluxes measured in location 2 (see Table 1)

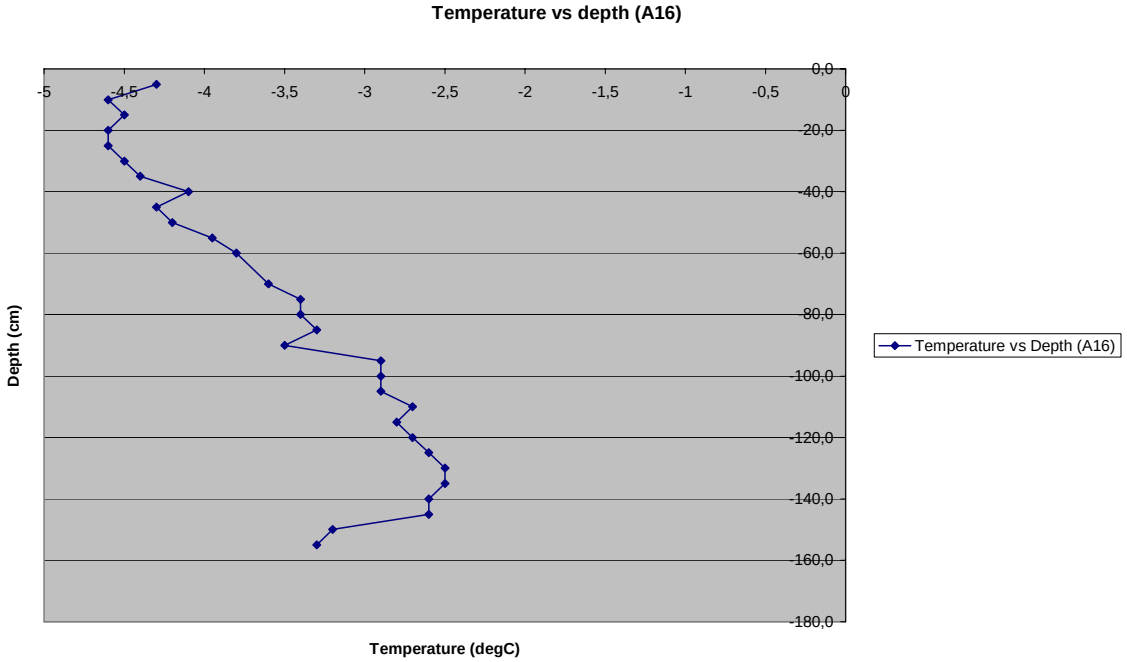

Figure 11. The temperature versus depth in hole A16 (close to point 4 of ADV and SBE measurements).

4. Conclusions

The coupled influence of wind, permanent sea currents and semidiurnal tides explain the shape of floes trajectories with many loops and corner points. Field studies and numerical simulations have been performed to study peculiarities of ice drift and water current in ice adjacent layer around the loops and between them.

The major findings of the study are:

- Ice drift velocity takes maximal values on parts of the floe trajectory between loops and corner points. Ice drift velocities and accelerations take minimal values inside loops and around corner points of the floe trajectory.
- Maximal measured velocity of the floe drift reached 25 cm/s
- Floes rotation reached 5^{o} per 5 hours
- Wind drag force has dominant influence on floe drift between consequent loops and corner points. Inside loops relative water velocity in ice adjacent layer takes maximal values.
- Heat fluxes to the ice bottom take maximal values when the floe passed loops of its trajectory.

References

Gorbatsky V.V., and A.V. Marchenko (2007): On the influence of turbulence in ice adjacent layer on water-ice drag forces and heat fluxes in the Barents Sea. Recent development of Offshore Engineering in Cold Regions. Yue (ed), POAC-07, Dalian, China, June 27-30, 2007, Dalian University Press, Dalian, ISBN 978-7-5611-3631-7, 648-659

Dmitriev, N.E., Proshutinsky, A.Yu., Loyning, T.B. and T.Vinje (1991): Tidal ice dynamics in the area of Svalbard and Franz Josef Land. Polar Research 9(2), 193-205.

Mironov, Ye. Uv. (2004): Ice conditions in the Greenland and Barents Seas and Their long-term Forecast. AARI. St.-Petersburg, 320 pp. (in Russian)

Marchenko, A., and V. Gorbatsky (2005). Internal Ice Stresses and Ridges in the North-East Barents Sea. Proc. of 18th Int. Conference on Port and Ocean Engineering under Arctic Conditions (POAC'05), Vol. 2, Clarkson University, Potsdam, NY, pp.927-937.

Marchenko, A., and A. Makshtas (2005): A dynamic model of ice ridge build up. *Cold Regions Science and Technology*, Vol 41/3, pp. 175-188.

Vinje, T., and A.S. Kvambekk (1990): Barents Sea drift ice characteristics. Proceedings of the Pro Mare Symposium on Polar Marine Ecology, E.Hopkins, C.C.E. and Oritsland, N.A. (eds.), Trondheim, 12-16 May 1990. Polar Research 10(1), 59-68.

Zubov, N.N. (1945): L'dy Arktiki (Arctic Ice). Moscow: Izdatel'stvo Glavsevmorputi. (English translation, U.S. Navy Electronics Laboratory)

19th IAHR International Symposium on Ice

"Using New Technology to Understand Water-Ice Interaction"
Vancouver, British Columbia, Canada, July 6 to 11, 2008

Surveying a Four-Week Old First-Year Ridge

A. Barker[1], G.W. Timco[1] and B. Wright[2]
[1]*Canadian Hydraulics Centre, National Research Council of Canada*
M-32, 1200 Montreal Road,Ottawa,ON, K1A 0R6 Canada
anne.barker@nrc-cnrc.gc.ca / garry.timco@nrc.gc.ca
[2]*B. Wright & Associates Limited,*
212 Sir Charles Carey Street, Canmore, AB T1W 2R6 Canada
bwright1@shaw.ca

Abstract

The date of formation of a large sea ice ridge in the Canadian Beaufort Sea was established within a one week time-frame, based upon satellite tracking of ridge development in the area of interest. During subsequent field work at the site, a single line across the ridge was surveyed and a number of holes were drilled to estimate the rate of consolidation of the ridge over the four-week period since its formation. It was observed that there were considerable differences in the morphology of the ridge along its length. In some cases there was a classic ridge shape whereas in other areas, the ridge was relatively flat. Limited profiling of the ridge was performed at one site in which the maximum sail height was 3.7 m. The profile values were directly compared or extrapolated to compare with the "average" first-year ridge values documented by Timco and Burden (1997). In general, there was good correlation. The depth of the measured consolidated layer was approximately twice the estimated thickness of level ice if it had grown under these meteorological conditions for the four weeks since its formation.

1. Introduction

Pressure ridges are abundant in the Beaufort Sea region of the Canadian Arctic. Their development and consolidation is of interest for shipping, oil and gas production/exploration systems, and search and rescue operations. Additionally, further understanding of ridge-building processes increases the knowledge base of pack ice driving forces, which is an important topic of consideration for any offshore development in this region. During the 1970s and 1980s, there were a number of ridges profiled and these have been summarized by Timco and Burden (1997). During a field trip to the Canadian Beaufort Sea in April 2007, the authors had an opportunity to investigate a first-year ridge that formed in a water depth of 18 m. Since the authors had been monitoring the Beaufort region using various types of satellite technology, it was known that the ridge had formed approximately four weeks before the field trip. Thus, this gave a unique opportunity to profile a ridge when its formation date was known. This paper summarizes the results of this study of this four-week old first-year ice ridge.

2. Ridge Formation

RADARSAT-1 Extended High and Fine beam mode images were collected over the course of the winter and spring, with the images covering a region north and west of Pelly Island. It was observed that an extensive ridge developed in the time frame between the image collected on March 22, 2007 and the one collected on March 29, 2007. The ridge extended from approximately 136°24'W to a location just east of 136°00'W, a distance of over 10 km, immediately north of the landfast ice edge. Figure 1 shows a satellite image of the ridge and the location of the field work site.

Prior to the ridge's formation, winds from the southeast (roughly) appeared to break up the ice that had formed north of the landfast ice edge, pushing the ice to the northwest. Open water leads and new ice formation as a result of this movement were visible in the March 22 RADARSAT-1 image. The wind records for that time period, from the Environment Canada weather records from Tuktoyaktuk airport for the week that the ridge formed (http://climate.weatheroffice.ec.gc.ca/climateData/canada_e.html), indicated one likely event that led to the formation of the ridge. On March 27, winds averaging 25 km/h with an average direction of 240° blew for almost twenty-four hours. This sustained wind may have been sufficient to close the leads that had opened, and to generate a number of pressure ridges that formed at that time.

Between the time of the ridge's formation and the field work that occurred at the end of April, 2007, the area immediately around the ridge became landfast, as evidenced through further RADARSAT-1 images of the region. At that point in time, the western end of the ridge was at the landfast ice edge, with predominantly local pack ice and open water conditions, as shown in Figure 2.

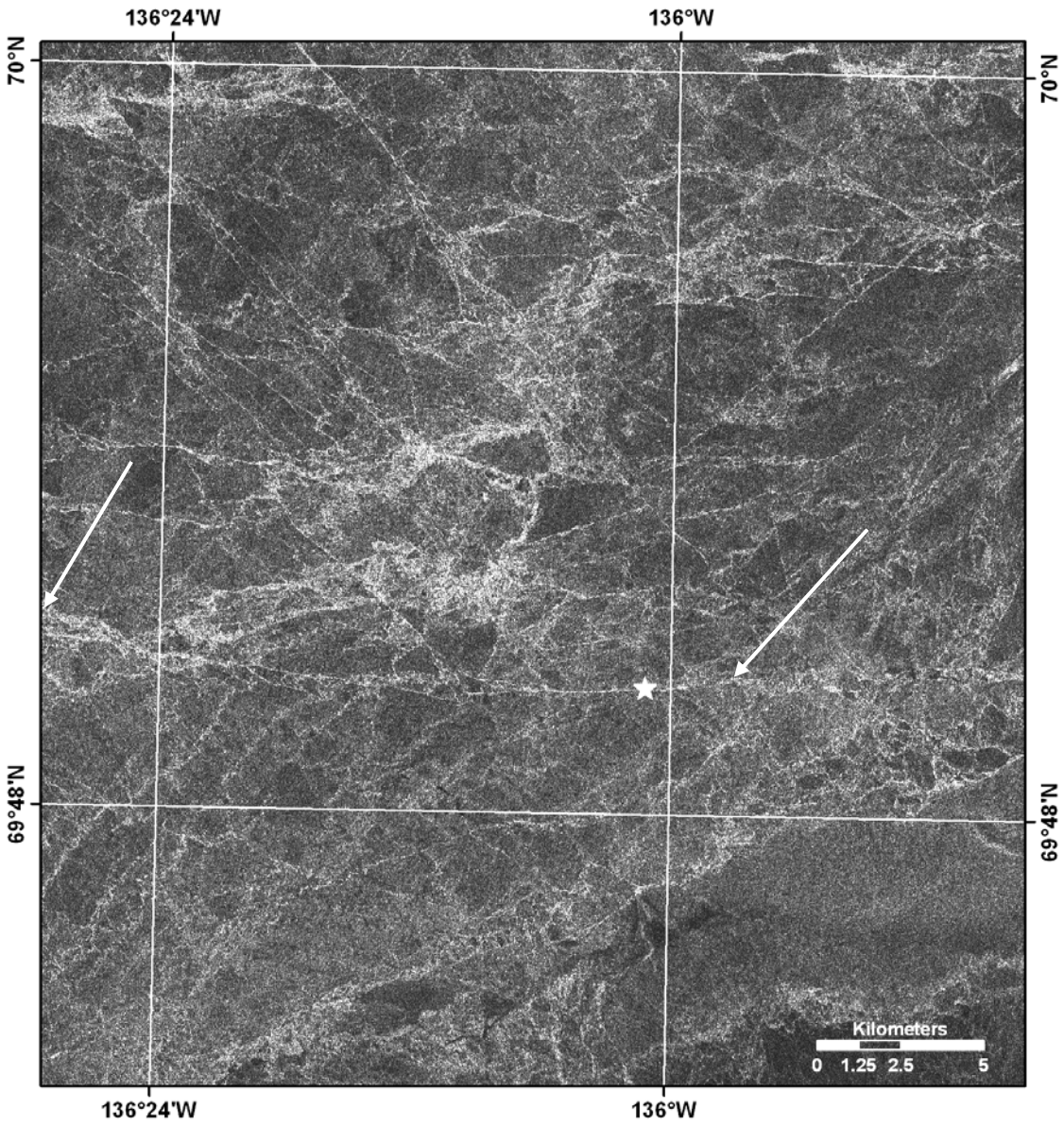

RADARSAT-1 data © CSA 2007. Received by the Canada Centre for Remote Sensing. Processed and distributed by MDA Geospatial Services Inc.

Figure 1. RADARSAT-1 image from March 29, 2007 showing the ridge, which begins at approximately 136°24'00"W, distinctly running west to east for over 10 km. Arrows indicate the approximate limits of the ridge in this image. The profile location is indicated by a star.

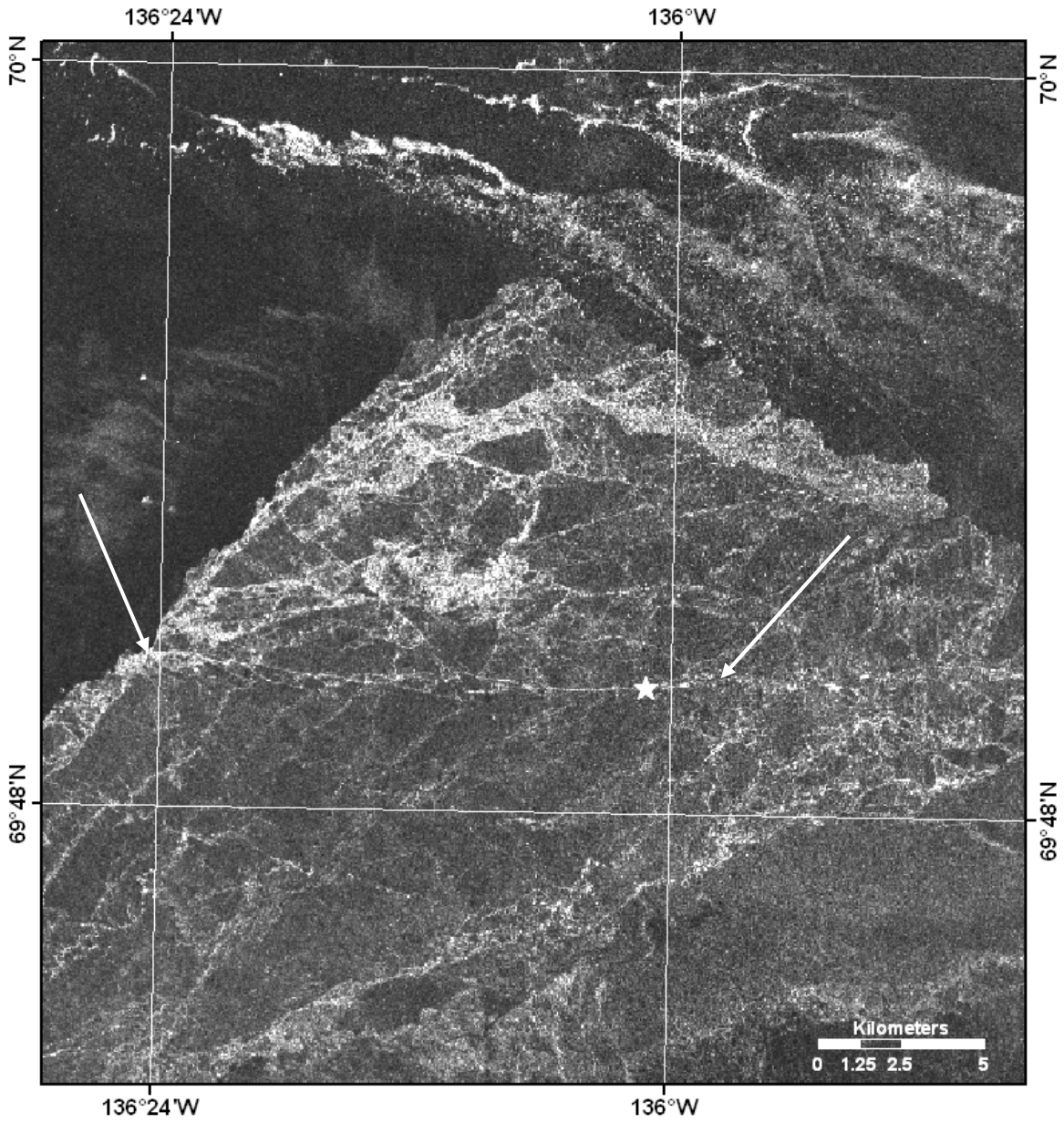

RADARSAT-1 data © CSA 2007. Received by the Canada Centre for Remote Sensing. Processed and distributed by MDA Geospatial Services Inc.

Figure 2. April 22, 2007 RADARSAT-1 image of the ridge. Open water and pack ice conditions predominate at the western end of the ridge, which is at the landfast ice edge.

3. Field Study

The field study of the ridge occurred on April 24, 2007, approximately four weeks after its formation. Initially, the authors flew by helicopter along the length of the ridge for a number of kilometres, in order to document its overall appearance. Figure 3 shows an aerial view of the ridge taken during this flight. Figure 4 shows variations in the ridge geometry, extracted from a

video taken whilst flying parallel to the ridge. These photographs illustrate both the extensiveness of such sea ice features in the Canadian Beaufort Sea, as well as the diversity in shape that a ridge feature may assume. In some locations, the ridge could be described as "textbook" in shape. In other locations, the ridge was nearly flat in elevation, compared with the surrounding level ice, or a jumbled mass of ice rubble, interspersed with small level ice floes that had not been compressed by the interactions that created the ridge. As can be seen in Figure 3, the ridge was extremely linear along its entire longitudinal axis, with only a few significant "jogs". This is not the case for many ridges, which often follow a far more irregular path.

Upon arrival at the site, the weather was initially sunny, with a temperature of approximately 0°C and wind speeds of approximately 50 km/hr. Extensive cloud cover could be seen moving in from the north. Surveying flags were established along a transect line across the ridge, approximately every five metres. The ridge at this location was comprised of a combination of large, loosely-sintered ice rubble that made up the ridge sail. The survey level was set on top of a level block of ice on the ridge west of the intended profile location, and this gave a clear sight line for the complete profile. The view from ice level is shown in Figure 5 and the view from the survey location is shown in Figure 6. The loose blocks of ice, as well as the much larger, smooth blocks that sometimes had a diameter over 1 m, made the placement of the surveying flags somewhat challenging; there was often either nothing to embed the flags in or smaller blocks of ice would shift upon walking near the flags. The ridge sail was approximately 15 m wide at the profile location, and the total profile line was approximately 70 m long, stretching across the level ice on both sides of the ridge.

Figure 3. Aerial view of ridge on April 24, 2007. Field of view across the photograph is approximately 7 km. Arrows indicate ridge extremities in the image.

Figure 4. Photographs showing the ridge geometry along the length of the ridge as viewed from helicopter. Note the large variation in the ridge shape along its length.

Figure 5. Photograph of the ridge close to the survey location.

Figure 6. Photographs showing either side and along the profiled ridge.

Unfortunately, because of time and weather constraints, a complete drilling profile of the ridge could not be obtained. Five holes were drilled at the first five survey flags, in the relatively level ice beside the ridge sail, and an additional four holes were drilled immediately beside the ridge sail (but not along the profile transect). Figure 7 shows the profile obtained from the surveying and drilling program.

Based upon the limited drilling data collected, the average depth of consolidation for the nine holes was 1.3 m. It is possible to compare this to estimates of the depth of the consolidation layer using the laboratory results of Timco and Goodrich (1988). They found that the depth to the consolidated layer was approximately twice the thickness of level ice grown under the same conditions. To make this comparison, it is necessary to know the thickness of level ice that would have grown under these conditions. This can be estimated by using an ice growth equation and the appropriate meteorological conditions for that site since the formation of the ridge. Information on the temperature during the time period from formation is available. These data were used in Anderson's (1961) ice growth equation giving a value of 0.66 m for a twenty-seven day period since the formation of the ridge. Using the two-to-one ratio provided by Timco and Goodrich suggests that the thickness of the consolidation layer would be approximately 1.3 m. This is in excellent agreement with the measured thickness of the consolidation layer thickness which averaged 1.3 m.

As an example of the level of effort involved in even a small ridge study, with three people conducting the survey/drilling, it took three hours to complete the survey and drill these nine holes. More thorough ridge survey programs, such as those reported in Shafrova and Høyland (2008) for example, can take five days or more to drill up to 50 holes and complete a comprehensive survey of a single ridge site. Profiling of ridges during the 1980s used four people to profile a ridge in about 5 to 6 hours. Such field data are important to collect for ground-truthing and empirical data collection purposes. New technology for thickness measurements would decrease the time necessary for these ridge studies.

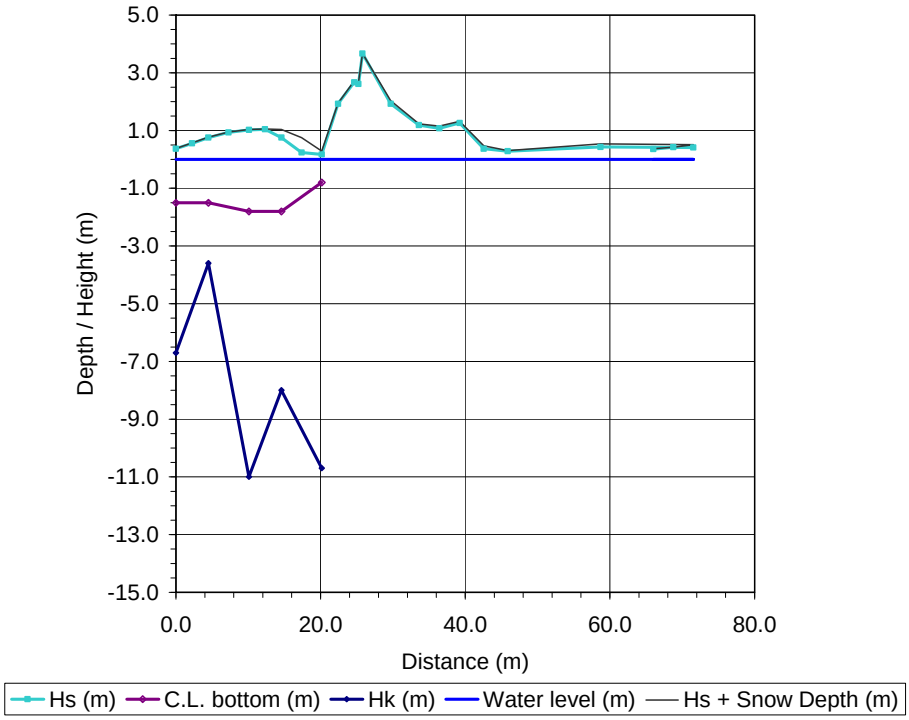

Figure 7. Available ridge profile data along surveyed transect, where Hs is the sail height, Hk is the keel depth and C.L. is the estimated bottom depth of the consolidated layer. The vertical direction is stretched in this plot for clarity.

4. Discussion

It is possible to compare the results of this limited survey (listed in Table 1 as "Measured" values) with past research in this particular geographical area. The sail height for this section of the ridge is at the high end of distributions for the Mackenzie mid-winter shear zone (first year ice only), where the majority (>97%) of the ridges in this area had previously been described as less than 3.0 m high (Spedding, 1982).

The available field data from the profiled ridge were compared with "average" sea ice ridge data, as discussed in Timco and Burden (1997). Despite the lack of complete keel information, the data, and estimations based upon the measured data, generally agree with their results. Figure 8 shows their definitions and values for "average" first-year ridges. Table 1 provides a comparison of these measurements with Timco and Burden's results showing good agreement. While the deepest measured keel depth was 11 m, it is likely that at the centre of the ridge, this depth would have been greater, increasing correspondence with the Timco and Burden relationships. It should be noted that the ridge height chosen was not the highest observed along this ridge. It is likely that the ridge was grounded in some locations along its length.

It is also of interest to consider the nature of how the profile location was chosen. Flying along the length of the ridge, numerous potential sites were rejected because they appeared to be either too difficult to survey with such a small team with limited equipment, or, conversely, too uninteresting. By choosing only those locations that seemed to be manageable and perhaps "typically" ridge-shaped, this type of decision-making could naturally affect how well a given profile meets the Timco and Burden relationships.

Table 1. Comparison of measured ridge properties with "average" ridge properties and relationships as discussed in Timco and Burden (1997).

	Measured	**Calculated**	
$Height_{sail}$ (m)	3.7	-	
$Height_{keel}$ (m)	11	16.3*	$Height_{keel} = 4.4 \times Height_{sail}$ (m)
$Width_{keel}$ (m)	42.6**	55.9	$Width_{keel} = 15.1 \times Height_{sail}$ (m)
$Width_{keel}$ (m)	42.6**	42.9	$Width_{keel} = 3.9 \times Height_{keel}$ (m)
$Area_{keel}$ (m²)	n/a	223	$Area_{keel} = 8 \times Area_{sail}$ (m²)
α_{sail} (°) (south)	32	32.9	α_{sail} (°)
α_{sail} (°) (north)	12	32.9	α_{sail} (°)
α_{keel} (°) (south)	22	26.6	α_{keel} (°)

* The water depth in this region was 18 m so it is possible that the ridge was grounded in some locations along its length.

** Keel width was crudely estimated by measuring the horizontal distance from the peak sail height to the shallowest measured keel depth, and multiplying this value by two.

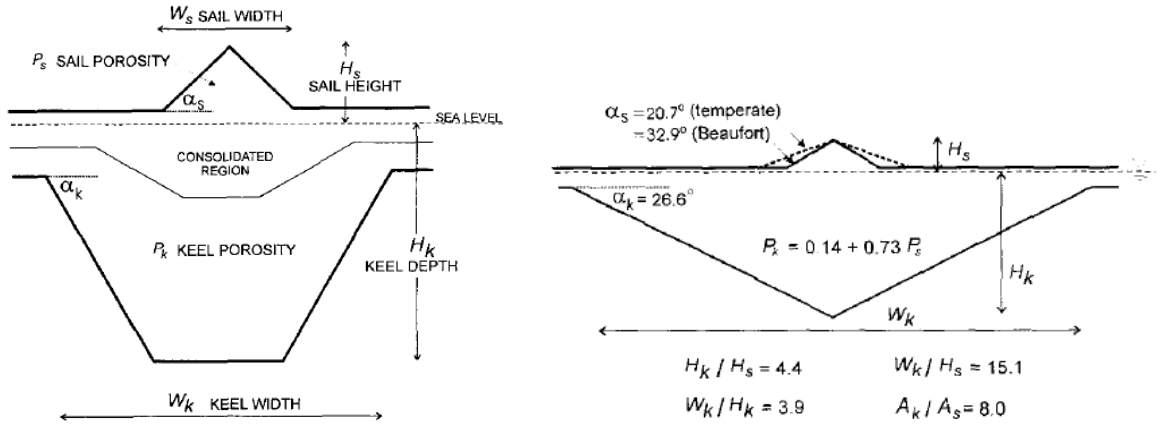

Figure 8. Illustrations from Timco and Burden (1997) showing the key terms and relationships established in that paper for first-year ridges.

5. Summary

This limited study illustrated the differences in the morphology of the ridge along its length. The survey of one location of the ridge showed good agreement with conventional predictions of the thickness of the consolidation layer and "average" ridge properties. This type of information is very important since it affects ice loads on offshore structures and also how a ship would transit a ridge. The knowledge of the formation date of the ridge proved very useful since it allowed a good estimate of the thickness of the consolidated layer of the ridge. Satellite observations provided this very valuable information.

Acknowledgements

The authors would like to acknowledge that the funding for the project from which this work was derived was provided by the Climate Change Technology and Innovation Initiative (CCTII) Unconventional Gas Supply, and the Program of Energy Research and Development.

References

Anderson, D.L., 1961. Growth rate of sea ice. Journal of Glaciology, Volume 3, pp 1170-1172.

Shafrova, S. and Høyland, K.V., 2008. Morphology and 2D spatial strength distribution in two Arctic first-year sea ice ridges. Cold Regions Science and Technology 51, No. 1, pp 38-55, *doi:10.1016/j.coldregions.2007.05.011*

Spedding, L.G., 1982. Rule of thumb ridge height distributions. *in* Proceedings of Workshop on Sea Ice Ridging and Pile-up. Compiled by R.M.W. Frederking and G.R. Pilkington, Associate Committee on Geotechnical Research, National Research Council of Canada. Technical Memorandum 134, pp 62-82, Ottawa, Canada

Timco, G.W. and Burden, R., 1997. An analysis of the shapes of sea ice ridges. Cold Regions Science and Technology 25, pp 65–77.

Timco, G.W. and Goodrich, L.E., 1988. Ice rubble consolidation. Proceedings of the 9th International Symposium on Ice (IAHR'88), Volume 1, pp. 427-438. Sapporo, Japan.